

Special Collection on Eye Disease

The initiation of retinal neo-vascularization is associated with downregulation of miR-106b expression, see Ménard et al. - "miR-106b suppresses pathological retinal angiogenesis"

**Eye
Disease**

AGING

Editorial and Publishing Office.

6666 E. Quaker Str., Suite 1B
Orchard Park, NY 14127
Phone: 1-800-922-0957, option 1
Fax: 1-716-508-8254
e-Fax: 1-716-608-1380

Submission

Please submit your manuscript on-line at <http://aging.msubmit.net>

Editorial

For editorial inquiries, please call us or email editors@impactaging.com

Production

For questions related to preparation of your article for publication, please call us or email krasnova@impactaging.com

Indexing

If you have questions about the indexing status of your paper, please email kurenova@impactaging.com

Printing

Each issue or paper can be printed on demand. To make a printing request, please call us or email printing@impactjournals.com

Billing/Payments

If you have questions about billing/invoicing or would like to make a payment, please call us or email payment@impactaging.com

Publisher's Office

Aging is published by Impact Journals, LLC
To contact the Publisher's Office, please email: publisher@impactjournals.com, or
call 1-800-922-0957, option 5

AGING

www.aging-us.com

EDITORIAL BOARD

EDITORS-IN-CHIEF

Jan Vijn - Albert Einstein College of Medicine, Bronx, NY, USA

David A. Sinclair - Harvard Medical School, Boston, MA, USA

Vera Gorbunova - University of Rochester, Rochester, NY, USA

Judith Campisi - The Buck Institute for Research on Aging, Novato, CA, USA

Mikhail V. Blagosklonny - Roswell Park Cancer Institute, Buffalo, NY, USA

EDITORIAL BOARD

Frederick Alt - Harvard Medical School, Boston, MA, USA

Vladimir Anisimov - Petrov Institute of Oncology, St.Petersburg, Russia

Johan Auwerx - Ecole Polytechnique Federale de Lausanne, Switzerland

Andrzej Bartke - Southern Illinois University, Springfield, IL, USA

Nir Barzilai - Albert Einstein College of Medicine, Bronx, NY, USA

Elizabeth H. Blackburn - University of California, San Francisco, CA, USA

Maria Blasco - Spanish National Cancer Center, Madrid, Spain

Vilhelm A. Bohr - National Institute on Aging, NIH, Baltimore, MD, USA

William M. Bonner - National Cancer Institute, NIH, Bethesda, MD, USA

Robert M. Brosh, Jr. - National Institute on Aging, NIH, Baltimore, MD, USA

Anne Brunet - Stanford University, Stanford, CA, USA

Rafael de Caba - NIA, NIH, Baltimore, MD, USA

Ronald A. DePinho - Dana-Farber Cancer Institute, Boston, MA, USA

Jan van Deursen - Mayo Clinic, Rochester, MN, USA

Lawrence A. Donehower - Baylor College of Medicine, Houston, TX, USA

Caleb E. Finch - University of Southern California, Los Angeles, CA, USA

Toren Finkel - National Institutes of Health, Bethesda, MD, USA

Luigi Fontana - Washington University, St. Louis, MO, USA

Claudio Franceschi - University of Bologna, Bologna, Italy

Myriam Gorospe - National Institute on Aging, NIH, Baltimore, MD, USA

Leonard Guarente - MIT, Cambridge, MA, USA

Andrei Gudkov - Roswell Park Cancer Institute, Buffalo, NY, USA

Michael Hall - University of Basel, Basel, Switzerland

Philip Hanawalt - Stanford University, CA, USA

Nissim Hay - University of Illinois at Chicago, Chicago, IL, USA

[Siegfried Hekimi](#) - McGill University, Montreal, Canada

[Stephen L. Helfand](#) - Brown University, Providence, RI, USA

[Jan H.J. Hoeijmakers](#) - Erasmus MC, Rotterdam, The Netherlands

[John 0. Holloszy](#) - Washington University, St. Louis, MO, USA

[Stephen P. Jackson](#) - University of Cambridge, Cambridge, UK

[Heinrich Jasper](#) - The Buck Institute for Research on Aging, Novato, CA, USA

[Pankaj Kapahi](#) - The Buck Institute for Research on Aging, Novato, CA, USA

[Jan Karlseder](#) - The Salk Institute, La Jolla, CA, USA

[Cynthia Kenyon](#) - University of California San Francisco, San Francisco, CA, USA

[James L. Kirkland](#) - Mayo Clinic, Rochester, MN, USA

[Guido Kroemer](#) - INSERM, Paris, France

[Titia de Lange](#) - Rockefeller University, New York, NY, USA

[Arnold Levine](#) - The Institute for Advanced Study, Princeton, NJ, USA

[Michael P. Lisanti](#) - University of Salford, Salford, UK

[Lawrence A. Loeb](#) - University of Washington, Seattle, WA, USA

[Valter Longo](#) - University of Southern California, Los Angeles, CA, USA

[Gerry Melino](#) - University of Rome, Rome, Italy

[Simon Melov](#) - The Buck Institute for Research on Aging, Novato, CA, USA

[Alexey Moskalev](#) - Komi Science Center of RAS, Syktyvkar, Russia

[Masashi Narita](#) - University of Cambridge, Cambridge, UK

[Andre Nussenzweig](#) - National Cancer Institute, NIH, Bethesda, MD, USA

[William C. Orr](#) - Southern Methodist University, Dallas, TX, USA

[Daniel S. Peeper](#) - The Netherlands Cancer Institute, Amsterdam, The Netherlands

[Thomas Rando](#) - Stanford University School of Medicine, Stanford, CA, USA

[Michael Ristow](#) - Swiss Federal Institute of Technology, Zurich, Switzerland

[Igor B. Roninson](#) - Ordway Research Institute, Albany, NY, USA

[Michael R. Rose](#) - University of California, Irvine, CA, USA

[K Lenhard Rudolph](#) - Hannover Medical School, Hannover, Germany

[Paolo Sassone-Corsi](#) - University of California, Irvine, CA, USA

[John Sedivy](#) - Brown University, Providence, RI, USA

[Manuel Serrano](#) - Spanish National Cancer Research Center, Madrid, Spain

[Gerald S. Shadel](#) - Yale University School of Medicine, New Haven, CT, USA

[Norman E. Sharpless](#) - University of North Carolina, Chapel Hill, NC, USA

[Vladimir P. Skulachev](#) - Moscow State University, Moscow, Russia

[Sally Temple](#) - NY Neural Stem Cell Institute, Albany, NY, USA

[George Thomas](#) - University of Cincinnati, Cincinnati, OH, USA

[Jonathan L. Tilly](#) - Massachusetts General Hospital, Boston, MA, USA

[John Tower](#) - University of Southern California, LA, CA, USA

[Eric Verdin](#) - University of California, San Francisco, CA, USA

[Thomas von Zglinicki](#) - Newcastle University, Newcastle, UK

[Alex Zhavoronkov](#) - Insilico Medicine, Baltimore, MD, USA

Table of Contents

miR-106b suppresses pathological retinal angiogenesis	1
Originally published Volume 12, Issue 24 pp 24836—24852	
Suppressing endoplasmic reticulum stress-related autophagy attenuates retinal light injury	18
Originally published Volume 12, Issue 16 pp 16579—16596	
Activation of C-reactive protein proinflammatory phenotype in the blood retinal barrier <i>in vitro</i> : implications for age-related macular degeneration	36
Originally published Volume 12, Issue 14 pp 13905—13923	
Role of Citicoline in an <i>in vitro</i> AMD model.....	55
Originally published Volume 12, Issue 10 pp 9031—9040	
Systemic administration of the di-apocarotenoid norbixin (BIO201) is neuroprotective, preserves photoreceptor function and inhibits A2E and lipofuscin accumulation in animal models of age-related macular degeneration and Stargardt disease.....	65
Originally published Volume 12, Issue 7 pp 6151—6171	
PU-91 drug rescues human age-related macular degeneration RPE cells; implications for AMD therapeutics	86
Originally published Volume 11, Issue 17 pp 6691—6713	
HMGB1 and Caveolin-1 related to RPE cell senescence in age-related macular degeneration	109
Originally published Volume 11, Issue 13 pp 4323—4337	
Nutraceutical effects of <i>Emblica officinalis</i> in age-related macular degeneration.....	124
Originally published Volume 11, Issue 4 pp 1177—1118	
A comprehensive evaluation of 181 reported CHST6 variants in patients with macular corneal dystrophy...	136
Originally published Volume 11, Issue 3 pp 1019—1029	
Circulating insulin-like growth factor-1: a new clue in the pathogenesis of age-related macular degeneration	147
Originally published Volume 10, Issue 12 pp 4241—4247	
Effects of senescent secretory phenotype acquisition on human retinal pigment epithelial stem cells	154
Originally published Volume 10, Issue 11 pp 3173—3184	
p62 /SQSTM1 coding plasmid prevents age related macular degeneration in a rat model.....	166
Originally published Volume 10, Issue 8 pp 2136—2147	

Loss of NAMPT in aging retinal pigment epithelium reduces NAD ⁺ availability and promotes cellular senescence	178
Originally published Volume 10, Issue 6 pp 1306—1323	
miR-106b suppresses pathological retinal angiogenesis	196
Originally published Volume 12, Issue 24 pp 24836—24852	
ALDH2 protects naturally aged mouse retina <i>via</i> inhibiting oxidative stress-related apoptosis and enhancing unfolded protein response in endoplasmic reticulum	213
Originally published Volume 13, Issue 2 pp 2750—2767	
Exosomes derived from BDNF-expressing 293T attenuate ischemic retinal injury <i>in vitro</i> and <i>in vivo</i>	231
Advance	
Exploration of age-related mitochondrial dysfunction and the anti-aging effects of resveratrol in zebrafish retina	244
Originally published Volume 11, Issue 10 pp 3117—3137	
The senescent vision: dysfunction or neuronal loss?	265
Originally published Volume 11, Issue 1 pp 15—17	
Long-term intake of <i>Lactobacillus paracasei</i> KW3110 prevents age-related chronic inflammation and retinal cell loss in physiologically aged mice	268
Originally published Volume 10, Issue 10 pp 2723—2740	
The expression of C1 inhibitor (C1INH) in macrophages is upregulated by retinal pigment epithelial cells – implication in subretinal immune privilege in the aging eye	286
Originally published Volume 10, Issue 6 pp 1380—1389	
Age-related changes in eye lens biomechanics, morphology, refractive index and transparency	296
Originally published Volume 11, Issue 24 pp 12497—12531	
Pineal gland volume is associated with prevalent and incident isolated rapid eye movement sleep behavior disorder	331
Originally published Volume 12, Issue 1 pp 884—893	
Abnormalities of saccadic eye movements in dementia due to Alzheimer’s disease and mild cognitive impairment	341
Originally published Volume 11, Issue 15 pp 5389—5398	
Involvement of adiponectin in age-related increases in tear production in mice	351
Originally published Volume 11, Issue 19 pp 8329—8346	

ALKBH5-mediated m⁶A demethylation of FOXM1 mRNA promotes progression of uveal melanoma..... 369
[Originally published Volume 13, Issue 3 pp 4045—4062](#)

Development and validation of an immune and stromal prognostic signature in uveal melanoma to guide clinical therapy 387
[Originally published Volume 12, Issue 20 pp 20254—20267](#)

Loss of macroH2A1 decreases mitochondrial metabolism and reduces the aggressiveness of uveal melanoma cells 401
[Originally published Volume 12, Issue 10 pp 9745—9760](#)

Immunological analyses reveal an immune subtype of uveal melanoma with a poor prognosis..... 417
[Originally published Volume 12, Issue 2 pp 1446—1464](#)

miR-106b suppresses pathological retinal angiogenesis

Catherine Ménard¹, Ariel M. Wilson¹, Agnieszka Dejada², Khalil Miloudi³, François Binet², Sergio Crespo-Garcia², Célia Parinot², Frédérique Pilon², Rachel Juneau², Elisabeth MMA Andriessen², Gaëlle Mawambo¹, John Paul SanGiovanni⁴, Vincent De Guire¹, Przemyslaw Sapieha^{1,2,3}

¹Department of Biochemistry, Maisonneuve-Rosemont Hospital Research Centre, University of Montreal, Montreal H1T 2M4, Quebec, Canada

²Department of Ophthalmology, Maisonneuve-Rosemont Hospital Research Centre, University of Montreal, Montreal H1T 2M4, Quebec, Canada

³Department of Neurology-Neurosurgery, McGill University, Montreal H3A 2B4, Quebec, Canada

⁴Department of Nutritional Sciences, University of Arizona, Tucson, AZ 85719, USA

Correspondence to: Przemyslaw Sapieha, Vincent De Guire; email: mike.sapieha@umontreal.ca, vdeguire.hmr@ssss.gouv.qc.ca

Keywords: age related macular degeneration, miR-106b, PERK, choroidal neovascularization, angiogenesis

Received: July 4, 2020

Accepted: November 13, 2020

Published: December 23, 2020

Copyright: © 2020 Ménard et al. This is an open access article distributed under the terms of the [Creative Commons Attribution License](https://creativecommons.org/licenses/by/3.0/) (CC BY 3.0), which permits unrestricted use, distribution, and reproduction in any medium, provided the original author and source are credited.

ABSTRACT

MicroRNAs are small non-coding RNAs that post-transcriptionally regulate gene expression. We recently demonstrated that levels of miR-106b were significantly decreased in the vitreous and plasma of patients with neovascular age-related macular degeneration (AMD). Here we show that expression of the miR-106b-25 cluster is negatively regulated by the unfolded protein response pathway of protein kinase RNA-like ER kinase (PERK) in a mouse model of neovascular AMD. A reduction in levels of miR-106b triggers vascular growth both *in vivo* and *in vitro* by inducing production of pro-angiogenic factors. We demonstrate that therapeutic delivery of miR-106b to the retina with lentiviral vectors protects against aberrant retinal angiogenesis in two distinct mouse models of pathological retinal neovascularization. Results from this study suggest that miRNAs such as miR-106b have the potential to be used as multitarget therapeutics for conditions characterized by pathological retinal angiogenesis.

INTRODUCTION

Age-related macular degeneration (AMD) is a common [1] and complex [2, 3] disease of aging and the leading cause of irreversible loss of sight in elderly people [4–6]. Early forms of AMD are characterized by subretinal lipoproteinaceous deposits, local attrition of photoreceptors [7] and loss of visual sensitivity [8]. Late forms of AMD are defined by geographic atrophy (loss of retinal pigment epithelium and photoreceptors) [9] and/or pathologic choroidal neovascularization (CNV) characterized by vascular sprouting from the choriocapillaris into the neural retina or subretinal space [10]. The neovascular form (NV AMD or exudative

AMD) accounts for over 80% of the vision loss associated with AMD [11].

The advent of therapies targeting vascular endothelial growth factor (VEGF) has significantly improved the quality of life of patients suffering from NV AMD [12–15]. However, not all patients with AMD respond to anti-VEGF therapies [16]. Sustained reduction in retinal VEGF levels can lead to neurotoxicity [17] and degeneration of RPE-choriocapillaris in mouse models [18]. Importantly, assessment by fundus photography and fundus fluorescein angiography of patients on anti-VEGF therapy showed accelerated development of geographic atrophy [19, 20]. These findings justify the

need for continued exploration of novel therapeutic interventions.

Given that several inflammatory and growth factors in addition to VEGF [10, 21, 22] are associated with the pathogenesis of NV AMD, a multi-targeted approach is warranted. In this regard, therapeutic delivery of miRNAs may offer a promising avenue. miRNAs are small non-coding RNAs of around 20 nucleotides that act as post-transcriptional regulatory elements of most cellular processes [23]. miRNAs mediate repression of gene expression with the potential of a single miRNA to target mRNA transcripts from hundreds of genes [24]. We previously elucidated a specific miRNA signature in the vitreous and plasma of patients with NV AMD and observed a disease-associated increase in miR-146a and a decrease in miR-106b and miR-152 [25]. Interestingly, within our cohort, we found that both vitreous- and plasma-based miR-146a/miR-106b ratios had greater than 90% discriminatory power for classification of patients with NV AMD with an area under the receiver operating characteristic curve of 0,977 in vitreous humour and 0,915 in plasma, suggesting potential for a blood-based diagnostic. These results are concordant with the evidence based in humans and model systems where upregulation of miR-146a, miR-17 (a miR containing the same seed sequence as miR-106b), miR-125 and miR-155 are associated with human AMD and a mouse model of oxygen induced retinopathy (OIR) [26–30]. miRNAs targeting VEGFA (miR-184, miR-150 and miR-106b) have also been found to be downregulated in human AMD and in animal models [25, 28, 31]. Here, we aimed to determine the mechanism leading to the downregulation of miR-106b in AMD and to characterize the therapeutic potential of upregulating miR-106b for NV AMD.

RESULTS

miR-106b is downregulated in the choroid after laser-induced CNV

In order to evaluate the potential role of miR-106b in CNV and NV AMD, we employed a laser burn-induced neovascularization mouse model. In this model, Bruch's membrane is ruptured using an argon laser, initiating sprouting of subretinal blood vessels from the choroid, mimicking NV AMD (Figure 1A) [32]. This model is characterized by a reproducible pattern of reduced neovascularization 3 days post-burn, followed by a significant increase in neovascularization that peaks on the 7th day, then vascular regression and wound healing by 14 days post-burn [32]. To illustrate the vascular changes occurring in this model, we took serial ocular fundus images of infrared reflectance and fluorescein

angiography after laser burn and subcutaneous injection of fluorescein, revealing fluorescein leakage surrounding burn sites that regressed over time (Figure 1B). In line with our previously reported findings for human vitreous and plasma from patients with active NV AMD [25], choroidal miR-106b expression was significantly downregulated in retinal specimens at all investigated time points, with statistically significant decreases of ~40% at day 3, and ~50% at days 7 and 14, relative to control animals (Figure 1C–1E). The significant downregulation of miR-106b three days post-burn corresponds to the neovascularization nadir in the laser burn model. This suggests that the observed decrease in miR-106b directly precedes initiation of CNV.

The PERK arm of the unfolded protein response is involved in retinal suppression of the mmu-miR-106b~25 cluster in laser-induced CNV

Upon confirmation of a reduction in retinal miR-106b in the CNV mouse model, we next sought to investigate the underlying mechanism. MiR-106b is a member of the miR-106b~25 cluster (mmu-miR-106b, mmu-miR-25 and mmu-miR-93) and is located in the 13th intron of protein-coding gene minichromosome maintenance complex component 7 (*MCM7*) [33]. Regulation of miR-106b expression is tightly correlated with *MCM7* transcription. Previous studies have suggested that activation of the protein kinase RNA-like ER kinase (PERK) arm of the UPR and consequent triggering of activating transcription factor 4 (ATF4) as a potential mechanism causing downregulation of the *MCM7* gene and the mmu-miR-106b~25 cluster [34] (Figure 2A). We therefore investigated if the regulation of mmu-miR-106b occurred at the transcriptional level through activation of ER stress effector pathway PERK.

To better characterize PERK activation, we examined its downstream effectors. Phosphorylation of eIF2 α was increased after laser burn as was total eIF2 α with a significant ~2-fold rise in pEIF2 α at 7 days (Figure 2B, 2C). Moreover, a significant upregulation of the ATF4 transcript was also detected with an increase at both 3 and 7 days after laser burn (Figure 2D). We then assessed the effect of PERK activation on the *MCM7* gene transcript and miR-106b~25 cluster by qPCR analysis. We observed significant decreases of ~50% and ~35% in *MCM7* transcript expression at 3 and 7 days after laser burn respectively (Figure 2E). Additionally, all members of the miR-106b~25 cluster (miR-106b, miR-25 and miR-93) were downregulated 3 days after laser burn with decreases of ~0.24-fold, ~0.37-fold and ~0.60-fold for miR-25, miR-93 and miR-106b, respectively (Figure 2F). To confirm that PERK can mediate repression of hsa-miR-106b, we

infected Human Retinal Microvascular Endothelial Cells (HRMECs) with a lentivirus carrying short hairpin (sh) RNA against PERK. After 72 hours, we observed a significant ~2-fold increase in hsa-miR-106b expression in cultured cells (Figure 2G). Taken together, these results support a PERK-associated decrease in miR-106b in laser-induced CNV.

miR-106b targets effectors of angiogenesis

To confirm the involvement of miR-106b in the regulation of AMD-related angiogenesis, we quantified protein levels of experimentally validated targets of miR-106b involved in the neovascularization process. Previous studies demonstrated that miR-106b can

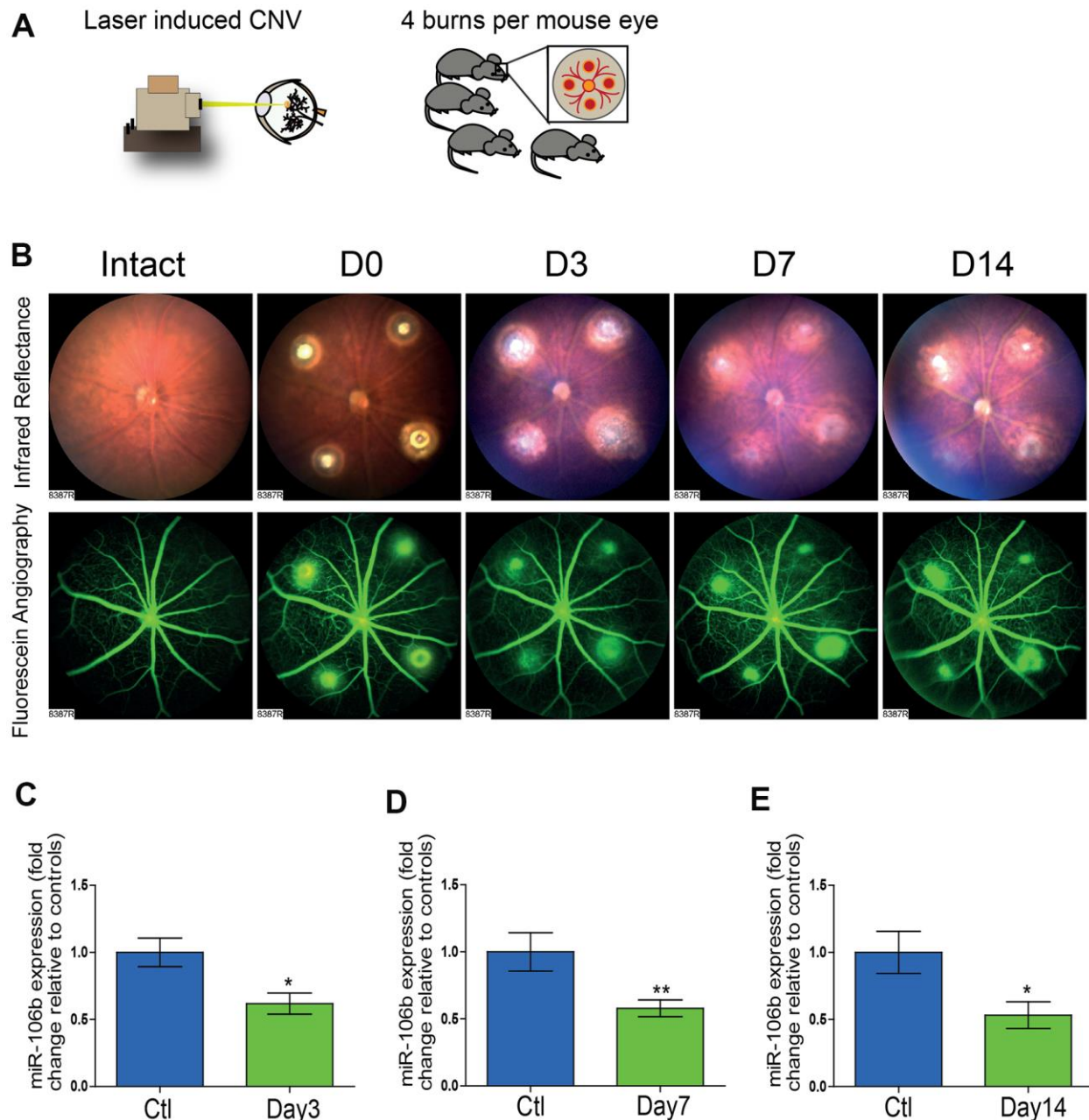


Figure 1. The initiation of retinal neo-vascularization is associated with downregulation of miR-106b expression. (A) Schematic of laser burn CNV mouse model. (B) Representative retinal fundus of a mouse before and after undergoing laser-induced choroidal neovascularization. Serial images depict the progression of neovascularization over a time-course of 14 days in the same eye. Choroidal expression of miR-106b by qPCR relative to intact controls assessed (C) 3 days after burns (n=8), (D) 7 days after burns (n=13) and (E) 14 days after burns (n=10); Scale bar = 50µm. Data are expressed as the mean ± S.E.M. Unpaired Two-tailed Student's t-test was used for the analysis, *P < 0.05; **P < 0.001.

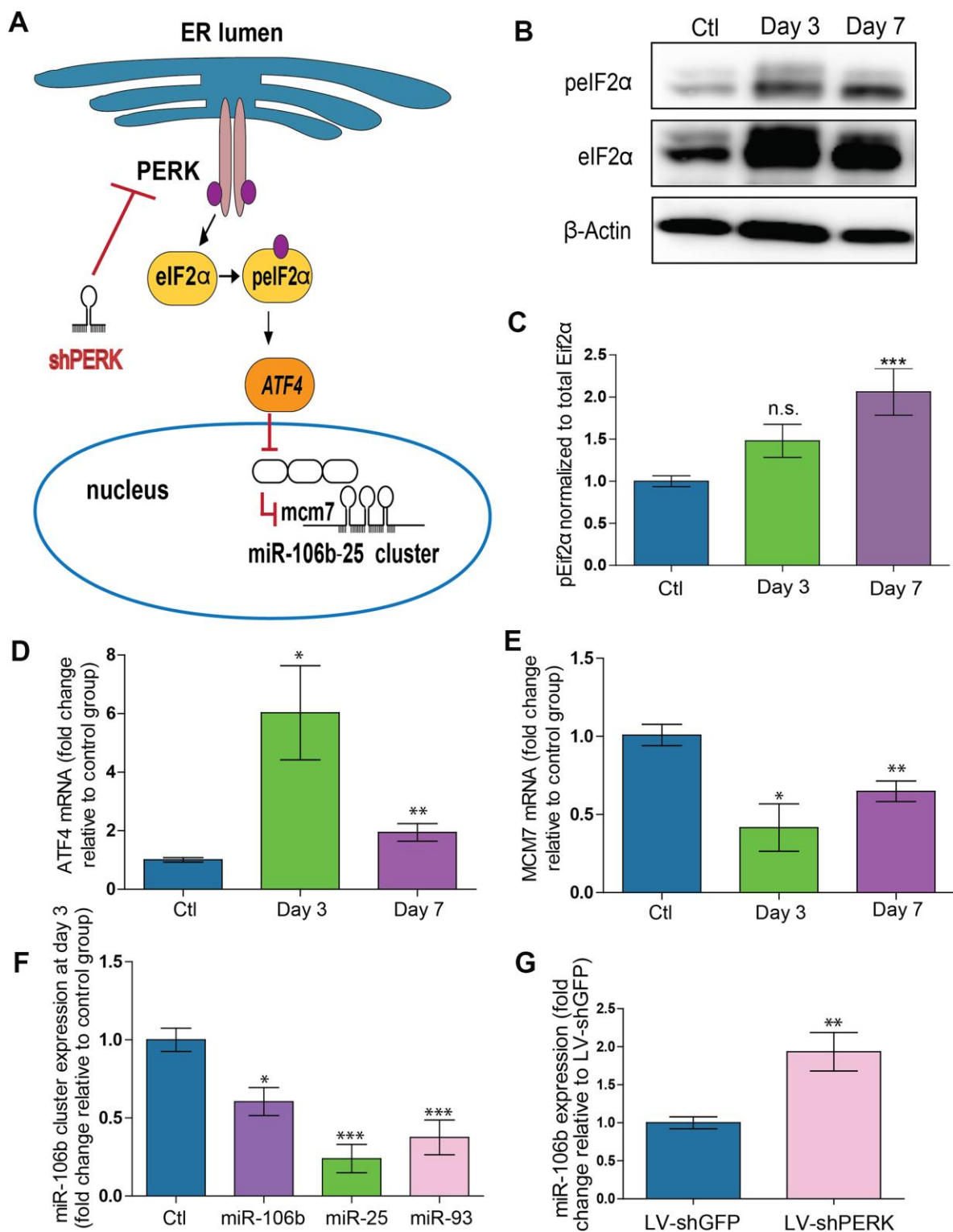


Figure 2. PERK activation provokes downregulation of miR-106b-25 cluster and MCM7 host gene in a mouse model of CNV.

(A) Schematic of ER stress activation of PERK pathway. (B) Western blot of Phospho-EIF2 α , total-EIF2 α and β -actin in control choroids, and 3 and 7 days after burns. (C) Western blot quantification in control choroids, 3 days (n=7) and 7 days after burns (n=6). (D) *Aft4* mRNA expression in control choroids, 3 days (n=6) and 7 days after burns (n=10). (E) *Mcm7* mRNA expression in control choroids, 3 days (n=6) and 7 days after laser burn (n=14). (F) miR106~25 cluster member expression in choroids 3 days after laser burn (miR-106b (n=7), miR-25 (n=6) and miR-93 (n=5)). (G) miR-106b expression after infection of HRMECs with LV.shGFP (negative control), and LV.shPERK (n=5). Data are expressed as mean \pm S.E.M. One-way ANOVA with Bonferroni post-hoc test was performed on groups of 3 or more, and unpaired Two-tailed Student's t-test was used for the analysis of groups of 2, *P < 0.05; **P < 0.001; ***P < 0.0001.

influence expression of VEGFA and HIF1 α [31]. In line with a decrease in miR-106b, we confirmed the upregulation of VEGFA (~3-fold) and HIF1 α (~1.71-fold) in choroid specimens 3 days after laser burn (Figure 3A–3D). Importantly, we did not observe variations at the mRNA level for these targets, suggesting post-transcriptional regulation of their protein expression or altered translation efficiency, characteristic of miRNA regulation (Supplementary Figure 1A). These results further suggest that the loss of miR-106b expression can contribute to the expression of angiogenic proteins that promote neovascularization.

miR-106b influences HRMEC migration and choroidal vascular sprouting

We sought to characterize the effects of miR-106b on cellular processes involved in angiogenesis. We first evaluated the role of miR-106b on HRMEC migration in a wound healing/cell migration assay performed by electric cell-substrate impedance sensing (ECIS) assay. Cells were infected with LV.miR-106b, LV.shVEGFA, LV.shPERK or control LV.shGFP for 72 hours, plated at confluence and submitted to an electric pulse in the center of the well to provoke cell detachment, resulting in a 250 μ m diameter region devoid of cells (Figure 3E). Cell migration was quantified at 8 hours by measurement of impedance, which increases as cells repopulate the empty space. We found that HRMEC migration was reduced in all three LV-treated dishes compared to control LV.shGFP (blue line) (Figure 3F–3H). Cells infected with LV.shPERK became the least migratory (Figure 3H). LV.miR-106b prevented migration of HRMECs to a similar extent as LV.shVEGFA (Figure 3F, 3G). To confirm that miR-106b reduced migration of HRMECs, we performed a scratch assay (Figure 3I). As above, significant decreases in cell migration were observed in all treatment groups when compared to controls with a ~45% reduction in LV.shVEGFA, ~50% reduction with LV.miR-106b and ~45% with LV.shPERK when compared to control LV.shGFP (100% of migration) (Figure 3I, 3J).

NV AMD is characterized by pathological neovascularization of the choriocapillaris. We therefore used *ex vivo* mouse choroid explants and assessed sprouting angiogenesis. Similar to findings reported above, we observed a ~70% reduction in sprouting area with LV.miR-106b, a ~80% reduction with LV.shPERK, while LV.shVEGFA resulted in a reduction of ~60% compared to control LV.shGFP (Figure 3K, 3L). Taken together, these results further highlight the anti-angiogenic properties of miR-106b and provide rationale to test miR-106b delivery *in vivo*.

Intraocular injection of LV.miR-106b decreases choroidal and retinal neovascularization

Endothelial cell migration and sprouting are key processes involved in angiogenesis. We next tested the outcome of therapeutic delivery of miR-106b in models of pathological retinal angiogenesis. We first performed laser burns on 8 week-old mice to trigger CNV, directly followed by intravitreal injection of either LV.miR-106b or positive control LV.shVEGF or negative control LV.shGFP. Choroids were collected 7 days after laser burns and quantified (Figure 4A). LV.miR-106b led to ~45% reduction of neo-angiogenesis and prevented CNV to a similar extent as LV.shVEGF (Figure 4B–4D).

We subsequently assessed the anti-angiogenic properties of miR-106b in the mouse model of oxygen-induced retinopathy [35]. Mouse pups were injected at P4 and P7 with LV.miR-106b, negative control LV.shGFP or positive control LV.shVEGFA. From P7 to P12 pups were exposed to 75% oxygen and returned to room air from P12 until maximal neovascularization at P17 (Figure 5A). Similar to what was observed for CNV, retinas treated with LV.miR-106b showed a significant ~50% reduction in pathological neovascularization compared to LV.shGFP and a similar reduction to levels observed with LV.shVEGFA (Figure 5B–5I). Collectively, these results suggest that therapeutic delivery of miR-106b prevents pathological retinal angiogenesis (Figure 6).

DISCUSSION

The diagnostic and therapeutic potential of miRNAs for ocular diseases is promising yet still requires proof of concept. We have previously shown that levels of miR-106b decrease in the vitreous and plasma of human patients with NV AMD [25]. In the current study, we demonstrate that much like in patients, there is a reduction in choroidal miR-106b in mouse retinas following laser burn induced-CNV. Furthermore, we provide evidence that the downregulation involves transcriptional inhibition of the 106b~25 cluster by the PERK pathway. Consequently, therapeutic intravitreal administration of miR-106b via lentiviral vectors inhibited pathological retinal neovascularization across models. These findings were supported by *in vitro* and *ex vivo* data that confirmed the role of miR-106b in preventing cellular mechanisms that lead to angiogenesis including cell migration and sprouting.

The pathogenesis of AMD is associated with oxidative stress, hypoxia, inflammation and proteotoxic stress, which can trigger pathways of ER-stress [36]. We observed activation of the PERK axis with phosphorylation

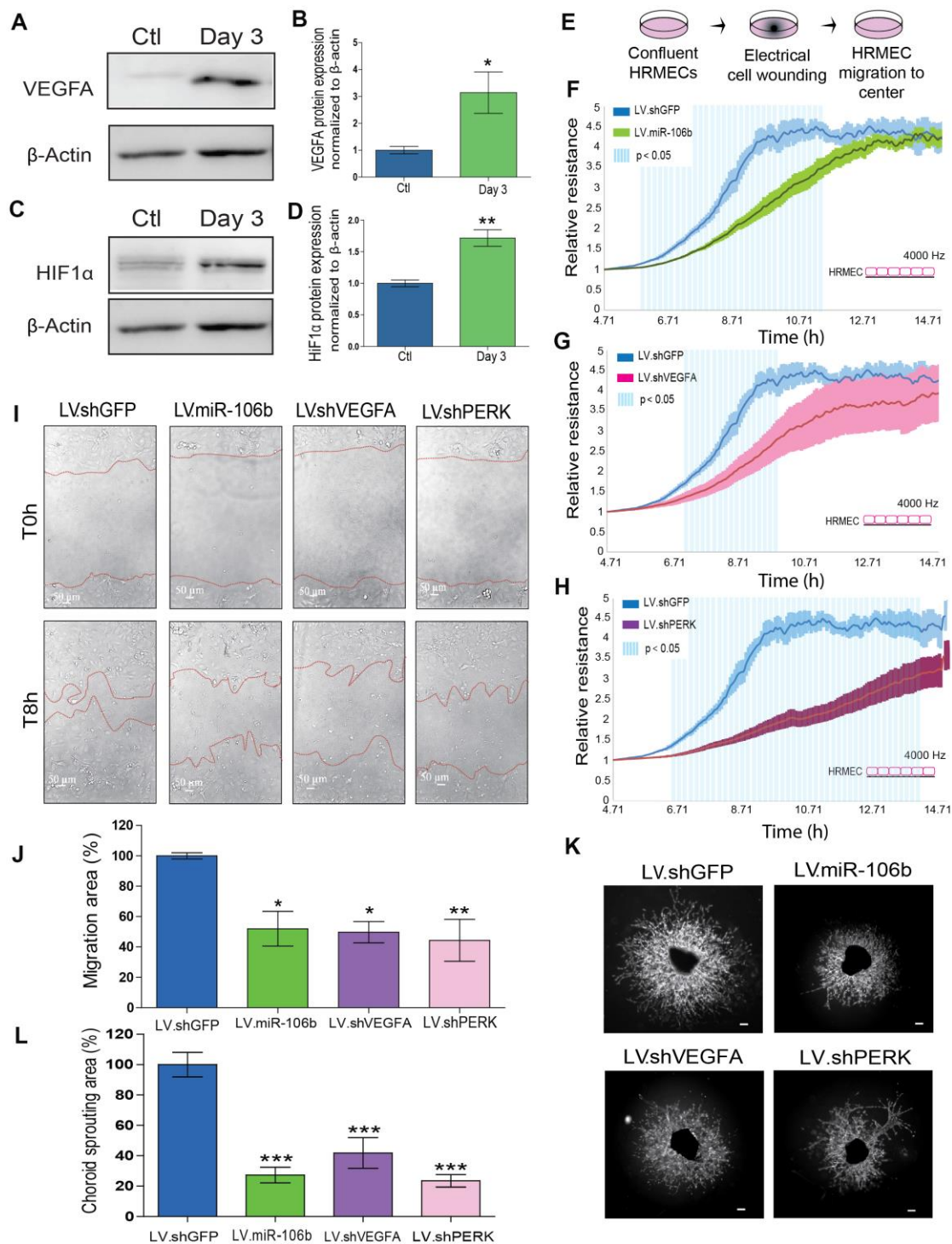


Figure 3. miR-106b exerts an anti-angiogenic effect and impairs retinal endothelial cell migration. (A) Western blot of VEGFA and β -actin from control choroids and 3 days after burns, and (B) quantification (n=4). (C) Western blot of HIF1 α and β -actin from control choroids and 3 days after burns, and (D) quantification (n=4). (E) Schematic of ECIS cell migration assay procedure. HRMEC ECIS with (F) LV.miR-106b (n=4), (G) LV.shVEGFA (n=4) and (H) LV.shPERK (n=4) compared to LV.shGFP control. (I) HRMEC scratch assay infected 72h with LV.shGFP, LV.miR-106b, LV.shVEGFA and LV.shPERK at T0h and after 8h. (J) Migration area quantification of scratch assay with LV.miR-106b (n=4), LV.shVEGFA (n=4), and LV.shPERK (n=4) compared to LV.shGFP. (K) Sprouting assay with choroid explants infected with LV.shGFP, LV.miR-106b, LV.shVEGFA, and LV.shPERK. (L) Sprouting area quantification with LV.miR-106b (n=9), LV.shVEGFA (n=9), LV.shPERK (n=8) compared to LV.shGFP control. Scale bar = 500 μ m. Data are expressed as mean \pm S.E.M. Unpaired Two-tailed Student's t-test was used for the analysis of groups of 2, and one-way ANOVA with Bonferroni post-hoc test was performed on groups of 3 or more, * $P < 0.05$; ** $P < 0.001$; *** $P < 0.0001$.

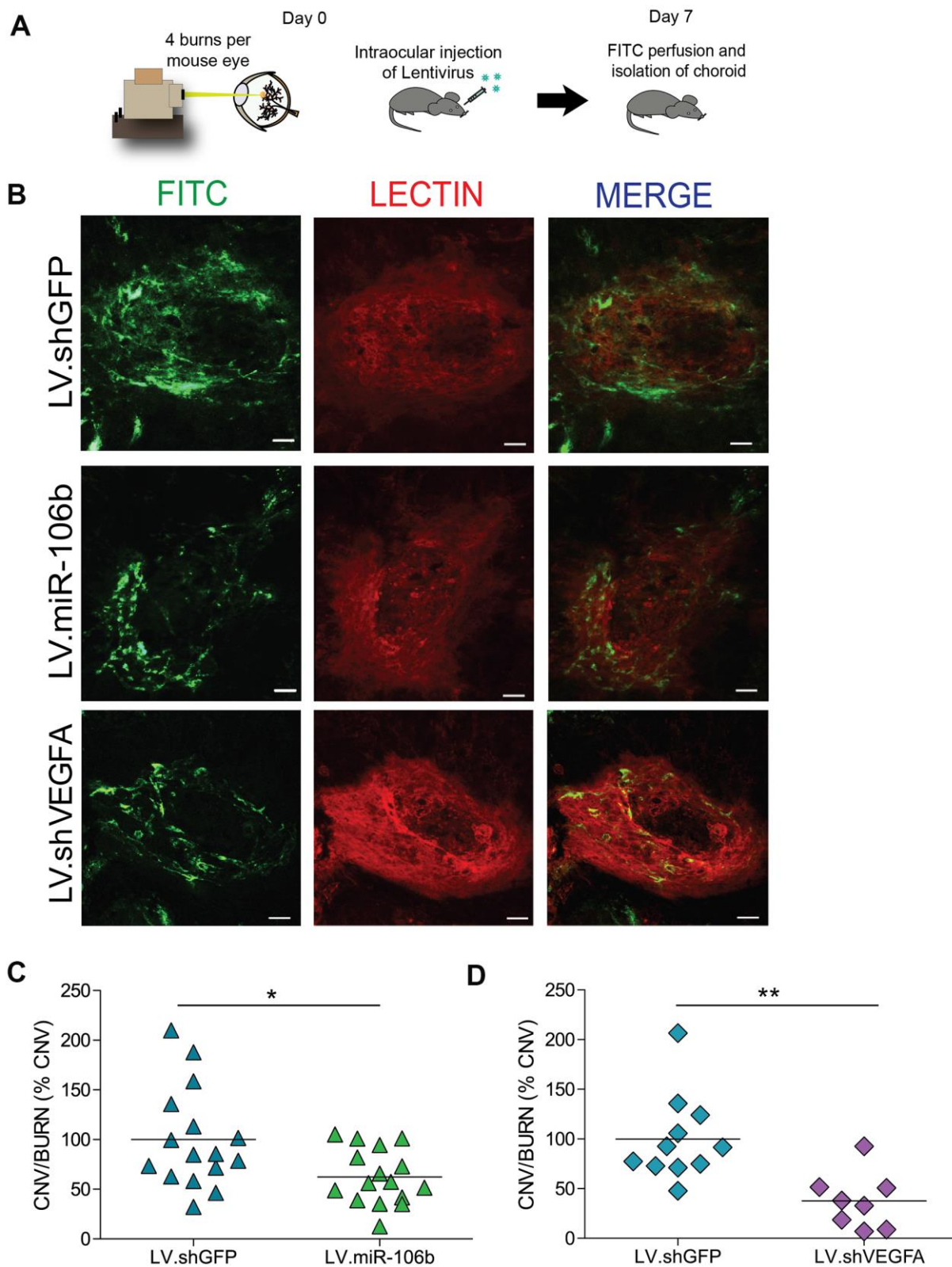


Figure 4. miR-106b decreases choroidal neovascularization in a CNV mouse model. (A) Schematic of intraocular injection of LV.miR-106b or LV.shVEGFA in laser burn mouse model. (B) Burn in red (lectin), CNV in green (FITC) and merge with LV.miR-106b or LV.shVEGFA compared with LV.shGFP. (C) CNV/Burns ratios quantification after LV.miR-106b treatment (n=16 burns/4 mice) and (D) CNV/Burns ratios quantification after LV.shVEGFA treatment (n=12 burns/3 mice). Scale bar = 50 μ m. Data are expressed as mean \pm S.E.M. Unpaired Two-tailed Student's t-test were used *P < 0.05; **P < 0.001.

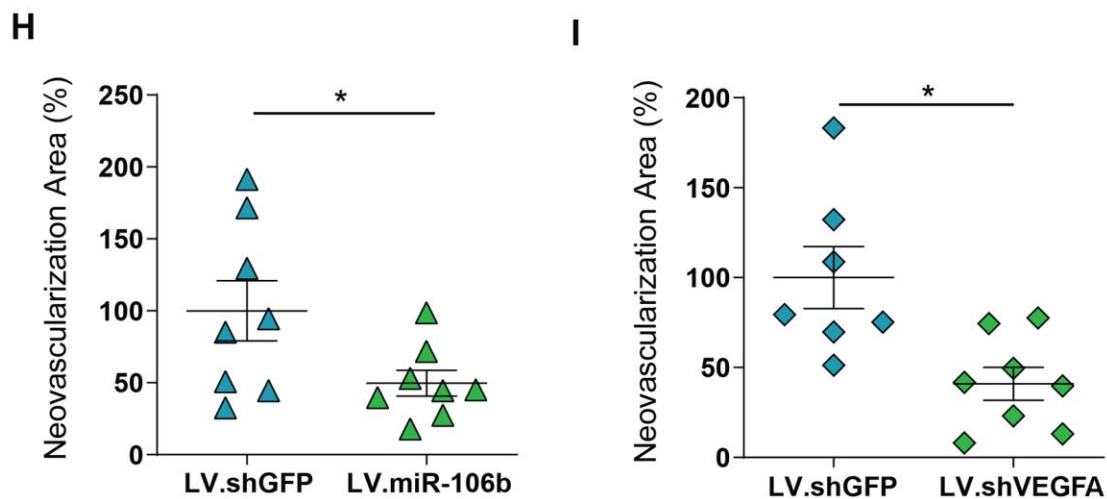
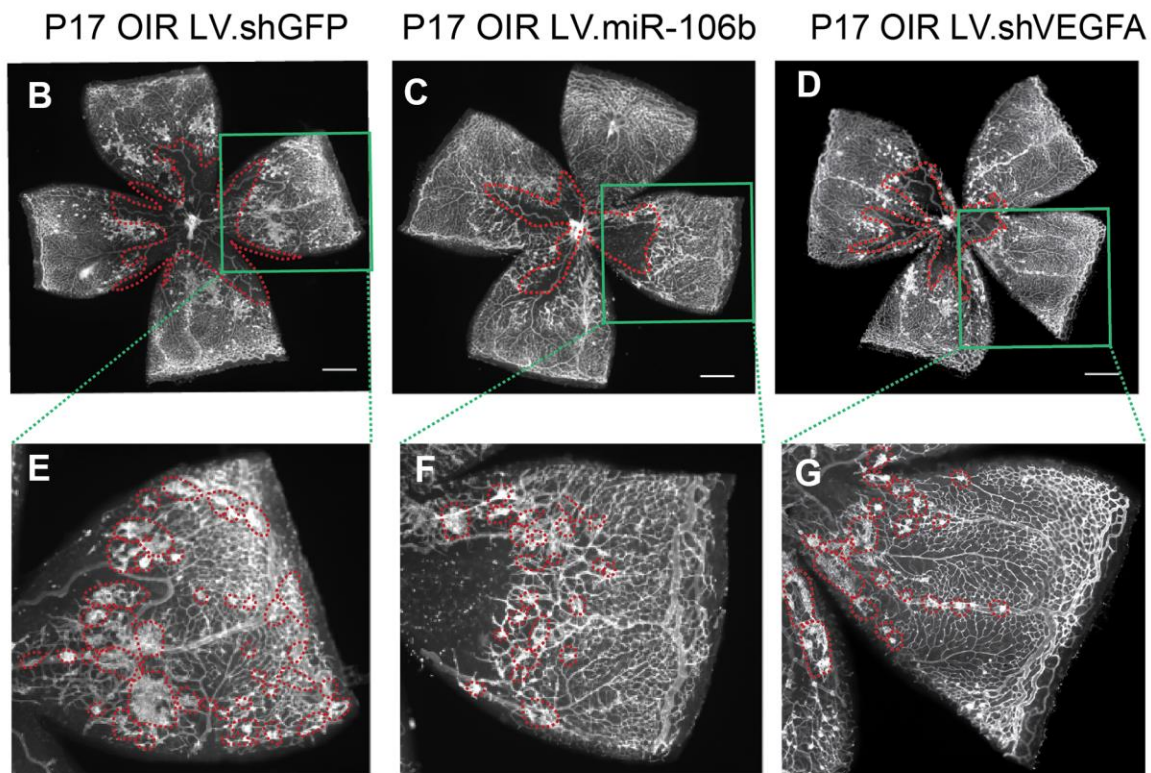
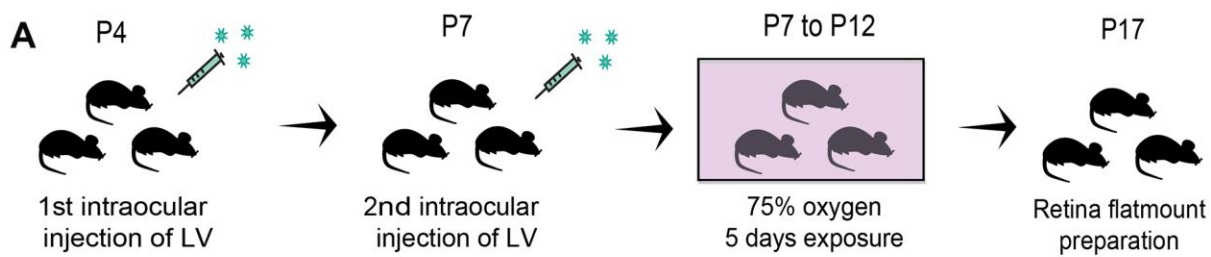


Figure 5. miR-106b decreases retinal neovascularization in the OIR mouse model. (A) Schematic of intraocular injection of LV.miR-106b or LV.shVEGFA in the OIR mouse model. P17 retinas were flatmounted after exposure to 75% O₂, having received intraocular injection of LV.shGFP (B), LV.miR-106b (C), or LV.shVEGFA (D) and magnified (E–G). Neovascular area quantification (H) after LV.miR-106b injection (n=8), and (I) LV.shVEGFA injection (n=8). Scale bars, 500 μ m (B–D) and 200 μ m (E–G). Data are expressed as mean \pm S.E.M. Unpaired Two-tailed Student's t-tests were used. *P < 0.05.

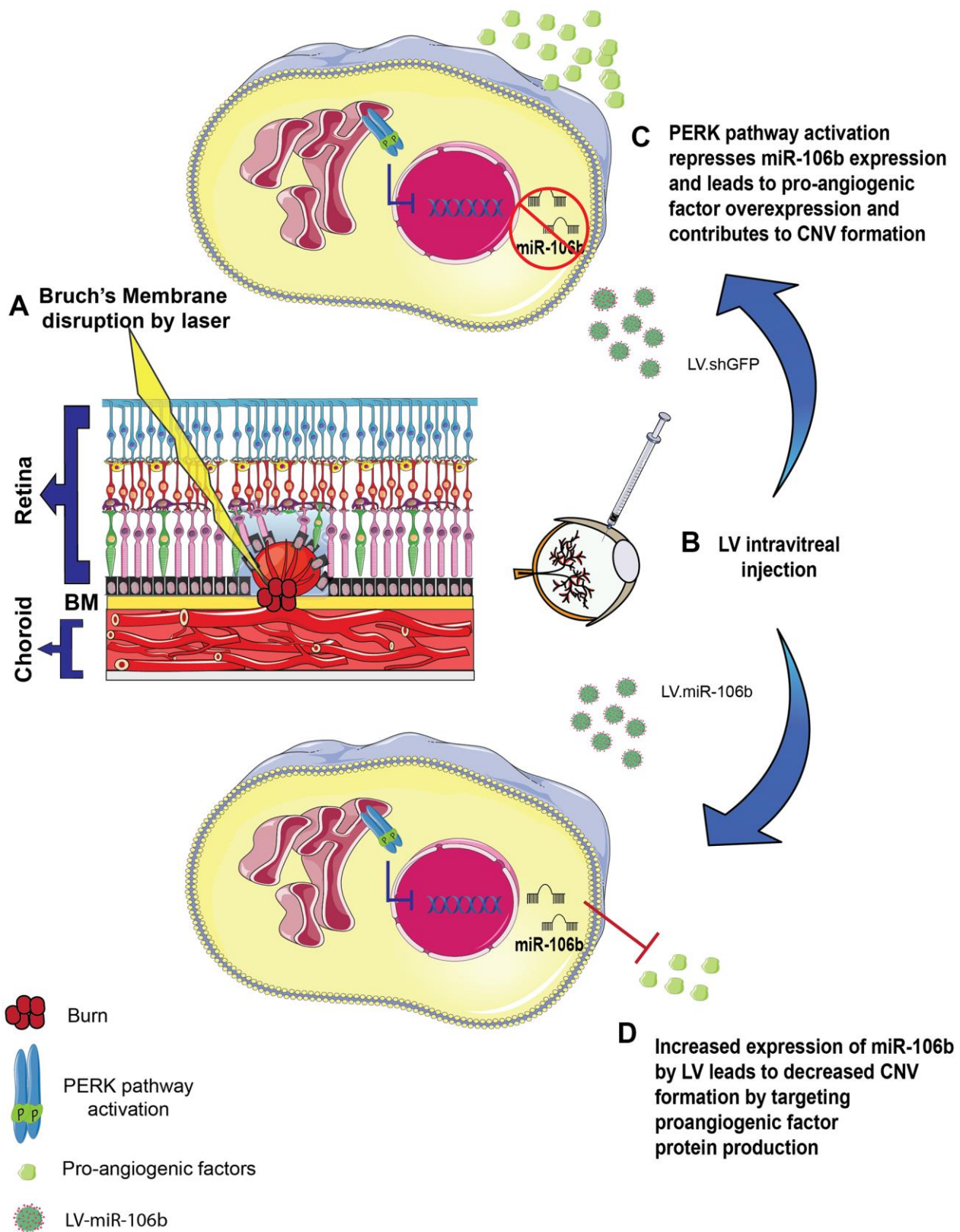


Figure 6. Schematic of miR-106b impact on CNV in mouse laser burn model. (A) Bruch's membrane disruption following laser burn. (B) Intravitreal injection of LV.shGFP or LV.miR-106b. (C) PERK activation represses miR-106b expression and leads to pro-angiogenic factor overexpression, contributing to CNV formation. (D) Increased expression of miR-106b by LV leads to decreased CNV formation by targeting proangiogenic factor protein production. (CNV: choroidal neovascularization, LV: lentivirus).

of eIF2 α and increase in ATF4 mRNA after laser burn. Activated PERK typically influences protein synthesis through phosphorylation of eIF2 α , leading to global translation arrest [37] while transcripts with alternative upstream open reading frames, such as ATF4, are translated and can mediate an antioxidant response and expand the ER's folding capacity [38]. With sustained activation, ATF4 can also drive transcription of pro-apoptotic factors and lead to apoptosis by inducing CHOP [38]. The PERK pathway is thought to be influenced by miRNAs. For example, miR-204 represses PERK [39] while miR-30b-5p and miR-30c-5p regulate eIF2 α , and miR-214 downregulates ATF4 expression [40]. Similarly, to what has been reported in mouse embryonic fibroblasts [34], our data suggest that PERK suppresses miR-106b during choroidal neovascularization and thus renders the retina more conducive to neovascularization.

We demonstrated the anti-angiogenic properties of miR-106b in models of retinal (OIR) and choroidal neovascularization (laser CNV). The magnitude of suppression was comparable to that of suppression of VEGFA or PERK inhibition by shRNA. MiR-106b, a member of miR-17 family with reported anti-angiogenic properties [41, 42], also significantly decreased choroidal sprouting. Our results are consistent with previous studies demonstrating the anti-angiogenic properties of miR-106b in cell culture via STAT3 inhibition [43] and in mice in a hind limb ischemia model.

Currently, there are efforts to devise therapeutics that simultaneously inhibit several factors involved in retinal vascular disease given the clinical success of compounds such as Aflibercept [44]. miRNAs regulate translation of multiple genes and hence may be considered as multi-target inhibitors. Their potential to mitigate retinal disease will grow as comprehensive landscapes of miRNAs in health and disease are established [26, 45]. Preclinical studies are underway for mimics or inhibition of specific miRNAs [46]. Overall, this study demonstrates a new role for miR-106b and highlights its potential for suppressing pathological retinal neovascularization.

MATERIALS AND METHODS

Animals

All studies were performed according to the Association for Research in Vision and Ophthalmology (ARVO) Statement for the Use of Animals in Ophthalmic and Vision Research and were approved by the Animal Care Committee of the University of Montreal in agreement with the guidelines established by the Canadian Council

on Animal Care. C57Bl/6 wild-type were purchased from Jackson Laboratory and CD1 nursing mothers from Charles River Laboratory.

Cell line

Human retinal microvascular endothelial cells (HRMECs) (Cell System, Kirkland, USA) were used from passages 6 to 11. HRMECs were cultured in EGM-2 microvascular medium (Lonza, Switzerland). For scratch assay experiments and for Electric Cell-substrate Impedance Sensing (ECIS), cells were starved overnight then cultured in EBM-2 medium (2% fetal bovine serum).

O₂-induced retinopathy (OIR)

Mouse pups (C57Bl/6, Jackson Labs) and their fostering mothers (CD1, Charles River) were exposed to 75% O₂ from postnatal day 7 (P7) until day 12 and returned to room air. This model serves as a proxy to human ocular neovascular diseases such as ROP and diabetic retinopathy characterized by a late phase of destructive pathological angiogenesis [47, 48]. Upon return to room air, hypoxia-driven neovascularization (NV) develops from P14 onwards [35]. Dissected retinas were flatmounted and incubated overnight with fluoresceinated isolectin B4 (1:100) in 1mM CaCl₂ to determine extent of avascular area or neovascularization area at P17 using ImageJ and the SWIFT-NV method [49].

In vivo imaging following laser-induced choroidal neovascularization (CNV)

In vivo imaging was performed using a scanning laser ophthalmoscope (Micron IV; Phoenix Laboratories, Pleasanton, CA, USA). Mice of 9 to 11 weeks of age were subjected to pupil dilation (Mydriacyl; Alcon, Mississauga, ON, Canada) and anesthetized with a mix of 10% ketamine and 4% xylazine (10 μ l/g body weight). Fluorescein (Alcon, 1 unit/g body weight of a 5% fluorescein dilution in 0.9% sodium chloride) was injected subcutaneously and corneas were lubricated with Optixcare ophthalmic gel (Aventix Animal Health, Burlington, ON, Canada). After a fluorescein circulation of 5 minutes, retinas were imaged before and after inducing choroidal neovascularization with 4 distinct laser burns (50 μ m, 300mW, 0.05s). Animals were followed-up 3, 7 and 14 days after laser burn.

CNV induction and neovascularization labeling by perfusion with FITC

For lentiviral treatment mice of 9 to 11 weeks of age were intraocularly injected with lentivirus and their

Bruch's membranes were ruptured using an argon laser as described previously [32]. At day 3, 7 and 14 after CNV induction, mice were injected with 0.5 ml of 15 mg/ml of fluorescein isothiocyanate (FITC)-dextran (average molecular weight 20,000) (Sigma Aldrich, CA) and euthanized.

Immunohistofluorescence

Eyes were fixed for 30 min in 4% PFA at room temperature before dissection to isolate retinas (OIR) or choroids (LB-CNV). Flatmounted retinas or choroids were stained with Rhodamine labeled Griffonia (Bandeiraea) Simplicifolia Lectin I (RL-1102; Vector Laboratories) in 1 mM CaCl₂ in PBS. The sclera-choroid-RPE cell complex was mounted onto a slide, and the burns photographed with an Olympus FV1000 microscope.

Neovascularization quantifications

Retinal neovascularization (OIR model): For visualization of pan-retinal vasculature, dissected retinas were flatmounted and incubated overnight with rhodamine-labeled Griffonia (Bandeiraea) Simplicifolia Lectin I (Vector Laboratories Inc.) in 1 mM CaCl₂ in PBS for retinal vasculature. The extent of avascular area or neovascularization area at P17 was determined using ImageJ and the SWIFT_NV method [49].

Choroidal neovascularization (laser burn model): The neovascularization was captured in a Z-stack, and the lesion caused by the laser impact was captured in a single-plane image. The Z-stacks were compressed into one image, and the FITC-dextran-labeled neovascular area and the area of the lesion were measured per lesion in ImageJ.

Western blot analysis

For assessment of choroidal protein levels, eyes were enucleated from mice 3 days after burn. RIPA buffer with anti-protease and anti-phosphatase (BioRad) was freshly prepared to manually with a piston to homogenize tissues and for cells lysis. Protein concentration was assessed by BCA assay (Sigma-Aldrich, Oakville, CA), and 30µg of protein analyzed for each condition by standard SDS-PAGE technique using Bis-Acrylamide gel 10% or 12.5% depending of protein size. Total protein transfer on nitrocellulose or PVDF membranes (Bio-Rad, Mississauga, ON, CA) was evaluated with Ponceau Red (Sigma-Aldrich, Oakville, CA). Antibody solutions and dilutions were prepared as per manufacturers' recommendations.

Antibodies

Phospho-eIF2 α (Ser51) (Cell signaling Technology, Whitby, CA), Total-eIF2 α (Cell signaling Technology,

Whitby, CA), β -actin (8H10D10) (Cell signaling Technology, Whitby, CA), VEGFA (C1) (Santa Cruz Biotechnology, INC, Texas, USA), HIF1 α (H1alpha67) (Novus Biologicals, Oakville, CA).

Quantitative real time polymerase chain reaction analysis

RNA extraction was performed with TRIzol® Reagent (Life Technology, Waltham, USA) as suggested by manufacturer protocol. DNase digestion was then performed to prevent amplification of genomic DNA (Invitrogen, Waltham, USA). iScript™ Reverse Transcription Supermix for RT-qPCR (Bio-Rad, Mississauga, CA) was used to generate cDNA from 1µg of total RNA. Real time qPCR was performed to quantify gene expression using SYBR® Green reagent (Applied Biosystem TM, USA) and was processed with an ABI 7500 Real-Time PCR machine. β -actin was used as a reference gene. Primer sequences (Integrated DNA Technologies) are listed in Supplementary Table 1. miRNA extraction was performed with TRIzol® Reagent, Retrotranscription reaction was done with TaqMan MicroRNA Reverse Transcription kit (Applied Biosystem, USA) using 100ng of total RNA in each reaction following manufacturer protocol. Real-time PCR was processed with TaqMan miR assay 20X and Universal master mix II No-UNG 2x for TaqMan Reaction (Applied Biosystem, USA). Primers are listed in the Supplementary Table 1.

Lentivirus plasmid constructions

Lentiviral constructs were produced with the PCR insertion kit (Q5 Site-Directed Mutagenesis kit, New England BioLabs®inc). The following sequence for shVEGFA and mature miR-106b sequence were inserted shVEGFA: 5' GAGCGGAGAAAGC ATTTG TTTCTCGAGAAACAAATGCTTTCTCCGC TCTTTT 3', miR-106b: 5'TAAAGTGCT GACAGTG CAGATCTCGAGATCTGCACTGTCAGCACTTTAT TTT-3'. All constructs were verified by Genome Quebec sequencing. Constructs of shIRE1 α and shPERK were previously published by our group [50].

Preparation of lentivirus

We produced infectious lentiviral vectors by transfecting lentivector and packaging vectors into HEK293T cells (Invitrogen) as previously described (Dull et al. Journal of Virology, 1998). Viral supernatants were concentrated by ultracentrifugation (>500-fold). Viral efficiency was confirmed by real-time-PCR and Western blot.

Intravitreal injections

For the OIR model, P4, P7, C57BL/6 pups were anesthetized with 3.0% isoflurane and injected in the vitreous chamber with 0.5 μ l of lentivirus. Retinas were collected at P17 for vasculature analysis. For the laser burn model, 8 to 10 week old C57BL/6 mice were injected following laser burn in the vitreous chamber with 1 μ l of lentivirus. Choroids were collected 7 days post burns for CNV quantification.

Scratch assay

Scratch assays were performed with pre-infected HRMECs cells (72hr) in 6 well plates until confluency was reached. Scratches were done with 200 μ l sterile tips and culture media was replaced with with EBM-2 medium (2% fetal bovine serum). Pictures were taken at time 0 (moment of the scratch) and after 8 hours with a 2x objective using an inverted microscope (Zeiss Axio Imager) and migration distances were quantified with Image J software.

Electric cell-substrate impedance sensing migration assay (ECIS)

Real time analysis of trans and inter-endothelial impedance was performed by plating 1×10^5 pre-infected (72 hours) HRMECs cells into 8 well arrays (8W10E for migration assays, 40 electrodes per well) (Applied BioPhysics, Troy, NY, USA). Cells were plated at confluency and submitted to an electric pulse in the center of each well, causing localized cell detachment, resulting in a 250 μ m diameter devoid of cells. Cell migration was quantified by measurement of impedance, which increases as cells repopulate the empty space. The results were then normalized to the vehicle control and expressed as relative resistance. Graphical representation depicts mean and S.E.M., and light blue zones highlight time points where statistically significant differences are observed (student's t-test, $P < 0.05$).

Choroid *ex vivo* explant assay

Adult C57Bl/6 mice were euthanized, and eyes were immediately enucleated and kept in ice-cold EBM basal medium (Lonza) before dissection. Choroid explants were placed in growth factor-reduced Matrigel (Corning) seeded in 24 well plates, and incubated at 37° C for 10 minutes to allow the Matrigel to solidify. 500 μ L of medium was then added to each well and incubated at 37° C with 5% CO² for 24 hours before lentiviral infections. Explant pictures were taken after 48 hours (at the beginning of choroid vessel growth), and at 72 hours to 96 hours post-infection to follow vessel growth. Phase contrast photos of individual

explants were captured with a ZEISS Axio Oberver.Z1 microscope. Sprouting area quantification was performed using the semi-automated macro plug-in to the Image J software designed for this purpose [51].

Statistical analyses

Data are presented as mean \pm S.E.M. GraphPad Prism (GraphPad Software, San Diego, CA) was used to perform statistical analyses. We used Student's t test to compare groups of two, and one-way ANOVA with Bonferroni post-hoc analysis for groups of 3 and more; data with $P < 0.05$ were considered statistically different: * denotes $P < 0.05$, ** $P < 0.01$, and *** $P < 0.001$.

AUTHOR CONTRIBUTIONS

C.M., V.D., J.P.S. and P.S. designed the research and study. C.M., A.D., K.M., F.B., S.C.G., C.P., F.P., R.J., E.M.M.A., and G.M., carried out experimental work. C.M., A.M.W. and A.D. analyzed the data. C.M., A.M.W., V.D. J.P.S. and P.S. wrote the manuscript with valuable input from authors.

CONFLICTS OF INTEREST

We do not have any disclosure or conflicts of interest in the study.

FUNDING

This work was supported by operating grants from The Foundation Fighting Blindness Canada, the Canadian Diabetes Association (DI-3-18-5444-PS), the Canadian Institutes of Health Research (Foundation grant #353770 to P.S), the Canadian the Heart and Stroke Foundation Canada (G-16-00014658 to P.S.), and Natural Sciences and Engineering Research Council of Canada (418637 to P.S.). P.S. holds the Wolfe Professorship in Translational Research and a Canada Research Chair in Retinal Cell Biology. We also thank the Fonds de Recherche en Ophtalmologie de l'Université de Montréal (FROUM) and the RRSV.

REFERENCES

1. Klein R, Klein BE. The prevalence of age-related eye diseases and visual impairment in aging: current estimates. Invest Ophthalmol Vis Sci. 2013; 54:ORSF5–RSF13.
<https://doi.org/10.1167/iovs.13-12789>
PMID:[24335069](https://pubmed.ncbi.nlm.nih.gov/24335069/)
2. Miller JW. Age-related macular degeneration revisited—piecing the puzzle: the LXIX Edward Jackson

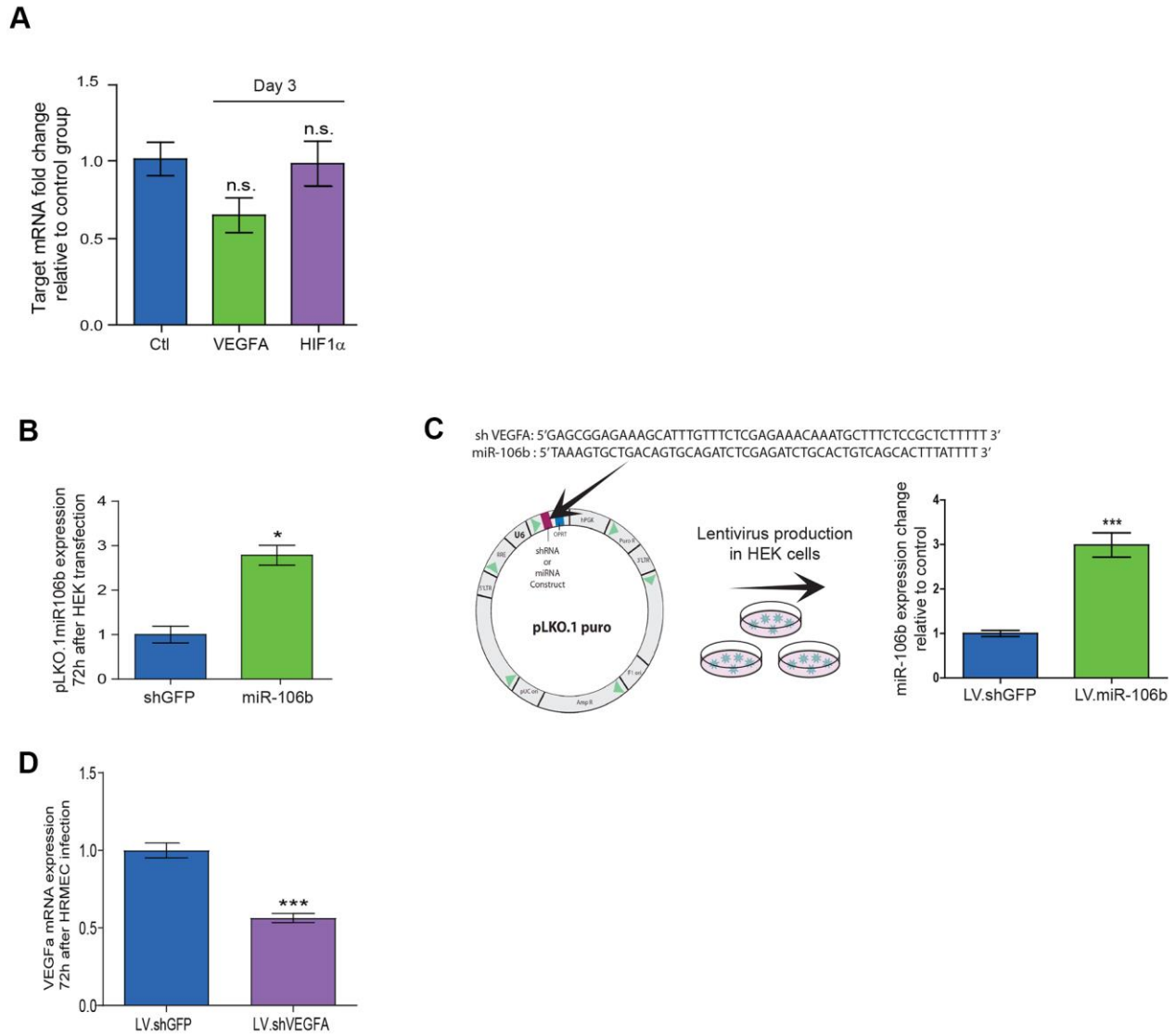
- memorial lecture. *Am J Ophthalmol.* 2013; 155:1–35.e13.
<https://doi.org/10.1016/j.ajo.2012.10.018>
 PMID:[23245386](https://pubmed.ncbi.nlm.nih.gov/23245386/)
3. Gorin MB. Genetic insights into age-related macular degeneration: controversies addressing risk, causality, and therapeutics. *Mol Aspects Med.* 2012; 33:467–86.
<https://doi.org/10.1016/j.mam.2012.04.004>
 PMID:[22561651](https://pubmed.ncbi.nlm.nih.gov/22561651/)
 4. Friedman DS, O’Colmain BJ, Muñoz B, Tomany SC, McCarty C, de Jong PT, Nemesure B, Mitchell P, Kempen J, and Eye Diseases Prevalence Research Group. Prevalence of age-related macular degeneration in the United States. *Arch Ophthalmol.* 2004; 122:564–72.
<https://doi.org/10.1001/archophth.122.4.564>
 PMID:[15078675](https://pubmed.ncbi.nlm.nih.gov/15078675/)
 5. Kempen JH, O’Colmain BJ, Leske MC, Haffner SM, Klein R, Moss SE, Taylor HR, Hamman RF, and Eye Diseases Prevalence Research Group. The prevalence of diabetic retinopathy among adults in the United States. *Arch Ophthalmol.* 2004; 122:552–63.
<https://doi.org/10.1001/archophth.122.4.552>
 PMID:[15078674](https://pubmed.ncbi.nlm.nih.gov/15078674/)
 6. Maberley DA, Hollands H, Chuo J, Tam G, Konkall J, Roesch M, Veselinovic A, Witzigmann M, Bassett K. The prevalence of low vision and blindness in Canada. *Eye (Lond).* 2006; 20:341–46.
<https://doi.org/10.1038/sj.eye.6701879>
 PMID:[15905873](https://pubmed.ncbi.nlm.nih.gov/15905873/)
 7. Schuman SG, Koreishi AF, Farsiu S, Jung SH, Izatt JA, Toth CA. Photoreceptor layer thinning over drusen in eyes with age-related macular degeneration imaged in vivo with spectral-domain optical coherence tomography. *Ophthalmology.* 2009; 116:488–96.e2.
<https://doi.org/10.1016/j.ophtha.2008.10.006>
 PMID:[19167082](https://pubmed.ncbi.nlm.nih.gov/19167082/)
 8. Midena E, Vujosevic S, Convento E, Manfre’ A, Cavarzeran F, Pilotto E. Microperimetry and fundus autofluorescence in patients with early age-related macular degeneration. *Br J Ophthalmol.* 2007; 91:1499–503.
<https://doi.org/10.1136/bjo.2007.119685>
 PMID:[17504849](https://pubmed.ncbi.nlm.nih.gov/17504849/)
 9. Sarks SH. Ageing and degeneration in the macular region: a clinico-pathological study. *Br J Ophthalmol.* 1976; 60:324–41.
<https://doi.org/10.1136/bjo.60.5.324>
 PMID:[952802](https://pubmed.ncbi.nlm.nih.gov/952802/)
 10. Guillonneau X, Eandi CM, Paques M, Sahel JA, Sapieha P, Sennlaub F. On phagocytes and macular degeneration. *Prog Retin Eye Res.* 2017; 61:98–128.
<https://doi.org/10.1016/j.preteyeres.2017.06.002>
 PMID:[28602950](https://pubmed.ncbi.nlm.nih.gov/28602950/)
 11. Sobrin L, Seddon JM. Nature and nurture- genes and environment- predict onset and progression of macular degeneration. *Prog Retin Eye Res.* 2014; 40:1–15.
<https://doi.org/10.1016/j.preteyeres.2013.12.004>
 PMID:[24374240](https://pubmed.ncbi.nlm.nih.gov/24374240/)
 12. Brown DM, Kaiser PK, Michels M, Soubrane G, Heier JS, Kim RY, Sy JP, Schneider S, and ANCHOR Study Group. Ranibizumab versus verteporfin for neovascular age-related macular degeneration. *N Engl J Med.* 2006; 355:1432–44.
<https://doi.org/10.1056/NEJMoa062655>
 PMID:[17021319](https://pubmed.ncbi.nlm.nih.gov/17021319/)
 13. Rosenfeld PJ, Brown DM, Heier JS, Boyer DS, Kaiser PK, Chung CY, Kim RY, and MARINA Study Group. Ranibizumab for neovascular age-related macular degeneration. *N Engl J Med.* 2006; 355:1419–31.
<https://doi.org/10.1056/NEJMoa054481>
 PMID:[17021318](https://pubmed.ncbi.nlm.nih.gov/17021318/)
 14. Mitchell P. A systematic review of the efficacy and safety outcomes of anti-VEGF agents used for treating neovascular age-related macular degeneration: comparison of ranibizumab and bevacizumab. *Curr Med Res Opin.* 2011; 27:1465–75.
<https://doi.org/10.1185/03007995.2011.585394>
 PMID:[21623685](https://pubmed.ncbi.nlm.nih.gov/21623685/)
 15. Jacob J, Brié H, Leys A, Levecq L, Mergaerts F, Denhaerynck K, Vancayzeele S, Van Craeyveld E, Abraham I, MacDonald K. Six-year outcomes in neovascular age-related macular degeneration with ranibizumab. *Int J Ophthalmol.* 2017; 10:81–90.
<https://doi.org/10.18240/ijo.2017.01.14>
 PMID:[28149782](https://pubmed.ncbi.nlm.nih.gov/28149782/)
 16. Amoaku WM, Chakravarthy U, Gale R, Gavin M, Ghanchi F, Gibson J, Harding S, Johnston RL, Kelly SP, Lotery A, Mahmood S, Menon G, Sivaprasad S, et al. Defining response to anti-VEGF therapies in neovascular AMD. *Eye (Lond).* 2015; 29:1397–98.
<https://doi.org/10.1038/eye.2015.159> PMID:[26446737](https://pubmed.ncbi.nlm.nih.gov/26446737/)
 17. Robinson GS, Ju M, Shih SC, Xu X, McMahon G, Caldwell RB, Smith LE. Nonvascular role for VEGF: VEGFR-1, 2 activity is critical for neural retinal development. *FASEB J.* 2001; 15:1215–17.
<https://doi.org/10.1096/fj.00-0598fje>
 PMID:[11344092](https://pubmed.ncbi.nlm.nih.gov/11344092/)
 18. Saint-Geniez M, Maharaj AS, Walshe TE, Tucker BA, Sekiyama E, Kurihara T, Darland DC, Young MJ, D’Amore PA. Endogenous VEGF is required for visual function: evidence for a survival role on müller cells and photoreceptors. *PLoS One.* 2008; 3:e3554.

- <https://doi.org/10.1371/journal.pone.0003554>
PMID:[18978936](https://pubmed.ncbi.nlm.nih.gov/18978936/)
19. Grunwald JE, Daniel E, Huang J, Ying GS, Maguire MG, Toth CA, Jaffe GJ, Fine SL, Blodi B, Klein ML, Martin AA, Hagstrom SA, Martin DF, and CATT Research Group. Risk of geographic atrophy in the comparison of age-related macular degeneration treatments trials. *Ophthalmology*. 2014; 121:150–161.
<https://doi.org/10.1016/j.ophtha.2013.08.015>
PMID:[24084496](https://pubmed.ncbi.nlm.nih.gov/24084496/)
20. Grunwald JE, Pistilli M, Ying GS, Maguire MG, Daniel E, Martin DF, and Comparison of Age-related Macular Degeneration Treatments Trials Research Group. Growth of geographic atrophy in the comparison of age-related macular degeneration treatments trials. *Ophthalmology*. 2015; 122:809–16.
<https://doi.org/10.1016/j.ophtha.2014.11.007>
PMID:[25542520](https://pubmed.ncbi.nlm.nih.gov/25542520/)
21. Klein R, Knudtson MD, Klein BE, Wong TY, Cotch MF, Liu K, Cheng CY, Burke GL, Saad MF, Jacobs DR Jr, Sharrett AR. Inflammation, complement factor h, and age-related macular degeneration: the multi-ethnic study of atherosclerosis. *Ophthalmology*. 2008; 115:1742–49.
<https://doi.org/10.1016/j.ophtha.2008.03.021>
PMID:[18538409](https://pubmed.ncbi.nlm.nih.gov/18538409/)
22. Ambati J, Fowler BJ. Mechanisms of age-related macular degeneration. *Neuron*. 2012; 75:26–39.
<https://doi.org/10.1016/j.neuron.2012.06.018>
PMID:[22794258](https://pubmed.ncbi.nlm.nih.gov/22794258/)
23. Huang Y, Shen XJ, Zou Q, Wang SP, Tang SM, Zhang GZ. Biological functions of microRNAs: a review. *J Physiol Biochem*. 2011; 67:129–39.
<https://doi.org/10.1007/s13105-010-0050-6>
PMID:[20981514](https://pubmed.ncbi.nlm.nih.gov/20981514/)
24. Baek D, Villén J, Shin C, Camargo FD, Gygi SP, Bartel DP. The impact of microRNAs on protein output. *Nature*. 2008; 455:64–71.
<https://doi.org/10.1038/nature07242>
PMID:[18668037](https://pubmed.ncbi.nlm.nih.gov/18668037/)
25. Ménard C, Rezende FA, Miloudi K, Wilson A, Tétreault N, Hardy P, SanGiovanni JP, De Guire V, Sapiéha P. MicroRNA signatures in vitreous humour and plasma of patients with exudative AMD. *Oncotarget*. 2016; 7:19171–84.
<https://doi.org/10.18632/oncotarget.8280>
PMID:[27015561](https://pubmed.ncbi.nlm.nih.gov/27015561/)
26. Liu CH, Sun Y, Li J, Gong Y, Tian KT, Evans LP, Morss PC, Fredrick TW, Saba NJ, Chen J. Endothelial microRNA-150 is an intrinsic suppressor of pathologic ocular neovascularization. *Proc Natl Acad Sci USA*. 2015; 112:12163–68.
<https://doi.org/10.1073/pnas.1508426112>
PMID:[26374840](https://pubmed.ncbi.nlm.nih.gov/26374840/)
27. Yan L, Lee S, Lazzaro DR, Aranda J, Grant MB, Chaqour B. Single and compound knock-outs of MicroRNA (miRNA)-155 and its angiogenic gene target CCN1 in mice alter vascular and neovascular growth in the retina via resident microglia. *J Biol Chem*. 2015; 290:23264–81.
<https://doi.org/10.1074/jbc.M115.646950>
PMID:[26242736](https://pubmed.ncbi.nlm.nih.gov/26242736/)
28. Shen J, Yang X, Xie B, Chen Y, Swaim M, Hackett SF, Campochiaro PA. MicroRNAs regulate ocular neovascularization. *Mol Ther*. 2008; 16:1208–16.
<https://doi.org/10.1038/mt.2008.104>
PMID:[18500251](https://pubmed.ncbi.nlm.nih.gov/18500251/)
29. Ertekin S, Yıldırım O, Dinç E, Ayaz L, Fidancı SB, Tamer L. Evaluation of circulating miRNAs in wet age-related macular degeneration. *Mol Vis*. 2014; 20:1057–66.
PMID:[25221421](https://pubmed.ncbi.nlm.nih.gov/25221421/)
30. Berber P, Grassmann F, Kiel C, Weber BH. An eye on age-related macular degeneration: the role of MicroRNAs in disease pathology. *Mol Diagn Ther*. 2017; 21:31–43.
<https://doi.org/10.1007/s40291-016-0234-z>
PMID:[27658786](https://pubmed.ncbi.nlm.nih.gov/27658786/)
31. Nunes DN, Dias-Neto E, Cardó-Vila M, Edwards JK, Dobroff AS, Giordano RJ, Mandelin J, Brentani HP, Hasselgren C, Yao VJ, Marchiò S, Pereira CA, Passetti F, et al. Synchronous down-modulation of miR-17 family members is an early causative event in the retinal angiogenic switch. *Proc Natl Acad Sci USA*. 2015; 112:3770–75.
<https://doi.org/10.1073/pnas.150008112>
PMID:[25775553](https://pubmed.ncbi.nlm.nih.gov/25775553/)
32. Lambert V, Lecomte J, Hansen S, Blacher S, Gonzalez ML, Struman I, Sounni NE, Rozet E, de Tullio P, Foidart JM, Rakic JM, Noel A. Laser-induced choroidal neovascularization model to study age-related macular degeneration in mice. *Nat Protoc*. 2013; 8:2197–211.
<https://doi.org/10.1038/nprot.2013.135>
PMID:[24136346](https://pubmed.ncbi.nlm.nih.gov/24136346/)
33. Mendell JT. miRiad roles for the miR-17-92 cluster in development and disease. *Cell*. 2008; 133:217–22.
<https://doi.org/10.1016/j.cell.2008.04.001>
PMID:[18423194](https://pubmed.ncbi.nlm.nih.gov/18423194/)
34. Gupta S, Read DE, Deepti A, Cawley K, Gupta A, Oommen D, Verfaillie T, Matus S, Smith MA, Mott JL, Agostinis P, Hetz C, Samali A. Perk-dependent repression of miR-106b-25 cluster is required for ER stress-induced apoptosis. *Cell Death Dis*. 2012; 3:e333.
<https://doi.org/10.1038/cddis.2012.74>
PMID:[22739985](https://pubmed.ncbi.nlm.nih.gov/22739985/)

35. Smith LE, Wesolowski E, McLellan A, Kostyk SK, D'Amato R, Sullivan R, D'Amore PA. Oxygen-induced retinopathy in the mouse. *Invest Ophthalmol Vis Sci*. 1994; 35:101–11. PMID:[7507904](https://pubmed.ncbi.nlm.nih.gov/7507904/)
36. Salminen A, Kauppinen A, Hyttinen JM, Toropainen E, Kaarniranta K. Endoplasmic reticulum stress in age-related macular degeneration: trigger for neovascularization. *Mol Med*. 2010; 16:535–42. <https://doi.org/10.2119/molmed.2010.00070> PMID:[20683548](https://pubmed.ncbi.nlm.nih.gov/20683548/)
37. Harding HP, Zhang Y, Ron D. Protein translation and folding are coupled by an endoplasmic-reticulum-resident kinase. *Nature*. 1999; 397:271–74. <https://doi.org/10.1038/16729> PMID:[9930704](https://pubmed.ncbi.nlm.nih.gov/9930704/)
38. Binet F, Sapieha P. ER stress and angiogenesis. *Cell Metab*. 2015; 22:560–75. <https://doi.org/10.1016/j.cmet.2015.07.010> PMID:[26278049](https://pubmed.ncbi.nlm.nih.gov/26278049/)
39. Xu G, Chen J, Jing G, Grayson TB, Shalev A. miR-204 targets PERK and regulates UPR signaling and β -cell apoptosis. *Mol Endocrinol*. 2016; 30:917–24. <https://doi.org/10.1210/me.2016-1056> PMID:[27384111](https://pubmed.ncbi.nlm.nih.gov/27384111/)
40. McMahon M, Samali A, Chevet E. Regulation of the unfolded protein response by noncoding RNA. *Am J Physiol Cell Physiol*. 2017; 313:C243–54. <https://doi.org/10.1152/ajpcell.00293.2016> PMID:[28637678](https://pubmed.ncbi.nlm.nih.gov/28637678/)
41. Bonauer A, Carmona G, Iwasaki M, Mione M, Koyanagi M, Fischer A, Burchfield J, Fox H, Doebele C, Ohtani K, Chavakis E, Potente M, Tjwa M, et al. MicroRNA-92a controls angiogenesis and functional recovery of ischemic tissues in mice. *Science*. 2009; 324:1710–13. <https://doi.org/10.1126/science.1174381> PMID:[19460962](https://pubmed.ncbi.nlm.nih.gov/19460962/)
42. Doebele C, Bonauer A, Fischer A, Scholz A, Reiss Y, Urbich C, Hofmann WK, Zeiher AM, Dimmeler S. Members of the microRNA-17-92 cluster exhibit a cell-intrinsic antiangiogenic function in endothelial cells. *Blood*. 2010; 115:4944–50. <https://doi.org/10.1182/blood-2010-01-264812> PMID:[20299512](https://pubmed.ncbi.nlm.nih.gov/20299512/)
43. Maimaiti A, Maimaiti A, Yang Y, Ma Y. MiR-106b exhibits an anti-angiogenic function by inhibiting STAT3 expression in endothelial cells. *Lipids Health Dis*. 2016; 15:51. <https://doi.org/10.1186/s12944-016-0216-5> PMID:[26956882](https://pubmed.ncbi.nlm.nih.gov/26956882/)
44. Sarwar S, Clearfield E, Soliman MK, Sadiq MA, Baldwin AJ, Hanout M, Agarwal A, Sepah YJ, Do DV, Nguyen QD. Aflibercept for neovascular age-related macular degeneration. *Cochrane Database Syst Rev*. 2016; 2:CD011346. <https://doi.org/10.1002/14651858.CD011346.pub2> PMID:[26857947](https://pubmed.ncbi.nlm.nih.gov/26857947/)
45. Desjarlais M, Rivera JC, Lahaie I, Cagnone G, Wirt M, Omri S, Chemtob S. MicroRNA expression profile in retina and choroid in oxygen-induced retinopathy model. *PLoS One*. 2019; 14:e0218282. <https://doi.org/10.1371/journal.pone.0218282> PMID:[31188886](https://pubmed.ncbi.nlm.nih.gov/31188886/)
46. Hanna J, Hossain GS, Kocerha J. The potential for microRNA therapeutics and clinical research. *Front Genet*. 2019; 10:478. <https://doi.org/10.3389/fgene.2019.00478> PMID:[31156715](https://pubmed.ncbi.nlm.nih.gov/31156715/)
47. Sapieha P, Joyal JS, Rivera JC, Kermorvant-Duchemin E, Sennlaub F, Hardy P, Lachapelle P, Chemtob S. Retinopathy of prematurity: understanding ischemic retinal vasculopathies at an extreme of life. *J Clin Invest*. 2010; 120:3022–32. <https://doi.org/10.1172/JCI42142> PMID:[20811158](https://pubmed.ncbi.nlm.nih.gov/20811158/)
48. Stahl A, Connor KM, Sapieha P, Chen J, Dennison RJ, Krah NM, Seaward MR, Willett KL, Aderman CM, Guerin KI, Hua J, Löfqvist C, Hellström A, Smith LE. The mouse retina as an angiogenesis model. *Invest Ophthalmol Vis Sci*. 2010; 51:2813–26. <https://doi.org/10.1167/iovs.10-5176> PMID:[20484600](https://pubmed.ncbi.nlm.nih.gov/20484600/)
49. Stahl A, Connor KM, Sapieha P, Willett KL, Krah NM, Dennison RJ, Chen J, Guerin KI, Smith LE. Computer-aided quantification of retinal neovascularization. *Angiogenesis*. 2009; 12:297–301. <https://doi.org/10.1007/s10456-009-9155-3> PMID:[19757106](https://pubmed.ncbi.nlm.nih.gov/19757106/)
50. Binet F, Mawambo G, Sitaras N, Tetreault N, Lapalme E, Favret S, Cerani A, Leboeuf D, Tremblay S, Rezende F, Juan AM, Stahl A, Joyal JS, et al. Neuronal ER stress impedes myeloid-cell-induced vascular regeneration through IRE1 α degradation of netrin-1. *Cell Metab*. 2013; 17:353–71. <https://doi.org/10.1016/j.cmet.2013.02.003> PMID:[23473031](https://pubmed.ncbi.nlm.nih.gov/23473031/)
51. Shao Z, Friedlander M, Hurst CG, Cui Z, Pei DT, Evans LP, Juan AM, Tahiri H, Duhamel F, Chen J, Sapieha P, Chemtob S, Joyal JS, Smith LE. Choroid sprouting assay: an *ex vivo* model of microvascular angiogenesis. *PLoS One*. 2013; 8:e69552. <https://doi.org/10.1371/journal.pone.0069552> PMID:[23922736](https://pubmed.ncbi.nlm.nih.gov/23922736/)

SUPPLEMENTARY MATERIALS

Supplementary Figure



Supplemental Figure 1. (A) VEGFA and HIF1 α mRNA expression in choroids 3 days after laser burn (VEGFA n=5, HIF1 α n=7). (B) LV.miR-106b expression after plasmid transfection in HEK cells (n=4). (C) Schematic of plasmid construction, virus production and LV.miR-106b expression 72hrs after viral infection of HRMECs. (D) VEGFA mRNA expression in HRMECs 72hrs after LV.shVEGFA infection. Data are expressed as mean \pm S.E.M. Unpaired Two-tailed Student's t-test was used for the analysis of groups of 2, and one-way ANOVA with Bonferroni post-hoc test was performed on groups of 3 or more, *P<0.05; **P<0.001; ***P<0.0001.

Supplementary Table

Supplementary Table 1. List of human and mouse primers.

Genes (human)	Foward primers	Reverse primers
B-ACTIN (ACTB)	5' GTCATTCCAAATATGAGATGCGT 5'	5' TGTGGACTTGGGAGAGGACT 3'
VEGFA	5' CTCTACCTCCACCATGCCAAG 3'	5' AGACATCCATGAACTTCACCACTTC 3'
Genes (mouse)	Foward primers	Reverse primers
B-ACTIN (ACTB)	5' GACGGCCAGGTCATCACTATTG 3'	5' CCACAGGATTCCATACCCAAG 3'
VEGFA	5' GCCCTGAGTCAAGAGGACAG 3'	5' CTCCTAGGCCCCCTCAGAAGT 3'
MCM7	5' ATGGCGCTTAAGGACTACG 3'	5' ATCCAGGTCCACATACAGTG 3'
ATF4	5' CTACTAGGTACCGCCAGAAG 3'	5' GCCTTACGGACCTCTTCTAT 3'
HIF1 α	5' CGAGAACGAGAAGAAAAAGATGAG 3'	5' AAGCCATCTAGGGCTTTCAG 3'

RT-qPCR primer sequences to quantify mRNA expression in choroids (mouse) or HRMECs (human).

Suppressing endoplasmic reticulum stress-related autophagy attenuates retinal light injury

Jing-Yao Song¹, Bin Fan¹, Lin Che¹, Yi-Ran Pan¹, Si-Ming Zhang¹, Ying Wang², Victoria Bunik³, Guang-Yu Li¹

¹Department of Ophthalmology, Second Hospital of Jilin University, Changchun, China

²Department of Hemooncolog, Second Hospital of Jilin University, Changchun, China

³A.N.Belozersky Institute of Physico-Chemical Biology, Lomonosov Moscow State University, Moscow, Russia

Correspondence to: Guang-Yu Li; **email:** l_gy@jlu.edu.cn

Keywords: oxidative stress, ER stress, autophagy, AMD, PERK

Received: February 11, 2020

Accepted: June 30, 2020

Published: August 28, 2020

Copyright: Song et al. This is an open-access article distributed under the terms of the Creative Commons Attribution License (CC BY 3.0), which permits unrestricted use, distribution, and reproduction in any medium, provided the original author and source are credited.

ABSTRACT

Excessive light exposure is a principal environmental factor, which can cause damage to photoreceptors and retinal pigment epithelium (RPE) cells and may accelerate the progression of age-related macular degeneration (AMD). In this study, oxidative stress, endoplasmic reticulum (ER) stress and autophagy caused by light exposure were evaluated *in vitro* and *in vivo*. Light exposure caused severe photo-oxidative stress and ER stress in photoreceptors (661W cells) and RPE cells (ARPE-19 cells). Suppressing either oxidative stress or ER stress was protective against light damage in 661W and ARPE-19 cells and N-acetyl-L-cysteine treatment markedly inhibited the activation of ER stress caused by light exposure. Moreover, suppressing autophagy with 3-methyladenine significantly attenuated light-induced cell death. Additionally, inhibiting ER stress either by knocking down PERK signals or with GSK2606414 treatment remarkably suppressed prolonged autophagy and protected the cells against light injury. *In vivo* experiments verified neuroprotection via inhibiting ER stress-related autophagy in light-damaged retinas of mice. In conclusion, the above results suggest that light-induced photo-oxidative stress may trigger subsequent activation of ER stress and prolonged autophagy in photoreceptors and RPE cells. Suppressing ER stress may abrogate over-activated autophagy and protect the retina against light injury.

INTRODUCTION

Age-related macular degeneration (AMD) is a degenerative retinal disease, which often occurs in the elderly and causes irreversible loss of central vision. Indeed, excessive and prolonged light exposure may damage the retina and is an environmental factor that can accelerate AMD [1]. With the rapid development of technology, many electronic devices with screens, and ophthalmic equipment with intensive illumination, have become widely used. Therefore, an increasing amount of attention has been focused on issues of light pollution and retinal light damage. Among the molecular mechanisms involved in light-induced retinal damage,

photochemical damage is regarded as the main culprit [2]. Excessive photons from visible light exposure are absorbed by opsin in photoreceptor cells or melanosomes in pigment epithelial cells, causing a series of photochemical reactions, which may further trigger programmed cell death [3]. However, the exact molecular mechanism of light-induced retinal injury remains unclear.

Two stereoisomers, 11-cis-retinal and all-trans-retinal, exist in the retina and play roles in the visual cycle. A photon from visible light triggers cis-trans isomerization, converting the bent chromophore into a straight conformation, causing a separation between the

two stereoisomers [4, 5]. When oxygen is present and upon photoexcitation by light, all-transretinal is a potent photosensitizer that generates reactive oxygen species (ROS), such as singlet oxygen, superoxide and hydrogen peroxide [6, 7]. The excessive ROS may lead to oxidative-stress damage in both photoreceptors and RPE cells following disk phagocytosis [3, 8]. There is growing evidence that photo-oxidative reactions might be an important step in triggering the death cascade in light-damaged retinal neurons [2, 9–12].

The endoplasmic reticulum (ER) is an important organelle that mediates protein synthesis, processing and transport and participates in maintaining homeostasis of the intracellular environment [13, 14]. In the process of protein folding, resident protein disulfide isomerases (PDI), endoplasmic reticulum oxidoreduction 1 (ERO1) and glutathione (GSH) cooperate as a chaperone-like assisted mechanism to prevent and correct aberrant disulfide bonds [15]. Previous studies have shown that excessive intracellular ROS may lead to depletion of the GSH pool and compromise the function of PDI, which disrupts the folding process of proteins in the ER and produces a massive amount of misfolded proteins [16, 17]. However, the excessive accumulation of misfolded proteins in the ER may trigger an unfolded-protein response (UPR), which may enhance protein folding ability, as well as the homeostasis of protein translation and accelerate protein degradation to recover ER function [18]. Normally, the UPR is activated by 3 transmembrane ER stress sensors: activating transcription factor 6 (ATF6), inositol-requiring enzyme 1 (IRE1) and protein kinase RNA-like ER kinase (PERK). When ER stress happens, ATF6 is transported to the Golgi in the form of vesicles and is then cleaved by protease [sites 1 and 2 protease (S1P and S2P)] to produce a transcriptionally active polypeptide [19]; IRE1 is phosphorylated and causes the activation of endoribonuclease, splicing of the 26-nucleotide (nt) sequence from the X-box binding protein (XBP1) messenger ribonucleic acid (mRNA) and production of functional XBP1(S), which is transferred to the nucleus and activates transcription of the genes encoding the ER chaperone [20]; PERK is activated by phosphorylation, which in turn phosphorylates eukaryotic translation initiation factor 2 (EIF2) to inhibit protein translation and reduce protein synthesis [21]. However, phosphorylated EIF2 may selectively increase activating transcription factor 4 (ATF4) translation [22], which causes the activation of transcription factor C/EBP homologous protein (CHOP). Under physiological conditions, these three transmembrane proteins bind to the glucose regulatory protein 78kDa (Grp78; also known as BiP) in the ER lumen. Once misfolded proteins accumulate in the ER, they titrate

BiP away from these sensors to cause activation of the downstream signals, which may further accelerate protein degradation, termed ER-related degradation (ERAD) [23]. ERAD is mainly composed of the following mechanisms: ubiquitin proteasome-dependent ERAD and autophagy lysosome-dependent ERAD [24].

Autophagy is an important and complex metabolic pathway in eukaryotic cells. It normally consists of four main phases: nucleation, expansion, maturation, and degradation/recycling [25]. Autophagy is often classified as basic autophagy, which exists at a relatively low level in cells, and induced autophagy, which is caused by various stresses, such as starvation, aging and inflammation [26–28]. Autophagy is a major intracellular degradation system and is responsible for the degradation of long-lived proteins, organelles and other cellular contents [29]. Moreover, autophagy is an important mechanism of ERAD and participates in the degradation of misfolded proteins and protein aggregates following ER stress [30]. However, prolonged autophagy may lead to cell death and is specifically termed autophagy-dependent cell death [31]. The role of autophagy in retinal light injury is controversial. Autophagy might be a double-edged sword among the molecular mechanisms that lead to retinal light damage. Midorikawa et al. reported that moderate autophagy combined with endosomal degradation pathway activity is neuroprotective and attenuates light-dependent retinal degeneration [32]. However, Zhang et al. showed that over-activated autophagy is detrimental to light damaged photoreceptors and that suppressing autophagy with 3-methyladenine (3MA) may protect photoreceptors against light injury [33]. Therefore, further clarifying the role of autophagy in retinal light injury is still necessary and whether autophagy activation is related to ER stress-related pathways needs further investigation.

Previous studies employing histopathological analysis of retinal sections have shown that visible light-induced damage predominantly occurs in the outer layer of the retina, especially in the layer of photoreceptor cells and pigment epithelial cells [3, 34]. Therefore, in this study the light-induced death mechanism was investigated with *in vitro* experiments using two kinds of cell lines: photoreceptor cells (661W) and pigment epithelial cells (ARPE-19). The *in vivo* experiments, specifically focused on light-induced alternations in the outer layer of the retina and the RPE layer, in order to determine the changes in the retina and RPE/choroid mixture. It was found that visible light exposure caused severe photo-oxidative-stress damage in photoreceptors and RPEs following ER stress-related autophagy and that inhibiting oxidative stress with the antioxidant N-acetyl-L-cysteine (NAC) suppressed ER stress caused by light

exposure and protected cells against light damage. In addition, either directly inhibiting prolonged autophagy with 3MA or suppressing over-activated autophagy by inhibiting ER stress (knockdown PERK or treated with SAL, an ER stress inhibitor) also protected photoreceptors and RPE cells from light injury. Finally, the potent role of ER stress-related autophagy was further verified with *in vivo* experiments. This study suggests that visible light exposure may cause prolonged autophagy in photoreceptors and RPE cells and that suppressing ER stress-related autophagy may effectively protect the retina against light injury. Furthermore, this research deciphered the molecular mechanisms involved in retinal light injury, which may lay the experimental foundation for further development of neuroprotective drugs for light damage-related retinal degenerative diseases.

RESULTS

Light exposure induces oxidative stress in photoreceptors and RPE cells

Photo-oxidative-stress damage may be the initial step triggering neuronal death in the outer layer of the retina, the imbalance of the cellular redox status induced by light exposure was first evaluated by exposing 661W cells and ARPE-19 cells to 1500 Lux light for 1–3 days. The induced isomer of heme oxygenase, HO-1 is a protein marker that indicates cellular redox status [35] and was quantitatively determined via western blot. As shown in Figure 1, light exposure led to the gradual

activation of HO-1 from 1 to 3 days. The level of HO-1 was significantly elevated, even on the first day of light exposure, compared with the level in the dark control group ($P < 0.05$), and reached a peak on the third day. Reduced glutathione (GSH) and oxidized glutathione (GSSG) make up an important intracellular defense system for anti-oxidation, thus GSH and GSSG levels were determined, and the ratio of GSH/GSSG was calculated. As shown in Figure 2B, the ratio of GSH/GSSG was significantly decreased on the third day after light exposure compared with the GSH/GSSG ratio in the dark control group ($P < 0.05$), suggesting a severe imbalanced redox status in the cells caused by light exposure. In addition, to further verify the role of oxidative stress in the death pathway, the protective effect of suppressing oxidative stress on light-damaged cells was examined using the antioxidant, NAC. As shown in Figure 2A and 2C, NAC treatment (5 mM for 661W cells and 2.5 mM for ARPE-19 cells) significantly reduced intracellular ROS generation and the level of HO-1, but increased the ratio of GSH/GSSG on the third day of light exposure compared to the vehicle group ($P < 0.05$). Most importantly, treatment with NAC (5 mM for 661W cells and 2.5 mM for ARPE-19 cells) significantly attenuated the percentage of cell death caused by light damage compared with the light-damaged vehicle group ($P < 0.05$; Figure 2D). Taken together, these results suggest that light exposure leads to severe oxidative-stress injury in photoreceptors and RPE cells, and may function as an upstream step triggering the subsequent activation of the death cascade.

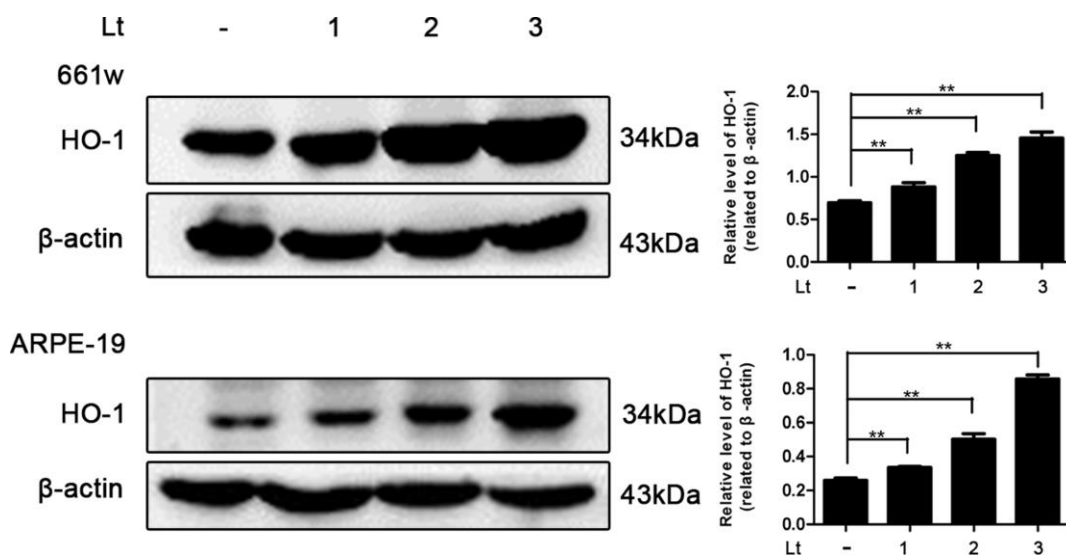


Figure 1. Light exposure increases the level of HO-1 in photoreceptors and RPEs. 661W cells/ARPE-19 cells were cultured in dark conditions or exposed to 1500 Lux light for 1–3 days. The level of HO-1 protein in the whole cell lysate was determined with western blotting, and β-actin was referenced as an internal control. Three independent experiments are conducted two weeks apart. The results are presented as the mean ± SEM. n (per group) = 3, ** $P < 0.01$.

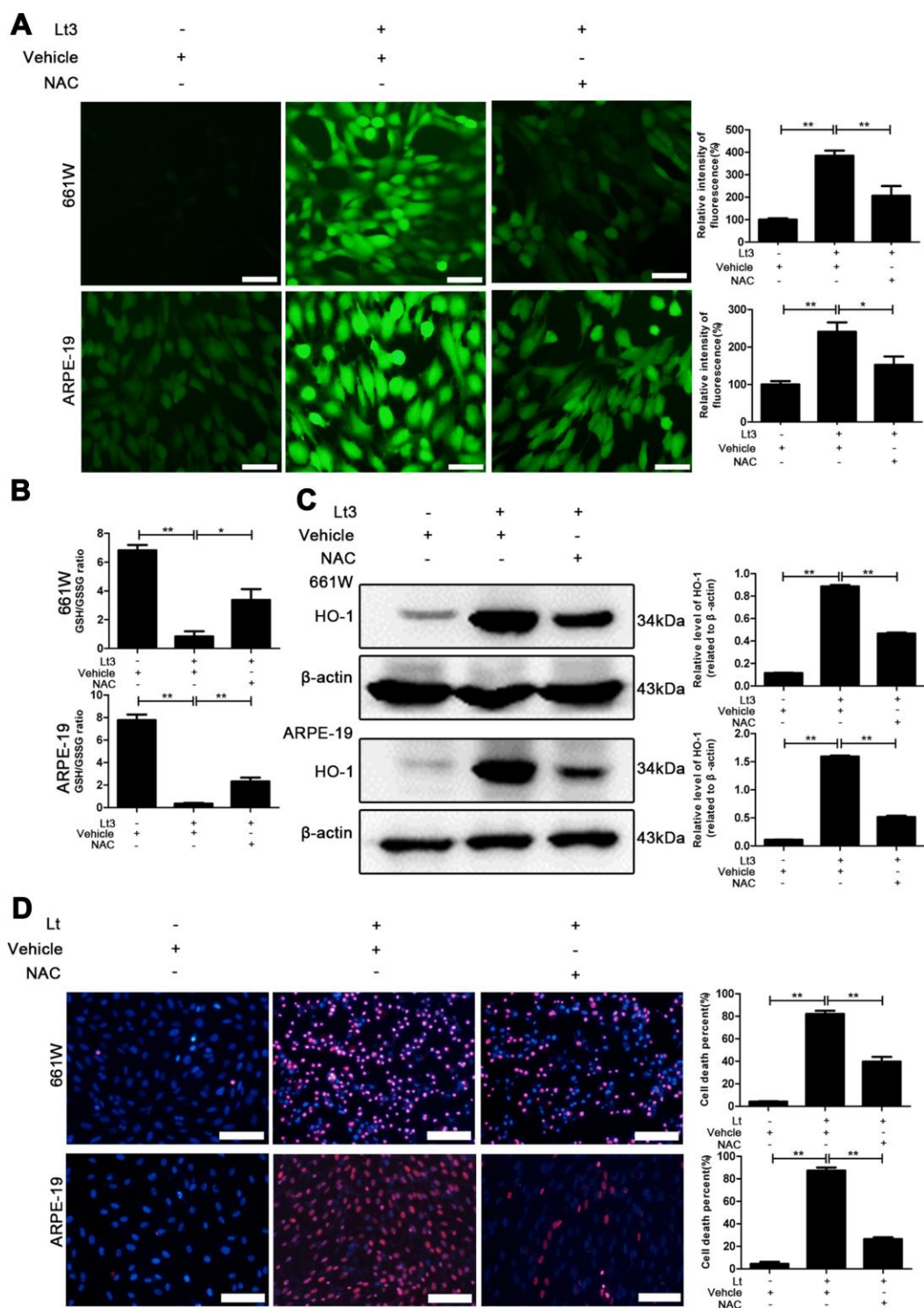


Figure 2. NAC treatment suppresses light-induced oxidative stress. 661W cells/ARPE-19 cells were pretreated with NAC (5 mM for 661W cells and 2.5 mM for ARPE-19 cells) or vehicle and cultured under light/dark conditions for 3 days. **(A)** The intracellular ROS were stained with DCFH-DA fluorescent probe identified by green fluorescence. Scale bar=50 μ m. Relative fluorescence intensities were calculated and compared. **(B)** The GSH/GSSG ratio was measured with a GSH/GSSG Assay Kit. **(C)** The HO-1 level was determined with western blotting, and β -actin was referred as an internal control. **(D)** 661W cells pretreated with 5 mM NAC/vehicle were cultured under light/dark conditions for 3 days. ARPE-19 cells pretreated with 2.5 mM NAC/vehicle were cultured under light/dark conditions for 6 days. The cell death percentage was evaluated with PI/Hoechst staining. Scale bar=100 μ m. The percentage of cell death was calculated as PI-positive cells/total cells%. Three independent experiments are conducted two weeks apart. The results are presented as the mean \pm SEM. n (per group) =3, *P < 0.05, **P < 0.01.

Light exposure induces ER stress in photoreceptors and RPE cells

Excessive ROS in cells may lead to depletion of the GSH pool and compromise of the function of PDI, which disrupts the folding process of proteins in the ER, causing the accumulation of unfolded or misfolded proteins and triggering ER stress [16]. Therefore, the markers in three signal pathways of ER stress were determined after 661W and ARPE-19 cells were exposed to 1500 Lux light for 1–3 days. As shown in Figure 3, light exposure significantly caused activation of cleaved-ATF6, p-IRE1a/IRE1a, p-PERK/PERK, p-EIF2a/EIF2a, ATF4 and CHOP compared with the dark control group. The levels of these markers reached a peak on the third day of light exposure indicating that light exposure indeed induces ER stress in photoreceptors and RPE cells. To further assess the role of ER stress in the light-induced cell death pathway, salubrinal (SAL), an ER stress inhibitor, was used to suppress ER stress under light-exposure conditions. As shown in Figure 4A, treatments with SAL (1 μ M, 10 μ M, 20 μ M, and 50 μ M) were protective against light damage compared with the vehicle group, as determined using the PI/Hoechst staining assay. The optimum SAL concentration, which provided the best protection against light damage and led to the lowest cell death rate was around 20 μ M for 661W cells and 10 μ M for ARPE-19s. Treatment with SAL (20 μ M for 661W cells and 10 μ M for ARPE-19s) consistently suppressed the activation of ER stress, reducing the levels of cleaved-ATF6, p-IRE1a/IRE1a, p-PERK/PERK, p-EIF2a/EIF2a, ATF4 and CHOP after 3 days of light exposure compared with the light vehicle group (Figure 4B). However, treatment with SAL under dark conditions

caused a slight increase in p-EIF2a ($P < 0.05$, vs dark vehicle group), suggesting that SAL is pharmacologically functional since SAL treatment may prevent EIF2 α dephosphorylation by inhibiting the protein complex GADD34/protein phosphatase 1 (PP1) [36]. The correlation between oxidative stress and ER stress under the light-exposed condition was then examined. As shown in Figure 5, treatment with the antioxidant NAC (5 mM for 661W cells and 2.5 mM for ARPE-19s) significantly suppressed ER stress, markedly reducing the levels of cleaved-ATF6, p-IRE1a/IRE1a, p-PERK/PERK, p-EIF2a/EIF2a, ATF4 and CHOP on the third day of light exposure compared with the vehicle group, which suggests that light induced-oxidative stress might be the upstream step, prior to ER stress, in the death cascade.

Autophagy is over-activated in cells under light conditions

Prolonged ER stress may trigger autophagy-lysosome-dependent ERAD to remove accumulated abnormal proteins and protein aggregates thus, light-induced autophagy in photoreceptors and RPEs was further investigated. BECN1 is a widely used marker for assessing autophagy because it participates in the initial stage of autophagosome formation [37]. The transformation from LC3BI to LC3BII is another important process employed in the study of autophagy activation [38]. Klionsky et al suggested LC3BII / β -actin as an indicator for detecting autophagy [39]. As shown in Figure 6A, after 661W and ARPE-19 cells were exposed to light for 1–3 days, the levels of BECN1 and LC3BII in the light-damaged group significantly increased in a dose-dependent manner

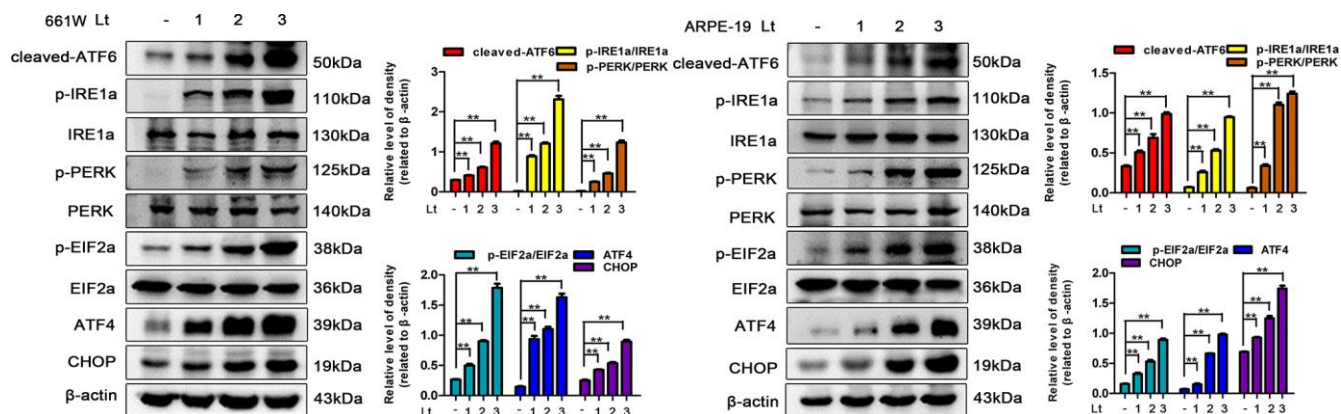


Figure 3. Light exposure induces ER stress in photoreceptors and RPEs. 661W cells and ARPE-19 cells were cultured in a dark condition or exposed to 1500 Lux light for 1–3 days after which the levels of ER stress markers were determined by western blotting. β -actin was referenced as an internal control. Three independent experiments are conducted two weeks apart. The results are presented as the mean \pm SEM. n (per group) = 3, ** $P < 0.01$.

compared with the dark control group ($P < 0.05$). In addition, the autophagic flux caused by light exposure was monitored. Hydroxychloroquine (HCO) may compromise the acidity of lysosomes. This interrupts autophagic clearance, which may cause the accumulation of LC3BII if the autophagic flux is blocked [38]. As shown in Figure 6B, treatment with 20 μM HCO remarkably caused the accumulation of LC3BII in 661W cells and ARPE-19s under the light-exposure condition compared with the light vehicle group ($P < 0.05$), indicating that light exposure induces a complete autophagic process, which may be blocked by HCO treatment. In addition, p62, another marker protein of autophagy, whose expression level was negatively correlated with autophagy flux, was detected [40–42]. As shown in Figure 6B, the level of p62 in the light damaged group was significantly lower than in the

dark control group, and HCO treatment was able to attenuate the decrease of p62 under the light exposure condition, indicating that light exposure induced autophagy and increased autophagy flux. Next, the role of autophagy in the light-induced death cascade was investigated. As shown in Figure 6C, treatment with 3-methyladenine (3MA; 2.5 mM for 661W cells, 1 mM for ARPE-19 cells) significantly reduced the levels of BECN1 and LC3BII in the cells exposed to light for 3 days compared with the light vehicle group and remarkably reduced the cell death rate assessed by PI/Hoechst staining under the light-exposed condition, as shown in Figure 6D. However, the levels of BECN1 and LC3BII in the 3MA-treated light-exposed group were still slightly higher than those in the vehicle dark group, suggesting that 3MA treatment simply suppresses over-activated autophagy caused by light exposure.

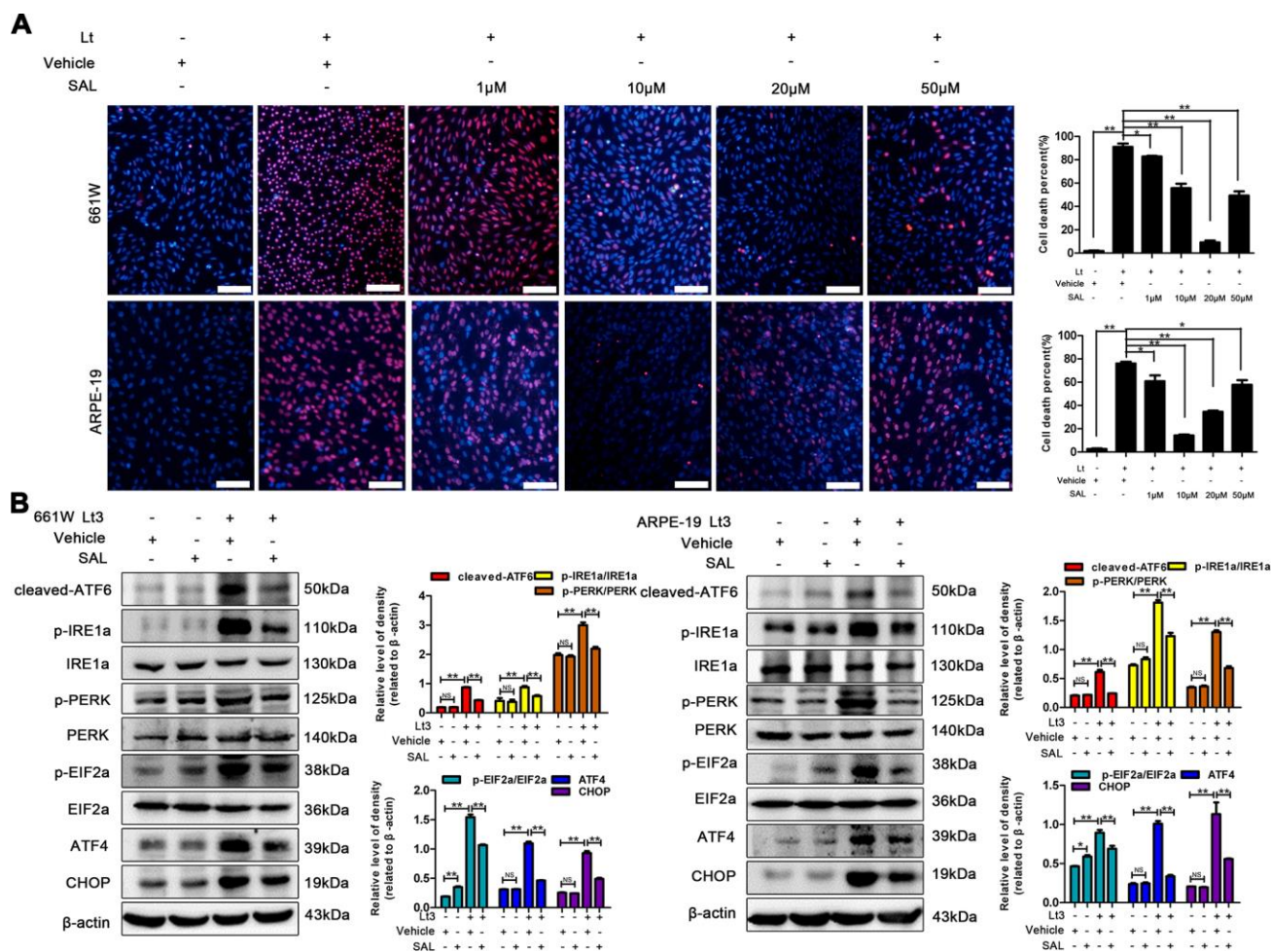


Figure 4. SAL treatment suppresses light-induced ER stress and protects photoreceptors and RPEs. (A) 661W cells/RPE cells were treated with SAL (1 μM , 10 μM , 20 μM and 50 μM) and cultured under 1500 Lux light or dark conditions for the indicated times. The percentage of cell death was evaluated with PI/Hoechst staining. Scale bar=100 μm . (B) The cells were treated with SAL (20 μM for 661W cells; 10 μM for ARPE-19 cells) or vehicle and cultured under light/dark conditions for 3 days, after which the levels of ER stress markers in the whole cell lysate were determined with western blotting, and β -actin was referenced as an internal control. Three independent experiments are conducted two weeks apart. The results are presented as the mean \pm SEM. n (per group) =3, NS: no significance, * $P < 0.05$, ** $P < 0.01$.

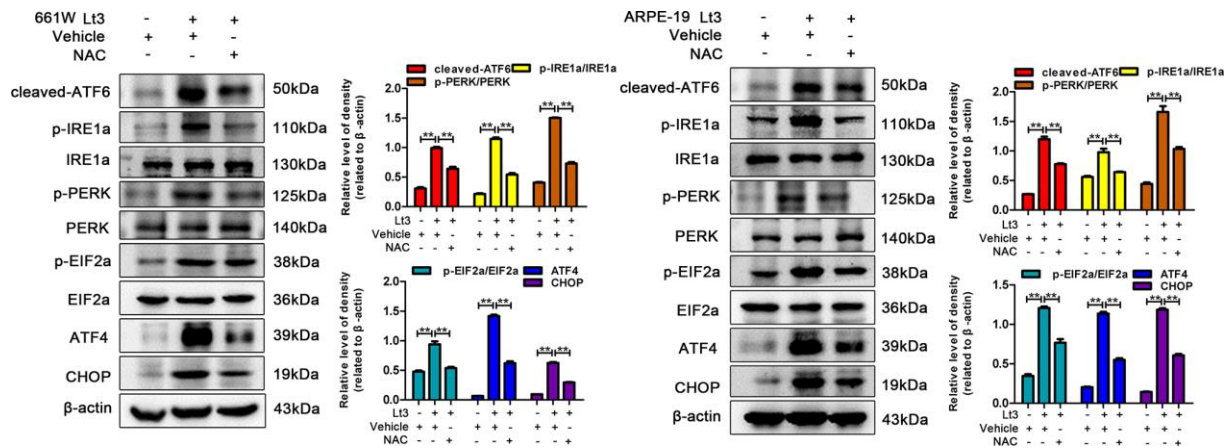


Figure 5. NAC treatment suppresses light-induced ER stress in photoreceptors and RPEs. The cells were treated with NAC (5 mM for 661W cells; 2.5 mM for ARPE-19 cells) or vehicle and cultured under light/dark conditions for 3 days, the levels of ER stress markers were determined with western blotting, and β -actin was referenced as an internal control. Three independent experiments are conducted two weeks apart. The results are presented as the mean \pm SEM. n (per group) = 3, **P < 0.01.

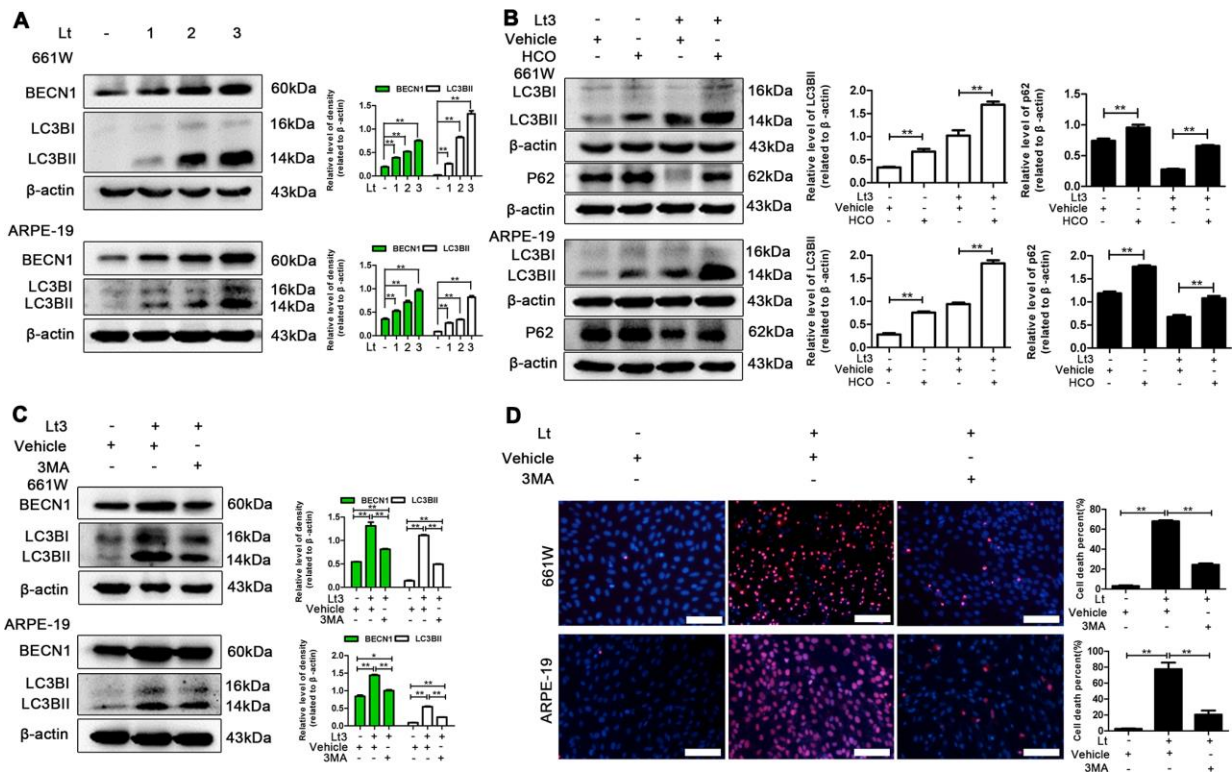


Figure 6. Inhibiting light-induced prolonged autophagy is protective. (A) 661W cells/ARPE-19 cells were cultured in a dark condition or exposed to 1500 Lux light for 1–3 days. The levels of BECN1 and LC3BII in the whole cell lysate was determined with western blotting, and β -actin was referenced as an internal control. (B) After 661W cells and ARPE-19 cells were treated with HCO (20 μ M) or vehicle and cultured under light/dark conditions for 3 days, the level of LC3BII and P62 in the whole cell lysate were determined with western blotting, and β -actin was referenced as an internal control. (C) The cells were treated with 3MA (2.5 mM for 661W cells; 1 mM for ARPE-19) or vehicle and cultured under light/dark conditions for 3 days. The level of BECN1 and LC3BII in the whole cell lysate were determined with western blotting, and β -actin was referenced as an internal control. (D) 661W cells pretreated with 2.5 mM 3MA/vehicle were cultured under light/dark conditions for 3 days. ARPE-19 cells pretreated with 1 mM 3MA/vehicle were cultured under light/dark conditions for 6 days. The percentage of cell death was evaluated with PI/Hoechst staining. Scale bar=100 μ m. Three independent experiments are conducted two weeks apart. The results are presented as the mean \pm SEM. n (per group) = 3, *P < 0.05, **P < 0.01.

Inhibiting ER stress suppresses autophagy and protects cells under light conditions

To further verify whether light exposure induces ER stress-related autophagy, ER stress was further suppressed with SAL and the influence of ER stress on autophagy activation was examined. As shown in Figure 7, treatment with SAL significantly reduced the levels of BECN1 and LC3BII compared with the vehicle light damaged group ($P < 0.05$), indicating that suppressing ER stress may block the light-induced activation of autophagy. Previous studies have shown that the PERK signal may participate in activation of ER-related autophagy. Therefore, in the current study, PERK activity was suppressed using one of the following two methods: knocking down PERK expression with lentivirus-mediated shRNA in 661W cells or treatment with GSK2606414 (GSK), a specific inhibitor of PERK in ARPE-19 cells. As shown in Figure 8A, the expression of PERK in 661W cells was significantly knocked down by the specific shRNA (sh-PERK) compared with the negative control (NC) group ($P < 0.05$). In addition, activation of the downstream factors of the PERK pathway (p-PERK/PERK, p-EIF2a/EIF2a, ATF4 and CHOP) was also markedly suppressed under the light-exposed condition. Similarly, treatment with GSK also significantly suppressed

activation of the PERK signal in RPE cells under the light-exposed condition, as shown in Figure 8B, causing obvious reductions in the levels of p-PERK/PERK, p-EIF2a/EIF2a, ATF4 and CHOP compared with the vehicle light damaged group. Next, the influence of PERK inhibition on the activation of autophagy was assessed. Figure 8B shows that both PERK knockdown and GSK treatment caused significant reduction in the levels of BECN1 and LC3BII in light-exposed cells compared with the light vehicle group ($P < 0.05$). Furthermore, the influence of PERK inhibition on light-induced autophagy flux was evaluated by tracking mCherry-GFP-LC3B double labeled autophagosomes expressed by adenoviruses. The green fluorescence of GFP-labeled LC3B is quenched due to the acidic environment after autophagosomes integrate with lysosomes. Therefore, the autolysosomes with mCherry-GFP double labeled-LC3B simply turn red (the color of cherries). However, when autophagy is blocked, the number of autolysosomes is reduced and some autophagosomes with mCherry-GFP double labeled-LC3B show the overlaid yellow color. As shown in Figure 9A, the number of autolysosomes was greatly reduced in the cells with PERK inhibition. Some autophagosomes show the overlaid yellow color, yet a large number of autolysosomes in the control cells show the red color, indicating that either PERK knockdown

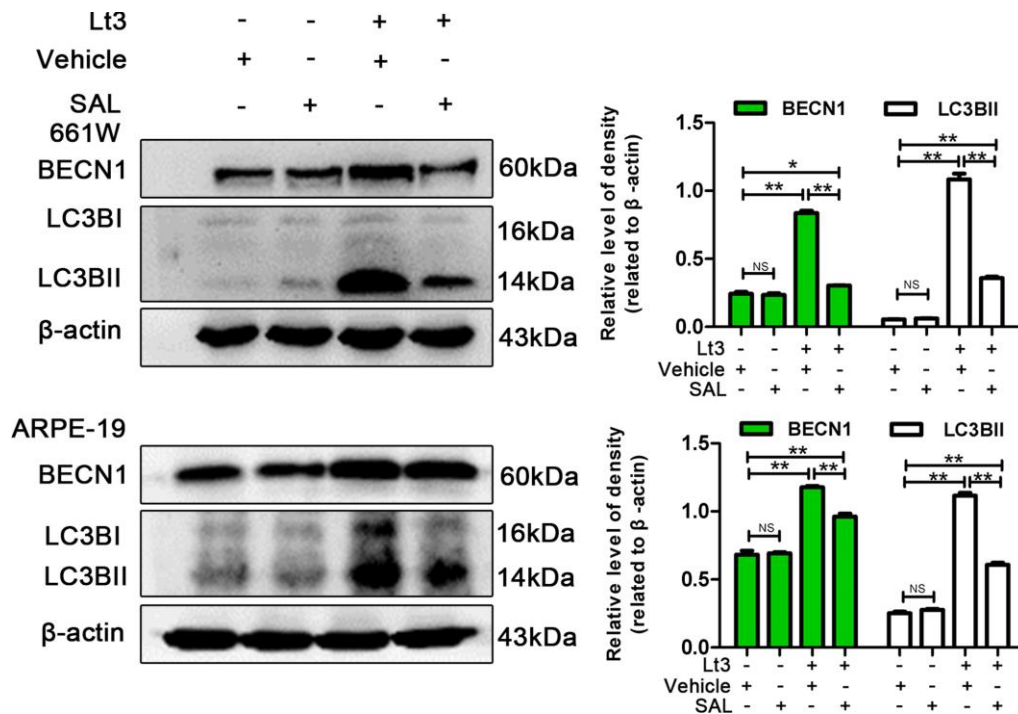


Figure 7. Inhibiting ER stress suppresses light-related autophagy. 661W cells/ARPE-19 cells were treated with SAL (20 μ M for 661W cells; 10 μ M for ARPE-19 cells) or vehicle and cultured under light/dark conditions for 3 days. The level of BECN1 and LC3BII in the whole cell lysate were determined with western blotting, and β -actin was referenced as an internal control. Three independent experiments are conducted two weeks apart. The results are presented as the mean \pm SEM. n (per group) = 3, NS: no significance, * $P < 0.05$, ** $P < 0.01$.

or GSK treatment may block autophagy. Importantly, PERK knockdown and GSK treatment significantly reduced the death rate in 661W and ARPE-19 cells in the light-exposed condition as evaluated with PI/Hoechst staining, as shown in Figure 9B. Taken together, these results suggest that inhibiting ER stress via PERK signal may suppress light-induced prolonged autophagy, and that inhibiting ER stress-related autophagy protects photoreceptors and RPE cells against light damage.

Suppressing ER stress inhibits prolonged autophagy and protects the retina against light injury

Next, ER stress-related autophagy was verified in light-injured retinas of mice. As shown in Figure 10A, intensive light exposure for 12 h caused a significant increase in the levels of ER stress markers, including cleaved-ATF6, p-IRE1a/IRE1a, p-PERK/PERK, p-EIF2a/EIF2a, ATF4 and CHOP, and elevated the levels

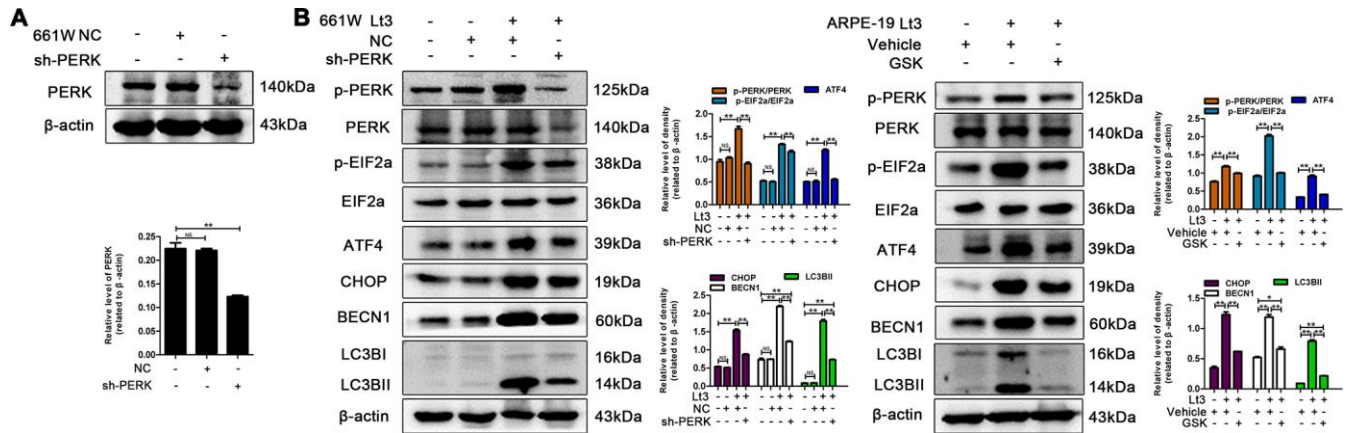


Figure 8. Inhibiting PERK suppresses light-related autophagy. (A) 661W cells were infected with lentivirus-expressed PERK shRNA (sh-PERK) or negative control shRNA (NC). The level of PERK in the whole cell lysate was determined with western blotting, and β-actin was referenced as an internal control. (B) 661W cells with stable PERK knockdown/ARPE-19 cells treated with GSK (5 μM) or vehicle were cultured under light/dark conditions for 3 days. The target proteins in the whole cell lysate were determined with western blotting, and β-actin was referenced as an internal control. Three independent experiments are conducted two weeks apart. The results are presented as the mean ± SEM. n (per group) = 3, NS: no significance, *P < 0.05, **P < 0.01.

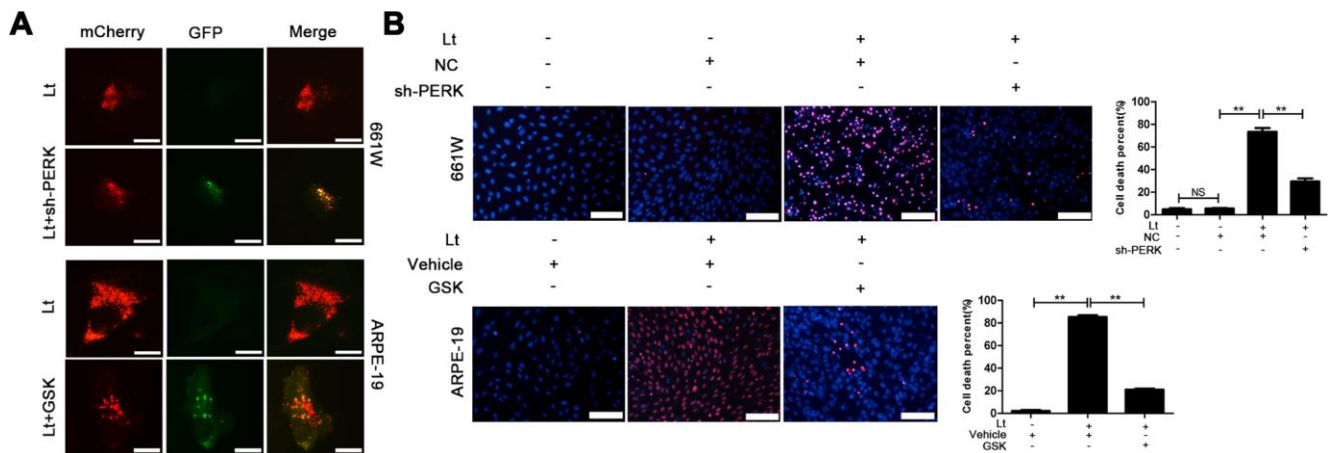


Figure 9. Inhibiting PERK blocks autophagic flow and protects the light-damaged cells. (A) 661W cells with stable PERK knockdown and ARPE-19 cells were infected with mCherry-GFP double labeled-LC3B mediated by adenovirus. At 48 h after infection, the ARPE-19 cells were treated with GSK (5 μM) or vehicle. The cells were cultured under 1500 Lux light condition for 3 days and photographed under fluorescence microscopy. Scale bar = 20 μm. (B) 661W cells with PERK knockdown were cultured under light/dark conditions for 3 days, but ARPE-19 cells treated with GSK (5 μM) or vehicle were cultured under light/dark conditions for 6 days. The percentage of cell death was evaluated with PI/Hoechst staining. Scale bar = 100 μm. Three independent experiments are conducted two weeks apart. The results are presented as the mean ± SEM. n (per group) = 3, NS: no significance, **P < 0.01.

of autophagy markers BECN1 and LC3BII in both the retina and RPE/choroid samples compared to the control samples as determined with western blot. However, intraperitoneal injection of SAL significantly suppressed the light-induced activation of ER stress and autophagy, resulting in reduced levels of cleaved-ATF6, p-IRE1a/IRE1a, p-PERK/PERK, p-EIF2a/EIF2a, ATF4, CHOP, BECN1 and LC3BII compared with the light-damaged vehicle group ($P < 0.05$; Figure 10A). In addition, light-induced retinal injury was quantitatively evaluated by measuring the level of rhodopsin, a marker of photoreceptors, and RPE65, a marker of RPE cells. Figure 10A shows that intensive light exposure resulted in marked damage to photoreceptors and RPEs,

significantly reducing the levels of rhodopsin and RPE65, while SAL injection markedly attenuated the decreased levels of these two markers compared with the light-damaged vehicle group ($P < 0.05$). Moreover, histological analysis showed that light exposure caused obvious structural disorders in the ONL of the retina and significantly reduced the thickness of the ONL, while SAL injection attenuated the light-induced decrease of ONL thickness and maintained the normal structure of the retina (Figure 10B). These results suggest that excessive light exposure may cause ER stress and prolonged autophagy in the retina; however, suppressing ER stress may inhibit over-activated autophagy and protect the retina against light injury.

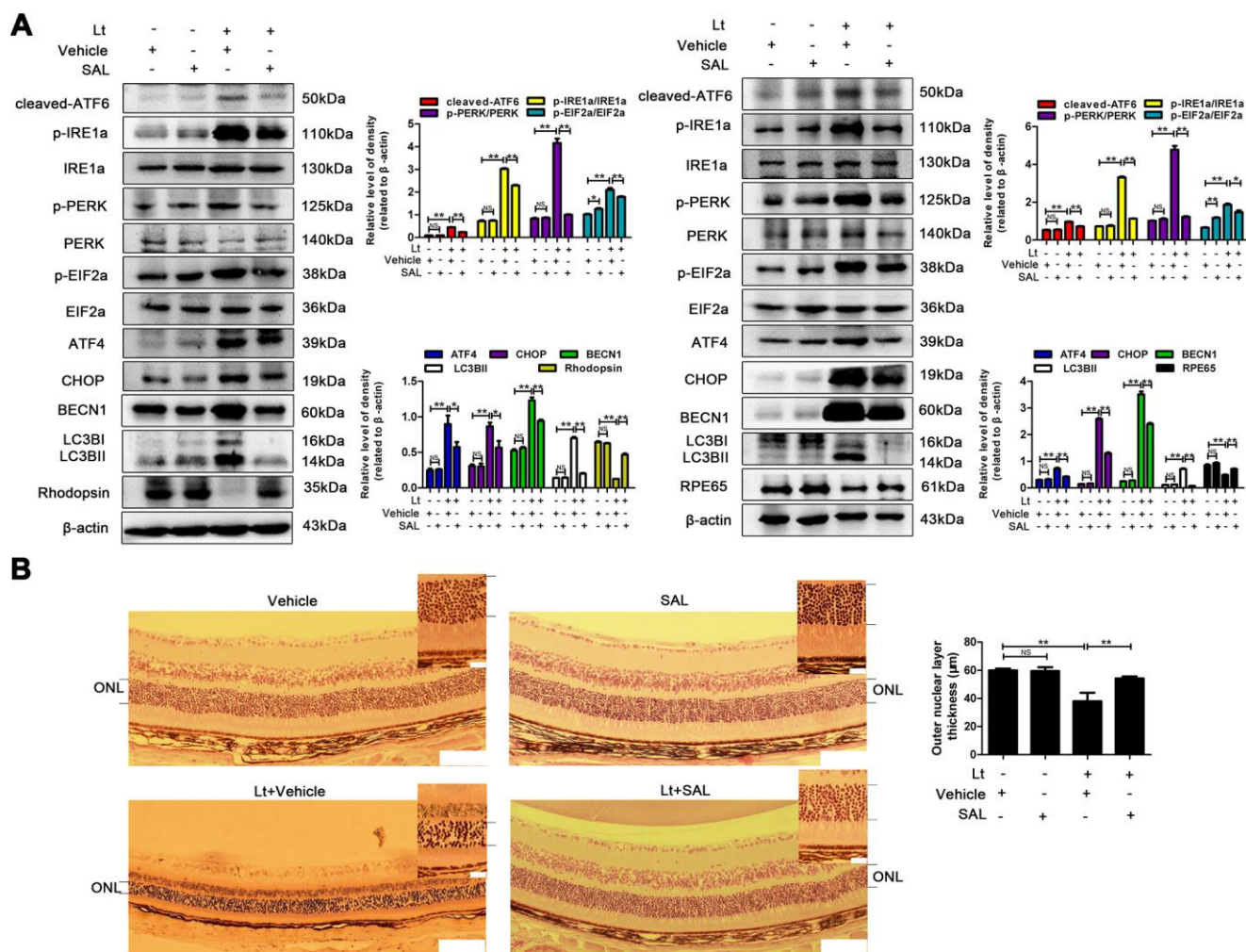


Figure 10. Suppressing ER stress inhibits prolonged autophagy and protects the retina against light injury. The mice were intraperitoneally injected with a dose of 1 mg/kg once a day for 7 days. On the third day of administration, the mice were exposed to continuous 7000 Lux visible light for 12 h. After light exposure, the mice were fed in the animal room with the normal light/dark cycle. On the fifth day of light exposure, the mice were sacrificed, and the eyeballs were enucleated. (A) The retinas were collected, and target proteins were determined with western blotting. β -actin was referenced as an internal control. Three independent experiments are conducted three weeks apart. The results are presented as the mean \pm SEM. n (per group) = 3, NS: no significance, * $P < 0.05$, ** $P < 0.01$. (B) The retinas were sectioned and stained with H&E and photographed under a microscope. Scale bar = 100 μ m; 20 μ m. The thickness of the outer nuclear layer (ONL) was measured and quantitatively analyzed. The results are presented as the mean \pm SEM, n (per group) = 6, NS: no significance, ** $P < 0.01$.

DISCUSSION

The death of photoreceptors/RPEs is the principal event in the pathogenesis of AMD, and it is known that the excessive exposure to natural or unnatural light may accelerate this death or the death process [8]. Schick reported that sunlight exposure during working life is an important risk factor for AMD [43] and Sui reported that individuals with more sunlight exposure are at a significantly increased risk of AMD [11]. Photoreceptors and RPE cells are rich in photosensitizers [3, 44]. The excessive electromagnetic energy of photons is absorbed by these photosensitizers, which may break the bonds of other molecules via direct electron exchange or hydrogen exchange and generate excessive free radicals [2, 3]. In this study, oxidative-stress damage caused by visible light exposure in photoreceptors (661W cells) and RPE cells (ARPE-19 cells) was verified by the increased HO-1 and the decreased GSH/GSSG ratio. These results suggest that light exposure led to a severe redox imbalance in the cells and that suppressing oxidative stress with the antioxidant NAC protects photoreceptors and RPE cells against light damage. Light-induced oxidative damage might be an important step in the pathogenesis of light-related retinal diseases, especially in AMD, in which increased reactive oxygen species (ROS) production, and mitochondria dysfunction are observed together with increased abnormal protein aggregation and inflammation in the photoreceptor/RPE layer, leading to oxidative stress-induced damage to the retinal pigment epithelium which is considered to be a key factor in the pathogenesis of AMD [45].

When the cells are undergoing oxidative stress, the chaperones available for protein folding are inactivated, and the disulfide bond reduction needed for ER-associated degradation is impeded. Together, these may lead to accumulation of unfolded or misfolded proteins and trigger UPR [46]. In the current study, it was demonstrated that continuous light exposure markedly induced the activation of UPR both *in vitro* and *in vivo*. The levels of key factors in the UPR signal pathway, including cleaved-ATF6, p-IRE1a/IRE1a, p-PERK/PERK, p-EIF2a/EIF2a, ATF4 and CHOP, were significantly increased in both photoreceptors/RPE and the retina after visible light exposure. In addition, treatment with the ER stress inhibitor SAL significantly suppressed the elevated levels of ER stress markers and attenuated light-induced cell death and injury in the retina. To verify the relationship between the oxidative stress and ER stress, the influence of the antioxidant, NAC on UPR signals was further investigated. The results showed that treatment with NAC may significantly suppress the light-induced activation of ER stress, indicating that photo-oxidation might be the

upstream step prior to the activation of UPR in the light-induced death cascade in photoreceptors/RPEs.

Moderate UPR is beneficial for sustaining cellular homeostasis by reducing the synthesis of unfolded or misfolded proteins. However, prolonged UPR may trigger the downstream death signal, leading cells to a programmed death [18]. Previous studies have reported that autophagy is involved in the pathogenesis of light-related retina degeneration diseases, such as AMD. Therefore, the light-induced cell death pattern and the role of autophagy in the light-induced death cascade was examined and activation of autophagy was detected in both light-injured *in vitro* and *in vivo* models. The levels of typically autophagic markers, BECN1 and LC3BII were significantly increased after light exposure. Furthermore, the results of the LC3B turnover assay and p62 degradation assay suggest that the light-induced autophagic flux, which encompasses autophagosome formation and the late phases of autolysosome formation, in photoreceptors/RPEs increased. More importantly, it was also verified that blocking autophagy with specific inhibitor 3MA was neuroprotective against light damage in photoreceptors/RPEs. This evidence strongly suggests that autophagy is over-activated in light-damaged cells. Previous studies have shown that AMD is a multifactorial disease of the retina featured by degeneration and loss of photoreceptors and RPE cells and that autophagy is involved in its pathology. Although some studies suggest that the decline of autophagy with age contributes to the age-related disease [39], there is currently no consensus on whether autophagic activity increases or decreases with age and AMD. Kozhevnikova et al. reported that the basal level of autophagy is elevated during the early stage of retinopathy and declines at progressive stages [47]. The autophagy process is increased in two mouse models of AMD and in early-onset human AMD samples but declines in late AMD [48]. Results of the current study suggest that prolonged autophagy damages photoreceptors and RPEs in light exposure conditions, and that suppressing overactivated autophagy is neuroprotective against light injury; this may be a potential therapeutic strategy for early AMD.

The excessive accumulation of misfolded proteins and protein aggregates in cells may trigger ER stress, yet autophagy is an important mechanism for degrading abnormal proteins. Recent studies have shown that both ER stress and autophagy are involved in the pathogenesis of retinal degenerative diseases [49]. Therefore, the relationship between ER stress and autophagy in light-damaged photoreceptors/RPEs was further investigated. The results showed that either pharmacologically inhibiting PERK with GSK

treatment (a specific inhibitor) or genetically knocking down PERK with lentivirus expressed shRNA significantly suppressed light-induced autophagy, reducing the level of BECN1 and LC3BII, indicating that light-induced ER stress may be closely related to autophagy and that the PERK signal may be a major pathway activating ER stress-related autophagy. ER stress-related autophagy was further verified with *in vivo* experiments. Intraperitoneal injection of SAL (an ER stress inhibitor) markedly suppressed the activation of light-induced autophagy and attenuated light-induced ONL thickening in mice retinas. Wafa et al. reported that ATF4, the downstream factor of PERK, may function as a transcription factor directly or in cooperation with CHOP increasing the expression of various autophagy-related genes, including LC3B, ATG5, Atg7, and Beclin1, in mouse embryonic fibroblasts under amino acid-starved conditions [50]. Thus, further experiments are needed to verify the more detailed signal links involved in ER stress-related autophagy in the light-induced death cascade.

In conclusion, the current study demonstrated that ER stress and autophagy are both involved in light-induced death of photoreceptors and RPE cells. As an upstream step, photo-oxidation may cause an imbalance in the cellular redox status and interrupt the folding process of proteins, further triggering ER stress in photoreceptors and RPEs. Suppressing ER stress via PERK signals may inhibit prolonged autophagy and protect photoreceptors/RPEs against light damage. Inhibiting ER stress-related autophagy is neuroprotective for retina against light injury, which may be a potential treatment strategy for AMD.

MATERIALS AND METHODS

Ethics approval

All animal experiments were performed according to the Association of Research in Vision and Ophthalmology (ARVO) statement regarding the use of animals in ophthalmology and vision research. The animal experiments were performed according to the protocols approved by the Institutional Animal Care and Use Committee and the Ethics Committee of the Second Hospital of Jilin University, Changchun, China (approval number: 2018038).

Reagents and materials

Cell culture media and additives were obtained from the HyClone Company (Beijing, China). N-acetyl-L-cysteine (>99%), Salubrinal, Hoechst/PI and a Reactive Oxygen Species Assay Kit were purchased from Beyotime Biotechnology (Shanghai, China). The 3-methyladenine

was purchased from Sigma-Aldrich (Shanghai, China). Hydroxychloroquine was purchased from Tokyo Chemical Industry (Shanghai, China). GSK2606414 (>99.38) was purchased from Med Chen Express (New Zealand, USA). PERK (Cat. No. 3192), IRE1a (Cat. No. 3294) and p62 (Cat. No. 5114) antibodies were purchased from Cell Signaling Technology (Shanghai, China). EIF2a (Cat. No. sc-133132) antibodies were acquired from Santa Cruz Biotechnology (Beijing, China). Rhodopsin (Cat. No. OM186133) antibodies were purchased from OmnimAbs (Shanghai, China). LC3B (Cat. No. ab192890) antibodies were purchased from Abcam (Cambridge, MA, USA). BECN1 (Cat. No. 11306-1-AP) antibodies were purchased from Proteintech (Wuhan, China). P-IRE1a (Cat. No. 13013), p-PERK (Cat. No. 12814), ATF6 (Cat. No. 24382), p-EIF2a (Cat. No. 11279), ATF4 (Cat. No. 32007), CHOP (Cat. No. 40744), RPE65 (Cat. No. 49495), β -actin (Cat. No. 21800) and secondary antibodies were obtained from Signalway Technology (St. Louis, MO, USA).

Cell culture

The 661W cell line was a gift from Dr. Muayyad Al-Ubaidi (University of Oklahoma Health Sciences Center, USA). The 661W cells were grown in Dulbecco's modified Eagle's medium (DMEM) supplemented with 10% heat-inactivated fetal bovine serum, 100 U/ml penicillin and 100 mg/ml streptomycin. ARPE-19 cells were purchased from the American Type Culture Collection (ATCC, USA) and maintained in Dulbecco's modified Eagle's medium/nutrient mixture F-12 (DMEM/F-12) supplemented with 10% FBS, 100 U/ml penicillin and 100 mg/ml streptomycin. The 661W cells were passaged by 0.05% trypsin-EDTA every 2–3 days. ARPE-19 was passaged by trypsin with 0.05% EDTA every 3–4 days. The cells were cultured in a humidified atmosphere of 95% air and 5% CO₂ at 37°C. Cell culture medium and additives were purchased from the HyClone Company (Beijing, China).

Visual light exposure

A standard 8-W fluorescent strip light was fixed in the incubator and covered with a filter to ensure that the cells were exposed to visible light (400–800 nm), and the distance between the light source and plates was 20 cm to ensure that all cells received the same intensity of light (1500 Lux, measured with a digital light meter, TES-1332A, Taipei, China). The light exposure experiment was performed as previously described [33]. Briefly, the cells were precultured in 96 or 6 well plates for 24 h, and light exposure was started until the cell confluence reached 75%. For the dark control group, a paper box was placed in the same incubator to create a dark chamber. The cell culture medium was replaced

every two days, and the temperature of the culture medium under dark or light conditions was maintained; no substantial difference in temperature was found between the two groups.

PERK knockdown with lentiviral-mediated short hairpin RNA (shRNA)

The lentivirus expressed short hairpin RNA (shRNA) targeting the PERK gene was constructed by GeneCopoeia (Shanghai, China), and the lentivirus-mediated scrambled shRNA was produced as a negative control. The interfering sequence specifically targeting the PERK gene was as follows: forward sequence 5'-CAGGTCCTGGTAATCATTCAAGAGAATGATTA CCAAGGACCTG-3'. The lentivirus particle was produced according to a previous protocol [51]. Briefly, a third-generation lentiviral package system was used to package lentivirus particles. Three auxiliary plasmids (pRRE, pRSV-Rev and pCMV-VSVG) and the core plasmid were mixed with lipo6000 transfection reagent (Beyotime Biotechnology, Shanghai, China) in proportion and then transfected into human embryonic kidney 293T (HEK293T) cells. After 72 h, virus particles were collected, and the virus particles were concentrated. The 661W cells were infected with the concentrated virus particles. To avoid toxicity, the virus medium was replaced with fresh complete DMEM medium 24 h after infection. To obtain cells with stable PERK knockdown, the cells were treated with puromycin (Beyotime, Biotechnology, Shanghai, China) at an initial concentration of 8 $\mu\text{g}/\text{mL}$ three days after the infection, and the puromycin containing medium was replaced with fresh complete medium 48 h after the screening program. After repeating the screening program three times, cell clones with stable PERK knockdown were obtained.

Autophagic flux measurement

The cells were infected with adenovirus-mediated mCherry-GFP-LC3B (Beyotime Biotechnology, Shanghai, China) to monitor autophagic flux, according to the commercial instructions. Briefly, the cells were precultured in a 96-well plate for 24 h, and then the medium was replaced with virus-fresh medium mixture (2 $\mu\text{l}/100 \mu\text{l}$). After culturing for 24 h, the virus medium was replaced with complete fresh medium, and the cells were further cultured for 24 h. After infection, the cells were exposed to the light condition, and then they were observed and photographed under an inverted fluorescence microscope (Olympus, Japan).

Propidium iodide (PI)/Hoechst staining

The cells were stained with Hoechst 33258 dye (2 $\mu\text{g}/\text{mL}$, Beyotime Biotechnology, Shanghai, China) for

30 min in the dark at 37°C, after which the cells were stained with PI (Beyotime Biotechnology, Shanghai, China) at a final concentration of 5 $\mu\text{g}/\text{mL}$ for 10 min in the dark at 4°C. The images were photographed under an inverted microscope (Olympus, Japan), and the images were quantitatively analyzed with Image J software (v1.51, NIH, USA). The cell death rate = PI-positive cells/total cells%.

Intracellular ROS measurement

The intracellular ROS level was determined with a dichloro-dihydro-fluorescein diacetate (DCFH-DA, Beyotime Biotechnology, Shanghai, China) staining assay. Briefly, the cells were precultured in 96-well plates for 24 h. Next, the cells were washed twice with fresh medium and then cultured with FBS-free medium containing 10 μM DCFH-DA for 20 min at 37°C in the dark. After washing twice with serum-free medium, the cells were observed and photographed under a fluorescence microscope (Olympus, Japan). Fluorescence intensities were quantitatively determined with ImageJ software (v1.51, NIH, USA). All of the images were converted to grayscale images and then inverted and calibrated while using ImageJ, and the mean fluorescence intensity was obtained by dividing the gray value of all pixels in the selected area by the number of pixels [52, 53]. The relative intensity of the fluorescence was calculated as a percentage of the fluorescence intensity of the vehicle cells.

Measurement of GSH/GSSG

The intracellular reduced/oxidized glutathione was quantitatively determined according to the commercial instructions of the GSH/GSSG Kit (Beyotime, Shanghai, China). Briefly, after 3 days of light exposure, the cells were washed twice with PBS and then harvested with a scraper and centrifuged at 1,000 rpm for 5 min at 4°C. The cell pellet was further resolved with reagent A (removing the cellular proteins) and frozen-thawed twice in liquid nitrogen and a 37°C water bath. The supernatant was collected after the cell mixture was centrifuged at 10,000 g for 10 min at 4°C for determining total glutathione and oxidized glutathione. To measure the total glutathione, solution B (containing GSH reductase, 5,5'-dithiobis-2-nitrobenzoic acid) was mixed with the supernatant and incubated at 25°C for 5 min. Then NADPH was added to the mixture to obtain a color reaction. Similarly, to measure GSSG, the cellular GSH was removed with a GSH scavenging reagent, and then the GSSG was determined following the above procedure. The absorbance at 412 nm was measured with a microplate reader (Tecan, Mannedorf, Switzerland). The concentrations of total glutathione and GSSG were

calculated from the standard curve. The ratio of GSH/GSSG was calculated with the formula, $GSH/GSSG = (Total\ glutathione - GSSG \times 2) / GSSG \%$

Western blot analysis

Cell, retina and RPE/choroid mixture samples were sonicated in protein lysate buffer (Beyotime, Shanghai, China) containing 1% protease inhibitor cocktails (Beyotime, Shanghai, China). A bicinchoninic acid assay was used to measure the protein concentration. An equal amount (20 µg) of cell lysate was dissolved in the sample buffer, after which samples were boiled for 6 min. After denaturation, electrophoresis was performed with 10% polyacrylamide gels containing 0.1% SDS, and then proteins were transferred to nitrocellulose membranes. The membranes were blocked with 5% non-fat dry milk in Tris-buffered saline with 0.1% Tween-20 (TBS-T) for 1 h at room temperature and rinsed in TBS-T three times. Then the membranes were subsequently incubated with the specific primary antibody overnight at 4°C. The membranes were washed three times with TBS-T and incubated with the corresponding biotinylated secondary antibodies for 1 h at room temperature. Signals were subsequently developed using enhanced chemiluminescence, after which images were captured using a microscope equipped with a CCD camera (Tanon, Shanghai). Finally, the band density of proteins was calculated with the ImageJ software (v1.51, NIH, USA).

Animals

Six-week-old male C57BL/6J mice were purchased from the Animal Center of Jilin University (Changchun) and maintained with free intake of food and water, the indoor temperature was maintained at 21°C–23°C, and a 12 h light/dark cycle was guaranteed.

SAL treatment and light exposure protocol

The mice were divided into four groups: vehicle group (n=6), SAL-treated group (n=6), light-damaged vehicle group (n=6), and light-damaged SAL-treated group (n=6). SAL (dissolved in 1% DMSO saline) was intraperitoneally injected with a dose of 1 mg/kg once a day for 7 days. On the third day of administration, the pupils were dilated with 1% Atropine eye drops, and the mice were exposed to continuous 7000 Lux visible light for 12 h. After light exposure, the mice were fed in the animal room with the normal light/dark cycle. On the fifth day of light exposure, the mice were sacrificed by intraperitoneal injection of excessive pentobarbital sodium, and the eyeballs were enucleated. One eye was sectioned for further histological analysis, and another eye's retina was collected for western blot analysis.

RPE/choroid mixture isolation

The RPE/choroid mixture was separated according to a previous protocol [54]. Briefly, the cornea and lens from enucleated eyeballs were carefully removed under a surgery microscope, and then the retina and the soft tissue surrounding the sclera were removed. After sonication in RIPA lysis buffer containing 1% protease inhibitor cocktails at 4°C, the sclera tissue was separated from the RPE/choroid by centrifuge at 10,000 rpm. The supernatant containing RPE/choroid proteins was collected and stored at -20°C for western blot analysis.

Histological analysis

The enucleated eyeballs were marked at 12 o'clock with a surgical suture and fixed with 4% paraformaldehyde solution for 24 h at room temperature. After fixation, the eyeball was rinsed twice with PBS and dehydrated with gradient concentrations of alcohol. Next, the eyeballs were plastically embedded and sectioned, and the retina was sliced along the sagittal plane. The retina slice was stained with hematoxylin and eosin (H&E), and the thickness of the outer nuclear layer at 0.5 mm apart from the optic nerve head was measured with Image J software (v1.51, NIH, USA). The morphological structure of the retina and RPE was observed and photographed under a microscope.

Statistical analysis

Statistical analysis was performed with SPSS v 23.0 (SPSS, Chicago, Illinois, USA), and each experiment was repeated at least three times. Data are expressed as the mean ± mean standard error (SEM). Levene's test was conducted to evaluate the variance between different groups for comparative statistical analysis. Based on the homogeneity of variance, the difference between the two means was evaluated by one-way ANOVA followed by Tukey test or Dunnett's T3 test. $P < 0.05$ was considered statistically significant.

Abbreviations

SAL: Salubrinal; 3MA: 3-methyladenine; NAC: N-acetyl-L-cysteine; HCO: Hydroxychloroquine; ROS: reactive oxygen species; GSH: glutathione; GSSG: oxidized glutathione; PDI: resident protein disulfide isomerases; ERO1: endoplasmic reticulum oxidoreduction 1; UPR: unfolded-protein response; ER: endoplasmic reticulum; ATF6: activating transcription factor 6; IRE1: inositol-requiring enzyme 1; XBP1: X-box binding protein; EIF2: eukaryotic translation initiation factor 2; ATF4: activating transcription factor 4; CHOP: C/EBP homologous protein; AMD: age-related macular degeneration; Lt: Light exposure.

AUTHOR CONTRIBUTIONS

JYS, VB and GYL planned the study and wrote the manuscript. JYS performed most experimental work and BF guided the project. LC and YW coordinated and performed experimental work. YRP and SMZ performed statistical analyses. All the authors approved the final draft.

ACKNOWLEDGMENTS

We thank Dr. Muayyad Al-Ubaidi, Department of Cell Biology, University of Oklahoma Health Sciences Center, Oklahoma City, OK, USA for generously providing the 661W cell line.

CONFLICTS OF INTEREST

The authors have no conflicts of interest to disclose.

FUNDING

This work was supported by grants from the National Natural Science Foundation of China (No. 81570864), the Natural Science Foundation of Jilin Province (No. 20200801043GH, No.20200201379JC, No.20190201083JC) and the Science and Technology Project of Jilin Provincial Education Department (No. JJKH20190046KJ, No. JJKH20190049KJ). The funders had no role in study design, data collection and analysis, decision to publish, or preparation of the manuscript.

REFERENCES

1. Marquioni-Ramella MD, Suburo AM. Photo-damage, photo-protection and age-related macular degeneration. *Photochem Photobiol Sci.* 2015; 14:1560–77. <https://doi.org/10.1039/c5pp00188a> PMID:26198091
2. Wu J, Seregard S, Algvere PV. Photochemical damage of the retina. *Surv Ophthalmol.* 2006; 51:461–81. <https://doi.org/10.1016/j.survophthal.2006.06.009> PMID:16950247
3. Hunter JJ, Morgan JJ, Merigan WH, Sliney DH, Sparrow JR, Williams DR. The susceptibility of the retina to photochemical damage from visible light. *Prog Retin Eye Res.* 2012; 31:28–42. <https://doi.org/10.1016/j.preteyeres.2011.11.001> PMID:22085795
4. Ye S, Zaitseva E, Caltabiano G, Schertler GF, Sakmar TP, Deupi X, Vogel R. Tracking g-protein-coupled receptor activation using genetically encoded infrared probes. *Nature.* 2010; 464:1386–89. <https://doi.org/10.1038/nature08948> PMID:20383122
5. Park PS. Constitutively active rhodopsin and retinal disease. *Adv Pharmacol.* 2014; 70:1–36. <https://doi.org/10.1016/B978-0-12-417197-8.00001-8> PMID:24931191
6. Rózanowska M, Sarna T. Light-induced damage to the retina: role of rhodopsin chromophore revisited. *Photochem Photobiol.* 2005; 81:1305–30. <https://doi.org/10.1562/2004-11-13-IR-371> PMID:16120006
7. Fanjul-Moles ML, López-Riquelme GO. Relationship between oxidative stress, circadian rhythms, and AMD. *Oxid Med Cell Longev.* 2016; 2016:7420637. <https://doi.org/10.1155/2016/7420637> PMID:26885250
8. Contín MA, Benedetto MM, Quinteros-Quintana ML, Guido ME. Light pollution: the possible consequences of excessive illumination on retina. *Eye (Lond).* 2016; 30:255–63. <https://doi.org/10.1038/eye.2015.221> PMID:26541085
9. Yu L, Kelly U, Ebright JN, Malek G, Saloupis P, Rickman DW, McKay BS, Arshavsky VY, Bowes Rickman C. Oxidative stress-induced expression and modulation of phosphatase of regenerating liver-1 (PRL-1) in mammalian retina. *Biochim Biophys Acta.* 2007; 1773:1473–82. <https://doi.org/10.1016/j.bbamcr.2007.06.005> PMID:17673310
10. Tanito M, Kwon YW, Kondo N, Bai J, Masutani H, Nakamura H, Fujii J, Ohira A, Yodoi J. Cytoprotective effects of geranylgeranylacetone against retinal photooxidative damage. *J Neurosci.* 2005; 25:2396–404. <https://doi.org/10.1523/JNEUROSCI.4866-04.2005> PMID:15745966
11. Sui GY, Liu GC, Liu GY, Gao YY, Deng Y, Wang WY, Tong SH, Wang L. Is sunlight exposure a risk factor for age-related macular degeneration? a systematic review and meta-analysis. *Br J Ophthalmol.* 2013; 97:389–94. <https://doi.org/10.1136/bjophthalmol-2012-302281> PMID:23143904
12. Ivanov IV, Mappes T, Schaupp P, Lappe C, Wahl S. Ultraviolet radiation oxidative stress affects eye health. *J Biophotonics.* 2018; 11:e201700377. <https://doi.org/10.1002/jbio.201700377> PMID:29603665
13. Fregno I, Molinari M. Endoplasmic reticulum turnover: ER-phagy and other flavors in selective and non-selective ER clearance. *F1000Res.* 2018; 7:454. <https://doi.org/10.12688/f1000research.13968.1> PMID:29744037
14. Wang WA, Groenendyk J, Michalak M. Endoplasmic reticulum stress associated responses in cancer. *Biochim Biophys Acta.* 2014; 1843:2143–49.

- <https://doi.org/10.1016/j.bbamcr.2014.01.012>
PMID:24440276
15. Zeeshan HM, Lee GH, Kim HR, Chae HJ. Endoplasmic reticulum stress and associated ROS. *Int J Mol Sci*. 2016; 17:327.
<https://doi.org/10.3390/ijms17030327>
PMID:26950115
16. Malhotra JD, Kaufman RJ. Endoplasmic reticulum stress and oxidative stress: a vicious cycle or a double-edged sword? *Antioxid Redox Signal*. 2007; 9:2277–93.
<https://doi.org/10.1089/ars.2007.1782>
PMID:17979528
17. Kheitan S, Minuchehr Z, Soheili ZS. Exploring the cross talk between ER stress and inflammation in age-related macular degeneration. *PLoS One*. 2017; 12:e0181667.
<https://doi.org/10.1371/journal.pone.0181667>
PMID:28742151
18. Walter P, Ron D. The unfolded protein response: from stress pathway to homeostatic regulation. *Science*. 2011; 334:1081–86.
<https://doi.org/10.1126/science.1209038>
PMID:22116877
19. Chen X, Shen J, Prywes R. The luminal domain of ATF6 senses endoplasmic reticulum (ER) stress and causes translocation of ATF6 from the ER to the golgi. *J Biol Chem*. 2002; 277:13045–52.
<https://doi.org/10.1074/jbc.M110636200>
PMID:11821395
20. Wakabayashi S, Yoshida H. The essential biology of the endoplasmic reticulum stress response for structural and computational biologists. *Comput Struct Biotechnol J*. 2013; 6:e201303010.
<https://doi.org/10.5936/csbj.201303010>
PMID:24688718
21. Fels DR, Koumenis C. The PERK/eIF2alpha/ATF4 module of the UPR in hypoxia resistance and tumor growth. *Cancer Biol Ther*. 2006; 5:723–28.
<https://doi.org/10.4161/cbt.5.7.2967> PMID:16861899
22. Rzymiski T, Milani M, Singleton DC, Harris AL. Role of ATF4 in regulation of autophagy and resistance to drugs and hypoxia. *Cell Cycle*. 2009; 8:3838–47.
<https://doi.org/10.4161/cc.8.23.10086>
PMID:19887912
23. Song S, Tan J, Miao Y, Zhang Q. Crosstalk of ER stress-mediated autophagy and ER-phagy: involvement of UPR and the core autophagy machinery. *J Cell Physiol*. 2018; 233:3867–74.
<https://doi.org/10.1002/jcp.26137> PMID:28777470
24. Fujita E, Kouroku Y, Isoai A, Kumagai H, Misutani A, Matsuda C, Hayashi YK, Momoi T. Two endoplasmic reticulum-associated degradation (ERAD) systems for the novel variant of the mutant dysferlin: ubiquitin/proteasome ERAD(I) and autophagy/lysosome ERAD(II). *Hum Mol Genet*. 2007; 16:618–29.
<https://doi.org/10.1093/hmg/ddm002> PMID:17331981
25. Kesidou E, Lagoudaki R, Touloumi O, Poulatsidou KN, Simeonidou C. Autophagy and neurodegenerative disorders. *Neural Regen Res*. 2013; 8:2275–83.
<https://doi.org/10.3969/j.issn.1673-5374.2013.24.007>
PMID:25206537
26. Kuma A, Mizushima N. Physiological role of autophagy as an intracellular recycling system: with an emphasis on nutrient metabolism. *Semin Cell Dev Biol*. 2010; 21:683–90.
<https://doi.org/10.1016/j.semcdb.2010.03.002>
PMID:20223289
27. Simonsen A, Cumming RC, Finley KD. Linking lysosomal trafficking defects with changes in aging and stress response in drosophila. *Autophagy*. 2007; 3:499–501.
<https://doi.org/10.4161/auto.4604> PMID:17617737
28. Lapaquette P, Guzzo J, Bretillon L, Bringer MA. Cellular and Molecular Connections between Autophagy and Inflammation. *Mediators Inflamm*. 2015; 2015:398483.
<https://doi.org/10.1155/2015/398483> PMID:26221063
29. Liu C, DeRoo EP, Stecyk C, Wolsey M, Szuchnicki M, Hagos EG. Impaired autophagy in mouse embryonic fibroblasts null for krüppel-like factor 4 promotes DNA damage and increases apoptosis upon serum starvation. *Mol Cancer*. 2015; 14:101.
<https://doi.org/10.1186/s12943-015-0373-6>
PMID:25944097
30. Lee WS, Yoo WH, Chae HJ. ER stress and autophagy. *Curr Mol Med*. 2015; 15:735–45.
<https://doi.org/10.2174/1566524015666150921105453>
PMID:26391548
31. Galluzzi L, Vitale I, Aaronson SA, Abrams JM, Adam D, Agostinis P, Alnemri ES, Altucci L, Amelio I, Andrews DW, Annicchiarico-Petruzzelli M, Antonov AV, Arama E, et al. Molecular mechanisms of cell death: recommendations of the nomenclature committee on cell death 2018. *Cell Death Differ*. 2018; 25:486–541.
<https://doi.org/10.1038/s41418-017-0012-4>
PMID:29362479
32. Midorikawa R, Yamamoto-Hino M, Awano W, Hinohara Y, Suzuki E, Ueda R, Goto S. Autophagy-dependent rhodopsin degradation prevents retinal degeneration in drosophila. *J Neurosci*. 2010; 30:10703–19.
<https://doi.org/10.1523/JNEUROSCI.2061-10.2010>
PMID:20702701
33. Zhang TZ, Fan B, Chen X, Wang WJ, Jiao YY, Su GF, Li GY. Suppressing autophagy protects photoreceptor cells from light-induced injury. *Biochem Biophys Res Commun*. 2014; 450:966–72.

- <https://doi.org/10.1016/j.bbrc.2014.06.082>
PMID: [24971547](https://pubmed.ncbi.nlm.nih.gov/24971547/)
34. Organisciak DT, Vaughan DK. Retinal light damage: mechanisms and protection. *Prog Retin Eye Res.* 2010; 29:113–34.
<https://doi.org/10.1016/j.preteyeres.2009.11.004>
PMID: [19951742](https://pubmed.ncbi.nlm.nih.gov/19951742/)
35. Baglolo CJ, Sime PJ, Phipps RP. Cigarette smoke-induced expression of heme oxygenase-1 in human lung fibroblasts is regulated by intracellular glutathione. *Am J Physiol Lung Cell Mol Physiol.* 2008; 295:L624–36.
<https://doi.org/10.1152/ajplung.90215.2008>
PMID: [18689604](https://pubmed.ncbi.nlm.nih.gov/18689604/)
36. Lin W, Kunkler PE, Harding HP, Ron D, Kraig RP, Popko B. Enhanced integrated stress response promotes myelinating oligodendrocyte survival in response to interferon-gamma. *Am J Pathol.* 2008; 173:1508–17.
<https://doi.org/10.2353/ajpath.2008.080449>
PMID: [18818381](https://pubmed.ncbi.nlm.nih.gov/18818381/)
37. Guo ML, Liao K, Periyasamy P, Yang L, Cai Y, Callen SE, Buch S. Cocaine-mediated microglial activation involves the ER stress-autophagy axis. *Autophagy.* 2015; 11:995–1009.
<https://doi.org/10.1080/15548627.2015.1052205>
PMID: [26043790](https://pubmed.ncbi.nlm.nih.gov/26043790/)
38. Mizushima N, Yoshimori T. How to interpret LC3 immunoblotting. *Autophagy.* 2007; 3:542–45.
<https://doi.org/10.4161/auto.4600> PMID: [17611390](https://pubmed.ncbi.nlm.nih.gov/17611390/)
39. Klionsky DJ, Abdelmohsen K, Abe A, Abedin MJ, Abeliovich H, Acevedo Arozena A, Adachi H, Adams CM, Adams PD, Adeli K, Adhietty PJ, Adler SG, Agam G, et al. Guidelines for the use and interpretation of assays for monitoring autophagy (3rd edition). *Autophagy.* 2016; 12:1–222.
<https://doi.org/10.1080/15548627.2015.1100356>
PMID: [26799652](https://pubmed.ncbi.nlm.nih.gov/26799652/)
40. Caccamo A, Ferreira E, Branca C, Oddo S. P62 improves AD-like pathology by increasing autophagy. *Mol Psychiatry.* 2017; 22:865–73.
<https://doi.org/10.1038/mp.2016.139> PMID: [27573878](https://pubmed.ncbi.nlm.nih.gov/27573878/)
41. Wu CL, Chen CH, Hwang CS, Chen SD, Hwang WC, Yang DI. Roles of p62 in BDNF-dependent autophagy suppression and neuroprotection against mitochondrial dysfunction in rat cortical neurons. *J Neurochem.* 2017; 140:845–61.
<https://doi.org/10.1111/jnc.13937>
PMID: [28027414](https://pubmed.ncbi.nlm.nih.gov/28027414/)
42. Wang Y, Zhu WG, Zhao Y. Autophagy substrate SQSTM1/p62 regulates chromatin ubiquitination during the DNA damage response. *Autophagy.* 2017; 13:212–13.
<https://doi.org/10.1080/15548627.2016.1245262>
PMID: [27791533](https://pubmed.ncbi.nlm.nih.gov/27791533/)
43. Schick T, Ersoy L, Lechanteur YT, Saksens NT, Hoyng CB, den Hollander AI, Kirchhof B, Fauser S. History of sunlight exposure is a risk factor for age-related macular degeneration. *Retina.* 2016; 36:787–90.
<https://doi.org/10.1097/IAE.0000000000000756>
PMID: [26441265](https://pubmed.ncbi.nlm.nih.gov/26441265/)
44. Delmelle M. Possible implication of photooxidation reactions in retinal photo-damage. *Photochem Photobiol.* 1979; 29:713–16.
<https://doi.org/10.1111/j.1751-1097.1979.tb07755.x>
PMID: [221949](https://pubmed.ncbi.nlm.nih.gov/221949/)
45. Kaarniranta K, Uusitalo H, Blasiak J, Felszeghy S, Kannan R, Kauppinen A, Salminen A, Sinha D, Ferrington D. Mechanisms of mitochondrial dysfunction and their impact on age-related macular degeneration. *Prog Retin Eye Res.* 2020. [Epub ahead of print].
<https://doi.org/10.1016/j.preteyeres.2020.100858>
PMID: [32298788](https://pubmed.ncbi.nlm.nih.gov/32298788/)
46. Kupsco A, Schlenk D. Oxidative stress, unfolded protein response, and apoptosis in developmental toxicity. *Int Rev Cell Mol Biol.* 2015; 317:1–66.
<https://doi.org/10.1016/bs.ircmb.2015.02.002>
PMID: [26008783](https://pubmed.ncbi.nlm.nih.gov/26008783/)
47. Kozhevnikova OS, Telegina DV, Devyatkin VA, Kolosova NG. Involvement of the autophagic pathway in the progression of AMD-like retinopathy in senescence-accelerated OXYS rats. *Biogerontology.* 2018; 19:223–35.
<https://doi.org/10.1007/s10522-018-9751-y>
PMID: [29492791](https://pubmed.ncbi.nlm.nih.gov/29492791/)
48. Mitter SK, Song C, Qi X, Mao H, Rao H, Akin D, Lewin A, Grant M, Dunn W Jr, Ding J, Bowes Rickman C, Boulton M. Dysregulated autophagy in the RPE is associated with increased susceptibility to oxidative stress and AMD. *Autophagy.* 2014; 10:1989–2005.
<https://doi.org/10.4161/auto.36184>
PMID: [25484094](https://pubmed.ncbi.nlm.nih.gov/25484094/)
49. Zhang J, Zhao X, Cai Y, Li Y, Yu X, Lu L. Protection of retina by mini- α A in NaIO₃-induced retinal pigment epithelium degeneration mice. *Int J Mol Sci.* 2015; 16:1644–56.
<https://doi.org/10.3390/ijms16011644>
PMID: [25588217](https://pubmed.ncbi.nlm.nih.gov/25588217/)
50. B'chir W, Maurin AC, Carraro V, Averous J, Jousse C, Muranishi Y, Parry L, Stepien G, Fafournoux P, Bruhat A. The eIF2 α /ATF4 pathway is essential for stress-induced autophagy gene expression. *Nucleic Acids Res.* 2013; 41:7683–99.
<https://doi.org/10.1093/nar/gkt563>

PMID:[23804767](#)

51. Liu SY, Song JY, Fan B, Wang Y, Pan YR, Che L, Sun YJ, Li GY. Resveratrol protects photoreceptors by blocking caspase- and PARP-dependent cell death pathways. *Free Radic Biol Med*. 2018; 129:569–81. <https://doi.org/10.1016/j.freeradbiomed.2018.10.431> PMID:[30342188](#)
52. Hu YN, Sung TJ, Chou CH, Liu KL, Hsieh LP, Hsieh CW. Characterization and antioxidant activities of yellow strain *Flammulina velutipes* (Jinhua mushroom) polysaccharides and their effects on ROS content in L929 cell. *Antioxidants (Basel)*. 2019; 8:298. <https://doi.org/10.3390/antiox8080298> PMID:[31405147](#)
53. Buranasin P, Mizutani K, Iwasaki K, Pawaputanon Na Mahasarakham C, Kido D, Takeda K, Izumi Y. High glucose-induced oxidative stress impairs proliferation and migration of human gingival fibroblasts. *PLoS One*. 2018; 13:e0201855. <https://doi.org/10.1371/journal.pone.0201855> PMID:[30092096](#)
54. Zhu S, Yam M, Wang Y, Linton JD, Grenell A, Hurley JB, Du J. Impact of euthanasia, dissection and postmortem delay on metabolic profile in mouse retina and RPE/choroid. *Exp Eye Res*. 2018; 174:113–20. <https://doi.org/10.1016/j.exer.2018.05.032> PMID:[29864440](#)

Activation of C-reactive protein proinflammatory phenotype in the blood retinal barrier *in vitro*: implications for age-related macular degeneration

Sara Romero-Vázquez¹, Alfredo Adán¹, Marc Figueras-Roca¹, Victor Llorenç¹, Mark Slevin², Gemma Vilahur³, Lina Badimon³, Andrew D. Dick^{4,5}, Blanca Molins¹

¹Group of Ocular Inflammation, Clinical and Experimental Studies, Institut d'Investigacions Biomèdiques Agustí Pi i Sunyer (IDIBAPS), Hospital Clínic de Barcelona, Barcelona, Spain

²Department of Life Sciences, Manchester Metropolitan University, Manchester, UK

³Cardiovascular Research Center-ICCC, Hospital de la Santa Creu i Sant Pau, IIB-Sant Pau, CiberCV, Institute Carlos III, Barcelona, Spain

⁴Academic Unit of Ophthalmology, School of Clinical Sciences and School of Cellular and Molecular Medicine, University of Bristol, Bristol, UK

⁵National Institute for Health Research (NIHR) Biomedical Research Centre at Moorfields Eye Hospital and University College London Institute of Ophthalmology, London, UK

Correspondence to: Blanca Molins; email: bmolins@clinic.cat

Keywords: age-related macular degeneration, retinal pigment epithelium, inflammation, C-reactive protein

Received: April 9, 2020

Accepted: June 20, 2020

Published: July 16, 2020

Copyright: Romero-Vázquez et al. This is an open-access article distributed under the terms of the Creative Commons Attribution License (CC BY 3.0), which permits unrestricted use, distribution, and reproduction in any medium, provided the original author and source are credited.

ABSTRACT

The retinal pigment epithelium (RPE) is considered one of the main targets of age-related macular degeneration (AMD), the leading cause of irreversible vision loss among the ageing population worldwide. Persistent low grade inflammation and oxidative stress eventually lead to RPE dysfunction and disruption of the outer blood-retinal barrier (oBRB). Increased levels of circulating pentameric C-reactive protein (pCRP) are associated with higher risk of AMD. The monomeric form (mCRP) has been detected in drusen, the hallmark deposits associated with AMD, and we have found that mCRP induces oBRB disruption. However, it is unknown how mCRP is generated in the subretinal space. Using a Transwell model we found that both pCRP and mCRP can cross choroidal endothelial cells and reach the RPE *in vitro* and that mCRP, but not pCRP, is able to cross the RPE monolayer in ARPE-19 cells. Alternatively, mCRP can originate from the dissociation of pCRP in the surface of lipopolysaccharide-damaged RPE in both ARPE-19 and primary porcine RPE lines. In addition, we found that the proinflammatory phenotype of mCRP in the RPE depends on its topological localization. Together, our findings further support mCRP contribution to AMD progression enhancing oBRB disruption.

INTRODUCTION

Age-related macular degeneration (AMD) is the primary cause of irreversible vision loss among the ageing population worldwide. The number of people with AMD worldwide is expected to reach 196 million in 2020, increasing to 288 million in 2040 [1]. AMD is a degenerative and progressive disease involving

multiple genetic and environmental factors, age being the primary risk factor.

The retinal pigment epithelium (RPE) monolayer is believed to be among the initial targets of early disease. AMD presents RPE cell abnormalities, disruption of the outer blood-retinal-barrier (oBRB), and degeneration of photoreceptors, which require a normally functioning

RPE to survive [2, 3]. Prior research has implicated strong roles for inflammation, oxidative stress, lipid abnormalities, and RPE dysfunction in AMD pathobiology, but their precise mechanisms and their relative contribution are unclear [4]. A multitude of systemic changes occur with ageing that contribute to the initiation and development of inflammation. Indeed, the immune system of elderly individuals is characterized by a basal systemic inflammatory state [5].

Altered immune responses are thought to contribute to the dry AMD phenotype. Parainflammation is a low-grade cytoprotective adaptation to local stress that is intermediate between immune-mediated homeostasis and chronic inflammation that maintains cellular and tissue function. Loss of parainflammation control contributes to AMD by invoking a chronic, heightened immune response that causes tissue destruction [6–8]. Histochemical and proteomic analysis of ocular drusen, the hallmark deposits of AMD, have shown that these deposits contain inflammatory proteins and complement components that mediate local inflammation [9, 10]. Furthermore, the strongest genetic risk factor for AMD known to date is a common polymorphism in the *complement factor H (CFH)* gene (c.1277T > C, p.Tyr402His), a gene essential for the regulation of complement activation [11, 12].

C-reactive protein (CRP), a prototypical acute-phase reactant, is an active regulator of the innate immune system. Among the multiple functions ascribed to CRP are activation of the classical complement pathway and inactivation of the alternative pathway [13]. CRP is considered to be a serum biomarker for chronic inflammation, heart disease and, more recently, also AMD [14, 15]. In plasma, CRP typically exists as a cyclic, disk-shaped pentamer (pentameric CRP, pCRP) composed of five noncovalently linked subunits of 23 kDa [16]. However, pCRP can undergo dissociation into its subunits, acquiring distinct biological functions. Oxidative stress and bioactive lipids from activated or damaged cells can dissociate pCRP into its 23-kDa subunits [17–19] through a mechanism that is dependent on lysophosphatidylcholine (LPC) exposure after phospholipase A₂ activation [20]. This alternative conformation of CRP, termed monomeric CRP (mCRP), has different antigenicity-expressing neoepitopes than pCRP and represents the tissue-based insoluble form of CRP. Unlike pCRP, mCRP displays a proinflammatory phenotype in several cell types [21–23].

mCRP has been identified in ocular drusen and other subepithelial deposits [24, 25], as well as in the choroid, and we have shown that mCRP, but not pCRP, contributes to oBRB disruption *in vitro* [26]. Moreover, we also showed that the “non-risk” Factor H (FH)

variant can effectively bind to mCRP to dampen mCRP pro-inflammatory activity [27]. Notably, FH from AMD patients carrying the risk polymorphism for AMD shows an impaired binding to mCRP and, therefore, its proinflammatory effects remain unrestrained [28]. In line with these findings, data demonstrates that mCRP is the more abundant form of CRP in human RPE-choroid [29], and that mCRP levels are elevated in individuals with the high-risk *CFH* genotype [29, 30].

If mCRP pro-inflammatory capacity is unrestrained in AMD and particularly in high risk patients, then we need to determine how mCRP is generated or accumulates in the subretinal space as there is no CRP transcription in the retinal tissue [30, 31]. In addition, it is also unclear whether mCRP-induced barrier disruption depends on its topological localization.

RESULTS

Choroidal endothelial cells allow diffusion of CRP isoforms

We first interrogated whether circulating CRP could reach the subretinal space using a Transwell model, in which confluent monolayers of primary porcine choroidal endothelial cells (CECs) were grown on porous filters with their apical and basolateral surfaces exposed to separate chambers (Figure 1A). Addition of mCRP to the apical chamber that mimics blood vessel lumen (A to B red arrow in Figure 1A) resulted in CRP diffusion into the basolateral chamber (tissue side) as Western blot (Figure 1B) and ELISA (Figure 1C) of the culture media of the different compartments revealed the presence of mCRP in both chambers. Similarly, pCRP was able to reach the abluminal side of the CEC monolayer, as seen by Western blot (Figure 1D). CRP isoforms were also able to reach the apical chamber when added in the abluminal compartment (B to A blue arrow in Figure 1A), suggesting bidirectional diffusion of the proteins. Immunofluorescence imaging showed that mCRP delivered to the apical compartment was extensively bound to the CEC surface compared to pCRP and to CRP (either mCRP or pCRP) delivered in the basolateral chamber (Figure 1E–1G).

Diffusion of CRP across the RPE

Given that CRP isoforms were able to cross the CEC monolayer in our *in vitro* model, we next evaluated whether CRP isoforms could also reach the subretinal space and cross the RPE, using the Transwell model. In this scenario the basolateral side of the RPE monolayer represents the Bruch’s membrane/choriocapillaris side, whereas the apical side represents the subretinal space (Figure 2A). Western blot experiments revealed that

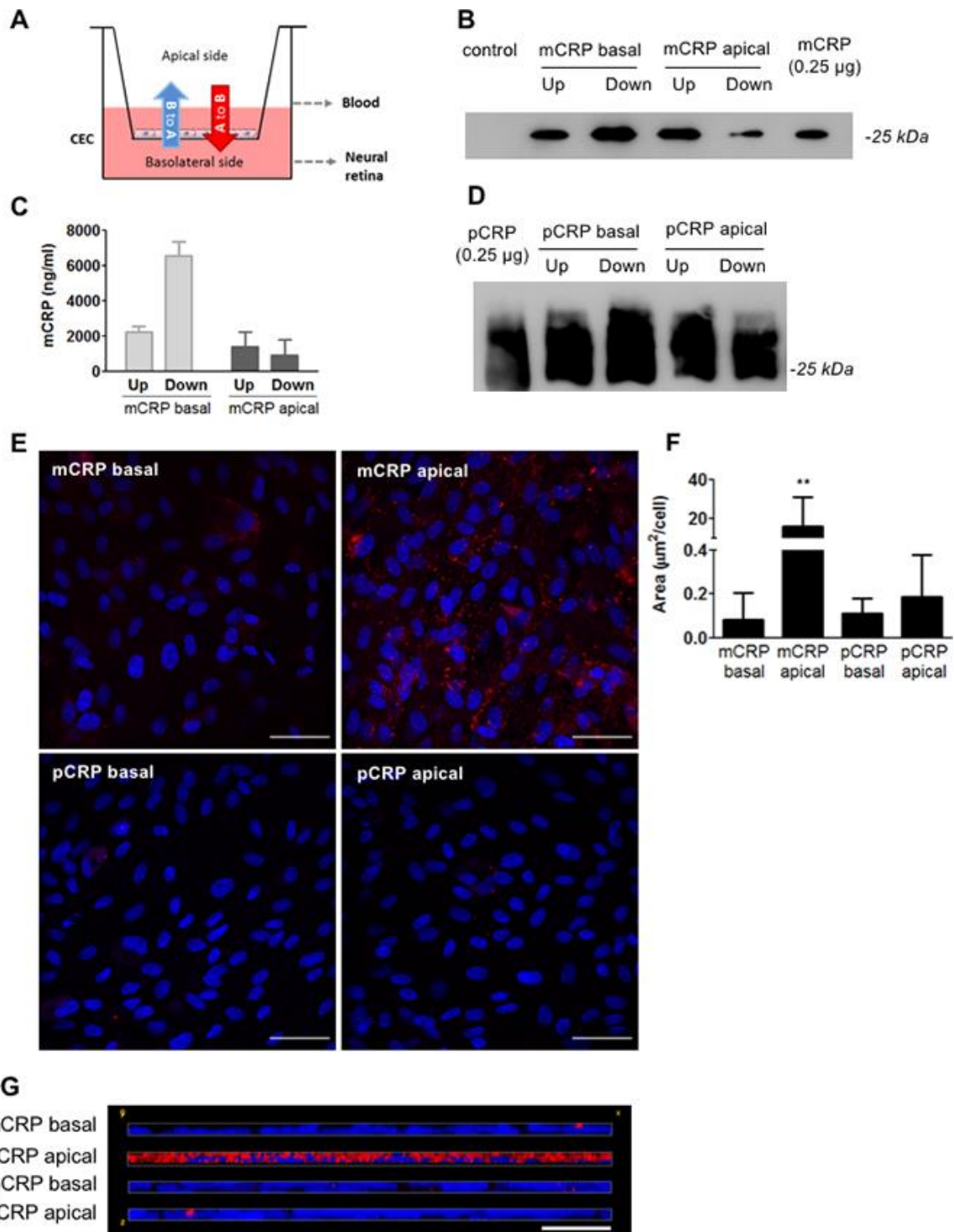


Figure 1. CRP isoforms are able to cross CECs. (A) Experimental setup. CRP (10 µg/ml) was added to either the apical or basolateral chamber of the Transwell for 48h, mimicking blood vessel lumen and RPE, respectively. The presence of CRP in the opposite chamber where it was added was determined by Western blot and ELISA, and CRP bound to the cell surface was determined by immunofluorescence. (B) Western blot of mCRP present in apical (Up) and basolateral (Down) chamber (N=4). (C) ELISA of mCRP (ng/ml) from apical (Up) and basolateral (Down) supernatants. Values are expressed as mean ± SD (N=3). (D) Western-blot of pCRP present in apical (Up) and basolateral (Down) supernatants (N=5). (E) Immunofluorescence of CRP (red) stained with monoclonal antibodies against mCRP (3H12) or pCRP (1C6). Nuclei stained with DAPI. Scale bar = 50 µm (N=6). (F) Quantification of CRP binding measured as stained area divided by the number of cells per image (µm²/cell). Results are expressed as mean area (µm²/cell) ± SD. Statistical analysis was performed by One-Way ANOVA and Tukey's posthoc. **P<0.01 vs. all conditions. (G) Reconstruction of x-z sections with a 0.3 µm z axis step of immunofluorescence images. Images shown are representative of six independent experiments.

mCRP was able to diffuse across ARPE-19 cell monolayer, as it was present in the apical chamber when added in the basolateral chamber (B to A, red arrow in Figure 2A). Diffusion of mCRP was greater at 48 hours compared to 24 hours (Figure 2B). We also detected the presence of mCRP by ELISA 48 hours after treatment in the opposite chamber where it was added (Figure 2C). By contrast, pCRP did not seem to cross the ARPE-19 monolayer. Western blot experiments showed that pCRP was not present in the supernatant of the opposite chamber where it was added, neither at 24h nor at 48h after treatment (Figure 2D). Immunofluorescence imaging showed that mCRP delivered to the apical compartment was extensively bound to the ARPE-19 cell monolayer compared to pCRP and to CRP (either mCRP or pCRP) delivered in the basolateral chamber (Figure 2E–2G).

We then tested whether mCRP was also able to cross porcine primary RPE cells. Primary RPE cells represent a healthier and younger RPE than ARPE-19 cells, as they show more than 5 times higher TEER values (Supplementary Figure 1D, 1E). Interestingly, unlike ARPE-19 cells, primary porcine RPE cells did not allow mCRP diffusion as mCRP was not detected in the opposite chamber where it was added, neither in Western blot (Figure 3A) nor ELISA (Figure 3B). As expected, pCRP was also unable to cross the RPE monolayer (Figure 3C). Immunofluorescence imaging showed similar results to those with ARPE-19; mCRP delivered to the apical compartment was extensively bound to the RPE cell monolayer compared to pCRP and to CRP (either mCRP or pCRP) delivered in the basolateral chamber (Figure 3D–3F).

Damaged RPE dissociates pCRP into mCRP

Given that pCRP is able to cross the CEC monolayer and reach the subepithelial space *in vitro*, we next studied whether pCRP could dissociate into its monomeric subunits within the RPE. It has been previously described that LPS-induced inflammation induces CRP dissociation in the cremaster muscle [20], and therefore we studied whether LPS-induced inflammation could also lead to CRP dissociation in RPE cells. RPE cells were treated with 100 µg/mL LPS for 24h before adding pCRP. After 24h, RPE cells were treated with pCRP for 48h and the presence of mCRP on the surface of RPE cells was measured by immunofluorescence. As observed in Figure 4, LPS-induced inflammation triggered pCRP dissociation into mCRP in both ARPE-19 (Figure 4A, 4B) and primary porcine RPE cells (Figure 4C, 4D). Altogether these results show that mCRP present in drusen and in the subretinal space may either arrive from the choroidal circulation or it may originate from local dissociation of pCRP in damaged RPE.

Topological localization of mCRP determines the impact on barrier disruption in RPE cells

Next, we evaluated whether mCRP-induced barrier disruption depended on the topological localization of mCRP. For this purpose, ARPE-19 cells grown on inserts for at least 3 weeks were treated with CRP isoforms (10 µg/mL) either in the apical or basolateral compartment for 48h. As expected, mCRP delivered in the apical chamber, significantly decreased TEER values (Figure 5A). This observation was accompanied by an increase in paracellular permeability (Figure 5B) and an increased ZO-1 disorganization (Figure 5C, 5D, Supplementary Figure 3). Interestingly, abluminal treatment of mCRP also induced a significant decrease in TEER values.

We then aimed to replicate the experiments in primary porcine RPE cells, which are less permeable to mCRP diffusion. As seen in Figure 6, apical treatment of mCRP, but not pCRP, induced barrier disruption also in primary RPE cells as seen by significant decrease in TEER (Figure 6A), increase in paracellular permeability (Figure 6B) and increased ZO-1 disorganization (Figure 6C, 6D, Supplementary Figure 4). However, when mCRP was delivered into the abluminal compartment it failed to induce barrier disruption, showing that mCRP-induced barrier disruption depends on its topological localization.

DISCUSSION

The present study aimed to understand the relative contribution of mCRP to the pathophysiology of AMD. Our *in vitro* work demonstrates that mCRP is capable of traversing through choroidal vascular endothelium and across RPE. Although no direct *in vivo* correlate, the data suggest that mCRP can reach the subretinal space. Alternatively, mCRP may derive from the dissociation of pCRP on the surface of damaged RPE. Moreover, we found that the proinflammatory phenotype of mCRP in the RPE depends on its topological localization. Together the data continues to build the evidence of mCRP accentuation of AMD pathology and detriment to RPE health.

CRP is mainly produced in the liver and, although extrahepatic synthesis has been reported in some tissues, no evidence of *CRP* gene transcription has been detected in the retinal tissue [30, 31]. This indicates that the systemic circulation is the main source of CRP in the sub-RPE deposits. Indeed, we observed that both CRP isoforms, at clinically relevant concentrations, are able to cross CECs from their apical side -simulating blood side- and reach the basolateral side of the endothelium -simulating the subepithelial side- in a Transwell model

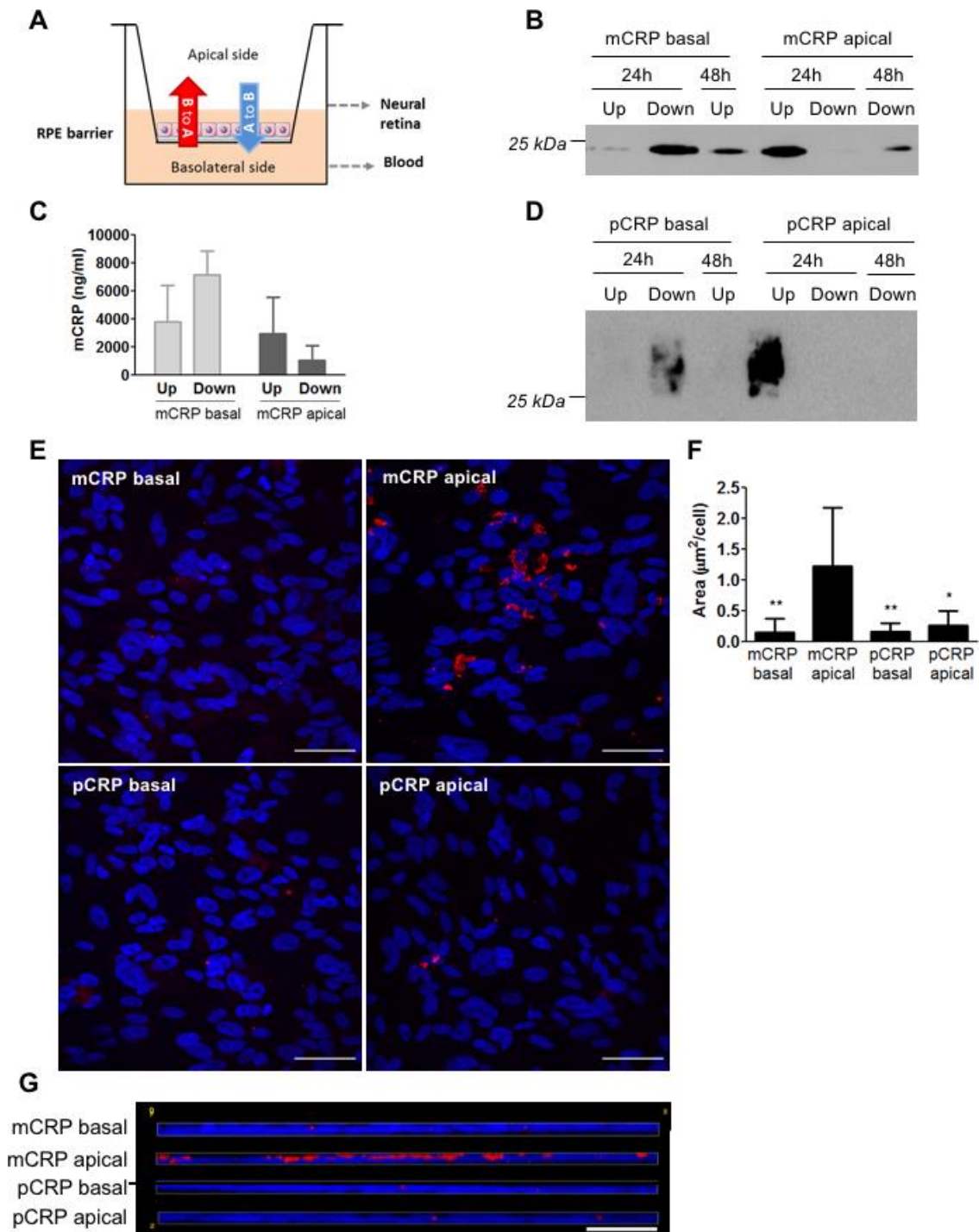


Figure 2. Diffusion of CRP isoforms across ARPE-19 cells. (A) Experimental setup. CRP (10 $\mu\text{g}/\text{ml}$) was added to either the apical or basolateral chamber of Transwell for 48h, mimicking neural retina and choriocapillaris, respectively. The presence of CRP in the opposite chamber where it was added was determined by Western blot and ELISA, and CRP bound to the cell surface was determined by immunofluorescence. (B) Western blot of mCRP present in apical (Up) and basolateral (Down) supernatants after 24 and 48 hours of treatment (N=4). (C) ELISA of mCRP (ng/ml) from apical (Up) and basolateral (Down) supernatants 48 hours after treatment. Values are expressed as mean \pm SD (N=3). (D) Western blot of pCRP present in apical (Up) and basolateral (Down) supernatants after 24 and 48 hours of treatment (N=4). (E) Immunofluorescence of CRP (red) stained with monoclonal antibodies against mCRP (3H12) or pCRP (1C6). Nuclei stained with DAPI. Scale bar = 50 μm (N=6). (F) Quantification of CRP binding measured as stained area divided by the number of cells per image ($\mu\text{m}^2/\text{cell}$). Results are expressed as mean area ($\mu\text{m}^2/\text{cell}$) \pm SD. Statistical analysis was performed by One-Way ANOVA and Tukey's posthoc. * $P < 0.05$, ** $P < 0.01$ vs. mCRP apical. (G) Reconstruction of x-z sections with a 0.3 μm z axis step of immunofluorescence images. Images shown are representative of six independent experiments.

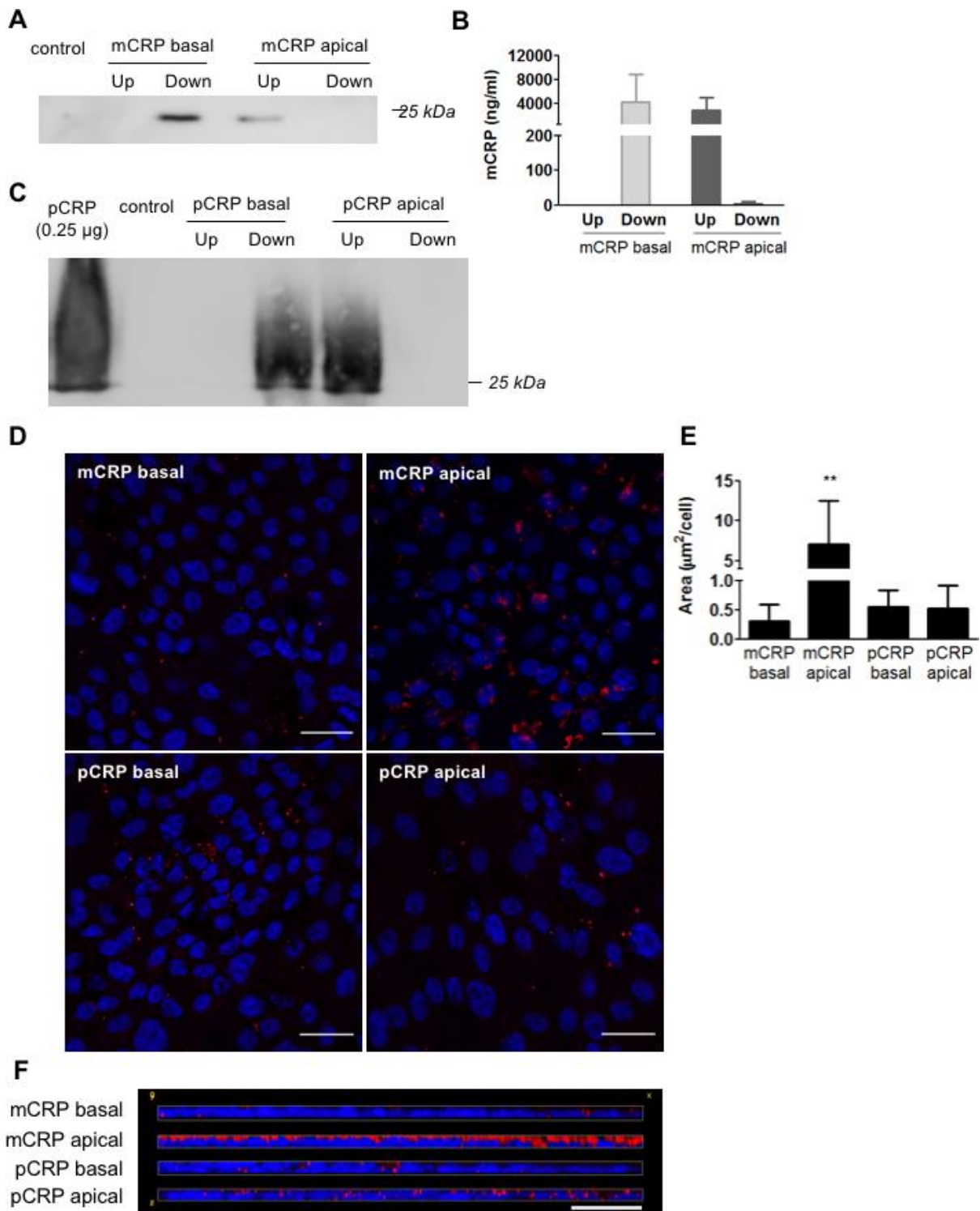


Figure 3. Diffusion of CRP isoforms across primary porcine RPE cells. (A) Western blot of mCRP present in apical (Up) and basolateral (Down) supernatants 48 hours after addition of mCRP (N=4). (B) ELISA of mCRP (ng/ml) from apical (Up) and basolateral (Down) supernatants. Values are expressed as mean \pm SD (N=5). (C) Western blot of pCRP present in apical (Up) and basolateral (Down) supernatants 48 hours after treatment (N=3). (D) Immunofluorescence of CRP (red) stained with monoclonal antibodies against mCRP (3H12) or pCRP (1C6). Nuclei stained with DAPI. Scale bar = 30 μ m (N=3). (E) Quantification of CRP binding measured as stained area divided by the number of cells per image ($\mu\text{m}^2/\text{cell}$). Results are expressed as mean area ($\mu\text{m}^2/\text{cell}$) \pm SD. Statistical analysis was performed by One-Way ANOVA and Tukey's posthoc. **P<0.01 vs. all conditions. (F) Reconstruction of x-z sections with a 0.3 μ m z axis step of immunofluorescence images. Images shown are representative of three independent experiments.

(Figure 1). The choroidal endothelium is fenestrated, which allows the movement of macromolecules and nutrients to nourish the RPE cells [32]. Although mCRP could extravasate the endothelium and reach the subepithelial space, we observed by immunofluorescence that most mCRP was retained in the apical side of the endothelium. Indeed, mCRP promiscuously interacts with a variety of immunoglobulins and other proteins [33]. Thus, we tested whether mCRP in the subepithelial space could also originate from the dissociation of pCRP in the RPE. Using the approach of Thiele et al. [20], we found that LPS-induced inflammation lead to pCRP dissociation also in RPE cells (Figure 4). Mechanistically, this process is dependent on exposure of LPC, a bioactive lipid that is generated after phospholipase A₂ activation on activated cell membranes [20]. Chirco et al. found that mCRP is predominantly localized in the choriocapillaris and Bruch's membrane [29] and a previous work by *Johnson and colleagues*, looking at total CRP, showed that CRP was more abundant in donor eyes with the high-risk *CFH* polymorphism compared to age-matched controls,

especially in regions containing drusen-like deposits [30]. A similar study compared differences in total CRP immunoreactivity in the retina based on AMD status and found that early and wet AMD eyes had higher levels of CRP compared to controls and that CRP was primarily detected into the BM [34]. In their work, Chirco et al. also showed that mCRP exerts an inflammatory effect on CEC, as it increases CEC migration and paracellular permeability and upregulates inflammatory gene expression including *ICAM1*, suggesting a role for mCRP in promoting inflammation in the choroid.

Besides the proinflammatory effect in the choroid, we have previously demonstrated that clinically relevant concentrations of mCRP induce barrier disruption and have a proinflammatory effect in RPE *in vitro* and potential for driving angiogenesis [26, 27]. With respect to angiogenesis and neovessels, in the context of vascular disease, CRP inhibits VEGF production and angiogenesis [35, 36]. Conversely, others have shown CRP upregulates VEGF expression in adipose-derived stem cells and in monocytes [37, 38]. mCRP has been

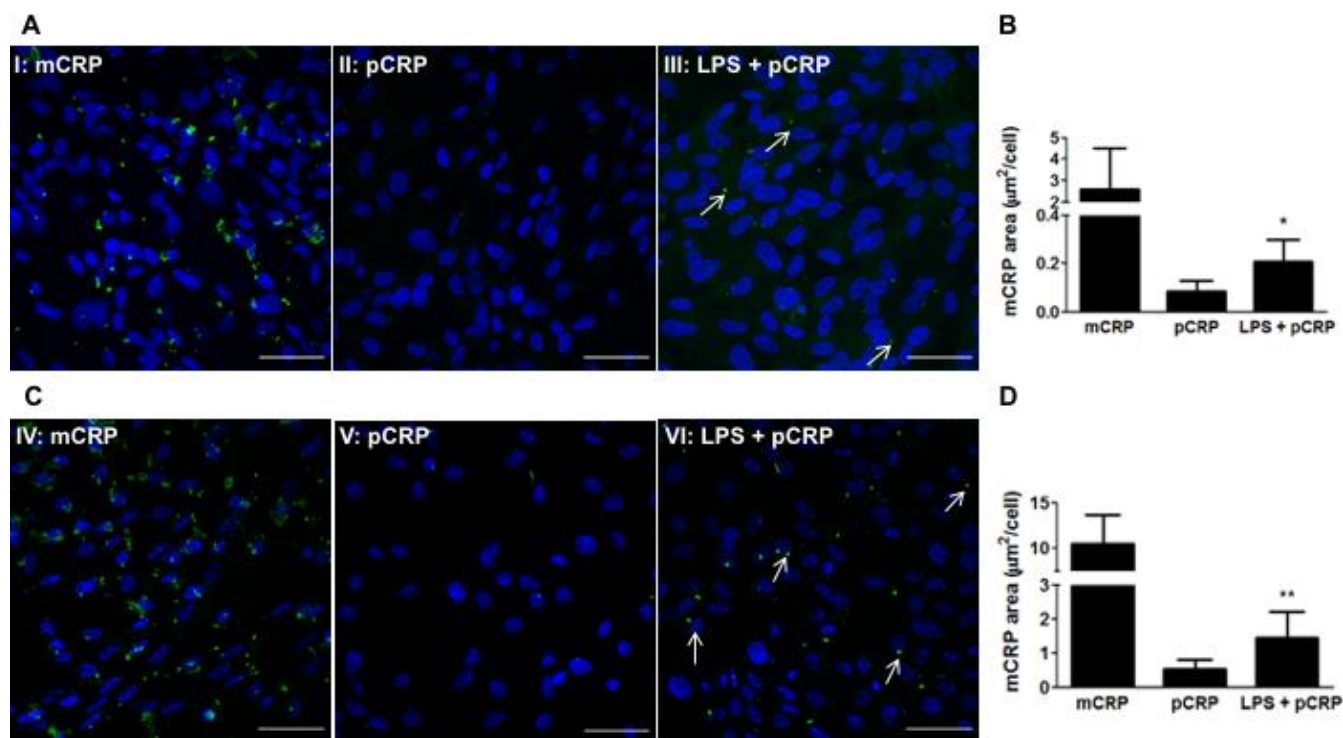


Figure 4. LPS-induced inflammation promotes CRP dissociation in RPE cells. RPE cells were treated with 100 μg/mL LPS for 24h before adding pCRP. After 24h, RPE cells were treated with pCRP for 48h and the presence of mCRP on the surface of RPE cells was measured by immunofluorescence. mCRP immunostaining of ARPE-19 (A) and primary porcine RPE (B) cells treated with 10 μg/ml mCRP for 48h (I, IV), 25 μg/ml pCRP for 48h (II, V), or 100 μg/ml LPS 24h before treatment with 25 μg/ml pCRP for 48h (III, VI). Arrows point mCRP dissociated from pCRP on RPE surface. Nuclei stained with DAPI. Scale bar = 50 μm. Images shown are representative of three independent experiments. (C, D) Quantification of CRP dissociation measured as stained area with the monoclonal antibody 3H12 against mCRP (green) divided by the number of cells per image (μm²/cell). Results are expressed as mean area (μm²/cell) ± SD (N=3). Statistical analysis was performed by student t-test. *P<0.05 vs. pCRP.

localized around newly formed microvessels in carotid artery plaques and in peri-infarct regions after an acute ischemic stroke [39, 40], promoting angiogenesis and inducing inflammation [41]. One notion is understanding of mCRP role is context dependent and in vivo studies are required to determine the contribution of mCRP to neovessel formation in the context of AMD, either via VEGF dependent or -independent mechanisms. On the other hand, Lauer et al. showed that mCRP binds necrotic RPE cells and that complement regulation at necrotic cell lesions is impaired by the FH His402 risk variant [17]. In these studies, RPE cells were stimulated with mCRP from the apical side. However, given the polarized nature of RPE cells it could be possible that the proinflammatory effect of mCRP on RPE cells depends on its topological localization. Our results showed a polarized stimulation of mCRP on barrier disruption in RPE cells, in both ARPE-19 and primary porcine RPE cells. The addition of mCRP to the apical side of RPE cells resulted in a significantly greater barrier disruption -decreased TEER, increased permeability and disrupted membrane ZO-1- than the addition of mCRP to the basolateral side. This effect was more pronounced in primary RPE cells, where mCRP

had no effect on barrier disruption when added from the basolateral side, than in ARPE-19 cells. Indeed, we observed by immunofluorescence a preferential binding of mCRP to the apical side (Figures 2, 3). The polarized proinflammatory effect of mCRP has been already observed in endothelial cells using a similar approach [42]. These observations could be due to a polarized distribution of the surface sensors for mCRP in the cell surface.

The receptors that mediate mCRP activities have not been fully characterized. In human neutrophils, mCRP binds FcγRIII (CD16) [21]. However, functional blockade of CD16 showed only a slight attenuation of mCRP-induced activation in RPE and endothelial cells (ECs) [27, 43]. Instead, in ECs, lipid raft microdomains seem to be the major sensors for mCRP [44]. Therefore, it could be speculated that mCRP interacts with RPE cells through lipid raft microdomains. Nevertheless, unlike many other surface receptors in epithelial tissues, caveolae seem to have a bipolar distribution in RPE cells [45]. The increased immunoreactivity of mCRP when added to the apical side could be also attributed to the presence of the Transwell filter in the basolateral

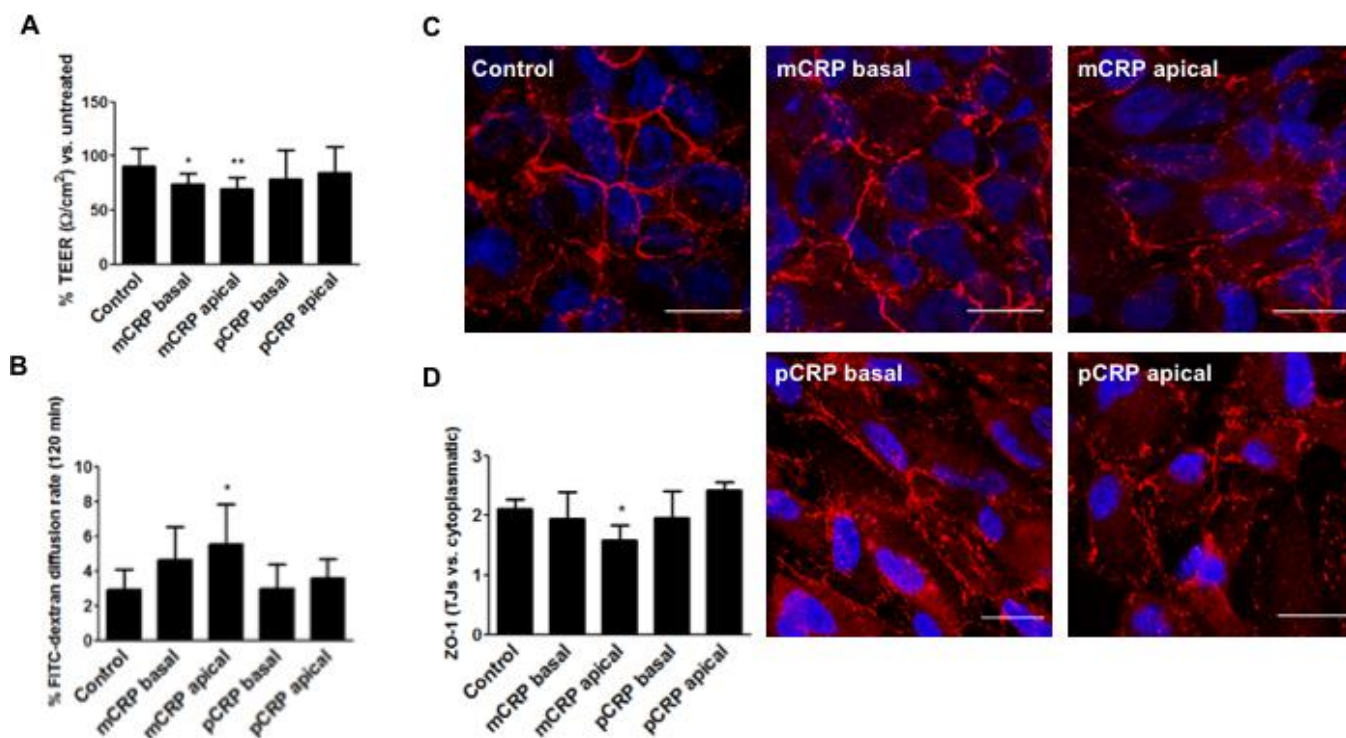


Figure 5. mCRP induces barrier disruption in ARPE-19 cells in a polarized manner. ARPE-19 cells were treated with CRP isoforms for 48h either from the apical side or the basolateral chamber and TEER (A) and paracellular permeability as determined by FITC-dextran diffusion rate (B) was determined. (C) Cells were then fixed and immunostained with anti ZO-1 (red) and DAPI (blue). Images shown are representative of four independent experiments. Scale bar = 20 μ m. (D) Quantification of ZO-1 at the TJs expressed as relative (intercellular/cytoplasmatic) ZO-1 distribution. Values are expressed as mean \pm SD and statistical analysis was performed by one-way ANOVA and Dunnett's posthoc analysis (N=4). * P<0.05, ** P<0.01 vs. control.

side that could hamper the binding of mCRP to the basolateral side. This could also prevent mCRP to induce barrier disruption when added from the basolateral side. However, we used filters with a pore size of 0.4 μm , big enough to allow mCRP to reach the basolateral side of the RPE cells. It could be also possible that the receptors on the apical side of the cells have a greater affinity for mCRP than those in the basolateral side. However, we observed a similar pattern with different cell types (CEC, ARPE-19, and primary RPE), and therefore it is likely that our observations are mainly the consequence of mCRP settling on the cell surface.

Given that mCRP seems to induce higher barrier disruption when present in the apical side of RPE cells, we tested whether mCRP could cross the RPE and reach the apical side when added in the basolateral side. RPE cells are critical for oBRB function, enabling selective transport of molecules in and out of the retina to preserve its immune privilege [7]. We found that pCRP was unable to reach the apical side -representing the subretinal space- of RPE cells. However, mCRP was

able to reach the apical side only in ARPE-19 cells, but not in primary porcine RPE cells (Figures 2, 3). ARPE-19, is a spontaneously arising RPE cell line that behaves in many ways like primary RPE cultures as they exhibit barrier functions mediated by tight junctions and secrete cytokines. However, they exhibit reduced TEER [46]. Indeed, ARPE-19 cells are commonly used for studying oxidative stress and cell signaling in AMD because they exhibit features of aged RPE [47]. Thus, the fact that ARPE-19 cells but not primary RPE cells allow mCRP diffusion to the apical side suggest that mCRP could reach the subretinal space when the RPE is damaged. These findings may explain why mCRP had some effect on barrier disruption on ARPE-19 cells but not in primary RPE cells when added from the basolateral side. As such, some mCRP may have crossed the ARPE-19 monolayer reaching the apical side, thereby inducing barrier disruption.

Our current work suggests a plausible mechanism by which mCRP may contribute to RPE dysfunction and AMD progression: the serum-associated isoform of CRP (pCRP), would reach the oBRB by diffusion

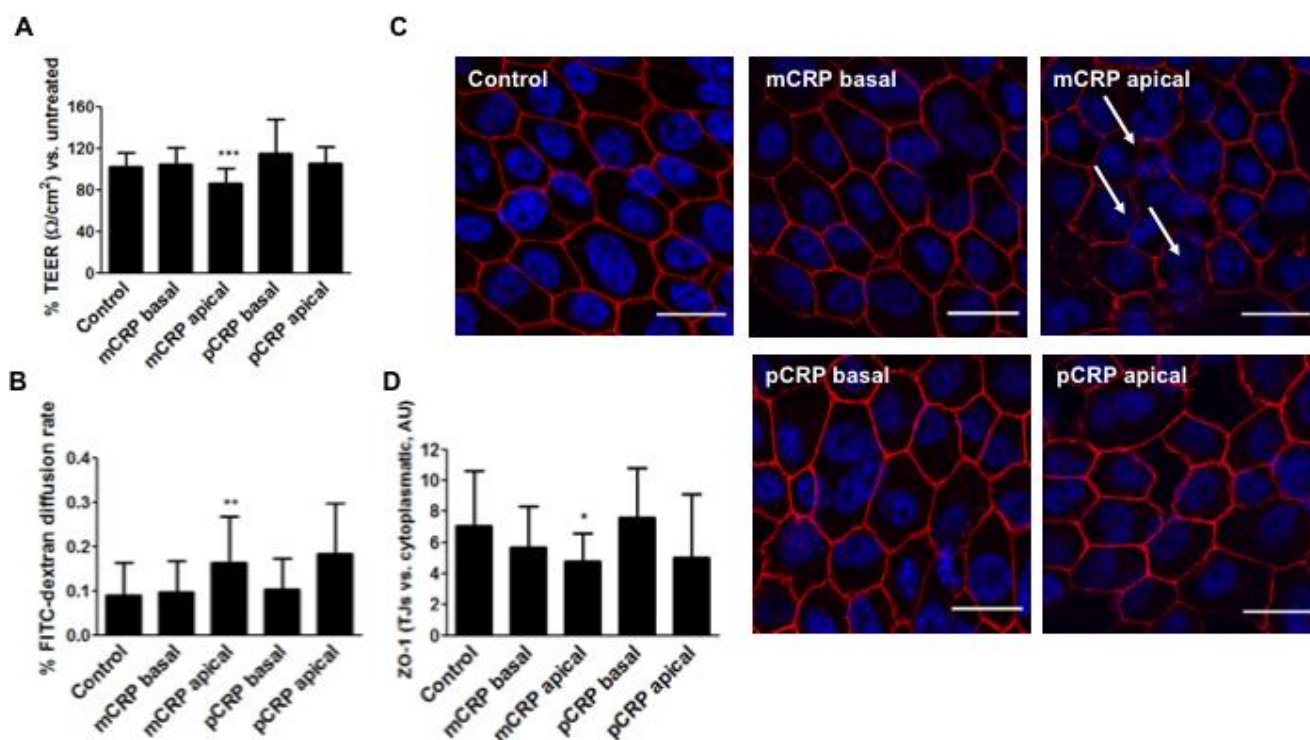


Figure 6. mCRP induces barrier disruption in primary porcine RPE cells in a polarized manner. Primary porcine RPE cells were treated with CRP isoforms for 48h either from the apical side or the basolateral chamber and TEER (A) and paracellular permeability as determined by FITC-dextran diffusion rate (B) was determined. (C) Cells were then fixed and immunostained with anti ZO-1 (red) and DAPI (blue). Images shown are representative of four independent experiments. Arrows show disruption of ZO-1. Scale bar = 20 μm . (D) Quantification of ZO-1 at the TJs expressed as relative (intercellular/cytoplasmic) ZO-1 distribution. Values are expressed as mean \pm SD and statistical analysis was performed by one-way ANOVA and Dunnett's posthoc analysis (N=6). * P<0.05, ** P<0.01, *** P<0.0001 vs. control.

through CECs from the choroidal circulation. Once there, it would undergo dissociation into mCRP via LPC exposed in RPE surface in an inflammatory microenvironment. Alternatively, mCRP could also be generated elsewhere -although in small amounts- or in the surface of CECs before reaching the oBRB. The mCRP in the subepithelial space could reach the apical side of a damaged RPE and amplify the inflammation further disrupting the RPE barrier integrity.

The present work carries some limitations. Firstly, we used a simple model that did not incorporate a proper analogue of the Bruch's membrane. We used fibronectin to grow CECs, laminin to grow primary porcine RPE cells, and ARPE-19 cells were grown without any protein coating in the Transwell filters. Secondly, we did not use RPE cells derived from inducible pluripotent stem cells which would have added more translatability to our work. However, we used two different models of RPE to understand how mCRP contributes to AMD progression, albeit in an *in vitro* setting.

In summary, our findings further support mCRP direct contribution to progression of AMD, at least at the RPE level. The topological experiments elicit that mCRP is proinflammatory when present on the apical side of the RPE. However, mCRP is likely to only reach the apical side of the RPE in compromised RPE health and where barrier functions are compromised. Thus, a plausible scenario would infer that, in the presence of an already aged/damaged RPE, mCRP reaches the apical side of the RPE to amplify the proinflammatory microenvironment and enhance barrier disruption. With respect to previous findings, this pathologic mechanism will be more prevalent in patients carrying the *FH* risk polymorphism for AMD, where mCRP proinflammatory effects remain unrestrained [28].

MATERIALS AND METHODS

CRP isoforms

High purity human pCRP (Calbiochem) was stored in 10 mM Tris, 140 mM NaCl buffer (pH 8.0) containing 2 mM CaCl₂ to prevent spontaneous formation of mCRP from the native pentamer. mCRP was obtained by urea chelation from purified human CRP as previously described [23]. Briefly, pCRP at 1 mg/mL was chelated with 10 mM ethylene diaminetetraacetic acid (EDTA) and incubated in 8.0 M urea for 4 h at 37°C. Urea was removed via dialysis against low ionic strength TBS (0.01 M Tris-HCl and 0.05 M NaCl, pH 7.3). Monomeric CRP concentration was determined by the BCA protein assay. The filtered solution was stored at

4 °C. pCRP was also dialyzed with TBS to remove sodium azide.

Cell culture

ARPE-19, a spontaneously arising human retinal pigment epithelium cell line, was obtained from the American Type Culture Collection (ATCC®CRL-2302™). ARPE-19 (passages 15-20) were cultured in a 50:50 mixture of Dulbecco modified Eagle medium (DMEM) and Ham's F12 (Biowest) supplemented with 10% fetal bovine serum (FBS, Biowest), 2 mM L-glutamine (Biowest), 100 U/mL penicillin (PAA), 0.1 mg/mL streptomycin (Biowest), and 1mM sodium pyruvate (Sigma) in a humidified incubator at 37°C in 5% CO₂. Cells were passed every 4 to 6 days by trypsinization. ARPE-19 cells were plated at confluence onto semi-permeable polycarbonate Transwell® filters, 0.4 µm pore size. At day 3 FBS was reduced to 2 % and cells were maintained in a 37°C and 5% CO₂ incubator for 2–4 weeks, changing media every 3–4 days.

Primary porcine RPE cells were isolated and cultured following the protocol described by [48] with some modifications. Eyes were trimmed of excess tissue and placed in 0.2% povidone iodine for 10 minutes on ice. Eyes were rinsed with sterile distilled water and placed in 1000 U/mL Penicillin-Streptomycin on ice for a minimum of 5 minutes. Anterior segments were removed with a scalpel at the ora serrata. Eyecups were filled with 1 mM EDTA and incubated at 37°C for 30 minutes to loosen the neural retina from the RPE sheet. The retina was gently pulled and detached from the RPE sheet. RPE cells were collected after incubation of the eyecups with 0.05% trypsin with 0.67 mM EDTA at 37°C. After trypsin inactivation with 10% FBS, RPE suspension was centrifuged and plated in DMEM High Glucose (Capricorn Scientific), with L-glutamine and sodium pyruvate, supplemented with 1% penicillin-streptomycin, 1% non-essential amino acids (Corning) and 10% FBS. At day 3 of culture, 5 µg/ml of ciprofloxacin (Sigma) was added to the medium and at day 7, serum was decreased to 1%. Cell monolayers were pigmented and showed the characteristic cobblestone morphology. At day 14, RPE cells were trypsinized and plated at confluence onto semi-permeable polycarbonate Transwell® filters, 0.4 µm pore size, previously coated with laminin. RPE cells were maintained in a 37°C and 5% CO₂ incubator for 2–4 weeks and fed with 1% FBS growth medium every 3–4 days. These RPE cells expressed RPE-specific markers and showed high levels of TEER (see Supplementary Figure 1).

Choroidal endothelial cells from porcine eyes were isolated and cultured as described by Browning et al. [49]

with few modifications. Briefly, after the retina and RPE cell layer were removed with a cell scraper, the complex choroid-Bruch's membrane was peeled off from the sclera, cut into small pieces and washed three times with Minimum Essential Medium (MEM, ThermoFisher). The pieces were incubated with 0.1% collagenase (Sigma) for 2 hours at 37°C. The collagenase was neutralized with MEM containing 10% FBS and the mixture was passed through a 20G syringe. After centrifugation and washing with isolation medium, cells were resuspended in 0.1% BSA-PBS, adjusted to 1×10^7 cells/ml, and incubated with rabbit anti-CD31 (Abcam) (20 μ l per ml of cell suspension) for 1 hour at room temperature (RT) with agitation. Cells were centrifuged, washed with PBS and incubated with Dynabeads® for 45 minutes at 4°C. Endothelial cells positively selected were resuspended in EGM-MV2 (PromoCell) without hydrocortisone and seeded onto 0.5% gelatin coated wells. CECs expressed characteristic endothelial markers (CD31, and VWF) and showed the capacity of endothelial tube formation for up to passage 8 (see Supplementary Figure 2). CECs were plated at confluence onto semi-permeable polycarbonate Transwell® filters, 0.4 μ m pore size, previously coated with 10 μ g/mL fibronectin and maintained at 37°C and 5% CO₂ incubator in EGM-MV2 media (Promocell).

Measurement of transepithelial electrical resistance (TEER)

TEER was measured using a commercial electrical resistance system (Millicell; Millipore) in ARPE-19 and primary porcine RPE monolayers grown on Transwell filters as described above. TEER values were calculated by subtracting the value of a blank (transwell filter without cells). Measurements were repeated at least three times for each filter, and each experiment was repeated at least five times using 2 filters.

Permeability assay

The paracellular permeability of ARPE-19 and primary porcine RPE monolayers was assessed by measuring the passive permeation of FITC-dextran (40 kDa, Sigma-Aldrich) across confluent cells grown on filters for a minimum of 3 weeks. Then, the RPE monolayers were treated with CRP isoforms (10 μ g/mL) for 48h. After 48h treatment, 500 μ g/ml FITC-dextran were added to the apical compartment of the chamber and samples (200 μ l) from the basal medium (lower chamber) were collected 120 min after addition of FITC-dextran. The absorbance of basal and apical medium samples was measured at 485 nm of excitation and 528 nm of emission in a microplate reader (Infinite 200 PRO multimode, Tecan Group Ltd., Switzerland). Each condition was assayed in triplicate and repeated in at least five independent experiments. The diffusion rate

was expressed as a percentage and calculated as follows: (amount of dextran lower chamber) x100 / (amount of dextran upper chamber).

Immunofluorescence

The distribution of ZO-1 and RPE65 in RPE monolayers, CD31 and VWF expression in CECs, and CRP binding to RPE and CECs was examined by immunofluorescence. Filters were cut out, washed with PBS and fixed with 3.8% paraformaldehyde in PBS for 15 min at room temperature (RT). Cells were then washed with PBS, permeabilized with Triton X-100 (0.2% for ZO-1 and CD31, and 0.5 % for RPE65) for 15 minutes and blocked twice with filtered 1% BSA. Cells were then incubated with primary antibody anti-ZO-1 (clone 1A12, Thermo Scientific), anti-RPE65 (clone 401.8B11.3D9, Abcam), anti-CD31 (Abcam), anti-mCRP (3H12 gently provided by Dr LA Potempa) or anti-pCRP (1D6, gently provided by Dr LA Potempa) overnight. After washing three times with PBS, cells were incubated with secondary antibody Alexa Fluor anti-mouse 488 or 568 IgG or anti-rabbit 568 IgG for 1h at RT. Nuclei were counterstained with DAPI. Controls were stained with secondary antibodies only. Stained cells were washed and covered with Prolong Gold antifade reagent (Life Technologies). Images of immunostained cells were recorded on the high-speed spectral confocal microscope Leica TCS-SP5 and analyzed with ImageJ software. ZO-1 was intensity at the tight junctions (TJs) was measured as intensity at the intercellular junction divided by the intensity at the cytoplasm [50].

SDS-PAGE and immunoblotting

The presence of CRP isoforms on apical and basolateral compartments was detected by SDS-PAGE and immunoblotting. Supernatants were centrifuged at 1,000 g for 10 minutes, loaded onto 12.5% polyacrylamide gels and run at 30 mA for 60 minutes. In order to avoid denaturalization of pCRP, samples were not heated and the amount of SDS in the acrylamide gels and the loading and electrophoresis buffers was reduced to 1/20 [51]. Proteins were transferred to a 0.22 μ m nitrocellulose membrane performing a semi-dry transfer protocol. Non-specific binding sites were blocked with 5% non-fat dry milk in 0.1% PBS-Tween for 1 hour at RT, before incubation with anti-mCRP-specific monoclonal antibody 3H12 1:300 in blocking buffer ON at 4°C. Membranes were incubated with the secondary antibody linked to HRP (GAM-HRP, Bio-Rad) for 1 hour at RT. Chemiluminescent signal was detected with the Amersham ECL™ Prime Western blotting detection reagent (GE Healthcare) with ImageQuant LAS4000 (GE Healthcare) and bands were analyzed using ImageJ software.

Determination of mCRP in cell supernatants

mCRP was detected in cellular supernatants (previously centrifuged at 1,000 g for 10 min) by an ELISA assay following the protocol recently described by Zhang et al. [52]. For this purpose, mouse anti-human CRP mAb CRP-8 (Sigma-Aldrich, C1688) was immobilized as capture antibody at 1:1,000 in coating buffer (10 mM sodium carbonate/bicarbonate, pH 9.6) overnight at 4°C. After washing three times for 2 minutes each with TBS, non-specific binding sites were blocked with filtered 1% BSA-TBS for 1 hour at RT. Samples diluted 1:100 in blocking buffer were added into wells for 1 hour at RT. Then, washing step was repeated and samples were incubated with sheep anti-human CRP polyclonal antibody (1:2,000 in blocking buffer) (BindingSite), prior incubation with a HRP-labeled donkey anti-sheep IgG (1:10,000 in blocking buffer) (Abcam). Signaling was detected with VersaMax Microplate Reader and The OD value of each sample was calculated as $OD_{450} - OD_{570}$ nm.

Statistical analysis

Results were expressed as mean \pm SD. Student's *t* test or ANOVA followed by Dunnett's posthoc analysis were used to determine statistical significance between treatments. A value of $P < 0.05$ was considered significant. All calculations were performed using GraphPad Prism (GraphPad Software, San Diego, CA, USA).

CONFLICTS OF INTEREST

Authors have no conflicts of interest to declare.

FUNDING

This work was supported by the Ministry of Science and Innovation of Spain, 'Instituto de Salud Carlos III', 'Fondo de Investigación Sanitaria' (PI19/00265) to B.M. This work was supported by Plan Nacional de Salud (PNS) [PGC2018-094025-B-I00 to G.V and SAF2016-76819-R to L.B.] from the Spanish Ministry of Science and Innovation and funds FEDER "Una Manera de Hacer Europa"; and CIBERCV (to L.B). We thank the support of the Generalitat of Catalunya (Secretaria d'Universitats i Recerca del Departament d'Economia i Coneixement de la Generalitat, 2017 SGR 0701 and 2017 SGR 1480 and the Fundació Investigación Cardiovascular-Fundación Jesus Serra for their continuous support.

REFERENCES

1. Wong WL, Su X, Li X, Cheung CM, Klein R, Cheng CY, Wong TY. Global prevalence of age-related macular degeneration and disease burden projection for 2020 and 2040: a systematic review and meta-analysis. *Lancet Glob Health*. 2014; 2:e106–16. [https://doi.org/10.1016/S2214-109X\(13\)70145-1](https://doi.org/10.1016/S2214-109X(13)70145-1) PMID:25104651
2. Zarbin MA. Current concepts in the pathogenesis of age-related macular degeneration. *Arch Ophthalmol*. 2004; 122:598–614. <https://doi.org/10.1001/archophth.122.4.598> PMID:15078679
3. McLeod DS, Taomoto M, Otsuji T, Green WR, Sunness JS, Luty GA. Quantifying changes in RPE and choroidal vasculature in eyes with age-related macular degeneration. *Invest Ophthalmol Vis Sci*. 2002; 43:1986–93. PMID:12037009
4. Ambati J, Atkinson JP, Gelfand BD. Immunology of age-related macular degeneration. *Nat Rev Immunol*. 2013; 13:438–51. <https://doi.org/10.1038/nri3459> PMID:23702979
5. Shaw AC, Goldstein DR, Montgomery RR. Age-dependent dysregulation of innate immunity. *Nat Rev Immunol*. 2013; 13:875–87. <https://doi.org/10.1038/nri3547> PMID:24157572
6. Donoso LA, Kim D, Frost A, Callahan A, Hageman G. The role of inflammation in the pathogenesis of age-related macular degeneration. *Surv Ophthalmol*. 2006; 51:137–52. <https://doi.org/10.1016/j.survophthal.2005.12.001> PMID:16500214
7. Dick AD. Doyne lecture 2016: intraocular health and the many faces of inflammation. *Eye (Lond)*. 2017; 31:87–96. <https://doi.org/10.1038/eye.2016.177> PMID:27636226
8. Chen M, Luo C, Zhao J, Devarajan G, Xu H. Immune regulation in the aging retina. *Prog Retin Eye Res*. 2019; 69:159–72. <https://doi.org/10.1016/j.preteyeres.2018.10.003> PMID:30352305
9. Crabb JW, Miyagi M, Gu X, Shadrach K, West KA, Sakaguchi H, Kamei M, Hasan A, Yan L, Rayborn ME, Salomon RG, Hollyfield JG. Drusen proteome analysis: an approach to the etiology of age-related macular degeneration. *Proc Natl Acad Sci USA*. 2002; 99:14682–87. <https://doi.org/10.1073/pnas.222551899> PMID:12391305
10. Johnson LV, Leitner WP, Staples MK, Anderson DH. Complement activation and inflammatory processes in

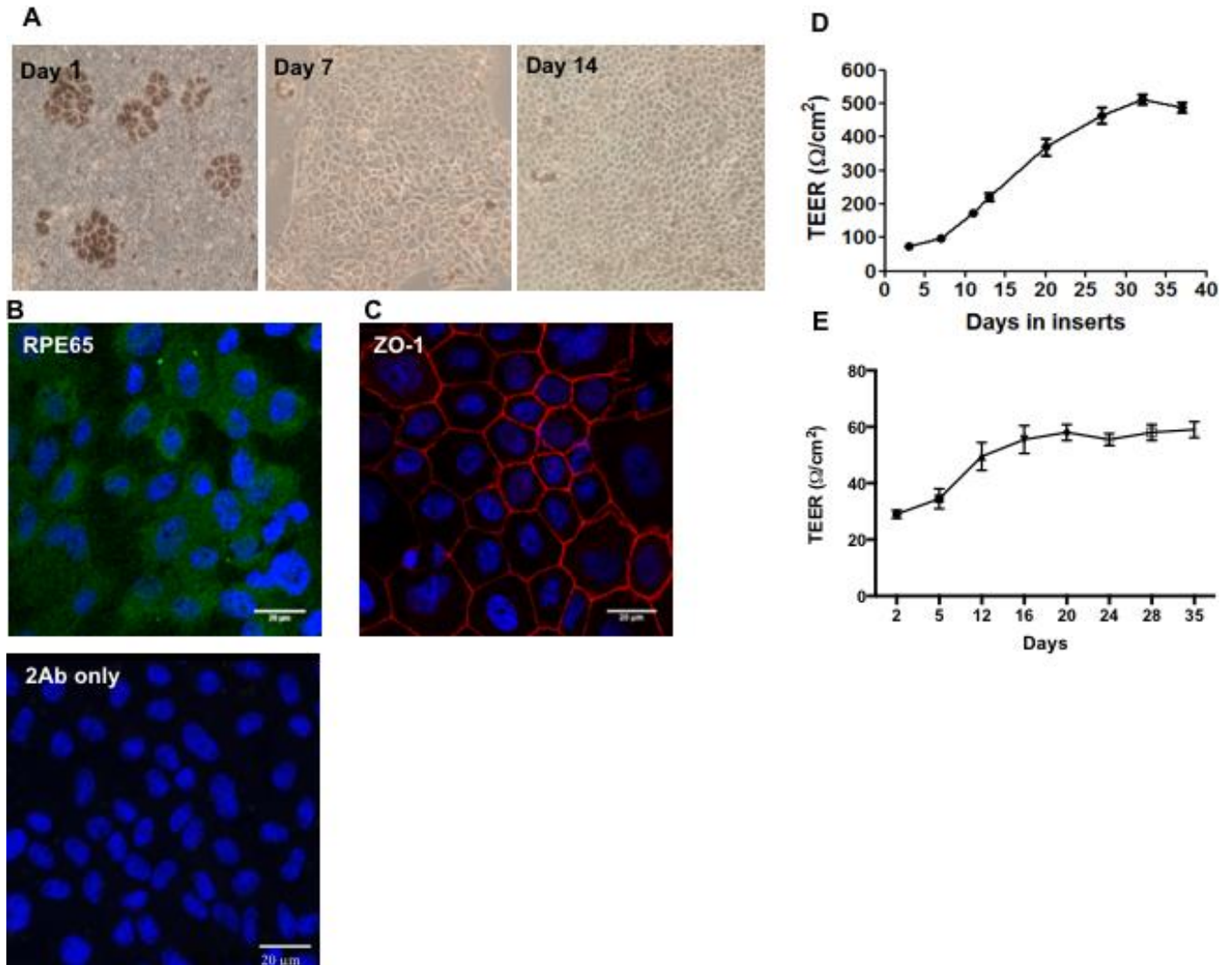
- drusen formation and age related macular degeneration. *Exp Eye Res.* 2001; 73:887–96.
<https://doi.org/10.1006/exer.2001.1094>
PMID:11846519
11. Haines JL, Hauser MA, Schmidt S, Scott WK, Olson LM, Gallins P, Spencer KL, Kwan SY, Nouredine M, Gilbert JR, Schnetz-Boutaud N, Agarwal A, Postel EA, Pericak-Vance MA. Complement factor H variant increases the risk of age-related macular degeneration. *Science.* 2005; 308:419–21.
<https://doi.org/10.1126/science.1110359>
PMID:15761120
 12. Edwards AO, Ritter R 3rd, Abel KJ, Manning A, Panhuysen C, Farrer LA. Complement factor H polymorphism and age-related macular degeneration. *Science.* 2005; 308:421–24.
<https://doi.org/10.1126/science.1110189>
PMID:15761121
 13. Black S, Kushner I, Samols D. C-reactive protein. *J Biol Chem.* 2004; 279:48487–90.
<https://doi.org/10.1074/jbc.R400025200>
PMID:15337754
 14. Seddon JM, George S, Rosner B, Rifai N. Progression of age-related macular degeneration: prospective assessment of c-reactive protein, interleukin 6, and other cardiovascular biomarkers. *Arch Ophthalmol.* 2005; 123:774–82.
<https://doi.org/10.1001/archophth.123.6.774>
PMID:15955978
 15. Vine AK, Stader J, Branham K, Musch DC, Swaroop A. Biomarkers of cardiovascular disease as risk factors for age-related macular degeneration. *Ophthalmology.* 2005; 112:2076–80.
<https://doi.org/10.1016/j.ophtha.2005.07.004>
PMID:16225921
 16. Volanakis JE. Human C-reactive protein: expression, structure, and function. *Mol Immunol.* 2001; 38:189–97.
[https://doi.org/10.1016/s0161-5890\(01\)00042-6](https://doi.org/10.1016/s0161-5890(01)00042-6)
PMID:11532280
 17. Lauer N, Mihlan M, Hartmann A, Schlötzer-Schrehardt U, Keilhauer C, Scholl HP, Charbel Issa P, Holz F, Weber BH, Skerka C, Zipfel PF. Complement regulation at necrotic cell lesions is impaired by the age-related macular degeneration-associated factor-H His402 risk variant. *J Immunol.* 2011; 187:4374–83.
<https://doi.org/10.4049/jimmunol.1002488>
PMID:21930971
 18. Ji SR, Wu Y, Zhu L, Potempa LA, Sheng FL, Lu W, Zhao J. Cell membranes and liposomes dissociate c-reactive protein (CRP) to form a new, biologically active structural intermediate: mCRP(m). *FASEB J.* 2007; 21:284–94.
<https://doi.org/10.1096/fj.06-6722com>
PMID:17116742
 19. Eisenhardt SU, Habersberger J, Murphy A, Chen YC, Woollard KJ, Bassler N, Qian H, von Zur Muhlen C, Hagemeyer CE, Ahrens I, Chin-Dusting J, Bobik A, Peter K. Dissociation of pentameric to monomeric c-reactive protein on activated platelets localizes inflammation to atherosclerotic plaques. *Circ Res.* 2009; 105:128–37.
<https://doi.org/10.1161/CIRCRESAHA.108.190611>
PMID:19520972
 20. Thiele JR, Habersberger J, Braig D, Schmidt Y, Goerendt K, Maurer V, Bannasch H, Scheichl A, Woollard KJ, von Dobschütz E, Kolodgie F, Virmani R, Stark GB, et al. Dissociation of pentameric to monomeric c-reactive protein localizes and aggravates inflammation: in vivo proof of a powerful proinflammatory mechanism and a new anti-inflammatory strategy. *Circulation.* 2014; 130:35–50.
<https://doi.org/10.1161/CIRCULATIONAHA.113.007124>
PMID:24982116
 21. Kheiss T, József L, Hossain S, Chan JS, Potempa LA, Filep JG. Loss of pentameric symmetry of c-reactive protein is associated with delayed apoptosis of human neutrophils. *J Biol Chem.* 2002; 277:40775–81.
<https://doi.org/10.1074/jbc.M205378200>
PMID:12198121
 22. Kheiss T, József L, Potempa LA, Filep JG. Conformational rearrangement in c-reactive protein is required for proinflammatory actions on human endothelial cells. *Circulation.* 2004; 109:2016–22.
<https://doi.org/10.1161/01.CIR.0000125527.41598.68>
PMID:15051635
 23. Molins B, Peña E, Vilahur G, Mendieta C, Slevin M, Badimon L. C-reactive protein isoforms differ in their effects on thrombus growth. *Arterioscler Thromb Vasc Biol.* 2008; 28:2239–46.
<https://doi.org/10.1161/ATVBAHA.108.174359>
PMID:18787187
 24. Mullins RF, Russell SR, Anderson DH, Hageman GS. Drusen associated with aging and age-related macular degeneration contain proteins common to extracellular deposits associated with atherosclerosis, elastosis, amyloidosis, and dense deposit disease. *FASEB J.* 2000; 14:835–46.
PMID:10783137
 25. Anderson DH, Mullins RF, Hageman GS, Johnson LV. A role for local inflammation in the formation of drusen in the aging eye. *Am J Ophthalmol.* 2002; 134:411–31.
[https://doi.org/10.1016/s0002-9394\(02\)01624-0](https://doi.org/10.1016/s0002-9394(02)01624-0)
PMID:12208254

26. Molins B, Pascual-Méndez A, Llorenç V, Zarranz-Ventura J, Mesquida M, Adán A, Martorell J. C-reactive protein isoforms differentially affect outer blood-retinal barrier integrity and function. *Am J Physiol Cell Physiol*. 2017; 312:C244–53.
<https://doi.org/10.1152/ajpcell.00057.2016>
PMID:[28003224](https://pubmed.ncbi.nlm.nih.gov/28003224/)
27. Molins B, Fuentes-Prior P, Adán A, Antón R, Arostegui JI, Yagüe J, Dick AD. Complement factor H binding of monomeric c-reactive protein downregulates proinflammatory activity and is impaired with at risk polymorphic CFH variants. *Sci Rep*. 2016; 6:22889.
<https://doi.org/10.1038/srep22889> PMID:[26961257](https://pubmed.ncbi.nlm.nih.gov/26961257/)
28. Molins B, Romero-Vázquez S, Fuentes-Prior P, Adán A, Dick AD. C-reactive protein as a therapeutic target in age-related macular degeneration. *Front Immunol*. 2018; 9:808.
<https://doi.org/10.3389/fimmu.2018.00808>
PMID:[29725335](https://pubmed.ncbi.nlm.nih.gov/29725335/)
29. Chirco KR, Whitmore SS, Wang K, Potempa LA, Halder JA, Stone EM, Tucker BA, Mullins RF. Monomeric c-reactive protein and inflammation in age-related macular degeneration. *J Pathol*. 2016; 240:173–83.
<https://doi.org/10.1002/path.4766> PMID:[27376713](https://pubmed.ncbi.nlm.nih.gov/27376713/)
30. Johnson PT, Betts KE, Radeke MJ, Hageman GS, Anderson DH, Johnson LV. Individuals homozygous for the age-related macular degeneration risk-conferring variant of complement factor H have elevated levels of CRP in the choroid. *Proc Natl Acad Sci USA*. 2006; 103:17456–61.
<https://doi.org/10.1073/pnas.0606234103>
PMID:[17079491](https://pubmed.ncbi.nlm.nih.gov/17079491/)
31. Chirco KR, Flamme-Wiese MJ, Wiley JS, Potempa LA, Stone EM, Tucker BA, Mullins RF. Evaluation of serum and ocular levels of membrane attack complex and c-reactive protein in CFH-genotyped human donors. *Eye (Lond)*. 2018; 32:1740–42.
<https://doi.org/10.1038/s41433-018-0170-8>
PMID:[30013157](https://pubmed.ncbi.nlm.nih.gov/30013157/)
32. Alizadeh E, Mammadzada P, André H. The different facades of retinal and choroidal endothelial cells in response to hypoxia. *Int J Mol Sci*. 2018; 19:3846.
<https://doi.org/10.3390/ijms19123846>
PMID:[30513885](https://pubmed.ncbi.nlm.nih.gov/30513885/)
33. Boguslawski G, McGlynn PW, Potempa LA, Filep JG, Labarrere CA. Conduct unbecoming: c-reactive protein interactions with a broad range of protein molecules. *J Heart Lung Transplant*. 2007; 26:705–13.
<https://doi.org/10.1016/j.healun.2007.04.006>
PMID:[17613401](https://pubmed.ncbi.nlm.nih.gov/17613401/)
34. Bhutto IA, Baba T, Merges C, Juriasinghani V, McLeod DS, Luttly GA. C-reactive protein and complement factor H in aged human eyes and eyes with age-related macular degeneration. *Br J Ophthalmol*. 2011; 95:1323–30.
<https://doi.org/10.1136/bjo.2010.199216>
PMID:[21633121](https://pubmed.ncbi.nlm.nih.gov/21633121/)
35. Schneeweis C, Gräfe M, Bungenstock A, Spencer-Hänsch C, Fleck E, Goetze S. Chronic CRP-exposure inhibits VEGF-induced endothelial cell migration. *J Atheroscler Thromb*. 2010; 17:203–12.
<https://doi.org/10.5551/jat.3004>
PMID:[20173307](https://pubmed.ncbi.nlm.nih.gov/20173307/)
36. Verma S, Wang CH, Li SH, Dumont AS, Fedak PW, Badiwala MV, Dhillon B, Weisel RD, Li RK, Mickle DA, Stewart DJ. A self-fulfilling prophecy: c-reactive protein attenuates nitric oxide production and inhibits angiogenesis. *Circulation*. 2002; 106:913–19.
<https://doi.org/10.1161/01.cir.0000029802.88087.5e>
PMID:[12186793](https://pubmed.ncbi.nlm.nih.gov/12186793/)
37. Bello G, Cailotto F, Hanriot D, Kolopp-Sarda MN, Latger-Cannard V, Hess K, Zannad F, Longrois D, Ropars A. C-reactive protein (CRP) increases VEGF-a expression in monocytic cells via a PI3-kinase and ERK 1/2 signaling dependent pathway. *Atherosclerosis*. 2008; 200:286–93.
<https://doi.org/10.1016/j.atherosclerosis.2007.12.046>
PMID:[18280482](https://pubmed.ncbi.nlm.nih.gov/18280482/)
38. Chen J, Gu Z, Wu M, Yang Y, Zhang J, Ou J, Zuo Z, Wang J, Chen Y. C-reactive protein can upregulate VEGF expression to promote ADSC-induced angiogenesis by activating HIF-1 α via CD64/PI3k/Akt and MAPK/ERK signaling pathways. *Stem Cell Res Ther*. 2016; 7:114.
<https://doi.org/10.1186/s13287-016-0377-1>
PMID:[27526687](https://pubmed.ncbi.nlm.nih.gov/27526687/)
39. Slevin M, Matou-Nasri S, Turu M, Luque A, Rovira N, Badimon L, Boluda S, Potempa L, Sanfeliu C, de Vera N, Krupinski J. Modified c-reactive protein is expressed by stroke neovessels and is a potent activator of angiogenesis in vitro. *Brain Pathol*. 2010; 20:151–65.
<https://doi.org/10.1111/j.1750-3639.2008.00256.x>
PMID:[19170684](https://pubmed.ncbi.nlm.nih.gov/19170684/)
40. Krupinski J, Turu MM, Martinez-Gonzalez J, Carvajal A, Juan-Babot JO, Iborra E, Slevin M, Rubio F, Badimon L. Endogenous expression of c-reactive protein is increased in active (ulcerated noncomplicated) human carotid artery plaques. *Stroke*. 2006; 37:1200–04.
<https://doi.org/10.1161/01.STR.0000217386.37107.be>
PMID:[16601222](https://pubmed.ncbi.nlm.nih.gov/16601222/)
41. Slevin M, Matou S, Zeinolabediny Y, Corpas R, Weston R, Liu D, Boras E, Di Napoli M, Petcu E, Sarroca S, Popa-Wagner A, Love S, Font MA, et al. Monomeric c-reactive protein—a key molecule driving development of Alzheimer’s disease associated with brain ischaemia? *Sci Rep*. 2015; 5:13281.

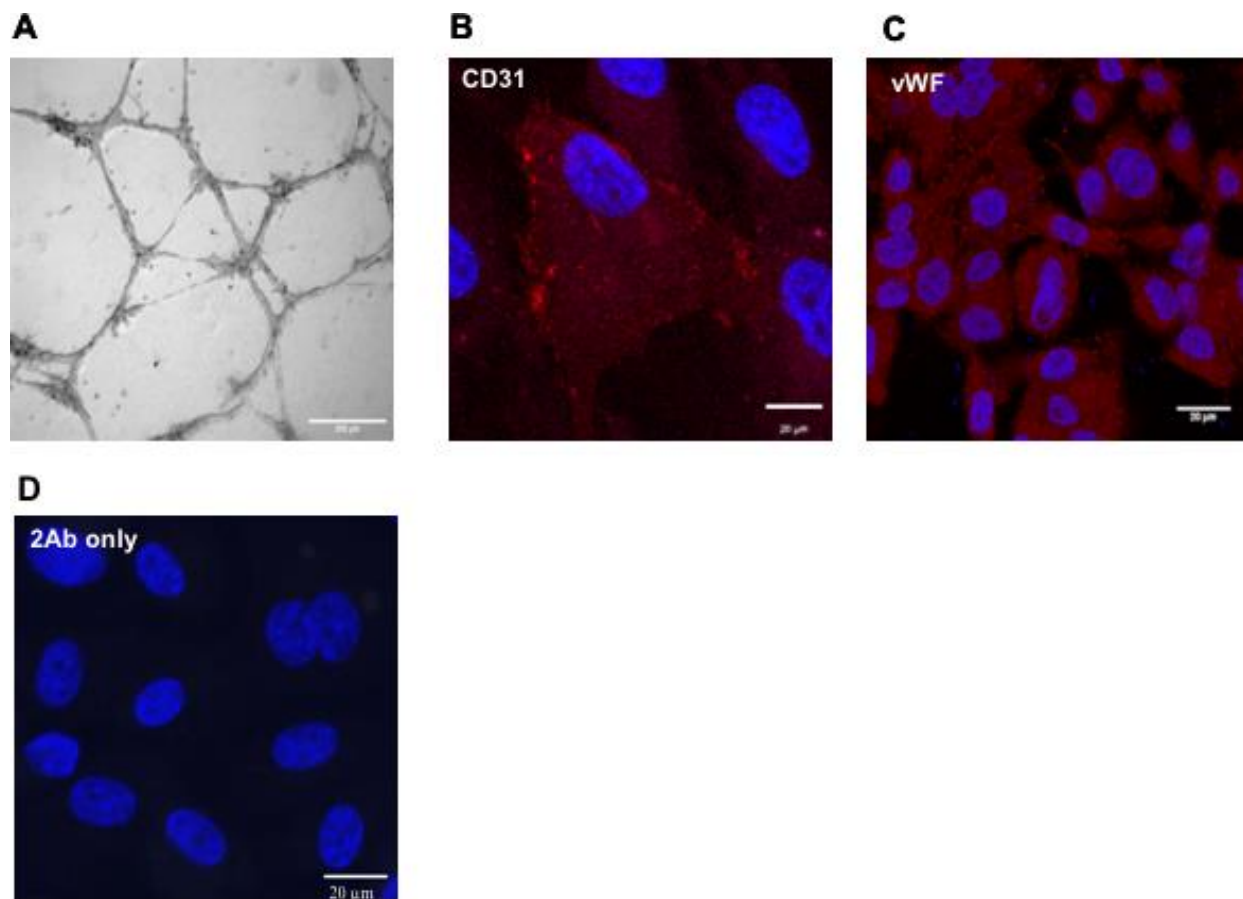
- <https://doi.org/10.1038/srep13281>
PMID:26335098
42. Li HY, Wang J, Wu YX, Zhang L, Liu ZP, Filep JG, Potempa LA, Wu Y, Ji SR. Topological localization of monomeric c-reactive protein determines proinflammatory endothelial cell responses. *J Biol Chem*. 2014; 289:14283–90.
<https://doi.org/10.1074/jbc.M114.555318>
PMID:24711458
43. Singh U, Devaraj S, Dasu MR, Ciobanu D, Reusch J, Jialal I. C-reactive protein decreases interleukin-10 secretion in activated human monocyte-derived macrophages via inhibition of cyclic AMP production. *Arterioscler Thromb Vasc Biol*. 2006; 26:2469–75.
<https://doi.org/10.1161/01.ATV.0000241572.05292.fb>
PMID:16917108
44. Ji SR, Ma L, Bai CJ, Shi JM, Li HY, Potempa LA, Filep JG, Zhao J, Wu Y. Monomeric c-reactive protein activates endothelial cells via interaction with lipid raft microdomains. *FASEB J*. 2009; 23:1806–16.
<https://doi.org/10.1096/fj.08-116962>
PMID:19136614
45. Mora RC, Bonilha VL, Shin BC, Hu J, Cohen-Gould L, Bok D, Rodriguez-Boulan E. Bipolar assembly of caveolae in retinal pigment epithelium. *Am J Physiol Cell Physiol*. 2006; 290:C832–43.
<https://doi.org/10.1152/ajpcell.00405.2005>
PMID:16251472
46. Ablonczy Z, Dahrouj M, Tang PH, Liu Y, Sambamurti K, Marmorstein AD, Crosson CE. Human retinal pigment epithelium cells as functional models for the RPE in vivo. *Invest Ophthalmol Vis Sci*. 2011; 52:8614–20.
<https://doi.org/10.1167/iovs.11-8021>
PMID:21960553
47. Tong N, Jin R, Zhou Z, Wu X. Involvement of microRNA-34a in age-related susceptibility to oxidative stress in ARPE-19 cells by targeting the silent mating type information regulation 2 homolog 1/p66shc pathway: implications for age-related macular degeneration. *Front Aging Neurosci*. 2019; 11:137.
<https://doi.org/10.3389/fnagi.2019.00137>
PMID:31249522
48. Toops KA, Tan LX, Lakkaraju A. A detailed three-step protocol for live imaging of intracellular traffic in polarized primary porcine RPE monolayers. *Exp Eye Res*. 2014; 124:74–85.
<https://doi.org/10.1016/j.exer.2014.05.003>
PMID:24861273
49. Browning AC, Gray T, Amoaku WM. Isolation, culture, and characterisation of human macular inner choroidal microvascular endothelial cells. *Br J Ophthalmol*. 2005; 89:1343–47.
<https://doi.org/10.1136/bjo.2004.063602>
PMID:16170129
50. Molins B, Mora A, Romero-Vázquez S, Pascual-Méndez A, Rovira S, Figueras-Roca M, Balcells M, Adán A, Martorell J. Shear stress modulates inner blood retinal barrier phenotype. *Exp Eye Res*. 2019; 187:107751.
<https://doi.org/10.1016/j.exer.2019.107751>
PMID:31394104
51. Taylor KE, van den Berg CW. Structural and functional comparison of native pentameric, denatured monomeric and biotinylated c-reactive protein. *Immunology*. 2007; 120:404–11.
<https://doi.org/10.1111/j.1365-2567.2006.02516.x>
PMID:17163961
52. Zhang L, Li HY, Li W, Shen ZY, Wang YD, Ji SR, Wu Y. An ELISA assay for quantifying monomeric c-reactive protein in plasma. *Front Immunol*. 2018; 9:511.
<https://doi.org/10.3389/fimmu.2018.00511>
PMID:29593741

SUPPLEMENTARY MATERIALS

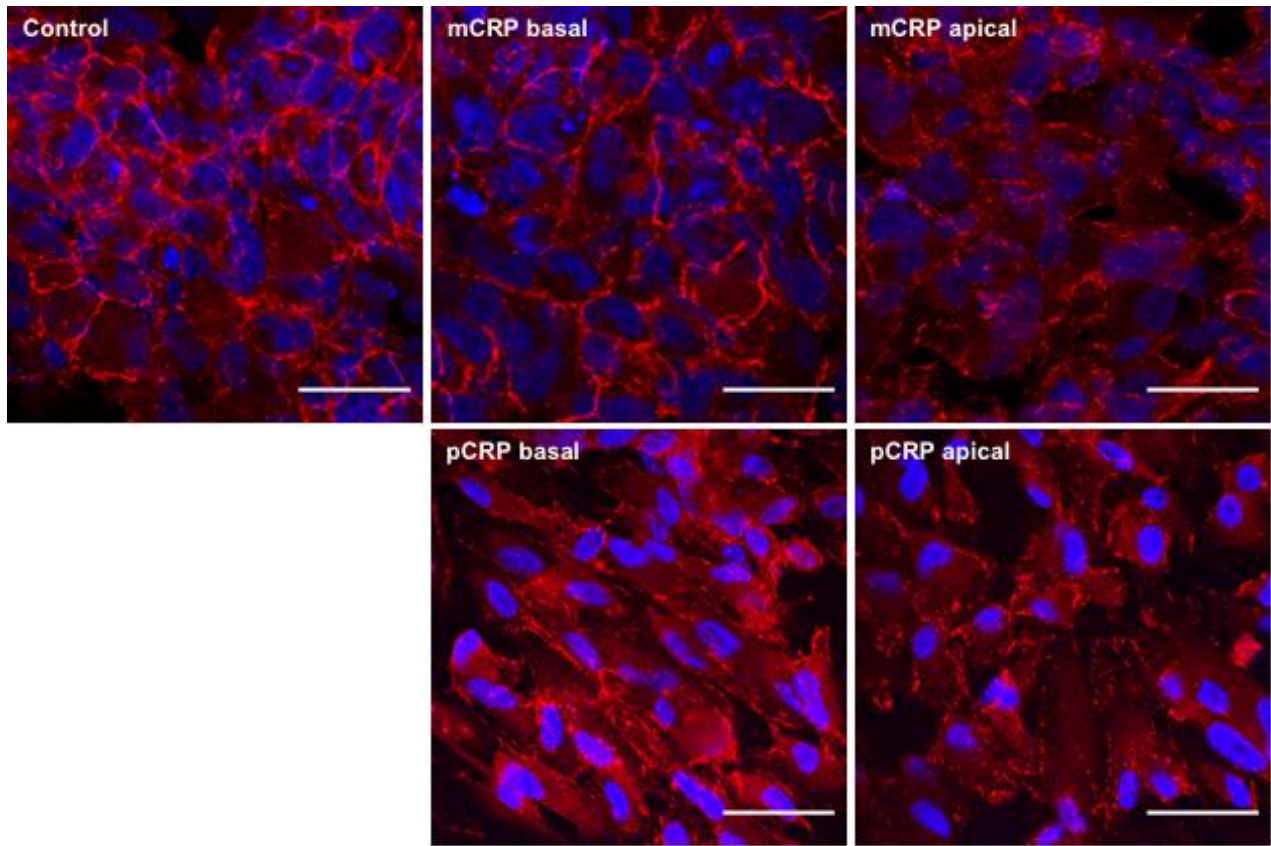
Supplementary Figures



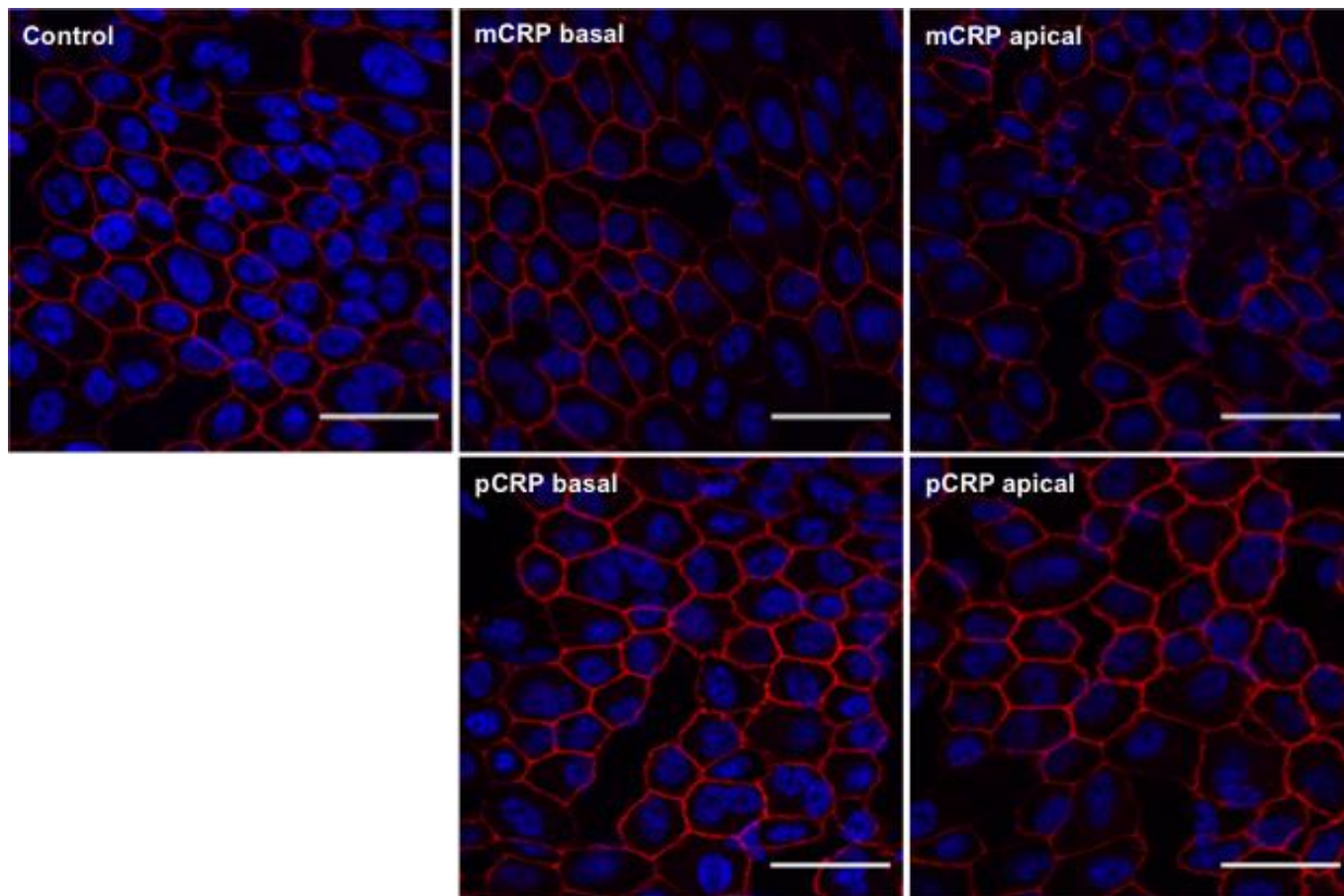
Supplementary Figure 1. Characterization of RPE cells. (A) Cells harvested for 1, 7 and 14 days after plating. Objective lens 10x. Primary porcine RPE cells cultured for 30 days were stained with antibodies to RPE65 (green) (B) and ZO-1 (red) (C). Scale bar = 20 μm . (D) TEER values of primary porcine RPE cells plated at 280,000 cells/ cm^2 on laminin coated Transwell™ filters. (E) TEER values of ARPE-19 cells plated at 250,000 cells/ cm^2 on Transwell™ filters for 35 days.



Supplementary Figure 2. Characterization of primary porcine CECs. (A) Primary porcine CECs were cultured into pure matrigel-coated wells and allowed to form capillary-like structures for 24 hours. Scale bar = 500 μm . Primary porcine CECs were stained with antibodies against CD31 (B) and VWF (C). Scale bar = 20 μm . (D) Negative control with cells stained without primary antibody.



Supplementary Figure 3. Effect of CRP isoforms on ZO-1 expression in ARPE-19 cells. Cells were fixed and immunostained with anti ZO-1 (red) and DAPI (blue). Scale bar = 30 μ m.



Supplementary Figure 4. Effect of CRP isoforms on ZO-1 expression in primary porcine RPE cells. Cells were fixed and immunostained with anti ZO-1 (red) and DAPI (blue). Scale bar = 30 μ m.

Role of Citicoline in an *in vitro* AMD model

Sonali Nashine¹, M. Cristina Kenney^{1,2}

¹Department of Ophthalmology, Gavin Herbert Eye Institute, University of California Irvine, Irvine, CA 92697, USA

²Department of Pathology and Laboratory Medicine, University of California Irvine, Irvine, CA 92697, USA

Correspondence to: M. Cristina Kenney; **email:** mkenney@uci.edu

Keywords: Citicoline, age-related macular degeneration (AMD), neuroprotection, RPE, mitochondria

Received: January 2, 2020

Accepted: March 31, 2020

Published: May 29, 2020

Copyright: Nashine et al. This is an open-access article distributed under the terms of the Creative Commons Attribution License (CC BY 3.0), which permits unrestricted use, distribution, and reproduction in any medium, provided the original author and source are credited.

ABSTRACT

Citicoline is the exogenous form of the nootropic, Cytidine 5'-diphosphate-choline that exerts its neuroprotective effects in the brain as well as in the eye. The current study characterized the cytoprotective effects of purified Citicoline in transmitochondrial AMD (Age-related Macular Degeneration) RPE cybrid cells which carry diseased mitochondria from clinically characterized AMD patients. The effects of Citicoline were examined via flow cytometry analysis of AnnexinV/ PI-stained cells, IncuCyte live-cell imaging analysis to quantify cells undergoing caspase-3/7-mediated apoptosis, analyses of gene expression profiles of apoptosis, hypoxia, and angiogenesis markers, and measurement of ROS levels and cell viability. Our results demonstrated that Citicoline when added exogenously alleviates apoptotic effects as evidenced by diminished AnnexinV/PI and Caspase-3/7 staining, downregulation of apoptosis genes, enhanced cell viability, and reduced oxidative stress in AMD RPE cybrid cells. In conclusion, our study identified Citicoline as a protector in AMD RPE cybrid cells *in vitro*. However, further studies are required to establish the merit of Citicoline as a cytoprotective molecule in AMD and to decipher the molecular underpinnings of its mechanism of action in AMD.

INTRODUCTION

Citicoline is the international nonproprietary name given to the exogenous pharmacological form of Cytidine 5'-diphosphate-choline (CDP-Choline, CDPCho), a naturally occurring endogenous nucleotide compound that is water-soluble and has a molecular weight of 488.32 g/mol [1, 2]. CDP-Choline is comprised of cytosine base, ribose, pyrophosphate, and choline. The endogenous production of CDP-Choline from choline is an intermediate step in the *de novo* synthesis of phosphatidylcholine which is one of the most abundant cell membrane lipids in human and animal tissues [3]. By activating the biosynthesis of structural phospholipids, Citicoline maintains neuronal membrane integrity, influences neurotransmitter levels, increases norepinephrine and dopamine levels in the central nervous system, restores the activity of membrane sodium/potassium ATPase and mitochondrial ATPase, and enhances brain function [1]. Owing to these mechanisms, Citicoline has been

successfully used as a neuroprotective agent to prevent neuronal aging and improve memory and learning *in vivo* [4]. Furthermore, it has been extensively used in preclinical studies and clinical trials for neurodegenerative diseases including Parkinson's disease and glaucoma. Citicoline administration improves motor responses in Parkinson's disease via stimulation of dopaminergic system [5]. Furthermore, Citicoline preserves the function of the retina and the visual cortex in glaucoma patients, and delays the progression of glaucoma disease [6–8]. Parisi et al. demonstrated that Citicoline injected intramuscularly improves retinal and visual function in glaucoma patients [9].

The primary advantages of Citicoline as a neuroprotective compound are: a) negligible toxicity in humans and animals, b) >90 % bioavailability, c) administration feasible via intravenous, intramuscular, or oral routes, and d) following oral ingestion, Citicoline is metabolized to cytidine and choline which enter the systemic circulation where cytidine is converted to

uridine; both choline and uridine cross the blood-brain barrier [10–12]. Although the use of Citicoline in the rescue of neuronal cells and attenuation of retinal neurodegeneration is well-established, its potential role in preventing apoptotic cell death in retinal pigment epithelium (RPE) cells and in Age-related Macular Degeneration (AMD) pathology remains uncharacterized and awaits detailed investigation.

In quest of identifying novel therapeutic candidates for AMD, the goal of this study was to test the hypothesis that Citicoline, a naturally occurring nootropic, will protect against apoptotic cell death in an *in vitro* AMD model i.e., transmitochondrial AMD RPE cybrid cells which are created by fusing mitochondrial DNA-deficient APRE-19 (*Rho0*) cells with platelets isolated from AMD patients. Since nuclear content is the same and the cells differ only in mitochondrial DNA (mtDNA) content, the differences in biochemical or molecular profiles in AMD RPE cybrid cell lines can be attributed to variations in mitochondrial DNA of AMD patients. Our previous studies have shown that the AMD RPE cybrid cells carry mtDNA damage from the AMD patients. Extensive characterization studies using various endpoints that measure cellular and mitochondrial health have demonstrated dysfunctional AMD mitochondria, significantly higher mitochondrial superoxide generation, increased oxidative stress and apoptosis, and reduced mtGFP (Green Fluorescent Protein) staining in AMD

RPE cybrids compared to normal RPE cybrids. Therefore, our previous findings have established substantive cellular damage due to increased oxidative stress and apoptotic cell death in AMD RPE cybrid cell lines compared to the normal RPE cybrid cell lines [13–15].

This *in vitro* study supports our hypothesis as Citicoline conferred significant protection against apoptotic cell death that was in-part mediated by damaged mtDNA from AMD patients in transmitochondrial AMD RPE cybrid cells.

RESULTS

Citicoline reduces apoptotic cells as shown by diminished Annexin V fluorescence intensity

The ability of Citicoline to attenuate apoptosis was examined via Flow Cytometry analysis of untreated and Citicoline-treated AMD RPE cybrid cells stained with apoptotic and dead cell markers, namely Annexin V and Propidium Iodide (PI), respectively (Figure 1A–1E). Figure 1A and 1C show representative Flow cytometry images and Figure 1B and 1D show representative scatter plots of untreated and Citicoline-treated AMD RPE cells stained with Annexin V/ PI.

Figure 1E quantifies the Annexin V/ PI fluorescence intensity in AMD RPE cybrid cells and demonstrates that

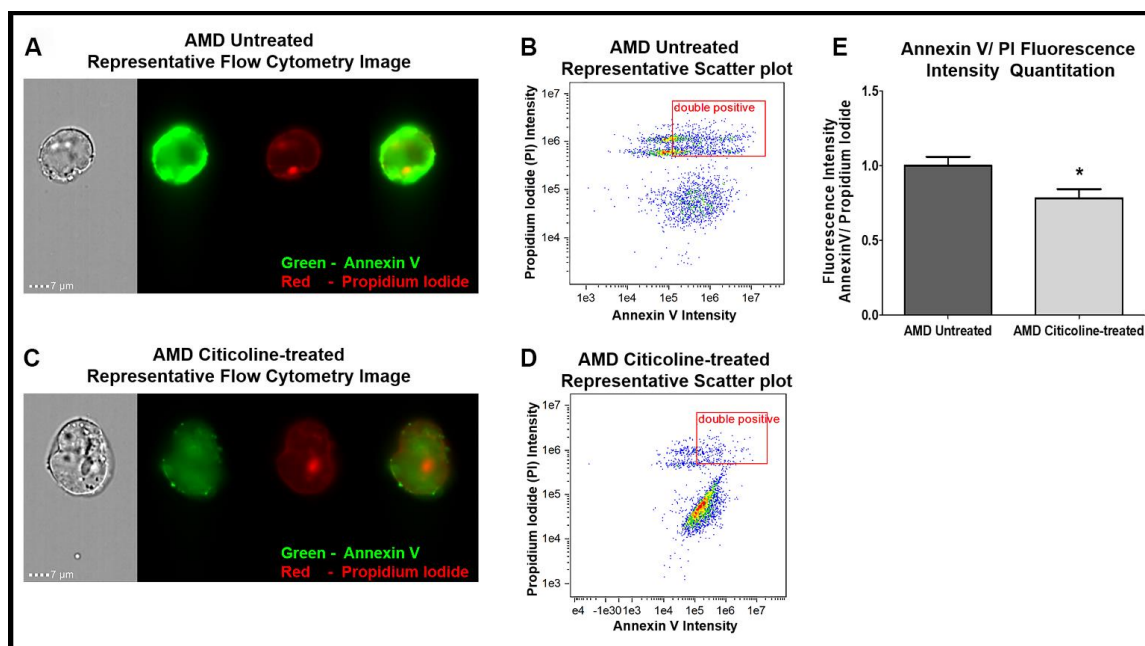


Figure 1. (A) AMD Untreated cells' Representative Annexin V/ PI staining flow cytometry image; (B) AMD Untreated cells' Representative Annexin V/ PI fluorescence intensity scatter plot; (C) AMD Citicoline-treated cells' Representative Annexin V/ PI staining flow cytometry image; (D) AMD Citicoline-treated cells' Representative Annexin V/ PI fluorescence intensity scatter plot; (E) AMD Untreated vs. AMD Citicoline-treated Annexin V/ PI fluorescence intensity quantitation.

Citicoline caused significant reduction in apoptotic cells. Flow cytometry analysis revealed a 21.67 % decrease in Annexin V/ PI double positives' fluorescence intensity in Citicoline-treated AMD RPE cybrid cells (0.783 ± 0.06 a.u.) compared to their untreated counterparts (1 ± 0.059 a.u.) ($p=0.04$, $n=6$).

Citicoline downregulates apoptosis-associated genes

Apoptosis is regulated by multiple genes that act at various levels of the apoptotic cell death pathway. Exogenous addition of Citicoline downregulated the pro-apoptotic genes significantly (Figure 2A–2D). Compared to their untreated counterparts, Citicoline-treated AMD RPE cybrid cells showed decreased gene expression of: *BAX* gene by 28.6 % (AMD Untreated: 1 ± 0.096 , AMD Citicoline-treated: 0.714 ± 0.068 ; $p=0.03$, $n=8$) (Figure 2A), *Caspase-3* gene by 77.2 % (AMD Untreated: 1 ± 0.248 , AMD Citicoline-treated: 0.228 ± 0.043 ; $p=0.0079$, $n=5$) (Figure 2B), *Caspase-9* gene by 37.2 % (AMD Untreated: 1 ± 0.147 , AMD Citicoline-treated: 0.628 ± 0.028 ; $p=0.03$, $n=5$) (Figure 2C), and *BCL2L13* gene by 28.4 % (AMD Untreated: 1 ± 0.065 , AMD Citicoline-treated: 0.716 ± 0.064 ; $p=0.010$, $n=8$) (Figure 2D). Furthermore, Citicoline treatment led to a 32.4 % increase in cell viability (AMD Untreated: 1 ± 0.081 , AMD Citicoline-treated: 1.324 ± 0.084 ; $p=0.015$, $n=6$) (Figure 2E).

Citicoline reduces Caspase-3/7-mediated apoptosis

To examine and compare Caspase-3/7-mediated apoptosis between untreated and Citicoline-treated AMD RPE cybrid cells, we performed IncuCyte® Live-Cell Imaging Analysis using Caspase-3/7 Green and NucLight Red dyes (Figure 3A–3C). Figure 3A shows representative IncuCyte live-cell images. The upper panel represents untreated AMD group and the lower panel represents the Citicoline-treated AMD group. Addition of Citicoline led to a 55.99 % decrease in Overlap object count (i.e., Caspase-3/7 Green+NucLight Red staining)/ NucLight Red object count in AMD RPE cybrid cells: Untreated - 1 ± 0.078 a.u. and Citicoline-treated - 0.440 ± 0.125 a.u. ($p=0.03$, $n=4$) at 48 h (Figure 3B). At 72 h, a 47.54 % drop in Overlap object count was observed in Citicoline-treated AMD RPE cybrid cells (0.52 ± 0.11 a.u.) compared to their untreated counterparts (1 ± 0.082 a.u.) ($p=0.03$, $n=4$) (Figure 3C). Therefore, Citicoline prevents Caspase-3/7-mediated apoptosis in AMD RPE cybrid cells.

Citicoline reduces oxidative stress

To measure reactive oxygen species levels, we performed ROS assay using H2DCFDA reagent. Compared to their untreated counterparts, Citicoline-treated AMD RPE cybrid cells showed decreased ROS

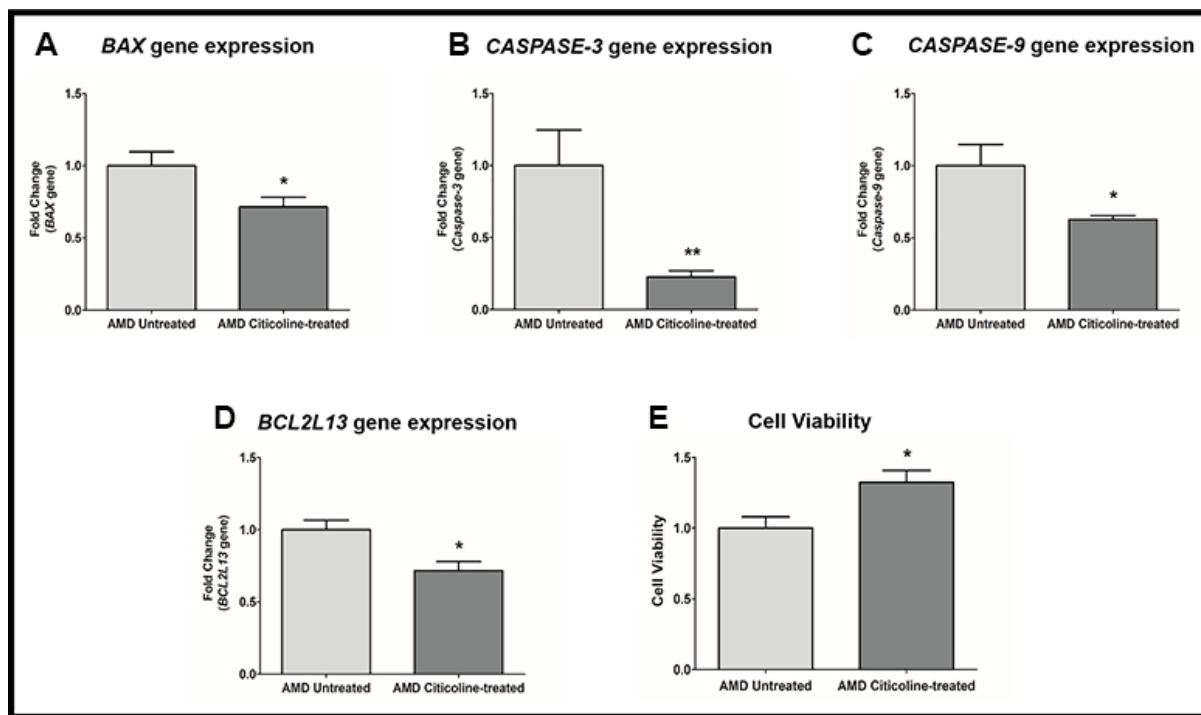


Figure 2. (A) *BAX* gene expression in AMD Untreated and AMD Citicoline-treated cells. (B) *Caspase-3* gene expression in AMD Untreated and AMD Citicoline-treated cells. (C) *Caspase-9* gene expression in AMD Untreated and AMD Citicoline-treated cells. (D) *Caspase-9* gene expression in AMD Untreated and AMD Citicoline-treated cells. (E) Cell viability MTT assay.

levels by 22.8 % (AMD Untreated: 1 ± 0.059 , AMD Citicoline-treated: 0.772 ± 0.040 ; $p=0.013$, $n=5$) (Figure 4A). Compared to their untreated counterparts, Citicoline-treated AMD RPE cybrid cells showed increased gene expression of: *HMOX1* gene by 76.6 %

(AMD Untreated: 1 ± 0.1267 , AMD Citicoline-treated: 1.766 ± 0.28 ; $p=0.0379$, $n=8$) (Figure 4B) and *HMOX2* gene by 20.4 % (AMD Untreated: 1 ± 0.0214 , AMD Citicoline-treated: 1.204 ± 0.020 ; $p=0.0286$, $n=4$) (Figure 4C).

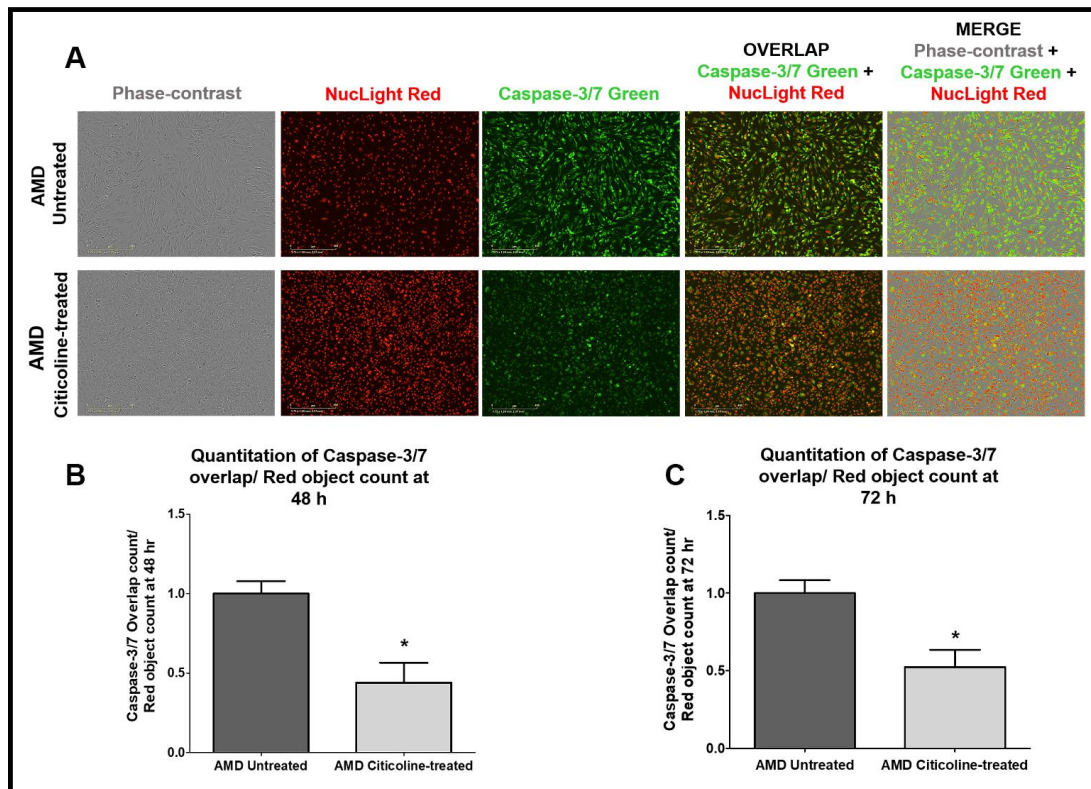


Figure 3. (A) Upper and lower panels show Representative Incucyte live-cell images of untreated and Citicoline-treated AMD cells, respectively, in phase-contrast (first column), stained with NuLight Red (second column), stained with Caspase-3/7 Green (third column), overlap i.e., Caspase-3/7 + NuLight (fourth column), and Merge i.e., Phase-contrast + Caspase-3/7 + NuLight (fifth column). Scale bar = 400 μ m. (B) Quantitation of Caspase-3/7 overlap/ Red object count at the 48 h time point. (C) Quantitation of Caspase-3/7 overlap/ Red object count at the 72 h time point.

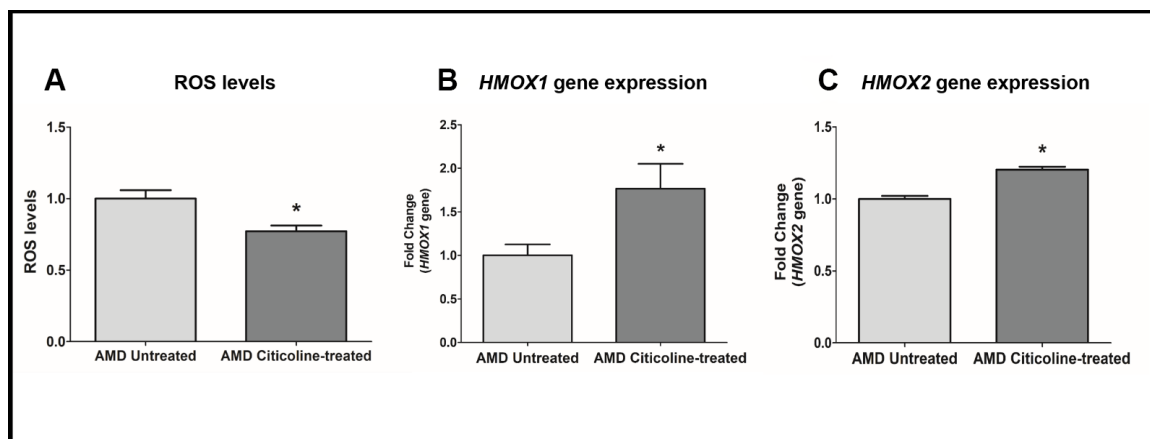


Figure 4. (A) ROS levels in AMD Untreated and AMD Citicoline-treated cells, (B) *HMOX1* gene expression levels in AMD Untreated and AMD Citicoline-treated cells, and (C) *HMOX2* gene expression levels in AMD Untreated and AMD Citicoline-treated cells.

Citicoline downregulates *HIF-1α* and *VEGF* genes

HIF1α (Hypoxia-inducible factor 1- α), a transcription factor, is a master regulator of cellular response to hypoxic stress. *HIF-1α* activation leads to up-regulation of *VEGF*, which in turn plays a key role in angiogenesis in choroidal neovascularization in AMD. Compared to their untreated counterparts, Citicoline-treated AMD RPE cybrid cells showed decreased gene expression of: *HIF-1α* gene by 34 % (AMD Untreated: 1 ± 0.123 , AMD Citicoline-treated: 0.66 ± 0.041 ; $p=0.01$, $n=7$) (Figure 5A) and *VEGF* gene by 32.8 % (AMD Untreated: 1 ± 0.069 , AMD Citicoline-treated: 0.672 ± 0.077 ; $p=0.015$, $n=6$) (Figure 5B).

DISCUSSION

Our current study identified the cytoprotective potential of exogenously added purified Citicoline in trans-mitochondrial AMD RPE cybrid cells *in vitro*. Using a combination of apoptotic assays, we found that Citicoline mitigates apoptotic cell death as evidenced by diminished Annexin V/ PI positive cell population, reduced Caspase-3/7-mediated apoptosis in live cells, downregulation of apoptotic genes, and enhanced cell viability in Citicoline-treated transmitochondrial AMD RPE cybrid cells. Additionally, treatment with Citicoline led to a significant reduction in reactive oxygen species and upregulation of *HMOX1* and *HMOX2* genes, thereby suppressing oxidative stress and supporting cell survival. Furthermore, significantly decreased expression of *HIF-1α* (hypoxia marker) and *VEGF* (angio-genesis marker) genes, post-Citicoline treatment, may in part have contributed to the cytoprotective action of Citicoline in AMD RPE cybrid cells. To our knowledge, this is the first report to identify the anti-apoptotic potential of Citicoline in an *in vitro* transmitochondrial AMD RPE cybrid cell model.

Apoptosis is characterized by specific morphological and biochemical changes in the cell, which can be detected via varied techniques. Annexin V is a eukaryotic cellular protein commonly used as a probe to detect apoptotic cells due to its ability to bind phosphatidylserine i.e., a cell membrane phospholipid that faces the cytoplasmic surface in healthy cells but is translocated to the extracellular side in apoptotic cells. Phosphatidylserine(s) exposure on the outer leaflet of the plasma membrane signals macrophages and marks the apoptotic cells for phagocytosis [16]. In this study, we used a recombinant Annexin V conjugated to the Alexa Fluor® 488 fluorophore to create a photostable conjugate with maximum sensitivity. Along with Annexin V, we used the red-fluorescent propidium iodide (PI) nucleic acid binding dye which is impermeant to live cells and apoptotic cells, but stains dead cells with red fluorescence. Flow cytometry analyses enabled us to distinguish viable cells from apoptotic cells and necrotic cells. In this study, Citicoline treatment led to diminished Annexin V/ PI fluorescence intensity, indicating the ability of Citicoline to lower apoptotic cell death in trans-mitochondrial AMD cells. This is consistent with a previous study in which the apoptosis inhibitory action of Citicoline was demonstrated using Annexin V/ FITC Flow cytometry analysis in a mouse model of cerebral malaria (CM); administration of Citicoline rescued cells in an experimental model of CM *in vitro* as well conferred partial protection against cell death and neurological syndrome in murine CM [17].

In the current study, Citicoline treatment in AMD RPE cybrid cells caused downregulation of *BAX*, *Caspase-3*, *Caspase-9*, and *BCL2L13* genes indicating that Citicoline mediates its cytoprotective effects by influencing both the intrinsic and extrinsic pathways of apoptosis. Our previous studies have demonstrated that

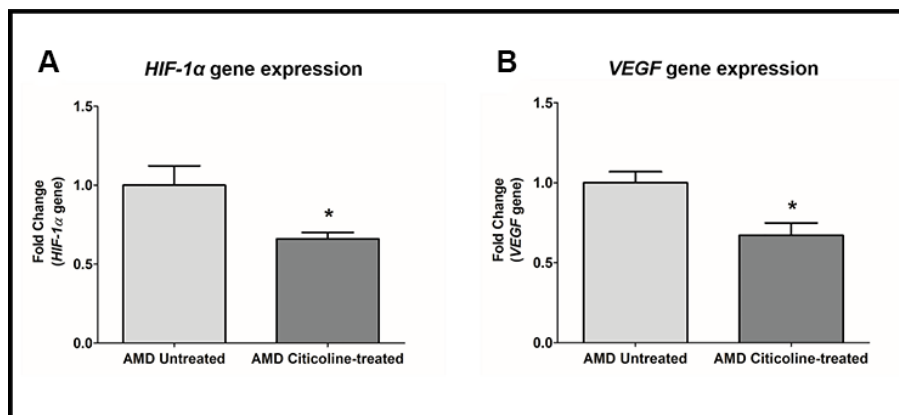


Figure 5. (A) *HIF-1α* gene expression in AMD Untreated and AMD Citicoline-treated cells. (B) *VEGF* gene expression in AMD Untreated and AMD Citicoline-treated cells.

dysfunctional AMD mitochondria in the AMD RPE cybrid cells contribute to the activation of apoptosis and enhanced expression of apoptotic markers such as *BAX* and *Caspase-3* [14]. BAX (Bcl-2-Associated X protein) is a member of the Bcl-2 family and a key regulator of the intrinsic apoptotic pathway. Apoptotic stimuli activate BAX and BAK (Bcl-2 homologous Antagonist/Killer) which oligomerize and initiate permeabilization of the mitochondrial outer membrane, which is considered a critical step in apoptosis [18]. Caspase-3 is an effector caspase that via its protease activity initiates and coordinates crucial apoptotic events such as the exposure of Phosphatidylserine to the extracellular side of the plasma membrane and cellular degradation processes including DNA fragmentation and cytoskeletal disruption. Caspase-3 is the point of convergence for the extrinsic and intrinsic apoptotic pathways [19]. On receiving apoptotic stimuli, the mitochondria release cytochrome c which binds to Apaf-1 and recruits Caspase-9 thereby activating the latter. Caspase-9 is a part of the apoptosome and initiates the activation of downstream effector caspases [20]. BCL2L13/Bcl-rambo is a member of the Bcl-2 family of proteins that regulate apoptosis. In cells, Bcl-rambo is localized to the mitochondria, and its overexpression induces apoptosis. Bcl-rambo mediates apoptosis by associating with adenine nucleotide translocator (ANT), a component of the mitochondrial permeability transition pore, to induce its opening [21]. Previous studies have attributed the Citicoline-mediated suppression of apoptosis to its ability to upregulate the Sirtuin1 (SIRT1) protein, downregulate procaspase and caspase expression, and neutralization of BAX family proteins thereby preventing cleavage of PARP and subsequent DNA damage [22–24].

Next, we compared Caspase-3/7-mediated apoptosis between untreated and Citicoline-treated AMD RPE cybrid cells using InCuCyte® Live-Cell Imaging Analysis system and Caspase-3/7 Green and NucLight Red reagents. The InCuCyte Caspase-3/7 Green Apoptosis Reagent couples the activated Caspase-3/7 recognition motif (DEVD) to a DNA intercalating dye and enables real-time quantification of cells undergoing caspase-3/7 mediated apoptosis. This reagent is an inert, non-fluorescent substrate which when added to culture medium, crosses the cell membrane where it is cleaved by activated caspase-3/7 resulting in the release of the DNA dye and fluorescent staining of the nuclear DNA. The InCuCyte NucLight Rapid Red Reagent is a cell permeable DNA stain that specifically stains nuclei in live cells and enables real-time quantification of cell proliferation. Addition of this reagent to normal healthy cells does not interfere with cell growth and morphology and provides homogenous staining of nuclei. In the culture medium, this inert stain crosses the

cell membrane and has excellent specificity for DNA without the need for a wash step. In the current study, Citicoline-treated AMD cells showed significantly lower Overlap object count (i.e., (Caspase-3/7 Green + NucLight Red staining)/ Red object count) at 48 h and 72 h compared to their untreated counterparts. To our knowledge, this is the first study to demonstrate the role of Citicoline in reducing Caspase-3/7-mediated apoptosis in live cell imaging systems.

Our current results are consistent with previous studies which have demonstrated the apoptosis inhibitory effect of Citicoline in various *in vitro* and *in vivo* models of neurodegenerative conditions. For instance, Alvarez et al. showed Citicoline-mediated protection of hippocampal neurons against apoptosis induced by brain beta-amyloid deposits plus cerebral hypoperfusion in rats [25]. Moreover, Citicoline protects against high-glucose-induced neurotoxicity and against excitotoxic cell damage in retina [26]. As demonstrated in recent studies, one mechanism by which Citicoline mediates its cytoprotective action could be via suppression of ERK1/2 signaling which is known to induce apoptosis in the inner and outer retina [27]. Additionally, Citicoline is known to exert its pro-survival action in diabetic retina by preventing glial activation and suppressing the expression of NF- κ B and TNF- α [28].

The current study also revealed that Citicoline alleviates ROS production and downregulates *HIF-1 α* and *VEGF* genes in AMD RPE cybrid cells. These results are corroborated by previous findings that demonstrate that Citicoline reduces ROS species, stabilizes cell membranes, reduces the volume of ischemic lesions, and provides neuroprotection in ischemic and hypoxic conditions via: a) attenuating the accumulation of free fatty acids especially arachidonic acid, b) preventing the activation of phospholipase A2 in both membrane and mitochondrial fractions, and c) stimulating the synthesis of glutathione [29, 30].

In summary, although further studies with Citicoline/AMD RPE cybrid cells are underway, these results present novel findings that identify Citicoline to be a potential protector that attenuates apoptotic cell death in AMD. Citicoline is available as an over-the-counter dietary supplement in the U.S. and offers the advantage of easy access that shortens considerably the transition from lab bench to clinic.

MATERIALS AND METHODS

Human subjects

The University of California Irvine's IRB (Institutional Review Board) approved research with human subjects

(Approval #2003–3131). All participants provided informed consent and clinical investigations were performed according to the tenets of Declaration of Helsinki.

Cell culture

Passage 5 AMD ARPE-19 transmitochondrial cybrid cell lines were created as described previously [14]. Briefly, these cybrid cell lines were prepared by polyethylene glycol fusion of mitochondria DNA-deficient ARPE-19 (*Rho⁰*) cell line with platelets isolated from AMD patients. Cybrid status and that the cybrids have acquired their mtDNAs from the donor individuals was confirmed using allelic discrimination, Sanger sequencing, and Next-Generation Sequencing.

Culture conditions

The base medium for this cybrid cell line is DMEM-F12 Medium (Cat. # 10-092CM, Fisher Scientific, Pittsburgh, PA). DMEM-F12 Medium contains 3.15 g/L D-glucose, 2.5 mM L-glutamine, 15 mM HEPES, 0.5 mM sodium pyruvate, and 1200 mg/L sodium bicarbonate. To make the complete growth medium, fetal bovine serum was added to the base medium to a final concentration of 10 %.

Treatment with Citicoline

Purified Citicoline was obtained from Sigma-Aldrich (St. Louis, MO) and used at a concentration of 1mM for all experiments. Water was used as an initial solvent. Citicoline was subsequently dissolved in culture media for treatment of cells.

Flow cytometry

Cells were stained with recombinant Annexin V conjugated to fluorescein (FITC annexin V), as well as red-fluorescent propidium iodide (PI) nucleic acid binding dye (Life Technologies). The stained cells were analyzed by flow cytometry, measuring the fluorescence emission at 530 nm and >575 nm. Live cells show only a low level of fluorescence, apoptotic cells show green fluorescence and dead cells show both red and green fluorescence.

Quantitative Real-Time PCR (qRT-PCR)

RNA extraction, cDNA synthesis, and qRT-PCR analysis were performed as described previously [14]. QuantiTect Primer Assays were used to study the expression of *Caspase-3* gene (Cat. # QT00023947, Qiagen, Germantown, MD), *BAX* gene (Cat. # QT00031192, Qiagen), *HIF-1 α* gene (Cat. # QT00083664, Qiagen),

HMOX1 gene (Cat. # QT00092645, Qiagen), and *HMOX2* gene (Cat. # QT00039942, Qiagen). KiCqStart® SYBR® green primers were used to examine the expression of *VEGF* gene (Cat. # kspq12012, Sigma). Specific housekeeper gene used was *HPRT1* (Cat. # QT00059066, Qiagen). Data analysis was performed using $\Delta\Delta C_t$ method which was calculated by subtracting ΔC_t of the AMD group from ΔC_t of the normal group. ΔC_t was the difference between the C_t s (threshold cycles) of the target gene and C_t s of the housekeeper gene (reference gene). Fold change was calculated using the following formula: Fold change = $2^{\Delta\Delta C_t}$.

Cell viability assay

The numbers of viable cells were measured using the MTT (3-(4,5-dimethylthiazol-2-yl)-2,5-diphenyltetrazolium bromide) assay. Cells were plated in 96-well tissue culture plates, treated with 1 mM Citicoline followed by addition of MTT. Cells were incubated at 37 °C for 1 h, followed by addition of DMSO (Dimethyl SulfOxide). Signal absorbance was measured at 570 nm and background absorbance measured at 630 nm. Normalized absorbance values were obtained by subtracting background absorbance from signal absorbance. The colorimetric signal obtained was proportional to the cell number.

IncuCyte live-cell imaging

IncuCyte live-cell imaging was performed as described previously [31, 32]. Cells were seeded in 96-well plates at a density of 5,000 – 10,000 cells/well followed by staining with IncuCyte® NucLight Rapid Red (1:500) and Caspase-3/7 Green (1:1000) labeling reagents. Stained cell plates were placed into the IncuCyte® live-cell analysis system and allowed to warm to 37 °C for 30 min prior to scanning. Phase Contrast, Green, and Red channels were selected, 5 images were taken per well with an average scan interval of 2 h until the experiment was complete. Fluorescent objects were quantified using the IncuCyte® integrated analysis software that minimizes background fluorescence.

Reactive oxygen species (ROS) assay

To quantitate ROS levels, the cell-permeant H2DCFDA (2', 7'-dichlorodihydrofluorescein diacetate) was used as an indicator for ROS in cells. Stock solution of 5mM H2DCFDA was prepared in DMSO. Stock solution was then diluted in DPBS (Dulbecco's Phosphate-Buffered Saline) to obtain a working concentration of 10 μ M. Cells were plated in 96-well tissue culture plates followed by treatment with 1mM Citicoline. 10 μ M H2DCFDA solution was added to cells and incubated

for 30 min at 37 °C. H2DCFDA was then replaced with DPBS. Fluorescence which was measured at excitation 492 nm and emission 520 nm was proportional to ROS levels in cells.

Statistical analysis

Non-parametric Mann-Whitney test (GraphPad Prism 5.0; GraphPad Software, CA, USA) was used to analyze data between groups and to determine significance; $p \leq 0.05$ was statistically significant. 'n' represents the number of biological replicates i.e., the number of individual AMD cybrid cell lines used in the experiment.

AUTHOR CONTRIBUTIONS

S.N.: Designed and performed the experiments; acquired, analyzed, and interpreted data; wrote and edited the manuscript. M.C.K.: Reviewed data and the manuscript; provided resources.

CONFLICTS OF INTEREST

The authors declare no conflicts of interest.

FUNDING

This research was funded by Arnold and Mabel Beckman Foundation, Discovery Eye Foundation, Polly and Michael Smith, Edith and Roy Carver, Iris and B. Gerald Cantor Foundation, Unrestricted Departmental Grant from Research to Prevent Blindness and NEI R01 EY0127363, UCI School of Medicine, and support of the Institute for Clinical and Translational Science (ICTS) at University of California Irvine. S.N. is a recipient of the 2017 Genentech/ ARVO AMD Translational Research Fellowship and the 2016 RPB pilot research grant.

REFERENCES

1. Grieb P. Neuroprotective properties of citicoline: facts, doubts and unresolved issues. *CNS Drugs*. 2014; 28:185–93.
<https://doi.org/10.1007/s40263-014-0144-8>
PMID:[24504829](https://pubmed.ncbi.nlm.nih.gov/24504829/)
2. Conant R, Schauss AG. Therapeutic applications of citicoline for stroke and cognitive dysfunction in the elderly: a review of the literature. *Altern Med Rev*. 2004; 9:17–31.
PMID:[15005642](https://pubmed.ncbi.nlm.nih.gov/15005642/)
3. Fagone P, Jackowski S. Phosphatidylcholine and the CDP-choline cycle. *Biochim Biophys Acta*. 2013; 1831:523–32.
<https://doi.org/10.1016/j.bbalip.2012.09.009>

- PMID:[23010477](https://pubmed.ncbi.nlm.nih.gov/23010477/)
4. Gareri P, Castagna A, Cotroneo AM, Putignano S, De Sarro G, Bruni AC. The role of citicoline in cognitive impairment: pharmacological characteristics, possible advantages, and doubts for an old drug with new perspectives. *Clin Interv Aging*. 2015; 10:1421–9.
<https://doi.org/10.2147/CIA.S87886>
PMID:[26366063](https://pubmed.ncbi.nlm.nih.gov/26366063/)
 5. Eberhardt R, Birbamer G, Gerstenbrand F, Rainer E, Traegner H. Citicoline in the treatment of parkinson's disease. *Clin Ther*. 1990; 12:489–95.
PMID:[2289218](https://pubmed.ncbi.nlm.nih.gov/2289218/)
 6. Parisi V. Electrophysiological assessment of glaucomatous visual dysfunction during treatment with cytidine-5'-diphosphocholine (Citicoline): a study of 8 years of follow-up. *Doc Ophthalmol*. 2005; 110:91–102.
<https://doi.org/10.1007/s10633-005-7348-7>
PMID:[16249960](https://pubmed.ncbi.nlm.nih.gov/16249960/)
 7. Parisi V, Coppola G, Centofanti M, Oddone F, Angrisani AM, Ziccardi L, Ricci B, Quaranta L, Manni G. Evidence of the neuroprotective role of citicoline in glaucoma patients. *Prog Brain Res*. 2008; 173:541–54.
[https://doi.org/10.1016/S0079-6123\(08\)01137-0](https://doi.org/10.1016/S0079-6123(08)01137-0)
PMID:[18929133](https://pubmed.ncbi.nlm.nih.gov/18929133/)
 8. Ottobelli L, Manni GL, Centofanti M, Iester M, Alleva F, Rossetti L. Citicoline oral solution in glaucoma: is there a role in slowing disease progression? *Ophthalmologica*. 2013; 229:219–26.
<https://doi.org/10.1159/000350496>
PMID:[23615390](https://pubmed.ncbi.nlm.nih.gov/23615390/)
 9. Parisi V, Manni G, Colacino G, Bucci MG. Cytidine-5'-diphosphocholine (Citicoline) improves retinal and cortical responses in patients with glaucoma. *Ophthalmology*. 1999; 106:1126–34.
[https://doi.org/10.1016/S0161-6420\(99\)90269-5](https://doi.org/10.1016/S0161-6420(99)90269-5)
PMID:[10366081](https://pubmed.ncbi.nlm.nih.gov/10366081/)
 10. Cho HJ, Kim YJ. Efficacy and safety of oral citicoline in acute ischemic stroke: drug surveillance study in 4,191 cases. *Methods Find Exp Clin Pharmacol*. 2009; 31:171–76.
<https://doi.org/10.1358/mf.2009.31.3.1364241>
PMID:[19536360](https://pubmed.ncbi.nlm.nih.gov/19536360/)
 11. Cotroneo AM, Castagna A, Putignano S, Lacava R, Fantò F, Monteleone F, Rocca F, Malara A, Gareri P. Effectiveness and safety of citicoline in mild vascular cognitive impairment: the IDEALE study. *Clin Interv Aging*. 2013; 8:131–37.
<https://doi.org/10.2147/CIA.S38420>
PMID:[23403474](https://pubmed.ncbi.nlm.nih.gov/23403474/)
 12. Weiss GB. Metabolism and actions of CDP-choline as an endogenous compound and administered

- exogenously as citicoline. *Life Sci.* 1995; 56:637–60.
[https://doi.org/10.1016/0024-3205\(94\)00427-t](https://doi.org/10.1016/0024-3205(94)00427-t)
PMID:[7869846](https://pubmed.ncbi.nlm.nih.gov/7869846/)
13. Nashine S, Chwa M, Kazemian M, Thaker K, Lu S, Nesburn A, Kuppermann BD, Kenney MC. Differential expression of complement markers in normal and AMD transmitochondrial cybrids. *PLoS One.* 2016; 11:e0159828.
<https://doi.org/10.1371/journal.pone.0159828>
PMID:[27486856](https://pubmed.ncbi.nlm.nih.gov/27486856/)
 14. Nashine S, Cohen P, Chwa M, Lu S, Nesburn AB, Kuppermann BD, Kenney MC. Humanin G (HNG) protects age-related macular degeneration (AMD) transmitochondrial ARPE-19 cybrids from mitochondrial and cellular damage. *Cell Death Dis.* 2017; 8:e2951.
<https://doi.org/10.1038/cddis.2017.348>
PMID:[28726777](https://pubmed.ncbi.nlm.nih.gov/28726777/)
 15. Nashine S, Cohen P, Nesburn AB, Kuppermann BD, Kenney MC. Characterizing the protective effects of SHLP2, a mitochondrial-derived peptide, in macular degeneration. *Sci Rep.* 2018; 8:15175.
<https://doi.org/10.1038/s41598-018-33290-5>
PMID:[30310092](https://pubmed.ncbi.nlm.nih.gov/30310092/)
 16. Kay JG, Grinstein S. Sensing phosphatidylserine in cellular membranes. *Sensors (Basel).* 2011; 11:1744–55.
<https://doi.org/10.3390/s110201744>
PMID:[22319379](https://pubmed.ncbi.nlm.nih.gov/22319379/)
 17. El-Assaad F, Combes V, Grau GE, Jambou R. Potential efficacy of citicoline as adjunct therapy in treatment of cerebral malaria. *Antimicrob Agents Chemother.* 2014; 58:602–05.
<https://doi.org/10.1128/AAC.02591-12>
PMID:[24165175](https://pubmed.ncbi.nlm.nih.gov/24165175/)
 18. Shamas-Din A, Kale J, Leber B, Andrews DW. Mechanisms of action of Bcl-2 family proteins. *Cold Spring Harb Perspect Biol.* 2013; 5:a008714.
<https://doi.org/10.1101/cshperspect.a008714>
PMID:[23545417](https://pubmed.ncbi.nlm.nih.gov/23545417/)
 19. Porter AG, Jänicke RU. Emerging roles of caspase-3 in apoptosis. *Cell Death Differ.* 1999; 6:99–104.
<https://doi.org/10.1038/sj.cdd.4400476>
PMID:[10200555](https://pubmed.ncbi.nlm.nih.gov/10200555/)
 20. Kuida K. Caspase-9. *Int J Biochem Cell Biol.* 2000; 32:121–24.
[https://doi.org/10.1016/s1357-2725\(99\)00024-2](https://doi.org/10.1016/s1357-2725(99)00024-2)
PMID:[10687948](https://pubmed.ncbi.nlm.nih.gov/10687948/)
 21. Ju L, Chen S, Alimujiang M, Bai N, Yan H, Fang Q, Han J, Ma X, Yang Y, Jia W. A novel role for Bcl2l13 in promoting beige adipocyte biogenesis. *Biochem Biophys Res Commun.* 2018; 506:485–91.
<https://doi.org/10.1016/j.bbrc.2018.10.034>
PMID:[30352689](https://pubmed.ncbi.nlm.nih.gov/30352689/)
 22. Hurtado O, Hernández-Jiménez M, Zarruk JG, Cuartero MI, Ballesteros I, Camarero G, Moraga A, Pradillo JM, Moro MA, Lizasoain I. Citicoline (CDP-choline) increases Sirtuin1 expression concomitant to neuroprotection in experimental stroke. *J Neurochem.* 2013; 126:819–26.
<https://doi.org/10.1111/jnc.12269>
PMID:[23600725](https://pubmed.ncbi.nlm.nih.gov/23600725/)
 23. Sobrado M, López MG, Carceller F, García AG, Roda JM. Combined nimodipine and citicoline reduce infarct size, attenuate apoptosis and increase bcl-2 expression after focal cerebral ischemia. *Neuroscience.* 2003; 118:107–13.
[https://doi.org/10.1016/s0306-4522\(02\)00912-0](https://doi.org/10.1016/s0306-4522(02)00912-0)
PMID:[12676142](https://pubmed.ncbi.nlm.nih.gov/12676142/)
 24. Krupinski J, Ferrer I, Barrachina M, Secades JJ, Mercadal J, Lozano R. CDP-choline reduces pro-caspase and cleaved caspase-3 expression, nuclear DNA fragmentation, and specific PARP-cleaved products of caspase activation following middle cerebral artery occlusion in the rat. *Neuropharmacology.* 2002; 42:846–54.
[https://doi.org/10.1016/s0028-3908\(02\)00032-1](https://doi.org/10.1016/s0028-3908(02)00032-1)
PMID:[12015211](https://pubmed.ncbi.nlm.nih.gov/12015211/)
 25. Alvarez XA, Sampedro C, Lozano R, Cacabelos R. Citicoline protects hippocampal neurons against apoptosis induced by brain beta-amyloid deposits plus cerebral hypoperfusion in rats. *Methods Find Exp Clin Pharmacol.* 1999; 21:535–40.
<https://doi.org/10.1358/mf.1999.21.8.794835>
PMID:[10599052](https://pubmed.ncbi.nlm.nih.gov/10599052/)
 26. Matteucci A, Varano M, Gaddini L, Mallozzi C, Villa M, Pricci F, Malchiodi-Albedi F. Neuroprotective effects of citicoline in in vitro models of retinal neurodegeneration. *Int J Mol Sci.* 2014; 15:6286–97.
<https://doi.org/10.3390/ijms15046286>
PMID:[24736780](https://pubmed.ncbi.nlm.nih.gov/24736780/)
 27. Park CH, Kim YS, Cheon EW, Noh HS, Cho CH, Chung IY, Yoo JM, Kang SS, Choi WS, Cho GJ. Action of citicoline on rat retinal expression of extracellular-signal-regulated kinase (ERK1/2). *Brain Res.* 2006; 1081:203–10.
<https://doi.org/10.1016/j.brainres.2005.12.128>
PMID:[16696125](https://pubmed.ncbi.nlm.nih.gov/16696125/)
 28. Bogdanov P, Sampedro J, Solà-Adell C, Simó-Servat O, Russo C, Varela-Sende L, Simó R, Hernández C. Effects of liposomal formulation of citicoline in experimental diabetes-induced retinal neurodegeneration. *Int J Mol Sci.* 2018; 19:2458.
<https://doi.org/10.3390/ijms19082458>
PMID:[30127248](https://pubmed.ncbi.nlm.nih.gov/30127248/)

29. Trovarelli G, de Medio GE, Dorman RV, Piccinin GL, Horrocks LA, Porcellati G. Effect of cytidine diphosphate choline (CDP-choline) on ischemia-induced alterations of brain lipid in the gerbil. *Neurochem Res.* 1981; 6:821–33.
<https://doi.org/10.1007/BF00965041>
PMID:[6796897](https://pubmed.ncbi.nlm.nih.gov/6796897/)
30. Adibhatla RM, Hatcher JF. Citicoline decreases phospholipase A2 stimulation and hydroxyl radical generation in transient cerebral ischemia. *J Neurosci Res.* 2003; 73:308–15.
<https://doi.org/10.1002/jnr.10672>
PMID:[12868064](https://pubmed.ncbi.nlm.nih.gov/12868064/)
31. Nashine S, Subramaniam SR, Chwa M, Nesburn A, Kuppermann BD, Federoff H, Kenney MC. PU-91 drug rescues human age-related macular degeneration RPE cells; implications for AMD therapeutics. *Aging (Albany NY).* 2019; 11:6691–713.
<https://doi.org/10.18632/aging.102179>
PMID:[31477635](https://pubmed.ncbi.nlm.nih.gov/31477635/)
32. Nashine S, Kanodia R, Nesburn AB, Soman G, Kuppermann BD, Kenney MC. Nutraceutical effects of *Emblica officinalis* in age-related macular degeneration. *Aging (Albany NY).* 2019; 11:1177–88.
<https://doi.org/10.18632/aging.101820>
PMID:[30792375](https://pubmed.ncbi.nlm.nih.gov/30792375/)

Systemic administration of the di-apocarotenoid norbixin (BIO201) is neuroprotective, preserves photoreceptor function and inhibits A2E and lipofuscin accumulation in animal models of age-related macular degeneration and Stargardt disease

Valérie Fontaine¹, Elodie Monteiro¹, Mylène Fournié¹, Elena Brazhnikova¹, Thinhinane Boumedine¹, Cécile Vidal¹, Christine Balducci², Louis Guibout², Mathilde Latil², Pierre J. Dilda², Stanislas Veillet², José-Alain Sahel¹, René Lafont², Serge Camelo²

¹Sorbonne Université, INSERM, CNRS, Institut de la Vision, Paris 75012, France

²Biophytis, Sorbonne Université, Campus Pierre and Marie Curie, Paris 75005, France

Correspondence to: Serge Camelo; email: serge.camelo@biophytis.com

Keywords: norbixin, retinal function, A2E, AMD, Stargardt disease

Received: November 5, 2019

Accepted: March 2, 2020

Published: April 7, 2020

Copyright: Fontaine et al. This is an open-access article distributed under the terms of the Creative Commons Attribution License (CC BY 3.0), which permits unrestricted use, distribution, and reproduction in any medium, provided the original author and source are credited.

ABSTRACT

Atrophic age-related macular degeneration (AMD) and Stargardt disease (STGD) are major blinding diseases affecting millions of patients worldwide, but no treatment is available. In dry AMD and STGD oxidative stress and subretinal accumulation of *N*-retinylidene-*N*-retinylethanolamine (A2E), a toxic by-product of the visual cycle, causes retinal pigment epithelium (RPE) and photoreceptor degeneration leading to visual impairment. Acute and chronic retinal degeneration following blue light damage (BLD) in BALB/c mice and aging of *Abca4*^{-/-} *Rdh8*^{-/-} mice, respectively, reproduce features of AMD and STGD. Efficacy of systemic administrations of 9'-*cis*-norbixin (norbixin), a natural di-apocarotenoid, prepared from *Bixa orellana* seeds with anti-oxidative properties, was evaluated during BLD in BALB/c mice, and in *Abca4*^{-/-} *Rdh8*^{-/-} mice of different ages, following three experimental designs: "preventive", "early curative" and "late curative" supplementations. Norbixin injected intraperitoneally in BALB/c mice, maintained scotopic and photopic electroretinogram amplitude and was neuroprotective. Norbixin chronic oral administration for 6 months in *Abca4*^{-/-} *Rdh8*^{-/-} mice following the "early curative" supplementation showed optimal neuroprotection and maintenance of photoreceptor function and reduced ocular A2E accumulation. Thus, norbixin appears promising as a systemic drug candidate for both AMD and STGD treatment.

INTRODUCTION

Age-related macular degeneration (AMD) is the commonest cause of severe visual loss and blindness in developed countries among individuals aged 60 and older [1]. AMD is a major unmet medical need as it is estimated that more than 20 million patients will be affected by 2050 in the US alone. STGD is the most common hereditary macular dystrophy, mostly affecting young patients aged between 6 and 15 years old with a prevalence of 1/8,000-1/10,000 [2, 3]. It has an

autosomal recessive mode of inheritance and may lead to registered blindness within the second or third decade of life. STGD is caused by mutations in the *ABCR* gene encoding the ATP-binding cassette gene, subfamily A, member 4 (*ABCA4*) transporter which is expressed by photoreceptors and retinal pigmented epithelium (RPE) cells and plays an important role in the visual cycle [4, 5]. Polymorphisms of the gene coding for *ABCA4* have also been associated with increased risk of developing AMD [6]. Other genetic polymorphisms, especially in the *complement factor H*

(*CFH*) gene [7] have also been associated with AMD, but risk factors are mostly linked to age [8, 9] and environmental such as smoking [10]. AMD can either evolve towards neovascular AMD, also called wet AMD, characterized by the growth of new choroidal blood vessels in the subretinal space, or towards geographic atrophy also named dry AMD, characterized by RPE and photoreceptor degeneration. In STGD patients, neovascularization is extremely rare and RPE and photoreceptor atrophy occurs in the vast majority of cases [11]. Thus, despite some differences, dry AMD and STGD share similar pathophysiological mechanisms [11]. In both pathologies, early signs of evolution are characterized by subretinal accumulation of lipids and proteins forming drusen in AMD and flecks in STGD [2, 12]. AMD and STGD evolution are associated with Bruch's membrane thickening, RPE alterations and ultimately to RPE and photoreceptor degeneration. Rod photoreceptors, responsible for scotopic/mesopic vision (i.e. under dim light conditions) are the first visual cells dying in the retina. The cones mediating colored photopic vision under normal light conditions are essentially preserved until late stages of AMD and STGD [13, 14]. Therefore, both AMD and STGD induce the progressive loss of night vision followed by loss of color vision and central vision [3]. To date, no treatment is available for either STGD [11] or dry AMD [15].

Both drusen in AMD and flecks in STGD contain *N*-retinylidene-*N*-retinylethanolamine (A2E), which is a toxic by-product of the visual cycle [16]. It is formed by the reaction of 2 all-*trans* retinal molecules with phosphatidylethanolamine generating *N*-retinylidene-PE (A2E precursor: A2-PE), as a detoxication mechanism of retinal isomers including all-*trans* and 11-*cis*-retinal [17]. Under normal conditions the ABCA4 protein participates in the elimination of A2-PE from the photoreceptors and inhibition of this clearance increases the accumulation of A2E and all-*trans*-retinal dimer in the RPE [18, 19]. Recently, it has been shown that ABCA4 is also expressed in RPE cells where it would participate in the recycling of retinaldehyde released during proteolysis of rhodopsin in endolysosomes following phagocytosis of photoreceptor outer segments [5]. The authors also demonstrated that A2E accumulates at similar rates in RPE from *Abca4*^{-/-} mice reared under cyclic light or total darkness suggesting that *de novo* bis-retinoids formation within RPE endolysosomes contributes more to lipofuscin build-up than do bis-retinoids formed in outer segment discs during light exposure. Therefore, they propose that the clearance of retinaldehydes from RPE phagolysosomes may be more critical for photoreceptor viability than the clearance of retinaldehydes from outer segment discs [5]. *In vitro*, it has been shown that the combination of

blue-light illumination and A2E is toxic for RPE cells; either the ARPE19 cell line or primary porcine RPE cells [20–22]. Indeed, in the presence of blue light and oxygen, A2E undergoes photo-oxidation as evidenced by the appearance of toxic oxygen adducts [23]. It generates small amounts of singlet oxygen and is finally cleaved to small reactive aldehydes, which contribute to its deleterious effects on RPE cells [23]. A2E photo-oxidation products also damage DNA [20, 21] and activate the complement system [24]. Moreover, photosensitization of A2E triggers telomere dysfunction and accelerates RPE senescence [25]. In the absence of illumination, A2E alone affects normal RPE functions by inducing membrane permeabilization and thereby impairing lysosomal function [26]. It also impairs mitochondrial homeostasis and function resulting in the reduction of ATP production [27–30]. Furthermore, high A2E concentrations increase oxidative stress [31] and secretion of inflammatory cytokines by RPE cells *in vitro* [25, 32, 33]. In addition, A2E induces the expression of vascular endothelial growth factor *in vitro* [34] and *in vivo* [32, 35].

A rapid accumulation of A2E and of lipofuscin is observed in 3-month-old *Abca4*^{-/-} *Rdh8*^{-/-} mice [36] and increases in 6-month-old mice [36]. In these mice, progressive A2E accumulation is associated with retinal degeneration and loss of both scotopic and photopic full-field electroretinogram (ERG) responses indicate that both rods and cones are dysfunctional (rod-cone dystrophy) [36, 37]. Indeed, it has been shown that as early as in 3-month-old *Abca4*^{-/-} *Rdh8*^{-/-} mice, the amplitudes of scotopic A and B waves and flicker ERG are reduced [36]. *Abca4*^{-/-} *Rdh8*^{-/-} mice recapitulate most phenotypic retinal alterations observed during STGD and AMD [36, 37], and represent a chronic model of these diseases.

Acute white-light exposure is known to induce apoptosis of photoreceptors in albino mice retinas [38]. The model of light-induced retinopathy is used as an amenable model of AMD and has been used to test several neuroprotective molecules [39].

Norbixin (9'-*cis*-norbixin) is a 6,6'-*di-apo*-carotenoid extracted from annatto (*Bixa orellana*) seeds [40]. Tolerability of norbixin is well known, based on animal and human studies, and supports its use as food additive/dye [41]. Norbixin protects primary porcine RPE cells against phototoxicity induced by A2E and blue-light illumination *in vitro* [22]. Norbixin also reduces the accumulation of A2E by primary porcine RPE cells *in vitro* [22]. We have previously reported that a 3-month supplementation with norbixin in water reduced A2E ocular accumulation *in vivo* in *Abca4*^{-/-} *Rdh8*^{-/-} double-knockout mice [22]. In the same

mouse model, the local treatment with norbixin via intraocular injections inhibited retinal degeneration and the loss of full-field ERG, induced following blue-light illumination [22]. In addition, norbixin was neuroprotective against blue-light damage (BLD) in rats [22].

Here we used an acute BLD model in BALB/c mice modified from our previous article [22] and that is used to rapidly study some features of AMD and the chronic model of AMD and STGD in aging *Abca4*^{-/-} *Rdh8*^{-/-} mice to evaluate the protective efficacy of norbixin. In the present article we demonstrate that norbixin administered systemically is neuroprotective against blue-light-induced retinal degeneration in BALB/c mice. Moreover, we report for the first time that 6-month oral supplementation of *Abca4*^{-/-} *Rdh8*^{-/-} double-knockout mice with chow containing norbixin is neuroprotective and partially preserves the function of both rods and cones *in vivo*. Oral supplementation with norbixin also reduces A2E and lipofuscin accumulation in RPE cells. We define the therapeutic window during which oral supplementation with norbixin is the most effective in relation to progressive photoreceptor loss of function and A2E accumulation.

RESULTS

Norbixin protects the retina of albino BALB/c mice against blue-light-induced photoreceptor degeneration

To determine whether norbixin could protect the retina via a systemic effect we used a model of BLD in albino BALB/c mice. Norbixin (10 mg/kg of body weight) was injected intraperitoneally 30 minutes prior to BLD and 1, 2.5 and 4 hours after the beginning of exposure to blue light (Figure 1A). Four hours of blue-light exposure induced severe loss of retinal function in vehicle-dosed mice, as measured seven days after exposure by scotopic A wave (Figure 1B), scotopic B wave (Figure 1C) and photopic B wave (Figure 1D) ERGs. In the light-exposed mice, intraperitoneal administration of norbixin maintained 40.4 % of the scotopic A wave and 58.4 % of scotopic B wave amplitudes at a flash intensity of 10 cd.s/m² compared to the non-injected group ($p < 0.0001$), whereas there was no effect in the vehicle group. Norbixin treatment also allowed a 60.4 % ($p < 0.001$) preservation of the photopic B wave intensity (Figure 1D). The neuroprotective effect of norbixin was confirmed by morphological evaluation of the retina, 7 days following BLD (Figure 1E). Consistently, treatment with norbixin partially protected photoreceptors against degeneration induced by BLD. Indeed, more photoreceptors were preserved in the norbixin group (+43 %; $p < 0.01$)

than in the non-injected or the vehicle treated groups (Figure 1F and 1G).

Determination of retinal degeneration, ERG amplitudes and A2E accumulation kinetics in *Abca4*^{-/-} *Rdh8*^{-/-} mice of different ages

We characterized precisely the kinetics of i) photoreceptor degeneration of ii) the progressive loss of visual function and of iii) the accumulation of A2E in eyes of *Abca4*^{-/-} *Rdh8*^{-/-} mice in a systematic analysis of this mice model between 2 and 18 months of age. First, in the *Abca4*^{-/-} *Rdh8*^{-/-} mouse model we measured scotopic and photopic ERGs. We found that the amplitude of scotopic A and B waves and photopic B wave decreased progressively between 2 and 18 months of age (Figure 2A–2C). The progressive loss of visual function was paralleled by reduction of the number of photoreceptor nuclei (Figure 2D). Interestingly, losses of visual function and of photoreceptor nuclei started early during the course of aging since diminution were significantly different (scotopic A wave $p < 0.0001$, scotopic B wave $p < 0.001$, photopic A wave $p < 0.01$ and photoreceptor loss $p < 0.0001$) between 2 and 6 months (Figure 2A–2D). At later time points, a significant alteration of ERG was also observed between 6 and 12 months (scotopic A wave only), 9 and 15 months (scotopic A and photopic B waves), and 12 and 18 months (scotopic and photopic A and B waves). The decrease of photoreceptor layers number occurred in three steps: a strong loss between 2 and 6 months followed by a plateau until 12 months, and a second decrease period between 12 and 18 months (Figure 2D). We then determined ocular A2E accumulation in the eyes of *Abca4*^{-/-} *Rdh8*^{-/-} mice. A2E ocular concentration increased significantly between 2 and 6 months ($p < 0.0001$), reached a maximum at 9 months of age followed by a plateau (Figure 2E).

RPE65, cathepsin D and GFAP immunostaining in *Abca4*^{-/-} *Rdh8*^{-/-} mice of different ages

Next, we performed immunohistochemistry studies to characterize RPE65 (an enzyme of the visual cycle), cathepsin D, a lysosomal enzyme expressed in RPE, and GFAP, a marker of astrocytes and reactive Müller cells, expression in 2- and 18-month-old *Abca4*^{-/-} *Rdh8*^{-/-} mice. At 2 months of age, as expected, cathepsin D expression was observed in various retinal cells but was more intense at the level of the RPE (Figure 3A). The same pattern of expression was noted in 18-month-old mice, however we noted that RPE cells appeared thicker both on bright light image and following fluorescent staining (Figure 3B). An increase in intensity of cathepsin D expression could be detected between young and old mice (Figure 3B). Similarly, in 2-month-old *Abca4*^{-/-}

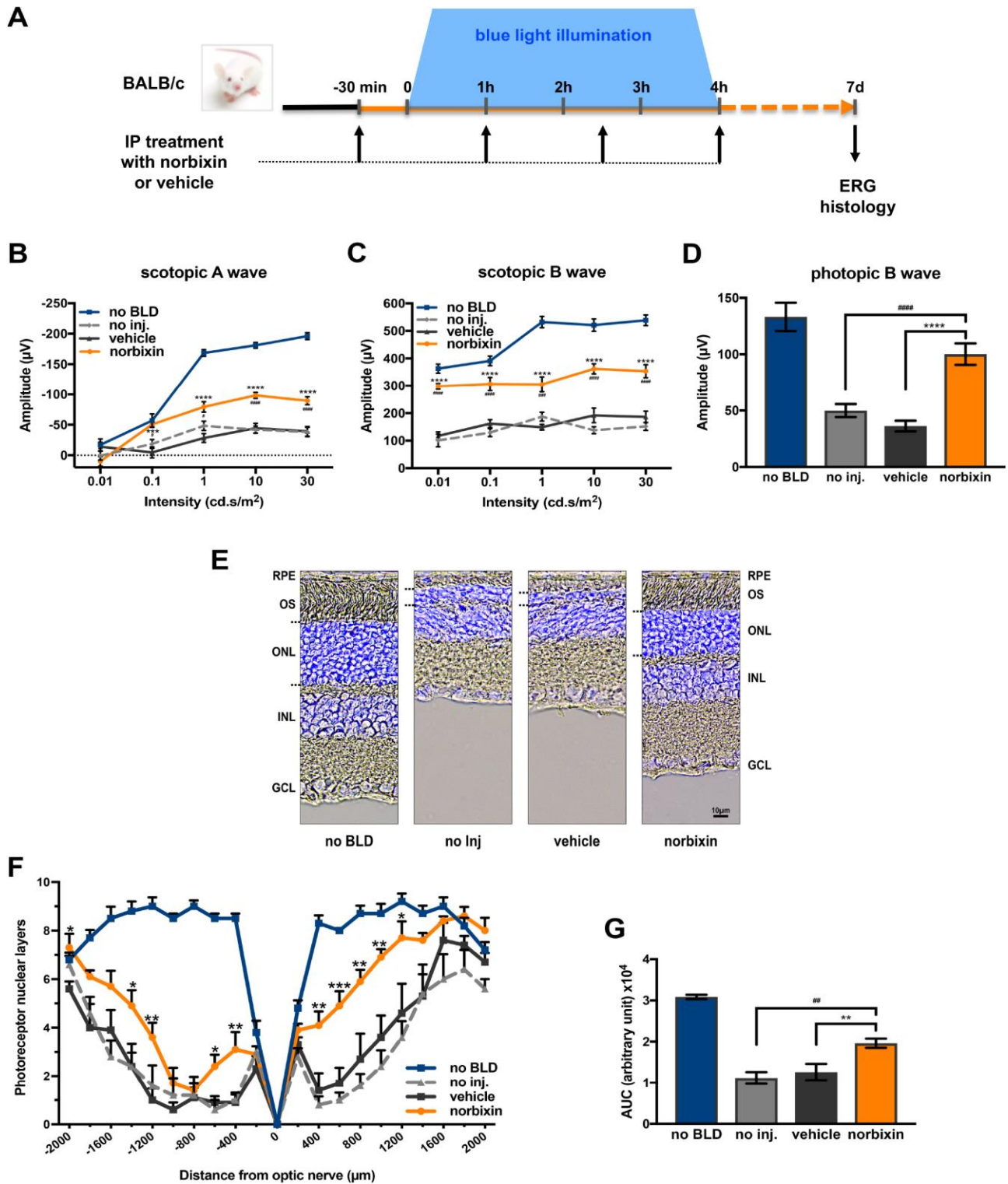


Figure 1. Effect of norbixin on ERG and retinal phototoxicity after BLD in BALB/c mice. (A) schematic representation of the protocol design. (B) Scotopic A wave, (C) Scotopic B wave, (D) Photopic B wave, ERG recorded 7 days after BLD. (E) Representative cryosection pictures showing Hoechst 33342 staining of the retinal cell nuclei one week after BLD. (F) Graph showing the number of photoreceptor layers measured along the retina each 200 µm from the optic nerve. (G) Histograms showing the area under the curve (AUC) calculated from the photoreceptor layer quantification and used to perform statistical analyses. IP: intra-peritoneal; no BLD: no blue light damage; no inj.: no injection; OS: outer segment; ONL: outer nuclear layer; INL: inner nuclear layer; GCL: ganglion cell layer. Bars represent mean ± s.e.m. with n = 8 per group. # or * $p < 0.05$, ## or ** $p < 0.01$, ### or *** $p < 0.001$, #### or **** $p < 0.0001$ compared to non-injected or to vehicle, respectively (One-way ANOVA, Dunnett's post-test).

Rdh8^{-/-} mice, RPE layer was thin and RPE cells appeared uniformly immunoreactive for RPE65 (Figure 3C). By contrast, at 18 months, the RPE cells were thicker. In addition, RPE65 expression almost disappeared completely from the apical face. The weak remaining staining appeared mostly basal (Figure 3D). Finally, we performed immunohistochemistry for GFAP that showed that GFAP expression was limited to astrocytes in 2-month-old *Abca4*^{-/-} *Rdh8*^{-/-} mice (Figure 3E), but that in 18-month-old mice, Müller cells were also GFAP positive, which is consistent with retinal stress (Figure 3E). Altogether, we described progressive reduction in ERG amplitudes, increased A2E accumulation, modifications of the RPE layer and apparition of retinal stress which are linked to progressive photoreceptor loss, as the *Abca4*^{-/-} *Rdh8*^{-/-} mice got older. The observations that the kinetics of evolution of these parameters could vary over time, prompted us to test the efficacy of norbixin administered by oral supplementation for 5 to 6 months in mice of various ages. In an attempt to determine the norbixin supplementation therapeutic window, we decided to follow three experimental designs: “preventive”, “early curative” and “late curative”

supplementations in which norbixin administration started at 1.5 months, 9 months, and 12 months of age, respectively.

Effect of norbixin in the preventive supplementation study

In the preventive supplementation experiment, 1.5-month-old *Abca4*^{-/-} *Rdh8*^{-/-} mice were fed with normal pellets or norbixin-containing pellets for 6 months (Figure 4A). Norbixin concentrations in the eye were below detection limits (data not shown). However, total norbixin concentration including isomers and glucuronide-conjugated forms and norbixin-conjugated glucuronides were detected in the plasma after 6 months of supplementation, confirming the exposure of mice to norbixin administered via food complementation (Table 1). After 3 months of supplementation no difference was measured in scotopic and photopic ERG in mice fed with norbixin-containing pellets or with normal pellets (data not shown). In contrast, after 6 months of supplementation we observed a limited, but significant ($p < 0.01$), protection of scotopic A-wave ERG in mice supplemented with norbixin-containing

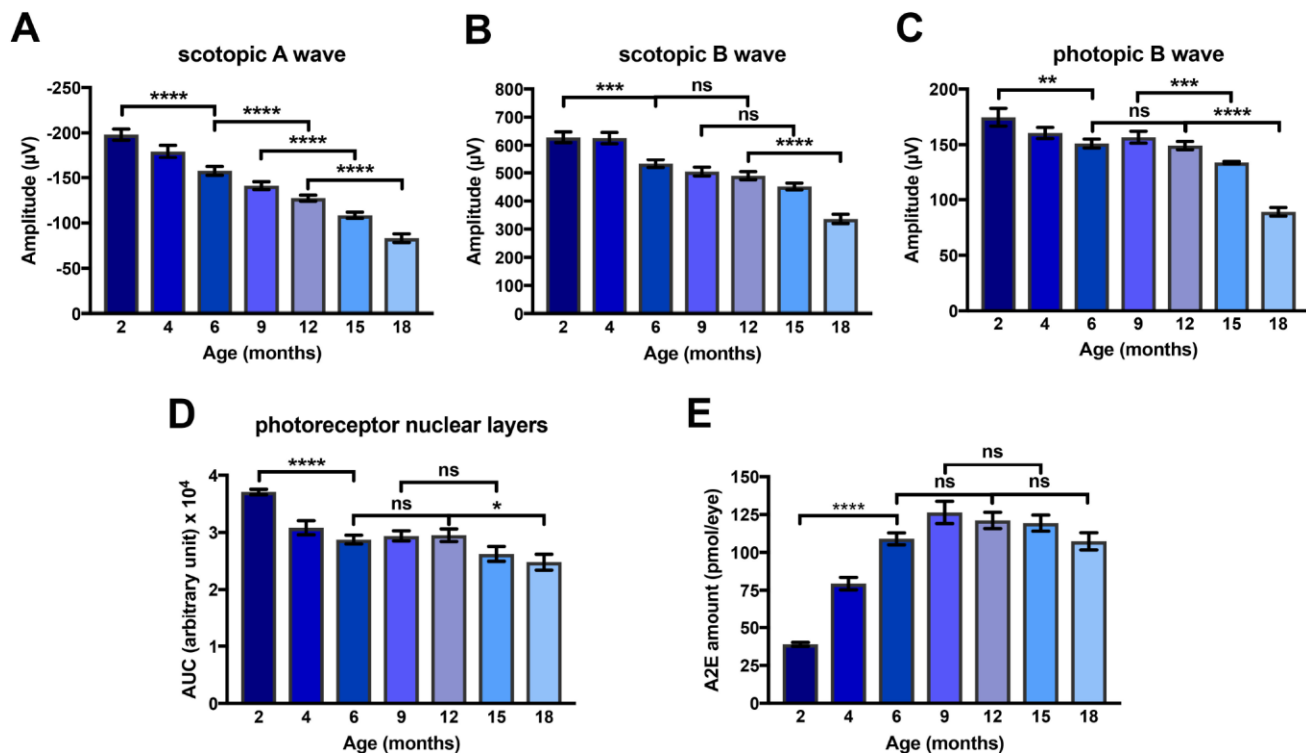


Figure 2. Kinetics of loss of amplitude of scotopic A and B waves and photopic B wave, of A2E accumulation and of loss of photoreceptor nuclear layers in *Abca4*^{-/-} *Rdh8*^{-/-} mice aged between 2 and 18 months. (A) Scotopic A wave recorded at a flash intensity of 10 cd.s/m² (n = 30-50). (B) Scotopic B wave recorded at a flash intensity of 10 cd.s/m² (n = 30-50). (C) Photopic B wave recorded at a flash intensity of 30 cd.s/m² (n = 30-50). (D) Kinetics of loss of photoreceptor nuclear layers (n = 7-14). (E) Kinetics of A2E accumulation (n = 15-40). Bars represent mean ± s.e.m. * $p < 0.05$, ** $p < 0.01$, * $p < 0.001$, **** $p < 0.0001$ (One-way ANOVA, Dunnett's post-test).**

chow compared to mice fed with normal pellets. Indeed, at a 10 cd.s/m² flash intensity (that corresponds to a mixed rod and cone response), in 7.5-month-old mice fed with normal chow, A wave amplitude was reduced by 44.2% compared to the 1.5-month-old mice (Figure 4B) whereas in 7.5-month-old mice fed with norbixin-containing-chow, A wave amplitude was only reduced by 26.8% compared to the 1.5-month-old mice (Figure 4B). Therefore, norbixin pellet administration reduced the loss of scotopic A wave intensity by 60.7% when compared with normal pellets (Figure 4B). However, no significant difference in either scotopic B nor photopic B waves were observed between the two groups of mice (Figure 4C, 4D). Compared to normal chow, norbixin-containing pellet supplementation had

no effect on photoreceptor degeneration at 7.5 months (Figure 4E). We observed a dramatic increase in A2E accumulation between 1.5 and 7.5 months in mice fed with normal pellets (Figure 4F). Interestingly, we measured a reduction (18.3 %, $p < 0.01$) in A2E accumulation in mice supplemented for 6 months with norbixin (Figure 4F).

Effect of norbixin in the early curative supplementation study

In the early curative supplementation experiment, untreated 9-month-old *Abca4*^{-/-} *Rdh8*^{-/-} mice were fed with normal pellets or norbixin-containing pellets for 6 months (Figure 5A). At the beginning of treatment, the

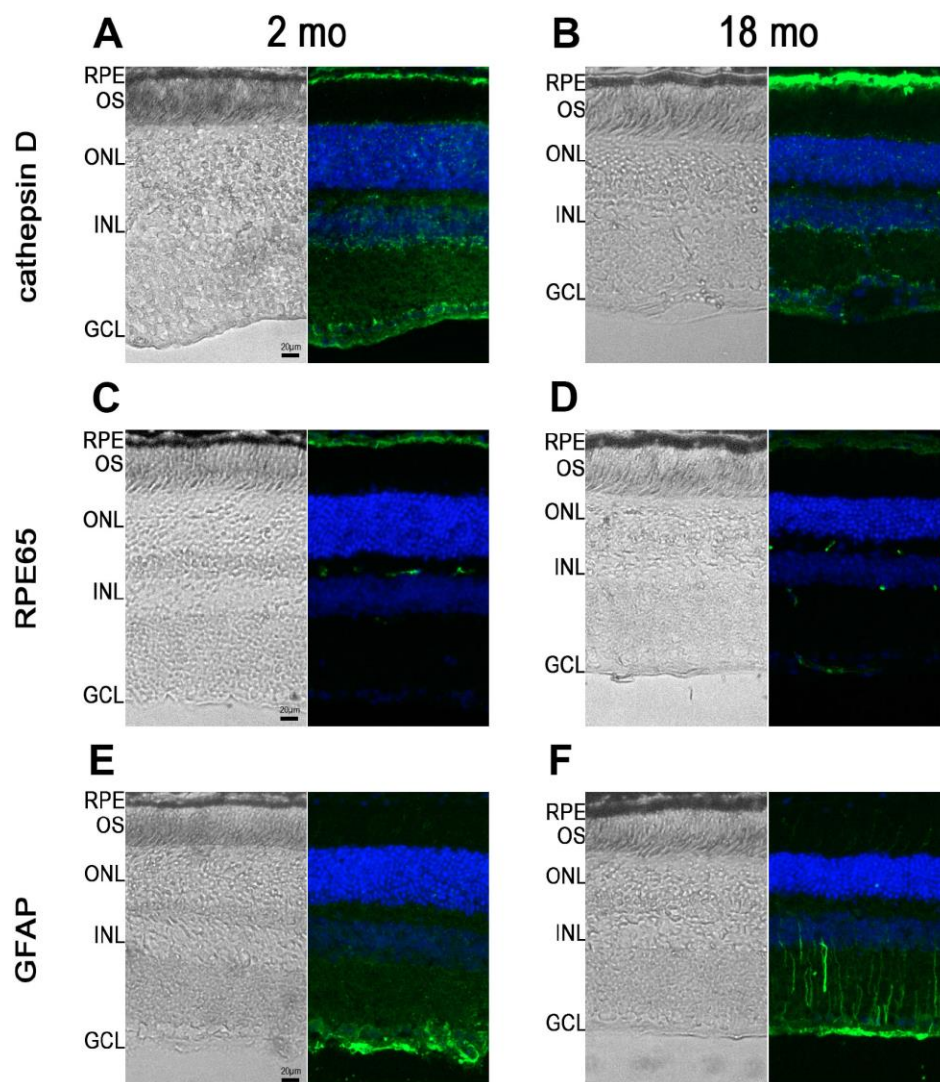


Figure 3. RPE65, cathepsin D and GFAP immunostaining in *Abca4*^{-/-} *Rdh8*^{-/-} mice of different ages. Pictures showing retinal cryosections of 2-month-old (A, C, E) and 18-month-old (B, D, F) mice captured in bright field (left pictures) or after immunostaining for cathepsin D (A, B), RPE65 (C, D) and GFAP (E, F). OS: outer segment; ONL: outer nuclear layer; INL: inner nuclear layer; GCL: ganglion cell layer.

retinal function of 9-month-old *Abca4*^{-/-}*Rdh8*^{-/-} mice was already decreased by 28.5% and 19.8 % for scotopic A and B waves (flash intensity: 10 cd.s/m²), respectively and by 10.3 % for the photopic B wave compared to 2-month-old mice (Figure 2A–2C). At the end of the early curative supplementation experiment (15-month-old mice), norbixin concentration in the eye was again below detection limits (data not shown). Significant amounts of norbixin (including free norbixin and norbixin glucuronide conjugates) were detected in plasma after 6 months of supplementation (Table 1), confirming norbixin exposure. After 3 months of

supplementation, we observed no statistical difference between norbixin-treated and control animals in scotopic A and B waves and photopic B wave measured by full-field ERG (data not shown). By contrast, after 6 months of supplementation we observed a strong and significant preservation of scotopic A (Figure 5B) and B waves (Figure 5C), as well as photopic B wave (Figure 5D) in mice supplemented with norbixin compared to mice fed with normal pellets. Most interestingly, the photopic B wave amplitude in 15-month-old mice that were fed with norbixin-containing pellets for 6 months was similar to the photopic B wave amplitude of

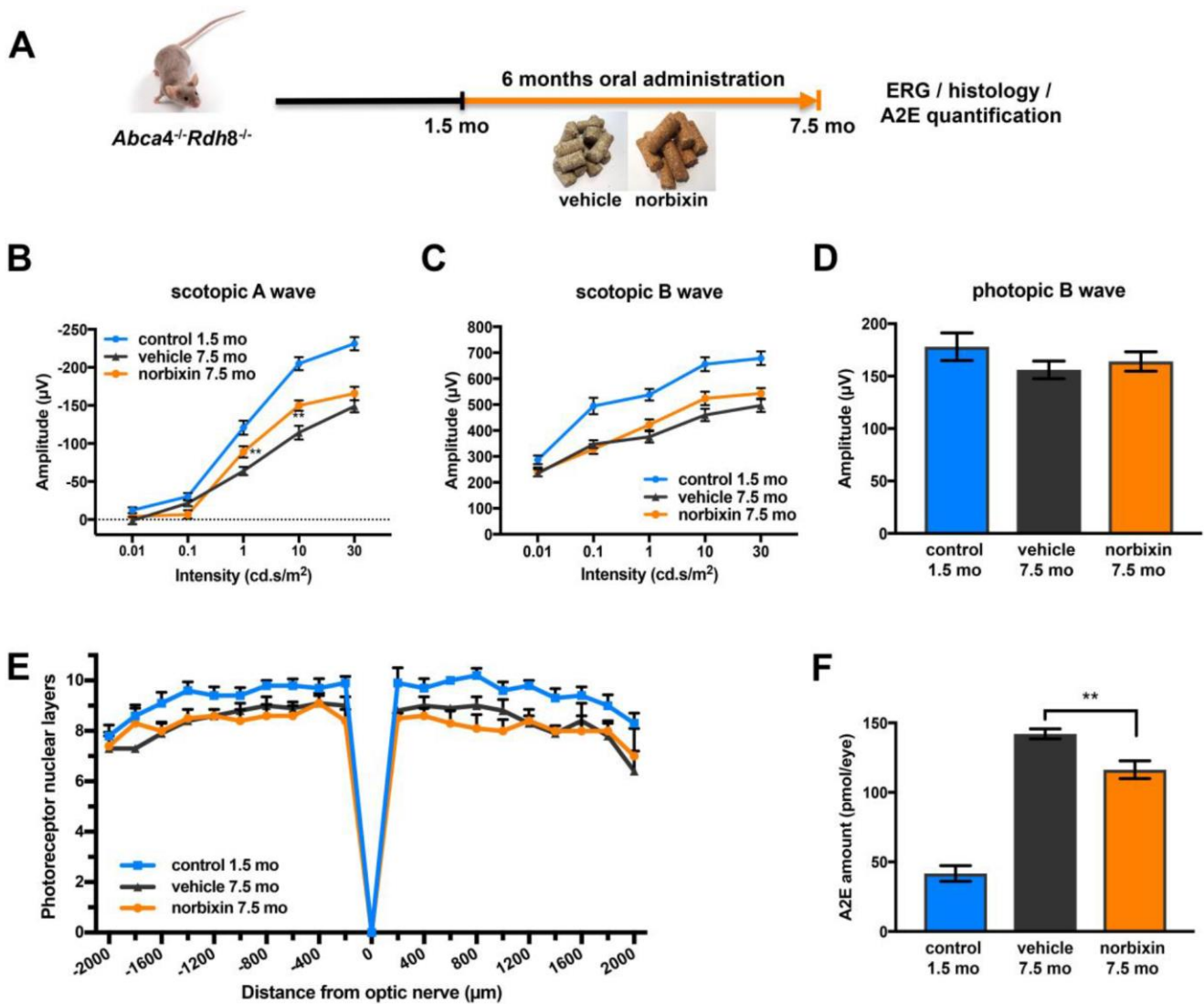


Figure 4. Effect of norbixin preventive supplementation from 1.5 to 7.5 months in *Abca4*^{-/-}*Rdh8*^{-/-} mice. (A) schematic representation of the 6-month preventive supplementation protocol design. (B) Scotopic A wave, (C) Scotopic B wave, (D) Photopic B wave, recorded after 6 months of oral supplementation with norbixin in *Abca4*^{-/-}*Rdh8*^{-/-} mice compared to mice fed with normal chow (vehicle) and to 1.5-month-old mice. (E) Quantification of photoreceptor nuclear layers along the superior and inferior poles of the retina each measured every 200 µm apart from the optic nerve. (F) A2E quantification in eyes from 1.5-month-old *Abca4*^{-/-}*Rdh8*^{-/-} mice, 7.5-month-old mice fed with normal chow or with norbixin-containing pellets. Bars represent mean ± s.e.m. with n= 8 mice per group (i.e. n=16 eyes per group for ERG). ***p*<0.01 compared to vehicle (One-way ANOVA, Dunnett's post-test).

Table 1. norbixin + isomers + norbixin glucuronide conjugate plasma concentrations.

Experiment	Mean ± SD (nM)
Preventive	1201 ± 256.5
Early curative	887,4 ± 295.7
Late curative	1782 ± 346.1

9-month-old mice at the beginning of treatment with norbixin (Figure 5D). This result demonstrates that norbixin supplementation fully preserves the function of cone photoreceptors. In 15-month-old mice supplemented during 6 months with norbixin, a statistically significant protection of photoreceptor degeneration was observed in the inferior retina compared to mice fed with normal chow (Figure 5E; $p < 0.05$). Consistent with functional protection, A2E accumulation in RPE was strongly reduced (-40 %; $p < 0.001$) in mice fed with pellets containing norbixin compared to mice fed with normal pellets (Figure 5F). No difference in lipofuscin granule accumulation was observed following transmission electronic microscopy (TEM) analysis of mice supplemented with norbixin compared to mice fed with normal chow (data not shown). No differences were either noted regarding RPE65 nor cathepsin D expression in the RPE layer of mice treated with norbixin compared to mice fed with normal chow (data not shown). By contrast an increase of Müller cells GFAP staining was observed following supplementation with norbixin (data not shown).

Effect of norbixin in the late curative supplementation study

During the late curative supplementation experiment 12-month-old *Abca4^{-/-} Rdh8^{-/-}* mice were fed with normal pellets or norbixin-containing pellets for 5 months (Figure 6A). Norbixin was not detected in the eyes of mice fed during 5 months with norbixin-containing pellets (data not shown). Norbixin + norbixin-glucuronide conjugate plasma concentration was approximately 1.5- to 2- times higher than in the preventive and early curative supplementation experiments, respectively (Table 1). Nevertheless, after three months of supplementation, norbixin did not preserve scotopic A and B waves and photopic B wave (data not shown). After 5 months of supplementation with norbixin containing pellets, the loss of scotopic A wave ERG (flash intensity: 10 cd.s/m²) was reduced by 67.3 % when compared with ERG of animals that received normal pellets (Figure 6B; $p < 0.01$). However, no significant difference in neither scotopic nor photopic B wave ERGs was observed between the two groups of mice (Figure 6C, 6D). No significant difference in photoreceptor degeneration was noted

between 17-month-old mice fed with pellets containing norbixin or normal pellets for 5 months (Figure 6E). A2E accumulation in 17-month-old mice did not differ between mice fed during 5 months with normal chow and with norbixin-containing pellets (Figure 6F). Interestingly, the number of lipofuscin granules quantified in RPE cells by TEM was slightly, but significantly, reduced (-23.2 %; $p < 0.05$) in 17-month-old mice fed with norbixin-containing pellets compared to same-age mice fed with normal pellets (Figure 6G, 6H). The cytoplasm surface occupied by this material reached 23.4 % in the normal chow-fed mice, whereas it was significantly reduced to 17.3 % ($p < 0.01$) in the norbixin-fed mice (Figure 6I).

DISCUSSION

We have previously shown that 9'-*cis*-norbixin, a 6,6'-*di-*apo**-carotenoid extracted from annatto (*Bixa orellana*) seeds, protects primary porcine RPE cells against phototoxicity induced by A2E and blue-light illumination *in vitro* [22]. Norbixin was also shown to reduce the uptake of A2E by primary porcine RPE cells *in vitro* [22]. In addition, 3 months of oral supplementation with norbixin in drinking water reduced the A2E ocular accumulation *in vivo* in *Abca4^{-/-} Rdh8^{-/-}* mice [22]. In the same mouse model, a single norbixin intraocular injection inhibited retinal degeneration and the loss of full-field ERG, induced following blue-light illumination [22]. In addition, when 50 to 100 mg/mL of norbixin was injected intraperitoneally, almost complete neuroprotection was achieved in albino rats subjected to BLD [22]. In the present study, we tested on one hand, the effect of four intraperitoneal injections of 10 mg/kg of norbixin administered before and during the course of a modified BLD exposure in BALB/c mice, an acute model used to rapidly study the neurodegeneration symptomatic of AMD, and, on the other hand, the effect of norbixin supplementation for 5 to 6 months in *Abca4^{-/-} Rdh8^{-/-}* mice of different ages, a chronic model of AMD and STGD.

Here, we demonstrate that norbixin IP injections are partially neuroprotective and protect photoreceptor function following retinal degeneration induced by blue-light exposure. The protective effect of norbixin in

the blue-light model is probably associated with its antioxidative properties as previously demonstrated *in vitro* [22, 42] and *in vivo* [43]. Despite the fact that we haven't measured the specific effect of norbixin on expression of inflammatory markers in retina of Balb/c mice subjected to BLD we quantified sub-retinal infiltration in this model. We observed a small trend toward reduction of macrophages infiltration by norbixin, however this was not statistically significant (data not shown). The absence of a significant effect of

norbixin on macrophages infiltration in the BLD model could be explained by the limited dose of norbixin used in this experiment. Indeed, the dose of norbixin only induced a 30 % neuroprotective effect in the retina. It could be hypothesized that a higher dose of norbixin would induce a significant reduction of macrophages infiltration in the sub-retinal space. Further experiments to confirm this hypothesis and to decipher the neuroprotective mechanism of norbixin in this model are therefore still required.

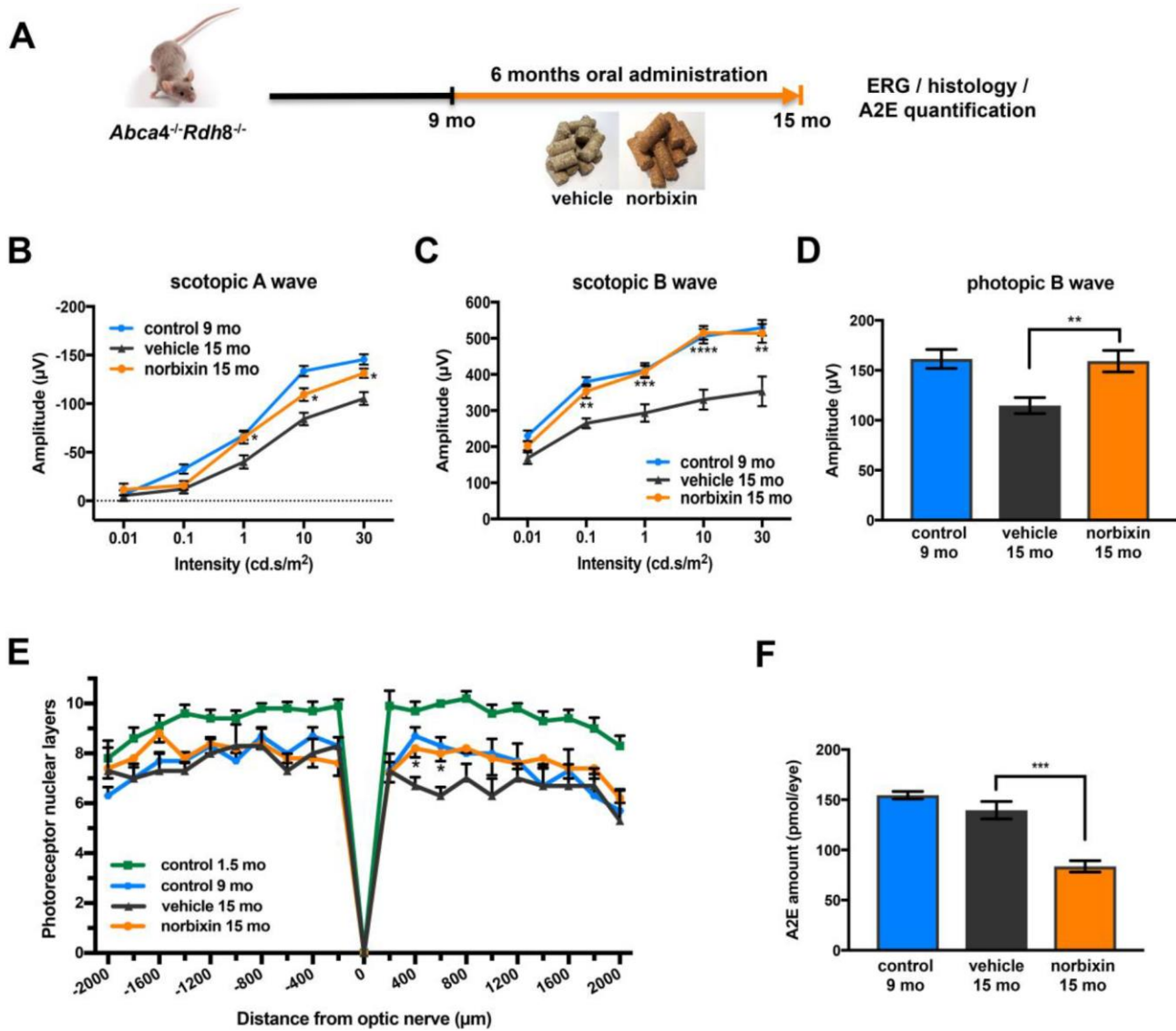


Figure 5. Effect of norbixin early curative supplementation from 9 to 15 months in *Abca4^{-/-}Rdh8^{-/-}* mice. (A) Schematic representation of the 6-month early curative supplementation protocol design. (B) Scotopic A wave, (C) Scotopic B wave, (D) Photopic B wave ERG recorded after 6 months of oral supplementation with norbixin in *Abca4^{-/-}Rdh8^{-/-}* mice compared to mice fed with normal chow (vehicle) and to 1.5 and 9-month-old mice. (E) Quantification of photoreceptor nuclear layers along the superior and inferior poles of the retina each measured every 200 µm apart from the optic nerve. (F) A2E quantification in eyes from 9-month-old *Abca4^{-/-}Rdh8^{-/-}* mice, 15-month-old mice fed with normal chow or with norbixin-containing pellets. Bars represent mean ± s.e.m. with n = 6 per group (i.e. n=12 eyes for the norbixin treated group and n=11 eyes for the vehicle treated group for ERG). **p*<0.05, ***p*<0.01, ****p*<0.001, *****p*<0.0001 compared to vehicle (One-way ANOVA, Dunnett's post-test).

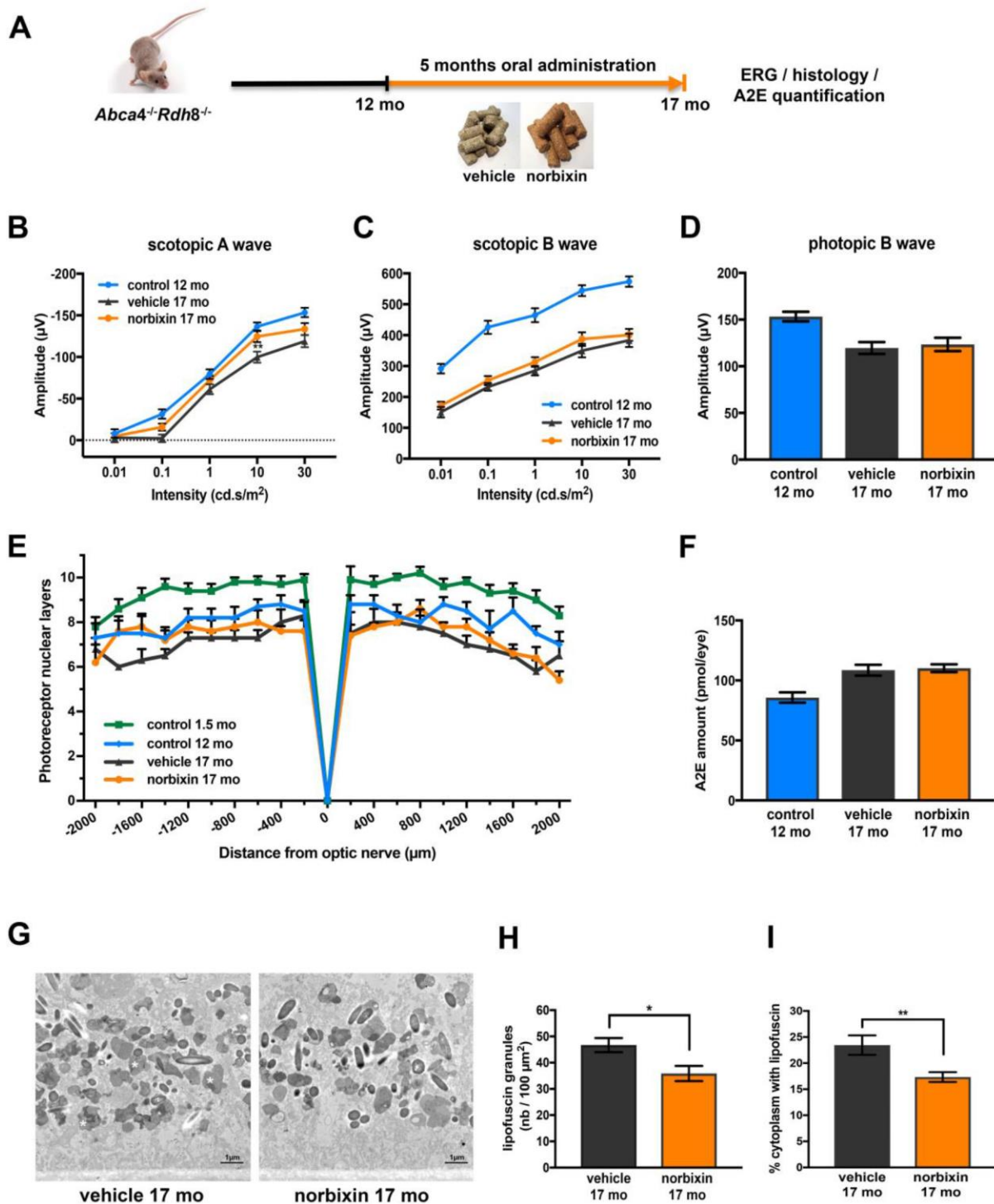


Figure 6. Effect of norbixin late curative supplementation from 12 to 17 months in *Abca4*^{-/-} *Rdh8*^{-/-} mice. (A) Schematic representation of the 5-month late curative supplementation protocol design. (B) Scotopic A wave ERG recorded after 5 months of oral supplementation with norbixin in *Abca4*^{-/-} *Rdh8*^{-/-} mice compared to mice fed with normal chow (vehicle) and to 1.5- and 12-month-old mice. (C) Scotopic B wave. (D) Photopic B wave. (E) Quantification of photoreceptor nuclear layers along the superior and inferior poles of the retina each measured every 200 µm apart from the optic nerve. (F) A2E quantification in eyes from 12-month-old *Abca4*^{-/-} *Rdh8*^{-/-} mice, 17-month-old mice fed with normal chow or with norbixin-containing pellets. (G) Representative images of lipofuscin content in RPE cells of 17-month-old vehicle and norbixin-treated mice. Large granules of lipofuscin are found in the RPE cytoplasm (white asterisk). (H) Histograms showing the quantified lipofuscin granules expressed by area of 100 µm². (I) Histograms representing the surface of cytoplasm occupied by lipofuscin and expressed in percentage of total cytoplasm surface. Bars represent mean ± s.e.m. with n = 8 per group (i.e. n=16 eyes per group for ERG). **p*<0.05, ***p*<0.01 compared to vehicle (One-way ANOVA, Dunnett's post-test).

Abca4^{-/-} Rdh8^{-/-} mice are a model of STGD but also a broader model of retinal degeneration such as AMD [36, 37]. Indeed, both STGD and AMD are characterized by progressive accumulation of A2E and lipofuscin, RPE cell and photoreceptor degeneration eventually leading to the gradual “night” and “day” vision loss that are mediated by rods and cones, respectively [13, 14]. Structural and morphological alterations over time of the retina of *Abca4^{-/-} Rdh8^{-/-}* mice has been extensively described [37]. It is noteworthy that despite the fact that the mice we used also carried the *rd8* mutation in the *Crb1* gene, we haven’t observed the formation of photoreceptor “rosettes” in the retina nor focal inferior retinal degeneration characterized by the formation of local retinal folds representative of *rd8^{-/-}* mouse retinal phenotype [44] (data not shown). It has been shown that *Crb1^{rd8/rd8}* mutation is necessary but not sufficient for the development of these degenerative features and that the influence of small genetic background difference is involved in the resulting phenotype [45]. Therefore, we can expect that our strain does not express gene mutations necessary to induce a degenerative phenotype as it was already the case in our previous publication [22].

In the present study, we describe the kinetics of expression of cathepsin D, RPE65 and GFAP expression and the progressive loss of visual function in relation with photoreceptor degeneration, and of the accumulation of A2E in eyes of *Abca4^{-/-} Rdh8^{-/-}* mice as they aged between 2 months and 18 months. Ocular A2E accumulation in the eyes of *Abca4^{-/-} Rdh8^{-/-}* mice appeared to be biphasic with a maximum observed at 9 months followed by a plateau afterwards. The rapid increase of ocular A2E concentration has been previously reported in “young” *Abca4^{-/-} Rdh8^{-/-}* mice up to the age of 6 months [36]. Interestingly, while retinal degeneration and loss of ERGs appeared constant during aging, we noted that photoreceptor loss and decrease in retinal function was more pronounced between 2 and 6 months and 12 and 18 months than between 9 and 15 months. Evolution of photoreceptor function over time might be related to the kinetics of A2E accumulation during the early phase in young mice and following its stabilization during the late phase in old animals. A2E and other toxic all-*trans*-retinal derivatives accumulate with age in the retina and RPE as by-products of the visual cycle even in non-pathological conditions [46]. In *Abca4^{-/-} Rdh8^{-/-}* mice, lacking two proteins essential for avoiding accumulation of all-*trans*-retinal derivatives in photoreceptors and RPE, high amounts of A2E are found in the RPE. Similarly, in the retina of AMD and STGD patients, A2E also accumulates faster and leads to retinal degeneration [46]. A2E promotes the release

of Ca²⁺ from the endoplasmic reticulum leading to the production of reactive oxygen species (ROS) by NADPH oxidase [46, 47]. Excessive ROS production and oxidative stress in general contributes to photoreceptor cell death and retinal degeneration [23] and is recognized as a major risk factor for dry AMD development [48–50]. It could be hypothesized that in young *Abca4^{-/-} Rdh8^{-/-}* mice, rapid accumulation of toxic A2E is responsible for the early decline in photoreceptor counts and visual function that we observed. Then, approximately around 9 months of age, due to the reduction of the number of photoreceptors and reduction in the visual cycle activation, demonstrated by reduced ERG amplitudes, the production of A2E may be progressively slowed, reaching an equilibrium illustrated by the plateau observed thereafter. During this intermediate period, when A2E is produced at a slower rate, A2E may also be more sensitive to photodegradation. Indeed, due to the reduced number of photoreceptor nuclei, the retina is thinner, allowing increased light intensity to reach A2E internalized in RPE cells [51]. In the meantime, apoptosis of photoreceptors continues at a slower rate, probably secondary to the early phase of photoreceptor degeneration progressively displacing the equilibrium between A2E concentrations and numbers of photoreceptors established at 9 months. It is to note that A2E ocular concentrations measured in our experiments are slightly higher and retinal degeneration slightly milder when compared to results found in the article by Maeda and colleagues [36], but are consistent with reported values by others [52]. Moreover, during the long-term studies presented here we used the same eyes to dose A2E and norbixin. Since norbixin could have been present in ocular fluids and to avoid losing vitreous/aqueous humor, we did not perform dissections of eyes from *Abca4^{-/-} Rdh8^{-/-}* mice to determine the exact location of A2E in these mice. However, we assume that A2E is mostly present in the RPE layer. Indeed, in previous dosing experiments performed on mice and dog eyes we noted that A2E is almost exclusively found in the RPE (data not shown). This observation is also consistent with the publication from Lenis et al. [5]. Altogether, the observations that the kinetics of evolution of ERG amplitudes, A2E accumulation and photoreceptor loss were not constant over time, suggest that the efficacy of a systemic treatment might be dependent on pathological course.

In the present study, we attempted to determine the optimal therapeutic window during which oral supplementation with norbixin is the most effective in relation to kinetics of A2E accumulation and of loss of visual function in *Abca4^{-/-} Rdh8^{-/-}* mice. Here we report that 6-month oral supplementation of 9-month-old *Abca4^{-/-} Rdh8^{-/-}* mice with chow containing norbixin

totally preserves cone function and limits loss of function in rods, as well as photoreceptor degeneration and A2E accumulation. By contrast, during norbixin supplementation of younger mice (starting at 1.5 months), we only observed a slight but significant protective effect of norbixin on scotopic A wave ERG and on retinal accumulation of A2E. This might be related to the fact that sharp decrease in scotopic A wave amplitude and an important A2E accumulation occur during the early retinal degeneration phase. The neuroprotective effect of norbixin in *Abca4^{-/-} Rdh8^{-/-}* mice during the early curative supplementation confirms our previous observations in acute blue-light induced retinal degeneration model *in vivo* in the same mice [22]. In the three supplementation protocols (preventive, early and late curative), norbixin prevented the loss of scotopic A wave amplitude measured by ERGs. This suggests a protective effect on rod photoreceptors by norbixin. Rods are the first neurons affected during the early stages of AMD and STGD [13, 14]. They are also much more abundant in the mouse retina than cones [13, 14]. In the preventive supplementation the protective effect of norbixin on rod function, was associated with a slight reduction of A2E concentration (Figure 2). This slight reduction however appears insufficient to prevent the loss of cone function as demonstrated by the absence of effect on photopic B wave. The loss of rod's function is a progressive phenomenon observed even in 15-month-old *Abca4^{-/-} Rdh8^{-/-}* mice and was also reduced by norbixin supplementation in the late curative supplementation protocol. It is important to note that the late curative experiment presented here, was performed in female mice rather than male mice in the other protocols. However, we compared ERG results obtained in 17 months male mice treated with norbixin for 5 months (between 12 and 17 months) and ERG amplitudes data obtained in male mice aged 18 months from the experimental group used in Figure 2. We observed a protection of scotopic A wave ERG (but not scotopic B wave) linked with rod function in norbixin complemented male mice (data not shown). Due to the difference of age between the two groups of male mice we cannot conclude that these effects are solely related with norbixin treatment with the exclusion of age, but this observation is consistent with the preferential preservation of rod photoreceptors reported for female mice in the late curative experiment (Figure 5B). Therefore, we are confident that the results reported here on the late curative complementation in female are representative of a phenomenon also occurring in male mice. The protective action of norbixin extended to cone photoreceptor function in mice supplemented between 9 and 15 months of age. Norbixin treatment during the early curative supplementation reduced by 40 % the A2E retinal concentration. This suggests that a

sharp reduction of A2E concentration is necessary to protect cone photoreceptor function, whereas a more limited reduction of A2E concentration appears to be sufficient to protect rod photoreceptor function. Other compounds including retinylamine [36, 53], C20-d3-vitamin A, [54], Emixustat [55], primary amines [56], omega-3 fatty acids [57] and the selective oestrogen receptor modulator raloxifene [47], among others, have been shown to reduce A2E accumulation and concomitantly to “rescue” retinal degeneration in *Abca4^{-/-} Rdh8^{-/-}* mice or *Abca4^{-/-}* *in vivo*. Altogether, this supports the hypothesis that norbixin effectiveness is at least partly linked to the level of reduction of ocular A2E concentration.

The exact mechanism(s) of reduction of A2E concentration *in vitro* and *in vivo* by norbixin remain(s) to be determined. But, based on our ERG results, it seems unlikely that norbixin supplementation limits A2E production *in vivo* by slowing down the visual cycle. We also showed previously *in vitro* that norbixin reduces the amounts of A2E internalized by porcine RPE cells as determined by HPLC-MS/MS [22]. Therefore, norbixin-induced reduction of intraocular A2E concentration in *Abca4^{-/-} Rdh8^{-/-}* mice could be due to direct effects on RPE cells *in vivo*. We could also hypothesize that in the BLD experiments reported here, the neuroprotective effect of norbixin observed in *Abca4^{-/-} Rdh8^{-/-}* mice *in vivo* may be due to a reduction of oxidative stress and ROS production. Indeed, norbixin has been shown to reduce oxidative stress in rats [42] and humans [43] following a high-fat meal diet. Further experiments to confirm the antioxidant properties of norbixin in the context of retinal degeneration *in vivo* and in RPE cells *in vitro* are still required. In the present article which focuses on the effect of norbixin *in vivo* in mice models of AMD and STGD we haven't described any mechanistic processes of norbixin. However, experiments *in vitro* on primary porcine RPE cells are actually performed to decipher the potential mechanism of action of norbixin (V. Fontaine et al. in preparation). Indeed, in addition with reduction of A2E accumulation, anti-apoptotic, antioxidant and anti-inflammatory properties of norbixin could play a role in the protection of visual function and in the neuroprotective effect of norbixin that we report in the present study *in vivo*. In order to determine if norbixin displayed an anti-inflammatory effect in the late curative experiment we quantified macrophages infiltration in the subretinal space of *Abca4^{-/-} Rdh8^{-/-}* mice (data not shown) *in vivo* but we did not observe any significative differences. It has been proposed that A2E may potentiate subretinal macrophage accumulation [58]. Therefore, the slight reduction of A2E accumulation obtained in our model by norbixin may not be sufficient to significantly reduce

macrophage recruitment. However, it could be hypothesized that norbixin may alter macrophage activation or differentiation *in vivo*. This will be the aim of future experiments. In order to better understand the effects of norbixin in the retina *in vivo* and to determine whether norbixin effects target specifically the retina or RPE or both, we performed GFAP, RPE65 and cathepsin D stainings on retinal sections of eyes obtained from *Abca4^{-/-}Rdh8^{-/-}* mice treated with norbixin versus untreated in the early curative supplementation experiment. However, we did not observe any differences in RPE65 nor cathepsin D expression in both groups. Surprisingly, we observed enhanced GFAP staining of Müller cells in the retina of norbixin supplemented mice. Further experiments are required to decipher the mechanisms behind the protective effects of norbixin.

To our knowledge, this is the first report demonstrating the efficiency of treatment given orally through food complementation on the photoreceptor function in the aging *Abca4^{-/-}Rdh8^{-/-}* mouse model. Most of the previous studies performed to measure the efficacy of molecules on the retinal function, using this *Abca4^{-/-}Rdh8^{-/-}* mouse model, were done by intraperitoneal or intravitreal injections and after light damage in young mice [36, 47, 53, 56, 59–61]. Maeda and colleagues also showed the beneficial effect of 9-*cis*-retinal administrated by monthly oral gavage over 6 or 10 months in 4-month-old C57BL/6 mice on scotopic A and B waves, as well as flicker ERG [62]. Similar observations were reported following weekly gavage for one month in 12-month-old *Rdh5^{-/-}Rdh11^{-/-}* mice [63]. In another study, the same group showed that 3 months treatment with primary amines in 1-month-old *Abca4^{-/-}Rdh8^{-/-}* mice force-fed daily reduced A2E accumulation, photoreceptor degeneration, and retinal functions [56].

Based on our previous results showing that norbixin increases RPE survival and reduces A2E internalization *in vitro* [22], we assume that norbixin's neuroprotective effect is local. However, free norbixin concentrations in the eyes were below detection limits in all supplementation experiments. It could be hypothesized that limited amounts of free norbixin present in the plasma access the eye and are consumed in a continuous fashion. Oral supplementation exposure of norbixin in mice depends on the quantity of food absorbed by each mouse and also depends on the time of day of the analysis of plasma concentrations relative to food consumption which occurs mainly at night time. Therefore, we cannot assume that all mice received the same amount of norbixin during supplementations. Nevertheless, at 3 and 6 months, norbixin was detected in the plasma of all supplemented mice across all experimental designs, confirming the exposure of mice to

norbixin administered via food as early as 3 months. Interestingly, in the early curative supplementation experiment, plasma norbixin and norbixin glucuronide conjugate concentration was the lowest. Nevertheless, the observed partial neuroprotection, and full preservation of scotopic and photopic ERG amplitudes, suggest that this level of plasma exposure is sufficient to support norbixin biological effects. As a mean, we calculated that norbixin consumption represents approximately a daily intake of 47.5 mg +/- 5 mg per kg/mouse. This value is in the same range of administration in the BLD study, where mice received four intraperitoneal injections of 10 mg/kg each. Nevertheless, we have reported previously in acute BLD model in albino rats a more profound effect of our tested compound. The partial efficacy reported here in acute and long-term models of retinal degeneration may be due to the small doses used and might be improved by increasing the doses of norbixin administered. Increasing bio-availability of norbixin into the eye following systemic administration may also improve efficacy and we are actually working on these two options.

In conclusion, our present study demonstrates that systemic administration of norbixin in the acute BLD model of dry AMD is neuroprotective and partially preserves photoreceptor function. In addition, 6 months of oral supplementation with norbixin is effective in *Abca4^{-/-}Rdh8^{-/-}* mice. We show that chronic norbixin supplementation reduces the concentration of A2E in the eye, that norbixin is neuroprotective, and preserves visual function of *Abca4^{-/-}Rdh8^{-/-}* mice, modelling retinal degenerative conditions such as STGD and dry AMD. We believe that treatment using norbixin could potentially preserve “night” and “day” visual acuity in humans affected by dry AMD and STGD. It is essential for patient care to develop drugs that are effective on visual function following oral administration rather than by repeated local intraocular injections. These results demonstrated the effectiveness of the norbixin in a chronic and acute model of retinal degeneration and could offer a new therapeutic strategy, alone or in combination with gene therapies, for AMD and/or STGD patients. Thus, norbixin is a good drug candidate to treat patients and may provide a cure for these very debilitating diseases.

MATERIALS AND METHODS

Ethics statement

All procedures were carried out according to the guidelines on the ethical use of animals from the European Community Council Directive (86/609/EEC) and were approved by the French Ministry of Agriculture (OGM agreement 6193) and by the Committee on the Ethics of Animal Experiments of the

French Ministry of Research. All efforts were made to minimize suffering.

Animals

BALB/c mice were provided by Envigo (Gannat, France). Pigmented *Abca4*^{-/-} *Rdh8*^{-/-} mice carrying the Rpe65-Leu450 mutation and the *rd8* mutation in the *Crb1* gene were obtained from Case Western Reserve University [36]. All animals were housed under 12-hour on/off cyclic normal lighting.

Reagents/chemicals

All general chemicals were from Sigma (St. Louis, MO, USA). Reagents for cell culture and Alexa Fluor® 488 - conjugated secondary antibodies were from Thermo Fisher Scientific (Waltham, MA, USA). TrueBlack® was from Biotium (Fremont, CA, USA). Goat anti-human Cathepsin D antibody was from Santa Cruz Biotechnology (Dallas, TX, USA), mouse anti-bovine RPE65 antibody and rabbit anti-human GFAP were from Abcam (Cambridge, UK). Ketamine, xylazine, tropicamide and oxybuprocaine chlorhydrate were from Centravet (Maison-Alfort, France). Lubrithal eye gel was from Dechra Pharmaceuticals (Northwich, UK). Optimal cutting temperature compound and other reagents for histology were from Roth Sochiel (Lauterbourg, France). Agar 100 resin kit was from Agar Scientific (Stansted, UK). 9'-*cis*-Norbixin was prepared from 9'-*cis*-bixin (AICABIX P, purity 92 %) purchased from Aica-Color (CUSCO, Peru) upon alkaline hydrolysis as previously described [22] and according to Santos et al. [64]. The obtained product (the 9'-*cis* isomer) showed an HPLC purity of 97 % as confirmed by ¹H-nuclear magnetic resonance (using malonic acid as internal standard). Fresh solutions of 9'-*cis*-norbixin, stored as powder at -80°C, were prepared in DMSO.

Immunohistochemistry

Retinal cryosections of *Abca4*^{-/-} *Rdh8*^{-/-} mice aged 2 and 18 months were permeabilized with Triton X100 (0.05% in PBS; 5 min at RT) and saturated with NGS (10% in PBS) or BSA (3% in PBS) during 1 h at RT. For cathepsin D immunostaining sections were depigmented in H₂O₂ (3% in PBS) during 24 h before staining. Primary antibodies against GFAP, RPE65 and cathepsin D were diluted in 2% NGS or 1% BSA and incubated over night at 4°C and followed by Alexa Fluor® 488 - conjugated secondary antibodies during 1 h at RT. In order to quench lipofuscin auto-fluorescence in RPE a final incubation with TrueBlack® was performed. Sections were stained with Hoechst 33342 to label nuclei and representative pictures were taken using a fluorescence microscope (Nikon TiE) equipped

with a CoolSNAP HQ2 camera. For each age retinal cryosections from 3 different mice were used.

Synthesis of A2E and A2E-Propylamine

A2E (*N*-retinylidene-*N*-retinylethanolamine) was synthesized by Orga-link (Magny-Les-Hameaux, France) as described before [65]. Briefly, all-*trans*-retinal, ethanolamine and acetic acid were mixed in absolute ethanol in darkness at room temperature over 7 days. The crude product was purified by preparative HPLC in the dark to isolate A2E with a purity of 98 % as determined by HPLC. A2E (20 mM in DMSO under argon) was stored at -20°C. A2E-propylamine (an analogue of A2E) was synthesized as previously described [22] using propylamine instead of ethanolamine.

Intraperitoneal treatment and blue-light damage (BLD)

Four groups of 8 BALB/c mice were used for this study. Mice were injected intraperitoneally with either norbixin (10 mg/kg in 5 % Tween 80 in PBS), or an equivalent volume of vehicle (5 % Tween 80 in PBS) 30 min prior to light damage and 1, 2.5 and 4 hours after the beginning of the exposure. A custom-made light-damage device equipped with fluorescent lamps (Phillips TL-D 36W/18) with UV filter was used to induce BLD in mice (Durand, St-Clair de la Tour, France). All manipulations with the animals were performed in dim red light. Pupils were dilated with 1 % atropine eye solution before illumination. Mice, previously maintained in a 12-hour light (≈ 10 lux)/ 12-hour dark cycle environment for two weeks, were dark-adapted for 24 hours and light damage was induced at 4000 lux for 4 hours. Following exposure to light damage, animals were placed in the dark for 24 hours and then returned to the dim cyclic light environment for 7 days. Two control groups were used: i) non-injected and illuminated mice and ii) non-injected and non-illuminated mice.

Kinetics of ERGs, photoreceptor loss and A2E accumulation in *Abca4*^{-/-} *Rdh8*^{-/-} mice

A total of 300 *Abca4*^{-/-} *Rdh8*^{-/-} male and female mice of different ages (2, 4, 6, 9, 12, 15 and 18 months) were used in order to perform a kinetic analysis of ERGs, photoreceptor loss and A2E accumulation.

Norbixin-containing pellet preparation preservation and consumption

Custom rodent diet was formulated and irradiated (25 kGy) by Special Diet Services (Witham, UK). Norbixin (600 µg/g) was incorporated in 10 mm RM1

compression pellets. The pellets were stored at -20°C until use and were administered as standard diet (*ad libitum*). The concentration of norbixin in the pellets at the end of each batch was determined by HPLC MS/MS. The mean concentration was $377.9 \mu\text{g/g} \pm 40.93 \mu\text{g/g}$. Based on the norbixin pellet concentration, we calculated that male mice weighing 42.1 g after 3 months supplementation consumed 5.3 g of pellets every day, which correspond to a daily dose of $47.5 \text{ mg} \pm 5 \text{ mg}$ per kg.

In vivo norbixin supplementation

In order to test the preventive/curative actions of oral norbixin against retinal neurodegeneration a total of 54 *Abca4^{-/-}Rdh8^{-/-}* mice of different ages were used. In the first “preventive study”, two groups of 8 males aged 1.5 months received control chow or chow containing norbixin orally for 6 months. In a second experiment “early curative study” two groups of 6 males aged 9 months received norbixin mixed with chow or control chow orally for 6 months. In a third experiment “late curative study”, two groups of 8 females aged 12 months received norbixin mixed with chow or control chow orally for 5 months. In each experiment full-field ERG was performed after 3 months of supplementation. After 5 or 6 months of supplementation, ERG was measured in both eyes ($n=16$ per group in the preventive and late curative experiments and $n=12$ for norbixin treated group and $n=11$ in the vehicle group of the early curative study). Blood was collected by cardiac puncture in all mice before being euthanized. In each group half of the eyes were removed for A2E and norbixin measurements and half of the eyes were used for histological analyses.

Full-field electroretinogram

ERG recordings were performed with the Espion visual electrophysiology system (Diagnosys LLC, Lowell, MA, USA) that includes a ColorDome Ganzfeld. ERG was performed one week after BLD. After overnight dark adaptation, mice were anesthetized with ketamine (100 mg/kg) and xylazine (10 mg/kg). Eye drops were used to dilate the pupils (0.5% tropicamide+ 5% phenylephrine hydrochloride) and anesthetize the cornea (0.4% oxybuprocaine chlorhydrate). Body temperature was maintained at 37°C using a circulating hot-water heating pad. Corneal electrodes (Ocuscience, a subsidiary of Xenolec Inc., USA) were placed on the corneal surface of each eye. Lubrithal eye gel was used to maintain good contact and corneal moisture. Needle electrodes placed subcutaneously in cheeks served as reference and a needle electrode placed in the back served as earth. The ERG was recorded from both eyes simultaneously after placing the animal into the

Ganzfeld bowl. Five responses to light stimulus at increasing intensities ($0.01, 0.1, 1, 10$ and 30 cd.s.m^{-2}) were averaged for scotopic response. After 5 min of light adaptation, the photopic response was recorded at the highest stimulus (average of 5 measurements at 30 cd.s.m^{-2}).

Histology and photoreceptor counting

Following ERG measures, mice were euthanized and eyes were enucleated and dissected to remove the cornea and lens. For cryosection, eyes were fixed in 4% paraformaldehyde/ 5% sucrose (in PBS) for one hour at 4°C . The eye cups were then cryoprotected by successive bathing in 5% sucrose (1h), 10% sucrose (1h) and 20% sucrose (overnight), embedded in optimal cutting temperature compound, and cryosections ($10 \mu\text{m}$) were prepared using Superfrost® Plus slides and stored at -20°C until analysis. Sections were stained with Hoechst 33342 to label nuclei and were scanned using a nanozoomer (NDP.scan v2.5.86, Hamamatsu, Japan) with fluorescence imaging modules. Photoreceptor nuclei were quantified at $200 \mu\text{m}$ intervals superior and inferior to the edge of the optic nerve head along the vertical meridian using the NDP.view software.

Electronic microscopy analysis

After enucleation and anterior segment removal, eye cups were fixed in 1.5% glutaraldehyde and 1% paraformaldehyde diluted in 0.1 M sodium cacodylate. One mm^2 sections of eye cups were cut and incubated for 1 h in 1% osmium tetroxide. Cells were dehydrated through graded concentrations of ethanol ($50\text{-}70\text{-}96\text{-}100 \%$) and infiltrated in epoxy resin (Agar 100 resin kit) at room temperature according to the manufacturer’s instructions and polymerized for 48 h at 60°C . Ultrathin sections (70 nm) were cut with an ultramicrotome (Ultracut, Leica Microsystems) and collected on 200 Mesh copper grids (EMS). Observations were made with a Field Emission Scanning Electron Microscope (Gemini 500, Zeiss). Lipofuscin quantification was carried out with Fiji software using the «Cell Counter» plugin. Three different images of RPE cells were counted for each eye in each group. The total area of RPE cytoplasm was systematically quantified. Nuclei areas were excluded from the measure. Results are expressed as number of lipofuscin granules / $100 \mu\text{m}^2$ of cytoplasm and as the cytoplasmic volume occupied by lipofuscin.

A2E measurement by HPLC-MS/MS

HPLC-MS/MS analysis was performed on an Agilent 1100 in-line triple quadrupole mass spectrometer

(API365 or API3200, Applied Biosystems, Les Ulis, France) operated in MRM positive-ion mode. A2E was eluted on a reverse-phase C18 column (2.1x50 mm; 3.5 µm particle size; Symmetry, Waters, Guyancourt, France) with the following gradient of acetonitrile in water (containing 0.1 % formic acid): 65 to 100 % (4 min), 100 % (5 min), (flow-rate: 0.3 mL/min). A2E-propylamine (25 ng) was used as internal standard. The AUC of A2E and A2E-propylamine were determined in MRM mode with precursor ion/product ion settings, A2E (m/z 592.5/105.1) and A2E-propylamine (m/z 590.6/186.2). For A2E quantification, a calibration curve was performed using various concentrations of A2E (5 to 10000 nM). A2E-propylamine was used as internal standard for A2E quantification by HPLC coupled with tandem mass spectrometry (HPLC-MS/MS).

A2E measurement in mice eyes

A2E present in eyes was determined with the HPLC-MS/MS method described above. Each eye was homogenized in CHCl₃/MeOH (1:1, v/v) (0.5 mL) with homogenizer (Precellys-24) during 2 cycles (30 s) at 6500 rpm. The internal standard (A2E-propylamine) was added and the organic layer was extracted. The homogenate was then extracted two times with CHCl₃/CH₂Cl₂ (0.5 mL). The combined organic extracts were dried *in vacuo* without heating (EZ2, Genevac Ltd Ipswich, U.K.). Then they were dissolved in 100 µL DMSO/MeOH (1:1, v/v) and transferred to microtitre plates. The calibration curve of A2E was prepared in CHCl₃/MeOH (1:1, v/v) and dried *in vacuo* without heating (EZ2, Genevac), then dissolved in 100 µL DMSO/MeOH (1:1, v/v). Under these conditions, with an injection volume of 10 µL, the limit of quantification (LOQ) was 10 nM.

Norbixin concentration determination in pellets, mice plasma and eye samples

HPLC analysis was performed on an Agilent 1200 with DAD. Norbixin was eluted from a reverse-phase C18 column (2.1x50 mm; 5 µm particles; Purospher Star, Merck, Molsheim, France) with the following gradient of acetonitrile in water (containing 0.1 % formic acid): 0 to 90 % (1.5 min), 90 % (1 min), (flow-rate: 0.5 mL/min) and they were monitored at 460 nm. For quantification of norbixin, a calibration curve was performed under the same conditions as the sample matrix, with various amounts of norbixin (10 to 50000 ng/mL). Plasma samples (30 µL) from different animals, and methanol (100 µL) were distributed in a 96-well microtitre plate, mixed for 10 min and precipitated. The microtiter plate was frozen at -20°C for 30 min, thawed and then centrifuged. The hydro-

alcoholic phase was removed from each well and transferred into another microtitre plate for LC-MS/MS analysis. Under these conditions, with 20 µL injections, the limit of quantification (LOQ) was 50 ng/mL (= *ca.* 2.5 pmol). Eye samples were treated with the same protocol as for A2E measurements (see above). Norbixin isomers were analyzed by LC-MS/MS on an Agilent 1200 with DAD and in-line triple quadrupole mass spectrometer (6420, Agilent, Les Ulis, France) operated in MRM positive-ion mode. HPLC used a reverse-phase C18-column (2.1x50 mm; Fortis-18) eluted with the following gradient of acetonitrile in water (containing 0.1 % formic acid): 60 to 95 % (2.5 min), 95 % (2 min), (flow-rate: 0.3 mL/min). Norbixin and its isomers or conjugates (= glucuronides) were monitored at 460 nm and MRM mode with precursor ion/product ion ratio (m/z 381.1/144.9).

Statistical analyses

For statistical analyses, one-way ANOVA followed by Dunnett's tests were performed using Prism 7 (GraphPad Software, La Jolla, CA, USA) depending of the sample size.

ACKNOWLEDGMENTS

This work was supported by Biophytis. The contribution of Dr L.N. Dinan for critical reading of the manuscript and language improvement is acknowledged. This work was completed with the support of the Programme Investissements d'Avenir IHU FOReSIGHT (ANR-18-IAHU-01). We are grateful to Michaël Trichet from the IBPS EM platform for his help in analysing RPE cytoplasm lipofuscin.

CONFLICTS OF INTEREST

A patent "Composition for the protection of retinal pigment epithelium" covering the topic of this manuscript has been filed on April 30, 2015 (FR 15 53957) and is owned by Stanislas Veillet, René Lafont, José-Alain Sahel and Valérie Fontaine. René Lafont is founder, CSO and shareholder of Biophytis. S. Veillet is founder, CEO and shareholder of Biophytis. This does not alter our adherence to AGING policies on sharing data and materials. We have no restriction to share these data.

FUNDING

This manuscript results from a collaborative work between one public laboratory (Institut de la Vision) and one private company (Biophytis). The experimental work was shared between the two organisations. Biophytis participated to the design and realization of the experiments. They declare, however, that their potential

commercial interests had no impact on the scientific conduct of the study or the analysis/interpretation of data. CB, LG, ML, PJD, RL, SC, and SV are employees of Biophytis.

REFERENCES

1. Rein DB, Wittenborn JS, Zhang X, Honeycutt AA, Lesesne SB, Saaddine J, and Vision Health Cost-Effectiveness Study Group. Forecasting age-related macular degeneration through the year 2050: the potential impact of new treatments. *Arch Ophthalmol*. 2009; 127:533–40.
<https://doi.org/10.1001/archophthalmol.2009.58>
PMID:[19365036](https://pubmed.ncbi.nlm.nih.gov/19365036/)
2. Lois N, Holder GE, Bunce C, Fitzke FW, Bird AC. Phenotypic subtypes of Stargardt macular dystrophy-fundus flavimaculatus. *Arch Ophthalmol*. 2001; 119:359–69.
<https://doi.org/10.1001/archophth.119.3.359>
PMID:[11231769](https://pubmed.ncbi.nlm.nih.gov/11231769/)
3. Rotenstreich Y, Fishman GA, Anderson RJ. Visual acuity loss and clinical observations in a large series of patients with Stargardt disease. *Ophthalmology*. 2003; 110:1151–58.
[https://doi.org/10.1016/S0161-6420\(03\)00333-6](https://doi.org/10.1016/S0161-6420(03)00333-6)
PMID:[12799240](https://pubmed.ncbi.nlm.nih.gov/12799240/)
4. Klevering BJ, Blankenagel A, Maugeri A, Cremers FP, Hoyng CB, Rohrschneider K. Phenotypic spectrum of autosomal recessive cone-rod dystrophies caused by mutations in the ABCA4 (ABCR) gene. *Invest Ophthalmol Vis Sci*. 2002; 43:1980–85.
PMID:[12037008](https://pubmed.ncbi.nlm.nih.gov/12037008/)
5. Lenis TL, Hu J, Ng SY, Jiang Z, Sarfare S, Lloyd MB, Esposito NJ, Samuel W, Jaworski C, Bok D, Finnemann SC, Radeke MJ, Redmond TM, et al. Expression of ABCA4 in the retinal pigment epithelium and its implications for Stargardt macular degeneration. *Proc Natl Acad Sci USA*. 2018; 115:E11120–27.
<https://doi.org/10.1073/pnas.1802519115>
PMID:[30397118](https://pubmed.ncbi.nlm.nih.gov/30397118/)
6. Wu Y, Tian L, Huang Y. Correlation between the interactions of ABCA4 polymorphisms and smoking with the susceptibility to age-related macular degeneration. *Int J Clin Exp Pathol*. 2015; 8:7403–08.
PMID:[26261643](https://pubmed.ncbi.nlm.nih.gov/26261643/)
7. Edwards AO, Ritter R 3rd, Abel KJ, Manning A, Panhuysen C, Farrer LA. Complement factor H polymorphism and age-related macular degeneration. *Science*. 2005; 308:421–24.
<https://doi.org/10.1126/science.1110189>
PMID:[15761121](https://pubmed.ncbi.nlm.nih.gov/15761121/)
8. Bonilha VL. Age and disease-related structural changes in the retinal pigment epithelium. *Clin Ophthalmol*. 2008; 2:413–24.
<https://doi.org/10.2147/OPHT.S2151>
PMID:[19668732](https://pubmed.ncbi.nlm.nih.gov/19668732/)
9. Kinnunen K, Petrovski G, Moe MC, Berta A, Kaarniranta K. Molecular mechanisms of retinal pigment epithelium damage and development of age-related macular degeneration. *Acta Ophthalmol*. 2012; 90:299–309.
<https://doi.org/10.1111/j.1755-3768.2011.02179.x>
PMID:[22112056](https://pubmed.ncbi.nlm.nih.gov/22112056/)
10. Neuner B, Komm A, Wellmann J, Dietzel M, Pauleikhoff D, Walter J, Busch M, Hense HW. Smoking history and the incidence of age-related macular degeneration—results from the Muenster Aging and Retina Study (MARS) cohort and systematic review and meta-analysis of observational longitudinal studies. *Addict Behav*. 2009; 34:938–47.
<https://doi.org/10.1016/j.addbeh.2009.05.015>
PMID:[19539431](https://pubmed.ncbi.nlm.nih.gov/19539431/)
11. Sears AE, Bernstein PS, Cideciyan AV, Hoyng C, Charbel Issa P, Palczewski K, Rosenfeld PJ, Sadda S, Schraermeyer U, Sparrow JR, Washington I, Scholl HP. Towards Treatment of Stargardt Disease: Workshop Organized and Sponsored by the Foundation Fighting Blindness. *Transl Vis Sci Technol*. 2017; 6:6.
<https://doi.org/10.1167/tvst.6.5.6> PMID:[28920007](https://pubmed.ncbi.nlm.nih.gov/28920007/)
12. Veerappan M, El-Hage-Sleiman AM, Tai V, Chiu SJ, Winter KP, Stinnett SS, Hwang TS, Hubbard GB 3rd, Michelson M, Gunther R, Wong WT, Chew EY, Toth CA, et al, and Age-related Eye Disease Study 2 Ancillary Spectral Domain Optical Coherence Tomography Study Group. Optical Coherence Tomography Reflective Drusen Substructures Predict Progression to Geographic Atrophy in Age-related Macular Degeneration. *Ophthalmology*. 2016; 123:2554–70.
<https://doi.org/10.1016/j.ophtha.2016.08.047>
PMID:[27793356](https://pubmed.ncbi.nlm.nih.gov/27793356/)
13. Curcio CA, Medeiros NE, Millican CL. Photoreceptor loss in age-related macular degeneration. *Invest Ophthalmol Vis Sci*. 1996; 37:1236–49.
PMID:[8641827](https://pubmed.ncbi.nlm.nih.gov/8641827/)
14. Jackson GR, Owsley C, Curcio CA. Photoreceptor degeneration and dysfunction in aging and age-related maculopathy. *Ageing Res Rev*. 2002; 1:381–96.
[https://doi.org/10.1016/S1568-1637\(02\)00007-7](https://doi.org/10.1016/S1568-1637(02)00007-7)
PMID:[12067593](https://pubmed.ncbi.nlm.nih.gov/12067593/)
15. Sacconi R, Corbelli E, Querques L, Bandello F, Querques G. A Review of Current and Future Management of Geographic Atrophy. *Ophthalmol Ther*. 2017; 6:69–77.
<https://doi.org/10.1007/s40123-017-0086-6>
PMID:[28391446](https://pubmed.ncbi.nlm.nih.gov/28391446/)
16. Eldred GE, Lasky MR. Retinal age pigments generated

- by self-assembling lysosomotropic detergents. *Nature*. 1993; 361:724–26.
<https://doi.org/10.1038/361724a0>
PMID:[8441466](https://pubmed.ncbi.nlm.nih.gov/8441466/)
17. Poliakov E, Strunnikova NV, Jiang JK, Martinez B, Parikh T, Lakkaraju A, Thomas C, Brooks BP, Redmond TM. Multiple A2E treatments lead to melanization of rod outer segment-challenged ARPE-19 cells. *Mol Vis*. 2014; 20:285–300.
PMID:[24644403](https://pubmed.ncbi.nlm.nih.gov/24644403/)
 18. Roehlecke C, Schaller A, Knels L, Funk RH. The influence of sublethal blue light exposure on human RPE cells. *Mol Vis*. 2009; 15:1929–38.
PMID:[19784391](https://pubmed.ncbi.nlm.nih.gov/19784391/)
 19. Gao Z, Liao Y, Chen C, Liao C, He D, Chen J, Ma J, Liu Z, Wu Y. Conversion of all-*trans*-retinal into all-*trans*-retinal dimer reflects an alternative metabolic/antidotal pathway of all-*trans*-retinal in the retina. *J Biol Chem*. 2018; 293:14507–19.
<https://doi.org/10.1074/jbc.RA118.002447>
PMID:[30049796](https://pubmed.ncbi.nlm.nih.gov/30049796/)
 20. Sparrow JR, Nakanishi K, Parish CA. The lipofuscin fluorophore A2E mediates blue light-induced damage to retinal pigmented epithelial cells. *Invest Ophthalmol Vis Sci*. 2000; 41:1981–89.
PMID:[10845625](https://pubmed.ncbi.nlm.nih.gov/10845625/)
 21. Sparrow JR, Zhou J, Cai B. DNA is a target of the photodynamic effects elicited in A2E-laden RPE by blue-light illumination. *Invest Ophthalmol Vis Sci*. 2003; 44:2245–51.
<https://doi.org/10.1167/iovs.02-0746>
PMID:[12714667](https://pubmed.ncbi.nlm.nih.gov/12714667/)
 22. Fontaine V, Monteiro E, Brazhnikova E, Lesage L, Balducci C, Guibout L, Feraille L, Elena PP, Sahel JA, Veillet S, Lafont R. Norbixin Protects Retinal Pigmented Epithelium Cells and Photoreceptors against A2E-Mediated Phototoxicity In Vitro and In Vivo. *PLoS One*. 2016; 11:e0167793.
<https://doi.org/10.1371/journal.pone.0167793>
PMID:[27992460](https://pubmed.ncbi.nlm.nih.gov/27992460/)
 23. Wu Y, Yanase E, Feng X, Siegel MM, Sparrow JR. Structural characterization of bisretinoid A2E photocleavage products and implications for age-related macular degeneration. *Proc Natl Acad Sci USA*. 2010; 107:7275–80.
<https://doi.org/10.1073/pnas.0913112107>
PMID:[20368460](https://pubmed.ncbi.nlm.nih.gov/20368460/)
 24. Zhou J, Jang YP, Kim SR, Sparrow JR. Complement activation by photooxidation products of A2E, a lipofuscin constituent of the retinal pigment epithelium. *Proc Natl Acad Sci USA*. 2006; 103:16182–87.
<https://doi.org/10.1073/pnas.0604255103>
PMID:[17060630](https://pubmed.ncbi.nlm.nih.gov/17060630/)
 25. Wang J, Feng Y, Han P, Wang F, Luo X, Liang J, Sun X, Ye J, Lu Y, Sun X. Photosensitization of A2E triggers telomere dysfunction and accelerates retinal pigment epithelium senescence. *Cell Death Dis*. 2018; 9:178.
<https://doi.org/10.1038/s41419-017-0200-7>
PMID:[29415988](https://pubmed.ncbi.nlm.nih.gov/29415988/)
 26. Finnemann SC, Leung LW, Rodriguez-Boulan E. The lipofuscin component A2E selectively inhibits phagolysosomal degradation of photoreceptor phospholipid by the retinal pigment epithelium. *Proc Natl Acad Sci USA*. 2002; 99:3842–47.
<https://doi.org/10.1073/pnas.052025899>
PMID:[11904436](https://pubmed.ncbi.nlm.nih.gov/11904436/)
 27. Suter M, Remé C, Grimm C, Wenzel A, Jäätelä M, Esser P, Kociok N, Leist M, Richter C. Age-related macular degeneration. The lipofuscin component N-retinyl-N-retinylidene ethanolamine detaches proapoptotic proteins from mitochondria and induces apoptosis in mammalian retinal pigment epithelial cells. *J Biol Chem*. 2000; 275:39625–30.
<https://doi.org/10.1074/jbc.M007049200>
PMID:[11006290](https://pubmed.ncbi.nlm.nih.gov/11006290/)
 28. Guha S, Coffey EE, Lu W, Lim JC, Beckel JM, Laties AM, Boesze-Battaglia K, Mitchell CH. Approaches for detecting lysosomal alkalization and impaired degradation in fresh and cultured RPE cells: evidence for a role in retinal degenerations. *Exp Eye Res*. 2014; 126:68–76.
<https://doi.org/10.1016/j.exer.2014.05.013>
PMID:[25152362](https://pubmed.ncbi.nlm.nih.gov/25152362/)
 29. Moon J, Yun J, Yoon YD, Park SI, Seo YJ, Park WS, Chu HY, Park KH, Lee MY, Lee CW, Oh SJ, Kwak YS, Jang YP, Kang JS. Blue light effect on retinal pigment epithelial cells by display devices. *Integr Biol*. 2017; 9:436–43.
<https://doi.org/10.1039/C7IB00032D>
PMID:[28386617](https://pubmed.ncbi.nlm.nih.gov/28386617/)
 30. Alaimo A, Liñares GG, Bujjamer JM, Gorojod RM, Alcon SP, Martínez JH, Baldessari A, Grecco HE, Kotler ML. Toxicity of blue led light and A2E is associated to mitochondrial dynamics impairment in ARPE-19 cells: implications for age-related macular degeneration. *Arch Toxicol*. 2019; 93:1401–15.
<https://doi.org/10.1007/s00204-019-02409-6>
PMID:[30778631](https://pubmed.ncbi.nlm.nih.gov/30778631/)
 31. Feng J, Chen X, Sun X, Wang F, Sun X. Expression of endoplasmic reticulum stress markers GRP78 and CHOP induced by oxidative stress in blue light-mediated damage of A2E-containing retinal pigment epithelium cells. *Ophthalmic Res*. 2014; 52:224–33.
<https://doi.org/10.1159/000363387>
PMID:[25402962](https://pubmed.ncbi.nlm.nih.gov/25402962/)

32. Anderson OA, Finkelstein A, Shima DT. A2E induces IL-1 β production in retinal pigment epithelial cells via the NLRP3 inflammasome. *PLoS One*. 2013; 8:e67263. <https://doi.org/10.1371/journal.pone.0067263> PMID:[23840644](https://pubmed.ncbi.nlm.nih.gov/23840644/)
33. Brandstetter C, Mohr LK, Latz E, Holz FG, Krohne TU. Light induces NLRP3 inflammasome activation in retinal pigment epithelial cells via lipofuscin-mediated photooxidative damage. *J Mol Med (Berl)*. 2015; 93:905–16. <https://doi.org/10.1007/s00109-015-1275-1> PMID:[25783493](https://pubmed.ncbi.nlm.nih.gov/25783493/)
34. Iriyama A, Fujiki R, Inoue Y, Takahashi H, Tamaki Y, Takezawa S, Takeyama K, Jang WD, Kato S, Yanagi Y. A2E, a pigment of the lipofuscin of retinal pigment epithelial cells, is an endogenous ligand for retinoic acid receptor. *J Biol Chem*. 2008; 283:11947–53. <https://doi.org/10.1074/jbc.M708989200> PMID:[18326047](https://pubmed.ncbi.nlm.nih.gov/18326047/)
35. Iriyama A, Inoue Y, Takahashi H, Tamaki Y, Jang WD, Yanagi Y. A2E, a component of lipofuscin, is pro-angiogenic in vivo. *J Cell Physiol*. 2009; 220:469–75. <https://doi.org/10.1002/jcp.21792> PMID:[19418485](https://pubmed.ncbi.nlm.nih.gov/19418485/)
36. Maeda A, Maeda T, Golczak M, Palczewski K. Retinopathy in mice induced by disrupted all-trans-retinal clearance. *J Biol Chem*. 2008; 283:26684–93. <https://doi.org/10.1074/jbc.M804505200> PMID:[18658157](https://pubmed.ncbi.nlm.nih.gov/18658157/)
37. Taubitz T, Tschulakow AV, Tikhonovich M, Illing B, Fang Y, Biesemeier A, Julien-Schraermeyer S, Schraermeyer U. Ultrastructural alterations in the retinal pigment epithelium and photoreceptors of a Stargardt patient and three Stargardt mouse models: indication for the central role of RPE melanin in oxidative stress. *PeerJ*. 2018; 6:e5215. <https://doi.org/10.7717/peerj.5215> PMID:[30038866](https://pubmed.ncbi.nlm.nih.gov/30038866/)
38. Wenzel A, Grimm C, Samardzija M, Remé CE. Molecular mechanisms of light-induced photoreceptor apoptosis and neuroprotection for retinal degeneration. *Prog Retin Eye Res*. 2005; 24:275–306. <https://doi.org/10.1016/j.preteyeres.2004.08.002> PMID:[15610977](https://pubmed.ncbi.nlm.nih.gov/15610977/)
39. Jiang D, Ryals RC, Huang SJ, Weller KK, Titus HE, Robb BM, Saad FW, Salam RA, Hammad H, Yang P, Marks DL, Pennesi ME. Monomethyl Fumarate Protects the Retina From Light-Induced Retinopathy. *Invest Ophthalmol Vis Sci*. 2019; 60:1275–85. <https://doi.org/10.1167/iovs.18-24398> PMID:[30924852](https://pubmed.ncbi.nlm.nih.gov/30924852/)
40. Satyanarayana A, Prabhakara Rao PG, Rao DG. Chemistry processing and toxicology of Anatto (Bixa orellana L). *J Food Sci Technol*. 2003; 40:131–41.
41. Fernandes AC, Almeida CA, Albano F, Laranja GA, Felzenszwalb I, Lage CL, de Sa CC, Moura AS, Kovary K. Norbixin ingestion did not induce any detectable DNA breakage in liver and kidney but caused a considerable impairment in plasma glucose levels of rats and mice. *J Nutr Biochem*. 2002; 13:411–20. [https://doi.org/10.1016/S0955-2863\(02\)00177-8](https://doi.org/10.1016/S0955-2863(02)00177-8) PMID:[12121828](https://pubmed.ncbi.nlm.nih.gov/12121828/)
42. A R, Agrawal N, Kumar H, Nath V, Kumar V. Norbixin, an apocarotenoid derivative activates PPAR γ in cardiometabolic syndrome: validation by in silico and in vivo experimental assessment. *Life Sci*. 2018; 209:69–77. <https://doi.org/10.1016/j.lfs.2018.08.001> PMID:[30076922](https://pubmed.ncbi.nlm.nih.gov/30076922/)
43. Roehrs M, Conte L, da Silva DT, Duarte T, Maurer LH, de Carvalho JA, Moresco RN, Somacal S, Emanuelli T. Anatto carotenoids attenuate oxidative stress and inflammatory response after high-calorie meal in healthy subjects. *Food Res Int*. 2017; 100:771–79. <https://doi.org/10.1016/j.foodres.2017.08.005> PMID:[28873749](https://pubmed.ncbi.nlm.nih.gov/28873749/)
44. Mattapallil MJ, Wawrousek EF, Chan CC, Zhao H, Roychoudhury J, Ferguson TA, Caspi RR. The Rd8 mutation of the *Crb1* gene is present in vendor lines of C57BL/6N mice and embryonic stem cells, and confounds ocular induced mutant phenotypes. *Invest Ophthalmol Vis Sci*. 2012; 53:2921–27. <https://doi.org/10.1167/iovs.12-9662> PMID:[22447858](https://pubmed.ncbi.nlm.nih.gov/22447858/)
45. Luhmann UF, Carvalho LS, Holthaus SM, Cowing JA, Greenaway S, Chu CJ, Herrmann P, Smith AJ, Munro PM, Potter P, Bainbridge JW, Ali RR. The severity of retinal pathology in homozygous *Crb1*rd8/rd8 mice is dependent on additional genetic factors. *Hum Mol Genet*. 2015; 24:128–41. <https://doi.org/10.1093/hmg/ddu424> PMID:[25147295](https://pubmed.ncbi.nlm.nih.gov/25147295/)
46. Chen Y, Zhao Z, Sternberg P, Cai J. NRF2 and age-dependent RPE degeneration. 2012. <https://doi.org/10.5772/28167>
47. Getter T, Suh S, Hoang T, Handa JT, Dong Z, Ma X, Chen Y, Blackshaw S, Palczewski K. The selective estrogen receptor modulator raloxifene mitigates the effect of all-trans-retinal toxicity in photoreceptor degeneration. *J Biol Chem*. 2019; 294:9461–75. <https://doi.org/10.1074/jbc.RA119.008697> PMID:[31073029](https://pubmed.ncbi.nlm.nih.gov/31073029/)
48. Shen JK, Dong A, Hackett SF, Bell WR, Green WR, Campochiaro PA. Oxidative damage in age-related macular degeneration. *Histol Histopathol*. 2007; 22:1301–08.

- <https://doi.org/10.14670/HH-22.1301> PMID:[17701910](https://pubmed.ncbi.nlm.nih.gov/17701910/)
49. Hollyfield JG, Bonilha VL, Rayborn ME, Yang X, Shadrach KG, Lu L, Ufret RL, Salomon RG, Perez VL. Oxidative damage-induced inflammation initiates age-related macular degeneration. *Nat Med*. 2008; 14:194–98.
<https://doi.org/10.1038/nm1709> PMID:[18223656](https://pubmed.ncbi.nlm.nih.gov/18223656/)
50. Buschini E, Piras A, Nuzzi R, Vercelli A. Age related macular degeneration and drusen: neuroinflammation in the retina. *Prog Neurobiol*. 2011; 95:14–25.
<https://doi.org/10.1016/j.pneurobio.2011.05.011> PMID:[21740956](https://pubmed.ncbi.nlm.nih.gov/21740956/)
51. Ueda K, Zhao J, Kim HJ, Sparrow JR. Photodegradation of retinal bisretinoids in mouse models and implications for macular degeneration. *Proc Natl Acad Sci USA*. 2016; 113:6904–09.
<https://doi.org/10.1073/pnas.1524774113> PMID:[27274068](https://pubmed.ncbi.nlm.nih.gov/27274068/)
52. Flynn E, Ueda K, Auran E, Sullivan JM, Sparrow JR. Fundus autofluorescence and photoreceptor cell rosettes in mouse models. *Invest Ophthalmol Vis Sci*. 2014; 55:5643–52.
<https://doi.org/10.1167/iovs.14-14136> PMID:[25015357](https://pubmed.ncbi.nlm.nih.gov/25015357/)
53. Puntel A, Maeda A, Golczak M, Gao SQ, Yu G, Palczewski K, Lu ZR. Prolonged prevention of retinal degeneration with retinylamine loaded nanoparticles. *Biomaterials*. 2015; 44:103–10.
<https://doi.org/10.1016/j.biomaterials.2014.12.019> PMID:[25617130](https://pubmed.ncbi.nlm.nih.gov/25617130/)
54. Charbel Issa P, Barnard AR, Herrmann P, Washington I, MacLaren RE. Rescue of the Stargardt phenotype in Abca4 knockout mice through inhibition of vitamin A dimerization. *Proc Natl Acad Sci USA*. 2015; 112:8415–20.
<https://doi.org/10.1073/pnas.1506960112> PMID:[26106163](https://pubmed.ncbi.nlm.nih.gov/26106163/)
55. Zhang J, Kiser PD, Badiie M, Palczewska G, Dong Z, Golczak M, Tochtrop GP, Palczewski K. Molecular pharmacodynamics of emixustat in protection against retinal degeneration. *J Clin Invest*. 2015; 125:2781–94.
<https://doi.org/10.1172/JCI80950> PMID:[26075817](https://pubmed.ncbi.nlm.nih.gov/26075817/)
56. Maeda A, Golczak M, Chen Y, Okano K, Kohno H, Shiose S, Ishikawa K, Harte W, Palczewska G, Maeda T, Palczewski K. Primary amines protect against retinal degeneration in mouse models of retinopathies. *Nat Chem Biol*. 2011; 8:170–78.
<https://doi.org/10.1038/nchembio.759> PMID:[22198730](https://pubmed.ncbi.nlm.nih.gov/22198730/)
57. Prokopiou E, Kolovos P, Kalogerou M, Neokleous A, Nicolaou O, Sokratous K, Kyriacou K, Georgiou T. Omega-3 Fatty Acids Supplementation: Therapeutic Potential in a Mouse Model of Stargardt Disease. *Invest Ophthalmol Vis Sci*. 2018; 59:2757–67.
<https://doi.org/10.1167/iovs.17-23523> PMID:[29860462](https://pubmed.ncbi.nlm.nih.gov/29860462/)
58. Ma W, Coon S, Zhao L, Fariss RN, Wong WT. A2E accumulation influences retinal microglial activation and complement regulation. *Neurobiol Aging*. 2013; 34:943–60.
<https://doi.org/10.1016/j.neurobiolaging.2012.06.010> PMID:[22819137](https://pubmed.ncbi.nlm.nih.gov/22819137/)
59. Maeda T, Golczak M, Maeda A. Retinal photodamage mediated by all-trans-retinal. *Photochem Photobiol*. 2012; 88:1309–19.
<https://doi.org/10.1111/j.1751-1097.2012.01143.x> PMID:[22428905](https://pubmed.ncbi.nlm.nih.gov/22428905/)
60. Schur RM, Sheng L, Sahu B, Yu G, Gao S, Yu X, Maeda A, Palczewski K, Lu ZR. Manganese-Enhanced MRI for Preclinical Evaluation of Retinal Degeneration Treatments. *Invest Ophthalmol Vis Sci*. 2015; 56:4936–42.
<https://doi.org/10.1167/iovs.15-16522> PMID:[26225634](https://pubmed.ncbi.nlm.nih.gov/26225634/)
61. Parmar T, Parmar VM, Arai E, Sahu B, Perusek L, Maeda A. Acute Stress Responses Are Early Molecular Events of Retinal Degeneration in Abca4-/-Rdh8-/- Mice After Light Exposure. *Invest Ophthalmol Vis Sci*. 2016; 57:3257–67.
<https://doi.org/10.1167/iovs.15-18993> PMID:[27315541](https://pubmed.ncbi.nlm.nih.gov/27315541/)
62. Maeda T, Maeda A, Leahy P, Saperstein DA, Palczewski K. Effects of long-term administration of 9-cis-retinyl acetate on visual function in mice. *Invest Ophthalmol Vis Sci*. 2009; 50:322–33.
<https://doi.org/10.1167/iovs.08-2301> PMID:[18708622](https://pubmed.ncbi.nlm.nih.gov/18708622/)
63. Maeda A, Maeda T, Palczewski K. Improvement in rod and cone function in mouse model of Fundus albipunctatus after pharmacologic treatment with 9-cis-retinal. *Invest Ophthalmol Vis Sci*. 2006; 47:4540–46.
<https://doi.org/10.1167/iovs.06-0215> PMID:[17003450](https://pubmed.ncbi.nlm.nih.gov/17003450/)
64. Santos AA, Silva MV, Guerreiro LT, Alves MV, Cunha Bastos VL, Bastos JC, Kovary K. Influence of norbixin on plasma cholesterol-associated lipoproteins, plasma arylesterase/paraonase activity and hepatic lipid peroxidation of swiss mice on a high fat diet. *Food Chem*. 2002; 77:393–99.
[https://doi.org/10.1016/S0308-8146\(01\)00363-6](https://doi.org/10.1016/S0308-8146(01)00363-6)
65. Arnault E, Barrau C, Nanteau C, Gondouin P, Bigot K, Viénot F, Gutman E, Fontaine V, Villette T, Cohen-Tannoudji D, Sahel JA, Picaud S. Phototoxic action

spectrum on a retinal pigment epithelium model of age-related macular degeneration exposed to sunlight normalized conditions. PLoS One. 2013; 8:e71398.
<https://doi.org/10.1371/journal.pone.0071398>
PMID:[24058402](https://pubmed.ncbi.nlm.nih.gov/24058402/)

PU-91 drug rescues human age-related macular degeneration RPE cells; implications for AMD therapeutics

Sonali Nashine¹, Sudhakar R. Subramaniam², Marilyn Chwa¹, Anthony Nesburn^{1,3}, Baruch D. Kuppermann¹, Howard Federoff², M. Cristina Kenney^{1,4}

¹Department of Ophthalmology, Gavin Herbert Eye Institute, University of California Irvine, Irvine, CA 92697, USA

²Department of Neurology, University of California Irvine, Irvine, CA 92697, USA

³Cedars-Sinai Medical Center, Los Angeles, CA 90048, USA

⁴Department of Pathology and Laboratory Medicine, University of California Irvine, Irvine, CA 92697, USA

Correspondence to: M. Cristina Kenney; **email:** mkenney@uci.edu

Keywords: age-related macular degeneration (AMD), RPE, PGC-1 α , mitochondria, FDA-approved drugs

Received: June 3, 2019

Accepted: August 9, 2019

Published: September 2, 2019

Copyright: Nashine et al. This is an open-access article distributed under the terms of the Creative Commons Attribution License (CC BY 3.0), which permits unrestricted use, distribution, and reproduction in any medium, provided the original author and source are credited.

ABSTRACT

Since mitochondrial dysfunction is implicated in the pathogenesis of AMD, this study is based on the premise that repurposing of mitochondria-stabilizing FDA-approved drugs such as PU-91, might rescue AMD RPE cells from AMD mitochondria-induced damage. The PU-91 drug upregulates *PGC-1 α* which is a critical regulator of mitochondrial biogenesis. Herein, we tested the therapeutic potential of PU-91 drug and examined the additive effects of treatment with PU-91 and esterase inhibitors i.e., EI-12 and EI-78, using the *in vitro* transmitochondrial AMD cell model. This model was created by fusing platelets obtained from AMD patients with *Rho⁰* i.e., mitochondria-deficient, ARPE-19 cell lines. The resulting AMD RPE cell lines have identical nuclei but differ in their mitochondrial DNA content, which is derived from individual AMD patients. Briefly, we report significant improvement in cell survival, mitochondrial health, and antioxidant potential in PU-91-treated AMD RPE cells compared to their untreated counterparts. In conclusion, this study identifies PU 91 as a therapeutic candidate drug for AMD and repurposing of PU-91 will be a smoother transition from lab bench to clinic since the pharmacological profiles of PU-91 have been examined already.

INTRODUCTION

The incidence of Age-related Macular Degeneration (AMD) is increasing at an alarming rate in elderly population in the United States. Per the National Eye Institute projection, the estimated number of AMD patients is expected to rise to 5.44 million by 2050. Most AMD cases occur among Caucasian Americans, followed by Hispanic and other populations. AMD – a disease which damages the macula and affects central vision, remains a leading cause of uncorrectable vision loss in the United States [1]. Despite intensive study, a limited number of FDA-approved treatment options are available for treatment of AMD. Anti-VEGF drugs such

as Ranibizumab, Bevacizumab, and Aflibercept have been demonstrated to reduce choroidal neovascularization in AMD. Therefore, injections of these anti-VEGF drugs into the vitreous cavity are by far the most viable treatment option available for wet AMD [2]. Furthermore, AREDS (Age-Related Eye Disease Study) supplements, which are over-the-counter antioxidant/zinc supplements, are known to slow down the progression of AMD [3].

Mitochondrial (mt) DNA damage due to mutations or oxidative stress has long been implicated in the development of AMD [4]. Mitochondrial DNA damage induces ARPE-19 cells to secrete pro-inflammatory

cytokines associated with onset and progression of AMD [5]. Macular RPE cells from aged and AMD human donor eyes have higher frequencies of mtDNA lesions and mtDNA genomic heteroplasmic mutations, compared to their age-matched controls. AMD severity has been associated with decreased expression of a DNA repair enzyme OGG1, which is involved in excision repair of oxidatively-damaged DNA. Accumulation of mtDNA lesions and reduced DNA repair capacity contribute to loss of RPE cells in AMD and aging retinas [6]. Therefore, several mitochondria-targeting therapeutic molecules have been identified in the hope of rescuing mtDNA and subsequently RPE cells in AMD. For instance, a mitochondria-targeted antioxidant SkQ1 prevents AMD progression in an *in vivo* model of AMD [7]. A mitochondria-targeting peptide called MTP-131 (Bendavia) targets cardiolipin and improves mitochondrial function [8]. Furthermore, our recent work has shown that Humanin G (HNG) which is a more potent variant of Humanin, a mitochondrial-derived peptide, rescues AMD RPE cybrid cells *in vitro* [9]. In that study, we demonstrated that mitochondria from AMD patients were dysfunctional compared to the normal mitochondria which were derived from age-matched normal subjects. Mitochondrial DNA damage was evidenced by significant reduction in mtDNA copy numbers and higher numbers of mtDNA lesions in the AMD cybrids compared to that in the normal cybrids. Furthermore, decreased expression of mitochondrial transcription and replication genes suggesting impaired mitochondrial transcription and replication was observed in the AMD cybrid cells compared to their normal counterparts. Moreover, this work with AMD cybrids revealed higher mitochondrial superoxide generation and reduced mtGFP fluorescent staining in AMD cybrids compared to normal cybrids [9]. Therefore, our previous findings established substantive mitochondrial damage in AMD cybrid cell lines compared to the normal cybrid cell lines which served as controls.

Since mitochondrial biogenesis is influenced by PGC-1 α (Peroxisome-proliferator-activated receptor γ Coactivator-1 α) expression and activity [10,11], numerous pharmacological interventions in retinal and neurodegenerative diseases have been directed toward PGC-1 α upregulation [12-15].

The purpose of this study was to test the following hypothesis: PU-91, an FDA-approved mitochondrion-stabilizing drug, will protect RPE cells in an *in vitro* macular degeneration model. PU-91 is a pro-drug that when metabolized is PPAR α ligand and which was developed for the treatment of dyslipidemia. The drug is estimated to have seen >5 million-years of patient exposure and remains an effective agent for certain

dyslipidemias. PU-91, not its metabolite, is the chemical matter that produces the upregulation of PGC-1 α (data not shown, manuscript in preparation). Our *in vitro* AMD model was created by fusion of mitochondria-deficient APRE-19 (*Rho*⁰) cell line with platelets isolated from AMD patients. The resulting AMD RPE transmitochondrial cybrids have identical nuclei derived from ARPE-19 cells but mitochondria from different AMD patients (Supplementary Table 1). We investigated the effect of PU-91 drug on mitochondrial biogenesis, apoptosis, oxidative stress, mitochondrial membrane potential, mitochondrial superoxide production, mtGFP staining, and finally examined the additive effects of PU-91 and esterase inhibitors i.e., EI-12 and EI-78 in AMD RPE transmitochondrial cybrids. Our findings demonstrated that PU-91 preserved AMD mitochondrial function and integrity, and protected AMD RPE cybrids against oxidative stress-induced and mtDNA-induced apoptotic cell death. This study suggests a potential role for PU-91 as a candidate drug for AMD treatment. Since PU-91 is an FDA-approved drug, its repositioning for treatment for AMD would encounter a smoother pathway because its side effects and other risks are already known. This shortens considerably the journey from lab bench to clinic. However, further studies are required to establish the merit of PU-91 as a cytoprotective molecule in AMD.

RESULTS

PU-91 increases mitochondrial DNA copy number and upregulates the genes involved in mitochondrial biogenesis pathway in AMD RPE cells

Mitochondrial biogenesis involves the orchestration of expression of multiple nuclear encoded genes, in large part, mediated through the transcriptional action of PGC-1 α gene product in concert with others. As PU-91 is posited to upregulate mitochondrial biogenesis, we sought to measure mitochondrial DNA (mtDNA) copy number and transcriptional outputs in AMD RPE cybrid cells treated with this repositioned drug.

Accordingly, PU-91 significantly increased relative mtDNA copy numbers by 50% ($p=0.03$; AMD UN: 1 ± 0.03 , $n=4$; AMD PU-91: 1.50 ± 0.13 , $n=4$) (Figure 1A) and upregulated the gene expression of PGC-1 α by 208 % ($p=0.016$; AMD UN: 1 ± 0.29 , $n=5$; AMD PU-91: 3.08 ± 0.35 , $n=5$) (Figure 1B), *NRF-1* by 46 % ($p=0.03$; AMD UN: 1 ± 0.09 , $n=4$; AMD PU-91: 1.46 ± 0.1 , $n=4$) (Figure 1C), *NRF-2* by 38 % ($p=0.03$; AMD UN: 1 ± 0.13 , $n=5$; AMD PU-91: 1.38 ± 0.06 , $n=5$) (Figure 1D), *PPAR- α* by 19 % ($p=0.03$; AMD UN: 1 ± 0.05 , $n=5$; AMD PU-91: 1.19 ± 0.05 , $n=5$) (Figure 1E), and *PPAR- γ* by 32 % ($p=0.03$; AMD UN: 1 ± 0.09 ,

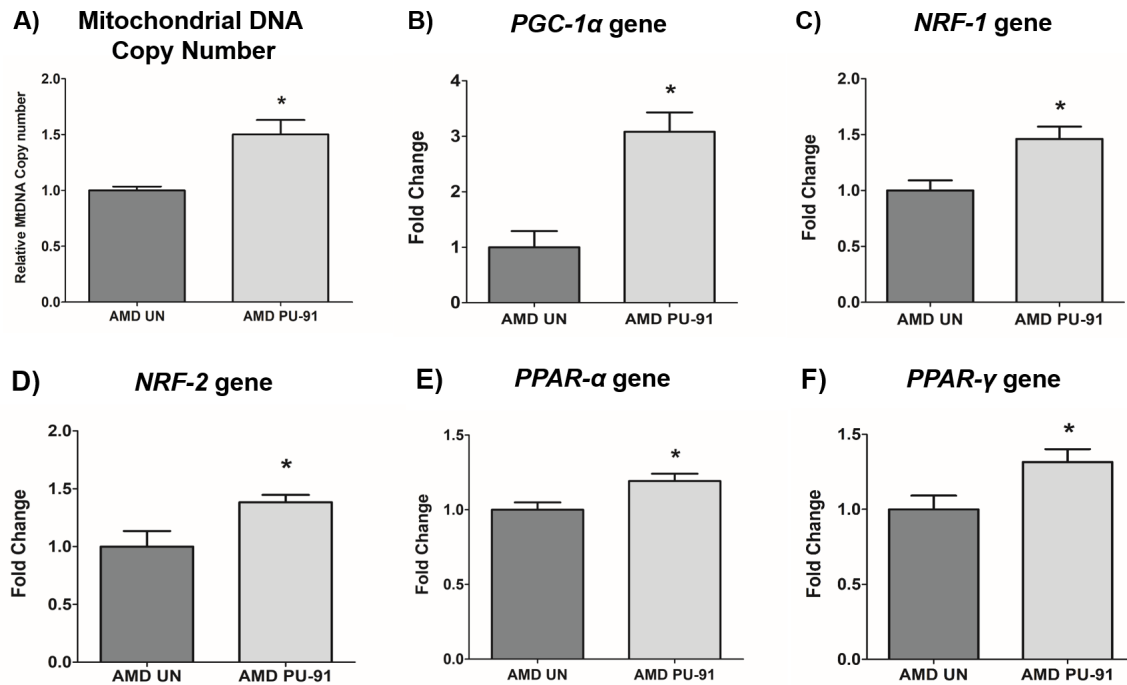


Figure 1. PU-91 regulates the mitochondrial biogenesis pathway. We used quantitative qRT-PCR to measure the relative mtDNA copy number (A), and the gene expression of markers of the mitochondrial biogenesis pathway such as *PGC-1α* (B), *NRF-1* (C), *NRF-2* (D), *PPAR-α* (E), and *PPAR-γ* (F). PU-91-treated AMD cybrids (AMD PU-91) had higher mtDNA copy numbers and increased gene expression levels of all the above-mentioned markers ($p < 0.05$, $n = 4-5$). Data are presented as mean \pm SEM and normalized to untreated (UN) AMD cybrids which were assigned a value of 1. Mann-Whitney test was used to measure statistical differences; $*p < 0.05$.

$n = 5$; AMD PU-91: 1.32 ± 0.08 , $n = 5$) (Figure 1F) in AMD cybrids compared to their untreated counterparts.

PU-91 improves mitochondrial function in AMD RPE cells

It would be anticipated that transcriptional activation of genes that promote mitochondrial biogenesis would be accompanied by evidence of improved mitochondrial function. As shown in Figure 2, PU-91-treated AMD cybrid cells had increased mitochondrial membrane potential (JC-1 assay) (116 % increase; $p = 0.03$; AMD UN: 1 ± 0.09 , $n = 3$; AMD PU-91: 2.16 ± 0.26 , $n = 4$), (Figure 2A), and significantly lower levels of mitochondrial superoxides (MitoSOX assay) (22 % increase; $p = 0.04$; AMD UN: 1 ± 0.06 , $n = 4$; AMD PU-91: 0.78 ± 0.038 , $n = 4$), (Figure. 2B). Furthermore, PU-91-treated AMD cells showed upregulation of *SOD2*, a mitochondrial antioxidant gene, by 160 %, ($p = 0.0079$; AMD UN: 1 ± 0.11 , $n = 5$; AMD PU-91: 2.6 ± 0.37 , $n = 5$) (Figure 2C), and reduced gene expression of *HIF1α* (47 % increase; $p = 0.03$; AMD UN: 1 ± 0.14 , $n = 4$; AMD PU-91: 0.53 ± 0.03 , $n = 4$) (Figure 2D). PU-91 upregulated *MT-RNR2* (Mitochondrially Encoded 16S rRNA) gene in AMD RPE cybrid cells. Treatment with

PU-91 drug caused a 104 % higher expression of *MT-RNR2* gene in AMD RPE cybrid cells ($p = 0.0079$; AMD UN: 1 ± 0.15 , $n = 5$; AMD PU-91: 2.04 ± 0.39 , $n = 5$) (Figure 2E), suggesting that increased production of Mitochondrial Derived Peptides (MDPs) could be one of the mechanisms by which PU-91 rescues cells.

PU-91 enhances mitochondrial GFP (mtGFP) fluorescence in AMD RPE cells

The cell biological features of mitochondria integrity are best observed in whole cells where mitochondria are visualized. Figure. 3A shows representative confocal images of AMD RPE cells stained with DAPI (blue) and mitochondrial GFP stain (green). Panel 1 shows bright-field images, panel 2 shows DAPI (blue)-stained images, panel 3 shows mtGFP (green)-stained images, and panel 4 shows merge (DAPI + mtGFP) images. The qualitative appearance of the mitochondrial network is vastly different in PU-91 treated cells compared with untreated controls (panel 3). When quantitated, PU-91-treated AMD cells showed an increase in mtGFP fluorescence intensity by 168 % ($p = 0.03$; AMD UN: 1 ± 0.22 , $n = 4$; AMD PU-91: 2.68 ± 0.25 , $n = 4$) (Figure 3B) compared to the untreated AMD cells.

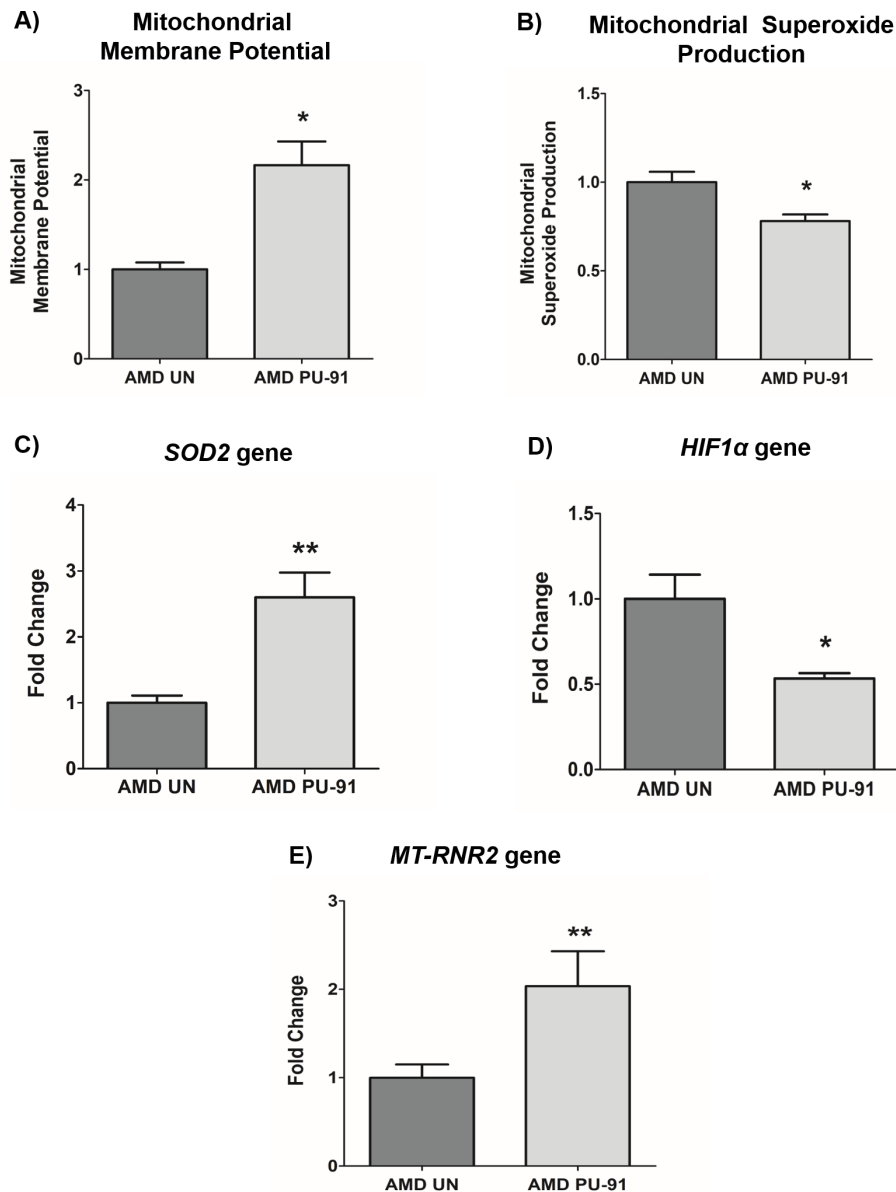


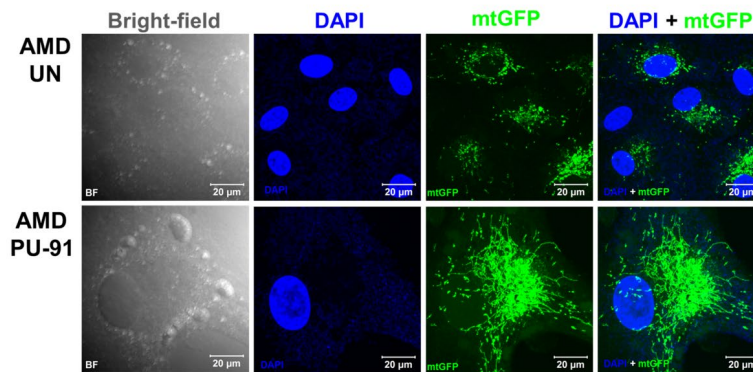
Figure 2. PU-91 regulates mitochondrial function. We used the fluorometric JC-1 assay and MitoSOX assay to measure mitochondrial membrane potential and mitochondrial superoxide production, respectively. Treatment with PU-91 led to elevated mitochondrial membrane potential ($p \leq 0.05$, $n=3$) (A) and reduced mitochondrial superoxide production ($p \leq 0.05$, $n=3$) (B) in AMD cybrids (AMD PU-91) compared to the untreated group (AMD UN). Furthermore, PU-91-treated AMD cybrids showed upregulation of the mitochondrial superoxide dismutase, *SOD2* gene ($p \leq 0.05$, $n=5$) (C) and reduced expression of *HIF1α* gene ($p \leq 0.05$, $n=3-4$) (D). (E) PU-91 upregulates *MT-RNR2* gene. Using TaqMan probe for the *MT-RNR2* gene, qRT-PCR analysis revealed that PU-91 increases *MT-RNR2* gene expression by 104% compared to untreated control ($p \leq 0.05$, $n=5$). Data are presented as mean \pm SEM and normalized to untreated (UN) AMD cybrids which were assigned a value of 1. Mann-Whitney test was used to measure statistical differences; * $p \leq 0.05$, ** $p \leq 0.01$.

PU-91 rescues AMD RPE cells from apoptotic cell death

Apart from promoting mitochondrial biogenesis, *PGC-1α* also partners to promote the expression of additional gene networks that are cytoprotective. Treatment of AMD RPE cells with PU-91 decreased expression of

Caspase-3 gene by 34 % ($p=0.016$; AMD UN: 1 ± 0.099 , $n=5$; AMD PU-91: 0.66 ± 0.03 , $n=5$) (Figure 4A) and *BAX* gene by 21 % ($p=0.0079$; AMD UN: 1 ± 0.05 , $n=5$; AMD PU-91: 0.79 ± 0.03 , $n=5$) (Figure 4B), and significantly increased cell viability by 55 % ($p=0.03$; AMD UN: 1 ± 0.11 , $n=4$; AMD PU-91: 1.55 ± 0.086 , $n=4$) (Figure 4C) compared to their untreated counter-

A) Representative mtGFP and DAPI-stained confocal images



B) MtGFP Fluorescence Intensity

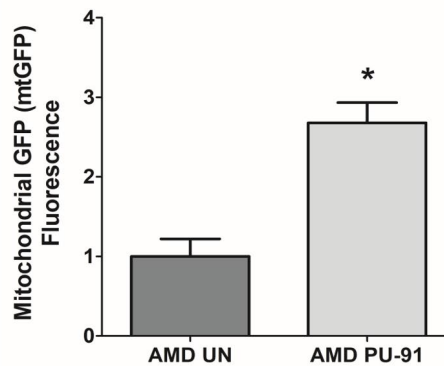


Figure 3. PU-91 alters mitochondrial GFP fluorescence intensity. Untreated (AMD UN) and PU-91-treated AMD cybrids (AMD PU-91) were stained with CellLight mitochondrial GFP stain followed by confocal imaging of cells. (A) Shows representative bright-field, DAPI, mtGFP, and overlay (DAPI + mtGFP) confocal images. PU-91-treated AMD cybrids had a drastic increase in mtGFP fluorescence intensity compared to the untreated group ($p \leq 0.05$, $n=3$) (B). Data are presented as mean \pm SEM and normalized to untreated (UN) AMD cybrids which were assigned a value of 1. Mann-Whitney test was used to measure statistical differences; * $p \leq 0.05$.

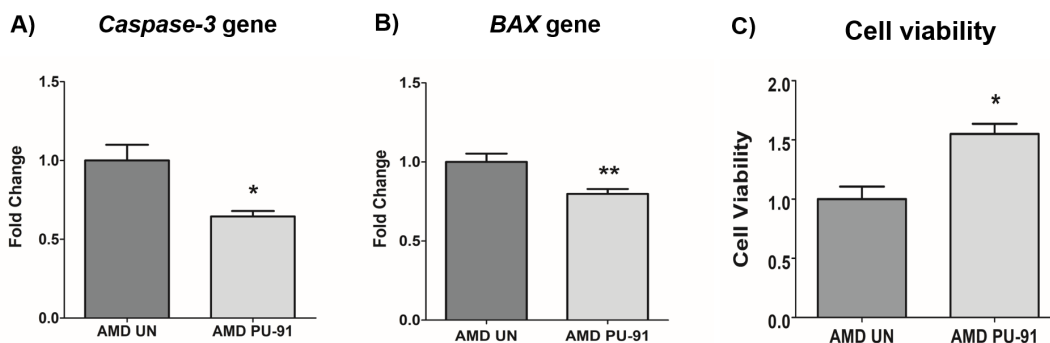
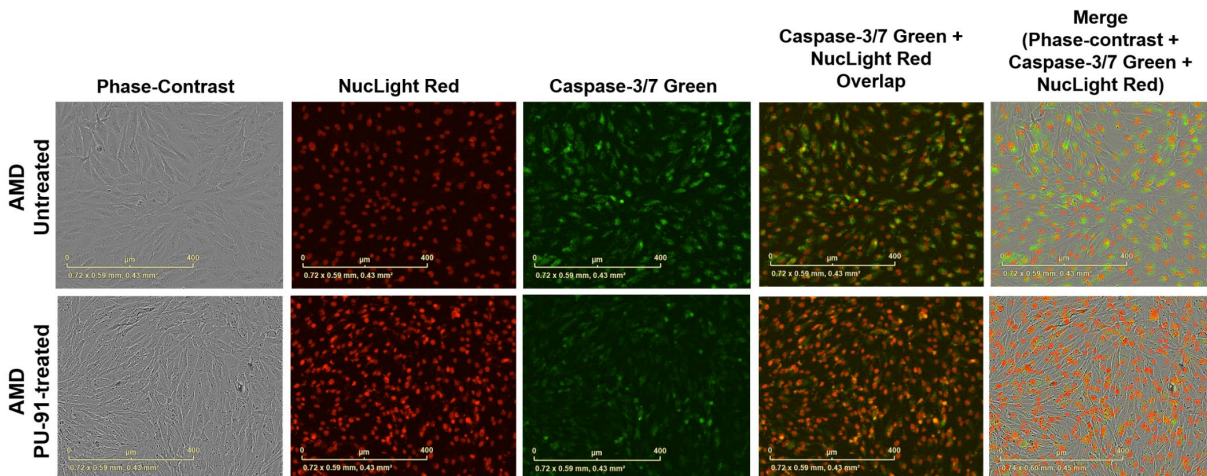


Figure 4. PU-91 regulates apoptotic cell death. qRT-PCR analysis showed downregulation of apoptotic genes such as *Caspase-3* ($p \leq 0.05$, $n=4$) (A) and *BAX* ($p \leq 0.05$, $n=4$) (B) in AMD cybrids treated with PU-91. Using the MTT assay, it was observed that PU-91-treated AMD cybrids had a higher number of viable cells compared to the untreated group ($p \leq 0.05$, $n=4$) (C). Data are presented as mean \pm SEM and normalized to untreated (UN) AMD cybrids which were assigned a value of 1. Mann-Whitney test was used to measure statistical differences; * $p \leq 0.05$, ** $p \leq 0.01$.

A) Representative IncuCyte live cell images showing NuLight Red and Caspase-3/7 Green staining



B) IncuCyte live cell imaging Quantitation

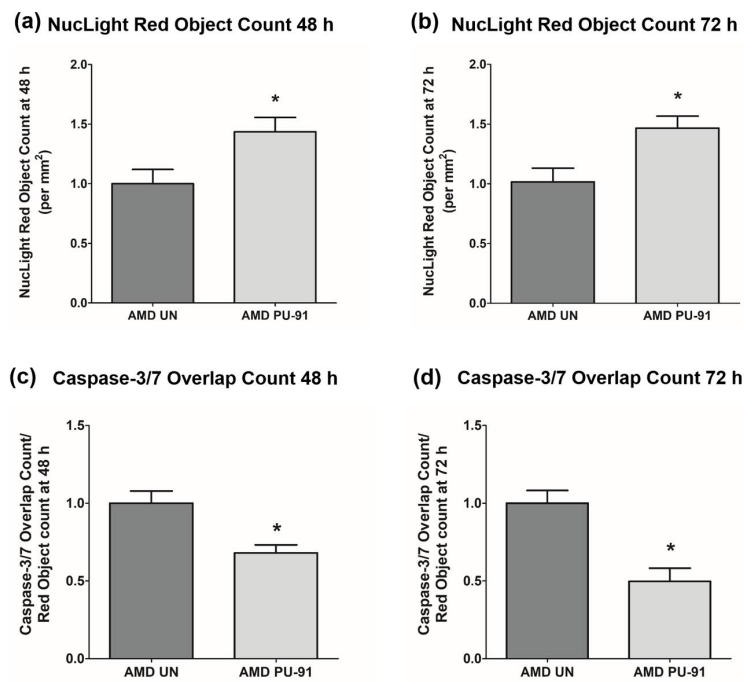


Figure 5. PU-91 regulates apoptotic cell death – Caspase-3/7 staining. (A) Shows representative IncuCyte live-cell images of untreated (AMD UN) and PU-91-treated AMD cybrid cells (AMD PU-91) stained with NuLight Red and Caspase-3/7 Green reagent. (B) Shows quantitation graphs for the 48 h and 72 h time points. Data are presented as mean \pm SEM and normalized to untreated (UN) AMD cybrids which were assigned a value of 1. Mann-Whitney test was used to measure statistical differences; * $p < 0.05$.

parts. Furthermore, to examine and compare cell proliferation and apoptosis between untreated and PU-91-treated AMD cells, we performed IncuCyte® Live-Cell Imaging Analysis using Caspase- 3/7 Green and NuLight Red reagents (Figures 5A and 5B). Figure. 5A shows representative IncuCyte live-cell images. The upper panel represents untreated AMD group and the lower panel represents the PU-91-treated AMD group.

Panel 1 shows phase-contrast images; panel 2 shows NuLight Red-stained images; panel 3 shows Caspase-3/7 Green-stained images; panel 4 shows Overlap i.e., Caspase-3/7 + NuLight Red images; and panel 5 shows Merged i.e., Phase-contrast + NuLight Red + Caspase-3/7 Green images. Compared to untreated AMD cells, PU-91-treated AMD cells showed 43.6 % and 46.6 % higher NuLight Red object count at the 48 h ($p=0.03$;

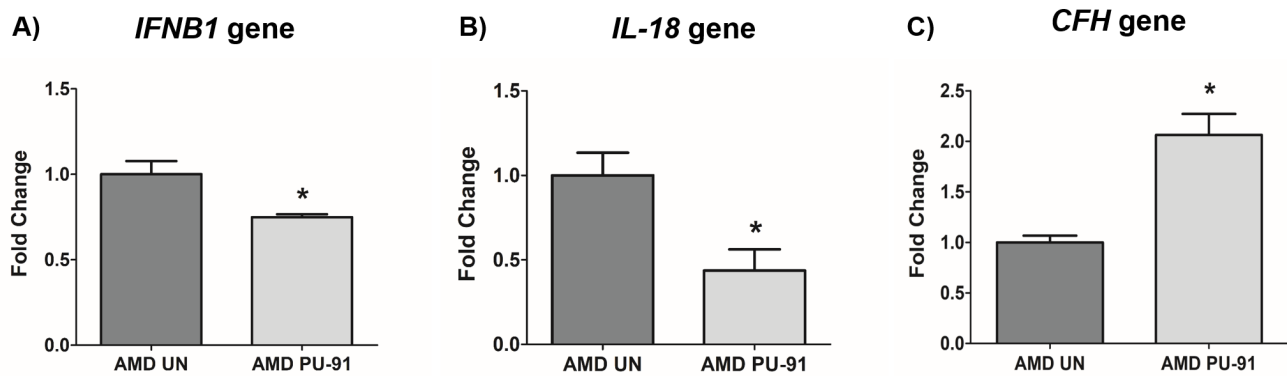


Figure 6. PU-91 regulates inflammation and complement. qRT-PCR analysis showed lower gene expression of inflammation markers such as *IFNB1* ($p \leq 0.05$, $n=4$) (A), *IL-18* ($p \leq 0.05$, $n=4$) (B) in PU-91-treated AMD cybrids (AMD PU-91) compared to untreated AMD cybrids (AMD UN). However, PU-91 upregulated the complement inhibitor *CFH* gene ($p \leq 0.05$, $n=3-4$) (C). Data are presented as mean \pm SEM and normalized to untreated (UN) AMD cybrids which were assigned a value of 1. Mann-Whitney test was used to measure statistical differences; * $p \leq 0.05$.

AMD UN: 1 ± 0.119 , $n=4$; AMD PU-91: 1.436 ± 0.119 , $n=4$) (Figure 5B (a)) and 72 h ($p=0.03$; AMD UN: 1 ± 0.115 , $n=4$; AMD PU-91: 1.466 ± 0.099 , $n=4$) (Figure 5B (b)) timepoints respectively. Furthermore, as hypothesized, PU-91-treated AMD cells showed lower Overlap object count (i.e., Caspase-3/7 Green + NucLight Red staining (Yellow))/ Red object count compared to their untreated counterparts i.e., at 48 h – 32 % decrease; $p=0.03$; AMD UN: 1 ± 0.079 , $n=4$; AMD PU-91: 0.68 ± 0.05 , $n=4$) (Figure 5B (c)) and at 72 h – 50.21 % decrease; $p=0.03$; AMD UN: 1 ± 0.082 , $n=4$, AMD PU-91: 0.498 ± 0.084 , $n=4$) (Figure 5B (d)).

PU-91 regulates inflammation and complement in AMD RPE cells

Molecular correlates of AMD include chronic inflammation and dysregulation of the complement pathway. We sought to determine whether PU-91 regulated these pathogenic features. Treatment with PU-91 altered the gene expression of inflammatory markers, *IFNB1* (25 % decrease; $p=0.03$; AMD UN: 1 ± 0.08 , $n=4$; AMD PU-91: 0.75 ± 0.02 , $n=4$) (Figure 6A), *IL-18* (56 % decrease; $p=0.03$; AMD UN: 1 ± 0.13 , $n=4$; AMD PU-91: 0.44 ± 0.12 , $n=4$) (Figure 6B), and of a complement inhibitor *CFH* (106 % increase; $p=0.03$; AMD UN: 1 ± 0.07 , $n=4$; AMD PU-91: 2.06 ± 0.21 , $n=3$) (Figure 6C).

Additive effects of PU-91 + Esterase Inhibitors (EI) i.e., EI-12 and EI-78 on cell viability in AMD RPE cells

To drive higher levels of PU-91 into tissues such as the neuroretina we evaluated co-administration with

esterase inhibitors (EI) namely EI-12 and EI-78. To determine whether addition of either of these esterase inhibitors to PU-91 alters pharmacodynamic responses and/or produce independent effects, we studied these on AMD RPE cybrids. Figure 7A and 7B and Supplementary Table 2 show the effects of treatment with PU-91+EI-12 at varying concentrations i.e., EI-12 5 μ M, 10 μ M, and 20 μ M, on the cell viability of AMD cybrid cells at 48 h (Figure 7A) and at 72 h (Figure 7B). Compared to untreated AMD cybrids, a significant increase in cell viability was observed in PU-91 treated AMD cybrids and in the PU-91+EI-12 20 μ M group at 48 h.

Also, a significant difference in cell viability was observed between the untreated AMD group and the group treated with PU-91+EI-12 5 μ M, PU-91+EI-12 10 μ M and PU-91+EI-12 20 μ M at 72 h (Figure 7B). Compared to untreated AMD cells, treatment with PU-91+EI-78 at varying concentrations i.e., EI-78 2.5 μ M, 5 μ M and 10 μ M, eliminated the cell viability cytoprotection of PU-91 alone on AMD RPE cells at 48 h (Figure 7C). Compared to untreated AMD cells, treatment with PU-91+EI-78 at concentrations 5 μ M and 10 μ M eliminated the cell viability cytoprotection of PU-91 alone on AMD RPE cells at 72 h time points. A significant increase in cell viability was observed between the untreated AMD group and the group treated with PU-91+EI-78 2.5 μ M (Figure 7D, Supplementary Table 3).

No significant changes in cell viability were observed between AMD cells treated with only PU-91 and those treated with PU-91+EI-12 or PU-91+EI-78 (Supplementary Tables 2 and 3).

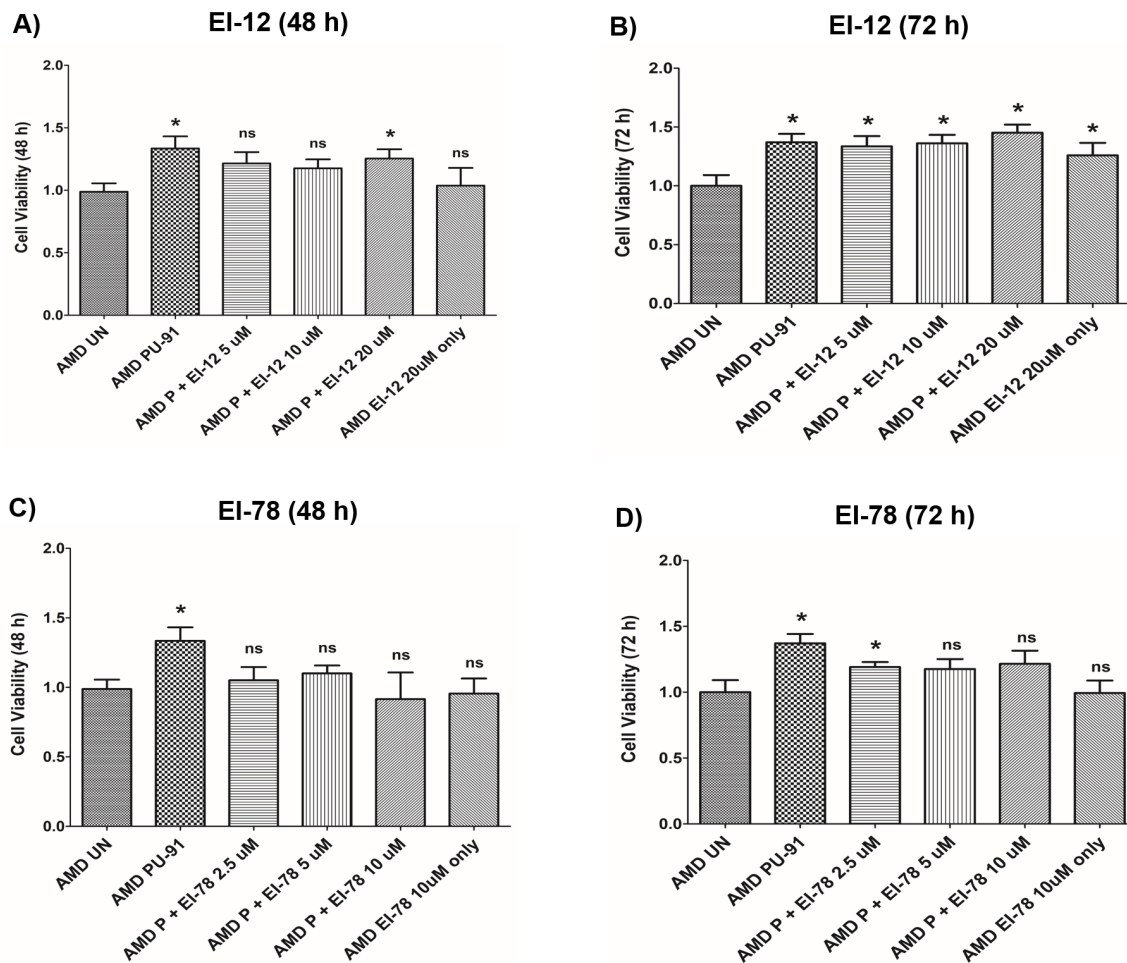


Figure 7. Effect of PU-91 + EI-12/ EI-78 on cell viability. This figure shows cell viability differences using MTT assay in AMD cells treated with P + EI-12 (A and B) / EI-78 (C and D) at 48 h and 72 h. Data (n=3) are presented as mean ± SEM and normalized to untreated (UN) AMD cybrids which were assigned a value of 1. Mann-Whitney test were used to measure statistical differences; *p<0.05. P = PU-91; EI = Esterase Inhibitor.

Additive effects of PU-91 + EI-12 and EI-78 on gene expression in AMD RPE cells

We extended the observations of PU-91 with esterase inhibitors EI-12 and EI-78, on gene expression changes. Treatment with PU-91 + EI-12/ EI-78 at different concentrations i.e., EI-12: 5 μM, 10 μM, and 20 μM; EI-78: 2.5 μM, 5 μM, and 10 μM altered the expression of *PGC-1α*, *Caspase-3*, *IL-18*, *VEGF*, *SOD2* genes in AMD RPE cybrid cells (n=3) at the 72 h time point.

***PGC-1α*: EI-12** - Compared to untreated AMD cybrids, significant *PGC-1α* upregulation was observed in PU-91-treated, P (PU-91)+EI-12 5 μM (216 %), P+EI-12 10 μM (263 %), P+EI-12 20 μM (115 %) groups, and only EI-12 20 μM (82 %) groups (Figure 8A, Supplementary Table 4). **EI-78** - Compared to untreated AMD cybrids, significant *PGC-1α* upregulation was observed in PU-

91-treated, P+EI-78 2.5 μM (189 %), P+EI-78 5 μM (109 %), and P+EI-78 10 μM (126 %) groups, (Figure 9A, Supplementary Table 5).

***Caspase-3*: EI-12** - Compared to untreated AMD cybrids, significant *Caspase-3* downregulation was observed in PU-91-treated, P+EI-12 5 μM (22 %), P+EI-12 10 μM (27 %), P+EI-12 20 μM (34 %), and only EI-12 20 μM (26 %) groups (Figure 8B, Supplementary Table 4). **EI-78** - Compared to untreated AMD cybrids, significant *Caspase-3* downregulation was observed in PU-91-treated, P+EI-78 2.5 μM (26 %), P+EI-78 10 μM (34 %), and only EI-78 10 μM (13.8 %) groups (Figure 9B, Supplementary Table 5).

***IL-18*: EI-12** - Compared to untreated AMD cybrids, significant *IL-18* downregulation was observed only in the PU-91-treated group, P+EI-12 5 μM (18.3 %),

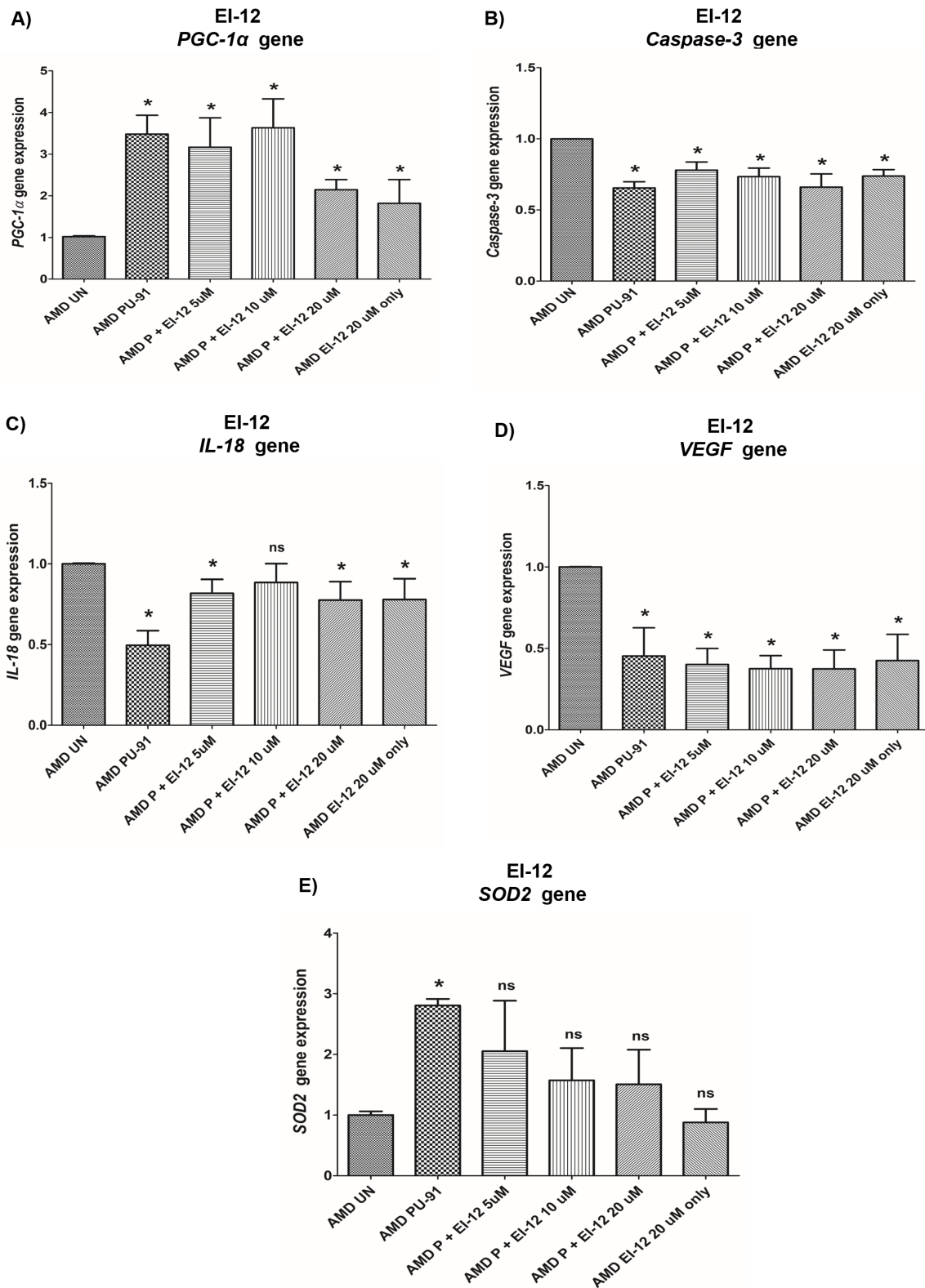


Figure 8. Effect of PU-91 + EI-12 on gene expression. qRT-PCR analysis showed differential expression of *PGC-1α* (A), *Caspase-3* (B), *IL-18* (C), *VEGF* (D), and *SOD2* (E) genes in AMD RPE cells at the 72 h time point. Data (n=3) are presented as mean \pm SEM and normalized to untreated (UN) AMD cybrids which were assigned a value of 1. Mann-Whitney test was used to measure statistical differences; * $p < 0.05$. P = PU-91; EI = Esterase Inhibitor.

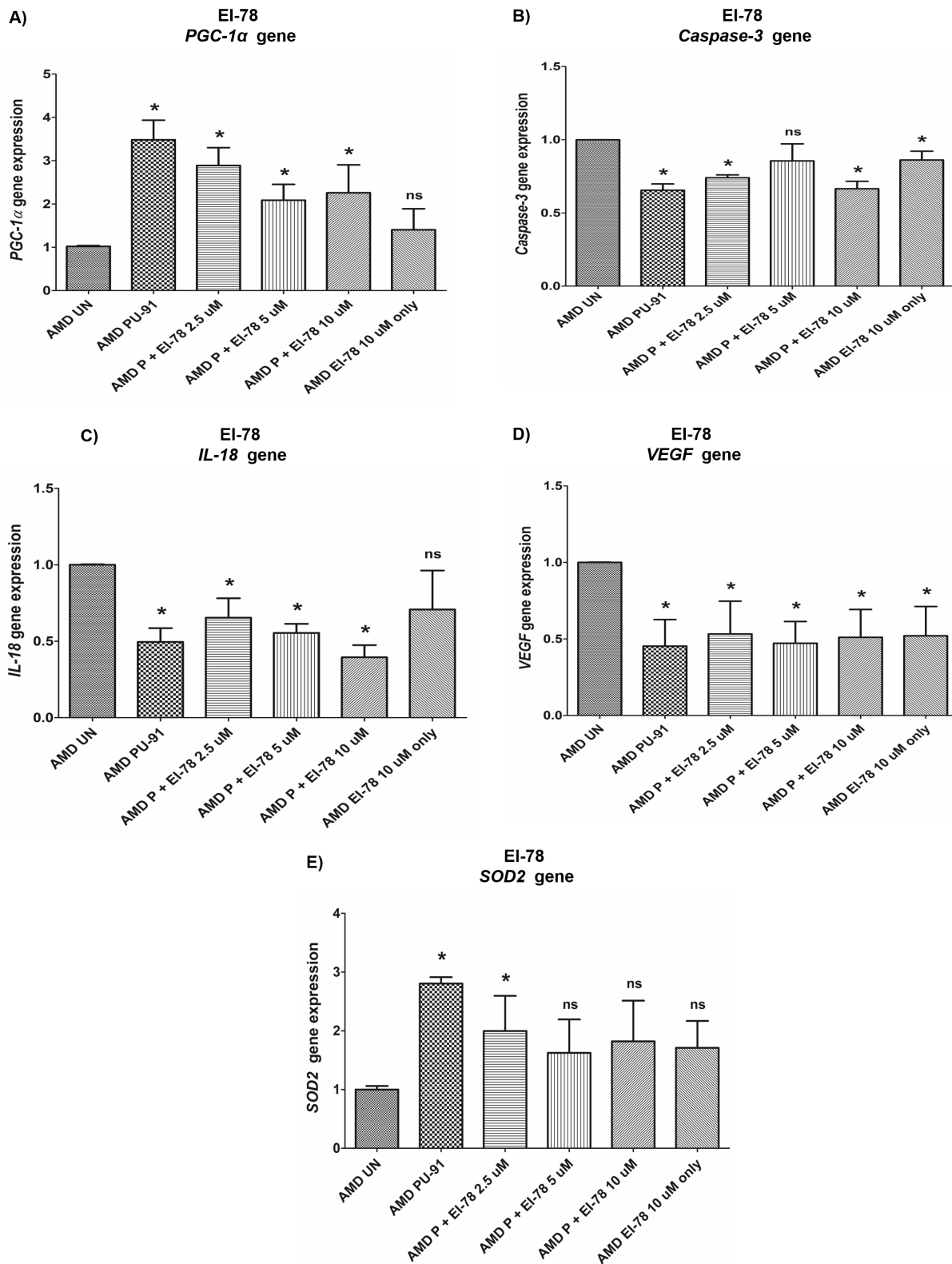


Figure 9. Effect of PU-91 + EI-78 on gene expression. qRT-PCR analysis showed differential expression of *PGC-1α* (A), *Caspase-3* (B), *IL-18* (C), *VEGF* (D), and *SOD2* (E) genes in AMD RPE cells at the 72 h time point. Data (n=3) are presented as mean \pm SEM and normalized to untreated (UN) AMD cybrids which were assigned a value of 1. Mann-Whitney test was used to measure statistical differences; *p<0.05. P = PU-91; EI = Esterase Inhibitor.

P+EI-12 20 μ M (22.4 %), and only EI-12 20 μ M (22 %) groups (Figure 8C, Supplementary Table 4). **EI-78** - Compared to untreated AMD cybrids, significant *IL-18* downregulation was observed in PU-91-treated, P+EI-78 2.5 μ M (34.6 %), P+EI-78 5 μ M (45 %), and P+EI-78 10 μ M (61 %) groups (Figure 9C, Supplementary Table 5).

VEGF: EI-12 - Compared to untreated AMD cybrids, significant *VEGF* downregulation was observed in PU-91-treated, P+EI-12 5 μ M (60 %), P+EI-12 10 μ M (63 %), P+EI-12 20 μ M (63 %), and only EI-12 20 μ M (58 %) groups (Figure 8D, Supplementary Table 4). **EI-78** - Compared to untreated AMD cybrids, significant *VEGF* downregulation was observed in PU-91-treated, P+EI-78 2.5 μ M (46.7 %), and P+EI-78 5 μ M (53 %), P+EI-78 10 μ M (48.9 %), and only EI-78 10 μ M (47.9 %) groups (Figure 9D, Supplementary Table 5).

SOD2: EI-12 - Compared to untreated AMD cybrids, significant *SOD2* upregulation was observed only in the PU-91-treated group (Figure 8E, Supplementary Table 4). **EI-78** - Compared to untreated AMD cybrids, significant *SOD2* upregulation was observed only in the PU-91-treated and P+EI-78 2.5 μ M (99.7 %) groups (Figure 9E, Supplementary Table 5).

DISCUSSION

We report that PU-91, an FDA-approved drug, promotes mitochondrial-stabilization, *PGC-1 α* upregulation, cytoprotection of AMD ARPE-19 trans-mitochondrial cybrid cells by preserving mitochondrial health, reducing apoptotic cell loss, and inducing upregulation of the MDP-coding *MT-RNR2* gene. Our study establishes PU-91 as a potential candidate drug for AMD therapy.

Gene expression analyses revealed significant upregulation of mitochondrial biogenesis pathway genes i.e., *PGC-1 α* , *NRF-1*, *NRF-2*, *PPAR- α* , and *PPAR- γ* in PU-91-treated AMD cybrids. PU-91 positively regulates the expression of nucleus-encoded markers of mitochondrial biogenesis in AMD mitochondria-containing cybrid cell lines. Dysregulation of mitochondrial function and decreased *PGC-1 α* levels have been implicated in neurodegeneration [16, 17]. *PGC-1 α* is a master regulator of mitochondrial biogenesis in several disease models including cardiac disorders, Parkinson's disease, Huntington's disease and Alzheimer's disease [18-24]. A study demonstrated that *PGC-1 α* activity and signaling are induced to regulate detoxifying responses to oxidative and metabolic stress in inner retina [25]. The same study identified *PGC-1 α* as an important regulator of retinal ganglion cell (RGC) homeostasis

and astrocyte reactivity. Moreover, *PGC-1 α* , by regulating senescence, protects RPE cells against oxidative damage in aging retina in AMD-like pathology *in vivo* [26]. Iacovelli et al. reported major involvement of *PGC-1 α* in mitochondrial function and in antioxidant capacity in primary human RPE cells and in ARPE-19 cell lines *in vitro* [13]. *PGC-1 α* increases the expression of mitochondrial enzymes such as ATP synthase and Cytochrome c Oxidase (COX), and induces mitochondrial biogenesis by activating various transcription factors, including *NRF-1* and *NRF-2*, which in turn induce *TFAM*, *PPARs*, estrogen and *ERRs* [27].

NRF-1 and *NRF-2* are redox-sensitive transcription factors that are activated in response to oxidative stress. By inducing cytoprotective molecules, they orchestrate a defense mechanism against reactive oxygen species (ROS)-induced cytotoxicity. Moreover, *NRF-1* and *NRF-2* are known to protect neurons against acute brain injury [28]. *NRF2* binds to the antioxidant response element (ARE) in the promoter regions of its target genes, thereby activating antioxidant gene transcription [29]. Activation of *NRF-2* conferred neuroprotective effects in the retina post-ischemia/reperfusion injury *in vivo* [30]. Both *NRF-1* and *NRF-2* activate the genes involved in oxidative homeostasis. Deletion of *PGC-1 α* and *NRF-2*, as found in *NRF-2/PGC-1 α* dKO mice, resulted in significant age-dependent RPE degeneration [31]. Substantial *in vivo* evidence demonstrates the involvement of *NRF-1* and *NRF-2* in early development, and their absence causes embryonic lethality and oxidative stress-induced toxicity [32]. *NRF-1* activates the *Cytochrome c* gene and therefore plays a role in nuclear-mitochondrial interactions [33].

PPARs, a subfamily of nuclear receptors, are transcription factors that can heterodimerize with partners, such as the retinoid X receptor (*RXR*) and bind to DNA of target genes [34]. Ding et al. demonstrated that *PPAR- α* (Peroxisome Proliferator-Activated Receptor α) improves mitochondrial oxygen consumption and protects capillary pericytes in the retina [35]. Pearsall et al. showed that *PPAR- α* plays a pivotal role in retinal neuronal survival, lipid metabolism and improves retinal energy efficiency. Since energy deficits due to dysfunctional mitochondria have been implicated in AMD, *PPAR- α* was suggested to be a putative therapeutic target in AMD [36]. Zhu et al. reported a potential role of *PPAR- γ* in differentiation and maturation of retinal cells [37]. Studies also highlighted potential neuroprotective function of *PPAR- γ* agonists *in vivo* and *in vitro* in neurodegenerative diseases such as Alzheimer's [38], Parkinson's [39], and ALS [40]. Addition of the *PPAR- γ* agonists such as Pioglitazone

is known to induce neuronal survival and protection from apoptotic cell death in the retina [41]. Furthermore, PPAR- γ ligands inhibit corneal neovascularization [42-44] and injury-induced scarring in the conjunctiva after glaucoma surgery [45]. Murata et al. demonstrated inhibition of choroidal angiogenesis and VEGF-induced RPE migration and proliferation *in vitro* by PPAR- γ ligands namely troglitazone/ rosiglitazone. This group also showed that intravitreal injection of troglitazone caused significant reduction in lesions and leakage in the eyes of choroidal neovascular (CNV) animal models [46]. In summary, by modulating the expression of mitochondrial biogenesis mediators, PU-91 orchestrates mitochondrial and cellular health.

We next performed JC-1 dye assay to compare mitochondrial membrane potential ($\Delta\Psi_m$) between untreated and PU-91-treated AMD cybrids. Previously, it has been established that any imbalance in oxidative redox state causes mitochondrial depolarization, opening of mitochondrial permeability transition pore, and collapse of mitochondrial membrane potential, subsequently leading to apoptosis [47, 48]. These events hold true in the retina as well [49]. We know that AMD cybrids have damaged mitochondria, which likely contribute to compromised mitochondrial membrane potential. However, PU-91 administration improved $\Delta\Psi_m$ significantly in AMD cybrid cells, suggesting that PU-91 can protect mitochondrial membrane integrity and function. Potential mechanisms of PU-91-mediated $\Delta\Psi_m$ restoration including attenuation of mitochondrial depolarization should be further examined. Consistent with our study, Chong et al. demonstrated that Artemisinin, an FDA-approved drug improves $\Delta\Psi_m$ as measured by JC-1 assay and protects human retinal pigment epithelial cells from oxidative damage [50]. Moreover, *in vivo* studies by Ellis et al. showed that addition of Sigma-1 receptor agonists restored $\Delta\Psi_m$ in oxygen-deprived retina [51].

Mitochondria are a major source of reactive oxygen species (ROS) in a cell, and the principal mitochondrial ROS is superoxide anion, which is a by-product of leakage from the Electron Transport Chain. We have previously shown that AMD RPE cybrid cells have higher mitochondrial superoxide production compared to age-matched normal cybrid cells [9]. In the current study, we used a fluorogenic MitoSOX Red dye for specific detection of mitochondrial superoxide. Once inside the mitochondria, the MitoSOX Red reagent is oxidized by superoxide and exhibits red fluorescence. Our results revealed significantly diminished mitochondrial superoxide production in PU-91-treated AMD cybrids compared to untreated AMD cybrids. This finding is important because elevated levels of

intracellular ROS and mitochondrial superoxides contribute to retinal and neurological diseases [52-54], and reduction in mitochondrial superoxide is critical to protect against oxidative stress-related diseases.

We also examined in AMD cybrids the gene expression of *SOD2*, the mitochondrial Super Oxide Dismutase, also known as MnSOD (Manganese SOD). *SOD2* prevents binding of mitochondrial superoxide to nitric oxide thereby preventing apoptosis, necrosis, mitophagy, and autophagy [55]. Deficiency of *SOD2* causes extensive oxidative damage in the RPE and has been associated with AMD pathogenesis [56]. Recent Genome-Wide Association Studies (GWAS) have suggested an association between a susceptible locus - rs2842992 near the *SOD2* gene and geographic atrophy in AMD [57]. In the present study, PU-91 treatment upregulated *SOD2* gene levels significantly, which would enhance the antioxidant effects in AMD cybrids. Hypoxic stress and activation of HIF1 α has been implicated in AMD. ROS and HIF1 α cause VEGF activation thereby triggering angiogenesis and subsequent choroidal neovascularization in wet AMD [58, 59]. PU-91-treated AMD cybrids had lower expression of *HIF1 α* gene, suggesting that PU-91 may exhibit hypoxia-suppressing effects. Cumulatively, these results highlight a key pharmacological role of PU-91 in decreasing oxidative stress in AMD cells.

We have established previously that dysfunctional mitochondria in the AMD cybrids contribute to activation of cleaved Caspase-3 and BAX, which are markers of cell apoptosis [9]. Other studies have demonstrated the role of apoptotic and necrotic cascades in death of retinal cells in AMD [60, 61]. Therefore, treatment with drugs that inhibit apoptosis is essential to prevent retinal cell loss and to preserve cellular health. We observed higher number of viable cells and downregulation of *Caspase-3* and *BAX* genes in PU-91-treated AMD cybrids, indicating that PU-91 prevents mitochondria-induced apoptotic cell death in these cells. Next, we compared cell proliferation and apoptosis between untreated and PU-91-treated AMD cells using IncuCyte® Live-Cell Imaging Analysis system and Caspase-3/7 Green and NucLight Red reagents. PU-91-treated AMD cells showed significantly higher NucLight Red object count at the 48 h and 72 h compared to untreated AMD cells. Furthermore, as hypothesized, PU-91-treated AMD cells showed lower Overlap object count (i.e., Caspase-3/7 Green + NucLight Red staining (Yellow))/ Red object count compared to their untreated counterparts. Our IncuCyte data revealed that PU-91 enhanced cell proliferation and reduced Caspase-3/7 activity in AMD cybrids. To our knowledge, this is the first study to report these findings.

The *MT-RNR2* gene contains small open-reading frames for mitochondrial-derived peptides (MDPs) such as Humanin and SHLPs that possess cytoprotective and neuroprotective properties [9, 62, 63]. Interestingly, addition of PU-91 upregulated the MDP-coding *MT-RNR2* gene in AMD cybrids, suggesting that PU-91-mediated protective effects in AMD cybrids may be partly attributed to MDP production. Therefore, PU-91 may ameliorate cell health by triggering production of MDPs including Humanin, which is cytoprotective in AMD [9].

Mitochondrial stabilization and protection are potential mechanisms by which PU-91 protects AMD RPE cybrids. To compare mitochondrial density between untreated and PU-91-treated AMD cells, we transduced the cells with CellLight reagent, which is a GFP-E1 alpha pyruvate dehydrogenase leader peptide construct driven by a mammalian promoter. This fluorescent fusion construct provides precise targeting to mitochondria. Herein, treatment with PU-91 enhanced mitochondrial GFP fluorescence appreciably in AMD cells compared to their untreated counterparts, indicating that PU-91 can augment and/or prevent mitochondrial loss in AMD cybrids. These results are consistent with a previous study wherein Humanin G, a mitochondrial-derived peptide, rescued AMD mitochondria in RPE cybrid cells [9].

PU-91 attenuated *IL-18* gene expression, thereby reducing mtDNA damage-induced inflammation in AMD cybrids. This is significant because elevation of pro-inflammatory cytokines in the serum and ocular fluids of AMD patients accompanies pathogenesis. Ijima et al. suggested association of IL-18 with dry AMD since patients with dry AMD had higher IL-18 serum levels; this study also demonstrated IL-18-induced RPE cell degeneration in mouse eye [64]. AMD cybrids treated with PU-91 showed reduced expression of *IFNBI* gene which has been demonstrated to reduce human RPE cell proliferation [65]. As shown previously, AMD cybrids have decreased expression of CFH, an inhibitor of complement pathway, consistent with complement activation [66]. Moreover, AMD patients carrying the high-risk allele for CFH showed substantial retinal mtDNA damage [67]. MtDNA dysfunction has been associated with AMD due to increased mtDNA lesions with aging [68]. Significant increase in *CFH* gene expression was observed in PU-91-treated AMD cybrids, suggesting inhibition of complement by PU-91.

Next, we investigated the effects of co-administration of PU-91 with esterase inhibitors (EI) - EI-12 and EI-78, which are being evaluated to augment PU-91

penetration into retina and neural tissue *in vivo*. Administration of PU-91 in humans/animals results in a large first pass effect, converting the vast majority of PU-91 to its primary metabolite, PU-91*, which is *inactive* as a PGC-1 α upregulator. We identified the mechanism of PU-91 to PU-91* conversion and identified two esterase inhibitors namely EI-12 and EI-78, that when co-administered with PU-91 largely block conversion to PU-91*, thereby markedly increasing CNS bioavailability of PU-91. We tested the following co-administration combinations – 1) PU-91 50 μ M + EI-12 5 μ M, 2) PU-91 50 μ M + EI-12 10 μ M, 3) PU-91 50 μ M + EI-12 20 μ M, 4) PU-91 50 μ M + EI-78 2.5 μ M, 5) PU-91 50 μ M + EI-78 5 μ M, 6) PU-91 50 μ M + EI-78 10 μ M, 7) EI-12 20 μ M, 8) EI-78 10 μ M, 9) PU-91 50 μ M, and 10) AMD untreated. No substantive changes either in cell viability or gene expression (*PGC-1 α* , *Caspase-3*, *IL-18*, *VEGF*, and *SOD2*) were observed when treated with a combination of PU-91 + EI-12/EI-78 compared to treatment with PU-91 alone.

In summary, in the *in vitro* AMD RPE transmitochondrial cybrids, the PU-91 drug: 1) regulates the mitochondrial biogenesis pathway, 2) improves mitochondrial function, 3) enhances mitochondrial GFP fluorescence, 4) prevents apoptotic cell death, 5) favorably regulates inflammation and complement, 6) favorably regulates the MDP-coding *MT-RNR2* gene, 7) when co-administered with EI-12/EI-78, does not impact either the viable cell count or gene expression (*PGC-1 α* , *Caspase-3*, *IL-18*, *VEGF*, and *SOD2*) substantially compared to treatment with PU-91 alone. In conclusion, PU-91 rescues AMD RPE cybrids, and potentially could be repurposed as an FDA-approved drug to prevent/treat AMD. Since it improves mitochondrial function and has already been FDA-approved, the candidate therapeutic PU-91 will be an excellent treatment option for AMD. Repositioning of PU-91 will be a smoother transition from lab bench to clinic since the pharmacological profiles of PU-91 have been examined already. Furthermore, because of its extensive safety record it could be potentially prosecuted through NDA more rapidly than a drug-like new chemical entity. Bringing a disease modifying therapeutic to market for the most prevalent form of blindness, AMD, has substantial potential benefit for our aging populations world-wide.

MATERIALS AND METHODS

Human subjects

The University of California Irvine's Institutional review board approved research with human subjects (Approval #2003–3131). All participants provided

informed consent and clinical investigations were performed according to the tenets of Declaration of Helsinki.

Cell culture

Passage 5 AMD ARPE-19 transmitochondrial cybrids were created as described previously [9]. Briefly, these cybrid cells were prepared by polyethylene glycol fusion of mitochondrial DNA-deficient ARPE-19 (*Rho*⁰) cell line with platelets isolated from AMD patients. All cybrids used in this study (Supplementary Table 1) belonged to the 'H' mtDNA haplogroup. Our ARPE-19 cells have been validated using RPE-specific markers such as Bestrophin 1, Cellular retinaldehyde binding protein-1, and Keratin-18. Cybrid status and that the cybrids have acquired their mtDNAs from the donor individuals was confirmed using allelic discrimination, Sanger Sequencing, and Next-Generation Sequencing.

Culture conditions: The base medium for this cybrid cell line is DMEM-F12 Medium (Cat. # 10-092CM, Fisher Scientific, Pittsburgh, PA). DMEM-F12 Medium contains 3.15 g/L D-glucose, 2.5 mM L-glutamine, 15 mM HEPES, 0.5 mM sodium pyruvate, and 1200 mg/L sodium bicarbonate. To make the complete growth medium, fetal bovine serum was added to the base medium to a final concentration of 10 %.

Treatment with PU-91 and esterase inhibitors (EI-12 and EI-78)

PU-91 stock solution of 40 mM concentration was prepared at 15 mg/mL in DMSO. PU-91 stock was diluted in culture media to obtain a working concentration of 50 μ M, which was used for all experiments in this study. PU-91 has been estimated to have clinical exposure in greater than 5 million patient years. 50 μ M was selected as this concentration produces an optimal response in cell culture studies. Stock solutions of 20 mM EI-12 and 10 mM EI-78 were prepared in DMSO and were diluted in culture media to obtain the following working concentrations: EI-12 at 5 μ M, 10 μ M, and 20 μ M; EI-78 at 2.5 μ M, 5 μ M, and 10 μ M.

Mitochondrial copy number

Total DNA was extracted from AMD cybrids followed by quantitative real-time PCR (qRT-PCR). QRT-PCR was performed using TaqMan gene expression assays for *18S* and *MT-ND2* (Cat. # 4331182, Thermo Fisher Scientific) genes and TaqMan gene expression master mix (Cat. # 4369016, Thermo Fisher Scientific). Relative mtDNA copy numbers were determined using delta Cts.

Quantitative Real-Time PCR

RNA extraction, cDNA synthesis, and qRT-PCR analysis were performed as described previously [9]. QuantiTect Primer Assays were used to study the expression of *Caspase-3* gene (Cat. # QT00023947, Qiagen, Germantown, MD), *BAX* gene (Cat. # QT00031192, Qiagen), *HIF1 α* gene (Cat. # QT00083664, Qiagen), *CFH* gene (Cat. # QT00001624, Qiagen), and *SOD2* gene (Cat. # QT01008693, Qiagen). KiCqStart® SYBR® green primers were used to examine the expression of *PGC-1 α* , *NRF-1*, *NRF-2*, *PPAR- α* , *PPAR- γ* , *VEGF*, *IL-18*, and *IFN β* genes (Cat. # kspq12012, Sigma, St. Louis, MO). Specific housekeeper genes used were *HPRT1* (Cat. # QT00059066, Qiagen) for *Caspase-3*, *BAX*, *SOD2*, *VEGF*, *IL-18*, *NRF-1*, *NRF-2*, *PPAR- α* , and *PPAR- γ* ; *HMBS* (Cat. # QT00014462) for *CFH*, *PGC-1 α* and *TUBB* (Cat. # QT00089775, Qiagen) for *HIF-1 α* . TaqMan gene expression master mix (Cat. # 4369016, Life Technologies) and TaqMan gene expression assays were used to examine the expression of the *MT-RNR2* gene (Assay ID: Hs02596860_s1, Life Technologies), for which *GAPDH* (Assay ID: Hs02786624_g1, Life Technologies) was used as a housekeeper gene. Data analysis was performed using $\Delta\Delta$ Ct method. Δ Ct was the difference between the Cts (threshold cycles) of the target gene and Cts of the housekeeper gene (reference gene). Fold change was calculated using the following formula: Fold change = $2^{\Delta\Delta$ Ct}.

Cell viability assay

The numbers of viable cells were measured using the MTT (3-(4,5-dimethylthiazol-2-yl)-2,5-diphenyltetrazolium bromide) assay. Cells were plated in 96-well tissue culture plates, treated with 50 μ M PU-91 followed by addition of MTT. Cells were incubated at 37 °C for 1 h, followed by addition of DMSO. Absorbance was measured at 570 nm and background absorbance measured at 630 nm. Normalized absorbance values were obtained by subtracting background absorbance from signal absorbance. The colorimetric signal obtained was proportional to the cell number.

IncuCyte live-cell imaging

IncuCyte live-cell imaging was performed as described previously [69]. The IncuCyte NucLight Rapid Red Reagent is a cell permeable DNA stain that specifically stains nuclei in live cells and enables real-time quantification of cell proliferation. Addition of this reagent to normal healthy cells does not interfere with cell growth and morphology and provides homogenous staining of nuclei. In the culture medium, this inert stain crosses the cell membrane and has excellent specificity for DNA without the need for a wash step.

The IncuCyte Caspase-3/7 Green Apoptosis Reagent couples the activated Caspase-3/7 recognition motif (DEVD) to a DNA intercalating dye and enables real-time quantification of cells undergoing caspase-3/7 mediated apoptosis. This reagent is an inert, non-fluorescent substrate which when added to culture medium, crosses the cell membrane where it is cleaved by activated caspase-3/7 resulting in the release of the DNA dye and fluorescent staining of the nuclear DNA.

Cells were seeded in 96-well plates at a density of 5,000 – 10,000 cells/well followed by staining with IncuCyte® NucLight Rapid Red (1:500) and Caspase-3/7 Green (1:1000) labeling reagents. Stained cell plates were placed into the IncuCyte® live-cell analysis system and allowed to warm to 37 °C for 30 min prior to scanning. Phase Contrast, Green, and Red channels were selected, 5 images were taken per well with an average scan interval of 2 h until the experiment was complete. Fluorescent objects were quantified using the IncuCyte® integrated analysis software that minimizes background fluorescence.

Mitochondrial membrane potential assay

The JC-1 assay uses a unique cationic dye i.e., 5,5',6,6'-tetrachloro-1,1',3,3'- tetraethylbenzimidazolylcarbocyanine iodide, to detect loss of mitochondrial membrane potential. JC-1 1X reagent was prepared by diluting 100X JC-1 reagent in assay buffer to 1:100 dilutions. AMD cybrids were plated in 24-well tissue culture plates for 24 h followed by treatment with 50 µM PU-91. 1X JC-1 reagent was added to cells and incubated for 15 min at 37 °C. JC-1 reagent in the wells was then replaced with DPBS and fluorescence was measured as follows: Red fluorescence (Live cells): Excitation 550 nm and Emission 600nm; Green fluorescence (Apoptotic cells): Excitation 485 nm and Emission 535 nm. Ratio of Red/Green was used for analysis. Lower ratio corresponded to higher apoptotic/dead cell number.

MitoSOX assay

The fluorogenic MitoSOX Red dye (Cat. # M36008, Invitrogen, Grand Island, NY, USA) is a live-cell permeant reagent that detects mitochondrial superoxide in cells. MitoSOX Red reagent oxidized by superoxide has red fluorescence that can be quantified. AMD cybrids were plated in 24-well tissue culture plates. Stock solution of 5 mM MitoSOX reagent was diluted with HBSS (Hank's balanced salt solution) buffer to obtain a 5 µM working solution. Cells were treated with 5 µM MitoSOX reagent and incubated for 10 min at 37 °C. Cells were then washed with HBSS buffer, and fluorescence was measured at excitation/emission maxima of 510/580 nm.

CellLight mitochondrial GFP staining and confocal microscopy

Staining with CellLight Mitochondrial GFP probe (Cat. # C10600, Thermo Fisher Scientific, MA, USA) and confocal microscopy were performed as described previously [9]. Cells were plated in 4-well tissue culture chamber slides, stained with CellLight mtGFP for 24 h and incubated overnight at 37 °C. The cells were washed with 1X TBS (Tris buffered saline), fixed in paraformaldehyde and mounted in DAPI. Confocal z-stack images were captured using the LSM-700 Confocal microscope (Zeiss, Thornwood, NY, USA). ZEN 2 lite software (Zeiss) was used for fluorescence quantitation.

Statistical analysis

Non-parametric Mann-Whitney test (GraphPad Prism 5.0; GraphPad Software, CA, USA) was used to analyze data between groups and to determine significance. $p \leq 0.05$ was statistically significant.

AUTHOR CONTRIBUTIONS

S.N.: Designed and performed the experiments; acquired, analyzed, and interpreted data; wrote and edited the manuscript. S.R.S and H.F.: Collaborators provided stocks of PU-91 and Esterase inhibitors EI-12 and EI-78; provided technical guidance and reviewed data. M.C.: Initial PU-91 treatment experiment. M.C.K. and H.F.: Reviewed data and the manuscript. M.C.K., H.F., A.B.N., and B.D.K.: Contributed research materials.

CONFLICTS OF INTEREST

S.N.: None; S.R.S.: None; M.C.: None; A.B.N.: None; B.D.K.: *Clinical research*: Alcon, Allergan, Apellis, Genentech, G.S.K. Ophthotech, Regeneron; *Consultant*: Alcon, Allergan, Catalyst, Genentech, Novartis, Ophthotech, Regeneron; *Recipient*: Allergan, Genentech, Novartis, Regeneron. M.C.K.: Allegro; H.F.: None.

FUNDING

This research work was supported by the 2017 Genentech/ARVO AMD Translational Research Fellowship, RPB (Research to Prevent Blindness) pilot research grant, Arnold and Mabel Beckman Foundation, UCI School of Medicine, Discovery Eye Foundation, Guenther Foundation, Beckman Initiative for Macular Research, Polly and Michael Smith, Max Factor Family Foundation, Iris and B. Gerald Cantor Foundation; research was supported in part by an unrestricted grant

from RPB. SN is a recipient of the 2017 Genentech/ARVO AMD Translational Research Fellowship and the 2016 RPB pilot research grant.

REFERENCES

1. Modenese A, Gobba F. Macular degeneration and occupational risk factors: a systematic review. *Int Arch Occup Environ Health*. 2019; 92:1–11. <https://doi.org/10.1007/s00420-018-1355-y> PMID:30191305
2. Villegas VM, Aranguren LA, Kovach JL, Schwartz SG, Flynn HW Jr. Current advances in the treatment of neovascular age-related macular degeneration. *Expert Opin Drug Deliv*. 2017; 14:273–82. <https://doi.org/10.1080/17425247.2016.1213240> PMID:27434329
3. Krishnadev N, Meleth AD, Chew EY. Nutritional supplements for age-related macular degeneration. *Curr Opin Ophthalmol*. 2010; 21:184–89. <https://doi.org/10.1097/ICU.0b013e32833866ee> PMID:20216418
4. Dib B, Lin H, Maidana DE, Tian B, Miller JB, Bouzika P, Miller JW, Vavvas DG. Mitochondrial DNA has a pro-inflammatory role in AMD. *Biochim Biophys Acta*. 2015 (11 Pt A); 1853:2897–906. <https://doi.org/10.1016/j.bbamcr.2015.08.012> PMID:26305120
5. Jarrett SG, Lewin AS, Boulton ME. The importance of mitochondria in age-related and inherited eye disorders. *Ophthalmic Res*. 2010; 44:179–90. <https://doi.org/10.1159/000316480> PMID:20829642
6. Lin H, Xu H, Liang FQ, Liang H, Gupta P, Havey AN, Boulton ME, Godley BF. Mitochondrial DNA damage and repair in RPE associated with aging and age-related macular degeneration. *Invest Ophthalmol Vis Sci*. 2011; 52:3521–29. <https://doi.org/10.1167/iovs.10-6163> PMID:21273542
7. Markovets AM, Fursova AZ, Kolosova NG. Therapeutic action of the mitochondria-targeted antioxidant SkQ1 on retinopathy in OXYS rats linked with improvement of VEGF and PEDF gene expression. *PLoS One*. 2011; 6:e21682. <https://doi.org/10.1371/journal.pone.0021682> PMID:21750722
8. Cousins SW. Role of mitochondrial dysfunction in dry age-related macular degeneration: The site of intracellular metabolism may be a relevant drug target in dry AMD. *Retina Today*. 2015; 83-85.
9. Nashine S, Cohen P, Chwa M, Lu S, Nesburn AB, Kuppermann BD, Kenney MC. Humanin G (HNG) protects age-related macular degeneration (AMD) trans-mitochondrial ARPE-19 cybrids from mitochondrial and cellular damage. *Cell Death Dis*. 2017; 8:e2951. <https://doi.org/10.1038/cddis.2017.348> PMID:28726777
10. Scarpulla RC. Metabolic control of mitochondrial biogenesis through the PGC-1 family regulatory network. *Biochim Biophys Acta*. 2011; 1813:1269–78. <https://doi.org/10.1016/j.bbamcr.2010.09.019> PMID:20933024
11. Lin J, Handschin C, Spiegelman BM. Metabolic control through the PGC-1 family of transcription coactivators. *Cell Metab*. 2005; 1:361–70. <https://doi.org/10.1016/j.cmet.2005.05.004> PMID:16054085
12. Saint-Geniez M, Jiang A, Abend S, Liu L, Sweigard H, Connor KM, Arany Z. PGC-1 α regulates normal and pathological angiogenesis in the retina. *Am J Pathol*. 2013; 182:255–65. <https://doi.org/10.1016/j.ajpath.2012.09.003> PMID:23141926
13. Iacovelli J, Rowe GC, Khadka A, Diaz-Aguilar D, Spencer C, Arany Z, Saint-Geniez M. PGC-1 α Induces Human RPE Oxidative Metabolism and Antioxidant Capacity. *Invest Ophthalmol Vis Sci*. 2016; 57:1038–51. <https://doi.org/10.1167/iovs.15-17758> PMID:26962700
14. Zheng B, Liao Z, Locascio JJ, Lesniak KA, Roderick SS, Watt ML, Eklund AC, Zhang-James Y, Kim PD, Hauser MA, Grünblatt E, Moran LB, Mandel SA, et al, and Global PD Gene Expression (GPEX) Consortium. PGC-1 α , a potential therapeutic target for early intervention in Parkinson’s disease. *Sci Transl Med*. 2010; 2:52ra73. <https://doi.org/10.1126/scitranslmed.3001059> PMID:20926834
15. Handschin C, Spiegelman BM. Peroxisome proliferator-activated receptor gamma coactivator 1 coactivators, energy homeostasis, and metabolism. *Endocr Rev*. 2006; 27:728–35. <https://doi.org/10.1210/er.2006-0037> PMID:17018837
16. Wang B, Abraham N, Gao G, Yang Q. Dysregulation of autophagy and mitochondrial function in Parkinson’s disease. *Transl Neurodegener*. 2016; 5:19. <https://doi.org/10.1186/s40035-016-0065-1> PMID:27822367

17. Róna-Vörös K, Weydt P. The role of PGC-1 α in the pathogenesis of neurodegenerative disorders. *Curr Drug Targets*. 2010; 11:1262–69. <https://doi.org/10.2174/1389450111007011262> PMID:20840068
18. Ventura-Clapier R, Garnier A, Veksler V. Transcriptional control of mitochondrial biogenesis: the central role of PGC-1 α . *Cardiovasc Res*. 2008; 79:208–17. <https://doi.org/10.1093/cvr/cvn098> PMID:18430751
19. Rao J, Li J, Liu Y, Lu P, Sun X, Sugumaran PK, Zhu D. The key role of PGC-1 α in mitochondrial biogenesis and the proliferation of pulmonary artery vascular smooth muscle cells at an early stage of hypoxic exposure. *Mol Cell Biochem*. 2012; 367:9–18. <https://doi.org/10.1007/s11010-012-1313-z> PMID:22527940
20. Corona JC, Duchon MR. PPAR γ and PGC-1 α as therapeutic targets in Parkinson's. *Neurochem Res*. 2015; 40:308–16. <https://doi.org/10.1007/s11064-014-1377-0> PMID:25007880
21. Ciron C, Lengacher S, Dusonchet J, Aebischer P, Schneider BL. Sustained expression of PGC-1 α in the rat nigrostriatal system selectively impairs dopaminergic function. *Hum Mol Genet*. 2012; 21:1861–76. <https://doi.org/10.1093/hmg/ddr618> PMID:22246294
22. McGill JK, Beal MF. PGC-1 α , a new therapeutic target in Huntington's disease? *Cell*. 2006; 127:465–68. <https://doi.org/10.1016/j.cell.2006.10.023> PMID:17081970
23. Johri A, Chandra A, Flint Beal M. PGC-1 α , mitochondrial dysfunction, and Huntington's disease. *Free Radic Biol Med*. 2013; 62:37–46. <https://doi.org/10.1016/j.freeradbiomed.2013.04.016> PMID:23602910
24. Sweeney G, Song J. The association between PGC-1 α and Alzheimer's disease. *Anat Cell Biol*. 2016; 49:1–6. <https://doi.org/10.5115/acb.2016.49.1.1> PMID:27051562
25. Guo X, Dason ES, Zanon-Moreno V, Jiang Q, Nahirnyj A, Chan D, Flanagan JG, Sivak JM. PGC-1 α signaling coordinates susceptibility to metabolic and oxidative injury in the inner retina. *Am J Pathol*. 2014; 184:1017–29. <https://doi.org/10.1016/j.ajpath.2013.12.012> PMID:24508229
26. Kaarniranta K, Kajdaneck J, Morawiec J, Pawlowska E, Blasiak J. PGC-1 α Protects RPE Cells of the Aging Retina against Oxidative Stress-Induced Degeneration through the Regulation of Senescence and Mitochondrial Quality Control. The Significance for AMD Pathogenesis. *Int J Mol Sci*. 2018; 19:E2317. <https://doi.org/10.3390/ijms19082317> PMID:30087287
27. Jornayvaz FR, Shulman GI. Regulation of mitochondrial biogenesis. *Essays Biochem*. 2010; 47:69–84. <https://doi.org/10.1042/bse0470069> PMID:20533901
28. Hertel M, Braun S, Durka S, Alzheimer C, Werner S. Upregulation and activation of the Nrf-1 transcription factor in the lesioned hippocampus. *Eur J Neurosci*. 2002; 15:1707–11. <https://doi.org/10.1046/j.1460-9568.2002.01992.x> PMID:12059978
29. Radhakrishnan SK, Lee CS, Young P, Beskow A, Chan JY, Deshaies RJ. Transcription factor Nrf1 mediates the proteasome recovery pathway after proteasome inhibition in mammalian cells. *Mol Cell*. 2010; 38:17–28. <https://doi.org/10.1016/j.molcel.2010.02.029> PMID:20385086
30. He M, Pan H, Chang RC, So KF, Brecha NC, Pu M. Activation of the Nrf2/HO-1 antioxidant pathway contributes to the protective effects of Lycium barbarum polysaccharides in the rodent retina after ischemia-reperfusion-induced damage. *PLoS One*. 2014; 9:e84800. <https://doi.org/10.1371/journal.pone.0084800> PMID:24400114
31. Felszeghy S, Viiri J, Paterno JJ, Hyttinen JM, Koskela A, Chen M, Leinonen H, Tanila H, Kivinen N, Koistinen A, Toropainen E, Amadio M, Smedowski A, et al. Loss of NRF-2 and PGC-1 α genes leads to retinal pigment epithelium damage resembling dry age-related macular degeneration. *Redox Biol*. 2019; 20:1–12. <https://doi.org/10.1016/j.redox.2018.09.011> PMID:30253279
32. Leung L, Kwong M, Hou S, Lee C, Chan JY. Deficiency of the Nrf1 and Nrf2 transcription factors results in early embryonic lethality and severe oxidative stress. *J Biol Chem*. 2003; 278:48021–29. <https://doi.org/10.1074/jbc.M308439200> PMID:12968018
33. Virbasius CA, Virbasius JV, Scarpulla RC. NRF-1, an activator involved in nuclear-mitochondrial interactions, utilizes a new DNA-binding domain conserved in a family of developmental regulators. *Genes Dev*. 1993; 7:2431–45. <https://doi.org/10.1101/gad.7.12a.2431> PMID:8253388

34. Michalik L, Auwerx J, Berger JP, Chatterjee VK, Glass CK, Gonzalez FJ, Grimaldi PA, Kadowaki T, Lazar MA, O'Rahilly S, Palmer CN, Plutzky J, Reddy JK, et al. International Union of Pharmacology. LXI. Peroxisome proliferator-activated receptors. *Pharmacol Rev.* 2006; 58:726–41. <https://doi.org/10.1124/pr.58.4.5> PMID:17132851
35. Ding L, Cheng R, Hu Y, Takahashi Y, Jenkins AJ, Keech AC, Humphries KM, Gu X, Elliott MH, Xia X, Ma JX. Peroxisome proliferator-activated receptor α protects capillary pericytes in the retina. *Am J Pathol.* 2014; 184:2709–20. <https://doi.org/10.1016/j.ajpath.2014.06.021> PMID:25108226
36. Pearsall EA, Cheng R, Zhou K, Takahashi Y, Matlock HG, Vadvalkar SS, Shin Y, Fredrick TW, Gantner ML, Meng S, Fu Z, Gong Y, Kinter M, et al. PPAR α is essential for retinal lipid metabolism and neuronal survival. *BMC Biol.* 2017; 15:113. <https://doi.org/10.1186/s12915-017-0451-x> PMID:29183319
37. Zhu JM, Hu N. Expression of peroxisome proliferator-activated receptor γ in rat retina during development. *Int J Ophthalmol.* 2015; 8:52–56. <https://doi.org/10.3980/j.issn.2222-3959.2015.01.09> PMID:25709907
38. Carta AR, Frau L, Pisanu A, Wardas J, Spiga S, Carboni E. Rosiglitazone decreases peroxisome proliferator receptor- γ levels in microglia and inhibits TNF- α production: new evidences on neuroprotection in a progressive Parkinson's disease model. *Neuroscience.* 2011; 194:250–61. <https://doi.org/10.1016/j.neuroscience.2011.07.046> PMID:21839812
39. Escribano L, Simón AM, Pérez-Mediavilla A, Salazar-Colocho P, Del Río J, Frechilla D. Rosiglitazone reverses memory decline and hippocampal glucocorticoid receptor down-regulation in an Alzheimer's disease mouse model. *Biochem Biophys Res Commun.* 2009; 379:406–10. <https://doi.org/10.1016/j.bbrc.2008.12.071> PMID:19109927
40. Kiaei M, Kipiani K, Chen J, Calingasan NY, Beal MF. Peroxisome proliferator-activated receptor-gamma agonist extends survival in transgenic mouse model of amyotrophic lateral sclerosis. *Exp Neurol.* 2005; 191:331–36. <https://doi.org/10.1016/j.expneurol.2004.10.007> PMID:15649489
41. Zhu J, Zhang J, Ji M, Gu H, Xu Y, Chen C, Hu N. The role of peroxisome proliferator-activated receptor and effects of its agonist, pioglitazone, on a rat model of optic nerve crush: PPAR γ in retinal neuroprotection. *PLoS One.* 2013; 8:e68935. <https://doi.org/10.1371/journal.pone.0068935> PMID:23874818
42. Usui T, Sugisaki K, Iriyama A, Yokoo S, Yamagami S, Nagai N, Ishida S, Amano S. Inhibition of corneal neovascularization by blocking the angiotensin II type 1 receptor. *Invest Ophthalmol Vis Sci.* 2008; 49:4370–76. <https://doi.org/10.1167/iovs.07-0964> PMID:18829859
43. Uchiyama M, Shimizu A, Masuda Y, Nagasaka S, Fukuda Y, Takahashi H. An ophthalmic solution of a peroxisome proliferator-activated receptor gamma agonist prevents corneal inflammation in a rat alkali burn model. *Mol Vis.* 2013; 19:2135–50. PMID:24194635
44. Sarayba MA, Li L, Tungsiripat T, Liu NH, Sweet PM, Patel AJ, Osann KE, Chittiboyina A, Benson SC, Pershadsingh HA, Chuck RS. Inhibition of corneal neovascularization by a peroxisome proliferator-activated receptor-gamma ligand. *Exp Eye Res.* 2005; 80:435–42. <https://doi.org/10.1016/j.exer.2004.10.009> PMID:15721625
45. Yamanaka O, Miyazaki K, Kitano A, Saika S, Nakajima Y, Ikeda K. Suppression of injury-induced conjunctiva scarring by peroxisome proliferator-activated receptor gamma gene transfer in mice. *Invest Ophthalmol Vis Sci.* 2009; 50:187–93. <https://doi.org/10.1167/iovs.08-2282> PMID:18658087
46. Murata T, He S, Hangai M, Ishibashi T, Xi XP, Kim S, Hsueh WA, Ryan SJ, Law RE, Hinton DR. Peroxisome proliferator-activated receptor-gamma ligands inhibit choroidal neovascularization. *Invest Ophthalmol Vis Sci.* 2000; 41:2309–17. PMID:10892878
47. Wigdal SS, Kirkland RA, Franklin JL, Haak-Frendscho M. Cytochrome c release precedes mitochondrial membrane potential loss in cerebellar granule neuron apoptosis: lack of mitochondrial swelling. *J Neurochem.* 2002; 82:1029–38. <https://doi.org/10.1046/j.1471-4159.2002.01049.x> PMID:12358750
48. Kroemer G, Zamzami N, Susin SA. Mitochondrial control of apoptosis. *Immunol Today.* 1997; 18:44–51. [https://doi.org/10.1016/S0167-5699\(97\)80014-X](https://doi.org/10.1016/S0167-5699(97)80014-X) PMID:9018974
49. Lieven CJ, Vrabec JP, Levin LA. The effects of oxidative stress on mitochondrial transmembrane potential in retinal ganglion cells. *Antioxid Redox Signal.* 2003; 5:641–46.

- <https://doi.org/10.1089/152308603770310310>
PMID:[14580321](https://pubmed.ncbi.nlm.nih.gov/14580321/)
50. Chong CM, Zheng W. Artemisinin protects human retinal pigment epithelial cells from hydrogen peroxide-induced oxidative damage through activation of ERK/CREB signaling. *Redox Biol.* 2016; 9:50–56. <https://doi.org/10.1016/j.redox.2016.06.002> PMID:[27372058](https://pubmed.ncbi.nlm.nih.gov/27372058/)
51. Ellis DZ, Li L, Park Y, He S, Mueller B, Yorio T. Sigma-1 Receptor Regulates Mitochondrial Function in Glucose- and Oxygen-Deprived Retinal Ganglion Cells. *Invest Ophthalmol Vis Sci.* 2017; 58:2755–64. <https://doi.org/10.1167/iovs.16-19199> PMID:[28549090](https://pubmed.ncbi.nlm.nih.gov/28549090/)
52. Seo SJ, Krebs MP, Mao H, Jones K, Connors M, Lewin AS. Pathological consequences of long-term mitochondrial oxidative stress in the mouse retinal pigment epithelium. *Exp Eye Res.* 2012; 101:60–71. <https://doi.org/10.1016/j.exer.2012.05.013> PMID:[22687918](https://pubmed.ncbi.nlm.nih.gov/22687918/)
53. Beckman JS, Estévez AG, Crow JP, Barbeito L. Superoxide dismutase and the death of motoneurons in ALS. *Trends Neurosci.* 2001 (11 Suppl); 24:S15–20. [https://doi.org/10.1016/S0166-2236\(00\)01981-0](https://doi.org/10.1016/S0166-2236(00)01981-0) PMID:[11881740](https://pubmed.ncbi.nlm.nih.gov/11881740/)
54. Estévez AG, Spear N, Manuel SM, Radi R, Henderson CE, Barbeito L, Beckman JS. Nitric oxide and superoxide contribute to motor neuron apoptosis induced by trophic factor deprivation. *J Neurosci.* 1998; 18:923–31. <https://doi.org/10.1523/JNEUROSCI.18-03-00923.1998> PMID:[9437014](https://pubmed.ncbi.nlm.nih.gov/9437014/)
55. Indo HP, Yen HC, Nakanishi I, Matsumoto K, Tamura M, Nagano Y, Matsui H, Gusev O, Cornette R, Okuda T, Minamiyama Y, Ichikawa H, Suenaga S, et al. A mitochondrial superoxide theory for oxidative stress diseases and aging. *J Clin Biochem Nutr.* 2015; 56:1–7. <https://doi.org/10.3164/jcfn.14-42> PMID:[25834301](https://pubmed.ncbi.nlm.nih.gov/25834301/)
56. Justilien V, Pang JJ, Renganathan K, Zhan X, Crabb JW, Kim SR, Sparrow JR, Hauswirth WW, Lewin AS. SOD2 knockdown mouse model of early AMD. *Invest Ophthalmol Vis Sci.* 2007; 48:4407–20. <https://doi.org/10.1167/iovs.07-0432> PMID:[17898259](https://pubmed.ncbi.nlm.nih.gov/17898259/)
57. Kan M, Liu F, Weng X, Ye J, Wang T, Xu M, He L, Liu Y. Association study of newly identified age-related macular degeneration susceptible loci SOD2, MBP, and C8orf42 in Han Chinese population. *Diagn Pathol.* 2014; 9:73. <https://doi.org/10.1186/1746-1596-9-73> PMID:[24667176](https://pubmed.ncbi.nlm.nih.gov/24667176/)
58. Schlingemann RO. Role of growth factors and the wound healing response in age-related macular degeneration. *Graefes Arch Clin Exp Ophthalmol.* 2004; 242:91–101. <https://doi.org/10.1007/s00417-003-0828-0> PMID:[14685874](https://pubmed.ncbi.nlm.nih.gov/14685874/)
59. Martin G, Schlunck G, Hansen LL, Agostini HT. Differential expression of angioregulatory factors in normal and CNV-derived human retinal pigment epithelium. *Graefes Arch Clin Exp Ophthalmol.* 2004; 242:321–26. <https://doi.org/10.1007/s00417-003-0838-y> PMID:[14722782](https://pubmed.ncbi.nlm.nih.gov/14722782/)
60. Telegina DV, Kozhevnikova OS, Kolosova NG. [Molecular mechanisms of cell death in the retina during the development of age-related macular degeneration]. *Adv Gerontol.* 2016; 29:424–32. PMID:[28525689](https://pubmed.ncbi.nlm.nih.gov/28525689/)
61. Adler R, Curcio C, Hicks D, Price D, Wong F. Cell death in age-related macular degeneration. *Mol Vis.* 1999; 5:31. PMID:[10562655](https://pubmed.ncbi.nlm.nih.gov/10562655/)
62. Okada AK, Teranishi K, Lobo F, Isas JM, Xiao J, Yen K, Cohen P, Langen R. The Mitochondrial-Derived Peptides, HumaninS14G and Small Humanin-like Peptide 2, Exhibit Chaperone-like Activity. *Sci Rep.* 2017; 7:7802. <https://doi.org/10.1038/s41598-017-08372-5> PMID:[28798389](https://pubmed.ncbi.nlm.nih.gov/28798389/)
63. Nashine S, Cohen P, Nesburn AB, Kuppermann BD, Kenney MC. Characterizing the protective effects of SHLP2, a mitochondrial-derived peptide, in macular degeneration. *Sci Rep.* 2018; 8:15175. <https://doi.org/10.1038/s41598-018-33290-5> PMID:[30310092](https://pubmed.ncbi.nlm.nih.gov/30310092/)
64. Ijima R, Kaneko H, Ye F, Nagasaka Y, Takayama K, Kataoka K, Kachi S, Iwase T, Terasaki H. Interleukin-18 induces retinal pigment epithelium degeneration in mice. *Invest Ophthalmol Vis Sci.* 2014; 55:6673–78. <https://doi.org/10.1167/iovs.14-15367> PMID:[25237159](https://pubmed.ncbi.nlm.nih.gov/25237159/)
65. Qiao H, Sakamoto T, Hinton DR, Gopalakrishna R, Ishibashi T, Ryan SJ, Inomata H. Interferon beta affects retinal pigment epithelial cell proliferation via protein kinase C pathways. *Ophthalmologica.* 2001; 215:401–07. <https://doi.org/10.1159/000050897> PMID:[11741104](https://pubmed.ncbi.nlm.nih.gov/11741104/)
66. Nashine S, Chwa M, Kazemian M, Thaker K, Lu S, Nesburn A, Kuppermann BD, Kenney MC. Differential Expression of Complement Markers in Normal and AMD Transmitochondrial Cybrids. *PLoS One.* 2016; 11:e0159828. <https://doi.org/10.1371/journal.pone.0159828> PMID:[27486856](https://pubmed.ncbi.nlm.nih.gov/27486856/)

67. Ferrington DA, Kapphahn RJ, Leary MM, Atilano SR, Terluk MR, Karunadharma P, Chen GK, Ratnapriya R, Swaroop A, Montezuma SR, Kenney MC. Increased retinal mtDNA damage in the CFH variant associated with age-related macular degeneration. *Exp Eye Res.* 2016; 145:269–77. <https://doi.org/10.1016/j.exer.2016.01.018> PMID:[26854823](https://pubmed.ncbi.nlm.nih.gov/26854823/)
68. Karunadharma PP, Nordgaard CL, Olsen TW, Ferrington DA. Mitochondrial DNA damage as a potential mechanism for age-related macular degeneration. *Invest Ophthalmol Vis Sci.* 2010; 51:5470–79. <https://doi.org/10.1167/iovs.10-5429> PMID:[20505194](https://pubmed.ncbi.nlm.nih.gov/20505194/)
69. Nashine S, Kanodia R, Nesburn AB, Soman G, Kuppermann BD, Kenney MC. Nutraceutical effects of *Emblicaofficinalis* in age-related macular degeneration. *Aging (Albany NY).* 2019; 11:1177–88. <https://doi.org/10.18632/aging.101820> PMID:[30792375](https://pubmed.ncbi.nlm.nih.gov/30792375/)

SUPPLEMENTARY MATERIALS

Supplementary Tables

Supplementary Table 1. AMD Patient/ Cybrid cell lines' Patient Information.

CYBRID NUMBER	CYBRID TYPE	AGE	GENDER	RACE	HAPLOGROUP
1	AMD	81	Female	White	H
2	AMD	82	Female	White	H
3	AMD	86	Female	White	H
4	AMD	84	Female	White	H
5	AMD	75	Female	White	H
6	AMD	76	Male	White	H
7	AMD	83	Male	White	H
8	AMD	74	Male	White	H
9	AMD	76	Male	White	H
10	AMD	83	Male	White	H

This table provides information about the AMD patients and AMD cybrid cell lines.

Supplementary Table 2. Effects of PU-91 + EI-12 on cell viability.

Effect of EI-12 on cell viability 48 hr Time point	AMD UN	AMD Only PU-91-treated	AMD PU-91 + EI-12 5 μ M	AMD PU-91 + EI-12 10 μ M	AMD PU-91 + EI-12 20 μ M	AMD Only EI-12 20 μ M
Mean \pm SEM	1 \pm 0.07	1.33 \pm 0.09	1.215 \pm 0.09027	1.176 \pm 0.07125	1.253 \pm 0.07453	1.037 \pm 0.1413
Effect of EI-12 on cell viability 72 hr Time point	AMD UN	AMD Only PU-91-treated	AMD PU-91 + EI-12 5 μ M	AMD PU-91 + EI-12 10 μ M	AMD PU-91 + EI-12 20 μ M	AMD Only EI-12 20 μ M
Mean \pm SEM	1 \pm 0.09	1.37 \pm 0.07	1.335 \pm 0.08792	1.361 \pm 0.07264	1.452 \pm 0.06857	1.259 \pm 0.1060

This table shows the additive effects of PU-91 + EI-12 on cell viability. All values are normalized to 1 and are presented as Mean \pm SEM.

Supplementary Table 3. Effects of PU-91 + EI-78 on cell viability.

Effect of EI-78 on cell viability 48 hr Time point	AMD UN	AMD Only PU-91-treated	AMD PU-91 + EI-78 2.5 µM	AMD PU-91 + EI-78 5 µM	AMD PU-91 + EI-78 10 µM	AMD Only EI-78 10 µM
Mean ± SEM	1 ± 0.07	1.33 ± 0.09	1.05 ± 0.09	1.10 ± 0.06	0.91 ± 0.19	0.95 ± 0.11
Effect of EI-78 on cell viability 72 hr Time point	AMD UN	AMD Only PU-91-treated	AMD PU-91 + EI-78 2.5 µM	AMD PU-91 + EI-78 5 µM	AMD PU-91 + EI-78 10 µM	AMD Only EI-78 10 µM
Mean ± SEM	1 ± 0.09	1.37 ± 0.07	1.19 ± 0.04	1.17 ± 0.08	1.21 ± 0.09	0.99 ± 0.09

This table shows the additive effects of PU-91 + EI-78 on cell viability. All values are normalized to 1 and are presented as Mean ± SEM.

Supplementary Table 4. Effects of PU-91 + EI-12 on gene expression.

Effect of EI-12 on gene expression		AMD UN	AMD Only PU-91-treated	AMD PU-91 + EI-12 5 µM	AMD PU-91 + EI-12 10 µM	AMD PU-91 + EI-12 20 µM	AMD Only EI-12 20 µM
<i>PGC-1α</i>	Mean ± SEM	1 ± 0.02	3.48 ± 0.45	3.16 ± 0.71	3.63 ± 0.69	2.15 ± 0.24	1.82 ± 0.57
<i>Caspase-3</i>	Mean ± SEM	1 ± 0.0002	0.65 ± 0.04	0.78 ± 0.06	0.73 ± 0.06	0.66 ± 0.09	0.74 ± 0.045
<i>IL-18</i>	Mean ± SEM	1 ± 0.004	0.49 ± 0.09	0.82 ± 0.09	0.88 ± 0.12	0.77 ± 0.11	0.78 ± 0.13
<i>VEGF</i>	Mean ± SEM	1 ± 0.002	0.45 ± 0.17	0.40 ± 0.09	0.37 ± 0.08	0.37 ± 0.12	0.42 ± 0.16
<i>SOD2</i>	Mean ± SEM	1 ± 0.06	2.81 ± 0.11	2.05 ± 0.83	1.57 ± 0.53	1.51 ± 0.57	0.88 ± 0.22

This table shows the additive effects of PU-91 + EI-12 on gene expression. All values are normalized to 1 and are presented as Mean ± SEM.

Supplementary Table 5. Effects of PU-91 + EI-78 on gene expression.

Effect of EI-78 on gene expression		AMD UN	AMD Only PU-91-treated	AMD PU-91 + EI-78 2.5 μM	AMD PU-91 + EI-78 5 μM	AMD PU-91 + EI-78 10 μM	AMD Only EI-78 10 μM
<i>PGC-1α</i>	Mean ± SEM	1 ± 0.02	3.48 ± 0.45	2.89 ± 0.41	2.09 ± 0.37	2.26 ± 0.64	1.40 ± 0.48
<i>Caspase-3</i>	Mean ± SEM	1 ± 0.0002	0.65 ± 0.04	0.74 ± 0.019	0.85 ± 0.12	0.66 ± 0.05	0.86 ± 0.06
<i>IL-18</i>	Mean ± SEM	1 ± 0.004	0.49 ± 0.09	0.65 ± 0.13	0.55 ± 0.06	0.39 ± 0.08	0.71 ± 0.25
<i>VEGF</i>	Mean ± SEM	1 ± 0.002	0.45 ± 0.17	0.53 ± 0.21	0.47 ± 0.14	0.51 ± 0.18	0.52 ± 0.19
<i>SOD2</i>	Mean ± SEM	1 ± 0.06	2.81 ± 0.11	1.99 ± 0.59	1.62 ± 0.57	1.82 ± 0.69	1.71 ± 0.46

This table shows the additive effects of PU-91 + EI-78 on gene expression. All values are normalized to 1 and are presented as Mean ± SEM.

HMGB1 and Caveolin-1 related to RPE cell senescence in age-related macular degeneration

Shuo Sun¹, Bincui Cai¹, Yao Li^{2,3}, Wenqi Su¹, Xuzheng Zhao⁴, Boteng Gong¹, Zhiqing Li¹, Xiaomin Zhang¹, Yalin Wu⁵, Chao Chen⁵, Stephen H. Tsang^{2,3}, Jin Yang¹, Xiaorong Li¹

¹Tianjin Key Laboratory of Retinal Functions and Diseases, Eye Institute and School of Optometry, Tianjin Medical University Eye Hospital, Tianjin, People's Republic of China

²Edward S. Harkness Eye Institute, New York-Presbyterian Hospital, New York, NY 10032, USA

³Department of Ophthalmology, Columbia University, New York, NY 10027, USA

⁴Tangshan Eye Hospital, Tangshan, People's Republic of China

⁵Fujian Provincial Key Laboratory of Ophthalmology and Visual Science, Eye Institute of Xiamen University, College of Medicine, Xiamen University, Xiamen City, People's Republic of China

Correspondence to: Jin Yang, Xiaorong Li; email: yangjinchina324@gmail.com, lixiaorong@tmu.edu.cn

Keywords: A2E, HMGB1, Caveolin-1, RPE cell senescence, AMD

Received: July 30, 2018

Accepted: June 17, 2019

Published: July 7, 2019

Copyright: Sun et al. This is an open-access article distributed under the terms of the Creative Commons Attribution License (CC BY 3.0), which permits unrestricted use, distribution, and reproduction in any medium, provided the original author and source are credited.

ABSTRACT

Accumulation of lipofuscin in the retinal pigment epithelium (RPE) is considered a major cause of RPE dysfunction and senescence in age-related macular degeneration (AMD), and *N*-retinylidene-*N*-retinyl-ethanolamine (A2E) is the main fluorophore identified in lipofuscin from aged human eyes. Here, human-induced pluripotent stem cell (iPSC)-RPE was generated from healthy individuals to reveal proteomic changes associated with A2E-related RPE cell senescence. A novel RPE cell senescence-related protein, high-mobility group box 1 (HMGB1), was identified based on proteomic mass spectrometry measurements on iPSC-RPE with A2E treatment. Furthermore, HMGB1 upregulated Caveolin-1, which also was related RPE cell senescence. To investigate whether changes in HMGB1 and Caveolin-1 expression under A2E exposure contribute to RPE cell senescence, human ARPE-19 cells were stimulated with A2E; expression of HMGB1, Caveolin-1, tight junction proteins and senescent phenotypes were verified. HMGB1 inhibition alleviated A2E induced cell senescence. Migration of RPE cells was evaluated. Notably, A2E less than or equal to 10 μ M induced both HMGB1 and Caveolin-1 protein upregulation and HMGB1 translocation, while Caveolin-1 expression was downregulated when there was more than 10 μ M A2E. Our data indicate that A2E-induced upregulation of HMGB1, Caveolin-1 and HMGB1 release may relate to RPE cell senescence and play a role in the pathogenesis of AMD.

INTRODUCTION

Age-related macular degeneration (AMD) is the leading cause of vision loss in older adults worldwide [1]. AMD can be classified into early-stage or late-stage AMD. The latter is characterized by neovascularization (wet AMD), geographic atrophy (dry AMD), or both [2]. Conversely, early-stage AMD is characterized a limited amount of drusen, which is mainly caused by lipid and protein accumulation and thought to contribute to astro-

phic changes. As the disease progresses, neovascular changes or geographic atrophy involving the macular area can be present in patients for years. Dry AMD manifests as well-demarcated areas, providing direct visualization of the underlying choroidal vessels due to atrophy of photoreceptor and retinal pigment epithelium (RPE) cells; wet AMD is characterized by the development of choroidal neo-vascularization (CNV) [3]. Although anti-vascular endothelial growth factor (anti-VEGF) has become the main treatment approach

for wet AMD, there is a lack of consensus regarding the treatment of dry AMD. Most importantly, an appropriate disease model that can simulate the occurrence and development of AMD must be chosen [4]. Therefore, we explored the relationship between dry AMD and RPE dysfunction and senescence using proteomic mass spectrometry to examine differential expression in induced pluripotent stem cell (iPSC)-derived RPE cell lines with and without A2E treatment [5]. We have previously demonstrated that the iPSC-derived RPE is phenotypically and functionally similar to the native RPE [6]. In addition, the young status of iPSC-RPE may provide an excellent means for observing changes in protein expression during the process of RPE cell aging [7].

As a by-product of the visual cycle, *N*-retinylidene-*N*-retinylethanolamine (A2E) and its isomers are formed by the reaction of two trans-retinal molecules with phosphatidyl-ethanolamine. A2E is the major fluorophore identified in lipofuscin from aged human eyes, and it has been widely studied [8]. As a hallmark of aging, A2E continuously accumulates in the RPE [9]. The lipofuscin constituents consist of various molecules that have photoreactive properties and undergo photo-oxidation [10]. A2E photo-oxidation products can cause oxidative stress, membrane permeation, telomere dysfunction and accelerated RPE senescence [11]. Although A2E is clearly present in the retina, there are rather different opinions regarding its distribution. Ablonczy et al. showed that levels of A2E decreased from the periphery to the centre region in aging tissue of macaques and humans [12] but A2E was localized mainly in the centre region of young mouse retina. However, the distribution of A2E increases across the entire RPE with age [13]. Thus, the relationship between A2E and AMD is worthy of further study.

Our aim in the present study was to identify protein changes related to A2E in aging iPSC-RPE cells and to verify and explore the mechanism of these altered proteins in human ARPE-19 cells.

RESULTS

Proteomic mass spectrometry detection of differential expression of proteins, highlighting HMGB1 in iPSC-RPE cells with and without A2E treatment

We used proteomic mass spectrometry to explore differential expression of proteins in iPSC-RPE cells after A2E treatment. The method of iPSC-RPE cell culture was described previously [6]. For liquid chromatography with tandem mass spectrometry (LC-MS/MS) analysis, we extracted proteins from iPSC-derived RPE

cells with and without A2E treatment, with three biological replicates prepared from three separate cultures (Flow chart, Figure 1A). Representative proteomic MS-based analyses of proteins from A2E-treated cells versus untreated cells are depicted in a volcano plot in Figure 1B, where the $-\log_{10}(P \text{ value})$ was plotted against the $\log_2(\text{fold change A2E Treatment/Control})$. In the figure, black, green, and red splashes indicate proteins without significant differential expression, significantly downregulated proteins, and significantly upregulated proteins, respectively. We arranged the ratio of A2E treatment/control expression from large to small and found that the high-mobility group box 1 (HMGB1), which is marked with a red arrowhead, was upregulated 76-fold in the A2E treatment group compared to the control ($p \text{ value}=0.00578$, Table 1). Thus, based on MS results, HMGB1 was upregulated in iPSC-RPE cells by A2E treatment.

Upregulation and translocation of HMGB1 in ARPE-19 cells after A2E treatment

To determine the optimized concentration of A2E causing upregulation of HMGB1 without undue influence on cell viability, ARPE-19 cells were incubated with increasing concentrations of A2E with or without blue light (10min) for 48 h. After 24 h in fresh medium, cell viability was examined using the 3-(4, 5-dimethylthiazol-2-yl)-2,5-diphenyl tetrazolium bromide (MTT) assay. The viability of ARPE-19 cells decreased with increasing A2E concentration, especially at 25 μM A2E and 50 μM A2E with blue light (Figure 2A). Therefore, we used A2E at a concentration of 10 μM in this study to mimic aged ARPE-19 cells with lipofuscin accumulation. Western blotting of cells incubated with 10 μM A2E with blue light for 48 h showed higher levels of HMGB1 than that the control and blue light alone (Figure 2C). Moreover, fluorescein diacetate (FDA)/propidium iodide (PI) staining showed that most of the ARPE-19 cells were alive (Figure 2B), confirming that A2E can increase expression of HMGB1 at an early stage and low dose (* indicates a $p \text{ value} < 0.05$, ** indicates a $p \text{ value} < 0.01$, *** indicates a $p \text{ value} < 0.001$). In the presence of A2E, a large amount of HMGB1 was translocated from the nucleus to the cytoplasm (Figure 2D). The results confirm that A2E can induce upregulation and translocation of HMGB1.

HMGB1 upregulation and release increased the expression of Caveolin-1

The potential role of HMGB1 upregulation and translocation in ARPE-19 cells was then investigated. Cell senescence can be caused by various factors, including DNA damage and oxidative stress. It has been

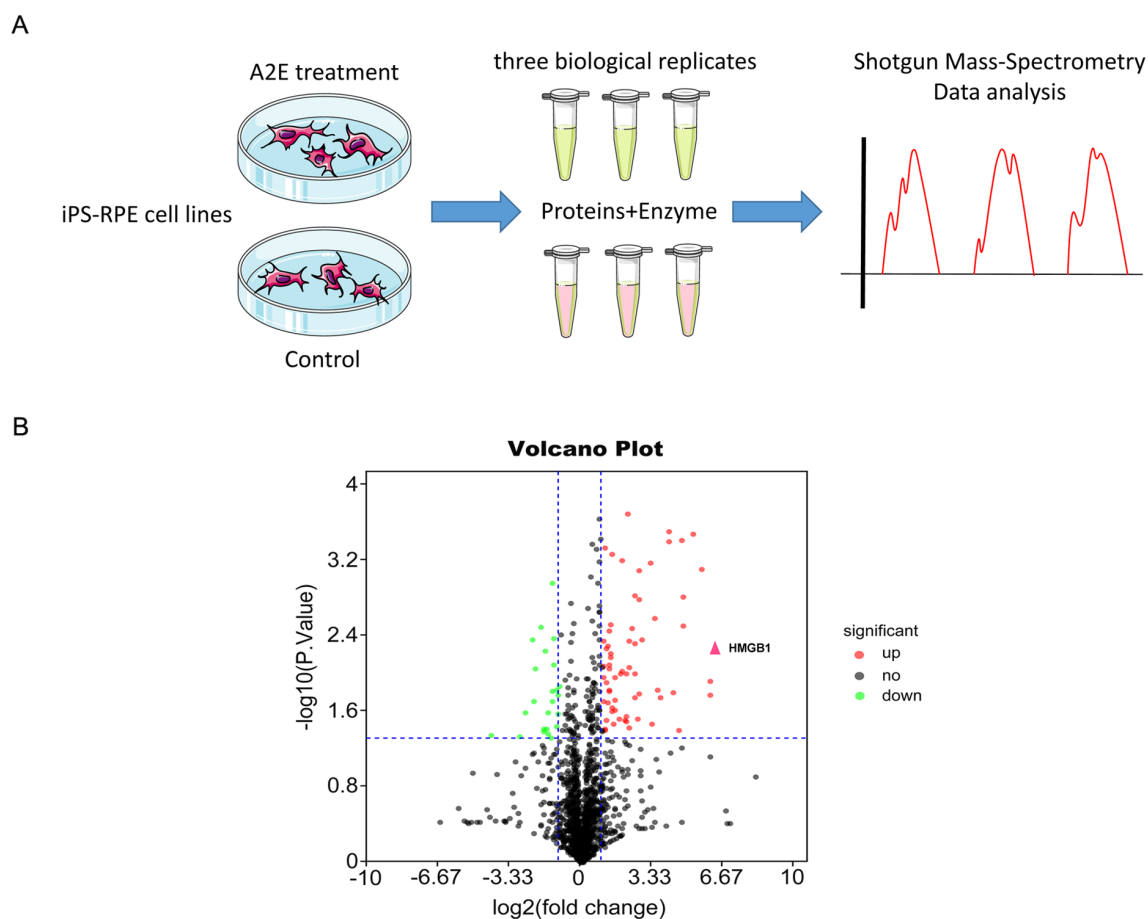


Figure 1. Proteomic mass spectrometry-based measurement of differential expression of HMGB1. (A) The flow chart of shotgun mass spectrometry. (B) Volcano plot illustrating significant differential abundant proteins based on quantitative analysis. The $-\log_{10}$ (P value) was plotted against \log_2 (fold change A2E treatment/Control). Proteins were significantly upregulated (red dots) or downregulated (green dots) between the A2E treatment and control. The red arrowhead indicates HMGB1.

reported that Caveolin-1 plays a major role in cell senescence and that HMGB1 increases its expression [14, 15]. The interaction between HMGB1 with Caveolin-1 was assessed using the Search Tool for the Retrieval of Interacting Genes/Proteins (STRING) database (Figure 3B). Thus, RPE cells were infected with HMGB1 overexpression lentivirus. LV-empty-vector (NC) and stimulated with recombinant HMGB1. Then, Real-time Quantitative polymerase chain reaction (qPCR), western blot and immunofluorescence analyses indicated that Caveolin-1 expression was increased by HMGB1 in ARPE-19 cells (Figure 3A, C). Furthermore, lentiviral infection of ARPE-19 cells using shHMGB1 and sh-NC (scramble shRNA) constructs was performed. Effective knock-down of HMGB1 and decrease of Caveolin-1 in ARPE-19 cells transfected with shHMGB1 was demonstrated.

Meanwhile, shHMGB1-expressing cells indicated a sig-

nificant reduction in Toll-like receptor2 (TLR2) and Toll-like receptor4 (TLR4) protein expression but not in Receptor of Advanced Glycation Endproducts (RAGE) which three proteins were reported as potential connection with HMGB1 and Caveolin-1 compared to sh-NC (scramble shRNA) cells. (Figure 3D, * indicates a p value < 0.05, ** indicates a p value < 0.01, *** indicates a p value < 0.001). Together, these results showed that HMGB1 regulates the expression of Caveolin-1 via TLR2 and TLR4.

Caveolin-1 upregulation induced ARPE-19 cell senescence

We investigated the effect of stable Caveolin-1 overexpression on ARPE-19 cell senescence. ARPE-19 cells were infected with lentivirus-Caveolin-1, and β -galactosidase staining showed that Caveolin-1-overexpressing RPE cells were more aged compared with the negative control (LV-empty-vector) RPE cells (Figure 4E).

Table 1. The data set was arranged by the ratio of A2E treatment/control, and HMGB1 was found to be upregulated more than 76-fold in the A2E-treated group.

Uniprot#	Gene Names	Ratio A2E treatment/ control	P-Value A2E treatment/control
P09429	HMGB1	76.95828543	0.0057787
Q06210	GFPT1	65.83452999	0.0167382
G5E9P1	ITPR1	64.99257944	0.0757587
Q7Z4H8	KDELC2	64.17736137	0.0116703
P20591	MX1	50.71424385	0.000773586
P04179	SOD2	37.3876135	0.000328524
H9KVA0	TYMP	27.61593536	0.00153441
F5H090	UNC13C	26.74494289	0.00305275
H3BPK7	AARS	26.39582865	0.000375675
P51911	CNN1	26.24793326	0.0604881
Q8IYM0	FAM186B	25.5978875	0.373977
P21281	ATP6V1B2	23.45846962	0.0387506
Q562R1	ACTBL2	19.38697164	0.0155401
P42785	PRCP PCP	17.65006048	0.0672487
Q15349	RPS6KA2	17.34576845	0.000390284
H0Y9R5	SNX25	17.23254402	0.000304062
Q14240	EIF4A2	15.7087038	0.402011
J3KSW2	POLI	13.22929896	0.0174629
E7EX17	EIF4B	12.53696128	0.106437
P62310	LSM3	11.81044422	0.0147819
Q03135	CAV1	0.810928595	0.289982
P42224	STAT1	4.42761394	0.000198283
P05362	ICAM1	2.45723684	0.00874002

Inhibition of cell motility by Caveolin-1 upregulation in ARPE-19 cells

Since cell senescence may result in reduced migration and invasion, we further investigated whether Caveolin-1 affects RPE cell migration and invasion capacities using wound-healing and Transwell invasion assays. The results showed that Caveolin-1 overexpression significantly reduced migration (Figure 4Fi and Gi) and invasion (Figure 4Fii and Gii). In addition, expression of Zo-1 and β -catenin was increased by Caveolin-1 upregulation, according to quantitative real-time PCR, western blot and immunofluorescence analysis (Figure 4A, B, C, D). In contrast, the mRNA levels of other tight junction proteins, such as Claudin-1, Claudin-3, Occludin, and N-cadherin, did not change (Figure 4C,* indicates a p value < 0.05, ** indicates a p value < 0.01, *** indicates a p value < 0.001).

Relationships among A2E induced cell senescence, HMGB1 and Caveolin-1

Because HMGB1 increases expression of Caveolin-1, we further explored the relationship among A2E, HMGB1 and Caveolin-1. We assessed HMGB1 and Caveolin-1 expression in ARPE-19 cells by western blot and found that A2E increased the levels of both, compared with unstimulated cells. Interestingly, A2E enhanced expression of Caveolin-1, though Caveolin-1 levels did not increase with higher concentrations of A2E. The tendency of Caveolin-1 expression first increased and then decreased at more than 10 μ M A2E (Figure 5A, * indicates a p value < 0.05, ** indicates a p value < 0.01, *** indicates a p value < 0.001). Furthermore, although the tendency of Caveolin-1 expression first increased and then decreased at more than 10 μ M A2E, the senescence of cells was still in process (Fi-

Figure 5B). Since we have found A2E could induce translocation of HMGB1, we collected the supernatants from ARPE-19 cells stimulated by different concentrations of A2E to investigate the level of HMGB1 secretion into the extracellular space. Enzyme Linked Immunosorbent Assay (ELISA) revealed the secretion of HMGB1 was increased along with increasing concentrations of A2E (Figure 5C). These data showed that A2E increases HMGB1 and Caveolin-1 expression, with links to cell senescence, but the expression of Caveolin-1 was changing dynamically based on different A2E concentration.

Glycyrrhizic acid inhibited the release of HMGB1 alleviated A2E induced cell senescence

To further confirm the role of ARPE cell-secreted HMGB1 in cell senescence, we used a HMGB1 inhibitor, glycyrrhizic acid (GA), which binds directly to HMGB1, to block HMGB1 released into the extracellular space and inhibit its extracellular cytokine activities [16] (Figure 6E). MTT assay was used to identify candidate concentrations of GA that were not cytotoxic to ARPE-19. Shown in Figure 6A, these data revealed that glycyrrhizic acid showed no toxicity at

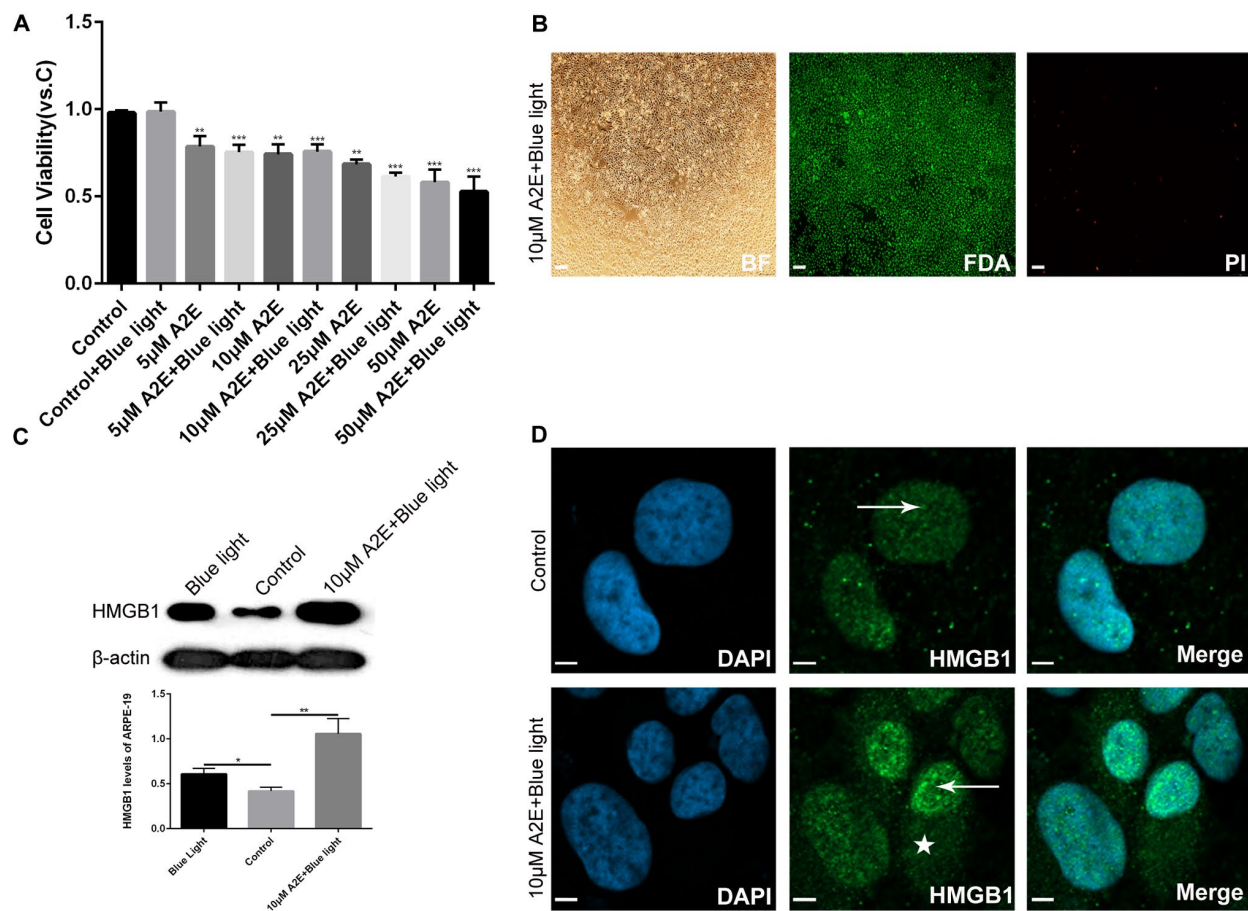


Figure 2. Experimental validation that blue light exposure of A2E-treated ARPE-19 cells induces HMGB1 upregulation and translocation. (A) An MTT assay was performed on RPE cells treated with different concentrations of A2E with or without blue light photosensitization. Data are presented as means \pm SD; * indicates a p value $<$ 0.05, ** indicates a p value $<$ 0.01, *** indicates a p value $<$ 0.001, compared to the control, $n=3$. (B) FDA/PI staining of RPE cells after *in vitro* culture for 48 h with 10 μ M A2E + blue light (10 min). Most living RPE cells were stained green by fluorescein diacetate (FDA); a few dead cells were stained red by propidium iodide (PI). (C) Western blot analyses showed that HMGB1 protein expression was higher in 10 μ M A2E + blue light-treated cells compared to the control and also higher in the blue light treatment, as quantified by densitometry; the results are expressed as a ratio with β -actin. Data are presented as means \pm SD; * indicates a p value $<$ 0.05, ** indicates a p value $<$ 0.01, $n=3$. (D) HMGB1 localization in RPE cells was assessed by confocal microscopy after 10 μ M A2E + blue light treatment. HMGB1 moved from the nucleus (arrow) to the cytoplasm (star) after 10 μ M A2E + blue light treatment. Nuclei are labelled with DAPI (blue); HMGB1 is stained green.

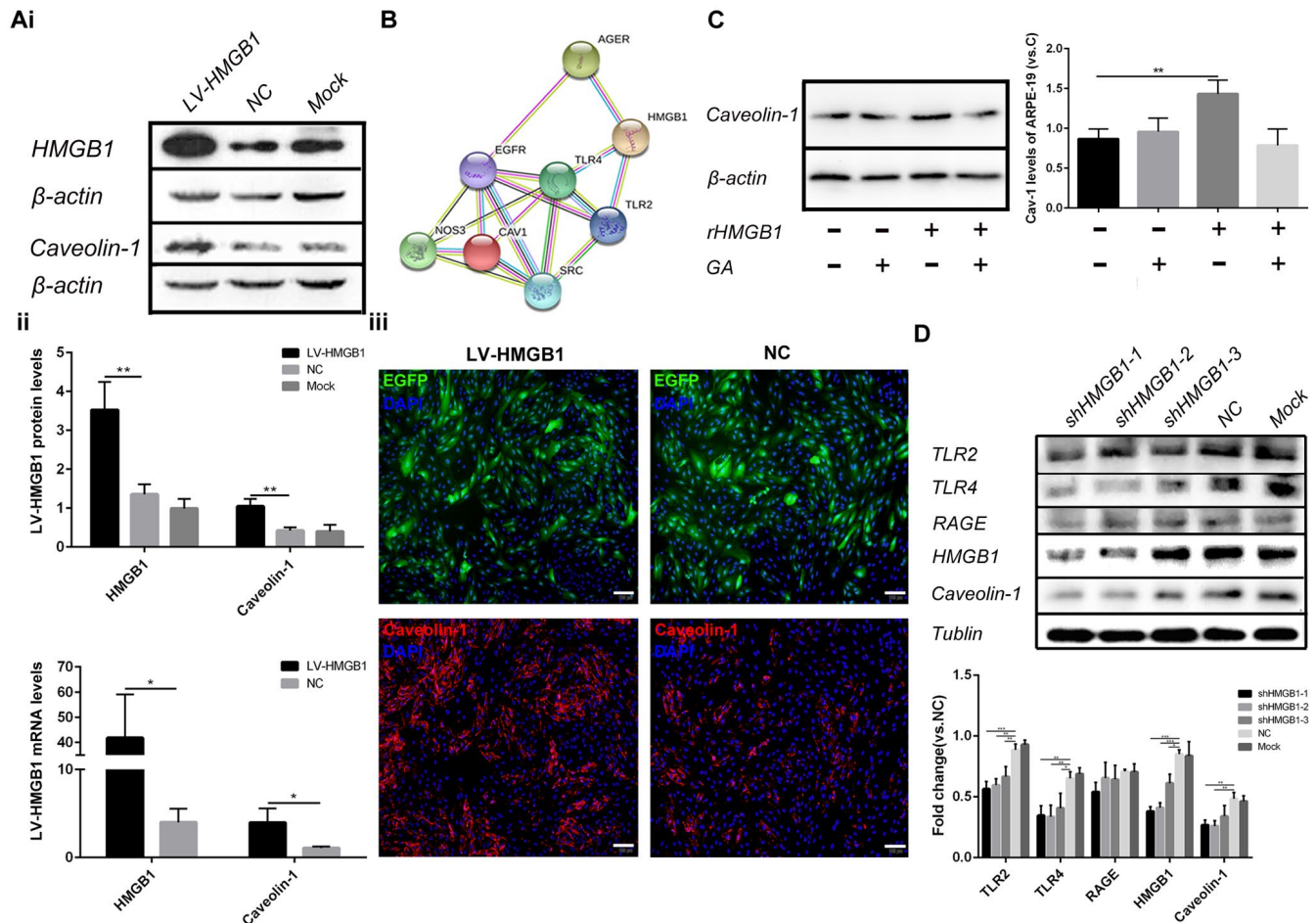


Figure 3. HMGB1 upregulation and release increase the expression of Caveolin-1. (A) (i) Western blot analyses showed that overexpression of HMGB1 upregulated Caveolin-1; β -actin was used as the loading control; Western blot results were quantified by densitometry, and the results are expressed as a ratio with β -actin. (ii) qPCR analyses showed that overexpression of HMGB1 upregulated Caveolin-1. Data are presented as means \pm SD; * indicates a p value < 0.05 , ** indicates a p value < 0.01 , $n=3$. (iii) Expression of EGFP and Caveolin-1 was assessed by immunofluorescence in HMGB1-overexpressing RPE cells and negative-control RPE cells. (B) Protein interaction between HMGB1 and Caveolin-1 was revealed by the STRING version 9.1 program. (C) Relative Caveolin-1 expression in RPE cell incubated with normal medium, $1\mu\text{g/ml}$ rHMGB1, $100\mu\text{M}$ GA, or $1\mu\text{g/ml}$ rHMGB1+ $100\mu\text{M}$ GA, Data are presented as means \pm SD; * indicates a p value < 0.05 , ** indicates a p value < 0.01 , $n=3$. (D) Western blot analyses showed that knock-down of HMGB1 downregulated Caveolin-1; Tubulin was used as the loading control, western blot results were quantified by densitometry, and the results are expressed as a ratio with Tubulin. Data are presented as means \pm SD; * indicates a p value < 0.05 , ** indicates a p value < 0.01 , $n=3$.

various concentrations from $5\mu\text{M}$ to $200\mu\text{M}$. Then we explored the effect of GA on ARPE-19 cells treated with A2E and blue light, and $50\mu\text{M}$ A2E induced ARPE-19 cell senescence used as a positive control. The results showed that GA blocked the release of HMGB1 into the extracellular space and A2E induced cell senescence was mitigated correspondingly. (Figure 6B, C, D) These results indicated that blocking HMGB1 by directly inhibiting its extracellular cytokine activities could alleviate A2E induced cell senescence.

DISCUSSION

Cellular senescence is a process during which physiological function and proliferation and differentiation capacities decline gradually [17]. It is also a state of permanent cellular division arrest that only concerns only mitotic cells. Although RPE cells are quiescent in the retina, they can undergo oxidative stress-induced senescence. Therefore, cellular senescence can be considered as an important molecular pathway of AMD pathology [18]. The reason we chose RPE cells differen-

tiated from iPSCs is because their young age allows for observing the process of ageing under certain stimulation. This approach has been applied to several studies on age-related diseases, including Parkinson's disease and Alzheimer's disease [19, 20]. Although it has been reported that A2E accumulation causes RPE cell senescence and dysfunction, including complement factor activation and oxidative stress [21], there is thus far no unanimous conclusion regarding the specific mechanism.

HMGB1 organizes DNA, regulates transcription and is a damage-associated molecular pattern molecule that is related to oxidative stress and downstream apoptosis or survival [22]. Under pathological conditions such as hypoxia, cell death, atherosclerosis and ischaemia-induced angiogenesis [23,24,14] and in senescent cells, HMGB1 is upregulated and translocated from the nucleus to the cytoplasm and extracellular space. Indeed, HMGB1 is deemed a more reliable and accurate

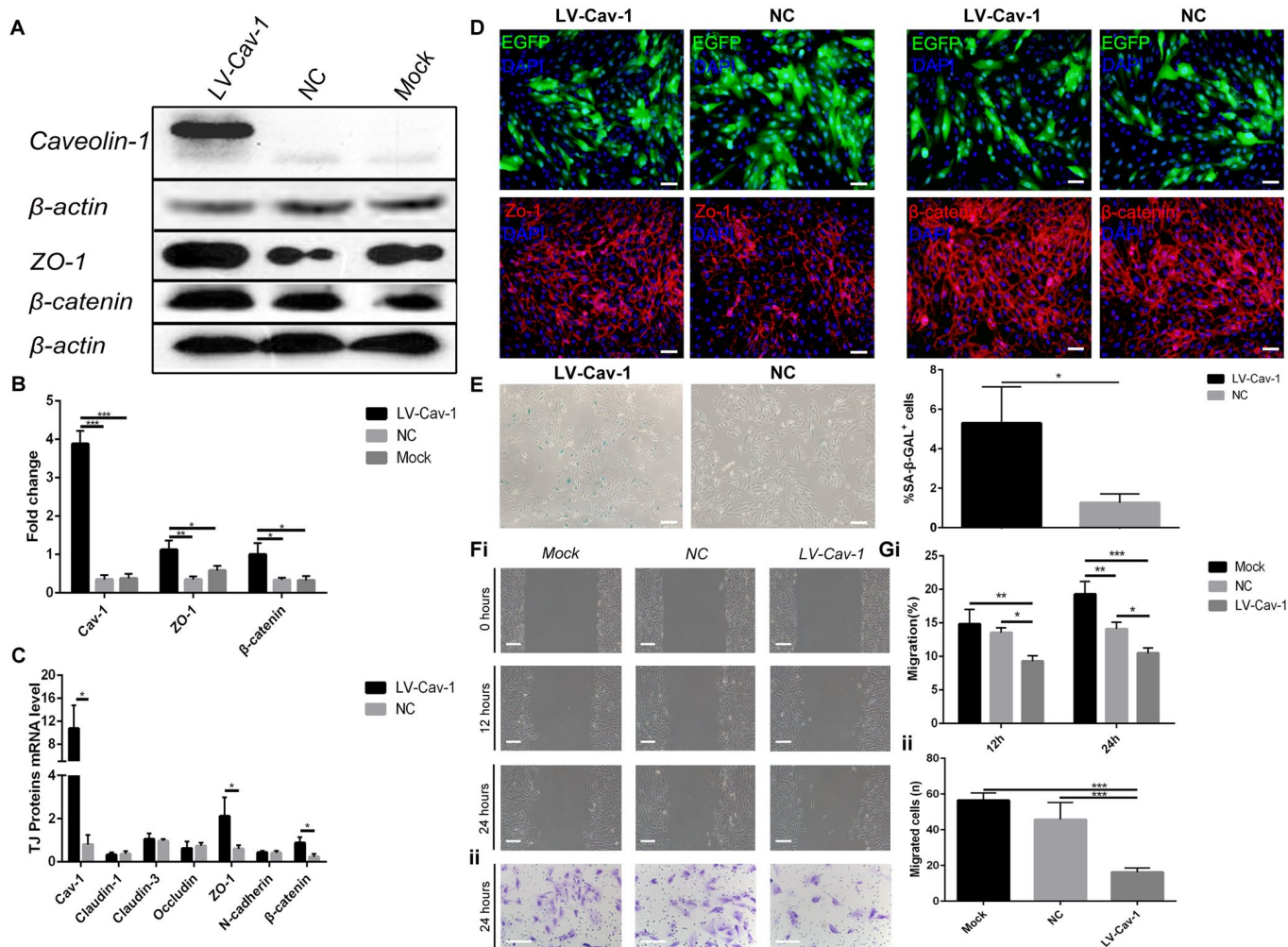


Figure 4. Overexpression of Caveolin-1 induced ARPE-19 cell senescence and inhibited migration and invasion. (A) Western blot analyses showed that overexpression of Caveolin-1 upregulated Zo-1 and β-catenin; β-actin was used as the loading control. (B) Western blot results were quantified by densitometry, and the results are expressed as a ratio with β-actin. Data are presented as means ± SD; * indicates a *p* value < 0.05, ** indicates a *p* value < 0.01, *** indicates a *p* value < 0.001, *n*=3. (C) qPCR analyses showed that overexpression of Caveolin-1 upregulated Zo-1 and β-catenin. Data are presented as means ± SD; * indicates a *p* value < 0.05, *n*=3. (D) Expression of EGFP, Zo-1 and β-catenin was assessed by immunofluorescence in Caveolin-1-overexpressing RPE cells and negative-control RPE cells. (E) Representative microscopic images of β-galactosidase staining in RPE cells showed overexpression of Caveolin-1 in RPE cells compared with that in negative-control RPE cells. Quantification of percentage of cells with positive SA-β-gal staining. Data are presented as means ± SD; * indicates a *p* value < 0.05, ** indicates a *p* value < 0.01, *n*=3. (F) (i) Wound-healing assays in Caveolin-1-overexpressing RPE cells. (ii) Transwell invasion assays in Caveolin-1-overexpressing RPE cells. (G) (i) The rate of cell migration in different groups was measured at different time points. Note that cell migration was decreased in Caveolin-1-overexpressing RPE cells. (ii) The mean number of invaded cells was assessed in 5 fields. Note that cell invasion was decreased in Caveolin-1-overexpressing RPE cells. Data are presented as means ± SD; * indicates a *p* value < 0.05, ** indicates a *p* value < 0.01, *** indicates a *p* value < 0.001, *n*=3.

evaluation of the senescent state than using SA- β -gal positive staining alone. Importantly, HMGB1 is regarded as a central mediator of senescent phenotypes [25]. After identification by proteomic MS-based measurement, we detected HMGB1 expression and localization in A2E-treated RPE cells and confirmed that the protein was upregulated and released from the nucleus into the cytoplasm. This is consistent with the findings of CoCl₂-induced hypoxia and senescent human and mouse cells in culture and *in vivo* [25, 26]. GA, extracted from the root of *G.glabra* was recently found to suppress HMGB1-induced injury by binding directly HMGB1. Furthermore, the effect of GA was demonstrated against photo-aging in skin, which indicated the potential role of GA against aging [27]. GA can inhibit the release of HMGB1. Alleviated A2E induced cell senescence confirmed the important role of HMGB1 in cell senescence.

Another RPE cell age-related protein detected in our study is Caveolin-1, which is the main component of the caveolae found in most cell types and is involved in the regulation of many cellular processes, such as mitochondrial function, proliferation, migration and senescence [28]. Senescence is strongly associated with decreased responses to growth factors that interact with Caveolin-1 via caveolae [29], and it has been reported that Caveolin-1 plays a major role in both replicative senescence and stress-induced premature senescence [15]. Our results showed that HMGB1 upregulation and release enhanced expression of Caveolin-1, suggesting that both HMGB1 and Caveolin-1 had a synergistic effect on RPE cell senescence. Caveolin-1 and translocation of HMGB1 significantly and consistently suppress cancer cell migration and invasion, with little effect on cell viability [30]. HMGB1 binding to RAGE up-regulates Caveolin-1 expression during macrophage

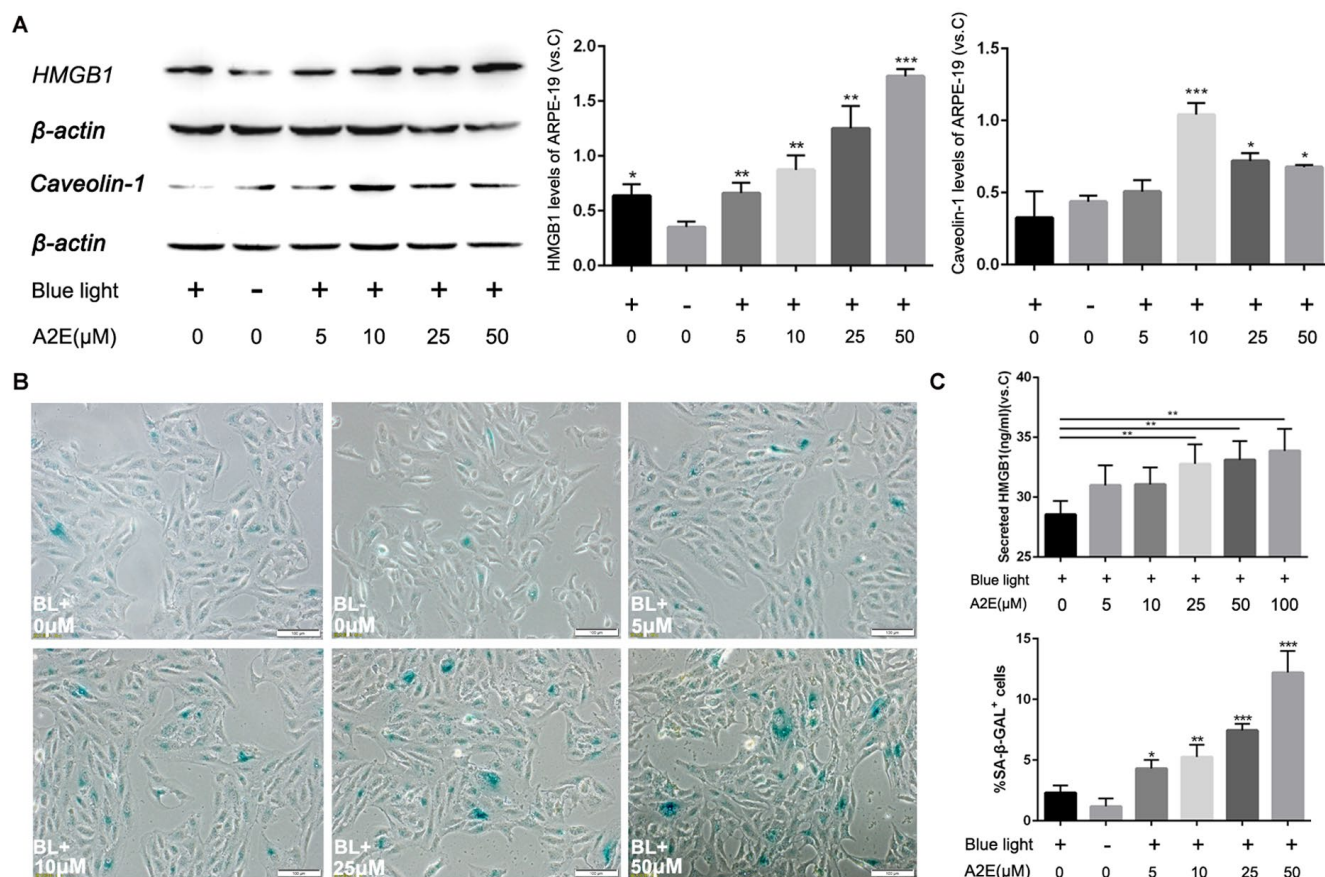


Figure 5. Blue light exposure of A2E-treated ARPE-19 cells increased HMGB1 and Caveolin-1 expression. (A) Western blot assay for HMGB1 and Caveolin-1 in RPE cells treated with a concentration gradient of A2E with or without blue light, quantified by densitometry, and the results are expressed as a ratio with β -actin. Data are presented as means \pm SD; * indicates a p value $<$ 0.05, ** indicates a p value $<$ 0.01, $n=3$. (B) Representative microscopic images of β -galactosidase staining in RPE cells with various concentrations of A2E. Quantification of percentage of cells with positive SA- β -gal staining. Data are presented as means \pm SD; * indicates a p value $<$ 0.05, ** indicates a p value $<$ 0.01, $n=3$. (C) The release of HMGB1 induced by A2E treatment were detected by ELISA assays.

necroptosis [31]. Therefore, it is worth studying this synergistic effect in RPE cells.

Although interaction between HMGB1 with Caveolin-1 was indicated by the STRING program, there is no evidence to date for this in RPE cells. Furthermore, research on the pathophysiology of pre-eclampsia (PE), hypoxic trophoblasts displayed higher intracellular HMGB1 protein levels which could increase TLR4 and Caveolin-1 [14]. However, Shang et al. suggested that RAGE mediated HMGB1-induced Caveolin-1 phosphorylation but did not raise the expression level; Lin et al. showed that Caveolin-1 phosphorylation, which promotes HMGB1 release, regulates endothelial cell apoptosis [32, 33]. Therefore, it is also worth addressing how HMGB1 interacts with Caveolin-1.

Upregulation of Caveolin-1 inhibits cell proliferation by suppressing receptor tyrosine kinase activities. In contrast, Caveolin-1 causes an enlarged and flattened shape in senescent cells via upregulation of Rb family and focal adhesion proteins [34]. Furthermore, the senescent phenotype can be reversed by downregulation of Caveolin-1, which suggests that it is a major switch in cellular senescence [35]. Our results demonstrate that cell aging reduces migration and invasion, which was consistent with previous reports [36], and that Zo-1 and β -catenin are upregulated, despite the results of other studies indicating that all tight junction proteins increased [37]. The upregulation of Zo-1 may be associated with activation of Src tyrosine kinases and matrix metalloproteinases (MMPs), which can be negatively regulated by the scaffolding domain of

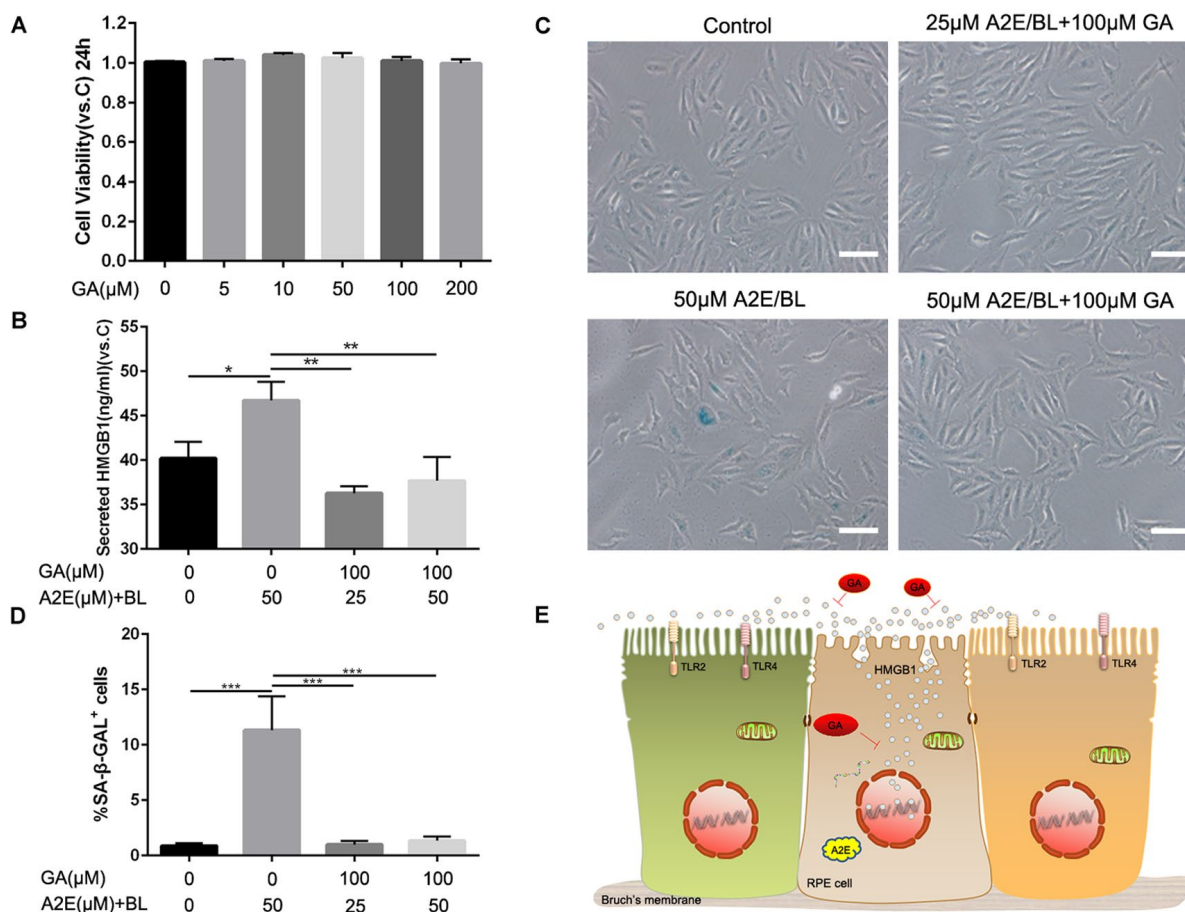


Figure 6. Glycyrrhizic acid alleviated A2E induced cell senescence. (A) An MTT assay was performed on RPE cells treated with different concentrations of GA. Data are presented as means \pm SD; * indicates a p value $<$ 0.05, ** indicates a p value $<$ 0.01, $n=3$. (B) The release of HMGB1 induced by different concentrations of A2E+BL with or without 100 μ M GA were detected by ELISA assays. Data are presented as means \pm SD; * indicates a p value $<$ 0.05, ** indicates a p value $<$ 0.01, $n=3$. (C) Representative microscopic images of β -galactosidase staining in RPE cells induced by different concentrations of A2E+BL with or without 100 μ M GA. (D) Quantification of percentage of cells with positive SA- β -gal staining. Data are presented as means \pm SD; * indicates a p value $<$ 0.05, ** indicates a p value $<$ 0.01, $n=3$. (E) Proposed schematic model for strategies for HMGB1 inhibition in response to A2E treatment.

Caveolin-1 [38, 39]. For example, Hardyman et al. found that a Src kinase inhibitor was able to rescue structural destruction of the epithelial cell barrier [40], and Vermeer reported that activation of MMP-9 decreased expression of Claudin-1 and Occludin [41]. In addition, upregulating Caveolin-1 rescued expression of tight junction proteins under hyperoxic conditions [37]. Nonetheless, β -catenin is not only a type of tight junction protein but is also a key link for the Wnt pathway, which is related to cell proliferation. Galbiati et al. suggested both Caveolin-1 and β -catenin levels increased and decreased in parallel and Caveolin-1 inhibited Wnt-1 signaling [42]. Kook et al. showed that quercetin could protect RPE cells from oxidative damage and cellular senescence via decreasing the expression of Caveolin-1 [43].

Although our expected results were that expression of Caveolin-1 would increase with increasing concentrations of A2E, it exhibited a tendency of first increasing up to 10 μ M A2E and then decreasing above 10 μ M A2E. However, there is no relevant research on changes in Caveolin-1 expression during RPE aging. These results may be due to the following reasons. First, we found that cell growth began to decline and that cell morphology began to change under high concentrations of A2E (Figure 5B). Yu et al. confirmed that Caveolin-1 deficiency induces premature senescence, with mitochondrial dysfunction, in human diploid fibroblasts [44]. Second, we surmised that cumulative feedback inhibition of Caveolin-1 may be associated with RPE cell senescence because upregulation of Caveolin-1 inhibits cellular levels of nitric oxide (NO) by regulating NO synthase activity [45]. Regardless, the mechanism responsible for these changes remains to be determined.

In summary, upregulation of HMGB1 and Caveolin-1 caused RPE cell senescence and suppressed migration and invasion, and β -catenin and Zo-1 accumulation was enhanced by A2E in RPE cells. In particular, the results showed a change in expression of HMGB1 and Caveolin-1, which suggests that they are prime gatekeepers in RPE cell senescence. The above results indicate that stabilizing expression of HMGB1 and Caveolin-1 is a potential therapeutic target to prevent the progression of RPE cell senescence.

MATERIALS AND METHODS

Cell culture

iPSC-derived RPE cell lines were created from healthy individuals, as described in Yang et al. and Lin et al. [6, 46]. In short, lentiviral vectors were used to transduce fibroblasts into iPS cell lines with *OCT4*, *SOC2*, *KLF4*, and *MYC*, which were cultured in human embryonic

stem cell medium with 10 mM basic fibroblast growth factor (FGF). iPS cell lines were co-cultured with mitomycin-C-treated stromal cells from the PA6 line and were further incubated in differentiation medium under 5% CO₂ at 37°C. Differentiation medium contained human embryonic stem cell medium (HUESM)–bFGF with 10 nm Nicotinamide (from d 0 to 20) and 20 ng/ml Activin A (from day 20 to 40). The first two generations of cells were plated onto 12-well dishes with feeder cells to induce RPE differentiation. After 6 weeks, pigmented colonies were re-plated on Matrigel-coated plates in RPE culture medium. ARPE-19 was purchased from American Type Culture Collection (ATCC, Manassas, VA, USA) and cultured in complete Dulbecco's modified Eagle's medium F-12 nutrient mixture (DMEM F12, Gibco Life Technology, China) containing 10% fetal bovine serum (FBS) and 1% penicillin/streptomycin (100 unit penicillin/100 μ g streptomycin per mL) (Invitrogen, USA) at 37°C with 5% CO₂. All cells were cultured in a humidified 5% CO₂ atmosphere at 37°C and passaged every 5 to 7 days.

Proteomic MS-based measurements

The process described in Yang et al. and Lin et al. [6, 46] consisted of three steps. (1) The third passage of iPSC-derived RPE cell lines were treated with and without A2E. Three biological replicates were prepared representing three separate cultures derived from each cell line and were also performed separately for A2E-treated samples. (2) Proteins were extracted from each cell line, reduced and alkylated before tryptic digestion, and RapiGest was cleaved with acid. The resulting peptides were analysed using a Synapt G2 quadrupole-time-of-flight mass spectrometer (Waters Corp.) with MSE data-independent scanning. (3) Initial data were processed using ProteinLynx Global Server (Version 2.5 RC9, Waters Corp.). Further analysis was performed with TransOmics software (Waters Corp.) and the NCBI database of human sequences.

Lentivirus-mediated transduction

For overexpression and knock-down of human HMGB1 and Caveolin-1, lentiviruses were purchased from Genechem (Shanghai, China). For infection of ARPE-19 cells, we used 5 μ M polybrene, and the medium was changed after 11 h. To acquire stable clones, 2 μ M puromycin (Solarbio, China) was added to the culture medium, and the medium was replaced every 3 days with fresh puromycin-containing medium until resistant colonies were identified.

Drug treatment

A2E was purchased from Gene And Cell Technologies (310 Georgia St, Vallejo CA, 94590, USA), dissolved in

dimethyl sulfoxide (DMSO) at a concentration of 25 mM and stored at -80°C in the dark as a stock solution. ARPE-19 cells were incubated with different concentrations of A2E in culture medium without FBS for 48 h. After A2E loading, RPE cells were exposed to 470 ± 20 nm light at 2000 ± 500 lx (Yingze, Tianjin) for 10 min, as described previously [47]; the cells were then returned to complete medium and incubated for 24 h. GA was purchased from MCE, ARPE-19 cells were pretreated with GA for 2h, then the cell culture medium was replaced with medium containing A2E and GA for 48h. Mammalian recombinant HMGB1 (rHMGB1) protein was purchased from Sigma–Aldrich, ARPE-19 cells were treated with rHMGB1 for 24h.

Cell viability assays

Cytotoxicity was assessed using the MTT assay. After treatment with different concentrations of A2E/Blue light, 20 μL MTT labelling reagent (Solarbio, China) was added to 200 μL medium in each well. After 4h of incubation at 37°C , the labelling reagent was replaced with 200 μL DMSO, and the sample was shaken for 15 min to dissolve the crystals. Optical density (OD) was measured at 490 nm using a Full Wavelength Microplate Reader (Infinite 200 PRO, TECAN). FDA/PI staining was also performed.

Quantitative real-time PCR

Expression of tight junction genes, Claudin-1, Claudin-3, Zo-1, Occludin, N-cadherin, β -catenin, and HMGB1, Caveolin-1, was analysed by RT-PCR. Each gene expression value was normalized to the endogenous control glyceraldehyde-3-phosphate dehydrogenase (GAPDH). RNA was extracted from cells in 6-well plates using 1mL of Trizol® (Invitrogen, USA) and re-suspended in 20 μL diethyl pyrocarbonate (DEPC)-treated water. The total RNA concentration was determined using a Nanodrop 2000 (Thermo Scientific). Total RNA (1 μg) was used for reverse transcription

with a retroscript kit (Revert Aid First Strand cDNA Synthesis Kit, Thermo Scientific), and real-time PCR was performed using a 7900HT Fast Real-Time PCR system (Applied Biosystems, USA). For quantification, the relative expression of different gene transcripts was calculated with the $\Delta\Delta\text{Ct}$ method. The Ct of any gene of interest was normalized to the Ct of GAPDH. Fold changes were determined as $2^{-\Delta\Delta\text{Ct}}$. All reactions were performed 3 times. Primer information is provided in Table 2.

Western blot analysis

ARPE-19 cells were collected in RIPA buffer (Solarbio, China) with protease inhibitors (Thermo Fisher Scientific). Protein concentrations were measured using a bicinchoninic acid (BCA) assay kit (Solarbio, China) A total of 20 or 40 μg of protein was loaded per lane, separated by sodium dodecyl-sulfate polyacrylamide gel electrophoresis (SDS-PAGE), and transferred to Immobilon-FL polyvinylidene difluoride (PVDF) membranes. Subsequently, the membranes were blocked in 10% bovine serum albumin (BSA, BD Biosciences) in phosphate-buffered saline with Tween 20 (PBST) for 1.5 h at room temperature and incubated overnight at 4°C with primary antibodies against TLR2(1:1000, Rabbit, Abcam), TLR4(1:2000, Mouse, Proteintech), RAGE(1:1000, Rabbit, Abcam), Tublin(1:1000, Mouse, Proteintech), β -actin (1:1000, Mouse, Abcam), Caveolin-1 (1:10000, Rabbit, Abcam), HMGB1 (1:1000, Mouse, Abcam), Zo-1 (1:1000, Rabbit, Proteintech), or β -catenin (1:5000, Rabbit, Abcam). After washing 3 times, the membranes were incubated for 2 h in the dark at room temperature with horseradish peroxidase (HRP)-conjugated secondary antibodies diluted 1:3000 in PBST. The membranes were washed in PBST 3 times before visualizing using Immobilon Western Chemiluminescent HRP Substrate (MILLIPORE, USA). Blots shown are representative of at least three biological repeats for each experiment. Every immuno-

Table 2. Primers used for quantitative RT-PCR.

	Forward (5'to 3')	Reverse (5'to 3')
GAPDH	TGTGGGCATCAATGGATTTGG	ACACCATGTATTCCGGGTCAAT
HMGB1	GAGAGGCCAAAATGTCATCAT	GGGATCCTTGAACCTTCTTTT
Caveolin-1	CGGGAACAGGGCAACATCTAC	CTTCTGGTTCCGCAATCACATC
Zo-1	AAGGAAGGCTTAGAGGAAGGTGA	GTCCATAGGGAGATTCCTTTTCA
β -catenin	CCTGAGGAAGAGGATGTGGATAC	CATTTAGCAGTTTTGTGTCAGTTCAGG
Claudin-1	CTGGGAGGTGCCCTACTTTG	ACACGTAGTCTTTCCCGCTG
Claudin-3	ACGCGAGAAGAAGTACACGG	GTAGTCCTTGCGGTCGTAGC
Occludin	AGGTTCCATCCGAAGCAGG	GTGTAGGTGTGGTGTGTCGG
N-cadherin	CCTTTCAAACACAGCCACGG	TGTTTGGGTCGGTCTGGATG

reactive band was detected using the ECL detection system (UVP, USA), and densitometric values were quantitated using ImageJ software (version 1.45). The relative expression of each immunoreactive band was normalized to that of β -actin.

Immunofluorescence and confocal microscopy

ARPE-19 cells in a 24-well cell culture plate were fixed with 4% paraformaldehyde (PFA) for 20 min and then permeabilized in 0.1% Triton X-100 in PBS for 20 min at room temperature. After being blocked with 10% goat serum in PBS for 1.5 h, the samples were incubated with the primary antibodies described above at 4°C overnight. Coverslips were washed with PBST 3 times and incubated with Alexa Fluor 488-conjugated (1:500; ThermoFisher) and Alexa Fluor 594-conjugated (1:500; ThermoFisher) secondary antibodies diluted in PBST at room temperature in the dark for 1 h. Coverslips were washed 3 times and stained with 4',6-diamidino-2-phenylindole (DAPI) for 3-5 min and then imaged by confocal microscopy (Zeiss).

Migration assays

For the wound-healing assay, cells were transfected with Caveolin-1 for 24 h and then cultured in 6-well plates. When reaching 80% confluence, we used a sterilized pipette to scratch the cell monolayer. After washing three times with PBS, the cells were cultured in medium without FBS. Images shown are from three time points, 0, 12 and 24h, and demonstrate wound closure, which was measured using ImageJ. For transwell assays, cells were transfected with Caveolin-1 for 24 h, trypsinized and counted; 1×10^5 cells in medium without FBS were placed in the top chamber of a Transwell device (24-well insert; 8 μ m, pore size; Corning Incorporated). Medium with 20% FBS was used as a chemical attractant in the lower chamber. After incubation at 37°C for 24 h, the membranes were fixed with 4% PFA for 30 min and stained. Cells migrated to the lower side of the membranes were counted using an inverted microscope.

ELISA assays

The amount of HMGB1 in cell culture medium was assessed using the HMGB1 ELISA kit (Mlbio, China).

SA- β -gal staining

The SA- β -gal staining assay was performed using an SA- β -gal staining kit (Solarbio, China) following the manufacturer's instructions.

Data and statistical analysis

All figures are representative of at least 3 separate experiments. All quantitative data were analysed with SPSS (Version 22), and the results are expressed as the mean \pm SEM, with $p < 0.05$ considered statistically significant. Differences between groups were assessed using either an independent *t*-test or one-way analysis of variance (ANOVA) with Tukey's post hoc or Dunnett's tests.

Abbreviations

AMD: age-related macular degeneration; A2E: *N*-retinylidene-*N*-retinylethanolamine; ANOVA: one-way analysis of variance; BCA: bicinchoninic acid; BSA: bovine serum albumin; CNV: choroidal neovascularization; DMSO: dimethyl sulfoxide; DMEM/F12: Dulbecco's modified Eagle's medium F-12 nutrient mixture; DEPC: diethyl pyrocarbonate; DAPI: 4',6-diamidino-2-phenylindole; ELISA: Enzyme Linked Immunosorbent Assay; EP: ethyl pyruvate; FDA/PI: fluorescein diacetate /propidium iodide; FBS: foetal bovine serum; FGF: fibroblast growth factor; GA: Glycyrrhizic acid; GAPDH: glyceraldehyde-3-phosphate dehydrogenase; HUESM: human embryonic stem cell medium; HRP: horseradish peroxidase; HMGB1: High-mobility group box 1; iPSC: induced pluripotent stem cell; LC-MS/MS: liquid chromatography with tandem mass spectrometry; MTT: 3-(4,5-dimethylthiazol-2-yl)-2,5-diphenylbromide; MMPs: matrix metalloproteinases; NO: nitric oxide; OD: optical density; PBS: phosphate-buffered saline; PVDF: polyvinylidene difluoride; PFA: paraformaldehyde; PE: pre-eclampsia; qRT-PCR: reverse transcription and quantitative PCR; RAGE: receptor for advanced glycation end products; RPE: retinal pigment epithelium; TLR: Toll-like receptor; VEGF: vascular endothelial growth factor.

AUTHOR CONTRIBUTIONS

S.S. wrote the first draft of the manuscript. S.H.T., Y.L.W., C.C., J.Y. and X.R.L. developed the structure and arguments for the paper. S.S., Y.L. and B.C.C. discussed and edited different parts of the manuscript. All authors read and approved the final manuscript.

ACKNOWLEDGEMENTS

We thank W.Q.S., B.T.G., X.Z.Z., X.M.Z., and Z.Q.L. for their thoughtful comments on the manuscript and thank Liang Wang for her revision.

CONFLICTS OF INTEREST

All the authors declare that they have no competing interests.

FUNDING

This study was supported by Natural Science Foundation of Tianjin City (18JCQNJC10700); National Natural Science Funds (81670875); Natural Science Foundation of Tianjin City (17JCYBJC27200); a grant of the Dr. Henry Norman Bethune LangMu Young Scientist scholarship (BJ-LM2015008L); the National Natural Science Funds (81400412).

REFERENCES

1. Evans JB, Syed BA. New hope for dry AMD? *Nat Rev Drug Discov.* 2013; 12:501–02. <https://doi.org/10.1038/nrd4038> PMID:23812264
2. Ferris FL 3rd, Wilkinson CP, Bird A, Chakravarthy U, Chew E, Csaky K, Sadda SR, and Beckman Initiative for Macular Research Classification Committee. Clinical classification of age-related macular degeneration. *Ophthalmology.* 2013; 120:844–51. <https://doi.org/10.1016/j.ophtha.2012.10.036> PMID:23332590
3. Jager RD, Mieler WF, Miller JW. Age-related macular degeneration. *N Engl J Med.* 2008; 358:2606–17. <https://doi.org/10.1056/NEJMra0801537> PMID:18550876
4. Bowes Rickman C, Farsiu S, Toth CA, Klingeborn M. Dry age-related macular degeneration: mechanisms, therapeutic targets, and imaging. *Invest Ophthalmol Vis Sci.* 2013; 54:ORSF68-80. <https://doi.org/10.1167/iovs.13-12757> PMID:24335072
5. Hanus J, Anderson C, Wang S. RPE necroptosis in response to oxidative stress and in AMD. *Ageing Res Rev.* 2015; 24:286–98. <https://doi.org/10.1016/j.arr.2015.09.002> PMID:26369358
6. Yang J, Li Y, Chan L, Tsai YT, Wu WH, Nguyen HV, Hsu CW, Li X, Brown LM, Egli D, Sparrow JR, Tsang SH. Validation of genome-wide association study (GWAS)-identified disease risk alleles with patient-specific stem cell lines. *Hum Mol Genet.* 2014; 23:3445–55. <https://doi.org/10.1093/hmg/ddu053> PMID:24497574
7. Kokkinaki M, Sahibzada N, Golestaneh N. Human induced pluripotent stem-derived retinal pigment epithelium (RPE) cells exhibit ion transport, membrane potential, polarized vascular endothelial growth factor secretion, and gene expression pattern similar to native RPE. *Stem Cells.* 2011; 29:825–35. <https://doi.org/10.1002/stem.635> PMID:21480547
8. Crouch RK, Koutalos Y, Kono M, Schey K, Ablonczy Z. A2E and Lipofuscin. *Prog Mol Biol Transl Sci.* 2015; 134:449–63. <https://doi.org/10.1016/bs.pmbts.2015.06.005> PMID:26310170
9. Sparrow JR, Boulton M. RPE lipofuscin and its role in retinal pathobiology. *Exp Eye Res.* 2005; 80:595–606. <https://doi.org/10.1016/j.exer.2005.01.007> PMID:15862166
10. Jang YP, Zhou J, Nakanishi K, Sparrow JR. Anthocyanins protect against A2E photooxidation and membrane permeabilization in retinal pigment epithelial cells. *Photochem Photobiol.* 2005; 81:529–36. PMID:15745429
11. Wang J, Feng Y, Han P, Wang F, Luo X, Liang J, Sun X, Ye J, Lu Y, Sun X. Photosensitization of A2E triggers telomere dysfunction and accelerates retinal pigment epithelium senescence. *Cell Death Dis.* 2018; 9:178. <https://doi.org/10.1038/s41419-017-0200-7> PMID:29415988
12. Ablonczy Z, Higbee D, Anderson DM, Dahrouj M, Grey AC, Gutierrez D, Koutalos Y, Schey KL, Hanneken A, Crouch RK. Lack of correlation between the spatial distribution of A2E and lipofuscin fluorescence in the human retinal pigment epithelium. *Invest Ophthalmol Vis Sci.* 2013; 54:5535–42. <https://doi.org/10.1167/iovs.13-12250> PMID:23847313
13. Grey AC, Crouch RK, Koutalos Y, Schey KL, Ablonczy Z. Spatial localization of A2E in the retinal pigment epithelium. *Invest Ophthalmol Vis Sci.* 2011; 52:3926–33. <https://doi.org/10.1167/iovs.10-7020> PMID:21357388
14. Jiang R, Cai J, Zhu Z, Chen D, Wang J, Wang Q, Teng Y, Huang Y, Tao M, Xia A, Xue M, Zhou S, Chen AF. Hypoxic trophoblast HMGB1 induces endothelial cell hyperpermeability via the TRL-4/caveolin-1 pathway. *J Immunol.* 2014; 193:5000–12. <https://doi.org/10.4049/jimmunol.1303445> PMID:25339669
15. Zou H, Stoppani E, Volonte D, Galbiati F. Caveolin-1, cellular senescence and age-related diseases. *Mech Ageing Dev.* 2011; 132:533–42. <https://doi.org/10.1016/j.mad.2011.11.001> PMID:22100852
16. Girard JP. A direct inhibitor of HMGB1 cytokine. *Chem Biol.* 2007; 14:345–47. <https://doi.org/10.1016/j.chembiol.2007.04.001> PMID:17462568

17. Collado M, Blasco MA, Serrano M. Cellular senescence in cancer and aging. *Cell*. 2007; 130:223–33. <https://doi.org/10.1016/j.cell.2007.07.003> PMID:17662938
18. Blasiak J, Piechota M, Pawlowska E, Szatkowska M, Sikora E, Kaarniranta K. Cellular Senescence in Age-Related Macular Degeneration: Can Autophagy and DNA Damage Response Play a Role? *Oxid Med Cell Longev*. 2017; 2017:5293258. <https://doi.org/10.1155/2017/5293258> PMID:29225722
19. Kikuchi T, Morizane A, Doi D, Magotani H, Onoe H, Hayashi T, Mizuma H, Takara S, Takahashi R, Inoue H, Morita S, Yamamoto M, Okita K, et al. Human iPS cell-derived dopaminergic neurons function in a primate Parkinson's disease model. *Nature*. 2017; 548:592–96. <https://doi.org/10.1038/nature23664> PMID:28858313
20. Kimura J, Shimizu K, Kajima K, Yokosuka A, Mimaki Y, Oku N, Ohizumi Y. Nobiletin Reduces Intracellular and Extracellular β -Amyloid in iPS Cell-Derived Alzheimer's Disease Model Neurons. *Biol Pharm Bull*. 2018; 41:451–57. <https://doi.org/10.1248/bpb.b17-00364> PMID:29607920
21. Marie M, Bigot K, Angebault C, Barrau C, Gondouin P, Pagan D, Fouquet S, Villette T, Sahel JA, Lenaers G, Picaud S. Light action spectrum on oxidative stress and mitochondrial damage in A2E-loaded retinal pigment epithelium cells. *Cell Death Dis*. 2018; 9:287. <https://doi.org/10.1038/s41419-018-0331-5> PMID:29459695
22. Tang D, Kang R, Zeh HJ 3rd, Lotze MT. High-mobility group box 1, oxidative stress, and disease. *Antioxid Redox Signal*. 2011; 14:1315–35. <https://doi.org/10.1089/ars.2010.3356> PMID:20969478
23. Bauer EM, Shapiro R, Zheng H, Ahmad F, Ishizawa D, Comhair SA, Erzurum SC, Billiar TR, Bauer PM. High mobility group box 1 contributes to the pathogenesis of experimental pulmonary hypertension via activation of Toll-like receptor 4. *Mol Med*. 2013; 18:1509–18. <https://doi.org/10.2119/molmed.2012.00283> PMID:23269975
24. Lei C, Lin S, Zhang C, Tao W, Dong W, Hao Z, Liu M, Wu B. Effects of high-mobility group box1 on cerebral angiogenesis and neurogenesis after intracerebral hemorrhage. *Neuroscience*. 2013; 229:12–19. <https://doi.org/10.1016/j.neuroscience.2012.10.054> PMID:23137544
25. Davalos AR, Kawahara M, Malhotra GK, Schaum N, Huang J, Ved U, Beausejour CM, Coppe JP, Rodier F, Campisi J. p53-dependent release of Alarmin HMGB1 is a central mediator of senescent phenotypes. *J Cell Biol*. 2013; 201:613–29. <https://doi.org/10.1083/jcb.201206006> PMID:23649808
26. Zhang G, Zhang X, Li D, Tian J, Jiang W. Long-term oral atazanavir attenuates myocardial infarction-induced cardiac fibrosis. *Eur J Pharmacol*. 2018; 828:97–102. <https://doi.org/10.1016/j.ejphar.2018.03.041> PMID:29605419
27. Tundis R, Loizzo MR, Bonesi M, Menichini F. Potential role of natural compounds against skin aging. *Curr Med Chem*. 2015; 22:1515–38. <https://doi.org/10.2174/0929867322666150227151809> PMID:25723509
28. Baker N, Tuan RS. The less-often-traveled surface of stem cells: caveolin-1 and caveolae in stem cells, tissue repair and regeneration. *Stem Cell Res Ther*. 2013; 4:90. <https://doi.org/10.1186/scrt276> PMID:23899671
29. Yeo EJ, Jang IS, Lim HK, Ha KS, Park SC. Agonist-specific differential changes of cellular signal transduction pathways in senescent human diploid fibroblasts. *Exp Gerontol*. 2002; 37:871–83. [https://doi.org/10.1016/S0531-5565\(02\)00027-X](https://doi.org/10.1016/S0531-5565(02)00027-X) PMID:12086695
30. Ma J, Fu G, Wu J, Han S, Zhang L, Yang M, Yu Y, Zhang M, Lin Y, Wang Y. 4-cholesten-3-one suppresses lung adenocarcinoma metastasis by regulating translocation of HMGB1, HIF1 α and Caveolin-1. *Cell Death Dis*. 2016; 7:e2372. <https://doi.org/10.1038/cddis.2016.281> PMID:27899819
31. Li Z, Scott MJ, Fan EK, Li Y, Liu J, Xiao G, Li S, Billiar TR, Wilson MA, Jiang Y, Fan J. Tissue damage negatively regulates LPS-induced macrophage necroptosis. *Cell Death Differ*. 2016; 23:1428–47. <https://doi.org/10.1038/cdd.2016.21> PMID:26943325
32. Lin F, Pei L, Zhang Q, Han W, Jiang S, Lin Y, Dong B, Cui L, Li M. Ox-LDL induces endothelial cell apoptosis and macrophage migration by regulating caveolin-1 phosphorylation. *J Cell Physiol*. 2018; 233:6683–92. <https://doi.org/10.1002/jcp.26468> PMID:29323707
33. Shang D, Peng T, Gou S, Li Y, Wu H, Wang C, Yang Z. High Mobility Group Box Protein 1 Boosts Endothelial Albumin Transcytosis through the RAGE/Src/Caveolin-1 Pathway. *Sci Rep*. 2016; 6:32180. <https://doi.org/10.1038/srep32180> PMID:27572515
34. Chen QM, Tu VC, Catania J, Burton M, Toussaint O, Dilley T. Involvement of Rb family proteins, focal adhesion proteins and protein synthesis in senescent

- morphogenesis induced by hydrogen peroxide. *J Cell Sci.* 2000; 113:4087–97. PMID:[11058095](https://pubmed.ncbi.nlm.nih.gov/11058095/)
35. Cho KA, Park SC. Caveolin-1 as a prime modulator of aging: a new modality for phenotypic restoration? *Mech Ageing Dev.* 2005; 126:105–10. <https://doi.org/10.1016/j.mad.2004.09.029> PMID:[15610768](https://pubmed.ncbi.nlm.nih.gov/15610768/)
36. Nagasaka Y, Kaneko H, Ye F, Kachi S, Asami T, Kato S, Takayama K, Hwang SJ, Kataoka K, Shimizu H, Iwase T, Funahashi Y, Higuchi A, et al. Role of Caveolin-1 for Blocking the Epithelial-Mesenchymal Transition in Proliferative Vitreoretinopathy. *Invest Ophthalmol Vis Sci.* 2017; 58:221–29. <https://doi.org/10.1167/iovs.16-20513> PMID:[28114583](https://pubmed.ncbi.nlm.nih.gov/28114583/)
37. Xu S, Xue X, You K, Fu J. Caveolin-1 regulates the expression of tight junction proteins during hyperoxia-induced pulmonary epithelial barrier breakdown. *Respir Res.* 2016; 17:50. <https://doi.org/10.1186/s12931-016-0364-1> PMID:[27176222](https://pubmed.ncbi.nlm.nih.gov/27176222/)
38. Haines P, Samuel GH, Cohen H, Trojanowska M, Bujor AM. Caveolin-1 is a negative regulator of MMP-1 gene expression in human dermal fibroblasts via inhibition of Erk1/2/Ets1 signaling pathway. *J Dermatol Sci.* 2011; 64:210–16. <https://doi.org/10.1016/j.jdermsci.2011.08.005> PMID:[21925842](https://pubmed.ncbi.nlm.nih.gov/21925842/)
39. Li S, Couet J, Lisanti MP. Src tyrosine kinases, Galpha subunits, and H-Ras share a common membrane-anchored scaffolding protein, caveolin. Caveolin binding negatively regulates the auto-activation of Src tyrosine kinases. *J Biol Chem.* 1996; 271:29182–90. <https://doi.org/10.1074/jbc.271.46.29182> PMID:[8910575](https://pubmed.ncbi.nlm.nih.gov/8910575/)
40. Hardyman MA, Wilkinson E, Martin E, Jayasekera NP, Blume C, Swindle EJ, Gozzard N, Holgate ST, Howarth PH, Davies DE, Collins JE. TNF- α -mediated bronchial barrier disruption and regulation by src-family kinase activation. *J Allergy Clin Immunol.* 2013; 132:665–675.e8. <https://doi.org/10.1016/j.jaci.2013.03.005> PMID:[23632299](https://pubmed.ncbi.nlm.nih.gov/23632299/)
41. Vermeer PD, Denker J, Estin M, Moninger TO, Keshavjee S, Karp P, Kline JN, Zabner J. MMP9 modulates tight junction integrity and cell viability in human airway epithelia. *Am J Physiol Lung Cell Mol Physiol.* 2009; 296:L751–62. <https://doi.org/10.1152/ajplung.90578.2008> PMID:[19270179](https://pubmed.ncbi.nlm.nih.gov/19270179/)
42. Galbiati F, Volonte D, Brown AM, Weinstein DE, Ben-Ze'ev A, Pestell RG, Lisanti MP. Caveolin-1 expression inhibits Wnt/beta-catenin/Lef-1 signaling by recruiting beta-catenin to caveolae membrane domains. *J Biol Chem.* 2000; 275:23368–77. <https://doi.org/10.1074/jbc.M002020200> PMID:[10816572](https://pubmed.ncbi.nlm.nih.gov/10816572/)
43. Kook D, Wolf AH, Yu AL, Neubauer AS, Priglinger SG, Kampik A, Welge-Lüssen UC. The protective effect of quercetin against oxidative stress in the human RPE in vitro. *Invest Ophthalmol Vis Sci.* 2008; 49:1712–20. <https://doi.org/10.1167/iovs.07-0477> PMID:[18385095](https://pubmed.ncbi.nlm.nih.gov/18385095/)
44. Yu DM, Jung SH, An HT, Lee S, Hong J, Park JS, Lee H, Lee H, Bahn MS, Lee HC, Han NK, Ko J, Lee JS, Ko YG. Caveolin-1 deficiency induces premature senescence with mitochondrial dysfunction. *Aging Cell.* 2017; 16:773–84. <https://doi.org/10.1111/accel.12606> PMID:[28514055](https://pubmed.ncbi.nlm.nih.gov/28514055/)
45. Chen Z, Bakhshi FR, Shajahan AN, Sharma T, Mao M, Trane A, Bernatchez P, van Nieuw Amerongen GP, Bonini MG, Skidgel RA, Malik AB, Minshall RD. Nitric oxide-dependent Src activation and resultant caveolin-1 phosphorylation promote eNOS/caveolin-1 binding and eNOS inhibition. *Mol Biol Cell.* 2012; 23:1388–98. <https://doi.org/10.1091/mbc.e11-09-0811> PMID:[22323292](https://pubmed.ncbi.nlm.nih.gov/22323292/)
46. Lin MK, Yang J, Hsu CW, Gore A, Bassuk AG, Brown LM, Colligan R, Sengillo JD, Mahajan VB, Tsang SH. HTRA1, an age-related macular degeneration protease, processes extracellular matrix proteins EFEMP1 and TSP1. *Aging Cell.* 2018; 17:e12710. <https://doi.org/10.1111/accel.12710> PMID:[29730901](https://pubmed.ncbi.nlm.nih.gov/29730901/)
47. Wang Y, Kim HJ, Sparrow JR. Quercetin and cyanidin-3-glucoside protect against photooxidation and photodegradation of A2E in retinal pigment epithelial cells. *Exp Eye Res.* 2017; 160:45–55. <https://doi.org/10.1016/j.exer.2017.04.010> PMID:[28461203](https://pubmed.ncbi.nlm.nih.gov/28461203/)

Nutraceutical effects of *Emblica officinalis* in age-related macular degeneration

Sonali Nashine¹, Raj Kanodia², Anthony B. Nesburn^{1,3}, Girish Soman⁴, Baruch D. Kuppermann¹, M. Cristina Kenney^{1,5}

¹Department of Ophthalmology, Gavin Herbert Eye Institute, University of California Irvine, Irvine, CA 92697, USA

²Rhinoplasty Surgeon, Dr. Raj Kanodia Medical Group, Beverly Hills, CA 90210, USA

³Cedars-Sinai Medical Center, Los Angeles, CA 90048, USA

⁴Nisarga Biotech Pvt Ltd, Janai Malai, Satara, Maharashtra 415004, India

⁵Department of Pathology and Laboratory Medicine, University of California Irvine, Irvine, CA 92697, USA

Correspondence to: M. Cristina Kenney; **email:** mkenney@uci.edu

Keywords: *Emblica officinalis*, *Phyllanthus emblica*, Indian gooseberry, Amla, nutraceutical, age-related macular degeneration, AMD

Received: December 26, 2018

Accepted: February 6, 2019

Published: February 21, 2019

Copyright: Nashine et al. This is an open-access article distributed under the terms of the Creative Commons Attribution License (CC BY 3.0), which permits unrestricted use, distribution, and reproduction in any medium, provided the original author and source are credited.

ABSTRACT

Emblica officinalis Gaetrn (i.e., *Phyllanthus emblica*/ Indian gooseberry/ Amla) (EO) has been used extensively as a nutraceutical in several diseases since it is known to boost immunity and offers numerous health benefits such as antioxidant, anti-inflammatory, and anti-aging effects. The goal of our study was to test the hypothesis that EO will rescue human AMD RPE transmitochondrial cells from mitochondria-induced cellular damage. AMD RPE transmitochondrial cell lines were created by fusing mitochondria DNA-deficient APRE-19 (*Rho0*) cells with platelets isolated from AMD patients, and therefore had identical nuclei but differed in mitochondrial DNA content. These AMD RPE cells were treated with EO extract followed by characterization of effects of EO using cellular and molecular assays. Herein, EO significantly improved live cell number and mitochondrial membrane potential, reduced apoptosis and oxidative stress, down-regulated *VEGF*, and up-regulated *PGC-1 α* . In conclusion, EO improved cellular and mitochondrial health, thereby playing a key cytoprotective role in AMD *in vitro*. Further studies are required to examine the mechanisms that mediate the cytoprotective effects of EO.

INTRODUCTION

Emblica officinalis Gaetrn (*Phyllanthus emblica*), commonly known as Indian gooseberry or Amla, is an edible fruit which is borne on a deciduous tree of the same name. All parts of the *Emblica officinalis* (EO) tree i.e, fruits, bark, leaves, seeds, flowers, and roots are known to have medicinal properties. EO is native to the tropical and subtropical regions of Southeast Asia including India, China, Malaysia, Bangladesh, Sri Lanka, and Mascarene Island. EO is a vital medicinal plant in Ayurveda which is the ancient holistic system of medicine practiced in the Indian subcontinent.

Several health rejuvenating Ayurvedic formulations have been prepared using EO fruit (referred to as EO throughout the paper) as a primary ingredient [1]. Phytochemically, EO is composed of several bioactive compounds such as flavonoids (i.e., Quercetin, Kaempferol), phenolic compounds (i.e., gallic acid, methyl gallate, ellagic acid, trigallayl glucose), tannins (i.e., Emblicanin A and B, phyllaemblicin B, punigluconin, pedunculagin, Chebulinic acid, Corilagin, Geraniin, Ellagotannin), amino acids (i.e., glutamic acid, aspartic acid, alanine, lysine, proline, cystine), fatty acids (i.e., stearic acid, oleic acid, palmitic acid, myristic acid, linolenic acid, linoleic acid), alkaloids

(i.e., Phyllantine, Phyllembain, Phyllantidine), pectin, citric acid, ascorbic acid (Vitamin C), cellulose, gum, and albumin. Based on the stage of ripening, the vitamin C content of EO varies and is the highest in ripe EO fruits (~800 mg/100 g) compared to unripe (~560 mg/100 g) or semi-ripe (~600 mg/100g) EO fruits [2].

Due to its high Vitamin C content which on an average is ~600 mg/100 g, EO is well-known as an immunity boosting food. In addition to vitamin C, EO is a rich source of antioxidants, including polyphenols, which confer EO its free radical scavenging potential [3]. A study by Carlson et al. revealed that EO has an antioxidant content of ~261.5 mmol/100 g which was substantially higher than numerous other plant-based foods and supplements that were tested using the FRAP assay in the same study [4]. Substantive evidence validates the antioxidant and cytoprotective properties of EO in several disease models including Alzheimer's, diabetes, cardiac diseases, inflammatory disorders, hepatic diseases, atherosclerosis, cancer, and pulmonary fibrosis [5-11].

The goal of the current study was to examine and characterize the nutraceutical potential of EO in a human retinal pigment epithelial (RPE) age-related macular degeneration (AMD) transmitochondrial cybrid cell model [12]. We hypothesized that EO will rescue AMD RPE transmitochondrial cells from cellular and mitochondrial damage *in vitro*. The results of this novel

study the cytoprotective role of EO in AMD RPE cybrid cells in terms of increased viability and reduction in oxidative stress and apoptosis.

RESULTS

EO concentration optimization

To determine the optimum working concentration of EO for all experiments, we performed an initial concentration titration experiment wherein AMD cybrids were treated with increasing doses of EO i.e, 10, 15, 20, and 25 mg/mL of EO (Figure 1) followed by measurement of viable cell numbers using MTT assay. Although compared to untreated AMD cybrids (Bar 1; 1 ± 0.382 (Mean \pm SEM) arbitrary unit (a.u.), $n=3$), 10 mg/mL EO-treated AMD cybrids (Bar 3; 1.59 ± 0.191 a.u.; $n=3$) showed a 59 % higher viable cell number, the difference was not statistically significant ($p=0.2387$). However, EO-treated cybrids showed significantly improved viable cell number at 15 mg/mL (Bar 4; 295 % increase; 3.95 ± 0.240 a.u.; $p<0.001$; $n=3$), 20 mg/mL (Bar 5; 330 % increase; 4.30 ± 0.193 a.u.; $p<0.001$; $n=3$), and 25 mg/mL (Bar 6; 357.5 % increase; 4.575 ± 0.297 a.u.; $p<0.001$; $n=3$) compared to their untreated counterparts. No difference ($p=0.96$) in cell viability was observed between the untreated and solvent control (Bar 2; 1.018 ± 0.018 a.u.; $n=3$) groups. Based on these results, we chose 25 mg/mL as the optimal working concentration of EO for all experiments performed in this study.

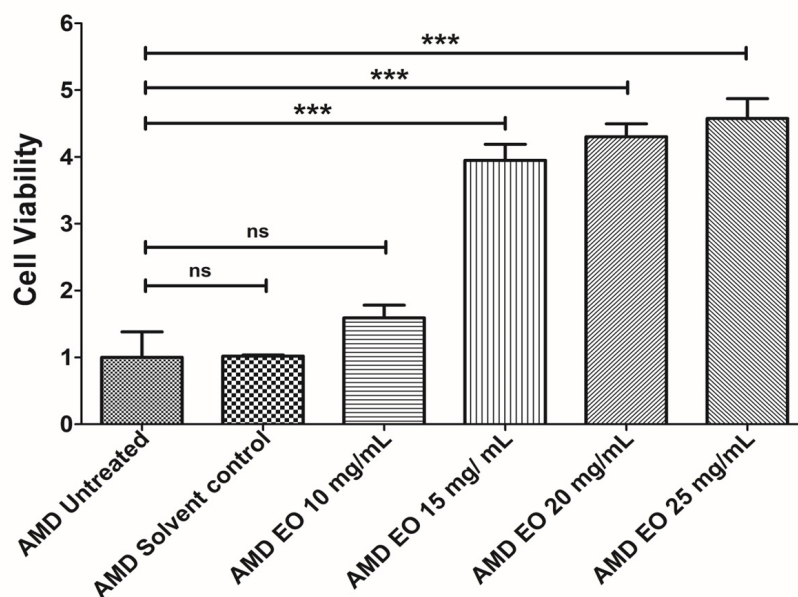


Figure 1. EO concentration optimization. Bar graph showing the effects of EO on cell death in AMD RPE cybrid cells. No difference was observed between the AMD untreated (bar 1) vs. AMD solvent control (bar 2) groups. Furthermore, no statistically significant difference was observed between untreated (bar 1) and 10 mg/mL EO-treated (bar 3) AMD cybrids. Higher viable cell numbers were observed in EO-treated AMD cybrids at concentrations of 15 mg/mL (bar 4), 20 mg/mL (bar 5), and 25 mg/mL (bar 6). *** indicates $p<0.001$; ns indicates non-significant p-value. Data are presented as mean \pm SEM and normalized to untreated AMD cybrids which were assigned a value of 1. Experiments were performed at the 24 h time-point.

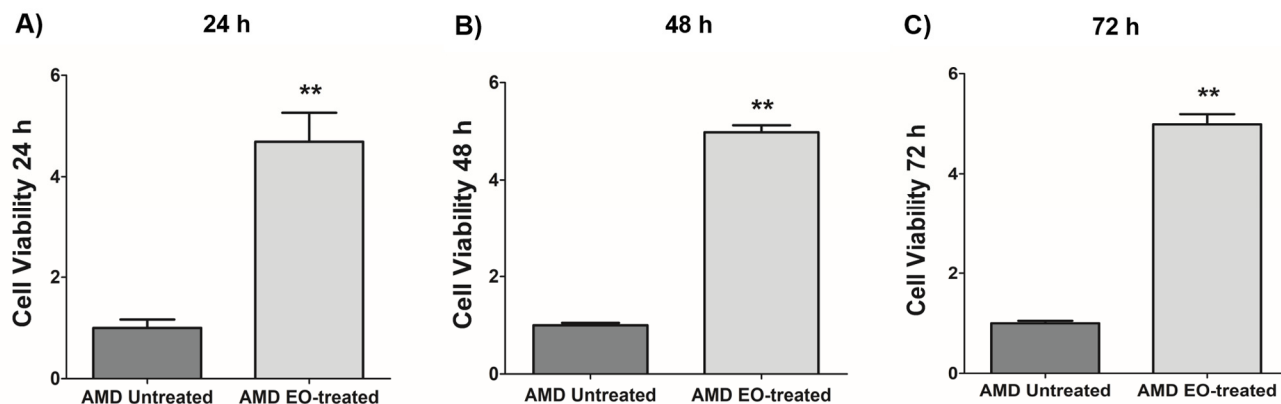


Figure 2. Effect of EO on cell viability. When treated with 25 mg/mL EO, AMD cybrid cells showed consistently increased viable cell numbers at 24 h (A), 48 h (B), and 72 h (C) compared to their untreated counterparts. ** indicates $p < 0.01$. Data are presented as mean \pm SEM and normalized to untreated AMD cybrids which were assigned a value of 1.

Effect of EO on cell viability

We next examined the effects of treatment of AMD RPE cybrids with 25 mg/mL EO over a time course i.e., at 24 h, 48 h, and 72 h post EO treatment (Figure 2). As anticipated, compared to their untreated counterparts, we observed significantly higher viable cell numbers in EO-treated AMD cybrids at 24 h (369 % increase; AMD untreated: 1 ± 0.166 a.u., AMD EO-treated: 4.69 ± 0.571 a.u.; $p=0.002$; $n=6$) (Figure 2A), 48 h (398.1 % increase; AMD untreated: 1 ± 0.049 a.u., AMD EO-treated: 4.981 ± 0.145 a.u.; $p=0.008$; $n=5$) (Figure 2B), and 72 h (398.8 % increase; AMD untreated: 1 ± 0.049 a.u., AMD EO-treated: 4.988 ± 0.203 a.u.; $p=0.008$; $n=5$) (Figure 2C), suggesting that EO is able to rescue AMD cybrids from cell death [13].

Effect of EO on Caspase-3/7 and NucLight staining

To compare the effects of EO on Caspase-3/7 activity, we morphologically monitored the kinetic activation of Caspase-3/7 using IncuCyte® live-cell imaging (Figure 3). Figure 3A shows representative overlap live-cell images of AMD RPE cybrids stained with Caspase-3/7 Green + NucLight Red reagents. The left panel represents untreated AMD cybrids and the right panel represents EO-treated AMD cybrids. We observed that EO reduced the number of Overlap object count (Yellow) (i.e., Caspase-3/7 Green + NucLight Red staining / NucLight Red object count) at 24 h (34.8 % decrease; AMD untreated: 1 ± 0.076 a.u., AMD EO-treated: 0.652 ± 0.032 a.u.; $p=0.029$; $n=4$) (Figure 3B) and 48 h (22.7 % decrease; AMD untreated: 1 ± 0.032 a.u., AMD EO-treated: 0.773 ± 0.023 a.u.; $p=0.001$, $n=4$) (Figure 3C).

These results suggest that EO can mitigate Caspase-3/7 mediated apoptosis in AMD RPE cybrids.

Effect of EO on Caspase-3 and MT-RNR2 gene expression

Treatment with EO led to significant downregulation of *Caspase-3* gene (60 % decrease; AMD untreated: 1 ± 0.063 a.u.; AMD EO-treated: 0.400 ± 0.112 a.u.; $p=0.008$; $n=5$) (Figure 4A), suggesting that EO reduces caspase-3-mediated apoptosis in AMD cybrids. Moreover, upregulation of the mitochondria derived peptide (MDP)-coding *MT-RNR2* gene (3006 % increase; AMD untreated: 1 ± 0.231 a.u.; AMD EO-treated: 31.06 ± 11.93 a.u.; $p=0.008$; $n=5$) (Figure 4B) was observed in EO-treated AMD cybrids compared to untreated cells, suggesting higher MDP production as a result of EO treatment.

Effect of EO on ROS assay and SOD2 gene expression

To measure reactive oxygen species levels, we performed ROS assay using H2DCFDA reagent. Addition of EO to AMD cybrids reduced ROS levels at 24 h, 48 h and 72 h time points: 24 h (39.4 % decrease; AMD untreated: 1 ± 0.082 a.u., AMD EO-treated: 0.606 ± 0.023 a.u.; $p=0.008$, $n=5$) (Figure 5A), 48 h (41.1 % decrease; AMD untreated: 1 ± 0.076 a.u., AMD EO-treated: 0.589 ± 0.011 a.u.; $p=0.008$, $n=5$) (Figure 5B), and 72 h (43.9 % decrease; AMD untreated: 1 ± 0.166 a.u., AMD EO-treated: 0.561 ± 0.009 a.u.; $p=0.008$, $n=5$) (Figure 5C). Furthermore, EO-treated AMD cybrids showed upregulation of *SOD2* gene compared to their untreated counterparts (357.3 % increase; AMD

untreated: 1 ± 0.133 a.u.; AMD EO-treated: 4.573 ± 0.533 a.u.; $p=0.029$; $n=4$) (Figure 5D). These results

suggest that EO can reduce oxidative stress in AMD cybrids.

A) Caspase-3/7 Green + NuLight Red Overlap Representative images

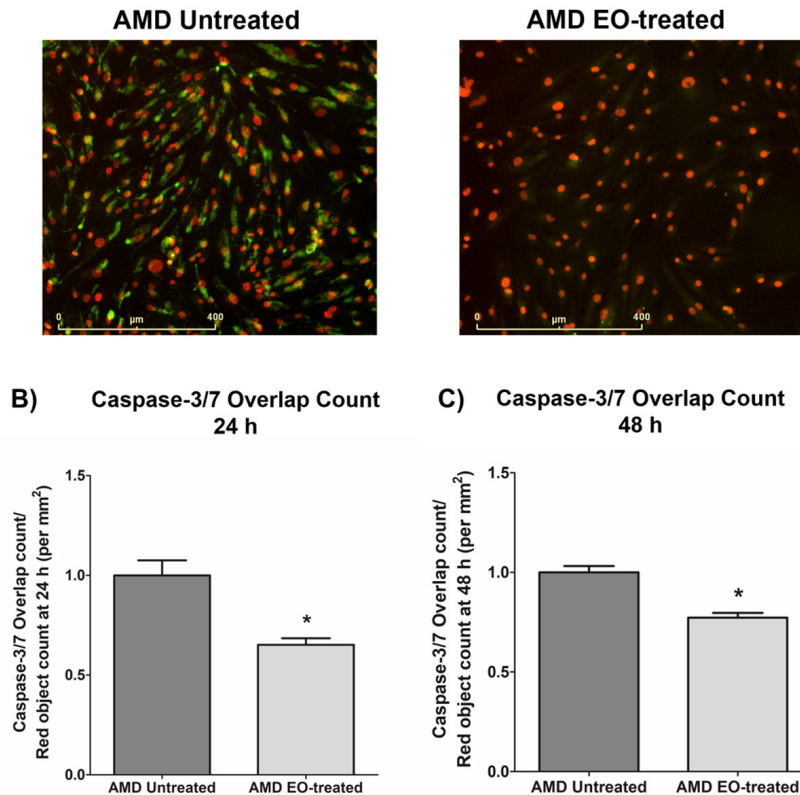


Figure 3. Effect of EO on Caspase-3/7 and NuLight staining. This figure shows representative IncuCyte live-cell images of untreated and EO-treated AMD cybrid cells stained with NuLight Red and Caspase-3/7 Green reagent (A), and quantitation graphs for Caspase-3/7 Green and NuLight Red staining at the 24 h (B) and 48 h (C) time points. * indicates $p<0.05$. Data are presented as mean \pm SEM, normalized to untreated AMD cybrids, which were assigned a value of 1.

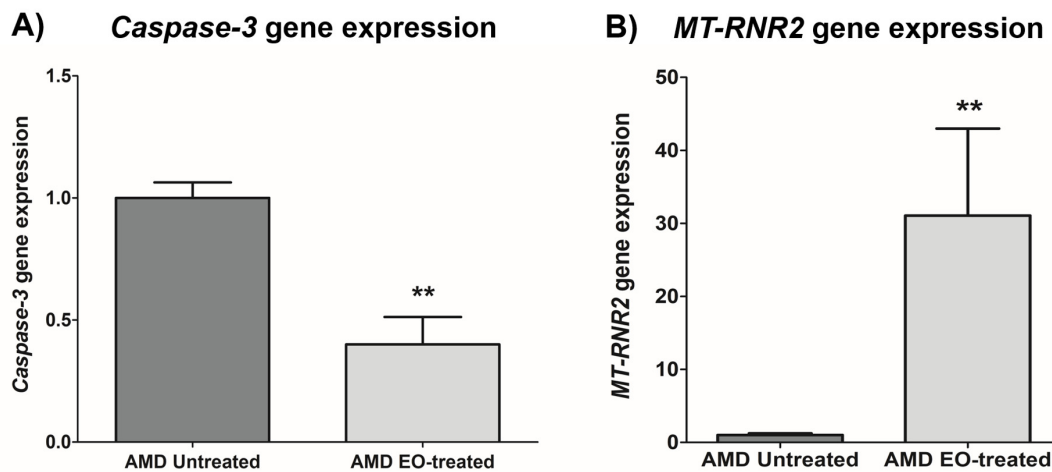


Figure 4. Effect of EO on Caspase-3 and MT-RNR2 gene expression. Treatment of AMD cybrids with EO reduced the gene expression of Caspase-3 (A) and up-regulated MT-RNR2 gene (B). ** indicates $p<0.01$. Data are presented as mean \pm SEM and normalized to untreated AMD cybrids which were assigned a value of 1.

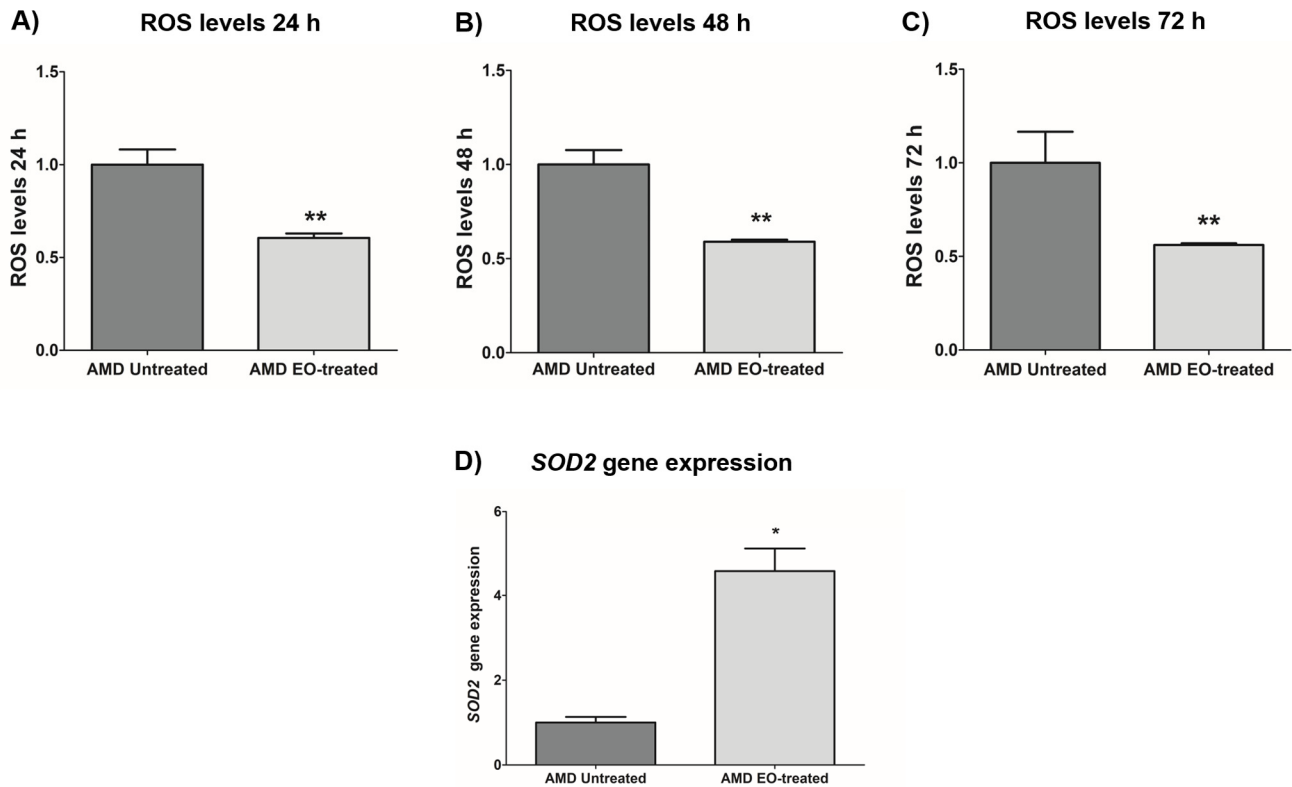


Figure 5. Effect of EO on ROS assay and *SOD2* gene expression. Addition of EO lowered ROS levels in AMD cybrids at 24 h (A), 48 h (B), and 72 h (C) time points. (D) shows increased expression of the antioxidant gene, *SOD2*, as a result of treatment with EO. ** and * indicate $p < 0.01$ and $p < 0.05$ respectively. Data are presented as mean \pm SEM and normalized to untreated AMD cybrids which were assigned a value of 1.

Effect of EO on mitochondrial membrane potential and *PGC-1 α* gene expression

Compared to their untreated counterparts, EO-treated AMD cybrids showed elevated mitochondrial membrane potential at 24 h post-treatment (169.3 % increase; AMD untreated: 1 ± 0.139 a.u., AMD EO-treated: 2.693 ± 0.246 a.u.; $p = 0.029$, $n = 4$) (Figure 6A). Moreover, EO-treated AMD cybrids showed up-regulation of the *PGC-1 α* gene (1498 % increase; AMD untreated: 1 ± 0.277 a.u.; AMD EO-treated: 15.98 ± 1.589 a.u.; $p = 0.029$; $n = 4$) (Figure 6B). These results suggest that EO promotes mitochondrial health and function in AMD cybrids.

Effect of EO on *VEGF* gene expression and on cell viability and ROS levels in amyloid- β -stressed AMD cells

Since VEGF has been implicated in the etiology of AMD, we next sought to compare *VEGF* gene expression between untreated and EO-treated AMD cybrids. We observed significant downregulation of *VEGF* gene

in EO-treated AMD cybrids compared to untreated cybrids (64.7 % decrease; AMD untreated: 1 ± 0.066 a.u.; AMD EO-treated: 0.353 ± 0.132 a.u.; $p = 0.029$; $n = 4$) (Figure 7A).

As amyloid- β is a component of drusen deposits formed in AMD, it is also important to determine the effect of EO treatment on amyloid- β -induced damage in AMD cybrids. Our previous studies have established that exogenously added amyloid- β_{1-42} (active form) peptides stressed AMD RPE cybrid cells. [13-14] Therefore, we analyzed the effects of EO against amyloid- β -induced damage in AMD cybrids using amyloid- β_{1-42} (active form) and amyloid- β_{42-1} (inactive scrambled control) peptides. Pretreatment with EO preserved the viable cell number and reduced ROS levels in amyloid- β_{1-42} -treated AMD cybrids. In terms of cell viability (Figure 7B), there was a 263.36 % increase in viable cell number in EO + amyloid- β_{1-42} treated versus amyloid- β_{1-42} alone-treated AMD cybrids (AMD amyloid- β_{1-42} : 0.625 ± 0.039 a.u.; AMD EO + amyloid- β_{1-42} : 2.271 ± 0.258 ; $p < 0.001$; $n = 4$) (Figure 7B – bar 2 vs. bar 5). No difference in cell viability was observed between untreated

and amyloid- β_{42-1} (scrambled control)-treated (0.927 ± 0.054 ; $p=0.364$; $n=4$) AMD cybrids. AMD cybrids treated with EO-alone (4.213 ± 0.242 , $n=4$) served as one of the controls. Furthermore, as shown in Figure 7C, pretreatment with EO reduced ROS levels by 74.1 % in EO + amyloid- β_{1-42} treated versus amyloid- β_{1-42} alone-treated AMD cells (AMD amyloid- β_{1-42} : 1.193 ± 0.025 a.u.; AMD EO + amyloid- β_{1-42} : 0.309 ± 0.028

a.u.; $p<0.001$; $n=3$) (Figure 7C – bar 2 vs. bar 5). No difference in ROS levels was observed between untreated and amyloid- β_{42-1} (scrambled control)-treated (1.047 ± 0.112 ; $p=0.723$; $n=3$) AMD cybrids. EO-alone-treated AMD cybrids (0.316 ± 0.015 , $n=3$) served as one of the controls. These results suggest that EO can rescue AMD RPE cybrid cells from cellular stress induced by amyloid- β *in vitro*.

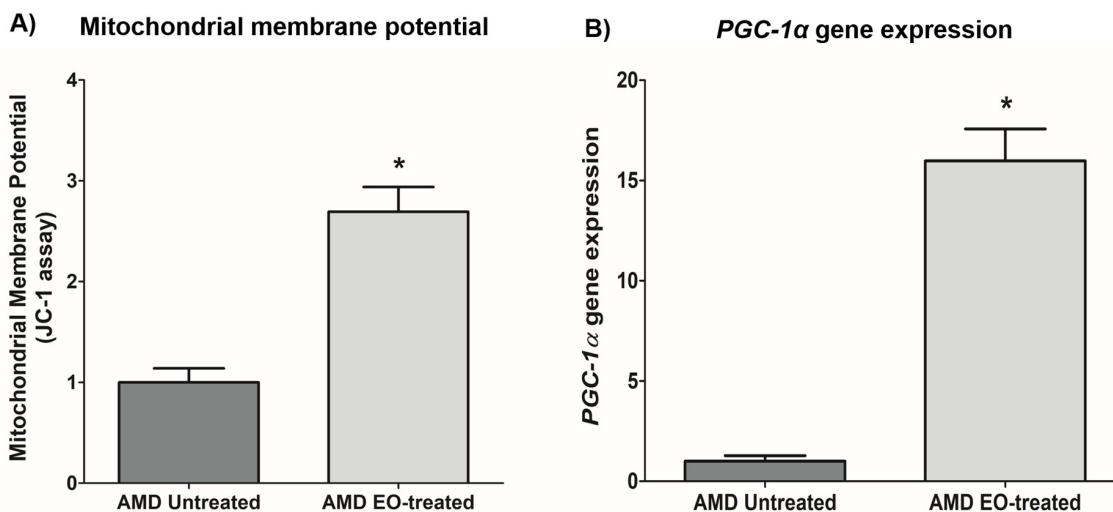


Figure 6. Effect of EO on mitochondrial membrane potential and *PGC-1 α* gene expression. This figure shows increased mitochondrial membrane potential in EO-treated AMD RPE cells (A), and increased *PGC-1 α* gene expression in EO-treated AMD cybrids (B). * indicates $p<0.05$. Data are presented as mean \pm SEM and normalized to untreated AMD cybrids which were assigned a value of 1.

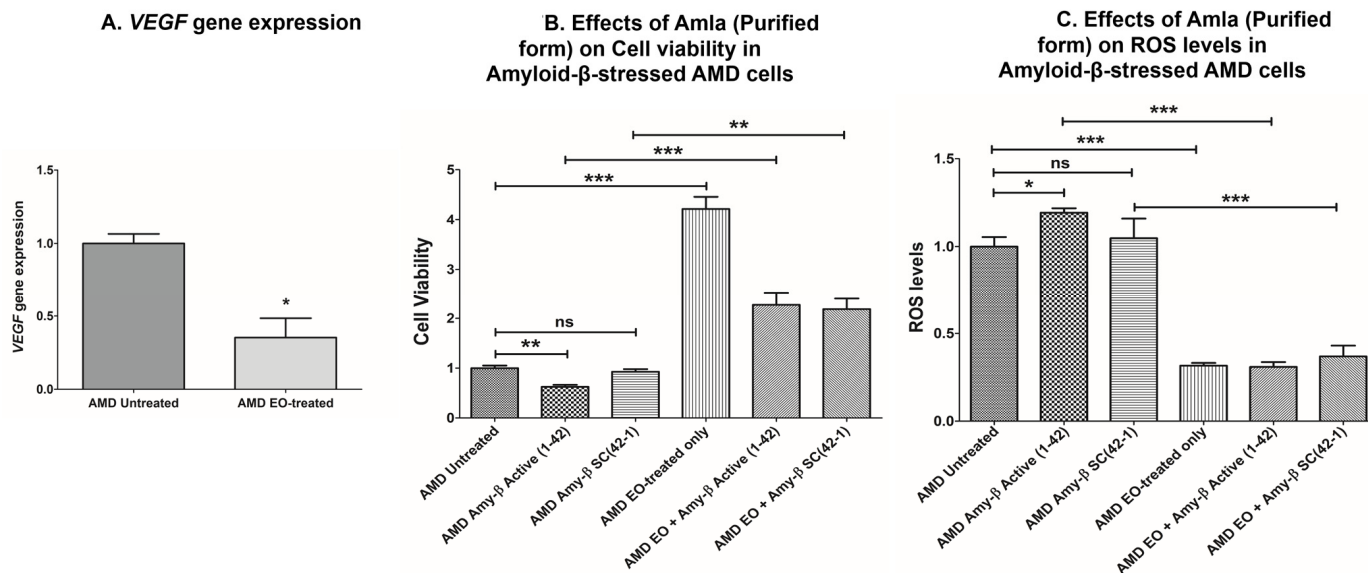


Figure 7. Effect of EO on *VEGF* gene expression, and on cell viability and ROS levels in amyloid- β -stressed AMD cells. This figure showed down-regulation of *VEGF* gene in EO-treated AMD cybrids (A). Pretreatment with EO rescued AMD cybrids from amyloid- β -induced damage as shown by changes in cell viability (B) (bar 2 versus bar 5) and ROS levels (C) (bar 2 versus bar 5). *, **, and *** indicate $p<0.05$, $p<0.01$, and $p<0.001$ respectively; ns indicates non-significant p-value. Data are presented as mean \pm SEM and normalized to untreated AMD cybrids which were assigned a value of 1.

DISCUSSION

In the present study, we report the protective role of *Emblica officinalis* in rescuing human AMD RPE cybrid cells from damage. Herein, we analyzed the effects of exogenously added EO on the viable cell numbers, ROS levels, mitochondrial membrane potential, gene expression of *Caspase-3*, *SOD2*, *PGC-1 α* , *MT-RNR2*, and *VEGF*, and against amyloid- β -induced toxicity in AMD RPE transmitochondrial cybrid cell lines *in vitro*.

We began our EO study by testing a varying range of concentrations of EO i.e., 10, 15, 20, and 25 mg/mL in AMD RPE cybrids *in vitro* and chose EO concentration of 25 mg/mL as the final optimal working concentration for all experiments. To our knowledge, this is the first study investigating the effects of EO on RPE cybrids containing damaged AMD mitochondria [13]. According to previous literature, varying doses of EO fruit extract are administered depending on the species, the model system, and nature of the study. For instance, Rao et al. found clinically relevant concentrations at 1–100 μ g/ml of EO fruit extract to be effective in human umbilical vein endothelial cells (HUVEC) *in vitro* [15]. Yamamoto et al. demonstrated that treatment with 100–200 μ g/mL EO was effective in C2C12 myoblasts, a skeletal muscle cell line, *in vitro* [16]. However, *in vivo* and human studies required higher concentrations of EO fruit extract. For example, Lim et al. showed administration of 300 mg/kg EO to Sprague-Dawley (SD) rats was effective [17]. In diabetic studies, human subjects were given oral concentrations of EO at 1 g/mL, 2 g/mL, and 3 g/mL in water [6].

We next characterized the cytoprotective role of EO in AMD cybrids. Comparison of cell viability between untreated and EO-treated AMD cybrids demonstrated consistently higher viable cell numbers in EO-treated AMD cybrids at 24 h, 48 h and 72 h post EO-treatment. Our observations were consistent with previous studies that have highlighted the cytoprotective role of EO. For example, EO at a concentration of 500 mg/kg significantly increased cell viability, thereby rescuing splenocytes from arsenic-induced cell damage in mice [18]. Another recent finding revealed attenuation of t-BHP-induced cytotoxicity by pretreatment with EO for 48 h in a murine skeletal muscle cell line [16]. EO was shown to inhibit chromium-induced toxicity by enhancing percent cell survival and cell proliferation in an *in vitro* murine macrophage model [19]. In addition, EO prevented apoptotic cell death and enhanced cell proliferation in lymphocytes isolated from Sprague-Dawley rats [20]. Another study demonstrated the role of EO as a cytoprotectant *in vivo* [21].

It has been established previously that AMD RPE transmitochondrial cybrid cells are damaged due to diseased AMD mitochondria and undergo apoptotic cell death [13–14]. Therefore, to examine the effects of EO on apoptosis markers, we next examined the effects of EO administration on Caspase-3/7 activity using IncuCyte® live-cell imaging system and reagents. The NucLight reagent (Red) stains nuclei in live cells and the Caspase-3/7 reagent (Green) enables real-time quantification of cells undergoing caspase-3/7 mediated apoptosis. Our data revealed that EO-treated AMD cybrids had reduced Caspase-3/7 activity compared to their untreated counterparts. Moreover, AMD cybrids treated with EO had reduced expression levels of *Caspase-3* gene compared to untreated AMD cybrids. To our knowledge, this is the first study to report such EO effects in human AMD cybrids. However, addition of EO has been reported to decrease caspase-3 activity and to protect against arsenic-induced toxicity in thymocytes of mice [22]. Another study reported that co-treatment with EO reduced caspase-3 activity in splenocytes *in vitro* [18]. The same study used Annexin V/PI binding experiment to demonstrate that co-treatment with EO reduced the number of apoptotic and necrotic cells [18].

Enhanced production of reactive oxygen species (ROS) is associated with damaged mitochondria and deterioration of mitochondrial health and function [23]. AMD RPE transmitochondrial cybrid cells used in this study have higher levels of mitochondrial ROS compared to normal RPE transmitochondrial cells [13]. In the current study, we used H2DCFDA, a chemically reduced form of fluorescein, as an indicator of ROS in AMD cybrids and observed that EO induces a consistent ROS-reducing effect in AMD cybrids at 24 h, 48 h, and 72 h post treatment. This finding is critical since elevated ROS levels have been implicated in the pathogenesis of numerous aging-related diseases [24–26] including retinal diseases such as AMD, diabetic retinopathy, glaucoma, etc. [27]. Quantitative RT-PCR analyses revealed that treatment with EO increased the transcript levels of *SOD2*, the mitochondrial superoxide dismutase which plays an antioxidant role in preserving cellular health in AMD. [28] This is a key finding since *SOD2* deficiency contributes to oxidative damage in RPE and development of AMD pathogenesis [29]. Our current results are consistent with previous studies that have highlighted the crucial role of EO as a potential antioxidant [4,30–31] in combating oxidative stress in aging-related diseases/disorders such as diabetes, renal dysfunction, hyperlipidaemia, etc. [32–34]. Elevated ROS levels can cause VEGF (Vascular Endothelial Growth Factor) activation thereby triggering angiogenesis and subsequent choroidal neovascularization in wet AMD [35–36]. In our previous studies, we found

significant up-regulation of *VEGF* gene in AMD RPE transmitochondrial cybrid cells compared to age-matched normal RPE transmitochondrial cybrid cells (Data not shown). Interestingly, in the present study, EO decreased the *VEGF* gene levels in AMD cybrids, suggesting that EO might help in reducing VEGF-induced neovascularization in AMD. This data is consistent with reports by Lu et al. wherein an EO preparation inhibited VEGF-induced angiogenesis via suppression of VEGF receptor activity [37].

Using the JC-1 dye, we compared the mitochondrial membrane potential ($\Delta\Psi_m$) between untreated and EO-treated AMD cybrids, and found significantly higher $\Delta\Psi_m$ in EO-treated AMD cybrids. Therefore, EO can enhance the oxidative redox state of AMD cybrids, contributing to preservation of mitochondrial integrity and function in AMD cybrids. Our data were in agreement with recent studies showing that EO positively contributes to mitochondrial health by enhancing the spare respiratory capacity [16]. QRT-PCR analyses demonstrated that EO-treated AMD cybrids had significant upregulation of *PGC-1 α* (peroxisome proliferator-activated receptor gamma coactivator 1- α) gene compared to untreated AMD cybrids. *PGC-1 α* is an important regulator of mitochondrial biogenesis and its downregulation contributes to AMD pathology [38]. Moreover, PGC-1 α drives human RPE mitochondrial function and induces antioxidant capacity [39].

Drusen deposit formation under the retina is a characteristic feature in AMD [40]. Amyloid- β is a common protein found in retinal drusen deposits [41-42] and in the brains of patients with Alzheimer's disease [43-44]. Therefore, we tested the effects of EO on amyloid- β -induced toxicity. The AMD cybrids were pretreated with EO followed by exposure to amyloid- β peptides. The EO pretreatment rescued AMD cybrids from amyloid- β -induced cellular damage as demonstrated by higher cell viability and lower ROS levels. Similar results were observed in an *in vivo* model of Alzheimer's disease wherein oral administration of EO attenuated amyloid-induced toxicity [5].

To speculate a mechanism by which EO mediates its protective action in AMD cybrids, we measured the expression of *MT-RNR2* gene using TaqMan probes. Significant up-regulation of the MDP-coding *MT-RNR2* gene was observed in EO-treated AMD cybrids compared to the untreated cells. Since MDPs have been assigned a cytoprotective role in AMD [13-14] and other age-related diseases [45], EO-mediated cytoprotection in the AMD cybrids may be partly attributed to higher expression of the *MT-RNR2* gene. Another plausible mechanism by which EO confers its protective

effects in AMD cybrids could be via aldose reductase inhibition. It is known that tannins, which are one of the components of EO, possess aldose reductase inhibitor activity [46]. Aldose reductase, an enzyme involved in glucose metabolism, has been associated with the pathogenesis of retinal diseases including diabetic retinopathy and cataract [47-50]. Chang et al. demonstrated that overexpression of aldose reductase is associated with activation of retinal microglia in mice. Since retinal microglia are immune cells that mediate inflammatory responses in the eye, their activation causes secretion of pro-inflammatory cytokines thereby contributing to the pathogenesis of eye diseases. However, suppression of aldose reductase prevents retinal microglia activation and migration, subsequently preventing ocular inflammation and disease development [51].

In conclusion, treatment with purified EO extract preserves mitochondrial and cellular health and function in human AMD RPE cybrids, implying that EO mitigates aging-related damage in AMD. Since EO extract is an over-the-counter nutraceutical and is available in both liquid and capsule forms for easy consumption, it might serve as an effective, inexpensive, and non-invasive therapeutic option for treatment of AMD. Further studies are required to fully understand the precise mechanisms that orchestrate the protective events post EO treatment in AMD cells.

MATERIALS AND METHODS

Human Subjects

The Institutional review board of the University of California Irvine approved research with human subjects (Approval #2003-3131). All participating subjects provided informed consent and clinical investigations were performed according to the tenets of Declaration of Helsinki.

Cell culture

Human AMD RPE transmitochondrial cells were created by fusing mitochondria DNA-deficient APRE-19 (*Rho0*) cells with platelets isolated from AMD patient's blood as described previously. [13] Passage 5 cells were used for all experiments (n=3-6).

Treatment with *Emblca Officinalis* (EO)

Purified EO extract was obtained and used at a concentration of 25 mg/mL for all experiments. DMSO was used as an initial solvent. EO was subsequently dissolved in culture media for cell treatment.

Cell viability assay (MTT assay)

The numbers of viable cells were measured using the MTT (3-(4,5-dimethylthiazol-2-yl)-2,5-diphenyltetrazolium bromide) assay (Cat.# 30006, Biotium, Fremont, CA). Cells were plated in 96-well tissue culture plates and treated with 25 mg/mL EO for 24 h and 48 h. Cells were incubated with MTT reagent at 37 °C for 1 h, followed by addition of DMSO. Signal absorbance was measured at 570 nm and background absorbance was measured at 630 nm. Normalized absorbance values were obtained by subtracting background absorbance from signal absorbance. The colorimetric signal obtained was proportional to the cell number.

IncuCyte Live-cell imaging

The IncuCyte NuLight Rapid Red Reagent (Cat.# 4717, IncuCyte, Ann Arbor, MI) is a cell permeable DNA stain that specifically stains nuclei in live cells and enables real-time quantification of cell proliferation.

The IncuCyte Caspase-3/7 Green Apoptosis Reagent (Cat.# 4440, IncuCyte) couples the activated Caspase-3/7 recognition motif (DEVD) to a DNA intercalating dye and enables real-time quantification of cells undergoing caspase-3/7 mediated apoptosis. This reagent is an inert, non-fluorescent substrate which when added to culture medium, crosses the cell membrane where it is cleaved by activated caspase-3/7 resulting in the release of the DNA dye and fluorescent staining of the nuclear DNA.

Cells were seeded in 96-well plates at a density of 5000 – 10,000 cells/well, treated with EO, followed by staining with IncuCyte® NuLight Rapid Red (1:500) and Caspase-3/7 Green (1:1000) labeling reagents. Stained cell plates were placed into the IncuCyte® live-cell analysis system and allowed to warm to 37 °C for 30 min prior to scanning. Phase Contrast, Green, and Red channels were selected, 5 images were taken per well with an average scan interval of ~2 h until the experiment was complete. Fluorescent objects were quantified using the IncuCyte® integrated analysis software that minimizes background fluorescence.

Reactive Oxygen Species (ROS) assay

To quantitate ROS levels, the cell-permeant H2DCFDA (2', 7'-dichlorodihydrofluorescein diacetate) was used as an indicator for ROS in cells. Stock solution of 5mM H2DCFDA was prepared in DMSO. Stock solution was then diluted in DPBS to obtain a working concentration of 10 μM. Cells were plated in 96-well tissue culture plates followed by treatment with 25 mg/mL EO. 10

μM H2DCFDA solution was added to cells and incubated for 30 min at 37 °C. H2DCFDA was then replaced with DPBS. Fluorescence which was measured at excitation 4924 nm and emission 520 nm was proportional to ROS levels in cells.

Mitochondrial membrane potential (JC-1) assay

The JC-1 assay (Cat.# 30001-T, Biotium) uses a unique cationic dye i.e., 5,5',6,6'-tetrachloro-1,1',3,3'- tetraethylbenzimidazolylcarbocyanine iodide, to detect loss of mitochondrial membrane potential. JC-1 1X reagent was prepared by diluting 100X JC-1 reagent in assay buffer to 1:100 dilutions. Cells were plated in 24-well tissue culture plates followed by treatment with 25 mg/mL EO. 1X JC-1 reagent was added to cells and incubated for 15 min at 37 °C. JC-1 reagent in the wells was then replaced with DPBS and fluorescence was measured as follows: Red fluorescence (Live cells): Excitation 550 nm and Emission 600 nm; Green fluorescence (Apoptotic cells): Excitation 485 nm and Emission 535 nm. Ratio of Red/Green was used for analysis. Lower ratio corresponded to higher apoptotic/dead cell number.

Quantitative Real-Time PCR

RNA extraction, cDNA synthesis, and qRT-PCR analysis from EO-treated AMD cybrids were performed as described previously. [14] QuantiTect Primer Assays were used to study the expression of *Caspase-3* gene (Cat. # QT00023947, Qiagen, Germantown, MD), and *SOD2* gene (Cat. # QT01008693, Qiagen). KiCqStart® SYBR® green primers were used to examine the expression of *PGC-1α* and *VEGF* genes (Cat. # kspq12012, Sigma, St. Louis, MO). Specific housekeeper genes used were *HPRT1* (Cat. # QT00059066, Qiagen) and *HMBS* (Cat. # QT00014462). TaqMan gene expression master mix (Cat. # 4369016, Life Technologies) and TaqMan gene expression assays were used to examine the expression of the *MT-RNR2* gene (Assay ID: Hs02596860_s1, Life Technologies), for which *GAPDH* (Assay ID: Hs02786624_g1, Life Technologies) was used as a housekeeper gene. Data analysis was performed using $\Delta\Delta C_t$ method which was calculated by subtracting ΔC_t of the AMD group from ΔC_t of the normal group. ΔC_t was the difference between the C_t s (threshold cycles) of the target gene and C_t s of the housekeeper gene (reference gene). Fold change was calculated using the following formula: Fold change = $2^{\Delta\Delta C_t}$.

Statistical analysis

Non-parametric Mann-Whitney test (for 2 groups) or one-way ANOVA (for 3 or more groups) followed by

post-hoc Tukey–Kramer test (GraphPad Prism 5.0; GraphPad Software, CA, USA) were performed to analyze data between groups. P values < 0.05 were considered statistically significant.

AUTHOR CONTRIBUTIONS

S.N.: Designed and performed the experiments; acquired, analyzed, and interpreted data; wrote and edited the manuscript. R.K. and G.S.: Provided EO extract. M.C.K. and A.B.N.: Reviewed data and the manuscript. M.C.K., A.B.N., and B.D.K.: contributed reagents/materials/analysis tools.

CONFLICTS OF INTEREST

S.N.: none; R.K.: none; A.B.N.: none; G.S.: Nisarga Biotech Pvt Ltd.; B.D.K.: Clinical research: Alcon, Allergan, Apellis, Genentech, G.S.K. Ophthotech, Regeneron; Consultant: Alcon, Allergan, Catalyst, Genentech, Novartis, Ophthotech, Regeneron; Recipient: Allergan, Genentech, Novartis, Regeneron. M.C.K.: none

FUNDING

This research work was supported by the 2017 Genentech/ARVO AMD Translational Research Fellowship, RPB (Research to Prevent Blindness) pilot research grant, Arnold and Mabel Beckman Foundation, UCI School of Medicine, Discovery Eye Foundation, Guenther Foundation, Beckman Initiative for Macular Research, Polly and Michael Smith Foundation, Max Factor Family Foundation, Iris and B. Gerald Cantor Foundation; research was supported in part by an unrestricted grant from RPB. SN is a recipient of the 2017 Genentech/ARVO AMD Translational Research Fellowship and the 2016 RPB pilot research grant.

REFERENCES

1. Hasan R, Islam N, Islam R. Phytochemistry, pharmacological activities and traditional uses of *Emblica officinalis*: A review. *Int Curr Pharm J*. 2016; 5:14–21. <https://doi.org/10.3329/icpj.v5i2.26441>
2. Agte V, Bhute R, Pathare P, Nilegaonkar S. Factors Influencing the Antioxidant Potential of Amla and Its Products. *Br J Pharm Res*. 2014; 4:2575–84. <https://doi.org/10.9734/BJPR/2014/6643>
3. Middha SK, Goyal AK, Lokesh P, Yardi V, Mojamdar L, Keni DS, Babu D, Usha T. Toxicological Evaluation of *Emblica officinalis* Fruit Extract and its Anti-inflammatory and Free Radical Scavenging Properties. *Pharmacogn Mag*. 2015 (Suppl 3); 11:S427–33. <https://doi.org/10.4103/0973-1296.168982>
4. Carlsen MH, Halvorsen BL, Holte K, Bøhn SK, Dragland S, Sampson L, Willey C, Senoo H, Umezono Y, Sanada C, Barikmo I, Berhe N, Willett WC, et al. The total antioxidant content of more than 3100 foods, beverages, spices, herbs and supplements used worldwide. *Nutr J*. 2010; 9:3. <https://doi.org/10.1186/1475-2891-9-3>
5. Justin Thenmozhi A, Dhivyabharathi M, William Raja TR, Manivasagam T, Essa MM. Tannoid principles of *Emblica officinalis* renovate cognitive deficits and attenuate amyloid pathologies against aluminum chloride induced rat model of Alzheimer’s disease. *Nutr Neurosci*. 2016; 19:269–78. <https://doi.org/10.1179/1476830515Y.0000000016>
6. Akhtar MS, Ramzan A, Ali A, Ahmad M. Effect of Amla fruit (*Emblica officinalis* Gaertn.) on blood glucose and lipid profile of normal subjects and type 2 diabetic patients. *Int J Food Sci Nutr*. 2011; 62:609–16. <https://doi.org/10.3109/09637486.2011.560565>
7. Kanthe PS, Patil BS, Bagali SC, Reddy RC, Aithala MR, Das KK. Protective effects of Ethanolic Extract of *Emblica officinalis* (amla) on Cardiovascular Pathophysiology of Rats, Fed with High Fat Diet. *J Clin Diagn Res*. 2017; 11:CC05–09. <https://doi.org/10.7860/JCDR/2017/28474.10628>
8. Golechha M, Sarangal V, Ojha S, Bhatia J, Arya DS. Anti-Inflammatory Effect of *Emblica officinalis* in Rodent Models of Acute and Chronic Inflammation: Involvement of Possible Mechanisms. *Int J Inflam*. 2014; 2014:178408. <https://doi.org/10.1155/2014/178408>
9. Thilakchand KR, Mathai RT, Simon P, Ravi RT, Baliga-Rao MP, Baliga MS. Hepatoprotective properties of the Indian gooseberry (*Emblica officinalis* Gaertn): a review. *Food Funct*. 2013; 4:1431–41. <https://doi.org/10.1039/c3fo60237k>
10. Ngamkitidechakul C, Jaijoy K, Hansakul P, Soonthornchareonnon N, Sireeratawong S. Antitumour effects of *Phyllanthus emblica* L.: induction of cancer cell apoptosis and inhibition of in vivo tumour promotion and in vitro invasion of human cancer cells. *Phytother Res*. 2010; 24:1405–13. <https://doi.org/10.1002/ptr.3127>
11. Tahir I, Khan MR, Shah NA, Aftab M. Evaluation of phytochemicals, antioxidant activity and amelioration of pulmonary fibrosis with *Phyllanthus emblica* leaves. *BMC Complement Altern Med*. 2016; 16:406. <https://doi.org/10.1186/s12906-016-1387-3>
12. Nashine S, Chwa M, Kazemian M, Thaker K, Lu S, Nesburn A, Kuppermann BD, Kenney MC. Differential Expression of Complement Markers in Normal and

- AMD Transmitochondrial Cybrids. *PLoS One*. 2016; 11:e0159828. <https://doi.org/10.1371/journal.pone.0159828>
13. Nashine S, Cohen P, Chwa M, Lu S, Nesburn AB, Kuppermann BD, Kenney MC, Humanin G. Humanin G (HNG) protects age-related macular degeneration (AMD) transmitochondrial ARPE-19 cybrids from mitochondrial and cellular damage. *Cell Death Dis*. 2017; 8:e2951. <https://doi.org/10.1038/cddis.2017.348>
 14. Nashine S, Cohen P, Nesburn AB, Kuppermann BD, Kenney MC. Characterizing the protective effects of SHLP2, a mitochondrial-derived peptide, in macular degeneration. *Sci Rep*. 2018; 8:15175. <https://doi.org/10.1038/s41598-018-33290-5>
 15. Rao TP, Okamoto T, Akita N, Hayashi T, Kato-Yasuda N, Suzuki K. Amla (*Embllica officinalis* Gaertn.) extract inhibits lipopolysaccharide-induced procoagulant and pro-inflammatory factors in cultured vascular endothelial cells. *Br J Nutr*. 2013; 110:2201–06. <https://doi.org/10.1017/S0007114513001669>
 16. Yamamoto H, Morino K, Mengistu L, Ishibashi T, Kiriyaama K, Ikami T, Maegawa H. Amla Enhances Mitochondrial Spare Respiratory Capacity by Increasing Mitochondrial Biogenesis and Antioxidant Systems in a Murine Skeletal Muscle Cell Line. *Oxid Med Cell Longev*. 2016; 2016:1735841. <https://doi.org/10.1155/2016/1735841>
 17. Lim DW, Kim JG, Kim YT. Analgesic Effect of Indian Gooseberry (*Embllica officinalis* Fruit) Extracts on Postoperative and Neuropathic Pain in Rats. *Nutrients*. 2016; 8:E760. <https://doi.org/10.3390/nu8120760>
 18. Singh MK, Yadav SS, Yadav RS, Singh US, Shukla Y, Pant KK, Khattri S. Efficacy of crude extract of *Embllica officinalis* (amla) in arsenic-induced oxidative damage and apoptosis in splenocytes of mice. *Toxicol Int*. 2014; 21:8–17. <https://doi.org/10.4103/0971-6580.128784>
 19. Sai Ram M, Neetu D, Deepti P, Vandana M, Ilavazhagan G, Kumar D, Selvamurthy W. Cyto-protective activity of Amla (*Embllica officinalis*) against chromium (VI) induced oxidative injury in murine macrophages. *Phytother Res*. 2003; 17:430–33. <https://doi.org/10.1002/ptr.1157>
 20. Sai Ram M, Neetu D, Yogesh B, Anju B, Dipti P, Pauline T, Sharma SK, Sarada SK, Ilavazhagan G, Kumar D, Selvamurthy W. Cyto-protective and immunomodulating properties of Amla (*Embllica officinalis*) on lymphocytes: an in-vitro study. *J Ethnopharmacol*. 2002; 81:5–10. [https://doi.org/10.1016/S0378-8741\(01\)00421-4](https://doi.org/10.1016/S0378-8741(01)00421-4)
 21. Joshi S, Thatte U, and Shirish Joshi and Urmila Thatte. Pharmacological evaluation of cytoprotective potential of *Phyllanthus Emblica* (PE) and *Asparagus Racemosus* (AR) in preventing gastric erosions, ulcerations and inflammation induced in rats. *Natl J Physiol Pharm Pharmacol*. 2012; 2:172–78. <https://doi.org/10.5455/njppp.2012.2.172-178>
 22. Singh MK, Yadav SS, Gupta V, Khattri S. Immunomodulatory role of *Embllica officinalis* in arsenic induced oxidative damage and apoptosis in thymocytes of mice. *BMC Complement Altern Med*. 2013; 13:193. <https://doi.org/10.1186/1472-6882-13-193>
 23. Wang W, Gong G, Wang X, Wei-LaPierre L, Cheng H, Dirksen R, Sheu SS. Mitochondrial Flash: Integrative Reactive Oxygen Species and pH Signals in Cell and Organelle Biology. *Antioxid Redox Signal*. 2016; 25:534–49. <https://doi.org/10.1089/ars.2016.6739>
 24. Chandrasekaran A, Idelchik MD, Melendez JA. Redox control of senescence and age-related disease. *Redox Biol*. 2017; 11:91–102. <https://doi.org/10.1016/j.redox.2016.11.005>
 25. Jacob KD, Noren Hooten N, Trzeciak AR, Evans MK. Markers of oxidant stress that are clinically relevant in aging and age-related disease. *Mech Ageing Dev*. 2013; 134:139–57. <https://doi.org/10.1016/j.mad.2013.02.008>
 26. De la Fuente M, Miquel J. An update of the oxidation-inflammation theory of aging: the involvement of the immune system in oxi-inflamm-aging. *Curr Pharm Des*. 2009; 15:3003–26. <https://doi.org/10.2174/138161209789058110>
 27. Jarrett SG, Boulton ME. Consequences of oxidative stress in age-related macular degeneration. *Mol Aspects Med*. 2012; 33:399–417. <https://doi.org/10.1016/j.mam.2012.03.009>
 28. Kasahara E, Lin LR, Ho YS, Reddy VN. SOD2 protects against oxidation-induced apoptosis in mouse retinal pigment epithelium: implications for age-related macular degeneration. *Invest Ophthalmol Vis Sci*. 2005; 46:3426–34. <https://doi.org/10.1167/iovs.05-0344>
 29. Justilien V, Pang JJ, Renganathan K, Zhan X, Crabb JW, Kim SR, Sparrow JR, Hauswirth WW, Lewin AS. SOD2 knockdown mouse model of early AMD. *Invest Ophthalmol Vis Sci*. 2007; 48:4407–20. <https://doi.org/10.1167/iovs.07-0432>
 30. Kumari P, Khatkar BS. Assessment of total polyphenols, antioxidants and antimicrobial properties of aonla varieties. *J Food Sci Technol*. 2016; 53:3093–103. <https://doi.org/10.1007/s13197-016-2282-0>

31. Charoenteeraboon J, Wongnoppavich A, Soonthornchareonnon N, Jaijoy K, Sireeratawong S. Antioxidant activities of the standardized water extract from fruit of *Phyllanthus emblica* Linn. *Songklanakarin J Sci Technol*. 2010; 32:599–604.
32. Rao TP, Sakaguchi N, Juneja LR, Wada E, Yokozawa T. Amla (*Emblica officinalis* Gaertn.) extracts reduce oxidative stress in streptozotocin-induced diabetic rats. *J Med Food*. 2005; 8:362–68. <https://doi.org/10.1089/jmf.2005.8.362>
33. Yokozawa T, Kim HY, Kim HJ, Tanaka T, Sugino H, Okubo T, Chu DC, Juneja LR. Amla (*Emblica officinalis* Gaertn.) attenuates age-related renal dysfunction by oxidative stress. *J Agric Food Chem*. 2007; 55:7744–52. <https://doi.org/10.1021/jf072105s>
34. Yokozawa T, Kim HY, Kim HJ, Okubo T, Chu DC, Juneja LR. Amla (*Emblica officinalis* Gaertn.) prevents dyslipidaemia and oxidative stress in the ageing process. *Br J Nutr*. 2007; 97:1187–95. <https://doi.org/10.1017/S0007114507691971>
35. Schlingemann RO. Role of growth factors and the wound healing response in age-related macular degeneration. *Graefes Arch Clin Exp Ophthalmol*. 2004; 242:91–101. <https://doi.org/10.1007/s00417-003-0828-0>
36. Martin G, Schlunck G, Hansen LL, Agostini HT. Differential expression of angioregulatory factors in normal and CNV-derived human retinal pigment epithelium. *Graefes Arch Clin Exp Ophthalmol*. 2004; 242:321–26. <https://doi.org/10.1007/s00417-003-0838-y>
37. Lu K, Chakroborty D, Sarkar C, Lu T, Xie Z, Liu Z, Basu S. Triphala and its active constituent chebulinic acid are natural inhibitors of vascular endothelial growth factor- α mediated angiogenesis. *PLoS One*. 2012; 7:e43934. <https://doi.org/10.1371/journal.pone.0043934>
38. Kaarniranta K, Kajdanek J, Morawiec J, Pawlowska E, Blasiak J. PGC-1 α Protects RPE Cells of the Aging Retina against Oxidative Stress-Induced Degeneration through the Regulation of Senescence and Mitochondrial Quality Control. The Significance for AMD Pathogenesis. *Int J Mol Sci*. 2018; 19:E2317. <https://doi.org/10.3390/ijms19082317>
39. Iacovelli J, Rowe GC, Khadka A, Diaz-Aguilar D, Spencer C, Arany Z, Saint-Geniez M. PGC-1 α Induces Human RPE Oxidative Metabolism and Antioxidant Capacity. *Invest Ophthalmol Vis Sci*. 2016; 57:1038–51. <https://doi.org/10.1167/iovs.15-17758>
40. Schlanitz FG, Sacu S, Baumann B, Bolz M, Platzer M, Pircher M, Hitzengerger CK, Schmidt-Erfurth U. Identification of Drusen Characteristics in Age-Related Macular Degeneration by Polarization-Sensitive Optical Coherence Tomography. *Am J Ophthalmol*. 2015; 160:335–344.e1. <https://doi.org/10.1016/j.ajo.2015.05.008>
41. Crabb JW, Miyagi M, Gu X, Shadrach K, West KA, Sakaguchi H, Kamei M, Hasan A, Yan L, Rayborn ME, Salomon RG, Hollyfield JG. Drusen proteome analysis: an approach to the etiology of age-related macular degeneration. *Proc Natl Acad Sci USA*. 2002; 99:14682–87. <https://doi.org/10.1073/pnas.222551899>
42. Spaide RF, Curcio CA. Drusen characterization with multimodal imaging. *Retina*. 2010; 30:1441–54. <https://doi.org/10.1097/IAE.0b013e3181ee5ce8>
43. Allsop D, Mayes J. Amyloid β -peptide and Alzheimer's disease. *Essays Biochem*. 2014; 56:99–110. <https://doi.org/10.1042/bse0560099>
44. Murphy MP, LeVine H 3rd. Alzheimer's disease and the amyloid-beta peptide. *J Alzheimers Dis*. 2010; 19:311–23. <https://doi.org/10.3233/JAD-2010-1221>
45. Gong Z, Tas E, Muzumdar R. Humanin and age-related diseases: a new link? *Front Endocrinol (Lausanne)*. 2014; 5:210. <https://doi.org/10.3389/fendo.2014.00210>
46. Suryanarayana P, Kumar PA, Saraswat M, Petrash JM, Reddy GB. Inhibition of aldose reductase by tannoid principles of *Emblica officinalis*: implications for the prevention of sugar cataract. *Mol Vis*. 2004; 10:148–54.
47. Vineros SA, Campochiaro PA, Williams EH, May EE, Green WR, Sorenson RL. Aldose reductase expression in human diabetic retina and retinal pigment epithelium. *Diabetes*. 1988; 37:1658–64. <https://doi.org/10.2337/diab.37.12.1658>
48. Kinoshita JH, Fukushi S, Kador P, Merola LO. Aldose reductase in diabetic complications of the eye. *Metabolism*. 1979 (Suppl 1); 28:462–69.
49. Yadav UC, Srivastava SK, Ramana KV. Understanding the role of aldose reductase in ocular inflammation. *Curr Mol Med*. 2010; 10:540–49.
50. Snow A, Shieh B, Chang KC, Pal A, Lenhart P, Ammar D, Ruzycski P, Palla S, Reddy GB, Petrash JM. Aldose reductase expression as a risk factor for cataract. *Chem Biol Interact*. 2015; 234:247–53. <https://doi.org/10.1016/j.cbi.2014.12.017>
51. Chang KC, Shieh B, Petrash JM. Aldose reductase mediates retinal microglia activation. *Biochem Biophys Res Commun*. 2016; 473:565–71. <https://doi.org/10.1016/j.bbrc.2016.03.122>

A comprehensive evaluation of 181 reported *CHST6* variants in patients with macular corneal dystrophy

Jing Zhang¹, Dan Wu¹, Yue Li¹, Yidan Fan¹, Yiqin Dai¹, Jianjiang Xu¹

¹Department of Ophthalmology and Visual Science, Eye and ENT Hospital, Shanghai Medical College of Fudan University, NHC Key Laboratory of Myopia (Fudan University), Shanghai Key Laboratory of Visual Impairment and Restoration, Shanghai, China

Correspondence to: Jianjiang Xu; email: jianjiangxu@126.com

Keywords: *CHST6*, macular corneal dystrophy, genetic variants

Received: October 23, 2018

Accepted: January 25, 2019

Published: February 4, 2019

Copyright: Zhang et al. This is an open-access article distributed under the terms of the Creative Commons Attribution License (CC BY 3.0), which permits unrestricted use, distribution, and reproduction in any medium, provided the original author and source are credited.

ABSTRACT

Macular corneal dystrophy (MCD) is an autosomal recessive disease featured by bilateral progressive stromal clouding and loss of vision, consequently necessitating corneal transplantation. Variants in *CHST6* gene have been recognized as the most critical genetic components in MCD. Although many *CHST6* variants have been described until now, the detailed mechanisms underlying MCD are still far from understood. In this study, we integrated all the reported *CHST6* variants described in 408 MCD cases, and performed a comprehensive evaluation to better illustrate the causality of these variants. The results showed that majority of these variants (165 out of 181) could be classified as pathogenic or likely pathogenic. Interestingly, we also identified several disease causal variants with ethnic specificity. In addition, the results underscored the strong correlation between mutant frequency and residue conservation in the general population (Spearman's correlation coefficient = -0.311, $P = 1.20E-05$), thus providing potential candidate targets for further genetic manipulation. The current study highlighted the demand of further functional investigations to evaluate the causality of *CHST6* variants, so as to promote earlier accurate diagnosis of MCD and future development of potential targets for genetic therapy.

INTRODUCTION

Macular corneal dystrophy (MCD; OMIM 217800) is an autosomal recessive disease featured by bilateral progressive stromal clouding and loss of vision, finally necessitating corneal transplantation [1, 2]. Cases of MCD have been recognized worldwide, while it is found to have high prevalence in India, Saudi Arabia, and Iceland [3]. The clinical symptoms usually manifest in the first decade of life, presented by a diffuse central stromal haze that progressively extends to the periphery of the cornea, which yields loss of corneal transparency and decreased vision. It is reported that MCD constitutes 10% to 75% of the corneal dystrophies that demand corneal grafting [4]. Generally, MCD could be divided into three immunophenotypes (MCD types IA, I

and II) depending on the levels of keratan sulfate (KS) that detected in the serum and in the cornea. Patients with MCD type I lack KS in the serum and cornea, whilst patients with MCD type II contain detectable KS both in the serum and cornea [5]. The third type, IA, in which sulfated KS can be detected in the keratocytes instead of the serum and the cornea, has also been described [6].

Keratan sulfate plays a central role in maintaining corneal transparency. It is the major component of keratocan and lumican that are critical in collagen fibril organization. The sulfation of keratin in cornea is mediated through the corneal isoform of carbohydrate sulfotransferase 6 (*CHST6*), an enzyme which functions in catalyzing the transfer of a sulfate group to the GlcNAc residues of

keratan [7]. The *CHST6* (OMIM 605294) gene spans approximate 23 kb of the short arm of chromosome 16 (16q23.1) and consists of 4 exons and a 1,187 bp open reading frame. The encoded protein CHST6 contains 395 amino acids with a molecular weight of 44 kDa. Like other members of the carbohydrate sulfotransferase family, it includes a short cytosolic tail at the N-terminal, a single transmembrane span, and a C-terminal domain. The sulfate donor PAPS binding site that located in the C-terminal domain determines carbohydrate specificity in vivo [8]. Deficiency in *CHST6* may generate unsulfated polyactosamine chains that are less water-soluble than the fully sulfated keratan sulfate, and result in malformations in fibril organization in the cornea, which finally leads to progressive corneal opacification in MCD patients [9].

Variants in *CHST6* gene have been recognized as the most critical genetic components in MCD. To date, more than 100 frameshift, nonsense, or missense variants in *CHST6* were described in patients with MCD I/IA. In MCD II patients, large rearrangements and deletions in the upstream of *CHST6* were initially reported, followed by subsequent identification of mutations within the coding region of *CHST6* [4, 9–45]. However, substantial genetic heterogeneity still exists, and there is no study systematically evaluating *CHST6* variants in MCD patients, in particular with regards to genotype-phenotype correlation and informing on the significance of specific variants.

In the current study, we conducted a comprehensive evaluation of all 181 *CHST6* variants described in MCD patients, and then classified the pathogenicity of those variants according to the American College of Medical Genetics and Genomics (ACMG) guidelines [46].

RESULTS

The spectrum of *CHST6* variants

Totally, we retrieved information of 436 MCD cases reported in 38 articles. Most of these cases were Asian ethnicity (65%, 284 families), followed by Europeans (21%), Americans (12%) and Africans (2%, Figure 1). The age of disease onset in these reported MCD patients was highly variable, ranging from 6 to 57 years old, with the average onset age of 25.2 ± 11.8 years old. The number of females and males were almost identical, with no obvious gender preference. Four hundred and eight MCD cases were found to harbor potential pathogenic *CHST6* variants. Among them, 270 cases had homozygous *CHST6* variants, 98 cases carried compound heterozygous variants, and 40 cases have only a single variant. A total of 181 unique *CHST6* variants were previously reported, including 128 missense, 29 frameshift, 17 nonsense, and 4 non-frameshift variants, together with 3 deletions and/or rearrangements in the upstream region of *CHST6* (Supplementary Table 1).

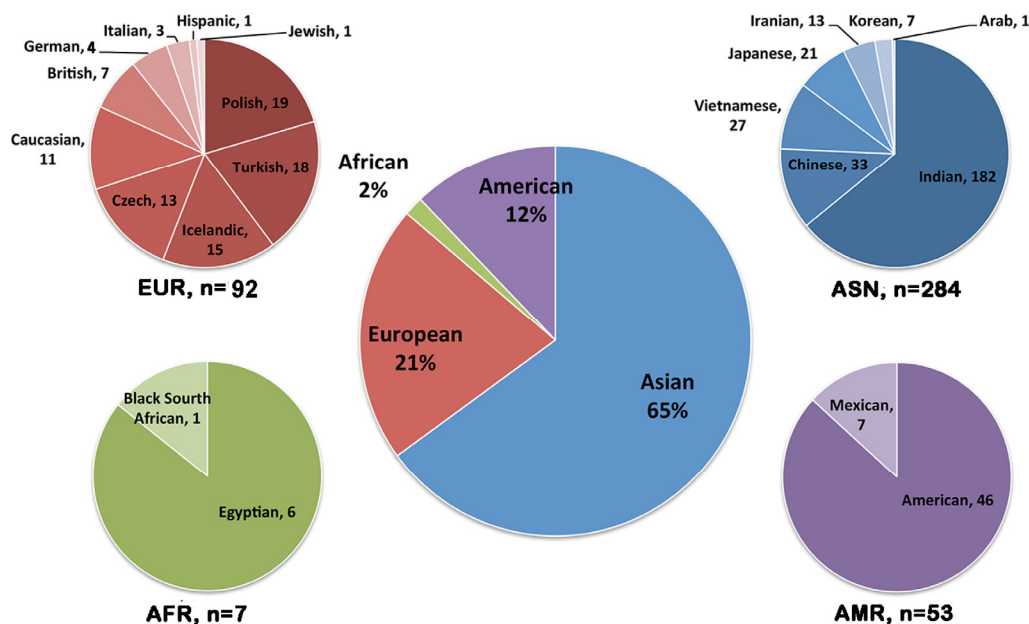


Figure 1. Population distribution of *CHST6* variants found in patients with macular corneal dystrophy (MCD). Pie-chart showing the number of MCD patients carrying *CHST6* variants in different countries and the percentage in the general population (middle).

Frequent CHST6 variants

The most frequently described *CHST6* variant was p.L200R, which was observed in 37 cases. This mutation was only described in Europeans and Americans, and many of the affected cases (23/37) were compound heterozygous for this mutation. The second most frequent variant was located at position 211, which has been observed in 21 cases. Three types of amino acid substitutions, including p.R211G, p.R211Q and p.R211W were identified here. Interestingly, these mutations were mainly found in Asian populations, except for a homozygous p.R211W mutation that was reported in three Turkish cases, as well as a compound heterozygous p.R211Q mutation found in a Germany patient. Of note, these frequent variants were located quite close to the sulfate donor (PAPS) binding site, implying their potential roles in affecting protein function. In general however, most of *CHST6* variants were identified in only one or a few patients, indicating the substantial genetic heterogeneity of MCD caused by *CHST6* variants. A complete list of *CHST6* variants with nucleotide and predicted amino acid changes was shown in Supplementary Table 1. The position of these variants, with regard to key domains, was illustrated in a schematic representation of the CHST6 protein (Figure 2).

Protein sequence alignment revealed that at least half of the reported *CHST6* variants that caused amino acid changes are conserved among various vertebrate species (Figure 3). Further, the normalized conservation score

of each residue in the CHST6 protein was calculated using the empirical Bayesian method, as implemented in the ConSurf Server (Shown in Supplementary Table 4), and compared with its mutated frequency detected in MCD patients. Both of the two measurements were transformed into z-scores before comparison. It was interesting to find that the number of patients who carried *CHST6* variants at each position was significantly correlated with the conservation score of the corresponding residue (Spearman's correlation coefficient = -0.311, $P = 0.000012$, shown in Figure 4).

Pathogenicity classification of all CHST6 variants

All the reported *CHST6* variants were classified based on the ACMG guidelines as described in Materials and Methods part. Finally, 62 variants were classified as pathogenic, 103 variants as likely pathogenic and 16 as being of uncertain significance.

Among the 49 protein-truncating variants, 32 of them were leading to a frameshift (including large deletions) and 17 were nonsense mutations. Majority of the truncating variants were rare, because only nine of them existed in the gnomAD database, with the frequency lower than $4.67E-05$. Protein truncating variants were considered to be pathogenic if they caused a termination of the protein before residue 298, since the p.Q298X variant has already been classified as pathogenic by the ClinVar database. It thus showed that 41 of them were classified to be pathogenic.

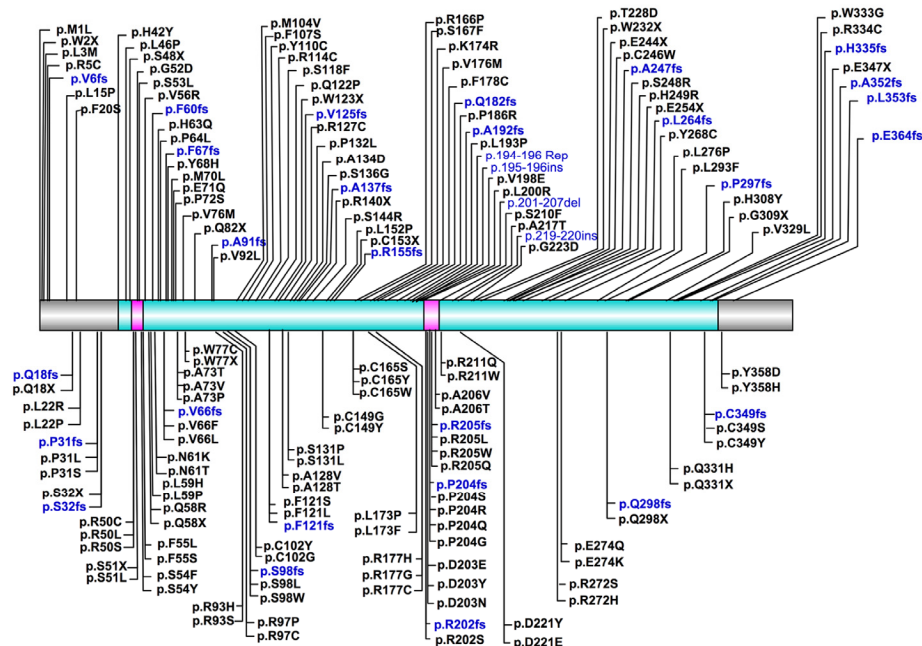


Figure 2. Schematic representation of position of CHST6 variants and its protein domains. The sulfotransferase domain (residue 42-356) was labeled in cyan, and the two PAPS binding sites (residue 49-55 and 202-210) were labeled in carmine.

A total of 128 missense variants in *CHST6* were identified in MCD patients, and 25 of them were classified as pathogenic by UniProt, and thereby were counted as strong evidence (PS1) of pathogenicity. Additional 31 variants occurred at the same amino acid residue with those established pathogenic variants were considered to show moderate evidence (PM5) of pathogenicity. Meanwhile, all the variants were absent from controls or at extremely low frequency in general populations, which was recognized as a moderate piece of evidence for pathogenicity (PM2). Majority of the in silico programs tested agreed on the protein-damaging prediction of these missense variants, and missense variations in *CHST6* were already recognized as a common cause of the disease, then these evidences can be counted as supporting (PP2 and PP3). Besides, the SMART prediction tool (<http://smart.emblheidelberg.de/>) was applied to retrieve *CHST6* protein domains and their location. It was shown that the key sulfotransferase domain ranged from residue 42 to 356, thus moderate evidence (PM2) for a variant to be pathogenic was considered if it occurred within this domain. Finally, after combining all the information in the pathogenicity evaluation, 21 missense variants were classified to be pathogenic, 100 missense variants to be likely pathogenic and 7 as being of uncertain significance. Of note, the most frequently described variant p.L200R has been classified as likely pathogenic, given the evidences of PM1, PM2, PP2, PP3 and PP5. The detailed results of ACMG classification for protein-truncating variants and missense variants were shown in Supplementary Tables 2 and 3, respectively.

DISCUSSION

To date, many efforts have been made on the molecular diagnosis of MCD, and the implementation of next-generation sequencing (NGS) in clinical diagnosis

greatly helps expand the genetic spectrums of MCD worldwide. In the current study, we performed a comprehensive evaluation on all the reported *CHST6* variants found in MCD patients, including the distribution of these variants across populations, the conservation scores among residues, the correlation between mutant frequency and residue conservation, and the potential genotype phenotype correlation. Accordingly, we further classified all the reported *CHST6* variants based on the ACMG guideline. To our knowledge, this is the first study comprehensively analyzing the genetic findings on MCD pathogenesis, and the current study may help shed light on earlier accurate diagnosis of MCD and future development of potential targets for genetic therapy.

In this study, we observed a high prevalence of MCD in Asians, in particular India, which can be attributed to the known high rate of consanguinity there [3]. We also found some causal variants with potential ethnic specificity, such as variant p.L200R and p.R211G, which have been discovered in Europeans/Americans or Asians, respectively. Importantly, we found a significant correlation between the mutant frequency and the conservation score of the corresponding residue. The top-5 most conserved residues were Ser53, Ser210, Asp203, Arg50, and Arg93, and four of them were located in the important PAPS binding site. For the most described variant p.L200R, its residue conservation score was -1.217, ranked 16. Currently, there are no animal models available that mimic human MCD, since the large number of genetic mutations in *CHST6* gene identified in MCD patients made it difficult to find a single target for genetic manipulation. However, those most conserved residues or the highly mutated residues in the general population might be potential candidates for further functional studies.

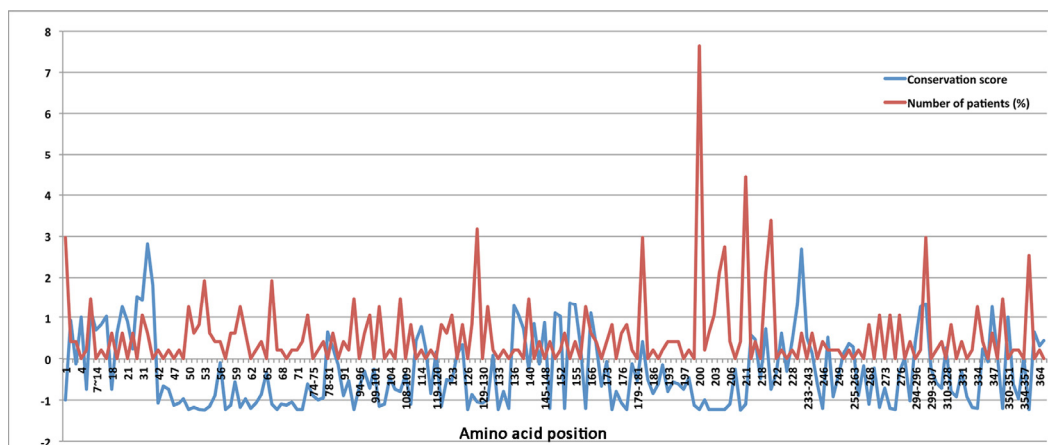


Figure 4. The normalized conservation scores (blue curve) for each residue in *CHST6* protein and the percentage of reported MCD patients who carried mutations in the corresponding position (red curve).

Functionally, owing to the abnormal sulfation caused by CHST6 variants, the keratin molecules cannot be metabolized and then were deposited in the cornea [47]. In addition, the collagen fibrils turned to be smaller, with a decrease in the interfibrillar spacing [48]. They together contributed to the loss of corneal transparency in MCD. It has also been demonstrated that CHST6 revealed a protective role on cell survival. For example, repression of CHST6 increased radiation-induced apoptosis of human Burkitt's lymphoma cells [49], and more relevantly, CHST6 deficiencies were found to trigger ER stress with considerable GRP78/CHOP upregulation and cell apoptosis in MCD keratocytes [23]. All of these evidences collectively highlighted the pivotal role of CHST6 in many cellular processes, such as ECM constitution, ER stress, apoptosis and so on. Individuals with CHST6 variants might experience similar corneal dystrophy symptoms, but the underlying mechanisms for their diseases might be different at the molecular level. For example, conserved variants located within the 5'PB domain like Arg205 or Asp203 may substantially reduce the ability to combine with PAPS [50], while other conserved variants with significant changes on residue polar or physiochemical property may impact the enzymatic activity. Whether and how these crucial variants act on different cellular processes need to be clarified. Therefore, further functional investigations on some potential key variants prioritized by this study may help promote the understanding of MCD pathogenesis to a much more in-depth level.

Several limitations of this study should also be noted here. Firstly, among the 408 MCD cases that harbored pathogenic *CHST6* variants, 298 of them carried homozygous or compound heterozygous variants, fulfilling the recessive inherited model of MCD. However, there was still 40 cases carried only one single heterozygous mutation. It was quite possible that a second mutation was missed by previous sequencing methods. Thus, some state of art techniques like targeted region deep sequencing of the complete gene or whole genome sequencing can be used. In addition, for some variants that weighted to be uncertain significance in this study, additional evidences are required to push them to robustly meet the criteria of pathogenicity categories, although these data are not available at this moment.

Secondly, although we collected clinical information including age of onset, gender, and disease phenotype of MCD patients recruited in previous studies, when available. Unfortunately, approximate two thirds of patients lacked phenotypic details, and most of previous studies did not investigate the distribution and reactivity of the KS in serum and cornea in these MCD patients.

Thus, we were unable to draw any conclusions with regards to the correlation between CHST6 variants and MCD immunophenotypes. The available data are still too scarce to make any correlations, implying the need for better characterization of this rare disease.

In summary, the current comprehensive evaluation contributed to the most updated *in-silico* classification of all reported CHST6 variants till now. Although the vast majority of CHST6 variants are likely to be protein damaging, systematic functional investigations are still in urgent need to demonstrate the pathogenicity of these variants.

MATERIALS AND METHODS

Databases and literature search

We retrieved all publications (assessed on Dec 10, 2018) from the following electronic databases: PubMed, EMBASE, and Medline, using the keywords "mutation" or "variant" combined with "CHST6" and "corneal dystrophy". All the relevant studies, including original articles, reviews, or case reports were carefully screened. The inclusion criteria applied in this process was shown as the following: (1) sequencing studies that report CHST6 variants found in corneal dystrophy patients; (2) sufficient data for collecting variants information and disease phenotype. Reviews or obvious duplicates were removed. Variant combinations, patients' ethnicity, and disease phenotype were collected. The number of MCD patients included in each study was recorded. Simultaneously, public databases were assessed through searches for "CHST6" in ClinVar, ClinVita, EmvClass, and Human Gene Mutation Database (HGMD). Identified variants were compared with those from the literature search. The whole research progress was approved by the Ethics Committee of Eye and ENT Hospital of Fudan University and was performed following the declaration of Helsinki.

Variant analysis

Each published variant was checked for accuracy and compared to the corresponding wide-type reference. When different reference sequences were used among publications, nucleotide and codon numbers were converted to ensure that their annotation matched with reference transcript NM_021615.4 for *CHST6*. The A of the ATG translation initiation codon was numbered as +1 and the initial codon as codon 1. Frequencies of the variants in control subjects were retrieved from the Genome Aggregation Database (gnomAD), which contains 123,136 exomes and 15,496 genomes from unrelated individuals worldwide (<http://gnomad.broadinstitute.org>).

Classification of variant pathogenicity

We evaluated the pathogenicity of all reported *CHST6* variants according to the ACMG guidelines, to classify all variants into one of the five following categories: benign, likely benign, uncertain significance, pathogenic, or likely pathogenic. Briefly, all variants were subjected to the ANNOVAR package (<http://www.openbioinformatics.org/annovar/>) for variant annotation, to obtain their allele frequency in public databases, in silico prediction scores, and other evidence of pathogenicity. Then, each pathogenic criterion was evaluated to be very strong (PVS1), strong (PS1-4), moderate (PM1-6), or supporting (PP1-5), and each benign criterion was evaluated to be stand-alone (BA1), strong (BS1-4), or supporting (BP1-6). After weighting these variants based on the observed evidence of pathogenicity, the criteria were then combined to choose a classification from the five-tier system.

Calculating the conservation scores

The conservation scores for all residues of *CHST6* protein, as well as their confidence intervals were calculated by the ConSurf package (<http://consurf.tau.ac.il/>), using the empirical Bayesian method with the default parameters. The scores were then normalized, so that the average score for all residues was zero, and the standard deviation was one. The lowest score represented the most conserved position in a protein.

AUTHOR CONTRIBUTIONS

JX and JZ designed the study; JZ, DW, YL, YF and YD collected the publications and analyzed the data; JZ drafted the manuscript; JX, DW, YL, YF, and YD revised the manuscript.

ACKNOWLEDGMENTS

The authors were sponsored by the National Natural Science Foundation of China (81870630, 81700806, 81670820); the Natural Science Foundation of Shanghai (17ZR1404400); The sponsor or funding organization had no role in the design or conduct of this research.

CONFLICTS OF INTEREST

The authors declare no conflicts of interest.

REFERENCES

1. Klintworth GK. Research into the pathogenesis of macular corneal dystrophy. *Trans Ophthalmol Soc U K*. 1980; 100:186–194.
2. Donnenfeld ED, Cohen EJ, Ingraham HJ, Poleski SA, Goldsmith E, Laibson PR. Corneal thinning in macular corneal dystrophy. *Am J Ophthalmol Case Rep*. 1986; 101:112–113. [https://doi.org/10.1016/0002-9394\(86\)90473-3](https://doi.org/10.1016/0002-9394(86)90473-3)
3. Aggarwal S, Peck T, Golen J, Karcioğlu ZA. Macular corneal dystrophy: A review. *Surv Ophthalmol*. 2018; 63:609–617. <https://doi.org/10.1016/j.survophthal.2018.03.004>
4. El-Ashry MF, Abd El-Aziz MM, Wilkins S, Cheetham ME, Wilkie SE, Hardcastle AJ, Halford S, Bayoumi AY, Ficker LA, Tuft S, Bhattacharya SS, Ebenezer ND. Identification of novel mutations in the carbohydrate sulfotransferase gene (*CHST6*) causing macular corneal dystrophy. *Invest Ophthalmol Vis Sci*. 2002; 43:377–382.
5. Yang CJ, SundarRaj N, Thonar EJ, Klintworth GK. Immunohistochemical evidence of heterogeneity in macular corneal dystrophy. *Am J Ophthalmol Case Rep*. 1988; 106:65–71. [https://doi.org/10.1016/S0002-9394\(14\)76390-1](https://doi.org/10.1016/S0002-9394(14)76390-1)
6. Klintworth GK, Oshima E, al-Rajhi A, al-Saif A, Thonar EJ, Karcioğlu ZA. Macular corneal dystrophy in Saudi Arabia: a study of 56 cases and recognition of a new immunophenotype. *Am J Ophthalmol*. 1997; 124:9–18. [https://doi.org/10.1016/S0002-9394\(14\)71637-X](https://doi.org/10.1016/S0002-9394(14)71637-X)
7. Akama TO, Nakayama J, Nishida K, Hiraoka N, Suzuki M, McAuliffe J, Hindsgaul O, Fukuda M, Fukuda MN. Human corneal GlcNac 6-O-sulfotransferase and mouse intestinal GlcNac 6-O-sulfotransferase both produce keratan sulfate. *J Biol Chem*. 2001; 276:16271–16278. <https://doi.org/10.1074/jbc.M009995200>
8. Musselmann K, Hassell JR. Focus on molecules: *CHST6* (carbohydrate sulfotransferase 6; corneal N-acetylglucosamine-6-sulfotransferase). *Exp Eye Res*. 2006; 83:707–708. <https://doi.org/10.1016/j.exer.2005.11.020>
9. Akama TO, Nishida K, Nakayama J, Watanabe H, Ozaki K, Nakamura T, Dota A, Kawasaki S, Inoue Y, Maeda N, Yamamoto S, Fujiwara T, Thonar EJ, et al. Macular corneal dystrophy type I and type II are caused by distinct mutations in a new sulphotransferase gene. *Nat Genet*. 2000; 26:237–241. <https://doi.org/10.1038/79987>
10. Klintworth GK, Smith CF, Bowling BL. *CHST6* mutations in North American subjects with macular corneal dystrophy: a comprehensive molecular genetic review. *Mol Vis*. 2006; 12:159–176.
11. Dudakova L, Palos M, Svobodova M, Bydzovsky J, Huna L, Jirsova K, Hardcastle AJ, Tuft SJ, Liskova P.

- Macular corneal dystrophy and associated corneal thinning. *Eye*. 2014; 28:1201–1205.
<https://doi.org/10.1038/eye.2014.164>
12. Liskova P, Veraitch B, Jirsova K, Filipec M, Neuwirth A, Ebenezer ND, Hysi PG, Hardcastle AJ, Tuft SJ, Bhattacharya SS. Sequencing of the CHST6 gene in Czech macular corneal dystrophy patients supports the evidence of a founder mutation. *Br J Ophthalmol*. 2008; 92:265–267.
<https://doi.org/10.1136/bjo.2007.125252>
 13. Nowinska AK, Wylegala E, Teper S, Wroblewska-Czajka E, Aragona P, Roszkowska AM, Micali A, Pisani A, Puzzolo D. Phenotype and genotype analysis in patients with macular corneal dystrophy. *Br J Ophthalmol*. 2014; 98:1514–1521.
<https://doi.org/10.1136/bjophthalmol-2014-305098>
 14. Gruenauer-Kloevekorner C, Braeutigam S, Heinritz W, Froster UG, Duncker GI. Macular corneal dystrophy: mutational spectrum in German patients, novel mutations and therapeutic options. *Graefes Arch Clin Exp Ophthalmol*. 2008; 246:1441–1447.
<https://doi.org/10.1007/s00417-008-0836-1>
 15. Yaylacioglu Tuncay F, Kayman Kurekci G, Guntekin Ergun S, Pasaoglu OT, Akata RF, Dincer PR. Genetic analysis of CHST6 and TGFBI in Turkish patients with corneal dystrophies: Five novel variations in CHST6. *Mol Vis*. 2016; 22:1267–1279.
 16. Sultana A, Klintworth GK, Thonar EJ, Vemuganti GK, Kannabiran C. Immunophenotypes of macular corneal dystrophy in India and correlation with mutations in CHST6. *Mol Vis*. 2009; 15:319–325.
 17. Sultana A, Sridhar MS, Jagannathan A, Balasubramanian D, Kannabiran C, Klintworth GK. Novel mutations of the carbohydrate sulfotransferase-6 (CHST6) gene causing macular corneal dystrophy in India. *Mol Vis*. 2003; 9:730–734.
 18. Sultana A, Sridhar MS, Klintworth GK, Balasubramanian D, Kannabiran C. Allelic heterogeneity of the carbohydrate sulfotransferase-6 gene in patients with macular corneal dystrophy. *Clin Genet*. 2005; 68:454–460.
<https://doi.org/10.1111/j.1399-0004.2005.00517.x>
 19. Liu NP, Dew-Knight S, Rayner M, Jonasson F, Akama TO, Fukuda MN, Bao W, Gilbert JR, Vance JM, Klintworth GK. Mutations in corneal carbohydrate sulfotransferase 6 gene (CHST6) cause macular corneal dystrophy in Iceland. *Mol Vis*. 2000; 6:261–264.
 20. Liu NP, Smith CF, Bowling BL, Jonasson F, Klintworth GK. Macular corneal dystrophy types I and II are caused by distinct mutations in the CHST6 gene in Iceland. *Mol Vis*. 2006; 12:1148–1152.
 21. Warren JF, Aldave AJ, Srinivasan M, Thonar EJ, Kumar AB, Cevallos V, Witcher JP, Margolis TP. Novel mutations in the CHST6 gene associated with macular corneal dystrophy in southern India. *Arch Ophthalmol*. 2003; 121:1608–1612.
<https://doi.org/10.1001/archophth.121.11.1608>
 22. Niel F, Ellies P, Dighiero P, Soria J, Sabbagh C, San C, Renard G, Delpech M, Valleix S. Truncating mutations in the carbohydrate sulfotransferase 6 gene (CHST6) result in macular corneal dystrophy. *Invest Ophthalmol Vis Sci*. 2003; 44:2949–2953.
<https://doi.org/10.1167/iov.02-0740>
 23. Wang L, Tang X, Lv X, Sun E, Wu D, Wang C, Liu P. CHST6 mutation screening and endoplasmic reticulum stress in macular corneal dystrophy. *Oncotarget*. 2017; 8:96301–96312.
<https://doi.org/10.18632/oncotarget.22028>
 24. Liu Z, Tian X, Iida N, Fujiki K, Xie P, Wang W, Ma Z, Kanai A, Murakami A. Mutation analysis of CHST6 gene in Chinese patients with macular corneal dystrophy. *Cornea*. 2010; 29:883–888.
<https://doi.org/10.1097/ICO.0b013e3181ca2e74>
 25. El-Ashry MF, Abd El-Aziz MM, Shalaby O, Bhattacharya SS. Molecular genetic study of Egyptian patients with macular corneal dystrophy. *Br J Ophthalmol*. 2010; 94:250–255.
<https://doi.org/10.1136/bjo.2009.161810>
 26. Paliwal P, Sharma A, Tandon R, Sharma N, Titiyal JS, Sen S, Vajpayee RB. Molecular genetic analysis of macular corneal dystrophy patients from North India. *Ophthalmic Res*. 2012; 48:28–32.
<https://doi.org/10.1159/000334911>
 27. Birgani SA, Salehi Z, Houshmand M, Mohamadi MJ, Promehr LA, Mozafarzadeh Z. Novel mutations of CHST6 in Iranian patients with macular corneal dystrophy. *Mol Vis*. 2009; 15:373–377.
 28. Park SH, Ahn YJ, Chae H, Kim Y, Kim MS, Kim M. Molecular analysis of the CHST6 gene in Korean patients with macular corneal dystrophy: Identification of three novel mutations. *Mol Vis*. [structural features]. *Arch Soc Esp Oftalmol*. 2006; 81:315–320.
<https://doi.org/10.4321/S0365-66912006000600004>
 29. Aldave AJ, Yellore VS, Thonar EJ, Udari N, Warren JF, Yoon MK, Cohen EJ, Rapuano CJ, Laibson PR, Margolis TP, Small K. Novel mutations in the carbohydrate sulfotransferase gene (CHST6) in American patients with macular corneal dystrophy. *Am J Ophthalmol Case Rep*. 2004; 137:465–473.
<https://doi.org/10.1016/j.ajo.2003.09.036>
 30. Ha NT, Chau HM, Cung le X, Thanh TK, Fujiki K, Murakami A, Hiratsuka Y, Kanai A. Mutation analysis of the carbohydrate sulfotransferase gene in

- Vietnamese with macular corneal dystrophy. *Invest Ophthalmol Vis Sci.* 2003; 44:3310–3316.
<https://doi.org/10.1167/iovs.03-0031>
31. Huo YN, Yao YF, Yu P. Pathogenic mutations of TGFBI and CHST6 genes in Chinese patients with Avellino, lattice, and macular corneal dystrophies. *J Zhejiang Univ Sci.* 2011; 12:687–693.
<https://doi.org/10.1631/jzus.B1100011>
 32. Rubinstein Y, Weiner C, Einan-Lifshitz A, Chetrit N, Shoshany N, Zadok D, Avni I, Pras E. Macular Corneal Dystrophy and Posterior Corneal Abnormalities. *Cornea.* 2016; 35:1605–1610.
<https://doi.org/10.1097/ICO.0000000000001054>
 33. Gulias-Canizo R, Castaneda-Diez R, Gomez-Leal A, Klintworth GK, Rodriguez-Reyes AA. [Corneal macular dystrophy: clinical, histopathologic and ultrastructural features]. *Arch Soc Esp Ophthalmol.* 2006; 81:315–320.
<https://doi.org/10.4321/S0365-66912006000600004>
 34. Carstens N, Williams S, Goolam S, Carmichael T, Cheung MS, Buchmann-Moller S, Sultan M, Staedtler F, Zou C, Swart P, Rice DS, Lacoste A, Paes K, et al. Novel mutation in the CHST6 gene causes macular corneal dystrophy in a black South African family. *BMC Med Genet.* 2016; 17:47.
<https://doi.org/10.1186/s12881-016-0308-0>
 35. Ha NT, Chau HM, Cung le X, Thanh TK, Fujiki K, Murakami A, Hiratsuka Y, Hasegawa N, Kanai A. Identification of novel mutations of the CHST6 gene in Vietnamese families affected with macular corneal dystrophy in two generations. *Cornea.* 2003; 22:508–511.
<https://doi.org/10.1097/00003226-200308000-00004>
 36. Abbruzzese C, Kuhn U, Molina F, Rama P, De Luca M. Novel mutations in the CHST6 gene causing macular corneal dystrophy. *Clin Genet.* 2004; 65:120–125.
<https://doi.org/10.1111/j.0009-9163.2004.00191.x>
 37. Gonzalez-Rodriguez J, Ramirez-Miranda A, Hernandez-Da Mota SE, Zenteno JC. TGFBI, CHST6, and GSN gene analysis in Mexican patients with stromal corneal dystrophies. *Graefes Arch Clin Exp Ophthalmol.* 2014; 252:1267–1272.
<https://doi.org/10.1007/s00417-014-2648-9>
 38. El-Ashry MF, Abd El-Aziz MM, Shalaby O, Wilkins S, Poopalasundaram S, Cheetham M, Tuft SJ, Hardcastle AJ, Bhattacharya SS, Ebenezer ND. Novel CHST6 nonsense and missense mutations responsible for macular corneal dystrophy. *Am J Ophthalmol.* 2005; 139:192–193.
<https://doi.org/10.1016/j.ajo.2004.07.001>
 39. Liu NP, Bao W, Smith CF, Vance JM, Klintworth GK. Different mutations in carbohydrate sulfotransferase 6 (CHST6) gene cause macular corneal dystrophy types I and II in a single sibship. *Am J Ophthalmol.* 2005; 139:1118–1120.
<https://doi.org/10.1016/j.ajo.2004.11.054>
 40. Yellore VS, Sonmez B, Chen MC, Rayner SA, Thonar EJ, Aldave AJ. An unusual presentation of macular corneal dystrophy associated with uniparental isodisomy and a novel Leu173Pro mutation. *Ophthalmic Genet.* 2007; 28:169–174.
<https://doi.org/10.1080/13816810701407925>
 41. Patel DA, Harocopos GJ, Chang SH, Vora SC, Lubniewski AJ, Huang AJ. Novel CHST6 gene mutations in 2 unrelated cases of macular corneal dystrophy. *Cornea.* 2011; 30:664–669.
<https://doi.org/10.1097/ICO.0b013e3182012888>
 42. Iida-Hasegawa N, Furuhashi A, Hayatsu H, Murakami A, Fujiki K, Nakayasu K, Kanai A. Mutations in the CHST6 gene in patients with macular corneal dystrophy: immunohistochemical evidence of heterogeneity. *Invest Ophthalmol Vis Sci.* 2003; 44:3272–3277.
<https://doi.org/10.1167/iovs.02-0910>
 43. Kobayashi A, Fujiki K, Fujimaki T, Murakami A, Sugiyama K. In vivo laser confocal microscopic findings of corneal stromal dystrophies. *Arch Ophthalmol.* 2007; 125:1168–1173.
<https://doi.org/10.1001/archophth.125.9.1168>
 44. Dang X, Zhu Q, Wang L, Su H, Lin H, Zhou N, Liang T, Wang Z, Huang S, Ren Q, Qi Y. Macular corneal dystrophy in a Chinese family related with novel mutations of CHST6. *Mol Vis.* 2009; 15:700–705.
 45. Young RD, Akama TO, Liskova P, Ebenezer ND, Allan B, Kerr B, Catterson B, Fukuda MN, Quantock AJ. Differential immunogold localisation of sulphated and unsulphated keratan sulphate proteoglycans in normal and macular dystrophy cornea using sulphation motif-specific antibodies. *Histochem Cell Biol.* 2007; 127:115–120.
<https://doi.org/10.1007/s00418-006-0228-8>
 46. Richards S, Aziz N, Bale S, Bick D, Das S, Gastier-Foster J, Grody WW, Hegde M, Lyon E, Spector E, Voelkerding K, Rehml HL, Committee ALQA. Standards and guidelines for the interpretation of sequence variants: a joint consensus recommendation of the American College of Medical Genetics and Genomics and the Association for Molecular Pathology. *Genet Med.* 2015; 17:405–424.
<https://doi.org/10.1038/gim.2015.30>
 47. Musselmann K, Kane B, Alexandrou B, Hassell JR. Stimulation of collagen synthesis by insulin and proteoglycan accumulation by ascorbate in bovine keratocytes in vitro. *Invest Ophthalmol Vis Sci.* 2006; 47:5260–5266.

<https://doi.org/10.1167/iavs.06-0612>

48. Akhtar S, Alkatan HM, Kirat O, Khan AA, Almubrad T. Collagen Fibrils and Proteoglycans of Macular Dystrophy Cornea: Ultrastructure and 3D Transmission Electron Tomography. *Microsc Microanal.* 2015; 21:666–679.
<https://doi.org/10.1017/S1431927615000483>
49. Nakayama F, Umeda S, Ichimiya T, Kamiyama S, Hazawa M, Yasuda T, Nishihara S, Imai T. Sulfation of keratan sulfate proteoglycan reduces radiation-induced apoptosis in human Burkitt's lymphoma cell lines. *FEBS Lett.* 2013; 587:231–237.
<https://doi.org/10.1016/j.febslet.2012.12.002>
50. Kakuta Y, Pedersen LG, Pedersen LC, Negishi M. Conserved structural motifs in the sulfotransferase family. *Trends Biochem Sci.* 1998; 23:129–130.
[https://doi.org/10.1016/S0968-0004\(98\)01182-7](https://doi.org/10.1016/S0968-0004(98)01182-7)

SUPPLEMENTARY MATERIAL

Please browse Full Text version to see the data of Supplementary Tables:

Supplementary Table 1. Summary of variants reported in *CHST6* gene.

Supplementary Table 2. ACMG classification for missense variants in *CHST6* gene.

Supplementary Table 3. ACMG classification for protein-truncating variants in *CHST6* gene.

Supplementary Table 4. The normalized conservation score of each residue in the CHST6 protein calculated by the ConSurf Server.

Circulating insulin-like growth factor-1: a new clue in the pathogenesis of age-related macular degeneration

Niccolò Castellino¹, Antonio Longo¹, Teresio Avitabile¹, Andrea Russo¹, Matteo Fallico¹, Vincenza Bonfiglio¹, Mario Damiano Toro^{1,3}, Robert Rejdak³, Katarzyna Nowomiejska³, Paolo Murabito¹, Claudio Furino², Michele Reibaldi¹

¹Policlinico Gaspare Rodolico-University of Catania, Catania, Italy

²Eye Clinic, University of Bari, Bari, Italy

³Department of General Ophthalmology, Medical University in Lublin, Lublin, Poland

Correspondence to: Antonio Longo; **email:** antlongo@unict.it

Keywords: age-related macular degeneration, neovascular AMD, IGF-1, anti-VEGF, senescence, somatomedin C.

Received: October 17, 2018 **Accepted:** December 12, 2018 **Published:** December 29, 2018

Correction: This article has been corrected. See Aging 2019; 3: <https://doi.org/10.18632/aging.101833>

Copyright: Castellino et al. This is an open-access article distributed under the terms of the Creative Commons Attribution License (CC BY 3.0), which permits unrestricted use, distribution, and reproduction in any medium, provided the original author and source are credited.

ABSTRACT

In order to investigate Insulin-like growth factor-1 (IGF-1) blood levels in male and female age-matched patients affected by early, intermediate, neovascular age related macular degeneration (AMD) and healthy subjects (no AMD) were enrolled in a prospective, observational study. All patients enrolled were classified according to 4 stages classification of AMD from Age-related eye disease study (AREDS). Each subject underwent a complete ophthalmic examination including best corrected visual acuity (BCVA), applanation tonometry, slit-lamp biomicroscopic examination, color fundus photography, optical coherence tomography (OCT) and, if needed, fluorescein angiography. Overall, 224 anti-VEGF naïve subjects including 56 patients in early AMD group, 56 patients in intermediate AMD group, 56 patients in neovascular AMD group and 56 patients in no AMD group were recruited. For each group 28 male patients and 28 female patients were enrolled. IGF-1 hematic levels were significantly higher ($p < 0.005$) in the neovascular AMD group and in the intermediate AMD group in comparison to no AMD group; no significant difference between early AMD group and no AMD group was found. Our analysis has shown an increment of IGF-1 levels in both neovascular and intermediate stage of AMD supporting the hypothesis that IGF-1 may play a role in the pathogenesis of AMD.

INTRODUCTION

Age related macular degeneration (AMD) is one of the leading cause of visual impairment in developed countries [1,2]. AMD has been classified in two major clinical patterns: the “dry” form which is associated with an atrophic evolution and a slow visual decline and the “neovascular” form which is characterized by choroidal neovascularization (cnv) associated with a rapid and abrupt visual loss [3,4].

AMD is the result of a complex interaction between environmental factors and genetic. Smoking is the most

consistently identified modifiable risk factor, but dietary factors, solar insolation, and season of birth may also affect AMD incidence and progression [5,6]. The pathogenesis of neovascular AMD has long been debated but at present it remains not fully elucidated. It encompasses the presence of an inflammatory network involving the macula and the active role of pro-angiogenic factors which lead to choroidal neovascularization and visual loss [7].

Among the various pro-angiogenic factors, vascular endothelial growth factor (VEGF) seems to play a pivotal role in neovascular AMD, and actually anti-

VEGF drugs are the only approved therapeutic approach for the treatment of the disease [8–11]. Nevertheless, in addition to VEGF several humoral mediators including fibroblast growth factor, platelet-derived growth factor, interleukin-6 (IL-6), interleukin-8 (IL-8), monocyte chemoattractant protein-1, and insulin-like growth factor-1 (IGF-1) are altered in patients affected by neovascular AMD [12–15].

IGF-1, also called somatomedin C, is a protein that is mainly secreted by the liver as a result of stimulation by growth hormone. IGF-1 is important for both the regulation of normal physiology, as well as a number of pathological states, including cancer [16]. High IGF-1 levels were associated with increased all cause mortality, human studies support the notion that attenuation of GH/IGF-1 signaling may protect from age-related diseases and functional decline [17].

In eyes affected by neovascular AMD, IGF-1 is increased in ocular fluid. Furthermore IGF-1 receptors are expressed in retinal pigmented epithelium cells which are involved in neovascular AMD [18].

To date, only one study investigated systemic IGF-1 concentration in neovascular AMD patients, showing an increment in circulating IGF-1 levels in comparison to healthy controls. The authors demonstrated that early endothelial cells are increased in neovascular AMD and may contribute to IGF-1 elevation [19].

However, in this study only patients with neovascular AMD were included, whereas patients with less advanced stages of AMD were not evaluated. Therefore, it remains unclear if IGF-1 elevation is a consequence of neovascular development in AMD patients, or if IGF-1 is primary involved in the pathogenesis of AMD, as in others aging related diseases, being a causal factor instead of the effect of AMD.

The present study was therefore designed to evaluate the circulating IGF-1 levels in early, intermediate, and neovascular AMD patients in comparison to healthy matched controls.

RESULTS

Overall 224 subjects met the study inclusion criteria and were included in the study, 56 patients in neovascular AMD group (32 type 1 cnv, 18 type 2 cnv, 6 type 3 cnv) (mean age 74±8 years), 56 patients in intermediate AMD group (mean age 73±8 years), 56 patients in early AMD group (mean age 74±1 years), and 56 patients in no AMD group (mean age 73±4 years). Mean best corrected visual acuity (BCVA) and intraocular pressure in four groups are reported in Table 1. For each group 28 male patients and 28 female patients were enrolled.

Mean IGF-1 values in all patients

As shown in Table 2 the overall mean ± standard deviations (SD) IGF-1 values was significantly different

Table 1. Mean ± standard deviations (SD) Best Corrected Visual Acuity and Intraocular Pressure values detected in four groups.

		Neovascular AMD (n=56)	Intermediate AMD (n=56)	Early AMD (n=56)	No AMD (n=56)	P (ANOVA)
BCVA	logMAR	0.58±0.06 *	0.09±0.05 *	0.04±0.05 °	0.01±0.02	<0.001
Intraocular pressure	mmHg	14.2±2.6	14.6±2.5	14.3±2.1	14.4±2.5	0.787

BCVA: Best Corrected Visual Acuity

Tukey HSD vs no AMD: * p<0.001, ° p=0.007

Table 2. Table 2. Mean ± standard deviations (SD) IGF-1 values detected in four groups.

	Neovascular AMD (n=56)	Intermediate AMD (n=56)	Early AMD (n=56)	No AMD (n=56)	P (ANOVA)
Overall	146±40 *	127±29 °	107±32	103±36	<0.001
Males	169±34 *	143±30 °	118±35	114±38	<0.001
Females	123±32 *	111±16 §	97±25	92±30	<0.001

Tukey HSD vs no AMD: * p<0.001, ° p=0.002, ° p=0.011, § p=0.038

between groups ($P < 0.001$, ANOVA). Compared with the no AMD group, the mean IGF-1 values was significantly higher in the neovascular AMD group (Tukey HSD $p < 0.001$) and in the intermediate AMD group (Tukey HSD $p = 0.002$); no significant difference between early AMD group and no AMD group (Tukey HSD $p = 0.911$), Figure 1.

Mean IGF-1 values in male patients

The overall mean \pm (SD) IGF-1 values in male patients was significantly different between groups ($P < 0.001$, ANOVA). Compared with the no AMD group, the mean \pm (SD) IGF-1 values was significantly higher in the neovascular AMD group (Tukey HSD $p < 0.001$) and in the intermediate AMD group (Tukey HSD $p = 0.011$); no difference was seen with early AMD group (Tukey HSD $p = 0.975$).

Mean IGF-1 values in female patients

The overall mean \pm (SD) IGF-1 values was significantly different between groups ($P < 0.001$, ANOVA). Compared with the no AMD group, the mean \pm (SD) IGF-1 values was significantly higher in the neovascular AMD group (Tukey HSD $p < 0.001$) and in the in-

termediate AMD group (Tukey HSD $p = 0.038$), but not in early AMD group (Tukey HSD $p = 0.905$).

Correlation between IGF-1 and age

A significant correlation was found between mean IGF-1 values and age in early AMD group ($r = -0.342$, $p = 0.010$) and no AMD group ($r = -0.317$, $p = 0.017$), but no significant in neovascular AMD group ($r = -0.117$, $p = 0.389$) and intermediate AMD ($r = -0.211$, $p = 0.118$), Figure 2.

DISCUSSION

AMD is a retinal degenerative disorder characterized by complex and not entirely understood pathogenesis. Several cytokines that promote retinal inflammation and angiogenesis has been suggested to be involved. Among these, there are clinical and experimental evidences on the role of retinal IGF-1 as a mediator of retinal inflammation and neovascular formation [20,21]. To address this hypothesis, we evaluated circulating IGF-1 levels in patients with various stages of AMD. Our results indicate that serum levels of IGF-1 are higher in intermediate and neovascular AMD patients in comparison with early and no AMD patients.

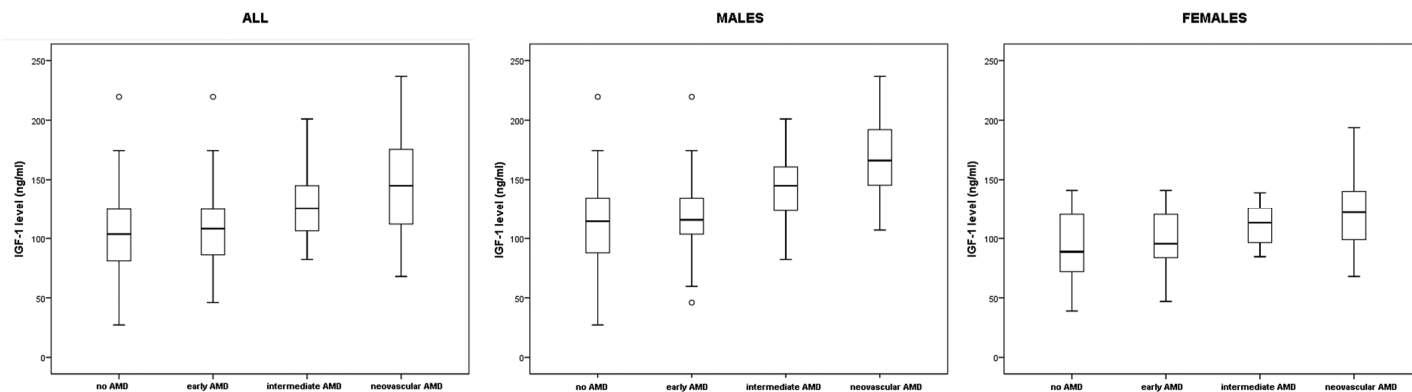


Figure 1. IGF-1 levels in all patients, males and females, in four groups.

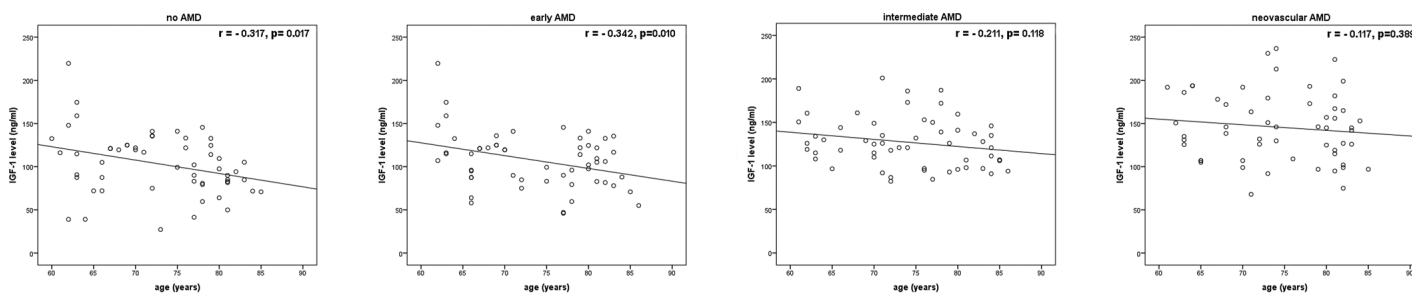


Figure 2. Correlations between IGF-1 levels and age in four groups.

Dong Min Cha and associates [18] demonstrated the presence of higher levels of various cytokines, chemokines and growth factors, including IGF-1, in the aqueous humor samples of patients affected by AMD in comparison with control subjects.

In a previous study Machalinska and associates demonstrated higher IGF-1 plasma concentration of IGF-1 in patients with neovascular AMD in comparison to healthy subjects. Furthermore in their study the authors also reported an association of higher IGF-1 levels with an increase of early endothelial progenitor cells. Albeit the latter association does not prove a cause to effect relationship, the authors hypothesized that angiogenesis under hypoxic conditions may represent the trigger that may explain the above mentioned observations [19]. They also suggested as a possible explanation a disturbed local synthesis of the cytokines and growth factors under conditions of chronic vascular endothelial injury. It should be kept in mind that IGF-1 is a well-known retinal pro-angiogenic cytokine, and it has been demonstrated that IGF-1 induces retinal neovascularization in animal models [22]. This may be of particular relevance under condition of long-term chronic hypoxia, in contrast to VEGF which may be more readily increased in the early phases of retinal ischemia.

In agreement with the study of Machalinska, our results showed an increase in IGF-1 values in patients with neovascular AMD compared to healthy patients. However, a novel contribution of our present study is the observation of a significant increase in IGF-1 levels also in patients with intermediate stages of the disease. These data suggest that IGF-1 may be already elevated in stages of the retinal degeneration prior to the neovascular formation. The association between IGF-1 and microvascular impairment in AMD may be not limited to the neovascular stage but may be already evident in a less severe stage (intermediate) of the disease. This hypothesis is also corroborated by the observed grading in IGF-1 levels that were higher in the more advanced stages of the disease. IGF-1 levels in AMD may be considered a predisposing factor to the disease or, alternatively it may be a consequence of the degenerative processes which characterize AMD. Thus, these data are consistent with previous available data and may provide evidences for a pathogenetic or at least facilitating role of IGF-1 in AMD.

Furthermore, an indirect confirmation of the role of changes in circulating IGF-1 values in patients with intermediate and neovascular AMD is that, in these groups of patients, our results did not show a significant correlation with age, which instead was found in healthy patients and in the group with early stage of disease.

In a recent study Westwood and associates reported that IGF-1 plasma alterations are present in various neurodegenerative disorders. They demonstrated that lower serum levels of IGF-1 are associated with an increased risk of developing Alzheimer Disease (AD) dementia [23]. AMD is also characterized by retinal neurodegenerative processes [24] and previous studies have shown common pathogenetic features with AD [25]. Accordingly, is possible to suppose that IGF-1 is altered in various aging-related and neurodegenerative disorders [26]. As a result, the role of IGF-1 in neuronal inflammation needs to be elucidated.

It should be kept in mind that serum concentrations of IGF-1 are influenced by several factors, such as nutritional factors, energy and protein intake, and BMI. These factors may play as confounders in data analysis and interpretation. Our data also confirmed gender-differences in IGF-1 levels that were previously observed. [27]

Our study has several limitations including the cross-sectional nature of the study design with no longitudinal follow-up. In addition we didn't evaluate IGF-1 levels in AMD patient affected by geographic atrophy, not clarifying whether the higher levels of IGF-1 in neovascular stage are linked to neovascular development or to the progression of neurodegenerative processes.

In conclusion circulating IGF-1 levels are significantly higher in patients affected by intermediate and neovascular AMD in comparison with control subjects. Although future studies with larger sample are needed, our results suggest IGF-1 as a possible contributing factor in the pathogenesis of this disease.

METHODS

In this observational, prospective, controlled study we recruited consecutive patients of more than 60 years with a diagnosis of early AMD, intermediate AMD, neovascular AMD, and healthy controls examined at the Department of Ophthalmology, University of Catania, Catania, Italy, between January 2017 and May 2018. In each group, according to the power of the study, 28 male and 28 female patients were enrolled. The study was approved by the Institutional review board of the University of Catania. Written informed consent was obtained from all subjects enrolled in the study.

Exclusion criteria were diabetes and any systemic condition which could bias IGF-1 measurements, including any clinical condition which may have caused an elevation of systemic inflammatory markers, regardless of the cause that may have generated the rise.

Patients in overweight or obese were excluded from the study (BMI above 29). Similarly patients with low body weight (BMI below 17.5) or patient with clinically evident sarcopenia were excluded. In addition, patients who had undergone to any previous intravitreal therapy, previous cataract surgery in the last six months or patients who had clinical evidence of other retinal and ocular disease were also excluded.

All patients enrolled were classified according to 4 stages classification of AMD from Age-related eye disease study (AREDS)[28]:

- No AMD (AREDS category 1) none or a few small drusen (<63 microns in diameter).
- Early AMD (AREDS category 2) any or all of the following: multiple small drusen, few intermediate drusen (63 to 124 microns in diameter), or retinal pigment epithelial abnormalities.
- Intermediate AMD (AREDS category 3) any or all of the following: extensive intermediate drusen, and at least one large drusen (\geq 125 microns in diameter), or geographic atrophy not involving the center of the fovea.
- Neovascular AMD (AREDS category 4); any of the features of neovascular AMD.

All patients underwent an ophthalmic examination including: best corrected visual acuity (BCVA), applanation tonometry, slit-lamp biomicroscopic examination, Color fundus photography, optical coherence tomography (OCT) and, if needed, fluorescein angiography (FA) and indocyanine green angiography (ICGA).

Color fundus photography of the central retina was performed by Visucam (Carl Zeiss Meditec, Inc, Dublin, California, USA). At least two color fundus images of each eye were acquired capturing the central field of the retina within a 45° view. Images were defined as gradable, if they fulfilled the following quality criteria allowing for the assessment of AMD: sufficient brightness and color contrast as well as full macular region captured. Images were excluded from AMD grading, if they revealed obscuring lesions or lesions considered to be the result of a competing retinal disease hampering AMD grading. Gradable images were examined by an experienced and trained ophthalmology consultant (M.R.); questionable findings were discussed with a second trained grader (T.A.).

Spectral-domain OCT was carried out using the Spectralis HRA by Heidelberg (SD-OCT; Heidelberg Engineering, Heidelberg, Germany), FA and ICGA (Heidelberg retinal angiograph, Heidelberg Engine-

ering, Heidelberg, Germany) were performed in order to confirm the diagnoses in the neovascular AMD group.

Serum IGF-1 was measured by standard immunoassay in all patients. A 3 mL blood sample was drawn. This was obtained in the early morning at 08.00 after a 10 h overnight fasting. Prior to blood sampling patients were maintained in the supine position for 15 minutes. Samples were centrifuged, serum was aliquoted immediately and stored at -80°C in the central laboratory of our institution.

The primary outcome measure of our study was the evaluation of IGF-1 circulating levels in case and control groups in male and female patients. Secondary outcome was to evaluate the correlation between circulating IGF-1 levels and age in each group.

Statistical analysis

The sample size (at least 26 males and 26 females in each group) was determined from the results of our preliminary data to detect, with an alpha of 0.05 and a 90% power (two-tailed), a difference of 25 ng/ml in IGF-1 serum level between females with neovascular AMD and females with no AMD

The values of parameters in four groups were compared by ANOVA; if significant, comparison with baseline value was performed by Tukey HSD (honestly significant difference) test. In each group, correlation between IGF-1 levels and age was analyzed by Pearson's Correlation Coefficient. SPSS 21.0 (V.21, Armonk, NY, USA) was used for statistical analysis. P values < 0.05 was considered as statistically significant.

CONFLICTS OF INTEREST

The authors have no conflicts of interest to declare.

FUNDING

No financial support was provided to this work.

REFERENCES

1. Bressler NM. Age-related macular degeneration is the leading cause of blindness. *JAMA*. 2004; 291:1900–01. <https://doi.org/10.1001/jama.291.15.1900>
2. Wong WL, Su X, Li X, Cheung CM, Klein R, Cheng CY, Wong TY. Global prevalence of age-related macular degeneration and disease burden projection for 2020 and 2040: a systematic review and meta-analysis. *Lancet Glob Health*. 2014; 2:e106–16. [https://doi.org/10.1016/S2214-109X\(13\)70145-1](https://doi.org/10.1016/S2214-109X(13)70145-1)

3. Ferris FL 3rd, Wilkinson CP, Bird A, Chakravarthy U, Chew E, Csaky K, Sadda SR, and Beckman Initiative for Macular Research Classification Committee. Clinical classification of age-related macular degeneration. *Ophthalmology*. 2013; 120:844–51. <https://doi.org/10.1016/j.ophtha.2012.10.036>
4. Ferris FL 3rd, Fine SL, Hyman L. Age-related macular degeneration and blindness due to neovascular maculopathy. *Arch Ophthalmol*. 1984; 102:1640–42. <https://doi.org/10.1001/archophth.1984.01040031330019>
5. Reibaldi M, Longo A, Pulvirenti A, Avitabile T, Russo A, Cillino S, Mariotti C, Casuccio A. Geo-Epidemiology of Age-Related Macular Degeneration: New Clues Into the Pathogenesis. *Am J Ophthalmol*. 2016; 161:78–93.e1, 2. <https://doi.org/10.1016/j.ajo.2015.09.031>
6. Longo A, Casuccio A, Pani L, Avitabile T, Cillino S, Uva MG, Bonfiglio V, Russo A, Parisi G, Cennamo G, Furino C, Parravano M, Xoxi E, Reibaldi M. Association of neovascular age-related macular degeneration with month and season of birth in Italy. *Aging (Albany NY)*. 2016; 9:133–41. <https://doi.org/10.18632/aging.101137>
7. Wong TY, Chakravarthy U, Klein R, Mitchell P, Zlateva G, Buggage R, Fahrbach K, Probst C, Sledge I, Sledge I. The natural history and prognosis of neovascular age-related macular degeneration: a systematic review of the literature and meta-analysis. *Ophthalmology*. 2008; 115:116–26. <https://doi.org/10.1016/j.ophtha.2007.03.008>
8. Witmer AN, Vrensen GF, Van Noorden CJ, Schlingemann RO. Vascular endothelial growth factors and angiogenesis in eye disease. *Prog Retin Eye Res*. 2003; 22:1–29. [https://doi.org/10.1016/S1350-9462\(02\)00043-5](https://doi.org/10.1016/S1350-9462(02)00043-5)
9. Brown DM, Regillo CD. Anti-VEGF agents in the treatment of neovascular age-related macular degeneration: applying clinical trial results to the treatment of everyday patients. *Am J Ophthalmol*. 2007; 144:627–37. <https://doi.org/10.1016/j.ajo.2007.06.039>
10. Ferrara N, Damico L, Shams N, Lowman H, Kim R. Development of ranibizumab, an anti-vascular endothelial growth factor antigen binding fragment, as therapy for neovascular age-related macular degeneration. *Retina*. 2006; 26:859–70. <https://doi.org/10.1097/01.iae.0000242842.14624.e7>
11. Reibaldi M, Pulvirenti A, Avitabile T, Bonfiglio V, Russo A, Mariotti C, Bucolo C, Mastropasqua R, Parisi G, Longo A. Pooled estimates of incidence of endophthalmitis after intravitreal injection of anti-vascular endothelial growth factor agents with and without topical antibiotic prophylaxis. *Retina*. 2018; 38:1–11. <https://doi.org/10.1097/IAE.0000000000001583>
12. Haddad S, Chen CA, Santangelo SL, Seddon JM. The genetics of age-related macular degeneration: a review of progress to date. *Surv Ophthalmol*. 2006; 51:316–63. <https://doi.org/10.1016/j.survophthal.2006.05.001>
13. Jonas JB, Tao Y, Neumaier M, Findeisen P. Monocyte chemoattractant protein 1, intercellular adhesion molecule 1, and vascular cell adhesion molecule 1 in exudative age-related macular degeneration. *Arch Ophthalmol*. 2010; 128:1281–86. <https://doi.org/10.1001/archophthalmol.2010.227>
14. Jonas JB, Tao Y, Neumaier M, Findeisen P. Cytokine concentration in aqueous humour of eyes with exudative age-related macular degeneration. *Acta Ophthalmol*. 2012; 90:e381–88. <https://doi.org/10.1111/j.1755-3768.2012.02414.x>
15. Kramer M, Hasanreisoglu M, Feldman A, Axer-Siegel R, Sonis P, Maharshak I, Monselise Y, Gurevich M, Weinberger D. Monocyte chemoattractant protein-1 in the aqueous humour of patients with age-related macular degeneration. *Clin Experiment Ophthalmol*. 2012; 40:617–25. <https://doi.org/10.1111/j.1442-9071.2011.02747.x>
16. Samani AA, Yakar S, LeRoith D, Brodt P. The role of the IGF system in cancer growth and metastasis: overview and recent insights. *Endocr Rev*. 2007; 28:20–47. <https://doi.org/10.1210/er.2006-0001>
17. Balasubramanian P, Longo VD. Growth factors, aging and age-related diseases. *Growth Horm IGF Res*. 2016; 28:66–68. <https://doi.org/10.1016/j.ghir.2016.01.001>
18. Cha DM, Woo SJ, Kim HJ, Lee C, Park KH. Comparative analysis of aqueous humor cytokine levels between patients with exudative age-related macular degeneration and normal controls. *Invest Ophthalmol Vis Sci*. 2013; 54:7038–44. <https://doi.org/10.1167/iovs.13-12730>
19. Machalinska A, Safranow K, Dziedziejko V, Mozolewska-Piotrowska K, Paczkowska E, Klos P, Pius E, Grymula K, Wiszniewska B, Karczewicz D, Machalinski B. Different populations of circulating endothelial cells in patients with age-related macular degeneration: a novel insight into pathogenesis. *Invest Ophthalmol Vis Sci*. 2011; 52:93–100. <https://doi.org/10.1167/iovs.10-5756>
20. Lambooy AC, van Wely KH, Lindenbergh-Kortleve DJ, Kuijpers RW, Kliffen M, Mooy CM. Insulin-like growth factor-I and its receptor in neovascular age-related macular degeneration. *Invest Ophthalmol Vis Sci*. 2003; 44:2192–98. <https://doi.org/10.1167/iovs.02-0410>

21. Economou MA, Wu J, Vasilcanu D, Rosengren L, All-Ericsson C, van der Ploeg I, Menu E, Girnita L, Axelson M, Larsson O, Seregard S, Kvanta A. Inhibition of VEGF secretion and experimental choroidal neovascularization by picropodophyllin (PPP), an inhibitor of the insulin-like growth factor-1 receptor. *Acta Ophthalmol.* 2008; 86 Thesis 4:42–49.
<https://doi.org/10.1111/j.1755-3768.2008.01185.x>
22. Grant MB, Mames RN, Fitzgerald C, Ellis EA, Aboufrikha M, Guy J. Insulin-like growth factor I acts as an angiogenic agent in rabbit cornea and retina: comparative studies with basic fibroblast growth factor. *Diabetologia.* 1993; 36:282–91.
<https://doi.org/10.1007/BF00400229>
23. Westwood AJ, Beiser A, Decarli C, Harris TB, Chen TC, He XM, Roubenoff R, Pikula A, Au R, Braverman LE, Wolf PA, Vasan RS, Seshadri S. Insulin-like growth factor-1 and risk of Alzheimer dementia and brain atrophy. *Neurology.* 2014; 82:1613–19.
<https://doi.org/10.1212/WNL.0000000000000382>
24. Zucchiatti I, Parodi MB, Pierro L, Cicinelli MV, Gagliardi M, Castellino N, Bandello F. Macular ganglion cell complex and retinal nerve fiber layer comparison in different stages of age-related macular degeneration. *Am J Ophthalmol.* 2015; 160:602–607.e1. <https://doi.org/10.1016/j.ajo.2015.05.030>
25. Ong SS, Proia AD, Whitson HE, Farsiu S, Doraiswamy PM, Lad EM. Ocular amyloid imaging at the crossroad of Alzheimer's disease and age-related macular degeneration: implications for diagnosis and therapy. *J Neurol.* <https://doi.org/10.1007/s00415-018-9028-z>. Epub ahead of print
26. Pennington KL, DeAngelis MM. Epidemiology of age-related macular degeneration (AMD): associations with cardiovascular disease phenotypes and lipid factors. *Eye Vis (Lond).* 2016; 3:34.
<https://doi.org/10.1186/s40662-016-0063-5>
27. Austad SN, Bartke A. Sex Differences in Longevity and in Responses to Anti-Aging Interventions: A Mini-Review. *Gerontology.* 2015; 62:40–46.
<https://doi.org/10.1159/000381472>
28. Age-Related Eye Disease Study Research Group. A randomized, placebo-controlled, clinical trial of high-dose supplementation with vitamins C and E, beta carotene, and zinc for age-related macular degeneration and vision loss: AREDS report no. 8. *Arch Ophthalmol.* 2001; 119:1417–36.
<https://doi.org/10.1001/archopht.119.10.1417>

Effects of senescent secretory phenotype acquisition on human retinal pigment epithelial stem cells

Raffaella Lazzarini^{1,*}, Michele Nicolai^{2,*}, Vittorio Pirani², Cesare Mariotti², Roberto Di Primio¹

¹Department of Clinical and Molecular Sciences-Histology, Università Politecnica delle Marche, Ancona 60020, Italy

²Ophthalmology Clinic, Università Politecnica delle Marche, Ancona 60020, Italy

*Equal contribution

Correspondence to: Cesare Mariotti; **email:** mariottiocul@gmail.com

Keywords: AMD, RPESCs, age-related diseases, senescence, inflammation

Received: June 20, 2018 **Accepted:** October 27, 2018 **Published:** November 16, 2018

Copyright: Lazzarini et al. This is an open-access article distributed under the terms of the Creative Commons Attribution License (CC BY 3.0), which permits unrestricted use, distribution, and reproduction in any medium, provided the original author and source are credited.

ABSTRACT

Regenerative medicine approaches based on mesenchymal stem cells (MSCs) are being investigated to treat several aging-associated diseases, including age-related macular degeneration (AMD). Loss of retinal pigment epithelium (RPE) cells occurs early in AMD, and their transplant has the potential to slow disease progression. The human RPE contains a subpopulation of cells - adult RPE stem cells (RPESCs) – that are capable of self-renewal and of differentiating into RPE cells *in vitro*. However, age-related MSC changes involve loss of function and acquisition of a senescence-associated secretory phenotype (SASP), which can contribute to the maintenance of a chronic state of low-grade inflammation in tissues and organs.

In a previous study we isolated, characterized, and differentiated RPESCs. Here, we induced replicative senescence in RPESCs and tested their acquisition of the senescence phenotype and the SASP as well as the differentiation ability of young and senescent RPESCs.

Senescent RPESCs showed a significantly reduced proliferation ability, high senescence-associated β -galactosidase activity, and SASP acquisition. RPE-specific genes were downregulated and p21 and p53 protein expression was upregulated.

These findings document the effects of senescence and SASP acquisition on RPESC differentiation ability and highlight the need for a greater understanding of their role in AMD pathogenesis.

INTRODUCTION

Age-related macular degeneration (AMD) is an eye disorder affecting the elderly which can induce an irreversible loss of central visual function [1]. Its limited treatment possibilities and the rising number of senior citizens in developed countries are reasons for concern; indeed, it has been estimated that 200 million individuals will suffer from AMD in 2020 and almost 300 million will be affected in 2040 [2]. Aging plays a major role in AMD pathogenesis [3]; smoking, cataract surgery, a high body mass index (BMI), a history of

cardiovascular disease, and a family history of AMD are additional risk factors [4-5].

The Age-Related Eye Disease Study (AREDS) has classified AMD into early, intermediate, and late stage [6], while the Clinical Age-Related Maculopathy Staging (CARMS) system divides patients into five mutually exclusive categories based on slit-lamp assessment of clinical features [7]. However, there is no consensus on the staging and progression terminology. In 2013, the Beckman Initiative for Macular Research Classification Committee proposed a new clinical

classification based on the three AREDS stages: stage 1, normal, aging phenotype (small drusen < 63 μm without pigmentary changes); stage 2, early AMD with medium drusen (63 - 125 μm) and no pigmentary abnormalities; and stage 3, which is subdivided into intermediate – large drusen and/or pigmentary changes – and advanced – choroidal neovascularization (CNV, exudative or neovascular AMD) or geographic atrophy (GA; dry or non-exudative AMD) [8]. Anti-vascular endothelial growth factor (anti-VEGF) has long been the mainstay of treatment for neovascular AMD, whereas no effective treatment is available for the more common dry form [9-12].

AMD is the result of complex interactions among metabolic, functional, genetic, and environmental factors [13]. It is characterized by degeneration of the retinal pigment epithelium (RPE), death of photoreceptors and degradation of choriocapillaries, which together lead to impairment and loss of central vision. The RPE is a polarized non-proliferative cell monolayer lying between the neural retina and the vascularized choroid. It serves several functions that are essential for vision and for the survival of retinal neurons. Its dysfunction, due to oxidative stress, mitochondrial destabilization, and complement dysregulation, has been implicated in AMD pathogenesis [14, 15]. During aging, RPE cells undergo a number of functional alterations that result in the development of age-related eye disorders, including AMD. RPE cell damage induced by proinflammatory factors – including tumor necrosis factor (TNF)- α – and cell death are able to promote activation of the alternative pathway (AP) of the complement system at the retina-choroid interface, a process that has been associated to RPE cell death; aging also induces a reduction in the number and an increase in the size and multinucleation of RPE cells [16]. The activation of different protein kinase C isoforms has also been implicated in the age-related formation of multinucleated RPE cells [17].

Neovascular AMD and GA are characterized by RPE dysfunction [18]; in GA, formation of large confluent drusen and hyperpigmentation (presumably related to the RPE dysfunction) seem to be the initial insult, while drusen resorption and RPE loss (hypopigmentation) are believed to predict its progression. Photoreceptor and choriocapillary dysfunction and death appear to be secondary to RPE loss; loss of choriocapillaries with an intact RPE has also been described in wet AMD [18]. According to a recent study, RPE cells from AMD patients show a different phenotype as well as functional changes such as altered autophagy, mitochondrial dysfunction, and susceptibility to

oxidative stress compared to those from normal individuals [19].

The early and intermediate stages of AMD are characterized by changes in lipid metabolism, autophagy, and inflammation; molecular signaling pathways, such as inflammation, cellular senescence and cell death, play a key role in the progression of late-stage dry AMD, whereas angiogenesis predominates in the neovascular form [3]. A greater understanding of the molecular pathways that are involved in the various stages of AMD would contribute to the development of innovative therapies.

An imbalance of circulating inflammatory molecules seems to characterize most age-related diseases (ARDs). Aging is characterized by a state of chronic, low-grade inflammation, known as inflammaging [20], which also appears to be involved in all stages of AMD development and progression.

Senescent cells are non-proliferating cells capable of secreting proinflammatory cytokines, thus contributing to ARD development and ARD-related morbidity. Cellular senescence is characterized by cell growth arrest, altered DNA synthesis and repair, resistance to apoptosis, and increased cell size [21]. Telomere shortening, DNA damage, and oxidative stress are capable of activating senescence processes [22].

Mesenchymal stem cells (MSCs) have been isolated from different adult tissues, including the RPE [23]. Ease of isolation, high proliferation potential, and low immunogenicity make them ideal for cell-based therapies. MSC function declines with age; senescent MSCs acquire a senescence-associated secretory phenotype (SASP) that contributes to driving aging and the development and progression of ARDs, including AMD [24].

The human RPE contains a subpopulation of stem-like MSCs (RPESCs) [23]. In a previous work, we isolated and characterized human RPESCs, demonstrated their ability to differentiate into mesenchymal (adipogenic, osteogenic and chondrogenic) lineages, and analyzed their differentiation potential into neuronal and retinal lineages [25]. In a recent study of an AMD rat model, transplantation of RPESCs isolated from human RPE was able to prevent visual loss [26].

The mechanisms involved in the activation of differentiation of resident RPESCs into mature RPE cells and the role of RPESCs in AMD pathogenesis are still unclear. A growing number of studies have been addressing the role of persistent inflammation in AMD development and progression. The aim of this work is

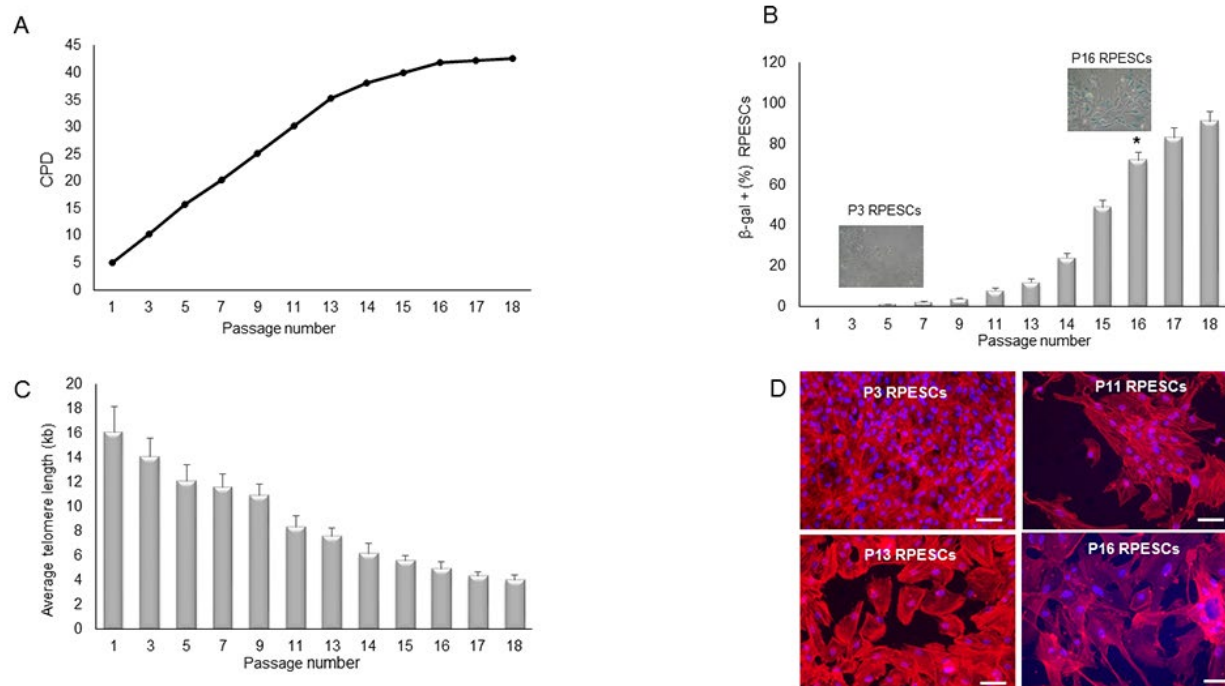


Figure 1. Proliferation rate, β -gal positivity, telomere length, and cell morphology during RPESC replicative senescence. RPESC replicative senescence. (A) Cumulative number of population doublings (CPD) in RPESCs grown to senescence. (B) Percentage of β -gal-positive cells detected during RPESC replicative senescence from P1 to P16. P11, number of culture passages. Data are reported as mean \pm SD. * $P=0.039$. (C) RPESC telomere length during replicative senescence was analyzed from P1 to P18; data are reported as mean \pm SD of 3 independent experiments. (D) Morphological analysis of young (P3) and senescent (P16) RPESCs by the TRIC-phalloidin immunofluorescence assay. Senescent RPESCs appear enlarged and flattened. Magnification 20X, scale bar 200 μ m. Pictures are representative of 3 independent experiments.

explore the molecular mechanisms that are involved in the acquisition of the senescent phenotype by RPESCs and the role of its proinflammatory factors in altering the function of aged RPE cells. To do so, we investigated the characteristics of replicative and stress-induced senescence of RPESCs, their morphological and genetic features, and their acquisition of the SASP, all of which seem to play a role in AMD pathogenesis.

RESULTS

Replicative senescence of human RPESCs

RPESCs were isolated, characterized, and cultured as described in a previous work by our group [25]. They were isolated from a healthy eye from a 21-year-old donor. All experiments were conducted using 3 different batches of exponentially growing cells at the 3rd passage (confluence about 75 %) in which replicative senescence was induced.

Replicative senescence was documented at the 16th passage (P16) by arrested proliferation, increased β -

galactosidase (SA β -gal) activity, and telomere length reduction. In particular, RPESC proliferation rate increased steeply from P2 to P11 and plateaued at P13; growth stopped at P18 (Figure 1A). As illustrated in Figure 1B, the proportion of β -gal-positive cells increased significantly ($P < 0.05$) from 6 ± 0.04 % in young cells (P3-P6) to 80 ± 12.1 % in senescent cells (P15-P18). Telomere length declined from 14 kb at P3 to 4 kb at P16 (Figure 1C). TRIC-phalloidin staining demonstrated that senescent RPESCs had a flatter and enlarged morphology compared to young cells (Figure 1D).

Acquisition of the secretory phenotype by senescent RPESCs

SASP acquisition by senescent RPESCs was determined by analyzing a panel of proinflammatory molecules: interleukin (IL)-6, interferon (INF)- γ , TNF- α , IL-12, and transforming growth factor β (TGF β)1 - in young (P3) and senescent (P16) RPESCs. The analysis was extended by determination of the levels of the anti-inflammatory molecules IL-4, IL-10, and IL-13.

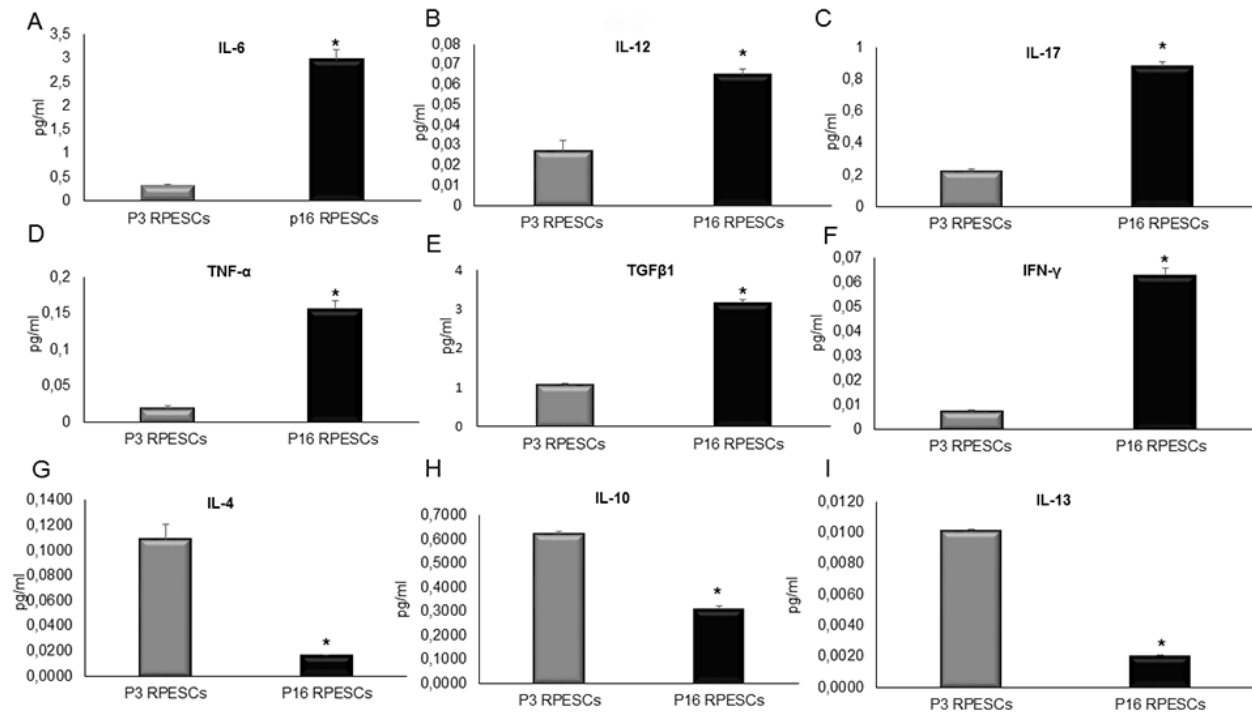


Figure 2. SASP induction in senescent RPESCs. Young (P3) and senescent (P16) RPESCs were maintained in culture for 48 h. The supernatant was analyzed for IL-6 (A), IL-12 (B), IL-17 (C), TNF- α (D), TGF β 1 (E), INF- γ (F), IL-4 (G), IL-10 (H), and IL-13 (I), by ELISA. Data are mean \pm SD of 3 independent experiments. * P = from 0.021 to 0.041.

The results of ELISA indicated that senescent RPESCs secreted higher levels of IL-6, IL-12, IL-17, TNF- α , TGF β 1, and INF- γ compared to young RPESCs (Figure 2A-F), reflecting a proinflammatory state and SASP acquisition. They also secreted lower levels of several anti-inflammatory molecules, including IL-4, IL-10, and IL-13, compared to young RPESCs (Figure 2G-I).

Expression of stemness, reprogramming, and RPE-specific genes in young and senescent RPESCs

The expression of RPE-specific (*OTX2*, *PEDF*, *PAX6*, *RPE65*, *MITF*, and *CRALBP*), stemness, and reprogramming (*SOX2*, *KLF4* and *c-MYC*) genes was investigated in young and senescent RPECS by qRT-PCR.

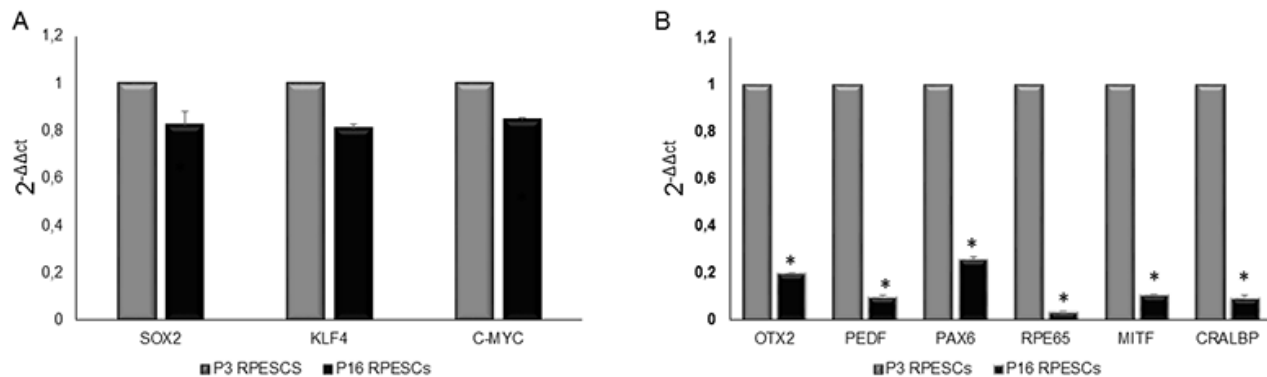


Figure 3. mRNA expression levels of stemness and RPE-specific genes in senescent and young RPESCs. (A) qRT-PCR analysis of the expression levels of stemness genes in senescent (P16) and young (P3) RPESCs. (B) qRT-PCR analysis of the mRNA levels of RPE-specific genes in senescent and young RPESCs. Data are mean \pm SD of 3 independent experiments. * P = from 0.026 to 0.036.

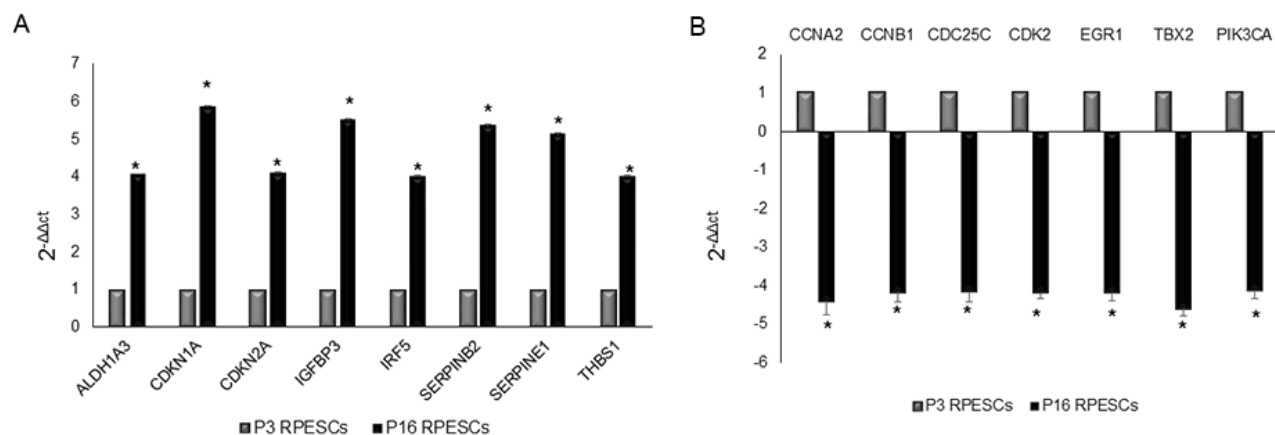


Figure 4. Senescence-associated gene expression profile in senescent and young RPESCs. PCR array performed to analyze the mRNA expression levels of senescence-associated genes in 3 senescent (P16) and 3 young (P3) RPESCs. Data are reported as fold change. A 4-fold difference was considered significant and only mRNAs with a $\Delta\Delta Ct$ greater than 4 (A) or lower than -4 (B) are reported. * $P =$ from 0.018 to 0.046.

As shown in Figure 3A, the two sets of cells showed similar expression levels of *SOX2*, *KLF4* and *c-MYC*, whereas senescent RPESCs exhibited downregulation of *OTX2*, *PEDF*, *PAX6*, *RPE65*, *MITF*, and *CRALBP* (Figure 3B).

Determination of the mRNA levels of senescence-associated genes in senescent and young RPESCs by PCR Array

The expression of senescence-associated genes in senescent and young RPESCs was measured by analyzing their mRNA levels using Cellular Senescence RT2 Profiler PCR Array (PAHS, Qiagen). Glyceraldehyde 3-phosphate dehydrogenase (*GAPDH*) and ribosomal protein, large, P0 (*RPLP0*) were used as inner controls to normalize gene expression levels.

Fifteen genes related to human cellular senescence were differentially expressed and showed a 4-fold change in senescent compared to young RPESCs: 8 genes, *ALDH1A3* (aldehyde dehydrogenase 1 family member A3), *CDKN1A* (cyclin-dependent kinase inhibitor 1A, p21), *CDKN2A* (cyclin-dependent kinase inhibitor 2A, P16INK4), *IGFBP3* (insulin-like growth factor binding protein 3), *IRF5* (interferon regulatory factor 5), *SERPINE2* (serpin family B member 2, PAI2), *SERPINE1* (serpin family E member 1, PAI1), and *THBS1* (thrombospondin 1), were upregulated (Figure 1A), whereas 7 genes, *CCNA2* (cyclin A2), *CCNB1* (cyclin B1), *CDC25C* (cell division cycle 25C), *CDK2* (cyclin-dependent kinase 2), *EGR1* (early growth response 1), *TBX2* (T-box 2), and *PIK3CA* (phosphatidylinositol-4,5-bisphosphate 3-kinase

catalytic subunit alpha), were downregulated (Figure 1B).

p21 and p53 protein expression in young and senescent RPESCs

Western blot analysis demonstrated that p21 and p53 protein were significantly upregulated in senescent compared to young RPESCs (Figure 5A) and that intermediate-passage cells (P11) were downregulated compared to both young and senescent RPESCs. The results of densitometric analysis and normalization to *GAPDH* expression (Figure 5B) were confirmed by real time PCR, which demonstrated that p21 and p53 mRNA was upregulated in senescent (P16) compared to young RPESCs (P3) (Figure 5C and D). In contrast, P11 RPESCs showed higher p21 and p53 mRNA and lower protein levels compared to young RPESCs (P3).

DISCUSSION

Age-related inflammation is a major risk factor in the aging process. AMD is a highly common, irreversible cause of severe loss of vision among the elderly in developed countries [2]. It has a multifactorial etiology, where advanced age and genetic predisposition are the strongest risk factors [27,28]. Although the mechanisms involved in its pathogenesis are unclear, inflammatory pathways have been reported to play a key role in its development and progression, as in the case of other ARDs [29]. Recent data have lent support to the hypothesis that senescent cells accumulate in the aging primate RPE [30]. Senescent cells accumulate with aging in human tissues and organs, promoting ARD

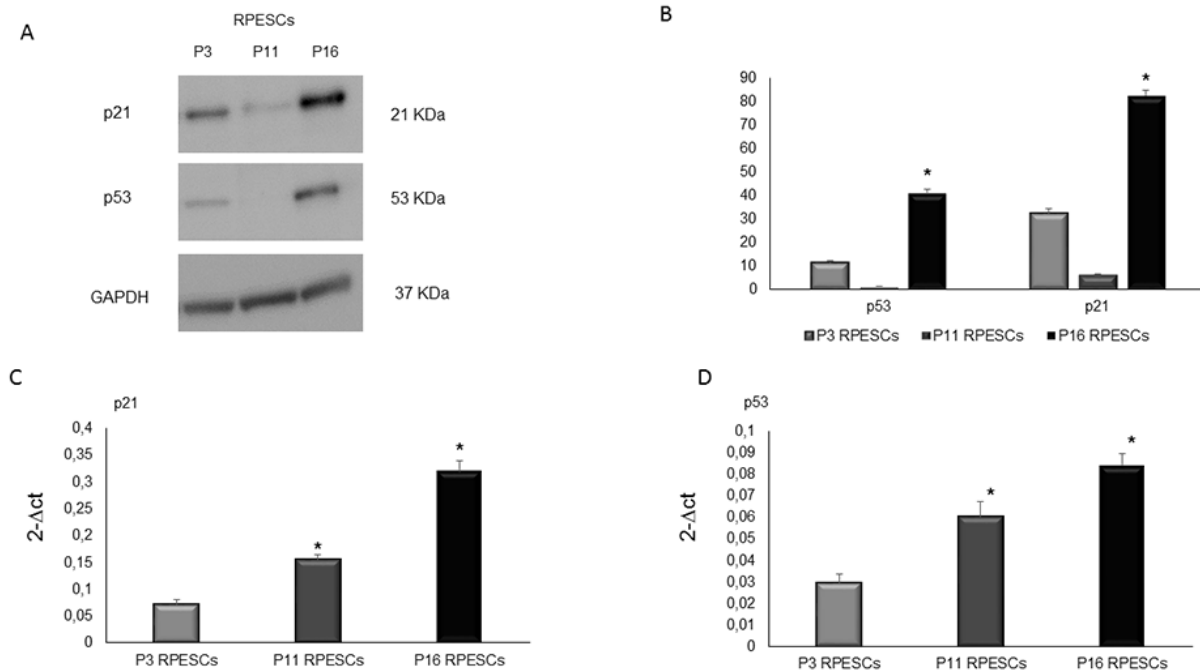


Figure 5. Human p53 and p21 protein expression levels in senescent and young RPESCs. p53 and p21 protein expression levels (A) Western blot analysis (B) and densitometric analysis of blots. Data are mean \pm SD of 3 independent experiments. * P = from 0.022 to 0.046. (C) Relative expression levels of mRNA related to p21 and (D) p53 genes in young (P3), pre-senescent (P11) and senescent (P16) RPESCs cells. Data are mean \pm SD of 3 independent experiments. * P = from 0.031 to 0.044.

development and progression; cell exposure to recurrent or chronic stress, including oxidative stress, may also result in their accumulation [31, 32]. Our group has recently characterized a stem cell-like population derived from the human RPE [25] as RPESCs (RPE progenitor cells). Notably, MSCs enter replicative senescence after a limited number of cell divisions, a fact that needs to be considered in experiments involving cell cultures, especially in investigations of regenerative medicine approaches. The effects of aging, senescence, and oxidative stress can induce loss of differentiation and proliferative potential in adult MSCs, including RPESCs [33]. Senescent cells acquire the SASP and release various proteins, including proinflammatory molecules, thus contributing to ARDs and the associated morbidity [34]. Critically, although human RPESCs have been identified as a stem-cell like population, they are unable to differentiate into mature RPE cells, replacing those that are lost due to AMD. In our previous study we isolated, cultured, and characterized RPESCs from the human RPE and investigated their differentiation potential [25]. In the present work, induction of replicative senescence in RPESCs resulted in reduced proliferative and multilineage differentiation potential, SASP acquisition, and release of inflammatory proteins that may be

involved in AMD development and progression. Senescent RPESCs exhibited telomere length shortening and a characteristic large and flattened morphology. They also stained for SA β -gal and showed upregulation of p21 and p53 protein compared to young RPESCs. p21 and p53 are key components of the senescence machinery, playing a critical role as regulators of stem cell functions [35]. Senescent RPESCs expressed higher mRNA levels of senescence-associated genes compared to their young counterparts. These genes, which include *CDKN1A* (p21), *IGFBP3*, *SERPINE1*, and *SERPINB2*, have been implicated in the maintenance of replicative and stress-induced cellular senescence mechanisms [36, 37]. In addition, *SERPINE1* (PAI1) is responsible for decreased extracellular matrix (ECM) degradation through inhibition of metalloprotease activation, mechanisms that may be involved in ECM accumulation in the RPE of AMD patients [38].

The irreversible growth arrest of senescent RPESCs was confirmed by the downregulation of the genes involved in cell cycle progression, including *CCNA2*, *CCNB1*, and *CDK2* [39, 40]. The transcription factors *SOX2*, *KLF4*, and *c-MYC* have been reported to play a regulatory role in stem cell self-renewal, i.e.

reprogramming. Interestingly, these stem-cell specific genes showed a similar expression level in senescent and young RPESCs, whereas the RPE-specific genes (*RPE65*, *MITF*, *OTX2*, *PAX6*, *CRALBP*, and *PEDF*) were downregulated in senescent RPESCs. These data suggest that despite their loss of differentiation potential during senescence, the reprogramming ability of these cells is preserved.

Senescent cells are metabolically active and release high concentrations of proinflammatory cytokines, chemokines, growth factors, and proteases into the culture medium [24, 41]. Senescent RPESCs (P16) secreted higher IL-6, IL-12, IL-17, INF- γ , TNF- α , and TGF β 1 concentrations compared to young RPESCs. INF- γ , TNF- α , and IL-17 are involved in Th1 and Th17 inflammation response pathways [42]. A recent study of the CD4⁺ T cell compartment in AMD patients has found that these cells play a proinflammatory role in an INF- γ - and IL-17-dependent fashion [43]. Such proinflammatory cytokines are also likely to play a key role in AMD pathogenesis, and their effect may well be reinforced by senescent RPESCs.

Interestingly, proinflammatory cytokines may induce activation of the anti-oxidative stress response in mature RPE cells, as reported in a study where protective anti-oxidant pathways were activated in mature RPE cells treated with oxidative agents and cultured with peripheral blood mononuclear cell-conditioned medium or with INF- γ /TNF- α [44]. Moreover, T-cell-derived proinflammatory cytokines were able to induce in mature RPE cells the production and secretion of multiple chemokines, which can affect the immune homeostasis in the retina [45]. Indeed, there is growing evidence for a role of the adaptive immune system in the pathogenesis of neovascular AMD. Several studies have addressed the crucial role of macrophages in the development of choroidal neovascularization [46, 47, 48] and of atrophic changes in the AMD retina [49], while an association has been described between AMD and systemic leukocyte activity [50].

Singh and co-workers have demonstrated that the age-related decrement in Th1 frequency seen in healthy controls is absent in AMD patients, since the percentage of CD4⁺ T-cells expressing CCR6 was significantly reduced in patients with non-exudative as well as exudative AMD [51]. There is also evidence that CCR2 expression in circulating monocytes may play a role in the development of neovascular AMD [52, 46]. Furthermore, significantly accelerated T-cell differentiation and aging have been described in the CD8⁺ T-cell compartment of patients with neovascular AMD [53].

As regards the pro/anti-inflammatory phenotype of senescent RPESCs, the present study found a significant downregulation of the anti-inflammatory cytokines IL-4, IL-10, and IL-13 in these cells. An increased or similar expression of these cytokines has been reported in the serum and aqueous humor of AMD patients compared with controls [54, 55], probably due to the acquisition by senescent RPESCs of a specific proinflammatory senescence-associated phenotype and to the downregulation of anti-inflammatory cytokines *in vitro*.

This study is preliminary and as such suffers from some limitations. Replicative senescence was induced *in vitro* in RPESCs isolated from the eye of a single healthy young donor. The examination of samples from aged AMD patients and healthy subjects is expected to provide insight into the senescent proinflammatory status of RPESCs in the elderly and into their role in disease pathogenesis. It would also be interesting to investigate the effects of oxidative agents on young and senescent RPESCs from the mature RPE in terms of induction of apoptosis or activation of anti-inflammatory anti-oxidant pathways.

Altogether, the present findings indicate that RPESCs can undergo replicative senescence, which affects their proliferation and differentiation ability. In addition, senescent RPESCs acquired the SASP, which probably compounds the inflammatory RPE microenvironment during AMD development and progression. A greater understanding of the role of RPESCs in AMD pathogenesis is needed to find means to control the disease and modulate its progression.

MATERIALS AND METHODS

RPESC culture

RPESCs were isolated, characterized, and cultured as described previously [25]. Cells were maintained in RPE medium [MEM- α modified medium containing 2 mM L-glutamine, penicillin/streptomycin (1:100), 1% Na-pyruvate, 10 % fetal bovine serum], supplemented with taurine, hydrocortisone, triiodothyronine (THT), and N1 (all from Sigma-Aldrich, Milano, Italy). RPESCs were incubated at 37°C in a 5% humidified CO₂ incubator. The medium was replaced every 3 days.

Replicative senescence was induced by culturing cells up to the 18th passage (P18). Viable cells were counted at each passage by trypan blue staining using an automated cell counter (Thermo Fisher, Milano, Italy). Population doublings (PDs) were determined as current PDs = last PDs + log₂ (collected cell number / seeded

cell number); cumulative PD (CPD) was calculated as the sum of PD changes, as described previously [56].

Telomere length measurement

Telomere length was measured using the Relative Human Telomere Length quantification qPCR assay kit (Sciencell Research Laboratories, San Diego, CA, USA) according to the manufacturer's protocol and a quantitative RT-PCR technique (Cawthon's method [57]), as described previously [56].

Senescence-associated β -galactosidase (SA β -gal) staining

β -gal staining was performed using the Senescence β -Galactosidase Staining kit (Cell Signaling Technology, Leiden, The Netherlands) according to the manufacturer's protocol.

Phalloidin staining

For phalloidin staining, young (P3), intermediate passage (P11) and senescent (P16) cells were seeded on chamber slides and cultured for 3 days in RPE medium. They were then fixed in 4% PFA for 30 min, blocked with bovine serum albumin (BSA), 2.5% in PBS for 30 min, and permeabilized with Triton X-100, 0.2% in BSA/PBS for 10 min at room temperature. Subsequently, cells were stained with TRITC-labeled phalloidin (Sigma Aldrich) according to the manufacturer's protocol. Nuclear staining was obtained by applying Hoechst solution (Molecular Probes, Thermo Fisher, Milano, Italy) for 10 min. Slides were mounted with Vectashield (Vector Laboratories, Burlingame, CA, USA).

Analysis of the secretory phenotype

The concentration of IL-4, IL-6, IL-10, IL-12, IL-13, INF- γ , TNF- α , and TGF β 1 was measured in the supernatant by an ELISA method (Multi-Analyte ELISArray kit, Qiagen; Affymetrix Ebiosciences, Vienna, Austria). Briefly, the supernatants were collected at the end of each passage before trypsinization, centrifuged, and stored at -20°C. Optical density at 450 nm was determined using a microtiter plate reader (Multiskan Go, Thermo Scientific, Monza, Italy). Cytokine concentration was determined as pg/ml by comparing their absorbance to the antigen standards. Each experiment was performed three times.

RNA isolation

Total RNA from P3 and P16 RPESCs was isolated using PerfectPure RNA Cell and Tissue Kit (5 PRIME,

Hamburg, Germany). The concentration and purity of total RNA samples were determined using a NanoDrop One Spectrophotometer (NanoDrop Technologies Inc., Wilmington, DE, USA). RNA was stored at -80 °C until use. About 300 ng of total RNA extracted from both RPESC sets was reverse transcribed using the GoScript™ Reverse Transcription System (Promega, Milano Italy) according to the manufacturer's protocol.

RT-PCR analysis

Real-time PCR was performed with a Master Cycle (Eppendorf, Hamburg, Germany) apparatus using EVA Green PCR Master Mix (Bio-Rad, Milano, Italy) according to the manufacturer's instructions. Conditions were as follows: denaturation 98°C for 2 min and 40 cycles of 98°C for 60 s and 60°C for 60 s. A melting stage was added at the end of amplification. There was no non-specific amplification as determined by the melting curve. All samples were tested in triplicate with the reference genes *β -actin* and *RPL30* for data normalization. Genes and related primer sequences (SOX2, KLF4, c-MYC, RPE65, CRALBP, PEDF, OTX2, MITF, p21 and p53) were as described previously [58]. The mRNA expression level of all tested genes was analyzed in young and senescent RPESCs with the $2^{-\Delta\Delta Ct}$ method: Δ (ΔCt) = ΔCt (senescent) - ΔCt (young). The relative expression values of the genes of interest are reported as mean \pm standard deviation (SD) of three independent experiments.

mRNA profiling

Total RNA from young (P3) and senescent (P16) RPESCs was isolated with the PerfectPure RNA Cell and Tissue Kit. cDNA synthesis was performed with RT² First Strand Kit (Qiagen, Milano, Italy) and Cellular Senescence RT Profiler PCR Array (PAHS-050ZA; Qiagen). The average of glyceraldehyde 3-phosphate dehydrogenase (*GAPDH*) and ribosomal protein, large, P0 (*RPLP0*) was used for normalization. Only mRNAs with reads < 35 Ct in all three biological replicates were included in the analysis. After amplification, melting curves were acquired. mRNA expression was quantified with the $2^{-\Delta\Delta Ct}$ method. Relative gene expression values are reported as mean \pm SD of three independent experiments.

Protein extraction and immunoblotting

Total protein was extracted from young (P3) and senescent (P16) RPESCs (1 x 10⁶ cells/sample) as described previously [16], with some modifications. Membranes were incubated overnight with the primary p21 and p53 antibody (Santa Cruz Biotechnology, Santa

Cruz, CA, USA) using GAPDH as the endogenous control, followed by incubation with the secondary antibody conjugated to horseradish peroxidase (Santa Cruz Biotechnology). Protein detection on the membrane was performed using the Clarity Western ECL Substrate Kit (Bio-Rad). The signals were captured with an Alliance Mini (UVITEC Cambridge, Cambridge, UK) system; the p21 and p53 bands were quantified with UVITEC software and their intensity was normalized by comparison to the housekeeping protein β -actin, used as a loading control. The intensity of each band was compared to the negative controls and any change was expressed as a percentage.

Statistical analysis

Results are expressed as mean \pm SD. Comparisons between groups were analyzed by paired-sample *t* test comparisons using SPSS 20.0 software. Significance was analyzed in data from at least three independent experiments. *P* values ≤ 0.05 were considered significant.

AUTHOR CONTRIBUTIONS

Raffaella Lazzarini, principal author, performed analysis on all samples, interpreted data and wrote manuscript. Michele Nicolai, principal co-author, helped in data interpretation and manuscript evaluation. Vittorio Pirani helped to evaluate and edit the manuscript. Cesare Mariotti, wrote manuscript and acted as corresponding author. Roberto Di Primio, supervised the findings of this work. All authors discussed the results and contributed to the final manuscript.

ACKNOWLEDGMENTS

The authors are grateful to Word Designs (www.silviamodena.com) for the language revision.

CONFLICTS OF INTEREST

The authors have declared that no competing interests exist.

REFERENCES

1. Hyttinen JM, Blasiak J, Niittykoski M, Kinnunen K, Kauppinen A, Salminen A, Kaarniranta K. DNA damage response and autophagy in the degeneration of retinal pigment epithelial cells—Implications for age-related macular degeneration (AMD). *Ageing Res Rev.* 2017; 36:64–77. <https://doi.org/10.1016/j.arr.2017.03.006>
2. Reibaldi M, Longo A, Pulvirenti A, Avitabile T, Russo A, Cillino S, Mariotti C, Casuccio A. Geo-Epidemiology of Age-Related Macular Degeneration: New Clues Into the Pathogenesis. *Am J Ophthalmol.* 2016; 161:78–93.e1, 2. <https://doi.org/10.1016/j.ajo.2015.09.031>
3. Blasiak J, Piechota M, Pawlowska E, Szatkowska M, Sikora E, Kaarniranta K. Cellular Senescence in Age-Related Macular Degeneration: Can Autophagy and DNA Damage Response Play a Role? *Oxid Med Cell Longev.* 2017; 2017:5293258. <https://doi.org/10.1155/2017/5293258>
4. Chakravarthy U, Wong TY, Fletcher A, Piau E, Evans C, Zlateva G, Buggage R, Pleil A, Mitchell P. Clinical risk factors for age-related macular degeneration: a systematic review and meta-analysis. *BMC Ophthalmol.* 2010; 10:31. <https://doi.org/10.1186/1471-2415-10-31>
5. Lim LS, Mitchell P, Seddon JM, Holz FG, Wong TY. Age-related macular degeneration. *Lancet.* 2012; 379:1728–38. [https://doi.org/10.1016/S0140-6736\(12\)60282-7](https://doi.org/10.1016/S0140-6736(12)60282-7)
6. Age-Related Eye Disease Study Research Group. Risk factors associated with age-related macular degeneration. A case-control study in the age-related eye disease study: Age-Related Eye Disease Study Report Number 3. *Ophthalmology.* 2000; 107:2224–32.
7. Seddon JM, Sharma S, Adelman RA. Evaluation of the clinical age-related maculopathy staging system. *Ophthalmology.* 2006; 113:260–66. <https://doi.org/10.1016/j.ophtha.2005.11.001>
8. Miller JW, Bagheri S, Vavvas DG. Advances in Age-related Macular Degeneration Understanding and Therapy. *US Ophthalmic Rev.* 2017; 10:119–30. <https://doi.org/10.17925/USOR.2017.10.02.119>
9. Abd AJ, Kanwar RK, Kanwar JR. Aged macular degeneration: current therapeutics for management and promising new drug candidates. *Drug Discov Today.* 2017; 22:1671–79. <https://doi.org/10.1016/j.drudis.2017.07.010>
10. Gillies MC, Campain A, Barthelmes D, Simpson JM, Arnold JJ, Guymer RH, McAllister IL, Essex RW, Morlet N, Hunyor AP, and Fight Retinal Blindness Study Group. Long-Term Outcomes of Treatment of Neovascular Age-Related Macular Degeneration: Data from an Observational Study. *Ophthalmology.* 2015; 122:1837–45. <https://doi.org/10.1016/j.ophtha.2015.05.010>
11. Yaspan BL, Williams DF, Holz FG, Regillo CD, Li Z, Dressen A, van Lookeren Campagne M, Le KN,

- Graham RR, Beres T, Bhangale TR, Honigberg LA, Smith A, et al, and MAHALO Study Investigators. Targeting factor D of the alternative complement pathway reduces geographic atrophy progression secondary to age-related macular degeneration. *Sci Transl Med*. 2017; 9:eaaf1443. <https://doi.org/10.1126/scitranslmed.aaf1443>
12. Holz FG, Sadda SR, Busbee B, Chew EY, Mitchell P, Tufail A, Brittain C, Ferrara D, Gray S, Honigberg L, Martin J, Tong B, Ehrlich JS, Bressler NM, and Chroma and Spectri Study Investigators. Efficacy and Safety of Lampalizumab for Geographic Atrophy Due to Age-Related Macular Degeneration: Chroma and Spectri Phase 3 Randomized Clinical Trials. *JAMA Ophthalmol*. 2018; 136:666–77. <https://doi.org/10.1001/jamaophthalmol.2018.1544>
 13. Nowak JZ. Age-related macular degeneration (AMD): pathogenesis and therapy. *Pharmacol Rep*. 2006; 58:353–63.
 14. Mitter SK, Song C, Qi X, Mao H, Rao H, Akin D, Lewin A, Grant M, Dunn W Jr, Ding J, Bowes Rickman C, Boulton M. Dysregulated autophagy in the RPE is associated with increased susceptibility to oxidative stress and AMD. *Autophagy*. 2014; 10:1989–2005. <https://doi.org/10.4161/auto.36184>
 15. Luo C, Zhao J, Chen M, Xu H. The expression of C1 inhibitor (C1INH) in macrophages is upregulated by retinal pigment epithelial cells - implication in subretinal immune privilege in the aging eye. *Aging (Albany NY)*. 2018; 10:1380–89. <https://doi.org/10.18632/aging.101474>
 16. Chen M, Rajapakse D, Fraczek M, Luo C, Forrester JV, Xu H. Retinal pigment epithelial cell multinucleation in the aging eye - a mechanism to repair damage and maintain homeostasis. *Aging Cell*. 2016; 15:436–45. <https://doi.org/10.1111/acel.12447>
 17. Rajapakse D, Chen M, Curtis TM, Xu H. PKC ζ -dependent upregulation of p27kip1 contributes to oxidative stress induced retinal pigment epithelial cell multinucleation. *Aging (Albany NY)*. 2017; 9:2052–68. <https://doi.org/10.18632/aging.101299>
 18. Bhutto I, Lutty G. Understanding age-related macular degeneration (AMD): relationships between the photoreceptor/retinal pigment epithelium/Bruch's membrane/choriocapillaris complex. *Mol Aspects Med*. 2012; 33:295–317. <https://doi.org/10.1016/j.mam.2012.04.005>
 19. Golestaneh N, Chu Y, Xiao YY, Stoleru GL, Theos AC. Dysfunctional autophagy in RPE, a contributing factor in age-related macular degeneration. *Cell Death Dis*. 2017; 8:e2537. <https://doi.org/10.1038/cddis.2016.453>
 20. Cevenini E, Monti D, Franceschi C. Inflamm-aging. *Curr Opin Clin Nutr Metab Care*. 2013; 16:14–20. <https://doi.org/10.1097/MCO.0b013e32835ada13>
 21. Rodier F, Campisi J. Four faces of cellular senescence. *J Cell Biol*. 2011; 192:547–56. <https://doi.org/10.1083/jcb.201009094>
 22. Muñoz-Espín D, Serrano M. Cellular senescence: from physiology to pathology. *Nat Rev Mol Cell Biol*. 2014; 15:482–96. <https://doi.org/10.1038/nrm3823>
 23. Salero E, Blenkinsop TA, Corneo B, Harris A, Rabin D, Stern JH, Temple S. Adult human RPE can be activated into a multipotent stem cell that produces mesenchymal derivatives. *Cell Stem Cell*. 2012; 10:88–95. <https://doi.org/10.1016/j.stem.2011.11.018>
 24. Lunyak VV, Amaro-Ortiz A, Gaur M. Mesenchymal Stem Cells Secretary Responses: Senescence Messaging Secretome and Immunomodulation Perspective. *Front Genet*. 2017; 8:220. <https://doi.org/10.3389/fgene.2017.00220>
 25. Mariotti C, Lazzarini R, Nicolai M, Saitta A, Orsini E, Orciani M, Di Primio R. Comparative study between amniotic-fluid mesenchymal stem cells and retinal pigmented epithelium (RPE) stem cells ability to differentiate towards RPE cells. *Cell Tissue Res*. 2015; 362:21–31. <https://doi.org/10.1007/s00441-015-2185-9>
 26. Davis RJ, Alam NM, Zhao C, Müller C, Saini JS, Blenkinsop TA, Mazzoni F, Campbell M, Borden SM, Charniga CJ, Lederman PL, Aguilar V, Naimark M, et al. The Developmental Stage of Adult Human Stem Cell-Derived Retinal Pigment Epithelium Cells Influences Transplant Efficacy for Vision Rescue. *Stem Cell Reports*. 2017; 9:42–49. <https://doi.org/10.1016/j.stemcr.2017.05.016>
 27. DeAngelis MM, Owen LA, Morrison MA, Morgan DJ, Li M, Shakoor A, Vitale A, Iyengar S, Stambolian D, Kim IK, Farrer LA. Genetics of age-related macular degeneration (AMD). *Hum Mol Genet*. 2017; 26:R45–50. <https://doi.org/10.1093/hmg/ddx228>
 28. Al-Zamil WM, Yassin SA. Recent developments in age-related macular degeneration: a review. *Clin Interv Aging*. 2017; 12:1313–30. <https://doi.org/10.2147/CIA.S143508>
 29. Nowak JZ. AMD--the retinal disease with an unprecised etiopathogenesis: in search of effective therapeutics. *Acta Pol Pharm*. 2014; 71:900–16.
 30. Mishima K, Handa JT, Aotaki-Keen A, Lutty GA, Morse LS, Hjelmeland LM. Senescence-associated beta-galactosidase histochemistry for the primate eye. *Invest Ophthalmol Vis Sci*. 1999; 40:1590–93.

31. Childs BG, Durik M, Baker DJ, van Deursen JM. Cellular senescence in aging and age-related disease: from mechanisms to therapy. *Nat Med.* 2015; 21:1424–35. <https://doi.org/10.1038/nm.4000>
32. Naylor RM, Baker DJ, van Deursen JM. Senescent cells: a novel therapeutic target for aging and age-related diseases. *Clin Pharmacol Ther.* 2013; 93:105–16. <https://doi.org/10.1038/clpt.2012.193>
33. Denu RA, Hematti P. Effects of Oxidative Stress on Mesenchymal Stem Cell Biology. *Oxid Med Cell Longev.* 2016; 2016:2989076. <https://doi.org/10.1155/2016/2989076>
34. He S, Sharpless NE. Senescence in Health and Disease. *Cell.* 2017; 169:1000–11. <https://doi.org/10.1016/j.cell.2017.05.015>
35. Zon LI. Intrinsic and extrinsic control of haematopoietic stem-cell self-renewal. *Nature.* 2008; 453:306–13. <https://doi.org/10.1038/nature07038>
36. Elzi DJ, Lai Y, Song M, Hakala K, Weintraub ST, Shiio Y. Plasminogen activator inhibitor 1--insulin-like growth factor binding protein 3 cascade regulates stress-induced senescence. *Proc Natl Acad Sci USA.* 2012; 109:12052–57. <https://doi.org/10.1073/pnas.1120437109>
37. Zhu Y, Tchkonja T, Pirtskhalava T, Gower AC, Ding H, Giorgadze N, Palmer AK, Ikeno Y, Hubbard GB, Lenburg M, O'Hara SP, LaRusso NF, Miller JD, et al. The Achilles' heel of senescent cells: from transcriptome to senolytic drugs. *Aging Cell.* 2015; 14:644–58. <https://doi.org/10.1111/acer.12344>
38. Fuchshofer R, Yu AL, Teng HH, Strauss R, Kampik A, Welge-Lussen U. Hypoxia/reoxygenation induces CTGF and PAI-1 in cultured human retinal pigment epithelium cells. *Exp Eye Res.* 2009; 88:889–99. <https://doi.org/10.1016/j.exer.2008.11.036>
39. Kim J, Kim Y, Choi H, Kwon A, Jekarl DW, Lee S, Jang W, Chae H, Kim JR, Kim JM, Kim M. Ubiquitin C decrement plays a pivotal role in replicative senescence of bone marrow mesenchymal stromal cells. *Cell Death Dis.* 2018; 9:139. <https://doi.org/10.1038/s41419-017-0032-5>
40. Krenning L, Feringa FM, Shaltiel IA, van den Berg J, Medema RH. Transient activation of p53 in G2 phase is sufficient to induce senescence. *Mol Cell.* 2014; 55:59–72. <https://doi.org/10.1016/j.molcel.2014.05.007>
41. Rodier F. Detection of the senescence-associated secretory phenotype (SASP). *Methods Mol Biol.* 2013; 965:165–73. https://doi.org/10.1007/978-1-62703-239-1_10
42. Leung S, Liu X, Fang L, Chen X, Guo T, Zhang J. The cytokine milieu in the interplay of pathogenic Th1/Th17 cells and regulatory T cells in autoimmune disease. *Cell Mol Immunol.* 2010; 7:182–89. <https://doi.org/10.1038/cmi.2010.22>
43. Chen J, Wang W, Li Q. Increased Th1/Th17 Responses Contribute to Low-Grade Inflammation in Age-Related Macular Degeneration. *Cell Physiol Biochem.* 2017; 44:357–67. <https://doi.org/10.1159/000484907>
44. Juel HB, Faber C, Svendsen SG, Vallejo AN, Nissen MH. Inflammatory cytokines protect retinal pigment epithelial cells from oxidative stress-induced death. *PLoS One.* 2013; 8:e64619. <https://doi.org/10.1371/journal.pone.0064619>
45. Juel HB, Faber C, Udsen MS, Folkersen L, Nissen MH. Chemokine expression in retinal pigment epithelial ARPE-19 cells in response to coculture with activated T cells. *Invest Ophthalmol Vis Sci.* 2012; 53:8472–80. <https://doi.org/10.1167/iovs.12-9963>
46. Tsutsumi C, Sonoda KH, Egashira K, Qiao H, Hisatomi T, Nakao S, Ishibashi M, Charo IF, Sakamoto T, Murata T, Ishibashi T. The critical role of ocular-infiltrating macrophages in the development of choroidal neovascularization. *J Leukoc Biol.* 2003; 74:25–32. <https://doi.org/10.1189/jlb.0902436>
47. McLeod DS, Bhutto I, Edwards MM, Silver RE, Seddon JM, Luttj DA. Distribution and Quantification of Choroidal Macrophages in Human Eyes With Age-Related Macular Degeneration. *Invest Ophthalmol Vis Sci.* 2016; 57:5843–55. <https://doi.org/10.1167/iovs.16-20049>
48. Camelo S, Calippe B, Lavalette S, Dominguez E, Hur J, Devevre E, Guillonnet X, Raoul W, Sennlaub F. Thinning of the RPE and choroid associated with T lymphocyte recruitment in aged and light-challenged mice. *Mol Vis.* 2015; 21:1051–59.
49. Sennlaub F, Auvynet C, Calippe B, Lavalette S, Poupel L, Hu SJ, Dominguez E, Camelo S, Levy O, Guyon E, Saederup N, Charo IF, Rooijen NV, et al. CCR2(+) monocytes infiltrate atrophic lesions in age-related macular disease and mediate photoreceptor degeneration in experimental subretinal inflammation in Cx3cr1 deficient mice. *EMBO Mol Med.* 2013; 5:1775–93. <https://doi.org/10.1002/emmm.201302692>
50. Subhi Y, Lykke Sørensen T. New neovascular age-related macular degeneration is associated with

- systemic leucocyte activity. *Acta Ophthalmol.* 2017; 95:472–80. <https://doi.org/10.1111/aos.13330>
51. Singh A, Subhi Y, Krogh Nielsen M, Falk MK, Matzen SM, Sellebjerg F, Sørensen TL. Systemic frequencies of T helper 1 and T helper 17 cells in patients with age-related macular degeneration: A case-control study. *Sci Rep.* 2017; 7:605. <https://doi.org/10.1038/s41598-017-00741-4>
 52. Subhi Y, Krogh Nielsen M, Molbech CR, Sørensen TL. Altered proportion of CCR2+ and CX3CR1+ circulating monocytes in neovascular age-related macular degeneration and polypoidal choroidal vasculopathy. *Clin Experiment Ophthalmol.* 2018; 46:661–69. <https://doi.org/10.1111/ceo.13152>
 53. Subhi Y, Nielsen MK, Molbech CR, Oishi A, Singh A, Nissen MH, Sørensen TL. T-cell differentiation and CD56+ levels in polypoidal choroidal vasculopathy and neovascular age-related macular degeneration. *Aging (Albany NY).* 2017; 9:2436–52 <https://doi.org/10.18632/aging.101329>
 54. Nassar K, Grisanti S, Elfar E, Lüke J, Lüke M, Grisanti S. Serum cytokines as biomarkers for age-related macular degeneration. *Graefes Arch Clin Exp Ophthalmol.* 2015; 253:699–704. <https://doi.org/10.1007/s00417-014-2738-8>
 55. Spindler J, Zandi S, Pfister IB, Gerhardt C, Garweg JG. Cytokine profiles in the aqueous humor and serum of patients with dry and treated wet age-related macular degeneration. *PLoS One.* 2018; 13:e0203337. <https://doi.org/10.1371/journal.pone.0203337>
 56. Olivieri F, Lazzarini R, Recchioni R, Marcheselli F, Rippo MR, Di Nuzzo S, Albertini MC, Graciotti L, Babini L, Mariotti S, Spada G, Abbatecola AM, Antonicelli R, et al. MiR-146a as marker of senescence-associated pro-inflammatory status in cells involved in vascular remodelling. *Age (Dordr).* 2013; 35:1157–72. <https://doi.org/10.1007/s11357-012-9440-8>
 57. Cawthon RM. Telomere measurement by quantitative PCR. *Nucleic Acids Res.* 2002; 30:e47. <https://doi.org/10.1093/nar/30.10.e47>
 58. Amatori S, Bagaloni I, Macedi E, Formica M, Giorgi L, Fusi V, Fanelli M. Malten, a new synthetic molecule showing in vitro antiproliferative activity against tumour cells and induction of complex DNA structural alterations. *Br J Cancer.* 2010; 103:239–48. <https://doi.org/10.1038/sj.bjc.6605745>

p62 /SQSTM1 coding plasmid prevents age related macular degeneration in a rat model

Nataliya G. Kolosova^{1,*}, Oyuna S. Kozhevnikova^{1,*}, Darya V. Telegina¹, Anzhela Zh. Fursova^{1,2}, Natalia A. Stefanova¹, Natalia A. Muraleva¹, Franco Venanzi⁴, Michael Y. Sherman⁵, Sergey I. Kolesnikov^{7,8,9}, Albert A. Sufianov^{6,11}, Vladimir L. Gabai^{3,10}, Alexander M. Shneider^{3,5,6}

¹Institute of Cytology and Genetics, SB RAS, Novosibirsk, Russia

²Novosibirsk State Regional Clinical Hospital, Novosibirsk, Russia

³CureLab Oncology, Inc, Deadham, MA 02492, USA

⁴School of Biosciences, University of Camerino, Camerino, Italy

⁵Department of Molecular Biology, Ariel University, Ariel, Israel

⁶Sechenov First Moscow State Medical University, Moscow, Russia

⁷Russian Academy of Sciences, Moscow, Russia

⁸Lomonosov Moscow State University, Moscow, Russia

⁹Research Center of Family Health and Reproduction Problems, Irkutsk, Russia

¹⁰Department of Biochemistry, Boston University School of Medicine, Boston, MA 02118, USA

¹¹Federal Center of Neurosurgery, Tyumen, Russia

* Equal contribution

Correspondence to: Alexander Shneider, Nataliya Kolosova; **email:** ashneider@curelab.com, kolosova@bionet.nsc.ru

Keywords: p62/SQSTM1, age-related macular degeneration, inflammation, gliosis, OXYS rats, aging, retina

Received: August 3, 2018

Accepted: August 21, 2018

Published: August 28, 2018

Copyright: Kolosova et al. This is an open-access article distributed under the terms of the Creative Commons Attribution License (CC BY 3.0), which permits unrestricted use, distribution, and reproduction in any medium, provided the original author and source are credited.

ABSTRACT

P62/SQSTM1, a multi-domain protein that regulates inflammation, apoptosis, and autophagy, has been linked to age-related pathologies. For example, previously we demonstrated that administration of p62/SQSTM1-encoding plasmid reduced chronic inflammation and alleviated osteoporosis and metabolic syndrome in animal models. Herein, we built upon these findings to investigate effect of the p62-encoding plasmid on an age-related macular degeneration (AMD), a progressive neurodegenerative ocular disease, using spontaneous retinopathy in senescence-accelerated OXYS rats, as a model. Overall, the p62DNA decreased the incidence and severity of retinopathy. In retinal pigment epithelium (RPE), p62DNA administration slowed down development of the destructive alterations of RPE cells, including loss of regular hexagonal shape, hypertrophy, and multinucleation. In neuroretina, p62DNA prevented gliosis, retinal thinning, and significantly inhibited microglia/macrophages migration to the outer retina, prohibiting their subretinal accumulation. Taken together, our results suggest that the p62DNA has a strong retinoprotective effect in AMD.

INTRODUCTION

Age-related macular degeneration (AMD) is the most common cause of irreversible vision loss in industrialized countries [1]. Prevalence of AMD is increasing

dramatically as the proportion of the elderly in the population continues to rise [1]. By clinical signs, there are two forms of AMD: dry and wet AMD forms, also known as geographic atrophy and exudative AMD, respectively. There are effective treatments of vascular

complications of neovascular AMD by anti-VEGF therapeutics. However, neither there is a treatment of the dry form of AMD (~ 90% of all cases) nor preventive strategies against progression to the nonexudative form of AMD [2]. Therefore, the development of effective therapeutic and prophylactic modalities against AMD is an urgent task. AMD is a multifactorial disease involving a complex interplay of genetic, environmental, metabolic, and functional factors [3]. Age-related alterations in the immune system, inflammation and autophagy as well as oxidative stress strongly interwoven into AMD pathogenesis and represent possible targets for new therapies [4].

To study age-associated disorders, we introduced a model of senescence-accelerated OXYS rats, which spontaneously develop a phenotype similar to human AMD-like retinopathy [5-10]. Retinopathy that develops in OXYS rats even at a young age corresponds (in terms of clinical manifestations and morphological characteristics) to the dry atrophic form of AMD in humans. Furthermore, neovascularisation develops in some (~10–20%) of these rats with age. The clinical signs of AMD-like retinopathy appear by the age of 3 months in 100% of OXYS rats against the background of a reduction in the transverse area of the RPE and impairment of choroidal microcirculation [7, 8]. Significant pathological changes in the RPE as well as clinical signs of advanced stages of retinopathy are evident in OXYS rats older than 12 months [6, 10]. These changes manifest themselves as excessive accumulation of lipofuscin and amyloid in the RPE regions [6], disturbances in the morphology of the RPE sheet, including an increase in the proportion of multinucleated cells, hypertrophy, distortion of cell shape, and reactive gliosis [10]. This animal model is successfully used to study the pathways and molecular alterations implicated in the development and progression of age-related diseases [11, 12] as well as to test new therapeutic interventions [8, 13, 14].

The adapter protein p62/SQSTM1 interacts with many signaling factors, and regulates major cellular functions including inflammation, apoptosis, and autophagy [15, 16]. In the retinal pigment epithelium (RPE), p62 promotes autophagy and simultaneously enhances an Nrf2-mediated antioxidant response to protect against acute oxidative stress [16]. Recently, a DNA plasmid encoding p62-SQSTM1 (p62DNA) has been developed as biological agent for treatment diseases associated with chronic inflammation. Indeed, it demonstrated strong anti-osteoporotic activity [17], and alleviated diet-induced obesity and metabolic dysfunctions [18] in animal models. Notably, suppression of osteoporosis and metabolic syndrome by p62DNA were associated with a sharp down-regulation of master pro-inflamma-

tory cytokines, and up-regulation of anti-inflammatory species [17, 18]. Because of a significant inflammatory component in AMD, we hypothesized that quenching chronic inflammatory reactions upon administration of p62DNA may alleviate the disease. Here, we assessed effects of p62DNA administration on the development of retinopathy in OXYS rats and evaluated possible mechanisms of its action.

RESULTS

p62DNA inhibits retinopathy development in OXYS rats

In the first series of experiments, we assessed possible prophylactic effects of p62DNA against the development of retinopathy. Set of six p62DNA weekly injections started at the age of 1.5 months prior to any signs of retinopathy. Preliminary examination of rats at the age of 1.5 months showed that in experimental and control groups of OXYS rats signs of the 1st stage (1 a.u.) of retinopathy were present in 15 and 10% of animals, respectively. Five injections of the p62DNA ones a week (from 1.5 months of age) significantly slowed down development of retinopathy in OXYS rats (Figure 1A). Indeed, by the age of 3 months, 55% of eyes in the control group developed the signs of the 1st stage of retinopathy, 30% developed the 2nd stage, and only 15% of eyes remained without the signs of the disease. In contrast, in the p62DNA treated group, 55% of eyes developed the signs of the 1st stage of retinopathy, while the rest 45% of eyes did not show any signs of degeneration. Accordingly, statistical analysis showed that the average level of retinopathy in the p62DNA-treated OXYS rat's eyes was 2.5 times lower than in the control animals (0.45 ± 0.11 and 1.15 ± 0.15 a.u., $p < 0.001$, respectively).

Another experiment was conducted testing if the plasmid effects progression of AMD in the older animals (Figure 1B). Examination of these animals at the age of 12 months revealed that all animals had signs of retinopathy in at least one eye. 75 percent of eyes in the control group manifested changes corresponding to the AMD predisciform stage (1 a.u.) and 25% did not have the signs of retinopathy. In the experimental group, 65% of eyes had changes corresponding to the predisciform stage (1 a.u.) and 35% of rats did not have the signs of retinopathy. Statistical analysis showed that retinopathy continued to progress in both control and experimental groups but p62DNA reduced the severity of patho-logical changes in the eyeground of OXYS rats ($p < 0.001$). By the time of the second eye inspection at the age of 13.5 months, all the eyes in the control group had signs of retinopathy corresponding to the 2nd stage of AMD (2 a.u.). At the same time, p62DNA-treated

OXYS rats demonstrated pathological changes corresponding to the 1st stage of AMD in the 45% of retinas, and to the 2st stage - in the 55% of eyes. These data indicate that administration of p62DNA in the prophylactic setting significantly delays development of AMD signs and alleviates the severity of the disease.

Effect of p62DNA remained for 6 months after the treatment

To assess the duration of the effect of p62DNA on AMD, groups of OXYS rats were administered weekly injections of either p62DNA or PBS control and then

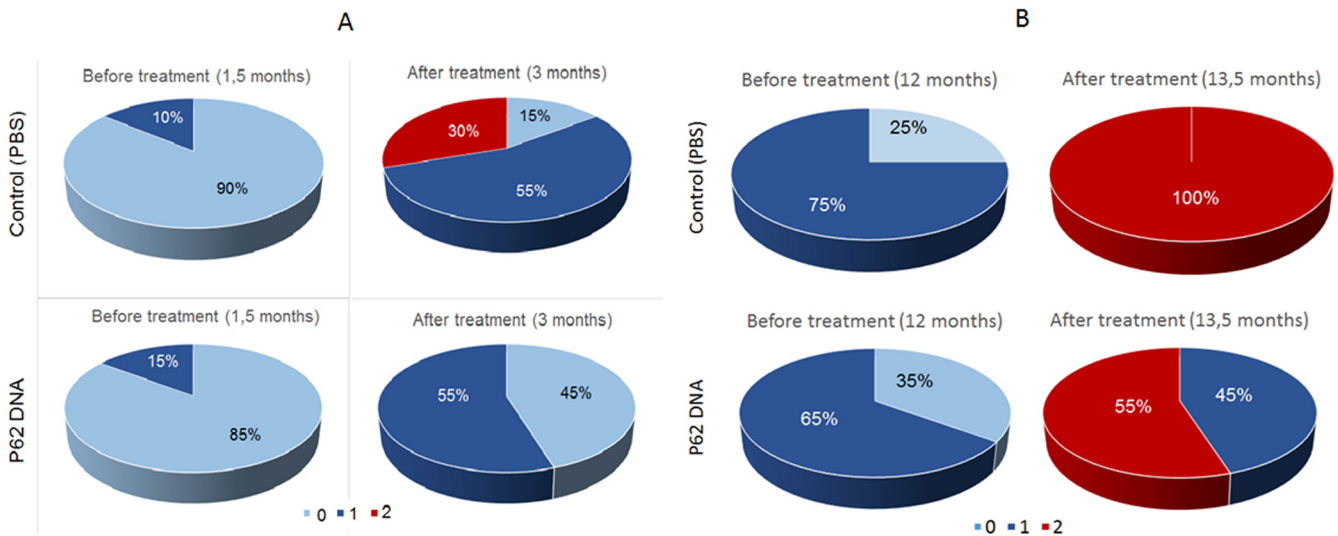


Figure 1. Effect of treatment with p62 - plasmid on the retinopathy developing in OXYS rats at 1.5 and 12 months of age. The data are presented as percentage of eyes with stages (0, 1 and 2) of retinopathy before and after treatment in control (PBS) and p62-treated OXYS rats. In each group, 20 eyes of 10 animals were examined.

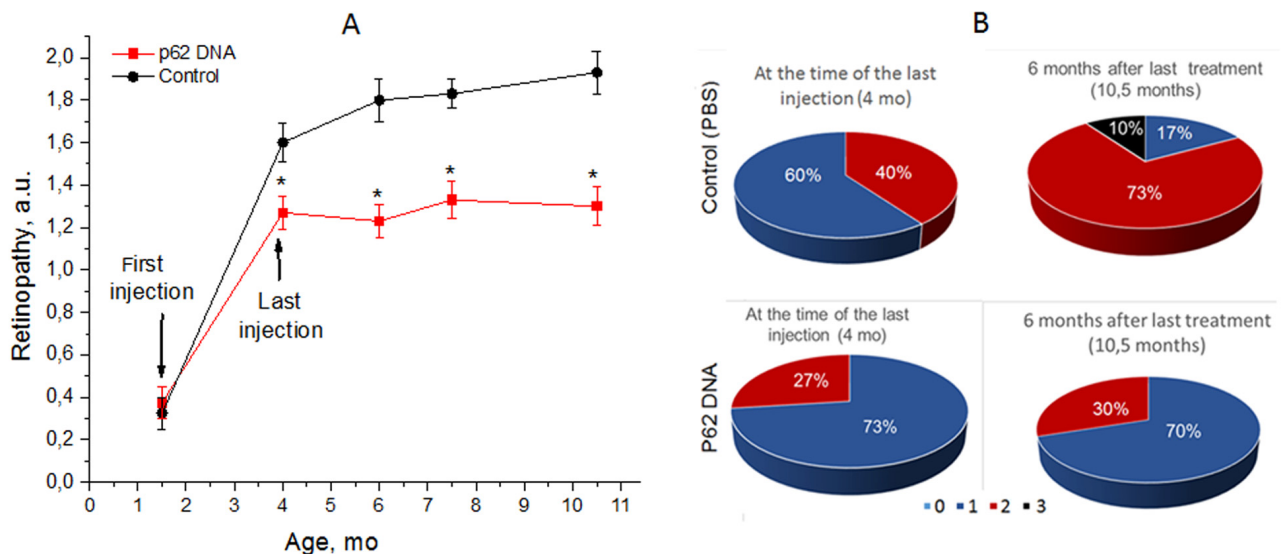


Figure 2. p62 DNA suppressed development of retinopathy and the effect persisted for 6 months after the last injection. (A) The data are presented as a.u. corresponding to the stages of retinopathy. *A significant increase in the severity of retinopathy according to the pairwise comparisons of the eye condition before and after treatment. (B) Stages of retinopathy in 4- and 10.5-month-old controls and p62 treated OXYS rats. Treatment was started at the age 1.5 months. In each group, 30 eyes of 15 animals were examined. The data are presented as the percentage of eyes with stages (0, 1, 2 and 3) of retinopathy.

observed for 6 months. The first injection took place at the age of 1.5 month, and the last one at 4.5 months. Each animal was examined by an ophthalmologist every second week. The results of examination are shown in Figure 2. The first (preliminary) examination of rats at the age of 1.5 months revealed that the same percentage of eyes in the experimental and the control group of OXYS rats had signs of the first stage of retinopathy (30% and 35% respectively). At the age of 4 months, 73% of eyes manifested signs of 1st stage retinopathy, and 27% - signs of the 2nd stage disease in p62-treated rats. At the same time in control rats, we found signs corresponding to the first and second stages of the disease in 40% and 60% of eyes respectively. According to the ANOVA analysis, an averaged stage of retinopathy in p62-treated rats was significantly reduced compared to the control ($p < 0.009$).

Starting 4 months of age, p62DNA completely prevented further development of retinopathy in OXYS rats. As a result, the severity of retinopathy signs at the age of 10.5 months remained at the level of 4-month-old animals: 70% of eyes of OXYS rats from this group had signs of first-stage and 30% second stage of retinopathy, indicating the disease remained stable during at least 6 months following the p62DNA injections. In contrast, examination of the control animals at the ages of 7.5 and 10.5 months indicated enhancements of the severity of pathological changes ($p < 0.015$). Indeed, at the age of 10.5 months, we detected signs of first-stage AMD in 17% of the eyes, second-stage - in 73%, and the third-stage - in 10% of eyes of the control OXYS rats (Figure 2). Therefore, administration of p62DNA precludes further disease progression, an effect that can last for 6 months.

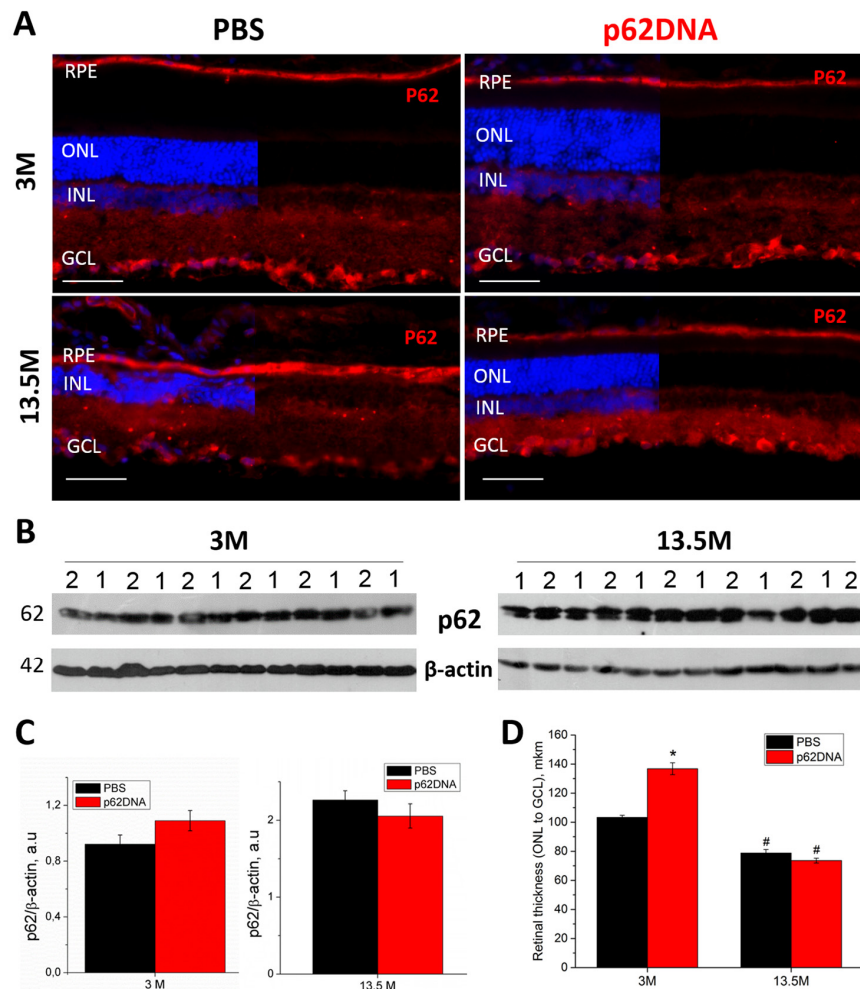


Figure 3. Effect of p62 DNA on p62 expression in the retina of OXYS rats at 3 and 13.5 months. (A) Representative p62 immunofluorescence of retinal cryosections from 3- and 13.5-month-old OXYS rats treated by PBS (left) or p62DNA plasmid (right). Scale bar: 50 μm. RPE: retinal pigment epithelium; ONL: outer nuclear layer; INL: inner nuclear layer; GCL: ganglion cells layer. (B) Representative immunoblots of p62 in the retina of OXYS rats. 1 - PBS; 2 - p62DNA. (C) Levels of p62 protein by immunoblot. (D) Measurements of retinal thickness (from ONL to GCL) in 3- and 13.5-month-old OXYS rats treated by p62DNA or PBS. * $p < 0.05$, statistically significant effect of p62DNA; # $p < 0.05$ between 3 and 13.5 months. Data are presented as mean ± SEM.

Administering of p62DNA does not change expression of retinal p62

Western blot analysis and immunohistochemistry were performed to determine expression of p62 in the retina of 3- and 13.5-month-old OXYS rats receiving injections of PBS (vehicle control) or p62DNA (Figure 3A-C). Immunohistochemical staining of the retinal slices revealed strong p62 expression in the RPE cells and around the nuclei of the inner nuclear (INL) and ganglion cells layers (GCL) in both control and treated animals. P62 expression was weaker in outer and inner plexiform layers (OPL and IPL) in rats of all groups (Figure 3A) (n=4 p62DNA, n=4 PBS). Also, immunostaining revealed p62 granules in plexiform layers, and the number of these granules increased with age. However, we did not detect any significant differences in the p62 immunostaining between plasmid-treated and PBS groups. The lack of difference in expression of p62 protein in rat retina in control and following p62DNA administration either at 3 months or 13.5 months old animals was further confirmed by immunoblotting with anti-p62 antibody (Figure 3B-C) (n=6 p62DNA, n=6 PBS).

Administering p62DNA prevents degeneration of neuroretina and RPE

We observed a higher overall retinal thickness (from GCL to ONL) in young OXYS rats treated with p62DNA compared to PBS-treated group (Figure 3D) ($p < 0.05$, n=4 p62DNA, n=4 PBS). In the control OXYS rats group, we observed a substantial reduction of the number of rows of photoreceptors (Figure 3A) and the retinal thickness (Figure 3D) by 13.5 months of age. These changes indicate progressive retinal neurodegeneration. At the same time, the age-associated reduction of the number of photoreceptor rows observed at the age of 13.5 months was substantially smaller in animals that received 6 weekly injections of p62 from 12 months. However, treatment of the older rats with the plasmid (starting at the age of 12 months) did not prevent or reverse the decline in retinal thickness.

RPE cells are first affected during AMD pathogenesis. In line with this observation, destructive alteration in RPE cells is a primary change during the development of retinopathy in OXYS rats [10]. We investigated the effect of p62DNA on the state of actin cytoskeleton in RPE cell by staining RPE flat mounts with phalloidin (Figure 4B). According to the commonly accepted practice assuring the highest quality and reproducibility, we analysed only the central zone of the RPE, which is in close proximity to the exit site of the optic nerve. In 3 months old PBS control OXYS rats, we observed hypertrophic and multinucleate RPE cells with loss of

hexagon shape, indicating significant abnormalities. By the age of 13.5-months in PBS control OXYS rats, the majority of RPE cells displayed disorganized morphology and the loss of hexagon shape. This qualitative assessment showed a significant increase in proportion of multinucleate and hypertrophic RPE cells upon aging. In contrast, in p62DNA treated groups, the RPE cell exhibited mostly a regular organized structure with a smaller proportion of pathologically altered cells (Figure 4B). Thus, p62DNA treatment significantly alleviated destructive alterations of RPE cells.

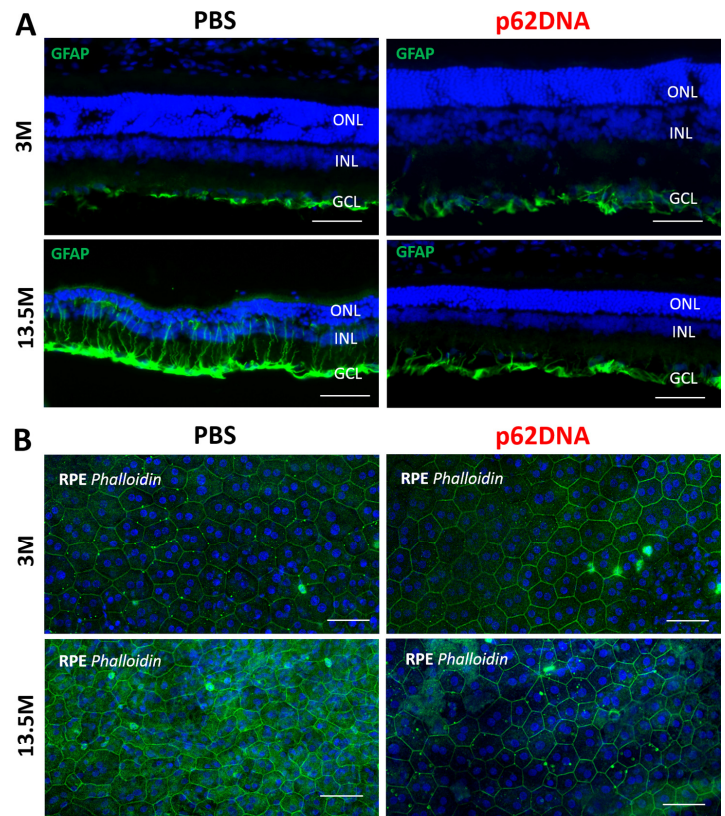


Figure 4. Effect of p62DNA on the GFAP expression and the state of RPE cells. (A) Representative GFAP immunostaining in retina of 3- and 13.5-month-old OXYS rats, treated by PBS (left) or p62DNA (right). GFAP staining was mainly confined to astrocytes and the ganglion cell layer at the inner limiting membrane in OXYS rats at the age of 3 months. In PBS-treated 13.5-month-old OXYS rats, the increased GFAP expression was observed along the Müller glial cell processes extending towards the outer limiting membrane, representing massive gliosis. p62DNA treatment prevented GFAP accumulation in 13.5-month-old OXYS rats. Scale bar: 50 μ m. ONL: outer nuclear layer; INL: inner nuclear layer; GCL: ganglion cells layer. (B) Representative images of phalloidin-stained RPE flat-mounts of 3- and 13.5-month-old OXYS rats, treated by PBS (left) or p62DNA (right). p62DNA treatment slowed down development of the destructive alterations of RPE cells (the loss of regular hexagonal shape, the hypertrophy, the multinucleation) in OXYS rats. Scale bar: 50 μ m.

Effect of administering p62DNA on GFAP expression

Upregulation of glial fibrillary acidic protein (GFAP) is a well-established indicator of retinal injury and reactive gliosis [19]. Accordingly, we investigated expression of GFAP by immunohistochemistry with the corresponding antibody. At the age of 3 months, GFAP staining was mainly confined to astrocytes and ganglion cell layer at the inner limiting membrane (Figure 4A),

and there was no significant difference between levels of GFAP in the retina of p62DNA and PBS groups. By the 13.5 months of age, astrocytes and Müller cells were strongly activated in control animals, as shown by the intense GFAP staining in the macroglial outgrowths from GCL towards the outer limiting membrane beyond ONL, re-presenting massive gliosis (Figure 4A). However, p62DNA treatment strongly reduced, and in some cases completely prevented GFAP upregulation in 13.5-month-old OXYS rats (Figure 4A) (n=4 p62DNA, n=4

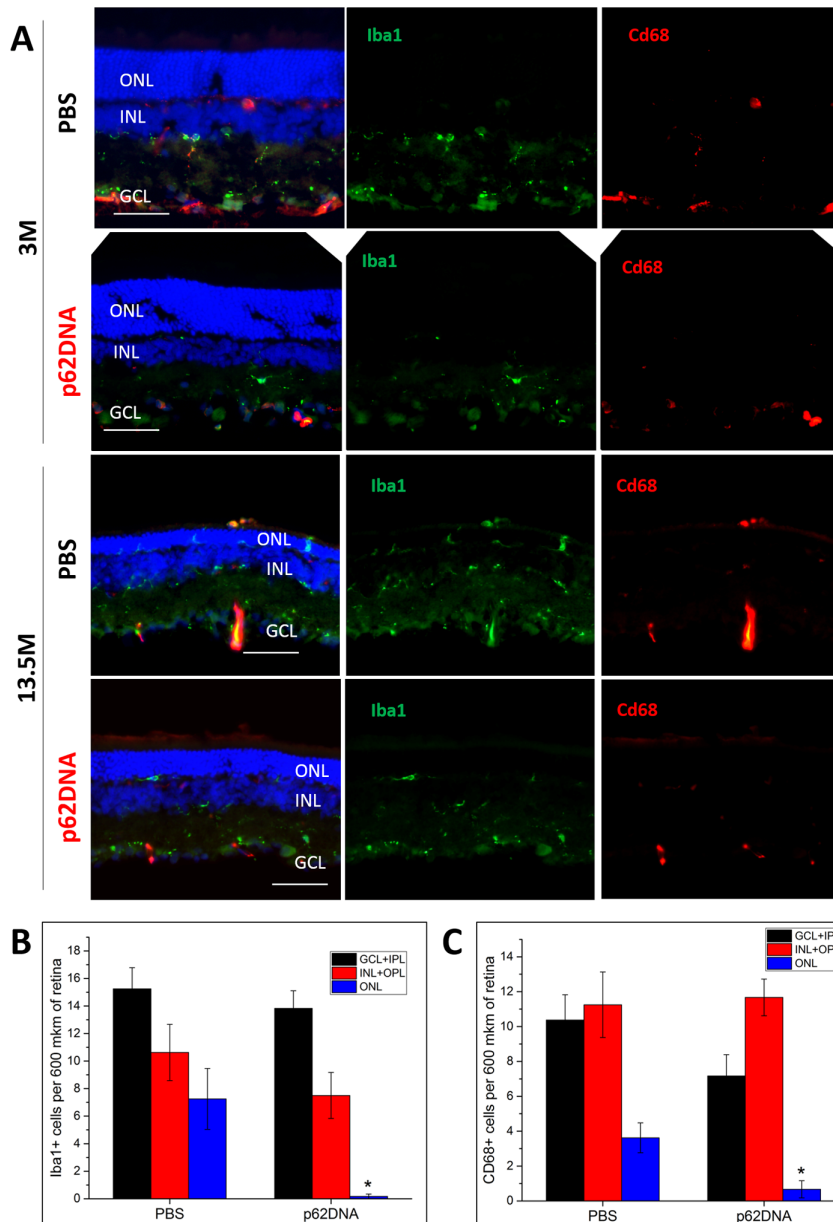


Figure 5. p62DNA abolished migration of Iba1+ and Cd68+ positive cells (microglia and macrophages) to the outer nuclear layer in 13.5-month-old OXYS rats. (A) Representative images of Iba1 (green) and Cd68 (red) immunostaining in OXYS rats treated with PBS or p62DNA at 3 and 13.5 months of age. The distribution of Iba1⁺ (B) and Cd68⁺ cells (C) in various layers of the retina: ganglion and inner plexiform layers (GCL+IPL, black), inner nuclear and outer plexiform layers (INL+OPL, red) and outer nuclear layer (ONL, blue). Scale bar: 50μm. ONL: outer nuclear layer; INL: inner nuclear layer; GCL: ganglion cells layer. *p < 0.05, statistically significant effect of p62DNA. Data are presented as mean ± SEM.

PBS). Therefore, administration of p62DNA has a strong preventive effect on multiple hallmarks of developing AMD.

Effect of p62DNA on retinal microglia and macrophages

In order to evaluate effects of the p62DNA on the inflammatory conditions in the retina and to quantify recruitment of microglia and macrophages to the outer retina, we performed double immunostaining of retinal cryosections with Iba1 (a microglial marker) and Cd68 (a marker of macrophages). Figure 5 depicts representative images of Iba1 and Cd68 immunoreactivity on retinal cryosections. At the age of 3 months, the Iba1⁺ and Cd68⁺ cells were located in the GCL, INL, IPL and OPL. At this age, we did not detect migration of microglia and macrophages into the photoreceptor layer, and p62DNA treatment did not affect the amounts Iba1 and Cd68 cell (Figure 5A-C). By the age of 13.5 months, PBS treated OXYS rats displayed Iba1⁺ and Cd68⁺ cells in ONL, indicating inflammatory processes (Figure 5C). In contrast, treatment with p62DNA almost completely blocked appearance of microglia and macrophages in the ONL, indicating little or no retinal inflammation following the p62 injection (Figure 5C) ($p < 0.05$, $n = 4$ p62DNA, $n = 4$ PBS). Overall these data indicate that p62 administration alleviates development of the age-related chronic inflammation and reverses retinal degeneration in the rat model of AMD.

DISCUSSION

Herein, we assessed preventive and/or therapeutic potency of a plasmid coding p62-SQSTM1. We report that administering the p62DNA to young OXYS rats substantially blocked AMD-like retinopathy limiting the disease signs. Unlike many other interventions manifesting withdrawal effect, the prophylactic effect of p62 DNA in young animals persisted for half a year after the last injection. The therapeutic effect was tested administering p62DNA to the rats at the age of 12 months when retinopathy has already actively progressed. Indeed, administering p62DNA to these animals suppressed further disease development. Therefore, the plasmid coding p62-SQSTM1 is a promising anti-AMD agent.

Degeneration and loss of RPE and choroidal involution with a secondary loss of photoreceptors are cardinal features of the dry form of AMD. Our prior data indicate that AMD-like pathology in OXYS rats is strongly associated with age-related alterations of the RPE and glia, and may derive from an imbalance of immune processes, including chronic inflammation [10, 11]. Normal RPE sheet is organized as a regular array of cells while upon AMD it exhibits strong spatial irregularity [20]. Other RPE changes typical for AMD include hypertrophy, multinucleation, and disruption of the hexagonal structure. Importantly, administering p62DNA prevented development of the destructive

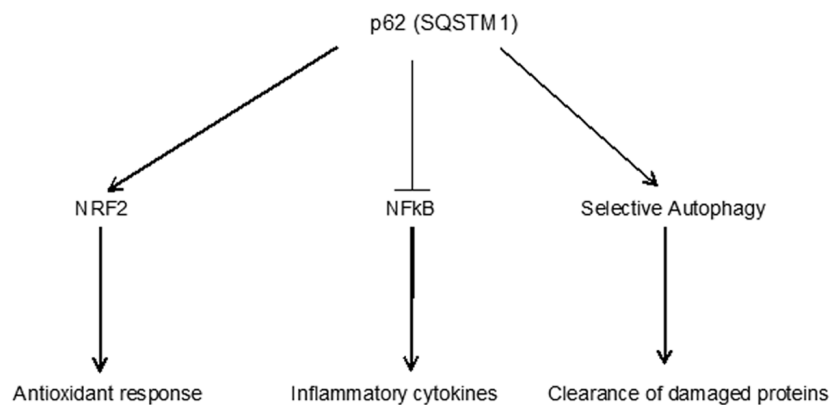


Figure 6. p62 (SQSTM1) as a mediator of several pathways. Anti-inflammatory effect of p62 can be mediated via inhibition of NF- κ B pathway as well as antioxidant response and clearance of damaged proteins/organelles (e.g., mitochondria) [25-28].

alterations of RPE cells (Figure 4) and thinning of the retina. Also, it reduced the loss of photoreceptor neurons, thus providing a neuroprotective effect in OXYS retina (Figure 3). To some extent, neuroprotection observed in AMD OXYS rat model may be due to primary protection of the RPE integrity.

Many diseases of retina are related to the gliosis of Müller cells and astrocytes, and upregulation of GFAP is a well-established indicator of retinal injury and reactive gliosis [21]. In AMD, regions of GFAP upregulation in Müller cells are associated with drusen formation [22]. Importantly, inhibition and/or reversal of the reactive gliosis prevents apoptotic death of retinal neurons and provides substantial neuroprotection [23, 24]. Here, we demonstrate that treatment with p62 DNA substantially prevents GFAP activation and decreases reactive gliosis in retina of OXYS rats.

In the present study we demonstrated that in aged OXYS rats macrophagal and microglial infiltration in outer retina (the number of Iba1- and Cd68-positive cells) was reduced in p62DNA treated rats compared to PBS control, which is consistent with the previously proposed anti-inflammatory protective role of p62 plasmid. Recently, we reported that p62-encoding plasmid administered intramuscularly reduces levels of pro-inflammatory cytokines, increases levels of anti-inflammatory cytokines and mitigates inflammation-related diseases such as osteoporosis and metabolic syndrome [17, 18]. There are two ways how administering p62DNA can lead to the anti-inflammatory effect, either directly influencing p62 level in the cells of the target organ or acting indirectly. Cells of the mammal organisms naturally express p62, also known as p62/sequestosome-1 (p62/SQSTM1), which plays a variety of biological roles ranging from oxidative stress, tumorigenesis, autophagy and degradation of misfolded proteins to inflammation and anti-inflammatory response (Figure 6) [16, 25]. For instance, p62 inhibited MYD88-TRAF6 complex formation, suppressing expression of IL-6 and nitric oxide synthase 2 [26]; and p62 overexpression decreased inflammatory cytokines production [27]. Also, inflammation may be controlled by interplay between the p62 level and NF- κ B activity [28] (Figure 6). Interestingly, mice deficient in p62 developed more severe atherosclerosis and showed greater macrophage infiltration of atherosclerotic plaques, a sign of increased inflammation [29]. Thus, if administering p62DNA leads to increased local expression of p62 in the organ, it may reduce local inflammation.

The suppression of osteoporosis by the p62DNA was associated with up-regulation of endogenous p62 protein in bone-marrow stromal cells [17]. However, in

the present study, we did not detect elevation of p62 levels in the RPE/retina of the p62DNA treated groups. Therefore tissue protection and suppression of inflammation can be achieved through a mechanism that does not involve elevation of endogenous p62 levels. Effects of p62DNA in this model seem to be indirect. The likely scenario is that the plasmid enters some cells remotely from the target organ, and expression of the plasmid-encoded p62 in these remote cells generates signals circulating in the body and causing therapeutic effects by reducing local inflammation. Thus, we believe that our work is fundamentally different from a direct gene therapy approach of Caccamo et al. [30] who have shown that increasing brain p62 expression might be a valid approach to restore neuronal function in proteinopathies.

Discovering the anti-inflammatory signal(s) induced by the p62DNA may be an important continuation of this line of research. A signal may be a secreted molecule, an exosome or even a reprogrammed cell. Although majority of the administered plasmid molecules do not leave the muscle they are injected to, some plasmid is delivered to a bone marrow. This fact lead to a hypothesis [18] that the plasmid transfects macrophages in the bone marrow shifting them to the anti-inflammatory M2-like phenotype. Then, these macrophages exit the bone marrow and circulate in the body.

In summary, our data suggests that a p62-encoding plasmid might be a novel preventive and/or therapeutic agent for AMD as it maintained retinal thickness and restored RPE morphology.

MATERIALS AND METHODS

DNA Plasmid

Human p62 (SQSTM, isoform 1) – encoding DNA vaccine (Elenagen) was previously described [31] and produced using EndoFree Plasmid Giga Kit (Qiagen).

Animals and treatments

All experimental procedures were in compliance with the European Communities Council Directive of 24 November 1986 (86/609/EEC). The protocol of the animal study was approved by the Commission on Bioethics of the Institute of Cytology and Genetics, Novosibirsk, Russia. Male senescence-accelerated OXYS rats were obtained from the Center for Genetic Resources of Laboratory Animals at the Institute of Cytology and Genetics, the Siberian Branch of the Russian Academy of Sciences. The OXYS strain was derived from the Wistar strain of rats at the Institute of Cytology and Genetics as described earlier [9]. At the

age of 4 weeks, the pups were weaned, housed in groups of five animals per cage (57 × 36 × 20 cm), and kept under standard laboratory conditions (22°C ± 2°C, 60% relative humidity, and 12-hour light/12-hour dark cycle; lights on at 9 a.m.). The animals were provided with standard rodent feed (PK-120-1; Laboratorsnab, Ltd., Moscow, Russia) and water *ad libitum*.

The first experiment

OXYS rats at the age of 1.5 months (n=20) and 12 months (n=20) were distributed in four groups (n = 10) and were injected intramuscularly (femoral quadriceps) with p62DNA in dose 150 mkg per rat in 60 µl (Elenagen, 2.5 mg/ml) on phosphate-buffered saline (PBS) or with only PBS. All groups were subjected to five injections at one-week intervals. Ophthalmoscopic examination was carried twice: before and 2 weeks after the last plasmid injection. The rats were euthanized using CO₂ inhalation and decapitated 8 d after the last examination of eyes. Eyes from four rats for group were used for immunohistochemistry (the right eyes) and RPE flat-mount staining (the left eyes). At least four tissue slices were analyzed per animal. To measure p62 protein level we used retinas obtained from six rats for group (the left and right eyes were mixed). The retina was separated from the other tissues, placed in microcentrifuge tubes for protein isolation, and frozen in liquid nitrogen. All specimens were stored at -70°C before the analysis.

The second experiment

1.5-month old OXYS rats were randomly distributed in two groups (n = 15) and were injected intramuscularly (femoral quadriceps) with p62DNA in dose 150 mkg per rat in 60 µl (Elenagen, 2.5 mg/ml) on PBS or with only PBS (n = 15). All groups were subjected to nine injections at one-week intervals. The animals received the last injection at the age of 4 months. An ophthalmologist examined all animals five times: before treatment at the age 1.5 months and at the ages 4, 6, 8, and 10,5 months, respectively.

Ophthalmoscopic examination

All rats underwent funduscopy with a Heine BETA 200 TL Direct Ophthalmoscope (Heine, Herrsching, Germany) after dilatation with 1% tropicamide. An assessment of stages of retinopathy was performed according to the Age-Related Eye Disease Study grade protocol (AREDS; <http://eyephoto.opth.wisc.edu>). The degree of retinopathy was estimated as follows: 0 arbitrary units (a.u.) corresponds to healthy retina; 1 a.u., appearance of drusen and other pathological changes in the RPE and partial atrophy of the choroid capillary layer; 2 a.u., exudative detachment of RPE and of retinal neuroepithelium, with further choroid

capillary layer atrophy; and 3 a.u., neovascularization and exudative-hemorrhagic detachment of RPE and neuroepithelium scarring.

Antibodies

Mouse monoclonal anti-p62 (ab56416), rabbit polyclonal anti-Gfap (ab7260), rabbit polyclonal anti-actin (ab1801), goat polyclonal anti-Iba1 (ab5076), mouse monoclonal anti-Cd68 (ab31630), and a secondary antibody – a donkey anti-goat IgG H&L antibody (conjugated with Alexa Fluor® 488; ab150129), donkey anti-rabbit IgG H&L antibody (conjugated with Alexa Fluor® 488; ab150073), donkey anti-mouse IgG H&L antibody (conjugated with Alexa Fluor® 568; ab175472) and goat anti-rabbit IgG H&L antibody (HRP; ab6721) were acquired from Abcam (Cambridge, UK).

RPE flat-mount staining

As described by previous work [12, 17], the enucleated eyes with an incision along the limbus were fixed in 4% paraformaldehyde in phosphate-buffered saline (PBS) for 2 h. The anterior segment of the eye (cornea, iris, ciliary body and lens) was removed. Retinal tissue was carefully excised from the eyecup, and the remaining cups containing RPE, choroid, and sclera were thoroughly washed in PBS with 0,1% Triton X-100 (PBST) and dissected into quarters by radial cuts. The RPE/choroid flat mounts were incubated in PBS/bovine serum albumin (BSA) 5% with 1% Triton X-100 for 1 h for blocking and permeabilization. Next, the samples were stained with fluorescein isothiocyanate (FITC)-phalloidin (1:100, P5282, Sigma-Aldrich) at 4°C 48 h to visualise the cytoskeleton and cell shapes during en face imaging. After washes in PBST, the RPE/choroids were flat-mounted on glass slides and were coverslipped with the Fluoro-shield mounting medium containing 4',6-diamidino-2-phenylindole (DAPI; ab104139, Abcam). Images were acquired with a confocal microscope (LSM 780 NLO, Zeiss).

Western blotting

Immunoblotting was performed as previously described [8]. To measure P62 protein level we used retinas obtained from six rats for group. The retina was separated from the other tissues, placed in microcentrifuge tubes for protein isolation, and frozen in liquid nitrogen. The retinas from the left and right eyes of one rat were mixed. Frozen tissues of retina were homogenized in protein lysis buffer radioimmuno-precipitation assay (50 mmol/L Tris-HCl, pH 7.4; 150 mmol/L NaCl; 1% Triton X-100; 1% sodium deoxycholate; 0.1% SDS; and 1 mmol/L EDTA) sup-

plemented with protease inhibitor cocktail (P8340; Sigma-Aldrich, St. Louis, MO). After incubation for 20 minutes on ice, samples were centrifuged at $9660 \times g$ at 4°C for 30 minutes and the supernatants were transferred to new tubes. Total proteins were measured with a Bio-Rad Bradford kit (Bio-Rad Laboratories). Samples were resolved on 12% SDS-PAGE on Tris-glycine buffer (25 mmol/L Tris base, 190 mmol/L glycine, and 0.1% SDS) and transferred to nitrocellulose membranes. Antibodies and dilutions used in immunoblotting included an anti-P62 antibody (1:1,000) and anti- β -actin antibody (1:1,000). After blockage with 5% bovine serum albumin (BSA; Sigma-Aldrich) in 0.01 M phosphate buffer with 0.1% Tween-20 (PBS-T) for 1 h, the membranes were incubated with the primary antibodies at 4°C overnight. After incubation with the respective secondary antibody (1:3,000), chemiluminescent signals were measured and scanned, and intensity of the bands was quantified in the ImageJ software (NIH, Bethesda, MD, USA). β -Actin served as an internal loading control.

Immunohistochemistry

Immunofluorescent staining was performed according to the standard method as described [5]. The eyes were removed and fixed in fresh 4% paraformaldehyde in PBS for 2 h, washed three times in PBS, and then cryoprotected in graded sucrose solutions (10%, 20%, and 30%). Posterior eyecups were embedded in Tissue-Tek® O.C.T. Compound (Sakura), frozen, and stored at -80°C . Tissue slices (10 μm thick) were prepared on a Microm HM-505N cryostat at -20°C , transferred onto Polysine® glass slides (Menzel-Glaser), and stored at -20°C . Primary antibodies and dilutions were as follows: anti-Iba1 (1:250), anti-Gfap (1:250), and anti-Cd68 (1:300). Primary antibodies were incubated for 18 h at 4°C . After incubation with the respective secondary antibodies diluted 1:300 for 1 h at room temperature, the tissue slices were coverslipped with the mounting medium containing DAPI (ab104139, Abcam) and were examined under the Zeiss microscope Axioplan 2. The negative control samples with the omitted primary antibody emitted only a minimal autofluorescent signal. For each image acquisition, all imaging parameters were the same. The morphometric parameters (the retinal thickness, Iba1⁺ and Cd68⁺ cell quantifications) were measured using quantitative analyses of the images performed with Axiovision software (SE64 4.9.1). Estimation was performed by examination of the five fields of view for each retina.

Statistical analysis

The data were analyzed using repeated-measures ANOVA (analysis of variance) and nonparametric tests

using the statistical package (Statistica 8.0 software). One-way analysis of variance was used for individual group comparisons. The Newman–Keuls test was applied to significant main effects and interactions in order to assess the differences between some sets of means. To assess the therapeutic effectiveness, we performed a dependent pairwise comparison of the eye states before and after treatment (t-test for dependent samples). The data of Iba⁺ and Cd68⁺ cells counting were analyzed by nonparametric method (the Mann–Whitney U test). The data are presented as mean \pm SEM. The differences were considered statistically significant at $p < 0.05$.

ACKNOWLEDGEMENTS

Microscopy was performed at the Microscopy Center of the Institute of Cytology and Genetics, SB RAS, Russia. We thank S.I. Baiborodin for technical assistance.

CONFLICTS OF INTEREST

A patent pending on anti-AMD application of p62-encoding vector belongs to CureLab Oncology, Inc.

FUNDING

The funduscopy, western blotting and immunohistochemical examination were supported by a Russian Scientific Foundation grant (18-75-00031). The DNA plasmid construction and the publication costs for this article were funded by CureLab Oncology, Inc.

REFERENCES

1. Yonekawa Y, Miller JW, Kim IK. Age-Related Macular Degeneration: Advances in Management and Diagnosis. *J Clin Med*. 2015; 4:343–59. <https://doi.org/10.3390/jcm4020343>
2. Hernández-Zimbrón LF, Zamora-Alvarado R, Ochoa-De la Paz L, Velez-Montoya R, Zenteno E, Gullias-Cañizo R, Quiroz-Mercado H, Gonzalez-Salinas R. Age-Related Macular Degeneration: New Paradigms for Treatment and Management of AMD. *Oxid Med Cell Longev*. 2018; 2018:8374647. <https://doi.org/10.1155/2018/8374647>
3. Datta S, Cano M, Ebrahimi K, Wang L, Handa JT. The impact of oxidative stress and inflammation on RPE degeneration in non-neovascular AMD. *Prog Retin Eye Res*. 2017; 60:201–18. <https://doi.org/10.1016/j.preteyeres.2017.03.002>
4. Kauppinen A, Paterno JJ, Blasiak J, Salminen A, Kaarniranta K. Inflammation and its role in age-related macular degeneration. *Cell Mol Life Sci*. 2016;

- 73:1765–86. <https://doi.org/10.1007/s00018-016-2147-8>
5. Kozhevnikova OS, Telegina DV, Devyatkin VA, Kolosova NG. Involvement of the autophagic pathway in the progression of AMD-like retinopathy in senescence-accelerated OXYS rats. *Biogerontology*. 2018; 19:223–35. <https://doi.org/10.1007/s10522-018-9751-y>
 6. Kozhevnikova OS, Korbolina EE, Stefanova NA, Muraleva NA, Orlov YL, Kolosova NG. Association of AMD-like retinopathy development with an Alzheimer's disease metabolic pathway in OXYS rats. *Biogerontology*. 2013; 14:753–62. <https://doi.org/10.1007/s10522-013-9439-2>
 7. Markovets AM, Saprunova VB, Zhdankina AA, Fursova AZ, Bakeeva LE, Kolosova NG. Alterations of retinal pigment epithelium cause AMD-like retinopathy in senescence-accelerated OXYS rats. *Aging (Albany NY)*. 2011; 3:44–54. <https://doi.org/10.18632/aging.100243>
 8. Muraleva NA, Kozhevnikova OS, Zhdankina AA, Stefanova NA, Karamysheva TV, Fursova AZ, Kolosova NG. The mitochondria-targeted antioxidant SkQ1 restores α B-crystallin expression and protects against AMD-like retinopathy in OXYS rats. *Cell Cycle*. 2014; 13:3499–505. <https://doi.org/10.4161/15384101.2014.958393>
 9. Stefanova NA, Kozhevnikova OS, Vitovtov AO, Maksimova KY, Logvinov SV, Rudnitskaya EA, Korbolina EE, Muraleva NA, Kolosova NG. Senescence-accelerated OXYS rats: a model of age-related cognitive decline with relevance to abnormalities in Alzheimer disease. *Cell Cycle*. 2014; 13:898–909. <https://doi.org/10.4161/cc.28255>
 10. Telegina DV, Kozhevnikova OS, Bayborodin SI, Kolosova NG. Contributions of age-related alterations of the retinal pigment epithelium and of glia to the AMD-like pathology in OXYS rats. *Sci Rep*. 2017; 7:41533. <https://doi.org/10.1038/srep41533>
 11. Kozhevnikova OS, Korbolina EE, Ershov NI, Kolosova NG. Rat retinal transcriptome: effects of aging and AMD-like retinopathy. *Cell Cycle*. 2013; 12:1745–61. <https://doi.org/10.4161/cc.24825>
 12. Telegina DV, Korbolina EE, Ershov NI, Kolosova NG, Kozhevnikova OS. Identification of functional networks associated with cell death in the retina of OXYS rats during the development of retinopathy. *Cell Cycle*. 2015; 14:3544–56. <https://doi.org/10.1080/15384101.2015.1080399>
 13. Kolosova NG, Muraleva NA, Zhdankina AA, Stefanova NA, Fursova AZ, Blagosklonny MV. Prevention of age-related macular degeneration-like retinopathy by rapamycin in rats. *Am J Pathol*. 2012; 181:472–77. <https://doi.org/10.1016/j.ajpath.2012.04.018>
 14. Stefanova NA, Muraleva NA, Maksimova KY, Rudnitskaya EA, Kiseleva E, Telegina DV, Kolosova NG. An antioxidant specifically targeting mitochondria delays progression of Alzheimer's disease-like pathology. *Aging (Albany NY)*. 2016; 8:2713–33. <https://doi.org/10.18632/aging.101054>
 15. Fan L, Yin S, Zhang E, Hu H. Role of p62 in the regulation of cell death induction. *Apoptosis*. 2018; 23:187–93. <https://doi.org/10.1007/s10495-018-1445-z>
 16. Wang L, Ebrahimi KB, Chyn M, Cano M, Handa JT. Biology of p62/sequestosome-1 in Age-Related Macular Degeneration (AMD). *Adv Exp Med Biol*. 2016; 854:17–22. https://doi.org/10.1007/978-3-319-17121-0_3
 17. Sabbieti MG, Agas D, Capitani M, Marchetti L, Concetti A, Vullo C, Catone G, Gabai V, Shifrin V, Sherman MY, Shneider A, Venanzi FM. Plasmid DNA-coding p62 as a bone effective anti-inflammatory/ana-bolic agent. *Oncotarget*. 2015; 6:3590–99. <https://doi.org/10.18632/oncotarget.2884>
 18. Halenova T, Savchuk O, Ostapchenko L, Chursov A, Fridlyand N, Komissarov AB, Venanzi F, Kolesnikov SI, Sufianov AA, Sherman MY, Gabai VL, Shneider AM. P62 plasmid can alleviate diet-induced obesity and metabolic dysfunctions. *Oncotarget*. 2017; 8:56030–40. <https://doi.org/10.18632/oncotarget.19840>
 19. Telegina DV, Kozhevnikova OS, Kolosova NG. Changes of glial cells in the retina with age and with the development of age-related macular degeneration. *Biochemistry (Mosc)*. 2018; 83:1009–17. <https://doi.org/10.1134/S000629791809002X>
 20. Rashid A, Bhatia SK, Mazzitello KI, Chrenek MA, Zhang Q, Boatright JH, Grossniklaus HE, Jiang Y, Nickerson JM. RPE cell and sheet properties in normal and diseased eyes. *Adv Exp Med Biol*. 2016; 854:757–63. https://doi.org/10.1007/978-3-319-17121-0_101
 21. Telegina DV, Kozhevnikova OS, Kolosova NG. Molecular mechanisms of cell death in retina during development of age-related macular degeneration. *Adv Gerontol*. 2017; 7:17–24. <https://doi.org/10.1134/S2079057017010155>
 22. Edwards MM, McLeod DS, Bhutto IA, Grebe R, Duffy M, Luty GA. Subretinal glial membranes in eyes with geographic atrophy. *Invest Ophthalmol Vis Sci*. 2017; 58:1352–67. <https://doi.org/10.1167/iovs.16-21229>
 23. de Hoz R, Rojas B, Ramírez AI, Salazar JJ, Gallego BI, Triviño A, Ramírez JM. Retinal macroglial responses in health and disease. *BioMed Res Int*. 2016;

2016:2954721.

<https://doi.org/10.1155/2016/2954721>

24. Ganesh BS, Chintala SK. Inhibition of reactive gliosis attenuates excitotoxicity-mediated death of retinal ganglion cells. *PLoS One*. 2011; 6:e18305.
<https://doi.org/10.1371/journal.pone.0018305>
25. Tilija Pun N, Park PH. Role of p62 in the suppression of inflammatory cytokine production by adiponectin in macrophages: involvement of autophagy and p21/Nrf2 axis. *Sci Rep*. 2017; 7:393.
<https://doi.org/10.1038/s41598-017-00456-6>
26. Into T, Inomata M, Niida S, Murakami Y, Shibata K. Regulation of MyD88 aggregation and the MyD88-dependent signaling pathway by sequestosome 1 and histone deacetylase 6. *J Biol Chem*. 2010; 285:35759–69. <https://doi.org/10.1074/jbc.M110.126904>
27. Kim JY, Ozato K. The sequestosome 1/p62 attenuates cytokine gene expression in activated macrophages by inhibiting IFN regulatory factor 8 and TNF receptor-associated factor 6/NF-kappaB activity. *J Immunol*. 2009; 182:2131–40.
<https://doi.org/10.4049/jimmunol.0802755>
28. Zhong Z, Umemura A, Sanchez-Lopez E, Liang S, Shalpour S, Wong J, He F, Boassa D, Perkins G, Ali SR, McGeough MD, Ellisman MH, Seki E, et al. NF-κB Restricts Inflammasome Activation via Elimination of Damaged Mitochondria. *Cell*. 2016; 164:896–910.
<https://doi.org/10.1016/j.cell.2015.12.057>
29. Sergin I, Bhattacharya S, Emanuel R, Esen E, Stokes CJ, Evans TD, Arif B, Curci JA, Razani B. Inclusion bodies enriched for p62 and polyubiquitinated proteins in macrophages protect against atherosclerosis. *Sci Signal*. 2016; 9:ra2.
<https://doi.org/10.1126/scisignal.aad5614>
30. Caccamo A, Ferreira E, Branca C, Oddo S. p62 improves AD-like pathology by increasing autophagy. *Mol Psychiatry*. 2017; 22:865–73.
<https://doi.org/10.1038/mp.2016.139>
31. Venanzi F, Shifrin V, Sherman M, Gabai V, Kiselev O, Komissarov A, Grudin M, Shartukova M, Romanovskaya-Romanko EA, Kudryavets Y, Bezdenezhnykh N, Lykhova O, Semesyuk N, et al. Broad-spectrum anti-tumor and anti-metastatic DNA vaccine based on p62-encoding vector. *Oncotarget*. 2013; 4:1829–35.
<https://doi.org/10.18632/oncotarget.1397>

Loss of NAMPT in aging retinal pigment epithelium reduces NAD⁺ availability and promotes cellular senescence

Ravirajsinh N. Jadeja¹, Folami L. Powell^{1,2,3}, Malita A. Jones¹, Jasmine Fuller¹, Ethan Joseph¹, Menaka C. Thounaojam⁴, Manuela Bartoli^{3,4}, Pamela M. Martin^{1,3,4,5}

¹Department of Biochemistry and Molecular Biology, Medical College of Georgia at Augusta University, Augusta, GA 30912, USA

²Education Innovation Institute, Medical College of Georgia at Augusta University, Augusta, GA 30912, USA

³James and Jean Culver Vision Discovery Institute, Medical College of Georgia at Augusta University, Augusta, GA 30912, USA

⁴Department of Ophthalmology, Medical College of Georgia at Augusta University, Augusta, GA 30912, USA

⁵Georgia Cancer Center, Medical College of Georgia at Augusta University, Augusta, GA 30912, USA

Correspondence to: Pamela M. Martin, Ravirajsinh N. Jadeja; **email:** pmmartin@augusta.edu, rjadeja@augusta.edu

Keywords: retinal pigment epithelium (RPE), aging, age-related macular degeneration (AMD), NAD⁺, NAMPT, senescence, SIRT1

Received: April 16, 2018

Accepted: June 4, 2018

Published: June 12, 2018

Copyright: Jadeja et al. This is an open-access article distributed under the terms of the Creative Commons Attribution License (CC BY 3.0), which permits unrestricted use, distribution, and reproduction in any medium, provided the original author and source are credited.

ABSTRACT

Retinal pigment epithelium (RPE) performs numerous functions critical to retinal health and visual function. RPE senescence is a hallmark of aging and degenerative retinal disease development. Here, we evaluated the temporal expression of key nicotinamide adenine dinucleotide (NAD⁺)-biosynthetic genes and associated levels of NAD⁺, a principal regulator of energy metabolism and cellular fate, in mouse RPE. NAD⁺ levels declined with age and correlated directly with decreased nicotinamide phosphoribosyltransferase (NAMPT) expression, increased expression of senescence markers (p16^{INK4a}, p21^{Waf/Cip1}, ApoJ, CTGF and β-galactosidase) and significant reductions in SIRT1 expression and activity. We simulated *in vitro* the age-dependent decline in NAD⁺ and the related increase in RPE senescence in human (ARPE-19) and mouse primary RPE using the NAMPT inhibitor FK866 and demonstrated the positive impact of NAD⁺-enhancing therapies on RPE cell viability. This, we confirmed *in vivo* in the RPE of mice injected sub-retinally with FK866 in the presence or absence of nicotinamide mononucleotide. Our data confirm the importance of NAD⁺ to RPE cell biology normally and in aging and demonstrate the potential utility of therapies targeting NAMPT and NAD⁺ biosynthesis to prevent or alleviate consequences of RPE senescence in aging and/or degenerative retinal diseases in which RPE dysfunction is a crucial element.

INTRODUCTION

The retinal pigment epithelium (RPE) performs numerous functions essential to normal retinal health and function [1]. RPE serves as a physiologic barrier between the photoreceptor cells and the choroidal blood supply and in doing so, plays an essential role in pro-

tecting the retina from systemic insults by regulating immune responses and thereby limiting the entry of infectious or otherwise detrimental agents into retina [1]. Additionally and importantly, RPE facilitates the delivery of nutrients and ions extracted from the choroidal blood to the photoreceptors and the counter movement of photoreceptor-derived waste products for

disposition in the choroid [2]. As such, damage to or dysfunction of RPE may have a domino effect on the health and function of photoreceptors that are obligatorily dependent upon it and therefore a significant impact on visual function. Hence, it is not surprising that RPE is implicated directly and prominently in the pathogenesis of most degenerative diseases of the retina, including age-related macular degeneration (AMD), the leading cause of blindness among persons aged 60 and above worldwide [3, 4].

AMD is a complex multifactorial disease and, as its name implies, age is a primary risk factor for its development [5]. RPE is principally affected in AMD [6]. Interestingly however, most available experimental models and related studies, including our own prior, have focused more heavily on identifying, understanding and limiting secondary consequences of aging and related RPE dysfunction (e.g., increased oxidative stress, inflammation, altered cholesterol metabolism) as opposed to targeting directly factors, such as energy deprivation, that precipitate accelerated aging at a cellular level. The consequence of the latter is an imbalance in homeostatic processes and subsequent damage, as shown in many specific cell types. This is the premise of a number of recent studies including the present investigation in which we focused on nicotinamide adenine dinucleotide (NAD⁺) and factors governing its bioavailability in relation to the overall impact on RPE viability.

NAD⁺, a central metabolic cofactor, plays a critical role in regulating cellular metabolism and energy homeostasis [7, 8]. The ratio of NAD⁺ to NADH (oxidized to reduced NAD⁺) regulates the activity of various enzymes essential to metabolic pathways including glycolysis, the Krebs's cycle, and fatty acid oxidation [8]. There is a wealth of clinical and experimental data stemming from studies of other primary diseases of aging (e.g., Alzheimer's disease, type 2 diabetes, non-alcoholic fatty liver disease, etc.) demonstrating clearly a generalized decline in the availability of NAD⁺ in association with increased age and the related reduction in the activity of a number of downstream metabolic pathways that contribute to the development and progression of degenerative processes [7,8]. Neuronal cells and tissues appear to be especially sensitive in this regard. Importantly, the aforementioned studies additionally suggest that age-related degenerative processes might be prevented or at the least, the consequences thereof lessened in severity by therapies that boost NAD⁺. The expression and activity of a number of key NAD⁺-dependent proteins (e.g., members of the sirtuin family, poly ADP-ribose polymerases (PARPs) and cyclic ADP-ribose synthases) and, the efficacy of therapies capable of impacting them

have been evaluated in the context of aging retina and RPE [9-11]. However, little attention has been given to upstream factors that regulate NAD⁺ biosynthesis, particularly in RPE. Given the importance of RPE to retinal health and function, in the present investigation we focused on evaluating the impact of NAD⁺ and factors that regulate its availability on RPE viability both *in vivo* and *in vitro*. Collectively, our results confirm the importance of NAD⁺ to RPE health and the positive potential impact of therapies that enhance NAD⁺ generation in this cell type hold with respect to limiting senescence and preserving RPE viability. This finding is highly relevant to the clinical management of AMD but perhaps also broadly to the management of other degenerative retinal diseases in which RPE is prominently affected.

RESULTS

NAD⁺ levels decline with increasing age in mouse RPE

NAD⁺ levels decline with age in many cell and tissue types [12, 13]. Whether the same occurs in aging RPE is unclear. As such, our first step was to evaluate temporally the availability of NAD⁺ in the RPE of the living animal. To do so, we isolated RPE tissue from the eyes of C57BL/6J mice that per the established average lifespan of a normal lab mouse (~24 months) belonged to one of the following three age groups: young-adult (age 1.5 - 6 months), middle-aged adult (age 7 - 11 months) or adults of advanced age (12 months of age or greater). Levels of NAD⁺ in mouse RPE correlated inversely with age (Fig. 1A). NAD⁺ levels remained stable in this cellular layer up to six months of age but began to decline significantly shortly thereafter such that by 12 months of age, there was on average, a 40-50 percent decrease in RPE-specific NAD⁺ content. Further reductions in NAD⁺ were detected in RPE obtained from mice of advanced age.

Nicotinamide phosphoribosyltransferase (NAMPT) is essential to NAD⁺ and down-stream SIRT1 expression in RPE

To identify the specific mechanism(s) responsible for the age-dependent decline in levels of NAD⁺ that we observed in mouse RPE, we next evaluated the expression of enzymes pertinent to NAD⁺ biosynthesis. In mammals, NAD⁺ is generated via one of two principal routes, the *de novo* or the salvage pathway ([8, 14]; Fig. 1B). Congruent with this, we monitored the expression of nicotinamide adenyltransferase (NMNAT), quinolinate phosphoribosyltransferase (QPRT) and nicotinamide phosphoribosyltransferase (NAMPT), key enzymes relevant to one or both of the

aforementioned major pathways to NAD⁺ generation. NMNAT and QPRT expression in RPE remained relatively stable across all ages tested despite the age-associated decline in NAD⁺ content (Fig. 1C and D, respectively). However, NAMPT expression (Fig. 1E) mirrored closely the age-dependent decline in NAD⁺, strongly implicating this enzyme as the principal enzyme driving NAD⁺ generation in RPE. This finding is consistent with findings in the existing scientific literature demonstrating that the bulk of NAD⁺ that is generated in mammals under physiological conditions is derived from the salvage pathway, also known as the deamidated route [14]. We evaluated also the expression of sirtuin family member 1 (SIRT1), a highly studied NAD⁺-dependent histone deacetylase touted as being a principal metabolic sensor and regulator of cellular energy metabolism and stress responses. Importantly, SIRT1 has also been linked to ocular aging

and/or processes associated with the development and progression of age-related retinal disease [15]. Like NAD⁺ and NAMPT mRNA expression, levels of SIRT1 protein declined significantly in mouse RPE in association with increasing age (Fig. 1F). Further, some of the senescence-associated markers were increased in aged mouse RPE (Fig. S1).

FK866 inhibits NAMPT thereby decreasing NAD⁺ levels and promoting RPE senescence

Our data to this point confirm that NAD⁺ levels decline in RPE as age increases. They also demonstrate the critical importance of NAMPT to the generation and maintenance of NAD⁺ levels in RPE. Hence, therapies targeting NAMPT and NAD⁺ may be of benefit in preserving RPE health and viability in aging and age-related retinal diseases like AMD. However, the deve-

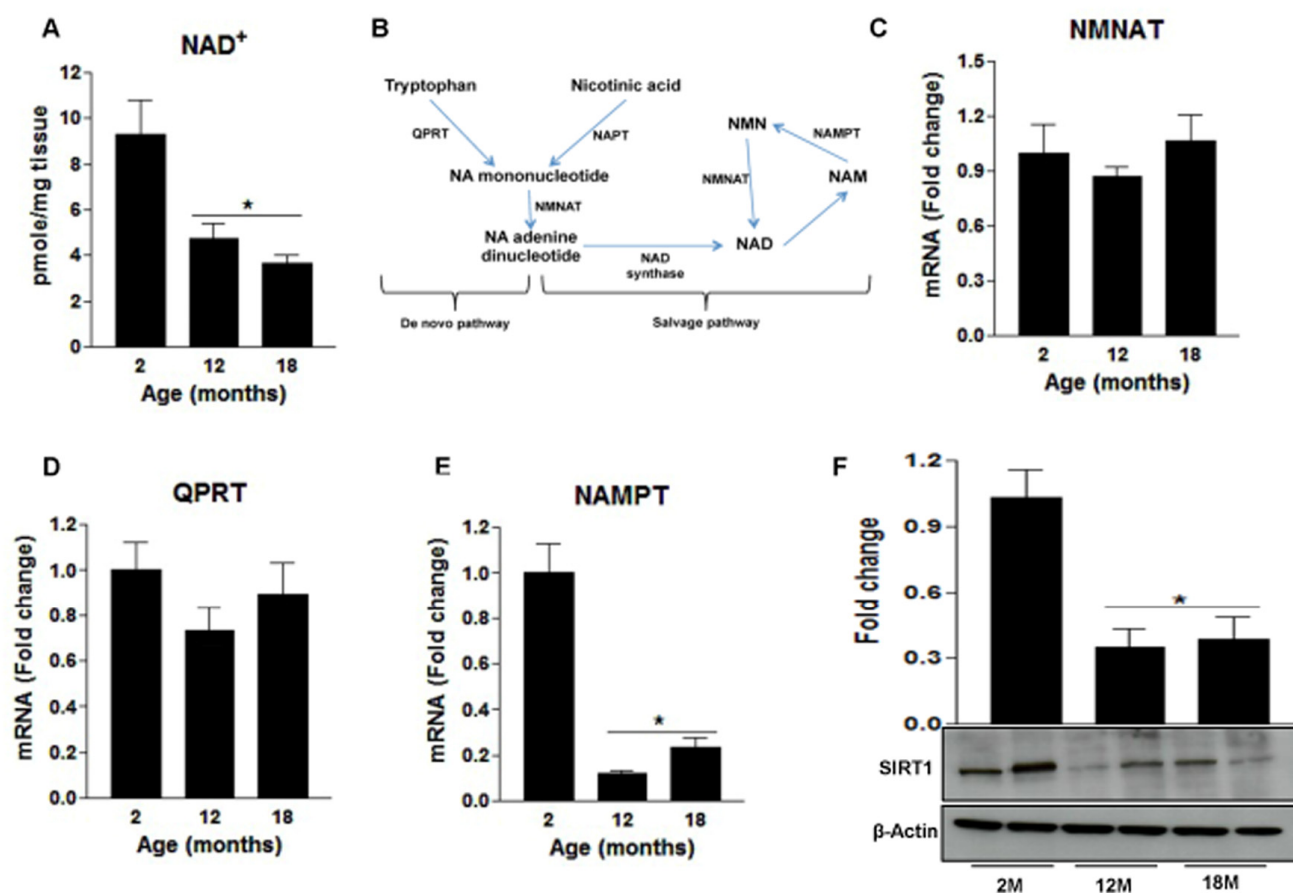


Figure 1. Changes in RPE NAD⁺ metabolism with aging in mice. RPE/eye cup was dissected from 2, 12 and 18 months old male C57BL/6J mice to evaluate changes in NAD⁺ metabolism. (A) NAD⁺ content was measured using a commercially available kit. (B) Overview of NAD synthesis pathways in mammals. (C-E) Changes in mRNA expression of enzymes regulating NAD⁺ synthesis were performed by qPCR. (F) Changes in SIRT-1 protein levels were measured by western blotting. Data is presented as mean ± S.E.M for n=5. A representative western blot image from three replicates is shown. mRNA expression of genes were normalized to 18s expression. *p<0.05 compared to 2M (two months old mice). NAMPT; Nicotinamide phosphoribosyltransferase, QPRT; Quinolinic Phosphoribosyltransferase, NMNAT; Nicotinamide mononucleotide adenylyltransferase.

lopment and testing of new therapies in this field of research is impeded significantly by the lack of experimental model systems that recapitulate accurately characteristics of human aging and age-related disease and/or, the extended time periods often required to generate reliable models and conduct such studies. Thus, to further our present studies and evaluate the impact of reduced NAMPT and consequent NAD⁺ availability on RPE cell viability, we used the highly specific and non-competitive NAMPT-inhibitor FK866 [16] to mimic acutely the age-related effect of decreased NAMPT expression and NAD⁺ content in cultured RPE cells and intact mouse retina.

Confluent, well-differentiated cultures of human RPE (ARPE-19) cells were exposed to varying concentrations of FK866 for 72 h. As anticipated, FK866 induced a dose-dependent decline in levels of NAD⁺ (Fig. 2A). Cell viability assays confirmed the absence of robust cellular toxicity due to FK866 exposure across the range of doses of the compound that were tested (0.01 – 10 μM; Fig. 2B). There was a significant and dose-dependent increase in the number of RPE cells positive for the expression of β-galactosidase, an estab-

lished marker of cellular senescence, in cells treated with FK866 (Fig. 2C-D), suggesting that while the compound did not induce robust cell death, it did on the other hand, stimulate cellular senescence. To confirm this, we evaluated also the mRNA and/or protein expression of cyclin-dependent kinase inhibitor 1 (p21^{Waf/Cip1}), cyclin-dependent kinase Inhibitor 2A (p16^{INK4a}), apolipoprotein J (ApoJ), and connective tissue growth factor (CTGF), key additional biomarkers of aging and cellular senescence [17-20]. Congruent with β-galactosidase staining, the expression of each of these markers was increased in association with increasing concentrations of FK866 and the associated decline in NAD⁺ (Fig. 3A-D). Additionally, the expression and activity of SIRT1 was dose-dependently decreased (Fig. 4A-B).

A common consequence of cellular senescence is the decreased ability of cells to handle the oxidative stress produced as a normal consequence of cellular metabolism [21]. This potentiates inflammatory processes and the further production of pro-oxidant by-products. This vicious cycle of oxidative stress and inflammation has been identified as key factor in the

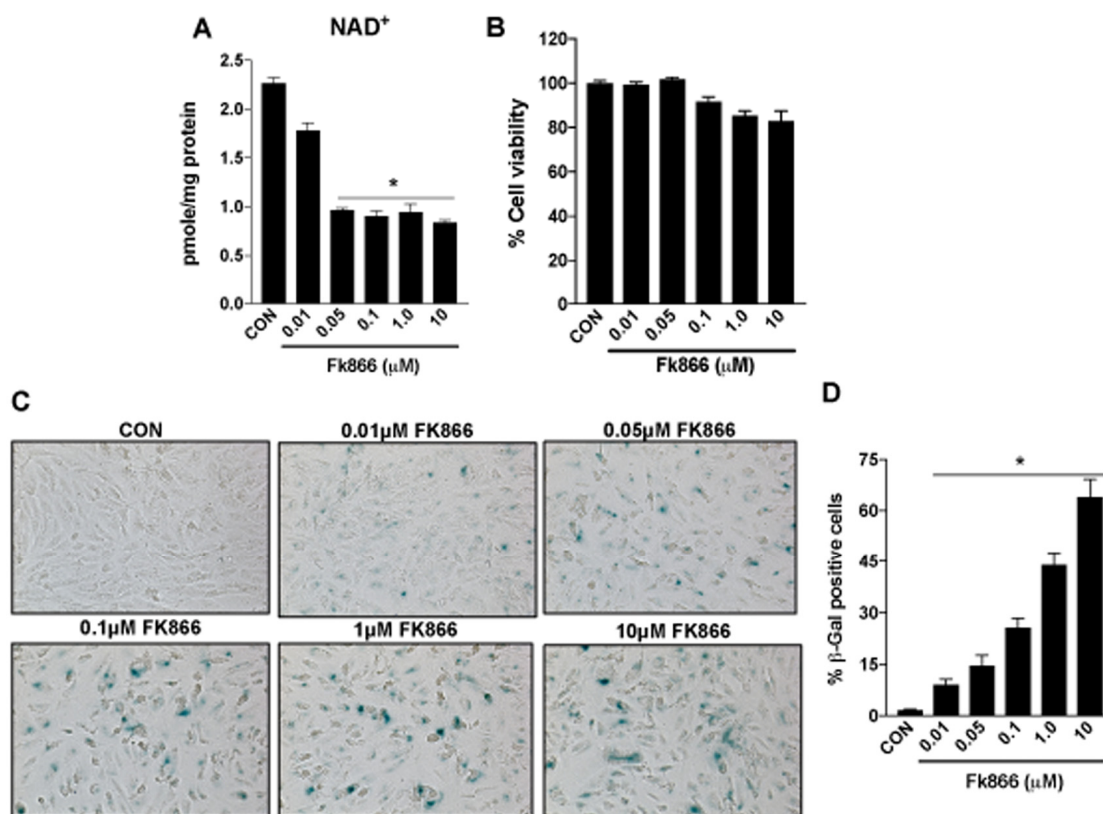


Figure 2. Inhibition of NAMPT activity in human retinal pigment epithelial cells decreases NAD⁺ levels to induce senescence. Human retinal pigment epithelial cells (ARPE-19) were treated with different doses (0.01-10μM) of a selective NAMPT activity blocker, FK866. Dose-dependent changes in (A) NAD⁺ content (B) cell viability and (C-D) senescence of FK866 treated human RPE cells were evaluated. Data is presented as mean ± S.E.M for n=3 independent experiments. *p<0.05 compared to CON (Vehicle treated).

development and progression of AMD and other degenerative retinal diseases. As such, we evaluated the effect of FK866 on the expression of interleukins 6 and 8 (IL-6 and IL-8, respectively), two pro-inflammatory cytokines that have been shown to be elevated commonly in degenerating RPE [17, 22]. Levels of IL-6 and IL-8 were increased in association with increasing concentrations of FK866 in our experimental system (Fig. 4C-D).

Based upon our immediate prior findings, a dose of 10 μ M FK866 was confirmed as the optimal standard dose. To confirm the optimal incubation period for FK866 treatment, additional cultures of ARPE-19 were treated with 10 μ M FK866 for 24, 48 or 72 h and parameters identical to those described above (Figs. 2-4) were evaluated. FK866 was effective at reducing NAD⁺ levels at each of the time points tested, however the greatest efficacy was achieved in association with a 72

h incubation period (Fig. 5A), the time period that was used in our initial studies. Cell viability assays were repeated in these additional batches of cells and the absence of cellular toxicity in cells exposed to 10 μ M FK866 at all-time points tested was confirmed (Fig. 5B). β -galactosidase staining and related quantification revealed a time-dependent increase in the number of β -gal-positive cells in FK866-treated cultures (Fig. 5C-D). Similarly, the expression of p21^{Waf/Cip1}, p16^{INK4a}, ApoJ and CTGF was increased (Fig. 6A-D) and SIRT1 expression and activity decreased (Fig. 7A-B) time-dependently, further supporting the optimality of the 72 h incubation period (Fig. 6A-D).

FK866 induces expression of inflammatory factors and ROS production in RPE

Senescent cells secrete numerous kinds of pro-inflammatory cytokines, chemokines, growth factors

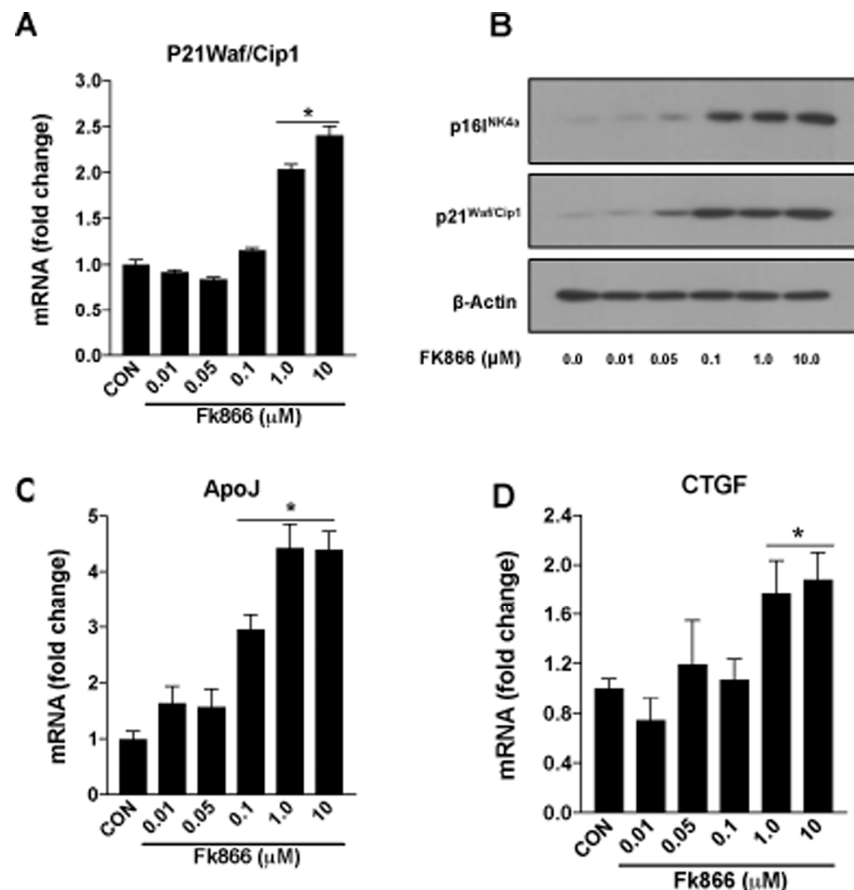


Figure 3. FK866 treatments induce changes in the markers of senescence in human retinal pigment epithelial cells. Human retinal pigment epithelial cells (ARPE-19) were treated with different doses (0.01-10 μ M) of FK866 and changes in the expression of various senescence markers were evaluated by qPCR and western blotting. Dose-dependent changes in (A) p21^{Waf/Cip1} mRNA, (B) p16^{INK4a} and p21^{Waf/Cip1} protein and, (C-D) CTGF and ApoJ mRNA levels are shown. A representative western blot image from three replicates is shown. mRNA expression of genes were normalized to 18s expression. Data are presented as mean \pm S.E.M for n=3 independent experiments. *p<0.05 compared to CON (Vehicle treated).

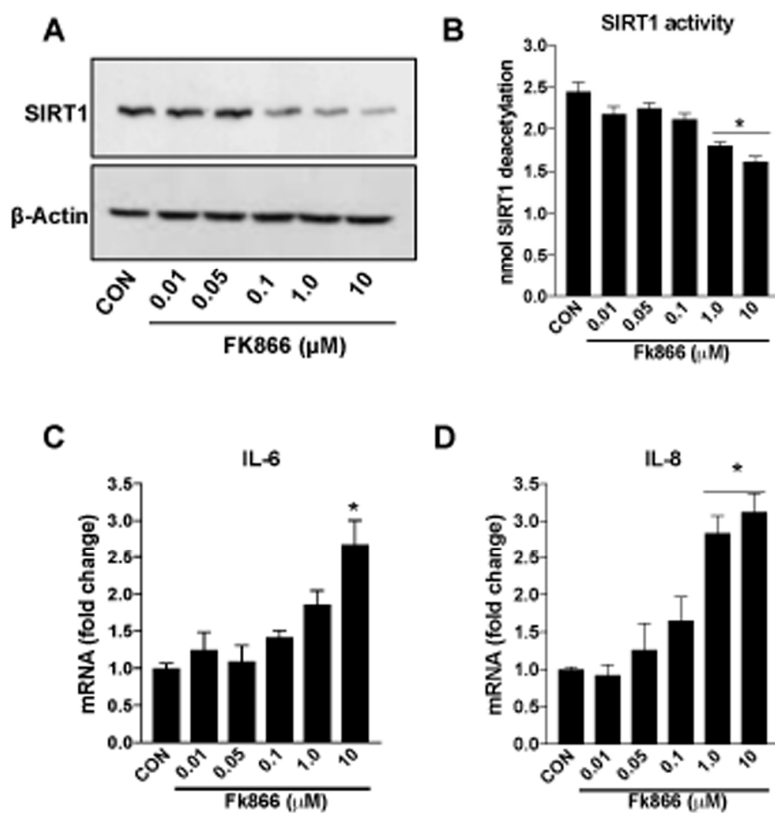


Figure 4. FK866 decreases SIRT-1 expression/activity and increases inflammation in human retinal pigment epithelial cells. Human retinal pigment epithelial cells (ARPE-19) were treated with different doses (0.01-10 μ M) of FK866 and (A) expression and (B) activity of SIRT1 was evaluated by western blotting and commercially available SIRT1 assay kit respectively. (C-D) Changes in inflammatory markers (IL-6 and IL-8) were evaluated by qPCR. A representative western blot image from three replicates is shown. mRNA expression of genes were normalized to 18s expression. Data are presented as mean \pm S.E.M for n=3 independent experiments. *p<0.05 compared to CON (Vehicle treated).

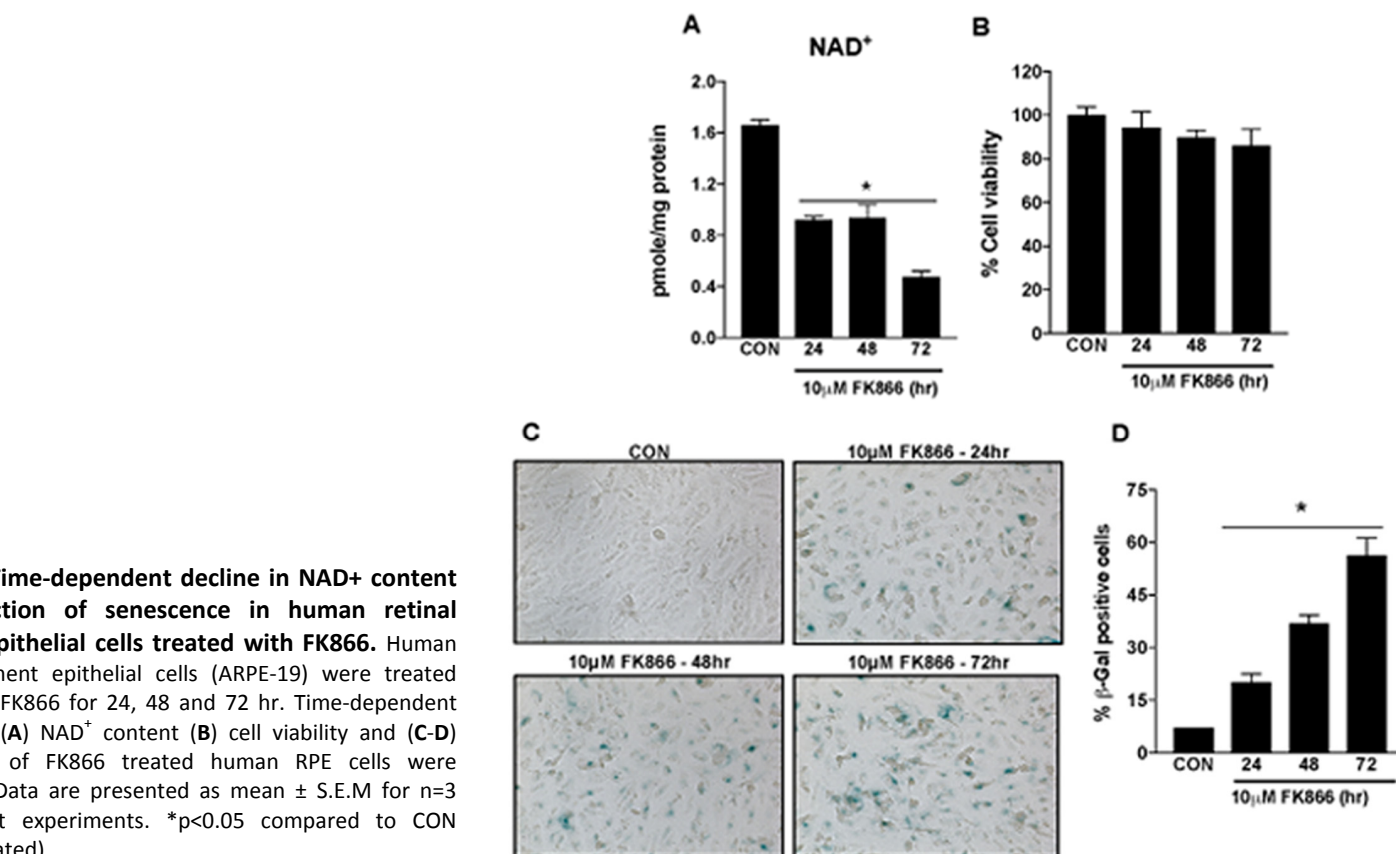


Figure 5. Time-dependent decline in NAD⁺ content and induction of senescence in human retinal pigment epithelial cells treated with FK866. Human retinal pigment epithelial cells (ARPE-19) were treated with 10 μ M FK866 for 24, 48 and 72 hr. Time-dependent changes in (A) NAD⁺ content (B) cell viability and (C-D) senescence of FK866 treated human RPE cells were evaluated. Data are presented as mean \pm S.E.M for n=3 independent experiments. *p<0.05 compared to CON (Vehicle treated).

and proteases, exemplifying what is referred to as a senescence-associated secretory phenotype (SASP) [23]. Further, oxidative stress also plays an important role in RPE senescence [24-26]. Congruent with this, we treated additional ARPE-19 cells with 10 μ M FK866 for 72 h, the dose and time-point most effective at reducing NAD⁺ and promoting cellular senescence without robust toxicity, and monitored them for expression of the pro-inflammatory cytokines IL-6 and IL-8 (Fig. 7C-D), and CellROX and MitoSOX positivity, a general marker of oxidative stress and a mitochondrial-specific superoxide marker, respectively (Fig. 7E). Like IL-6 and IL-8 expression, the number of cells positively stained with CellROX or MitoSOX dyes (green fluorescence and red fluorescence, respectively) and therefore in which there was an increased amount of oxidative stress, was increased in ARPE-19 cells exposed to FK866 compared to control, non-exposed cell cultures (Fig. 7E).

Nicotinamide mononucleotide (NMN) treatment preserves NAD⁺ and prevents RPE senescence *in vitro*

Therapies that enhance NAD⁺ have been shown to reduce the incidence and/or severity of age-associated complications [27-31]. However, it is unclear, whether the latter is also of benefit in aged RPE and associated degenerative retinal disease. Our studies up to this point have established the decline in NAMPT and related NAD⁺ availability in aged RPE and validated the FK866-treated cell culture system as a suitable *in vitro* model system in which to study these factors. Therefore, we used this experimental model to determine whether augmenting NAD⁺ content using the NAD⁺ precursor nicotinamide mononucleotide (NMN) could preserve NAD⁺ and prevent FK866-induced RPE senescence. NMN dose-dependently enhanced NAD⁺ levels in cells exposed to FK866 (Fig. 8A).

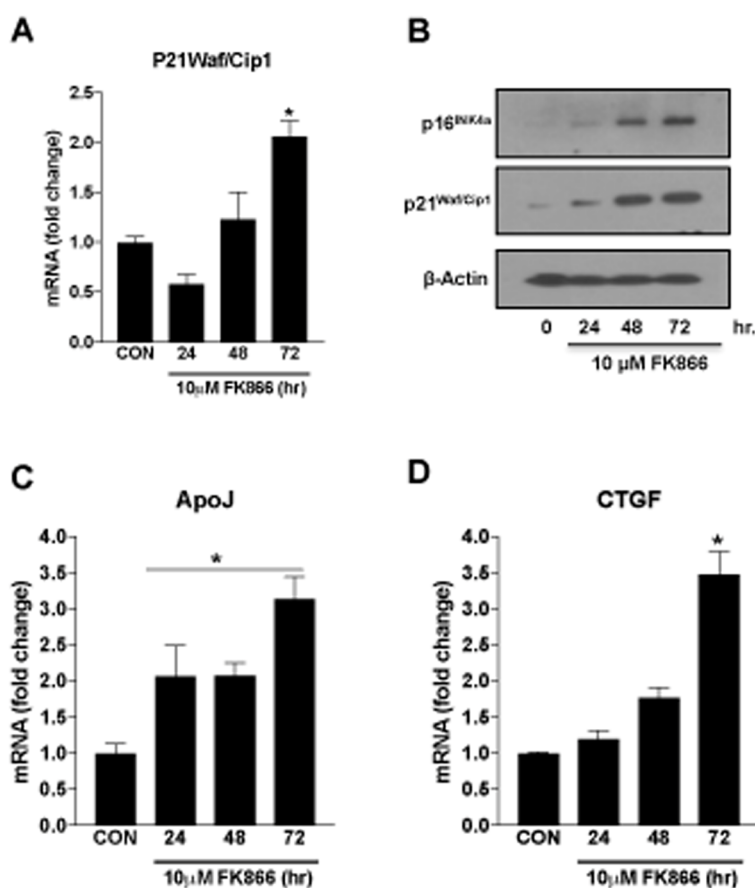


Figure 6. Time-dependent changes in markers of senescence in human retinal pigment epithelial cells treated with FK866. Human retinal pigment epithelial cells (ARPE-19) were treated with 10 μ M FK866 for 24, 48 and 72 hr. and changes in the expression of various senescence markers was evaluated by qPCR and western blotting. Time-dependent changes in (A) p21^{Waf/Cip1} mRNA, (B) p16^{INK4a} and p21^{Waf/Cip1} protein and, (C-D) CTGF and ApoJ mRNA levels are shown. A representative western blot image from three replicates is shown. mRNA expression of genes were normalized to 18s expression. Data are presented as mean \pm S.E.M for n=3 independent experiments. *p<0.05 compared to CON (Vehicle treated).

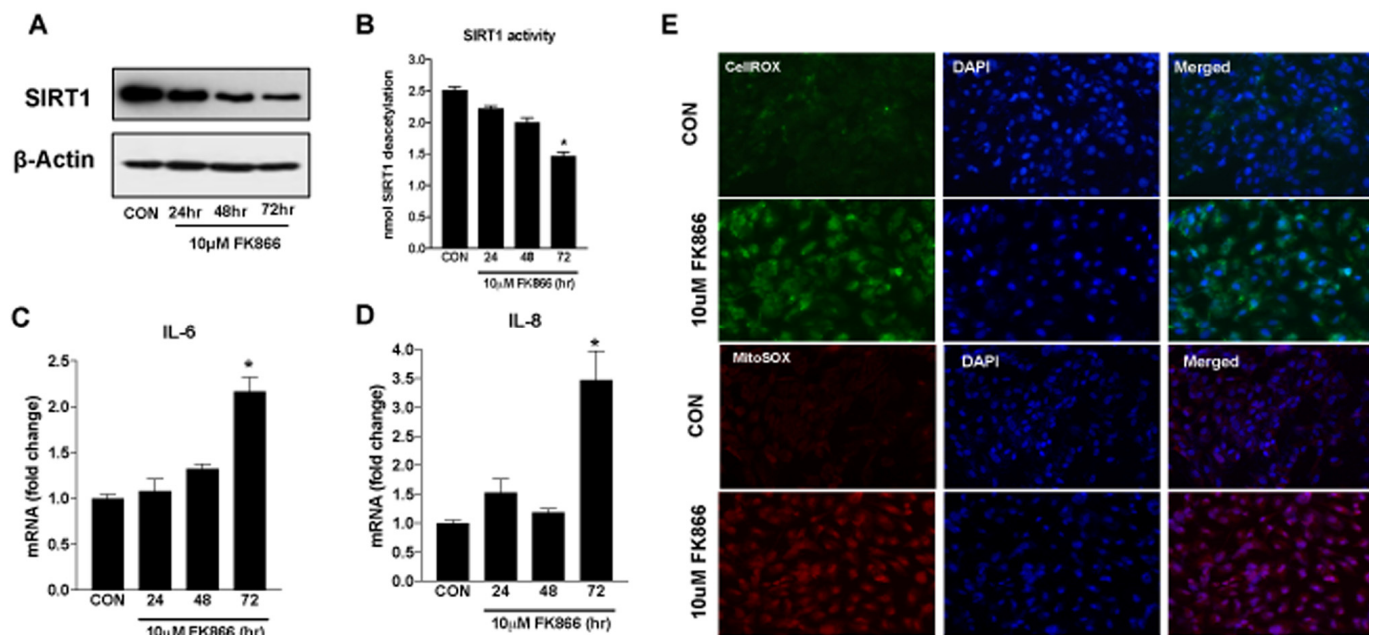


Figure 7. Time-dependent changes in SIRT-1 expression/activity and inflammatory markers in human retinal pigment epithelial cells treated with FK866. Human retinal pigment epithelial cells (ARPE-19) were treated with 10 μ M FK866 for 24, 48 and 72 hr. and (A) expression and (B) activity of SIRT-1 was evaluated by western blotting, and commercially available SIRT-1 assay kit respectively. (C-D) Changes in inflammatory markers (IL-6 and IL-8) were evaluated by qPCR. (E) Representative images of CellROX and MitoSOX stained 10 μ M FK866 treated (72 hr.) A representative western blot image from three replicates is shown. mRNA expression of genes were normalized to 18s expression. Data are presented as mean \pm S.E.M for n=3 independent experiments. *p<0.05 compared to CON (Vehicle treated).

Additionally, the compound prevented FK866-induced RPE senescence as indicated by the suppression of p16^{INK4a} and p21^{Waf/Cip1} expression and the reduction of SIRT1 expression (Fig. 8B). The number of β -galactosidase positive cells was also decreased in cultures exposed to NMN (Fig. 8C-D).

ARPE-19, though of human origin, is a “transformed” retinal cell line. Therefore, to validate findings obtained using ARPE-19 cell cultures, key experiments were repeated using cultures of primary mouse RPE (Fig. 9). FK866 was effective at reducing NAD⁺ expression in primary RPE though cell viability data indicate increased sensitivity in the form of cellular toxicity (Fig. 9A). Therefore, in subsequent studies using these cells, we refrained from using higher doses of the compound (Fig. 9B-G). As observed in ARPE-19 cells, exposure of RPE cells to FK866 potentiated cellular senescence (Fig. 9C), and these phenomena were inhibited by co-exposure of cells to NMN (Fig. 9D-F). Importantly, NMN also prevented the FK866-induced decrease in SIRT1 expression (Fig. 9G).

Nicotinamide mononucleotide (NMN) treatment preserves NAD⁺ and prevents RPE senescence *in vivo*

To determine whether our findings in the ARPE-19 and primary RPE cell culture model systems could be extrapolated to the living animal, we injected FK866 sub-retinally into the eyes and/or NMN intraperitoneally to adult C57BL/6J mice. NAD⁺ levels were significantly lower in RPE tissue isolated from mice injected with FK866 than in vehicle (PBS)-injected controls (Fig. 10A). On the other hand, NAD⁺ levels more than doubled in association with NMN injection only, and in animals that received NMN in conjunction with FK866, NAD⁺ levels were significantly preserved. SIRT1 expression was additionally preserved in conjunction with NMN injection (Fig. 10B).

DISCUSSION

RPE performs a number of highly diverse functions that are essential to maintenance of the normal health and function of the retina. Hence, it is not surprising that dysfunction of this cellular layer is implicated causally

in the development and progression of a number of degenerative diseases of the retina. Cellular senescence is a common consequence of aging hence, the decline in NAD⁺ in RPE and the associated upregulated expression of markers of senescence that we observed was not totally surprising. Though there has been some debate over whether dysfunction occurs first in the RPE or in the overlying photoreceptors, the contribution of senescence-associated RPE damage to age-related RPE dysfunction is undeniable. Irrespective of views on the exact chronology of the events that initiate degenerative processes in the aging outer retina, the importance of preserving a healthy RPE is emphasized by the fact that there is, to our knowledge, no experimental or clinical condition in which photoreceptors persist unaffected above an underlying region of RPE that is damaged, largely dysfunctional or dead. This is exemplified by the severe irreversible loss of central vision that can occur in association with geographic atrophy or RPE

cell dropout in advanced dry AMD. Thus, understanding the mechanisms that govern age-related changes in RPE is both important and essential to the development of therapies to effectively prevent and treat age-related degenerative retinal diseases like AMD. This is especially true regarding the dry form of the disease, which (a) generally presents first, (b) impacts the greatest number of patients, and (c) is not highly amenable to any form of therapeutic management that is presently available [32-34]. With these facts in mind, in the present study we focused on NAD⁺.

NAD⁺ levels decline with age in many cell and tissue types. In fact, altered NAD⁺ metabolism and concurrent alterations in mitochondrial function are inherent in metabolic disorders including type 2 diabetes, non-alcoholic fatty liver disease, and age-related diseases such as Parkinson's and Alzheimer's disease [7].

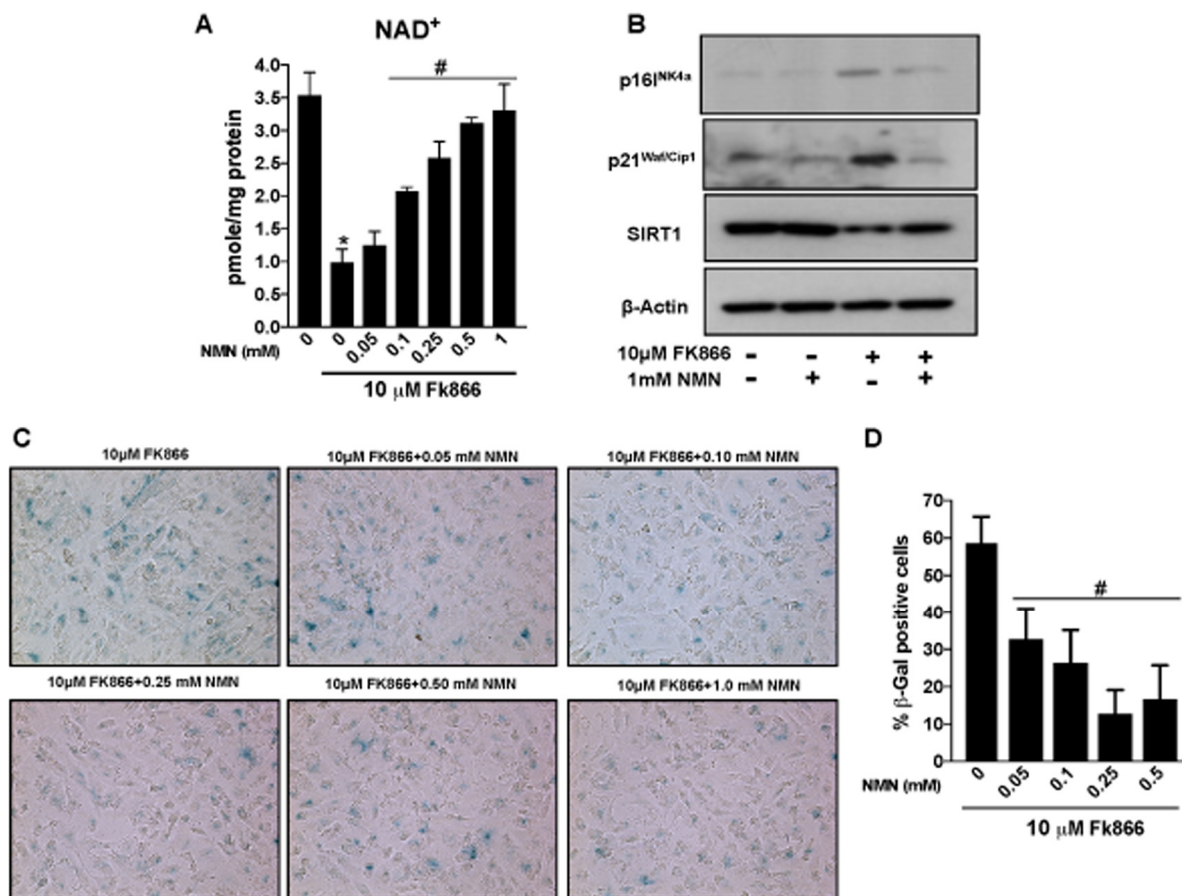


Figure 8. Nicotinamide mononucleotide (NMN) treatment preserves NAD⁺ and prevents senescence in human retinal pigment epithelial cells. Human retinal pigment epithelial cells (ARPE-19) were treated with 10 μM FK866 alone or in combination with different doses of NMN (0.05-1 mM) for 72 hr. (A) NAD⁺ content was measured using a NAD assay kit. (B) Changes in expression of SIRT1, p16^{INK4a} and p21^{Waf/Cip1} proteins levels were evaluated by western blotting. (C-D) RPE senescence was evaluated by β-galactosidase staining. A representative western blot image from three replicates is shown. Data are presented as mean ± S.E.M for n=3 independent experiments. *p<0.05 compared to CON (Vehicle treated) and #p<0.05 compared to FK866.

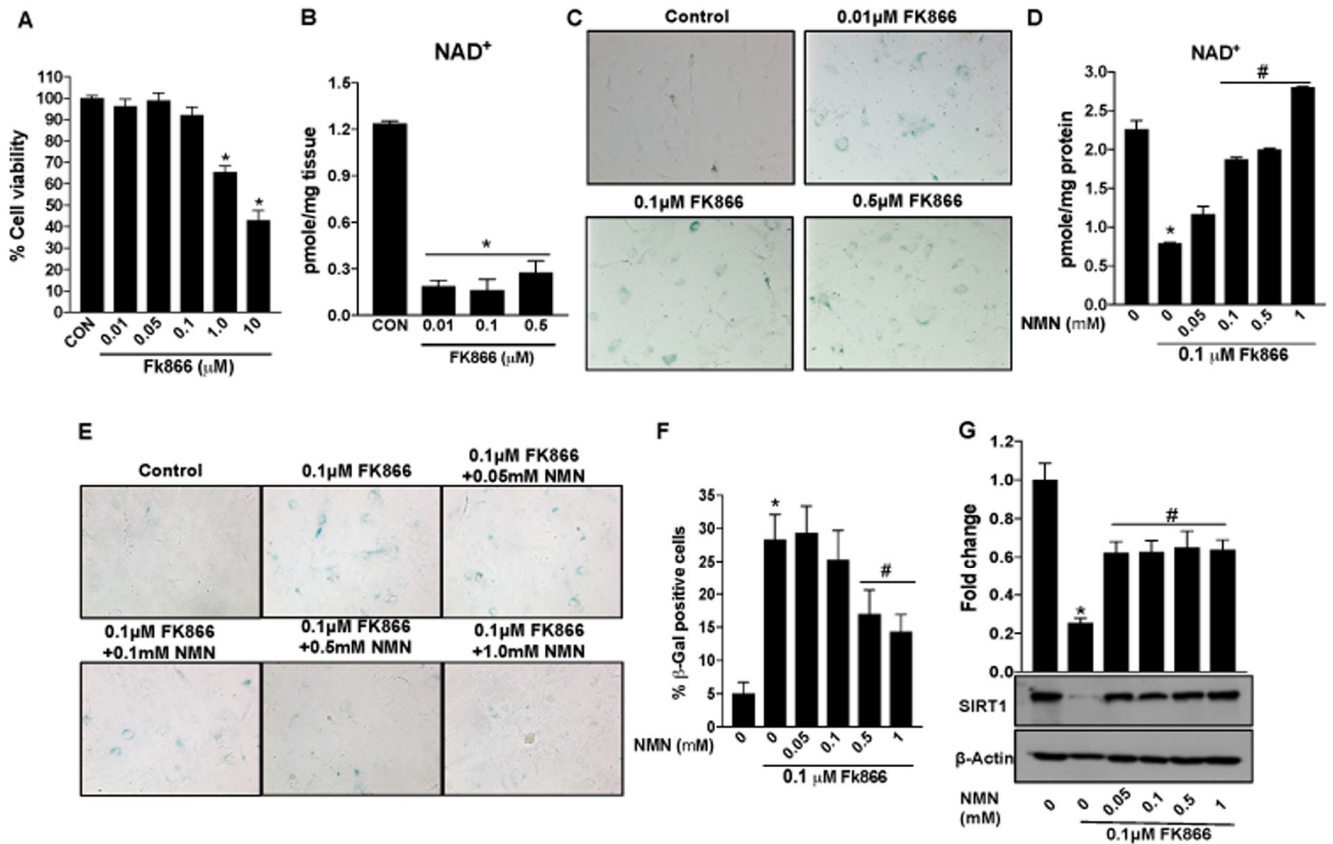


Figure 9. Nicotinamide mononucleotide (NMN) treatment preserves NAD⁺ and prevents senescence in mouse retinal pigment epithelial cells. Primary RPE cells were isolated from 17 days old mouse pups and cultured as described in materials and methods. Mouse primary RPE cells were treated with different doses of FK866 for 5 days to evaluate changes in cell viability, NAD⁺ content, senescence and SIRT1 expression. (A) Cell viability was evaluated by MTT assay. (B and D) NAD⁺ content was measured using a NAD assay kit. (C, E and F) RPE senescence were evaluated by and β -galactosidase staining. (G) Changes in expression of SIRT-1 protein levels were evaluated by western blotting. A representative western blot image from three replicates is shown. Data are presented as mean \pm S.E.M for n=3 independent experiments. *p<0.05 compared to CON (Vehicle treated) and #p<0.05 compared to FK866.

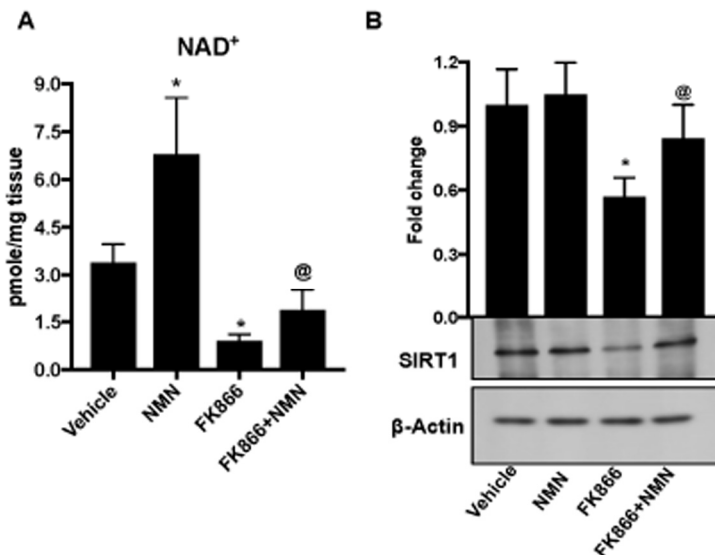


Figure 10. *In vivo* administration of nicotinamide mononucleotide (NMN) prevents FK866-induced NAD⁺ depletion and RPE senescence. Male C57BL/6J mice were injected sub-retinally with 10 μ M FK866 (right eye) at day 0 and day 7 and sacrificed on day 15 (7 days after the last dose). RPE/eye cup was then collected for further analysis. Simultaneously, mice were treated with 150 mg/kg NMN (i.p.) for 14 days. Left eye was injected with PBS to use as controls. (A) NAD⁺ content and (B) SIRT-1 expression was evaluated by NAD assay and western blotting respectively. A representative western blot image from three replicates is shown. Data are presented as mean \pm S.E.M for n=5. *p<0.05 compared to CON (Vehicle treated) and @p<0.05 compared to FK866.

Furthermore, therapies that enhance NAD⁺ production and/or the expression and activity of downstream NAD⁺-dependent enzymes have shown benefit in treating such diseases [35]. In retina specifically, the importance of NAD⁺ normally and in aging, has been evaluated directly in photoreceptors [36] but has not been studied extensively in the underlying RPE. This is both interesting and unfortunate given, as mentioned previously, the numerous essential primary and supportive functions that RPE performs and therefore, the obligatory commensal relationship that exists between the photoreceptors and RPE, the two cell types principally affected in AMD. A very recent report [37], demonstrated, using human-induced pluripotent stem cell derived RPE cells (hiPSC-RPE) prepared from donors with and without AMD, the benefit of the NAD⁺ precursor, nicotinamide, in limiting the expression of key complement and inflammatory proteins linked directly to drusen development and AMD. This study supports the feasibility of targeting NAD⁺ biosynthesis therapeutically to preserve RPE viability and thereby prevent and/or treat related degenerative processes in aged retina.

Here, using adult C57BL/6J mice across a broad range of ages (2 -18 months) and in which the absence of any underlying *rd* mutation that might impact adversely retinal phenotype or function has been verified [38], we first confirmed that NAD⁺ levels decline significantly in association with increased age as has been reported to occur in other retinal and non-retinal cell types. As a positive control, we monitored also the expression of SIRT1, a down-stream NAD⁺-dependent enzyme that is known to decrease in expression in association with increased age and decreased availability of NAD⁺ in various organisms, cell and tissue types. Our related evaluation of enzymes that drive key steps in NAD⁺ biosynthesis revealed NAMPT as the enzyme principally responsible for maintaining adequate NAD⁺ levels in RPE. This is congruent with recent work by others demonstrating that NAMPT-mediated NAD⁺ biosynthesis is essential for proper visual function [36].

A major limiting factor in AMD research is the lack of availability of acute experimental models that mimic accurately processes involved in disease pathogenesis while at the same time, affording a reliable preclinical system in which to rapidly test developmental therapies. FK866 has been used broadly in the cancer field and others to study the impact of NAMPT inhibition on various processes including cellular viability and immune signaling, inflammation, and energy metabolism [16, 39, 40]. Here, we used the compound to optimize a cell culture model system that allowed us to simulate and study the impact of decreased NAMPT expression and related NAD⁺ availability on RPE cell

viability relevant to aging. Our studies in the human RPE cell line ARPE-19 demonstrated an increase in RPE cell senescence in conjunction with reduced NAMPT and NAD⁺ availability as indicated by analyses of the expression of senescence markers like β -galactosidase, ApoJ, p16^{INK4a}, p21^{Waf/Cip1} and CTGF. Importantly, co-exposure of cells to the NAD⁺-precursor NMN stabilized levels of NAD⁺ and SIRT1 even in the presence of NAMPT inhibition and prevented the induction of senescence-associated gene expression. ARPE-19 is a transformed cell line and we simulated the age-related decline in NAD⁺ in these cells artificially using FK866. Therefore, we acknowledge that there may be differences between the way these cells respond compared to natural RPE. To alleviate this concern, we repeated key experiments in primary mouse RPE cells. The optimal age for isolating and culturing primary mouse RPE is 18-21 days. Cells can be isolated from mice of older age but do not persist well in culture for extended periods. This makes direct comparative studies between primary RPE cells obtained from young and old mice difficult to standardize. Hence, we again used FK866 to suppress NAMPT activity in primary RPE cells isolated from young mice. Importantly, the validity of our cell culture model systems and the data emanating there from was supported strongly by the fact that findings obtained in our cell cultures mirrored closely those obtained using intact RPE tissue obtained and analyzed immediately upon procurement from the eyes of living animals.

The risk and incidence of disease formation both within and outside of the eye increases proportionally with age. Though the cell and tissue types affected may differ from one disease to another, commonality is found in that the process of aging and the development of age-related degenerative disease generally appears to involve a progressive decline in cellular energy production and consequently, in the viability and function of cells. Neuronal tissues such as retina are especially sensitive. In AMD, gradual degenerative changes occur in both the photoreceptors and the RPE. RPE senescence is thought to be largely responsible for precipitating these changes [41-43]. Some promise with respect to preventing senescence-associated changes in RPE and potentially impacting AMD development has been demonstrated experimentally using compounds like resveratrol, which impact the expression and activity of SIRT1, a down-stream NAD⁺-dependent gene that in turn, governs processes essential to the maintenance of cellular viability [44-46]. However, few have explored directly the potential therapeutic impact of targeting NAMPT and NAD⁺ biosynthesis itself despite the knowledge that NAD⁺ is the starting point of most major metabolic pathways and therefore, the key governor of cellular aging and age-related processes.

Our present data demonstrating an age-dependent decline in NAMPT expression and in turn, NAD⁺ generation in RPE which ultimately promotes RPE senescence supports strongly the rationale for enhancing NAMPT expression and associated NAD⁺ generation therapeutically. Indeed, such therapies may represent a viable strategy for preventing and treating RPE and consequent photoreceptor damage in aging/AMD and broadly, in other degenerative retinal diseases in which RPE is prominently affected. AMD is the leading cause of blindness among persons aged 60 and above worldwide [47, 48]. Congruent with advancements in healthcare and the large number of “baby boomers”, the number of persons within this age bracket has and continues to increase steadily and substantially, and proportionate to that, the incidence of AMD. Indeed, it is estimated that by the year 2020, 200 million people will be affected by AMD [48]. Hence, AMD represents a significant present and future global health and economic burden [49], the impact of which is exacerbated by the fact that strategies to prevent and treat dry AMD, the form of the disease that is most common and therefore affects the greatest number of patients, are lacking. Based upon our present experimental observations, future preclinical studies evaluating NMN or other therapies that have a direct impact on NAMPT expression and NAD⁺ metabolism in the context of aging and age-related retinal disease development and progression are highly warranted.

MATERIALS AND METHODS

Animals

All experiments involving animals adhered to the Public Health Service Policy on the Humane Care and Use of Laboratory Animals (2015 Department of Health, Education and Welfare publication, NIH 80-23), the Association for Research in Vision and Ophthalmology Statement for use of Animals in Ophthalmic and Vision Research and were approved by the Augusta University Institutional Animal Care and Use Committee. Male C57BL/6J mice of different age groups obtained from a commercial vendor (Jackson Laboratories, Bar Harbor, ME, USA) and the National Institute of Aging (National Institutes of Health, Bethesda, MD, USA) were housed under identical conditions in a pathogen-free environment with a 12:12 h light/dark cycle and free access to laboratory chow and water. Mice were acclimatized for at least 1 week before the experiments.

Cell culture

Human retinal pigment epithelial (ARPE-19) cells were cultured in Dulbecco's modified Eagle medium DMEM/F12 medium (supplemented with 10% fetal

bovine serum, 100 U/ml penicillin, and 100 µg/ml streptomycin) and maintained at 37 °C in a humidified chamber with 5% CO₂. The culture medium was replaced with fresh medium every other day. Cultures were passaged by dissociation in 0.05% (w/v) trypsin in phosphate-buffered saline (PBS; 0.01 M phosphate buffer, 0.0027 M KCl, 0.137 M NaCl, pH 7.4). Completely confluent, well-differentiated cultures were used for experimentation.

Primary mouse RPE cells were prepared from C57BL/6J mouse eyes and the purity of these cultures was confirmed per our published method [50-53]. Primary mouse RPE cells were then maintained at 37 °C in a humidified chamber with 5% CO₂ and sub-cultured using trypsin–EDTA solution. All experiments were carried out using primary RPE cells in passages 1 and 2.

Reverse transcription–quantitative polymerase chain reaction

Total RNA was isolated from RPE/eyecup of mice (2, 12 and 18 months old) or ARPE-19 cells using RNAeasy mini kit (Qiagen, USA). cDNA was prepared from total RNA using the iScript cDNA Synthesis Kit (Bio-Rad) and subjected to qPCR assay. Assays were performed in 96-well PCR plates using All-in-One™ qPCR Mix (Genecopia, USA). The reaction volume of 20 µl contained 10.0 µl SYBR green master mix (2X), 1 µl cDNA, 1 µl of each primer and 7 µl nuclease-free water. Primer sequences are listed in Table 1. The following two-step thermal cycling profile was used (StepOnePlus Real-Time PCR, Life Technologies, Grand Island, NY): Step I (cycling): 95 °C for 5 min, 95 °C for 15 s, 60 °C for 30 s and 72 °C for 15s for 40 cycles. Step II (melting curve): 60 °C for 15 s, 60 °C 1 min and 95 °C for 30 s. The template amplification was confirmed by melting curve analysis. mRNA expression of genes were normalized to 18s expression and fold change in expression was calculated by 2^{-ΔΔCt} method.

FK866 and Nicotinamide mononucleotide (NMN) treatments

ARPE-19 cells were serum starved overnight and treated with varying doses (0.01-10µM) of FK866 (Sigma-Aldrich) for different time intervals (24, 48 or 72 h). Following FK866 treatment, cells were collected for one or more of the following analyses: MTT assay, NAD⁺ measurement, SIRT1 activity assay, RNA or protein studies. Primary mouse RPE cells were treated and analyzed similarly except that lower doses of FK866 (0.01, 0.1 and 0.5 µM) were employed. The above experiments were used to establish the optimal

Table 1. Primer sequences used for qPCR.

Gene	Forward (5'-3')	Reverse (5'-3')
<i>Homo sapiens</i>		
P21 ^{Waf/cip1}	AAGTCAGTTCCTTGTGGAGC	GCCATTAGCGCATCACAGTC
CTGF	ACATTAAGAAGGGCAAAAAGTGC	GTGCAGCCAGAAAGCTCAAA
APOJ	AGGGACTGTCATACCAGTGA	TTGTGCGACCTTGGTCAGAA
IL-6	CTCAATATTAGAGTCTCAACCCCA	TGTTACATGTTTGTGGAGAAGGAG
IL-8	GCTCTGTGTGAAGGTGCAGTT	ACCCAGTTTTCTTGGGGTC
18S	CCCGTTGAACCCCATTCGT	GCCTCACTAAACCATCCAATCGGTA
<i>Mus musculus</i>		
<i>Nmnat</i>	CCTTCAAGGCCTGACAACAT	ACCGACCGGTGAGATAATGC
<i>Nampt</i>	AACCAATGGCCTTGGGGTTA	TAACAAAGTTCCTCCGCTGGT
<i>Qprt</i>	GTGGAATGTAGCAGCCTGGA	TGCAGCTCCTCAGGCTTAAA
<i>18s</i>	CCAGAGCGAAAGCATTGCCAAGA	AGCATGCCAGAGTCTCGTTCGTTA

dose and time for use of FK866 to adequately inhibit NAMPT without inducing robust cellular toxicity in ARPE-19 and primary RPE cells. Congruent with these studies, ARPE-19 and primary mouse RPE cell cultures were exposed to FK866 (10 μ M) for 72 h in the presence or absence of varying concentrations of the NAD⁺ precursor, nicotinamide mononucleotide (NMN; 0.05 – 1.0 mM).

For *in vivo* studies, adult male C57BL/6J mice were deeply anesthetized via a single intraperitoneal injection of ketamine (80 mg/kg) and xylazine (12 mg/kg; Sigma-Aldrich, St. Louis, MO, USA). Upon confirmation of anesthetic depth via toe pinch, FK866 (10 μ M) was delivered sub-retinally in a total volume of 2 μ L using a 33-gauge Hamilton Syringe (Hamilton, Reno, NV, USA) at day 0 and again at day 7. Sham control eyes (left eyes) were injected in the same manner except with 2 μ L of 0.01M PBS. A group of FK866 injected mice were treated with 150 mg/kg NMN (*i.p.*) once daily for 2 weeks [36]. Mice were euthanized one-week post delivery of the second FK866 injection and RPE tissue harvested for measurement of NAD⁺ and protein analyses.

Western blot analysis

Protein was extracted from RPE/eyecup of mice (2, 12 and 18 months old) or ARPE-19 cells or primary RPE cells using RIPA cell lysis buffer (Thermo Scientific) containing protease and phosphatase inhibitors and concentration was determined using the coomassie protein

assay reagent (Sigma-Aldrich, USA). Equi-valent amount of protein samples were subjected to SDS-PAGE, transferred to PVDF membranes, and then incubated with primary antibodies: SIRT-1, p21^{Waf/Cip1} (1:1000; Cell signaling) and p16^{INK4a} (1:500; Abcam) overnight at 4°C. Next day, blots were washed with TBST and incubated with horseradish peroxidase conjugated secondary antibody (1:3000; Sigma-Aldrich, USA) for 60 min with gentle shaking at room temperature. Blots were then washed (with TBST) and developed with chemiluminescence reagent (Bio-Rad, Hercules, CA) using autoradiography films (Genesee Scientific, San Diego, CA). β -actin (1:3000; Sigma-Aldrich, USA) expression was evaluated to determine equivalent loading. Scanned images of blots were used to quantify protein expression using NIH ImageJ software (<http://rsb.info.nih.gov/ij/>).

NAD⁺ assay

NAD⁺ levels in cells and tissue were quantified with a commercially available kit (Sigma, MO, United States) according to the manufacturer's instructions.

SIRT1 activity assay

The SIRT-1 deacetylase assay in ARPE-19 cells was performed using a fluorometric SIRT1 assay kit (Sigma-Aldrich, USA), according to the manufacturer's protocol. Briefly, the reaction was carried out at 37°C for 30 min and deacetylase activity was detected as a fluorescence emission at 450 nm, using an excitation

wavelength of 360 nm. The intensity of the fluorescence emitted by the compounds at 450 nm was subtracted from initially determined assay values.

β-galactosidase assay

Senescence-associated beta-galactosidase (β-Gal) staining was performed according to the manufacturer's protocols (Cell Signaling Technology). At the end of treatments, cells were fixed for 15 minutes in 1x fixative solution (formaldehyde-glutaraldehyde mix), followed by PBS washes, and incubated overnight with β-Gal staining solution in a dry incubator at 37°C. Cells were viewed under brightfield microscopy (Leica BM5500B Microscope; Leica Biosystems, Wetzlar, Germany) for blue color development and were photographed using a Photometrics CoolSNAP HQ² camera and associated Leica Application Suite software v4.1.

CellROX and MitoSOX staining

ARPE-19 cells were treated with 10 μM FK866 for 72 hr. as mentioned above. At the end of treatments, cells were incubated for 5 μM CellROX for 30 min or 5 μM MitoSOX for 10 min. At the end of incubation, cells were washed with PBS, mounted using fluoroshield mounting medium with DAPI and images were captured using Zeiss Axioplan-2 imaging fluorescence microscope.

Statistical analysis

Results are presented as mean ± S.E.M for minimum of three independent experiments. Statistical significance was defined as $p < 0.05$ and determined using student's t-test (normally-distributed data). Graphs were prepared using GraphPad Prism 7 software.

AUTHOR CONTRIBUTIONS

Conceived and designed the experiments: RNJ, PMM; Performed the experiments: RNJ, FLP, MAJ, JF, EJ, MCT, Analyzed data: RNJ, MB, PMM; Wrote the manuscript: RNJ, PMM.

ACKNOWLEDGEMENTS

The authors would like to acknowledge Jianghe Yuan for helping with sub-retinal injections.

CONFLICTS OF INTEREST

The authors declare no conflicts of interest.

FUNDING

This study was supported by funding from National Institutes of Health grants EY022704 to P.M.M.

REFERENCES

1. Bok D. The retinal pigment epithelium: a versatile partner in vision. *J Cell Sci Suppl.* 1993 (Suppl 17); 17:189–95. https://doi.org/10.1242/jcs.1993.Supplement_17.27
2. Bonilha VL. Age and disease-related structural changes in the retinal pigment epithelium. *Clin Ophthalmol.* 2008; 2:413–24. <https://doi.org/10.2147/OPHTH.S2151>
3. Jonas JB, Cheung CM, Panda-Jonas S. Updates on the Epidemiology of Age-Related Macular Degeneration. *Asia Pac J Ophthalmol (Phila).* 2017; 6:493–97. <https://doi.org/10.22608/APO.2017251>
4. Pennington KL, DeAngelis MM. Epidemiology of age-related macular degeneration (AMD): associations with cardiovascular disease phenotypes and lipid factors. *Eye Vis (Lond).* 2016; 3:34. <https://doi.org/10.1186/s40662-016-0063-5>
5. Fritsche LG, Fariss RN, Stambolian D, Abecasis GR, Curcio CA, Swaroop A. Age-related macular degeneration: genetics and biology coming together. *Annu Rev Genomics Hum Genet.* 2014; 15:151–71. <https://doi.org/10.1146/annurev-genom-090413-025610>
6. Forest DL, Johnson LV, Clegg DO. Cellular models and therapies for age-related macular degeneration. *Dis Model Mech.* 2015; 8:421–27. <https://doi.org/10.1242/dmm.017236>
7. Elhassan YS, Philp AA, Lavery GG. Targeting NAD⁺ in Metabolic Disease: New Insights Into an Old Molecule. *J Endocr Soc.* 2017; 1:816–35. <https://doi.org/10.1210/js.2017-00092>
8. Srivastava S. Emerging therapeutic roles for NAD(+) metabolism in mitochondrial and age-related disorders. *Clin Transl Med.* 2016; 5:25. <https://doi.org/10.1186/s40169-016-0104-7>
9. Haigis MC, Sinclair DA. Mammalian sirtuins: biological insights and disease relevance. *Annu Rev Pathol.* 2010; 5:253–95. <https://doi.org/10.1146/annurev.pathol.4.110807.092250>
10. Fouquerel E, Sobol RW. ARTD1 (PARP1) activation and NAD(+) in DNA repair and cell death. *DNA Repair (Amst).* 2014; 23:27–32. <https://doi.org/10.1016/j.dnarep.2014.09.004>

11. Bai P. Biology of Poly(ADP-Ribose) Polymerases: The Factotums of Cell Maintenance. *Mol Cell*. 2015; 58:947–58. <https://doi.org/10.1016/j.molcel.2015.01.034>
12. Fang EF, Lautrup S, Hou Y, Demarest TG, Croteau DL, Mattson MP, Bohr VA. NAD⁺ in Aging: Molecular Mechanisms and Translational Implications. *Trends Mol Med*. 2017; 23:899–916. <https://doi.org/10.1016/j.molmed.2017.08.001>
13. Imai SI, Guarente L. It takes two to tango: NAD⁺ and sirtuins in aging/longevity control. *NPJ Aging Mech Dis*. 2016; 2:16017. <https://doi.org/10.1038/npjamd.2016.17>
14. Cantó C, Menzies KJ, Auwerx J. NAD(+) Metabolism and the Control of Energy Homeostasis: A Balancing Act between Mitochondria and the Nucleus. *Cell Metab*. 2015; 22:31–53. <https://doi.org/10.1016/j.cmet.2015.05.023>
15. Balaiya S, Abu-Amero KK, Kondkar AA, Chalam KV. Sirtuins Expression and Their Role in Retinal Diseases. *Oxid Med Cell Longev*. 2017; 2017:3187594. <https://doi.org/10.1155/2017/3187594>
16. Hasmann M, Schemainda I. FK866, a highly specific noncompetitive inhibitor of nicotinamide phosphoribosyltransferase, represents a novel mechanism for induction of tumor cell apoptosis. *Cancer Res*. 2003; 63:7436–42.
17. Marazita MC, Dugour A, Marquioni-Ramella MD, Figueroa JM, Suburo AM. Oxidative stress-induced premature senescence dysregulates VEGF and CFH expression in retinal pigment epithelial cells: Implications for Age-related Macular Degeneration. *Redox Biol*. 2016; 7:78–87. <https://doi.org/10.1016/j.redox.2015.11.011>
18. Zhu D, Wu J, Spee C, Ryan SJ, Hinton DR. BMP4 mediates oxidative stress-induced retinal pigment epithelial cell senescence and is overexpressed in age-related macular degeneration. *J Biol Chem*. 2009; 284:9529–39. <https://doi.org/10.1074/jbc.M809393200>
19. Han S, Lu Q, Wang N. Apr3 accelerates the senescence of human retinal pigment epithelial cells. *Mol Med Rep*. 2016; 13:3121–26. <https://doi.org/10.3892/mmr.2016.4926>
20. Yu AL, Birke K, Burger J, Welge-Lussen U. Biological effects of cigarette smoke in cultured human retinal pigment epithelial cells. *PLoS One*. 2012; 7:e48501. <https://doi.org/10.1371/journal.pone.0048501>
21. Davalli P, Mitic T, Caporali A, Lauriola A, D’Arca D. ROS, Cell Senescence, and Novel Molecular Mechanisms in Aging and Age-Related Diseases. *Oxid Med Cell Longev*. 2016; 2016:3565127. <https://doi.org/10.1155/2016/3565127>
22. Cao S, Walker GB, Wang X, Cui JZ, Matsubara JA. Altered cytokine profiles of human retinal pigment epithelium: oxidant injury and replicative senescence. *Mol Vis*. 2013; 19:718–28.
23. Meyer P, Maity P, Burkovski A, Schwab J, Müssel C, Singh K, Ferreira FF, Krug L, Maier HJ, Wlaschek M, Wirth T, Kestler HA, Scharffetter-Kochanek K. A model of the onset of the senescence associated secretory phenotype after DNA damage induced senescence. *PLOS Comput Biol*. 2017; 13:e1005741. <https://doi.org/10.1371/journal.pcbi.1005741>
24. Aryan N, Betts-Obregon BS, Perry G, Tsin AT. Oxidative Stress Induces Senescence in Cultured RPE Cells. *Open Neurol J*. 2016; 10:83–87. <https://doi.org/10.2174/1874205X01610010083>
25. Marazita MC, Dugour A, Marquioni-Ramella MD, Figueroa JM, Suburo AM. Oxidative stress-induced premature senescence dysregulates VEGF and CFH expression in retinal pigment epithelial cells: Implications for Age-related Macular Degeneration. *Redox Biol*. 2016; 7:78–87. <https://doi.org/10.1016/j.redox.2015.11.011>
26. Zhu D, Wu J, Spee C, Ryan SJ, Hinton DR. BMP4 mediates oxidative stress-induced retinal pigment epithelial cell senescence and is overexpressed in age-related macular degeneration. *J Biol Chem*. 2009; 284:9529–39. <https://doi.org/10.1074/jbc.M809393200>
27. Imai S, Guarente L. NAD⁺ and sirtuins in aging and disease. *Trends Cell Biol*. 2014; 24:464–71. <https://doi.org/10.1016/j.tcb.2014.04.002>
28. Braidy N, Guillemin GJ, Mansour H, Chan-Ling T, Poljak A, Grant R. Age related changes in NAD⁺ metabolism oxidative stress and Sirt1 activity in wistar rats. *PLoS One*. 2011; 6:e19194. <https://doi.org/10.1371/journal.pone.0019194>
29. Massudi H, Grant R, Braidy N, Guest J, Farnsworth B, Guillemin GJ. Age-associated changes in oxidative stress and NAD⁺ metabolism in human tissue. *PLoS One*. 2012; 7:e42357. <https://doi.org/10.1371/journal.pone.0042357>
30. Khan NA, Auranen M, Paetau I, Pirinen E, Euro L, Forsström S, Pasila L, Velagapudi V, Carroll CJ, Auwerx J, Suomalainen A. Effective treatment of mitochondrial myopathy by nicotinamide riboside, a vitamin B3. *EMBO Mol Med*. 2014; 6:721–31. <https://doi.org/10.1002/emmm.201403943>
31. Mouchiroud L, Houtkooper RH, Auwerx J. NAD⁺ metabolism: a therapeutic target for age-related metabolic

- disease. *Crit Rev Biochem Mol Biol.* 2013; 48:397–408. <https://doi.org/10.3109/10409238.2013.789479>
32. Hernández-Zimbrón LF, Zamora-Alvarado R, Ochoa-De la Paz L, Velez-Montoya R, Zenteno E, Gullias-Cañizo R, Quiroz-Mercado H, Gonzalez-Salinas R. Age-Related Macular Degeneration: New Paradigms for Treatment and Management of AMD. *Oxid Med Cell Longev.* 2018; 2018:8374647. <https://doi.org/10.1155/2018/8374647>
 33. Narayanan R, Kuppermann BD. Hot Topics in Dry AMD. *Curr Pharm Des.* 2017; 23:542–46. <https://doi.org/10.2174/1381612822666161221154424>
 34. Bandello F, Sacconi R, Querques L, Corbelli E, Cicinelli MV, Querques G. Recent advances in the management of dry age-related macular degeneration: A review. *F1000 Res.* 2017; 6:245. <https://doi.org/10.12688/f1000research.10664.1>
 35. Zhang MC, Ying WH. NAD(+) Deficiency Is a Common Central Pathological Factor of a Number of Diseases and Aging: Mechanisms and Therapeutic Implications. *Antioxid Redox Sign.* 2018. Epub ahead of print. <https://doi.org/10.1089/ars.2017.7445>.
 36. Lin JB, Kubota S, Ban N, Yoshida M, Santeford A, Sene A, Nakamura R, Zapata N, Kubota M, Tsubota K, Yoshino J, Imai SI, Apte RS. NAMPT-Mediated NAD(+) Biosynthesis Is Essential for Vision In Mice. *Cell Reports.* 2016; 17:69–85. <https://doi.org/10.1016/j.celrep.2016.08.073>
 37. Saini JS, Corneo B, Miller JD, Kiehl TR, Wang Q, Boles NC, Blenkinsop TA, Stern JH, Temple S. Nicotinamide Ameliorates Disease Phenotypes in a Human iPSC Model of Age-Related Macular Degeneration. *Cell Stem Cell.* 2017; 20:635–647.e7. <https://doi.org/10.1016/j.stem.2016.12.015>
 38. Chang B, Hurd R, Wang J, Nishina P. Survey of common eye diseases in laboratory mouse strains. *Invest Ophthalmol Vis Sci.* 2013; 54:4974–81. <https://doi.org/10.1167/iovs.13-12289>
 39. Montecucco F, Cea M, Cagnetta A, Damonte P, Nahimana A, Ballestrero A, Del Rio A, Bruzzone S, Nencioni A. Nicotinamide phosphoribosyltransferase as a target in inflammation- related disorders. *Curr Top Med Chem.* 2013; 13:2930–38. <https://doi.org/10.2174/15680266113136660208>
 40. Chen Y, Liang Y, Hu T, Wei R, Cai C, Wang P, Wang L, Qiao W, Feng L. Endogenous Nampt upregulation is associated with diabetic nephropathy inflammatory-fibrosis through the NF- κ B p65 and Sirt1 pathway; NMN alleviates diabetic nephropathy inflammatory-fibrosis by inhibiting endogenous Nampt. *Exp Ther Med.* 2017; 14:4181–93. <https://doi.org/10.3892/etm.2017.5098>
 41. Kozłowski MR. RPE cell senescence: a key contributor to age-related macular degeneration. *Med Hypotheses.* 2012; 78:505–10. <https://doi.org/10.1016/j.mehy.2012.01.018>
 42. Blasiak J, Piechota M, Pawłowska E, Szatkowska M, Sikora E, Kaarniranta K. Cellular Senescence in Age-Related Macular Degeneration: Can Autophagy and DNA Damage Response Play a Role? *Oxid Med Cell Longev.* 2017; 2017:5293258. <https://doi.org/10.1155/2017/5293258>
 43. Ambati J, Ambati BK, Yoo SH, Ianchulev S, Adamis AP. Age-related macular degeneration: etiology, pathogenesis, and therapeutic strategies. *Surv Ophthalmol.* 2003; 48:257–93. [https://doi.org/10.1016/S0039-6257\(03\)00030-4](https://doi.org/10.1016/S0039-6257(03)00030-4)
 44. Ishikawa K, He S, Terasaki H, Nazari H, Zhang H, Spee C, Kannan R, Hinton DR. Resveratrol inhibits epithelial-mesenchymal transition of retinal pigment epithelium and development of proliferative vitreoretinopathy. *Sci Rep.* 2015; 5:16386. <https://doi.org/10.1038/srep16386>
 45. King RE, Kent KD, Bomser JA. Resveratrol reduces oxidation and proliferation of human retinal pigment epithelial cells via extracellular signal-regulated kinase inhibition. *Chem Biol Interact.* 2005; 151:143–49. <https://doi.org/10.1016/j.cbi.2004.11.003>
 46. Sheu SJ, Liu NC, Ou CC, Bee YS, Chen SC, Lin HC, Chan JY. Resveratrol stimulates mitochondrial bioenergetics to protect retinal pigment epithelial cells from oxidative damage. *Invest Ophthalmol Vis Sci.* 2013; 54:6426–38. <https://doi.org/10.1167/iovs.13-12024>
 47. Sergejeva O, Botov R, Liutkevičienė R, Kriaučiūnienė L. Genetic factors associated with the development of age-related macular degeneration. *Medicina (Kaunas).* 2016; 52:79–88. <https://doi.org/10.1016/j.medici.2016.02.004>
 48. Wong WL, Su X, Li X, Cheung CM, Klein R, Cheng CY, Wong TY. Global prevalence of age-related macular degeneration and disease burden projection for 2020 and 2040: a systematic review and meta-analysis. *Lancet Glob Health.* 2014; 2:e106–16. [https://doi.org/10.1016/S2214-109X\(13\)70145-1](https://doi.org/10.1016/S2214-109X(13)70145-1)
 49. Gordoís A, Cutler H, Pezzullo L, Gordon K, Cruess A, Winyard S, Hamilton W, Chua K. An estimation of the worldwide economic and health burden of visual impairment. *Glob Public Health.* 2012; 7:465–81. <https://doi.org/10.1080/17441692.2011.634815>
 50. Gambhir D, Ananth S, Veeranan-Karmegam R, Elangovan S, Hester S, Jennings E, Offermanns S,

Nussbaum JJ, Smith SB, Thangaraju M, Ganapathy V, Martin PM. GPR109A as an anti-inflammatory receptor in retinal pigment epithelial cells and its relevance to diabetic retinopathy. *Invest Ophthalmol Vis Sci.* 2012; 53:2208–17.
<https://doi.org/10.1167/iops.11-8447>

51. Gnana-Prakasam JP, Martin PM, Mysona BA, Roon P, Smith SB, Ganapathy V. Hepcidin expression in mouse retina and its regulation via lipopolysaccharide/Toll-like receptor-4 pathway independent of Hfe. *Biochem J.* 2008; 411:79–88.
<https://doi.org/10.1042/BJ20071377>
52. Gnana-Prakasam JP, Reddy SK, Veeranan-Karmegam R, Smith SB, Martin PM, Ganapathy V. Polarized distribution of heme transporters in retinal pigment epithelium and their regulation in the iron-overload disease hemochromatosis. *Invest Ophthalmol Vis Sci.* 2011; 52:9279–86. <https://doi.org/10.1167/iops.11-8264>
53. Martin PM, Ananth S, Cresci G, Roon P, Smith S, Ganapathy V. Expression and localization of GPR109A (PUMA-G/HM74A) mRNA and protein in mammalian retinal pigment epithelium. *Mol Vis.* 2009; 15:362–72.

SUPPLEMENTARY MATERIAL

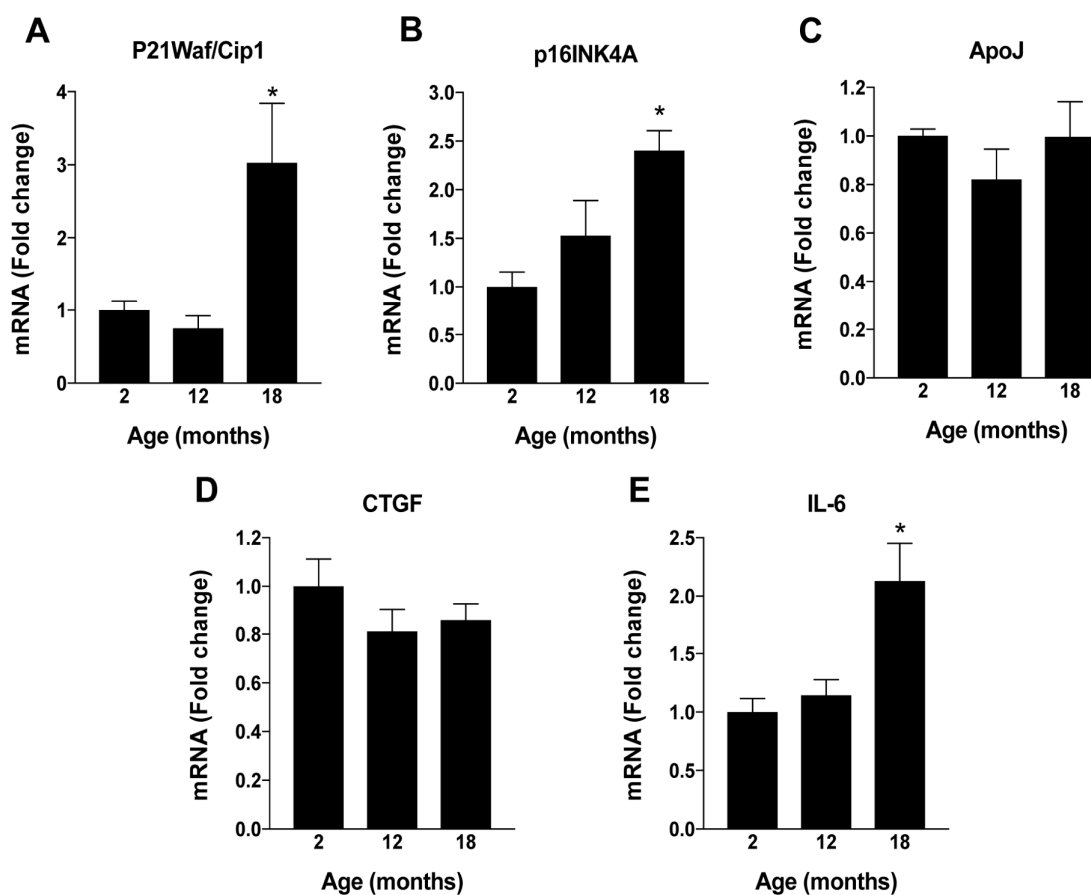


Figure S1. Changes in RPE senescence markers with aging in mice. RPE/eye cup was dissected from 2, 12 and 18 months old male C57BL/6J mice to evaluate changes in the expression of various senescence markers. (A-E) Changes in mRNA expression of markers associated with senescence were performed by qPCR. Data is presented as mean \pm S.E.M for n=5. mRNA expression of genes were normalized to 18s expression. *p<0.05 compared to 2M (two months old mice).

Table S1. Primer sequences used for qPCR.

<i>Mus musculus</i>		
<i>p21Waf/cip1</i>	TATCCAGACATTCAGAGCCAC	CGAAGTCAAAGTTCACCGT
<i>p16ink4a</i>	TCTTGGTCACTGTGAGGATTCA	GAACGTTGCCCATCATCATCA
<i>Ctgf</i>	TCCACCCGAGTTACCAATGA	TGCACTTTTGCCCTTCTTA
<i>ApoJ</i>	TAGGCTTCCAGAAAGCTCCT	ATAGCGCTCTGCTCAAGTACA
<i>IL-6</i>	CTTCTGGAGTACCATAGC	TCTGTTAGGAGAGCATTG
<i>18s</i>	CCAGAGCGAAAGCATTGCCAAGA	AGCATGCCAGAGTCTCGTTCGTTA

miR-106b suppresses pathological retinal angiogenesis

Catherine Ménard¹, Ariel M. Wilson¹, Agnieszka Dejada², Khalil Miloudi³, François Binet², Sergio Crespo-Garcia², Célia Parinot², Frédérique Pilon², Rachel Juneau², Elisabeth MMA Andriessen², Gaëlle Mawambo¹, John Paul SanGiovanni⁴, Vincent De Guire¹, Przemyslaw Sapieha^{1,2,3}

¹Department of Biochemistry, Maisonneuve-Rosemont Hospital Research Centre, University of Montreal, Montreal H1T 2M4, Quebec, Canada

²Department of Ophthalmology, Maisonneuve-Rosemont Hospital Research Centre, University of Montreal, Montreal H1T 2M4, Quebec, Canada

³Department of Neurology-Neurosurgery, McGill University, Montreal H3A 2B4, Quebec, Canada

⁴Department of Nutritional Sciences, University of Arizona, Tucson, AZ 85719, USA

Correspondence to: Przemyslaw Sapieha, Vincent De Guire; email: mike.sapieha@umontreal.ca, vdeguire.hmr@ssss.gouv.qc.ca

Keywords: age related macular degeneration, miR-106b, PERK, choroidal neovascularization, angiogenesis

Received: July 4, 2020

Accepted: November 13, 2020

Published: December 23, 2020

Copyright: © 2020 Ménard et al. This is an open access article distributed under the terms of the [Creative Commons Attribution License](https://creativecommons.org/licenses/by/3.0/) (CC BY 3.0), which permits unrestricted use, distribution, and reproduction in any medium, provided the original author and source are credited.

ABSTRACT

MicroRNAs are small non-coding RNAs that post-transcriptionally regulate gene expression. We recently demonstrated that levels of miR-106b were significantly decreased in the vitreous and plasma of patients with neovascular age-related macular degeneration (AMD). Here we show that expression of the miR-106b-25 cluster is negatively regulated by the unfolded protein response pathway of protein kinase RNA-like ER kinase (PERK) in a mouse model of neovascular AMD. A reduction in levels of miR-106b triggers vascular growth both *in vivo* and *in vitro* by inducing production of pro-angiogenic factors. We demonstrate that therapeutic delivery of miR-106b to the retina with lentiviral vectors protects against aberrant retinal angiogenesis in two distinct mouse models of pathological retinal neovascularization. Results from this study suggest that miRNAs such as miR-106b have the potential to be used as multitarget therapeutics for conditions characterized by pathological retinal angiogenesis.

INTRODUCTION

Age-related macular degeneration (AMD) is a common [1] and complex [2, 3] disease of aging and the leading cause of irreversible loss of sight in elderly people [4–6]. Early forms of AMD are characterized by subretinal lipoproteinaceous deposits, local attrition of photoreceptors [7] and loss of visual sensitivity [8]. Late forms of AMD are defined by geographic atrophy (loss of retinal pigment epithelium and photoreceptors) [9] and/or pathologic choroidal neovascularization (CNV) characterized by vascular sprouting from the choriocapillaris into the neural retina or subretinal space [10]. The neovascular form (NV AMD or exudative

AMD) accounts for over 80% of the vision loss associated with AMD [11].

The advent of therapies targeting vascular endothelial growth factor (VEGF) has significantly improved the quality of life of patients suffering from NV AMD [12–15]. However, not all patients with AMD respond to anti-VEGF therapies [16]. Sustained reduction in retinal VEGF levels can lead to neurotoxicity [17] and degeneration of RPE-choriocapillaris in mouse models [18]. Importantly, assessment by fundus photography and fundus fluorescein angiography of patients on anti-VEGF therapy showed accelerated development of geographic atrophy [19, 20]. These findings justify the

need for continued exploration of novel therapeutic interventions.

Given that several inflammatory and growth factors in addition to VEGF [10, 21, 22] are associated with the pathogenesis of NV AMD, a multi-targeted approach is warranted. In this regard, therapeutic delivery of miRNAs may offer a promising avenue. miRNAs are small non-coding RNAs of around 20 nucleotides that act as post-transcriptional regulatory elements of most cellular processes [23]. miRNAs mediate repression of gene expression with the potential of a single miRNA to target mRNA transcripts from hundreds of genes [24]. We previously elucidated a specific miRNA signature in the vitreous and plasma of patients with NV AMD and observed a disease-associated increase in miR-146a and a decrease in miR-106b and miR-152 [25]. Interestingly, within our cohort, we found that both vitreous- and plasma-based miR-146a/miR-106b ratios had greater than 90% discriminatory power for classification of patients with NV AMD with an area under the receiver operating characteristic curve of 0,977 in vitreous humour and 0,915 in plasma, suggesting potential for a blood-based diagnostic. These results are concordant with the evidence based in humans and model systems where upregulation of miR-146a, miR-17 (a miR containing the same seed sequence as miR-106b), miR-125 and miR-155 are associated with human AMD and a mouse model of oxygen induced retinopathy (OIR) [26–30]. miRNAs targeting VEGFA (miR-184, miR-150 and miR-106b) have also been found to be downregulated in human AMD and in animal models [25, 28, 31]. Here, we aimed to determine the mechanism leading to the downregulation of miR-106b in AMD and to characterize the therapeutic potential of upregulating miR-106b for NV AMD.

RESULTS

miR-106b is downregulated in the choroid after laser-induced CNV

In order to evaluate the potential role of miR-106b in CNV and NV AMD, we employed a laser burn-induced neovascularization mouse model. In this model, Bruch's membrane is ruptured using an argon laser, initiating sprouting of subretinal blood vessels from the choroid, mimicking NV AMD (Figure 1A) [32]. This model is characterized by a reproducible pattern of reduced neovascularization 3 days post-burn, followed by a significant increase in neovascularization that peaks on the 7th day, then vascular regression and wound healing by 14 days post-burn [32]. To illustrate the vascular changes occurring in this model, we took serial ocular fundus images of infrared reflectance and fluorescein

angiography after laser burn and subcutaneous injection of fluorescein, revealing fluorescein leakage surrounding burn sites that regressed over time (Figure 1B). In line with our previously reported findings for human vitreous and plasma from patients with active NV AMD [25], choroidal miR-106b expression was significantly downregulated in retinal specimens at all investigated time points, with statistically significant decreases of ~40% at day 3, and ~50% at days 7 and 14, relative to control animals (Figure 1C–1E). The significant downregulation of miR-106b three days post-burn corresponds to the neovascularization nadir in the laser burn model. This suggests that the observed decrease in miR-106b directly precedes initiation of CNV.

The PERK arm of the unfolded protein response is involved in retinal suppression of the mmu-miR-106b~25 cluster in laser-induced CNV

Upon confirmation of a reduction in retinal miR-106b in the CNV mouse model, we next sought to investigate the underlying mechanism. MiR-106b is a member of the miR-106b~25 cluster (mmu-miR-106b, mmu-miR-25 and mmu-miR-93) and is located in the 13th intron of protein-coding gene minichromosome maintenance complex component 7 (*MCM7*) [33]. Regulation of miR-106b expression is tightly correlated with *MCM7* transcription. Previous studies have suggested that activation of the protein kinase RNA-like ER kinase (PERK) arm of the UPR and consequent triggering of activating transcription factor 4 (ATF4) as a potential mechanism causing downregulation of the *MCM7* gene and the mmu-miR-106b~25 cluster [34] (Figure 2A). We therefore investigated if the regulation of mmu-miR-106b occurred at the transcriptional level through activation of ER stress effector pathway PERK.

To better characterize PERK activation, we examined its downstream effectors. Phosphorylation of eIF2 α was increased after laser burn as was total eIF2 α with a significant ~2-fold rise in p-eIF2 α at 7 days (Figure 2B, 2C). Moreover, a significant upregulation of the ATF4 transcript was also detected with an increase at both 3 and 7 days after laser burn (Figure 2D). We then assessed the effect of PERK activation on the *MCM7* gene transcript and miR-106b~25 cluster by qPCR analysis. We observed significant decreases of ~50% and ~35% in *MCM7* transcript expression at 3 and 7 days after laser burn respectively (Figure 2E). Additionally, all members of the miR-106b~25 cluster (miR-106b, miR-25 and miR-93) were downregulated 3 days after laser burn with decreases of ~0.24-fold, ~0.37-fold and ~0.60-fold for miR-25, miR-93 and miR-106b, respectively (Figure 2F). To confirm that PERK can mediate repression of hsa-miR-106b, we

infected Human Retinal Microvascular Endothelial Cells (HRMECs) with a lentivirus carrying short hairpin (sh) RNA against PERK. After 72 hours, we observed a significant ~2-fold increase in hsa-miR-106b expression in cultured cells (Figure 2G). Taken together, these results support a PERK-associated decrease in miR-106b in laser-induced CNV.

miR-106b targets effectors of angiogenesis

To confirm the involvement of miR-106b in the regulation of AMD-related angiogenesis, we quantified protein levels of experimentally validated targets of miR-106b involved in the neovascularization process. Previous studies demonstrated that miR-106b can

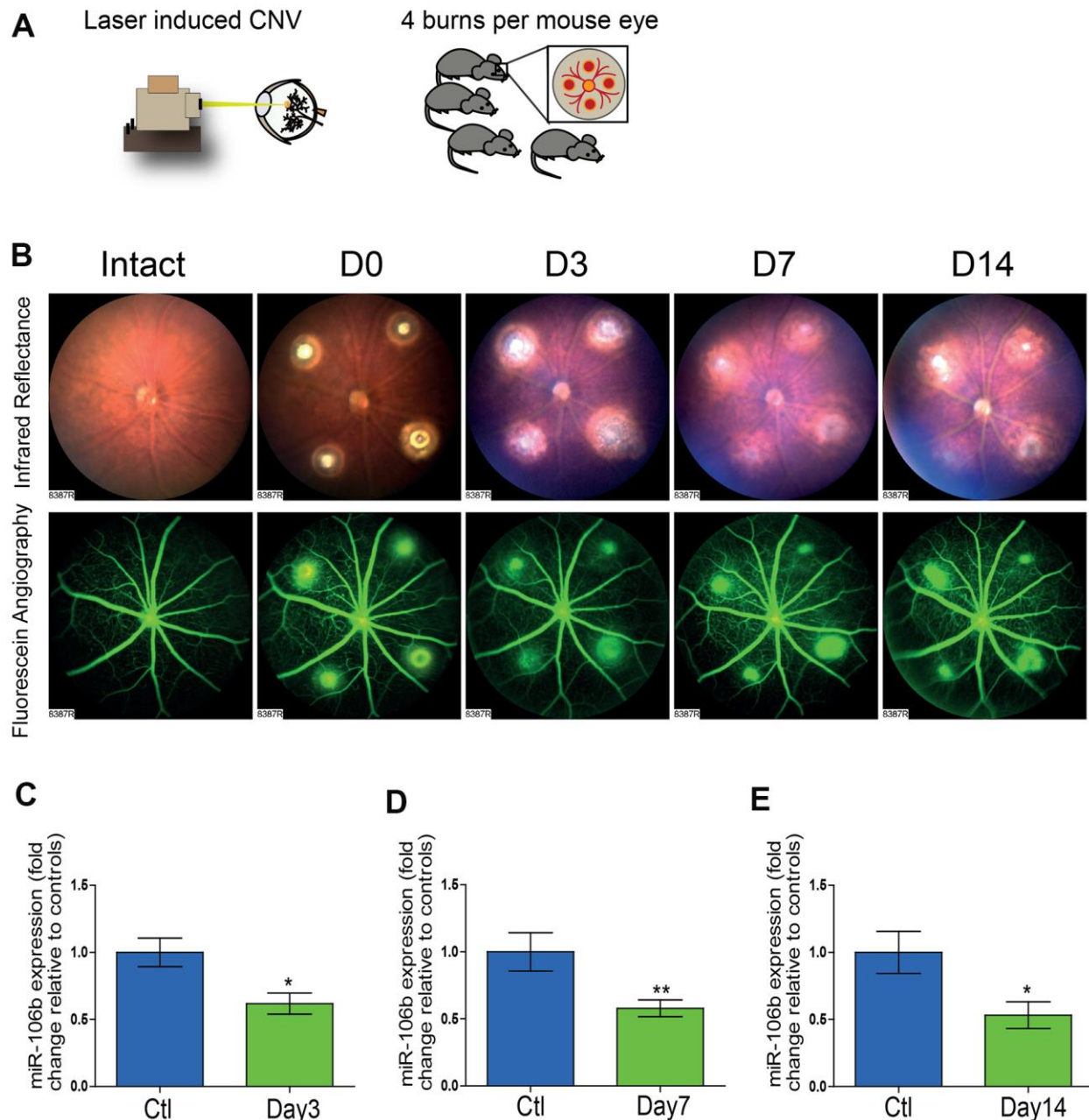


Figure 1. The initiation of retinal neo-vascularization is associated with downregulation of miR-106b expression. (A) Schematic of laser burn CNV mouse model. (B) Representative retinal fundus of a mouse before and after undergoing laser-induced choroidal neovascularization. Serial images depict the progression of neovascularization over a time-course of 14 days in the same eye. Choroidal expression of miR-106b by qPCR relative to intact controls assessed (C) 3 days after burns (n=8), (D) 7 days after burns (n=13) and (E) 14 days after burns (n=10); Scale bar = 50µm. Data are expressed as the mean ± S.E.M. Unpaired Two-tailed Student's t-test was used for the analysis, *P < 0.05; **P < 0.001.

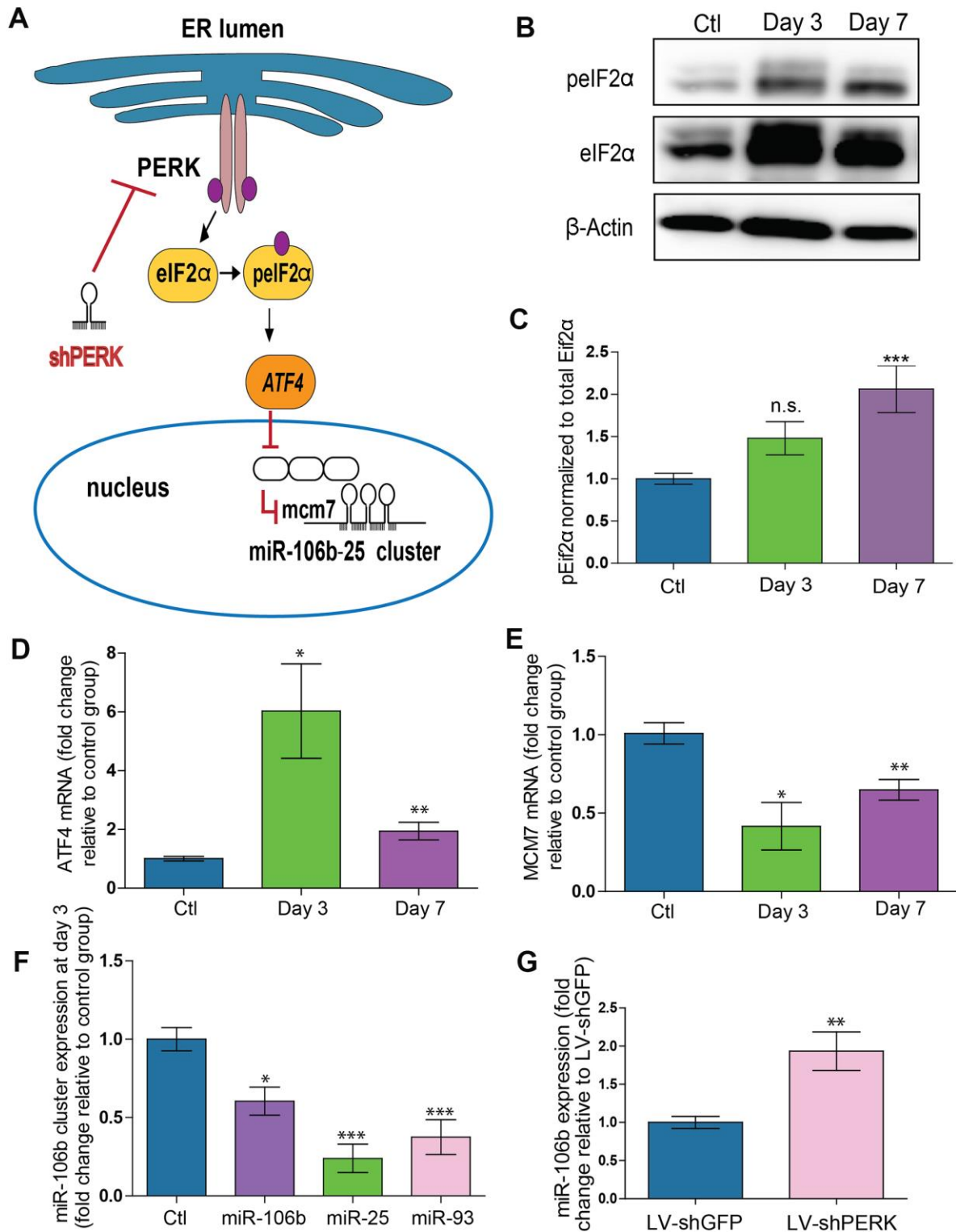


Figure 2. PERK activation provokes downregulation of miR-106b-25 cluster and MCM7 host gene in a mouse model of CNV. (A) Schematic of ER stress activation of PERK pathway. (B) Western blot of Phospho-eIF2 α , total-eIF2 α and β -actin in control choroids, and 3 and 7 days after burns. (C) Western blot quantification in control choroids, 3 days (n=7) and 7 days after burns (n=6). (D) *Aft4* mRNA expression in control choroids, 3 days (n=6) and 7 days after burns (n=10). (E) *Mcm7* mRNA expression in control choroids, 3 days (n=6) and 7 days after laser burn (n=14). (F) miR106~25 cluster member expression in choroids 3 days after laser burn (miR-106b (n=7), miR-25 (n=6) and miR-93 (n=5)). (G) miR-106b expression after infection of HRMECs with LV.shGFP (negative control), and LV.shPERK (n=5). Data are expressed as mean \pm S.E.M. One-way ANOVA with Bonferroni post-hoc test was performed on groups of 3 or more, and unpaired Two-tailed Student's t-test was used for the analysis of groups of 2, *P < 0.05; **P < 0.001; ***P < 0.0001.

influence expression of VEGFA and HIF1 α [31]. In line with a decrease in miR-106b, we confirmed the upregulation of VEGFA (~3-fold) and HIF1 α (~1.71-fold) in choroid specimens 3 days after laser burn (Figure 3A–3D). Importantly, we did not observe variations at the mRNA level for these targets, suggesting post-transcriptional regulation of their protein expression or altered translation efficiency, characteristic of miRNA regulation (Supplementary Figure 1A). These results further suggest that the loss of miR-106b expression can contribute to the expression of angiogenic proteins that promote neovascularization.

miR-106b influences HRMEC migration and choroidal vascular sprouting

We sought to characterize the effects of miR-106b on cellular processes involved in angiogenesis. We first evaluated the role of miR-106b on HRMEC migration in a wound healing/cell migration assay performed by electric cell-substrate impedance sensing (ECIS) assay. Cells were infected with LV.miR-106b, LV.shVEGFA, LV.shPERK or control LV.shGFP for 72 hours, plated at confluence and submitted to an electric pulse in the center of the well to provoke cell detachment, resulting in a 250 μ m diameter region devoid of cells (Figure 3E). Cell migration was quantified at 8 hours by measurement of impedance, which increases as cells repopulate the empty space. We found that HRMEC migration was reduced in all three LV-treated dishes compared to control LV.shGFP (blue line) (Figure 3F–3H). Cells infected with LV.shPERK became the least migratory (Figure 3H). LV.miR-106b prevented migration of HRMECs to a similar extent as LV.shVEGFA (Figure 3F, 3G). To confirm that miR-106b reduced migration of HRMECs, we performed a scratch assay (Figure 3I). As above, significant decreases in cell migration were observed in all treatment groups when compared to controls with a ~45% reduction in LV.shVEGFA, ~50% reduction with LV.miR-106b and ~45% with LV.shPERK when compared to control LV.shGFP (100% of migration) (Figure 3I, 3J).

NV AMD is characterized by pathological neovascularization of the choriocapillaris. We therefore used *ex vivo* mouse choroid explants and assessed sprouting angiogenesis. Similar to findings reported above, we observed a ~70% reduction in sprouting area with LV.miR-106b, a ~80% reduction with LV.shPERK, while LV.shVEGFA resulted in a reduction of ~60% compared to control LV.shGFP (Figure 3K, 3L). Taken together, these results further highlight the anti-angiogenic properties of miR-106b and provide rationale to test miR-106b delivery *in vivo*.

Intraocular injection of LV.miR-106b decreases choroidal and retinal neovascularization

Endothelial cell migration and sprouting are key processes involved in angiogenesis. We next tested the outcome of therapeutic delivery of miR-106b in models of pathological retinal angiogenesis. We first performed laser burns on 8 week-old mice to trigger CNV, directly followed by intravitreal injection of either LV.miR-106b or positive control LV.shVEGF or negative control LV.shGFP. Choroids were collected 7 days after laser burns and quantified (Figure 4A). LV.miR-106b led to ~45% reduction of neo-angiogenesis and prevented CNV to a similar extent as LV.shVEGF (Figure 4B–4D).

We subsequently assessed the anti-angiogenic properties of miR-106b in the mouse model of oxygen-induced retinopathy [35]. Mouse pups were injected at P4 and P7 with LV.miR-106b, negative control LV.shGFP or positive control LV.shVEGFA. From P7 to P12 pups were exposed to 75% oxygen and returned to room air from P12 until maximal neovascularization at P17 (Figure 5A). Similar to what was observed for CNV, retinas treated with LV.miR-106b showed a significant ~50% reduction in pathological neovascularization compared to LV.shGFP and a similar reduction to levels observed with LV.shVEGFA (Figure 5B–5I). Collectively, these results suggest that therapeutic delivery of miR-106b prevents pathological retinal angiogenesis (Figure 6).

DISCUSSION

The diagnostic and therapeutic potential of miRNAs for ocular diseases is promising yet still requires proof of concept. We have previously shown that levels of miR-106b decrease in the vitreous and plasma of human patients with NV AMD [25]. In the current study, we demonstrate that much like in patients, there is a reduction in choroidal miR-106b in mouse retinas following laser burn induced-CNV. Furthermore, we provide evidence that the downregulation involves transcriptional inhibition of the 106b~25 cluster by the PERK pathway. Consequently, therapeutic intravitreal administration of miR-106b via lentiviral vectors inhibited pathological retinal neovascularization across models. These findings were supported by *in vitro* and *ex vivo* data that confirmed the role of miR-106b in preventing cellular mechanisms that lead to angiogenesis including cell migration and sprouting.

The pathogenesis of AMD is associated with oxidative stress, hypoxia, inflammation and proteotoxic stress, which can trigger pathways of ER-stress [36]. We observed activation of the PERK axis with phosphorylation

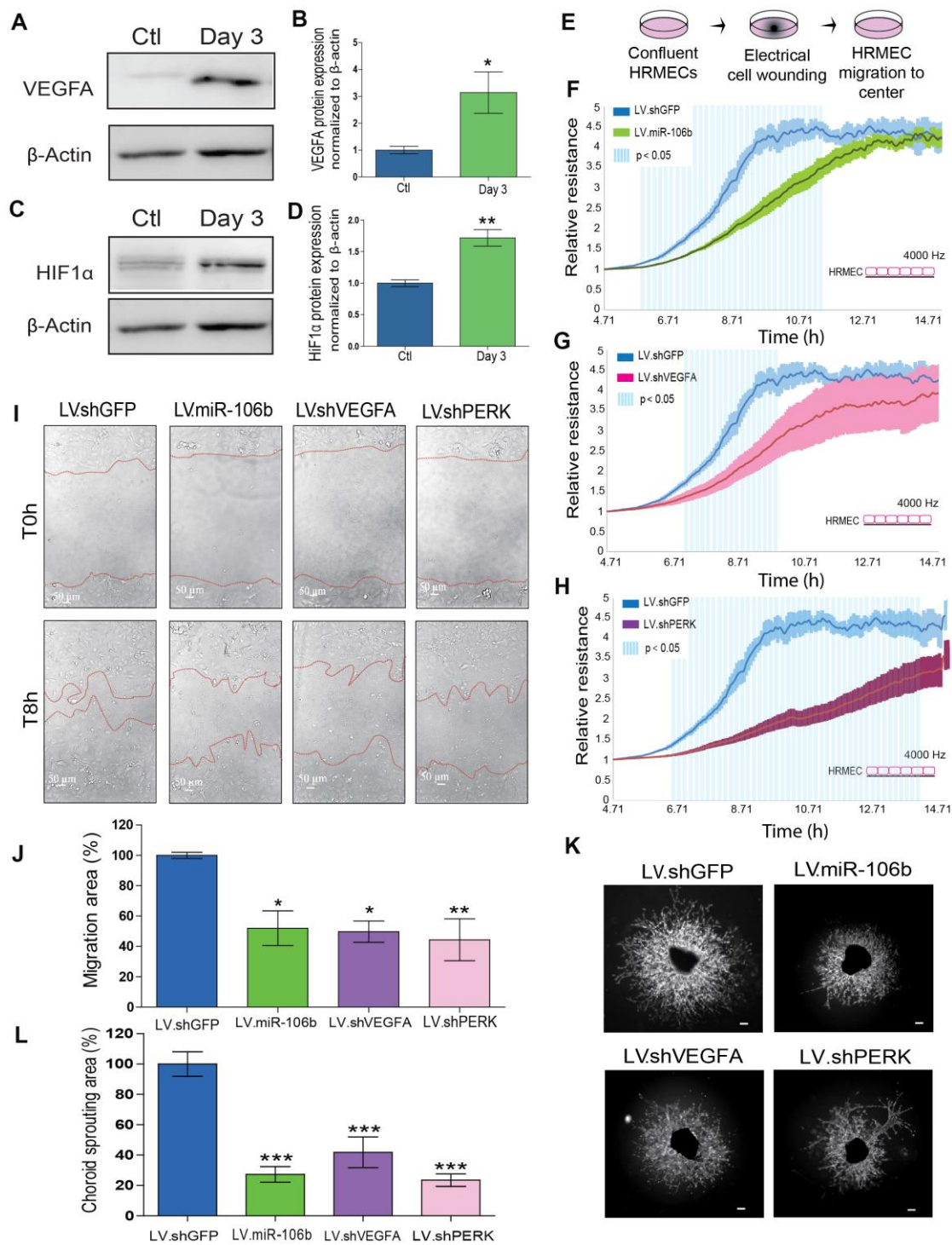


Figure 3. miR-106b exerts an anti-angiogenic effect and impairs retinal endothelial cell migration. (A) Western blot of VEGFA and β -actin from control choroids and 3 days after burns, and (B) quantification (n=4). (C) Western blot of HIF1 α and β -actin from control choroids and 3 days after burns, and (D) quantification (n=4). (E) Schematic of ECIS cell migration assay procedure. HRMEC ECIS with (F) LV.miR-106b (n=4), (G) LV.shVEGFA (n=4) and (H) LV.shPERK (n=4) compared to LV.shGFP control. (I) HRMEC scratch assay infected 72h with LV.shGFP, LV.miR-106b, LV.shVEGFA and LV.shPERK at T0h and after 8h. (J) Migration area quantification of scratch assay with LV.miR-106b (n=4), LV.shVEGFA (n=4), and LV.shPERK (n=4) compared to LV.shGFP. (K) Sprouting assay with choroid explants infected with LV.shGFP, LV.miR-106b, LV.shVEGFA, and LV.shPERK. (L) Sprouting area quantification with LV.miR-106b (n=9), LV.shVEGFA (n=9), LV.shPERK (n=8) compared to LV.shGFP control. Scale bar = 500 μ m. Data are expressed as mean \pm S.E.M. Unpaired Two-tailed Student's t-test was used for the analysis of groups of 2, and one-way ANOVA with Bonferroni post-hoc test was performed on groups of 3 or more, * $P < 0.05$; ** $P < 0.001$; *** $P < 0.0001$.

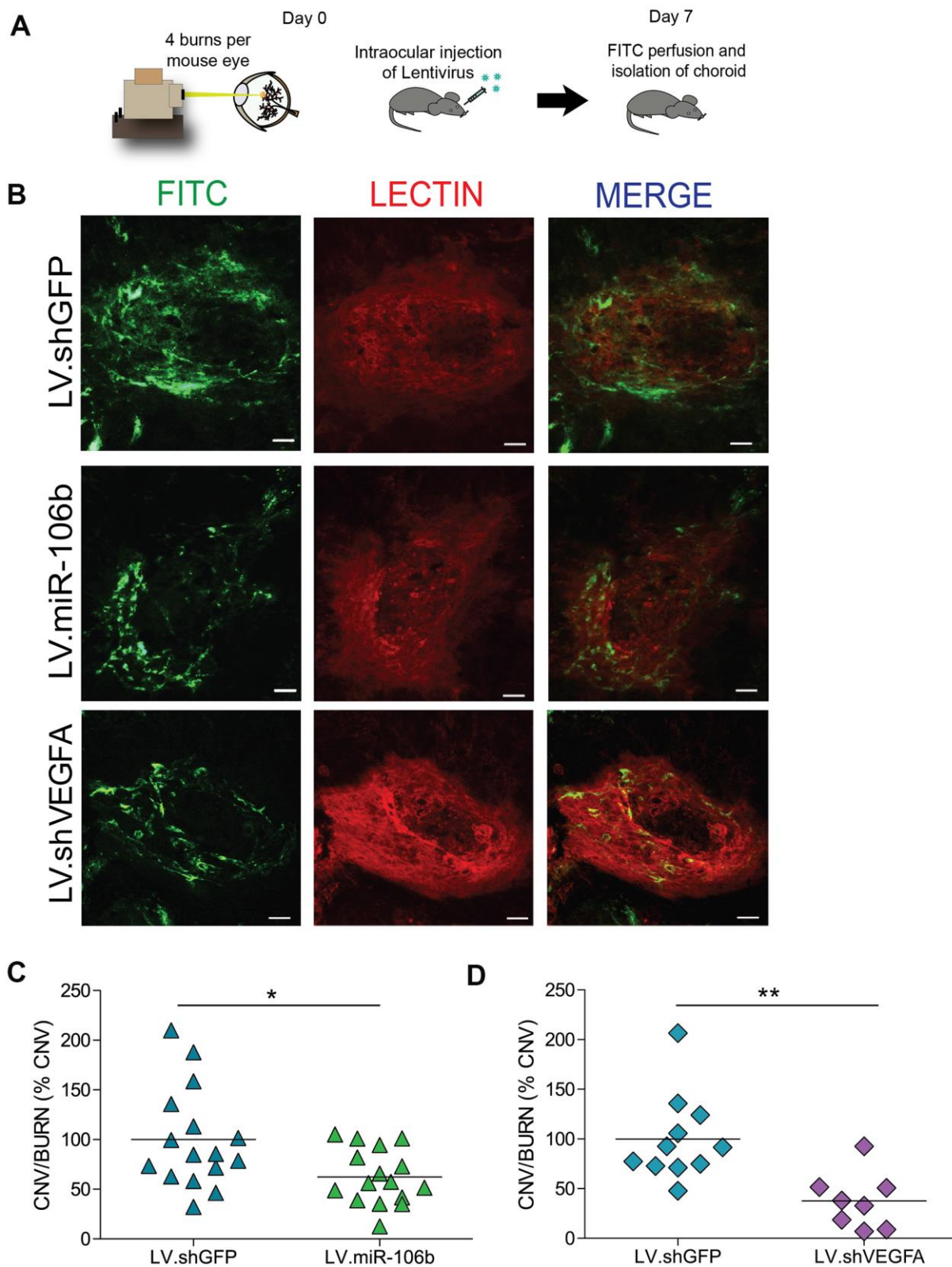


Figure 4. miR-106b decreases choroidal neovascularization in a CNV mouse model. (A) Schematic of intraocular injection of LV.miR-106b or LV.shVEGFA in laser burn mouse model. (B) Burn in red (lectin), CNV in green (FITC) and merge with LV.miR-106b or LV.shVEGFA compared with LV.shGFP. (C) CNV/Burns ratios quantification after LV.miR-106b treatment (n=16 burns/4 mice) and (D) CNV/Burns ratios quantification after LV.shVEGFA treatment (n=12 burns/3 mice). Scale bar = 50 μ m. Data are expressed as mean \pm S.E.M. Unpaired Two-tailed Student's t-test were used *P < 0.05; **P < 0.001.

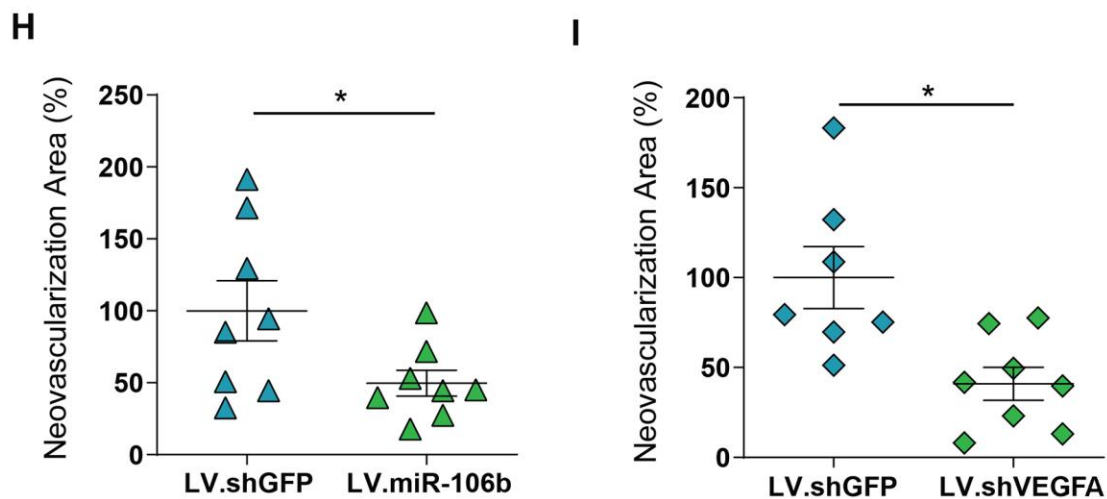
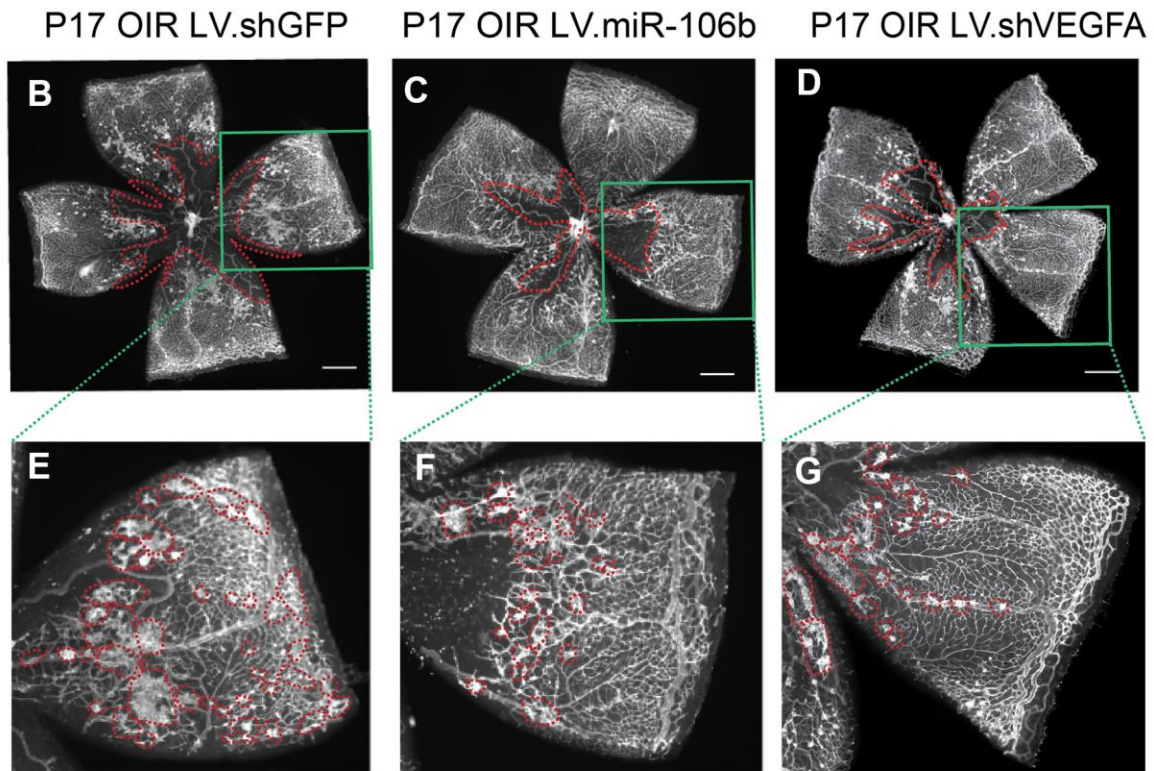
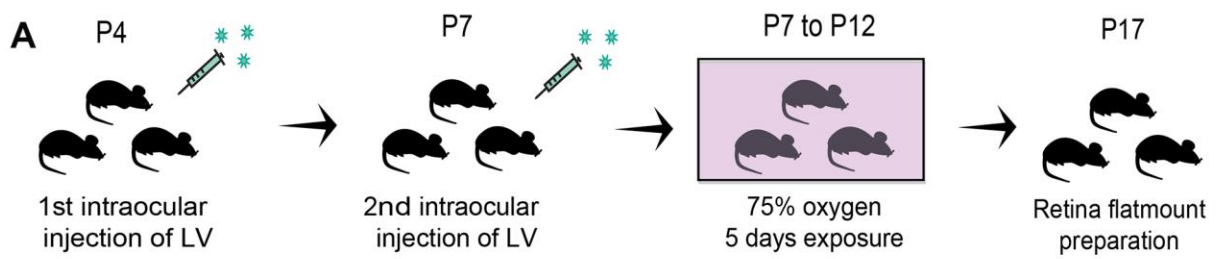


Figure 5. miR-106b decreases retinal neovascularization in the OIR mouse model. (A) Schematic of intraocular injection of LV.miR-106b or LV.shVEGFA in the OIR mouse model. P17 retinas were flatmounted after exposure to 75% O₂, having received intraocular injection of LV.shGFP (B), LV.miR-106b (C), or LV.shVEGFA (D) and magnified (E–G). Neovascular area quantification (H) after LV.miR-106b injection (n=8), and (I) LV.shVEGFA injection (n=8). Scale bars, 500 μ m (B–D) and 200 μ m (E–G). Data are expressed as mean \pm S.E.M. Unpaired Two-tailed Student's t-tests were used. *P < 0.05.

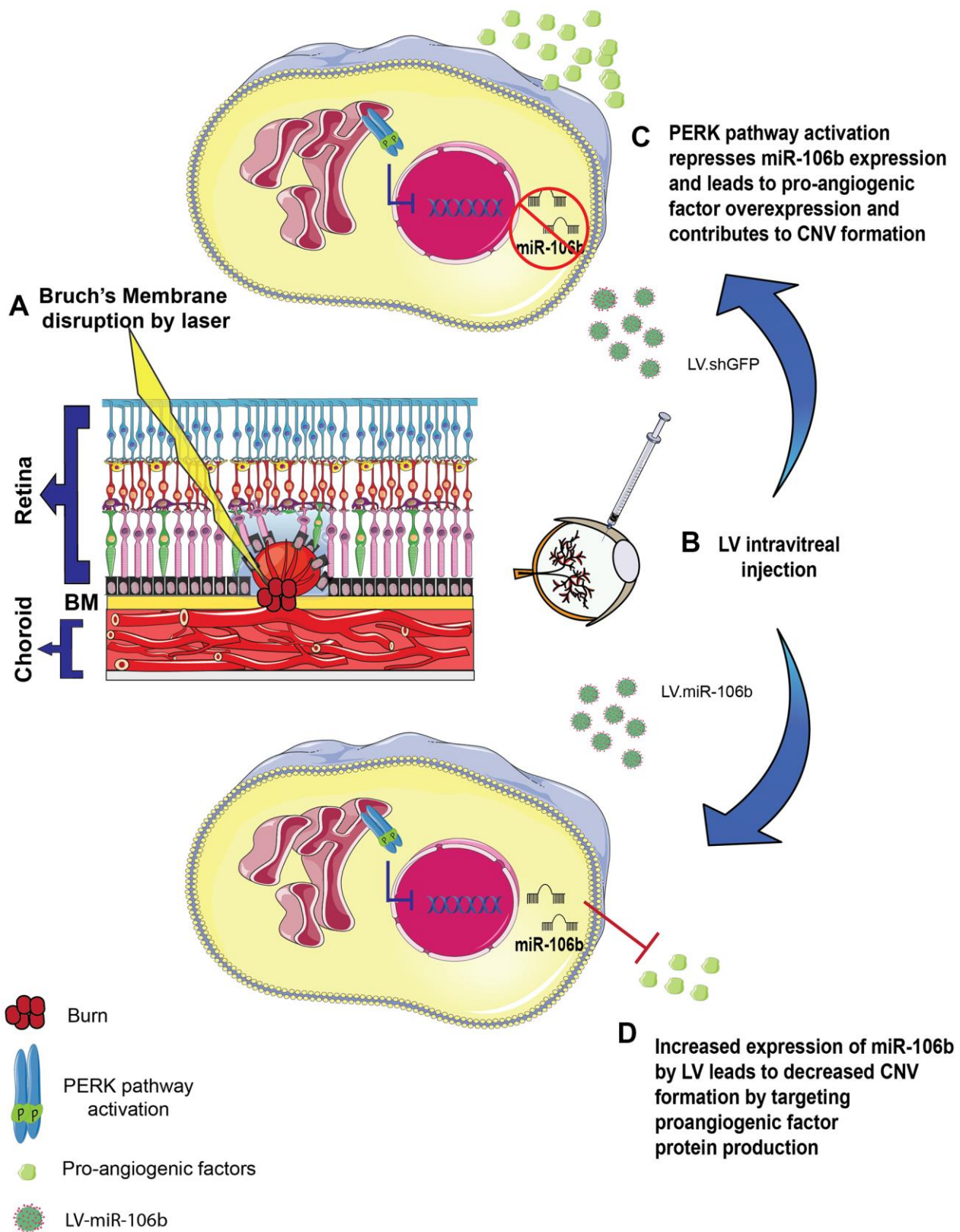


Figure 6. Schematic of miR-106b impact on CNV in mouse laser burn model. (A) Bruch's membrane disruption following laser burn. (B) Intravitreal injection of LV.shGFP or LV.miR-106b. (C) PERK activation represses miR-106b expression and leads to pro-angiogenic factor overexpression, contributing to CNV formation. (D) Increased expression of miR-106b by LV leads to decreased CNV formation by targeting proangiogenic factor protein production. (CNV: choroidal neovascularization, LV: lentivirus).

of eIF2 α and increase in ATF4 mRNA after laser burn. Activated PERK typically influences protein synthesis through phosphorylation of eIF2 α , leading to global translation arrest [37] while transcripts with alternative upstream open reading frames, such as ATF4, are translated and can mediate an antioxidant response and expand the ER's folding capacity [38]. With sustained activation, ATF4 can also drive transcription of pro-apoptotic factors and lead to apoptosis by inducing CHOP [38]. The PERK pathway is thought to be influenced by miRNAs. For example, miR-204 represses PERK [39] while miR-30b-5p and miR-30c-5p regulate eIF2 α , and miR-214 downregulates ATF4 expression [40]. Similarly, to what has been reported in mouse embryonic fibroblasts [34], our data suggest that PERK suppresses miR-106b during choroidal neovascularization and thus renders the retina more conducive to neovascularization.

We demonstrated the anti-angiogenic properties of miR-106b in models of retinal (OIR) and choroidal neovascularization (laser CNV). The magnitude of suppression was comparable to that of suppression of VEGFA or PERK inhibition by shRNA. MiR-106b, a member of miR-17 family with reported anti-angiogenic properties [41, 42], also significantly decreased choroidal sprouting. Our results are consistent with previous studies demonstrating the anti-angiogenic properties of miR-106b in cell culture via STAT3 inhibition [43] and in mice in a hind limb ischemia model.

Currently, there are efforts to devise therapeutics that simultaneously inhibit several factors involved in retinal vascular disease given the clinical success of compounds such as Aflibercept [44]. miRNAs regulate translation of multiple genes and hence may be considered as multi-target inhibitors. Their potential to mitigate retinal disease will grow as comprehensive landscapes of miRNAs in health and disease are established [26, 45]. Preclinical studies are underway for mimics or inhibition of specific miRNAs [46]. Overall, this study demonstrates a new role for miR-106b and highlights its potential for suppressing pathological retinal neovascularization.

MATERIALS AND METHODS

Animals

All studies were performed according to the Association for Research in Vision and Ophthalmology (ARVO) Statement for the Use of Animals in Ophthalmic and Vision Research and were approved by the Animal Care Committee of the University of Montreal in agreement with the guidelines established by the Canadian Council

on Animal Care. C57Bl/6 wild-type were purchased from Jackson Laboratory and CD1 nursing mothers from Charles River Laboratory.

Cell line

Human retinal microvascular endothelial cells (HRMECs) (Cell System, Kirkland, USA) were used from passages 6 to 11. HRMECs were cultured in EGM-2 microvascular medium (Lonza, Switzerland). For scratch assay experiments and for Electric Cell-substrate Impedance Sensing (ECIS), cells were starved overnight then cultured in EBM-2 medium (2% fetal bovine serum).

O₂-induced retinopathy (OIR)

Mouse pups (C57Bl/6, Jackson Labs) and their fostering mothers (CD1, Charles River) were exposed to 75% O₂ from postnatal day 7 (P7) until day 12 and returned to room air. This model serves as a proxy to human ocular neovascular diseases such as ROP and diabetic retinopathy characterized by a late phase of destructive pathological angiogenesis [47, 48]. Upon return to room air, hypoxia-driven neovascularization (NV) develops from P14 onwards [35]. Dissected retinas were flatmounted and incubated overnight with fluoresceinated isolectin B4 (1:100) in 1mM CaCl₂ to determine extent of avascular area or neovascularization area at P17 using ImageJ and the SWIFT-NV method [49].

In vivo imaging following laser-induced choroidal neovascularization (CNV)

In vivo imaging was performed using a scanning laser ophthalmoscope (Micron IV; Phoenix Laboratories, Pleasanton, CA, USA). Mice of 9 to 11 weeks of age were subjected to pupil dilation (Mydriacyl; Alcon, Mississauga, ON, Canada) and anesthetized with a mix of 10% ketamine and 4% xylazine (10 μ l/g body weight). Fluorescein (Alcon, 1 unit/g body weight of a 5% fluorescein dilution in 0.9% sodium chloride) was injected subcutaneously and corneas were lubricated with Optixcare ophthalmic gel (Aventix Animal Health, Burlington, ON, Canada). After a fluorescein circulation of 5 minutes, retinas were imaged before and after inducing choroidal neovascularization with 4 distinct laser burns (50 μ m, 300mW, 0.05s). Animals were followed-up 3, 7 and 14 days after laser burn.

CNV induction and neovascularization labeling by perfusion with FITC

For lentiviral treatment mice of 9 to 11 weeks of age were intraocularly injected with lentivirus and their

Bruch's membranes were ruptured using an argon laser as described previously [32]. At day 3, 7 and 14 after CNV induction, mice were injected with 0.5 ml of 15 mg/ml of fluorescein isothiocyanate (FITC)-dextran (average molecular weight 20,000) (Sigma Aldrich, CA) and euthanized.

Immunohistofluorescence

Eyes were fixed for 30 min in 4% PFA at room temperature before dissection to isolate retinas (OIR) or choroids (LB-CNV). Flatmounted retinas or choroids were stained with Rhodamine labeled Griffonia (Bandeiraea) Simplicifolia Lectin I (RL-1102; Vector Laboratories) in 1 mM CaCl₂ in PBS. The sclera-choroid-RPE cell complex was mounted onto a slide, and the burns photographed with an Olympus FV1000 microscope.

Neovascularization quantifications

Retinal neovascularization (OIR model): For visualization of pan-retinal vasculature, dissected retinas were flatmounted and incubated overnight with rhodamine-labeled Griffonia (Bandeiraea) Simplicifolia Lectin I (Vector Laboratories Inc.) in 1 mM CaCl₂ in PBS for retinal vasculature. The extent of avascular area or neovascularization area at P17 was determined using ImageJ and the SWIFT_NV method [49].

Choroidal neovascularization (laser burn model): The neovascularization was captured in a Z-stack, and the lesion caused by the laser impact was captured in a single-plane image. The Z-stacks were compressed into one image, and the FITC-dextran-labeled neovascular area and the area of the lesion were measured per lesion in ImageJ.

Western blot analysis

For assessment of choroidal protein levels, eyes were enucleated from mice 3 days after burn. RIPA buffer with anti-protease and anti-phosphatase (BioRad) was freshly prepared to manually with a piston to homogenize tissues and for cells lysis. Protein concentration was assessed by BCA assay (Sigma-Aldrich, Oakville, CA), and 30µg of protein analyzed for each condition by standard SDS-PAGE technique using Bis-Acrylamide gel 10% or 12.5% depending of protein size. Total protein transfer on nitrocellulose or PVDF membranes (Bio-Rad, Mississauga, ON, CA) was evaluated with Ponceau Red (Sigma-Aldrich, Oakville, CA). Antibody solutions and dilutions were prepared as per manufacturers' recommendations.

Antibodies

Phospho-eIF2 α (Ser51) (Cell signaling Technology, Whitby, CA), Total-eIF2 α (Cell signaling Technology,

Whitby, CA), β -actin (8H10D10) (Cell signaling Technology, Whitby, CA), VEGFA (C1) (Santa Cruz Biotechnology, INC, Texas, USA), HIF1 α (H1alpha67) (Novus Biologicals, Oakville, CA).

Quantitative real time polymerase chain reaction analysis

RNA extraction was performed with TRIzol® Reagent (Life Technology, Waltham, USA) as suggested by manufacturer protocol. DNase digestion was then performed to prevent amplification of genomic DNA (Invitrogen, Waltham, USA). iScript™ Reverse Transcription Supermix for RT-qPCR (Bio-Rad, Mississauga, CA) was used to generate cDNA from 1µg of total RNA. Real time qPCR was performed to quantify gene expression using SYBR® Green reagent (Applied Biosystem TM, USA) and was processed with an ABI 7500 Real-Time PCR machine. β -actin was used as a reference gene. Primer sequences (Integrated DNA Technologies) are listed in Supplementary Table 1. miRNA extraction was performed with TRIzol® Reagent, Retrotranscription reaction was done with TaqMan MicroRNA Reverse Transcription kit (Applied Biosystem, USA) using 100ng of total RNA in each reaction following manufacturer protocol. Real-time PCR was processed with TaqMan miR assay 20X and Universal master mix II No-UNG 2x for TaqMan Reaction (Applied Biosystem, USA). Primers are listed in the Supplementary Table 1.

Lentivirus plasmid constructions

Lentiviral constructs were produced with the PCR insertion kit (Q5 Site-Directed Mutagenesis kit, New England BioLabs®inc). The following sequence for shVEGFA and mature miR-106b sequence were inserted shVEGFA: 5' GAGCGGAGAAAGC ATTTG TTTCTCGAGAAACAAATGCTTTCTCCGC TCTTTT 3', miR-106b: 5'TAAAGTGCT GACAGTG CAGATCTCGAGATCTGCACTGTCAGCACTTTAT TTT-3'. All constructs were verified by Genome Quebec sequencing. Constructs of shIRE1 α and shPERK were previously published by our group [50].

Preparation of lentivirus

We produced infectious lentiviral vectors by transfecting lentivector and packaging vectors into HEK293T cells (Invitrogen) as previously described (Dull et al. Journal of Virology, 1998). Viral supernatants were concentrated by ultracentrifugation (>500-fold). Viral efficiency was confirmed by real-time-PCR and Western blot.

Intravitreal injections

For the OIR model, P4, P7, C57BL/6 pups were anesthetized with 3.0% isoflurane and injected in the vitreous chamber with 0.5 μ l of lentivirus. Retinas were collected at P17 for vasculature analysis. For the laser burn model, 8 to 10 week old C57BL/6 mice were injected following laser burn in the vitreous chamber with 1 μ l of lentivirus. Choroids were collected 7 days post burns for CNV quantification.

Scratch assay

Scratch assays were performed with pre-infected HRMECs cells (72hr) in 6 well plates until confluency was reached. Scratches were done with 200 μ l sterile tips and culture media was replaced with with EBM-2 medium (2% fetal bovine serum). Pictures were taken at time 0 (moment of the scratch) and after 8 hours with a 2x objective using an inverted microscope (Zeiss Axio Imager) and migration distances were quantified with Image J software.

Electric cell-substrate impedance sensing migration assay (ECIS)

Real time analysis of trans and inter-endothelial impedance was performed by plating 1×10^5 pre-infected (72 hours) HRMECs cells into 8 well arrays (8W10E for migration assays, 40 electrodes per well) (Applied BioPhysics, Troy, NY, USA). Cells were plated at confluency and submitted to an electric pulse in the center of each well, causing localized cell detachment, resulting in a 250 μ m diameter devoid of cells. Cell migration was quantified by measurement of impedance, which increases as cells repopulate the empty space. The results were then normalized to the vehicle control and expressed as relative resistance. Graphical representation depicts mean and S.E.M., and light blue zones highlight time points where statistically significant differences are observed (student's t-test, $P < 0.05$).

Choroid *ex vivo* explant assay

Adult C57Bl/6 mice were euthanized, and eyes were immediately enucleated and kept in ice-cold EBM basal medium (Lonza) before dissection. Choroid explants were placed in growth factor-reduced Matrigel (Corning) seeded in 24 well plates, and incubated at 37° C for 10 minutes to allow the Matrigel to solidify. 500 μ L of medium was then added to each well and incubated at 37° C with 5% CO₂ for 24 hours before lentiviral infections. Explant pictures were taken after 48 hours (at the beginning of choroid vessel growth), and at 72 hours to 96 hours post-infection to follow vessel growth. Phase contrast photos of individual

explants were captured with a ZEISS Axio Oberver.Z1 microscope. Sprouting area quantification was performed using the semi-automated macro plug-in to the Image J software designed for this purpose [51].

Statistical analyses

Data are presented as mean \pm S.E.M. GraphPad Prism (GraphPad Software, San Diego, CA) was used to perform statistical analyses. We used Student's t test to compare groups of two, and one-way ANOVA with Bonferroni post-hoc analysis for groups of 3 and more; data with $P < 0.05$ were considered statistically different: * denotes $P < 0.05$, ** $P < 0.01$, and *** $P < 0.001$.

AUTHOR CONTRIBUTIONS

C.M., V.D., J.P.S. and P.S. designed the research and study. C.M., A.D., K.M., F.B., S.C.G., C.P., F.P., R.J., E.M.M.A., and G.M., carried out experimental work. C.M., A.M.W. and A.D. analyzed the data. C.M., A.M.W., V.D. J.P.S. and P.S. wrote the manuscript with valuable input from authors.

CONFLICTS OF INTEREST

We do not have any disclosure or conflicts of interest in the study.

FUNDING

This work was supported by operating grants from The Foundation Fighting Blindness Canada, the Canadian Diabetes Association (DI-3-18-5444-PS), the Canadian Institutes of Health Research (Foundation grant #353770 to P.S), the Canadian the Heart and Stroke Foundation Canada (G-16-00014658 to P.S.), and Natural Sciences and Engineering Research Council of Canada (418637 to P.S.). P.S. holds the Wolfe Professorship in Translational Research and a Canada Research Chair in Retinal Cell Biology. We also thank the Fonds de Recherche en Ophtalmologie de l'Université de Montréal (FROUM) and the RRSV.

REFERENCES

1. Klein R, Klein BE. The prevalence of age-related eye diseases and visual impairment in aging: current estimates. Invest Ophthalmol Vis Sci. 2013; 54:ORSF5–RSF13.
<https://doi.org/10.1167/iops.13-12789>
PMID:[24335069](https://pubmed.ncbi.nlm.nih.gov/24335069/)
2. Miller JW. Age-related macular degeneration revisited—piecing the puzzle: the LXIX Edward Jackson

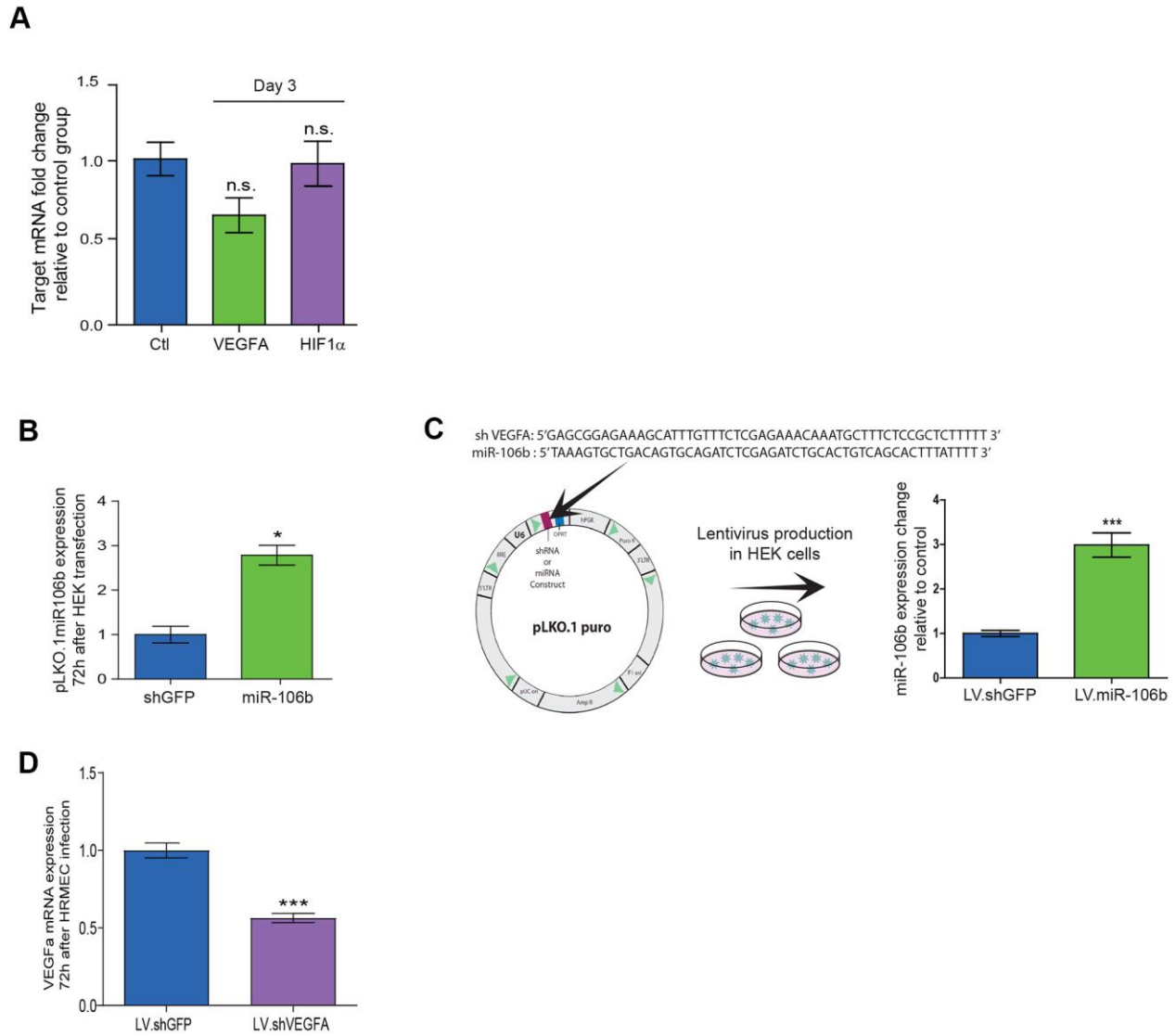
- memorial lecture. *Am J Ophthalmol.* 2013; 155:1–35.e13.
<https://doi.org/10.1016/j.ajo.2012.10.018>
 PMID:[23245386](https://pubmed.ncbi.nlm.nih.gov/23245386/)
3. Gorin MB. Genetic insights into age-related macular degeneration: controversies addressing risk, causality, and therapeutics. *Mol Aspects Med.* 2012; 33:467–86.
<https://doi.org/10.1016/j.mam.2012.04.004>
 PMID:[22561651](https://pubmed.ncbi.nlm.nih.gov/22561651/)
 4. Friedman DS, O’Colmain BJ, Muñoz B, Tomany SC, McCarty C, de Jong PT, Nemesure B, Mitchell P, Kempen J, and Eye Diseases Prevalence Research Group. Prevalence of age-related macular degeneration in the United States. *Arch Ophthalmol.* 2004; 122:564–72.
<https://doi.org/10.1001/archophth.122.4.564>
 PMID:[15078675](https://pubmed.ncbi.nlm.nih.gov/15078675/)
 5. Kempen JH, O’Colmain BJ, Leske MC, Haffner SM, Klein R, Moss SE, Taylor HR, Hamman RF, and Eye Diseases Prevalence Research Group. The prevalence of diabetic retinopathy among adults in the United States. *Arch Ophthalmol.* 2004; 122:552–63.
<https://doi.org/10.1001/archophth.122.4.552>
 PMID:[15078674](https://pubmed.ncbi.nlm.nih.gov/15078674/)
 6. Maberley DA, Hollands H, Chuo J, Tam G, Konkala J, Roesch M, Veselinovic A, Witzigmann M, Bassett K. The prevalence of low vision and blindness in Canada. *Eye (Lond).* 2006; 20:341–46.
<https://doi.org/10.1038/sj.eye.6701879>
 PMID:[15905873](https://pubmed.ncbi.nlm.nih.gov/15905873/)
 7. Schuman SG, Koreishi AF, Farsiu S, Jung SH, Izatt JA, Toth CA. Photoreceptor layer thinning over drusen in eyes with age-related macular degeneration imaged in vivo with spectral-domain optical coherence tomography. *Ophthalmology.* 2009; 116:488–96.e2.
<https://doi.org/10.1016/j.ophtha.2008.10.006>
 PMID:[19167082](https://pubmed.ncbi.nlm.nih.gov/19167082/)
 8. Midena E, Vujosevic S, Convento E, Manfre’ A, Cavarzeran F, Pilotto E. Microperimetry and fundus autofluorescence in patients with early age-related macular degeneration. *Br J Ophthalmol.* 2007; 91:1499–503.
<https://doi.org/10.1136/bjo.2007.119685>
 PMID:[17504849](https://pubmed.ncbi.nlm.nih.gov/17504849/)
 9. Sarks SH. Ageing and degeneration in the macular region: a clinico-pathological study. *Br J Ophthalmol.* 1976; 60:324–41.
<https://doi.org/10.1136/bjo.60.5.324>
 PMID:[952802](https://pubmed.ncbi.nlm.nih.gov/952802/)
 10. Guillonneau X, Eandi CM, Paques M, Sahel JA, Sapieha P, Sennlaub F. On phagocytes and macular degeneration. *Prog Retin Eye Res.* 2017; 61:98–128.
<https://doi.org/10.1016/j.preteyeres.2017.06.002>
 PMID:[28602950](https://pubmed.ncbi.nlm.nih.gov/28602950/)
 11. Sobrin L, Seddon JM. Nature and nurture- genes and environment- predict onset and progression of macular degeneration. *Prog Retin Eye Res.* 2014; 40:1–15.
<https://doi.org/10.1016/j.preteyeres.2013.12.004>
 PMID:[24374240](https://pubmed.ncbi.nlm.nih.gov/24374240/)
 12. Brown DM, Kaiser PK, Michels M, Soubrane G, Heier JS, Kim RY, Sy JP, Schneider S, and ANCHOR Study Group. Ranibizumab versus verteporfin for neovascular age-related macular degeneration. *N Engl J Med.* 2006; 355:1432–44.
<https://doi.org/10.1056/NEJMoa062655>
 PMID:[17021319](https://pubmed.ncbi.nlm.nih.gov/17021319/)
 13. Rosenfeld PJ, Brown DM, Heier JS, Boyer DS, Kaiser PK, Chung CY, Kim RY, and MARINA Study Group. Ranibizumab for neovascular age-related macular degeneration. *N Engl J Med.* 2006; 355:1419–31.
<https://doi.org/10.1056/NEJMoa054481>
 PMID:[17021318](https://pubmed.ncbi.nlm.nih.gov/17021318/)
 14. Mitchell P. A systematic review of the efficacy and safety outcomes of anti-VEGF agents used for treating neovascular age-related macular degeneration: comparison of ranibizumab and bevacizumab. *Curr Med Res Opin.* 2011; 27:1465–75.
<https://doi.org/10.1185/03007995.2011.585394>
 PMID:[21623685](https://pubmed.ncbi.nlm.nih.gov/21623685/)
 15. Jacob J, Brié H, Leys A, Levecq L, Mergaerts F, Denhaerynck K, Vancayzeele S, Van Craeyveld E, Abraham I, MacDonald K. Six-year outcomes in neovascular age-related macular degeneration with ranibizumab. *Int J Ophthalmol.* 2017; 10:81–90.
<https://doi.org/10.18240/ijo.2017.01.14>
 PMID:[28149782](https://pubmed.ncbi.nlm.nih.gov/28149782/)
 16. Amoaku WM, Chakravarthy U, Gale R, Gavin M, Ghanchi F, Gibson J, Harding S, Johnston RL, Kelly SP, Lotery A, Mahmood S, Menon G, Sivaprasad S, et al. Defining response to anti-VEGF therapies in neovascular AMD. *Eye (Lond).* 2015; 29:1397–98.
<https://doi.org/10.1038/eye.2015.159> PMID:[26446737](https://pubmed.ncbi.nlm.nih.gov/26446737/)
 17. Robinson GS, Ju M, Shih SC, Xu X, McMahon G, Caldwell RB, Smith LE. Nonvascular role for VEGF: VEGFR-1, 2 activity is critical for neural retinal development. *FASEB J.* 2001; 15:1215–17.
<https://doi.org/10.1096/fj.00-0598fje>
 PMID:[11344092](https://pubmed.ncbi.nlm.nih.gov/11344092/)
 18. Saint-Geniez M, Maharaj AS, Walshe TE, Tucker BA, Sekiyama E, Kurihara T, Darland DC, Young MJ, D’Amore PA. Endogenous VEGF is required for visual function: evidence for a survival role on müller cells and photoreceptors. *PLoS One.* 2008; 3:e3554.

- <https://doi.org/10.1371/journal.pone.0003554>
PMID:[18978936](https://pubmed.ncbi.nlm.nih.gov/18978936/)
19. Grunwald JE, Daniel E, Huang J, Ying GS, Maguire MG, Toth CA, Jaffe GJ, Fine SL, Blodi B, Klein ML, Martin AA, Hagstrom SA, Martin DF, and CATT Research Group. Risk of geographic atrophy in the comparison of age-related macular degeneration treatments trials. *Ophthalmology*. 2014; 121:150–161.
<https://doi.org/10.1016/j.ophtha.2013.08.015>
PMID:[24084496](https://pubmed.ncbi.nlm.nih.gov/24084496/)
20. Grunwald JE, Pistilli M, Ying GS, Maguire MG, Daniel E, Martin DF, and Comparison of Age-related Macular Degeneration Treatments Trials Research Group. Growth of geographic atrophy in the comparison of age-related macular degeneration treatments trials. *Ophthalmology*. 2015; 122:809–16.
<https://doi.org/10.1016/j.ophtha.2014.11.007>
PMID:[25542520](https://pubmed.ncbi.nlm.nih.gov/25542520/)
21. Klein R, Knudtson MD, Klein BE, Wong TY, Cotch MF, Liu K, Cheng CY, Burke GL, Saad MF, Jacobs DR Jr, Sharrett AR. Inflammation, complement factor h, and age-related macular degeneration: the multi-ethnic study of atherosclerosis. *Ophthalmology*. 2008; 115:1742–49.
<https://doi.org/10.1016/j.ophtha.2008.03.021>
PMID:[18538409](https://pubmed.ncbi.nlm.nih.gov/18538409/)
22. Ambati J, Fowler BJ. Mechanisms of age-related macular degeneration. *Neuron*. 2012; 75:26–39.
<https://doi.org/10.1016/j.neuron.2012.06.018>
PMID:[22794258](https://pubmed.ncbi.nlm.nih.gov/22794258/)
23. Huang Y, Shen XJ, Zou Q, Wang SP, Tang SM, Zhang GZ. Biological functions of microRNAs: a review. *J Physiol Biochem*. 2011; 67:129–39.
<https://doi.org/10.1007/s13105-010-0050-6>
PMID:[20981514](https://pubmed.ncbi.nlm.nih.gov/20981514/)
24. Baek D, Villén J, Shin C, Camargo FD, Gygi SP, Bartel DP. The impact of microRNAs on protein output. *Nature*. 2008; 455:64–71.
<https://doi.org/10.1038/nature07242>
PMID:[18668037](https://pubmed.ncbi.nlm.nih.gov/18668037/)
25. Ménard C, Rezende FA, Miloudi K, Wilson A, Tétreault N, Hardy P, SanGiovanni JP, De Guire V, Sapiéha P. MicroRNA signatures in vitreous humour and plasma of patients with exudative AMD. *Oncotarget*. 2016; 7:19171–84.
<https://doi.org/10.18632/oncotarget.8280>
PMID:[27015561](https://pubmed.ncbi.nlm.nih.gov/27015561/)
26. Liu CH, Sun Y, Li J, Gong Y, Tian KT, Evans LP, Morss PC, Fredrick TW, Saba NJ, Chen J. Endothelial microRNA-150 is an intrinsic suppressor of pathologic ocular neovascularization. *Proc Natl Acad Sci USA*. 2015; 112:12163–68.
<https://doi.org/10.1073/pnas.1508426112>
PMID:[26374840](https://pubmed.ncbi.nlm.nih.gov/26374840/)
27. Yan L, Lee S, Lazzaro DR, Aranda J, Grant MB, Chaqour B. Single and compound knock-outs of MicroRNA (miRNA)-155 and its angiogenic gene target CCN1 in mice alter vascular and neovascular growth in the retina via resident microglia. *J Biol Chem*. 2015; 290:23264–81.
<https://doi.org/10.1074/jbc.M115.646950>
PMID:[26242736](https://pubmed.ncbi.nlm.nih.gov/26242736/)
28. Shen J, Yang X, Xie B, Chen Y, Swaim M, Hackett SF, Campochiaro PA. MicroRNAs regulate ocular neovascularization. *Mol Ther*. 2008; 16:1208–16.
<https://doi.org/10.1038/mt.2008.104>
PMID:[18500251](https://pubmed.ncbi.nlm.nih.gov/18500251/)
29. Ertekin S, Yıldırım O, Dinç E, Ayaz L, Fidancı SB, Tamer L. Evaluation of circulating miRNAs in wet age-related macular degeneration. *Mol Vis*. 2014; 20:1057–66.
PMID:[25221421](https://pubmed.ncbi.nlm.nih.gov/25221421/)
30. Berber P, Grassmann F, Kiel C, Weber BH. An eye on age-related macular degeneration: the role of MicroRNAs in disease pathology. *Mol Diagn Ther*. 2017; 21:31–43.
<https://doi.org/10.1007/s40291-016-0234-z>
PMID:[27658786](https://pubmed.ncbi.nlm.nih.gov/27658786/)
31. Nunes DN, Dias-Neto E, Cardó-Vila M, Edwards JK, Dobroff AS, Giordano RJ, Mandelin J, Brentani HP, Hasselgren C, Yao VJ, Marchiò S, Pereira CA, Passetti F, et al. Synchronous down-modulation of miR-17 family members is an early causative event in the retinal angiogenic switch. *Proc Natl Acad Sci USA*. 2015; 112:3770–75.
<https://doi.org/10.1073/pnas.150008112>
PMID:[25775553](https://pubmed.ncbi.nlm.nih.gov/25775553/)
32. Lambert V, Lecomte J, Hansen S, Blacher S, Gonzalez ML, Struman I, Sounni NE, Rozet E, de Tullio P, Foidart JM, Rakic JM, Noel A. Laser-induced choroidal neovascularization model to study age-related macular degeneration in mice. *Nat Protoc*. 2013; 8:2197–211.
<https://doi.org/10.1038/nprot.2013.135>
PMID:[24136346](https://pubmed.ncbi.nlm.nih.gov/24136346/)
33. Mendell JT. miRiad roles for the miR-17-92 cluster in development and disease. *Cell*. 2008; 133:217–22.
<https://doi.org/10.1016/j.cell.2008.04.001>
PMID:[18423194](https://pubmed.ncbi.nlm.nih.gov/18423194/)
34. Gupta S, Read DE, Deepti A, Cawley K, Gupta A, Oommen D, Verfaillie T, Matus S, Smith MA, Mott JL, Agostinis P, Hetz C, Samali A. Perk-dependent repression of miR-106b-25 cluster is required for ER stress-induced apoptosis. *Cell Death Dis*. 2012; 3:e333.
<https://doi.org/10.1038/cddis.2012.74>
PMID:[22739985](https://pubmed.ncbi.nlm.nih.gov/22739985/)

35. Smith LE, Wesolowski E, McLellan A, Kostyk SK, D'Amato R, Sullivan R, D'Amore PA. Oxygen-induced retinopathy in the mouse. *Invest Ophthalmol Vis Sci*. 1994; 35:101–11. PMID:[7507904](https://pubmed.ncbi.nlm.nih.gov/7507904/)
36. Salminen A, Kauppinen A, Hyttinen JM, Toropainen E, Kaarniranta K. Endoplasmic reticulum stress in age-related macular degeneration: trigger for neovascularization. *Mol Med*. 2010; 16:535–42. <https://doi.org/10.2119/molmed.2010.00070> PMID:[20683548](https://pubmed.ncbi.nlm.nih.gov/20683548/)
37. Harding HP, Zhang Y, Ron D. Protein translation and folding are coupled by an endoplasmic-reticulum-resident kinase. *Nature*. 1999; 397:271–74. <https://doi.org/10.1038/16729> PMID:[9930704](https://pubmed.ncbi.nlm.nih.gov/9930704/)
38. Binet F, Sapiéha P. ER stress and angiogenesis. *Cell Metab*. 2015; 22:560–75. <https://doi.org/10.1016/j.cmet.2015.07.010> PMID:[26278049](https://pubmed.ncbi.nlm.nih.gov/26278049/)
39. Xu G, Chen J, Jing G, Grayson TB, Shalev A. miR-204 targets PERK and regulates UPR signaling and β -cell apoptosis. *Mol Endocrinol*. 2016; 30:917–24. <https://doi.org/10.1210/me.2016-1056> PMID:[27384111](https://pubmed.ncbi.nlm.nih.gov/27384111/)
40. McMahon M, Samali A, Chevet E. Regulation of the unfolded protein response by noncoding RNA. *Am J Physiol Cell Physiol*. 2017; 313:C243–54. <https://doi.org/10.1152/ajpcell.00293.2016> PMID:[28637678](https://pubmed.ncbi.nlm.nih.gov/28637678/)
41. Bonauer A, Carmona G, Iwasaki M, Mione M, Koyanagi M, Fischer A, Burchfield J, Fox H, Doebele C, Ohtani K, Chavakis E, Potente M, Tjwa M, et al. MicroRNA-92a controls angiogenesis and functional recovery of ischemic tissues in mice. *Science*. 2009; 324:1710–13. <https://doi.org/10.1126/science.1174381> PMID:[19460962](https://pubmed.ncbi.nlm.nih.gov/19460962/)
42. Doebele C, Bonauer A, Fischer A, Scholz A, Reiss Y, Urbich C, Hofmann WK, Zeiher AM, Dimmeler S. Members of the microRNA-17-92 cluster exhibit a cell-intrinsic antiangiogenic function in endothelial cells. *Blood*. 2010; 115:4944–50. <https://doi.org/10.1182/blood-2010-01-264812> PMID:[20299512](https://pubmed.ncbi.nlm.nih.gov/20299512/)
43. Maimaiti A, Maimaiti A, Yang Y, Ma Y. MiR-106b exhibits an anti-angiogenic function by inhibiting STAT3 expression in endothelial cells. *Lipids Health Dis*. 2016; 15:51. <https://doi.org/10.1186/s12944-016-0216-5> PMID:[26956882](https://pubmed.ncbi.nlm.nih.gov/26956882/)
44. Sarwar S, Clearfield E, Soliman MK, Sadiq MA, Baldwin AJ, Hanout M, Agarwal A, Sepah YJ, Do DV, Nguyen QD. Aflibercept for neovascular age-related macular degeneration. *Cochrane Database Syst Rev*. 2016; 2:CD011346. <https://doi.org/10.1002/14651858.CD011346.pub2> PMID:[26857947](https://pubmed.ncbi.nlm.nih.gov/26857947/)
45. Desjarlais M, Rivera JC, Lahaie I, Cagnone G, Wirt M, Omri S, Chemtob S. MicroRNA expression profile in retina and choroid in oxygen-induced retinopathy model. *PLoS One*. 2019; 14:e0218282. <https://doi.org/10.1371/journal.pone.0218282> PMID:[31188886](https://pubmed.ncbi.nlm.nih.gov/31188886/)
46. Hanna J, Hossain GS, Kocerha J. The potential for microRNA therapeutics and clinical research. *Front Genet*. 2019; 10:478. <https://doi.org/10.3389/fgene.2019.00478> PMID:[31156715](https://pubmed.ncbi.nlm.nih.gov/31156715/)
47. Sapiéha P, Joyal JS, Rivera JC, Kermorvant-Duchemin E, Sennlaub F, Hardy P, Lachapelle P, Chemtob S. Retinopathy of prematurity: understanding ischemic retinal vasculopathies at an extreme of life. *J Clin Invest*. 2010; 120:3022–32. <https://doi.org/10.1172/JCI42142> PMID:[20811158](https://pubmed.ncbi.nlm.nih.gov/20811158/)
48. Stahl A, Connor KM, Sapiéha P, Chen J, Dennison RJ, Krah NM, Seaward MR, Willett KL, Aderman CM, Guerin KI, Hua J, Löfqvist C, Hellström A, Smith LE. The mouse retina as an angiogenesis model. *Invest Ophthalmol Vis Sci*. 2010; 51:2813–26. <https://doi.org/10.1167/iovs.10-5176> PMID:[20484600](https://pubmed.ncbi.nlm.nih.gov/20484600/)
49. Stahl A, Connor KM, Sapiéha P, Willett KL, Krah NM, Dennison RJ, Chen J, Guerin KI, Smith LE. Computer-aided quantification of retinal neovascularization. *Angiogenesis*. 2009; 12:297–301. <https://doi.org/10.1007/s10456-009-9155-3> PMID:[19757106](https://pubmed.ncbi.nlm.nih.gov/19757106/)
50. Binet F, Mawambo G, Sitaras N, Tetreault N, Lapalme E, Favret S, Cerani A, Leboeuf D, Tremblay S, Rezende F, Juan AM, Stahl A, Joyal JS, et al. Neuronal ER stress impedes myeloid-cell-induced vascular regeneration through IRE1 α degradation of netrin-1. *Cell Metab*. 2013; 17:353–71. <https://doi.org/10.1016/j.cmet.2013.02.003> PMID:[23473031](https://pubmed.ncbi.nlm.nih.gov/23473031/)
51. Shao Z, Friedlander M, Hurst CG, Cui Z, Pei DT, Evans LP, Juan AM, Tahiri H, Duhamel F, Chen J, Sapiéha P, Chemtob S, Joyal JS, Smith LE. Choroid sprouting assay: an *ex vivo* model of microvascular angiogenesis. *PLoS One*. 2013; 8:e69552. <https://doi.org/10.1371/journal.pone.0069552> PMID:[23922736](https://pubmed.ncbi.nlm.nih.gov/23922736/)

SUPPLEMENTARY MATERIALS

Supplementary Figure



Supplemental Figure 1. (A) VEGFA and HIF1 α mRNA expression in choroids 3 days after laser burn (VEGFA n=5, HIF1 α n=7). (B) LV.miR-106b expression after plasmid transfection in HEK cells (n=4). (C) Schematic of plasmid construction, virus production and LV.miR-106b expression 72hrs after viral infection of HRMECs. (D) VEGFA mRNA expression in HRMECs 72hrs after LV.shVEGFA infection. Data are expressed as mean \pm S.E.M. Unpaired Two-tailed Student's t-test was used for the analysis of groups of 2, and one-way ANOVA with Bonferroni post-hoc test was performed on groups of 3 or more, *P<0.05; **P<0.001; ***P<0.0001.

Supplementary Table

Supplementary Table 1. List of human and mouse primers.

Genes (human)	Foward primers	Reverse primers
B-ACTIN (ACTB)	5' GTCATTCCAATATGAGATGCGT 5'	5' TGTGGACTTGGGAGAGGACT 3'
VEGFA	5' CTCTACCTCCACCATGCCAAG 3'	5' AGACATCCATGAACTTCACCACTTC 3'
Genes (mouse)	Foward primers	Reverse primers
B-ACTIN (ACTB)	5' GACGGCCAGGTCATCACTATTG 3'	5' CCACAGGATCCATACCCAAG 3'
VEGFA	5' GCCCTGAGTCAAGAGGACAG 3'	5' CTCCTAGGCCCTCAGAAGT 3'
MCM7	5' ATGGCGCTTAAGGACTACG 3'	5' ATCCAGGTCCACATACAGTG 3'
ATF4	5' CTACTAGGTACCGCCAGAAG 3'	5' GCCTTACGGACCTTCTCTAT 3'
HIF1 α	5' CGAGAACGAGAAGAAAAAGATGAG 3'	5' AAGCCATCTAGGGCTTTCAG 3'

RT-qPCR primer sequences to quantify mRNA expression in choroids (mouse) or HRMECs (human).

ALDH2 protects naturally aged mouse retina *via* inhibiting oxidative stress-related apoptosis and enhancing unfolded protein response in endoplasmic reticulum

Pan Long^{1,2,5,*}, Mengshan He^{3,7,*}, Weiming Yan^{4,*}, Wei Chen¹, Dongyu Wei^{5,6}, Siwang Wang³, Zuoming Zhang^{5,6}, Wei Ge¹, Tao Chen^{5,6}

¹Department of General Practice, Xijing Hospital, Fourth Military Medical University, Xi'an 710032, Shaanxi Province, China

²Department of Ophthalmology, The General Hospital of Western Theater Command, Chengdu 610083, Sichuan Province, China

³Department of Chinese Material Medical and Natural Medicines, Fourth Military Medical University, Xi'an 710032, Shaanxi Province, China

⁴Department of Ophthalmology, The 900th Hospital of Joint Logistic Support Force, PLA, Clinical Medical College of Fujian Medical University, Dongfang Hospital Affiliated to Xiamen University, Fuzhou 350025, Fujian Province, China

⁵Center of Clinical Aerospace Medicine, Fourth Military Medical University, Xi'an 710032, Shaanxi Province, China

⁶Department of Aviation Medicine, Xijing Hospital, Fourth Military Medical University, Xi'an 710032, Shaanxi Province, China

⁷Department of Pharmacy, Xijing Hospital, Fourth Military Medical University, Xi'an 710032, Shaanxi Province, China

*Equal contribution

Correspondence to: Tao Chen, Wei Ge; **email:** ct1988@fmmu.edu.cn, geweidr@fmmu.edu.cn

Keywords: ALDH2, UPR^{ER}, retina, aged mice, oxidative stress

Received: January 9, 2020

Accepted: October 1, 2020

Published: December 19, 2020

Copyright: © 2020 Long et al. This is an open access article distributed under the terms of the [Creative Commons Attribution License](https://creativecommons.org/licenses/by/3.0/) (CC BY 3.0), which permits unrestricted use, distribution, and reproduction in any medium, provided the original author and source are credited.

ABSTRACT

During the process of aging, the retina exhibits chronic oxidative stress (OS) damage. Our preliminary experiment showed that acetaldehyde dehydrogenase 2 (ALDH2) could alleviate retinal damage caused by OS. This study aimed to explore whether ALDH2 could inhibit mice retinal cell apoptosis and enhance the function of unfolded protein response in endoplasmic reticulum (UPR^{ER}) through reducing OS in aging process. Retinal function and structure *in vivo* and *in vitro* were examined in aged *ALDH2+* overexpression mice and ALDH2 agonist Alda1-treated aged mice. Levels of ALDH2, endoplasmic reticulum stress (ERS), apoptosis and inflammatory cytokines were evaluated. Higher expression of ALDH2 was observed at the outer nuclear layer (ONL) and the inner nuclear layer (INL) in aged *ALDH2+* overexpression and aged Alda1-treated mice. Moreover, aged *ALDH2+* overexpression mice and aged Alda1-treated mice exhibited better retinal function and structure. Increased expression of glucose-regulated protein 78 (GRP78) and ERS-related protein phosphorylated eukaryotic initiation factor 2 (peIF2 α) and decreased expression of apoptosis-related protein, including C/EBP homologous protein (CHOP), caspase12 and caspase9, and retinal inflammatory cytokines were detected in the retina of aged *ALDH2+* overexpression mice and aged Alda1-treated mice. The expression of ALDH2 in the retina was decreased in aging process. ALDH2 could reduce retinal oxidative stress and apoptosis, strengthen UPR^{ER} during the aging process to improve retinal function and structure.

INTRODUCTION

The aging process is characterized by a decline in systematic tissue function and the onset of serious of age-related disease [1–3]. However, it remained elusive that the potential mechanisms accounting for these phenomena and strategies to intervene to improve cell functions.

Recently, the imbalance of protein homeostasis was proposed to be responsible for aging and age-related diseases [4, 5]. As we known that the protein homeostasis is an essential component of the cell survival process and often refers to the maintenance of the proteome. And the unfolded protein response in the endoplasmic reticulum (UPR^{ER}) is considered as the most well-known mechanisms of protein homeostasis. The endoplasmic reticulum (ER) is responsible for folding and quality control through the activation of chaperones and foldases that assist in protein folding and preventing abnormal protein aggregation [6]. The key proteins involved in UPR^{ER} include the sensors inositol requiring element-1 (IRE1), protein kinase R-like endoplasmic reticulum kinase (PERK) and activating transcription factor 6 (ATF6) and the molecular chaperone glucose-regulated protein 78 (GRP78), which is also called immunoglobulin heavy chain binding protein (BiP/GRP78). When superfluous unfolded or misfolded proteins accumulate in the ER, GRP78 disassociates from these three sensors, thus triggering the UPR^{ER} response [7]. In this time, GRP78, with this single existence, is easily encountered with oxidative stress damage, especially in aging process. Furthermore, eukaryotic translation initiation factor 2 α (eIF2 α), a protein translation component, is the downstream of PERK. When endoplasmic reticulum stress (ERS) happens, eIF2 α is phosphorylated to slow down protein production and reduce the unfolded and misfolded proteins. [8]

During the aging process, protein glycosylation, oxidative imbalance, and protein folding defection cause abnormal protein accumulation in the ER and affect the UPR^{ER} to regulate the protein homeostasis capacity [9]. Moreover, increased free radicals damage during senescence leads to cell apoptosis via the caspase pathway, which is an important contributor to many human pathological conditions [10, 11]. Related studies have shown that the UPR^{ER} declined and its related chaperones were significantly reduced following with advancing age [12]. Traditionally, the UPR^{ER} is activated under the condition of energy deficiency with the aim of restoring protein homeostasis [13]. More importantly, the retina is one of the most energy-demanding tissues in the body. Both clinical and animal studies have found that retinal function and structure were worsen along with aging [14]. Nevertheless, the

underlying mechanisms of UPR^{ER} related to aged retinal behaviour remain largely unclear, and effective therapies to intervene aging-related injury to the retina by targeting the UPR^{ER} have not been developed.

Mitochondrial aldehyde dehydrogenase 2 (ALDH2) is essential for the catabolism of exogenous and endogenous toxic aldehydes associated with oxidative stress-induced lipid peroxidation and adducts with DNA, RNA and protein [15]. The available evidence suggested that chronic accumulation of aldehydes resulting from ALDH2 deficiency was responsible for the age-related diseases [16]. Recently, genetic polymorphism analysis of ALDH2 revealed that ALDH2*1*1 (wild homozygous GG) individuals had superior physical functions and diabetic or ischaemic stroke-related diseases resistance ability [17]. Interestingly, diabetic retinopathy (DR) was also closely related to ALDH2 polymorphisms [18, 19]. Moreover, ALDH2 has a certain protective effect in age-related disease, such as Alzheimer's Disease (AD), Parkinson's Disease (PD) and aged cardiopathy by decreasing free radicals damage [20]. Simultaneously, our previous animal experiments have also shown that ALDH2 could play a certain role in aged diabetic retinopathy [21] and retinitis pigmentosa (RP) [22]. Furthermore, our clinical retrospective data analysis showed that the aged with ALDH2*1*1 (G/G) genotype possessed a better retinal function and a thicker macula compared with ALDH2*2*2 (mutant heterozygous AA) while the young with different ALDH2 genotype, including ALDH2*1*1, ALDH2*1*2 (mutant heterozygous GA) and ALDH2*2*2, showed no significant difference (Supplementary Figure 1).

Considering that ALDH2 could alleviate OS damage, ALDH2 overexpression in aged mice (transgenic mice controlled by EF1 α and chicken β -actin promoters) and aged mice treated with the ALDH2 activator Alda1 (N-[1,3-benzodioxol-5-ylmethyl]-2,6-dichlorobenzamide) were examined to evaluate the effect of ALDH2 on aged mice retinal function and structure, and explore the underlying mechanisms.

RESULTS

Expression of ALDH2 in different groups

Total retinal proteins detected by western blotting (WB) showed that the expression of ALDH2 was dramatically decreased in the aged (WT) group compared with the young (WT) group ($P < 0.05$). Furthermore, ALDH2 expression was significantly increased in the aged (ALDH2+) group and aged (Alda1) group compared with the aged (WT) group and aged (DMSO) group, respectively (all $P < 0.05$) (Figure 1A, 1B, Figure 2A, 2B). Moreover, as shown in Figure 1C, 1D and Figure 2C, 2D,

immunofluorescence staining of retinal paraffin sections from the young (WT) group showed higher ALDH2 expression in the ONL and INL of the retinas. In contrast, retinas from the aged (WT) group exhibited lower ALDH2 expression in the ONL and INL. Interestingly, the retinas from the aged (ALDH2+) group and aged (Alda1) group showed obvious enhancing expression of ALDH2 in the ONL and INL compared with the aged (WT) group and aged (DMSO) group, respectively (all $P < 0.05$). Thus, the immunofluorescence staining and western blotting results were consistent.

ALDH2 improved aged mouse total retinal function

To evaluate the potential role of ALDH2 in retinal function, electroretinography (ERG) detection was performed. The value of the b wave (dark-adaptation 3.0 response) was selected to evaluate the mice total retinal function as the dark-adaptation 3.0 response is related to both cone cell and rod cell functions.

As shown in Figure 3A, 3B, the value of the b wave (dark-adaptation 3.0 response) was significantly decreased in the aged (WT) group compared with the young (WT) group ($P < 0.05$). However, the value of the b wave (dark-adaptation 3.0 response) was

increased in the aged (ALDH2+) group compared with the aged (WT) group ($P < 0.05$), while there was no significant difference between the aged (ALDH2+) group and young (WT) group ($P > 0.05$). Moreover, as shown in Figure 3C, 3D, the value of the b wave (dark-adaptation 3.0 response) was significantly decreased in the aged (DMSO) group compared with the young group ($P < 0.05$), and the value of the b wave (dark-adaptation 3.0 response) was increased in the aged (Alda1) group compared with the aged (DMSO) group ($P < 0.05$). There were no significant differences between the aged (Alda1) group and young group ($P > 0.05$).

ALDH2 enhanced aged mouse vessel function

To explore the retinal vessel protective effect of ALDH2, retinal vessel related ERG response (oscillatory potentials, OPs response) and FFA detection (the operation procedure pattern diagram was showed in Figure 4E) were performed. The OPs wave, as an ERG component, could be used to indirectly evaluate retinal vessel function, because retinal amacrine cells are accompanied by retinal vessels.

The results showed that the OPs2 wave (a typical wave of OPs) value was significantly decreased in the aged

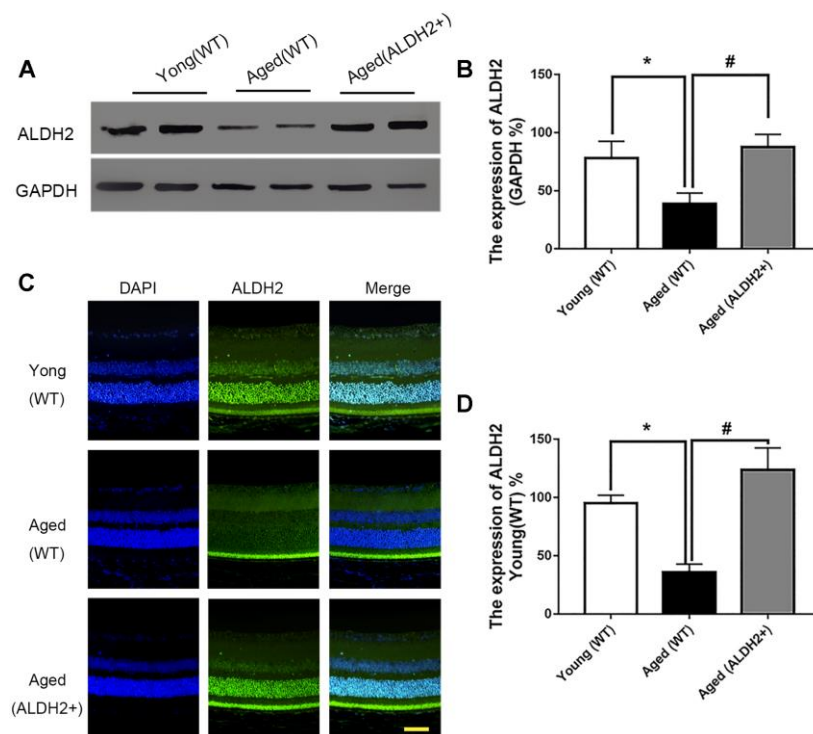


Figure 1. The expression of ALDH2 in the young (WT) group, aged (WT) group and aged (ALDH2+) group. (A, B) A typical ALDH2 WB image and the expression of ALDH2; (C, D) A typical ALDH2 immunofluorescence image and the expression of ALDH2. All analyses were performed in duplicate. Scale bar: 50 μ m. Values are presented as the mean \pm SD, $n = 4$ mice per group. * $P < 0.05$: aged (WT) group and aged (ALDH2+) group vs young (WT) group; # $P < 0.05$: aged (ALDH2+) group vs aged (WT) group.

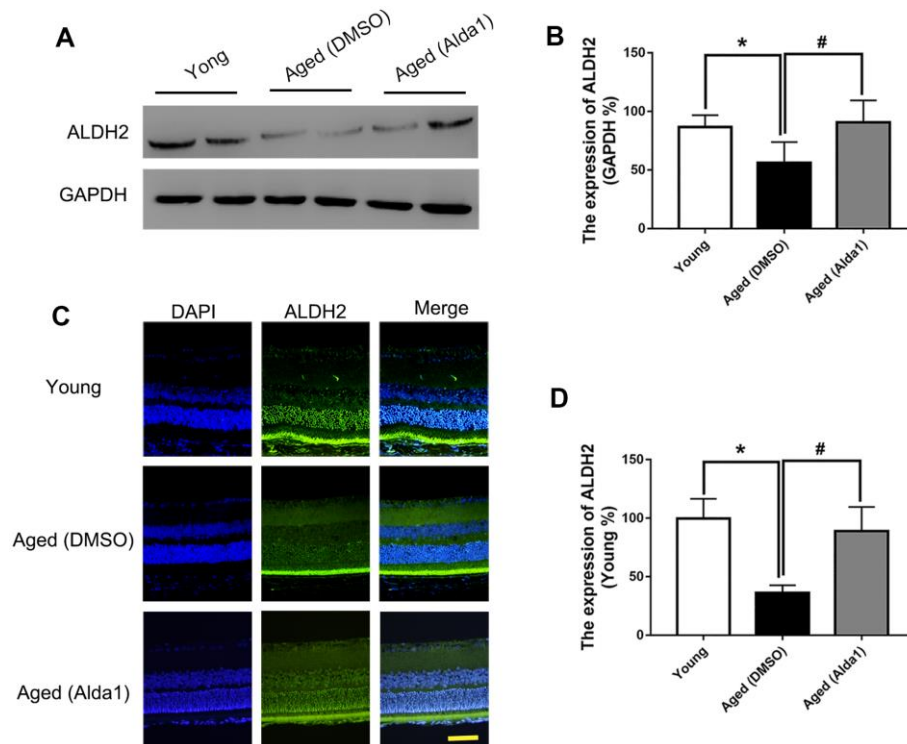


Figure 2. The expression of ALDH2 in the young group, aged (DMSO) group and aged (Alda1) group. (A, B) A typical ALDH2 WB image and the expression of ALDH2; (C, D) A typical ALDH2 immunofluorescence image and the expression of ALDH2. All analyses were performed in duplicate. Scale bar: 50 μ m. Values are presented as the mean \pm SD, n = 4 mice per group. * P <0.05: aged (DMSO) group and aged (Alda1) group vs young group; # P <0.05: aged (Alda1) group vs aged (DMSO) group.

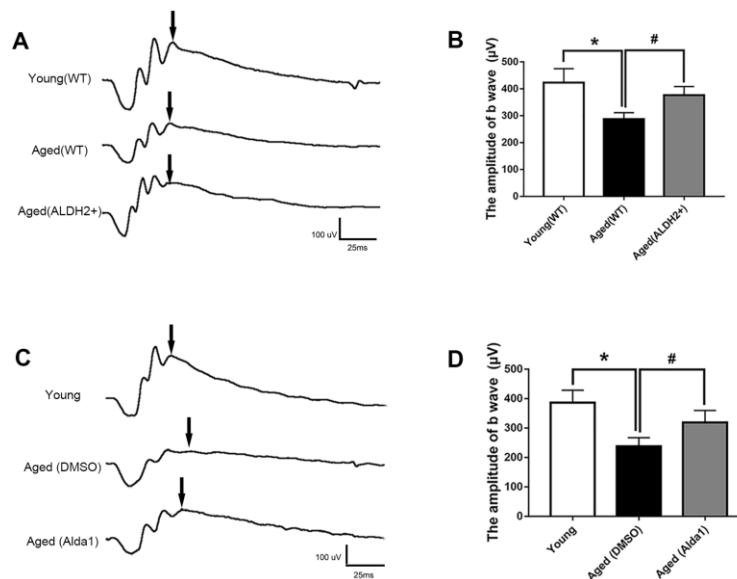


Figure 3. ALDH2 enhanced aged mouse retinal function. (A, B) A typical dark-adaptation 3.0 response image and amplification of the dark-adaptation 3.0 response b wave in ALDH2 overexpression mice; (C, D) A typical dark-adaptation 3.0 response image and the amplification of the dark-adaptation 3.0 response b wave in Alda1-treated mice. All analyses were performed in duplicate. Values are presented as the mean \pm SD, n = 10 mice per group. * P <0.05: aged (WT) group and aged (ALDH2+) group vs young (WT) group or aged (DMSO) group and aged (Alda1) group vs young group; # P <0.05: aged (ALDH2+) group vs aged (WT) group or aged (Alda1) group vs aged (DMSO) group.

(WT) group compared with the young (WT) group ($P < 0.05$) (Figure 4A, 4B). Moreover, the value of the OPs2 wave was increased in the aged (ALDH2+) group compared with the aged (WT) group ($P < 0.05$), while there was no significant difference compared with the young (WT) group ($P > 0.05$) (Figure 4A, 4B). In addition, the OPs2 wave value was significantly decreased in the aged (DMSO) group compared with the young group ($P < 0.05$). Moreover, the OPs2 wave value was increased in the aged (Alda1) group compared with the aged (DMSO) group ($P < 0.05$), while

there was no significant difference compared with the young group ($P > 0.05$) (Figure 4C, 4D).

Furthermore, we calculated the time of appearance of fluorescein sodium in the retinal vein following the first intraperitoneal injection of fluorescein sodium to evaluate the function of the retinal vessel micro-circulation. As shown in Figure 4F, 4G, the time of appearance of fluorescein sodium was significantly prolonged in the aged (WT) group compared with the young (WT) group ($P < 0.05$). In the aged (ALDH2+)

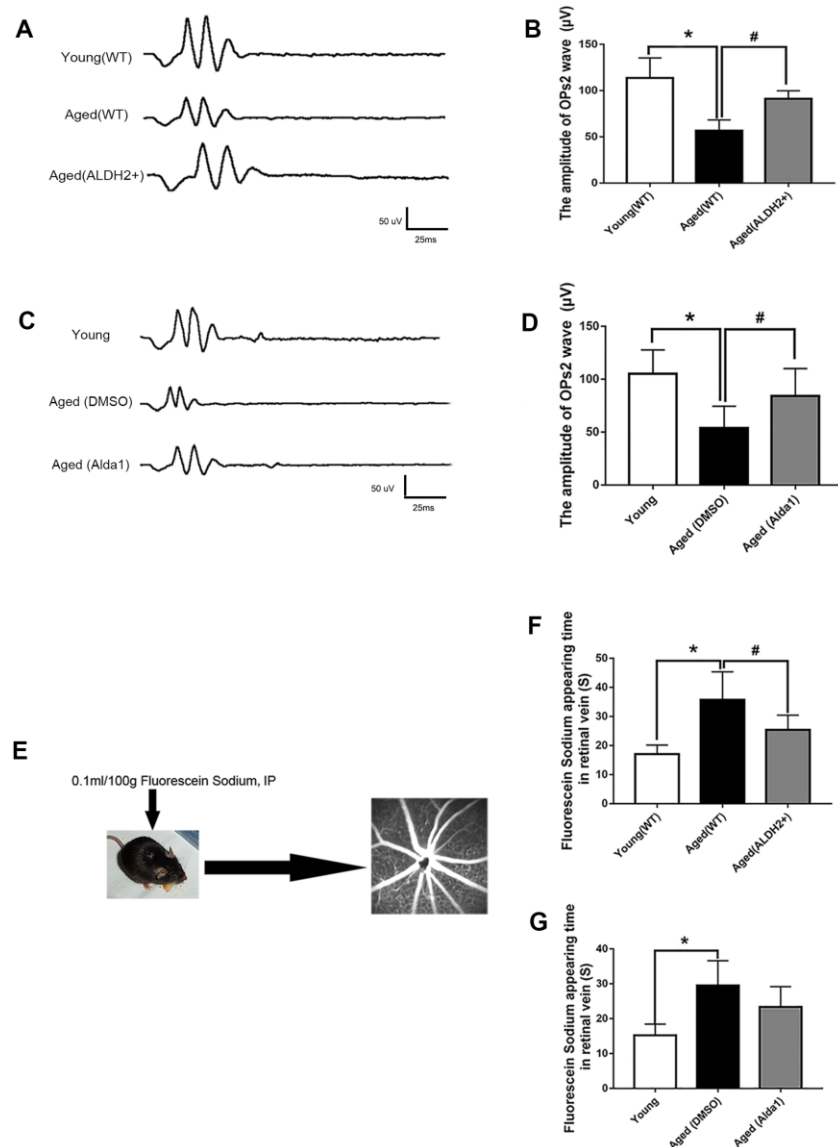


Figure 4. ALDH2 enhanced aged mouse retinal vessel function. (A, B) A typical OPs response image and amplification of the OPs2 response in ALDH2 overexpression mice; (C, D) A typical OPs response image and the amplification of OPs2 response in Alda1-treated mice; (E) The operation procedure pattern diagram for the FFA detection method; (F) The appearance time of fluorescein sodium in the retinal vessel in ALDH2 overexpression mice (G) and Alda1-treated mice. All analyses were performed in duplicate. Values are presented as the mean \pm SD, $n = 10$ mice per group. * $P < 0.05$: aged (WT) group and aged (ALDH2+) group vs young (WT) group or aged (DMSO) group and aged (Alda1) group vs Young group; # $P < 0.05$: aged (ALDH2+) group vs aged (WT) group or aged (Alda1) group vs aged (DMSO) group.

group, the time of appearance of fluorescein sodium was significantly reduced compared with the aged (WT) group ($P < 0.05$). In the aged (DMSO) group, the time of appearance of fluorescein sodium was significantly prolonged compared with the young group ($P < 0.05$). However, the time of appearance of fluorescein sodium showed no significant difference in the aged (Ald1) group compared with the aged (DMSO) group ($P > 0.05$).

ALDH2 protected the aged mouse retinal structure

To further examine the protective roles of ALDH2 in the aged mouse retinal structure, optical coherence tomography (OCT) and Hematoxylin-Eosin (HE) staining were performed. OCT could determine every retinal layer according to the different luminance reflective bands, such as the low-reflective band representative of ONL and INL and the high-reflective band representative of the retinal nerve fibre layer (RNFL), inner plexiform layer (IPL), outer plexiform

layer (OPL), photoreceptor inner segment/outer segment (IS/OS) junction line and retinal pigment epithelium (RPE) layer (Figure 5A).

As shown in Figure 5B, 5C, the thickness of the INL detected by OCT was significantly decreased in the aged (WT) group compared with the young (WT) group ($P < 0.05$). Interestingly, the thickness of INL was increased in the aged (ALDH2+) group compared with the aged (WT) group ($P < 0.05$). However, there were no significant differences in the ONL thickness among each group ($P > 0.05$). As shown in Figure 5D–5F, HE staining showed that the ONL cell and INL cell layers were significantly reduced in the aged (WT) group compared with those in the young (WT) group (all $P < 0.05$). Furthermore, the INL cell layer was more in the aged (ALDH2+) group than the aged (WT) group ($P < 0.05$). Moreover, the fundus photograph revealed a depigmentation change in the aged (WT) group but little depigmentation change in the aged (ALDH2+) group (Figure 5G).

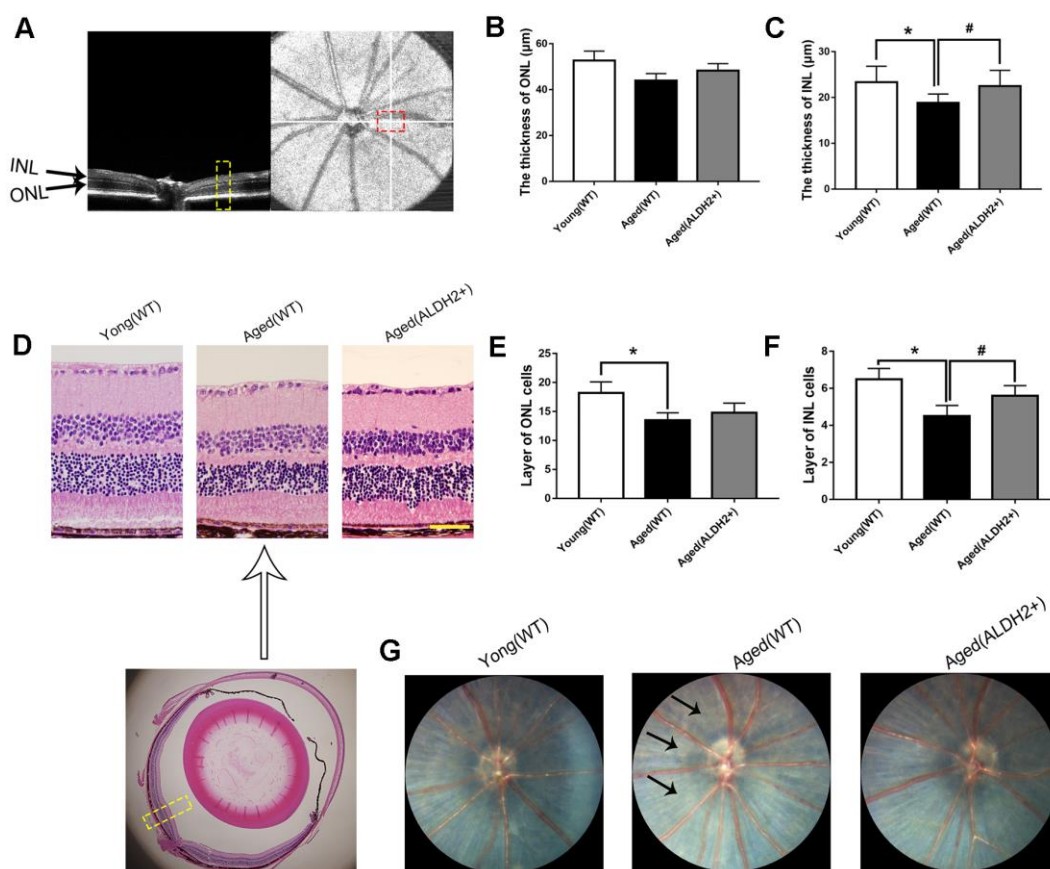


Figure 5. The retinal structures of ALDH2 overexpression aged mice. (A) A typical marked OCT image; (B) The thickness of the ONL; (C) The thickness of the INL; (D) A typical marked HE staining image; (E) The number of ONL cell layers; (F) The number of INL cell layers; (G) The fundus performance in the mice. All analyses were performed in duplicate. Scale bar: 50 µm. Black arrow showed retinal depigmentation change. Yellow box showed retinal structure analysis area. Values are presented as the mean ± SD, n = 6 mice per group. * $P < 0.05$: aged (WT) and aged (ALDH2+) vs young (WT); # $P < 0.05$: aged (ALDH2+) vs aged (WT).

Regarding the ALDH2 agonist, the total retinal thickness among the young, aged (DMSO) and aged (Alda1) groups was not significantly different (all $P>0.05$). However, the thickness of ELM+IS/OS was reduced in the aged (DMSO) group compared with the young group ($P<0.05$), while it was increased in the aged (Alda1) group compared with that in the aged (DMSO) group ($P<0.05$) (Figure 6A–6C). Moreover, HE staining showed that the number of INL cell layers was significantly reduced in the aged (DMSO) group compared with the young group ($P<0.05$). For the number of ONL cell layers, there existed no significant difference among the groups (Figure 6D–6F).

ALDH2 decreased the expression of TNF- α , IL-6 and IL-1 in aged mouse retina

In aging process, oxidation imbalance, accompanied by free radicals accumulation, affects retina working regularly. Retinal inflammatory factor, including tumor necrosis factor- α (TNF- α), interleukin-6 (IL-6) and interleukin-1 (IL-1) were detected to evaluate oxidative stress damage with aging. As shown in Figure 7A–7C, the expression levels of retinal TNF- α , IL-6 and IL-1 were significantly increased in the aged (WT) group compared with those in the young (WT) group, respectively (all $P<0.05$). However, the expression of

retinal TNF- α , IL-6 and IL-1 were decreased in the aged (ALDH2+) group compared with those in the aged (WT) group, respectively (all $P<0.05$). As for the agonist intervention experiment, the expression of retinal TNF- α , IL-6 and IL-1 were increased in the aged (DMSO) group compared with those in the young group, respectively (all $P<0.05$). Additionally, the expression of retinal TNF- α , IL-6 and IL-1 were decreased in the aged (Alda1) group compared with those in the aged (DMSO) group, respectively (all $P<0.05$) (Figure 7D–7F).

ALDH2 enhanced UPR^{ER} in aged mouse retina

To determine whether ALDH2 was involved in the enhancement of UPR^{ER} during the retinal aging process, the retinal UPR^{ER}-related proteins GRP78, eIF2 α and phosphorylated eIF2 α (peIF2 α) were assessed. As shown in Figure 8A, 8B, GRP78 expression was decreased in the aged (WT) group compared with the young (WT) group, as determined by western blotting ($P<0.05$). Additionally, GRP78 expression was increased in the aged (ALDH2+) group compared with the aged (WT) group, as confirmed by western blotting analysis ($P<0.05$). Immunofluorescence staining showed that GRP78 was highly expressed in ONL, which was consistent with the western blotting results (Figure 8C, 8D).

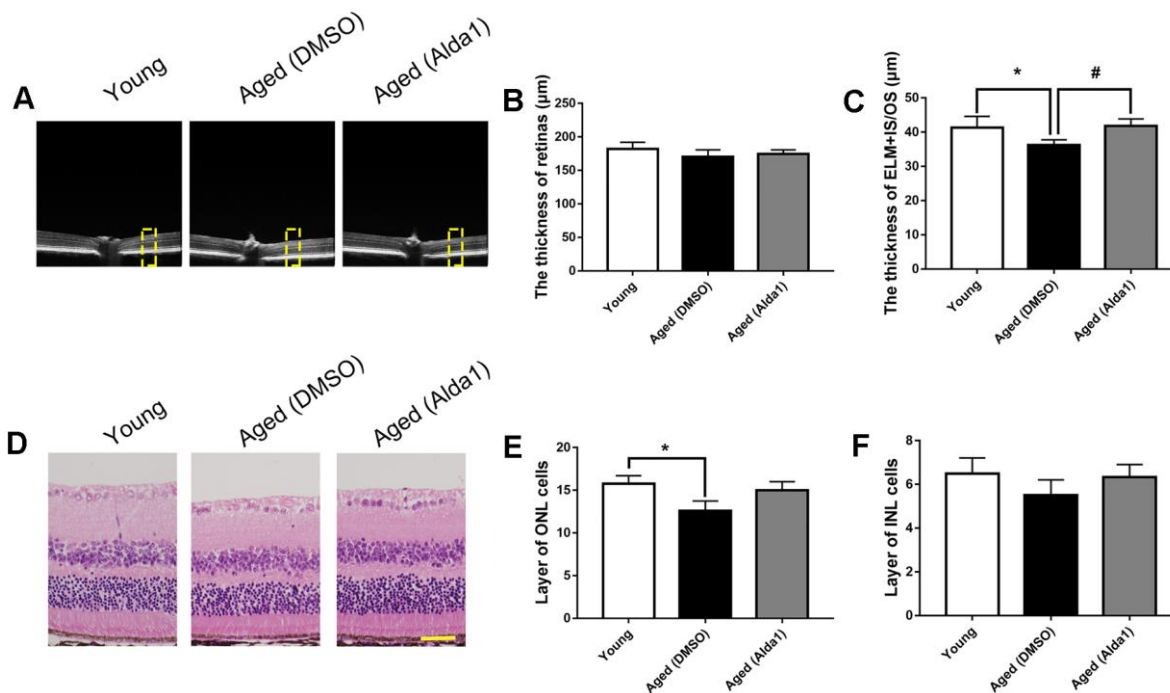


Figure 6. The retinal structures in Alda1-treated aged mice. (A) A typical marked OCT image; (B) The thickness of the total retina; (C) The thickness of the ELM+IS/OS. (D) A typical marked HE staining image; (E) The number of ONL cell layers; (F) The number of INL cell layers. All analyses were performed in duplicate. Scale bar: 50 μ m. Yellow box showed retinal structure analysis area. Values are presented as the mean \pm SD, $n = 6$ mice per group. * $P<0.05$: aged (WT) and aged (ALDH2+) vs young (WT); # $P<0.05$: aged (ALDH2+) vs aged (WT).

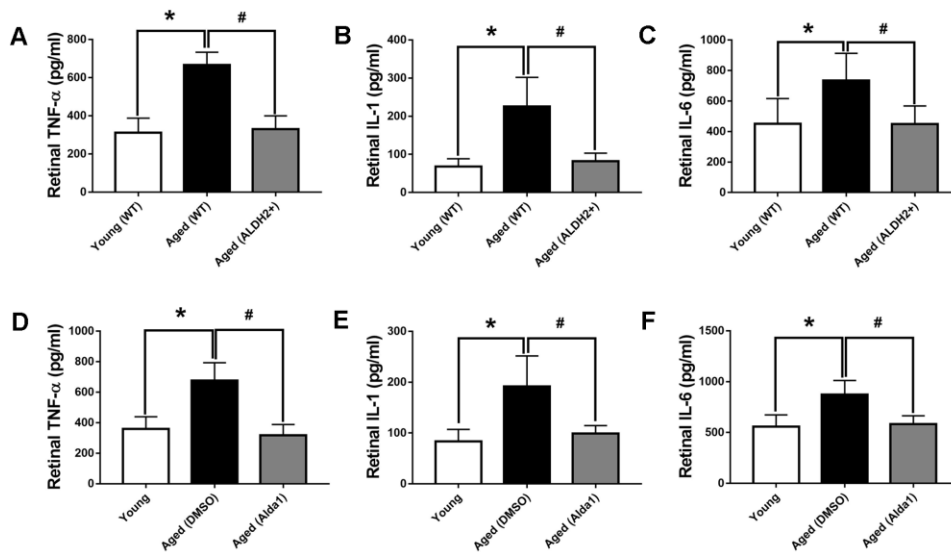


Figure 7. The expression of retinal TNF- α , IL-6 and IL-1 in aged ALDH2 overexpression and aged Alda1-treated mice. (A) The expression of retinal TNF- α in aged ALDH2 overexpression mice; (B) The expression of retinal IL-6 in aged ALDH2 overexpression mice; (C) The expression of retinal IL-1 in aged ALDH2 overexpression mice; (D) The expression of retinal TNF- α in aged Alda1-treated mice; (E) The expression of retinal IL-6 in aged Alda1-treated mice; (F) The expression of retinal IL-1 in aged Alda1-treated mice. All analyses were performed in duplicate. Values are presented as the mean \pm SD, n = 4 mice per group. * P <0.05: aged (WT) and aged (ALDH2+) vs young (WT) or Aged (DMSO) and aged (Alda1) vs young; # P <0.05: aged (ALDH2+) vs aged (WT) or aged (Alda1) vs aged (DMSO).

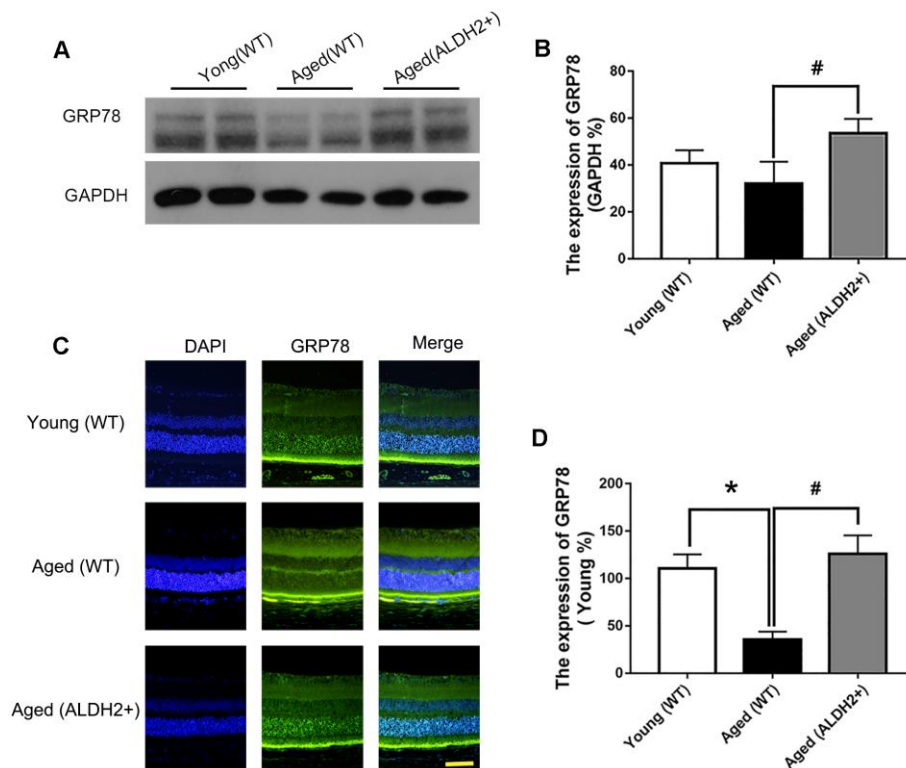


Figure 8. The expression of GRP78 in ALDH2+ overexpression mice during the normal aging process. (A, B) A typical WB image of GRP78 and the confirmation of GRP78 expression by WB; (C, D) A typical immunofluorescence image of GRP78 and the confirmation of GRP78 expression by immunofluorescence. All analyses were performed in duplicate. Scale bar: 50 μ m. Values are presented as the mean \pm SD, n = 4 mice per group. * P <0.05: aged (WT) and aged (ALDH2+) vs young (WT); # P <0.05: aged (ALDH2+) vs aged (WT).

Additionally, western blotting (Figure 9A, 9B) and immunofluorescence staining (Figure 9C, 9D) results showed that the expression of GRP78 was dramatically decreased in the aged (DMSO) group compared with that in the young group ($P<0.05$), while the expression of GRP78 was dramatically increased in the aged (Alda1) group compared with the aged (DMSO) group ($P<0.05$).

Moreover, the expression of pEIF2 α was obviously reduced in the aged (WT) group compared with that in the young (WT) group ($P<0.05$), while the expression of pEIF2 α was increased in the aged (ALDH2+) group compared with that in the aged (WT) group ($P<0.05$) (Figure 10A, 10B). Furthermore, the expression of pEIF2 α was decreased in the aged (DMSO) group compared with that in the young group ($P<0.05$), while its expression was increased in the aged (Alda1) group compared with that in the aged (DMSO) group ($P<0.05$) (Figure 10C, 10D).

ALDH2 decreased apoptosis-related protein in aged mouse retina

Apoptosis was accompanied with aging process, and we detected the proapoptotic protein CHOP and apoptosis protein caspase12 and caspase9. As shown in Figure 11A–11D, the expression of CHOP, caspase12 and caspase9 were significantly increased in the aged (WT) group compared with those in the young (WT) group (all $P<0.05$). However, the expression of CHOP, caspase12 and caspase9 were decreased in the aged (ALDH2+) group compared with the aged (WT) group (all $P<0.05$). Moreover, the expression of caspase12 existed no significant difference between the young (WT) group and aged (ALDH2+) group ($P>0.05$).

Regarding the agonist intervention experiment, the expression levels of CHOP, caspase12 and caspase9 were increased in the aged (DMSO) group compared with those in the young group (all $P<0.05$).

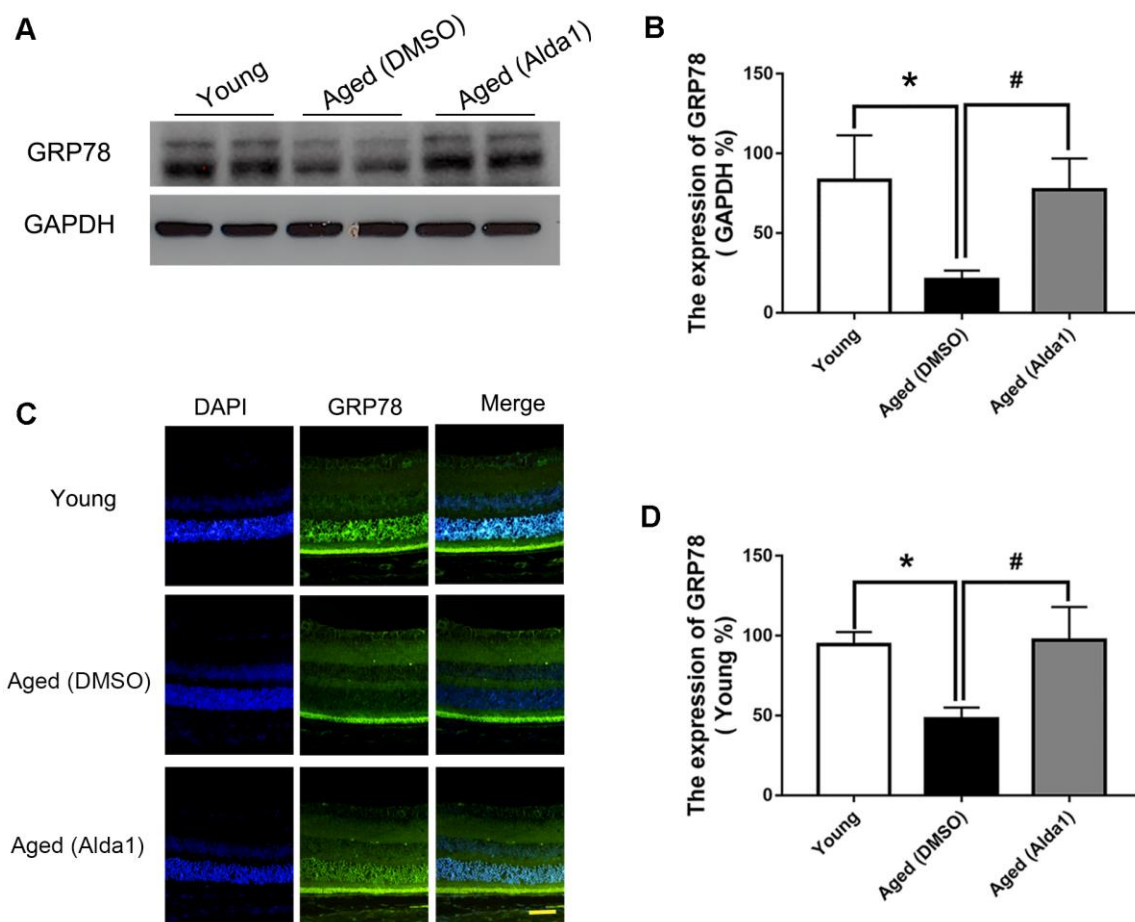


Figure 9. The expression of GRP78 in Alda1-treated mice during the normal aging process. (A, B) A typical WB image of GRP78 and the confirmation of GRP78 expression by WB; (C, D) A typical immunofluorescence image of GRP78 and the confirmation of GRP78 expression by immunofluorescence. Scale bar: 50 μ m. All analyses were performed in duplicate. Values are presented as the mean \pm SD, $n = 4$ mice per group. * $P<0.05$: aged (DMSO) and aged (Alda1) vs young; # $P<0.05$: aged (Alda1) vs aged (DMSO).

Additionally, the expressions of CHOP, caspase12 and caspase9 was with those in the young group (all $P<0.05$). Additionally, the expressions of CHOP, caspase12 and caspase9 was decreased in the aged (Alda1) group compared with those in the aged (DMSO) group (all $P<0.05$) (Figure 11E–11H).

DISCUSSION

The aging process is accompanied by the hypofunction of retinal cells, and specific interventions that could preserve retinal function are highly desired. Here we confirmed a reduction of retinal function and structure during the natural aging process. More importantly, we found that ALDH2 could effectively improve the aged mice retina, and the potential mechanism might be related with a decreased oxidative stress induced apoptosis activity and an enhanced UPR^{ER}.

Recent studies have explored the reduction of retinal function and structure in clinical and animal studies during the aging process. Specifically, clinical studies found a prolonged implicit time and declining OPs and b wave (dark-adaptation 3.0 response) amplitudes by 40 years of age [23]. Compared with the younger group, the b wave (dark-adaptation 3.0 response) amplitudes showed 25-40% smaller and longer implicit times [24]. Moreover, the bleaching restoration (dark adaptation ability) of amplitude was slower in older subjects [25]. Moreover, a recent study found that retinal thickness was reduced by 0.24 μm for every year with aging [26]. In a study of aging mice, it was found that aging disease-free retina underwent a reduction of photoreceptor density and ERG amplitudes [27]. It was found that aging was associated with a decrease in thickness of the photoreceptor layer [28]. Additionally, a reduction in the retinal nerve fibre layer (RNFL) thickness were correlated with increasing age [29].

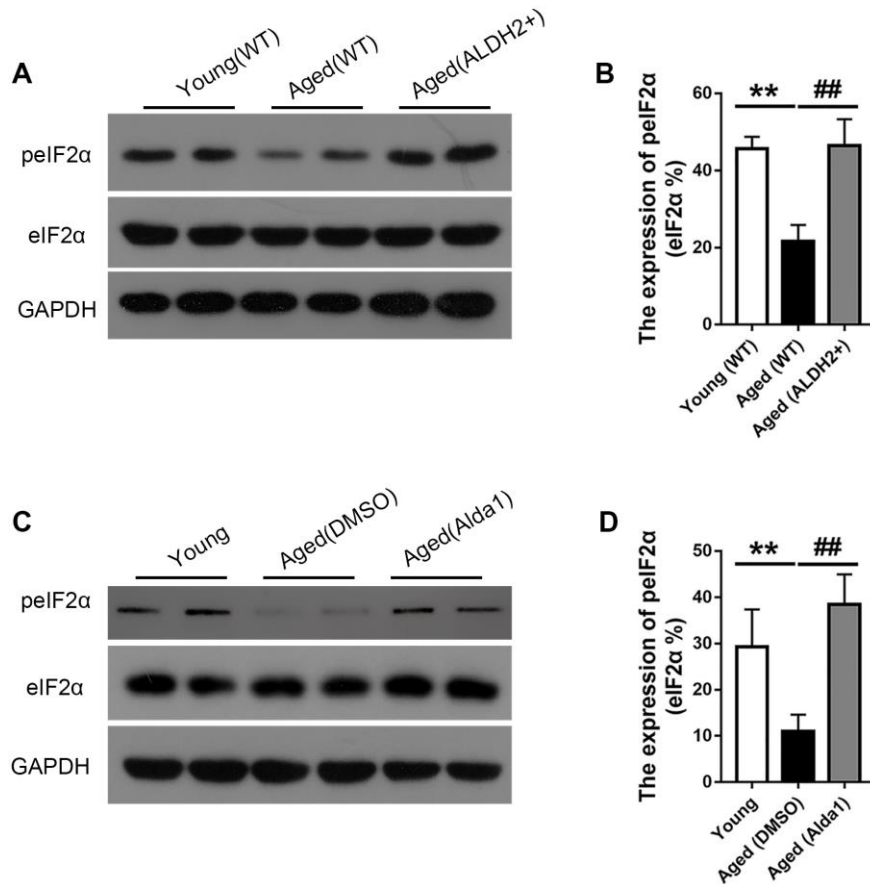


Figure 10. The expression of eIF2 α and pelf2 α in aged ALDH2 overexpression mice and aged Alda1-treated mice. (A) A typical WB image of eIF2 α and pelf2 α in aged ALDH2 overexpression mice; (B) The expression of pelf2 α /eIF2 α in aged ALDH2 overexpression mice; (C) a typical WB image of eIF2 α and pelf2 α in aged Alda1-treated mice; (D) The expression of pelf2 α /eIF2 α in aged Alda1-treated mice. All analyses were performed in duplicate. Values are presented as the mean \pm SD, n = 4 mice per group. ** $P<0.01$: aged (WT) group and aged (ALDH2+) group vs young (WT) group or aged (DMSO) group and aged (Alda1) group vs Young group; ## $P<0.01$: aged (ALDH2+) group vs aged (WT) group or aged (Alda1) group vs aged (DMSO) group.

During the aging process, functional protein, DNA and RNA, suffer from accumulated chronic oxidative damage, leading to mitochondrial dysfunction, cell apoptosis and endoplasmic reticulum dysfunction. As we known the endoplasmic reticulum (ER) could play essential roles in folding and transporting protein. When faced with unfolded or misfolded proteins, endoplasmic reticulum chaperone proteins, especially BiP/GRP78, would initiate correct protein folding. Recent studies have found a decrease of UPR^{ER}-related proteins in the patients with aging diseases [30]. These ER chaperones encounter with oxidative damage, which may limit their ability to perform appropriate protein folding and therefore reduce the ability of the UPR^{ER} to regulate protein homeostasis [31, 32]. Among the ER stress pathways, GRP78 is a master regulator of the UPR^{ER} by handling abnormal proteins to recover ER homeostasis [33]. Therefore, the aging process is associated with a prominent reduction in the buffering capacity of the

protein homeostasis network [34]. Moreover, studies have confirmed that the ability to activate the UPR^{ER} declined along with aging, while its constitutive activation could extend longevity [35]. For retinas, the activation of UPR^{ER} is a protective response to abnormal protein accumulation that ultimately restricts photoreceptor cell death [36]. And overexpression of GRP78 could regulate the UPR^{ER} and preserve photoreceptor function [37]. Moreover, increasing expression of GRP78 could downregulate the key proapoptotic cascade activator CHOP [38].

Our studies showed that the UPR^{ER} remained deficient for successful disposing of abnormal proteins during the aging process. Related studies have shown that wild type aged mouse retinas showed a significant reduction basal level of X-box Binding Protein 1 spliced (XBP1s), a key ERS signalling pathway downstream protein, and decreased activation of the UPR^{ER}. Moreover, XBP1s

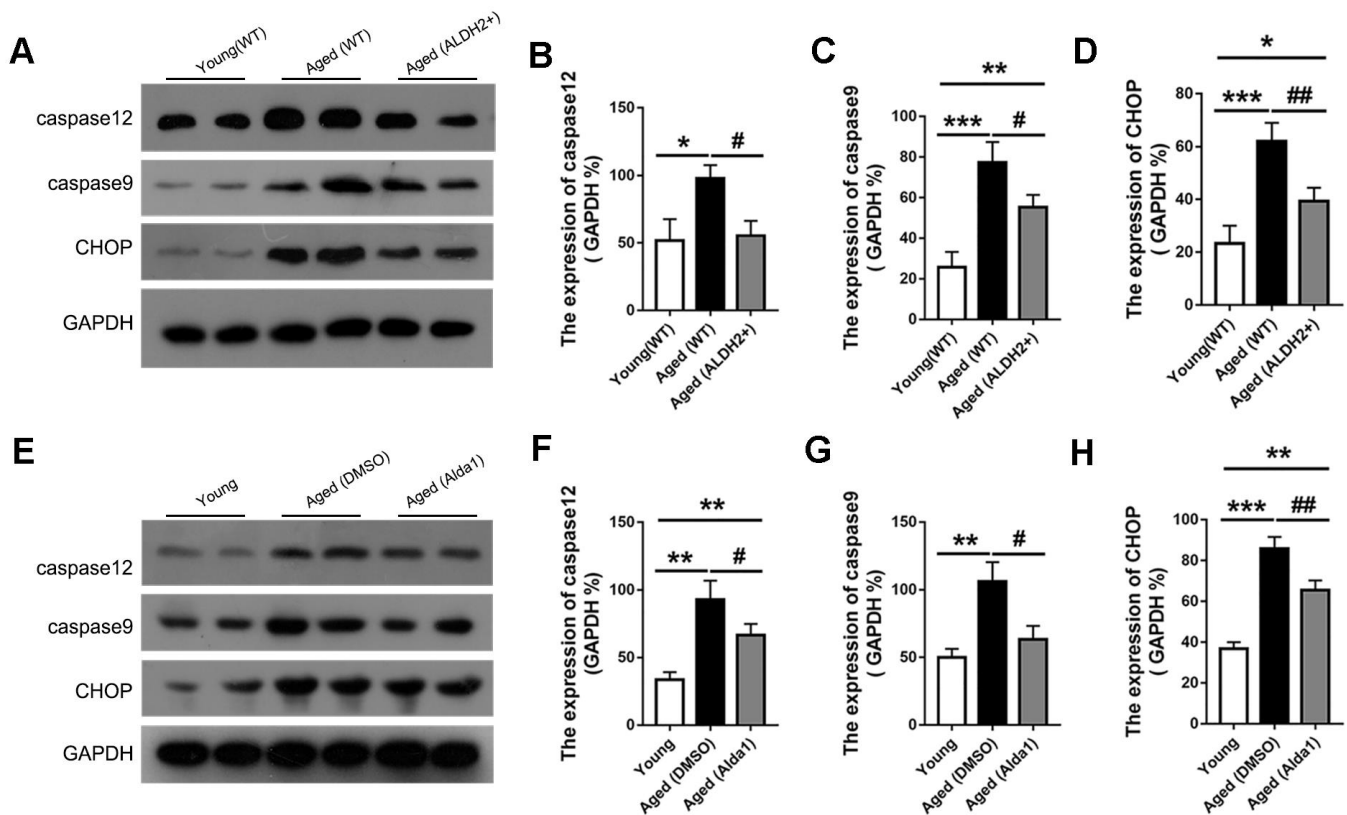


Figure 11. The expression of apoptosis related proteins in aged ALDH2 overexpression and aged Alda1-treated mice. (A) A typical WB image of CHOP, caspase9 and caspase12 in aged ALDH2 overexpression mice; (B–D) The expression of CHOP, caspase9 and caspase12 in aged ALDH2 overexpression mice; (E) A typical WB picture of CHOP, caspase9 and caspase12 in aged Alda1-treated mice; (F–H) The expression of CHOP, caspase9 and caspase12 in aged Alda1-treated mice. All analyses were performed in duplicate. Values are presented as the mean \pm SD, n = 4 mice per group. * $P < 0.05$: aged (WT) and aged (ALDH2+) vs young (WT) or Aged (DMSO) and aged (Alda1) vs young; ** $P < 0.01$: aged (WT) and aged (ALDH2+) vs young (WT) or Aged (DMSO) and aged (Alda1) vs young; *** $P < 0.001$: aged (WT) and aged (ALDH2+) vs young (WT) or Aged (DMSO) and aged (Alda1) vs young; # $P < 0.05$: aged (ALDH2+) vs aged (WT) or aged (Alda1) vs aged (DMSO), ## $P < 0.01$: aged (ALDH2+) vs aged (WT) or aged (Alda1) vs aged (DMSO).

KO mice showed significant retinal layer thinning and retinal ganglion cell (RGC) loss, as well as functional defects at 12-14 months of age [39]. To our knowledge, the UPR^{ER} is characterized by acute UPR^{ER} induced by hypoxia, nutrient deprivation, increased protein oxidation, and a disturbance of the secretory pathway, and chronic UPR^{ER} induced especially by the senescence process. Acute UPR^{ER}, with stronger and uncontrolled features, could lead to cell death, while chronic UPR^{ER}, with limited and insufficient features, could also trigger cell apoptosis through the CHOP and caspase12 pathways [35]. Furthermore, metabolism studies have shown that aging mice have diminished ERG responses and a reduced number of photoreceptors [40].

In this study, ALDH2 could effectively prevent the decline in retinal function and structure damage, as confirmed both by ALDH2 overexpression mice and intervention with the ALDH2 agonist Alda1. It is well-known that ALDH2 possesses potential roles of protecting cellular bioactive molecules, such as DNA, RNA and protein, from the damage of toxic aldehydes. Therefore, ALDH2 could decrease the production of unfolded or misfolded protein. As a result, in different stages of life or diverse diseases, the key roles of ALDH2 could differ during their involvement in the UPR^{ER} process. In the early stage of life, ALDH2 mainly sustains cell protein homeostasis by reducing unfolded or misfolded protein production, and thus the activation of ALDH2 could decelerate the progression of diseases such as atherosclerosis via decreasing ERS and apoptosis [41]. Recent studies have revealed that ALDH2 overexpression could effectively antagonize chronic alcohol intake-induced cardiac injury and contractile defects via decreasing ERS-related cell apoptosis [42]. In contrast, ALDH2 deficiency aggravates cardiac dysfunction with an accumulation of abnormal protein, leading to an increase in related cell apoptosis [43]. However, during the aging process, ALDH2 could enhance the UPR^{ER} to improve the ability to correct the activity of unfolded or misfolded protein. Our study showed that ALDH2 effectively preserved the UPR^{ER} by protecting the molecular chaperone GRP78 away from the sustained oxidative stress injury, thus improving cell survival ability. Unfortunately, the accurate regulatory mechanisms of ALDH2 in the aging process are still unclear. We could be certain that during the aging process, the expression levels of retinal CHOP, caspase12 and caspase9 were increasing and retinal inflammatory factor, including IL-1, IL-6 and TNF- α expression were enhanced. And ALDH2 could attenuate those hazardous substances expression, therefore alleviate aging retina oxidative damage and free radical attack by eliminating oxidizing substances, especially organic peroxides. The potential aging retina protective effect of ALDH2 could include: 1. Participate in

sustaining mitochondria homeostasis to reduce the production of peroxide; 2. Regulate nuclear gene expression (our additional data showed ALDH2 could interact with histone deacetylase); 3. Influence cell stress response in ER or ribosome.

In the present study, overexpression of ALDH2 and treatment with the ALDH2 agonist Alda1 in aging mice could both result in good retinal function and structural integrity via attenuating oxidative stress and apoptosis, and enhancing UPR^{ER}. Therefore, an increasing expression of ALDH2 could serve to preserve retinal function during the normal aging process or the onset of age-related retinal disease.

MATERIALS AND METHODS

Animals

Healthy male young C57/B6 mice (6-8 weeks old) made up the young (WT) group. Healthy male aged C57/B6 mice (72-80 weeks old) made up the aged (WT) group. Healthy male aged C57/B6 mice (72-80 weeks old) and aged *ALDH2*⁺ C57/B6 mice (72-80 weeks old) made up the aged (WT) group and aged (ALDH2⁺) group, respectively. These mice were selected to directly examine retinal function and structure *in vivo* and ERS, apoptosis proteins and inflammatory factor *in vitro*. Furthermore, mice (48-56 weeks old) were subjected to (N-[1,3-benzodioxol-5-ylmethyl]-2,6-dichlorobenzamide) Alda1 (Molecular Weight: 324.16; Formula: C₁₅H₁₁Cl₂NO₃) (MedChemExpress, USA) (10 mg/kg, 50% DMSO: 50% H₂O) [44] or DMSO, as the aged (Alda1) group and the aged (DMSO) group, via daily intraperitoneal injection for 24 weeks. Moreover, young C57/B6 mice (6-8 weeks old) served as the young group. After the last treatment, retinal function and structures *in vivo* and ERS, apoptosis proteins and inflammatory factor *in vitro* were examined. Young mice were purchased from the Laboratory Animal Center of the Fourth Military Medical University (license: 2014270138S). Aged mice were purchased from Beijing Vital River Laboratory Animal Technology Co., Ltd. (license: SCXK2016-0006). ALDH2 overexpression C57/B6 mice (transgenic mice controlled by EF1 α and chicken β -actin promoters) were obtained from professor Ren Jun (Center for Cardiovascular Research and Alternative Medicine, School of Pharmacy, University of Wyoming College of Health Sciences).

All animals were raised under clean laboratory conditions (temperature: 23° C \pm 3° C; 12-h light/ 12-h dark cycles). All animals in the experiments were handled in accordance with the Association for Research in Vision and Ophthalmology (ARVO) Statements for the use of Animals in Ophthalmic and

Vision Research. All protocols were approved by the research ethics committee for the care of laboratory animals at Fourth Military Medical University, and the experiments were conducted in accordance with its guidelines for experimental animals.

Electroretinography

ERG measurements were performed as described previously [45]. Briefly, the animals were placed in a dark environment for 12 hours, and all operation processes were recorded under dim red-light conditions. Mice were anaesthetized with 3 mL/kg 1% sodium pentobarbital (Sigma, St Louis, MO, USA) and 50 μ L sumianxin II (Jilin Shengda Animal Pharmaceutical Co., Ltd., Jilin, China) via intraperitoneal administration. Tropicamide-phenylephrine ophthalmic solution (Shenyang Xingji Corporation, Shenyang, Liaoning Province, China) was used to dilate the mouse pupil. ERG was recorded by full-field stimulation using a computer system (RETI port; Roland Consult GmbH, Brandenburg, Germany) equipped with international standards for visual electrophysiology (ISEVE) procedures. Moreover, a silver chloride electrode was placed at the centre of the cornea as the recode electrode. Stainless steel needle electrodes placed in the cheek and tail served as the reference and ground electrodes, respectively. We analysed the b wave (dark-adaptation 3.0 response) and dark-adaptation oscillatory potentials. Levofloxacin eye drops (Shenyang Xingji Corporation, Shenyang, Liaoning Province, China) were used three times a day after ERG testing to avoid infection.

OCT, fundus photograph and FFA detection

The mice were anaesthetized as described before and corresponding optical coherence tomography (OCT) scans were performed using a Micron IV fundus camera and an OCT Scan Head equipped with a mouse objective lens. Right eyes were dilated with 0.5% tropicamide, and Gatifloxacin Eye Gel (Shenyang Xingji Corporation, Shenyang, Liaoning Province, China) was used to protect the corneas. Fundus and OCT images were captured from 20 positions for each eye using a Retinal Imaging System (OPTO-RIS, Optoprobe, Canada) and 4D-ISOCT Microscope Imaging System (ISOCT, Optoprobe, Canada). The original OCT data were analysed by using OCT Image Analysis software (Version 2.0, Optoprobe, Canada). Moreover, FFA was applied to detect retinal vessel microcirculation function by HRAplusII (Ger) after injecting 0.1 mL/100 g 10% fluorescence sodium (Baiyunshan Mingxing Corporation, Guangzhou, Guangdong Province, China) via intraperitoneal injection (Figure 4E). The sodium fluorescein

intravenous imaging time was recorded to evaluate retinal vessel function.

HE staining

Mice were euthanized with an overdose of sodium pentobarbital and the eyes of the mice were rapidly removed, and HE staining was implemented as we described previously [46]. Specifically, the eyes used for histological analysis were kept immersed for 24 h at 4° C in 4% paraformaldehyde. Three paraffin-embedded sections (thickness, 4 μ m) were prepared and subjected to HE staining. Light microscope images were obtained using a digital imaging system (DP71, Olympus, Japan). The numbers of outer nuclear layer (ONL) and inner nuclear layer (INL) cell layers were then counted.

Immunofluorescence staining

Eye paraffin sections were deparaffinized and dehydrated. Endogenous peroxidase activity was blocked with 3% H₂O₂ for 15 min followed by 3 washes with phosphate-buffered saline (PBS: 0.1 mM, pH 7.2) at room temperature every 5 minutes. Antigen was retrieved by boiling (100° C) in citric acid buffer (PH 6.0) for 20 min and addition of 10% goat serum (including 0.3% Triton) for 1 h at room temperature to block non-specific labelling. Then, the sections were incubated overnight at 4° C with primary antibody against GRP78 (Proteintech, 11587-1-AP, Wuhan, Hubei Province) at a 1:200 dilution and ALDH2 (Abcam, ab108306, Cambridge, MA) at a 1:200 dilution. Slides incubated without any primary antibody served as the control. The slides were washed 3 times with PBS and incubated for 1 h with the IgG (H+L), Alexa Fluor 488 fluorescence secondary antibody (Zhuangzhi, EK021, Xi'an, Shaanxi Province, China) at a 1:400 dilution. Nuclei were stained by incubating the sections in a 100 ng/mL DAPI after 3 rinses with PBS. Images of the slides were captured under a fluorescence microscope (BX53, Olympus, Japan).

Western blot detection

Mice retinal tissues were separated and extracted on ice in RIPA buffer (Beyotime, Nantong, Jiangsu Province, China). The mixtures were then centrifuged at 12,000 rpm at 4° C for 15 min to collect the supernatant. A bicinchoninic acid (BCA) protein assay kit (Beyotime, Nantong, Jiangsu Province, China) was applied to calculate the concentration of the protein sample. An equal amount of protein was denatured by boiling with loading sample buffer followed by loading and separation of 25 μ g protein by sodium dodecyl sulphate-polyacrylamide gel electrophoresis. Next, the protein was transferred onto a 0.22 μ m PVDF membrane at 100 V for 90 min. The membranes were incubated with 5% non-fat

milk solution (Sangon Biotech Co., Ltd, Shanghai, China) for 1 h at room temperature and then reacted with ALDH2 (Abcam, ab108306, Cambridge, MA) at a 1:1000 dilution, eIF2 α (Abcam, ab169528, Cambridge, MA) at a 1:500 dilution, phospho-eIF2 α (Ser51) (Cell Signaling Technology, #3398, Danvers, MA) at a 1:1000 dilution, caspase9 (Cell Signaling Technology, D11A8, Danvers, MA) at a 1:500 dilution, caspase12 (Proteintech, 10380-1-AP, Wuhan, Hubei Province, China) at a 1:1000 dilution, GRP78 (Proteintech, 11587-1-AP, Wuhan, Hubei Province, China) at a 1:1000 dilution, and CHOP (Cell Signaling Technology, #5554, Danvers, MA) and GAPDH (Zhuangzhi Bioscience Technology Company, Xi'an, Shaanxi Province, China) at a 1:1000 dilution at 4° C overnight. The membranes were then incubated with the HRP-conjugated secondary antibody (Zhuangzhi Bioscience Technology Company, #EK020, Xi'an, Shaanxi Province, China) at a 1:10000 dilution at room temperature for 1 h, and then enhanced chemiluminescence was used for protein visualization. The intensity of immunoreactivity was quantified by densitometry using ImageJ software.

ELISA

Retinal tissues were collected and interleukin-1 (IL-1), interleukin-6 (IL-6) and tumor necrosis factor- α (TNF- α) levels in retinas were estimated using commercially available enzyme-linked immunosorbent assay (ELISA) kit (Westang Bio-Tech Co., LTD, Shanghai, China) according to the manufacturer's instructions.

Statistical analyses

Statistical analyses were performed using analysis of variance (ANOVA) followed by Bonferroni's post hoc analysis to examine the differences among all groups. Quantitative data are presented as the mean \pm standard deviation (SD), and $p \leq 0.05$ was considered statistically significant.

Abbreviations

AD: Alzheimer's disease; AGEs: advanced glycation end products; ALDH2: acetaldehyde dehydrogenase2; ARVO: Association for Research in Vision and Ophthalmology; ATF6: activating transcription factor 6; BiP: immunoglobulin heavy chain binding protein; CHOP: C/EBP homologous protein; DR: diabetic retinopathy; ERG: electroretinography; ERS: endoplasmic reticulum stress; FFA: fluorescence fundus angiography; GRP78: glucose-regulated protein 78; INL: inner nuclear layer; IPL: inner plexiform layer; IRE1: inositol requiring element-1; IS/OS: inner segment/outer segment; ISEVE: International Standards for Visual Electrophysiology; OCT: optical coherence

tomography; ONL: outer nuclear layer; OPL: outer plexiform layer; OPs: oscillatory potentials; OS: oxidative stress; PD: Parkinson's disease; PERK: protein kinase R-like endoplasmic reticulum kinase; RNFL: retinal nerve fibre layer; RP: retinitis pigmentosa; RPE: retinal pigment epithelium; UPR^{ER}: unfolded protein response in the endoplasmic reticulum.

AUTHOR CONTRIBUTIONS

Zuoming Zhang, Wei Ge, Tao Chen and Siwang Wang conceived and designed the experiments; Pan Long, Mengshan He and Weiming Yan performed the experiments and analysed the data; Dongyu Wei and Wei Chen contributed reagents/materials/analysis tools; Pan Long and Mengshan He drafted the paper, which was reviewed by all authors. All authors read and approved the final manuscript.

CONFLICTS OF INTEREST

The authors declare that there are no conflicts of interest.

FUNDING

This work was supported by the Natural Science Foundation of China (grant no. 82001484 and 81471409) and a Foundation of Key Research Plan of Shaanxi Province, China (grant no. 2017ZDXM-SF-023).

REFERENCES

1. Melchiorretto EF, Zeni M, Veronez DA, Martins EL, Fraga R. Quantitative analysis of the renal aging in rats. Stereological study. *Acta Cir Bras.* 2016; 31:346–52.
<https://doi.org/10.1590/S0102-865020160050000009>
PMID:27275857
2. Isaev NK, Genrikhs EE, Oborina MV, Stelmashook EV. Accelerated aging and aging process in the brain. *Rev Neurosci.* 2018; 29:233–40.
<https://doi.org/10.1515/revneuro-2017-0051>
PMID:29150992
3. Harris J, Subhi Y, Sørensen TL. Effect of aging and lifestyle on photoreceptors and retinal pigment epithelium: cross-sectional study in a healthy Danish population. *Pathobiol Aging Age Relat Dis.* 2017; 7:1398016.
<https://doi.org/10.1080/20010001.2017.1398016>
PMID:29152163
4. Escobar KA, Cole NH, Mermier CM, VanDusseldorp TA. Autophagy and aging: maintaining the proteome through exercise and caloric restriction. *Aging Cell.* 2019; 18:e12876.

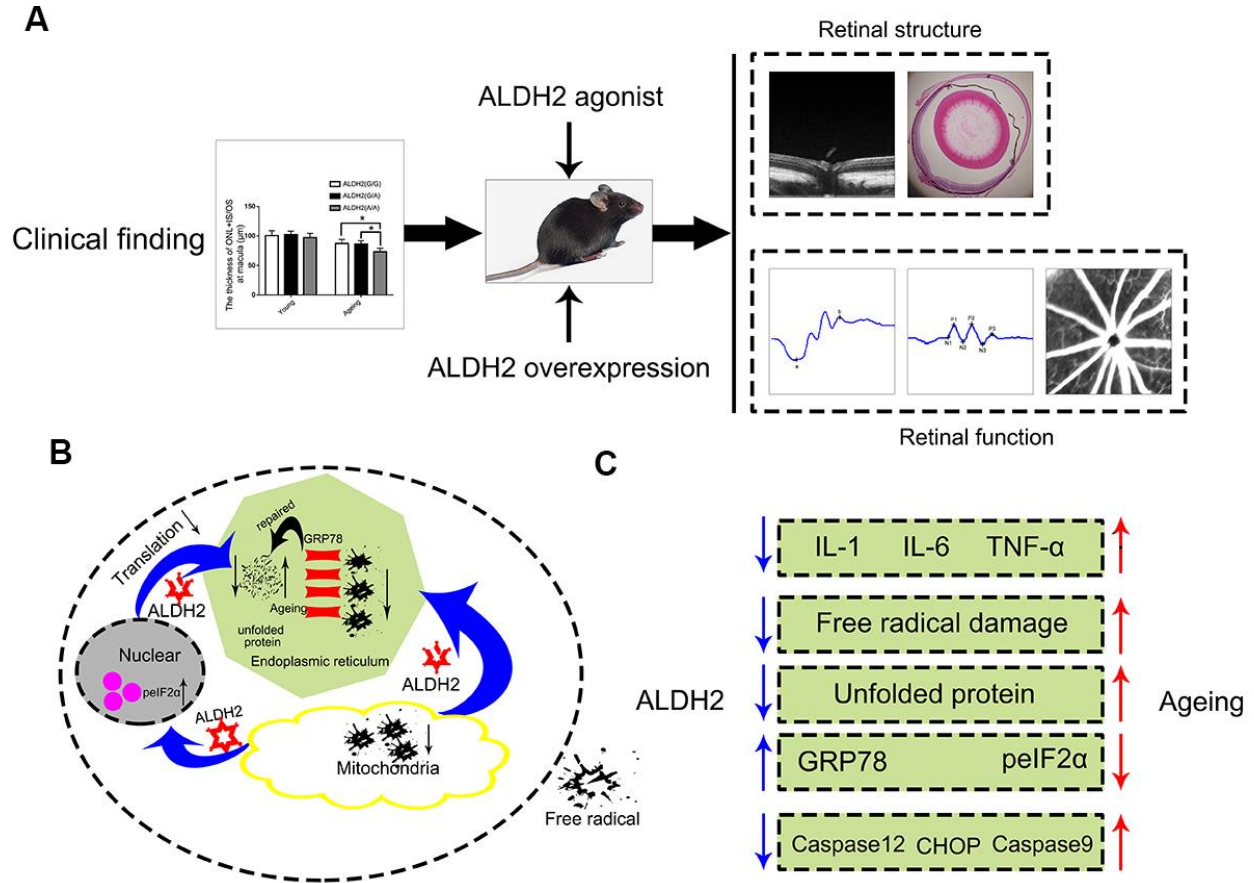
- <https://doi.org/10.1111/ace1.12876>
PMID:30430746
5. Morimoto RI, Cuervo AM. Proteostasis and the aging proteome in health and disease. *J Gerontol A Biol Sci Med Sci*. 2014 (Suppl 1); 69:S33–38.
<https://doi.org/10.1093/gerona/glu049>
PMID:24833584
 6. Kelly K, Wang JJ, Zhang SX. The unfolded protein response signaling and retinal müller cell metabolism. *Neural Regen Res*. 2018; 13:1861–70.
<https://doi.org/10.4103/1673-5374.239431>
PMID:30233053
 7. Beaupere C, Labunskyy VM. (un)folding mechanisms of adaptation to ER stress: lessons from aneuploidy. *Curr Genet*. 2019; 65:467–71.
<https://doi.org/10.1007/s00294-018-0914-9>
PMID:30511161
 8. Yang SY, Wei FL, Hu LH, Wang CL. PERK-eIF2 α -ATF4 pathway mediated by endoplasmic reticulum stress response is involved in osteodifferentiation of human periodontal ligament cells under cyclic mechanical force. *Cell Signal*. 2016; 28:880–86.
<https://doi.org/10.1016/j.cellsig.2016.04.003>
PMID:27079961
 9. Song S, Tan J, Miao Y, Li M, Zhang Q. Crosstalk of autophagy and apoptosis: involvement of the dual role of autophagy under ER stress. *J Cell Physiol*. 2017; 232:2977–84.
<https://doi.org/10.1002/jcp.25785> PMID:28067409
 10. Kroeger H, Chiang WC, Felden J, Nguyen A, Lin JH. ER stress and unfolded protein response in ocular health and disease. *FEBS J*. 2019; 286:399–412.
<https://doi.org/10.1111/febs.14522>
PMID:29802807
 11. Shi S, Tan P, Yan B, Gao R, Zhao J, Wang J, Guo J, Li N, Ma Z. ER stress and autophagy are involved in the apoptosis induced by cisplatin in human lung cancer cells. *Oncol Rep*. 2016; 35:2606–14.
<https://doi.org/10.3892/or.2016.4680>
PMID:26985651
 12. Paz Gavilán M, Vela J, Castaño A, Ramos B, del Río JC, Vitorica J, Ruano D. Cellular environment facilitates protein accumulation in aged rat hippocampus. *Neurobiol Aging*. 2006; 27:973–82.
<https://doi.org/10.1016/j.neurobiolaging.2005.05.010>
PMID:15964666
 13. van der Harg JM, van Heest JC, Bangel FN, Patiwaal S, van Weering JR, Scheper W. The UPR reduces glucose metabolism via IRE1 signaling. *Biochim Biophys Acta Mol Cell Res*. 2017; 1864:655–65.
<https://doi.org/10.1016/j.bbamcr.2017.01.009>
PMID:28093214
 14. Mohamed MEI, El-Shaarawy EAA, Youakim MF, Shuaib DMA, Ahmed MM. Aging changes in the retina of male albino rat: a histological, ultrastructural and immunohistochemical study. *Folia Morphol (Warsz)*. 2019; 78:237–58.
<https://doi.org/10.5603/FM.a2018.0075>
PMID:30155876
 15. Li SY, Gilbert SA, Li Q, Ren J. Aldehyde dehydrogenase-2 (ALDH2) ameliorates chronic alcohol ingestion-induced myocardial insulin resistance and endoplasmic reticulum stress. *J Mol Cell Cardiol*. 2009; 47:247–55.
<https://doi.org/10.1016/j.yjmcc.2009.03.017>
PMID:19344727
 16. Xue L, Cui S, Cui Z, Yang F, Pang J, Xu F, Chen Y. ALDH2: a new protector against age-independent myocardial senescence. *Int J Cardiol*. 2016; 210:38–40.
<https://doi.org/10.1016/j.ijcard.2016.02.098>
PMID:26925921
 17. Cheng X, Xu J, Gu M, Wang M, Sun B, Li Z, Ni G, Wang G, Weng Z, Shi Y, Zhang Z, Liu X. Genetic variants in ALDH2 predict risk of ischemic stroke in a Chinese population. *Gene*. 2018; 678:49–54.
<https://doi.org/10.1016/j.gene.2018.08.002>
PMID:30077765
 18. Li GY, Li ZB, Li F, Dong LP, Tang L, Xiang J, Li JM, Bao MH. Meta-analysis on the association of ALDH2 polymorphisms and type 2 diabetic mellitus, diabetic retinopathy. *Int J Environ Res Public Health*. 2017; 14:165.
<https://doi.org/10.3390/ijerph14020165>
PMID:28208752
 19. Morita K, Saruwatari J, Miyagawa H, Uchiyashiki Y, Oniki K, Sakata M, Kajiwara A, Yoshida A, Jinnouchi H, Nakagawa K. Association between aldehyde dehydrogenase 2 polymorphisms and the incidence of diabetic retinopathy among Japanese subjects with type 2 diabetes mellitus. *Cardiovasc Diabetol*. 2013; 12:132.
<https://doi.org/10.1186/1475-2840-12-132>
PMID:24028448
 20. Deza-Ponzio R, Herrera ML, Bellini MJ, Virgolini MB, Hereñú CB. Aldehyde dehydrogenase 2 in the spotlight: the link between mitochondria and neurodegeneration. *Neurotoxicology*. 2018; 68:19–24.
<https://doi.org/10.1016/j.neuro.2018.06.005>
PMID:29936317
 21. He M, Long P, Yan W, Chen T, Guo L, Zhang Z, Wang S. ALDH2 attenuates early-stage STZ-induced aged diabetic rats retinas damage via Sirt1/Nrf2 pathway. *Life Sci*. 2018; 215:227–35.
<https://doi.org/10.1016/j.lfs.2018.10.019>
PMID:30315856

22. Yan W, Long P, Wei D, Yan W, Zheng X, Chen G, Wang J, Zhang Z, Chen T, Chen M. Protection of retinal function and morphology in MNU-induced retinitis pigmentosa rats by ALDH2: an in-vivo study. *BMC Ophthalmol.* 2020; 20:55. <https://doi.org/10.1186/s12886-020-1330-8> PMID:[32070320](https://pubmed.ncbi.nlm.nih.gov/32070320/)
23. Dimopoulos IS, Freund PR, Redel T, Dornstauder B, Gilmour G, Sauvé Y. Changes in rod and cone-driven oscillatory potentials in the aging human retina. *Invest Ophthalmol Vis Sci.* 2014; 55:5058–73. <https://doi.org/10.1167/iovs.14-14219> PMID:[25034601](https://pubmed.ncbi.nlm.nih.gov/25034601/)
24. Freund PR, Watson J, Gilmour GS, Gaillard F, Sauvé Y. Differential changes in retina function with normal aging in humans. *Doc Ophthalmol.* 2011; 122:177–90. <https://doi.org/10.1007/s10633-011-9273-2> PMID:[21562738](https://pubmed.ncbi.nlm.nih.gov/21562738/)
25. Messenio D, Marano G, Gerosa S, Iannelli F, Biganzoli EM. The influence of age on the recovery of the ERG photostress test. *Doc Ophthalmol.* 2013; 126:87–97. <https://doi.org/10.1007/s10633-012-9361-y> PMID:[23184310](https://pubmed.ncbi.nlm.nih.gov/23184310/)
26. Nieves-Moreno M, Martínez-de-la-Casa JM, Morales-Fernández L, Sánchez-Jean R, Sáenz-Francés F, García-Feijó J. Impacts of age and sex on retinal layer thicknesses measured by spectral domain optical coherence tomography with spectralis. *PLoS One.* 2018; 13:e0194169. <https://doi.org/10.1371/journal.pone.0194169> PMID:[29522565](https://pubmed.ncbi.nlm.nih.gov/29522565/)
27. Williams GA, Jacobs GH. Cone-based vision in the aging mouse. *Vision Res.* 2007; 47:2037–46. <https://doi.org/10.1016/j.visres.2007.03.023> PMID:[17509638](https://pubmed.ncbi.nlm.nih.gov/17509638/)
28. Chauhan BC, Vianna JR, Sharpe GP, Demirel S, Girkin CA, Mardin CY, Scheuerle AF, Burgoyne CF. Differential Effects of Aging in the Macular Retinal Layers, Neuroretinal Rim, and Peripapillary Retinal Nerve Fiber Layer. *Ophthalmology.* 2020; 127:177–85. <https://doi.org/10.1016/j.ophtha.2019.09.013> PMID:[31668716](https://pubmed.ncbi.nlm.nih.gov/31668716/)
29. Chen CY, Huang EJ, Kuo CN, Wu PL, Chen CL, Wu PC, Wu SH, King YC, Lai CH. The relationship between age, axial length and retinal nerve fiber layer thickness in the normal elderly population in Taiwan: the Chiayi eye study in Taiwan. *PLoS One.* 2018; 13:e0194116. <https://doi.org/10.1371/journal.pone.0194116> PMID:[29522558](https://pubmed.ncbi.nlm.nih.gov/29522558/)
30. Frakes AE, Dillin A. The UPR^{ER}: sensor and coordinator of organismal homeostasis. *Mol Cell.* 2017; 66:761–71. <https://doi.org/10.1016/j.molcel.2017.05.031> PMID:[28622521](https://pubmed.ncbi.nlm.nih.gov/28622521/)
31. Naidoo N, Ferber M, Master M, Zhu Y, Pack AI. Aging impairs the unfolded protein response to sleep deprivation and leads to proapoptotic signaling. *J Neurosci.* 2008; 28:6539–48. <https://doi.org/10.1523/JNEUROSCI.5685-07.2008> PMID:[18579727](https://pubmed.ncbi.nlm.nih.gov/18579727/)
32. Nakka VP, Prakash-Babu P, Vemuganti R. Crosstalk between endoplasmic reticulum stress, oxidative stress, and autophagy: potential therapeutic targets for acute CNS injuries. *Mol Neurobiol.* 2016; 53:532–44. <https://doi.org/10.1007/s12035-014-9029-6> PMID:[25482050](https://pubmed.ncbi.nlm.nih.gov/25482050/)
33. Gorbatyuk MS, Gorbatyuk OS. The molecular chaperone GRP78/BiP as a therapeutic target for neurodegenerative disorders: a mini review. *J Genet Syndr Gene Ther.* 2013; 4:128. <https://doi.org/10.4172/2157-7412.1000128> PMID:[23750325](https://pubmed.ncbi.nlm.nih.gov/23750325/)
34. Martínez G, Duran-Aniotz C, Cabral-Miranda F, Vivar JP, Hetz C. Endoplasmic reticulum proteostasis impairment in aging. *Aging Cell.* 2017; 16:615–23. <https://doi.org/10.1111/acer.12599> PMID:[28436203](https://pubmed.ncbi.nlm.nih.gov/28436203/)
35. Taylor RC. Aging and the UPR(ER). *Brain Res.* 2016; 1648:588–93. <https://doi.org/10.1016/j.brainres.2016.04.017> PMID:[27067187](https://pubmed.ncbi.nlm.nih.gov/27067187/)
36. Athanasiou D, Aguila M, Bellingham J, Kanuga N, Adamson P, Cheetham ME. The role of the ER stress-response protein PERK in rhodopsin retinitis pigmentosa. *Hum Mol Genet.* 2017; 26:4896–905. <https://doi.org/10.1093/hmg/ddx370> PMID:[29036441](https://pubmed.ncbi.nlm.nih.gov/29036441/)
37. Gorbatyuk MS, Knox T, LaVail MM, Gorbatyuk OS, Noorwez SM, Hauswirth WW, Lin JH, Muzyczka N, Lewin AS. Restoration of visual function in P23H rhodopsin transgenic rats by gene delivery of BiP/Grp78. *Proc Natl Acad Sci USA.* 2010; 107:5961–66. <https://doi.org/10.1073/pnas.0911991107> PMID:[20231467](https://pubmed.ncbi.nlm.nih.gov/20231467/)
38. Ghaderi S, Ahmadian S, Soheili ZS, Ahmadi H, Samiei S, Kheitan S, Pirmardan ER. AAV delivery of GRP78/BiP promotes adaptation of human RPE cell to ER stress. *J Cell Biochem.* 2018; 119:1355–67. <https://doi.org/10.1002/jcb.26296> PMID:[28782832](https://pubmed.ncbi.nlm.nih.gov/28782832/)
39. McLaughlin T, Falkowski M, Park JW, Keegan S, Elliott M, Wang JJ, Zhang SX. Loss of XBP1 accelerates age-related decline in retinal function and neurodegeneration. *Mol Neurodegener.* 2018; 13:16. <https://doi.org/10.1186/s13024-018-0250-z> PMID:[29615095](https://pubmed.ncbi.nlm.nih.gov/29615095/)

40. Wang Y, Grenell A, Zhong F, Yam M, Hauer A, Gregor E, Zhu S, Lohner D, Zhu J, Du J. Metabolic signature of the aging eye in mice. *Neurobiol Aging*. 2018; 71:223–33. <https://doi.org/10.1016/j.neurobiolaging.2018.07.024> PMID:30172221
41. Yang MY, Wang YB, Han B, Yang B, Qiang YW, Zhang Y, Wang Z, Huang X, Liu J, Chen YD, Ren J, Cao F, Xu Y. Activation of aldehyde dehydrogenase 2 slows down the progression of atherosclerosis via attenuation of ER stress and apoptosis in smooth muscle cells. *Acta Pharmacol Sin*. 2018; 39:48–58. <https://doi.org/10.1038/aps.2017.81> PMID:28858301
42. Pang J, Peng H, Wang S, Xu X, Xu F, Wang Q, Chen Y, Barton LA, Chen Y, Zhang Y, Ren J. Mitochondrial ALDH2 protects against lipopolysaccharide-induced myocardial contractile dysfunction by suppression of ER stress and autophagy. *Biochim Biophys Acta Mol Basis Dis*. 2019; 1865:1627–41. <https://doi.org/10.1016/j.bbadis.2019.03.015> PMID:30946956
43. Liao J, Sun A, Xie Y, Isse T, Kawamoto T, Zou Y, Ge J. Aldehyde dehydrogenase-2 deficiency aggravates cardiac dysfunction elicited by endoplasmic reticulum stress induction. *Mol Med*. 2012; 18:785–93. <https://doi.org/10.2119/molmed.2011.00466> PMID:22430940
44. Stachowicz A, Głombik K, Olszanecki R, Basta-Kaim A, Suski M, Lasoń W, Korbut R. The impact of mitochondrial aldehyde dehydrogenase (ALDH2) activation by alda-1 on the behavioral and biochemical disturbances in animal model of depression. *Brain Behav Immun*. 2016; 51:144–53. <https://doi.org/10.1016/j.bbi.2015.08.004> PMID:26254233
45. Yan W, Long P, Chen T, Liu W, Yao L, Ren Z, Li X, Wang J, Xue J, Tao Y, Zhang L, Zhang Z. A natural occurring mouse model with Adgrv1 mutation of usher syndrome 2C and characterization of its recombinant inbred strains. *Cell Physiol Biochem*. 2018; 47:1883–97. <https://doi.org/10.1159/000491068> PMID:29961073
46. Chen W, Guo J, Guo H, Kong X, Bai J, Long P. Protective effect of vitamin C against infancy rat corneal injury caused by acute UVB irradiation. *Biomed Res Int*. 2020; 2020:8089273. <https://doi.org/10.1155/2020/8089273> PMID:32596375

SUPPLEMENTARY MATERIALS

Supplementary Figure



Supplementary Figure 1. (A) Clinical finding and animal experiments both showed ald2 could sustain aging retinal structure integrity and upregulate aging retinal function; (B) The pattern diagram of the potential roles of ald2; (C) The specific opposite effects of ald2 and aging.

Exosomes derived from BDNF-expressing 293T attenuate ischemic retinal injury in vitro and *in vivo*

Bojing Yan¹, Lixin Gao¹, Yingxiang Huang¹, Xiaolei Wang¹, Xuqiang Lang¹, Fancheng Yan¹, Bo Meng¹, Xiaowei Sun², Genlin Li³, Yanling Wang¹

¹Department of Ophthalmology, Beijing Friendship Hospital, Capital Medical University, Beijing 100050, China

²Department of Ophthalmology, Yantai Yuhuangding Hospital Affiliated to Medical College of Qingdao University, Qingdao 264000, China

³Beijing Tongren Eye Center, Beijing Tongren Hospital, Capital Medical University, Beijing Ophthalmology and Visual Sciences Key Lab, Beijing 100730, China

Correspondence to: Genlin Li, Yanling Wang; **email:** ligenlin2018@163.com, <https://orcid.org/0000-0001-8926-3592>; wangyanling999@vip.sina.com

Keywords: retinal ischemia, exosome, brain-derived neurotrophic factor, endocytosis, apoptosis

Received: March 11, 2020

Accepted: June 4, 2020

Published: November 29, 2020

Copyright: © 2020 Yan et al. This is an open access article distributed under the terms of the [Creative Commons Attribution License](https://creativecommons.org/licenses/by/3.0/) (CC BY 3.0), which permits unrestricted use, distribution, and reproduction in any medium, provided the original author and source are credited.

ABSTRACT

Retinal ischemia emerges in many ocular diseases and is a leading cause of neuronal death and dysfunction, resulting in irreversible visual impairment. We previously reported that brain-derived neurotrophic factor (BDNF)-expressing human 293T cells could steadily express BDNF and play a protective role in ARPE-19 cells, a human retinal epithelial cell line. Thus, we hypothesized that exosomes might be essential in the interaction between BDNF-expressing 293T cells and recipient cells. The study investigated whether exosomes derived from BDNF-expressing 293T cells (293T-Exo) can be internalized by ischemic retinal cells and exert neuroprotective roles. The results demonstrated that 293T-Exo significantly attenuated the loss of cell proliferation and cell death in R28 cells in response to oxygen-glucose deprivation treatment. Mechanistic studies revealed that the endocytosis of 293T-Exo by R28 cells displayed dose- and temperature-dependent patterns and may be mediated by the caveolar endocytic pathway via the integrin receptor. In the retinal ischemia rat model, the administration of 293T-Exo into the vitreous humor of ischemic eyes reduced apoptosis in the retina. Furthermore, 293T-Exo was mainly taken up by retinal neurons and retinal ganglion cells. Together, the results demonstrated that 293T-Exo has a neuroprotective effect in retinal ischemia and has therapeutic potential for retinal disorders.

INTRODUCTION

Retinal ischemia-reperfusion (I/R) emerges in many ocular diseases and is a leading cause of neuronal death and dysfunction, resulting in irreversible visual impairment or blindness [1, 2]. Growing reports demonstrated that retinal ischemia is a primary contributor to the pathogenesis of multiple diseases, such as retinal vascular occlusions, diabetic retinopathy, central retinal vein occlusion, as well as age-associated macular degeneration [3]. However, an effective treatment for retinal ischemia is currently unknown,

which leads to an urgent need to investigate the mechanisms and develop therapeutic strategies for retinal ischemia.

During ischemia, the deficiency of oxygen and other essential nutritional compounds generates reactive oxygen species due to subsequent restoration of oxygen supply, eventually leading to an inflammatory response and neurodegeneration [4, 5]. To study ischemia injury, retinal I/R animal models, including *in vivo* and *ex vivo*, have been established and widely employed to study the effect of I/R on neuronal

impairment in the retina [6]. In these animal models, intraocular pressure is dramatically raised above the systolic pressure for a specified time, followed by reperfusion treatment. Thus, several manifestations of I/R injury have been uncovered in such models, for example, the loss of retinal ganglion cells (RGCs), increased apoptosis in the inner retina, and decreased b waves [7].

Exosomes, 30-150 nm in diameter, are bi-lipid membrane extracellular vesicles (EVs) [8]. Due to their endocytic origin, EVs are categorized as exosomes, which contrasts with microvesicles that are produced from apoptotic bodies originated from fragments of dying cells or budding of the plasma membrane [9]. Exosomes are synthesized and released by various cell types and transport active biological molecules to regulate the physiological activities of recipient cells [10]. Thus, exosomes play an essential role in intercellular communication [11]. Over the past few decades, a growing number of studies suggest that the therapeutic effect of exosomes can facilitate repair and regeneration in multiple tissues, such as the heart [12], liver [13], and brain [14]. For retinal ischemia, bone marrow mesenchymal stem cells (MSCs)-derived exosomes can successfully transfer functional microRNAs into inner retinal layers and exert neuroprotective and axogenic roles in RGCs [15]. In addition, intravitreal administration of exosomes originated from human MSCs are well-tolerated and play a protective effect on retinal ischemia in a mouse model [16]. Together, exosome-mediated approaches are promising therapeutic strategies for retinal ischemia.

As the critical mediator in intercellular communication, the interaction between exosomes and recipients' cells is involved in a series of complicated processes [17]. In general, there are three main mechanisms involved in the exosome uptake, including 1) fusion with the recipient cells to transfer functional molecules, 2) binding to the surface receptor to initiate signaling cascades, and 3) internalization through phagocytosis, endocytosis, and macro-pinocytosis [18–20]. Also, several reports suggest that exosome-uptake proteins on the surface of exosomes and recipient cells also play an essential role in intercellular communication. For example, integrins are required for the exosome uptake in dendritic cells [19]. Clathrin and caveolin-associated pathways are two essential ways related to the endocytosis of exosomes [21]. So far, very few studies focus on the mechanism regarding how retinal cells uptake exosomes derived exogenous cells. Therefore, understanding the mechanism of exosome uptake would promote the development of more efficient delivery systems for disease treatment.

Brain-derived neurotrophic factor (BDNF), a member of the nerve growth factor gene family, is an essential multi-functional factor in various neuronal processes, including learning and memory, dendritic and synaptic plasticity, and axonal growth [22]. Beyond that, BDNF also has a broad effect on neuroprotection and regeneration in several neurodegenerative disorders, such as Alzheimer's, Parkinson's, and Huntington's disease [23, 24]. In addition, BDNF-transfected iris pigment epithelial (IPE) cells show a neuroprotective role against *N*-methyl-d-aspartate (NMDA)-associated neuroretinal cell death and phototoxic damage [25]. As previously reported [26], we constructed a eukaryotic BDNF-expressing plasmid from the human retina, and then subsequently used it to transfect human 293T cells. Our observations revealed that 293T cells transfected with the BDNF gene could steadily express BDNF mRNA and secrete the protein. Also, after coculturing with ARPE-19 cells, a human retinal epithelial cell line, increased level of BDNF is associated with higher viability and lower apoptosis in ARPE-19 cells, suggesting the potential neuroprotective role of BDNF in the retina.

Beyond that, several questions also emerged in this previous study: for example, what is the detailed mechanism underlying the role of BDNF-expressing cells and recipient cells and the role of BDNF in other retinal diseases? Given this, we hypothesized that exosomes might be an essential molecule-shuttle between BDNF-expressing 293T cells and recipient cells. We aimed to determine whether exosomes derived from BDNF-expressing 293T cells can be internalized by retinal cells and exert neuroprotective roles following ischemic injury and identify the related mechanism.

RESULTS

Characterization of 293T-Exo derived from BDNF-expressing 293T cells

We previously created human retina-derived BDNF plasmid construct in 293T cells. Next, we cocultured BDNF-expressing 293T cells with ARPE-19 in a Transwell chamber for 96 hours, and found that BDNF-engineered 293T cells exerted anti-apoptotic roles [26]. Given that, we assumed the potential role of exosomes in the interaction between BDNF-expressing 293T cells and recipient cells. Thus, we first isolated 293T-Exo from BDNF-expressing 293T cells. By NTA and TEM assays, the results showed that a majority of 293T-Exo (98.6%) were 144.2 nm in diameter and displayed a classic round-shape morphology (Figure 1A, 1B). In addition, the exosome surface markers CD9, CD63, CD81, and HSP70 α were positively expressed in 293T-

Exo, but not in 293T-Exo-conditioned medium (Figure 1C). These results together demonstrated that we successfully isolated exosomes from BDNF-expressing 293T cells.

BDNF expression increased in 293T-Exo and 293T-Exo-treated R28 cells

Consistent with our previous results [26], mRNA and protein expressions of BDNF were increased in BDNF-expressing 293T cells compared with control untreated 293T cells (Figure 2A, 2B). Also, 293T-Exo expressed a higher level of BDNF than exosomes derived from control 293T cells (Figure 2A, 2B). After treating with 293T-Exo-conditioned medium or 293T-Exo, both mRNA and protein levels of BDNF were increased in R28 cells (Figure 2C, 2D), suggesting BDNF can be transferred from BDNF-expressing 293T cells to recipient R28 cells.

293T-Exo were endocytosed by R28 cells

As shown in Figure 3A, green fluorescence-labeled 293T-Exo was internalized by R28 cells. The overlapping of green color 293T-Exo with the red

cytoskeleton demonstrated that 293T-Exo was uptaken in the cytoplasm. To determine the factors impacting the efficacy of endocytosis, we used different volumes of 293T-Exo (1-64 μ l) to treat R28 cells, and the results suggested that the endocytosis reached a saturable status when the volume of 293T-Exo was 16 μ l (Figure 3B). Also, we observed that higher temperatures (37 $^{\circ}$ C) exerted a positive role in endocytosis, whereas low temperatures (4 $^{\circ}$ C) inhibited the internalization of 293T-Exo (Figure 3C). Collectively, these results suggested that the endocytosis of 293T-Exo by R28 cells exhibited dose- and temperature-dependent patterns.

Integrin and caveolin-1 participated in the endocytosis of 293T-Exo

To determine more details of the endocytic process of 293T-Exo, we first used the specific ligands to test several critical endocytic receptors on the R28 plasma membrane, such as integrin and heparin sulfate proteoglycans (HSPGs) [27]. After pretreating R28 cells with RGD peptide, a specific ligand for integrin, we found that the endocytosis was significantly inhibited while no impact was observed on endocytosis when

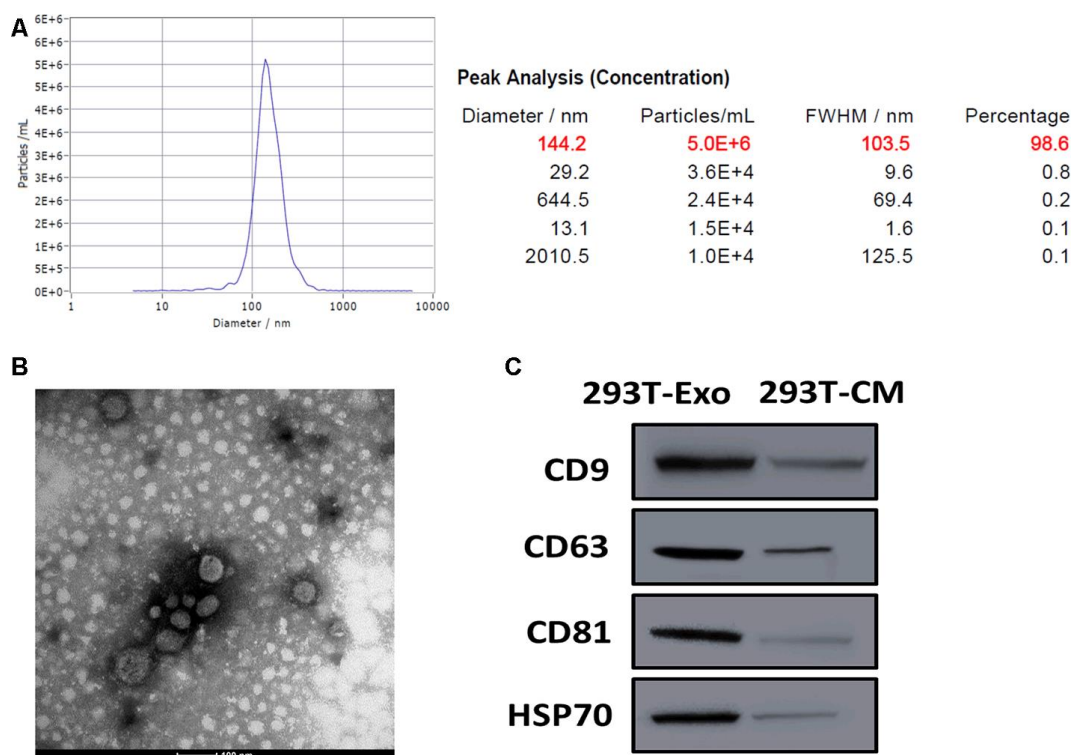


Figure 1. Characterization of 293T-Exo derived from BDNF-expressing 293T cells. (A) Diameter distribution of 293T-Exo determined by nanoparticle tracking analysis (NTA). (B) Representative image of 293T-Exo photographed by transmission electron microscopy (TEM). Scale bard = 100 nm. (C) Protein expressions of exosome surface markers, CD9, CD63, CD81, and HSP70 α in 293T-Exo and 293T-Exo-conditioned medium (293T-CM), as measured using western blots.

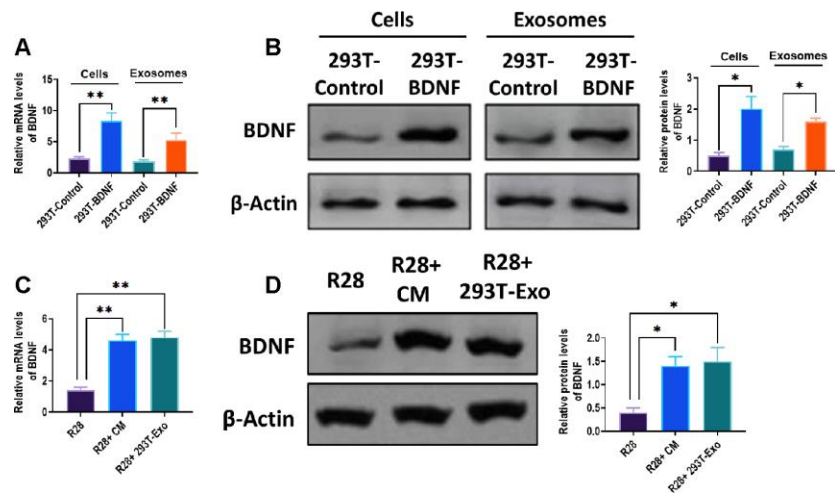


Figure 2. BDNF expression increased in 293T-Exo and 293T-Exo-treated R28 cells. mRNA (A) and protein (B) expressions of BDNF in control 293T cells, BDNF-expressing 293T cells, exosomes derived from control 293T cells, and BDNF-expressing 293T cells. mRNA (C) and protein (D) expressions in control R28 cells (R28), R28 cells treated with 293T-Exo-conditioned medium (R28+ CM), and R28 cells cocultured with 293T-Exo. Data are presented as mean \pm SD. * P < 0.05, ** P < 0.01.

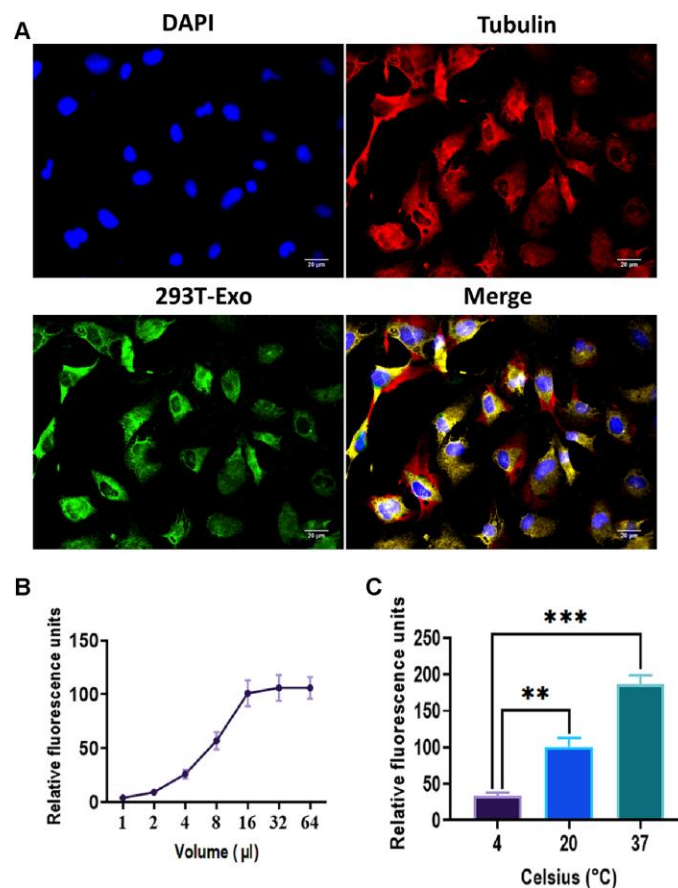


Figure 3. Endocytosis of 293T-Exo by R28 cells. (A) 293T-Exo uptake by R28 cells, as determined by the fluorescence assay. The nuclei were stained with DAPI (blue), the cytoskeleton was stained with tubulin (red), and 293T-Exo was stained with fluorescent-tag (green). Scale bar = 20 μ m. (B) Efficacy of endocytosis of 293T-Exo by R28 cells displayed a dose-dependent pattern and saturable (more than 16 μ l of 293T-Exo). (C) Efficacy of endocytosis of 293T-Exo by R28 cells displayed a temperature-dependent pattern. Data are presented as mean \pm SD. ** P < 0.01, *** P < 0.001.

R28 cells were pretreated with heparin, a ligand for HSPGs (Figure 4A). In addition, a dose-dependent pattern was found in the effect of RGD on endocytosis of 293T-Exo, but not in heparin (Figure 4B, 4C). Clathrin and caveolin are two main pathways of endocytosis [28], therefore, we labeled those two markers with red fluorescence and found that green-293T-Exo colocalized with caveolin-1, but not clathrin (Figure 5). Furthermore, we applied MBCD to block the caveolin-1-associated endocytic process [29]. The results revealed that the endocytosis of 293T-Exo could be inhibited by MBCD in a dose-dependent pattern (Figure 6A, 6B). Taken together, these results demonstrated the involvement of integrin and caveolin-1 pathways in the endocytosis of 293T-Exo.

293T-Exo reduced R28 cell death in response to oxygen-glucose deprivation (OGD) *in vitro*

The OGD is widely applied to mimic ischemic conditions *in vitro*, promoting cell death [30]. To determine the role of 293T-Exo in OGD-treated R28 cells, we applied the EdU assay to measure the proliferation of R28 cells in the

presence of OGD treatment. By flow cytometry analysis, we observed that both 293T-Exo and 293T-Exo-conditioned medium significantly increased the proliferative ability of R28 cells, compared with those treated with conditioned medium without 293T-Exo (Figure 7A). Meanwhile, the LDH assay showed that the reduction of cell death of OGD-treated R28 cells was accompanied by increasing doses of 293T-Exo (Figure 7B). These results together suggest a protective role of 293T-Exo for R28 cells in response to OGD.

Anti-apoptotic role of 293T-Exo *in vivo*

To determine whether 293T-Exo plays a protective role in retinal ischemia injury, we established a retinal ischemia rat model, and 293T-Exo was administered into the vitreous humor of ischemic eyes. Using the TUNEL assay, we observed that ischemia injury resulted in increased apoptosis in RGC, inner nuclear layers, and outer nuclear layers on the retinal tissue slides while the effect of ischemia injury was significantly attenuated by the administration of 293T-Exo (Figure 8A–8E).

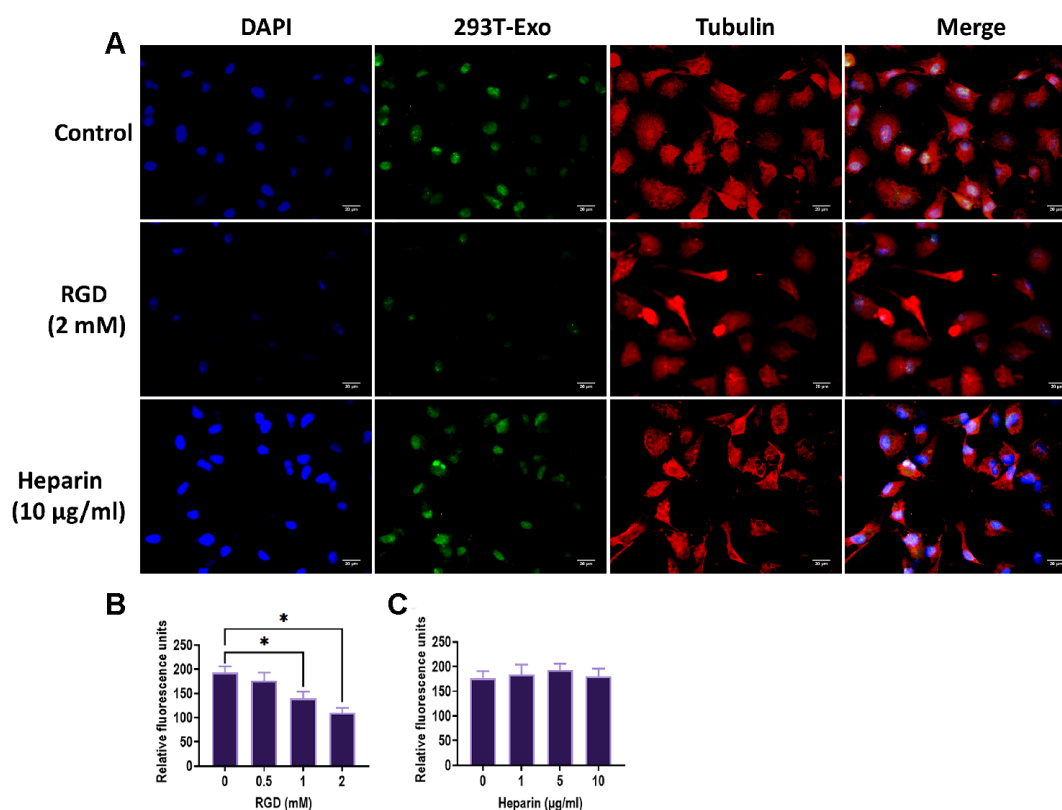


Figure 4. Integrins participated in the endocytosis of 293T-Exo by R28 cells. (A) Endocytosis was inhibited by pretreatment of RGD, but not by heparin. The nuclei were stained with DAPI (blue), the cytoskeleton was stained with tubulin (red), and 293T-Exo was stained with fluorescent-tag (green). Scale bar = 20 µm. (B) Efficacy of endocytosis of 293T-Exo by R28 cells was reversed due to increasing doses of RGD. (C) Efficacy of endocytosis of 293T-Exo by R28 cells was not affected by different doses of heparin. Data are presented as mean ± SD. * $P < 0.05$.

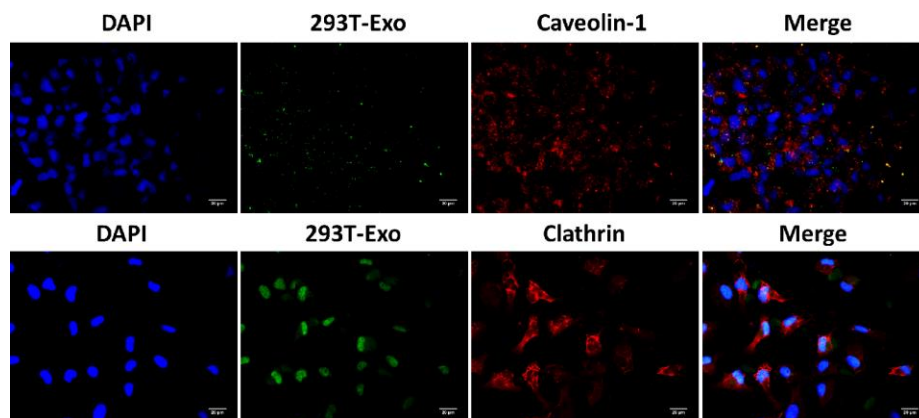


Figure 5. Caveolin-1 was involved in the endocytosis of 293T-Exo by R28 cells. The colocalization of 293T-Exo with caveolin-1, but not clathrin, was observed using the fluorescence assay. The nuclei were stained with DAPI (blue), 293T-Exo was stained with fluorescent-tag (green), and the caveolin-1 or clathrin was stained with corresponding antibodies (red), respectively. Scale bar = 20 μ m.

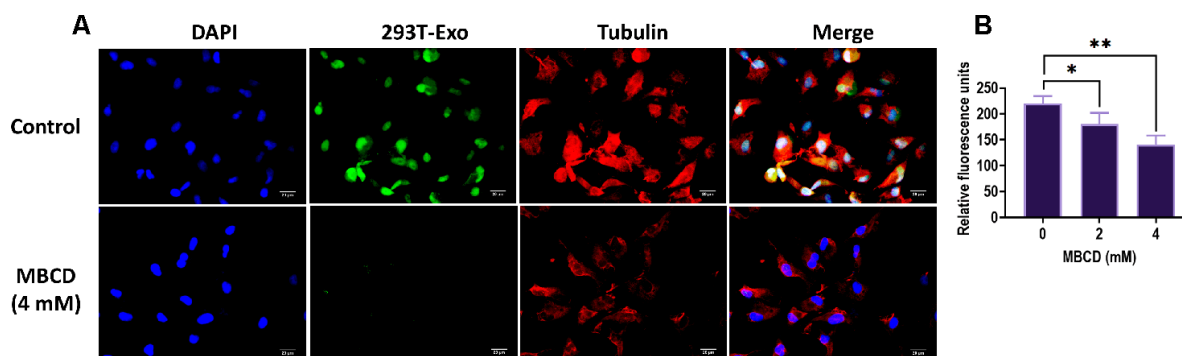


Figure 6. Caveolin-1-mediated endocytosis of 293T-Exo was inhibited by MBCD. (A) Pretreatment of MBCD in R28 cells inhibited the endocytosis of 293T-Exo, as determined by the fluorescence assay. The nuclei were stained with DAPI (blue), the cytoskeleton was stained with tubulin (red), and 293T-Exo was stained with fluorescent-tag (green). Scale bar = 20 μ m. (B) Efficacy of endocytosis of 293T-Exo by R28 cells was reversed due to increasing doses of MBCD. Data are presented as mean \pm SD. * P < 0.05, ** P < 0.01.

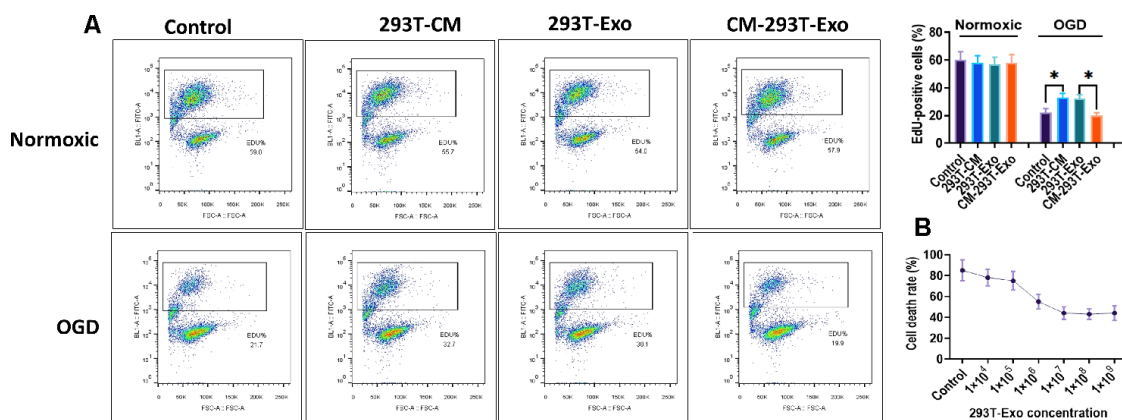


Figure 7. 293T-Exo inhibited OGD-induced cell death of R28 cells. (A) The percentage of EdU-positive in normoxic- or OGD-R28 cells with treatment of 293T-Exo, 293T-Exo-conditioned medium (293T-CM), and conditioned medium without 293T-Exo (CM-293T-Exo), as measured by flow cytometry. (B) Cell death rate was reduced by increasing concentration of 293T-Exo, as measured by the LDH assay. Data are presented as mean \pm SD. * P < 0.05.

293T-Exo was endocytosed by the retinal neurons and RGCs

To determine the specific cell types that uptake 293T-Exo, the axonal or dendritic projections of retinal neurons were stained with red Beta III tubulin and the nuclei of RGCs were stained with magenta BRN3A. As shown in Figure 9, more colocalization of 293T-Exo with retinal neurons of RGCs was observed in retinal tissue slides in response to ischemia injury. These findings suggest that retinal neurons and RGCs are two main cell types that endocytose 293T-Exo.

DISCUSSION

It has been reported that ischemic injury activates several key protective pathways, including the neurotrophic family [31]. As an essential member of this family, BDNF exerts a significant neuroprotective role and facilitates neural repair and regeneration [32, 33]. Elevated expression of BDNF can protect retinal function and suppress apoptosis of retinal pigment epithelial cells and photoreceptors [34]. Given such an important role of BDNF, we previously created a human retina-derived BDNF-expressing construct in

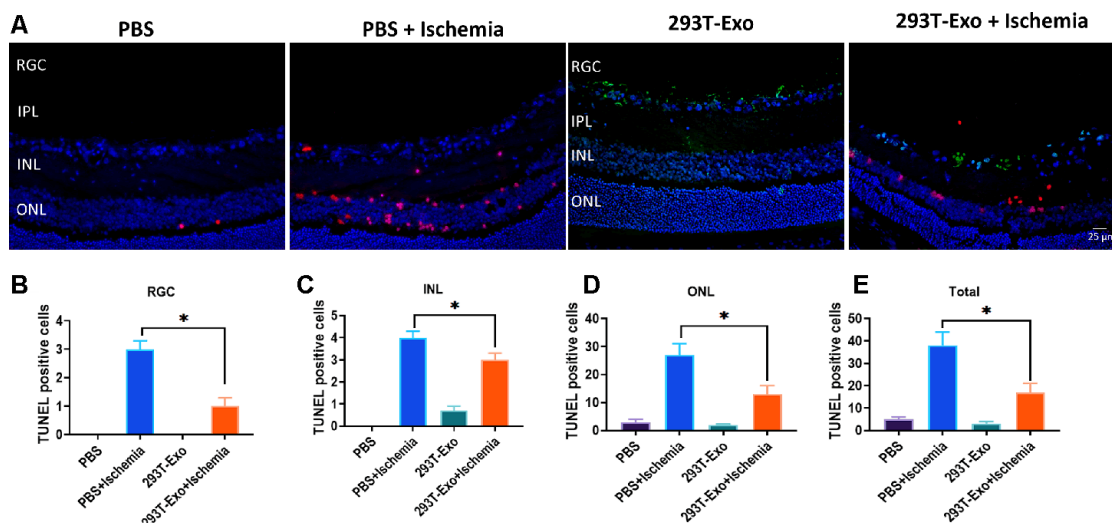


Figure 8. 293T-Exo inhibited OGD-induced apoptosis in the retinae in vivo. (A) 293T-Exo inhibited OGD-induced apoptosis in the retinae, as measured by the TUNEL fluorescence assay. The nuclei were stained with DAPI (blue), the TUNEL-positive cells were stained with TUNEL dye (red), and 293T-Exo was stained with fluorescent-tag (green). Scale bar = 25 μ m. (B–D) Number of TUNEL-positive cells in different structural layers in the retinae in response to treatment of PBS, PBS+ Ischemia, 293T-Exo, and 293T-Exo+ Ischemia, respectively. (E) Total number of TUNEL-positive cells in the retinae in response to treatment of PBS, PBS+ Ischemia, 293T-Exo, and 293T-Exo+ Ischemia. RGC: retinal ganglion cell; IPL: inner plexiform layer; INL: inner nuclear layers; ONL: outer nuclear layers. Data are presented as mean \pm SD. * $P < 0.05$.

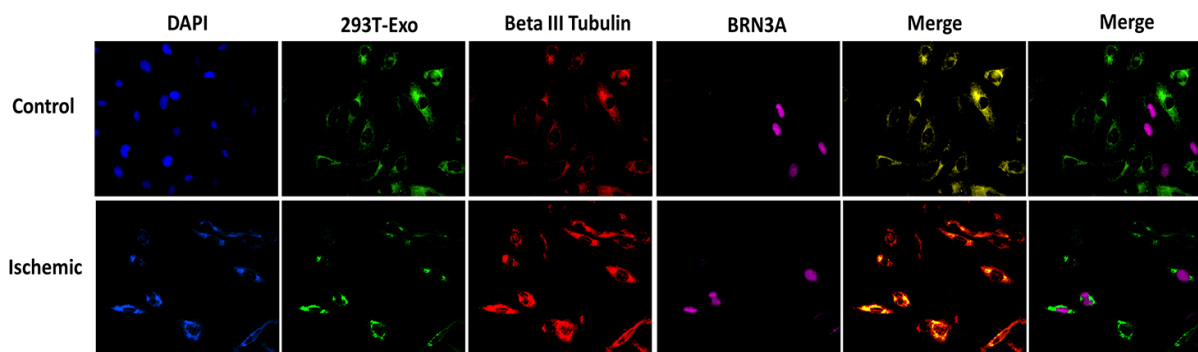


Figure 9. Endocytosis of 293T-Exo by retinal neurons and RGCs. Ischemia injury promoted endocytosis of 293T-Exo by retinal neurons and RGCs. The nuclei were stained with DAPI (blue), 293T-Exo was stained with fluorescent-tag (green), retinal neurons were stained with Beta III tubulin (red), and the nuclei of RGCs were stained with BRN3A (magenta). Scale bar = 25 μ m.

293T cells from human retina and then investigated the effect of BDNF-expressing 293T cells in ARPE-19 cells, a retinal pigment epithelial cell line [26]. After coculturing BDNF-expressing 293T cells with ARPE-19 cells in a Transwell chamber, we found that ARPE-19 cells are more viable and display lower apoptotic levels. Given this, in the present study, we aimed to further investigate the mechanism underlying the neuroprotective role of BDNF-expressing 293T cells, specifically, to understand how BDNF-expressing 293T cells affect the recipient ARPE-19 cells.

Given the experimental design previously described [26], BDNF-expressing 293T cells cocultured with ARPE-19 cells in a Transwell chamber without direct contact, suggesting there may be a potential mediator in this interaction. In the past decade, exosomes have been demonstrated to be an essential mediator in intercellular communication and play an essential role in regulating physiological processes in recipient cells [10, 11]. Thus, we hypothesized that exosomes might be involved in the communication between BDNF-expressing 293T and ARPE-19 cells. To address this question, we successfully isolated exosomes from BDNF-expressing 293T cells and found that the expression of BDNF was significantly increased in 293T-Exo. Furthermore, these observations revealed that 293T-Exo may be internalized by R28 cells and result in an increased level of BDNF in R28 cells.

To further explore the detailed mechanism of this endocytic process, we performed experiments to demonstrate that the endocytosis of 293T-Exo by R28 cells displayed dose- and temperature-dependent patterns, indicating that the endocytosis may be mediated by endocytic receptors. To date, several distinct endocytic mechanisms have been reported to participate in the endocytosis of exosomes [18–20], of which, clathrin- and caveolae-mediated pathways have been demonstrated to be involved in the endocytosis of exosomes [27, 35]. For example, PC12 cell-derived exosomes carrying microRNA-21 are endocytosed by bone MSCs through a clathrin-mediated pathway [36]. Also, lipid raft-associated protein caveolin-1 can negatively regulate the internalization of exosomes derived from glioblastoma cells [28]. In the present study, colocalization of 293T-Exo with caveolin-1, but not clathrin, was found in R28 cells. Furthermore, our results showed that the RGD peptide, a specific ligand for integrin, significantly inhibited endocytosis. In contrast, heparin, a ligand for HSPGs, did not affect the endocytic process, suggesting that the endocytosis of 293T-Exo may be mediated by the caveolar endocytic pathway via a cell surface integrin receptor, a heterodimeric transmembrane receptor [37].

Next, regarding the function of 293T-Exo in R28 cells, we designed both *in vitro* and *in vivo* experiments to investigate the effect of 293T-Exo in retinal ischemia. Our results, *in vitro*, revealed that 293T-Exo inhibited cell death of R28 cells in response to OGD treatment. Consistently, 293T-Exo displayed a remarkable neuroprotective role in a retinal ischemia rat model through decreasing apoptosis in the retina. Furthermore, we also demonstrated that 293T-Exo was primarily internalized by retinal neurons and RGCs. Retinal ischemic injury is characterized by increased cell death, apoptosis, as well as neuroinflammatory responses, ultimately leading to RGC loss, blood-retinal barrier permeability, and blindness [38]. A growing number of studies report that the exosomes derived from MSCs can attenuate ischemia-induced injury in the retina. For example, exosomes derived bone MSCs can transfer functional microRNAs, rather than protein, into inner retinal layers and exert a significant therapeutic role in RGCs [15]. In addition, exosomes derived hypoxic human MSCs inhibit oxygen-induced retinopathy-induced retinal thinning and preserve retinal vascular flow, ameliorating the severity of retinal ischemia in a murine model [16]. As such, these findings together provide a new understanding of the mechanism underlying the effect of exosomes in ischemic retina.

Exosome-mediated therapies provide a cell-free alternative, relative to MSCs-based approaches. It has several notable advantages, such as easy operation (*i.e.*, isolation, purification, storage, and delivery) and low risk (exosomes do not carry complications induced by transferring live cells into the vitreous). Meanwhile, there are still several challenges for exosome-based therapies. First, the safety and effectiveness of the dose of exosomes for each patient should be further investigated. Second, the timeframe of exosome-based therapies is essential for the clinical application. Third, the accuracy of delivering exosomes to the target tissue is a critical determinant for therapeutic purposes. Therefore, further studies should focus on addressing the above questions. Furthermore, it should be mentioned that we applied R28 retinal precursor cells, a transformed cell line [39], *in vitro*, which may not fully represent the function and structure of intact native retinal cells. Thus, it would be better to use native cells or tissues instead of transformed cells.

In conclusion, the results suggest that 293T-Exo is endocytosed by retinal cells through the caveolar endocytic pathway via the integrin receptor. In addition, 293T-Exo exerts a neuroprotective role in the ischemic retina, both *in vitro* and *in vivo*. The findings from the present study demonstrates a significant therapeutic potential of exosomes and provides an understanding of how to develop exosome-based therapies for retinal ischemia.

MATERIALS AND METHODS

Cell culture

As described in our previous study [26], human 293T cells were donated from the Functional Genomic Research Lab (Tsinghua University, China) and cultured in Dulbecco's Modified Eagle's Medium (DMEM; Cat#: A4192101; Thermo Fisher Scientific) supplemented with 10% heat-inactivated fetal bovine serum (FBS; Cat#: A3840001; Thermo Fisher Scientific) and 1% penicillin-streptomycin (Cat#: 15140122; Thermo Fisher Scientific) in a humidified incubator at 5% CO₂ and 37° C. Retinal cell line R28 (Cat#: EUR201; Kerafast) was cultured in DMEM supplemented with 10% fetal bovine serum (Cat#: A3160402; Thermo Fisher Scientific) and 100 µg/mL streptomycin (Cat#: 15140122; Thermo Fisher Scientific). The R28 cells were dissociated and used at a density of 1×10⁶ cells/mL for all subsequent experiments.

Isolation exosomes derived from BDNF-expressing 293T cells

Construction of BDNF-expressing 293T cells was performed as previously described [26]. The protocol for isolation of 293T cell-derived exosomes (293T-Exo) was conducted as previously described [40–42]. Briefly, 293T cells were incubated in the FBS-free culture medium in 225-cm² flasks for 48 hours, and then the supernatants were collected. Cells, shedding vesicles, and cell fragments were removed from the supernatant through a series of centrifugation (300g*5 min, 3000 g*30 min, and 10,000 g*60 min). Total Exosome Isolation Reagent (Cat#: 4478359; Thermo Fisher Scientific) was used to isolate exosomes from cell culture medium according to the manufacturer's instruction. Afterward, exosomes were harvested from the pellets and resuspended in PBS. Then, 0.22-µm pore size polyvinylidene difluoride (PVDF) membrane filters (Cat#: GVWP04700; MilliporeSigma) were used to filter any remaining cells or debris. The concentration of exosome was quantified through the BCA Protein Quantification Assay (Cat#: ab 102536; Abcam) [43].

Transmission electron microscopy (TEM) and nanoparticle-tracking analysis (NTA)

The 293T-Exo sample preparation, TEM, and NTA were performed as previously described [42]. Morphology of 293T-Exo was determined through TEM assay with the transmission electron microscope (JEM-1010; JEOL Ltd.). The 293T-Exo size distribution was assessed using the NanoSight NS500 instrument and NTA (software version 2.3; Build 0033; Malvern Panlytical).

Real-time PCR

Total RNA was isolated from cells or exosomes using the Trizol Reagent kit (Cat#: 12183555; Thermo Fisher Scientific) according to the manufacturer's instruction. Reverse transcription was performed using the High-Capacity cDNA Reverse Transcription Kit (Cat#: 4368814; Thermo Fisher Scientific). The mRNA expressions were measured using the Fast SYBR™ Green Master Mix (Cat#: 4385612; Thermo Fisher Scientific) and the 7500 Fast Real-Time PCR System (Applied Biosystems). Real-time PCR data were analyzed using 2^{-ΔΔCt} method [44], and β-Actin was used as a reference control.

Western blots

The 293T-Exo (4 µg/ml), cells (1×10⁶), or retinal tissues were lysed using T-PER™ Tissue Protein Extraction Reagent (Cat#: 78510; Thermo Fisher Scientific). Lysates were centrifuged and protein concentration was determined using the BCA Protein Quantification Assay (Cat#: ab 102536; Abcam). Ten µg protein was diluted with sodium dodecyl sulfate (SDS) sample buffer and loaded onto gels (4%–20%). Proteins were then electroblotted to polyvinylidene difluoride (PVDF) membranes (Cat#: 88518; Thermo Fisher Scientific). Protein-loaded membranes were incubated with primary antibodies overnight at 4° C on a shaker. The primary antibodies included: CD9 (1/500; Cat#: ab92726), CD63 (1/500; Cat#: ab134045), CD81 (1/500; Cat#: ab109201), HSP70 (1/1000; Cat#: ab5442), BDNF (1/500; Cat#: ab216443) and β-Actin (1/1000; Cat#: ab179467) (Abcam). Nonspecific binding was blocked with 5% non-fat dry milk in TBST. Protein band intensity was measured using Imagej software [45].

Fluorescence staining

The 293T-Exo was labeled with green fluorescent-tag using the ExoGlow-Protein Exosome/EV Protein Labeling Kit (Cat#: EXOGP300A-1-SBI; BioCat.) according to the manufacturer's instruction.

Establishment of retinal ischemia model in vitro

The R28 cells were subjected to the OGD assay to mimic ischemia injury [46]. Briefly, R28 cells (control) were cultured in normal medium to reach 80% confluence. For OGD treatment, R28 cells were cultured in glucose-free medium and then subjected to hypoxia condition (5% CO₂, 1% O₂) for 24 hours. Afterward, cells were supplied oxygen-enriched conditions (5% CO₂, 21% O₂) for 18 hours. Lactate dehydrogenase (LDH) assays (Cat#: ab102526; Abcam)

and ethynyl-deoxyuridine (EdU) assays (Cat#: ab219801; Abcam) were performed to measure cytotoxicity and proliferation according to the manufacturer's instruction.

Endocytosis assay

The R28 cells were plated in a 6-well plate and cocultured with 293T-Exo (50 μ l) labeled with green fluorescent-tag or PBS for 1 hour at 37° C. Then, coverslips were washed with PBS and fixed with 4% neutral buffered formalin and stained with antibodies: clathrin (1/1000; Cat#: MA1-065), tubulin (1/1000; Cat#: MA1-118), and caveolin-1 (1/500; Cat#: PA1-064) (Thermo Fisher Scientific). Slides were photographed using fluorescence microscopy Observer.Z1 (Zeiss Axio). For the exosome dose-dependent experiments, R28 cells were incubated with different amounts of 293T-Exo (1, 2, 4, 8, 16, 32, and 64 μ l) for 1 hour at 37° C. For the binding-blocking experiment, R28 cells (2×10^6) were pre-treated with Arginyl-glycyl-aspartic acid (RGD; 0, 0.5, 1 and 2 mM; Cat#: A9041-2MG; Sigma-Aldrich), heparin (0, 1, 5 and 10 μ M; Cat#: 9041-08-1; Sigma-Aldrich), or MBCD (Methyl- β - cyclodextrin; 0, 2 and 4 mM; Cat#: C4555-1G; Sigma-Aldrich) at 4° C for 1 hour and then incubated with 50 μ l 293T-Exo. Each well was washed with PBS three times and fixed with 4% neutral buffered formalin. The fluorescence was determined using fluorescence microscopy Observer.Z1 (Zeiss Axio).

Establishment of the retinal ischemia rat model

All animal-involved experimental procedures were approved by Beijing Friendship Hospital, Capital Medical University. Male Sprague Dawley rats (7-10 weeks old, 220-250 g, n=10) were used in this study. A retinal ischemia rat model was established as previously described [47]. Null-293T-Exo conditioned medium was prepared by isolating 293T-Exo from the medium. Normoxic Null-293T-Exo conditioned medium (5 μ l), 293T-Exo (5 μ l), or PBS (5 μ l) were injected into the vitreous humor of both non-ischemic (left) and ischemic (right) eyes, 24 hours after retinal ischemia. The left eye was used as the control for each animal. Retinal tissues were collected at seven days post-injection.

TUNEL fluorescence assay

The TUNEL fluorescence assay was performed at 24 hours post-injection using the Cell Meter™ TUNEL Apoptosis Assay Kit (Cat#: 22844; Bioquest) according to the manufacturer's instruction. The TUNEL-positive cells were quantified using Imagej software [45].

Fluorescent assay for localization of 293T-Exo in rat retinal tissues

Control and ischemic male Sprague Dawley rats (7-10 weeks old, 220-250 g, n=10) were intravitreally injected with 293T-Exo labeled with green fluorescent-tag and anesthetized at seven days post-injection. The eyecup samples were prepared as previously described [46]. The primary antibodies were as follows: BRN3A (1/500; Cat#: ab81213), Beta III Tubulin (1/1000; Cat#: ab18207), and Ibal (1/1000; Cat#: ab178846). Slides were photographed using the LSM 900 confocal microscope (ZEISS).

Statistical analysis

Data were presented as mean \pm standard deviation (SD). Statistical analyses were performed using SPSS 13.0 software. At least three independent replicates were available in each experimental group. Statistical difference was determined by one-way ANOVA and t-test. $P < 0.05$ was considered statistically significant.

AUTHOR CONTRIBUTIONS

Bojing Yan, Lixin Gao and Yingxiang Huang performed the experiments and analyzed the data; Xiaolei Wang, Xuqiang Lang and Fancheng Yan performed the molecular investigations; Bo Meng and Xiaowei Sun collected the data, designed and coordinated the research; Genlin Li and Yanling Wang wrote the paper.

CONFLICTS OF INTEREST

These authors declare no conflicts of interest.

FUNDING

This project is funded by the National Natural Science Foundation of China (No. 81870686), National Natural Science Foundation of China (No. 81271046), and the Capital's Funds for Health Improvement and Research (No.2018-1-2021).

REFERENCES

1. Minhas G, Sharma J, Khan N. Cellular stress response and immune signaling in retinal ischemia-reperfusion injury. *Front Immunol.* 2016; 7:444. <https://doi.org/10.3389/fimmu.2016.00444> PMID:[27822213](https://pubmed.ncbi.nlm.nih.gov/27822213/)
2. Peng PH, Ko ML, Chen CF. Epigallocatechin-3-gallate reduces retinal ischemia/reperfusion injury by attenuating neuronal nitric oxide synthase expression

- and activity. *Exp Eye Res.* 2008; 86:637–46.
<https://doi.org/10.1016/j.exer.2008.01.008>
PMID:[18289530](https://pubmed.ncbi.nlm.nih.gov/18289530/)
3. Osborne NN, Casson RJ, Wood JP, Chidlow G, Graham M, Melena J. Retinal ischemia: mechanisms of damage and potential therapeutic strategies. *Prog Retin Eye Res.* 2004; 23:91–147.
<https://doi.org/10.1016/j.preteyeres.2003.12.001>
PMID:[14766318](https://pubmed.ncbi.nlm.nih.gov/14766318/)
 4. Korthuis RJ, Granger DN. Reactive oxygen metabolites, neutrophils, and the pathogenesis of ischemic-tissue/reperfusion. *Clin Cardiol.* 1993; 16:19–26.
<https://doi.org/10.1002/clc.4960161307>
PMID:[8472394](https://pubmed.ncbi.nlm.nih.gov/8472394/)
 5. McCord JM. Oxygen-derived free radicals in postischemic tissue injury. *N Engl J Med.* 1985; 312:159–63.
<https://doi.org/10.1056/NEJM198501173120305>
PMID:[2981404](https://pubmed.ncbi.nlm.nih.gov/2981404/)
 6. Neufeld AH, Kawai Si, Das S, Vora S, Gachie E, Connor JR, Manning PT. Loss of retinal ganglion cells following retinal ischemia: the role of inducible nitric oxide synthase. *Exp Eye Res.* 2002; 75:521–28.
<https://doi.org/10.1006/exer.2002.2042>
PMID:[12457864](https://pubmed.ncbi.nlm.nih.gov/12457864/)
 7. Renner M, Stute G, Alzureiqi M, Reinhard J, Wiemann S, Schmid H, Faissner A, Dick HB, Joachim SC. Optic nerve degeneration after retinal ischemia/reperfusion in a rodent model. *Front Cell Neurosci.* 2017; 11:254.
<https://doi.org/10.3389/fncel.2017.00254>
PMID:[28878627](https://pubmed.ncbi.nlm.nih.gov/28878627/)
 8. Aguilera-Rojas M, Badewien-Rentzsch B, Plendl J, Kohn B, Einspanier R. Exploration of serum- and cell culture-derived exosomes from dogs. *BMC Vet Res.* 2018; 14:179.
<https://doi.org/10.1186/s12917-018-1509-x>
PMID:[29884196](https://pubmed.ncbi.nlm.nih.gov/29884196/)
 9. Merino-González C, Zuñiga FA, Escudero C, Ormazabal V, Reyes C, Nova-Lamperti E, Salomón C, Aguayo C. Mesenchymal stem cell-derived extracellular vesicles promote angiogenesis: potencial clinical application. *Front Physiol.* 2016; 7:24.
<https://doi.org/10.3389/fphys.2016.00024>
PMID:[26903875](https://pubmed.ncbi.nlm.nih.gov/26903875/)
 10. Ng YH, Rome S, Jalabert A, Forterre A, Singh H, Hincks CL, Salamonsen LA. Endometrial exosomes/microvesicles in the uterine microenvironment: a new paradigm for embryo-endometrial cross talk at implantation. *PLoS One.* 2013; 8:e58502.
<https://doi.org/10.1371/journal.pone.0058502>
PMID:[23516492](https://pubmed.ncbi.nlm.nih.gov/23516492/)
 11. Simons M, Raposo G. Exosomes—vesicular carriers for intercellular communication. *Curr Opin Cell Biol.* 2009; 21:575–81.
<https://doi.org/10.1016/j.ceb.2009.03.007>
PMID:[19442504](https://pubmed.ncbi.nlm.nih.gov/19442504/)
 12. Lai RC, Arslan F, Lee MM, Sze NS, Choo A, Chen TS, Salto-Tellez M, Timmers L, Lee CN, El Oakley RM, Pasterkamp G, de Kleijn DP, Lim SK. Exosome secreted by MSC reduces myocardial ischemia/reperfusion injury. *Stem Cell Res.* 2010; 4:214–22.
<https://doi.org/10.1016/j.scr.2009.12.003>
PMID:[20138817](https://pubmed.ncbi.nlm.nih.gov/20138817/)
 13. Tan CY, Lai RC, Wong W, Dan YY, Lim SK, Ho HK. Mesenchymal stem cell-derived exosomes promote hepatic regeneration in drug-induced liver injury models. *Stem Cell Res Ther.* 2014; 5:76.
<https://doi.org/10.1186/scrt465> PMID:[24915963](https://pubmed.ncbi.nlm.nih.gov/24915963/)
 14. Xiong Y, Mahmood A, Chopp M. Emerging potential of exosomes for treatment of traumatic brain injury. *Neural Regen Res.* 2017; 12:19–22.
<https://doi.org/10.4103/1673-5374.198966>
PMID:[28250732](https://pubmed.ncbi.nlm.nih.gov/28250732/)
 15. Mead B, Tomarev S. Bone marrow-derived mesenchymal stem cells-derived exosomes promote survival of retinal ganglion cells through miRNA-dependent mechanisms. *Stem Cells Transl Med.* 2017; 6:1273–85.
<https://doi.org/10.1002/sctm.16-0428> PMID:[28198592](https://pubmed.ncbi.nlm.nih.gov/28198592/)
 16. Moisseiev E, Anderson JD, Oltjen S, Goswami M, Zawadzki RJ, Nolta JA, Park SS. Protective effect of intravitreal administration of exosomes derived from mesenchymal stem cells on retinal ischemia. *Curr Eye Res.* 2017; 42:1358–67.
<https://doi.org/10.1080/02713683.2017.1319491>
PMID:[28636406](https://pubmed.ncbi.nlm.nih.gov/28636406/)
 17. Tian T, Zhu YL, Hu FH, Wang YY, Huang NP, Xiao ZD. Dynamics of exosome internalization and trafficking. *J Cell Physiol.* 2013; 228:1487–95.
<https://doi.org/10.1002/jcp.24304> PMID:[23254476](https://pubmed.ncbi.nlm.nih.gov/23254476/)
 18. Feng D, Zhao WL, Ye YY, Bai XC, Liu RQ, Chang LF, Zhou Q, Sui SF. Cellular internalization of exosomes occurs through phagocytosis. *Traffic.* 2010; 11:675–87.
<https://doi.org/10.1111/j.1600-0854.2010.01041.x>
PMID:[20136776](https://pubmed.ncbi.nlm.nih.gov/20136776/)
 19. Morelli AE, Larregina AT, Shufesky WJ, Sullivan ML, Stolz DB, Papworth GD, Zahorchak AF, Logar AJ, Wang Z, Watkins SC, Falo LD Jr, Thomson AW. Endocytosis, intracellular sorting, and processing of exosomes by dendritic cells. *Blood.* 2004; 104:3257–66.
<https://doi.org/10.1182/blood-2004-03-0824>
PMID:[15284116](https://pubmed.ncbi.nlm.nih.gov/15284116/)
 20. McKelvey KJ, Powell KL, Ashton AW, Morris JM, McCracken SA. Exosomes: mechanisms of uptake. *J*

- Circ Biomark. 2015; 4:7.
<https://doi.org/10.5772/61186>
PMID:28936243
21. Costa Verdera H, Gitz-Francois JJ, Schiffelers RM, Vader P. Cellular uptake of extracellular vesicles is mediated by clathrin-independent endocytosis and macropinocytosis. *J Control Release*. 2017; 266:100–08.
<https://doi.org/10.1016/j.jconrel.2017.09.019>
PMID:28919558
 22. Linker RA, Lee DH, Demir S, Wiese S, Kruse N, Siglienti I, Gerhardt E, Neumann H, Sendtner M, Lühder F, Gold R. Functional role of brain-derived neurotrophic factor in neuroprotective autoimmunity: therapeutic implications in a model of multiple sclerosis. *Brain*. 2010; 133:2248–63.
<https://doi.org/10.1093/brain/awq179>
PMID:20826430
 23. Zheng J, Sun J, Lu X, Zhao P, Li K, Li L. BDNF promotes the axonal regrowth after sciatic nerve crush through intrinsic neuronal capability upregulation and distal portion protection. *Neurosci Lett*. 2016; 621:1–8.
<https://doi.org/10.1016/j.neulet.2016.04.006>
PMID:27057731
 24. Zuccato C, Cattaneo E. Brain-derived neurotrophic factor in neurodegenerative diseases. *Nat Rev Neurol*. 2009; 5:311–22.
<https://doi.org/10.1038/nrneurol.2009.54>
PMID:19498435
 25. Kano T, Abe T, Tomita H, Sakata T, Ishiguro S, Tamai M. Protective effect against ischemia and light damage of iris pigment epithelial cells transfected with the BDNF gene. *Invest Ophthalmol Vis Sci*. 2002; 43:3744–53.
PMID:12454046
 26. Yan BJ, Wu ZZ, Chong WH, Li GL. Construction of a plasmid for human brain-derived neurotrophic factor and its effect on retinal pigment epithelial cell viability. *Neural Regen Res*. 2016; 11:1981–89.
<https://doi.org/10.4103/1673-5374.197142>
PMID:28197196
 27. Mulcahy LA, Pink RC, Carter DR. Routes and mechanisms of extracellular vesicle uptake. *J Extracell Vesicles*. 2014; 3.
<https://doi.org/10.3402/jev.v3.24641>
PMID:25143819
 28. Svensson KJ, Christianson HC, Wittrup A, Bourseau-Guilmain E, Lindqvist E, Svensson LM, Mörgelin M, Belting M. Exosome uptake depends on ERK1/2-heat shock protein 27 signaling and lipid raft-mediated endocytosis negatively regulated by caveolin-1. *J Biol Chem*. 2013; 288:17713–24.
<https://doi.org/10.1074/jbc.M112.445403>
PMID:23653359
 29. Mahammad S, Parmryd I. Cholesterol depletion using methyl- β -cyclodextrin. *Methods Mol Biol*. 2015; 1232:91–102.
https://doi.org/10.1007/978-1-4939-1752-5_8
PMID:25331130
 30. Zhang F, Wang S, Signore AP, Chen J. Neuroprotective effects of leptin against ischemic injury induced by oxygen-glucose deprivation and transient cerebral ischemia. *Stroke*. 2007; 38:2329–36.
<https://doi.org/10.1161/STROKEAHA.107.482786>
PMID:17600230
 31. Truettner J, Busto R, Zhao W, Ginsberg MD, Pérez-Pinzón MA. Effect of ischemic preconditioning on the expression of putative neuroprotective genes in the rat brain. *Brain Res Mol Brain Res*. 2002; 103:106–15.
[https://doi.org/10.1016/s0169-328x\(02\)00191-2](https://doi.org/10.1016/s0169-328x(02)00191-2)
PMID:12106696
 32. Neumann JT, Thompson JW, Raval AP, Cohan CH, Koronowski KB, Perez-Pinzon MA. Increased BDNF protein expression after ischemic or PKC epsilon preconditioning promotes electrophysiologic changes that lead to neuroprotection. *J Cereb Blood Flow Metab*. 2015; 35:121–30.
<https://doi.org/10.1038/jcbfm.2014.185>
PMID:25370861
 33. Zhang M, Mo X, Fang Y, Guo W, Wu J, Zhang S, Huang Q. Rescue of photoreceptors by BDNF gene transfer using in vivo electroporation in the RCS rat of retinitis pigmentosa. *Curr Eye Res*. 2009; 34:791–99.
<https://doi.org/10.1080/02713680903086018>
PMID:19839873
 34. Azadi S, Johnson LE, Paquet-Durand F, Perez MT, Zhang Y, Ekström PA, van Veen T. CNTF+BDNF treatment and neuroprotective pathways in the rd1 mouse retina. *Brain Res*. 2007; 1129:116–29.
<https://doi.org/10.1016/j.brainres.2006.10.031>
PMID:17156753
 35. Li C, Liu DR, Li GG, Wang HH, Li XW, Zhang W, Wu YL, Chen L. CD97 promotes gastric cancer cell proliferation and invasion through exosome-mediated MAPK signaling pathway. *World J Gastroenterol*. 2015; 21:6215–28.
<https://doi.org/10.3748/wjg.v21.i20.6215>
PMID:26034356
 36. Tian T, Zhu YL, Zhou YY, Liang GF, Wang YY, Hu FH, Xiao ZD. Exosome uptake through clathrin-mediated endocytosis and macropinocytosis and mediating miR-21 delivery. *J Biol Chem*. 2014; 289:22258–67.
<https://doi.org/10.1074/jbc.M114.588046>
PMID:24951588
 37. Lee HD, Kim YH, Kim DS. Exosomes derived from

- human macrophages suppress endothelial cell migration by controlling integrin trafficking. *Eur J Immunol.* 2014; 44:1156–69.
<https://doi.org/10.1002/eji.201343660>
PMID:[24338844](https://pubmed.ncbi.nlm.nih.gov/24338844/)
38. Mathew B, Poston JN, Dreixler JC, Torres L, Lopez J, Zelkha R, Balyasnikova I, Lesniak MS, Roth S. Bone-marrow mesenchymal stem-cell administration significantly improves outcome after retinal ischemia in rats. *Graefes Arch Clin Exp Ophthalmol.* 2017; 255:1581–1592.
<https://doi.org/10.1007/s00417-017-3690-1>
PMID:[28523456](https://pubmed.ncbi.nlm.nih.gov/28523456/)
39. Seigel GM. Review: R28 retinal precursor cells: the first 20 years. *Mol Vis.* 2014; 20:301–06.
PMID:[24644404](https://pubmed.ncbi.nlm.nih.gov/24644404/)
40. Hu Y, Yan C, Mu L, Huang K, Li X, Tao D, Wu Y, Qin J. Fibroblast-derived exosomes contribute to chemoresistance through priming cancer stem cells in colorectal cancer. *PLoS One.* 2015; 10:e0125625.
<https://doi.org/10.1371/journal.pone.0125625>
PMID:[25938772](https://pubmed.ncbi.nlm.nih.gov/25938772/)
41. Chairoungdua A, Smith DL, Pochard P, Hull M, Caplan MJ. Exosome release of β -catenin: a novel mechanism that antagonizes Wnt signaling. *J Cell Biol.* 2010; 190:1079–91.
<https://doi.org/10.1083/jcb.201002049>
PMID:[20837771](https://pubmed.ncbi.nlm.nih.gov/20837771/)
42. Li J, Chen X, Yi J, Liu Y, Li D, Wang J, Hou D, Jiang X, Zhang J, Wang J, Zen K, Yang F, Zhang CY, Zhang Y. Identification and characterization of 293T cell-derived exosomes by profiling the protein, mRNA and MicroRNA components. *PLoS One.* 2016; 11:e0163043.
<https://doi.org/10.1371/journal.pone.0163043>
PMID:[27649079](https://pubmed.ncbi.nlm.nih.gov/27649079/)
43. Villarroya-Beltri C, Gutiérrez-Vázquez C, Sánchez-Madrid F, Mittelbrunn M. Analysis of microRNA and protein transfer by exosomes during an immune synapse. *Methods Mol Biol.* 2013; 1024:41–51.
https://doi.org/10.1007/978-1-62703-453-1_4
PMID:[23719941](https://pubmed.ncbi.nlm.nih.gov/23719941/)
44. Schmittgen TD, Livak KJ. Analyzing real-time PCR data by the comparative C(T) method. *Nat Protoc.* 2008; 3:1101–08.
<https://doi.org/10.1038/nprot.2008.73>
PMID:[18546601](https://pubmed.ncbi.nlm.nih.gov/18546601/)
45. Schneider CA, Rasband WS, Eliceiri KW. NIH image to ImageJ: 25 years of image analysis. *Nat Methods.* 2012; 9:671–75.
<https://doi.org/10.1038/nmeth.2089>
PMID:[22930834](https://pubmed.ncbi.nlm.nih.gov/22930834/)
46. Mathew B, Ravindran S, Liu X, Torres L, Chennakesavalu M, Huang CC, Feng L, Zelka R, Lopez J, Sharma M, Roth S. Mesenchymal stem cell-derived extracellular vesicles and retinal ischemia-reperfusion. *Biomaterials.* 2019; 197:146–60.
<https://doi.org/10.1016/j.biomaterials.2019.01.016>
PMID:[30654160](https://pubmed.ncbi.nlm.nih.gov/30654160/)
47. Rosenbaum DM, Degtarev A, David J, Rosenbaum PS, Roth S, Grotta JC, Cuny GD, Yuan J, Savitz SI. Necroptosis, a novel form of caspase-independent cell death, contributes to neuronal damage in a retinal ischemia-reperfusion injury model. *J Neurosci Res.* 2010; 88:1569–76.
<https://doi.org/10.1002/jnr.22314>
PMID:[20025059](https://pubmed.ncbi.nlm.nih.gov/20025059/)

Exploration of age-related mitochondrial dysfunction and the anti-aging effects of resveratrol in zebrafish retina

Ning Wang^{1,2,*}, Zhiwen Luo^{1,2,*}, Ming Jin^{1,*}, Weiwei Sheng^{1,2}, Han-Tsing Wang^{3,4,5}, Xinyi Long^{1,2}, Yue Wu^{1,2}, Piaopiao Hu^{1,5}, Hong Xu^{3,4,5}, Xu Zhang^{1,5}

¹Affiliated Eye Hospital of Nanchang University, Jiangxi Research Institute of Ophthalmology and Visual Science, Nanchang, China

²Queen Mary School of Nanchang University, Nanchang, China

³Institute of Life Science of Nanchang University, Nanchang, China

⁴School of Life Sciences of Nanchang University, Nanchang, China

⁵Jiangxi Provincial Collaborative Innovation Center for Cardiovascular, Digestive and Neuropsychiatric Diseases, Nanchang, China

*Equal contribution

Correspondence to: Xu Zhang ; **email:** xuzhang19@163.com

Keywords: aging zebrafish, retina, mitochondrial dysfunction, mitophagy, mTOR, resveratrol

Received: February 1, 2019

Accepted: May 7, 2019

Published: May 19, 2019

Copyright: Wang et al. This is an open-access article distributed under the terms of the Creative Commons Attribution License (CC BY 3.0), which permits unrestricted use, distribution, and reproduction in any medium, provided the original author and source are credited.

ABSTRACT

It is currently believed that aging is closely linked with mitochondrial dysfunction, and that resveratrol exhibits anti-aging and neuroprotective effects by improving mitochondrial function, even though the mechanisms are not well defined. This study explored mitochondrial quality (mitochondrial DNA integrity and copy number), mitochondrial function (fusion/fission, mitophagy/autophagy), antioxidant system and activity of the Akt/mTOR and Ampk/Sirt1/Pgc1 α pathways, and inflammation in aging zebrafish retinas to identify the probable mechanisms of resveratrol's anti-aging and neuroprotective effects. mtDNA integrity, mtDNA copy number, mitochondrial fusion regulators, mitophagy, and antioxidant-related genes were all decreased whereas Akt/mTOR activity and inflammation was increased upon aging in zebrafish retinas. Resveratrol was shown to not only increase mitochondrial quality and function, but also to suppress Akt/mTOR activity in zebrafish retinas. These results support the notion that mitochondrial dysfunction and increased Akt/mTOR activity are major players in age-related retinal neuropathy in zebrafish, and demonstrate a trend towards mitochondrial fragmentation in the aging retina. Importantly, resveratrol promoted mitochondrial function, up-regulating Ampk/Sirt1/Pgc1 α , and down-regulated Akt/mTOR pathway activity in zebrafish retinas, suggesting that it may be able to prevent age-related ophthalmopathy.

INTRODUCTION

Aging is the biological process characterized by the accumulation of damage in structure and decline in function of cells and tissues over time, ultimately leading to organismal death [1]. The causes of aging are complex but include abnormal mitochondria, epigenetic

alterations, increased reactive oxygen species (ROS), increased DNA methylation, and decreased telomere length [2–4]. Recently, both dysfunctional mitochondria that overproduce ROS [5] and abnormal mitochondrial dynamics have been recognized as crucial contributors to the aging process as well as age-related neuronal diseases and age-related ophthalmopathies such as glaucoma,

age-related macular degeneration (AMD), and cataracts [6–8]. The detailed mechanism by which dysfunctional mitochondria influence the aging process, however, is complex and incompletely understood.

Mitochondrial dysfunction includes defective mitochondrial fusion/fission, decreased mitochondrial DNA (mtDNA) quality, and altered mitophagy [9]. Mitochondrial fusion/fission determines the mitochondrial mass and network structure in the cell. Mitochondrial fusion is the process of joining multiple mitochondria together and is mediated by optic atrophy 1 (Opa1) and mitochondrial fusion protein 1 and 2 (Mfn1 and Mfn2). Mitochondrial fission, on the other hand, divides a single large mitochondrion into multiple smaller mitochondria, which is mediated by dynamin related protein 1 (Drp1) and mitochondrial fission protein 1 (Fis1) [10]. Some studies have found that upon aging, mitochondria tend to be more fragmented, suggesting that fusion is decreased and/or fission is increased. A potential reason for this alteration in mitochondrial dynamics is that accumulated ROS damage reduces mitochondrial output, and in response the cell promotes mitochondrial fission to help cope with the decline in mitochondrial function [11].

The integrity of mtDNA, which is highly vulnerable to ROS damage, is a good indicator of mitochondrial quality, and defective mtDNA is ubiquitous in aged tissues [12]. Mitochondrial fusion/fission plays an important role in mitigating the effects of mtDNA damage, and its breakdown can exacerbate the effects of aging. Fusion can help relieve mtDNA damage by diluting mutant mtDNA with non-mutant mtDNA, whereas fission can allow for turnover of mutant mtDNA through mitophagy [13]. On the other hand, mitochondrial fragmentation is associated with apoptosis and cell death rather than mitophagy and must be distinguished from fission [14].

Autophagy is the process by which cells degrade damaged organelles and other cellular materials and recycle cellular building blocks such as amino acids [15]. A significant decline in autophagy is found in aging, and many studies have shown that increased autophagy can extend organismal lifespan [16,17]. Notably, centenarians have been found to retain active autophagy [18]. Mitophagy, mediated by PTEN-induced putative kinase 1 (Pink1), is the highly selective autophagic process by which cells eliminate damaged mitochondria [19]. It is believed that mtDNA repair mechanisms are less efficient than those for nuclear DNA repair, despite mtDNA being much more prone to damage particularly by ROS. Mitophagy is

therefore crucial for normal mitochondrial function by clearing damaged mtDNA. Similar to general autophagy, functional mitophagy has also been found to be decreased in aged cells including skin fibroblasts, muscle satellite cells, and neural cells [20–22]. Down-regulation of mitophagy also has a strong correlation with neurodegenerative disease [23]. It is therefore believed that a decline in mitophagy leads to higher oxidative stress, lower quality mitochondria, and apoptosis, which ultimately accelerates aging [24].

Resveratrol, a plant natural product found in high levels in peanuts and grape skin, has well-established antioxidant, anti-inflammatory, anti-mutagenic, neuroprotective, and anti-aging effects in many species [25–27]. Current evidence suggests that the anti-aging effects of resveratrol are related to its ability to modulate mitochondria [28,29]. Resveratrol has been found to increase mitochondrial fusion/fission as well as promote Pink1 expression and autophagic activity [30–33]. Additionally, some reports indicate these effects of resveratrol are due to its ability to decrease mammalian target of rapamycin (mTOR) levels and promote Ampk/Sirt1 activities [9,34]. In a prior study, we have demonstrated that resveratrol can protect against retinal neuron degeneration through activation of SIRT1 and inhibition of the mTOR pathway and inflammation-related proteins; however, the full effects of resveratrol on mitochondria remains unclear [30,35,36].

Zebrafish has become a powerful and widely used model organism as they are easy and cheap to maintain, are sensitive to neurotropic drugs, and a single pair can spawn 200–300 eggs in one week who grow to sexual maturity in only 3–4 months [37,38]. 70% of zebrafish genes have homologs in humans, 84% of human disease-related genes have homologs in zebrafish, and CNS protein-encoding genes have very similar functions with their human counterparts [39]. Moreover, the human retina is more closely related to the zebrafish retina than that of mice, which has rod-dominant vision unlike the cone-dominant vision found in humans and zebrafish [37]. Zebrafish is also an excellent aging model owing to its short lifespan, gradual aging progression as in mammals, and similar aging markers to those in humans [40].

The aim of the current study was to investigate mitochondrial DNA quality, mitochondrial function, AKT/mTOR, antioxidant system and Ampk/Sirt1/Pgc1 α activities in young and aging zebrafish retinas, and to analyze the anti-aging effect of resveratrol on these in the zebrafish retina. A mechanism related to mitochondrial quality control was investigated.

RESULTS

Zebrafish retinal mtDNA quality at different ages and after resveratrol treatment

To investigate the mitochondrial quality in aging zebrafish retinas, we first analyzed the ratio of mitochondrial long chain (mit-L) to mitochondrial short chain (mit-S) DNA which reflects the mitochondrial integrity and the ability to repair mitochondrial damage. Zebrafish retinas exhibited varying levels of mitochondrial integrity at different ages. While mitochondrial integrity was higher at 1 and 4 months compared to 5 days old, at 19 months old the mitochondrial integrity had returned to the level of the 5-day old retinas (Figure 1A). mtDNA copy number (mtCN) is proportional to mitochondrial mass, and we observed that at 4 months old the mtDNA copy number of retinas was substantially increased compared to 5-day and 1-month old retinas, however at 19 months it had also returned to the level of 5-day old retinas (Figure 1B). Resveratrol treatment of young zebrafish significantly increased the mitochondrial integrity after 1 day and 10 days treatment (Figure 1C). Interestingly, resveratrol did not alter the mtCN after 1 day of treatment but slightly decreased it after 10 days treatment (Figure 1D).

Mitochondrial fusion/fission were unbalanced in aging zebrafish retina and improved by resveratrol treatment

Mitochondrial dynamics is vital for maintaining mitochondrial quality, with fusion used to increase mitochondrial integrity and fission to increase mitCN [10]. We found Mfn2, one of the primary mitochondrial fusion regulators, was decreased in aging retinas compared to young retinas at both the mRNA and protein level (Figure 2A, E, F). This was particularly pronounced in the cytoplasm of the retinal ganglia cell layer (GCL) [41] (Figure 3H). Although the level of total Opa1, the other mitochondrial fusion regulator, was not significantly altered at the gene or protein level between young and aging retinas (Figure 2B, E, F), the ratio of long Opa1-L to short Opa1-S was decreased in the aging retinas (Figure 2G). Moreover, expression of Oma1, the metalloprotease that cleaves functional Opa1-L into the inactive Opa1-S, was increased in aging retinas (Figure 2C). Expression of the mitochondrial fission regulator gene Fis1 was increased in aging retinas versus young retinas (Figure 2D). Together, this suggests that mitochondrial fission is promoted in aging retinas through decreased Mfn2 expression, proteolytic inactivation of Opa1 by Oma1, and increased Fis1 expression.

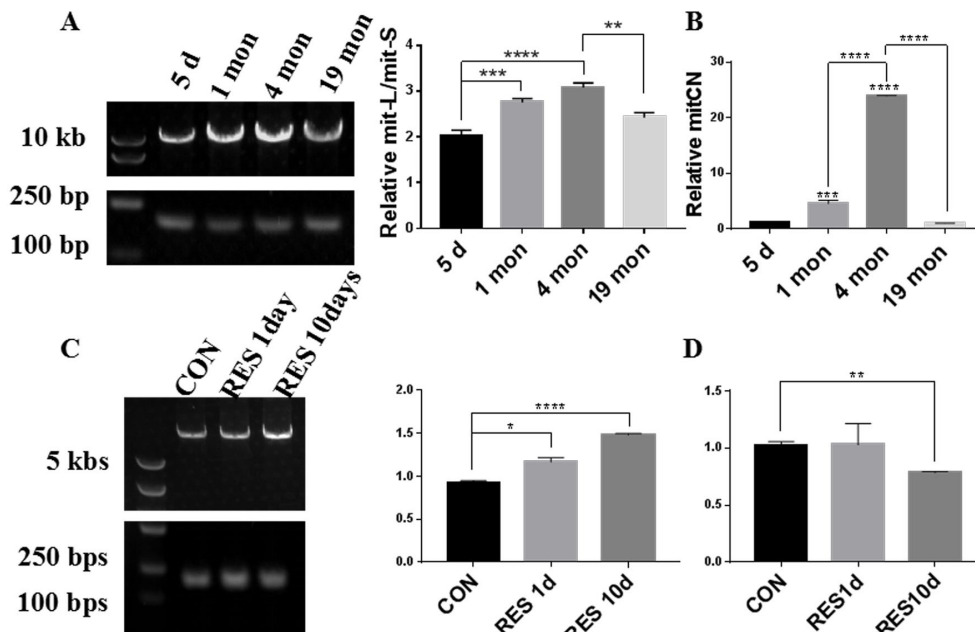


Figure 1. Zebrafish retinal mtDNA quality at different ages and after resveratrol treatment. (A, C) The bands in the left lane are DNA size markers. The top slice shows the long mitochondrial fragments (mit-L) while the bottom slice shows the short mitochondrial fragments (mit-S). The graphs show the ratio of mit-L/mit-S by densitometry analysis of each band (mean \pm SEM, * $P < 0.05$, ** $P < 0.01$, *** $P < 0.001$, **** $P < 0.0001$, $n=3$) (B) Comparison of mitochondrial copy number (mitCN) in 5 days, 1 month, 4 months, and 19 months old zebrafish retinas (mean \pm SEM, *** $P < 0.001$, **** $P < 0.0001$, $n=3$.) (D) Comparison of mitCN in zebrafish retinas after treatment with 20mg/L resveratrol for 1 or 10 days (mean \pm SEM, ** $P < 0.01$ compared to control, $n=3$.). CON, control. RES1d, resveratrol treated for 10 days; RES10d, resveratrol treated for 10 days.

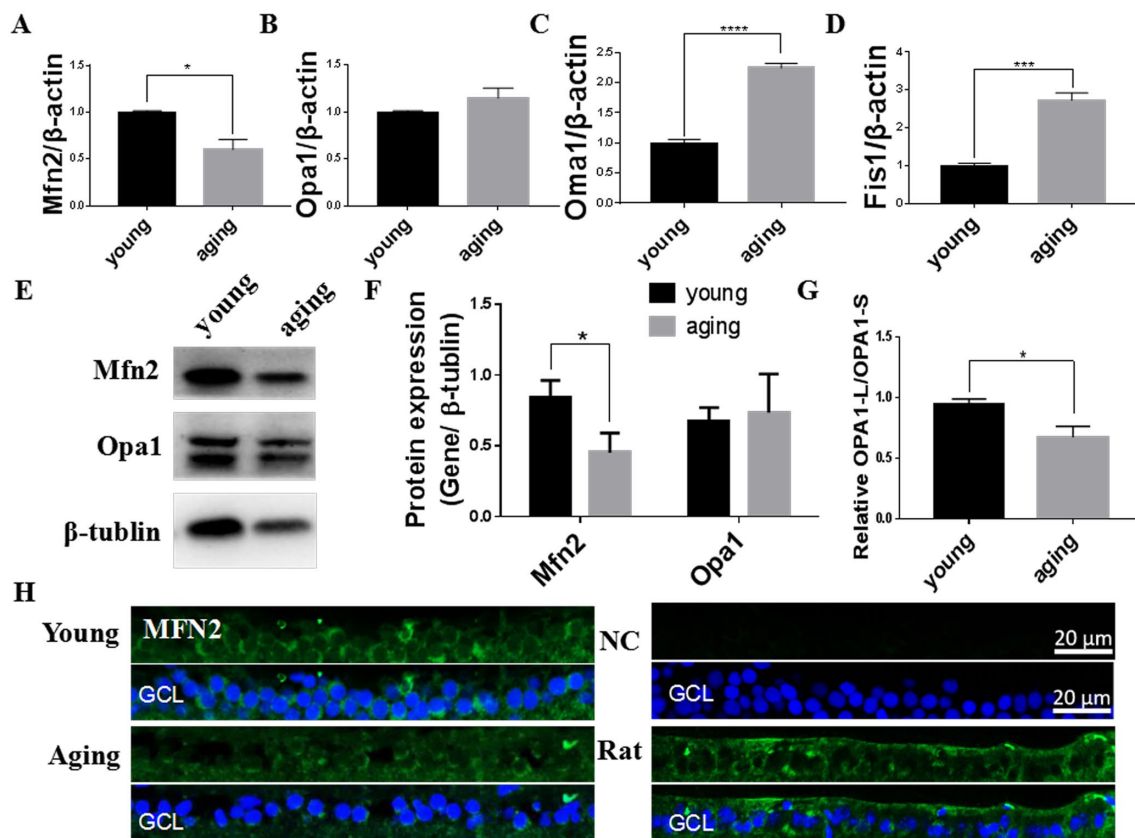


Figure 2. Mitochondrial fusion/fission imbalanced in aging zebrafish retinas. (A-D) Mfn2, Opa1, Oma1, and Fis1 expression in young and aging zebrafish retinas. Graphs represent (A) Mfn2, (B) Opa1, (C) Oma1, and (D) Fis1 gene expression by quantitative real-time PCR (mean \pm SEM, * P < 0.05, *** P < 0.001, **** P < 0.0001, n = 3). (E) Representative western blot showing the protein expression levels of Mfn2 and Opa1 in young and aging zebrafish retinas. (F) The graph depicts the densitometric mean and SEM normalized to the corresponding level of the loading control protein beta-tubulin (* P < 0.05, n = 3). (G) The ratio of Opa1-L/Opa1-S, as determined by densitometry of western blots as in E (* P < 0.05, n = 3). (H) Immunofluorescence localization and relative expression of Mfn2 in the RGC layer of young and aging zebrafish retina cross-sections. All photographs were taken at 40x magnification except rat sections were at 20x magnification. Young, 4-6 months old zebrafish; aging, 19-23 months old zebrafish; NC, negative control (no primary antibody); Rat, rat retina positive control; Opa1-L, Opa1 long segment; Opa1-S, Opa1 short segment; GCL, ganglion cell layer.

Resveratrol increased Mfn2 gene expression after both 1- and 10-days treatment in the young zebrafish. Opa1 and Oma1 gene expression increased after 1-day treatment but returned to their original levels after 10 days treatment, while Fis1 gene expression was steadily increased after 1- and 10-days treatment with resveratrol (Figure 3A-D). Increased cytoplasmic levels of Mfn2 in the RGC layer is also apparent upon resveratrol treatment (Figure 3E).

Mitophagy was decreased in the aging zebrafish retina and increased by resveratrol treatment

Mitophagy can both degrade damaged mitochondria and control the overall mitochondrial content of the cell [19]. Compared to young retinas, we observed that mRNA and protein levels of Pink1, a central regulator

of mitophagy, decreased in aging zebrafish retinas (Figure 4A-C). The decline in Pink1 expression was also observed in the nuclei and cytoplasm of the RGC layer of aging retinas [42] (Figure 4F). Microtubule-associated protein 1B light chain 3B (LC3B) is a marker of autophagy, and the ratio of LC3B short segment (LC3B-II) to LC3B long segment (LC3B-I) is representative of the level of autophagy [43]. Consistent with decreased mitophagy, there was also a significant decrease in the LC3B-II/LC3B-I ratio in aging versus young retinas, suggesting a decrease in overall autophagy levels (Figure 4D, E).

Young zebrafish treated with resveratrol for 1 or 10 days had increased Pink1 mRNA and protein levels (Figure 5A-C), which was also observable in the nuclei and cytoplasm of the RGC layer (Figure 5D).

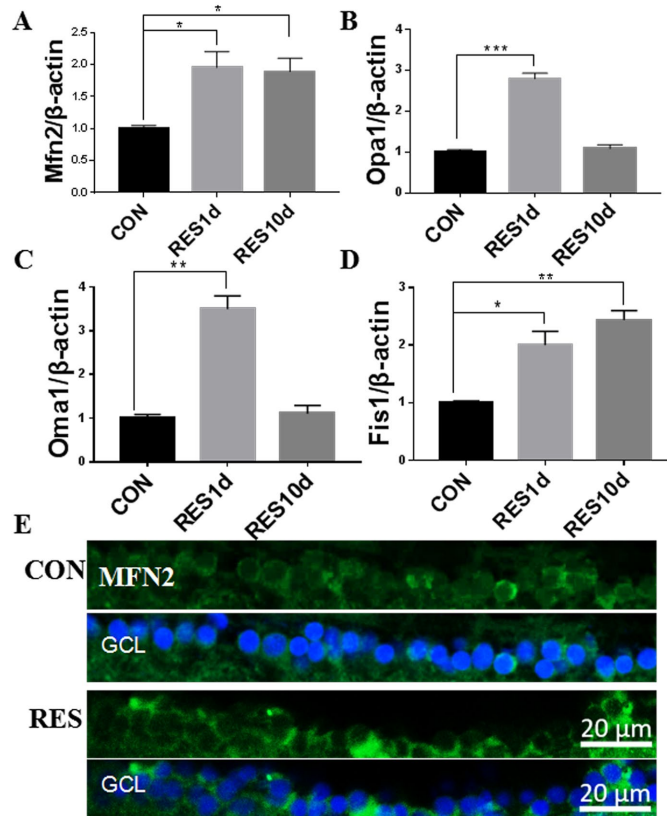


Figure 3. Resveratrol treatment increased mitochondrial fusion/fission expression in young zebrafish retina. (A-D) Mfn2, Opa1, Oma1, and Fis1 gene expression after resveratrol treatment for 1 or 10 days as determined by quantitative real-time PCR (mean \pm SEM, * $P < 0.05$, ** $P < 0.01$, *** $P < 0.001$ compared to control (CON), $n=3$). (E) Immunofluorescence localization and relative expression of Mfn2 in the RGC layer of adult zebrafish retina cross-sections after 10 days resveratrol treatment. All photographs were taken at 40x magnification. CON, control; RES1d, resveratrol treated for 1 days; RES/RES10d, resveratrol treated for 10 days; GCL, ganglion cell layer.

The Akt/mTOR pathway was up-regulated in aging zebrafish retinas and down-regulated by resveratrol treatment

Both autophagy and mitophagy are regulated by the protein kinase B (Akt)/mTOR pathway [9, 16]. In this study, we observed that the total protein level of mTOR as well as mTOR phosphorylation (p-mTOR) were up-regulated in aging retinas compared to young retinas (Figure 6A, B). The upstream activator of mTOR, Akt, also exhibited increased phosphorylation at threonine 308 (p-Akt-T308) and serine 473 (p-Akt-S473) (Figure 6C-D). The increased p-mTOR and p-Akt-T308 in aging retinas was also observed by immunostaining the RGC layer [44, 45] (Figure 6E). The elevated p-mTOR signal was primarily localized in the cytoplasm whereas (Figure 6E). In contrast, rat retinas exhibited p-Akt-the elevated p-Akt-T308 was largely located in the nuclei of aging zebrafish retinas T308 only in the cytoplasm, suggesting that there may be species-specific differences (Figure 6E).

Resveratrol treatment led to a significant decrease in p-mTOR, and had a small but insignificant effect on p-AKT-T308 in young zebrafish retinas (Figure 7 A-B). Immunofluorescence showed that p-mTOR was decreased in the RGC layers of resveratrol-treated young zebrafish retinas (Figure 7C).

Resveratrol treatment activated Mfn2, Fis1, Pink1, and suppressed p-mTOR in aging zebrafish retina

Similar to the young zebrafish, we observed that resveratrol also increased Mfn2 and Fis1 and Pink1 expression in aging zebrafish retinas (Figure 8). And importantly, p-mTOR was also decreased in the aging zebrafish retinas by resveratrol (Figure 8D-E, F).

Expression of antioxidant defense enzymes was suppressed in aging zebrafish retinas and increased by resveratrol treatment

The cellular ROS detoxification system includes the Superoxide dismutase (Sod) and Glutathione peroxidase

(Gpx) proteins [8]. Consistent with increased oxidative damage in aged tissues, we observed decreased expression of Cu/Zn-Sod, Mn-Sod, and Gpx in aging zebrafish retinas (Figure 9A-C). Although resveratrol had no significant effect on Cu/Zn-Sod, Mn-Sod, or Gpx expression in young zebrafish, it did increase expression of all three in aging zebrafish retinas (Figure 9A-C).

Resveratrol activated Ampk/Sirt1/Pgc1 α in zebrafish retinas

The Ampk/Sirt1/Pgc1 α pathway is crucial for regulating mitochondrial biogenesis and oxidative metabolism [9]. We observed that resveratrol increased Ampk, Sirt1, and Pgc1 α expression in both young and aging zebrafish retinas (Figure 9D-F). For Sirt1, young zebrafish had a greater response to resveratrol, while for Ampk and Pgc1 α the aging zebrafish had a higher increase due to resveratrol (Figure 9D-F).

Inflammation elevated in aging zebrafish retina and not regulated by resveratrol treatment

We found in aging zebrafish retina, expression of inflammation-related protein iNOS were increased, and inflammation-related genes Cox-2, TNF- α and IL-1 β were also increased (Figure 10) [46]. And resveratrol had no significant effect in young and aging zebrafish.

DISCUSSION

Mitochondrial dysfunction has been implicated as a leading cause of aging-related oculopathy, a very common ailment worldwide that can lead to visual impairment and blindness [7, 8]. In the present study, we used zebrafish as a model system to study aging-related alterations in retinas including mtDNA integrity, mtDNA copy number, mitochondrial fusion/fission regulators, mitophagy and autophagy, Akt/mTOR, Ampk/Sirt1/Pgc1 α and inflammation pathway activity.

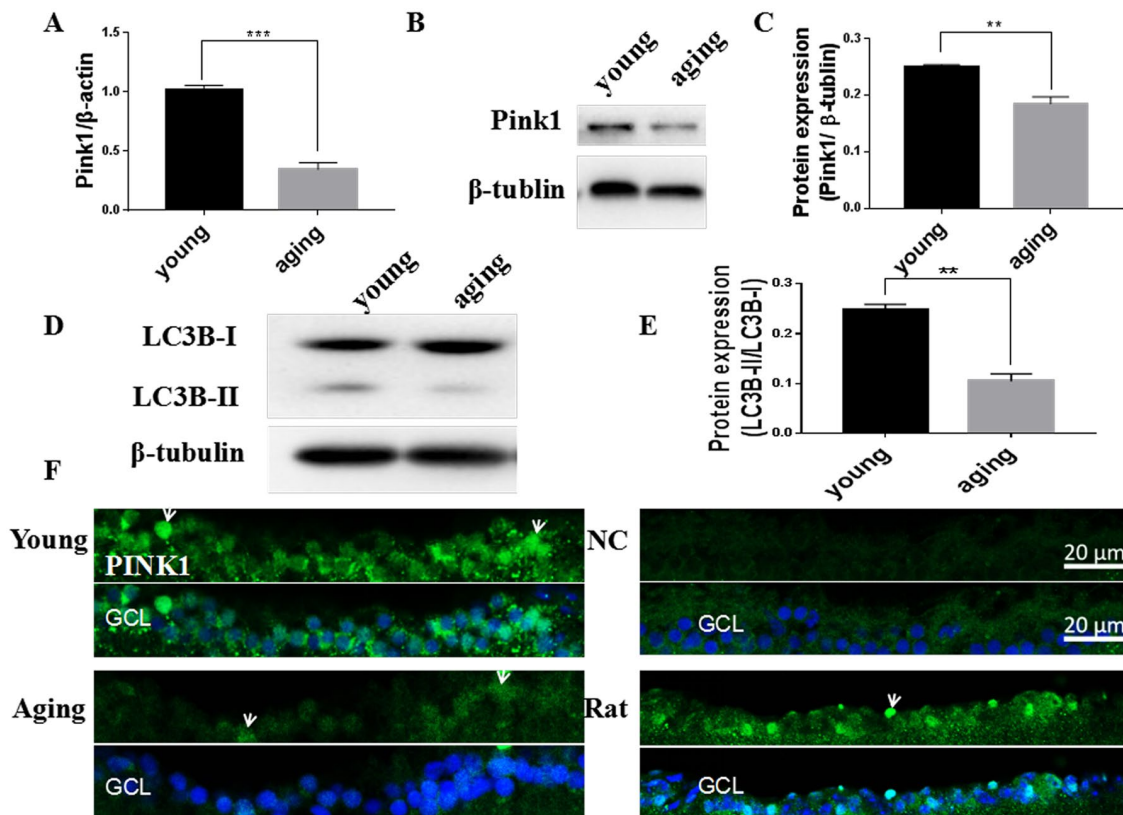


Figure 4. Decreased mitophagy and autophagy in aging zebrafish retinas. (A) Pink1 gene expression in young and aging zebrafish retinas as measured by quantitative real-time PCR (mean \pm SEM, *** P < 0.001, n = 3). (B) Representative western blot showing the protein expression level of Pink1 in young and aging zebrafish retinas. (C) Graph of the densitometric mean and SEM normalized to the corresponding level of the loading control protein beta-tubulin (** P < 0.01, n = 3). (D) Representative western blot showing the protein expression levels of LC3B-II and LC3B-I in young and aging zebrafish retina. (E) Graph of the ratio of LC3B-II to LC3B-I protein levels as determined by densitometry (** P < 0.01, n = 3). (F) Immunofluorescence analysis of Pink1 in the RGC layer of young and aging zebrafish retinas. Retina cross sections prepared from zebrafish eyes were immunostained with Pink1 antibody. All photographs were taken at 40x magnification except the rat sections that were at 20x. Young, 4-6 months old; aging, 19-23 months old; NC, negative control (without primary antibody); Rat, positive control; GCL, ganglion cell layer.

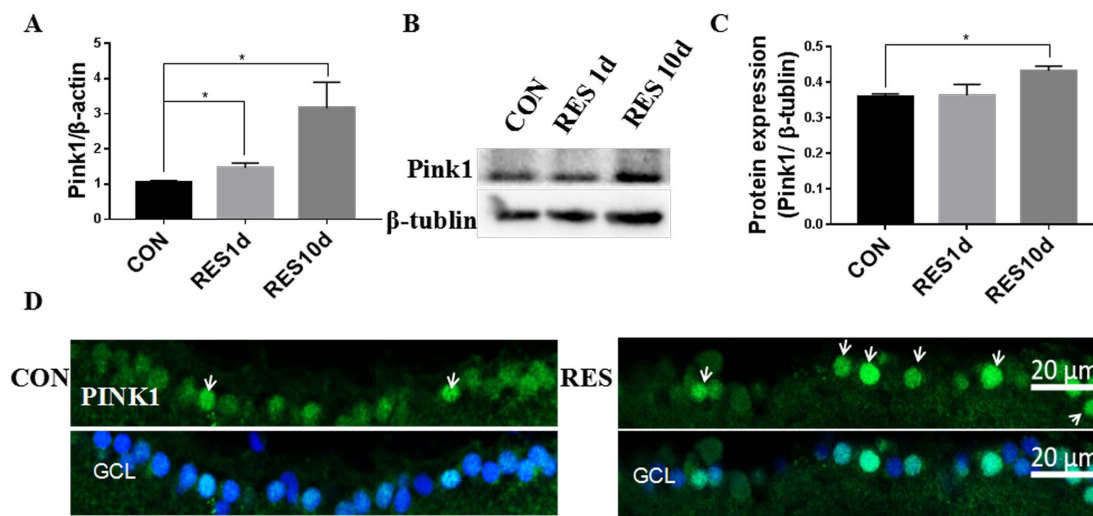


Figure 5. Resveratrol treatment increased mitophagy in young zebrafish retina. (A) Pink1 gene expression in adult zebrafish retina after treatment with resveratrol for 1 and 10 days as measured by quantitative real-time PCR (mean \pm SEM, * $P < 0.05$ compared to control (CON), $n=3$). (B) Representative western blot showing the protein expression of Pink1 in adult zebrafish retina after treatment with resveratrol for 1 and 10 days. (C) Graph of the densitometric mean and SEM normalized to the corresponding level of the loading control protein beta-tubulin from western blots as in B (* $P < 0.05$ compared to control (CON), $n=3$). (D) Immunofluorescence localization and relative expression of Pink1 in the RGC layer of adult zebrafish retinas after treatment with resveratrol for 10 days. Retina cross sections prepared from zebrafish eyes were immunostained with Pink1 antibody. All photographs were taken at 40x magnification. CON, control; RES1d, resveratrol treated for 1 days; RES/RES10d, resveratrol treated for 10 days; GCL, ganglion cell layer.

We also explored the ability of the anti-aging natural product resveratrol to modulate age-related alterations to the zebrafish retina.

We first explored mitochondrial quality and found that mtDNA integrity was lower in aging zebrafish retinas than in retinas of young zebrafish, suggesting that the mtDNA has suffered significant damage during aging [12,47]. Accumulation of ROS with age will harm mtDNA in particular, since mtDNA is more sensitive to oxidative damage due to its proximity to ROS production in the mitochondrial membrane. Moreover, a weaker antioxidant defense system in aging retinas further increases the mutation rate. The increased mutation load can then lead to a loss of mtDNA integrity [10,48,49]. Loss of mitochondrial content during aging has also been reported, and mitochondrial mass and mitochondrial copy number (mitCN) are decreased in neurodegeneration [31,50]. The mitCN was sharply decreased in aging compared to young retinas, indicating that the function of retinal mitochondria and their ability to efficiently produce energy are compromised during aging. Retinal cells and other neurons are particularly high energy-demanding tissues, so mitochondrial dysfunction has a higher impact on them compared to other tissues [9,51].

We observed that the mtDNA integrity of young zebrafish retinas was increased after 1- or 10-days treat-

ment with resveratrol, whereas the mitCN had a slight decrease after 10 days treatment but was not altered after only 1 day of treatment. One previous study found that resveratrol for one day can increase mtDNA integrity (the ratio of mit-L to mit-S) in adult zebrafish retinas but did not change the mitCN [30]. Another report indicated that resveratrol can decrease mitCN in mouse oocytes [52]. Our current results may be explained by an increase in mitophagy between 1 and 10 days of resveratrol treatment, which would increase the mitochondrial integrity by increasing the turnover of damaged mtDNA and thus decreasing the total mass of mitochondria.

Rather than existing as separate, individual units, a cell's mitochondria together make up a dynamic network of organelles in a constant state of flux between fusion and fission to regulate mitochondrial quality, maintain critical cellular functions, and ensure an adequate supply of energy. A healthy mitochondrial fusion/fission flux should balance the elimination of damaged mitochondria with the rate of new mitochondrial production to maintain mitochondrial homeostasis [10,44]. Mfn2 and Opa1 are vital regulators of fusion and are located at the outer- and inner-mitochondrial membrane, respectively, while Fis1 is a vital regulator of fission and is located at the outer-mitochondrial membrane [10,31,53]. Opa1 is a multi-domain protein that is cleaved by Oma1 from a long

isoform (Opa1-L) into a short isoform (Opa1-S). Opa1-L increases mitochondrial fusion, while Opa1-S increases fission, and therefore reduced Opa1 expression is believed to prolong lifespan because more Opa1-L will be present to prevent accumulation of damaged mitochondria. On the other hand, more Opa1-S may allow accumulation of dysfunctional mitochondria [54-56]. Fis1, the mitochondrial fission regulator, is also associated with age-related neuro-degeneration, and has been observed to be increased in AD and HD patient tissues [52,57]. In our study, we found that Mfn2 gene and protein expression was decreased, Opa1 gene and protein expression was unchanged, and Fis1 gene expression was increased in aging zebrafish retinas. These changes are consistent with previous reports and further support the notion that regulators of mitochondria

dynamics are mediators of aging in retinas as well as other neurons implicated in neurodegenerative diseases [5,53,58]. Moreover, our study was the first to show that Opa1 gene expression and the ratio of Opa1-L/Opa1-S was decreased during aging.

We postulated that mitochondria in aging zebrafish retinas are tipped to increased fragmentation, as the fusion activators are suppressed and fission activators are increased. Fragmentation is a compensatory means of adaptation to a low nutrition environment caused by ROS accumulation and loss of functional mitochondria. However, in the long term the vicious circle of increased fission and decreased fusion aggravates the aging process and likely plays a causative role in neurodegenerative diseases [5,11,21,44].

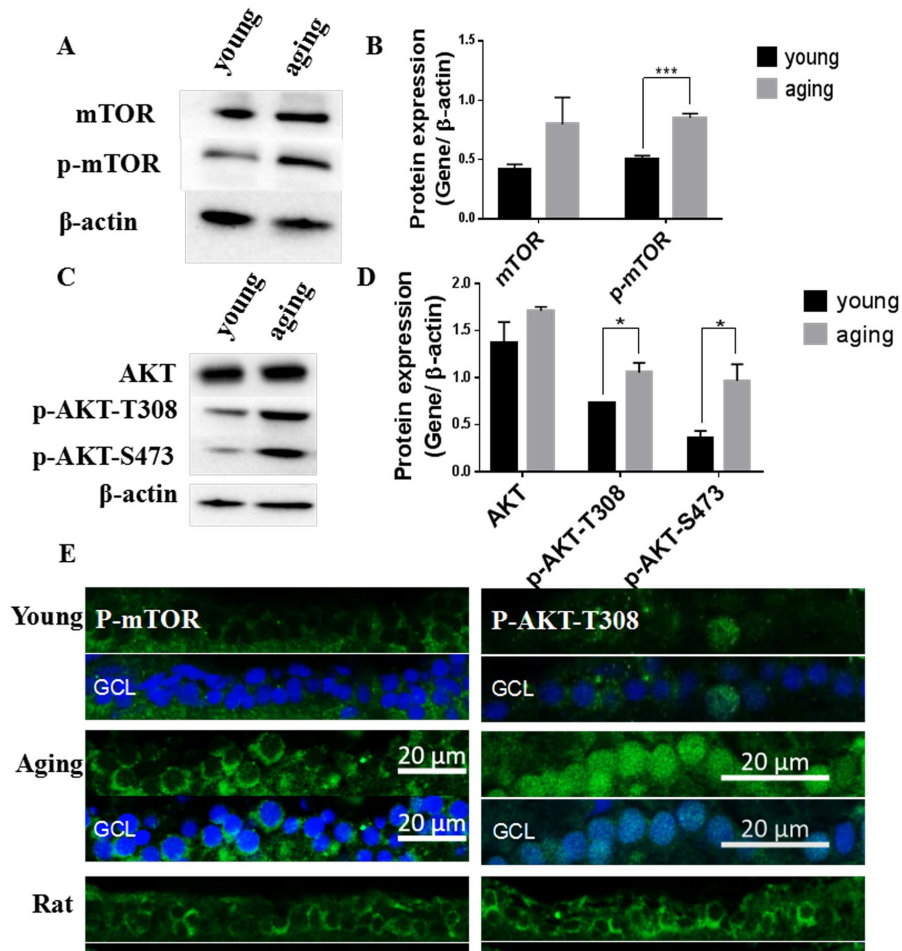


Figure 6. Activation of the Akt/mTOR pathway in aging zebrafish retinas. (A) Representative western blot showing the protein level of mTOR and p-mTOR in young and aging zebrafish retinas. (B) Densitometric mean and SEM normalized to the corresponding level of the loading control protein beta-actin (***P* < 0.001, *n* = 3). (C) Representative western blot showing the protein expression level of Akt and p-Akt-T308 and p-Akt-S473 in young and aging zebrafish retinas. (D) Densitometric mean and SEM normalized to the corresponding level of the loading control protein beta-actin (**P* < 0.05, *n* = 3). (E) Photographs of fluorescently immunostained retina cross-sections showing the localization and relative levels of p-mTOR and p-Akt-T308 in the RGC layers of young and aging zebrafish retinas. All photographs were taken at 40x magnification except rat sections were at 20x magnification and p-Akt-T308 at 60x magnification. Young, 4-6 months old zebra-fish; Aging, 19-23-month-old zebra-fish; Rat, positive control; GCL, ganglion cell layer.

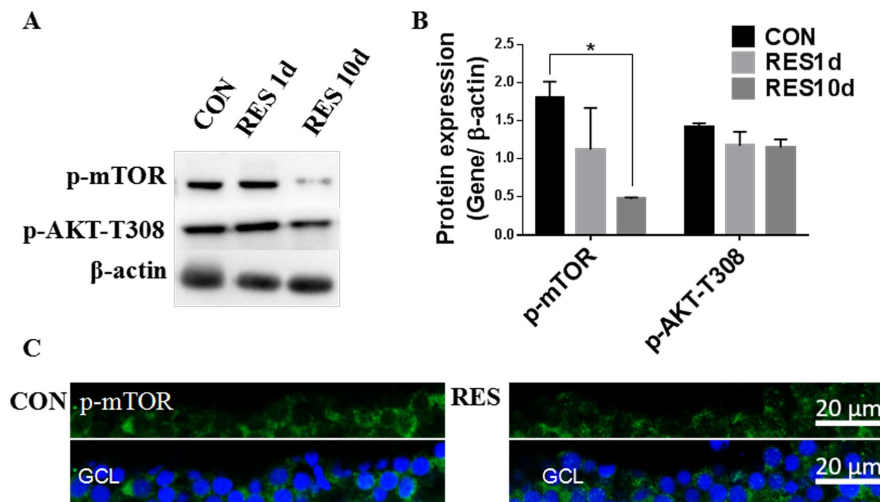


Figure 7. Resveratrol treatment suppressed the Akt/mTOR pathway in young zebrafish retinas. (A) Representative western blot showing the levels of p-mTOR and p-Akt-T308 in adult zebrafish retinas after being treated with resveratrol for 1 and 10 days. (B) Densitometric mean and SEM of p-mTOR and p-Akt-T308 normalized to the corresponding level of the loading control protein beta-actin (* $P < 0.05$ compared to control (CON), $n = 3$). (C) Photographs of fluorescence immunostained retina cross-sections showing the localization and relative levels of p-mTOR in the RGC layers of adult zebrafish retinas with or without resveratrol treatment for 10 days. All photographs were taken at 40x magnification. CON, control; RES1d, resveratrol treated for 1 day; RES/RES10d, resveratrol treated for 10 days; GCL, ganglion cell layer.

Many studies have provided evidence that resveratrol can improve mitochondrial function, particularly in old age, but the mechanisms remain unclear [31]. In the current study, we found that Mfn2, Opa1, Oma1, and Fis1 expression were all increased after 1 day of resveratrol treatment, but Opa1 and Oma1 levels returned to the level of control after 10 days treatment while Mfn2 and Fis1 remained elevated. Although resveratrol may act acutely on some genes that are nevertheless important for its beneficial effects, we postulated that the protective effects of resveratrol on mitochondrial dynamics may be primarily mediated by Mfn2 and Fis1 [30]. Kaige Peng et al. found that resveratrol can improve mitochondrial fusion-fission dynamics by promoting Mfn2, Opa1, and Fis1 expression to protect against the rotenone-induced neurotoxicity that would otherwise lead to mitochondrial homeostasis disorder, cellular damage, and dopaminergic neuron degeneration [31]. Although some suggest that inhibiting fission may be a beneficial target for neurodegenerative diseases, we believe that activating both fusion and fission together would be a better option [52]. Resveratrol, for example, appears to both promote fusion to dilute mitochondrial damage while also promoting fission to provide more energy generation and permit the elimination of unhealthy mitochondria through fission and mitophagy [10,23].

As the name suggests, mitophagy is the specialized autophagic process that digests unhealthy or excess mitochondria [59]. The relationship between autophagy and mitophagy is regulated by the p62 protein, which in vertebrates regulates autophagy via interacting with LC3 and mitophagy by controlling the Pink1/Parkin pathway [60]. We observed that the ratio of LC3B-II/LC3B-I protein, a marker of autophagy activity, was decreased in aging zebrafish retinas. Gene and protein expression of Pink1, a vital regulator of mitophagy, was also decreased in aging zebrafish retinas. Dysfunction of mitophagy and autophagy is implicated in neurodegenerative diseases including HD, AD, and Parkinson's disease (PD), where dysfunction of mitophagy and autophagy can lead to mitochondrial dysfunction and cell death [60]. The study by Wu et al. indicate that mitophagy and autophagy down-regulate mitochondrial ROS production through NLRP3 inflammasome activation [61], while a study by Lutz found an increase in mitochondrial fragmentation after loss of Pink1/Parkin function [62]. In the present study, we found that resveratrol can promote Pink1 gene and protein expression after 1- and 10-days treatment. Several other reports also showed that resveratrol can induce autophagy in neurons and promote Pink1/Parkin expression [21,34]. Over-expression of mitophagy activators can prolong drosophila and mouse lifespan, which occurred due to the activation of both fusion/fission and mitophagy [17,63,64].

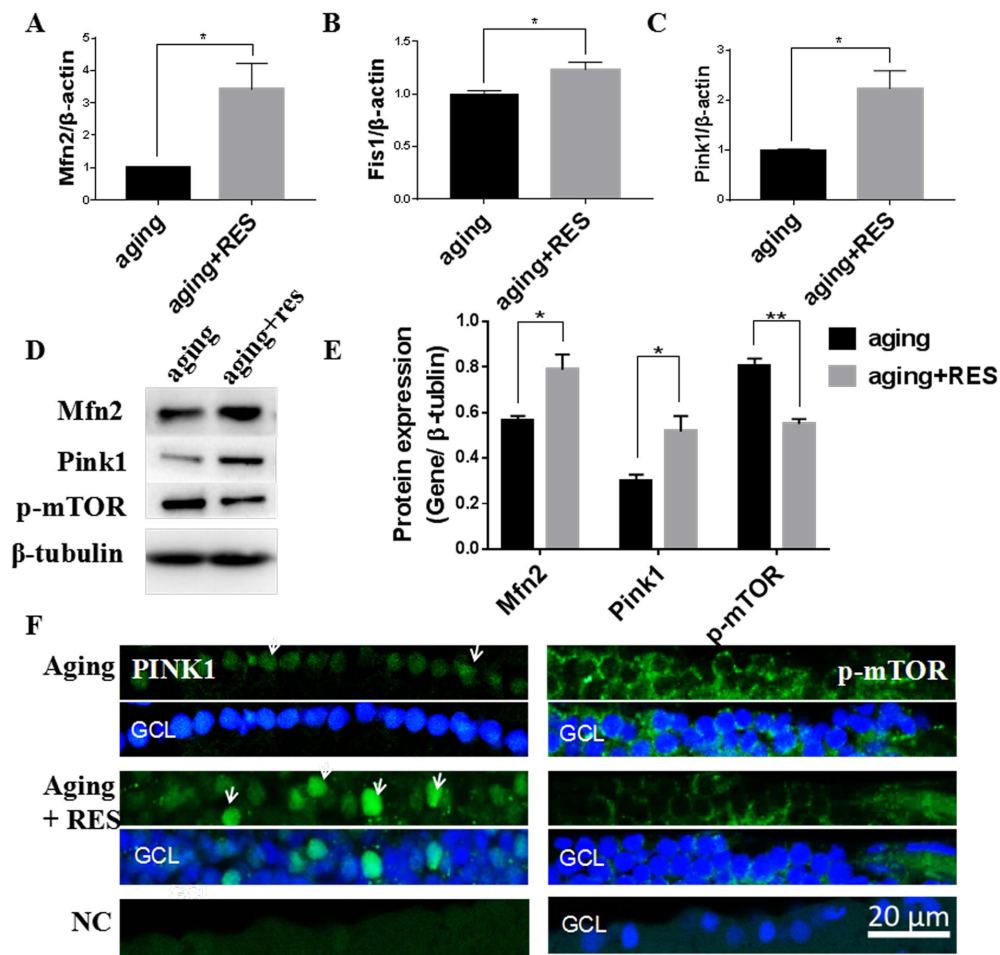


Figure 8. Resveratrol treatment activated Mfn2, Fis1, Pink1, and suppressed p-mTOR in aging zebrafish retina. (A-C) Mfn2, Fis1, Pink1 expression in aging and resveratrol-treated aging zebrafish retina. Graphs represent (A)Mfn2 (B) Fis1(C) Pink1 gene expression by quantitative real-time PCR (mean ± SEM, *P<0.05, n=3). (D)Representative western blot showing the protein expression levels of Mfn2,Pink1,p-mTOR in aging and resveratrol-treated aging zebrafish retina. (E)The graph showing the densitometric mean and SEM normalized to the corresponding level of the loading control protein beta-tubulin (*P<0.05, **P<0.01, n=3). (F) Immunolocalization and relative quantitative expression of Pink1 and p-mTOR on RGC in aging and resveratrol-treated aging zebrafish retina cross-sections. Retina cross sections prepared from zebrafish eyes were immunostained with Mfn2 or p-mTOR antibody. Results present aging, resveratrol-treated aging, and negative control (without primary antibody). All photographs were taken at 40 times. aging, 19-23 months zebrafish; aging + RES, resveratrol-treated aging zebrafish for 10 days; NC, negative control; GCL, ganglion cell layer.

Accumulation of mitochondrial damage will lead to aging, so it is of interest why cells would down-regulate protective mechanisms such as mitochondrial fusion/fission and mitophagy/autophagy who maintain mitochondrial activity during aging. Many studies have pointed to mTOR as a culprit in aging, showing that elevated mTOR activity can affect mitochondrial function and inhibit mitophagy/autophagy, thus contributing to the aging process [16,65]. Activated mTOR inhibits autophagy (including mitophagy), whereas inhibition of the Akt/mTOR pathway induces autophagy and increases the lifespan of many species [9,43,66]. Moreover, downregulation of mTOR has been shown to increase longevity by maintaining mitochondrial function and appropriate energy consum-

ption [63,65,67]. Increased mTOR activity is observed in aging tissues, and many believe that the PI3K/PTEN/Akt/mTOR pathway is one of the most important regulators of aging [68].

We found both increased expression and phosphorylation (indicating activation) of mTOR and Akt in aging zebrafish retinas. Moreover, resveratrol caused a significant decrease in p-mTOR after 10 days treatment, while p-Akt-T308 had no significant change. These results are consistent with those of Jun Wu et al. who found that resveratrol could promote mitophagy/autophagy in HMrSV5 cells by suppressing p-mTOR, and who also demonstrated that LC3-II accumulated with mTOR knockout [61].

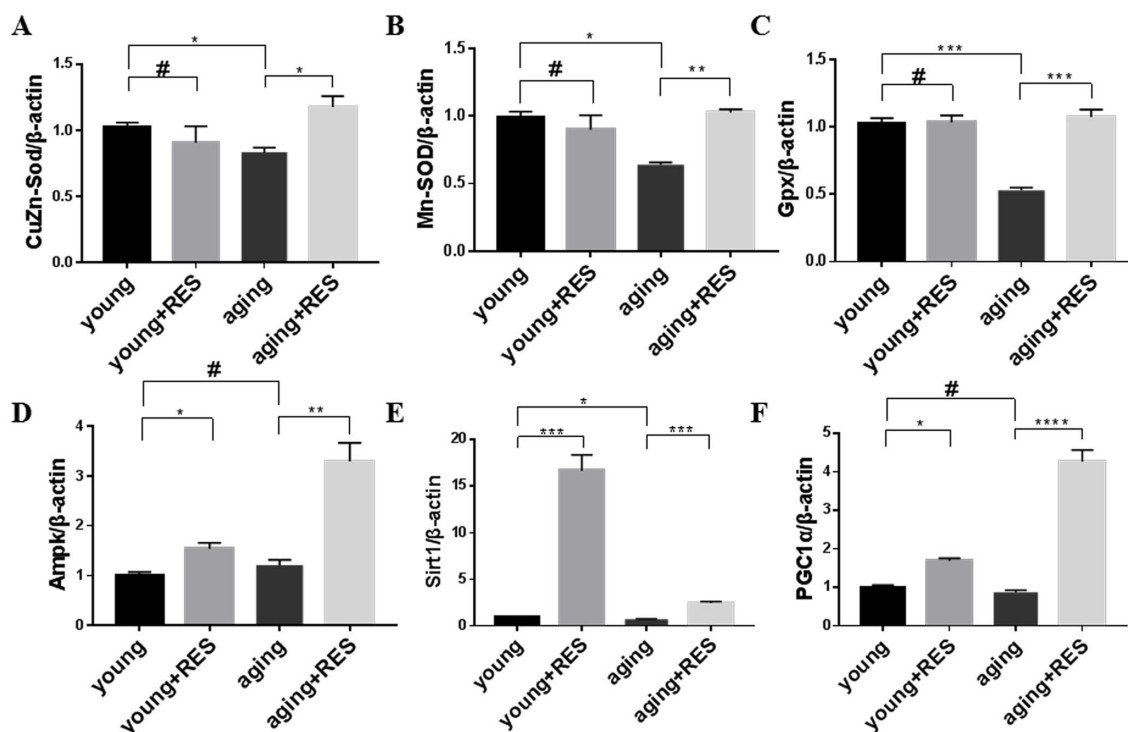


Figure 9. Resveratrol treatment activated the antioxidant system and Ampk/Sirt1/Pgc1α pathway in aging zebrafish retina. (A-F) Cu/Zn-Sod, Mn-Sod, Gpx, Ampk, Sirt1, and Pgc1α expression in young, resveratrol-treated young, aging, and resveratrol-treated aging zebrafish retinas. Graphs represent (A) Cu/Zn-Sod, (B) Mn-Sod, (C) Gpx, (D) Ampk, (E) Sirt1, and (F) Pgc1α gene expression by quantitative real-time PCR (mean ± SEM, *P < 0.05 **P < 0.01 ***P < 0.001 ****P < 0.0001, #P means no statistical significance, n=3). young, 4-6 month old zebrafish; young + RES, young zebrafish after resveratrol treatment for 10 days; aging, 19-23 month old zebrafish; aging + RES, aging zebrafish after resveratrol treatment for 10 days.

Regulation of mitochondrial function by mTOR is not solely through its regulation of mitophagy/autophagy [16]. Several reports suggest that mTOR can activate HIF-1, PGC1α, YY-1, and AMPK to regulate mitochondrial oxygen consumption, mitochondrial biogenesis, and mitochondrial metabolism [67,69,70]. Results from Masahiro Morita et al. suggest that the nutrient-sensing ability of mTOR promotes mitochondrial fission, and suppressing mTOR can elevate mitochondrial fusion to protect cells from mitochondrial degeneration [71]. It is therefore believed that mTOR inhibition should be targeted to protect neurons against age-related neurodegenerative diseases [72]. The current gold standard pharmacological inhibitor of mTOR is rapamycin, an extremely effective inhibitor of mTOR Complex 1, but it can cause many side effects including hyperglycemia, hyperlipidemia, anemia, eye diseases, and some testicle diseases [73]. Therefore, searching for other safer mTOR inhibitors that can improve mitochondrial function is required.

Given the relationships between aging, mitochondrial function, inflammation, and ROS, we explored what

effects resveratrol has on the cellular ROS detoxification system. Our prior study showed that I/R-induced inflammation can promote ROS accumulation and subsequent cellular damage in the rat retina leading to cell death, and that resveratrol could attenuate this inflammation and protect retinas [36]. However, in the current study we found that although expression of inflammation-related proteins was indeed increased in aging zebrafish retinas, resveratrol had no significant effect on their expression in young or aging zebrafish (Figure 10). And we found that in aging zebrafish retina, the antioxidant system such as CuZn-Sod, Mn-Sod and Gpx were decreased, which indicated the ability of cell to clean oxidative products was down-regulated, and the ROS level was increased in aging [9]. The result that resveratrol can activate oxidant system in aging but had no effect in young zebrafish retina illustrated resveratrol can maintain antioxidant system at a suitable level to improve mitochondrial quality and energy metabolism.

The Ampk/Sirt1/Pgc1α axis is considered to be a critical sensor of metabolic demand and regulator of

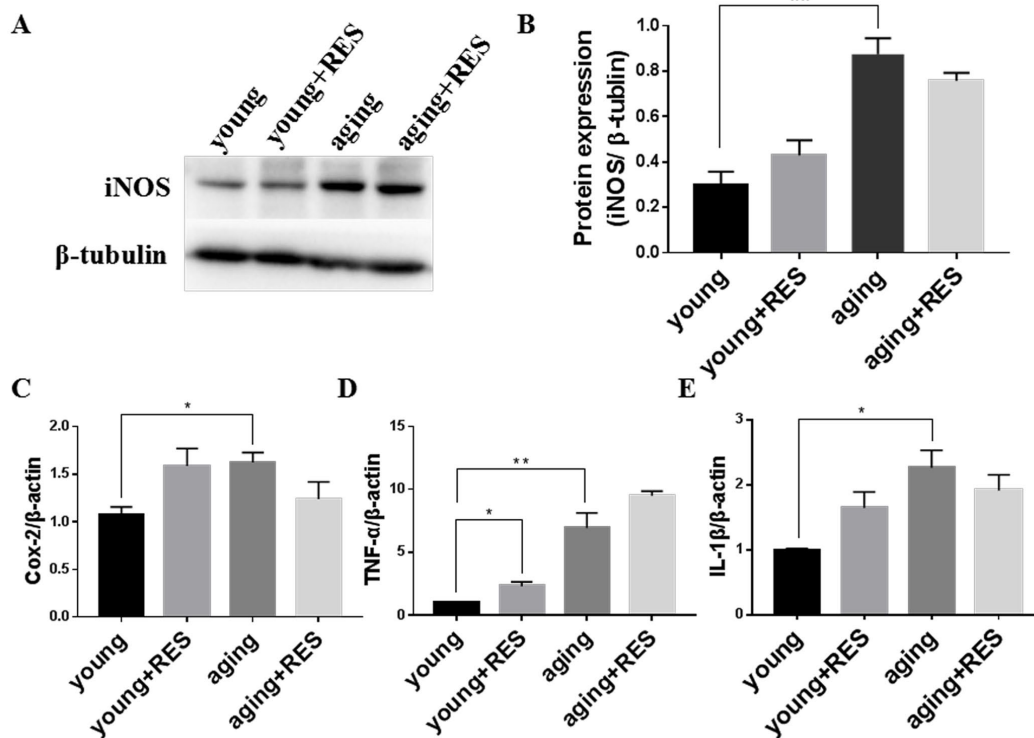


Figure 10. Inflammation elevated in aging zebrafish retina and not regulated by resveratrol treatment (A) Representative western blot showing the protein expression level of iNOS in young, resveratrol-treated young, aging, and resveratrol-treated aging zebrafish retinas. **(B)** The densitometric mean and SEM of bands from **A** normalized to the corresponding level of the loading control protein beta-tubulin (** $P < 0.01$, $n = 3$). **(C-E)** Cox-2, TNF- α , and IL-1 β expression in young, resveratrol-treated young, aging, and resveratrol-treated aging zebrafish retinas. Graphs represent **(C)** Cox-2, **(D)** TNF- α , and **(E)** IL-1 β gene expression by quantitative real-time PCR (mean \pm SEM, * $P < 0.05$ ** $P < 0.01$, $n = 3$). young, 4-6 month old zebrafish; young + RES, young zebrafish after resveratrol treatment for 10 day; aging, 19-23 month old zebrafish; aging + RES, aging zebrafish after resveratrol treatment for 10 days.

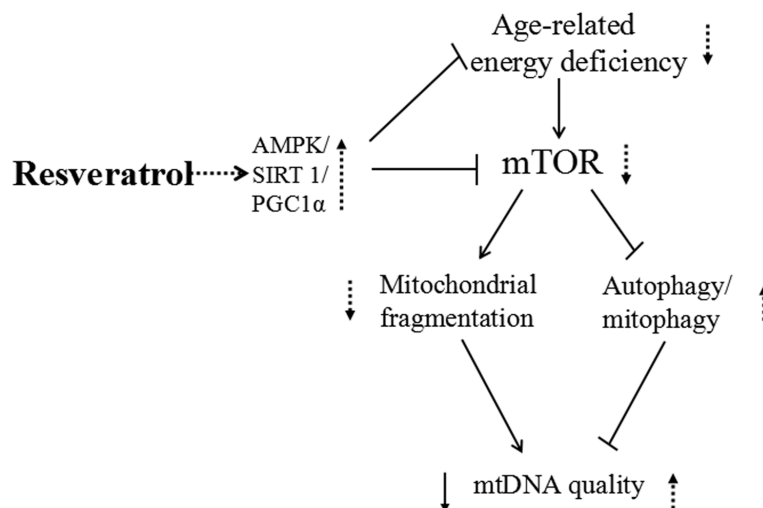


Figure 11. Schematic representation of resveratrol induced activation of AMPK/SIRT1/PGC1 α and inhibition of mTOR, leading to increased mitochondrial quality. Resveratrol treatment enhances AMPK/SIRT1/PGC1 α expression and decreases mTOR signaling, which leads to an increase in mtDNA quality and enhanced energy metabolism at least partly through decreased mitochondrial fragmentation and increased autophagy/mitophagy.

energy production and consumption [9,74]. By increasing levels of Ampk, Sirt1, and Pgc1 α , resveratrol can enhance mitochondrial biogenesis, oxidative metabolism, and cellular ROS defense enzymes to cope with the stress of aging in tissues such as the retina with a high metabolic demand. Increasing Ampk/Sirt1 activity can also inhibit mTOR downstream to promote mitophagy. Some reports also suggest that Sirt1/Pgc1 α activation can help prevent mitochondrial fragmentation to alleviate mitochondrial dysfunction [75]. Therefore, activation of the Ampk/Sirt1/Pgc1 α pathway by resveratrol is likely crucial for its ability to maintain healthy mitochondrial dynamics and regulate ROS levels for healthy aging.

Zebrafish has been utilized to study many age-related eye diseases including cataracts, glaucoma, and age-related macular degeneration (AMD). For example, NMDA treatment damages retinal neurons and was used to establish a zebrafish glaucoma model, while the gnn mutant or vascular endothelial growth factor (VEGF) treatment lead to AMD characteristics similar to those seen in human AMD [30,37,76-77]. We postulate that in aging zebrafish retinas the high demand for nutrition and energy will activate mTOR, which promotes mitochondrial fission to increase ATP production and suppresses fusion to compensate for the decreasing mitochondrial function. Increased oxygen consumption and inflammation leads to accumulation of excess ROS and an increase in oxidative to damage mtDNA. Mitophagy/autophagy are suppressed by mTOR, causing a buildup of unhealthy mitochondria that cannot be eliminated and this mitochondrial fragmentation can promote aging. Many studies have shown that resveratrol has anti-aging and neuroprotective properties, although the mechanisms are not completely understood [31]. We explored the effects of resveratrol on mtDNA integrity and copy number, mitochondrial fusion/fission, mitophagy and anti-ROS regulators, Akt/mTOR and Ampk/Sirt1/Pgc1 α pathway and found that it was able to alleviate or diminish many of the detrimental changes that occur during aging. Further studies are needed to analyze whether resveratrol

can protect against ROS accumulation and whether its beneficial molecular effects can translate to protection of the retina against age-related ophthalmopathy (Figure 11).

CONCLUSIONS

Maintaining mitochondrial health is crucial to prevent age-related neurodegenerative diseases, including ophthalmopathy. We utilized the zebrafish retina as a model for age-related ophthalmopathy and observed decreased mtDNA integrity, dysfunctional mitochondrial fission-fusion dynamics, decreased expression of antioxidant defense enzymes, and increased activity of the Akt/mTOR pathway in the aging retina. Consistent with its anti-aging effects in other species and model systems, resveratrol treatment helped alleviate most of the age-related changes observed in the zebrafish retina, suggesting its potential for the prevention of aging-induced ophthalmopathy in other species including humans. This study indicates that further testing of resveratrol for ophthalmopathy is warranted, and helps establish the zebrafish retina as a viable model of age-related ophthalmopathy for further studies on the molecular mechanisms and for novel drug screening.

MATERIALS AND METHODS

Animals

Male and female 4-6 months old (young/control) and 19-23 months old (aged) wild-type zebrafish of AB strain were obtained from the China Zebrafish Resource Center (CZRC, Wuhan, China) [40], and 5 days and 1 month old zebrafishes were offspring of the former. All fish were maintained in a 25 L aquarium at 28°C under 14-hour/10-hour light/dark cycles and were fed with brine shrimp twice a day. The maintenance and experimental manipulations of zebrafish were approved by the ethical review committee of Nanchang University (Nanchang, China) and were in accordance with the ARVO Statement for the Use of Animals in Ophthalmic and Vision Research.

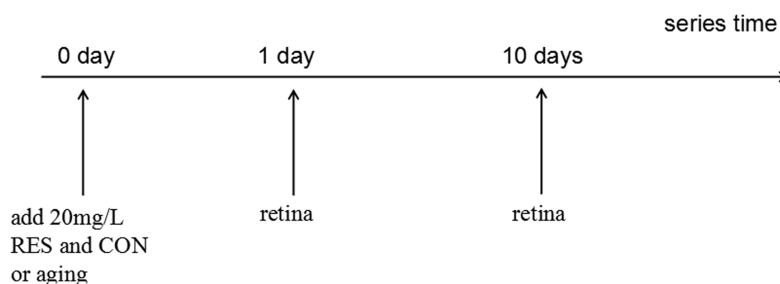


Figure 12. Resveratrol treatment timeline. All treatments began at 0 hour and the time points are post-resveratrol administration. CON/aging, 0.04% ethanol; RES, 20mg/L resveratrol + 0.04% ethanol.

Table 1. Primers used in the experiment.

Genes	Primers (5'-3')
Mfn2	F: GCGCCTACATCAAAGAAAGC R: CAGCATCCAAATCCTCATCC
Fis1	F: CTAGCTCCAGGGCCTGTTTGT R: GGTGAAAGGACCCGTTTCCAG
Opa1	F: GCTTGAGCGCTTGGAAAAGGAA R: TGGCAGGTGATCTTGAGTGTGT
Oma1	F: TGGAGGCGGAAGCGGATCAG R: GAATGAGGCGGTCCAACGTCTG
Pink1	F: CTGATGACGTTTCCAGCTGGTG R: CCACAGACTGATGTGCAGGA
Cox2	F: AACTAGGATTCCAAGACGCAGCATC R: AAATAAGAATGATGGCCGGAAGG
IL-1 β	F: TCGCCCAGTGCTCCGGCTAC R: GCAGCTGGTCGTATCCGTTTGG
TNF- α	F: AGGAACAAGTGCTTATGAGCCATGC R: AAATGGAAGGCAGCGCCGAG
CuZn-Sod	F: GTCGTCTGGCTTGTGGAGTG R: TGTCAGCGGGCTAGTGCTT
Mn-Sod	F: CCGGACTATGTAAAGGCCATCT R: AACTCGGTTGCTCTTTTCTCT
Gpx	F: AGATGTCATTCCTGCACACG R: AAGGAGAAGCTTCCTCAGCC
Ampk	F: ATCATAGACAACCGCCGCATTA R: TTGGCTCGCCGTACACCA
Sirt1	F: CAAGGAAATCTACCCCGGACAGT R: CAGTGTGTCGATATTCTGCGTGT
Pgc1 α	F: CCCCTTTGCCCTGACCTGCCTGAG R: GAAGGACAGCTCTGATCACTGGCATTGG
Beta-actin	F: CCCAAGGCCAACAGGGAAAA R: GGTACGACCGGAGGCATACA
Nuclear chain	F: ATGGGCTGGGCGATAAAATTGG R: ACATGTGCATGTCGCTCCCAA
Long mitochondrial chain	F: TTAAAGCCCCGAATCCAGGTGAGC R: GAGATGTTCTCGGGTGTGGGATGG
Short mitochondrial chain	F: CAAACACAAGCCTCGCCTGTTTAC R: CACTGACTTGATGGGGGAGACAGT

Resveratrol treatment

The control group was ethanol-control treated zebrafish while the resveratrol group was zebrafish exposed to resveratrol (R5010; Sigma-Aldrich Corp., St. Louis, MO, USA) dissolved in ethanol to the final concentration of 20mg/L for 1 or 10 days. For the resveratrol group, a day of treatment consisted of 10 hours a day under dark condition with resveratrol and another 14 hours under light condition with clean, untreated water[74]. For the control group, the zebrafish were exposed to the same volume of ethanol as the resveratrol group for 1 or 10 days. For immunofluorescence analysis, zebrafish treated for 10 days were used. (Figure 12).

Quantitative real-time PCR (qRT-PCR)

Total RNA of retinas (n=8 per group) were abstracted with Trizol Reagent (Cat. #92008, Ambion, USA; 15596-018) according to the manufacturer's instructions. Total RNA was reverse transcribed to cDNA using HiScript® Q RT SuperMix for qPCR (+ gDNA wiper) (Vazyme; R123-01). The cDNA was used as template for qPCR with TB Green™ Premix Ex Taq™ II (Tli RNaseH Plus) (Takara; RR820A). Specific primers used in the experiment are from PrimerBank and precursor articles (Table 1). The qPCR process, a three steps reaction (95°C denature for 15s, 60°C annealing for 30s and 72°C extension for 24s), was carried out with the StepOne Plus™ Real-time PCR System (Life Technologies, Carlsbad, CA, USA). All data were chosen from the linear phase of amplification for each gene.

Mitochondrial DNA analysis

Total DNA was extracted from retinas using the Ezup column animal genomic DNA extraction kit (B518251; Sangon Biotech, Shanghai, China). Short mitochondrial chain primers and long mitochondrial chain primers [78] (Table 1) were chosen to amplify DNA using Taq DNA Polymerase (Mg²⁺ plus buffer) (Vazyme; P101). The long mitochondrial chain reaction procedure was 19 cycles (94°C for 15 seconds and 68°C for 12 minutes), and then an extension step (72°C for 10 minutes). The short mitochondrial chain reaction procedure was 25 cycles (94°C for 30 seconds, 62°C for 45 seconds, and 72°C for 30 seconds), and then an extension step (72°C for 10 minutes). All data were chosen from the linear phase of amplification. Amplified DNA were analyzed on a 0.8% agarose gel (with ethidium bromide) and observed by Image Lab under UV light, and were quantified with ImageJ. A DNA Ladder and Low DNA mass ladder (Takara) were used to benchmark the DNA band sizes.

The total DNA extracted from retina was also used for analysis of mitochondrial copy number (mtCN). Short mitochondrial chain and Nuclear chain (Table 1) were chosen to amplify DNA using TB Green™ Premix Ex Taq™ II (Tli RNaseH Plus) (Takara; RR820A). The reaction procedure was 25 cycles (94°C for 30 seconds, 62°C for 45 seconds, and 72°C for 30 seconds), and then an extension step (72°C for 10 minutes) and was carried out with the StepOne Plus™ Real-time PCR System (Life Technologies, Carlsbad, CA, USA). All data were chosen from the linear phase of amplification for each sequence.

Table 2. Primary antibodies used in the experiment.

Antibody	Source	Catalog No.	Type	Dilution	MW(kD)
Mfn2	Abcam	Ab56889	Mouse mAb	1:1000(WB) 1:50(IF)	75
Pink1	Abcam	Ab23707	Rabbit mAb	1:1000(WB) 1:50(IF)	66.50
Opal	BD	612606	Mouse mAb	1:1000(WB)	80-100
mTOR	CST	#2983	Rabbit mAb	1:1000(WB)	289
P-mTOR	CST	#5536	Rabbit mAb	1:1000(WB) 1:50(IF)	289
AKT	CST	#4691	Rabbit mAb	1:1000(WB)	60
p-AKT-Thr308	CST	#13038	Rabbit mAb	1:1000(WB) 1:50(IF)	60
p-AKT-Ser473	CST	#4060	Rabbit mAb	1:1000(WB)	60
LC3B	CST	#2775	Rabbit mAb	1:1000(WB)	16.14
COX2	Gayman	#160106	Rabbit mAb	1:1000(WB)	75
iNOS	Invitrogen	PAI-036	Rabbit mAb	1:1000(WB)	130
Beta-actin	TRANS	HC201	Mouse mAb	1:1000(WB)	42
Beta-tubulin	TRANS	J10715	Donkey anti-mouse	1:1000(WB)	55

Western blot analysis

Proteins were extracted from zebrafish retinas (n=10) with RIPA buffer (R0010; Solarbio, Beijing, China) containing Phenylmethanesulfonyl fluoride (PMSF; Solarbio, Beijing, China). The concentration of protein was measured with the BCA Protein Assay Kit (Beyotime Biotechnology, Shanghai, China). Protein samples (10 µg each) were separated by 10% SDS-PAGE and transferred to nitrocellulose membranes. 5% non-fat milk dissolved in Tris-buffered saline containing Tween-20 was used to block the blots before applying primary antibodies for overnight at 4°C (Table 2). Then, peroxidase-conjugated secondary antibodies (goat anti-rabbit and goat anti-mouse (ZSGB-BIO, Beijing, China) were added at 1:2500 for 1 hour at room temp. Protein bands were then observed and analyzed using a SYNGENE imaging system (Cambridge, UK) and ImageJ (National Institutes of Health, Bethesda, MD, USA).

Immunofluorescence

Zebrafish were first anesthetized in ice water and then the eyeballs were carefully removed and fixed in 4% PFA overnight. After fixation, eyes were transferred to an EP tube for dehydration in 10%, 20%, and 30% sucrose solution until the eyes settled to the bottom in each sucrose concentration. Each eye was then solidified with OCT (optim alcutting tem perature) under -80°C for conservation or -20°C in a freezing microtome for slicing. The microtome maintained the temperature between -22°C to -20°C, and frozen eyes were sliced into 5µm thick slices. Slices were washed with 1×PBS 3×5 minutes. Water surrounding the tissue was blot up and circles were drawn on each tissue using a fluorescent pen. Retina slices were then blocked in PBS containing 0.3% BSA (Solarbio, Beijing, China) for an hour at room temperature and washed with 1×PBS 3x5 minutes before incubating with primary antibodies (Table 2) overnight at 4°C. Tissue slices incubated in PBS without primary antibodies were used as negative controls, and rat tissue slices incubated in PBS with same primary antibodies were used as positive controls. 1× TBST washing for 3x5 minutes was performed before and after incubation with Alexa Fluor 488 anti-mouse (H+L) or Alexa Fluor 488 anti-rabbit (H+L) secondary antibodies (dilution, 1:200; Life Technologies, Eugene, OR, USA) for one hour at room temperature. DAPI (Boster, Wuhan, China) staining of cellular nuclei was then performed prior to covering the slides with coverslips. Finally, retina slices were observed by confocal microscopy (OLYMPUS IX71, Japan).

Data analysis

Data were analyzed with GraphPad Prism 7.0 and ImageJ, and the error bars are mean ± SEM. Significance was checked by ANOVA followed by unpaired t-test, n ≥ 3. P < 0.05 was considered as significant.

AUTHOR CONTRIBUTIONS

N.W, Z.L, W.S, M.J, H.X and X.Z conceived the study. N.W, Z.L, W.S, M.J, H.W, S.L, Y.W, P.H and S.Z performed the experiments. N.W, Z.L, W.S, H.X and X.Z analyzed the data. N.W, H.X and X.Z drafted the manuscript. All authors read and approved the final version of manuscript.

ACKNOWLEDGEMENTS

The authors would like to acknowledge Suqi Zou and Hongdou Luo for helping guild experimental operation skills.

CONFLICTS OF INTEREST

The authors declare that they have no conflicts of interest.

FUNDING

This work was supported by the National Natural Science Foundation of China (81271425, 81260148, 31400988, 81160144, and 31171044) and Natural Science Foundation of Jiangxi (20151BBG70243, 20122BCB23007)..

REFERENCES

1. Fontana L, Partridge L, Longo VD. Extending healthy life span—from yeast to humans. *Science*. 2010; 328:321–26. <https://doi.org/10.1126/science.1172539> PMID:20395504
2. Mattson MP. Emerging neuroprotective strategies for Alzheimer's disease: dietary restriction, telomerase activation, and stem cell therapy. *Exp Gerontol*. 2000; 35:489–502. [https://doi.org/10.1016/S0531-5565\(00\)00115-7](https://doi.org/10.1016/S0531-5565(00)00115-7) PMID:10959037
3. Vijg J. Somatic mutations and aging: a re-evaluation. *Mutat Res*. 2000; 447:117–35. [https://doi.org/10.1016/S0027-5107\(99\)00202-X](https://doi.org/10.1016/S0027-5107(99)00202-X) PMID:10686308
4. Perry G, Nunomura A, Hirai K, Zhu X, Pérez M, Avila J, Castellani RJ, Atwood CS, Aliev G, Sayre LM, Takeda A,

- Smith MA. Is oxidative damage the fundamental pathogenic mechanism of Alzheimer's and other neurodegenerative diseases? *Free Radic Biol Med.* 2002; 33:1475–79. [https://doi.org/10.1016/S0891-5849\(02\)01113-9](https://doi.org/10.1016/S0891-5849(02)01113-9) PMID:12446204
5. Reddy PH, Reddy TP. Mitochondria as a therapeutic target for aging and neurodegenerative diseases. *Curr Alzheimer Res.* 2011; 8:393–409. <https://doi.org/10.2174/156720511795745401> PMID:21470101
 6. Swerdlow RH. Is aging part of Alzheimer's disease, or is Alzheimer's disease part of aging? *Neurobiol Aging.* 2007; 28:1465–80. <https://doi.org/10.1016/j.neurobiolaging.2006.06.021> PMID:16876913
 7. Klein R, Klein BE. The prevalence of age-related eye diseases and visual impairment in aging: current estimates. *Invest Ophthalmol Vis Sci.* 2013; 54:ORSF5-ORSF13 <https://doi.org/10.1167/iovs.13-12789> PMID: 24335069
 8. Takihara Y, Inatani M, Eto K, Inoue T, Kreymerman A, Miyake S, Ueno S, Nagaya M, Nakanishi A, Iwao K, Takamura Y, Sakamoto H, Satoh K, et al. In vivo imaging of axonal transport of mitochondria in the diseased and aged mammalian CNS. *Proc Natl Acad Sci USA.* 2015; 112:10515–20. <https://doi.org/10.1073/pnas.1509879112> PMID:26240337
 9. Gonzalez-Freire M, de Cabo R, Bernier M, Sollott SJ, Fabbri E, Navas P, Ferrucci L. Reconsidering the Role of Mitochondria in Aging. *J Gerontol A Biol Sci Med Sci.* 2015; 70:1334–42. <https://doi.org/10.1093/gerona/glv070> PMID:25995290
 10. Meyer JN, Leuthner TC, Luz AL. Mitochondrial fusion, fission, and mitochondrial toxicity. *Toxicology.* 2017; 391:42–53. <https://doi.org/10.1016/j.tox.2017.07.019> PMID:28789970
 11. Liesa M, Shirihai OS. Mitochondrial dynamics in the regulation of nutrient utilization and energy expenditure. *Cell Metab.* 2013; 17:491–506. <https://doi.org/10.1016/j.cmet.2013.03.002> PMID:23562075
 12. Wang AL, Lukas TJ, Yuan M, Neufeld AH. Age-related increase in mitochondrial DNA damage and loss of DNA repair capacity in the neural retina. *Neurobiol Aging.* 2010; 31:2002–10. <https://doi.org/10.1016/j.neurobiolaging.2008.10.019> PMID:19084291
 13. Tam ZY, Gruber J, Halliwell B, Gunawan R. Mathematical modeling of the role of mitochondrial fusion and fission in mitochondrial DNA maintenance. *PLoS One.* 2013; 8:e76230. <https://doi.org/10.1371/journal.pone.0076230> PMID:24146842
 14. Meira Martins LA, Vieira MQ, Ilha M, de Vasconcelos M, Biehl HB, Lima DB, Schein V, Barbé-Tuana F, Borojevic R, Guma FC. The interplay between apoptosis, mitophagy and mitochondrial biogenesis induced by resveratrol can determine activated hepatic stellate cells death or survival. *Cell Biochem Biophys.* 2015; 71:657–72. <https://doi.org/10.1007/s12013-014-0245-5> PMID:25234614
 15. Mizushima N, Levine B, Cuervo AM, Klionsky DJ. Autophagy fights disease through cellular self-digestion. *Nature.* 2008; 451:1069–75. <https://doi.org/10.1038/nature06639> PMID:18305538
 16. Johnson SC, Rabinovitch PS, Kaeberlein M. mTOR is a key modulator of ageing and age-related disease. *Nature.* 2013; 493:338–45. <https://doi.org/10.1038/nature11861> PMID:23325216
 17. Manner C, Ulgherait M, Rana A, Walker DW, Ulgherait M, Rana A, Rera M, Graniel J, Walker DW. MPK modulates tissue and organismal aging in a non-cell-autonomous manner. *Cell Reports.* 2014; 8:1767–80. <https://doi.org/10.1016/j.celrep.2014.08.006> PMID:25199830
 18. Sgarbi G, Matarrese P, Pinti M, Lanzarini C, Ascione B, Gibellini L, Dika E, Patrizi A, Tommasino C, Capri M, Cossarizza A, Baracca A, Lenaz G, et al. Mitochondria hyperfusion and elevated autophagic activity are key mechanisms for cellular bioenergetic preservation in centenarians. *Aging (Albany NY).* 2014; 6:296–310. <https://doi.org/10.18632/aging.100654> PMID:24799450
 19. Palikaras K, Lionaki E, Tavernarakis N. Coordination of mitophagy and mitochondrial biogenesis during ageing in *C. elegans*. *Nature.* 2015; 521:525–28. <https://doi.org/10.1038/nature14300> PMID:25896323
 20. Zhuang N, Li L, Chen S, Wang T. PINK1-dependent phosphorylation of PINK1 and Parkin is essential for mitochondrial quality control. *Cell Death Dis.* 2016; 7:e2501. <https://doi.org/10.1038/cddis.2016.396> PMID:27906179
 21. Diot A, Morten K, Poulton J. Mitophagy plays a central role in mitochondrial ageing. *Mamm Genome.* 2016; 27:381–95. <https://doi.org/10.1007/s00335-016-9651-x> PMID:27352213
 22. García-Prat L, Martínez-Vicente M, Perdiguero E,

- Ortet L, Rodríguez-Ubrea J, Rebollo E, Ruiz-Bonilla V, Gutarra S, Ballestar E, Serrano AL, Sandri M, Muñoz-Cánoves P. Autophagy maintains stemness by preventing senescence. *Nature*. 2016; 529:37–42. <https://doi.org/10.1038/nature16187> PMID:26738589
23. Grimm A, Eckert A. Brain aging and neurodegeneration: from a mitochondrial point of view. *J Neurochem*. 2017; 143:418–31. <https://doi.org/10.1111/jnc.14037> PMID:28397282
24. Cavallini G, Donati A, Taddei M, Bergamini E Evidence for Selective Mitochondrial Autophagy and Failure in Aging ND ES. *Autophagy*. 2007; 3:26–27. <https://doi.org/10.4161/auto.3268> PMID:16963838
25. Valenzano DR, Terzibas E, Genade T, Cattaneo A, Domenici L, Cellerino A. Resveratrol prolongs lifespan and retards the onset of age-related markers in a short-lived vertebrate. *Curr Biol*. 2006; 16:296–300. <https://doi.org/10.1016/j.cub.2005.12.038> PMID:16461283
26. Pangen R, Sahni JK, Ali J, Sharma S, Baboota S. Resveratrol: review on therapeutic potential and recent advances in drug delivery. *Expert Opin Drug Deliv*. 2014; 11:1285–98. <https://doi.org/10.1517/17425247.2014.919253> PMID:24830814
27. Blanchet J, Longpré F, Bureau G, Morissette M, DiPaolo T, Bronchti G, Martinoli MG. Resveratrol, a red wine polyphenol, protects dopaminergic neurons in MPTP-treated mice. *Prog Neuropsychopharmacol Biol Psychiatry*. 2008; 32:1243–50. <https://doi.org/10.1016/j.pnpbp.2008.03.024> PMID:18471948
28. Lagouge M, Argmann C, Gerhart-Hines Z, Meziane H, Lerin C, Daussin F, Messadeq N, Milne J, Lambert P, Elliott P, Geny B, Laakso M, Puigserver P, Auwerx J. Resveratrol improves mitochondrial function and protects against metabolic disease by activating SIRT1 and PGC-1 α . *Cell*. 2006; 127:1109–22. <https://doi.org/10.1016/j.cell.2006.11.013> PMID:17112576
29. Madreiter-Sokolowski CT, Sokolowski AA, Graier WF. Dosis Facit Sanitatem-Concentration-Dependent Effects of Resveratrol on Mitochondria. *Nutrients*. 2017; 9:1117. <https://doi.org/10.3390/nu9101117> PMID:29027961
30. Sheng W, Lu Y, Mei F, Wang N, Liu ZZ, Han YY, Wang HT, Zou S, Xu H, Zhang X. Effect of Resveratrol on Sirtuins, OPA1, and Fis1 Expression in Adult Zebrafish Retina. *Invest Ophthalmol Vis Sci*. 2018; 59:4542–51. <https://doi.org/10.1167/iovs.18-24539> PMID:30208422
31. Peng K, Tao Y, Zhang J, Wang J, Ye F, Dan G, Zhao Y, Cai Y, Zhao J, Wu Q, Zou Z, Cao J, Sai Y. Resveratrol Regulates Mitochondrial Biogenesis and Fission/Fusion to Attenuate Rotenone-Induced Neurotoxicity. *Oxid Med Cell Longev*. 2016; 2016:6705621. <https://doi.org/10.1155/2016/6705621> PMID:26770656
32. Sugiyama M, Kawahara-Miki R, Kawana H, Shirasuna K, Kuwayama T, Iwata H. Resveratrol-induced mitochondrial synthesis and autophagy in oocytes derived from early antral follicles of aged cows. *J Reprod Dev*. 2015; 61:251–59. <https://doi.org/10.1262/jrd.2015-001> PMID:25866375
33. Ren X, Chen L, Xie J, Zhang Z, Dong G, Liang J, Liu L, Zhou H, Luo P. Resveratrol Ameliorates Mitochondrial Elongation via Drp1/Parkin/PINK1 Signaling in Senescent-Like Cardiomyocytes. *Oxid Med Cell Longev*. 2017; 2017:4175353. <https://doi.org/10.1155/2017/4175353> PMID:29201272
34. Park D, Jeong H, Lee MN, Koh A, Kwon O, Yang YR, Noh J, Suh PG, Park H, Ryu SH. Resveratrol induces autophagy by directly inhibiting mTOR through ATP competition. *Sci Rep*. 2016; 6:21772. <https://doi.org/10.1038/srep21772> PMID:26902888
35. Li N, Wang F, Zhang Q, Jin M, Lu Y, Chen S, Guo C, Zhang X. Rapamycin mediates mTOR signaling in reactive astrocytes and reduces retinal ganglion cell loss. *Exp Eye Res*. 2018; 176:10–19. <https://doi.org/10.1016/j.exer.2018.06.014> PMID:29928901
36. Luo H, Zhuang J, Hu P, Ye W, Chen S, Pang Y, Li N, Deng C, Zhang X. Resveratrol Delays Retinal Ganglion Cell Loss and Attenuates Gliosis-Related Inflammation From Ischemia-Reperfusion Injury. *Invest Ophthalmol Vis Sci*. 2018; 59:3879–88. <https://doi.org/10.1167/iovs.18-23806> PMID:30073348
37. Chhetri J, Jacobson G, Gueven N. Zebrafish--on the move towards ophthalmological research. *Eye (Lond)*. 2014; 28:367–80. <https://doi.org/10.1038/eye.2014.19> PMID:24503724
38. Schirmer H, Pereira TC, Rico EP, Rosemberg DB, Bonan CD, Bogo MR, Souto AA. Modulatory effect of resveratrol on SIRT1, SIRT3, SIRT4, PGC1 α and NAMPT gene expression profiles in wild-type adult zebrafish liver. *Mol Biol Rep*. 2012; 39:3281–89. <https://doi.org/10.1007/s11033-011-1096-4> PMID:21706162
39. Howe K, Clark MD, Torroja CF, Torrance J, Berthelot C, Muffato M, Collins JE, Humphray S, McLaren K, Matt-

- hews L, McLaren S, Sealy I, Caccamo M, et al. The zebrafish reference genome sequence and its relationship to the human genome. *Nature*. 2014; 505:248. <https://doi.org/10.1038/nature12813> PMID:23594743
40. Van Houcke J, De Groef L, Dekeyser E, Moons L. The zebrafish as a gerontology model in nervous system aging, disease, and repair. *Ageing Res Rev*. 2015; 24:358–68. <https://doi.org/10.1016/j.arr.2015.10.004> PMID:26538520
41. Nivison MP, Ericson NG, Green VM, Bielas JH, Campbell JS, Horner PJ. Age-related accumulation of phosphorylated mitofusin 2 protein in retinal ganglion cells correlates with glaucoma progression. *Exp Neurol*. 2017; 296:49–61. <https://doi.org/10.1016/j.expneurol.2017.07.001> PMID:28684211
42. Yu W, Sun Y, Guo S, Lu B. The PINK1/Parkin pathway regulates mitochondrial dynamics and function in mammalian hippocampal and dopaminergic neurons. *Hum Mol Genet*. 2011; 20:3227–40. <https://doi.org/10.1093/hmg/ddr235> PMID:21613270
43. Gao S, Zhao Z, Wu R, Wu L, Tian X, Zhang Z. MiR-146b inhibits autophagy in prostate cancer by targeting the PTEN/Akt/mTOR signaling pathway. *Aging (Albany NY)*. 2018; 10:2113–21. <https://doi.org/10.18632/aging.101534> PMID:30153654
44. Reddy PH. Inhibitors of Mitochondrial Fission as a Therapeutic Strategy for Diseases with Oxidative Stress and Mitochondrial Dysfunction. *J Alzheimers Dis*. 2014; 40:245–56. <https://doi.org/10.3233/JAD-132060> PMID:24413616
45. Kim AJ, Chang JY, Shi L, Chang RC, Ko ML, Ko GY. The Effects of Metformin on Obesity-Induced Dysfunctional Retinas. *Invest Ophthalmol Vis Sci*. 2017; 58:106–18. <https://doi.org/10.1167/iovs.16-20691> PMID:28114566
46. Leite CE, Maboni LO, Cruz FF, Rosemberg DB, Zimmermann FF, Pereira TC, Bogo MR, Bonan CD, Campos MM, Morrone FB, Battastini AM. Involvement of purinergic system in inflammation and toxicity induced by copper in zebrafish larvae. *Toxicol Appl Pharmacol*. 2013; 272:681–89. <https://doi.org/10.1016/j.taap.2013.08.001> PMID:23933163
47. Sahin E, Depinho RA. Linking functional decline of telomeres, mitochondria and stem cells during aging. *Nature*. 2010; 464:520–28. <https://doi.org/10.1038/nature08982> PMID:20336134
48. Denham H. Free radical theory dietary implication & of aging. *Geroscience*. 1978; 1:145–52.
49. Larsson NG. Somatic mitochondrial DNA mutations in mammalian aging. *Annu Rev Biochem*. 2010; 79:683–706. <https://doi.org/10.1146/annurev-biochem-060408-093701> PMID:20350166
50. Short KR, Bigelow ML, Kahl J, Singh R, Coenen-Schimke J, Raghavakaimal S, Nair KS. Decline in skeletal muscle mitochondrial function with aging in humans. *Proc Natl Acad Sci USA*. 2005; 102:5618–23. <https://doi.org/10.1073/pnas.0501559102> PMID:15800038
51. Bua E, Johnson J, Herbst A, DeLong B, McKenzie D, Salamat S, Aiken JM. Mitochondrial DNA-deletion mutations accumulate intracellularly to detrimental levels in aged human skeletal muscle fibers. *Am J Hum Genet*. 2006; 79:469–80. <https://doi.org/10.1086/507132> PMID:16909385
52. Liang QX, Lin YH, Zhang CH, Sun HM, Zhou L, Schatten H, Sun QY, Qian WP. Resveratrol increases resistance of mouse oocytes to postovulatory aging *in vivo*. *Aging (Albany NY)*. 2018; 10:1586–96. <https://doi.org/10.18632/aging.101494> PMID:30036861
53. Huang Z, Ren S, Jiang Y, Wang T. PINK1 and Parkin cooperatively protect neurons against constitutively active TRP channel-induced retinal degeneration in *Drosophila*. *Cell Death Dis*. 2016; 7:e2179–11. <https://doi.org/10.1038/cddis.2016.82> PMID:27054334
54. MacVicar T, Langer T. OPA1 processing in cell death and disease - the long and short of it. *J Cell Sci*. 2016; 129:2297–306. <https://doi.org/10.1242/jcs.159186> PMID:27189080
55. Korwitz A, Merkwirth C, Richter-Dennerlein R, Tröder SE, Sprenger HG, Quirós PM, López-Otín C, Rugarli EI, Langer T. Loss of OMA1 delays neurodegeneration by preventing stress-induced OPA1 processing in mitochondria. *J Cell Biol*. 2016; 212:157–66. <https://doi.org/10.1083/jcb.201507022> PMID:26783299
56. Hering T, Kojer K, Birth N, Hallitsch J, Taanman JW, Orth M. Mitochondrial cristae remodelling is associated with disrupted OPA1 oligomerisation in the Huntington's disease R6/2 fragment model. *Exp Neurol*. 2017; 288:167–75. <https://doi.org/10.1016/j.expneurol.2016.10.017> PMID:27889468
57. Dabrowska A, Venero JL, Iwasawa R, Hankir MK, Rahman S, Boobis A, Hajji N. PGC-1 α controls

- mitochondrial biogenesis and dynamics in lead-induced neurotoxicity. *Aging* (Albany NY). 2015; 7:629–47. <https://doi.org/10.18632/aging.100790> PMID:26363853
58. Moreira OC, Estébanez B, Martínez-Florez S, de Paz JA, Cuevas MJ, González-Gallego J. Mitochondrial Function and Mitophagy in the Elderly: effects of Exercise. *Oxid Med Cell Longev*. 2017; 2017:2012798. <https://doi.org/10.1155/2017/2012798> PMID:28900532
 59. Liu H, Dai C, Fan Y, Guo B, Ren K, Sun T, Wang W. From autophagy to mitophagy: the roles of P62 in neurodegenerative diseases. *J Bioenerg Biomembr*. 2017; 49:413–22. <https://doi.org/10.1007/s10863-017-9727-7> PMID:28975445
 60. Wu J, Li X, Zhu G, Zhang Y, He M, Zhang J. The role of Resveratrol-induced mitophagy/autophagy in peritoneal mesothelial cells inflammatory injury via NLRP3 inflammasome activation triggered by mitochondrial ROS. *Exp Cell Res*. 2016; 341:42–53. <https://doi.org/10.1016/j.yexcr.2016.01.014> PMID:26825654
 61. Lutz AK, Exner N, Fett ME, Schlehe JS, Kloos K, Lämmermann K, Brunner B, Kurz-Drexler A, Vogel F, Reichert AS, Bouman L, Vogt-Weisenhorn D, Wurst W, et al. Loss of parkin or PINK1 function increases Drp1-dependent mitochondrial fragmentation. *J Biol Chem*. 2009; 284:22938–51. <https://doi.org/10.1074/jbc.M109.035774> PMID:19546216
 62. Wu JJ, Liu J, Chen EB, Wang JJ, Cao L, Narayan N, Fergusson MM, Rovira II, Allen M, Springer DA, Lago CU, Zhang S, DuBois W, et al. Increased mammalian lifespan and a segmental and tissue-specific slowing of aging after genetic reduction of mTOR expression. *Cell Reports*. 2013; 4:913–20. <https://doi.org/10.1016/j.celrep.2013.07.030> PMID:23994476
 63. Rana A, Rera M, Walker DW. Parkin overexpression during aging reduces proteotoxicity, alters mitochondrial dynamics, and extends lifespan. *Proc Natl Acad Sci USA*. 2013; 110:8638–43. <https://doi.org/10.1073/pnas.1216197110> PMID:23650379
 64. Shimobayashi M, Hall MN. Making new contacts: the mTOR network in metabolism and signalling crosstalk. *Nat Rev Mol Cell Biol*. 2014; 15:155–62. <https://doi.org/10.1038/nrm3757> PMID:24556838
 65. Zhao J, Brault JJ, Schild A, Cao P, Sandri M, Schiaffino S, Lecker SH, Goldberg AL. FoxO3 coordinately activates protein degradation by the autophagic/lysosomal and proteasomal pathways in atrophying muscle cells. *Cell Metab*. 2007; 6:472–83. <https://doi.org/10.1016/j.cmet.2007.11.004> PMID:18054316
 66. Guarente L. Aging research—where do we stand and where are we going? *Cell*. 2014; 159:15–19. <https://doi.org/10.1016/j.cell.2014.08.041> PMID:25259916
 67. Steelman LS, Chappell WH, Abrams SL, Kempf RC, Long J, Laidler P, Mijatovic S, Maksimovic-Ivanic D, Stivala F, Mazzarino MC, Donia M, Fagone P, Malaponte G, et al. Roles of the Raf/MEK/ERK and PI3K/PTEN/Akt/mTOR pathways in controlling growth and sensitivity to therapy—implications for cancer and aging. *Aging* (Albany NY). 2011; 3:192–222. <https://doi.org/10.18632/aging.100296> PMID:21422497
 68. Cunningham JT, Rodgers JT, Arlow DH, Vazquez F, Mootha VK, Puigserver P. mTOR controls mitochondrial oxidative function through a YY1-PGC-1alpha transcriptional complex. *Nature*. 2007; 450:736–40. <https://doi.org/10.1038/nature06322> PMID:18046414
 69. Hudson CC, Liu M, Chiang GG, Otterness DM, Loomis DC, Kaper F, Giaccia AJ, Abraham RT. Regulation of hypoxia-inducible factor 1alpha expression and function by the mammalian target of rapamycin. *Mol Cell Biol*. 2002; 22:7004–14. <https://doi.org/10.1128/MCB.22.20.7004-7014.2002> PMID:12242281
 70. Mtfp S, Basu K, McBride HM, Bergeron JJ, Sonenberg N, Morita M, Prudent J, Basu K, Goyon V, Katsumura S, Hulea L. mTOR Controls Mitochondrial Dynamics and Cell Article mTOR Controls Mitochondrial Dynamics and Cell Survival via MTFP1. *Mol Cell*. 2017; 67:1–14. <https://doi.org/10.1016/j.molcel.2017.08.013> PMID:28918902
 71. Maiese K. Targeting molecules to medicine with mTOR, autophagy and neurodegenerative disorders. *Br J Clin Pharmacol*. 2016; 82:1245–66. <https://doi.org/10.1111/bcp.12804> PMID:26469771
 72. Wilkinson JE, Burmeister L, Brooks SV, Chan CC, Friedline S, Harrison DE, Hejtmancik JF, Nadon N, Strong R, Wood LK, Woodward MA, Miller RA. Rapamycin slows aging in mice. *Aging Cell*. 2012; 11:675–82. <https://doi.org/10.1111/j.1474-9726.2012.00832.x> PMID:22587563
 73. Kacprzak V, Patel NA, Riley E, Yu L, Yeh JJ, Zhdanova IV. Dopaminergic control of anxiety in young and aged zebrafish. *Pharmacol Biochem Behav*. 2017; 157:1–8. <https://doi.org/10.1016/j.pbb.2017.01.005> PMID:28408289

74. Ran G, Ying L, Li L, Yan Q, Yi W, Ying C, Wu H, Ye X. Resveratrol ameliorates diet-induced dysregulation of lipid metabolism in zebrafish (*Danio rerio*). *PLoS One*. 2017; 12:e0180865. <https://doi.org/10.1371/journal.pone.0180865> PMID:28686680
75. Ding M, Feng N, Tang D, Feng J, Li Z, Jia M, Liu Z, Gu X, Wang Y, Fu F, Pei J. Melatonin prevents Drp1-mediated mitochondrial fission in diabetic hearts through SIRT1-PGC1 α pathway. *J Pineal Res*. 2018; 65:e12491. <https://doi.org/10.1111/jpi.12491> PMID:29575122
76. Cao Z, Jensen LD, Rouhi P, Hosaka K, Länne T, Steffensen JF, Wahlberg E, Cao Y. Hypoxia-induced retinopathy model in adult zebrafish. *Nat Protoc*. 2010; 5:1903–10. <https://doi.org/10.1038/nprot.2010.149> PMID:21127484
77. Biehlmaier O, Neuhauss SC, Kohler K. Double cone dystrophy and RPE degeneration in the retina of the zebrafish *gmn* mutant. *Invest Ophthalmol Vis Sci*. 2003; 44:1287–98. <https://doi.org/10.1167/iovs.02-0363> PMID:12601061
78. Hunter SE, Jung D, Di Giulio RT, Meyer JN. The QPCR assay for analysis of mitochondrial DNA damage, repair, and relative copy number. *Methods*. 2010; 51:444–51. <https://doi.org/10.1016/j.ymeth.2010.01.033> PMID:20123023

The senescent vision: dysfunction or neuronal loss?

Francisco M. Nadal-Nicolás, Manuel Vidal-Sanz, Marta Agudo-Barriuso

Aging is the most common degenerative process consequence of multiple cumulative mechanisms. The permanent effects of senescence are complex and heterogeneous; genetic heritage, nutrition, behavior, physis exercise and environment factors are tangled during the course of life. Aging is associated with chronic degenerations [1] and so, it is difficult to identify and characterize the intrinsic components of aging *per se*.

Visual aging is linked to a decline in functional activity causing lower visual acuity, lower contrast sensitivity and impaired dark adaptation. However, although it has been reported that the age-related visual impairment is mainly due to a neuronal malfunction together with cell loss, the subjacent and specific reasons of aging are still uncertain. How, and at what level, are the diverse neuronal populations affected? And how much are other retinal players involved?

By characterizing retinal aging in experimental animals (pigmented and albino rats) under controlled and healthy

conditions, we found that the retinal function, as measured with full field electroretinograms, decreased ~50% at 22-months compared with 2-month-old rats [2]. Whether neuronal malfunction or cell loss is mainly responsible for this reduced functionality is still an open question, even though structural changes in the optical components may contribute to this reduction. Interestingly, several studies suggest cell loss based on the retinal thinning that occurs with aging [3]. However, although when we measured the retinal layers *in vivo* we observed a decrease in thickness ~14% [2], we also saw that the constant retinal growth was responsible for the retinal thinning, since volumetric and quantification analyses indicated that the thinning did not involve neuronal loss (except for L/M-cones in pigmented rats) [2], (Figure 1).

The retina is a highly organized and specialized tissue. The light-sensitive photoreceptors are essential for an effective signal transduction and to initiate the efficient

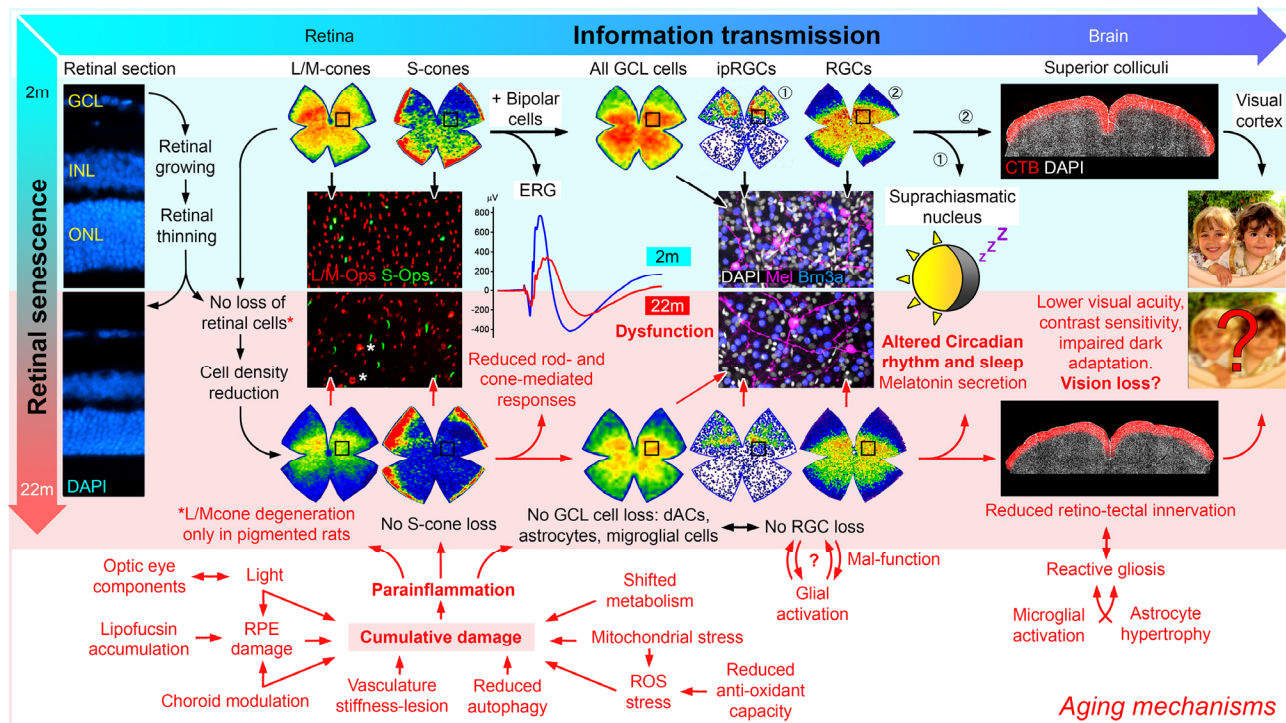


Figure 1. Aging effects on the visual pathway. In the retina, the continuous growth decreases both the retinal thickness and the density of the different retinal populations (details in [2]), however, although no neuronal loss was observed in aged retinas (except, L/M-cones in pigmented rats), the vision forming and the non-vision forming information, that reaches the brain, are likely affected by aging [7].

transmission of impulses through the retina. They are vulnerable to light-induced damage and many publications have shown the degeneration of outer segments during aging. Interestingly, we observed loss of L/M-cones in the central retina of 22-months-old pigmented rats [2], comparable to the photoreceptor-loss in the macular region of aged human retinas [4]. The central retina probably receives greater light exposure triggering different metabolic requirements that increases metabolic stress. In fact, a deficiency in DNA repair enzymes, damage induced by excitatory amino acids, specific age-related metabolic changes [5], a general decline in autophagy activity, and reduced energy production by mitochondrial metabolism collectively result in oxidative stress that may affect photoreceptor functionality. All that in addition to lipofuscin accumulation, morphological alterations and damage in the retinal pigmented epithelium [4] accompanied by a para-inflammatory response [6] are the signature signs of aging in the retina.

The reduced b-wave and increased implicit time observed in aged animals may be also explained by reduced function of bipolar cells [2]. But these results are difficult to interpret because, although we cannot rule out synaptic alterations, the b-wave would also reflect the corresponding diminished photoreceptor activity. Later, the signal reaches the retinal ganglion cells (RGCs), whose degeneration is widely accepted in aged retinas [3]. Our results show a decrease in RGC density, but not in the number of orthotopic or displaced RGC [2]. As above-mentioned, the decreased density is due to retinal growth, and it has been shown that animals with a reduced food intake maintain their RGC density, because the area could remain constant. Obviously, the fact that the number of RGCs does not change with age does not necessarily mean that these cells are healthy or functional. Furthermore, aged microglia show increased dystrophic signs in their morphology in the retina, i.e. reduced dendritic arbors with slow migration capability [7]. We cannot elucidate whether microglial cells become pathogenic with age, or whether they are trying to keep the changing retinal homeostasis under control.

Although our results did not show loss of ip-RGCs in aging retinas [2], morphological changes like reduced dendrites or even lower melanopsin expression have been recently reported, and this could explain an impaired function since circadian rhythm and sleep are strikingly influenced by aging [8].

Lastly, before the images are formed in the visual cortex, the information reaches the superior colliculi (SCi), the main retinorecipient area in rodents. In aged animals, there was a slight reduction of RGC projections to the SCi, as well as astrocyte hypertrophy and microglial cells activation, both symptoms of stress or

degeneration [2]. This may be a compensatory mechanism to maintain a lower neuronal activity of the aged neurons or to maintain the disrupted tissue homeostasis [7].

To preserve visual function, the eyes and brain require precisely tuned machinery. Any of the above-mentioned changes related to aging, including synapse remodelling or neuronal loss in response to age may contribute or play a crucial role in the continuous and irreversible decline in vision. Importantly, age may end causing a partial or complete distorted image formation, more so in a timeframe where our lifespan is increasing. So, could this retinal dysfunction be prevented or restored?

REFERENCES

1. Lin JB, et al. NPJ Aging Mech Dis. 2016; 2:16003. <https://doi.org/10.1038/npjamd.2016.3>
2. Nadal-Nicolás FM, et al. Neurobiol Aging. 2018; 61:146–68. <https://doi.org/10.1016/j.neurobiolaging.2017.09.021>
3. Cano J, et al. Arch Gerontol Geriatr. 1986; 5:41–50. [https://doi.org/10.1016/0167-4943\(86\)90006-3](https://doi.org/10.1016/0167-4943(86)90006-3)
4. Curcio CA, et al. Invest Ophthalmol Vis Sci. 1993; 34:3278–96.
5. Wang Y, et al. Neurobiol Aging. 2018; 71:223–33. <https://doi.org/10.1016/j.neurobiolaging.2018.07.024>
6. Xu H, et al. Prog Retin Eye Res. 2009; 28:348–68. <https://doi.org/10.1016/j.preteyeres.2009.06.001>
7. Damani MR, et al. Aging Cell. 2011; 10:263–76. <https://doi.org/10.1111/j.1474-9726.2010.00660.x>
8. Kondratova and Kondratov. Rev Neurosci. 2012; 7:325–35. <https://doi.org/10.1038/nrn3208>

Francisco M. Nadal-Nicolás: Retinal Neurophysiology Section, John Edward Porter Neuroscience Research Center, National Eye Institute, National Institutes of Health, Bethesda, MD 20892, USA

Correspondence: Francisco M. Nadal-Nicolás

Email: nadalnicolasfm@nih.gov

Keywords: aging, retina, retinal ganglion cells, melanopsin, photoreceptors, microglia, astrocytes

Funding: The work discussed in this editorial was funded by Fundación Séneca, Agencia de Ciencia y Tecnología Región de Murcia (19881/GERM/15), and the Spanish Ministry of Economy and Competitiveness, Instituto de Salud Carlos III, Fondo Europeo de Desarrollo Regional “Una Manera de Hacer Europa” (SAF2015-67643-P, PI16/00031).

Copyright: Nadal-Nicolás et al. This is an open-access article distributed under the terms of the Creative Commons Attribution License (CC BY 3.0), which permits unrestricted use, distribution, and reproduction in any medium, provided the original author and source are credited

Received: October 21, 2018

Published: December 26, 2018

Long-term intake of *Lactobacillus paracasei* KW3110 prevents age-related chronic inflammation and retinal cell loss in physiologically aged mice

Yuji Morita¹, Kenta Jounai², Akihiko Sakamoto³, Yasuyuki Tomita¹, Yoshihiko Sugihara¹, Hiroaki Suzuki¹, Konomi Ohshio¹, Masato Otake¹, Daisuke Fujiwara¹, Osamu Kanauchi¹, Mitsuo Maruyama^{3,4}

¹Research Laboratories for Health Science & Food Technologies, Kirin Company, Ltd., Yokohama, Kanagawa, Japan

²Technical Development Center, Koiwai Dairy Products Co Ltd., Sayama, Saitama 350-1321, Japan

³Department of Mechanism of Aging, National Center for Geriatrics and Gerontology, Obu, Aichi 474-8511, Japan

⁴Department of Aging Research, Nagoya University Graduate School of Medicine, Nagoya, Aichi 466-8550, Japan

Correspondence to: Mitsuo Maruyama, Yuji Morita; email: michan@ncgg.go.jp, Yuji_Morita@kirin.co.jp

Keywords: *Lactobacillus paracasei* KW3110, age-related inflammation, proinflammatory cytokine, retina

Received: May 23, 2018 **Accepted:** September 26, 2018 **Published:** October 19, 2018

Copyright: Morita et al. This is an open-access article distributed under the terms of the Creative Commons Attribution License (CC BY 3.0), which permits unrestricted use, distribution, and reproduction in any medium, provided the original author and source are credited.

ABSTRACT

Age-related chronic inflammation is a major risk factor for the incidence and prevalence of age-related diseases, including infectious and neurodegenerative diseases. We previously reported that a lactic acid bacteria, *Lactobacillus paracasei* KW3110, activated macrophages and suppressed inflammation in mice and humans. In this study, we investigated whether long-term intake of heat-killed *L. paracasei* KW3110 modulated age-related inflammation and altered the gut microbiota in physiologically aged mice. Compared with age-matched control mice, fecal analyses of gut microbiota revealed that intake of *L. paracasei* KW3110 mitigated age-related changes of beneficial bacterial composition, including the Bifidobacteriaceae family. *L. paracasei* KW3110 intake also mitigated age-related immune defects by reducing the prevalence of interferon-gamma (IFN- γ)-producing inflammatory CD4-positive T cells in the lamina propria of the small intestine, and reduced serum levels of proinflammatory cytokines. Furthermore, *L. paracasei* KW3110 intake suppressed retinal inflammation by reducing proinflammatory cytokine-producing macrophage, and age-related retinal cell loss. Taken together, these findings suggested that *L. paracasei* KW3110 mitigated age-related chronic inflammation through modulation of gut microbiota composition and immune system functions in aged mice, and also reduced age-related retinal ganglion cell (RGC) loss. Further studies are needed to evaluate the effect in age-related senescent changes of the retina.

INTRODUCTION

Aging involves a progressive decline of physiological functions in various organs, influenced by several factors, including genetic factors and environmental factors [1-3]. As the aged population has been growing rapidly around the world, the therapeutic and preventive

approaches to decelerate senescence are of great concern. Among the features of aging, the decline in immune function has been widely examined, because it results in chronic low grade inflammation, which is a major risk factor for the incidence and prevalence of age-related diseases, including infectious diseases, tumors, and neurodegenerative diseases [4-8].

The retina, one of the neural tissues, is also affected by chronic low grade inflammation. Age-related retinal neurodegenerative diseases, such as age-related macular degeneration (AMD), are major causes of blindness in the elderly [9-12]. The disease is caused by age-related retinal cell loss, including retinal ganglion cell (RGC) death [13] and photoreceptor cell death [14, 15], at least partly due to chronic inflammation [16-19]. Several therapeutic pharmacological agents for suppression of retinal diseases have been reported [20, 21]. However, human eyes are exposed to daily chronic stress, such as photo-oxidative stress, and as a result, safe and long-term approaches based on diet to mitigate retinal chronic inflammation are especially attractive.

Age-related immune dysfunctions leading to chronic inflammation have been previously reported. Thymic involution and disruption of homeostatic T cell proliferation, including decreased numbers of naïve T cells, accumulation of memory T cells, and increased numbers of regulatory T cells (Tregs), have been studied [22-24], and altered numbers of B cells with aging, reduced antibody production, and age-related dysfunction of other innate immune cells have also been reported [25-30]. Although some food materials or constituents, for example, prebiotics and probiotics, can improve age-related immune defects [31-34], their mechanism remains poorly understood. Recent studies suggested that the gut microbiota composition may be associated with age-related immune dysfunctions [35-37]. Disruption of gut microbiota composition has been also implicated in retinal diseases, including AMD, through a gut-retina axis [38]. Therefore, preventive dietary approaches involving alterations of gut microbiota composition for improving age-related retinal chronic inflammation should be studied.

Lactic acid bacteria are widely consumed as probiotics and paraprobiotics to enhance gut barrier function and improve immune systems. Studies have also demonstrated functional roles of several lactic acid bacterial strains in humans, including for the prevention of diarrhea, allergies, and metabolic disorders [39]. However, the long-term effects of lactic acid bacteria on age-related chronic inflammation remain unclear. We previously reported that *Lactobacillus paracasei* KW3110 activated macrophages and suppressed excessive inflammation in mice and humans [40-43]. In this study, we demonstrated the suppressive effects of the long-term intake of *L. paracasei* KW3110 on age-related alterations of gut microbiota composition and expansion of inflammatory CD4-positive T cells in the lamina propria of the small intestine (SI-LP). Furthermore, we also revealed the protective effects of the long-term intake of *L. paracasei* KW3110 on age-related retinal cell loss. We proposed that the long-term

intake of *L. paracasei* KW3110 contributed to the prevention of chronic inflammation and age-related retinal cell loss in physiologically aged mice.

RESULTS

Intake of *L. paracasei* KW3110 affected bacterial flora in aged mice

The gut microbiota plays a critical role in the immune system, and aging has been reported to alter gut bacterial flora composition [35]. Previous studies have reported that some prebiotics and probiotics can alter gut bacterial flora composition and improve immune defects [44, 45]. Therefore, to investigate whether intake of *L. paracasei* KW3110 affected the gut microbiota composition in aged mice, 16-month-old mice were fed a diet with or without *L. paracasei* KW3110 for 6 months. We analyzed bacterial 16S ribosomal RNA gene sequences in the feces. The microbiota composition at the phylum level revealed that the *Firmicutes/Bacteroidetes* ratio was lower in aged mice fed a control diet than in young mice fed a control diet (Fig. 1A, B). This result is consistent with a previous report [46]. However, in aged mice fed a diet containing *L. paracasei* KW3110 for 6 months, the *Firmicutes/Bacteroidetes* ratio was decreased compared with that in age-matched control mice (Fig. 1B).

At the bacterial family level, the bacterial ratios in the feces were altered in aged mice as compared with young control mice (Fig. 1C). In the aged mice groups, the intake of *L. paracasei* KW3110 affected some bacterial abundances. For example, the mean relative abundances of *Peptostreptococcaceae* ($p = 0.011$) and *Bifidobacteriaceae* ($p = 0.038$) were significantly higher in aged mice fed a diet containing *L. paracasei* KW3110 for 6 months than in age-matched mice fed a control diet (Fig. 1D). In contrast, the mean relative abundance of *Streptococcaceae* was significantly lower ($p = 0.0079$) in aged mice fed a diet containing *L. paracasei* KW3110 than in age-matched mice fed a control diet (Fig. 1D).

Intake of *L. paracasei* KW3110 affected the lymphocyte subpopulation of SI-LP in aged mice

We have previously shown that orally-provided *L. paracasei* KW3110 interacted with immune cells in the small intestine [43]. In addition, intake of *L. paracasei* KW3110 altered gut bacterial flora composition in aged mice (Fig. 1). Thus, to examine the effects of *L. paracasei* KW3110 on the immune system in the small intestine with aging, 11-month-old mice were fed a diet with or without *L. paracasei* KW3110 for 6 months. The ratio of CD3ε- and CD4-double positive T cells to live cells and the ratio of interferon-γ (IFN-γ)-producing

CD4-positive T cells to CD4-positive T cells, known as indicators of age-related inflammation in SI-LP cells, in aged mice fed a control diet, was higher than that in control young mice (Fig. 2B, D). The expression of programmed cell death protein 1 (PD-1), known as an indicator of immune senescence in CD4-positive T cells, in aged mice fed a control diet, was also higher than that in control young mice (Fig. 2E). However, the intake of *L. paracasei* KW3110 for 6 months in aged mice significantly decreased the ratio of CD3 ϵ - and CD4-double-positive T cells to live cells in SI-LP (Fig. 2A, B), the ratio of IFN- γ -producing CD4-positive T cells to CD4-positive T cells (Fig. 2C, D), and the expression of PD-1 in CD4-positive T cells (Figure 2E). In contrast, the ratio of CD4- and Foxp3-positive cells, known as regulatory T cells, in SI-LP was not changed in aged mice fed a diet either with or without *L. paracasei* KW3110 (Supplementary Fig. 1).

Intake of *L. paracasei* KW3110 decreased the levels of proinflammatory cytokines and chemokines in serum

The age-related inflammatory phenotypes in various tissues are associated with the serum levels of proinflammatory cytokines, which are produced from inflammatory immune cells. Therefore, we evaluated serum levels of proinflammatory cytokines and chemokines in aged mice. As shown in Fig. 3, the serum levels of proinflammatory cytokines and chemokines in aged mice were higher than those in control young mice (Fig. 3). Interestingly, serum levels of some cytokines and chemokines, interleukin-17 (IL-17), keratinocyte chemoattractant (KC), and interleukin-13 (IL-13), were significantly lower in aged mice fed a diet containing *L. paracasei* KW3110 from 16 months of age to 22 months of age for 6 months, than in age-matched mice

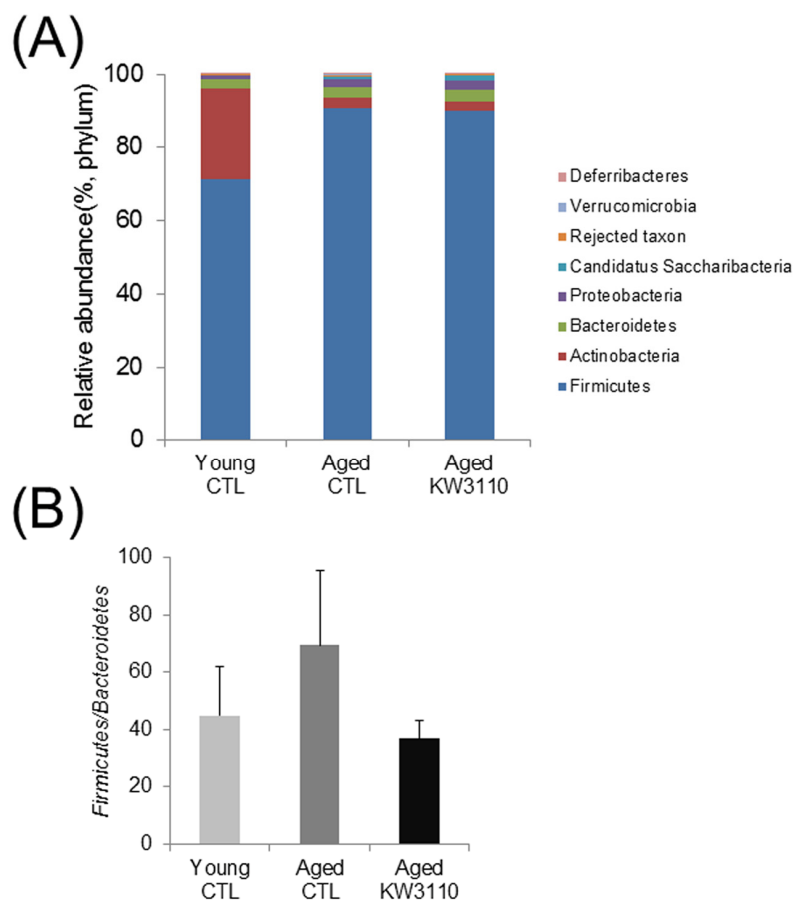


Figure 1. The intake of *Lactobacillus paracasei* KW3110 in aged mice affected the gut microbial composition. Feces were collected and subjected to flora analysis in young (3-months-old) and aged mice (22-months-old). **(A)** Distribution of gut microbiota (% of total 16S rDNA) at the phylum level. **(B)** Comparison of the *Firmicutes* to *Bacteroidetes* ratio. Values are presented as the means \pm SEM of relative abundance of each phylum.

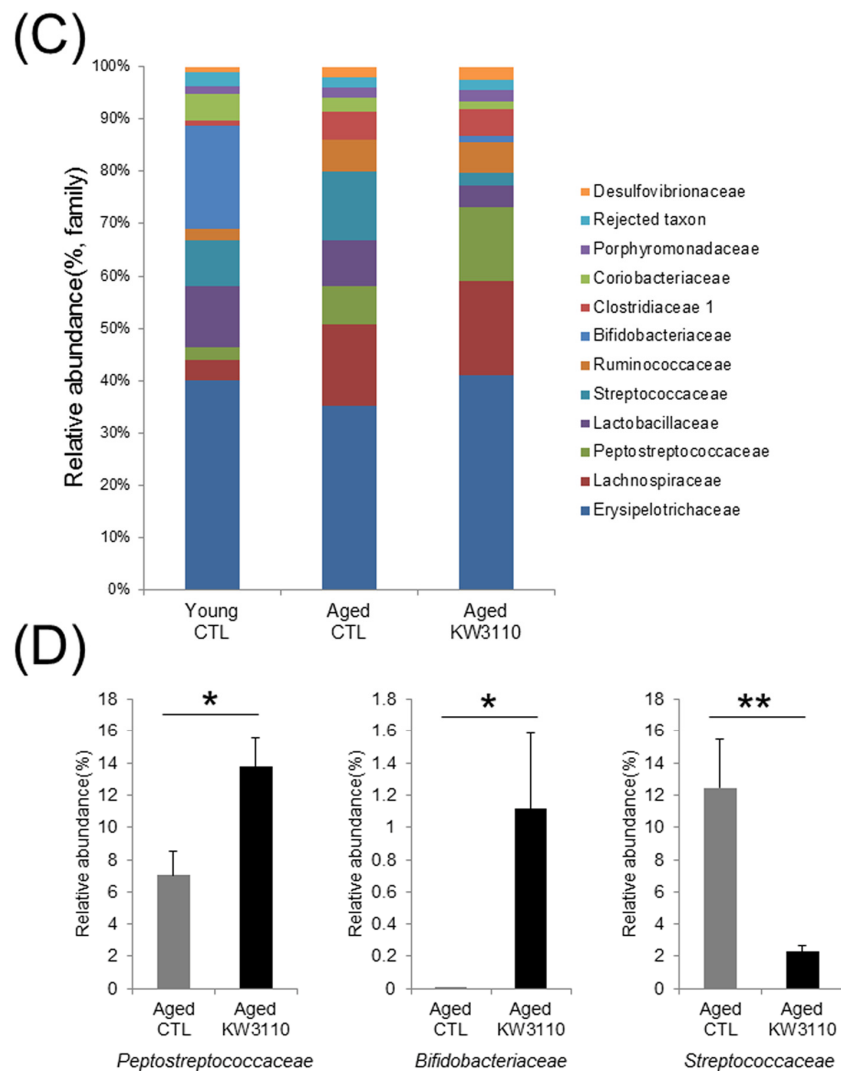


Figure 1. The intake of *Lactobacillus paracasei* KW3110 in aged mice affected the gut microbial composition. (C) Distribution of gut microbiota (% of total 16S rDNA) at the family level. Families with proportions less than 1% are not listed. (D) Comparisons of relative abundances of *Peptostreptococcaceae* (left panel), *Bifidobacteriaceae* (middle panel), and *Streptococcaceae* (right panel) families. Values are presented as the means \pm SEM. Significance was assumed if the p value was < 0.05. *p < 0.05, **p < 0.01. CTL = control diet; KW3110 = *Lactobacillus paracasei* KW3110 diet.

fed a control diet (Fig. 3). The concentrations of the other proinflammatory cytokines were also lower in aged mice fed a diet containing *L. paracasei* KW3110 for 6 months. These changes of proinflammatory cytokine levels could be observed in aged mice fed a diet containing *L. paracasei* KW3110 only for 2 months (Supplementary Fig. 2).

Intake of *L. paracasei* KW3110 mitigated retinal inflammation

As the lower serum levels of proinflammatory cytokines in aged mice were seemingly related to the suppression

of age-related inflammatory phenotypes in peripheral tissues, we investigated whether intake of *L. paracasei* KW3110 also mitigated age-related retinal inflammation. Intake of *L. paracasei* KW3110 from 11–17 months of age for 6 months, in aged mice, significantly decreased the expression of IFN- γ and interleukin-6 (IL-6) in CD11b-positive and F4/80-positive retinal immune cells and macrophage (Fig. 4A–C) as compared with in age-matched mice fed a control diet. The expression of tumor necrosis factor- α (TNF- α) in CD11b-positive and F4/80-positive retinal macrophage was also lower than in age-matched mice fed a control diet (Fig. 4D).

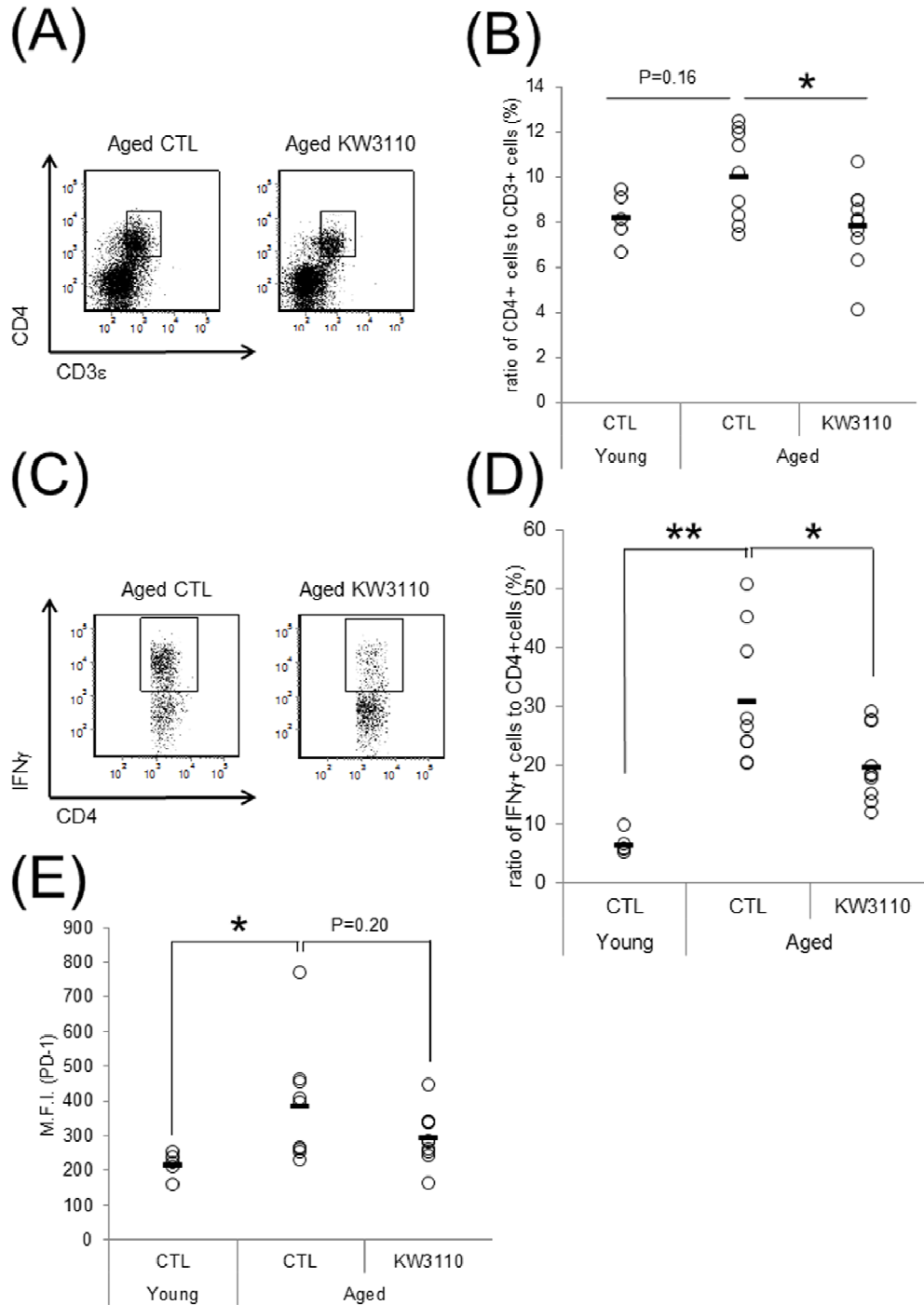


Figure 2. Intake of *Lactobacillus paracasei* KW3110 suppressed the inflammatory CD4-positive T cell expansion in the lamina propria of the small intestine (SI-LP). (A and B) To detect inflammatory cytokine-producing cells, SI-LP cells from young mice (3-months-old) and aged mice (17-months-old) were cultured under stimulation with Leukocyte Activation Cocktail plus BD GolgiPlug, and analyzed by flow cytometry. **(A)** Representative data of CD4-positive cells from aged mice fed a diet with (KW3110) or without (CTL) *L. paracasei* KW3110. **(B)** The ratio of CD3 ϵ - and CD4-positive to live cells. **(C)** Representative data of CD4- and interferon gamma (IFN- γ)-positive cells from aged mice fed a diet with or without *L. paracasei* KW3110. **(D)** The ratio of CD4- and IFN- γ -positive cells to CD4-positive cells. **(E)** The expressions of programmed cell death protein 1 (PD-1) in CD3 ϵ - and CD4-positive cells were analyzed by flow cytometry. M.F.I. indicates mean fluorescence intensity.

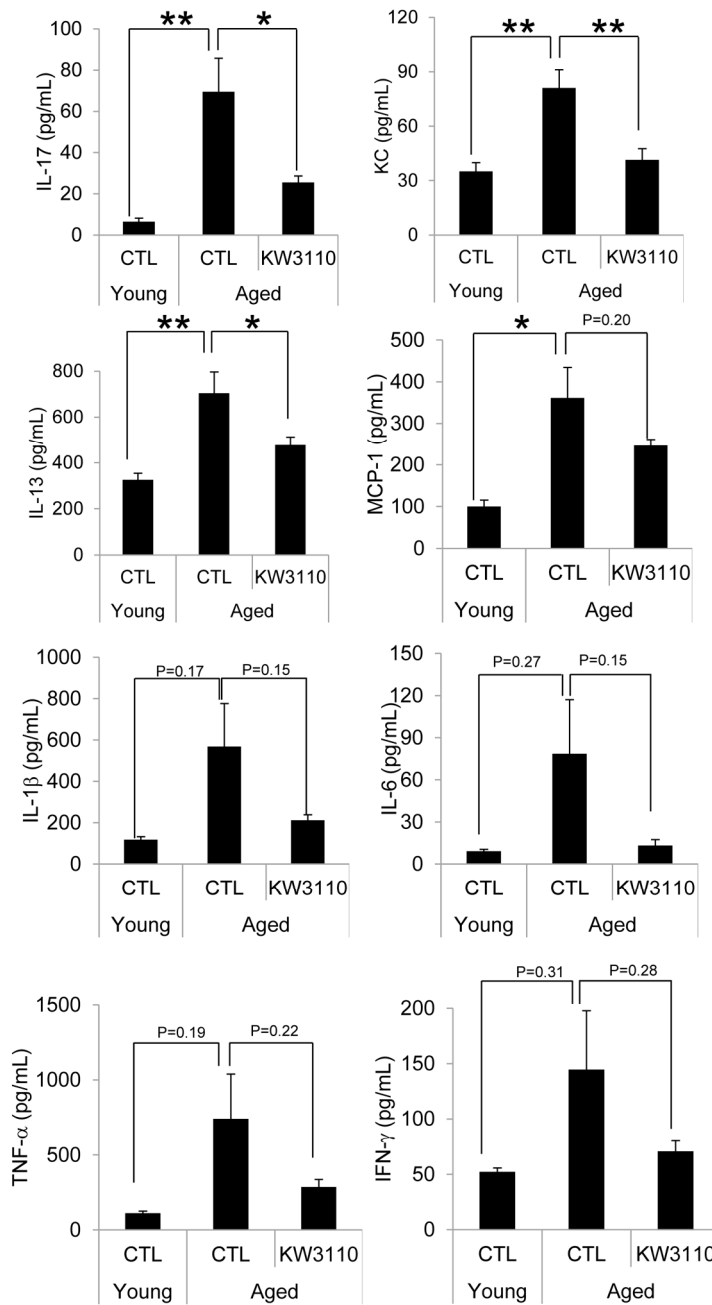


Figure 3. The levels of proinflammatory cytokines in the serum were mitigated in aged mice fed a diet containing *Lactobacillus paracasei* KW3110 as compared with age-matched control mice. Serum was collected and subjected to multiplex analyses to determine levels of cytokines (IL-1β, IL-6, IL-13, IL-17, IFN-γ, TNF-α, KC, and MCP1) in young (3-months-old) and aged mice (22-months-old). Values are presented as the means ± SEM. Significance was assumed if the p value was < 0.05. * p < 0.05; ** p < 0.01. CTL = control diet; KW3110 = *Lactobacillus paracasei* KW3110 diet; IL = interleukin; IFN = interferon; TNF = tumor necrosis factor; KC = keratinocyte chemoattractant; MCP1 = monocyte chemoattractant protein 1.

Intake of *L. paracasei* KW3110 suppressed age-related retinal cell loss

To elucidate the effects of the intake of *L. paracasei* KW3110 on age-related inflammatory phenotypes in retina, the number of RGCs was counted (Fig. 5A). The

survival of RGCs was significantly decreased in aged mice as compared with that of young control mice. However, the survival of RGCs was significantly improved in aged mice fed a diet containing *L. paracasei* KW3110 from 16–22 months of age for 6 months (Fig. 5A, B), as compared with age-matched

mice fed a control diet. In addition, the outer nuclear layer (ONL) thickness, corresponding to the photoreceptor layer, in aged mice fed a diet containing *L. paracasei* KW3110 for 6 months was also significantly thicker than in age-matched mice fed a control diet. These results were consistent with the suppressive results of proinflammatory cytokine levels in aged mice fed a diet containing *L. paracasei* KW3110.

DISCUSSION

Defective immune functions with aging are key triggers of age-related chronic inflammatory diseases, including infectious diseases, tumors, diabetes, and neurodegenerative diseases [8]. With rapid increases in the aging population, the prevention of age-related immunological dysfunctions and chronic inflammation are necessary to extend the healthy lifespan. In the present study, we demonstrated that long-term intake of heat-killed *L. paracasei* KW3110 in aged mice signi-

ficantly enhanced the population of beneficial gut bacteria, of the *Bifidobacterium* family, and slowed the age-related immune dysfunctions, expansion of the inflammatory IFN- γ -producing CD4-positive T cells in SI-LP, and lowered the serum levels of pro-inflammatory cytokines. We also found that intake of *L. paracasei* KW3110 mitigated retinal inflammation and age-related retinal cell death, probably associated with the prevention of age-related retinal diseases.

Age-related alterations of gut microbiota composition have been reported to cause immune senescence and intestinal chronic inflammation [34, 47]. Although some probiotics improve the intestinal environment and suppress inflammation, the effects of long-term ingestion of probiotics remain unclear. In the present study, we showed that intake of *L. paracasei* KW3110 improved the age-related changes of the gut microbiota composition (Fig. 1). The *Firmicutes* to *Bacteroidetes* bacterial ratio increased in aged mice fed a control diet

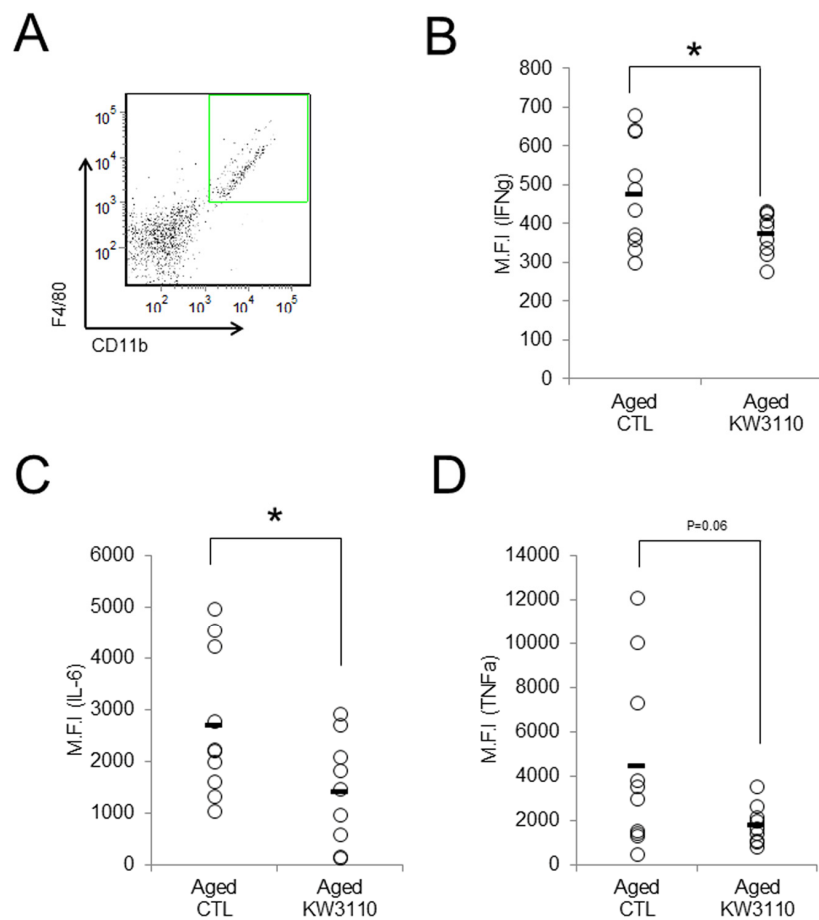


Figure 4. Intake of *Lactobacillus paracasei* KW3110 mitigated retinal inflammation. Intake of *L. paracasei* KW3110 in aged mice (17-months-old) suppressed the expression of inflammatory cytokines in retinal macrophage of aged mice. F4/80 and CD11b-positive macrophage in retina were gated as shown in (A), and median fluorescent intensity of intracellular IL-6, IFN- γ , and TNF- α were analyzed by flow cytometry (B-D). Significance was assumed if the p value was < 0.05; *p<0.05. All abbreviations are defined in the Figure 3 legend.

as compared with aged mice fed a diet containing *L. paracasei* KW3110 for 6 months. The age-related increase of *Firmicutes* to *Bacteroidetes* ratio was consistent with a previous study [48]. An increased *Firmicutes* to *Bacteroidetes* ratio has been reported to be associated with intestinal inflammation in obese patients [49]. The long-term intake of *L. paracasei*

KW3110 might mitigate intestinal inflammation and energy metabolic disorders by modulating the *Firmicutes* to *Bacteroidetes* ratio. The intake of *L. paracasei* KW3110 also increased the relative abundance of *Bifidobacteriaceae* families (Fig. 1D). *Bifidobacterium* is known as one of the most beneficial bacterial family, though the bacteria is not detected in

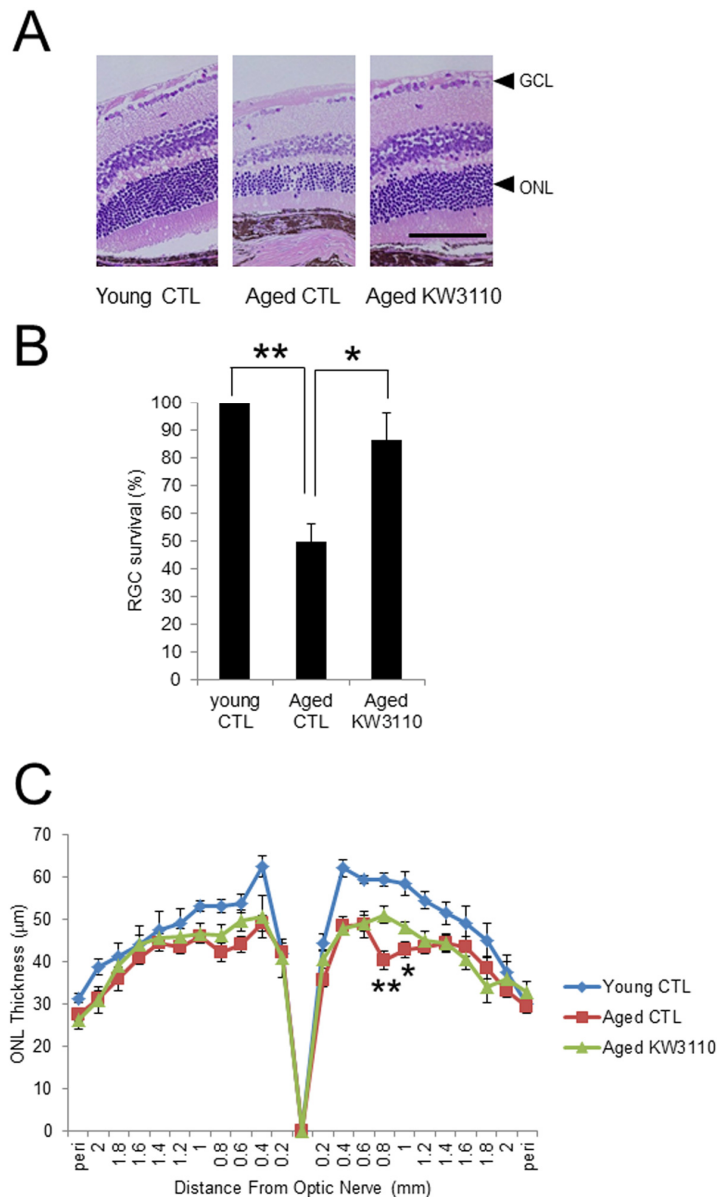


Figure 5. Protective effect of *Lactobacillus paracasei* KW3110 on age-induced histological changes and ganglion cell loss in the retina. (A) Hematoxylin and eosin staining of retinal sections in young mouse (3-months-old) fed a control (CTL) diet and aged mice (22-months-old) fed a diet either with or without *L. paracasei* KW3110 (KW3110 diet). Arrow heads indicate the ganglion cell layer (GCL) and outer nuclear layer (ONL), respectively. Scale bar represents 100 µm. (B) The survival rate of retinal ganglion cells (RGCs) in aged mice (22-months-old) fed a diet either with or without *L. paracasei* KW3110 (KW3110 diet) were analyzed compared to the survival of RGCs in young mice (3-months-old) fed a control diet. Values are presented as the means ± SEM. Significance was assumed if the p value was < 0.05. **p < 0.01. (C) ONL thickness was lower in aged mice (22-months-old) fed control diet than in aged mice fed a diet with *L. paracasei* KW3110. Values are presented as the means ± SEM. Significance was assumed if the p value was < 0.05. *p < 0.05; **p < 0.01.

the elderly [44, 50, 51]. In addition, the intake of *Bifidobacterium* has been reported to result in decreased levels of proinflammatory cytokines, such as TNF- α , in the elderly [44]. In contrast, intake of *L. paracasei* KW3110 decreased the relative abundance of *Streptococcaceae* (Fig. 1D). In a previous report, the *Streptococcaceae* bacteria stimulated the intestinal cells to induce CCL20 chemokine production [52] and inflammatory IFN- γ -producing CD4-positive T cells were attracted by the CCL20 chemokine [53]. In this study, the intake of *L. paracasei* KW3110 for 6 months in aged mice also significantly reduced *Ccl20* gene expression in SI-LP as compared with that of age-matched control mice (Supplementary Fig. 3). These results suggested that the mitigation of age-related alterations in gut microbiota composition by the intake of *L. paracasei* KW3110 was important to suppress age-related intestinal chronic inflammation.

Indeed, the intake of *L. paracasei* KW3110 in aged mice significantly suppressed the age-related increase of inflammatory CD4-positive T cells, producing inflammatory cytokines (IFN- γ) at high levels in the SI-LP (Fig. 2). The expression of PD-1, one of the senescence markers, in CD4-positive T cells in SI-LP was also lower in aged mice fed a diet containing *L. paracasei* KW3110 than that of aged mice fed a control diet. These anti-inflammatory effects on intestinal immune cells might be due to mitigation of age-related decreases of *Bifidobacterium*. The modulatory effects on intestinal immune cell subpopulations might be associated with a direct interaction between *L. paracasei* KW3110 and intestinal immune cells. In a previous study, our group showed that *L. paracasei* KW3110 interacted with intestinal macrophages and suppressed excessive inflammation, including dermatitis, in mice and humans [40-42]. Because lactic acid bacteria, including *L. paracasei* KW3110, have some toll-like receptor (TLR) ligands, such as lipoteichoic acid, *L. paracasei* KW3110 might modulate intestinal immune cell activation by a TLR-dependent pathway. Further studies are required to determine the mechanism underlying the relationship between the intake of *L. paracasei* KW3110 and suppressive effects on age-related expansions of intestinal inflammatory immune cells.

Proinflammatory cytokines produced by intestinal inflammatory immune cells are possibly transferred to other tissues, including the retina, through the blood. Age-related visual function declines and eye diseases, such as AMD, might be associated with retinal inflammation, because retinal chronic inflammation is toxic to retinal cells, including photoreceptor cells and RGCs [16-19]. In the present study, the intake of *L. paracasei* KW3110 mitigated the inflammation in the retinal macrophage in aged mice (Fig. 4). In addition,

the anti-inflammatory effects of *L. paracasei* KW3110 resulted in inhibition of age-related retinal cell death (Fig. 5). In previous studies, RGCs have been reported to mediate behaviors associated with response to light information and genetic ablation of RGCs results in loss of light-evoked behaviors [54-57]. We have obtained pre-liminary data that intake of *L. paracasei* KW3110 in aged mice could preserve the light-evoked locomotor activities as compared with age-matched control mice (data not shown). Although further studies, including immunohistochemical analysis, are needed, *L. paracasei* KW3110 might suppress age-related retinal cell death. Immunological phenomena are mainly regulated by macrophage in the retina. Macrophage consists of at least two subgroups, classic inflammatory M1 macrophage or alternative anti-inflammatory M2 macrophage [58, 59]. M1 macrophages produce inflammatory cytokines, such as TNF α and IL-6, whereas M2 macrophages are considered to be associated with anti-inflammatory responses, including tissue remodeling, through the production of neurotrophic factors and anti-inflammatory cytokines [60, 61]. Recently, we found that the intake of *L. paracasei* KW3110 suppressed light-induced retinal inflammation (unpublished data). Although further studies are required to evaluate the effects of *L. paracasei* KW3110 on macrophage activation in the retina, the inhibitory effects of *L. paracasei* KW3110 on age-related retinal cell death might be accompanied at least in part, by the regulation of macrophage activities. In addition, blood-borne macrophages have been reported to enter the retina via the optic nerve and ciliary body in light exposure mice model [62]. Our flow cytometry analysis showed that CD11b and f4/80-positive retinal cells, the retinal macrophages, in aged mice increased more than in young mice (Supplementary Fig. 4). Taken together, proinflammatory macrophages might penetrate into the retina under the age-related retinal degenerative condition.

In the present study, the anti-inflammatory effects of *L. paracasei* KW3110 on immune cells were observed in aged mice fed each diet from 11–17 months of age for 6 months (Figs. 2 and 4). However, in aged mice fed a diet containing *L. paracasei* KW3110 from 16–22 months of age for 6 months, such anti-inflammatory effects on immune cells were mild and not significantly different as compared with that of age-matched control mice (data not shown). These results suggested that 22 months of age was too old to evaluate the effects of *L. paracasei* KW3110 on intestinal immune cells.

Lactic acid bacteria are considered to be phagocytosed by intestinal M cells. In a previous report, M cells in aged mice (18 months of age) were not fully functional [63]. This may be because the effects of *L. paracasei*

KW3110 on immune cells in aged mice of 22 months of age were milder than in aged mice of 17 months of age. In the present study, we showed that intake of *L. paracasei* KW3110 from 16–22 months of age for 6 months significantly suppressed the serum levels of proinflammatory cytokines, alteration of gut microbiota composition, and retinal cell loss (Figs. 1, 3, and 5). Because the anti-inflammatory effects on serum cytokine levels were observed in aged mice fed a diet containing *L. paracasei* KW3110 (Supplementary Fig. 2), it was suggested that these phenotypes were reflected by the accumulation of anti-inflammatory effects for several months. In other words, continuous preventive methods, like dietary supplementation, might be much more effective in the delay of chronic inflammation.

In conclusion, the intake of *L. paracasei* KW3110 mitigated chronic inflammation in the intestine and retina, and reduced age-related retinal cell death. Further studies are needed to evaluate the effects in age-related senescent changes of the retina.

MATERIALS AND METHODS

Animals

The Mice (C57BL/6N, female) were purchased from Japan SLC (Hamamatsu, Japan). Young (1-month-old, $n = 5$), or aged (11-months-old, $n = 10$ in each group, or 16-months-old, $n = 12$ in each group) mice were acclimated until each aging study was started. Aged mice were divided by equal average weights into two groups. The control group mice were fed AIN93M (Oriental Yeast, Tokyo, Japan) and the *Lactobacillus paracasei* KW3110-fed mice (hereafter called the KW3110 group mice) were fed AIN93M containing 1 mg heat-killed *L. paracasei* KW3110/day/mouse for 6 months. The mice were housed in specific pathogen-free conditions under a 12-h light-dark photo cycle and had *ad libitum* access to water and the diet. The temperature in the room was kept at $25 \pm 1^\circ\text{C}$ and $60\% \pm 15\%$ humidity.

All animal procedures and experiments were performed in accordance with the Association for Research in Vision and Ophthalmology Statement for the Use of Animals in Ophthalmic and Vision Research and institutional guidelines following approval by the Animal Care and Use Committee of National Center for Geriatrics and Gerontology (NCGG) (Obu, Japan).

SI-LP and retinal cell preparations and flow cytometry analyses

The SI-LP cells and retinal cells were prepared for flow cytometric analyses. The SI-LP cells were prepared as

described previously [64]. Retinas were digested with 1 mg/mL collagenase II (Worthington, Lakewood, NJ, USA) for 40 minutes at 37°C in Hanks' Balanced Salt Solution (HBSS) buffer with 1.0 % bovine serum albumin (BSA). The tissue digest was then filtered through a $70 \mu\text{m}$ cell strainer, and washed with HBSS buffer with 1.0% BSA for 5 minutes at 1,300 rpm at 4°C . The supernatant was carefully removed and the digested tissue pellet was resuspended to form a single cell suspension. To investigate intracellular cytokine production, SI-LP and retinal cells were treated with a leukocyte activation cocktail with BD GolgiPlug (BD Biosciences, San Jose, CA, USA) for 4.5 hours and with a BD Cytotfix/Cytoperm Fixation/Permeabilization kit (BD Biosciences), and then stained with the following antibodies to: CD3 ϵ -BV421 (145-2C11) (Sony Biotechnology Inc., Tokyo, Japan), CD4-APC-Cy7 (GK1.5) (BioLegend, San Diego, CA, USA), IFN- γ -PE-Cy7 (XMG1.2) (eBiosciences, San Diego, CA, USA), TNF- α -BV421 (MP6-XT22) (BioLegend), IL-6-PE (MP5-20F3) (eBiosciences), IFN- γ -APC (XMG1.2) (eBiosciences), CD11b-APC-Cy7 (M1/70) (BD Biosciences), F4/80-PE-Cy7 (BM8) (BioLegend), programmed cell death protein 1 (PD-1)-BV421 (29F.1A12) (BioLegend), and 7-AAD (BD Pharmingen, San Jose, CA, USA). The 7-AAD-CD3 ϵ - and CD4-positive cells were defined as CD4-positive T cells and 7-AAD-CD11b-, and the f4/80-positive cells were defined as retinal macrophage cells. To detect Tregs, cells were treated with a Foxp3 Staining Kit (BD Biosciences) and stained with the following antibodies to: CD3 ϵ -FITC (145-2C11) (eBiosciences), Foxp3-PE-Cy7 (FJK-16s) (eBiosciences), CD4-APC-Cy7 (GK1.5) (BioLegend), and 7-AAD (BD Pharmingen). The 7-AAD-CD3 ϵ -, CD4-, and Foxp3-positive cells were defined as Tregs.

Data were collected using a FACS Canto II flow cytometer (BD Biosciences) and analyzed by FCS Express software (De Novo Software, Los Angeles, CA, USA).

Analysis of serum cytokine concentrations

Blood samples were collected into heparin-coated tubes and centrifuged at 3,000 rpm for 5 min. Supernatants were collected and analyzed for serum cytokine concentrations using a Bio-Plex Pro mouse cytokine assay kit (Bio-Rad, Hercules, CA, USA).

Analyses of gut microbiota

Feces were collected from young mice and aged mice fed control or KW3110-containing diets and stored at -80°C until further analyses. DNA was extracted according to a previous report [65]. Pyrosequencing of

16S ribosomal RNA was performed by Technosruqa Lab (Shizuoka, Japan). The 16S ribosomal RNA sequencing was performed using the MiSeqTMII system (Illumina, San Diego, CA, USA) according to a previously described method [65]. The V3-V4 regions of 16S ribosomal RNA genes were amplified by PCR from fecal genomic DNA using the following universal primers [66, 67]: 341F, 5'-AATGATACGGCGACCA CCGAGATCTACACTCTTTCCTACACGACGCTC TTCCGATCTCCTACGGGAGGCAGCAGCCTACGG GAGGCAGCAG-3', and 806R, 5'-CAAGCAGAAGA CGGCATAGAGATNNNNNGTGACTGGAGTTCA GACGTGTGCTCTCCGATCTGGACTACHVGGGT WTCTAAT-3'. PCR products were purified using a MultiScreen PCR filter plate (Merck Millipore, Darmstadt, Germany). All amplicons were sequenced using the paired-end, 2 × 250 bp cycle run on the MiSeqTMII system with a MiSeq Reagent Kit. The sequences were evaluated and filtered for their length and quality. Paired-end sequencing was joined using the fastq-join program (<http://code.google.com/p/ea-utils/>). The low quality reads, quality value scores < 20 for more than 99% of the sequence, were removed. The nucleotide sequence dataset was deposited in DNA Data Bank of Japan (DDBJ) with the accession numbers SAMD00118680-SAMD00118706.

Analyses of the extracted sequence reads were carried out using the Ribosomal Database Project (RDP) Multiclassifier version 2.11 [68] and Basic Local Alignment Search Tool (BLAST) search using the Metagenome@KIN analysis software (World Fusion, Tokyo, Japan). Reads showing > 97% similarity were grouped in each taxonomic rank.

Measurements of outer nuclear layer thickness in the retina and retinal ganglion cell survival

Retinal sections, which included the optic nerve head to the most peripheral region of the retina, were fixed in neutral 10% formalin and stained with hematoxylin and eosin (HE), and the outer nuclear layer (ONL) thickness was measured in all areas and averaged at each point from the optic nerve head. The number of RGCs was counted within whole retinal sections.

Statistical analysis

All values are expressed as the mean ± SEM. Statistical differences between three groups (young mice group fed a control diet, aged mice group fed a control diet, and aged mice group fed a diet containing KW3110) were analyzed by one-way analysis of variance (ANOVA), followed by the Tukey-Kramer test with significance set at $p < 0.05$. Statistical differences between two groups (aged mice group fed a control diet

versus aged mice group fed a diet containing KW3110) were determined using an unpaired, two-tailed Student's *t*-test with significance set at $p < 0.05$. All statistical analyses were performed by using the Ekuseru-Toukei 2012 software program (Social Survey Research Information, Tokyo, Japan).

ACKNOWLEDGEMENTS

We thank T. Kirisako and M. Sugamata of Kirin Company, I. Wakaya, of Koiwai Dairy Products Company for valuable discussion. We are also indebted to T. Matsuda and M. Sugimoto for stimulating and helpful suggestions and advice as well as grateful to our colleagues, Y. Ohta, M. Kondo, A. Yamada, N. Matsui, M. Nagasaka and M. Okayama for excellent technical assistance.

CONFLICTS OF INTEREST

The authors declare that they have no conflicts of interest with the content of this article.

FUNDING

This work was supported in part by the Research Funding for Longevity Sciences from National Center for Geriatrics and Gerontology (grant #29-26 to M.M.).

REFERENCES

1. Flatt T. A new definition of aging? *Front Genet.* 2012; 3:148. <https://doi.org/10.3389/fgene.2012.00148>
2. Rose MR, Flatt T, Graves JL, Greer LF, Martinez DE, Matos M, Mueller LD, Shmookler Reis RJ, Shahrestani P. What is Aging? *Front Genet.* 2012; 3:134. <https://doi.org/10.3389/fgene.2012.00134>
3. Kennedy BK, Berger SL, Brunet A, Campisi J, Cuervo AM, Epel ES, Franceschi C, Lithgow GJ, Morimoto RI, Pessin JE, Rando TA, Richardson A, Schadt EE, et al. Geroscience: linking aging to chronic disease. *Cell.* 2014; 159:709–13. <https://doi.org/10.1016/j.cell.2014.10.039>
4. Finkel T, Serrano M, Blasco MA. The common biology of cancer and ageing. *Nature.* 2007; 448:767–74. <https://doi.org/10.1038/nature05985>
5. Gavazzi G, Krause KH. Ageing and infection. *Lancet Infect Dis.* 2002; 2:659–66. [https://doi.org/10.1016/S1473-3099\(02\)00437-1](https://doi.org/10.1016/S1473-3099(02)00437-1)
6. Calçada D, Vianello D, Giampieri E, Sala C, Castellani G, de Graaf A, Kremer B, van Ommen B, Feskens E, Santoro A, Franceschi C, Bouwman J. The role of low-grade inflammation and metabolic flexibility in aging

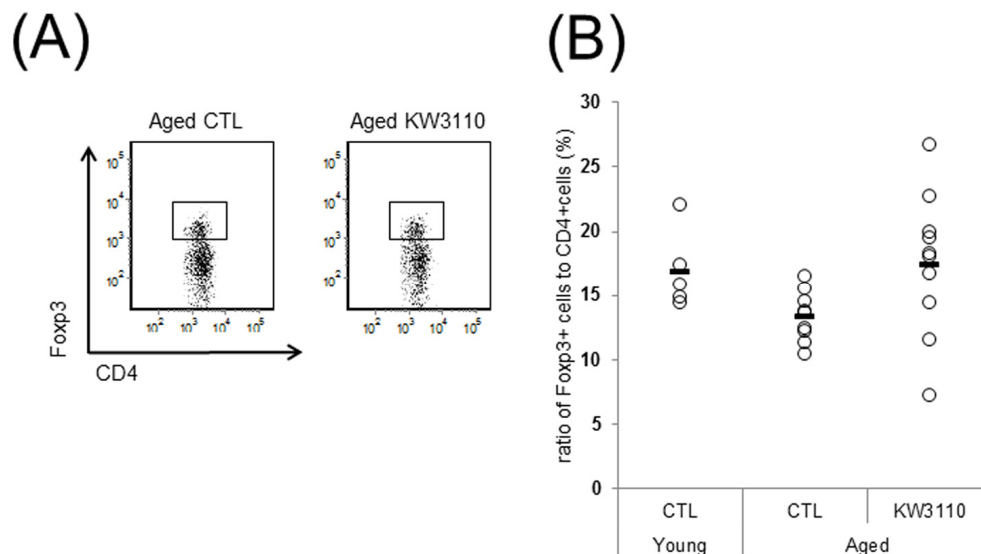
- and nutritional modulation thereof: a systems biology approach. *Mech Ageing Dev.* 2014; 136-137:138–47. <https://doi.org/10.1016/j.mad.2014.01.004>
7. Fulop T, Larbi A, Witkowski JM, Kotb R, Hirokawa K, Pawelec G. Immunosenescence and cancer. *Crit Rev Oncog.* 2013; 18:489–513. <https://doi.org/10.1615/CritRevOncog.2013010597>
 8. Deleidi M, Jäggle M, Rubino G. Immune aging, dysmetabolism, and inflammation in neurological diseases. *Front Neurosci.* 2015; 9:172. <https://doi.org/10.3389/fnins.2015.00172>
 9. Klein R, Cruickshanks KJ, Nash SD, Krantz EM, Nieto FJ, Huang GH, Pankow JS, Klein BE. The prevalence of age-related macular degeneration and associated risk factors. *Arch Ophthalmol.* 2010; 128:750–58. <https://doi.org/10.1001/archophthalmol.2010.92>
 10. Wong WL, Su X, Li X, Cheung CM, Klein R, Cheng CY, Wong TY. Global prevalence of age-related macular degeneration and disease burden projection for 2020 and 2040: a systematic review and meta-analysis. *Lancet Glob Health.* 2014; 2:e106–16. [https://doi.org/10.1016/S2214-109X\(13\)70145-1](https://doi.org/10.1016/S2214-109X(13)70145-1)
 11. Pezzullo L, Streatfeild J, Simkiss P, Shickle D. The economic impact of sight loss and blindness in the UK adult population. *BMC Health Serv Res.* 2018; 18:63. <https://doi.org/10.1186/s12913-018-2836-0>
 12. Flaxman SR, Bourne RR, Resnikoff S, Ackland P, Braithwaite T, Cicinelli MV, Das A, Jonas JB, Keeffe J, Kempen JH, Leasher J, Limburg H, Naidoo K, et al, and Vision Loss Expert Group of the Global Burden of Disease Study. Global causes of blindness and distance vision impairment 1990-2020: a systematic review and meta-analysis. *Lancet Glob Health.* 2017; 5:e1221–34. [https://doi.org/10.1016/S2214-109X\(17\)30393-5](https://doi.org/10.1016/S2214-109X(17)30393-5)
 13. Weinreb RN, Aung T, Medeiros FA. The pathophysiology and treatment of glaucoma: a review. *JAMA.* 2014; 311:1901–11. <https://doi.org/10.1001/jama.2014.3192>
 14. Beatty S, Koh H, Phil M, Henson D, Boulton M. The role of oxidative stress in the pathogenesis of age-related macular degeneration. *Surv Ophthalmol.* 2000; 45:115–34. [https://doi.org/10.1016/S0039-6257\(00\)00140-5](https://doi.org/10.1016/S0039-6257(00)00140-5)
 15. Shahinfar S, Edward DP, Tso MO. A pathologic study of photoreceptor cell death in retinal photic injury. *Curr Eye Res.* 1991; 10:47–59. <https://doi.org/10.3109/02713689109007610>
 16. Kauppinen A, Paterno JJ, Blasiak J, Salminen A, Kaarniranta K. Inflammation and its role in age-related macular degeneration. *Cell Mol Life Sci.* 2016; 73:1765–86. <https://doi.org/10.1007/s00018-016-2147-8>
 17. Ambati J, Atkinson JP, Gelfand BD. Immunology of age-related macular degeneration. *Nat Rev Immunol.* 2013; 13:438–51. <https://doi.org/10.1038/nri3459>
 18. Parmeggiani F, Romano MR, Costagliola C, Semeraro F, Incorvaia C, D'Angelo S, Perri P, De Palma P, De Nadai K, Sebastiani A. Mechanism of inflammation in age-related macular degeneration. *Mediators Inflamm.* 2012; 2012:546786. <https://doi.org/10.1155/2012/546786>
 19. Scholl HP, Charbel Issa P, Walier M, Janzer S, Pollok-Kopp B, Börncke F, Fritsche LG, Chong NV, Fimmers R, Wienker T, Holz FG, Weber BH, Oppermann M. Systemic complement activation in age-related macular degeneration. *PLoS One.* 2008; 3:e2593. <https://doi.org/10.1371/journal.pone.0002593>
 20. Chen Y, Palczewska G, Mustafi D, Golczak M, Dong Z, Sawada O, Maeda T, Maeda A, Palczewski K. Systems pharmacology identifies drug targets for Stargardt disease-associated retinal degeneration. *J Clin Invest.* 2013; 123:5119–34. <https://doi.org/10.1172/JCI69076>
 21. Chen Y, Okano K, Maeda T, Chauhan V, Golczak M, Maeda A, Palczewski K. Mechanism of all-trans-retinal toxicity with implications for stargardt disease and age-related macular degeneration. *J Biol Chem.* 2012; 287:5059–69. <https://doi.org/10.1074/jbc.M111.315432>
 22. Goronzy JJ, Fang F, Cavanagh MM, Qi Q, Weyand CM. Naive T cell maintenance and function in human aging. *J Immunol.* 2015; 194:4073–80. <https://doi.org/10.4049/jimmunol.1500046>
 23. Maue AC, Yager EJ, Swain SL, Woodland DL, Blackman MA, Haynes L. T-cell immunosenescence: lessons learned from mouse models of aging. *Trends Immunol.* 2009; 30:301–05. <https://doi.org/10.1016/j.it.2009.04.007>
 24. Spadaro O, Goldberg EL, Camell CD, Youm YH, Kopchick JJ, Nguyen KY, Bartke A, Sun LY, Dixit VD. Growth Hormone Receptor Deficiency Protects against Age-Related NLRP3 Inflammasome Activation and Immune Senescence. *Cell Reports.* 2016; 14:1571–80. <https://doi.org/10.1016/j.celrep.2016.01.044>
 25. Frasca D, Blomberg BB. Effects of aging on B cell function. *Curr Opin Immunol.* 2009; 21:425–30. <https://doi.org/10.1016/j.coi.2009.06.001>
 26. Miller JP, Allman D. The decline in B lymphopoiesis in aged mice reflects loss of very early B-lineage precursors. *J Immunol.* 2003; 171:2326–30.

- <https://doi.org/10.4049/jimmunol.171.5.2326>
27. Frasca D, Riley RL, Blomberg BB. Effect of age on the immunoglobulin class switch. *Crit Rev Immunol*. 2004; 24:297–320. <https://doi.org/10.1615/CritRevImmunol.v24.i5.10>
 28. Kovacs EJ, Palmer JL, Fortin CF, Fülöp T Jr, Goldstein DR, Linton PJ. Aging and innate immunity in the mouse: impact of intrinsic and extrinsic factors. *Trends Immunol*. 2009; 30:319–24. <https://doi.org/10.1016/j.it.2009.03.012>
 29. Shaw AC, Joshi S, Greenwood H, Panda A, Lord JM. Aging of the innate immune system. *Curr Opin Immunol*. 2010; 22:507–13. <https://doi.org/10.1016/j.coi.2010.05.003>
 30. Sakamoto A, Matsuda T, Kawaguchi K, Takaoka A, Maruyama M. Involvement of Zizimin2/3 in the age-related defect of peritoneal B-1a cells as a source of anti-bacterial IgM. *Int Immunol*. 2017; 29:431–38. <https://doi.org/10.1093/intimm/dxx054>
 31. Capri M, Monti D, Salvioli S, Lescai F, Pierini M, Altilia S, Sevini F, Valensin S, Ostan R, Bucci L, Franceschi C. Complexity of anti-immunosenescence strategies in humans. *Artif Organs*. 2006; 30:730–42. <https://doi.org/10.1111/j.1525-1594.2006.00295.x>
 32. Adolfsen O, Huber BT, Meydani SN. Vitamin E-enhanced IL-2 production in old mice: naive but not memory T cells show increased cell division cycling and IL-2-producing capacity. *J Immunol*. 2001; 167:3809–17. <https://doi.org/10.4049/jimmunol.167.7.3809>
 33. Candore G, Balistreri CR, Colonna-Romano G, Grimaldi MP, Lio D, Listi F, Scola L, Vasto S, Caruso C. Immunosenescence and anti-immunosenescence therapies: the case of probiotics. *Rejuvenation Res*. 2008; 11:425–32. <https://doi.org/10.1089/rej.2008.0662>
 34. Cho SY, Kim J, Lee JH, Sim JH, Cho DH, Bae IH, Lee H, Seol MA, Shin HM, Kim TJ, Kim DY, Lee SH, Shin SS, et al. Modulation of gut microbiota and delayed immunosenescence as a result of syringaresinol consumption in middle-aged mice. *Sci Rep*. 2016; 6:39026. <https://doi.org/10.1038/srep39026>
 35. Biagi E, Candela M, Turrone S, Garagnani P, Franceschi C, Brigidi P. Ageing and gut microbes: perspectives for health maintenance and longevity. *Pharmacol Res*. 2013; 69:11–20. <https://doi.org/10.1016/j.phrs.2012.10.005>
 36. Bartley JM, Zhou X, Kuchel GA, Weinstock GM, Haynes L. Impact of Age, Caloric Restriction, and Influenza Infection on Mouse Gut Microbiome: An Exploratory Study of the Role of Age-Related Microbiome Changes on Influenza Responses. *Front Immunol*. 2017; 8:1164. <https://doi.org/10.3389/fimmu.2017.01164>
 37. Shen X, Miao J, Wan Q, Wang S, Li M, Pu F, Wang G, Qian W, Yu Q, Marotta F, He F. Possible correlation between gut microbiota and immunity among healthy middle-aged and elderly people in southwest China. *Gut Pathog*. 2018; 10:4. <https://doi.org/10.1186/s13099-018-0231-3>
 38. Rowan S, Jiang S, Korem T, Szymanski J, Chang ML, Szelog J, Cassalman C, Dasuri K, McGuire C, Nagai R, Du XL, Brownlee M, Rabbani N, et al. Involvement of a gut-retina axis in protection against dietary glycemia-induced age-related macular degeneration. *Proc Natl Acad Sci USA*. 2017; 114:E4472–81. <https://doi.org/10.1073/pnas.1702302114>
 39. Fontana L, Bermudez-Brito M, Plaza-Diaz J, Muñoz-Quezada S, Gil A. Sources, isolation, characterisation and evaluation of probiotics. *Br J Nutr*. 2013 (Suppl 2); 109:S35–50. <https://doi.org/10.1017/S0007114512004011>
 40. Ichikawa S, Fujii R, Fujiwara D, Komiyama Y, Kaisho T, Sakaguchi M, Konishi Y. MyD88 but not TLR2, 4 or 9 is essential for IL-12 induction by lactic acid bacteria. *Biosci Biotechnol Biochem*. 2007; 71:3026–32. <https://doi.org/10.1271/bbb.70414>
 41. Fujiwara D, Inoue S, Wakabayashi H, Fujii T. The anti-allergic effects of lactic acid bacteria are strain dependent and mediated by effects on both Th1/Th2 cytokine expression and balance. *Int Arch Allergy Immunol*. 2004; 135:205–15. <https://doi.org/10.1159/000081305>
 42. Wakabayashi H, Nariai C, Takemura F, Nakao W, Fujiwara D. Dietary supplementation with lactic acid bacteria attenuates the development of atopic-dermatitis-like skin lesions in NC/Nga mice in a strain-dependent manner. *Int Arch Allergy Immunol*. 2008; 145:141–51. <https://doi.org/10.1159/000108139>
 43. Ichikawa S, Miyake M, Fujii R, Konishi Y. Orally administered *Lactobacillus paracasei* KW3110 induces in vivo IL-12 production. *Biosci Biotechnol Biochem*. 2009; 73:1561–65. <https://doi.org/10.1271/bbb.90058>
 44. Ouwehand AC, Bergsma N, Parhiala R, Lahtinen S, Gueimonde M, Finne-Soveri H, Strandberg T, Pitkälä K, Salminen S. Bifidobacterium microbiota and parameters of immune function in elderly subjects. *FEMS Immunol Med Microbiol*. 2008; 53:18–25. <https://doi.org/10.1111/j.1574-695X.2008.00392.x>
 45. Ibrahim F, Ruvio S, Granlund L, Salminen S, Viitanen M, Ouwehand AC. Probiotics and immunosenescence: cheese as a carrier. *FEMS Immunol Med*

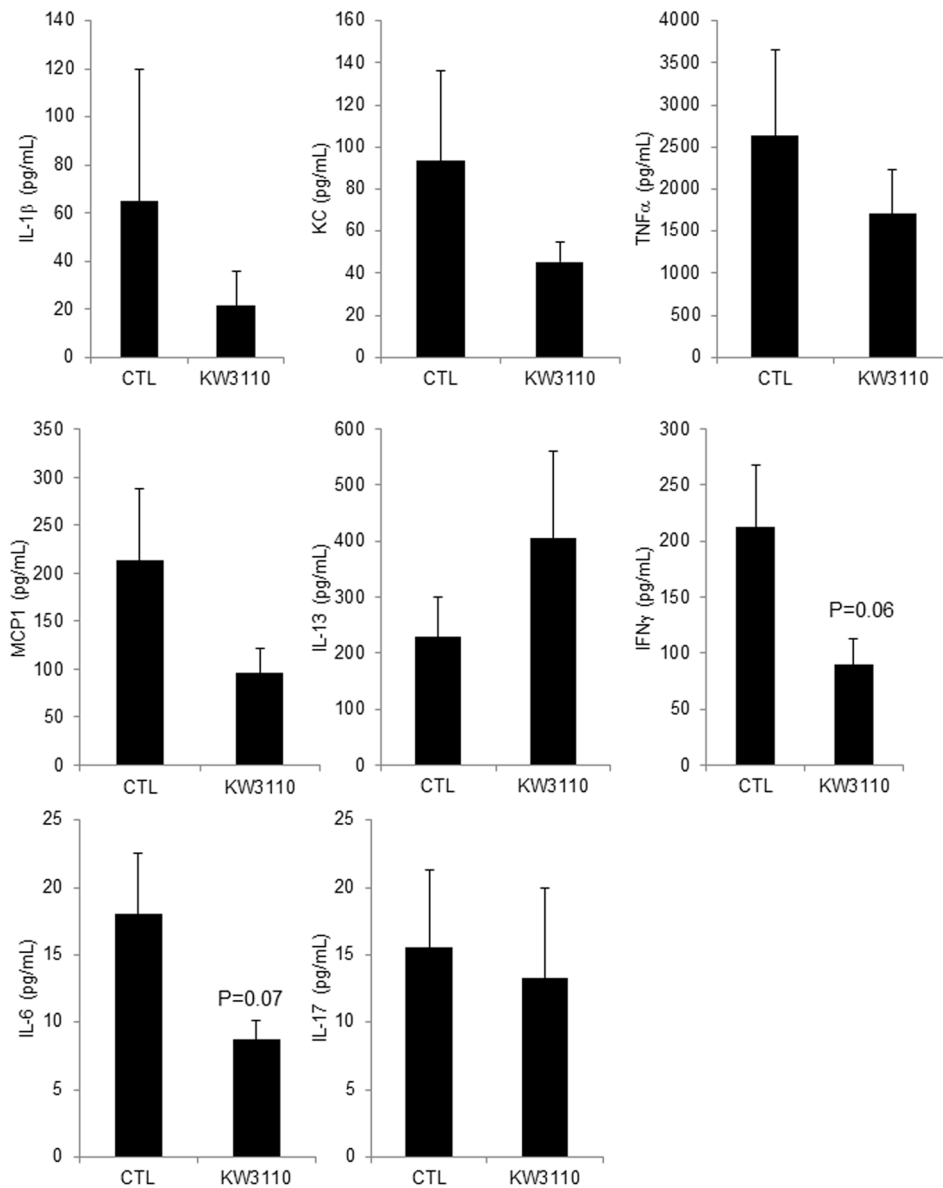
- Microbiol. 2010; 59:53–59.
<https://doi.org/10.1111/j.1574-695X.2010.00658.x>
46. Martinet KZ, Bloquet S, Bourgeois C. Ageing combines CD4 T cell lymphopenia in secondary lymphoid organs and T cell accumulation in gut associated lymphoid tissue. *Immun Ageing*. 2014; 11:8.
<https://doi.org/10.1186/1742-4933-11-8>
 47. Fransen F, van Beek AA, Borghuis T, Aidy SE, Hugenholtz F, van der Gaast-de Jongh C, Savelkoul HF, De Jonge MI, Boekschoten MV, Smidt H, Faas MM, de Vos P. Aged Gut Microbiota Contributes to Systemical Inflammation after Transfer to Germ-Free Mice. *Front Immunol*. 2017; 8:1385.
<https://doi.org/10.3389/fimmu.2017.01385>
 48. Hoffman JD, Parikh I, Green SJ, Chlipala G, Mohny RP, Keaton M, Bauer B, Hartz AM, Lin AL. Age Drives Distortion of Brain Metabolic, Vascular and Cognitive Functions, and the Gut Microbiome. *Front Aging Neurosci*. 2017; 9:298.
<https://doi.org/10.3389/fnagi.2017.00298>
 49. Verdam FJ, Fuentes S, de Jonge C, Zoetendal EG, Erbil R, Greve JW, Buurman WA, de Vos WM, Rensen SS. Human intestinal microbiota composition is associated with local and systemic inflammation in obesity. *Obesity (Silver Spring)*. 2013; 21:E607–15.
<https://doi.org/10.1002/oby.20466>
 50. Biagi E, Nylund L, Candela M, Ostan R, Bucci L, Pini E, Nikkila J, Monti D, Satokari R, Franceschi C, Brigidi P, De Vos W. Through ageing, and beyond: gut microbiota and inflammatory status in seniors and centenarians. *PLoS One*. 2010; 5:e10667.
<https://doi.org/10.1371/journal.pone.0010667>
 51. Drago L, Toscano M, Rodighiero V, De Vecchi E, Mogna G. Cultivable and pyrosequenced fecal microflora in centenarians and young subjects. *J Clin Gastroenterol*. 2012 (Suppl); 46:S81–84.
<https://doi.org/10.1097/MCG.0b013e3182693982>
 52. Veckman V, Miettinen M, Matikainen S, Lande R, Giacomini E, Coccia EM, Julkunen I. Lactobacilli and streptococci induce inflammatory chemokine production in human macrophages that stimulates Th1 cell chemotaxis. *J Leukoc Biol*. 2003; 74:395–402.
<https://doi.org/10.1189/jlb.0402212>
 53. Mony JT, Khoroshii R, Owens T. Chemokine receptor expression by inflammatory T cells in EAE. *Front Cell Neurosci*. 2014; 8:187.
<https://doi.org/10.3389/fncel.2014.00187>
 54. Hattar S, Liao HW, Takao M, Berson DM, Yau KW. Melanopsin-containing retinal ganglion cells: architecture, projections, and intrinsic photosensitivity. *Science*. 2002; 295:1065–70.
<https://doi.org/10.1126/science.1069609>
 55. Berson DM, Dunn FA, Takao M. Phototransduction by retinal ganglion cells that set the circadian clock. *Science*. 2002; 295:1070–73.
<https://doi.org/10.1126/science.1067262>
 56. Güler AD, Ecker JL, Lall GS, Haq S, Altimus CM, Liao HW, Barnard AR, Cahill H, Badea TC, Zhao H, Hankins MW, Berson DM, Lucas RJ, et al. Melanopsin cells are the principal conduits for rod-cone input to non-image-forming vision. *Nature*. 2008; 453:102–05.
<https://doi.org/10.1038/nature06829>
 57. Mure LS, Hatori M, Zhu Q, Demas J, Kim IM, Nayak SK, Panda S. Melanopsin-Encoded Response Properties of Intrinsically Photosensitive Retinal Ganglion Cells. *Neuron*. 2016; 90:1016–27.
<https://doi.org/10.1016/j.neuron.2016.04.016>
 58. Martinez FO, Helming L, Gordon S. Alternative activation of macrophages: an immunologic functional perspective. *Annu Rev Immunol*. 2009; 27:451–83.
<https://doi.org/10.1146/annurev.immunol.021908.132532>
 59. Biswas SK, Mantovani A. Macrophage plasticity and interaction with lymphocyte subsets: cancer as a paradigm. *Nat Immunol*. 2010; 11:889–96.
<https://doi.org/10.1038/ni.1937>
 60. Sica A, Mantovani A. Macrophage plasticity and polarization: in vivo veritas. *J Clin Invest*. 2012; 122:787–95. <https://doi.org/10.1172/JCI59643>
 61. Satoh T, Kidoya H, Naito H, Yamamoto M, Takemura N, Nakagawa K, Yoshioka Y, Morii E, Takakura N, Takeuchi O, Akira S. Critical role of Trib1 in differentiation of tissue-resident M2-like macrophages. *Nature*. 2013; 495:524–28.
<https://doi.org/10.1038/nature11930>
 62. Joly S, Francke M, Ulbricht E, Beck S, Seeliger M, Hirrlinger P, Hirrlinger J, Lang KS, Zinkernagel M, Odermatt B, Samardzija M, Reichenbach A, Grimm C, Remé CE. Cooperative phagocytes: resident microglia and bone marrow immigrants remove dead photoreceptors in retinal lesions. *Am J Pathol*. 2009; 174:2310–23.
<https://doi.org/10.2353/ajpath.2009.090023>
 63. Kobayashi A, Donaldson DS, Erridge C, Kanaya T, Williams IR, Ohno H, Mahajan A, Mabbott NA. The functional maturation of M cells is dramatically reduced in the Peyer's patches of aged mice. *Mucosal Immunol*. 2013; 6:1027–37.
<https://doi.org/10.1038/mi.2012.141>
 64. Sanos SL, Diefenbach A. Isolation of NK cells and NK-like cells from the intestinal lamina propria. *Methods Mol Biol*. 2010; 612:505–17.
https://doi.org/10.1007/978-1-60761-362-6_32

65. Takahashi S, Tomita J, Nishioka K, Hisada T, Nishijima M. Development of a prokaryotic universal primer for simultaneous analysis of Bacteria and Archaea using next-generation sequencing. *PLoS One*. 2014; 9:e105592.
<https://doi.org/10.1371/journal.pone.0105592>
66. Muyzer G, de Waal EC, Uitterlinden AG. Profiling of complex microbial populations by denaturing gradient gel electrophoresis analysis of polymerase chain reaction-amplified genes coding for 16S rRNA. *Appl Environ Microbiol*. 1993; 59:695–700.
67. Caporaso JG, Lauber CL, Walters WA, Berg-Lyons D, Lozupone CA, Turnbaugh PJ, Fierer N, Knight R. Global patterns of 16S rRNA diversity at a depth of millions of sequences per sample. *Proc Natl Acad Sci USA*. 2011 (Suppl 1); 108:4516–22.
<https://doi.org/10.1073/pnas.1000080107>
68. Wang Q, Garrity GM, Tiedje JM, Cole JR. Naive Bayesian classifier for rapid assignment of rRNA sequences into the new bacterial taxonomy. *Appl Environ Microbiol*. 2007; 73:5261–67.
<https://doi.org/10.1128/AEM.00062-07>

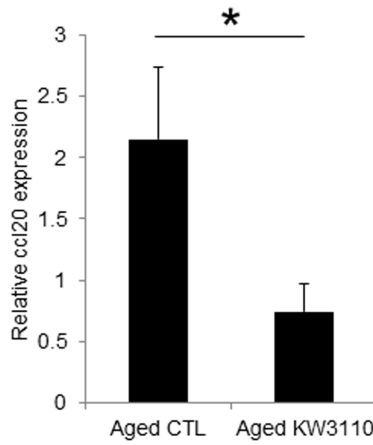
SUPPLEMENTARY FIGURES



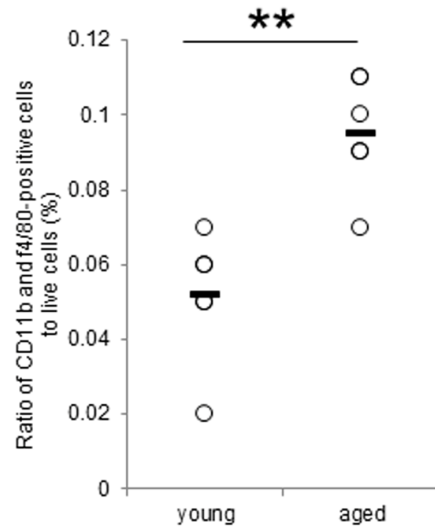
Supplementary Figure 1. Intake of *Lactobacillus paracasei* KW3110 did not affect the regulatory T cells (Tregs) population in the lamina propria of the small intestine (SI-LP). (A and B) To detect Tregs, SI-LP cells from young mice (3-months-old) and aged mice (17-months-old) were cultured and analyzed by flow cytometry. (A) Representative data of CD3 ϵ -, CD4-, and Foxp3-positive cells from aged mice fed a diet with or without *L. paracasei* KW3110. (B) The ratio of CD3 ϵ -, CD4-, and Foxp3-positive to CD3 ϵ - and CD4-positive cells. Statistical differences between three groups (young mice group fed a control diet, aged mice group fed a control diet, and aged mice group fed a diet containing KW3110) were analyzed by one-way analysis of variance (ANOVA), followed by the Tukey-Kramer test with significance set at $p < 0.05$. CTL = control diet; KW3110 = *Lactobacillus paracasei* KW3110 diet.



Supplementary Figure 2. The levels of cytokines in the serum of aged mice fed a diet either with or without *Lactobacillus paracasei* KW3110 for 2 months. Serum was collected and subjected to multiplex analyses to determine levels of cytokines (IL-1 β , IL-6, IL-13, IL-17, IFN- γ , TNF- α , KC, and MCP1) in aged mice (18-months-old) fed a diet with (KW3110) or without (CTL) *L. paracasei* KW3110 for 2 months. Values are presented as the means \pm SEM. Statistical differences between two groups (aged mice group fed a control diet versus aged mice group fed a diet containing KW3110) were determined using an unpaired, two-tailed Student's *t*-test with significance set at $p < 0.05$. IL = interleukin; IFN = interferon; TNF = tumor necrosis factor; KC = keratinocyte chemoattractant; MCP1 = monocyte chemoattractant protein 1.



Supplementary Figure 3. Suppression of chemokine expression in the lamina propria of the small intestine (SI-LP) by intake of *Lactobacillus paracasei* KW3110. Total mRNA was extracted from SI-LP cells from aged mice (17-months-old) fed a diet with (KW3110) or without (CTL) *L. paracasei* KW3110 for 6 months. *Ccl20* gene expression was estimated by qRT-PCR and normalized to *Gapdh* gene expression. Values are presented as the means ± SEM. Significance was assumed if the p value was < 0.05. * p < 0.05.



Supplementary Figure 4. The retinal macrophages increased in aged mice as compared with young mice. The ratio of CD11b and f4/80-positive to live cells. Significance was assumed if the p value was < 0.05; *p<0.05.

The expression of C1 inhibitor (C1INH) in macrophages is upregulated by retinal pigment epithelial cells – implication in subretinal immune privilege in the aging eye

Chang Luo^{1,2,3}, Jiawu Zhao¹, Mei Chen¹, Heping Xu^{1,2,3}

¹Centre for Experimental Medicine, School of Medicine, Dentistry & Biomedical Science, Queen's University Belfast, Belfast, UK

²AIER Eye Institute, Changsha, China

³AIER School of Ophthalmology, Central South University, Changsha, China

Correspondence to: Heping Xu; email: heping.xu@qub.ac.uk

Keywords: macrophages, retinal pigment epithelial cells, complement, aging, subretinal immune privilege

Received: April 29, 2018 **Accepted:** June 7, 2018 **Published:** June 13, 2018

Copyright: Luo et al. This is an open-access article distributed under the terms of the Creative Commons Attribution License (CC BY 3.0), which permits unrestricted use, distribution, and reproduction in any medium, provided the original author and source are credited.

ABSTRACT

Age-related para-inflammation in the retina-choroidal interface is featured by low-levels of complement activation and subretinal macrophage accumulation. This study aimed to understand how complement expression in macrophages is regulated by retinal pigment epithelium (RPE). Bone marrow-derived macrophages (BMDMs) and RPE cells were cultured from 8-10 weeks old C57BL/6J mice. The BMDMs were co-cultured with normal RPE, or oxidized photoreceptor outer segment (oxPOS) or TNF- α pre-treated RPE, or apoptotic RPE, or RPE-choroid eyecups. Macrophages were then isolated and processed for real-time RT-PCR. The expression of complement inhibitor C1INH in BMDMs was significantly upregulated by RPE and RPE-choroid eyecups. The eyecups also upregulated CFH, CD59a, and Crry in BMDMs. oxPOS pre-treated RPE upregulated C1qb but down-regulated C3 expression in BMDMs. TNF- α pre-treated RPE enhanced C1INH and CFB expression. When BMDMs were treated with apoptotic RPE, the expression of C1qb, CFH, and CD59a was reduced, whereas the expression of C3, CFB and C1INH was increased. Our results suggest that RPE can modulate macrophages complement expression at the retina-choroidal interface even under aging or oxidative conditions. However, during inflammation, they may promote the alternative pathway of complement activation through down-regulating CFH and CD59a and upregulating CFB and C3.

INTRODUCTION

The neuronal retina is segregated from the systemic immune system by the blood retina barriers (BRB) and is considered as an immune privileged tissue. In addition to the physical barrier, the immune suppressive microenvironment of the eye is also critical for retinal immune privilege [1-3]. The immune privilege reduces the likelihood of intraocular inflammation, thus protects the neuroretina from inflammation-mediated damage. Despite the lack of systemic immune surveillance, the retina is well-protected by its own innate immune

defence system, including innate immune cells (e.g., microglia and perivascular macrophages) and the complement system [4]. The pathophysiology of retinal innate immune cells, particularly microglia has been well-studied and the subject has been reviewed extensively recently (see review article [5-7]). However, how the complement system protects the retina remains poorly defined.

The complement system constitutes over 30 proteins and protein fragments. Most of the complement proteins are known to be synthesized in the liver and released

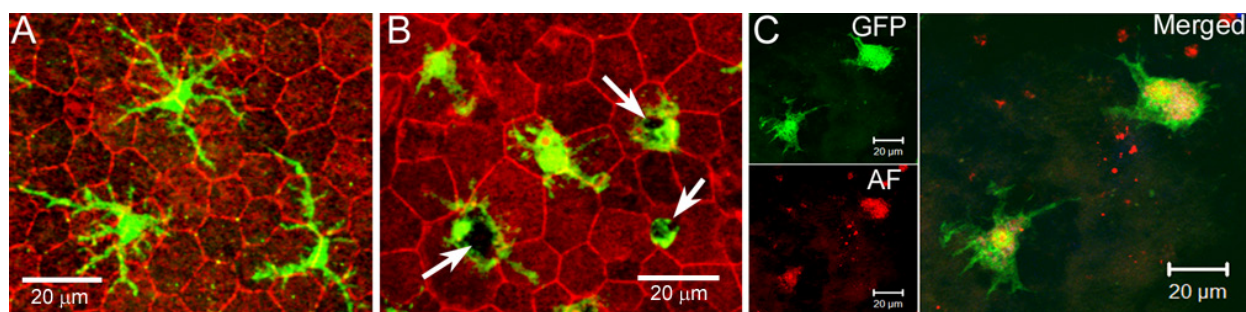


Figure 1. Subretinal macrophages in the aging eye. RPE/choroidal flatmount from 18 months (A) and 24 months (B) old CX3CR1^{GFp/+} mice were stained with phalloidin and imaged by confocal microscopy. Arrows - pigmented debris in subretinal macrophages. (C), RPE/choroidal flatmount from a 24 month old CX3CR1^{GFp/+} mouse was imaged by confocal microscopy. Green – GFP+ subretinal macrophages; Red – autofluorescence (AF).

into circulation as inactive precursors. Recent evidence suggests that complement components are also produced outside the liver by tissue cells [8]. Previous studies from our group and others have shown that the retina and retinal pigment epithelium (RPE)/choroidal tissue express a variety of complement components [9-11], and microglia and RPE are the major sources of local complement expression [9,12]. During aging, the expression of complement proteins or fragments is increased in the retina, particularly at the retina-choroid interface [4,11,13,14]. Together with a low level of microglial activation, the increased immune reactivity in the aging retina (also known as para-inflammation [14,15]) maintains retinal homeostasis and functionality [14].

The retina-choroid interface undergoes progressive changes during aging. For example, RPE cells increase in size and become multinucleate [16], phagocytes (microglia and macrophages) accumulate in the subretinal space (Figure 1) [17-19]. RPE cells and macrophages can both produce complement proteins [9,12], and they are the major sources of complement expression at the retina-choroid interface in the normal aging eye. How their complement expression is regulated during aging and at disease conditions is an important question. We have shown previously that complement expression in RPE cells is regulated by active macrophages [12]. We have also shown that complement expression in macrophages is regulated by cytokines presented at the microenvironment [20]. Macrophages are in close contact with RPE cells at the subretinal space in the aging eye (Figure 1). The aim of this study was, therefore, to investigate how complement expression in macrophages is regulated by RPE cells.

Under normal physiological conditions, RPE cells can suppress macrophage activation through pigment epithelial-derived factor (PEDF) [21-23] and α -

melanocyte stimulating hormone (α -MSH) [24]; whereas, under disease conditions, particularly when RPE cells undergo apoptotic death, the dead RPE cells can induce an angiogenic phenotype in macrophages [25]. Although substantial RPE death unlikely occurs in the normal aging eye, the cells are subjected to chronic oxidative stress and are constantly undergoing morphological remodeling [16]. The ability of RPE cells to modulate macrophage function in the subretinal space may depend on the condition of RPE cells. Indeed, subretinal macrophages in the healthy adult eyes (6 -12 months old) often have a small soma and long- fine-dendrites (Fig. 1A), whereas the cells in the aging eye (20 – 27 months) have a large cell body that often contains pigmented debris (Fig. 1B) [15], and they are autofluorescent (Fig. 1C) [17]. This suggests that they are active phagocytizing debris released by stressed RPE cells. In this study, we investigated the effect of different types of RPE cells in macrophage complement expression, including normal RPE cells, oxidized photoreceptor outer segments (oxPOS) pre-treated or TNF- α pre-treated RPE cells and apoptotic RPE cells.

RESULTS

The effects of normal RPE cells on BMDM complement gene expression

Previously we have shown that macrophages express a variety of complement components and regulatory genes [20]. In this study, we selectively investigated complement genes that were expressed at reasonable levels in macrophages in our previous study, including *c1qb* and *c1inh* of the classical pathway, *cfb* and *cfh* of the alternative pathway, and *c3* and *cd59a* of the terminal pathway. When BMDMs were co-cultured with normal RPE cells, the expression of C1qb and C3 mRNA was significantly reduced (Figure 2), whereas

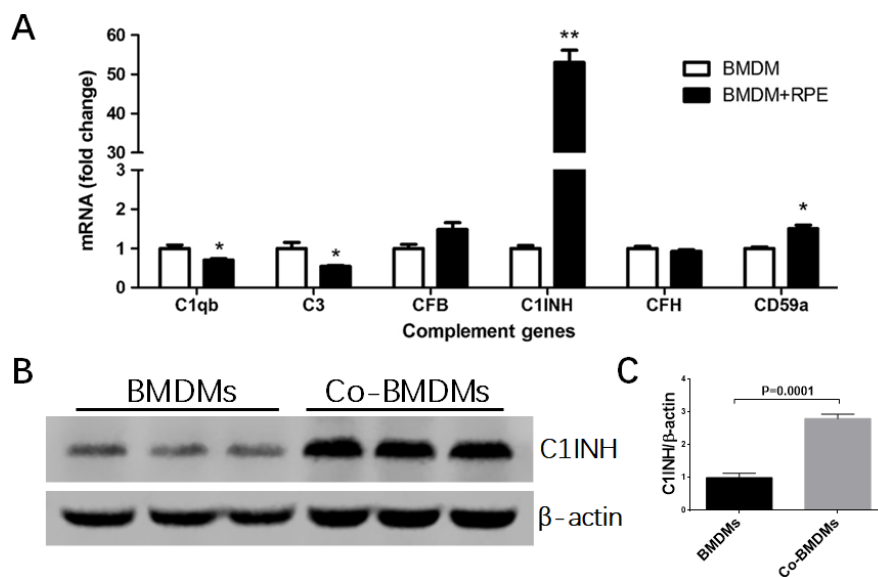


Figure 2. The effects of normal RPE cell on BMDM complement expression. BMDMs from C57BL/6J mice were co-cultured with primary mouse RPE cells for 7h (A) or 24h (B). Macrophages were then isolated by CD11b⁺ MACS kit and processed for real-time RT-PCR analysis of complement genes (A) and western blot analysis of C1INH protein expression (B). Fold change of C1INH protein expression by BMDMs after co-culture was analyzed by ImageJ (C). Mean ± SEM, n =3; *, P < 0.05; **, P < 0.01 compared to naïve BMDM alone. Unpaired Student t test.

the mRNA expression of CD59a, particularly C1INH was markedly increased (1.85-fold and 53.07-fold respectively) (Figure 2A). The upregulation of C1INH was further confirmed at protein level by Western Blot (Figure 2B, 2C). The expression of CFB and CFH was not affected. C1INH and CD59a negatively regulate complement activation. Our result suggests that under normal physiological conditions, RPE cells may suppress complement activation at the retina—choroid interface by modulating subretinal macrophage complement expression.

The effects of oxPOS pre-treated RPE cells on BMDM complement gene expression

Our recent work suggests that oxidized POS (oxPOS) suppresses RPE proliferation and induces multinucleation, a phenotype that is similar to RPE cells in the aging eye [16]. In this study, we further found that oxPOS treatment induced β-galactosidase expression in RPE cells (Figure 3A), an indicative of cell senescence. When BMDMs were co-cultured with oxPOS pre-treated RPE, the expression of C1qb

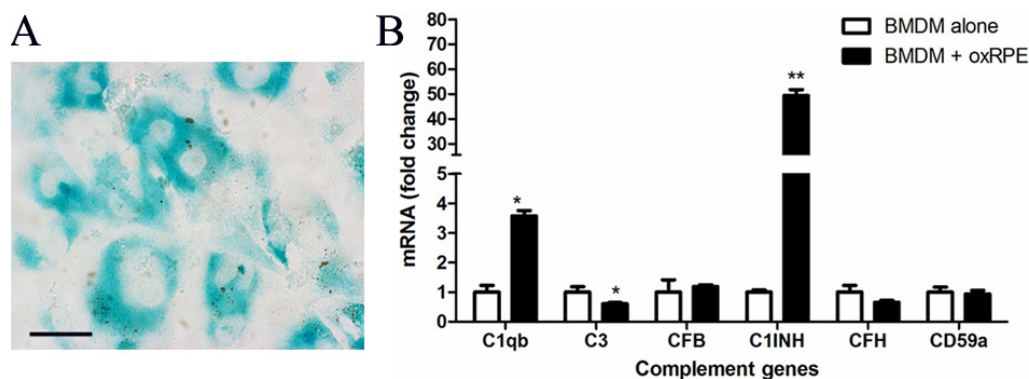


Figure 3. The effects of oxidized POS treated-RPE cell on BMDM complement gene expression. RPE cells were treated with oxidized photoreceptor outer segments (oxPOS) for 24h. oxPOS were then removed from the culture. (A) β-galactosidase expression in ox-POS-treated RPE cells. (B) The oxPOS pre-treated RPE cells were co-cultured with naïve BMDMs for 7h. Macrophages were isolated and processed for real-time RT-PCR analysis of complement genes. Mean ± SEM, n =3; *, P < 0.05; **, P < 0.01 compared to naïve BMDM alone, Unpaired Student t test.

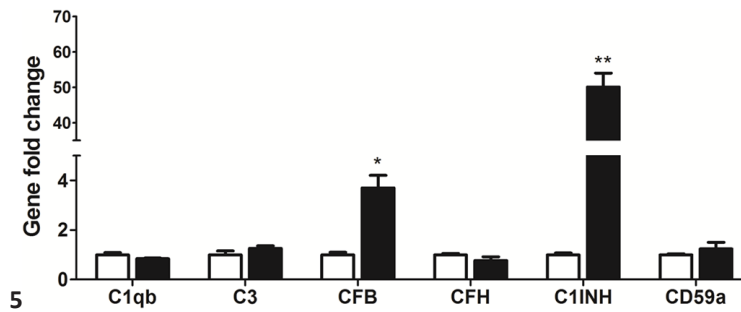


Figure 4. The effects of TNF- α treated-RPE cell on BMDM complement gene expression. RPE cells were treated with TNF- α for 16h. Naïve BMDMs were then co-cultured with TNF- α pre-treated RPE cells for 7h. Macrophages were isolated and processed for real-time RT-PCR analysis of complement genes. Mean \pm SEM, n =3; *, P < 0.05; **, P < 0.01 compared to naïve BMDM alone, Unpaired Student t test.

increased by more than 3-fold. The expression of C1INH remained at high levels (49.36-fold increment) compared with untreated BMDMs, whereas the expression of C3 was significantly decreased (Figure 3B). The expression of other genes, including CFB, CFH, and CD59a was not affected (Figure 3B). C1q is involved not only in the CP complement activation, but also in phagocytosis [26]. Our results suggest that, RPE cells in the aging eye may suppress complement activation through macrophage related C1INH and promote subretinal macrophage phagocytosis by enhancing C1q expression.

The effects of TNF- α pre-treated RPE cells on BMDM complement gene expression

TNF- α is one of the key inflammatory mediators in the inflamed eye e.g., uveoretinitis [27-29]. When BMDMs were co-cultured with TNF- α pre-treated RPE cells, the expression of CFB and C1INH was increased by 3.7-

fold and 50.1-fold respectively (Figure 4), whereas other complement component genes, including C1qb, C3, CFH and CD59a remained unchanged (Figure 4). The result suggests that under inflammatory conditions, RPE cells may convert macrophages into a phenotype that can promote complement activation through the alternative but not the classical or MBL pathway.

The effects of apoptotic RPE cells on BMDM complement gene expression

Apoptotic RPE cells were induced by exposing cells to 1mM H₂O₂ in serum-free DMEM overnight at 37°C [30]. Flow cytometry analysis confirmed that ~90% RPE cells were Annexin V⁺ or Annexin V⁺PI⁺ (Figure 5A). When BMDMs were incubated with apoptotic RPE cells, the expression of C3, CFB and C1INH was upregulated by 3.58-fold, 59.63-fold and 45.76-fold respectively, whereas the expression of C1q, CFH and CD59a was down-regulated to 0.20-fold, 0.03-fold and

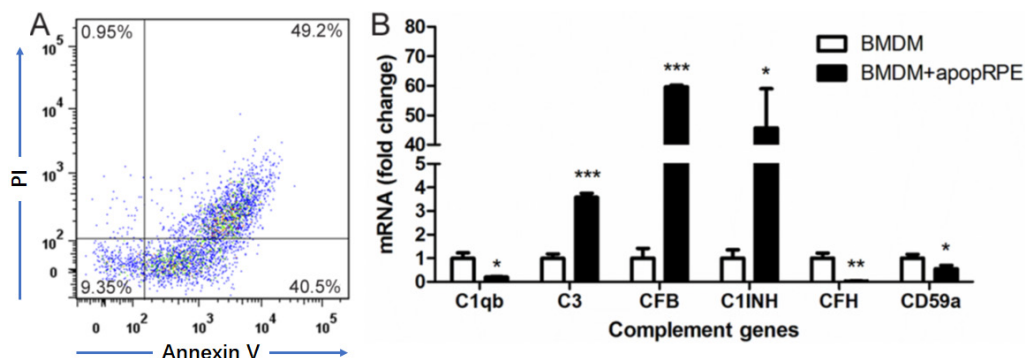


Figure 5. The effects of apoptotic RPE cell on BMDM complement gene expression. Primary mouse RPE cells were treated with H₂O₂ in serum-free DMEM overnight. Apoptotic RPE cells were confirmed by Propidium iodide (PI) and Annexin V staining (A). The apoptotic RPE cells were then incubated with naïve BMDMs for 7h. Macrophages were isolated and processed for real-time RT-PCR analysis of complement genes (B). Mean \pm SEM, n =3; *, P < 0.05; **, P < 0.01, ***, P < 0.001 compared to naïve BMDM alone, Unpaired Student t test.

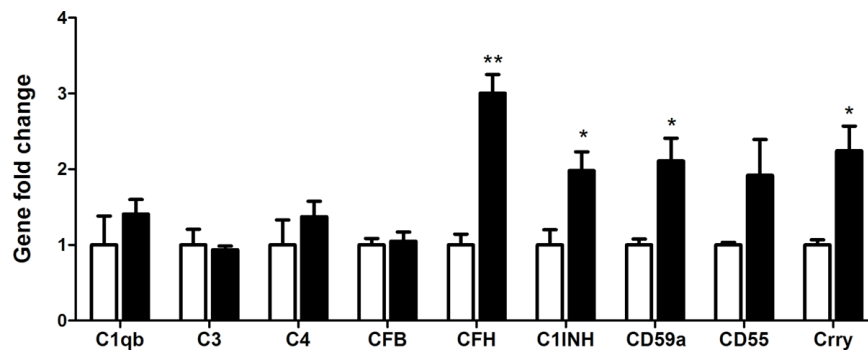


Figure 6. The effects of RPE/choroid eye-cup on BMDM complement gene expression. Naïve BMDMs were cultured in RPE/choroid eye cup from 18 months old mice for 7h. Macrophages were then isolated and processed for real-time RT-PCR analysis of complement genes. Mean \pm SEM, n=3; *, P<0.05; **, P<0.01 compared to naïve BMDM alone, Unpaired Student t test.

0.55-fold (compared to BMDM alone) respectively (Figure 5B). The result suggests that apoptotic RPE cells may promote AP complement activation in subretinal macrophages.

Changes in BMDM complement gene expression after culturing in RPE-choroid eyecup

To further understand how complement expression by subretinal macrophages is regulated by RPE cells in the aging eye, BMDMs were cultured in the eyecups of 18 months old mice. The cells were then removed from the eyecups and their complement gene expression was analyzed by real-time RT-PCR. Compared to naïve BMDMs, the eyecup treated macrophages expressed significantly higher levels of CFH, C1INH, CD59a and Crry (2~3-fold increment) (Figure 6). There was a trend of upregulation in CD55 mRNA in eyecup treated macrophages (Figure 6, P = 0.12 respectively). The expression of other complement genes, including C1qb, C3, C4 and CFB remained unchanged (Figure 6). CFH and C1INH are secretory types of complement inhibitors, whereas CD59a, Crry and CD55 are membrane-type inhibitors. Our results suggest that subretinal macrophages are likely to suppress complement activation at the retina-choroid interface in the normal aging eye.

DISCUSSION

RPE cells are known to critically control the immune suppressive microenvironment of the subretinal space through multiple mechanisms, including inducing the death of infiltrating immune cells (through the Fas Ligand and Tumor Necrosis Factor-related apoptosis-inducing ligand (TRAIL) [31-33]), releasing of immune suppressive mediators (e.g. TGF- β , retinoic acid, thrombospondin-1, CTLA4 and CLTA2) [34-37]). In this study, we show that RPE cells can modulate

macrophage towards an anti-complement activation phenotype although inflammatory or apoptotic RPE cells may promote the alternative pathway of complement activation by inducing relevant complement expression in macrophages. The immune modulatory role of RPE cells on macrophage complement expression may be an additional mechanism to maintain retinal homeostasis particularly in the aging eye where macrophages accumulate in the subretinal space.

Previously we have reported a low-level of complement activation (e.g., increased CFB and C3/C3b expression) at the retina-choroid interface in the aging eye [11,14]. We believe that this low-level of complement activation is beneficial and important to maintain retinal homeostasis [14]. Uncontrolled complement activation is believed to be involved in the pathogenesis of AMD [4,10,38-40]. How complement activation at the immune privileged site of subretinal space (i.e., retina-choroid interface) is regulated and why the activation becomes detrimental in AMD is not known. Previous studies have observed higher plasma levels of C3a, C4a and C5a in AMD patients compared to age-matched controls [39-41]. However, a recent study by Schick et al did not find significant difference in the plasma levels of C3a, Ba, sC5b-9, CFH, CFI between AMD patients and age-matched controls, but the aqueous levels of C3a and Ba were significantly higher in AMD patients [42], suggesting that uncontrolled local but not systemic complement activation may play an important role in AMD pathogenesis.

RPE and subretinal macrophages are the only two types of cells in the retina-choroid interface in the aging eye, and they may critically control local complement activation. Previously, we have shown that RPE cells express high levels of complement regulators (e.g., C4BP, MASP1, CFH, C1INH, DAF, Crry and CD59a),

but relative low levels of complement components (e.g., C2, C4, CFB and C5) [9,12]. This complement expression profile fits the immune suppressive nature of RPE cells and may contribute to the immune privilege of the subretinal space. Macrophages, on the other hand, express high levels of C1q under normal culture conditions [20]. C1q not only can initiate the classical pathway of complement activation, but also is critically involved in the phagocytosis of antibody-opsonized or FcR coated particles [26]. In this study, we show that normal RPE cultures are able to down-regulate the expression of C1qb and C3 and upregulate the expression of C1INH and CD59a in macrophages. The upregulation of complement regulators (CFH, CD59a, Crry, C1INH and CD55) was more prominent when macrophages were cultured in the RPE-choroid eye cups (Figure 6). Our results suggest that RPE cells may convert subretinal macrophages into a phenotype that can suppress complement activation. This “anti-complement activation” function of RPE may be a novel mechanism contributing to the immune suppressive microenvironment of the subretinal space.

The ability of RPE cells to regulate macrophage complement expression appears to rely on the physiological condition of the cells. After pre-treatment with oxPOS which induced RPE cells senescence, RPE cells further increased the expression of C1q and C1INH in macrophages (Figure 3). This phenotype allows macrophages to maintain complement suppressive property, but the phagocytosis function may be improved (as a result of increased C1q expression). oxPOS pre-treated RPE cells mimic the RPE cells in the aging eye [16], which may release debris into the subretinal space. This macrophage phenotype ensures effective clearance of the debris from the subretinal space to maintain homeostasis. Indeed, many subretinal macrophages in the aging eye contain pigmented inclusions (Figure 1B, 1C) [16].

Under disease conditions whereby RPE cells are subjected to inflammatory insult (e.g. TNF- α) or even undergo cell death, they may lose the immune suppressive property, instead become proinflammatory. TNF- α pre-treated RPE cells upregulated CFB and C1INH expression (Figure 4) in BMDMs, suggesting that they may suppress CP but promote AP complement activation. This macrophage phenotype was further enhanced by apoptotic RPE cells, evidenced by reduced expression of CP component (C1q) and AP inhibitor (CFH) and increased expression of CP inhibitor (C1INH) and AP components (CFB, C3) (Figure 5). This result suggests that under disease conditions, damaged or dead RPE cells may convert subretinal macrophages into a phenotype that can promote the AP complement activation at the retina-choroid interface.

This concept is supported by our previous observation that retinal complement activation in autoimmune uveoretinitis is mediated predominately by the AP [15].

In summary, we show that RPE cells can modulate macrophage complement expression. Under normal aging conditions, RPE cells may convert macrophages into a phenotype that can suppress complement activation with enhanced phagocytosis. This immune regulatory function of RPE cells on macrophages may be lost under inflammatory conditions. Instead, inflammatory or apoptotic RPE cells promote macrophages to produce complement components necessary for the AP activation. RPE cells together with subretinal macrophages critically control complement activation at the retina-choroid interface in the ageing eye.

MATERIALS AND METHODS

Preparation of photoreceptor outer segments

Photoreceptor outer segments (POS) were isolated from bovine eyes using the sucrose gradient density centrifugation as previous described [43]. Oxidized POS (ox-POS) was generated by exposing POS to 302 nm ultraviolet light for 18 hours [43], and lipid oxidation was confirmed using thiobarbituric acid reactive substance assay (TBARS) kit (OXI-TEK TBARS Assay kit, Alexis; Axxora Ltd, Nottingham, UK). The levels of TBARS were confirmed to be 60 - 92 nmol/10⁸ POS in oxPOS and 5 ~ 11 nmol/10⁸ POS in non-oxidized POS.

RPE cell culture

Primary mouse RPE cells were isolated and cultured from 3-month old wild type C56BL/6J mice as described previously [9,11]. Briefly, after removing the anterior segment of the eye, the vitreous and retina were peeled off from the eye cups. The RPE/choroid/sclera eye cups were incubated with 0.5% (w/v) trypsin-EDTA (ICN Flow, Irvin, UK) at 37°C for 30 min. RPE cells were harvested by gentle aspiration and the single-cell suspension was collected and seeded into culture plates with Dulbecco's Modified Eagle Medium (DMEM), supplemented with 10% Fetal Calf Serum (FCS) and 100 mg/ml primocin. Cells were subcultured when they reached confluence. RPE phenotype was confirmed by their cytokeratin 19 expression. Cells of passage 3-5 were used for experiments.

To induce apoptosis in RPE cells, the cell cultures were treated with 1mM H₂O₂ in serum-free DMEM for overnight at 37°C [30]. Cells were detached by washing with ice-cold PBS and processed for Annexin

V/Propidium Iodide (PI) staining according to manufacturer's instructions (Life Technologies, UK), and examined by FACS Canto II (BD Biosciences, Oxford, UK).

To generate oxRPE cells or TNF- α pre-treated RPE cells, RPE cells were incubated with 1×10^6 /ml ox-POS [43] or TNF- α (20 ng/ml) [11] for 24 h. Un-ingested POS or excessive TNF- α were then removed from the culture by thorough washes with warm PBS. RPE cells with different treatments were stained for β -Galactosidase using the Senescence β -Galactosidase Staining Kit (Sigma-Aldrich) as per manufacturer's instructions.

Culture of bone marrow-derived macrophages (BMDMs)

BMDMs were cultured using the protocol originally described by Weischenfeldt and Porse [44] with slight modification [20]. Briefly, tibias and femurs were collected from 8 to 12-week old wild-type C57BL/6J mice. Bone marrow was flushed with DMEM (Gibco BRL, Paisley, UK). Red Blood Cells (RBCs) were lysed by RBC Lysis Buffer (0.75% NH₄Cl, 0.02% Tris-HCl, pH 7.2). Cells were then washed and cultured in DMEM supplemented with 15% FCS and 15% L929 (a murine fibroblast cell line that secretes M-CSF) conditioned medium containing 100 mg/ml primocin (Invivogen, San Diego, California, USA) in 75 cm² Culture Flasks, and incubated at 37°C in 5% CO₂ incubator. After 6 days, cells were collected for further experiments. Flow cytometry confirmed that >92% of the cells were F4/80⁺CD11b⁺.

BMDM-RPE co-culture

1.5×10^6 BMDMs were seeded into T25 flask RPE cultures (5×10^5 of normal RPE, or ox-RPE or TNF- α -RPE or apoptotic RPE cells) and co-cultured for 7h or 24h. Cells were then detached in ice-cold PBS with 2mM EDTA and passed through 70 μ m cell strainer. BMDMs were isolated with the CD11b⁺ MACS kit (Miltenyi Biotec, UK). The phenotype of the BMDMs was confirmed to be 95-98% CD11b⁺F4/80⁺ by flow cytometry (FACS Canto, BD Biosciences, UK). The cells were processed further for downstream experiments.

Macrophage culture in the eye-cup

Eyes from 18 months old C57BL/6J mice were sterilized with 75% ethanol and dissected under microscope. The anterior segment of the eye, the lens and retinal tissue were removed. The eyecups

containing RPE, choroid and sclera were used for further studies.

1×10^4 BMDMs were added into the eyecup and cultured at 37 °C in 5% CO₂ incubator for 7h. BMDMs on eyecup were harvested by gently shaking the eyecup in a tube with culture medium. 90-95% of cells were F4/80⁺ by flow cytometry. The cells were collected and processed for real-time RT-PCR.

RNA isolation and reverse transcription

Total RNA was extracted from cultured BMDMs using the RNeasy mini kit (Qiagen Ltd., West Sussex, UK) according to the manufacturer's instructions. The quantity and quality of the RNA were determined using the NanoDrop ND-1000 spectrophotometer (NanoDrop Technologies, Wilmington, DE). First-strand cDNA synthesis was performed by a reaction of 1 μ g of total RNA with a random primer, using the SuperScriptTM II Reverse Transcriptase kit (Invitrogen, Paisley, UK).

Real-time Polymerase Chain Reaction (Real-time RT-PCR)

Real-time RT-PCR was performed in a total of 12 μ l mixture solution in 384-well plates using the LightCycler 480 system (Roche Applied Science, Mannheim, Germany). Each 12 μ l of reaction mixture contains 6 ml of LightCycler 480 SYBR Green Master (Roche Diagnostics GmbH, Mannheim, Germany), 0.5 mM primers and diluted cDNA. Real-time RT-PCR quantifications were run in triplicate for each sample and the average determined. PCR products were quantified by the LightCycler 480 software. Melting curve and gel electrophoretic analyses were used to determine amplification homogeneity and data quality. Expression levels were normalized to β -actin. The primer sequences have been described previously [12,20].

Western blot

BMDMs were lysed in RIPA buffer with protease inhibitors (Sigma Aldrich, USA). The total protein concentration was measured using a BCA kit (Solarbio, China). Ten micrograms of total protein were applied to 10% SDS-PAGE and blotted to an Immobilon-FL polyvinylidene difluoride membrane (Millipore, China). After blocking with 5% fat-free milk, the membrane was incubated with primary antibodies for C1INH (Abcam, UK) and β -actin (Arigo Biolaboratories, China) at 4 °C overnight, followed by incubation with secondary antibodies respectively at room temperature for 1-2 h. Quantitative imaging was performed using Odyssey infrared imaging system (Li-COR

Biotechnology, USA). Protein bands were quantified using ImageJ software.

Data analysis

All data were expressed of Mean \pm Standard error of mean (SEM). The difference in complement gene expression levels between normal un-treated BMDMs and different types of RPE treated BMDMs were compared using the unpaired Student t test with $P < 0.05$ considered to be statistically significant. All experiments were repeated at least twice.

CONFLICTS OF INTEREST

All authors disclose no commercial interests in any subjects presented in this paper.

FUNDING

The study was funded by Fight for Sight, UK (1361/1362; 5057/58), National Natural Science Foundation of China (81700827), Natural Science Foundation of Hunan Province, China (2018JJ3002), and AIER Eye Hospital Group Research Fund (AFM1713D3). The funders had no role in study design, data collection and analysis, decision to publish, or preparation of the manuscript.

REFERENCES

1. Forrester JV, Xu H. Good news-bad news: the Yin and Yang of immune privilege in the eye. *Front Immunol*. 2012; 3:338. <https://doi.org/10.3389/fimmu.2012.00338>
2. Forrester JV, Xu H, Lambe T, Cornall R. Immune privilege or privileged immunity? *Mucosal Immunol*. 2008; 1:372–81. <https://doi.org/10.1038/mi.2008.27>
3. Streilein JW. Immunoregulatory mechanisms of the eye. *Prog Retin Eye Res*. 1999; 18:357–70. [https://doi.org/10.1016/S1350-9462\(98\)00022-6](https://doi.org/10.1016/S1350-9462(98)00022-6)
4. Xu H, Chen M. Targeting the complement system for the management of retinal inflammatory and degenerative diseases. *Eur J Pharmacol*. 2016; 787:94–104. <https://doi.org/10.1016/j.ejphar.2016.03.001>
5. Forrester JV, Xu H, Kuffová L, Dick AD, McMenamin PG. Dendritic cell physiology and function in the eye. *Immunol Rev*. 2010; 234:282–304. <https://doi.org/10.1111/j.0105-2896.2009.00873.x>
6. Li L, Eter N, Heiduschka P. The microglia in healthy and diseased retina. *Exp Eye Res*. 2015; 136:116–30. <https://doi.org/10.1016/j.exer.2015.04.020>
7. Karlstetter M, Scholz R, Rutar M, Wong WT, Provis JM, Langmann T. Retinal microglia: just bystander or target for therapy? *Prog Retin Eye Res*. 2015; 45:30–57. <https://doi.org/10.1016/j.preteyeres.2014.11.004>
8. Marsh JE, Zhou W, Sacks SH. Local tissue complement synthesis--fine tuning a blunt instrument. *Arch Immunol Ther Exp (Warsz)*. 2001 (Suppl 1); 49:S41–46.
9. Luo C, Chen M, Xu H. Complement gene expression and regulation in mouse retina and retinal pigment epithelium/choroid. *Mol Vis*. 2011; 17:1588–97.
10. Anderson DH, Radeke MJ, Gallo NB, Chapin EA, Johnson PT, Curletti CR, Hancox LS, Hu J, Ebright JN, Malek G, Hauser MA, Rickman CB, Bok D, et al. The pivotal role of the complement system in aging and age-related macular degeneration: hypothesis revisited. *Prog Retin Eye Res*. 2010; 29:95–112. <https://doi.org/10.1016/j.preteyeres.2009.11.003>
11. Chen M, Muckersie E, Robertson M, Forrester JV, Xu H. Up-regulation of complement factor B in retinal pigment epithelial cells is accompanied by complement activation in the aged retina. *Exp Eye Res*. 2008; 87:543–50. <https://doi.org/10.1016/j.exer.2008.09.005>
12. Luo C, Zhao J, Madden A, Chen M, Xu H. Complement expression in retinal pigment epithelial cells is modulated by activated macrophages. *Exp Eye Res*. 2013; 112:93–101. <https://doi.org/10.1016/j.exer.2013.04.016>
13. Chen M, Muckersie E, Forrester JV, Xu H. Immune activation in retinal aging: a gene expression study. *Invest Ophthalmol Vis Sci*. 2010; 51:5888–96. <https://doi.org/10.1167/iovs.09-5103>
14. Xu H, Chen M, Forrester JV. Para-inflammation in the aging retina. *Prog Retin Eye Res*. 2009; 28:348–68. <https://doi.org/10.1016/j.preteyeres.2009.06.001>
15. Chen M, Xu H. Parainflammation, chronic inflammation, and age-related macular degeneration. *J Leukoc Biol*. 2015; 98:713–25. <https://doi.org/10.1189/jlb.3RI0615-239R>
16. Chen M, Rajapakse D, Fraczek M, Luo C, Forrester JV, Xu H. Retinal pigment epithelial cell multinucleation in the aging eye - a mechanism to repair damage and maintain homeostasis. *Aging Cell*. 2016; 15:436–45. <https://doi.org/10.1111/acer.12447>
17. Xu H, Chen M, Manivannan A, Lois N, Forrester JV. Age-dependent accumulation of lipofuscin in perivascular and subretinal microglia in experimental

- mice. *Aging Cell*. 2008; 7:58–68.
<https://doi.org/10.1111/j.1474-9726.2007.00351.x>
18. Combadière C, Feumi C, Raoul W, Keller N, Rodéro M, Pézard A, Lavalette S, Houssier M, Jonet L, Picard E, Debré P, Sirinyan M, Deterre P, et al. CX3CR1-dependent subretinal microglia cell accumulation is associated with cardinal features of age-related macular degeneration. *J Clin Invest*. 2007; 117:2920–28. <https://doi.org/10.1172/JCI31692>
 19. Chinnery HR, McLenachan S, Humphries T, Kezic JM, Chen X, Ruitenberg MJ, McMenamin PG. Accumulation of murine subretinal macrophages: effects of age, pigmentation and CX3CR1. *Neurobiol Aging*. 2012; 33:1769–76.
<https://doi.org/10.1016/j.neurobiolaging.2011.03.010>
 20. Luo C, Chen M, Madden A, Xu H. Expression of complement components and regulators by different subtypes of bone marrow-derived macrophages. *Inflammation*. 2012; 35:1448–61.
<https://doi.org/10.1007/s10753-012-9458-1>
 21. Zamiri P, Masli S, Streilein JW, Taylor AW. Pigment epithelial growth factor suppresses inflammation by modulating macrophage activation. *Invest Ophthalmol Vis Sci*. 2006; 47:3912–18.
<https://doi.org/10.1167/iovs.05-1267>
 22. Zamiri P, Masli S, Kitaichi N, Taylor AW, Streilein JW. Thrombospondin plays a vital role in the immune privilege of the eye. *Invest Ophthalmol Vis Sci*. 2005; 46:908–19. <https://doi.org/10.1167/iovs.04-0362>
 23. Zamiri P, Sugita S, Streilein JW. Immunosuppressive properties of the pigmented epithelial cells and the subretinal space. *Chem Immunol Allergy*. 2007; 92:86–93. <https://doi.org/10.1159/000099259>
 24. Taylor AW, Lee D. Applications of the role of α -MSH in ocular immune privilege. *Adv Exp Med Biol*. 2010; 681:143–49. https://doi.org/10.1007/978-1-4419-6354-3_12
 25. Liu J, Copland DA, Horie S, Wu WK, Chen M, Xu Y, Paul Morgan B, Mack M, Xu H, Nicholson LB, Dick AD. Myeloid cells expressing VEGF and arginase-1 following uptake of damaged retinal pigment epithelium suggests potential mechanism that drives the onset of choroidal angiogenesis in mice. *PLoS One*. 2013; 8:e72935.
<https://doi.org/10.1371/journal.pone.0072935>
 26. Galvan MD, Greenlee-Wacker MC, Bohlson SS. C1q and phagocytosis: the perfect complement to a good meal. *J Leukoc Biol*. 2012; 92:489–97.
<https://doi.org/10.1189/jlb.0212099>
 27. Calder CJ, Nicholson LB, Dick AD. A selective role for the TNF p55 receptor in autocrine signaling following IFN-gamma stimulation in experimental autoimmune uveoretinitis. *J Immunol*. 2005; 175:6286–93.
<https://doi.org/10.4049/jimmunol.175.10.6286>
 28. Dick AD, Forrester JV, Liversidge J, Cope AP. The role of tumour necrosis factor (TNF-alpha) in experimental autoimmune uveoretinitis (EAU). *Prog Retin Eye Res*. 2004; 23:617–37.
<https://doi.org/10.1016/j.preteyeres.2004.06.005>
 29. Sartani G, Silver PB, Rizzo LV, Chan CC, Wiggert B, Mastorakos G, Caspi RR. Anti-tumor necrosis factor alpha therapy suppresses the induction of experimental autoimmune uveoretinitis in mice by inhibiting antigen priming. *Invest Ophthalmol Vis Sci*. 1996; 37:2211–18.
 30. Liang FQ, Godley BF. Oxidative stress-induced mitochondrial DNA damage in human retinal pigment epithelial cells: a possible mechanism for RPE aging and age-related macular degeneration. *Exp Eye Res*. 2003; 76:397–403.
[https://doi.org/10.1016/S0014-4835\(03\)00023-X](https://doi.org/10.1016/S0014-4835(03)00023-X)
 31. Ferguson TA, Griffith TS. A vision of cell death: insights into immune privilege. *Immunol Rev*. 1997; 156:167–84.
<https://doi.org/10.1111/j.1600-065X.1997.tb00967.x>
 32. Kazama H, Ricci JE, Herndon JM, Hoppe G, Green DR, Ferguson TA. Induction of immunological tolerance by apoptotic cells requires caspase-dependent oxidation of high-mobility group box-1 protein. *Immunity*. 2008; 29:21–32.
<https://doi.org/10.1016/j.immuni.2008.05.013>
 33. Ferguson TA, Griffith TS. The role of Fas ligand and TNF-related apoptosis-inducing ligand (TRAIL) in the ocular immune response. *Chem Immunol Allergy*. 2007; 92:140–54.
<https://doi.org/10.1159/000099265>
 34. Mochizuki M, Sugita S, Kamoi K. Immunological homeostasis of the eye. *Prog Retin Eye Res*. 2013; 33:10–27.
<https://doi.org/10.1016/j.preteyeres.2012.10.002>
 35. Kawazoe Y, Sugita S, Keino H, Yamada Y, Imai A, Horie S, Mochizuki M. Retinoic acid from retinal pigment epithelium induces T regulatory cells. *Exp Eye Res*. 2012; 94:32–40.
<https://doi.org/10.1016/j.exer.2011.11.002>
 36. Horie S, Sugita S, Futagami Y, Yamada Y, Mochizuki M. Human retinal pigment epithelium-induced CD4+CD25+ regulatory T cells suppress activation of

- intraocular effector T cells. *Clin Immunol.* 2010; 136:83–95.
<https://doi.org/10.1016/j.clim.2010.03.001>
37. Sugita S, Horie S, Nakamura O, Futagami Y, Takase H, Keino H, Aburatani H, Katunuma N, Ishidoh K, Yamamoto Y, Mochizuki M. Retinal pigment epithelium-derived CTLA-2alpha induces TGFbeta-producing T regulatory cells. *J Immunol.* 2008; 181:7525–36.
<https://doi.org/10.4049/jimmunol.181.11.7525>
38. Whitmore SS, Sohn EH, Chirco KR, Drack AV, Stone EM, Tucker BA, Mullins RF. Complement activation and choriocapillaris loss in early AMD: implications for pathophysiology and therapy. *Prog Retin Eye Res.* 2015; 45:1–29.
<https://doi.org/10.1016/j.preteyeres.2014.11.005>
39. Bora NS, Matta B, Lyzogubov VV, Bora PS. Relationship between the complement system, risk factors and prediction models in age-related macular degeneration. *Mol Immunol.* 2015; 63:176–83.
<https://doi.org/10.1016/j.molimm.2014.07.012>
40. Warwick A, Khandhadia S, Ennis S, Lotery A. Age-related macular degeneration: a disease of systemic or local complement dysregulation? *J Clin Med.* 2014; 3:1234–57.
<https://doi.org/10.3390/jcm3041234>
41. Lechner J, Chen M, Hogg RE, Toth L, Silvestri G, Chakravarthy U, Xu H. Higher plasma levels of complement C3a, C4a and C5a increase the risk of subretinal fibrosis in neovascular age-related macular degeneration: complement activation in AMD. *Immun Ageing.* 2016; 13:4.
<https://doi.org/10.1186/s12979-016-0060-5>
42. Schick T, Steinhauer M, Aslanidis A, Altay L, Karlstetter M, Langmann T, Kirschfink M, Fauser S. Local complement activation in aqueous humor in patients with age-related macular degeneration. *Eye (Lond).* 2017; 31:810–13.
<https://doi.org/10.1038/eye.2016.328>
43. Chen M, Forrester JV, Xu H. Synthesis of complement factor H by retinal pigment epithelial cells is down-regulated by oxidized photoreceptor outer segments. *Exp Eye Res.* 2007; 84:635–45.
<https://doi.org/10.1016/j.exer.2006.11.015>
44. Weischenfeldt J, Porse B. Bone marrow-derived macrophages (BMM): isolation and applications. *CSH Protoc.* 2008; 2008: pdb.prot5080.
<https://doi.org/10.1101/pdb.prot5080>

Age-related changes in eye lens biomechanics, morphology, refractive index and transparency

Catherine Cheng^{1,2}, Justin Parreno^{2,3}, Roberta B. Nowak², Sondip K. Biswas⁴, Kehao Wang⁵, Masato Hoshino⁶, Kentaro Uesugi⁶, Naoto Yagi⁶, Juliet A. Moncaster⁷, Woo-Kuen Lo⁴, Barbara Pierscionek⁵, Velia M. Fowler^{2,3}

¹School of Optometry, Indiana University, Bloomington, IN 47405, USA

²Department of Molecular Medicine, The Scripps Research Institute, La Jolla, CA 92037, USA

³Department of Biological Sciences, University of Delaware, Newark, DE 19716, USA

⁴Department of Neurobiology, Morehouse School of Medicine, Atlanta, GA 30303, USA

⁵School of Science and Technology, Nottingham Trent University, Nottingham, United Kingdom

⁶Japan Synchrotron Radiation Research Institute (Spring-8), Sayo-cho, Sayo-gun, Hyogo, Japan

⁷Department of Radiology, Boston University School of Medicine, Boston, MA 02118, USA

Correspondence to: Velia M. Fowler, Catherine Cheng; **email:** vfowler@udel.edu, ckcheng@iu.edu

Keywords: fiber cell, strain, epithelial cell, cataract, stiffness

Received: August 30, 2019

Accepted: November 26, 2019

Published: December 16, 2019

Copyright: Cheng et al. This is an open-access article distributed under the terms of the Creative Commons Attribution License (CC BY 3.0), which permits unrestricted use, distribution, and reproduction in any medium, provided the original author and source are credited.

ABSTRACT

Life-long eye lens function requires an appropriate gradient refractive index, biomechanical integrity and transparency. We conducted an extensive study of wild-type mouse lenses 1-30 months of age to define common age-related changes. Biomechanical testing and morphometrics revealed an increase in lens volume and stiffness with age. Lens capsule thickness and peripheral fiber cell widths increased between 2 to 4 months of age but not further, and thus, cannot account for significant age-dependent increases in lens stiffness after 4 months. In lenses from mice older than 12 months, we routinely observed cataracts due to changes in cell structure, with anterior cataracts due to incomplete suture closure and a cortical ring cataract corresponding to a zone of compaction in cortical lens fiber cells. Refractive index measurements showed a rapid growth in peak refractive index between 1 to 6 months of age, and the area of highest refractive index is correlated with increases in lens nucleus size with age. These data provide a comprehensive overview of age-related changes in murine lenses, including lens size, stiffness, nuclear fraction, refractive index, transparency, capsule thickness and cell structure. Our results suggest similarities between murine and primate lenses and provide a baseline for future lens aging studies.

INTRODUCTION

The eye lens is required for fine focusing of light onto the retina to form a clear image, and the function of the lens is intimately tied to its shape, biomechanical properties, transparency and refractive index. It has long been known that age-related changes in these lens properties lead to two major lens pathologies, cataracts and presbyopia [1]. Cataracts, defined as any lens

opacity, are the leading cause of blindness in the world [2], and almost all mammalian and avian species develop age-related cataracts [3–15]. Changes in lens transparency occur in several locations, cortical, sub-capsular and nuclear, and there are many hypothesized causes for opacities, including UV light exposure, reactive oxygen species, nutrition and genetic variations [16–18]. Though previous studies have demonstrated that wild-type mouse lenses develop age-related

cataracts [10, 12–15, 19, 20], the age at which defects appear and the mechanisms for opacities in different locations in lenses from aged mice has not been thoroughly studied. Presbyopia is caused by a reduction in the lens' ability to change shape during focusing (accommodation), and, by extension, the need for reading glasses [21–23]. Studies have linked age-related increases in lens stiffness to presbyopia [21–26], and increased lens stiffness with age has been reported in humans [21, 26–34] and animal models [34–36], including mice [37–41].

The lens is composed of two cell types, a monolayer of epithelial cells covering the anterior hemisphere and a bulk mass of differentiated lens fiber cells (Supplementary Figure 1). A basement membrane, called the capsule, encapsulates the lens [42]. Life-long lens growth occurs through the proliferation, elongation and differentiation of equatorial epithelial cells into new fiber cells that are added in concentric layers surrounding previous generations of fibers [43–45]. Hexagonal packing of lens fibers is established by cell reorganization and shape changes in equatorial epithelial cells [46, 47]. High refractive index in the lens is established by the high concentration and short range order of crystallin proteins [48, 49]. Previous studies, including our work, suggest that cytoskeletal structures are important to maintain lens mechanical integrity [38, 40, 50, 51]. The lens is a unique organ where all the cells are retained since the formation of the tissue during embryonic development, and there is little or no protein turnover in cells at the center of the lens [42]. This presents a rare opportunity to study cellular aging by allowing comparison of cells made in the embryo vs. cells added during in adulthood vs. cells formed in old age.

Little is known about the morphological, mechanical, refractive and cellular changes that occur with advanced age in the lens. Mice offer an opportunity to investigate changes in lens morphometrics, stiffness, transparency and refractive properties with age in a relatively shortened period of time. We carried out a comprehensive study of the properties of mouse lenses from young adult mice (1–2 months old) to very old mice (24–30 months old), measuring size, Gradient Refractive Index (GRIN) and stiffness. We also determined that anterior subcapsular and cortical ring cataracts appear in wild-type mouse lenses around 12 months of age. Confocal and electron microscopy revealed morphological changes in lens fiber cells that are correlated with these changes in lens transparency, suggesting a cellular basis for these age-related cataracts. In all, we demonstrate that age-related changes in mouse lenses mimic some aspects of aging in human lenses.

RESULTS

Mouse lenses have increased size, nuclear fraction, stiffness and resilience with age

We first examined the morphometrics of mouse lenses between 2–30 months of age (Figure 1). We measured the axial (Figure 1, red double-headed arrows) and equatorial diameters (Figure 2, green double-headed arrows) for each lens to calculate lens volume, lens aspect ratio, nuclear volume and biomechanical properties. We observed that lenses from very old mice (24–30 months) have an optical discontinuity in the lens cortex (Figure 1, yellow arrowheads). For morphometric measurements, we used dot plots with lines to show the average and standard deviation, and also included a graph for each parameter of the Tukey 95% confidence interval from the statistical analysis, to assess the significance of the multiple comparisons between the age groups. The horizontal lines representing each comparison are statistically significant if they do not cross the vertical dotted line (95% confidence), which is similar in concept to a p -value less than 0.05. We found that lenses steadily increased in volume between 2 to 8 months of age, with growth slowing down between 8 to 18 months of age (Figures 1 and 2A). Mouse lenses do not increase significantly in volume after 18 months of age. The equatorial diameter of lenses does not increase significantly after 8 months of age while axial diameter increases slightly until 18 months of age (data not shown). Mouse lenses are nearly spherical in shape, becoming slightly more spherical between 2 and 4 months of age (Figure 2B). After 4 months, the lens aspect ratio does not change significantly with age. Lens fiber cells at the center, or nucleus, of the lens become compacted [21, 52], and in mouse lenses, the nucleus is a hard and spherical structure that can be isolated by removing the softer cells of the lens cortex [38, 41]. In contrast to the constant lens volume after 18 months of age, the size of the nucleus continues to increase with age up to 30 months of age (Figures 1 and 3). While the rate of increase is slow (no change from 8 to 12 months, or from 18 to 24 months), the size of the nucleus increases significantly between 24 to 30 months of age. These data suggest that while overall lens growth slows down, the remodelling and compaction of the nucleus continues in the mouse lens with age.

Next, we examined the biomechanical properties of lenses between 2–30 months of age. We utilized the application of sequential coverslips to compress the lens and then measured axial compressive strain (negative) and equatorial expansion strain (positive). Strain is a dimensionless measurement of percent change, allowing direct comparison between age groups regardless of changes in lens volume. Similar to previous reports

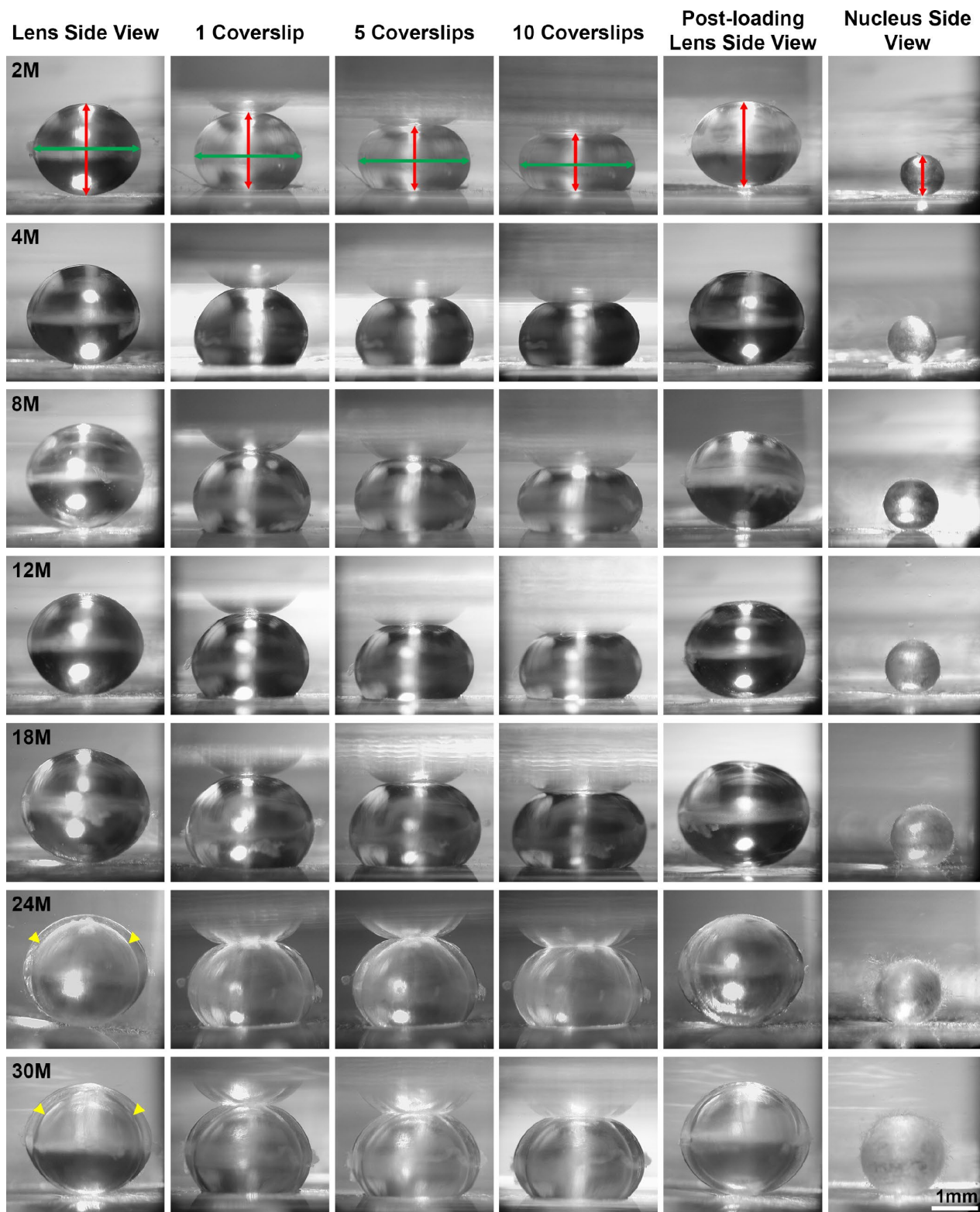


Figure 1. Side view pictures of mouse lenses between 2-30 months of age pre-compression, during coverslip compression (1, 5 and 10 coverslips) and post-compression, and the isolated lens nucleus. With age, the application of the same load compressed the older lenses less than young lenses. There is an overall increase in lens size and nucleus size with age. The axial diameter (red double-headed arrows) and the equatorial diameter (green double-headed arrows) for each lens were measured to calculate lens volume, lens aspect ratio, axial compressive strain, equatorial expansion strain, resilience and nuclear volume. In very old lenses (24-30 months), there is an area of optical discontinuity in the lens cortex (yellow arrowheads). Scale bar, 1mm.

[37–41], we observe that there is a steady increase in lens stiffness with age, demonstrated by the decrease in axial and equatorial strain under compressive load (Figures 1, 4A and 4B). After compression, we measured lens resilience (recovery after load removal)

by comparing the pre- and post-loading axial diameter of the lens. Between 2-24 months, the resilience of the lens is similar, recovering to 94–96% pre-loading diameter (Figure 4C). Surprisingly, at 30 months, the resilience of the lens is even better, recovering to 98.8%

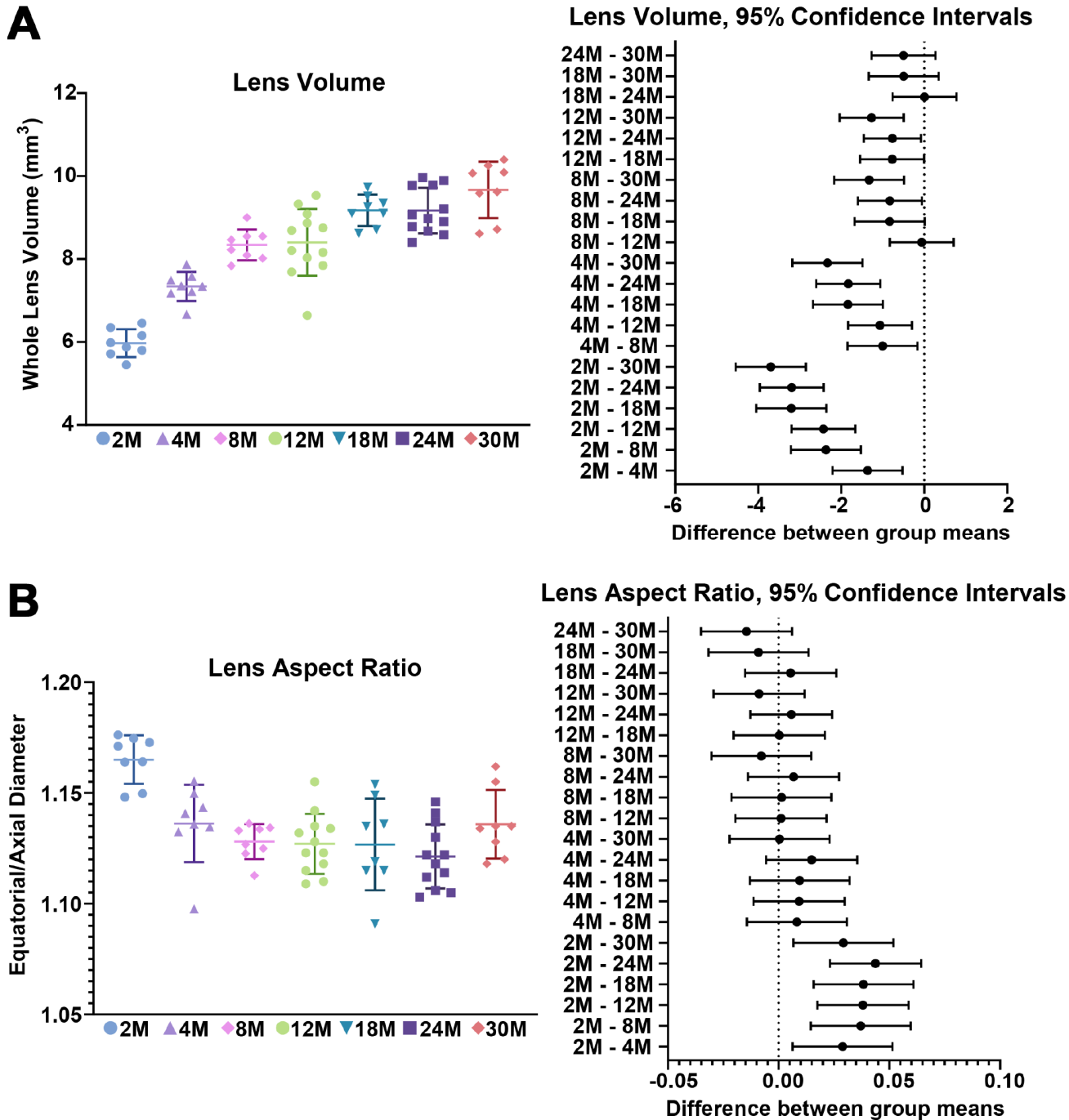


Figure 2. Lens volume and aspect ratio for mouse lenses between 2–30 months of age. Lines on the plots reflect mean \pm SD of $n =$ at least 8 lenses per age. The graph next to the data plots shows the 95% confidence interval. Any comparisons not crossing the dotted line are statistically significant ($p < 0.05$). (A) Lens volume (mm^3) from mice between 2–30 months of age. The volume increases steadily between 2-8 months of age and more slowly after 8 months. (B) The lens aspect ratio (axial/equatorial diameter) drops slightly between 2 to 4 months of age and then remains unchanged with age. Mouse lenses become slightly more spherical between 2 and 4 months.

$\pm 1.2\%$, and some of the lenses recovered completely to their pre-loading axial diameter. This may be linked to the dramatic increase in nuclear size in 30-month-old lenses. The mouse lens nucleus is very stiff and resists compression. Alternatively, very old lenses do not compress as much as the young lenses so it is possible that the increase in resilience may be because the oldest lenses do not need to recover as much after load removal.

Detailed analysis of strain data revealed that at the lowest load (129.3mg), there is an increase in stiffness of the lens between 2 to 8 months of age (Supplementary Figures 2A and 3A). Interestingly, lenses from mice over 4 months of age do not exhibit increased stiffness with age at this lowest load. This data suggests that the lens peripheral region, which is compressed by the lowest load, does not stiffen much with age. In contrast, at the highest load (1293mg),

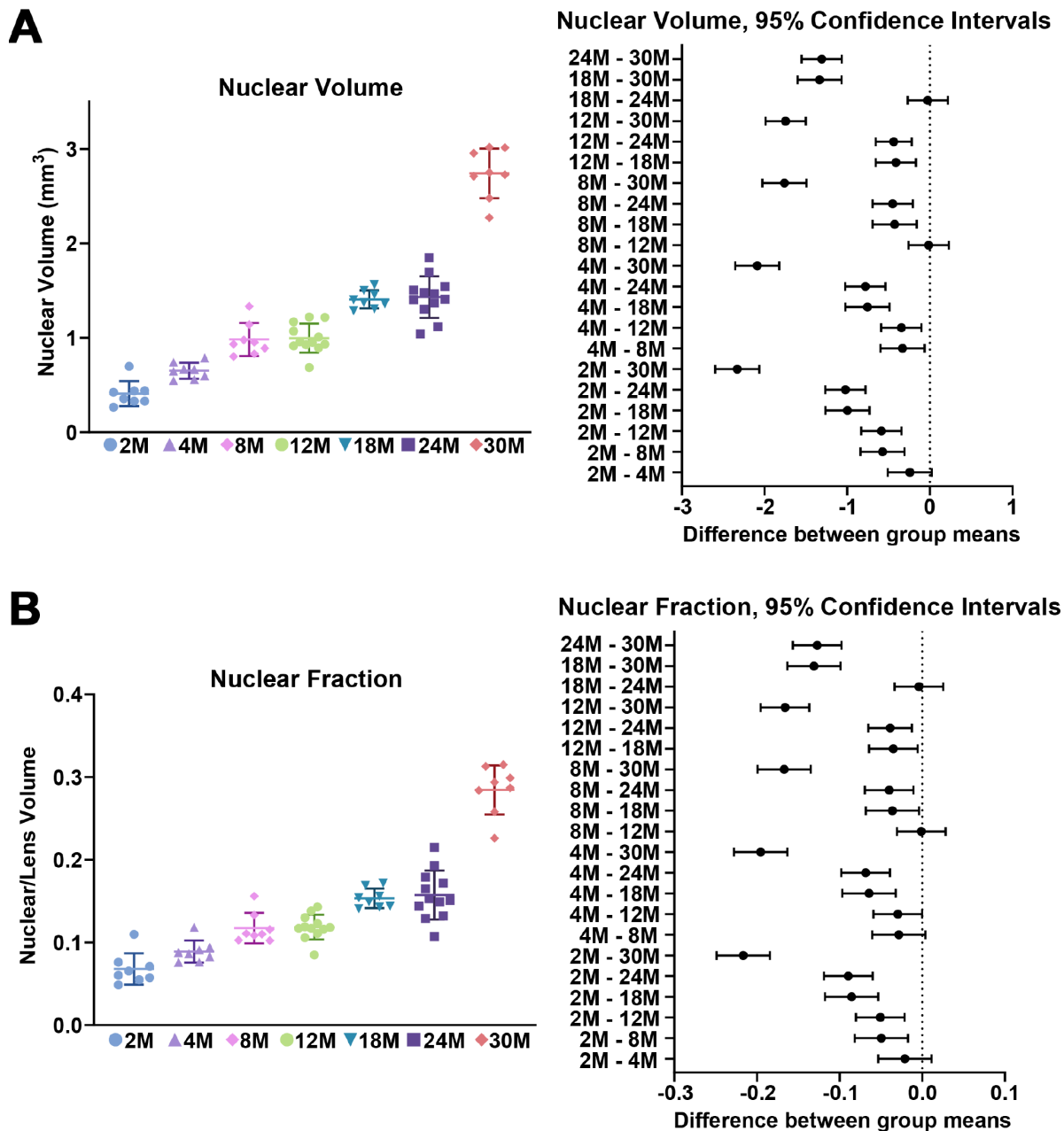


Figure 3. Nuclear volume and fraction for mouse lenses between 2–30 months of age. Lines on the plots reflect mean \pm SD of $n =$ at least 8 lenses per age. The graph next to the data plots shows the 95% confidence interval. Any comparisons not crossing the dotted line are statistically significant ($p < 0.05$). (A) The volume (mm^3) of the lens nucleus steadily increases with age. (B) Since nuclear volume increases more than lens volume with age, the nuclear fraction (nuclear/lens volume) increases with age.

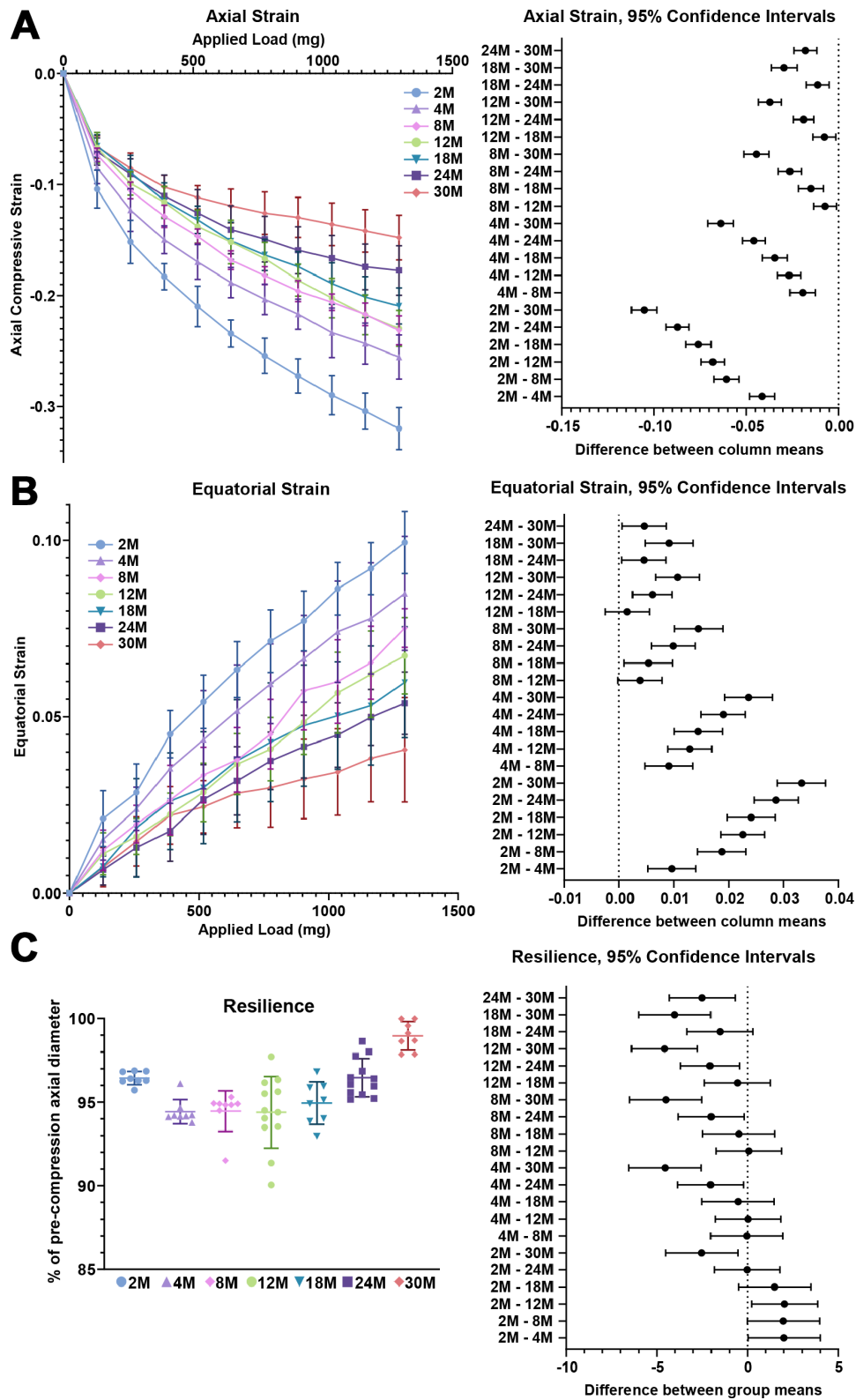


Figure 4. Lens stiffness and resilience for mouse lenses between 2–30 months of age. Plots reflect mean \pm SD of $n =$ at least 8 lenses per age. The graph next to the data plots shows the 95% confidence interval. Any comparisons not crossing the dotted line are statistically significant ($p < 0.05$). (A, B) Compression testing using sequential application of coverslips showed a steady decrease in axial and equatorial strain with age, indicating that lenses from older mice are stiffer. (C) Very old lenses from 30-month-old mice had increased resilience, calculated as the ratio of the pre-compression over post-compression axial diameter. Resilience for 30-month-old lenses was $98.8\% \pm 1.2\%$ while resilience for younger lenses was $\sim 94\%$.

there was a general decrease in strain with age, suggesting that whole lens stiffness increased with age (Supplementary Figures 2B and 3B).

Capsule thickness and fiber cell width do not increase after 4 months of age, but epithelial cell area increases slightly with age

We conducted a detailed study of the lens capsule and cell size in lenses from 2–12 months old mice. Utilizing WGA staining for the lens capsule and tdTomato+ labelled epithelial cell [53], we were able to measure capsule thickness in live lenses (Figure 5A). The lens capsule increased in thickness between 2 to 4 months of age but did not change in thickness beyond 4 months of age. Live lens imaging of anterior epithelial cells also revealed a small increase in epithelial cell area between

young 2- and 4-month old and older 12-month-old lenses (Figure 5B). The small change in anterior epithelial cell size likely reflects an increase in lens volume accompanied by a mild decrease in the number of quiescent anterior epithelial cells with age [54]. We also measured cortical fiber cell width in fixed lenses and observed a slight increase in fiber cell width between 2- and 4-month-old lenses, but no further changes in cortical fiber width after 4 months of age (Figure 5C). This indicates that newly formed fiber cells remain at a constant width after 4 months of age. Since the lens continues to grow after 4 months without an increase in fiber cell width, the number of cells in newly added outer shells would increase to fill the larger lens circumference, and we would also expect increased axial length of fibers in aging lenses to stretch from the anterior to posterior poles.

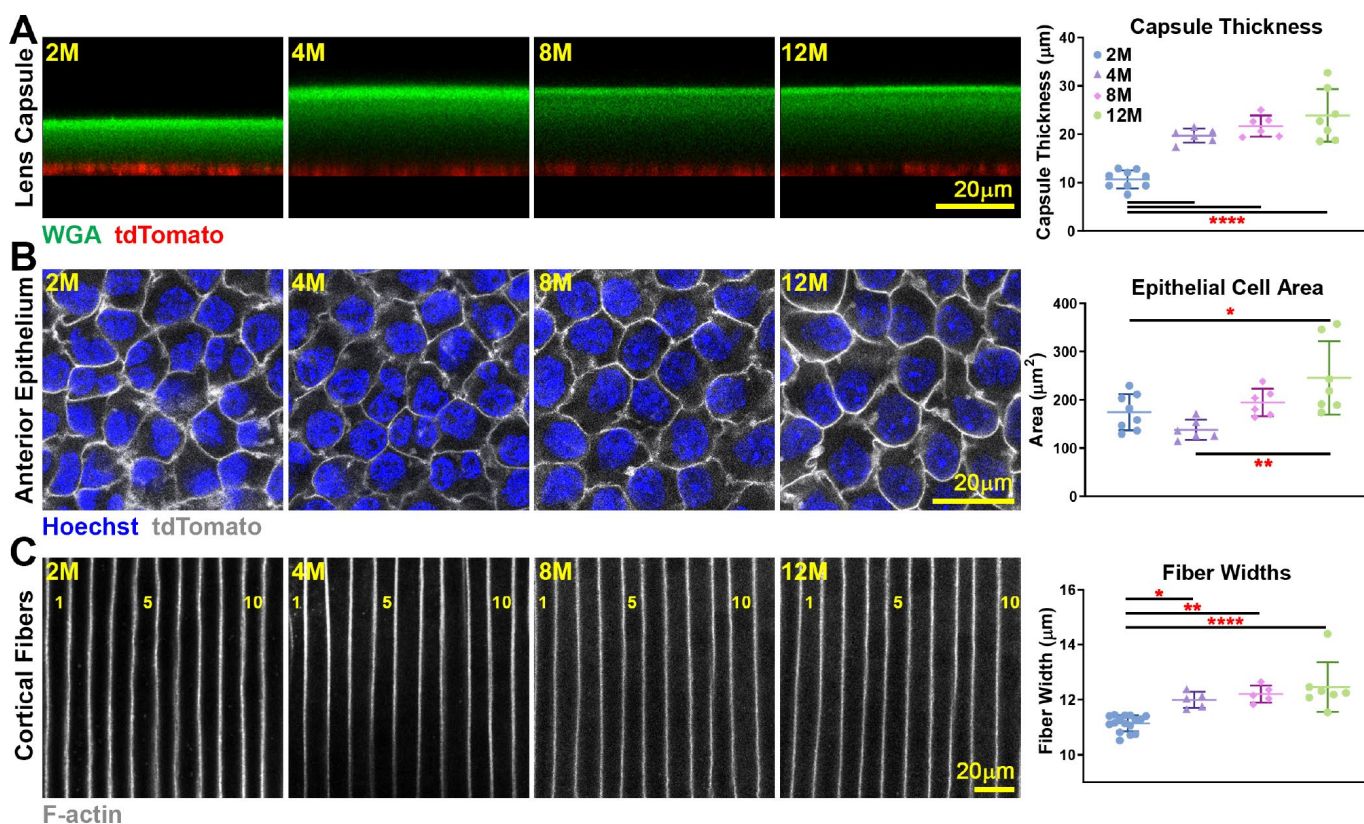


Figure 5. Live lens measurements of capsule thickness and anterior epithelial cell area and fixed lens measurements of cortical fiber cell width. Lines on the plots reflect mean \pm SD of $n =$ at least 6 lenses per age. Data from 2-month-old samples are reprinted from our previous publication [53]. *, $p < 0.05$; **, $p < 0.01$; ****, $p < 0.0001$. (A) Lens capsule thickness increases between 2 months and older ages, but the thickness is unchanged after 4 months of age. WGA (lens capsule) is shown in green, and tdTomato signal (basal surface of anterior epithelial cells) is shown in red. (B) Anterior epithelial cell area is increased between 2 and 4 months and 12 months of age. Cell nuclei (Hoechst) is shown in blue, and tdTomato signal (lateral membrane of anterior epithelial cells) is shown in grayscale. (C) Cortical fiber cell width increases between 2-month-old and older lenses, but there is no increase in fiber cell width after 4 months of age. The fiber cells are numbered showing 11 full-width cells in the 2-month-old lens and 10 full-width cells in lenses that were 4 months and older. These measurements show that although mouse lenses continue to increase in size with age, capsule thickness and fiber cell size only increase until about 4 months of age. There is a mild increase in epithelial cell size up to 12 months of age.

Anterior cataracts, cortical haziness and ring cataracts are observed in lenses from mice older than 12 months

Maintaining life-long transparency is essential for the function of the lens. We imaged freshly dissected lenses from 2-30-month-old mice, and determined that after 12 months of age, lenses very often developed anterior punctate cataracts (Figure 6A, arrowheads) and opacity in the lens cortex (Figure 6A, asterisks). The mild cortical haziness becomes a distinct ring in lenses by 24 months (Figure 6A, arrows). While the peripheral region of the lens outside the ring remained transparent, the inner portion of old lenses was translucent, but not transparent. The ring cataract causes a band of optical discontinuity that is more apparent when viewing the lens from the side (Figure 1, yellow arrowheads).

The mice we initially examined were in the B6-albino background from Jackson lab. Though there have been previous reports that mice in the C57BL6 genetic background develop cataracts with age [10, 12–15, 19, 20], these reports did not investigate the timing and location of cataracts in detail. Therefore, we also examined mouse lenses in two other B6 wild-type mouse lines to determine whether the timing of cataract occurrence and lens opacity locations were similar to the B6-albino wild-type mice. We found that B6 wild-type lenses from C57BL6 mice from Charles River and

B6SJL mice from Jackson Lab also develop anterior opacities, cortical haziness and ring cataracts at approximately the same age as lenses from B6-albino wild-type mice (Figures 6B and 6C).

Almost all lenses from wild-type mice in various B6 backgrounds over 12 months of age developed anterior cataracts, cortical haziness or ring cataracts with varying degrees of severity (Table 1). There were no lenses from mice over 12 months of age without cataracts, and most aged lenses had multiple areas of opacity. In 12-month-old lenses, ~59% had anterior cataracts, ~85% had cortical haziness and ~3% of lenses were clear. In 18-month-old lenses, ~70% had anterior cataracts, ~87% had cortical haziness and ~10% had ring cataracts. In 24-month-old lenses, ~92% of lenses had anterior cataracts, ~38% had cortical haziness and 75% of lenses had a ring cataract. In 30-month-old lenses, all lenses had anterior and ring cataracts.

Anterior cataracts in old lenses are due to incomplete suture closure and detachment of anterior epithelial cells from the underlying fiber cells

To determine the cause of anterior cataracts, we fixed lenses and performed whole lens staining and imaging of the lens anterior. We used phalloidin staining to determine whether there were changes in F-actin

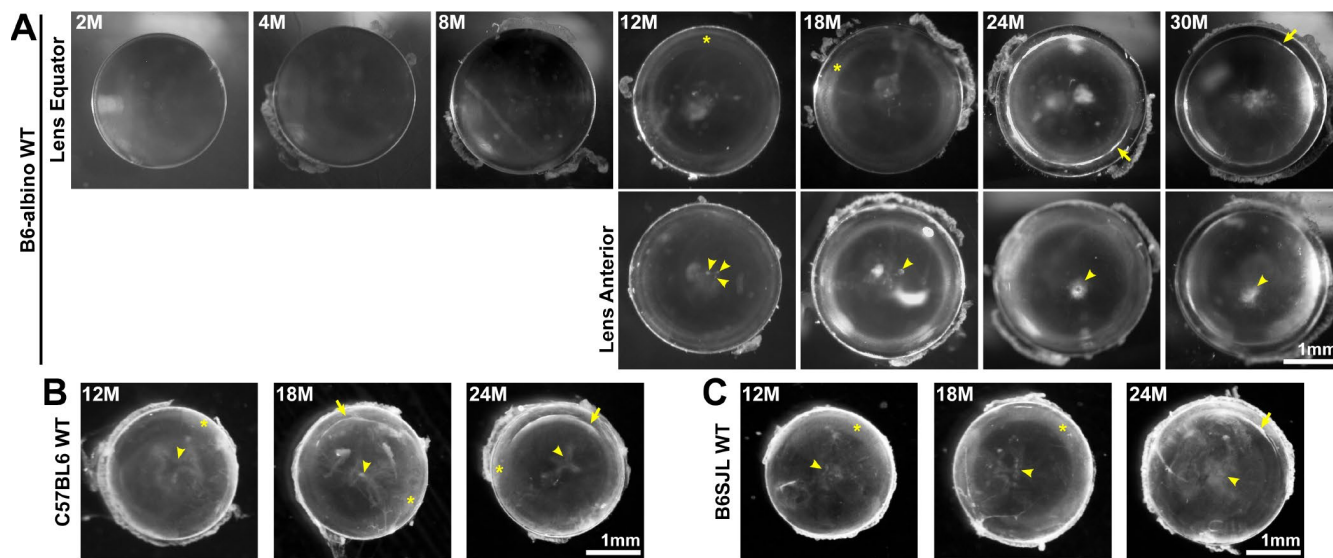


Figure 6. Lens images (top down view) from mice between 2-30 months of age in various B6 wild-type backgrounds. (A) B6-albino wild-type mice have clear lenses up to 8 months of age and develop small anterior opacities (arrowheads) by 12 months of age. Lenses from mice between 12-18 months develop cortical haziness (asterisks). Old lenses from mice between 24-30 months display ring cataracts (arrows) with a clear periphery and translucent, but not transparent, central regions. **(B, C)** Similar to B6-albino wild-type lenses, C57BL6 and B6SJL wild-type lenses also develop anterior opacities (arrowheads), cortical haziness (asterisks) and ring cataracts (arrows) at the same age as B6-albino wild-type mice. These images reveal that aged mouse lenses in the B6 genetic background develop cataracts around 12 months of age at the anterior pole and the lens cortex (haziness and ring opacity). Scale bars, 1mm.

Table 1. Cataract phenotypes in WT mice of various B6 backgrounds.

	Age	# of lenses	Cataract location		
			Anterior	Cortical	Ring
B6-albino	<8M	28	0	0	0
	12M	26	12	22	0
	18M	18	10	17	0
	24M	16	12	6	12
	30M	12	12	0	12
C57BL6	12M	4	4	3	0
	17-18M	5	5	2	3
	24-25M	5	5	0	5
B6SJL	12M	4	4	4	0
	18M	7	6	7	0
	24M	5	5	4	1
	30-32M	4	4	0	4

Analysis of lens opacities in WT mice in various B6 backgrounds between 2-30 months of age. Most aged lenses (12+ months) displayed anterior cataracts, cortical haziness or ring cataracts, and many lenses had multiple opacities in different locations of the lens. Only one lens from a B6-albino 12-month-old mouse was clear and did not have obvious cataracts.

organization in anterior epithelial and fiber cells. Previous studies had suggested anterior subcapsular opacities were due to abnormal epithelial cells undergoing epithelial-to-mesenchymal transition (EMT) [55–59]. Surprisingly, we found that anterior cataracts in 18-month-old lenses (Figure 6, arrowheads) were correlated with incomplete closure of the anterior suture (Figure 7A). In younger lenses, as expected, elongating lens fiber cell tips meet at the anterior and posterior poles to form a Y-shaped suture (Figure 7A and Supplementary Figure 1A) [60]. The fiber cell tips forming the anterior suture are directly below and attached to the apical surface of the anterior epithelial cells [60]. Compared to the tight adhesion of anterior epithelial cells and the underlying lens fibers at the suture location in the 4-month-old lens, the entire epithelial sheet appears wrinkled and collapsed into the gap of the anterior suture, and the epithelial cells appear to be partially detached from the underlying fiber cells in the 18-month-old lens (Figure 7B). The location of this morphological defect in the lens epithelium is directly correlated with the presence of anterior subcapsular cataracts observed in lenses from mice over 12 months of age. Yet, despite detachment from the underlying fibers, anterior epithelial cells of the 18-month-old lens remained in a monolayer with no evidence of abnormal proliferation.

Ring cataract in old lenses is linked to abnormal compaction of differentiating fiber cells

To determine whether there are cell morphology changes associated with the ring cataract in lenses from

mice older than 24 months of age (Figure 6, arrows), we performed SEM on dissected lens halves from 8 months and 24 months of age to visualize fiber cell profiles from the peripheral fibers in the cortex to the differentiating fibers in the inner cortex to the mature inner fibers (Figure 8 and Supplementary Figure 1B). In the 8-month-old lens, cortical fibers are organized with clear cell-cell boundaries. As these fibers differentiate, there is the appearance of small protrusions along the short sides of the fiber cells in the 8-month-old lens. After the fiber cells undergo final maturation in the 8-month-old lens, we observe the normal large paddles and small protrusions that form the complex interdigitations of lens fiber cells (Figure 8, Mature Inner Fibers). The images of fiber cells from 8-month-old lens at various stages of maturation (i.e., depth) are consistent with previous studies of fiber cell morphology [50, 61–66]. In contrast, in the 24-month-old lens, we observe disorganized cortical fiber cells, and the differentiating fibers of the old lens were compacted in the region corresponding to the ring cataract (Figure 8, red arrows and red box). Surprisingly, the inner mature fibers beyond the zone of compaction in the old lens have normal paddles and protrusions similar to cells in the young lens. Our data suggest that compaction of differentiating lens fibers within a narrow zone in the cortex is correlated with an optical discontinuity in the lens cortex leading to the ring cataract in the 24-month-old lens. This apparently differs significantly from the large, continuous areas of compaction normally seen in the nuclear fiber cells, which retain transparency in the aging lenses.

Hexagonal fiber cell packing of fiber cells is disrupted with age

Since we observed disorganization of the cortical fiber cells in the 24-month-old lens, we conducted TEM to determine the cell shape and organization of lenses from mice between 3–29 months of age (Figure 9). Cross sections through the lens periphery (Supplementary Figure 1B) include the epithelial cells on the left (labelled Epi), peripheral fiber cells and inner fiber cells on the right (Figure 9). The 3- and 8-month-old lens fibers are hexagonal in shape with uniform cell size. These young fiber cells are well aligned into neat rows and radial

columns. In the 12-month-old lens, the newly formed fibers at the lens periphery in this older lens have lost their distinct hexagonal shape but are still mostly uniform in size and organized into radial columns spanning neighboring layers. In contrast, in the 29-month-old lens, the fiber cells have all lost their normal hexagonal shape, are highly variable in size with tortuous membrane contours and are no longer aligned into radial columns. The electron density of the fiber cell cytoplasm is also highly variable, such that neighboring cells with dark and light gray cytoplasm are visible. There is also a general disorganization of cells in this very old lens, likely due to the change in cell shape and size.

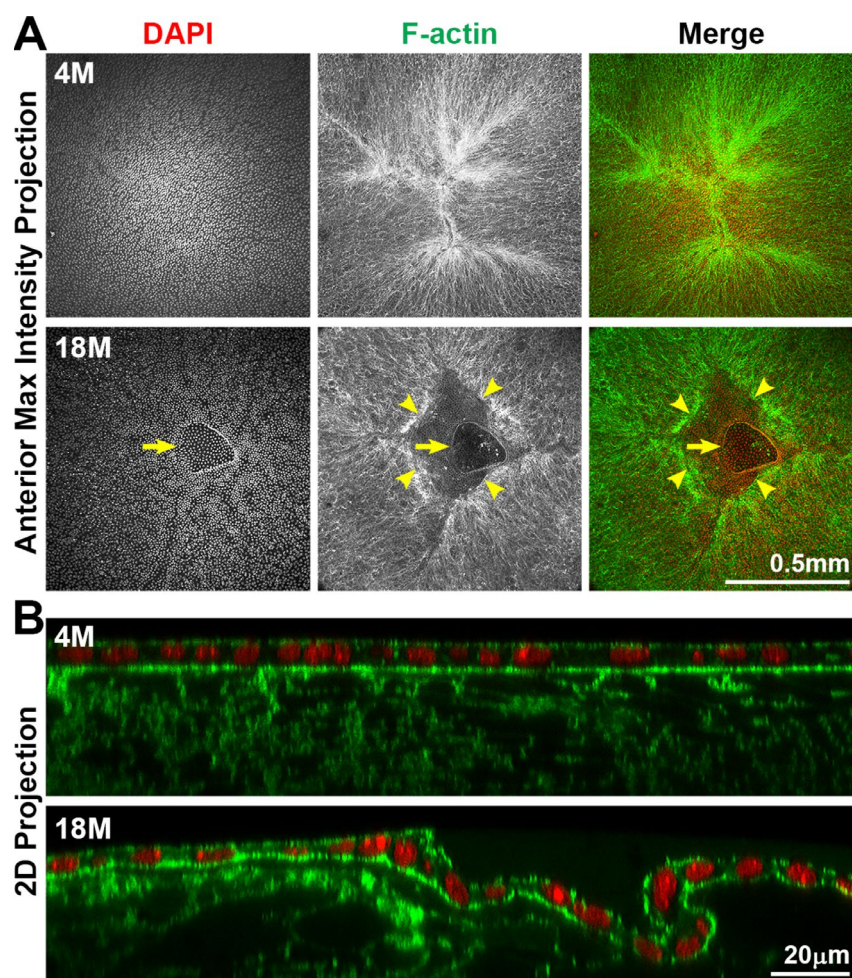


Figure 7. Whole lens staining for F-actin (phalloidin, green) and nuclei (DAPI, red) in 4-month-old and 18-month-old lenses. (A) The maximum intensity projection of the anterior lens epithelium and underlying fibers in the 4-month-old lens shows evenly distributed epithelial cell nuclei (DAPI) with a normal branched Y-suture (F-actin) under the epithelial cells. In contrast, there is an obvious defect at the apex of the 18-month-old lens with abnormal distribution of epithelial cell nuclei (DAPI, arrows) and a gap in the anterior suture (F-actin, arrowheads). (B) A 2D YZ projection of the 3D reconstruction of a Z-stack through the anterior epithelium and underlying fiber cells in the 4-month-old lens reveals tight adhesion of the anterior epithelial and fibers. In the 18-month-old lens near the fiber cell defect, the anterior epithelial cell layer is wrinkled and is depressed into the gap of the Y-suture. Although there was a defect in the epithelial cell sheet organization, there was no evidence of multilayered epithelial cells or abnormal epithelial cell proliferation in the 18-month-old lens. These results reveal that anterior cataracts in 18-month-old lenses are correlated with detachment and wrinkling of the anterior epithelial cells from the underlying Y-suture formed by fiber cells. Scale bars, 0.5mm in A and 20µm in B.

Hexagonal shape, packing and radial alignment of fiber cells originates from the F-actin dependent morphogenesis of the equatorial epithelial cells into meridional rows before fiber cell elongation and migration [46, 47]. F-actin polymerization can be affected by the redox state of the cell during aging and pathology (reviewed in [67]), and oxidative stress is a possible cause for cataractogenesis [1]. Therefore, we compared the packing and alignment of the anterior and equatorial epithelial cells, as well as the F-actin cytoskeleton in young and old lenses (Figure 10). We observed no obvious difference in the F-actin cytoskeleton of anterior epithelial cells between the 4-month-old and 18-month-old lenses (Figure 10A). Consistent with previous work [68–75], we observed

F-actin stress fibers and lamellipodia on the basal surface, sequestered actin bundles (SABs) and cortical F-actin near the lateral membrane and polygonal arrays on the apical surface of the anterior epithelial cells. At the lens equator, we observed organized hexagonal-shaped epithelial cells that are lined up in neat rows in the 4-month-old and 18-month-old lenses (Figure 10B). F-actin is enriched at the cell membrane with a basal F-actin meshwork, similar to previous reports [47, 69]. Thus, these data indicate that the F-actin cytoskeleton is not significantly altered with age in lens epithelial cells and that alterations in hexagonal cell shape in fiber cells of old lenses are unlikely to arise from a defect in equatorial epithelial cell shape, alignment and organization.

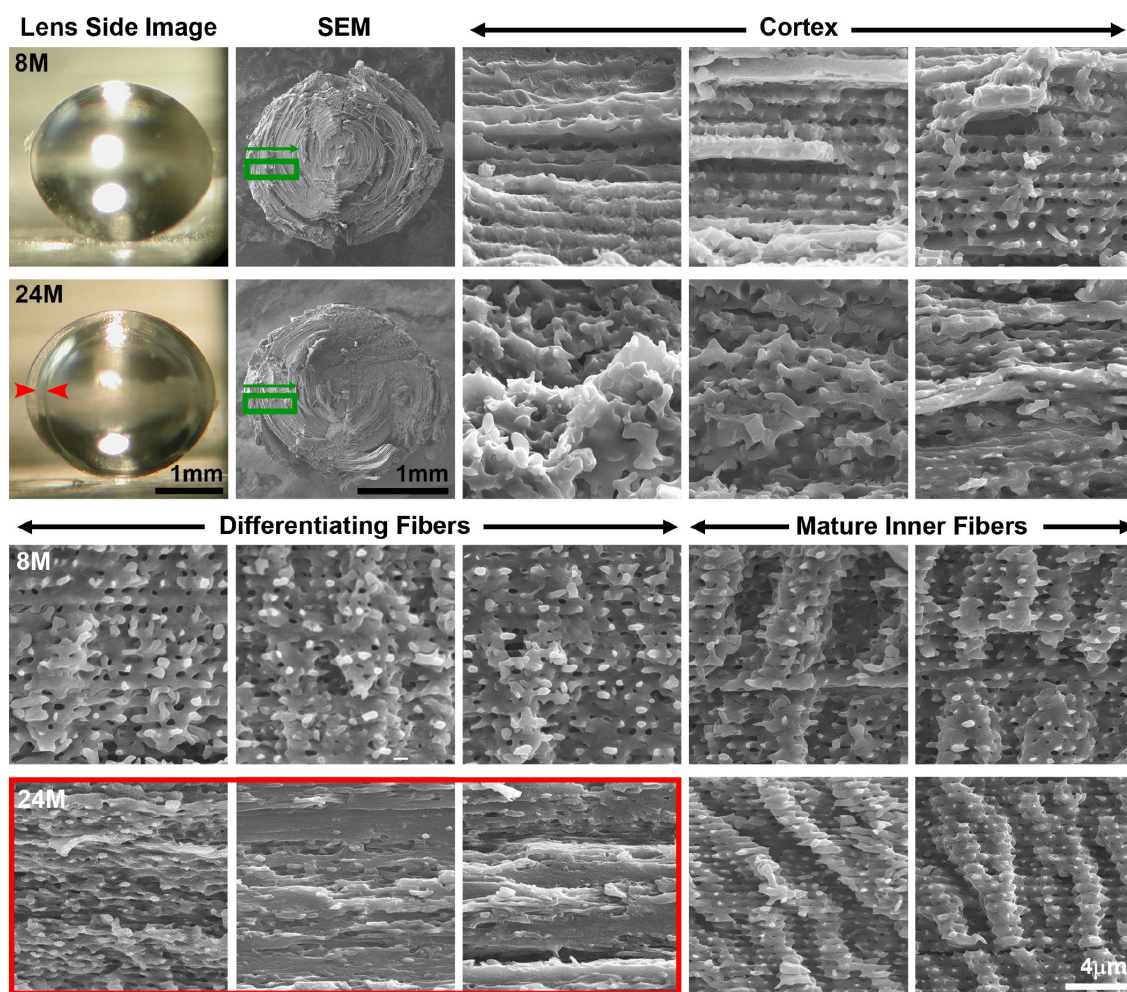


Figure 8. Side view lens images and scanning electron microscopy (SEM) at various depths in 8-month-old and 24-month-old lenses. Boxed regions in green on the low magnification SEM image indicate the approximate location where high magnification images were obtained. Cortical, newly formed fiber cells are disorganized in the 24-month-old lens compared to orderly cortical fibers in the 8-month-old lens. Differentiating fiber cells in deeper cortex layers (~100–200µm from the surface) of the 24-month-old lens lack normal small protrusions and formed a distinct zone of compaction. The location of the zone of compaction is correlated with the ring opacity (red arrows, red box). Mature inner fiber cells (~200–400µm from the surface) are comparable between the 8- and 24-month-old lenses with large paddles and small protrusions. Scale bars, 1mm (lens picture and low magnification SEM) and 4µm (high magnification SEM).

Gradient refractive index increases then plateaus with age

A high refractive index is necessary for the fine focusing power of the lens to transmit a sharp image onto the retina. We measured the refractive index in whole mouse eyes and generated 3D mesh plots and 2D contour plots of refractive index distribution in both the mid-sagittal plane and the mid-coronal plane passing

through each central lens nucleus. Representative plots are shown for mouse eyes from 2 weeks to 24 months of age (Figure 11). The magnitude of refractive index is indicated using colors ranging from low refractive index in dark blue (1.30) to high refractive index in dark red (1.55). Mouse lenses occupy around three quarters of the space inside the eye, and the lens is easily distinguished in the plots as the region with highest refractive index. Lenses at all ages have highest

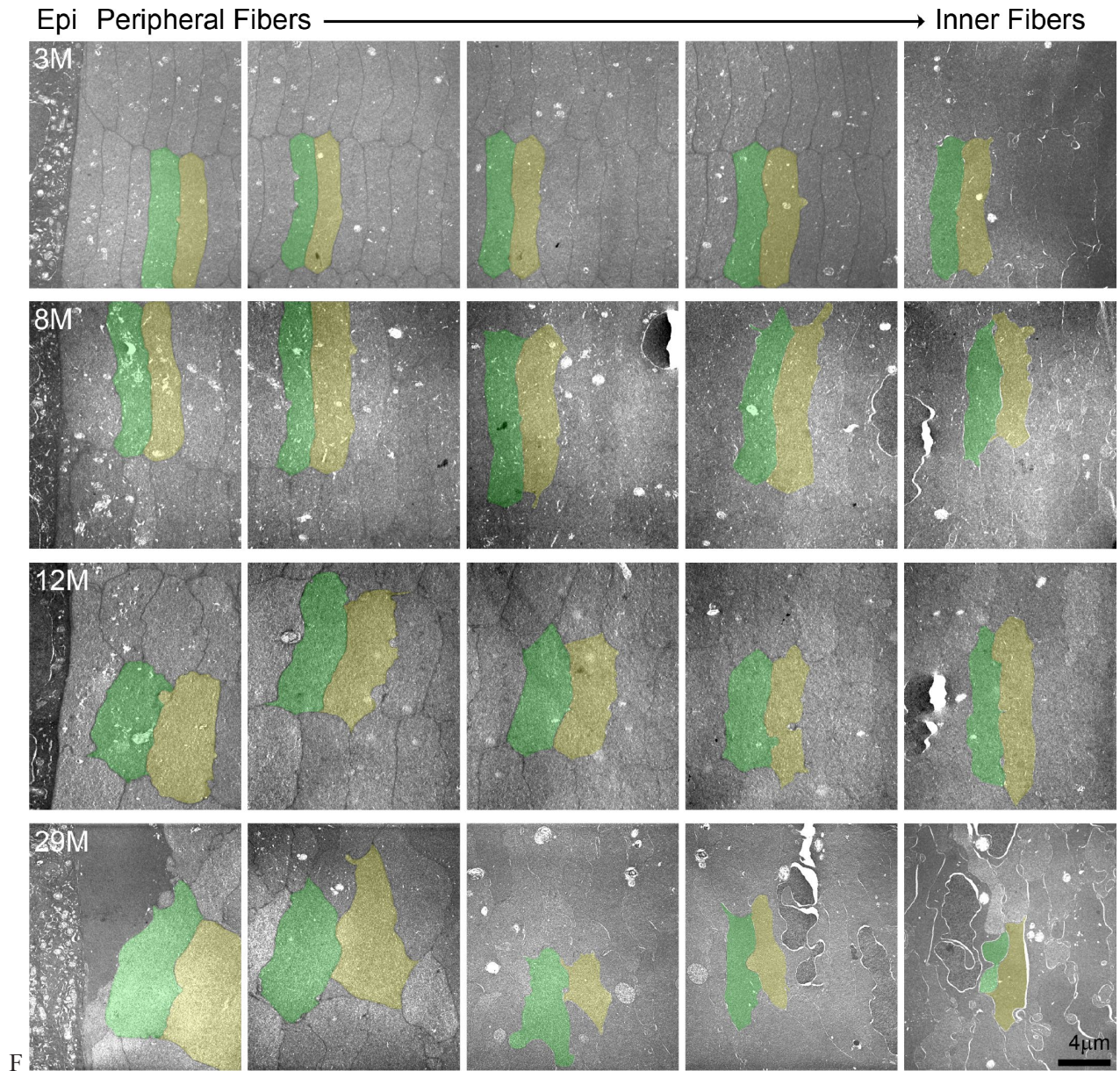


Figure 9. Transmission electron microscopy (TEM) of lens cross sections at various depths in 3–29-month-old lenses. Two neighboring cells in each panel are pseudo-colored green and yellow to show cell shape and size. In the 3- and 8-month-old lenses, fiber cells are hexagonal in shape and uniform in size from the periphery to the inner mature fiber cells. In the 12-month-old lens, the most peripheral fibers have lost their distinct hexagonal shape, but cells are still similarly sized between neighboring layers. In the 29-month-old lens, the cells have lost their characteristic hexagon cell shape and are highly variable in shape and size. There is also variability in electron density between neighboring cells in the 29-month-old lens with dark and light gray cells. Scale bar, 4µm.

magnitude of refractive index at the center, which plateaus over a limited region and decreases progressively toward the lens cortex, forming a Gradient Refractive Index (GRIN) in the lens. The GRIN profile is two-tiered with a ring of indentation that be clearly seen from the 3D mesh plot (bright yellow region). This indentation area separates the GRIN profile into two distinct regions: a cap (in red and orange) region and a bottom (in yellow and green) region. We measured the

diameter of the cap area in mid-sagittal 2D contour plots and compared that with the diameter of the isolated lens nucleus (Figure 12). The diameters of the cap area and the lens nucleus are very similar, with no statistically significant differences, suggesting that the highly compact lens nucleus is responsible for the high refractive index cap region on the 3D GRIN mesh plots. The bottom region of the GRIN profile, therefore, corresponds to the lens cortex.

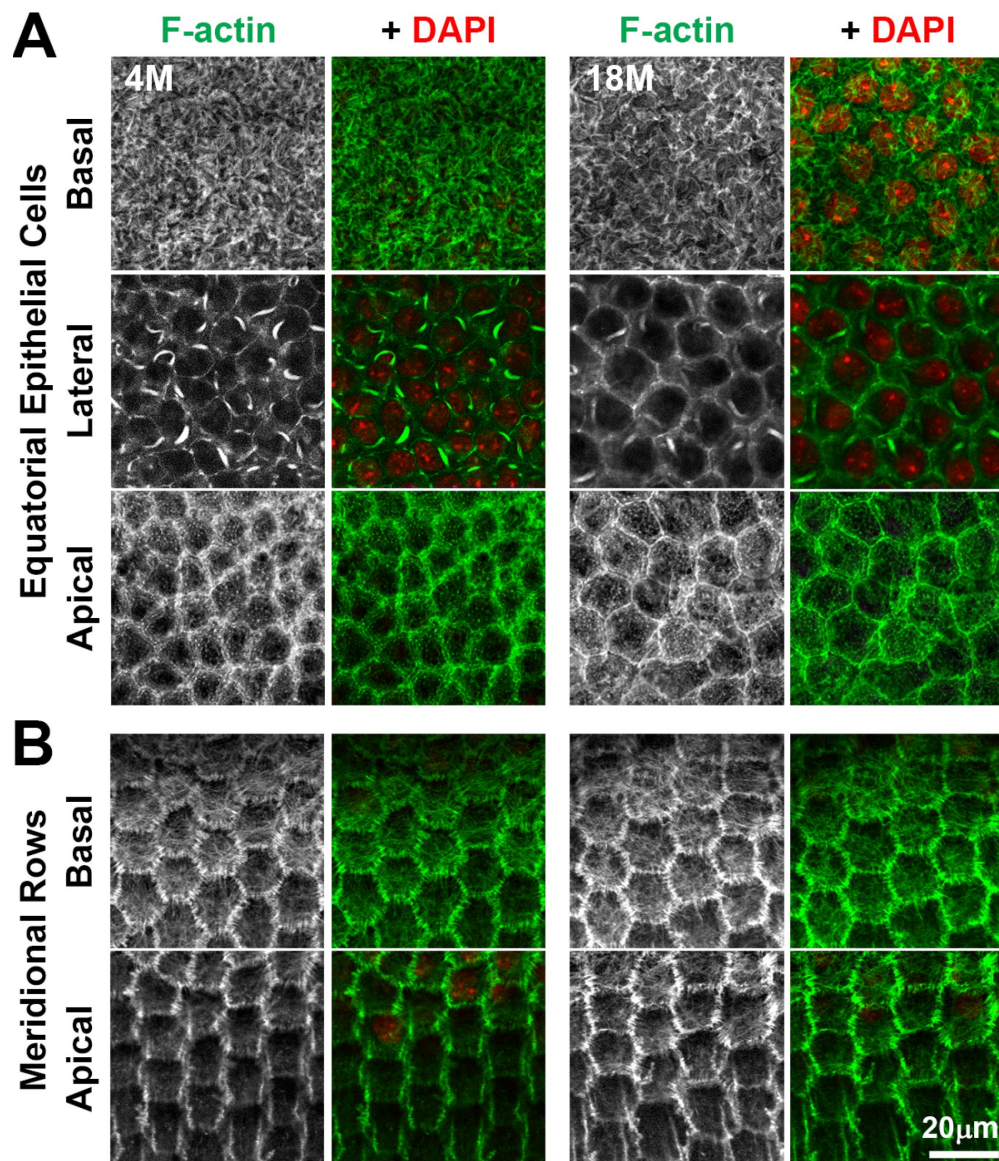


Figure 10. Whole lens staining for F-actin (phalloidin, green) and nuclei (DAPI, red) in 4-month-old and 18-month-old lenses reveal that the actin cytoskeleton in epithelial cells and the formation of organized meridional rows of hexagonal equatorial epithelial cells is similar between 4-month-old and 18-month-old lenses. (A) Single XY planes through anterior epithelial cells show similar F-actin staining and organization of equatorial epithelial cells between 4-month-old and 18-month-old lenses. These cells have a network of basal F-actin, membrane-adjacent F-actin and sequestered actin bundles near the lateral membrane, and polygonal arrays on the apical surface. **(B)** Single XY planes through the meridional rows at the lens equator reveals organized hexagonally-shaped epithelial cells with normal membrane-adjacent F-actin networks and a basal meshwork of F-actin in the 4-month-old and 18-month-old lenses. These data reveal that fiber cell shape changes and disorganization in older lenses is not due to altered shape or misalignment of equatorial epithelial cells. Scale bar, 20µm.

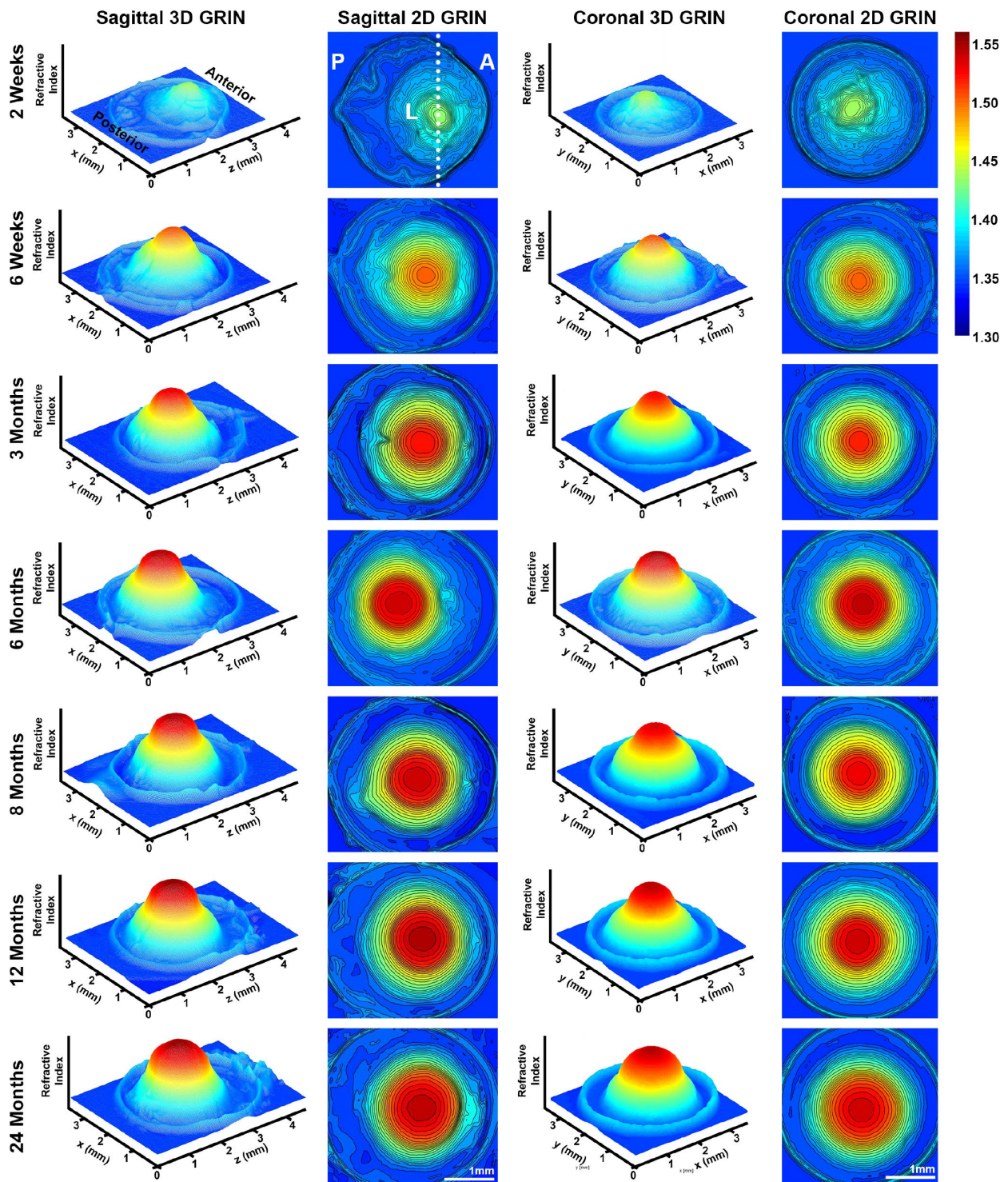
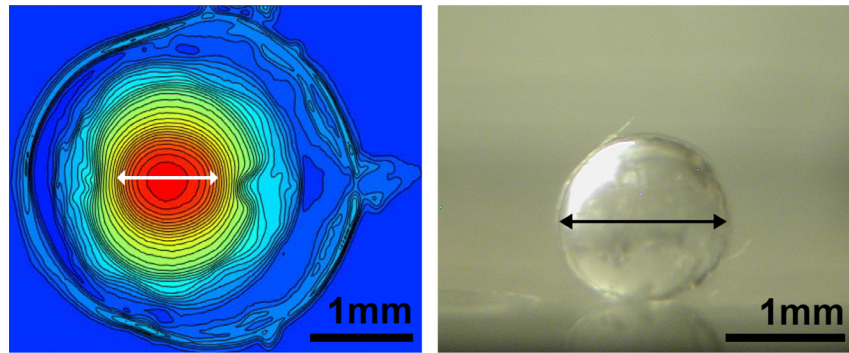


Figure 11. 3D mesh and 2D contour plots of the Gradient Refractive Index (GRIN) in whole eyes from mice between 2 weeks to 24 months of age. Plots are through the mid-sagittal plane and the mid-coronal plane passing through each central lens nucleus. The anterior of the eye (A), the posterior of the eye (P) and the lens (L) are marked on the mid-sagittal views of the 2-week-old eye. The dotted line through the 2D sagittal view of the 2-week-old eye represents the location of the mid-coronal 3D and 2D heat maps. All images are oriented in the same direction. Colors reflect the magnitude of refractive index from low refractive index in dark blue (1.30) to high refractive index in dark red (1.55). The areas with highest refractive index are the lens. Mouse lens GRIN profiles are two-tiered with a ring of indentation (bright yellow) clearly seen in the 3D mesh plots. There is a cap region of high refractive index (red and orange) and a bottom region (yellow and green). There is an increase in the size of the cap region with age. These data show that GRIN in the mouse lenses develops by 2 weeks of age, and there is a rapid increase and plateau of maximum refractive index at the center of the lens with age.

We also extracted and plotted the average GRIN profile of lenses through the visual axis (Figure 13A). The GRIN profiles of lenses from 2-week-old mice have relatively low refractive index, and with age, especially between the period from 2 weeks to 6 weeks, the GRIN increases over the entire lens. The GRIN profile shows a central plateau region that increases in magnitude with age until about 6 months of age, after which the magnitude of the central plateau region remains relatively unchanged. GRIN profiles are statistically different between all age groups except between 12 months and 24 months. This suggests that there was little or no change in the GRIN profile after 12 months

of age. This average GRIN profile obscures the indentation region separating the cap and bottom regions of the profile that are visible in the 3D mesh plots. We plotted representative 2D GRIN profiles from lenses at various ages (Supplementary Figure 4) with pairs of arrowheads to indicate the indentation at the edge of cap regions. From the GRIN profiles, we extracted and compared the max refractive index (Figure 13B). The maximum refractive index is ~ 1.55 and is reached at 6 months of age with no additional increase with age. Thus, while the region with high refractive index expands with age, the maximum refractive index does not increase significantly.



High Refractive Index Cap vs. Nuclear Diameter

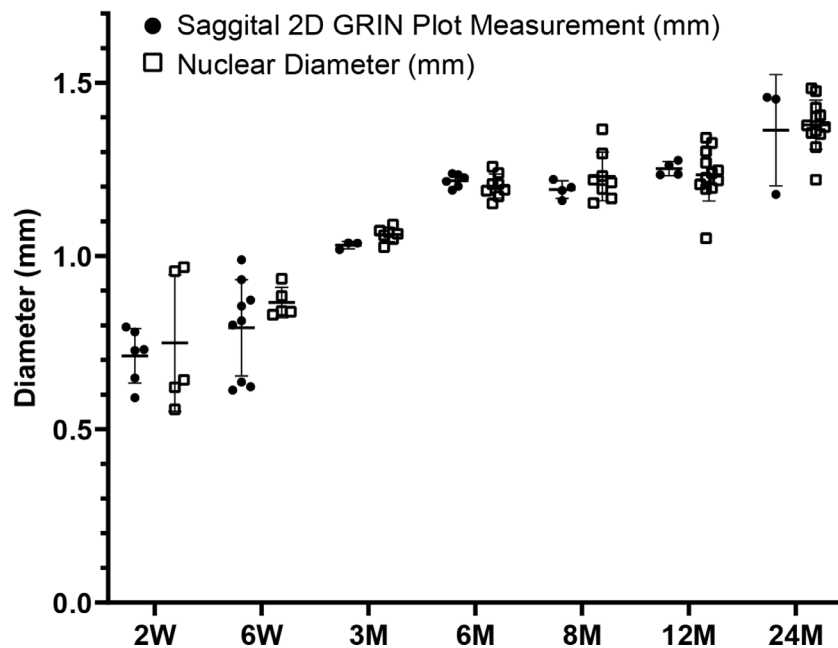


Figure 12. A comparison of the diameter of the cap region of high refractive index and the diameter of the extracted lens nucleus. The images show a representative mid-sagittal 2D contour plot and a representative lens nucleus with double-headed arrows indicating measured diameters. The graph compares the cap diameter in the sagittal 2D GRIN plot to the diameter of the lens nucleus. Lines on the plots reflect mean \pm SD of $n =$ at least 3 lenses from different mice per age. There was no statistically significant difference between the cap and nucleus diameters indicating that the area of high refractive index is directly correlated with the hard and compact lens nucleus. Scale bars, 1mm.

DISCUSSION

Our comprehensive study of aging in wild-type mouse lenses in the B6 genetic background showed increased stiffness along with appearance of anterior, cortical and ring cataracts with age (Figure 14). These data indicate that functional properties of wild-type mouse lenses change significantly with age and may be a suitable model to dissect the cellular and molecular mechanisms of age-related cataracts and changes in lens stiffness. The average life span of wild-type mice in the B6 genetic background is 26–29 months [76, 77]. Thus, in a relatively short period of time, we have been able to carry out this aging study. Our data shows that similar age-related cataracts are present in at least 3 different

wild-type mouse lines in the B6 background, demonstrating that the source of the mice (Jackson Lab or Charles River) and the environment (Scripps Research Institute or Boston University) does not affect the cataract phenotype. This suggests that there may be a universal mechanism underlying the age-related opacities seen in the B6 wild-type mouse lenses.

While the changes in lens opacity are similar between the different B6 wild-type mouse lines, we do observe slight difference in lens size and stiffness with age. Though all lenses increase in size with age, our lens imaging data showed that B6-albino wild-type lenses are slightly larger than age-matched C57BL6 and B6SJL wild-type lenses (Figure 6). The B6-albino

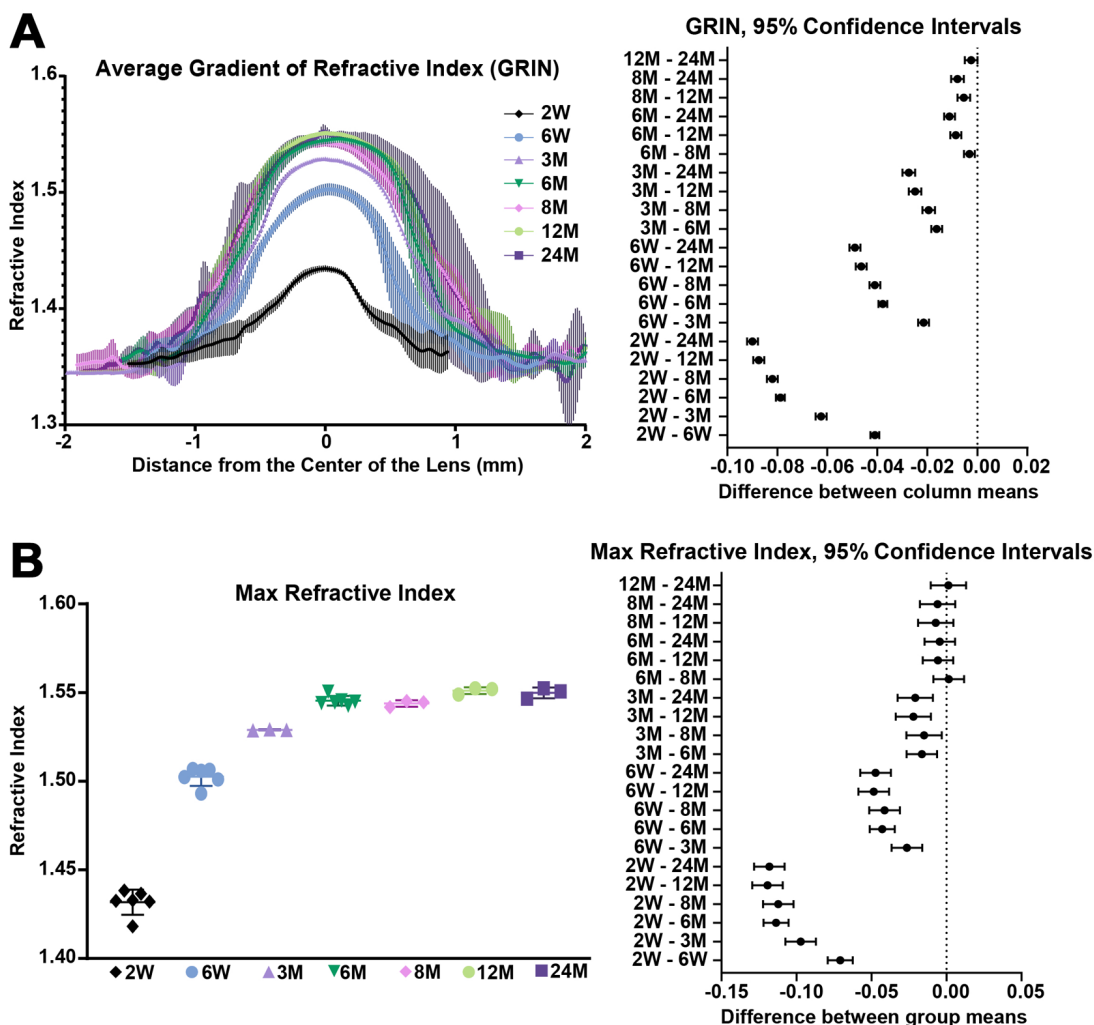


Figure 13. Average GRIN profiles along the visual axis and maximum refractive index in lenses from mice between 2 weeks to 24 months of age. Lines on the plots reflect mean \pm SD of $n =$ at least 3 lenses from different mice per age. The graph next to the data plots shows the 95% confidence interval. Any comparisons not crossing the dotted line are statistically significant ($p < 0.05$). (A) Average GRIN profiles increased in magnitude until about 6 months of age and then remained relatively unchanged with age. There is a statistically significant difference between profiles of different ages, except between the 12 months and 24 months profiles. (B) Max refractive index is ~ 1.55 in mouse lenses. Maximum refractive index rapidly increases until 6 months of age and then remains steady after 6 months of age.

lenses were also softer than age-matched C57BL6 wild-type lenses at 2–8 months of age [41]. A more detailed study of lens biomechanics and morphometrics in different wild-type mouse lines and at different ages would be required to determine the exact differences between the slightly different B6 genetic backgrounds. These differences highlight the importance of using control mice, preferably littermates, of the same genetic background for comparison in all lens studies as subtle differences in lens properties can occur even in wild-type mice of the same genetic background.

Mechanisms of age-related cataracts

Our data show that, in aged mouse lenses, anterior subcapsular cataracts arise due to detachment of the anterior epithelium from the underlying suture while the cortical ring cataracts are associated with an abnormal zone of compaction in the differentiating fiber cells. To our knowledge, this is the first report that age-related opacities in B6-albino wild-type lenses can be due to structural changes of the cells. These structural changes could themselves be caused by other better studied

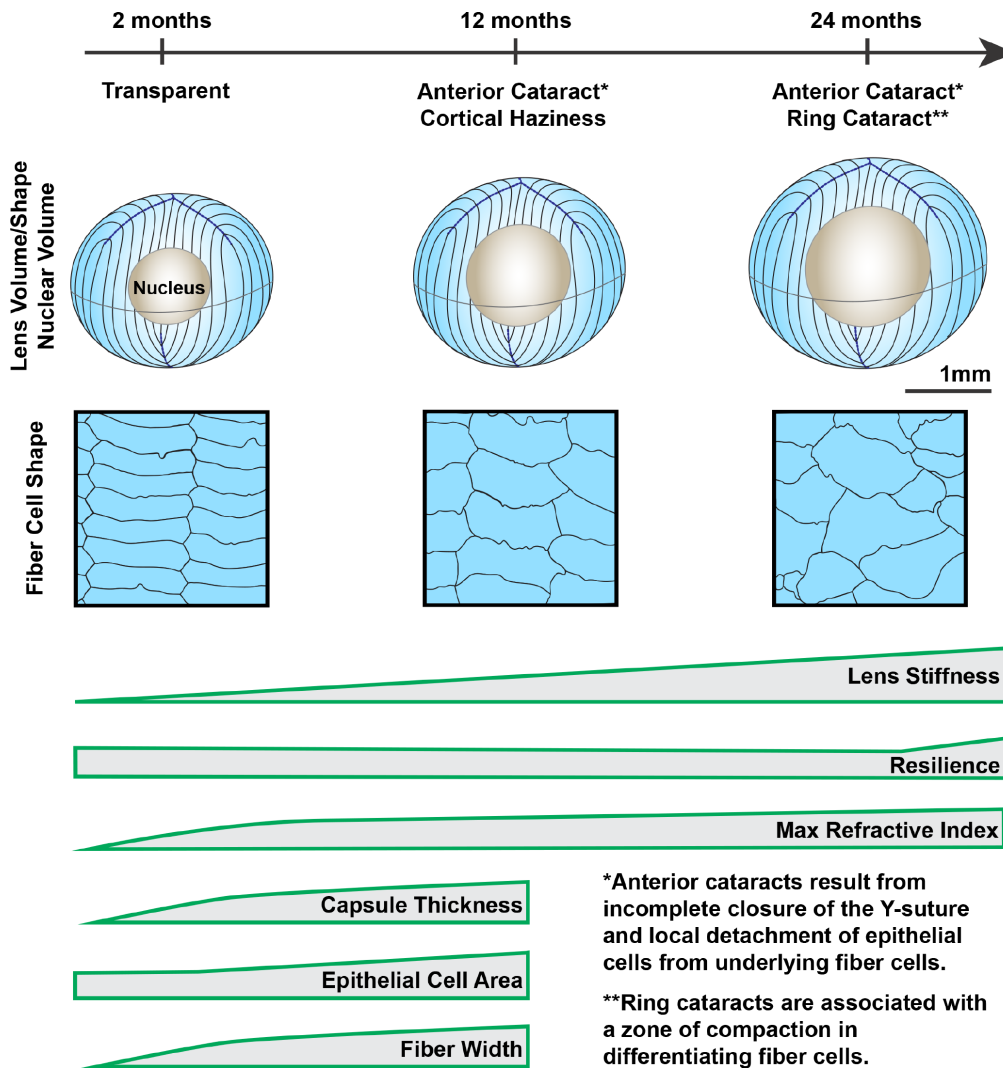


Figure 14. Wild-type mouse lenses in the B6 genetic background showed increased volume, nucleus size and overall stiffness, changes in cell morphology and microstructure along with appearance of anterior, cortical and ring cataracts with age. Lens volume and nucleus volume increase steadily with age. The shape and size of lens fiber cells become more disorganized in aged lenses. With age, mouse lenses develop anterior and cortical cataracts. Anterior cataracts are correlated with detachment of the anterior epithelial cells from the underlying fiber cells. Cortical ring opacities in the aged lenses are due to a zone of compaction in the cortical fiber cells leading to an optical discontinuity. While there is a steady increase in lens stiffness with age, resilience, or lens elasticity, is only increased in very old lenses. The maximum refractive index at the center of the lens (nucleus) increases rapidly until 6 months of age and reaches a plateau at 6 months. Lens capsule thickness and fiber cell width remain steady after 4 months of age, while epithelial cell area increases slightly between 4 and 12 months of age. Cartoons not all drawn to scale.

cataractogenesis mechanisms, such as oxidative stress, protein aggregation or disruption of lens fluid and ion homeostasis [1, 48, 78]. It is known that loss of both connexin 46 ($\alpha 3$) and connexin 50 ($\alpha 8$) and therefore gap junction coupling between fiber cells, in mouse lenses leads to incomplete anterior suture closure and severe cataracts [79]. Age-related loss of connexins, due to oxidative damage [78, 80], could lead to inadequate gap junction coupling and the formation of a suture gap in old lenses. The exact mechanism for suture disruptions with age require further study.

In human lenses, a barrier region has been observed at the interface between the lens cortex and the nucleus that forms during fiber cell maturation [81–83]. It is thought that the barrier limits antioxidant and metabolite movement into the lens and waste out of the lens leading to increased stiffness and decreased transparency with age [83]. Though the barrier observed in human lenses has not been reported in mouse lenses, previous reports have shown a diffusion barrier in rat lenses [84] and bovine lenses [85, 86]. In bovine lenses, the barrier region is in the approximate region of fiber cell compression (relative to lens size) [85, 86] that we observe in mouse lenses with advanced age. The exact structural and molecular basis for the barrier region remains unclear. In rat lenses [84], the diffusion barrier appears to be located near the site of membrane insertion for MP20, an abundant lens membrane protein. Our SEM data may suggest a possible structural alteration that leads to the formation of a diffusion barrier, in that the compaction of lens fiber cells could alter the fluid and ion outflow pathway. The avascular lens generates its own microcirculation system to allow transport of nutrients into and waste out of the tissue [87]. The outflow pathway is facilitated by a network of large micron-sized gap junction plaques in the differentiating lens fiber cells [88]. The disruption of gap junction plaques leads to decreased coupling between fiber cells [89], while loss of connexin proteins, due to genetic mutations or during aging, result in decreased gap junction coupling and cataracts [78, 80, 90–92]. Previous work also showed significantly decreased gap junction coupling in lenses from mice at 14 months of age as compared to those from mice between 2 and 6 months of age [78]. Further studies of connexins and gap junction plaque structures in the region of fiber cell compaction in the aging mouse lenses will be necessary to evaluate these mechanisms.

In our old lenses, the tissue inside the ring cataract appears hazy and translucent, rather than transparent. The hazy appearance may be due to compromised crystallin associations and organization in inner fiber cells due to decreased microcirculation in the old lens. While protein breakdown or aggregation may also lead to changes in

transparency, the GRIN profile suggests that protein concentration is not significantly altered in the central region of the old lenses but shows greater variation in the cortex (Figure 13A). Overall lens volume does not increase significantly after 18 months of age. This could be due to the reduction of the growth rate or the fact that as even if new fiber cells were added at a constant rate, newly differentiated cells in older, and hence, larger, lenses would be increasingly stretched to cover a larger surface area and consequently be much thinner and appear more compact. Our measurements indicate that lens capsule thickness plateaus at 4 months of age and remains a steady thickness thereafter, and this contrasts with the continuous increase in lens volume up to 18 months of age. Thus, the biomechanical properties of the lens capsule may restrict, to some extent, the amount of available space for addition of new cell layers and could impart a compressive force as new layers are continuously added. Any compression, however, would be of a low degree such that it would not increase the local protein concentration in the outermost cell layers as this would manifest in a localized rise in refractive index, which could cause scatter.

Cell morphology in aged lenses

We were surprised to find that lens fiber cells lose their characteristic hexagonal cell shape in lenses from mice over 12 months of age, and that the fiber cell membrane contours appear less straight with age. In human lenses, the loss of hexagonal cell shape and the increase in tortuosity of fiber cells membranes has also been reported [93, 94]. The cell shape change in older lenses leads to abnormal packing of fibers cells causing a disruption of the neat rows of cells. On the other hand, the hexagonal packing of the equatorial epithelial cells appears to be unaffected in old lenses, indicating that fiber cell shape is altered during subsequent differentiation and elongation. The disordered fiber cell packing near the lens periphery does not appear to affect the transparency of the lens since the outer cortex of very old lenses is transparent. There is little data in the literature regarding lens fiber cell shape changes with age, due in part to difficulty in fixation and sectioning of mouse lenses [62]. More work needs to be done to understand how fiber cell shape is altered in very old lenses and whether there are obvious changes in the cytoskeleton and membrane structures with age.

Increased lens stiffness with age

Increased stiffness in aging human lenses has been hypothesized to be caused by increased lens nucleus size and stiffness with age [21]. While our data shows increased nucleus size and overall tissue stiffness in aged mouse lenses, the correlation between nucleus size

and lens stiffness is not clear. Between 24 and 30 months of age, mouse lens nuclei increase dramatically in size, but lens stiffness, while statistically different, is not greatly increased between 24- and 30-month-old lenses. Moreover, our recent study of lenses with altered F-actin-binding proteins showed that in mouse lenses, it is possible to have a softer lens with an enlarged and stiff lens nucleus [61]. Unlike the human lens nucleus, the mouse lens nucleus is not likely to contribute to overall tissue stiffness because mouse lenses do not change shape to accommodate and are much more spherical in shape than human lenses.

We also considered the possibility that the zone of compaction may affect the stiffness of aged lenses. We measured the equatorial expansion (strain) of the ring in lenses from 24- and 30-month-old mice (data not shown). A comparison of equatorial strain of the overall lens vs the strain of the lens materials within the ring opacity revealed no statistically significant difference, suggesting that the zone of compaction expands along with the rest of the tissue under compression. This is not surprising since the zone of compaction is a very small percentage of the overall lens and thus, would be unlikely to account for the significant increase in lens stiffness with age. More sensitive lens biomechanical measurements along with modeling of the tissue changes under compression would be required to confirm this hypothesis.

We explored other possible mechanisms for increased lens stiffness with age. Our detailed measurements of capsule thickness in aging lenses are consistent with increased thickness previously reported in mouse [95] and human lenses with age [96, 97]. In human lenses, the capsule thickens and stiffens with age, and thus, it has been suggested that the lens capsule plays a role in increased human lens stiffness with age [97]. In contrast, while the mouse lens capsule thickness increases between 2–4 months of age, the capsule thickness remains constant after 4 months while the lens continues to stiffen. Therefore, while the lens capsule thickness may influence increases in stiffness at younger ages up to 4 months, the contribution of the capsule to overall lens biomechanics after 4 months is unlikely to be due to capsular thickness. However, other properties in the capsule may change with age. In human lenses, capsular thickness peaks at the age of ~80 years, but capsule stiffness continue to increase with age [97]. This suggests that other alterations, chemical and/or structural may occur to the capsule matrix network with age. Of note, advance glycation end product levels increase with age in the lens [98], and an increase in advance glycation end products can cause the formation of covalent collagen crosslinks, which lead to increases in matrix stiffness [99]. Further

work needs to be done to test whether mouse lens capsules have altered biomechanical properties with age and to examine the role the lens capsule plays in determining whole lens biomechanical properties.

Similar to previous studies in mouse and human lenses [54, 100–102], we observe increased epithelial cell area with age. We have recently shown that lens shape change requires epithelial cell expansion [53]. Therefore, it may be postulated that whole lens shape change under load is impaired in older lenses as epithelial cells are larger, flatter and have a decreased ability for further expansion. However, our findings show that epithelial cell area does not increase until 8 months of age. Thus, the increase in whole lens stiffness, at least between 2–8 months of age, is not due to a restriction in expansion ability of epithelial cell area. To our knowledge, we are the first to characterize fiber cell width changes with age, and our data shows that the increase in fiber cell width only occurs between 2 and 4 months of age with no further increases between 2–12 months. The age-dependent increase in peripheral fiber cell widths would not necessarily restrict whole lens shape change under load and therefore, cannot account for the continual increase in whole lens stiffness with age. Of note, a previous SEM study of adult mouse lens fiber reveals an average fiber cell width of 5.45 μ m in the mid-cortex region [43], a much deeper layer in the lens than our measurements. The difference in fiber cell width from the outermost cortex (our measurements of 11–12 μ m) with the differentiating cells of the mid-cortex (5–6 μ m) suggests that there is remodeling and compaction of the lens fibers during differentiation.

Finally, in very old and stiff mouse lenses, the misalignment of the lens fiber cells does not alter lens stiffness, suggesting that hexagonal fiber cell alignment does not contribute significantly to overall lens biomechanical properties. Our previous work has indicated that the intercellular interdigitations of mature fiber cells regulated by the actin cytoskeleton may be more important for lens stiffness [50]. The importance of fiber cell alignment in overall lens stiffness still needs to be tested via high resolution imaging of live lenses during compression combined with mathematical modeling of the distribution of load on organized vs. disorganized lens fibers.

Lens resilience

Elasticity and the ability to change shape during accommodation are essential for focusing on near objects in human lenses. The accommodative ability of human lenses decreases with age along with a sharp increase in stiffness, and presumably a decrease in

elasticity [21–26]. We used resilience (recovery after load removal) calculations as a parameter to reflect elasticity. Our data reveals that mouse lens resilience hovers around 95% for all ages tested, except 30-month-old lenses where resilience is close to 99%. This may be due in part to the abnormally large nucleus in 30-month-old lenses that resists compression, similar to increased stiffness and size of the human lens nucleus with age. Our previous data suggests that resilience in mouse lenses depends on the recovery of the anterior Y-suture that opens up under coverslip compression [53]. Further confocal microscopy studies of very old lenses under compression would be needed to understand the impact of the Y-suture on resilience with age. We also considered the impact of the zone of compaction on lens resilience. However, due to the location of the zone of compaction in the inner cortex of the lens and the very thin region of abnormal fiber cells, it is unlikely that this zone would affect the resilience of the lens.

Gradient refractive index in murine lenses

GRIN is a distinct characteristic of lens that helps correct spherical aberrations, and lenses from all species that have been measured, so far, have a GRIN profile (reviewed in [103]). The maximum refractive index value found in adult mouse lens (1.552 ± 0.006) is much higher than that of a human or a porcine lens, which are around 1.40 and 1.42, respectively [104, 105], and is slightly lower than that of fish lenses (1.57) [106]. Our data shows that the highest refractive index is reached in mouse lenses at 6 months of age and after that only the area of maximum refractive index increases with age. The shape of the GRIN profile varies between different species and changes during both the growth and aging processes. The GRIN profile of a mouse lens has a rounder central region than that of a human lens, which has a relatively constant index value at the center [103, 104, 107]. The area of highest refractive index in the mouse lens is correlated with the hard and compact nucleus (Figure 12). It is not clear whether nuclear compaction is required for high refractive index in the lens, though the region of highest refractive index in mouse and human lenses is correlated with the location of the nucleus [21, 52, 103]. In fish lenses, however, nuclear compaction does not seem to be required for high refractive index [106, 108, 109]. Alternatively, a high refractive index in the center of the lens could simply be a result of high protein concentrations. The central index reaches a maximum in lenses from some species where proteins in the nucleus are tightly packed because the cytoplasm is composed of almost pure protein [103]. During lens fiber cell maturation, cellular organelles are eliminated, leaving mature fibers without the ability to initiate *de novo* protein synthesis [42, 110]. Therefore, for the cytoplasm of the nuclear fibers

to have high levels of protein, there could be dehydration of the nucleus to decrease free water content in nuclear cells [111], possibly through increased bound water due to post-translational modifications and aggregation of lens proteins [112]. To validate this theory, proteomic and water content analysis of nuclei from young and old lenses would be needed to compare the differences in nuclear protein content and composition with age and how that correlates with the increase in GRIN. Another intriguing possibility is enhanced transport of proteins from peripheral fibers into nuclear fibers, which has been suggested to occur in fish lens nuclei [113], but this mechanism has not been explored in mammalian lenses.

Mouse lens GRIN profiles also display a unique discontinuity (or indentation) in the contour of the profile in peripheral region of the lens, which can be observed in the 3D GRIN mesh plots and 2D GRIN profiles (Figures 11 and Supplementary Figure 2). In other words, the mouse GRIN profile has two radii of curvature; one in the central region and one in the peripheral region. Compared to the two-tiered mouse GRIN, the GRIN profile in most other species is parabolic without a central plateau [103]. The two-tiered GRIN profile in mouse lenses can be observed at 2 weeks of age, the youngest lenses that were measured in the present study. It is hypothesized that formation of GRIN profile may take place during gestational age, though the exact age for each species is unknown. A study of the fetal bovine lens shows that shape of GRIN profile is irregular until the middle of gestation when it rapidly takes on a second-order polynomial shape [114]. Future measurements with embryonic mouse lenses would help determine when the GRIN is established during development, and whether variations in rate or extent of crystallin synthesis during lens growth can explain the peripheral discontinuity in the GRIN profile.

Concluding remarks

Our data reveals that not all properties of the lens continue to change with age and, at least in mouse lenses, most morphometric properties plateau by middle age (12–18 months). Though theoretically the lens continues to add more layers of fiber cells, there is no significant change in the lens size and shape after 18 months of age, suggesting there is a maximum size for the mouse lens. Nevertheless, lens stiffness continues to increase up to 30 months, indicating that increased lens size cannot explain the increase in lens stiffness. Thus, there must be other cellular and molecular mechanisms that contribute to the increased stiffness of very old lenses. This is just one example of the questions that still need to be investigated to identify the link between

morphometric measurements and lens functions (refraction, transparency and stiffness).

Collectively, the increases in lens size and nucleus size are correlated with increase stiffness with age. The addition of new fiber cells at the lens periphery becomes disordered with age, but this does not appear to impact lens biomechanical properties. Cataracts in aged lenses can be due to cell structural abnormalities, including incomplete suture closure, collapse of the lens epithelial cell layer into the suture gap and loss of epithelial-fiber cell attachments and compaction of the cortical lens fiber cells forming a circumferential light scattering ring. GRIN is present in the lens from 2 weeks of age and continues to increase until about 6 months of age, after which the maximum refractive index remains stable. The increase in the area of highest refractive index at the center of the lens is directly correlated with the increase in lens nucleus size, suggesting nuclear compaction drives the maximum GRIN. Whether there is a common molecular mechanism that drives changes in all the measured parameters remains unknown, but further biochemical and cell morphology studies will be needed to determine how subcellular aging affects the whole tissue. Thus, our study provides a baseline for future studies of lens aging by providing quantitative measurements of key parameters and identifying common age-related changes in the overall tissue and in individual cells.

MATERIALS AND METHODS

Mice and lens images

All animal procedures were performed in accordance with recommendations in the ARVO Statement for the use of Ophthalmic and Vision Research, the Guide for the Care and Use of Laboratory Animals by the National Institutes of Health and under approved protocols from the Institutional Animal Care and Use Committees at The Scripps Research Institute, Indiana University and Boston University.

Wild-type [B6-albino (Jackson Laboratories strain 000058), C57BL6 (Charles River strain 027) and B6SJLF1/J (hereafter referred to as B6SJL, Jackson Laboratories strain 100012)] and Rosa26-tdTomato mice tandem dimer-Tomato (B6.129(Cg)-Gt(ROSA) (hereafter referred to as tdTomato, Jackson Laboratories strain 007676) in the C57BL/6J background between the ages of 2 weeks-30 months were used for experiments. B6-albino mice (B6(Cg)-*Tyr^{cr-2J}*/J) are wild-type C57BL/6J mice with a spontaneous mutation in the tyrosinase gene [115, 116]. The B6-albino mice were a generous gift from Dr. William E. Balch (The Scripps Research Institute). The tdTomato-positive (tdTomato+) mice, used for live imaging, express a tdTomato tandem dimer protein fused

in frame to connexin 43 [117] (rendering it an inactive channel). Based on our previous study, tdTomato+ lenses are comparable in shape, size and stiffness to C57BL6/J wild-type lenses [53]. The tdTomato+ mice were maintained with a single copy of the transgene, and tdTomato-negative (tdTomato-) wild-type lenses were also used for experiments. Since previous studies revealed loss of specialized beaded intermediate filaments in the lens due to an endogenous mutation in the *Bfsp2/CP49* gene [118–120] results in changes in lens transparency and stiffness [38, 40], genotyping for *Bfsp2/CP49* were performed by automated qPCR on tail snips (Transnetyx, Cordova, TN) to confirm that all mice were wild-type for *Bfsp2/CP49*. Male and female mice were used for experiments.

Mouse lenses were dissected immediately from freshly enucleated eyeballs in 1X Dulbecco's phosphate buffered saline (DPBS, 14190, Thermo Fisher Scientific, Grand Island, New York). Images of freshly dissected lenses were captured using an Olympus SZ11 dissecting microscope with a digital camera (B6-albino wild-type) or an adapted Zeiss OpMi microscope with a D70 digital Nikon camera (C57BL6 and B6SJL wild-type). In side-view images, there is a band of mild opacity around the lens equator. This is due to lens dissection and severing of the attached zonular fibers from the lens capsule. This opacity is not a defect in the lenses.

Lens biomechanical testing and morphometrics

Morphometrics and stiffness of freshly dissected B6-albino mouse lenses were tested in 1X DPBS at room temperature using sequential application of glass coverslips as previously described [37, 38, 41]. Briefly, lenses were compressed with a series of glass coverslips, and images were acquired using an Olympus SZ11 dissecting microscope with digital camera. After mechanical testing, the lens capsule was gently removed, and soft cortical fiber cells were dissociated by rolling the lens between gloved fingertips leaving a very hard and round lens nucleus (center region of the lens) for imaging. FIJI software was used to perform image analysis, and Excel and GraphPad Prism 8 were used to calculate and plot strain [$\epsilon = (d-d_0)/d_0$, where ϵ is strain, d is the axial or equatorial diameter at a given load, and d_0 is the corresponding axial or equatorial diameter at zero load], resilience (ratio between pre-compression axial diameter over post-compression axial diameter), lens volume (volume = $4/3 \times \pi \times r_E^2 \times r_A$, where r_E is the equatorial radius and r_A is the axial radius), lens aspect ratio (ratio between axial and equatorial diameters), nuclear volume (volume = $4/3 \times \pi \times r_N^3$, where r_N is the radius of the lens nucleus) and nuclear fraction (ratio between the nuclear volume and the lens volume), respectively. Plots represent mean \pm standard deviation.

Two-way ANOVA with Tukey's multiple comparisons test were used to determine statistical significance.

Live lens imaging, capsule thickness and fiber cell width measurements

Imaging and analysis of live tdTomato+ and fixed tdTomato- wild-type lenses to determine lens capsule thickness, anterior epithelial cell shapes and fiber cell widths were performed as previously described [53]. Briefly, isolated lenses were stained with fluorescent CF640 dye conjugated to wheat germ agglutinin (WGA, 1:100, Biotium, Fremont, CA) and Hoechst 33342 (1:500, Biotium) in 1X PBS (137mM NaCl, 2.7mM KCl, 8.1mM Na₂HPO₄, 1.5mM KH₂PO₄; pH 8.1) for 15 minutes. Stained lenses were then transferred onto glass-bottomed culture dishes (10-mm microwell; MatTek, Ashland, MA) and immobilized anterior pole down, within 3-mm-diameter circular divots that were created, using a biopsy punch, in a thin layer of agarose (4% wt/vol in 1X PBS). Reactive oxygen species (ROS) are formed during confocal imaging of fluorescent probes in live tissues [121, 122]. Lenses were imaged in 3ml of 1X PBS containing 1.8 units of Oxyrase (Oxyrase, Mansfield, OH), an oxygen scavenger, to prevent ROS-related cell toxicity [122]. To determine fiber cell widths, tdTomato- wild-type lenses were fixed in 4% paraformaldehyde in 1X PBS for 30 minutes at room temperature. Following fixation, lenses were washed briefly in 1X PBS and placed in permeabilization/blocking solution for 30 minutes. Lenses were then incubated in permeabilization/blocking buffer containing rhodamine-conjugated phalloidin (1:20, Thermo Fisher Scientific, Waltham, MA) and Hoechst 33342 (1:500) for 2 hours followed by orienting them on their sides in the 3-mm-diameter circular divots described above.

Images were acquired on a Zeiss 880 laser-scanning confocal microscopy using a 20x air Plan-Apo 0.8 NA objective (equatorial lens region) or a 40x oil Plan-Apo 1.4 NA objective (anterior lens region). Z-stack images were acquired using step sizes of 0.7 μ m (20X objective) and 0.3 μ m (40X objective) and were processed using Zen (Zeiss) software.

Morphometric analysis was conducted using FIJI software as previously described [53]. To determine capsule thickness, line scan analysis was performed on XZ plane-view reconstructed images to obtain intensity distributions of WGA-stained capsules and tdTomato-labeled cell membranes. The distance between WGA and tdTomato peaks is indicative of capsule thickness. To determine epithelial cell areas, a region of interest (ROI) containing ~50–150 cells was traced using tdTomato-labeled cell membranes as a guide. The area occupied by the ROI was measured and the number of cells was determined by

counting the number of Hoechst-stained nuclei within the ROI. Average epithelial cell area was calculated by dividing the ROI area by the total number of cells. To determine fiber cell widths of fixed lenses, the equatorial region of the lens was imaged by propping lenses on their sides within an agarose wedge. Images were acquired and fiber cell widths were measured ~10 μ m inward from the fulcrum using Distributed Deconvolution (Ddecon) ImageJ plugin and the Z-line predictive model [123]. Data for 2 month old lenses were reprinted from our previous publication [53].

Phalloidin-staining of epithelial cells in whole lenses

Whole B6-albino lens fixation and staining was performed as previously described with a few modifications [47, 55]. Freshly enucleated eyes were collected from 4- and 18-month-old mice. An incision was made at the ora serata to allow fixative to penetrate the globe. Whole eyes were fixed in 4% paraformaldehyde in 1X PBS on ice for 30 minutes. Eyes were then washed and incubated overnight in 1X PBS at room temperature. After overnight incubation, lenses were microdissected out of the eye. Whole lenses were then permeabilized with 0.3% triton X-100 in 1X PBS for 15 minutes at room temperature. After permeabilization, lenses were immersed in Vectashield mounting medium with DAPI (H-1200, Vector Laboratories Burlingame, CA) for 30 minutes at room temperature. Samples were then washed 3 times, 5 minutes per wash, with 1X PBS. Lenses were then incubated for 2 hours at room temperature with Alexa-488-phalloidin (1:10, A12379, ThermoFisher), and Hoechst 33342 (1:250, Biotium, Fremont, CA) diluted in 1X PBS. Samples were then washed 4 times, 5 minutes per wash, in 1X PBS. Stained lenses were stored in Vectashield mounting medium at 4°C until imaging. Lenses were imaged in FluoroDishes (World Precision Instruments, Sarasota, FL) with optical quality glass bottoms, and equatorial images were collected by immobilizing the tissue on its side using agarose wedges [55]. Images and z-stacks (10X objective with 4 μ m steps or 40X objective with 0.3 μ m steps) were collected in the lens anterior and equator using a Zeiss LSM780 confocal microscope. Volocity (Quorum, Puslinch, Ontario, Canada) software were used to create max intensity projections, and 2D YZ projections of the 3D reconstruction of a Z-stack through the anterior epithelium and underlying fiber cells were rendered in ZEN 2.5 software (Zeiss). Staining was repeated on at least 4 lenses from 2 different mice for each age, and representative data are shown.

Scanning electron microscopy (SEM)

Eight- and 24-month-old B6-albino wild-type lenses were prepared for scanning electron microscopy (SEM)

as previously described [50, 61, 62]. Briefly, freshly dissected lenses were fixed in 2.5% glutaraldehyde in 0.1M sodium cacodylate buffer (pH 7.3) at room temperature for 2–3 days. A sharp needle was used to bisect lenses along the visual axis, and lens halves were post-fixed in 1% aqueous OsO₄ for 1 hour at room temperature. Samples were dehydrated using ethanol and were critical point dried in a Samdri-795 critical point dryer (Tousimis Inc., Rockville, MD). Lens halves were mounted and coated with gold/palladium in a Hummer 6.2 sputter coater (Anatech Inc., Union City, CA). Images were acquired with a JEOL 820 scanning electron microscope at 10 kV (JEOL, Tokyo, Japan). Using the lens nucleus as a reference, images from different regions of the lens were compared between samples (i.e., comparable regions were located based on measurements from the center outward). At least four lenses from 2 different mice were examined for each age, and representative images are shown.

Transmission electron microscopy (TEM)

Three-, 8-, 12- and 29-month-old B6-albino wild-type lenses were prepared for transmission electron microscopy using a method modified from a previous study [124]. Freshly dissected lenses were fixed in 2.5% glutaraldehyde, 0.1M cacodylate buffer (pH 7.3), 50 mM L-lysine and 1% tannic acid for 2–4 days (2 days for younger lenses and 4 days for older lenses). Fixative was removed and exchanged with fresh fixative at after day 1 or day 3. Fixed samples were stored in 0.1M sodium cacodylate buffer (pH 7.3) at 4°C until processing for EM. Lenses were mounted onto the specimen holder with superglue with the equatorial surface facing up, and then 200µm-thick lens section in the cross orientation were collected using a vibratome. Lens sections were post-fixed in 1% aqueous OsO₄ for 1 hour at room temperature. Sections were then rinsed in ddH₂O and stained en bloc at 4°C overnight with 0.5% uranyl acetate in 0.15M NaCl. Samples were dehydrated through graded ethanol and propylene oxide and embedded in Polybed 812 resin (Electron Microscopy Sciences, Hartfield, PA). One-micron-thick sections from the samples were cut with a diamond knife and stained with 1% toluidine blue. A Zeiss light microscope was used to examine sections before thin sections (70–80nm thick) were cut with a diamond knife. Thin sections were stained with 5% uranyl acetate followed by Reynold's lead citrate and examined in a JEOL 1200EX electron microscope at 80 kV (JEOL). At least 3 lenses from 3 different mice were examined at each age, and representative images are shown.

X-ray talbot interferometry

Whole B6-albino mouse eyes were stored in Dulbecco's Modified Eagle Medium without phenol red (21063-

029, ThermoFisher) with 2% penicillin/streptomycin (15-140-122, ThermoFisher) at room temperature before experiments. Three-dimensional refractive index distribution of mouse eyes were measured using X-ray Talbot interferometry, which is a synchrotron radiation-based phase contrast imaging modality [125–127]. Talbot interferometry is constructed at the bending magnet beamline BL20B2 at SPring-8. Experiments were conducted using monochromatic X-ray beam, finely tuned to 25 keV, which passes through a Si(111) double-crystal monochromator and two transmission gratings: a nickel phase grating (G1) and a gold absorption grating (G2). The pattern thicknesses of G1 and G2 are 4.35µm and 110µm, respectively. The pitch size of both gratings is 4.8µm, and the pattern size area is 50×50mm². A scientific CMOS detector (ORCA Flash 4.0, Hamamatsu Photonics) is used to detect the Moiré fringe patterns generated by X-ray beam passing through the sample and two gratings. A piezo stage and a 5-step fringe-scan method was used to shift G2 for phase retrieval, and a phase shift image was integrated from differential phase images obtained from the scan. To calibrate the phase shifts, experimentally obtained values for five different solutions of known density [127, 128] were compared to theoretically derived values per pixel. Linear relationships were found over the range of tested concentrations. X-ray refractive index difference was determined from the phase shifts per pixel using equations described previously [127]. Protein concentration, determined from the X-ray refractive index difference, is linearly related to the refractive index of the lens [129]. The total number of projections for tomography was 900, and the time of measurement is 50 minutes for each eye. Refractive index values measured by X-ray Talbot interferometry were processed by MatLab software (2018a, MathWorks, Natick, MA) to generate 2D iso-indicial index contours and 3D meshed index profiles in the mid-sagittal plane of each mouse eye. Gradient of refractive index (GRIN) profiles were generated along the visual axis by MatLab, and the average and standard deviation were calculated in Excel and plotted in GraphPad Prism 8. One-way and two-way ANOVA with Tukey's multiple comparisons test were used to determine statistical significance.

AUTHOR CONTRIBUTIONS

CC and VMF conceived and initiated this project. Most experiments described in this paper were performed by CC, JP and RBN. SKB and W-KL performed the EM experiments, and KW, MH, KU, NY and BP performed the GRIN measurements. KW, MH and BP conducted GRIN raw data analysis. JM provided lens pictures from C57BL6 and B6SJL mice. CC analyzed the data and prepared the figures. CC wrote the first draft of the

manuscript with input from JP and VMF, followed by feedback from other authors.

ACKNOWLEDGMENTS

We thank Michael B. Amadeo for assistance with experiment preparations.

CONFLICTS OF INTEREST

The authors report no conflicts of interest.

FUNDING

This work was supported by National Eye Institute grants R21 EY027389 (CC), R01 EY017724 (VMF and subcontract to W-KL), R01 EY005314 (W-KL) and beamtime grant 2018A1105 (to BP and KW) from SPring-8 synchrotron, Japan. JP was supported by a post-doctoral fellowship from the Natural Sciences and Engineering Research Council of Canada.

REFERENCES

1. Michael R, Bron AJ. The ageing lens and cataract: a model of normal and pathological ageing. *Philos Trans R Soc Lond B Biol Sci.* 2011; 366:1278–92.
<https://doi.org/10.1098/rstb.2010.0300>
PMID:21402586
2. Asbell PA, Dualan I, Mindel J, Brocks D, Ahmad M, Epstein S. Age-related cataract. *Lancet.* 2005; 365:599–609.
[https://doi.org/10.1016/S0140-6736\(05\)70803-5](https://doi.org/10.1016/S0140-6736(05)70803-5)
PMID:15708105
3. Fernandes A, Bradley DV, Tigges M, Tigges J, Herndon JG. Ocular measurements throughout the adult life span of rhesus monkeys. *Invest Ophthalmol Vis Sci.* 2003; 44:2373–80.
<https://doi.org/10.1167/iovs.02-0944>
PMID:12766033
4. Ohrloff C, Hockwin O. Lens metabolism and aging: enzyme activities and enzyme alterations in lenses of different species during the process of aging. *J Gerontol.* 1983; 38:271–77.
<https://doi.org/10.1093/geronj/38.3.271>
PMID:6841921
5. Williams DL, Heath MF, Wallis C. Prevalence of canine cataract: preliminary results of a cross-sectional study. *Vet Ophthalmol.* 2004; 7:29–35.
<https://doi.org/10.1111/j.1463-5224.2004.00317.x>
PMID:14738504
6. Keymer IF. Cataracts in birds. *Avian Pathol.* 1977; 6:335–41.
<https://doi.org/10.1080/03079457708418243>
PMID:18770343
7. Zigler JS Jr. Animal models for the study of maturity-onset and hereditary cataract. *Exp Eye Res.* 1990; 50:651–57.
[https://doi.org/10.1016/0014-4835\(90\)90109-8](https://doi.org/10.1016/0014-4835(90)90109-8)
PMID:2197105
8. Tripathi BJ, Tripathi RC, Borisuth NS, Dhaliwal R, Dhaliwal D. Rodent models of congenital and hereditary cataract in man. *Lens Eye Toxic Res.* 1991; 8:373–413.
PMID:1958636
9. Taylor A, Lipman RD, Jahngen-Hodge J, Palmer V, Smith D, Padhye N, Dallal GE, Cyr DE, Laxman E, Shepard D, Morrow F, Salomon R, Perrone G, et al. Dietary calorie restriction in the Emory mouse: effects on lifespan, eye lens cataract prevalence and progression, levels of ascorbate, glutathione, glucose, and glycohemoglobin, tail collagen breaktime, DNA and RNA oxidation, skin integrity, fecundity, and cancer. *Mech Ageing Dev.* 1995; 79:33–57.
[https://doi.org/10.1016/0047-6374\(94\)01541-S](https://doi.org/10.1016/0047-6374(94)01541-S)
PMID:7540704
10. Wolf NS, Li Y, Pendergrass W, Schmeider C, Turturro A. Normal mouse and rat strains as models for age-related cataract and the effect of caloric restriction on its development. *Exp Eye Res.* 2000; 70:683–92.
<https://doi.org/10.1006/exer.2000.0835>
PMID:10870527
11. Sapienza JS. Feline lens disorders. *Clin Tech Small Anim Pract.* 2005; 20:102–07.
<https://doi.org/10.1053/j.ctsap.2004.12.014>
PMID:15948424
12. Martin-Montalvo A, Mercken EM, Mitchell SJ, Palacios HH, Mote PL, Scheibye-Knudsen M, Gomes AP, Ward TM, Minor RK, Blouin MJ, Schwab M, Pollak M, Zhang Y, et al. Metformin improves healthspan and lifespan in mice. *Nat Commun.* 2013; 4:2192.
<https://doi.org/10.1038/ncomms3192> PMID:23900241
13. Pearson KJ, Baur JA, Lewis KN, Peshkin L, Price NL, Labinskyy N, Swindell WR, Kamara D, Minor RK, Perez E, Jamieson HA, Zhang Y, Dunn SR, et al. Resveratrol delays age-related deterioration and mimics transcriptional aspects of dietary restriction without extending life span. *Cell Metab.* 2008; 8:157–68.
<https://doi.org/10.1016/j.cmet.2008.06.011>
PMID:18599363
14. Pendergrass W, Penn P, Possin D, Wolf N. Accumulation of DNA, nuclear and mitochondrial debris, and ROS at sites of age-related cortical cataract in mice. *Invest Ophthalmol Vis Sci.* 2005; 46:4661–70.
<https://doi.org/10.1167/iovs.05-0808> PMID:16303963

15. Wolf N, Penn P, Pendergrass W, Van Remmen H, Bartke A, Rabinovitch P, Martin GM. Age-related cataract progression in five mouse models for anti-oxidant protection or hormonal influence. *Exp Eye Res.* 2005; 81:276–85.
<https://doi.org/10.1016/j.exer.2005.01.024>
PMID:[16129095](https://pubmed.ncbi.nlm.nih.gov/16129095/)
16. Shiels A, Hejtmancik JF. Mutations and mechanisms in congenital and age-related cataracts. *Exp Eye Res.* 2017; 156:95–102.
<https://doi.org/10.1016/j.exer.2016.06.011>
PMID:[27334249](https://pubmed.ncbi.nlm.nih.gov/27334249/)
17. Uwineza A, Kalligeraki AA, Hamada N, Jarrin M, Quinlan RA. Cataractogenic load - A concept to study the contribution of ionizing radiation to accelerated aging in the eye lens. *Mutat Res.* 2019; 779:68–81.
<https://doi.org/10.1016/j.mrrev.2019.02.004>
PMID:[31097153](https://pubmed.ncbi.nlm.nih.gov/31097153/)
18. Sella R, Afshari NA. Nutritional effect on age-related cataract formation and progression. *Curr Opin Ophthalmol.* 2019; 30:63–69.
<https://doi.org/10.1097/ICU.0000000000000537>
PMID:[30320615](https://pubmed.ncbi.nlm.nih.gov/30320615/)
19. Pendergrass WR, Penn PE, Li J, Wolf NS. Age-related telomere shortening occurs in lens epithelium from old rats and is slowed by caloric restriction. *Exp Eye Res.* 2001; 73:221–28.
<https://doi.org/10.1006/exer.2001.1033>
PMID:[11446772](https://pubmed.ncbi.nlm.nih.gov/11446772/)
20. Schriener SE, Linford NJ, Martin GM, Treuting P, Ogburn CE, Emond M, Coskun PE, Ladiges W, Wolf N, Van Remmen H, Wallace DC, Rabinovitch PS. Extension of murine life span by overexpression of catalase targeted to mitochondria. *Science.* 2005; 308:1909–11.
<https://doi.org/10.1126/science.1106653>
PMID:[15879174](https://pubmed.ncbi.nlm.nih.gov/15879174/)
21. Heys KR, Cram SL, Truscott RJ. Massive increase in the stiffness of the human lens nucleus with age: the basis for presbyopia? *Mol Vis.* 2004; 10:956–63.
PMID:[15616482](https://pubmed.ncbi.nlm.nih.gov/15616482/)
22. Glasser A, Campbell MC. Biometric, optical and physical changes in the isolated human crystalline lens with age in relation to presbyopia. *Vision Res.* 1999; 39:1991–2015.
[https://doi.org/10.1016/S0042-6989\(98\)00283-1](https://doi.org/10.1016/S0042-6989(98)00283-1)
PMID:[10343784](https://pubmed.ncbi.nlm.nih.gov/10343784/)
23. Weeber HA, Eckert G, Soergel F, Meyer CH, Pechhold W, van der Heijde RG. Dynamic mechanical properties of human lenses. *Exp Eye Res.* 2005; 80:425–34.
<https://doi.org/10.1016/j.exer.2004.10.010>
PMID:[15721624](https://pubmed.ncbi.nlm.nih.gov/15721624/)
24. Heys KR, Friedrich MG, Truscott RJ. Presbyopia and heat: changes associated with aging of the human lens suggest a functional role for the small heat shock protein, alpha-crystallin, in maintaining lens flexibility. *Aging Cell.* 2007; 6:807–15.
<https://doi.org/10.1111/j.1474-9726.2007.00342.x>
PMID:[17973972](https://pubmed.ncbi.nlm.nih.gov/17973972/)
25. Pierscionek BK. Age-related response of human lenses to stretching forces. *Exp Eye Res.* 1995; 60:325–32.
[https://doi.org/10.1016/S0014-4835\(05\)80114-9](https://doi.org/10.1016/S0014-4835(05)80114-9)
PMID:[7789412](https://pubmed.ncbi.nlm.nih.gov/7789412/)
26. Weeber HA, van der Heijde RG. On the relationship between lens stiffness and accommodative amplitude. *Exp Eye Res.* 2007; 85:602–07.
<https://doi.org/10.1016/j.exer.2007.07.012>
PMID:[17720158](https://pubmed.ncbi.nlm.nih.gov/17720158/)
27. Fisher RF. Elastic properties of the human lens. *Exp Eye Res.* 1971; 11:143.
[https://doi.org/10.1016/S0014-4835\(71\)80086-6](https://doi.org/10.1016/S0014-4835(71)80086-6)
PMID:[5130513](https://pubmed.ncbi.nlm.nih.gov/5130513/)
28. Krueger RR, Sun XK, Stroh J, Myers R. Experimental increase in accommodative potential after neodymium: yttrium-aluminum-garnet laser photodisruption of paired cadaver lenses. *Ophthalmology.* 2001; 108:2122–29.
[https://doi.org/10.1016/S0161-6420\(01\)00834-X](https://doi.org/10.1016/S0161-6420(01)00834-X)
PMID:[11713090](https://pubmed.ncbi.nlm.nih.gov/11713090/)
29. Burd HJ, Wilde GS, Judge SJ. An improved spinning lens test to determine the stiffness of the human lens. *Exp Eye Res.* 2011; 92:28–39.
<https://doi.org/10.1016/j.exer.2010.10.010>
PMID:[21040722](https://pubmed.ncbi.nlm.nih.gov/21040722/)
30. Glasser A, Campbell MC. Presbyopia and the optical changes in the human crystalline lens with age. *Vision Res.* 1998; 38:209–29.
[https://doi.org/10.1016/S0042-6989\(97\)00102-8](https://doi.org/10.1016/S0042-6989(97)00102-8)
PMID:[9536350](https://pubmed.ncbi.nlm.nih.gov/9536350/)
31. Pau H, Kranz J. The increasing sclerosis of the human lens with age and its relevance to accommodation and presbyopia. *Graefes Arch Clin Exp Ophthalmol.* 1991; 229:294–96.
<https://doi.org/10.1007/BF00167888>
PMID:[1869070](https://pubmed.ncbi.nlm.nih.gov/1869070/)
32. Hollman KW, O'Donnell M, Erpelding TN. Mapping elasticity in human lenses using bubble-based acoustic radiation force. *Exp Eye Res.* 2007; 85:890–93.
<https://doi.org/10.1016/j.exer.2007.09.006>
PMID:[17967452](https://pubmed.ncbi.nlm.nih.gov/17967452/)
33. Besner S, Scarcelli G, Pineda R, Yun SH. In Vivo Brillouin Analysis of the Aging Crystalline Lens. *Invest Ophthalmol Vis Sci.* 2016; 57:5093–100.
<https://doi.org/10.1167/iovs.16-20143>
PMID:[27699407](https://pubmed.ncbi.nlm.nih.gov/27699407/)

34. Sharma PK, Busscher HJ, Terwee T, Koopmans SA, van Kooten TG. A comparative study on the viscoelastic properties of human and animal lenses. *Exp Eye Res.* 2011; 93:681–88.
<https://doi.org/10.1016/j.exer.2011.08.009>
PMID:21910988
35. Zhang X, Wang Q, Lyu Z, Gao X, Zhang P, Lin H, Guo Y, Wang T, Chen S, Chen X. Noninvasive assessment of age-related stiffness of crystalline lenses in a rabbit model using ultrasound elastography. *Biomed Eng Online.* 2018; 17:75.
<https://doi.org/10.1186/s12938-018-0509-1>
PMID:29898725
36. Wu C, Han Z, Wang S, Li J, Singh M, Liu CH, Aglyamov S, Emelianov S, Manns F, Larin KV. Assessing age-related changes in the biomechanical properties of rabbit lens using a coaligned ultrasound and optical coherence elastography system. *Invest Ophthalmol Vis Sci.* 2015; 56:1292–300.
<https://doi.org/10.1167/iovs.14-15654>
PMID:25613945
37. Baradia H, Nikahd N, Glasser A. Mouse lens stiffness measurements. *Exp Eye Res.* 2010; 91:300–07.
<https://doi.org/10.1016/j.exer.2010.06.003>
PMID:20542031
38. Gokhin DS, Nowak RB, Kim NE, Arnett EE, Chen AC, Sah RL, Clark JI, Fowler VM. Tmod1 and CP49 synergize to control the fiber cell geometry, transparency, and mechanical stiffness of the mouse lens. *PLoS One.* 2012; 7:e48734.
<https://doi.org/10.1371/journal.pone.0048734>
PMID:23144950
39. Sindhu Kumari S, Gupta N, Shiels A, FitzGerald PG, Menon AG, Mathias RT, Varadaraj K. Role of Aquaporin 0 in lens biomechanics. *Biochem Biophys Res Commun.* 2015; 462:339–45.
<https://doi.org/10.1016/j.bbrc.2015.04.138>
PMID:25960294
40. Fudge DS, McCuaig JV, Van Stralen S, Hess JF, Wang H, Mathias RT, FitzGerald PG. Intermediate filaments regulate tissue size and stiffness in the murine lens. *Invest Ophthalmol Vis Sci.* 2011; 52:3860–67.
<https://doi.org/10.1167/iovs.10-6231> PMID:21345981
41. Cheng C, Gokhin DS, Nowak RB, Fowler VM. Sequential Application of Glass Coverslips to Assess the Compressive Stiffness of the Mouse Lens: Strain and Morphometric Analyses. *J Vis Exp.* 2016.
<https://doi.org/10.3791/53986> PMID:27166880
42. Lovicu FJ, Robinson ML. Development of the ocular lens. Cambridge, UK; New York: Cambridge University Press; 2004.
<https://doi.org/10.1017/CBO9780511529825>
43. Kuszak JR, Zoltoski RK, Sivertson C. Fibre cell organization in crystalline lenses. *Exp Eye Res.* 2004; 78:673–87.
<https://doi.org/10.1016/j.exer.2003.09.016>
PMID:15106947
44. Kuszak JR, Mazurkiewicz M, Jison L, Madurski A, Ngando A, Zoltoski RK. Quantitative analysis of animal model lens anatomy: accommodative range is related to fiber structure and organization. *Vet Ophthalmol.* 2006; 9:266–80.
<https://doi.org/10.1111/j.1463-5224.2006.00506.x>
PMID:16939454
45. Piatigorsky J. Lens differentiation in vertebrates. A review of cellular and molecular features. *Differentiation.* 1981; 19:134–53.
<https://doi.org/10.1111/j.1432-0436.1981.tb01141.x>
PMID:7030840
46. Bassnett S, Missey H, Vucemilo I. Molecular architecture of the lens fiber cell basal membrane complex. *J Cell Sci.* 1999; 112:2155–65.
PMID:10362545
47. Cheng C, Ansari MM, Cooper JA, Gong X. EphA2 and Src regulate equatorial cell morphogenesis during lens development. *Development.* 2013; 140:4237–45.
<https://doi.org/10.1242/dev.100727> PMID:24026120
48. Bloemendal H, de Jong W, Jaenicke R, Lubsen NH, Slingsby C, Tardieu A. Ageing and vision: structure, stability and function of lens crystallins. *Prog Biophys Mol Biol.* 2004; 86:407–85.
<https://doi.org/10.1016/j.pbiomolbio.2003.11.012>
PMID:15302206
49. Delaye M, Tardieu A. Short-range order of crystallin proteins accounts for eye lens transparency. *Nature.* 1983; 302:415–17.
<https://doi.org/10.1038/302415a0>
PMID:6835373
50. Cheng C, Nowak RB, Biswas SK, Lo WK, FitzGerald PG, Fowler VM. Tropomodulin 1 Regulation of Actin Is Required for the Formation of Large Paddle Protrusions Between Mature Lens Fiber Cells. *Invest Ophthalmol Vis Sci.* 2016; 57:4084–99.
<https://doi.org/10.1167/iovs.16-19949>
PMID:27537257
51. Cheng C, Nowak RB, Fowler VM. The lens actin filament cytoskeleton: diverse structures for complex functions. *Exp Eye Res.* 2017; 156:58–71.
<https://doi.org/10.1016/j.exer.2016.03.005>
PMID:26971460
52. Al-Ghoul KJ, Nordgren RK, Kuszak AJ, Freel CD, Costello MJ, Kuszak JR. Structural evidence of human nuclear fiber compaction as a function of ageing and cataractogenesis. *Exp Eye Res.* 2001; 72:199–214.

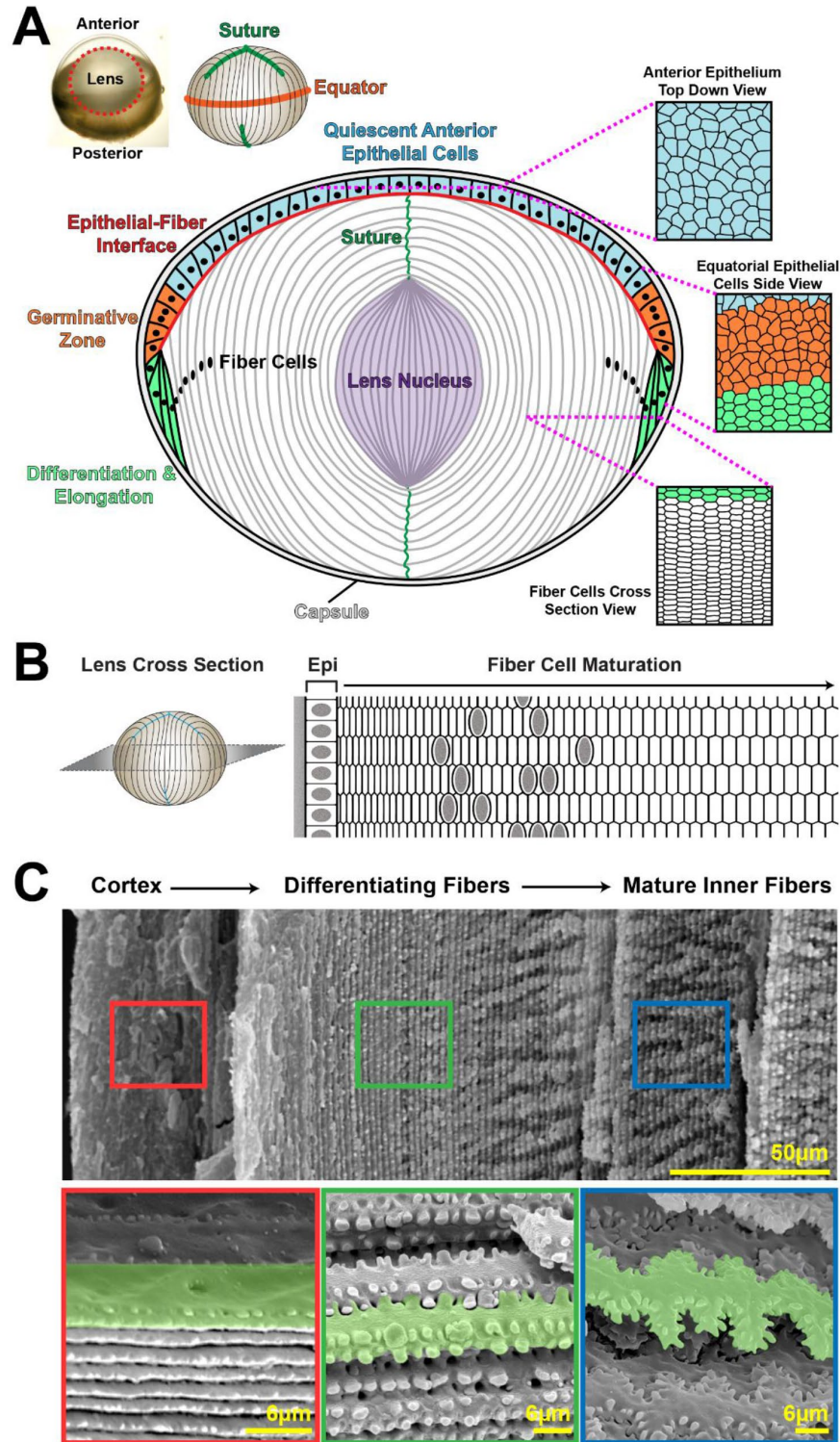
- <https://doi.org/10.1006/exer.2000.0937>
PMID:[11180969](https://pubmed.ncbi.nlm.nih.gov/11180969/)
53. Parreno J, Cheng C, Nowak RB, Fowler VM. The effects of mechanical strain on mouse eye lens capsule and cellular microstructure. *Mol Biol Cell*. 2018; 29:1963–74.
<https://doi.org/10.1091/mbc.E18-01-0035>
PMID:[30088796](https://pubmed.ncbi.nlm.nih.gov/30088796/)
54. Shi Y, De Maria A, Lubura S, Šikić H, Bassnett S. The penny pusher: a cellular model of lens growth. *Invest Ophthalmol Vis Sci*. 2014; 56:799–809.
<https://doi.org/10.1167/iovs.14-16028>
PMID:[25515574](https://pubmed.ncbi.nlm.nih.gov/25515574/)
55. Cheng C, Fowler VM, Gong X. EphA2 and ephrin-A5 are not a receptor-ligand pair in the ocular lens. *Exp Eye Res*. 2017; 162:9–17.
<https://doi.org/10.1016/j.exer.2017.06.016>
PMID:[28648759](https://pubmed.ncbi.nlm.nih.gov/28648759/)
56. Cheng C, Gong X. Diverse roles of Eph/ephrin signaling in the mouse lens. *PLoS One*. 2011; 6:e28147.
<https://doi.org/10.1371/journal.pone.0028147>
PMID:[22140528](https://pubmed.ncbi.nlm.nih.gov/22140528/)
57. Lovicu FJ, Schulz MW, Hales AM, Vincent LN, Overbeek PA, Chamberlain CG, McAvoy JW. TGFbeta induces morphological and molecular changes similar to human anterior subcapsular cataract. *Br J Ophthalmol*. 2002; 86:220–26.
<https://doi.org/10.1136/bjo.86.2.220>
PMID:[11815351](https://pubmed.ncbi.nlm.nih.gov/11815351/)
58. Lovicu FJ, Steven P, Saika S, McAvoy JW. Aberrant lens fiber differentiation in anterior subcapsular cataract formation: a process dependent on reduced levels of Pax6. *Invest Ophthalmol Vis Sci*. 2004; 45:1946–53.
<https://doi.org/10.1167/iovs.03-1206> PMID:[15161862](https://pubmed.ncbi.nlm.nih.gov/15161862/)
59. Srinivasan Y, Lovicu FJ, Overbeek PA. Lens-specific expression of transforming growth factor beta1 in transgenic mice causes anterior subcapsular cataracts. *J Clin Invest*. 1998; 101:625–34.
<https://doi.org/10.1172/JCI1360> PMID:[9449696](https://pubmed.ncbi.nlm.nih.gov/9449696/)
60. Bassnett S, Winzenburger PA. Morphometric analysis of fibre cell growth in the developing chicken lens. *Exp Eye Res*. 2003; 76:291–302.
[https://doi.org/10.1016/S0014-4835\(02\)00315-9](https://doi.org/10.1016/S0014-4835(02)00315-9)
PMID:[12573658](https://pubmed.ncbi.nlm.nih.gov/12573658/)
61. Cheng C, Nowak RB, Amadeo MB, Biswas SK, Lo WK, Fowler VM. Tropomyosin 3.5 protects the F-actin networks required for tissue biomechanical properties. *J Cell Sci*. 2018; 131:131.
<https://doi.org/10.1242/jcs.222042> PMID:[30333143](https://pubmed.ncbi.nlm.nih.gov/30333143/)
62. Blankenship T, Bradshaw L, Shibata B, Fitzgerald P. Structural specializations emerging late in mouse lens fiber cell differentiation. *Invest Ophthalmol Vis Sci*. 2007; 48:3269–76.
<https://doi.org/10.1167/iovs.07-0109> PMID:[17591898](https://pubmed.ncbi.nlm.nih.gov/17591898/)
63. Lo WK, Biswas SK, Brako L, Shiels A, Gu S, Jiang JX. Aquaporin-0 targets interlocking domains to control the integrity and transparency of the eye lens. *Invest Ophthalmol Vis Sci*. 2014; 55:1202–12.
<https://doi.org/10.1167/iovs.13-13379>
PMID:[24458158](https://pubmed.ncbi.nlm.nih.gov/24458158/)
64. Kuwabara T. The maturation of the lens cell: a morphologic study. *Exp Eye Res*. 1975; 20:427–43.
[https://doi.org/10.1016/0014-4835\(75\)90085-8](https://doi.org/10.1016/0014-4835(75)90085-8)
PMID:[1126408](https://pubmed.ncbi.nlm.nih.gov/1126408/)
65. Willekens B, Vrensen G. The three-dimensional organization of lens fibers in the rabbit. A scanning electron microscopic reinvestigation. *Albrecht Von Graefes Arch Klin Exp Ophthalmol*. 1981; 216:275–89.
<https://doi.org/10.1007/BF00455035> PMID:[6910997](https://pubmed.ncbi.nlm.nih.gov/6910997/)
66. Willekens B, Vrensen G. The three-dimensional organization of lens fibers in the rhesus monkey. *Graefes Arch Clin Exp Ophthalmol*. 1982; 219:112–20.
<https://doi.org/10.1007/BF02152295> PMID:[7173625](https://pubmed.ncbi.nlm.nih.gov/7173625/)
67. Wilson C, Terman JR, González-Billault C, Ahmed G. Actin filaments-A target for redox regulation. *Cytoskeleton (Hoboken)*. 2016; 73:577–95.
<https://doi.org/10.1002/cm.21315> PMID:[27309342](https://pubmed.ncbi.nlm.nih.gov/27309342/)
68. Liou W, Rafferty NS. Actin filament patterns in mouse lens epithelium: a study of the effects of aging, injury, and genetics. *Cell Motil Cytoskeleton*. 1988; 9:17–29.
<https://doi.org/10.1002/cm.970090104> PMID:[3356044](https://pubmed.ncbi.nlm.nih.gov/3356044/)
69. Weber GF, Menko AS. Actin filament organization regulates the induction of lens cell differentiation and survival. *Dev Biol*. 2006; 295:714–29.
<https://doi.org/10.1016/j.ydbio.2006.03.056>
PMID:[16678812](https://pubmed.ncbi.nlm.nih.gov/16678812/)
70. Rafferty NS. *Lens Morphology*. New York: Dekker; 1985.
71. Rafferty NS, Scholz DL. Actin in polygonal arrays of microfilaments and sequestered actin bundles (SABs) in lens epithelial cells of rabbits and mice. *Curr Eye Res*. 1985; 4:713–18.
<https://doi.org/10.3109/02713688509017667>
PMID:[4040842](https://pubmed.ncbi.nlm.nih.gov/4040842/)
72. Scholz DL, Rafferty NS. Immunogold-EM localization of actin and vimentin filaments in relation to polygonal arrays in lens epithelium in situ. *Curr Eye Res*. 1988; 7:705–19.
<https://doi.org/10.3109/02713688809033200>
PMID:[3046843](https://pubmed.ncbi.nlm.nih.gov/3046843/)
73. Rafferty NS, Scholz DL. Comparative study of actin filament patterns in lens epithelial cells. Are these

- determined by the mechanisms of lens accommodation? *Curr Eye Res.* 1989; 8:569–79.
<https://doi.org/10.3109/02713688908995756>
 PMID:[2743796](https://pubmed.ncbi.nlm.nih.gov/2743796/)
74. Rafferty NS, Scholz DL. Polygonal arrays of microfilaments in epithelial cells of the intact lens. *Curr Eye Res.* 1984; 3:1141–49.
<https://doi.org/10.3109/02713688409000814>
 PMID:[6541556](https://pubmed.ncbi.nlm.nih.gov/6541556/)
 75. Rafferty NS, Scholz DL, Goldberg M, Lewyckij M. Immunocytochemical evidence for an actin-myosin system in lens epithelial cells. *Exp Eye Res.* 1990; 51:591–600.
[https://doi.org/10.1016/0014-4835\(90\)90090-H](https://doi.org/10.1016/0014-4835(90)90090-H)
 PMID:[2249732](https://pubmed.ncbi.nlm.nih.gov/2249732/)
 76. Flurkey K, Currer J, Harrison D. *The Mouse in Aging Research.* 2007.
<https://doi.org/10.1016/B978-012369454-6/50074-1>
 77. Kunstyr I, Leuenberger HG. Gerontological data of C57BL/6J mice. I. Sex differences in survival curves. *J Gerontol.* 1975; 30:157–62.
<https://doi.org/10.1093/geronj/30.2.157>
 PMID:[1123533](https://pubmed.ncbi.nlm.nih.gov/1123533/)
 78. Gao J, Wang H, Sun X, Varadaraj K, Li L, White TW, Mathias RT. The effects of age on lens transport. *Invest Ophthalmol Vis Sci.* 2013; 54:7174–87.
<https://doi.org/10.1167/iovs.13-12593>
 PMID:[24065810](https://pubmed.ncbi.nlm.nih.gov/24065810/)
 79. Cheng C, Xia CH, Li L, White TW, Niimi J, Gong X. Gap junction communication influences intercellular protein distribution in the lens. *Exp Eye Res.* 2008; 86:966–74.
<https://doi.org/10.1016/j.exer.2008.03.015>
 PMID:[18462719](https://pubmed.ncbi.nlm.nih.gov/18462719/)
 80. Wang H, Gao J, Sun X, Martinez-Wittinghan FJ, Li L, Varadaraj K, Farrell M, Reddy VN, White TW, Mathias RT. The effects of GPX-1 knockout on membrane transport and intracellular homeostasis in the lens. *J Membr Biol.* 2009; 227:25–37.
<https://doi.org/10.1007/s00232-008-9141-5>
 PMID:[19067024](https://pubmed.ncbi.nlm.nih.gov/19067024/)
 81. Moffat BA, Landman KA, Truscott RJ, Sweeney MH, Pope JM. Age-related changes in the kinetics of water transport in normal human lenses. *Exp Eye Res.* 1999; 69:663–69.
<https://doi.org/10.1006/exer.1999.0747>
 PMID:[10620395](https://pubmed.ncbi.nlm.nih.gov/10620395/)
 82. Sweeney MH, Truscott RJ. An impediment to glutathione diffusion in older normal human lenses: a possible precondition for nuclear cataract. *Exp Eye Res.* 1998; 67:587–95.
<https://doi.org/10.1006/exer.1998.0549>
 PMID:[9878221](https://pubmed.ncbi.nlm.nih.gov/9878221/)
 83. Truscott RJ. Age-related nuclear cataract-oxidation is the key. *Exp Eye Res.* 2005; 80:709–25.
<https://doi.org/10.1016/j.exer.2004.12.007>
 PMID:[15862178](https://pubmed.ncbi.nlm.nih.gov/15862178/)
 84. Grey AC, Jacobs MD, Gonen T, Kistler J, Donaldson PJ. Insertion of MP20 into lens fibre cell plasma membranes correlates with the formation of an extracellular diffusion barrier. *Exp Eye Res.* 2003; 77:567–74.
[https://doi.org/10.1016/S0014-4835\(03\)00192-1](https://doi.org/10.1016/S0014-4835(03)00192-1)
 PMID:[14550398](https://pubmed.ncbi.nlm.nih.gov/14550398/)
 85. Vaghefi E, Donaldson PJ. The lens internal microcirculation system delivers solutes to the lens core faster than would be predicted by passive diffusion. *Am J Physiol Regul Integr Comp Physiol.* 2018; 315:R994–1002.
<https://doi.org/10.1152/ajpregu.00180.2018>
 PMID:[30156422](https://pubmed.ncbi.nlm.nih.gov/30156422/)
 86. Vaghefi E, Walker K, Pontre BP, Jacobs MD, Donaldson PJ. Magnetic resonance and confocal imaging of solute penetration into the lens reveals a zone of restricted extracellular space diffusion. *Am J Physiol Regul Integr Comp Physiol.* 2012; 302:R1250–59.
<https://doi.org/10.1152/ajpregu.00611.2011>
 PMID:[22496364](https://pubmed.ncbi.nlm.nih.gov/22496364/)
 87. Mathias RT, Rae JL, Baldo GJ. Physiological properties of the normal lens. *Physiol Rev.* 1997; 77:21–50.
<https://doi.org/10.1152/physrev.1997.77.1.21>
 PMID:[9016299](https://pubmed.ncbi.nlm.nih.gov/9016299/)
 88. Gao J, Sun X, Martinez-Wittinghan FJ, Gong X, White TW, Mathias RT. Connections between connexins, calcium, and cataracts in the lens. *J Gen Physiol.* 2004; 124:289–300.
<https://doi.org/10.1085/jgp.200409121>
 PMID:[15452195](https://pubmed.ncbi.nlm.nih.gov/15452195/)
 89. Cheng C, Nowak RB, Gao J, Sun X, Biswas SK, Lo WK, Mathias RT, Fowler VM. Lens ion homeostasis relies on the assembly and/or stability of large connexin 46 gap junction plaques on the broad sides of differentiating fiber cells. *Am J Physiol Cell Physiol.* 2015; 308:C835–47.
<https://doi.org/10.1152/ajpcell.00372.2014>
 PMID:[25740157](https://pubmed.ncbi.nlm.nih.gov/25740157/)
 90. Baldo GJ, Gong X, Martinez-Wittinghan FJ, Kumar NM, Gilula NB, Mathias RT. Gap junctional coupling in lenses from alpha(8) connexin knockout mice. *J Gen Physiol.* 2001; 118:447–56.
<https://doi.org/10.1085/jgp.118.5.447> PMID:[11696604](https://pubmed.ncbi.nlm.nih.gov/11696604/)
 91. Gao J, Minogue PJ, Beyer EC, Mathias RT, Berthoud VM. Disruption of the lens circulation causes calcium accumulation and precipitates in connexin mutant mice. *Am J Physiol Cell Physiol.* 2018; 314:C492–503.

- <https://doi.org/10.1152/ajpcell.00277.2017>
PMID:29351411
92. Gong X, Baldo GJ, Kumar NM, Gilula NB, Mathias RT. Gap junctional coupling in lenses lacking alpha3 connexin. *Proc Natl Acad Sci USA*. 1998; 95:15303–08.
<https://doi.org/10.1073/pnas.95.26.15303>
PMID:9860964
93. Costello MJ, Mohamed A, Gilliland KO, Fowler WC, Johnsen S. Ultrastructural analysis of the human lens fiber cell remodeling zone and the initiation of cellular compaction. *Exp Eye Res*. 2013; 116:411–18.
<https://doi.org/10.1016/j.exer.2013.10.015>
PMID:24183661
94. Taylor VL, al-Ghoul KJ, Lane CW, Davis VA, Kuszak JR, Costello MJ. Morphology of the normal human lens. *Invest Ophthalmol Vis Sci*. 1996; 37:1396–410.
[https://doi.org/10.1016/s0002-9394\(14\)72090-2](https://doi.org/10.1016/s0002-9394(14)72090-2)
PMID:8641842
95. Danysh BP, Czymmek KJ, Olurin PT, Sivak JG, Duncan MK. Contributions of mouse genetic background and age on anterior lens capsule thickness. *Anat Rec (Hoboken)*. 2008; 291:1619–27.
<https://doi.org/10.1002/ar.20753> PMID:18951502
96. Fisher RF, Pettet BE. The postnatal growth of the capsule of the human crystalline lens. *J Anat*. 1972; 112:207–14.
PMID:5077192
97. Krag S, Olsen T, Andreassen TT. Biomechanical characteristics of the human anterior lens capsule in relation to age. *Invest Ophthalmol Vis Sci*. 1997; 38:357–63.
PMID:9040468
98. Raghavan CT, Smuda M, Smith AJ, Howell S, Smith DG, Singh A, Gupta P, Glomb MA, Wormstone IM, Nagaraj RH. AGEs in human lens capsule promote the TGFβ2-mediated EMT of lens epithelial cells: implications for age-associated fibrosis. *Aging Cell*. 2016; 15:465–76.
<https://doi.org/10.1111/accel.12450> PMID:26853893
99. Dandia H, Makkad K, Tayalia P. Glycated collagen - a 3D matrix system to study pathological cell behavior. *Biomater Sci*. 2019; 7:3480–88.
<https://doi.org/10.1039/C9BM00184K> PMID:31282511
100. Oharazawa H, Ibaraki N, Matsui H, Ohara K. Age-related changes of human lens epithelial cells in vivo. *Ophthalmic Res*. 2001; 33:363–66.
<https://doi.org/10.1159/000055694> PMID:11721190
101. Balaram M, Tung WH, Kuszak JR, Ayaki M, Shinohara T, Chylack LT Jr. Noncontact specular microscopy of human lens epithelium. *Invest Ophthalmol Vis Sci*. 2000; 41:474–81.
PMID:10670478
102. Hara T, Hara T. Observations on lens epithelial cells and their removal in anterior capsule specimens. *Arch Ophthalmol*. 1988; 106:1683–87.
<https://doi.org/10.1001/archoph.1988.01060140855026> PMID:3058100
103. Pierscionek BK, Regini JW. The gradient index lens of the eye: an opto-biological synchrony. *Prog Retin Eye Res*. 2012; 31:332–49.
<https://doi.org/10.1016/j.preteyeres.2012.03.001>
PMID:22465790
104. Pierscionek B, Bahrami M, Hoshino M, Uesugi K, Regini J, Yagi N. The eye lens: age-related trends and individual variations in refractive index and shape parameters. *Oncotarget*. 2015; 6:30532–44.
<https://doi.org/10.18632/oncotarget.5762>
PMID:26416418
105. Pierscionek BK, Belaidi A, Bruun HH. Refractive index distribution in the porcine eye lens for 532 nm and 633 nm light. *Eye (Lond)*. 2005; 19:375–81.
<https://doi.org/10.1038/sj.eye.6701525>
PMID:15319785
106. Axelrod D, Lerner D, Sands PJ. Refractive index within the lens of a goldfish eye determined from the paths of thin laser beams. *Vision Res*. 1988; 28:57–65.
[https://doi.org/10.1016/S0042-6989\(88\)80006-3](https://doi.org/10.1016/S0042-6989(88)80006-3)
PMID:3413999
107. Bahrami M, Hoshino M, Pierscionek B, Yagi N, Regini J, Uesugi K. Optical properties of the lens: an explanation for the zones of discontinuity. *Exp Eye Res*. 2014; 124:93–99.
<https://doi.org/10.1016/j.exer.2014.05.009>
PMID:24880144
108. Verma Y, Rao KD, Suresh MK, Patel HS, Gupta PK. Measurement of gradient refractive index profile of crystalline lens of fish eye in vivo using optical coherence tomography. *Appl Phys B*. 2007; 87:607–10.
<https://doi.org/10.1007/s00340-007-2689-4>
109. Kozłowski TM, Kröger RH. Visualization of adult fish lens fiber cells. *Exp Eye Res*. 2019; 181:1–4.
<https://doi.org/10.1016/j.exer.2018.12.013>
PMID:30579924
110. Faulkner-Jones B, Zandy AJ, Bassnett S. RNA stability in terminally differentiating fibre cells of the ocular lens. *Exp Eye Res*. 2003; 77:463–76.
[https://doi.org/10.1016/S0014-4835\(03\)00172-6](https://doi.org/10.1016/S0014-4835(03)00172-6)
PMID:12957145
111. Bassnett S, Costello MJ. The cause and consequence of fiber cell compaction in the vertebrate lens. *Exp Eye Res*. 2017; 156:50–57.
<https://doi.org/10.1016/j.exer.2016.03.009>
PMID:26992780

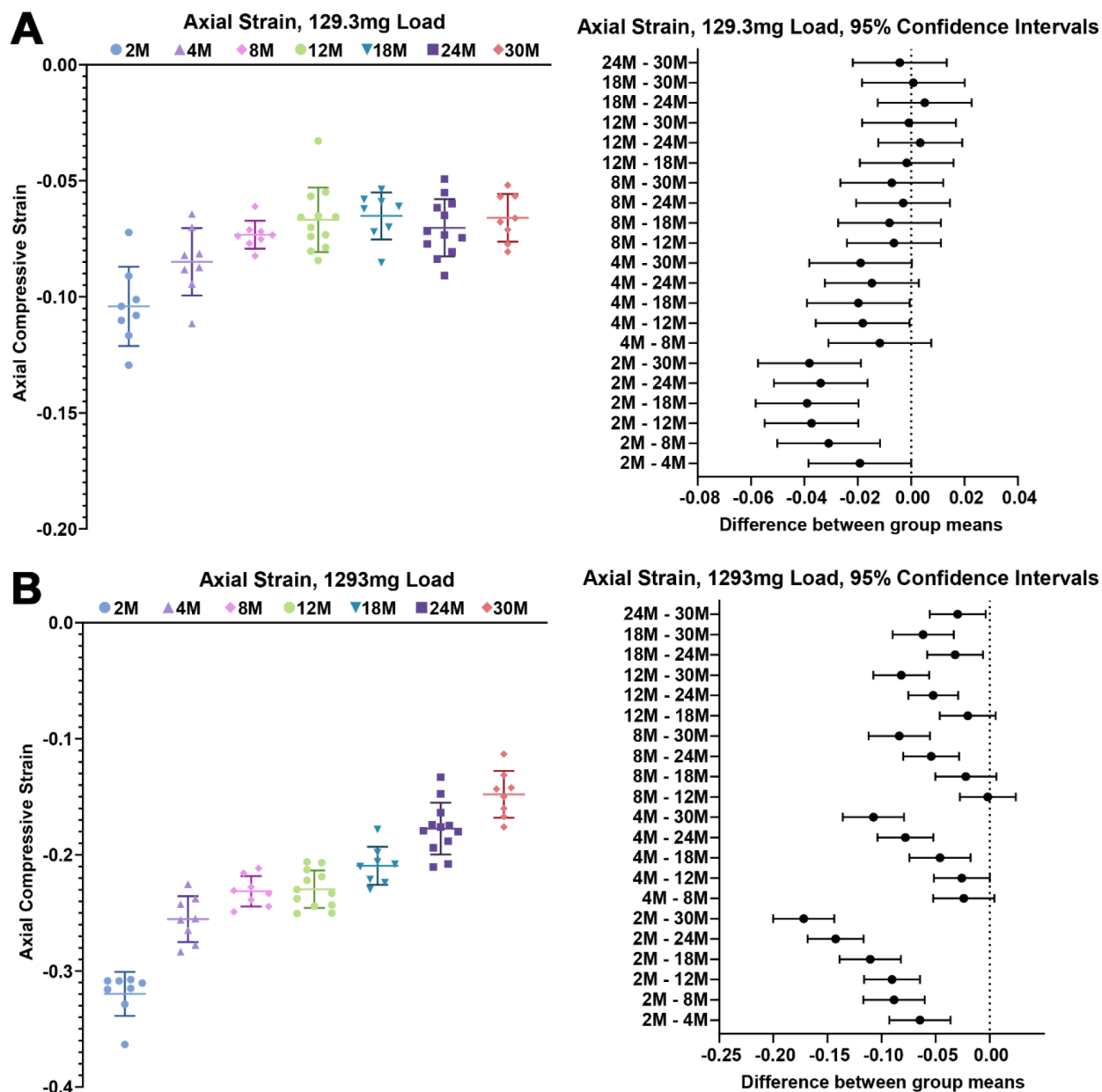
112. Heys KR, Friedrich MG, Truscott RJ. Free and bound water in normal and cataractous human lenses. *Invest Ophthalmol Vis Sci.* 2008; 49:1991–97. <https://doi.org/10.1167/iovs.07-1151> PMID:[18436831](https://pubmed.ncbi.nlm.nih.gov/18436831/)
113. Kozłowski TM, Kröger RH. Constant lens fiber cell thickness in fish suggests crystallin transport to denucleated cells. *Vision Res.* 2019; 162:29–34. <https://doi.org/10.1016/j.visres.2019.06.008> PMID:[31278970](https://pubmed.ncbi.nlm.nih.gov/31278970/)
114. Pierscionek BK, Belaidi A, Bruun HH. Optical development in the foetal bovine lens. *Exp Eye Res.* 2003; 77:639–41. [https://doi.org/10.1016/S0014-4835\(03\)00221-5](https://doi.org/10.1016/S0014-4835(03)00221-5) PMID:[14550406](https://pubmed.ncbi.nlm.nih.gov/14550406/)
115. Hughes ED, Qu YY, Genik SJ, Lyons RH, Pacheco CD, Lieberman AP, Samuelson LC, Nasonkin IO, Camper SA, Van Keuren ML, Saunders TL. Genetic variation in C57BL/6 ES cell lines and genetic instability in the Bruce4 C57BL/6 ES cell line. *Mamm Genome.* 2007; 18:549–58. <https://doi.org/10.1007/s00335-007-9054-0> PMID:[17828574](https://pubmed.ncbi.nlm.nih.gov/17828574/)
116. Townsend D, Witkop CJ Jr, Mattson J. Tyrosinase subcellular distribution and kinetic parameters in wild type and C-locus mutant C57BL/6J mice. *J Exp Zool.* 1981; 216:113–19. <https://doi.org/10.1002/jez.1402160112> PMID:[6793688](https://pubmed.ncbi.nlm.nih.gov/6793688/)
117. Muzumdar MD, Tasic B, Miyamichi K, Li L, Luo L. A global double-fluorescent Cre reporter mouse. *Genesis.* 2007; 45:593–605. <https://doi.org/10.1002/dvg.20335> PMID:[17868096](https://pubmed.ncbi.nlm.nih.gov/17868096/)
118. Simirskii VN, Lee RS, Wawrousek EF, Duncan MK. Inbred FVB/N mice are mutant at the cp49/Bfsp2 locus and lack beaded filament proteins in the lens. *Invest Ophthalmol Vis Sci.* 2006; 47:4931–34. <https://doi.org/10.1167/iovs.06-0423> PMID:[17065509](https://pubmed.ncbi.nlm.nih.gov/17065509/)
119. Alizadeh A, Clark J, Seeberger T, Hess J, Blankenship T, FitzGerald PG. Characterization of a mutation in the lens-specific CP49 in the 129 strain of mouse. *Invest Ophthalmol Vis Sci.* 2004; 45:884–91. <https://doi.org/10.1167/iovs.03-0677> PMID:[14985306](https://pubmed.ncbi.nlm.nih.gov/14985306/)
120. Sandilands A, Wang X, Hutcheson AM, James J, Prescott AR, Wegener A, Pekny M, Gong X, Quinlan RA. Bfsp2 mutation found in mouse 129 strains causes the loss of CP49' and induces vimentin-dependent changes in the lens fibre cell cytoskeleton. *Exp Eye Res.* 2004; 78:875–89. <https://doi.org/10.1016/j.exer.2003.09.028> PMID:[15037121](https://pubmed.ncbi.nlm.nih.gov/15037121/)
121. Dixit R, Cyr R. Cell damage and reactive oxygen species production induced by fluorescence microscopy: effect on mitosis and guidelines for non-invasive fluorescence microscopy. *Plant J.* 2003; 36:280–90. <https://doi.org/10.1046/j.1365-313X.2003.01868.x> PMID:[14535891](https://pubmed.ncbi.nlm.nih.gov/14535891/)
122. Wäldchen S, Lehmann J, Klein T, van de Linde S, Sauer M. Light-induced cell damage in live-cell super-resolution microscopy. *Sci Rep.* 2015; 5:15348. <https://doi.org/10.1038/srep15348> PMID:[26481189](https://pubmed.ncbi.nlm.nih.gov/26481189/)
123. Gokhin DS, Fowler VM. Software-based measurement of thin filament lengths: an open-source GUI for Distributed Deconvolution analysis of fluorescence images. *J Microsc.* 2017; 265:11–20. <https://doi.org/10.1111/jmi.12456> PMID:[27644080](https://pubmed.ncbi.nlm.nih.gov/27644080/)
124. Lo WK. Adherens junctions in the ocular lens of various species: ultrastructural analysis with an improved fixation. *Cell Tissue Res.* 1988; 254:31–40. <https://doi.org/10.1007/BF00220014> PMID:[3143480](https://pubmed.ncbi.nlm.nih.gov/3143480/)
125. Momose A. Recent Advances in X-ray Phase Imaging. *Jpn J Appl Phys.* 2005; 44:6355–67. <https://doi.org/10.1143/JJAP.44.6355>
126. Momose A, Kawamoto S, Koyama I, Hamaishi Y, Takai K, Suzuki Y. Demonstration of X-Ray Talbot Interferometry. *Jpn J Appl Phys.* 2003; 42:L866–68. <https://doi.org/10.1143/JJAP.42.L866>
127. Hoshino M, Uesugi K, Yagi N, Mohri S, Regini J, Pierscionek B. Optical properties of in situ eye lenses measured with X-ray Talbot interferometry: a novel measure of growth processes. *PLoS One.* 2011; 6:e25140. <https://doi.org/10.1371/journal.pone.0025140> PMID:[21949870](https://pubmed.ncbi.nlm.nih.gov/21949870/)
128. Hoshino M, Uesugi K, Yagi N, Mohri S, Siu KK. Investigation of Imaging Properties of Mouse Eyes Using X-ray Phase Contrast Tomography. *AIP Conf Proc.* 2010; 1266:57–61. <https://doi.org/10.1063/1.3478199>
129. Barer R, Joseph S. *Refractometry of Living Cells. Part I Basic Principles.* 1954; s3-95:399–423.

SUPPLEMENTARY MATERIALS

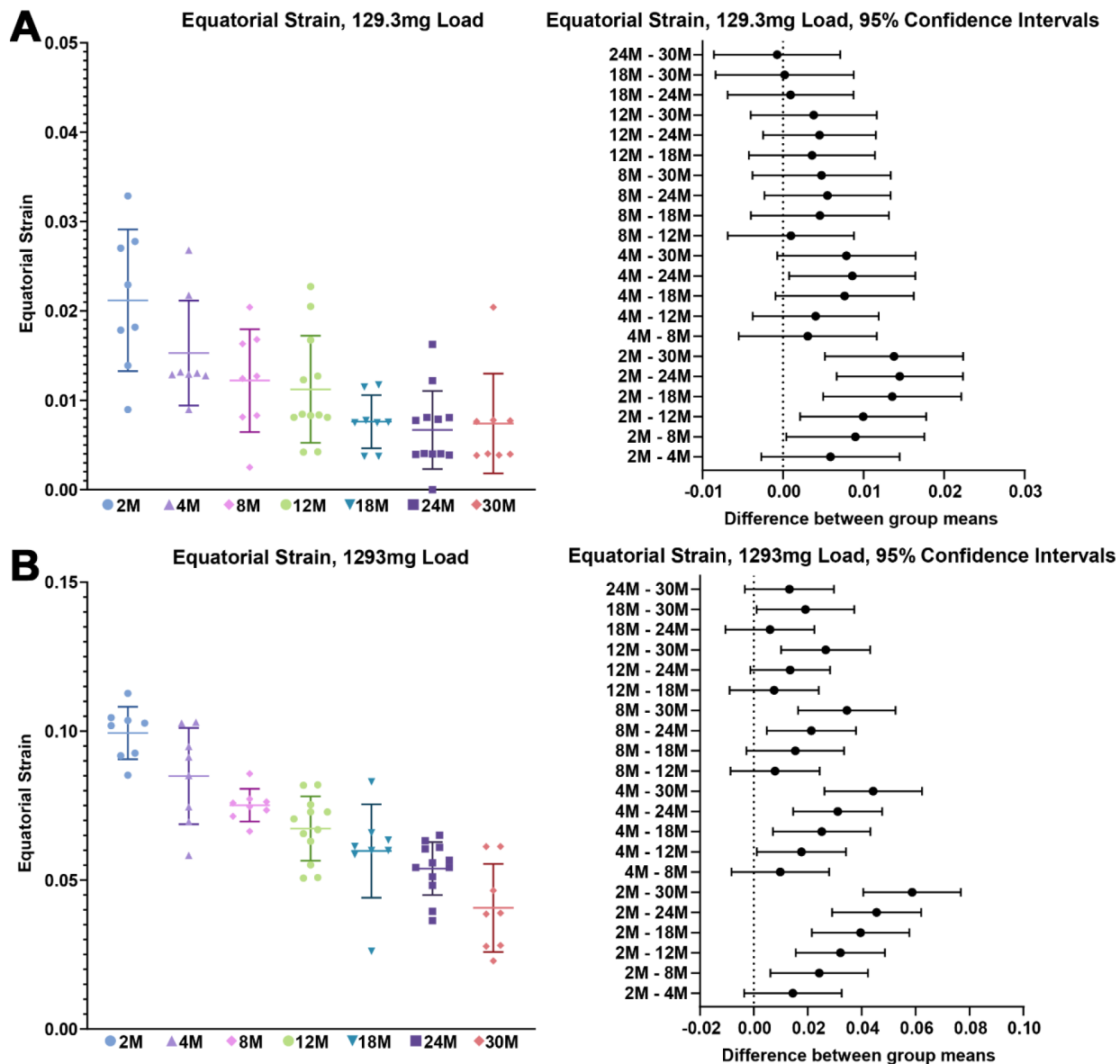


Supplementary Figure 1. Lens anatomy diagrams. (A) A cartoon (not drawn to scale) depicting a longitudinal section of the lens shows a monolayer of epithelial cells at the anterior surface (colored cells) and a bulk mass of elongated lens fibers (white cells) that extend from the anterior to posterior poles. The entire tissue is encapsulated by a thin collagenous basement membrane called the lens capsule. Anterior epithelial cells (blue) are quiescent and do not proliferate. These cells are cobblestone in shape, and their main function is to maintain the

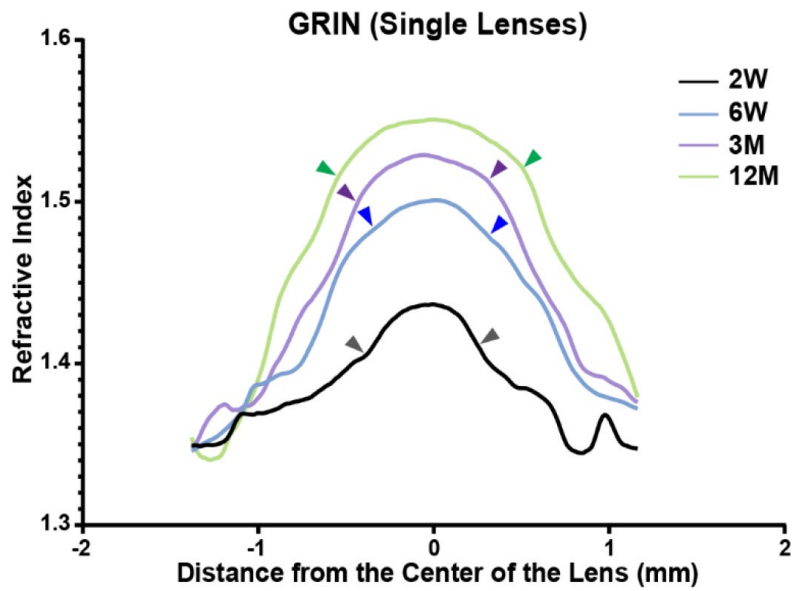
underlying fiber cells. Lifelong lens growth relies on the proliferation, migration and differentiation of equatorial epithelial cells (orange) in the germinative zone. Equatorial epithelial cells undergo a remarkable morphogenesis to transform from randomly organized cuboidal cells (orange) into organized rows with hexagon cell shape (green). A cross section through the fiber cells reveals that the organization and hexagon cell shape of the equatorial epithelial cells are retained in fiber cells. New layers of lens fiber cells are continuously added onto previous generations of fibers, and the lens grows in concentric shells. Newly formed fiber cells elongate toward the anterior and posterior poles. The apical tips of newly formed fibers migrate along the apical surface of epithelial cells toward the anterior pole while the basal tip of the newly formed fibers migrate along the lens capsule toward the posterior pole. At each pole, the elongating fibers will detach from the epithelial cells or lens capsule and contact the elongating fiber from the other side of the lens forming the Y-suture. Differentiating fiber cells also undergo a maturation process and lose all of their organelles to allow for a clear light path. The mature fiber cells in the middle of the lens without cellular organelles have very low metabolism and little or no protein turnover. The lens nucleus is composed of tightly compacted fiber cells in the middle of the lens (purple). **(B)** Diagram of a lens equatorial cross-section (not drawn to scale, modified from [51]). Epithelial cells (Epi) are on the periphery. Fiber cells are hexagonal in cross section with newly formed cells on the left (next to the epithelial cells) and maturing cells moving toward the right in concentric layers. **(C)** Scanning electron microscopy (SEM) at various depths in 3-month-old wild-type (WT) lenses (modified from [50]). Colored boxed regions indicate the approximate location where higher magnification images (lower panel) were obtained. Single fiber cells are highlighted in green as a comparison of the change in cell morphology during lens fiber maturation. Newly formed fiber cells in the cortex are straight with ball-and-socket protrusions along the broad sides and small protrusions along the short sides (red box). During maturation, differentiating fiber cells form larger protrusions along the short sides (green box). Mature inner fiber cells have large paddle domains decorated by small protrusions (blue box). These interlocking membrane interdigitations are thought to be important for mechanical stability in the lens. Scale bars, 50 μ m and 6 μ m in **(B)**.



Supplementary Figure 2. Dot plots of axial strain at the lowest load (129.3mg, 1 coverslip) and the maximum load (1293mg, 10 coverslips). Lines on the plots reflect mean \pm SD of $n =$ at least 8 lenses per age. The graph below the data plots shows the 95% confidence interval. Any comparisons not crossing the dotted line are statistically significant ($p < 0.05$). (A, B) Axial strain at the lowest load (129.3mg) decreased between 2 and 8 months of age but remained unchanged after 4 months of age. Axial strain was decreased with age at the highest load (1293mg).



Supplementary Figure 3. Dot plots of equatorial strain at the lowest load (129.3mg, 1 coverslip) and the maximum load (1293mg, 10 coverslips). Lines on the plots reflect mean \pm SD of $n =$ at least 8 lenses per age. The graph below the data plots shows the 95% confidence interval. Any comparisons not crossing the dotted line are statistically significant ($p < 0.05$). (A, B) Equatorial strain at the lowest load was decreased between 2 and 8 months of age with no significant change after 4 months of age. Equatorial strain at the highest load was generally decreased with age. These data suggest that the lens cortex, which is compressed at the lowest load, does not stiffen much with age after 4 months.



Supplementary Figure 4. Single GRIN profile plots from selected ages reveal the discontinuity in GRIN profile distinguishing the cap region from the bottom region. The curvature of the GRIN profile is therefore different in the center and periphery of the lens. The discontinuities are marked by pairs of arrowheads. The arrowheads mark the approximate location of the boundary between the nucleus and the cortex.

Pineal gland volume is associated with prevalent and incident isolated rapid eye movement sleep behavior disorder

Jeongbin Park¹, Ji Won Han², Seung Wan Suh², Seonjeong Byun², Ji Hyun Han², Jong Bin Bae², Jae Hyoung Kim^{3,4}, Ki Woong Kim^{1,2,5}

¹Department of Brain and Cognitive Science, Seoul National University College of Natural Sciences, Seoul, Korea

²Department of Neuropsychiatry, Seoul National University Bundang Hospital, Seongnam, Korea

³Department of Radiology, Seoul National University Bundang Hospital, Seongnam, Korea

⁴Department of Radiology, Seoul National University College of Medicine, Seoul, Korea

⁵Department of Psychiatry, Seoul National University College of Medicine, Seoul, Korea

Correspondence to: Ki Woong Kim; email: kwkimmd@snu.ac.kr

Keywords: pineal gland, RBD, MRI, aging, prospective

Received: September 11, 2019

Accepted: December 24, 2019

Published: January 9, 2020

Copyright: Park et al. This is an open-access article distributed under the terms of the Creative Commons Attribution License (CC BY 3.0), which permits unrestricted use, distribution, and reproduction in any medium, provided the original author and source are credited.

ABSTRACT

We aimed to investigate the association of pineal gland volume with the risk of isolated rapid eye movement (REM) sleep behavior disorder (RBD). We enrolled 245 community-dwelling cognitively normal elderly individuals without major psychiatric or neurological disorders at the baseline evaluation, of whom 146 completed the 2-year follow-up evaluation. We assessed RBD symptoms using the REM Sleep Behavior Disorder Screening Questionnaire (RBDSQ) and defined probable RBD (pRBD) as an RBDSQ score of ≥ 5 . We manually segmented the pineal gland on 3T T1-weighted brain magnetic resonance imaging and estimated its volume. The smaller the baseline pineal gland volume, the more severe the RBD symptoms at baseline. The individuals with isolated pRBD showed smaller pineal gland volumes than those without isolated pRBD. The larger the baseline pineal gland volume, the lower the risks of prevalent isolated pRBD at the baseline evaluation and incident isolated pRBD at the 2-year follow-up evaluation. Pineal gland volume showed good diagnostic accuracy for prevalent isolated pRBD and predictive accuracy for incident isolated pRBD in the receiver operator characteristic analysis. Our findings suggest that pineal gland volume may be associated with the severity of RBD symptoms and the risk of isolated RBD in cognitively normal elderly individuals.

INTRODUCTION

Rapid eye movement (REM) sleep behavior disorder (RBD) is a parasomnia characterized by the loss of normal skeletal muscle atonia during REM sleep and dream-enacting behaviors [1]. Its prevalence was estimated to be 1-2% in the general elderly populations [2, 3]. RBD can occur in association with (secondary RBD) or without (isolated RBD) a neurodegenerative disorder [1], and isolated RBD accounts for up to 60% at the diagnosis [4]. However, more than 80% of isolated RBD eventually developed a neurodegenerative disorder such as Parkinson's disease (PD) and Lewy

body disease (DLB) in 12-14 years [5, 6], which implies that a majority of isolated RBD may be a prodromal phase of α -synucleinopathies [1, 4].

A series of clinical trials found that the symptoms of RBD were improved by N-acetyl-5-methoxytryptamine (melatonin). In RBD patients, dream-enacting behaviors were reduced and REM sleep muscle atonia were restored by the administration of melatonin [7-11] but relapsed by discontinuation of melatonin [8]. Melatonin is a multifunctioning indoleamine produced by the pineal gland [12]. The pineal gland regulates sleep and circadian rhythm through the synthesis and secretion of

melatonin [12, 13]. In humans, roughly 80% of the pineal gland is composed of melatonin-producing pinealocytes [13], and the volume of pineal gland (VPG) is proportional to the levels of melatonin in plasma, urine or saliva [14–16]. Although the pineal gland is reported to fully develop after the first year of life and does not change in size or weight later in life [12, 17, 18], recent studies have found that VPG could be changed by lifestyle such as coffee consumption or pathological conditions that may change melatonin production [19–21]. Given the effects of melatonin on RBD symptoms and the association of melatonin with VPG [14–16], we may assume that RBD patients may have smaller VPG than the individuals without RBD, and VPG may predict the future risk of RBD in the individuals without RBD. In this study, we investigated the association of VPG with current RBD symptoms cross-sectionally and with the future risk of RBD symptoms prospectively in cognitively normal (CN) elderly individuals without neurological or psychiatric disorders.

RESULTS

The demographic and clinical characteristics of the participants are summarized in Table 1. The participants with probable RBD (pRBD) showed smaller volume of pineal parenchyma (VPP) and VPG than those without pRBD ($p < 0.001$).

Both VPP and VPG were inversely associated with the REM Sleep Behavior Disorder Screening Questionnaire (RBDSQ) total score (RBDSQ-T) (standardized $\beta = -0.352$, $p < 0.001$ for VPP; standardized $\beta = -0.301$, $p < 0.001$ for VPG) and the item 6 score of the RBDSQ (RBDSQ-6) (standardized $\beta = -0.239$, $p < 0.001$ for VPP; standardized $\beta = -0.198$, $p = 0.002$ for VPG), indicating that the individuals with smaller VPP or VPG may have more RBD symptoms (Figure 1). There was no evidence of multicollinearity in all regression models with the maximum variance inflation factor being 2.05.

Baseline VPP and VPG were inversely associated with the risk of prevalent pRBD at the baseline evaluation (odds ratio [OR] = 0.939, 95% CI = 0.912 - 0.966, $p < 0.001$ for VPP; OR = 0.947, 95% CI = 0.924 - 0.972, $p < 0.001$ for VPG), indicating that the individuals with larger VPP and VPG may have a lower risk of prevalent pRBD (Table 2). The baseline VPP and VPG were also inversely associated with the risk of incident pRBD at the 2-year follow-up evaluation (OR = 0.890, 95% CI = 0.798 - 0.993, $p = 0.036$ for VPP; OR = 0.912, 95% CI = 0.832 - 0.999, $p = 0.047$ for VPG), indicating that the individuals with larger VPP and VPG may have a lower risk of future pRBD (Table 2).

The diagnostic accuracies of the baseline VPP and VPG for prevalent pRBD at the baseline evaluation were good; area under the receiver operator characteristic curve (AUC) was 0.82 (95% CI = 0.762 - 0.863, $p < 0.0001$) for VPP and 0.81 (95% CI = 0.749 - 0.852, $p < 0.0001$) for VPG (Figure 2). The optimal cutoff values of the baseline VPP and VPG for classifying pRBD were 70 mm³ (sensitivity = 87.50%; specificity = 70.59%) and 77 mm³ (sensitivity = 83.33%; specificity = 64.25%), respectively. The predictive accuracies of baseline VPP and VPG for incident pRBD at the 2-year follow-up evaluation were also good; AUC was 0.89 (95% CI = 0.821 - 0.932, $p < 0.0001$) for VPP and 0.87 (95% CI = 0.799 - 0.916, $p < 0.0001$) for VPG (Figure 2). The optimal cutoff values of the baseline VPP and VPG for predicting incident pRBD at 2-year follow-up evaluation were 65 mm³ (sensitivity = 100.00%; specificity = 83.10%) and 69 mm³ (sensitivity = 100.00%; specificity = 78.87%), respectively.

DISCUSSION

In animals, nighttime REM sleep disturbances were induced by lesioning the pineal gland, which reduced pineal melatonin secretion [22]. However, the association between the pineal gland and RBD has never been investigated in humans. The current study directly showed that smaller pineal gland was associated with the more RBD symptoms and the higher risk of incident pRBD in CN elderly individuals.

Considering that the pineal gland volume was highly correlated with the endogenous melatonin level [14–16], our observation seems to be in line with previous studies on the effects of melatonin on RBD. Melatonin treatment decreased the frequency and severity of dream-enacting behaviors and the risk of falls in the elderly RBD patients [10], and the beneficial effects of melatonin (3–12 mg) lasted beyond a year in a series of RBD patients [9]. A couple of clinical trials on the polysomnography-diagnosed RBD patients found that the percentage of REM sleep without atonia and movement time in REM were reduced by administering melatonin before bedtime for 4–6 weeks [7, 8] but relapsed by discontinuing melatonin [8]. Another open-label trial reported that the percentage of tonic REM activity was reduced from 16% to 6% by administering 3–9 mg of melatonin at night, especially in the elderly patients with low endogenous melatonin secretion [23]. A placebo-controlled trial also reported that the percentage of REM sleep increased from 14.7% to 17.8% and the clinical global impression and daytime dysfunction were improved by administering 3 mg melatonin before bedtime in the individuals with disturbed and reduced REM sleep duration [11]. However, it remains unknown how melatonin improves

Table 1. Demographic and clinical characteristics of the participants.

	Prevalent pRBD at baseline			Incident pRBD at 2-year follow-up		
	Absent (n = 221)	Present (n = 24)	p	Absent (n = 142)	Present (n = 4)	p
Age (years, mean ± SD)	71.79 ± 6.17	72.50 ± 6.16	0.594 ^a	70.70 ± 5.87	76.00 ± 7.96	0.080 ^a
Women, n (%)	114 (51.58)	11 (45.83)	0.592 ^b	72 (50.70)	1 (25.00)	0.311 ^b
Education (years, mean ± SD)	11.43 ± 4.93	10.42 ± 5.03	0.341 ^a	11.35 ± 5.11	13.75 ± 4.03	0.352 ^a
Presence of cohabitants, n (%)	191 (86.43)	23 (95.83)	0.188 ^b	124 (87.32)	3 (75.00)	0.470 ^b
Alcohol drinking (standard units/week, mean ± SD)	3.03 ± 7.66	6.00 ± 11.17	0.215 ^a	3.67 ± 8.86	3.63 ± 5.71	0.992 ^a
Smoking (packs/day, mean ± SD)	0.03 ± 0.18	0.02 ± 0.08	0.797 ^a	0.04 ± 0.21	0.00 ± 0.00	0.680 ^a
History of head injury, n (%)	11 (4.98)	1 (4.17)	0.861 ^b	8 (5.63)	0 (0.00)	0.625 ^b
MMSE (points, mean ± SD)	27.40 ± 2.06	27.17 ± 2.81	0.616 ^a	27.29 ± 2.11	27.00 ± 0.82	0.786 ^a
GDS (points, mean ± SD)	7.71 ± 5.63	9.93 ± 7.69	0.199 ^a	7.49 ± 5.68	12.00 ± 6.38	0.121 ^a
CIRS (points, mean ± SD)	5.62 ± 2.83	6.33 ± 2.46	0.237 ^a	5.09 ± 2.64	6.50 ± 3.42	0.298 ^a
STOPBANG (points, mean ± SD)	2.54 ± 0.94	2.96 ± 0.75	0.037 ^a	2.50 ± 0.95	3.25 ± 0.96	0.121 ^a
RBDSQ (points, mean ± SD)						
Total score	1.48 ± 1.26	5.79 ± 1.22	< 0.001 ^a	1.37 ± 1.21	3.00 ± 1.16	0.009 ^a
Item 6 score	0.12 ± 0.37	1.17 ± 1.05	< 0.001 ^a	0.10 ± 0.32	0.75 ± 0.96	0.267 ^a
Intracranial volume (cm ³ , mean ± SD)	1565.40 ± 160.86	1553.13 ± 170.68	0.725 ^a	1576.95 ± 156.49	1530.15 ± 66.05	0.553 ^a
VPP (mm ³ , mean ± SD)	87.55 ± 30.04	58.42 ± 16.49	< 0.001 ^c	90.13 ± 30.15	53.00 ± 20.07	0.016 ^a
VPG (mm ³ , mean ± SD)	95.18 ± 39.96	61.13 ± 18.30	< 0.001 ^c	98.58 ± 42.12	56.25 ± 20.99	0.048 ^a

Abbreviations: pRBD = probable REM sleep behavior disorder; SD = standard deviation; MMSE = Mini-Mental State Examination; GDS = Geriatric Depression Scale; CIRS = Cumulative Illness Rating Scale; RBDSQ = REM Sleep Behavior Disorder Screening Questionnaire; VPP = pineal parenchyma volume; VPG = pineal gland volume.

^aIndependent sample t-test.

^bChi-square test.

^cAnalysis of covariance adjusted for age, sex, years of education, intracranial volume, head injury, amount of smoking, and amount of alcohol drinking.

the RBD symptoms. Multiple actions of melatonin such as decreasing muscle tonicity during REM sleep, enhancing GABAergic inhibition, stabilizing circadian clock variability and desynchronization, protecting cytoskeletal structure through its antagonism of calmodulin, enhancing sleep efficiency and shortening sleep latency may underlie its beneficial effect on RBD [1, 10]. In a glycine/GABA-A receptor knockout transgenic mouse model of RBD, melatonin was efficacious in decreasing REM motor behaviors and restoring REM muscle atonia [24].

VPP and VPG showed good diagnostic accuracy for prevalent pRBD and predictive accuracy for incident pRBD in the current study, indicating that VPP or VPG may be potential biomarkers of isolated RBD in

cognitively normal elderly individuals. However, the reduced VPP or VPG of the elderly individuals with isolated pRBD or those who are destined to have isolated pRBD in the future may be associated with prodromal α -synucleinopathies rather than RBD itself. Indeed, PD patients showed diminished endogenous melatonin production compared to controls [25]. In addition, melatonin directly blocked the α -synuclein fibril formation, destabilized preformed α -synuclein fibrils, and decreased α -synuclein-induced cytotoxicity [26]. Nevertheless, the changes of pineal gland volume in the patients with α -synucleinopathies have not been directly investigated yet.

This study has a couple of strengths. First, we excluded the volume of pineal cysts (VPC) when we

estimated the pineal parenchyma volume because pineal cysts do not contain pinealocytes [21, 27], and exclude the subjects with extremely large cystic glands from the current study. Although both VPP and VPG were associated with the prevalent and incident pRBD in the current study, pineal parenchyma volume (i.e., non-cystic volume) better reflected the levels of endogenous melatonin secretion than total pineal gland volume in adult individuals [14, 15]. Although we did not directly investigate the association between VPC and RBD, this result may suggest that the presence of the pineal cysts itself may not affect RBD symptoms. Second, we excluded the subjects who were depressive and/or were taking antidepressants since depression may increase the risk of RBD and antidepressants, selective serotonin reuptake inhibitor (SSRI) and serotonin norepinephrine reuptake inhibitor (SNRI) in particular, may produce dream-enacting behavior and loss of normal REM sleep atonia [1, 28]. However, this study also has several limitations. First, although the RBDSQ is well validated in polysomnography-confirmed RBD patients [1, 29], it may be subject to recall bias and misclassification bias. However, it seems unlikely that systematic errors would be made in reporting behavioral features of RBD since the current study included CN individuals who were examined only through comprehensive clinical and neuropsychological assessments. In addition, we tried to reduce the risk of misclassification bias by confirming the association of VPP and VPG with the RBDSQ item 6 score as well as RBDSQ total score. The RBDSQ item 6 queries the core symptoms of RBD with a good specificity [30]. Second, we cannot completely rule out the possibility that non-RBD

symptoms might have influence the RBDSQ scores. For example, some patients with restless leg syndrome (RLS) or severe obstructive sleep apnea (OSA) showed the behaviors mimicking RBD during sleep [31, 32]. Although we exclude the participants with OSA by excluding the participants who got 5 points or higher in STOPBANG, the participants with pRBD showed modestly higher STOPBANG score than those without pRBD at baseline. Third, we could not adjust for the volume of pineal calcification because we did not perform additional brain computed tomography or high-resolution T2-weighted MRI. Although the effects of pineal calcification on melatonin production or human REM sleep remain unclear, a couple of previous studies argue that pineal calcification may inhibit the capacity for pineal melatonin synthesis and be associated with polysomnographic sleep parameters in humans [19, 33]. Furthermore, calcifications can appear hypointense on T1-weighted images, which may lead underestimation of the VPP. Fourth, although we excluded individuals who took exogenous melatonin over the past 6 weeks, we did not directly quantify the endogenous nocturnal melatonin levels in the blood. Fifth, the sample size was small. In the statistical power analysis with α error probability of 0.05 (G*Power version 3.1; <http://www.gpower.hhu.de>), the statistical power (1-beta error) for the prevalent and incident pRBD was 0.52 and 0.54, respectively. However, the association of pineal gland volume and the prevalent and incident pRBD was statistically significant despite the low statistical power in the current study. Sixth, since the small number of converters at 2-year follow-up, the

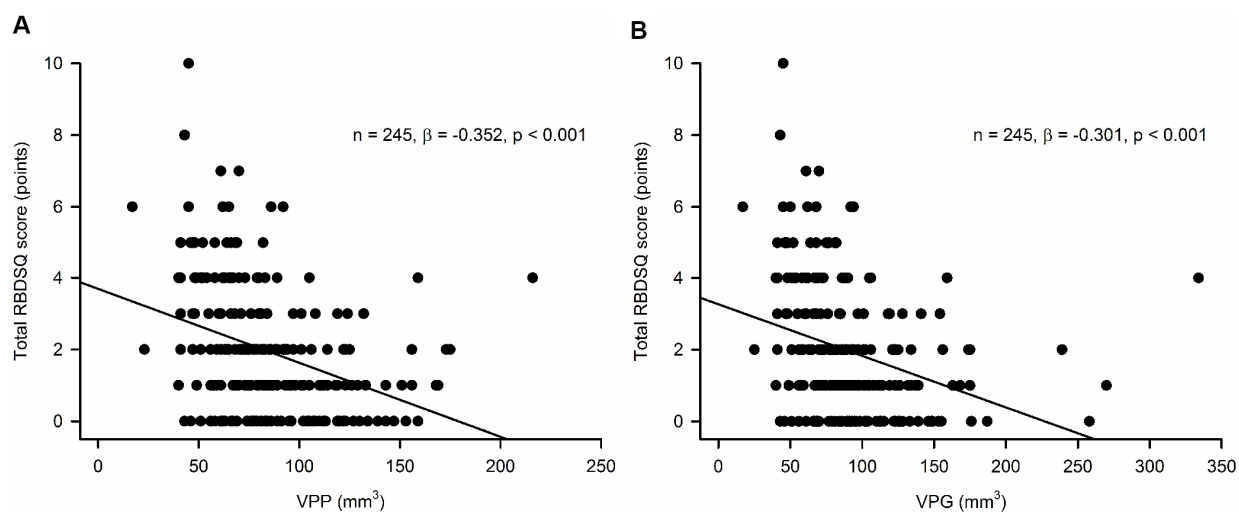


Figure 1. Association of (A) pineal parenchyma volume (VPP, mm³) and (B) pineal gland volume (VPG, mm³) with the REM Sleep Behavior Disorder Screening Questionnaire (RBDSQ) total score^a. ^aMultiple linear regression model adjusted for age, sex, years of education, intracranial volume, head injury, amount of smoking, and amount of alcohol drinking.

Table 2. Association of the baseline pineal parenchyma volume and pineal gland volume with the prevalent and incident probable REM sleep behavior disorder.

	Total, n	pRBD, n	OR (95% CI) ^a	p ^a
For prevalent pRBD				
VPP (mm ³)	245	24	0.939 (0.912 - 0.966)	< 0.001
VPG (mm ³)	245	24	0.947 (0.924 - 0.972)	< 0.001
For incident pRBD				
VPP (mm ³)	146 ^b	4	0.890 (0.798 - 0.993)	0.036
VPG (mm ³)	146 ^b	4	0.912 (0.832 - 0.999)	0.047

Abbreviations: pRBD = probable REM sleep behavior disorder; VPP = pineal parenchyma volume; VPG = pineal gland volume; OR = odds ratio; CI = confidence interval.

^aBinary logistic regression analyses adjusting age, sex, years of education, intracranial volume, head injury, amount of smoking, and amount of alcohol drinking at the baseline evaluation as covariates.

^bThe number of participants who did not have probable RBD at the baseline evaluation and completed the 2-year follow-up evaluation.

accuracies of cutoff values of the baseline VPP and VPG for predicting incident pRBD may need to be further validated in future studies with a larger sample size and longer follow-up. Finally, the follow-up duration was short.

In summary, the smaller pineal gland was associated with the more current RBD symptoms and the higher future risk of RBD in cognitively normal elderly individuals, and VPP or VPG may be a candidate biomarker of RBD.

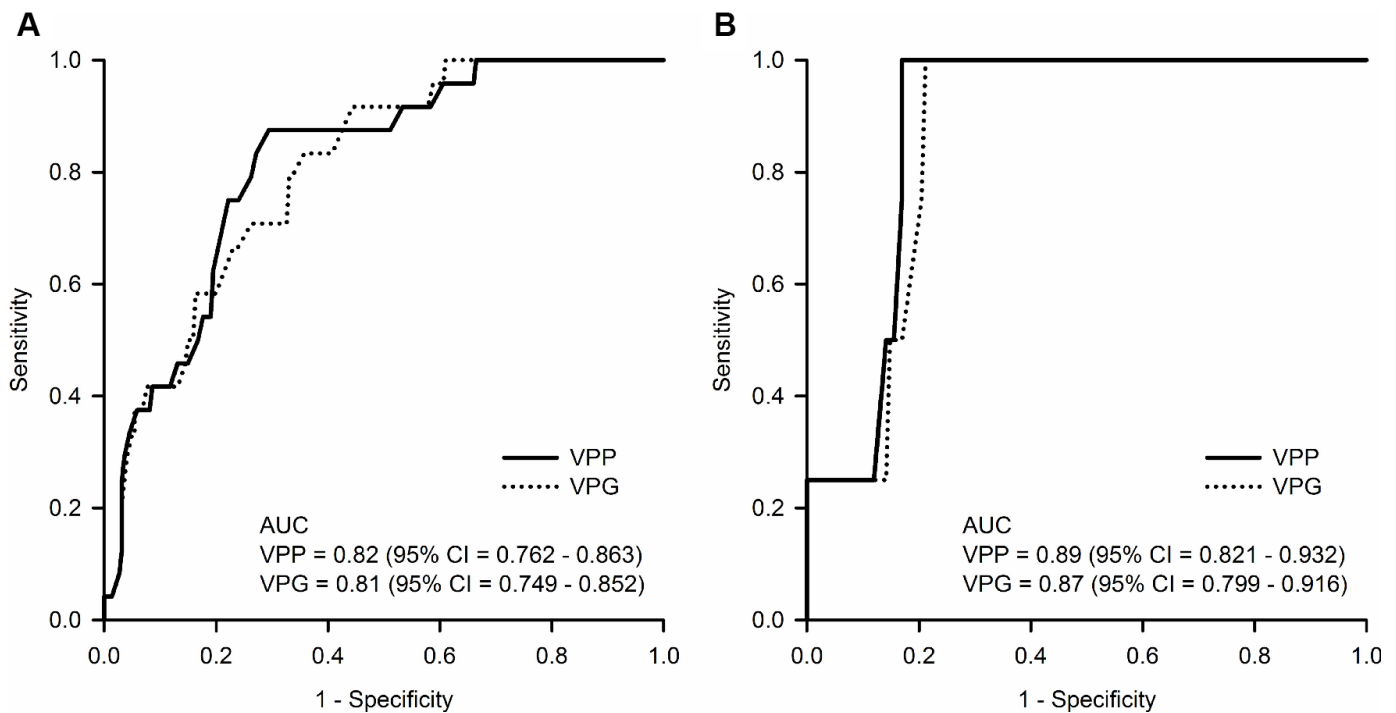


Figure 2. (A) Diagnostic accuracy for prevalent probable REM sleep behavior disorder (pRBD) at the baseline evaluation and (B) predictive accuracy for incident pRBD at the 2-year follow-up evaluation of the baseline pineal parenchyma volume (VPP, mm³) and pineal gland volume (VPG, mm³). Abbreviations: AUC = area under the receiver operator characteristic curve; CI = confidence intervals.

MATERIALS AND METHODS

Study participants

The present sample of 245 CN elderly individuals comprised 157 and 88 subjects from the participants of the baseline evaluation of the Korean Longitudinal Study on Cognitive Aging and Dementia (KLOSCAD) [34] and the first follow-up evaluation of the Korean Longitudinal Study on Health and Aging (KLOSHA) [35], respectively, which were conducted from November 2010 to October 2012. Both the KLOSCAD and KLOSHA were population-based prospective elderly cohort studies. The KLOSCAD study randomly sampled 30 villages and towns from 13 specific districts across South Korea, and randomly selected 10% and 20% of the elderly adults from urban and rural areas, respectively, using resident rosters and data on residents aged ≥ 60 years. The KLOSHA study randomly selected community-dwelling Korean elderly adults aged ≥ 65 years from the resident roster of Seongnam, one of the largest satellite cities of Seoul. Among the 221 participants who did not have pRBD at the baseline evaluation, 146 completed the 2-year follow-up evaluation. In the current study, we excluded the following conditions: cognitive disorders such as dementia and mild cognitive impairment (MCI); major psychiatric and/or neurologic disorders that could affect cognitive function; any history of brain tumors, substance abuse or dependence, and use of clonazepam, antidepressants (SSRI, SNRI, and others), or exogenous melatonin over the past 6 weeks; any serious medical condition that could affect the structure and/or function of the pineal gland or abnormalities in pineal gland morphology such as neoplastic lesions or extremely large cystic gland (diameter greater than 15.0 mm) [36]; and conditions that could mimic the symptoms of RBD such as RLS and OSA. We diagnosed RLS using the Cambridge-Hopkins Restless Leg Syndrome questionnaire (CHRLSq) [37] and defined OSA as a STOPBANG questionnaire [38] score of ≥ 5 points.

The study protocol was approved by the institutional review board of the Seoul National University Bundang Hospital. All the participants were fully informed of the study protocol, and written informed consent was provided by them or their legal guardians.

Assessment of cognitive function

In both the KLOSCAD and the KLOSHA, geriatric psychiatrists with expertise in dementia research administered face-to-face standardized diagnostic interviews, detail medical histories, laboratory tests, and physical and neurological examinations using the Korean version of the Consortium to Establish a

Registry for Alzheimer's Disease Assessment Packet Clinical Assessment Battery (CERAD-K) [39] and the Korean version of the Mini International Neuropsychiatric Interview [40]. In addition, research neuropsychologists administered the Digit Span Test [41], Frontal Assessment Battery [42], Geriatric Depression Scale (GDS) [43], Cumulative Illness Rating Scale (CIRS) [44], and CERAD-K Neuropsychological Assessment Battery (CERAD-K-N) [39, 45]. All participants performed -1.0 SD of the age-, gender-, and education-adjusted norms of elderly Koreans on the Mini-Mental State Examination (MMSE) [46]. Using a study-specific standard interview, trained research nurses collected data on age, sex, years of education, intracranial volume (ICV), history of head injury, amount of smoking (packs/day), and alcohol drinking (standard units/week) over the past twelve months period.

A panel of research neuropsychiatrists determined the participants' final diagnoses in both the KLOSCAD [34] and the KLOSHA [35]. Two neuropsychiatrists (K.W.K and J.W.H) participated in both panels. In both the KLOSCAD and the KLOSHA, we diagnosed dementia and other Axis I mental disorders according to the Diagnostic and Statistical Manual of Mental Disorders, 4th Edition, Text Revision (DSM-IV-TR) criteria [47] and MCI according to the criteria by the International Working Group on MCI [48]. We defined CN as functioning independently in the community and showing no evidence of cognitive impairment in objective neuropsychological tests.

Assessment of RBD symptoms

We evaluated behavioral features of RBD using the RBDSQ [29]. The RBDSQ is a self-reported screening instrument for diagnosing RBD and is comprised of 10 items assessing the most prominent clinical features of RBD: items 1 to 4, the frequency and content of dreams and their relationship to nocturnal movements and behavior; item 5, self-injuries and injuries to the bed partner; item 6, four subsections specifically assessing nocturnal motor behavior, e.g. questions about nocturnal vocalization (6.1), sudden limb movements (6.2), complex movements (6.3) or bedside items that fall down (6.4); items 7 and 8, nocturnal awakenings; item 9, disturbed sleep in general; and item 10, the presence of any neurological disorder. Each item could be answered as "yes" or "no". The RBDSQ score ranges from 0-13 points, with higher scores indicating more features associated with RBD. We defined pRBD individuals as having a total score of 5 or higher on the RBDSQ [29]. The questionnaire was completed by the subjects with aid from their partners if needed.

Segmentation of the pineal gland

We performed brain MRI using a Philips 3.0 Tesla Achieva scanners (Philips Medical Systems; Eindhoven, the Netherlands) within 3 months of the clinical assessments. We obtained 3D structural T1-weighted spoiled gradient echo sequences with the following parameters: acquisition voxel size = $1.0 \times 0.5 \times 0.5$ mm; 1.0 mm sagittal slice thickness with no inter-slice gap; repetition time = 4.61 ms; echo time = 8.15 ms; number of excitations = 1; flip angle = 8° ; field of view = 240×240 mm; and acquisition matrix size = $175 \times 256 \times 256$ mm in the x-, y-, and z-dimensions. We implemented bias field correction to remove the signal intensity inhomogeneity artifacts of MR images using Statistical Parametric Mapping software (version 8, SPM8; Wellcome Trust Centre for Neuroimaging, London; <https://www.fil.ion.ucl.ac.uk/spm>) in MATLAB R2014a (MathWorks Inc., Natick, MA, USA). We resliced the MR images into an isotropic voxel size of $1.0 \times 1.0 \times 1.0$ mm³. We measured ICV using FreeSurfer software (version 5.3.0; <http://surfer.nmr.mgh.harvard.edu>) to adjust for inter-individual variabilities in brain volume.

For each participant, trained researchers blinded to the demographics and clinical characteristics constructed a 3D mask of each pineal gland by manually segmenting the pineal gland slice-by-slice on the resliced T1-weighted MR images using the ITK-SNAP (version 3.4.0; <http://www.itksnap.org>) volumetric imaging software. We segmented the pineal glands primarily on the sagittal planes and corroborated the results on the axial and coronal planes. We identified the pineal gland using the following structures as guides: the quadrigeminal cisterna, posterior portion of the third ventricle, superior colliculus, and habenula. Except for the portion connected to the habenula, defining of the boundaries of the pineal gland was straightforward as it is surrounded by cerebrospinal fluid [13]. We carefully differentiated the pineal gland from the adjacent vascular structures, especially the vein of Galen and the paired internal cerebral veins. We defined a pineal cyst as an area of homogenous intensity that was isointense to cerebrospinal fluid in T1 sequence images [27, 49] with a diameter of 2.0 mm or greater [27]. We measured the VPG and VPC and estimated the VPP by subtracting VPC from VPG.

To determine inter-rater reliability, we assessed the intraclass correlation coefficients (ICCs) for 30 subjects who were randomly selected from the 258 participants with a time gap of 2 months. The ICCs were 0.971 (95% confidence interval [CI] = 0.940 - 0.986) for the VPG and 0.950 (95% CI = 0.894 - 0.976) for the VPC. The VPG was strongly correlated with the VPP ($r = 0.914$, $p < 0.001$) and the VPC ($r = 0.701$, $p < 0.001$) in our participants.

Statistical analysis

We compared continuous variables using independent samples t-tests and categorical variables using chi-square tests between groups. We examined the associations of VPP and VPG with RBDSQ-T using multiple linear regression model adjusted for age, sex, years of education, ICV, head injury, smoking, and alcohol drinking as covariates. To test the robustness of our observation, we also examined the associations of VPP and VPG with the RBDSQ-6 using multiple linear regression model adjusted for diagnosis, age, sex, years of education, ICV, head injury, smoking, and alcohol drinking as covariates. In each of the linear regression models, VPP, VPG, RBDSQ-T and RBDSQ-6 were entered as continuous variables. We assessed multicollinearity using collinearity statistical tests (tolerance and variance inflation factor). We compared VPP and VPG between the participants with pRBD and those without pRBD using analysis of covariance that adjusted for age, sex, years of education, ICV, head injury, smoking, and alcohol drinking as covariates. We examined the association of baseline VPP and VPG with the risk of prevalent pRBD at baseline and the risk of incident pRBD at 2-year follow-up evaluation using binary logistic regression analyses that adjusted for age, sex, years of education, ICV, head injury, smoking, and alcohol drinking at the baseline evaluation as covariates. We examined the diagnostic performances of the baseline VPP and VPG for prevalent pRBD at the baseline evaluation and the predictive accuracy for incident pRBD at the 2-year follow-up evaluation using the ROC analyses. We calculated the optimal cutoff values and AUC using Youden index maximum (sensitivity + specificity - 1) [50].

For all analyses, we considered a two-tailed p-value less than 0.05 as statistically significant, and we employed Bonferroni corrections to reduce type I error when multiple comparisons were conducted. We performed all statistical analyses using SPSS for Windows (version 20.0; IBM Corporation; Armonk, NY).

AUTHOR CONTRIBUTIONS

Conception and design: JP and KWK; Acquisition of the data: JWH, SWS, SB, JHH, JBB, JHK, KWK; Analysis and interpretation of data: All authors; Drafting of the manuscript and figures: JP and KWK; Critical revision of the manuscript for important intellectual content: All authors.

CONFLICTS OF INTEREST

The authors have no conflicts of interest to declare.

FUNDING

This study was supported by a grant from the Korean Health Technology R&D Project, Ministry of Health, Welfare, Republic of Korea (grant no. HI09C1379 [A092077]), the Basic Science Research Program through the National Research Foundation of Korea (NRF) funded by the Ministry of Education (2015R1D1A1A01059251), and Institute for Information and communications Technology Promotion (IITP) grant funded by the Korea government (MSIT) (2018-2-00861, Intelligent SW Technology Development for Medical Data Analysis).

REFERENCES

1. Boeve BF. REM sleep behavior disorder: updated review of the core features, the REM sleep behavior disorder-neurodegenerative disease association, evolving concepts, controversies, and future directions. *Ann N Y Acad Sci.* 2010; 1184:15–54. <https://doi.org/10.1111/j.1749-6632.2009.05115.x> PMID:20146689
2. Haba-Rubio J, Frauscher B, Marques-Vidal P, Toriel J, Tobback N, Andries D, Preisig M, Vollenweider P, Postuma R, Heinzer R. Prevalence and determinants of rapid eye movement sleep behavior disorder in the general population. *Sleep.* 2018; 41:zsx197. <https://doi.org/10.1093/sleep/zsx197> PMID:29216391
3. Kang SH, Yoon IY, Lee SD, Han JW, Kim TH, Kim KW. REM sleep behavior disorder in the Korean elderly population: prevalence and clinical characteristics. *Sleep.* 2013; 36:1147–52. <https://doi.org/10.5665/sleep.2874> PMID:23904674
4. Fantini ML, Ferini-Strambi L, Montplaisir J. Idiopathic REM sleep behavior disorder: toward a better nosologic definition. *Neurology.* 2005; 64:780–86. <https://doi.org/10.1212/01.WNL.0000152878.79429.00> PMID:15753409
5. Schenck CH, Boeve BF, Mahowald MW. Delayed emergence of a parkinsonian disorder or dementia in 81% of older men initially diagnosed with idiopathic rapid eye movement sleep behavior disorder: a 16-year update on a previously reported series. *Sleep Med.* 2013; 14:744–48. <https://doi.org/10.1016/j.sleep.2012.10.009> PMID:23347909
6. Iranzo A, Tolosa E, Gelpi E, Molinuevo JL, Valldeoriola F, Serradell M, Sanchez-Valle R, Vilaseca I, Lomeña F, Vilas D, Lladó A, Gaig C, Santamaria J. Neurodegenerative disease status and post-mortem pathology in idiopathic rapid-eye-movement sleep behaviour disorder: an observational cohort study. *Lancet Neurol.* 2013; 12:443–53. [https://doi.org/10.1016/S1474-4422\(13\)70056-5](https://doi.org/10.1016/S1474-4422(13)70056-5) PMID:23562390
7. Kunz D, Mahlberg R. A two-part, double-blind, placebo-controlled trial of exogenous melatonin in REM sleep behaviour disorder. *J Sleep Res.* 2010; 19:591–96. <https://doi.org/10.1111/j.1365-2869.2010.00848.x> PMID:20561180
8. Kunz D, Bes F. Melatonin as a therapy in REM sleep behavior disorder patients: an open-labeled pilot study on the possible influence of melatonin on REM-sleep regulation. *Mov Disord.* 1999; 14:507–11. [https://doi.org/10.1002/1531-8257\(199905\)14:3<507::AID-MDS1021>3.0.CO;2-8](https://doi.org/10.1002/1531-8257(199905)14:3<507::AID-MDS1021>3.0.CO;2-8) PMID:10348479
9. Boeve BF, Silber MH, Ferman TJ. Melatonin for treatment of REM sleep behavior disorder in neurologic disorders: results in 14 patients. *Sleep Med.* 2003; 4:281–84. [https://doi.org/10.1016/S1389-9457\(03\)00072-8](https://doi.org/10.1016/S1389-9457(03)00072-8) PMID:14592300
10. McCarter SJ, Boswell CL, St Louis EK, Dueffert LG, Slocumb N, Boeve BF, Silber MH, Olson EJ, Tippmann-Peikert M. Treatment outcomes in REM sleep behavior disorder. *Sleep Med.* 2013; 14:237–42. <https://doi.org/10.1016/j.sleep.2012.09.018> PMID:23352028
11. Kunz D, Mahlberg R, Müller C, Tilmann A, Bes F. Melatonin in patients with reduced REM sleep duration: two randomized controlled trials. *J Clin Endocrinol Metab.* 2004; 89:128–34. <https://doi.org/10.1210/jc.2002-021057> PMID:14715839
12. Arendt J. Melatonin: characteristics, concerns, and prospects. *J Biol Rhythms.* 2005; 20:291–303. <https://doi.org/10.1177/0748730405277492> PMID:16077149
13. Reiter RJ. The mammalian pineal gland: structure and function. *Am J Anat.* 1981; 162:287–313. <https://doi.org/10.1002/aja.1001620402> PMID:7325124
14. Nölte I, Lütkehoff AT, Stuck BA, Lemmer B, Schredl M, Findeisen P, Groden C. Pineal volume and circadian melatonin profile in healthy volunteers: an interdisciplinary approach. *J Magn Reson Imaging.* 2009; 30:499–505. <https://doi.org/10.1002/jmri.21872> PMID:19630077
15. Liebrich LS, Schredl M, Findeisen P, Groden C, Bumb JM, Nölte IS. Morphology and function: MR pineal volume and melatonin level in human saliva are correlated. *J Magn Reson Imaging.* 2014; 40:966–71. <https://doi.org/10.1002/jmri.24449> PMID:24214660

16. Sigurdardottir LG, Markt SC, Sigurdsson S, Aspelund T, Fall K, Schernhammer E, Rider JR, Launer L, Harris T, Stampfer MJ, Gudnason V, Czeisler CA, Lockley SW, et al. Pineal gland volume assessed by MRI and its correlation with 6-sulfatoxymelatonin levels among older men. *J Biol Rhythms*. 2016; 31:461–69. <https://doi.org/10.1177/0748730416656948> PMID:[27449477](https://pubmed.ncbi.nlm.nih.gov/27449477/)
17. Wetterberg L, Iselius L, Lindsten J. Genetic regulation of melatonin excretion in urine. A preliminary report. *Clin Genet*. 1983; 24:399–402. <https://doi.org/10.1111/j.1399-0004.1983.tb00093.x> PMID:[6652952](https://pubmed.ncbi.nlm.nih.gov/6652952/)
18. Schmidt F, Penka B, Trauner M, Reinsperger L, Ranner G, Ebner F, Waldhauser F. Lack of pineal growth during childhood. *J Clin Endocrinol Metab*. 1995; 80:1221–25. <https://doi.org/10.1210/jcem.80.4.7536203> PMID:[7536203](https://pubmed.ncbi.nlm.nih.gov/7536203/)
19. Tan DX, Xu B, Zhou X, Reiter RJ. Pineal Calcification, Melatonin Production, Aging, Associated Health Consequences and Rejuvenation of the Pineal Gland. *Molecules*. 2018; 23:301. <https://doi.org/10.3390/molecules23020301> PMID:[29385085](https://pubmed.ncbi.nlm.nih.gov/29385085/)
20. Park J, Han JW, Lee JR, Byun S, Suh SW, Kim T, Yoon IY, Kim KW. Lifetime coffee consumption, pineal gland volume, and sleep quality in late life. *Sleep*. 2018; 41:zsy127. <https://doi.org/10.1093/sleep/zsy127> PMID:[30011049](https://pubmed.ncbi.nlm.nih.gov/30011049/)
21. Gheban BA, Rosca IA, Crisan M. The morphological and functional characteristics of the pineal gland. *Med Pharm Rep*. 2019; 92:226–34. <https://doi.org/10.15386/mpr-1235> PMID:[31460502](https://pubmed.ncbi.nlm.nih.gov/31460502/)
22. Mouret J, Coindet J, Chouvet G. [Effect of pinealectomy on sleep stages and rhythms of the male rat]. *Brain Res*. 1974; 81:97–105. [https://doi.org/10.1016/0006-8993\(74\)90480-6](https://doi.org/10.1016/0006-8993(74)90480-6) PMID:[4373126](https://pubmed.ncbi.nlm.nih.gov/4373126/)
23. Takeuchi N, Uchimura N, Hashizume Y, Mukai M, Etoh Y, Yamamoto K, Kotorii T, Ohshima H, Ohshima M, Maeda H. Melatonin therapy for REM sleep behavior disorder. *Psychiatry Clin Neurosci*. 2001; 55:267–69. <https://doi.org/10.1046/j.1440-1819.2001.00854.x> PMID:[11422870](https://pubmed.ncbi.nlm.nih.gov/11422870/)
24. Brooks PL, Peever JH. Impaired GABA and glycine transmission triggers cardinal features of rapid eye movement sleep behavior disorder in mice. *J Neurosci*. 2011; 31:7111–21. <https://doi.org/10.1523/JNEUROSCI.0347-11.2011> PMID:[21562273](https://pubmed.ncbi.nlm.nih.gov/21562273/)
25. Videnovic A, Noble C, Reid KJ, Peng J, Turek FW, Marconi A, Rademaker AW, Simuni T, Zadikoff C, Zee PC. Circadian melatonin rhythm and excessive daytime sleepiness in Parkinson disease. *JAMA Neurol*. 2014; 71:463–69. <https://doi.org/10.1001/jamaneurol.2013.6239> PMID:[24566763](https://pubmed.ncbi.nlm.nih.gov/24566763/)
26. Ono K, Mochizuki H, Ikeda T, Nihira T, Takasaki J, Teplow DB, Yamada M. Effect of melatonin on α -synuclein self-assembly and cytotoxicity. *Neurobiol Aging*. 2012; 33:2172–85. <https://doi.org/10.1016/j.neurobiolaging.2011.10.015> PMID:[22118903](https://pubmed.ncbi.nlm.nih.gov/22118903/)
27. Pu Y, Mahankali S, Hou J, Li J, Lancaster JL, Gao JH, Appelbaum DE, Fox PT. High prevalence of pineal cysts in healthy adults demonstrated by high-resolution, noncontrast brain MR imaging. *AJNR Am J Neuroradiol*. 2007; 28:1706–09. <https://doi.org/10.3174/ajnr.A0656> PMID:[17885233](https://pubmed.ncbi.nlm.nih.gov/17885233/)
28. McCarter SJ, St Louis EK, Sandness DJ, Arndt K, Erickson M, Tabatabai G, Boeve BF, Silber MH. Antidepressants increase REM sleep muscle tone in patients with and without REM sleep behavior disorder. *Sleep*. 2015; 38:907–17. <https://doi.org/10.1016/j.sleep.2015.02.005> PMID:[25325487](https://pubmed.ncbi.nlm.nih.gov/25325487/)
29. Stiasny-Kolster K, Mayer G, Schäfer S, Möller JC, Heinzel-Gutenbrunner M, Oertel WH. The REM sleep behavior disorder screening questionnaire—a new diagnostic instrument. *Mov Disord*. 2007; 22:2386–93. <https://doi.org/10.1002/mds.21740> PMID:[17894337](https://pubmed.ncbi.nlm.nih.gov/17894337/)
30. Bolitho SJ, Naismith SL, Terpening Z, Grunstein RR, Melehan K, Yee BJ, Coeytaux A, Gilat M, Lewis SJ. Investigating rapid eye movement sleep without atonia in Parkinson’s disease using the rapid eye movement sleep behavior disorder screening questionnaire. *Mov Disord*. 2014; 29:736–42. <https://doi.org/10.1002/mds.25832> PMID:[24619826](https://pubmed.ncbi.nlm.nih.gov/24619826/)
31. Gaig C, Iranzo A, Pujol M, Perez H, Santamaria J. Periodic limb movements during sleep mimicking REM sleep behavior disorder: a new form of periodic limb movement disorder. *Sleep*. 2017; 40:zsw063. <https://doi.org/10.1093/sleep/zsw063> PMID:[28364416](https://pubmed.ncbi.nlm.nih.gov/28364416/)
32. Iranzo A, Santamaria J. Severe obstructive sleep apnea/hypopnea mimicking REM sleep behavior disorder. *Sleep*. 2005; 28:203–06. <https://doi.org/10.1093/sleep/28.2.203> PMID:[16171244](https://pubmed.ncbi.nlm.nih.gov/16171244/)
33. Mahlberg R, Kienast T, Hädel S, Heidenreich JO, Schmitz S, Kunz D. Degree of pineal calcification (DOC) is associated with polysomnographic sleep measures in primary insomnia patients. *Sleep Med*. 2009; 10:439–45.

- <https://doi.org/10.1016/j.sleep.2008.05.003>
PMID:[18755628](https://pubmed.ncbi.nlm.nih.gov/18755628/)
34. Han JW, Kim TH, Kwak KP, Kim K, Kim BJ, Kim SG, Kim JL, Kim TH, Moon SW, Park JY, Park JH, Byun S, Suh SW, et al. Overview of the Korean Longitudinal Study on Cognitive Aging and Dementia. *Psychiatry Investig.* 2018; 15:767–74.
<https://doi.org/10.30773/pi.2018.06.02>
PMID:[30086611](https://pubmed.ncbi.nlm.nih.gov/30086611/)
35. Park JH, Lim S, Lim J, Kim K, Han M, Yoon IY, Kim J, Chang Y, Chang CB, Chin HJ. An overview of the Korean longitudinal study on health and aging. *Psychiatry Investig.* 2007; 4:84–95.
36. Osborn AG, Preece MT. Intracranial cysts: radiologic-pathologic correlation and imaging approach. *Radiology.* 2006; 239:650–64.
<https://doi.org/10.1148/radiol.2393050823>
PMID:[16714456](https://pubmed.ncbi.nlm.nih.gov/16714456/)
37. Allen RP, Burchell BJ, MacDonald B, Hening WA, Earley CJ. Validation of the self-completed Cambridge-Hopkins questionnaire (CH-RLSq) for ascertainment of restless legs syndrome (RLS) in a population survey. *Sleep Med.* 2009; 10:1097–100.
<https://doi.org/10.1016/j.sleep.2008.10.007>
PMID:[19195928](https://pubmed.ncbi.nlm.nih.gov/19195928/)
38. Chung F, Elsaid H. Screening for obstructive sleep apnea before surgery: why is it important? *Curr Opin Anaesthesiol.* 2009; 22:405–11.
<https://doi.org/10.1097/ACO.0b013e32832a96e2>
PMID:[19412094](https://pubmed.ncbi.nlm.nih.gov/19412094/)
39. Lee JH, Lee KU, Lee DY, Kim KW, Jhoo JH, Kim JH, Lee KH, Kim SY, Han SH, Woo JI. Development of the Korean version of the Consortium to Establish a Registry for Alzheimer’s Disease Assessment Packet (CERAD-K): clinical and neuropsychological assessment batteries. *J Gerontol B Psychol Sci Soc Sci.* 2002; 57:47–53.
<https://doi.org/10.1093/geronb/57.1.P47>
PMID:[11773223](https://pubmed.ncbi.nlm.nih.gov/11773223/)
40. Yoo SW, Kim YS, Noh JS, Oh KS, Kim CH, NamKoong K, Chae JH, Lee GC, Jeon SI, Min KJ. Validity of Korean version of the mini-international neuropsychiatric interview. *Anxiety Mood.* 2006; 2:50–55.
41. Wechsler D. *Instruction Manual for the Wechsler Memory Scale Revised.* New York (NY): Psychological Corporation; 1987.
42. Kim TH, Huh Y, Choe JY, Jeong JW, Park JH, Lee SB, Lee JJ, Jhoo JH, Lee DY, Woo JI, Kim KW. Korean version of frontal assessment battery: psychometric properties and normative data. *Dement Geriatr Cogn Disord.* 2010; 29:363–70.
<https://doi.org/10.1159/000297523> PMID:[20424455](https://pubmed.ncbi.nlm.nih.gov/20424455/)
43. Kim JY, Park JH, Lee JJ, Huh Y, Lee SB, Han SK, Choi SW, Lee DY, Kim KW, Woo JI. Standardization of the Korean version of the geriatric depression scale: reliability, validity, and factor structure. *Psychiatry Investig.* 2008; 5:232–38.
<https://doi.org/10.4306/pi.2008.5.4.232>
PMID:[20046343](https://pubmed.ncbi.nlm.nih.gov/20046343/)
44. Miller MD, Paradis CF, Houck PR, Mazumdar S, Stack JA, Rifai AH, Mulsant B, Reynolds CF 3rd. Rating chronic medical illness burden in geropsychiatric practice and research: application of the Cumulative Illness Rating Scale. *Psychiatry Res.* 1992; 41:237–48.
[https://doi.org/10.1016/0165-1781\(92\)90005-N](https://doi.org/10.1016/0165-1781(92)90005-N)
PMID:[1594710](https://pubmed.ncbi.nlm.nih.gov/1594710/)
45. Lee DY, Lee KU, Lee JH, Kim KW, Jhoo JH, Kim SY, Yoon JC, Woo SI, Ha J, Woo JI. A normative study of the CERAD neuropsychological assessment battery in the Korean elderly. *J Int Neuropsychol Soc.* 2004; 10:72–81.
<https://doi.org/10.1017/S1355617704101094>
PMID:[14751009](https://pubmed.ncbi.nlm.nih.gov/14751009/)
46. Kim JL, Park JH, Kim BJ, Kim MD, Kim SK, Chi YK, Kim TH, Moon SW, Park MH, Bae JN, Woo JI, Ryu SH, Yoon JC, et al. Interactive influences of demographics on the Mini-Mental State Examination (MMSE) and the demographics-adjusted norms for MMSE in elderly Koreans. *Int Psychogeriatr.* 2012; 24:642–50.
<https://doi.org/10.1017/S1041610211002456>
PMID:[22166616](https://pubmed.ncbi.nlm.nih.gov/22166616/)
47. American Psychiatric Association. *Diagnostic and Statistical Manual of Mental Disorders. 4th Edition, Text Revision.* Washington (DC): American Psychiatric Association Press; 2000.
48. Winblad B, Palmer K, Kivipelto M, Jelic V, Fratiglioni L, Wahlund LO, Nordberg A, Bäckman L, Albert M, Almkvist O, Arai H, Basun H, Blennow K, et al. Mild cognitive impairment—beyond controversies, towards a consensus: report of the International Working Group on Mild Cognitive Impairment. *J Intern Med.* 2004; 256:240–46.
<https://doi.org/10.1111/j.1365-2796.2004.01380.x>
PMID:[15324367](https://pubmed.ncbi.nlm.nih.gov/15324367/)
49. Jinkins JR, Xiong L, Reiter RJ. The midline pineal “eye”: MR and CT characteristics of the pineal gland with and without benign cyst formation. *J Pineal Res.* 1995; 19:64–71.
<https://doi.org/10.1111/j.1600-079X.1995.tb00172.x>
PMID:[8609598](https://pubmed.ncbi.nlm.nih.gov/8609598/)
50. Youden WJ. Index for rating diagnostic tests. *Cancer.* 1950; 3:32–35.
[https://doi.org/10.1002/1097-0142\(1950\)3:1<32::AID-CNCR2820030106>3.0.CO;2-3](https://doi.org/10.1002/1097-0142(1950)3:1<32::AID-CNCR2820030106>3.0.CO;2-3) PMID:[15405679](https://pubmed.ncbi.nlm.nih.gov/15405679/)

Abnormalities of saccadic eye movements in dementia due to Alzheimer's disease and mild cognitive impairment

Thomas D.W. Wilcockson^{1,2}, Diako Mardanbegi³, Baiqiang Xia⁴, Simon Taylor⁵, Pete Sawyer⁶, Hans W. Gellersen³, Ira Leroi^{7,8,9}, Rebecca Killick⁵, Trevor J. Crawford²

¹School of Sport, Exercise and Health Sciences, Loughborough University, Loughborough, UK

²Psychology Department, Lancaster University, Lancaster, UK

³Computing and Communications Department, Lancaster University, Lancaster, UK

⁴Faculty of Information Technology and Electrical Engineering, University of Oulu, Oulu, Finland

⁵Maths and Statistics Department, Lancaster University, Lancaster, UK

⁶Engineering & Applied Science, Aston University, Birmingham, UK

⁷Global Brain Health Institute, Trinity College, Dublin, Ireland

⁸Division of Neuroscience and Experimental Psychology, University of Manchester, Manchester, UK

⁹Greater Manchester Mental Health NHS Foundation Trust, Manchester, UK

Correspondence to: Thomas D.W. Wilcockson; **email:** t.wilcockson@lboro.ac.uk

Keywords: mild cognitive impairment, Alzheimer's disease, inhibitory control, eye tracking, anti-saccade

Received: March 6, 2019 **Accepted:** July 19, 2019 **Published:** August 2, 2019

Copyright: Wilcockson et al. This is an open-access article distributed under the terms of the Creative Commons Attribution License (CC BY 3.0), which permits unrestricted use, distribution, and reproduction in any medium, provided the original author and source are credited.

ABSTRACT

Background: There is increasing evidence that people in the early stages of Alzheimer's disease (AD) have subtle impairments in cognitive inhibition that can be detected by using relatively simple eye-tracking paradigms, but these subtle impairments are often missed by traditional cognitive assessments. People with mild cognitive impairment (MCI) are at an increased likelihood of dementia due to AD. No study has yet investigated and contrasted the MCI subtypes in relation to eye movement performance. **Methods:** In this work we explore whether eye-tracking impairments can distinguish between patients with the amnesic and the non-amnesic variants of MCI. Participants were 68 people with dementia due to AD, 42 had a diagnosis of aMCI, and 47 had a diagnosis of naMCI, and 92 age-matched cognitively healthy controls. **Results:** The findings revealed that eye-tracking can distinguish between the two forms of MCI. **Conclusions:** The work provides further support for eye-tracking as a useful diagnostic biomarker in the assessment of dementia.

INTRODUCTION

Alzheimer's disease (AD) is a severe neurodegenerative disease of the human brain, for which there is as yet no cure. When a disease modifying therapy becomes available, it will be essential to administer this treatment in the very earliest stages of the disease, before pathological changes in the brain are widespread, rendering the treatment ineffective [1]. Thus,

identifying the presence of AD in the pre-dementia 'prodromal' or even 'preclinical' phase is essential [2]. Current biomarkers that are able to detect AD in the earliest stages are either invasive (i.e. involving a lumbar puncture to a cerebrospinal fluid sample) or expensive (i.e. involving neuroimaging). Thus, the discovery of a reliable non-invasive and low-cost biomarker would be an important development with implications for the early diagnosis and monitoring of

the disease, particularly on a global scale, since invasive and/or expensive biomarkers may not be widely available.

Eye movements provide a sensitive, low cost and non-invasive marker of cognitive change or deterioration [3,4]. People with AD gradually lose the efficient control of attention and develop impairments of both inhibitory control and eye movement error-correction [5]. Specifically, the inhibition of a gaze-shift towards a salient stimulus as well as the ability to direct a voluntary gaze-shift away from this stimulus is impaired. This difficulty in gaze control may be due to cognitive defects of either inhibitory control, working memory (WM), or both [6,7]. The error frequency in the antisaccade task (AST) also correlates with the severity of AD [3]. Importantly, eye movement deficits can develop early in the course of the disease, even before cognitive deficits are revealed by standard neuropsychological tests [3,7]. A critical issue then is whether eye-movement impairments are detectable in people who are in a preclinical stage of AD and therefore at a greater risk of developing clinical dementia.

A strong correlation has been reported [8] between antisaccade error rate with cortical thinning (brain atrophy) in a mild cognitive impairment (MCI) group. However, this work did not distinguish between the different types of MCI, thus the low and high-risk of dementia participants were conflated in their study. In a separate study, a group of amnesic MCI (aMCI) participants were contrasted to age-matched controls who were assessed both using the AST and with fMRI to measure structural changes [9]. The fMRI data revealed that participants with aMCI showed reduced activation in frontal eye fields and increased inhibitory errors when performing the AST. Although this work supports eye-tracking as a useful diagnostic tool in detecting individuals at high risk of dementia, the evidence was not conclusive, as there was no direct comparison between an aMCI and a non-amnesic MCI (naMCI) group. Evidence that saccadic impairment was significantly greater in the aMCI group with the higher risk for dementia due to AD, in comparison to the naMCI group who are at a lower risk, would clearly provide more compelling support for the validity of the AST as an early diagnostic marker.

A clinically useful biomarker should be able to detect subtle signs of impairment in a group of participants at higher risk of dementia such as those with MCI. MCI is a clinical syndrome characterised by impairments in cognition that are worse than would be expected for a person of their age. MCI has several outcomes; it can lead to dementia if the underlying cause is AD, or other

types of neurodegenerative conditions; or it may be transient, reversible [10] or even static. People with a diagnosis of MCI are at an increased risk of developing dementia compared to cognitively healthy adults with 5-10% of MCI patients progressing to dementia annually (see [11]). Traditionally, the clinical syndrome of MCI was considered to be a relatively distinct stage of dementia since the cognitive deficits were not severe enough to impact significantly on the individual's ability to conduct their activities of daily living [12]. However, there is a growing consensus [13,1,2] that MCI should be considered a prodromal and/or preclinical stage between normal cognitive health and AD. MCI can be further split into aMCI and naMCI types [12]. Those with aMCI experience greater memory impairment in comparison to naMCI. Further, [14] found evidence that there are structural differences between aMCI and naMCI in certain brain regions (the largest differences found for the hippocampus and entorhinal cortex). This suggests that memory differences may be the result of physical changes in the brain. Critically, there is a higher conversation rate to dementia due to AD for people diagnosed with aMCI, than naMCI [15-17]. Thus, people with aMCI are at much greater risk of progressing to AD than healthy adults or naMCI. No study has yet investigated the comparison of MCI subtypes in relation to eye movement performance. The principal aim of the current work was to explore and evaluate such evidence.

RESULTS

Antisaccade latency

The latencies for all correct saccades in the antisaccade are shown in Figure 1A. A one-way ANOVA on the mean antisaccade latencies revealed that there was a significant main effect of participant group ($F(3,238)=13.541; p<.005; \eta^2=.146$). AD ($N=65$; mean=404; SD=86; 95% CI=383-427) generated significantly longer latencies than the CP group ($N=91$; mean=338ms; SD=84; 95% CI=321 -355; $t(154)=4.801; p<.0005; d=.77$) and the naMCIs ($N=46$; mean=363ms; SD=62; 95% CI=346-381; $t(109)=2.78; p=.006; d=.53$). However, antisaccade latencies did not differ between the aMCI ($N=40$; mean=419ms; SD=82; 95% CI=394-444) and the AD group ($t(103)=-.857; p=.394; d=.17$). The mean latencies of aMCI group were significantly longer than the naMCI group ($t(84)=3.607; p=.001; d=.79$), and the CP group ($t(129)=5.116; p<.0005; d=.90$). The latencies for the naMCI did not differ from the CP group significantly ($t(135)=1.785; p=.077; d=.31$). Because age was not balanced between the groups we next performed an analysis of covariance. The ANCOVA,

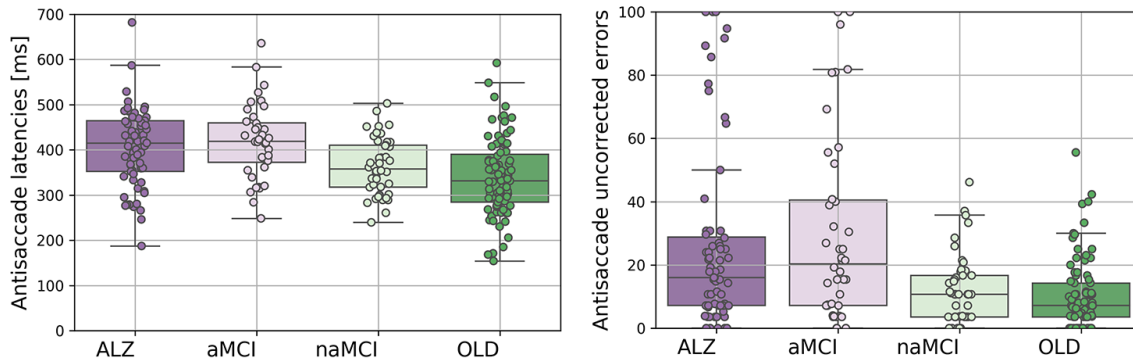


Figure 1. The eye movement variables for the Alzheimer's disease (AD), amnesic Mild Cognitive Impairment (aMCI), non-amnesic Mild Cognitive Impairment (naMCI), and control participants (CP). (A) Antisaccade latencies (left panel); (B) Antisaccade uncorrected errors (right panel).

with a between-subjects factor: group (AD, aMCI, naMCI, CP); and a covariate: age, revealed a significant main effect of age ($F(1,230)=32.115; p<.0005; \eta^2=.123$), and group ($F(3,230)=6.175; p<.0005; \eta^2=.075$). However, the corrected model, with age as a covariate was also significant ($F(4,230)=18.087; p<.0005; \eta^2=.239$), confirming that the group effect remained after age was partialled out. To provide further verification that age did not affect results we selected a subsample of age-matched participants. This age-matched sample was achieved by excluding the oldest AD ($N=4$) and aMCI ($N=3$) and the youngest CPs ($N=22$) and naMCI ($N=9$) participants from the sample. An ANOVA confirmed that the groups were matched across age ($F(3,201)=.800; p=.495; \eta^2=.012$). The antisaccade latency findings were replicated in this age-matched subsample. ANOVA revealed a significant main effect of participant group for mean antisaccade latencies ($F(3,201)=7.263; p<.0005; \eta^2=.098$). AD ($N=62$; mean=402ms; SD=88; 95% CI=381-425) revealed increased latencies in comparison to the CP group ($N=69$; mean=351ms; SD=88; 95% CI=331-374; $t(129)=3.304; p=.001; d=.58$), and the naMCI group ($N=37$; mean=363; SD=64; 95% CI=343-383; $t(97)=2.311; p=.023; d=.47$). Again, the aMCI ($N=37$; mean=418; SD=83; 95% CI=392-445) did not differ from AD ($t(97)=.910; p=.365; d=.19$). The aMCI group revealed significantly longer latencies compared to the naMCI group ($t(72)=3.160; p=.002; d=.75$), and the CP group ($t(104)=3.811; p<.0005; d=.75$). The antisaccade latencies for the naMCI group did not differ from CP group ($t(104)=.759; p=.449; d=.15$).

Antisaccade uncorrected errors

Figure 2B shows the mean frequency (%) total number of trials with uncorrected errors in each group for the

antisaccade experiment. A logistic regression [18] was fitted to the proportion of uncorrected errors, with weights proportional to the number of AST completed per participant and a dispersion parameter to account for potential higher than anticipated variation in the number of uncorrected errors. Estimated log-odds regression coefficients, presented in Table 1, identify that the proportion of uncorrected errors are significantly lower than 50% for all groups, and thereby revealing that there was a significant effect on participant group for the antisaccade errors ($F(3,245)=10.914; p<.0005$). The distribution of the standardised Pearson residuals did not visually appear to satisfy the assumption of the normal distribution. However, a one-way ANOVA test suggest that the residual contain no further dependence on group ($F(3,245)=.108; p=.956$) and likewise from a non-parametric analysis using the Kruskal Wallis H Test ($H(3)=3.073; p=.381$).

As expected, AD ($N=68$; mean proportion=26; SD=29; 95% CI=19-33) generated increased errors in comparison to the CP group ($N=91$; mean proportion=10; SD=11; 95% CI=8-13; $\chi^2(1)=18.459; p<.0005$). Critically, the aMCI group ($N=42$; mean proportion=30; SD=30; 95% CI=21-39) generated a higher proportion of antisaccade errors compared to the naMCI group ($N=46$; mean proportion=12; SD=11; 95% CI=9-16; $\chi^2(1)=11.774; p=.001$) and the CP group ($\chi^2(1)=21.806; p<.0005$). However, there was not a significant difference in the errors of the aMCI and the AD group ($\chi^2(1)=.665; p=.415$) and also between the naMCI and CP groups ($\chi^2(1)=.588; p=.446$). The difference between the AD and naMCI was shown to be significant ($\chi^2(1)=8.792; p=.003$).

An extension to the model that included participant age revealed that the group main effect remained significant

Table 1. Log-odds coefficient estimates for cognitive groups from the weighted logistic regression model for the proportion of uncorrected AST errors.

Group	Log-odds	SE	95% Confidence Interval		Wald Chi-Square
			Lower	Upper	
All participants (N=249), dispersion = 5.361					
AD	-1.242	0.1389	-1.515	-0.970	79.973
aMCI	-1.063	0.1699	-1.396	-0.730	39.192
naMCI	-1.974	0.2038	-2.373	-1.574	93.782
CP	-2.176	0.1670	-2.503	-1.848	169.688
Age matched (N=211), dispersion = 5.645					
AD	-1.226	0.1453	-1.511	-0.941	71.218
aMCI	-1.107	0.1827	-1.466	-0.749	36.742
naMCI	-1.959	0.2317	-2.413	-1.505	71.487
CP	-2.266	0.2066	-2.371	-1.861	120.267

All chi-squared Wald statistics are based on 1 degree of freedom and all correspond to p-values less than 0.0005.

($F(3,235)=8.173$; $p<.0005$), whilst age was not ($F(1,235)=.167$; $p=.684$). To provide further verification that age was not a confounding factor, an age-matched sample was entered in the analysis. The results, presented in Table 1, were essentially replicated. There was a significant main effect of participant group for antisaccade errors ($F(3,207)=9.295$; $p<.0005$). For antisaccade errors, the AD ($N=64$; mean proportion=26;

$SD=28$; 95% $CI=19-32$) revealed an increased error rate compared to the CP group ($N=69$; mean proportion=10; $SD=10$; 95% $CI=7-12$; $\chi^2(1)=16.945$; $p<.0005$) and the naMCI group ($N=37$; mean proportion=13; $SD=12$; 95% $CI=9-16$; $\chi^2(1)=7.183$; $p=.007$). Again, critically, the aMCI group ($N=39$; mean proportion=30; $SD=31$; 95% $CI=20-40$) revealed a significantly higher frequency of errors compared to the naMCI group

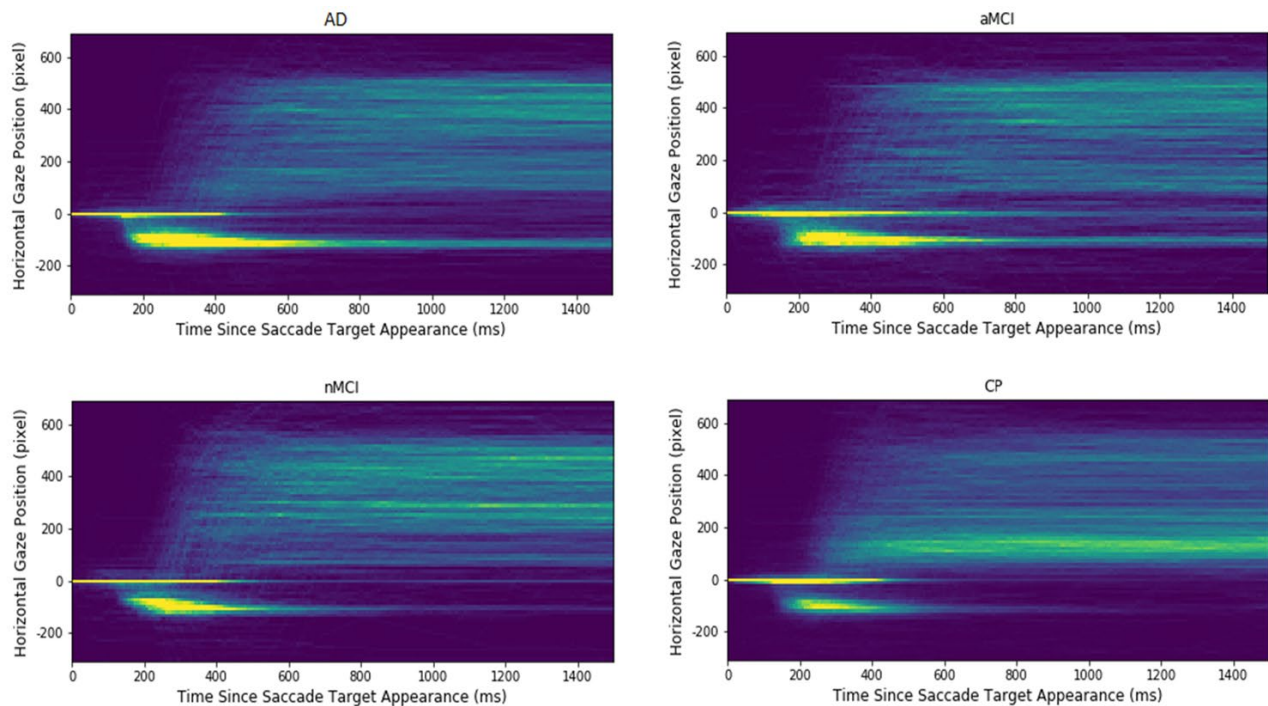


Figure 2. Heatmap plots of the extracted gaze signals in each of participant groups. The x-axis indicates the time since saccadic target appearance, and the y-axis presents the aligned horizontal gaze position. The warmer the colour; the higher is the gaze point density in the corresponding spatial-temporal location. Note that the longest "comet" tails, reflecting a high proportion of uncorrected errors, are evident for the Alzheimer's (AD) and the amnesic Mild Cognitive Impairment (aMCI) groups. The control participants (CP) and the non- amnesic MCI have distinctly shorter "comet" tails.

($\chi^2(1)=8.327$; $p=0.004$) and the CP group ($\chi^2(1)=17.635$; $p<.0005$). The aMCI group did not differ from the AD group ($\chi^2(1)=.258$; $p=.612$ and nor did the naMCI group from the CP group ($\chi^2(1)=.976$; $p=0.323$).

Further, to confirm whether AST error rate was associated with memory decline we performed a series of correlations between AST failure rate and FCSRT free recall score. Overall there was a negative association between AST error rate and FCSRT free recall ($r(180)=-.480$; $p<.0005$) which indicates that an increase in AST errors was associated with poorer free recall on the FCSRT task. This association was also observed when considering the participant groups separately: a significant negative association was found between AST error rate and FCSRT free recall within AD patients ($r(42)=-.430$; $p=.004$), aMCI ($r(39)=-.439$; $p=.004$), and marginally for naMCI ($r(44)=-.288$; $p=.052$). The association was not significant in control participants ($r(49)=-.166$; $p=.243$). The results indicate that AST inhibitory control is associated with memory decline in patient groups.

To clarify the spatial-temporal characteristics of the extracted signals in the AST, heatmaps of the gaze positions of each participant group are displayed in Figure 2. The heatmaps that the density and length of the “comet” (yellow) tail is shortest for the CP and naMCI groups; and longest for the AD and aMCI groups. This reflects the findings reported above, that the AD and aMCI generated a high proportion of errors in the AST which are uncorrected. Fewer of these uncorrected errors are seen in the traces of the control and naMCI group. In summary, three salient patterns emerge: (1) There were a number of reflexive saccades to the target location (which should have been inhibited) that increased from the level in CP participants, to the naMCI patients, to the aMCI patients, and finally showing the highest level in the AD patients. (2) Similarly, the time cost to correct the mistakes increases from the CP participants, to the naMCI patients, to the aMCI patients, and finally to the AD patients. Given 1500 milliseconds since target onset, the naMCI patients and the CP participants could correct almost all the mistakes, while the AD and aMCI patients have more uncorrected mistakes. (3) The CP participants revealed a higher proportion of correct antisaccades and corrected errors in comparison to the patient groups (AD, aMCI, naMCI).

DISCUSSION

We can summarise the key findings from this work: (1) These findings demonstrate for the first time, that the AST can discriminate between people with aMCI and

naMCI; and (2) The findings replicated the previously reported impairment in inhibitory control of antisaccades in people with dementia due to AD.

These results confirm that the AST is a promising biomarker for dementia. Given that people with MCI are more likely to develop dementia due to AD than cognitively healthy adults, and in particular that people with (aMCI) are at the highest risk of progressing to a full dementia syndrome, this may also offer an additional prognostic tool for predicting which people with a diagnosis of MCI are more likely to progress to dementia due to AD. Our results support previous literature which has also demonstrated that AD [3,5] and MCI [8,9] participants are impaired on the AST. These findings, when taken together, may therefore indicate that people with AD gradually lose the efficient control of attention and develop impairments of both inhibitory control and eye movement error-correction. There is a growing consensus that eye-tracking now provides an important opportunity for clinicians to detect the very early stages of Alzheimer’s disease, during the MCI phase. Several meta-analyses have been conducted all conclude that there is a clear excess of inhibition errors in AD (e.g. [19]). These findings are particularly compelling given the coupling of the impairments that have been replicated in these studies. For example, one recent study [20] replicated the increase in antisaccade errors together with a decrease in the frequency of corrected errors. This pattern of inhibitory impairment has not been found in other neuropsychiatric neurodegenerative such as schizophrenia [21] or Parkinson’s disease [5]. There is therefore little doubt that eye-tracking offers a highly reliable, simple, non-invasive assessment and patient-friendly tool for the cognitive assessment of dementia. In line with previous work, Holden et al [22] have shown that aMCI patients also show the increased antisaccade error rates. However, as one recent meta-analysis confirmed, no previous study has yet compared the different subtypes of MCI in a direct comparison of oculomotor function [19]. Here we show that people with aMCI have significant impairment of inhibitory control that is similar to AD; whilst people with naMCI are relatively unimpaired, with a level of inhibitory control that was more similar to the control group.

Our results suggest that inhibitory control of eye movement may be one of the earliest biomarkers of the onset of AD. Inhibitory control deficits appear to be associated with memory decline. There have been relatively few studies of antisaccades in MCI, and, to our knowledge, no longitudinal studies. In future work, the AST could be studied in people with MCI using a prospective longitudinal study design. We hypothesise that those people with increased antisaccade error rates

Table 2. Descriptive statistics (SD) of participants including cognitive assessment (MoCA) scores for each group.

	Dementia due to AD	Amnesic mild cognitive impairment	Non-amnesic mild cognitive impairment	Control participants	<i>p-value</i>
Age	74 (7.7)	74 (7.4)	69(6.9)	69 (7.2)	<.0005
Sex (% male)	50%	41%	57%	43%	.297 ns
MoCA total score	20 (5.7)	21(4.5)	25 (2.2)	28 (1.8)	<.0005
FCSRT – Free Recall	17.32 (12.0)	18.7 (7.7)	32.3 (4.2)	36.1 (5.7)	<.0005
FCSRT - Total	36.2 (14.8)	45.1 (4.4)	47.4 (1.3)	47.8 (0.8)	<.0005
Digit span total	15.6 (4.1)	16.4 (3.7)	16.7 (4.8)	18.7 (4.5)	<.0005
Spatial span total	11.3 (3.1)	12.6 (3.1)	13.0 (2.6)	14.6 (2.8)	<.0005

MoCA - Montreal Cognitive Assessment [25]; Free cued selective reminding task free recall and total score [26]; digit span and spatial span [27,28].

will be more likely to have poorer memories and may be at risk of developing dementia due to AD. Overall, our results support the role of the AST as a useful supplementary tool for the early detection of decline in people with MCI.

Inhibitory error rates in the antisaccade are sensitive to memory impairment, but may even precede it in a patient with dementia [5]. The results obtained from this study demonstrate that eye movements during the AST could be used to automatically classify participants as being at a higher risk of AD. There are potentially a number of practical implications for this observation. With early detection of AD, the potential for commencing effective interventions earlier are increased.

MATERIALS AND METHODS

Participants

Participants were men and women between the ages of 55 and 90, with at least 11 years of education and fluent English-speakers. Of these, 68 were people with dementia due to AD, 42 had a diagnosis of aMCI, and 47 had a diagnosis of naMCI. We also included 92 age-matched cognitively healthy people to act as control participants (see Table 2). Control participants were recruited from the local community or were the spouse/partner of the AD or MCI participants. All participants were white British or European. Participants with MCI or dementia due to AD were recruited through local memory clinics in the National Health Service (NHS) and had received a clinical diagnosis following a full assessment with a dementia

specialist. All those in the dementia group met clinical criteria for dementia due to AD, as per NINCDS-ADRDA criteria [23]. Those with a diagnosis of MCI met the following criteria [24]: (1) subjective complaints of memory decline (reported by the person themselves or an informant); (2) objective memory or other cognitive impairment (considered when scores on standard cognitive tests were >1.5 SDs below age/education adjusted norms) with or without deficits in other cognitive domains; (3) intact daily-life activities. To subtype the MCI group further into aMCI and naMCI, we applied the [24] criteria (see below). Participants with intact cognition (as assessed by a series of cognitive tasks; see below) were recruited from the local community. Participants were not eligible for the study if they had a previous history of head trauma, stroke, cardiovascular disease, active or past alcohol or substance misuse or dependence, or any physical or mental condition severe enough to interfere with their ability to participate in the study. Those with a global or specific learning disability were also not eligible to participate in the study. All participants had the capacity to consent to participation in the study and signed informed consent. Ethics' Committee approval was granted by Lancaster University and NHS Health Research Authority.

Stimuli and tasks

Eye-tracking was assessed using the AST. Cognition was assessed the Montreal Cognitive Assessment (MoCA: [25]), the Free and Cued Selective Reminding Test with Immediate Recall (FCSRT-IR: [26]), and the digit and spatial span [27,28].

Apparatus

We used an EyeLink Desktop 1000 eye-tracker (SR Research) with sampling at 500 Hz. Participants sat 55 cm away from the monitor (60 Hz). Their dominant eye was determined using the Miles test [29] and tracked accordingly. Experiment Builder software (SR Research) was used to control the stimulus events during the eye-tracking tasks.

Antisaccade task (AST)

Each antisaccade trial was preceded by a 1 second instruction screen stating that the participant should look toward the target. A central fixation target central fixation was displayed in white on a black background. This was displayed for one second. There was a 200ms blank interval before the appearance of the saccade distractor. The saccade distractor (in red) was then presented in a random order 4 degrees away from where the fixation target had been either on the left or right side for 2 seconds. Participants were asked to fixate at the central point then generate the saccade to the opposite position of the screen as soon as the distractor appeared. There were a total of 24 antisaccade trials in AST.

Montreal cognitive assessment (MoCA)

The MoCA is a brief screening tool for Alzheimer's dementia that includes the domains of attention and concentration, executive functions, memory, language, visuoconstructional skills, conceptual thinking, calculations, and orientation. The test generates a maximum score of 30; a scores of 26 or more is considered normal.

Free Cued Selective Reminding Task Immediate Recall (FCSRT-IR)

The International Working Group on Alzheimer's disease [30] recommended the free and cued selective reminding test (FCSRT: [26]) to assess memory, as it showed high sensitivity and specificity in the differentiation of dementia due to AD from healthy controls, and aMCI from naMCI (see [12]). Participants were asked to memorise line drawings of a set of easily recognised objects (e.g., grapes) which belonged to unique category cues (e.g., fruit). 16 items to be learned were presented four at a time on a card, one picture in each quadrant. Participants were asked to search each card, then point to and then name aloud each item (e.g., grapes) after its cue (fruit) was verbally presented. The card was then removed, and the participant immediately performed a cued recall of just those four items on the basis of the category cue. Participants were reminded of

any items that were not recalled by presenting the cue and the item together (e.g., the vehicle was a train). This procedure was repeated for all 16 pictures across the four cards. Participants were then given a test phase that consisted of three recall trials. Each test was preceded by a 20 second counting distractor task. Each recall trial consisted of two parts; after two minutes of free recall, category cues were provided for items not retrieved during the free recall phase. If subjects failed to retrieve the item when provided with the category cue, they were reminded by the presentation of both the cue and the item together. A measure of free recall and a measure of cued recall was obtained by calculating the correct responses (both out of a total of 48). This task has high validity as it has been used extensively in informing MCI and AD diagnoses [24]. [24] recommends that scores equal to or below 27 on the free recall score indicate aMCI, whilst scores of 28 and over indicate naMCI.

Digit span

In the digit span task [27,28], which assesses phonological memory function, participants were verbally presented with strings of single digit numbers. Once the string had been presented, the participant was asked to recall the digits in the correct serial order. The number of digits presented gradually increased during the course of the experiment, starting with two and going up to a maximum of nine. Two trials were presented at each level and a participant must get both correct in order to progress to the next level of the task. Participants then completed a reverse digit span task where participants need to reverse the order of the presented sequence. Again, the number of digits presented gradually increased from two to eight. Two trials were presented at each level with both correct needed in order to progress. A total digit span score was then calculated out of 30 by summing the correct trials together.

Spatial span

In the spatial span task [27,28], participants were presented with an array of nine squares. Squares in the array were selected one at a time by the experimenter. At the end of the sequence, it was the task of the participant to indicate the locations of the selected squares in the correct serial order. The number of squares selected in sequence increased over the course of the experiment from two up to a maximum of nine. Two trials were presented at each level and a participant had to get both correct in order to progress. A reverse version of the task was also performed with the participant indicating the sequence in the backwards order. A measure of total spatial span score was calculated out of a total of 32.

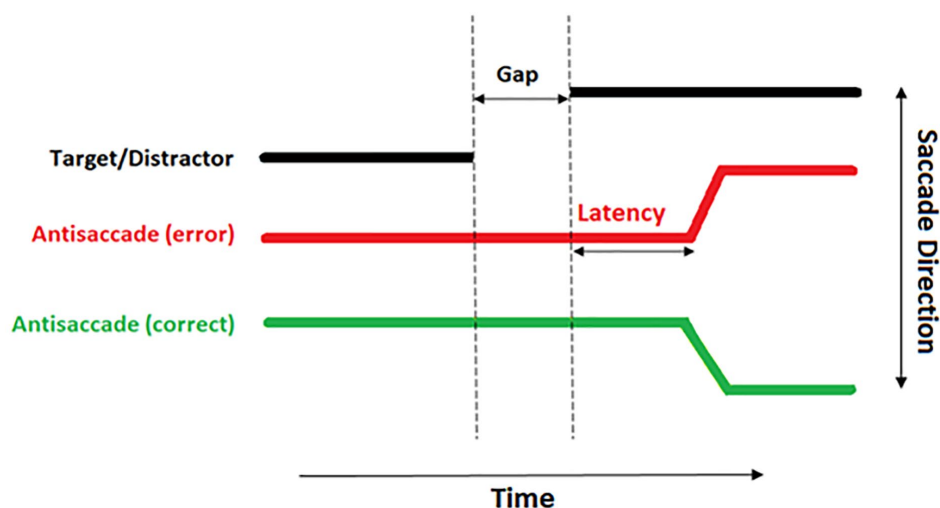


Figure 3. A diagrammatical representation of an antisaccade trial. The thick black line demonstrates the location of the distractor. The red line demonstrates the eye incorrectly moving toward the distractor. The green line demonstrates a correct antisaccade away from the distractor.

Data processing

The raw eye tracking data exported from the EyeLink DataViewer software were analysed offline in bespoke software [31] with the following features: Noise and spikes were filtered by removing all the frames where the velocity signal was greater than 1,500 deg/s or the acceleration signal was greater than 100,000 deg²/sec. All the fixations and saccadic events were detected by the EyeLink parser. All the saccades extracted for each trial as well as a range of spatial and temporal properties measured for each saccade were then stored in a table. Microsaccades with amplitude less than 0.7 deg were filtered from the data. The latency of the saccade was measured from the onset of the saccade to the target onset. Only the saccades made within the time window 80-700 ms after target onset (see Figure 3) were included to avoid ‘anticipatory saccades’ i.e. saccades which are initiated prior to the presentation of the distractor.

ACKNOWLEDGMENTS

The work described in this paper is funded by EPSRC project EP/M006255/1 Monitoring Of Dementia using Eye Movements (MODEM) and with support from the Sir John Fisher Foundation. We are grateful to Megan Polden, Nadia Maalin, and Claire Kelly for their help with data collection and to Joel Leakey.

CONFLICTS OF INTEREST

The authors have no conflicts of interest to report.

REFERENCES

1. Sperling RA, Aisen PS, Beckett LA, Bennett DA, Craft S, Fagan AM, Iwatsubo T, Jack CR Jr, Kaye J, Montine TJ, Park DC, Reiman EM, Rowe CC, et al. Toward defining the preclinical stages of Alzheimer’s disease: recommendations from the National Institute on Aging-Alzheimer’s Association workgroups on diagnostic guidelines for Alzheimer’s disease. *Alzheimers Dement.* 2011; 7:280–92. <https://doi.org/10.1016/j.jalz.2011.03.003> PMID:21514248
2. Ritchie CW, Russ TC, Banerjee S, Barber B, Boaden A, Fox NC, Holmes C, Isaacs JD, Leroi I, Lovestone S, Norton M, O’Brien J, Pearson J, et al. The Edinburgh Consensus: preparing for the advent of disease-modifying therapies for Alzheimer’s disease. *Alzheimers Res Ther.* 2017; 9:85. <https://doi.org/10.1186/s13195-017-0312-4> PMID:29070066
3. Crawford TJ, Higham S, Renvoize T, Patel J, Dale M, Suriya A, Tetley S. Inhibitory control of saccadic eye movements and cognitive impairment in Alzheimer’s disease. *Biol Psychiatry.* 2005; 57:1052–60. <https://doi.org/10.1016/j.biopsych.2005.01.017> PMID:15860346
4. Kaufman LD, Pratt J, Levine B, Black SE. Executive deficits detected in mild Alzheimer’s disease using the antisaccade task. *Brain Behav.* 2012; 2:15–21. <https://doi.org/10.1002/brb3.28> PMID:22574270

5. Crawford TJ, Higham S, Mayes J, Dale M, Shaunak S, Lekwuwa G. The role of working memory and attentional disengagement on inhibitory control: effects of aging and Alzheimer's disease. *Age (Dordr)*. 2013; 35:1637–50.
<https://doi.org/10.1007/s11357-012-9466-y>
PMID:[22903189](https://pubmed.ncbi.nlm.nih.gov/22903189/)
6. Crawford TJ, Parker E, Solis-Trapala I, Mayes J. Is the relationship of prosaccade reaction times and antisaccade errors mediated by working memory? *Exp Brain Res*. 2011; 208:385–97.
<https://doi.org/10.1007/s00221-010-2488-8>
PMID:[21107543](https://pubmed.ncbi.nlm.nih.gov/21107543/)
7. Crawford TJ, Higham S. Distinguishing between impairments of working memory and inhibitory control in cases of early dementia. *Neuropsychologia*. 2016; 81:61–67.
<https://doi.org/10.1016/j.neuropsychologia.2015.12.007> PMID:[26687733](https://pubmed.ncbi.nlm.nih.gov/26687733/)
8. Heuer HW, Mirsky JB, Kong EL, Dickerson BC, Miller BL, Kramer JH, Boxer AL. Antisaccade task reflects cortical involvement in mild cognitive impairment. *Neurology*. 2013; 81:1235–43.
<https://doi.org/10.1212/WNL.0b013e3182a6cbfe>
PMID:[23986300](https://pubmed.ncbi.nlm.nih.gov/23986300/)
9. Alichniewicz KK, Brunner F, Klünemann HH, Greenlee MW. Neural correlates of saccadic inhibition in healthy elderly and patients with amnesic mild cognitive impairment. *Front Psychol*. 2013; 4:467.
<https://doi.org/10.3389/fpsyg.2013.00467>
PMID:[23898312](https://pubmed.ncbi.nlm.nih.gov/23898312/)
10. Vos SJ, Verhey F, Frölich L, Kornhuber J, Wiltfang J, Maier W, Peters O, Rüter E, Nobili F, Morbelli S, Frisoni GB, Drzezga A, Didic M, et al, and Alzheimer's Disease Neuroimaging Initiative. Prevalence and prognosis of Alzheimer's disease at the mild cognitive impairment stage. *Brain*. 2015; 138:1327–38.
<https://doi.org/10.1093/brain/awv029>
PMID:[25693589](https://pubmed.ncbi.nlm.nih.gov/25693589/)
11. Mitchell AJ, Shiri-Feshki M. Rate of progression of mild cognitive impairment to dementia--meta-analysis of 41 robust inception cohort studies. *Acta Psychiatr Scand*. 2009; 119:252–65.
<https://doi.org/10.1111/j.1600-0447.2008.01326.x>
PMID:[19236314](https://pubmed.ncbi.nlm.nih.gov/19236314/)
12. Petersen RC. Mild cognitive impairment as a diagnostic entity. *J Intern Med*. 2004; 256:183–94.
<https://doi.org/10.1111/j.1365-2796.2004.01388.x>
PMID:[15324362](https://pubmed.ncbi.nlm.nih.gov/15324362/)
13. McKhann GM, Knopman DS, Chertkow H, Hyman BT, Jack CR Jr, Kawas CH, Klunk WE, Koroshetz WJ, Manly JJ, Mayeux R, Mohs RC, Morris JC, Rossor MN, et al. The diagnosis of dementia due to Alzheimer's disease: recommendations from the National Institute on Aging-Alzheimer's Association workgroups on diagnostic guidelines for Alzheimer's disease. *Alzheimers Dement*. 2011; 7:263–69.
<https://doi.org/10.1016/j.jalz.2011.03.005>
PMID:[21514250](https://pubmed.ncbi.nlm.nih.gov/21514250/)
14. Csukly G, Sirály E, Fodor Z, Horváth A, Salacz P, Hidasi Z, Csibri É, Rudas G, Szabó Á. The differentiation of amnesic type MCI from the non-amnesic types by structural MRI. *Front Aging Neurosci*. 2016; 8:52.
<https://doi.org/10.3389/fnagi.2016.00052>
PMID:[27065855](https://pubmed.ncbi.nlm.nih.gov/27065855/)
15. Fischer P, Jungwirth S, Zehetmayer S, Weissgram S, Hoenigschnabl S, Gelpi E, Krampla W, Tragl KH. Conversion from subtypes of mild cognitive impairment to Alzheimer dementia. *Neurology*. 2007; 68:288–91.
<https://doi.org/10.1212/01.wnl.0000252358.03285.9d> PMID:[17242334](https://pubmed.ncbi.nlm.nih.gov/17242334/)
16. Yaffe K, Petersen RC, Lindquist K, Kramer J, Miller B. Subtype of mild cognitive impairment and progression to dementia and death. *Dement Geriatr Cogn Disord*. 2006; 22:312–19.
<https://doi.org/10.1159/000095427> PMID:[16940725](https://pubmed.ncbi.nlm.nih.gov/16940725/)
17. Ward A, Tardiff S, Dye C, Arrighi HM. Rate of conversion from prodromal Alzheimer's disease to Alzheimer's dementia: a systematic review of the literature. *Dement Geriatr Cogn Dis Extra*. 2013; 3:320–32.
<https://doi.org/10.1159/000354370>
PMID:[24174927](https://pubmed.ncbi.nlm.nih.gov/24174927/)
18. Dobson AJ, Barnett AG. *An Introduction to generalized linear models* (Fourth ed.). Boca Raton, Florida: CRC Press; 2008.
19. Kahana Levy N, Lavidor M, Vakil E. Prosaccade and antisaccade paradigms in persons with Alzheimer's disease: a meta-analytic review. *Neuropsychol Rev*. 2018; 28:16–31.
<https://doi.org/10.1007/s11065-017-9362-4> PMID:[29079970](https://pubmed.ncbi.nlm.nih.gov/29079970/)
20. Noiret N, Carvalho N, Laurent É, Chopard G, Binetruy M, Nicolier M, Monnin J, Magnin E, Vandel P. Saccadic eye movements and attentional control in Alzheimer's disease. *Arch Clin Neuropsychol*. 2018; 33:1–13.
<https://doi.org/10.1093/arclin/acx044>
PMID:[28525567](https://pubmed.ncbi.nlm.nih.gov/28525567/)
21. Crawford TJ, Haeger B, Kennard C, Reveley MA, Henderson L. Saccadic abnormalities in psychotic patients. I. Neuroleptic-free psychotic patients. *Psychol Med*. 1995; 25:461–71.
<https://doi.org/10.1017/S0033291700033389>
PMID:[7480427](https://pubmed.ncbi.nlm.nih.gov/7480427/)

22. Holden JG, Cosnard A, Laurens B, Asselineau J, Biotti D, Cubizolle S, Dupouy S, Formaglio M, Koric L, Seassau M, Tilikete C, Vighetto A, Tison F. Prodromal Alzheimer's Disease Demonstrates Increased Errors at a Simple and Automated Anti-Saccade Task. *J Alzheimers Dis.* 2018; 65:1209–23.
<https://doi.org/10.3233/JAD-180082>
PMID:[30149445](https://pubmed.ncbi.nlm.nih.gov/30149445/)
23. McKhann G, Drachman D, Folstein M, Katzman R, Price D, Stadlan EM. Clinical diagnosis of Alzheimer's disease: report of the NINCDS-ADRDA Work Group under the auspices of Department of Health and Human Services Task Force on Alzheimer's Disease. *Neurology.* 1984; 34:939–44.
<https://doi.org/10.1212/WNL.34.7.939>
PMID:[6610841](https://pubmed.ncbi.nlm.nih.gov/6610841/)
24. Lemos R, Simões MR, Santiago B, Santana I. The free and cued selective reminding test: validation for mild cognitive impairment and Alzheimer's disease. *J Neuropsychol.* 2015; 9:242–57.
<https://doi.org/10.1111/jnp.12048> PMID:[24894485](https://pubmed.ncbi.nlm.nih.gov/24894485/)
25. Nasreddine ZS, Phillips NA, Bédirian V, Charbonneau S, Whitehead V, Collin I, Cummings JL, Chertkow H. The Montreal Cognitive Assessment, MoCA: a brief screening tool for mild cognitive impairment. *J Am Geriatr Soc.* 2005; 53:695–99.
<https://doi.org/10.1111/j.1532-5415.2005.53221.x>
PMID:[15817019](https://pubmed.ncbi.nlm.nih.gov/15817019/)
26. Grober E, Buschke H. Genuine memory deficits in dementia. *Dev Neuropsychol.* 1987; 3:13–36.
<https://doi.org/10.1080/87565648709540361>
27. Wechsler D. Wechsler Adult Intelligence Scale (WAIS-III) (3rd ed.). San Antonio, TX: The Psychological Corporation; 1997.
28. Wechsler D. Wechsler memory scale (WMS-III) (3rd ed.). San Antonio, TX: The Psychological corporation; 1997.
29. Roth HL, Lora AN, Heilman KM. Effects of monocular viewing and eye dominance on spatial attention. *Brain.* 2002; 125:2023–35.
<https://doi.org/10.1093/brain/awf210>
PMID:[12183348](https://pubmed.ncbi.nlm.nih.gov/12183348/)
30. Cummings JL, Dubois B, Molinuevo JL, Scheltens P. International Work Group criteria for the diagnosis of Alzheimer disease. *Med Clin North Am.* 2013; 97:363–68.
<https://doi.org/10.1016/j.mcna.2013.01.001>
PMID:[23642575](https://pubmed.ncbi.nlm.nih.gov/23642575/)
31. Mardanbegi D, Wilcockson T, Sawyer P, Gellersen HW, Crawford TJ. SaccadeMachine: Software for Analyzing Saccade Tests (Anti-saccade and Pro-saccade). In Proceedings of Communication by Gaze Interaction, Denver, CO, USA, June 25–28, 2019 (COGAIN@ETRA'19)

Involvement of adiponectin in age-related increases in tear production in mice

Yosuke Shikama^{1,*}, Mie Kurosawa^{1,*}, Masae Furukawa¹, Naozumi Ishimaru², Kenji Matsushita¹

¹Department of Oral Disease Research, National Center for Geriatrics and Gerontology, Obu 474-8511, Japan

²Department of Oral Molecular Pathology, Tokushima University Graduate School of Biomedical Sciences, Tokushima 770-8504, Japan

*Equal contribution

Correspondence to: Yosuke Shikama; email: shikama@ncgg.go.jp

Keywords: dry eye, adiponectin, peroxisome proliferator-activated receptor gamma, senescence-associated T cells, aging

Received: May 27, 2019

Accepted: September 21, 2019

Published: October 8, 2019

Copyright: Shikama et al. This is an open-access article distributed under the terms of the Creative Commons Attribution License (CC BY 3.0), which permits unrestricted use, distribution, and reproduction in any medium, provided the original author and source are credited.

ABSTRACT

Common age-related changes in the human eye contribute to the development of dry eye, including decreases in aqueous tear production. Although the infiltration of lymphocytes into the lacrimal glands occurs with age, age-related increases in tear production have also been observed in mice; however, the mechanisms underlying this increase remain unclear. We herein demonstrated that increases in tear production were not dependent on body weight gain or systemic conditions, such as insulin resistance, using aged mice and high-fat diet-fed mice. The results obtained also showed that senescence-associated T (SA-T) cells accumulated in the lacrimal glands of aged mice, particularly females. Expression levels of the nuclear transcription factor peroxisome proliferator-activated receptor- γ (PPAR γ) in whole lacrimal glands and epithelial cells isolated from lacrimal glands were significantly higher in aged mice than in young mice. The expression levels of adiponectin and one of its receptors, AdipoR2, also increased in the lacrimal glands of aged mice, but not in those of high-fat diet-fed mice. Collectively, the present results indicate that PPAR γ and adiponectin-mediated signaling contribute to age-related increases in tear production in mice and have potential as therapeutic targets for the treatment of dry eye in humans.

INTRODUCTION

Epidemiological studies have shown that the prevalence of dry eye increases every five years after the age of 50 years, with a higher prevalence being reported in women than in men [1–3]. Age and female sex have been identified as the greatest risk factors for dry eye, and this is supported by the clinical findings of decreased tear production in women through the 6th decade of life [4, 5]. The lacrimal glands are significantly affected by aging. Various histopathological changes, which cause tear dysfunction, have been reported in the lacrimal glands of humans, such as the infiltration of lymphocytes [6, 7]. However, a previous study reported that despite the age-related infiltration of lymphocytes into the lacrimal glands of aged mice, the volume of tears produced was

larger in aged mice than in young mice [8]. The mechanisms underlying these increases in tear production in aged mice have not yet been elucidated.

Metabolic disorders, such as diabetes, affect tear production and are associated with dry eye [9, 10]. Regarding the mechanisms responsible for type 2 diabetes, aging is known to induce insulin resistance [11], which is attributed to decreased plasma adiponectin levels in humans [12]. Adiponectin is a 30-kDa multimeric protein that is mainly secreted by white adipose tissue, and has insulin-sensitizing [13], anti-atherogenic, and anti-inflammatory properties [14, 15]. Moreover, adiponectin is secreted from adipocytes into the bloodstream as three oligomeric complexes: a trimer, hexamer, and high-molecular-weight multimer

comprising at least 18 monomers [16, 17]. Assembly into the high-molecular-weight form is essential for the function of adiponectin [18]. Globular adiponectin, the globular C1q domain of adiponectin generated from the full-length protein by proteolysis, is also biologically active [19]. AdipoR1 and AdipoR2, two structurally related seven-transmembrane receptors, function as adiponectin receptors. AdipoR1 exhibits high affinity for globular adiponectin and low affinity for full-length adiponectin. On the other hand, AdipoR2 mainly recognizes full-length adiponectin [20]. The nuclear transcription factor peroxisome proliferator-activated receptor- γ (PPAR γ) is a major regulator of adipocyte function and controls the secretion of adipokines, particularly adiponectin [21–23]. Previous studies reported that a PPAR γ ligand and adiponectin exerted therapeutic effects on tear production [24, 25].

In the present study, we examined the involvement of insulin resistance in stimulated tear secretion in aged [26] and high-fat diet-fed [27] mice. Although the volume of tears secreted increased with age, it slightly or significantly decreased in high-fat diet-fed mice in a gender-dependent manner. Neither high-fat diet feeding nor aging exerted significant effects on the mRNA expression levels of muscarinic acetylcholine receptor M3 (M3R), a selective receptor of pilocarpine, in the lacrimal glands. Moreover, we confirmed that not only lymphocytes, as previously reported [8], but also senescence-associated T (SA-T) cells, which mainly accumulate in lymphoid tissues with age [28], also accumulated in the lacrimal glands of aged mice. PPAR γ mRNA expression levels significantly increased in lacrimal glands as well as primary epithelial cells isolated from the lacrimal glands of aged mice. Adiponectin mRNA levels significantly increased in the white adipose tissue of aged mice. The present results also revealed that adiponectin and AdipoR2 mRNA expression levels significantly increased in the lacrimal glands of aged mice, but not in those of high-fat diet-fed mice. These results indicate that PPAR γ and adiponectin-mediated signaling is involved in age-related increases in tear production in mice.

RESULTS

Increases in pilocarpine-stimulated tear secretion in aged mice, but not in high-fat diet-fed mice

Body weight and the weight of the lacrimal glands were significantly higher in aged than in young male and female mice (Figure 1A, 1B). The volume of tears secreted also significantly increased with aging (Figure 1C), even when volumes were adjusted for body weight (Figure 1D) or the weight of the lacrimal

glands (Figure 1E). However, although body weight significantly or slightly increased in high-fat diet-fed male or female mice, respectively (Figure 1F), the volume of tears secreted significantly decreased in high-fat diet-fed female, but not male mice (Figure 1G, 1H). These results suggest that the volume of stimulated tear secretion was not dependent on body weight or systemic conditions, such as insulin resistance.

Effects of aging or high-fat diet feeding on M3R mRNA expression in murine lacrimal glands

M3R is strongly expressed in the lacrimal glands and is involved in the secretion of tears. Therefore, we examined M3R expression levels in the lacrimal glands of aged and high-fat diet-fed mice. No significant differences were observed in M3R mRNA expression levels between young and aged mice; expression levels were slightly lower in aged mice than in young mice (Figure 2A). On the other hand, no significant differences were noted in M3R mRNA expression levels between high-fat diet-fed mice and normal diet-fed mice independent of sex (Figure 2B). These results indicate that the increases and decreases observed in the volume of tears secreted in aged mice and high-fat diet-fed mice, respectively, were not dependent on M3R expression levels in the lacrimal glands.

SA-T cell accumulation in lacrimal glands of aged mice

The immune system undergoes aging, a typical feature of which is a chronic, low-grade inflammatory status called inflammaging [29], which is characterized by a general increase in the production of pro-inflammatory cytokines. Significant changes also occur in overall T-cell populations with age. In CD4⁺ T cells, the populations of naïve (CD44^{lo}CD62L^{hi}) T cells markedly decline in ontogeny, with age-dependent increases occurring in effector memory T cells (CD44^{hi}CD62L^{lo}) [30, 31]. Among effector memory CD4⁺ T cells, a unique population, SA-T cells, which express programmed cell death 1 (PD-1) and CD153, increase in lymphoid tissues with aging [28]. Moreover, Shirakawa et al. reported that SA-T cells also accumulated in the visceral adipose tissue of high-fat diet-fed mice, which induced chronic inflammation in visceral adipose tissue and insulin resistance [32]. We confirmed that effector memory CD4⁺ T cells markedly increased in the lacrimal glands of male and female aged mice (Figure 3A). The proportion of SA-T cells also significantly increased in male and female aged mice (Figure 3B, 3C), and the number of SA-T cells was approximately four-fold higher in female aged mice than in male aged mice (Figure 3D). Moreover, we

confirmed that SA-T cells did not accumulate in the lacrimal glands of high-fat diet-fed mice based on CD153 mRNA expression levels (Figure 3E). These results demonstrated that SA-T cells accumulated in the lacrimal glands of aged, but not high-fat diet-fed mice.

PPAR γ expression in lacrimal glands and adiponectin mRNA expression in the white adipose tissue of aged mice

PPAR γ expression levels in the white adipose tissue of humans and a rodent model were shown to significantly decrease with aging [33]. However, in the present study,

PPAR γ mRNA expression levels in the lacrimal glands significantly increased in aged mice (Figure 4A), but not in high-fat diet-fed mice (Figure 4B). By isolating primary epithelial cells from the lacrimal glands, we also confirmed that these expression levels significantly increased in epithelial cells isolated from aged mice (Figure 4C). PPAR γ exists as two isoforms, PPAR γ 1 and PPAR γ 2, with the latter containing an additional 30 amino acids at its N terminus. PPAR γ 1 is expressed in many tissues, while the expression of PPAR γ 2 is restricted to adipose tissue under physiological conditions [34]. We found that PPAR γ 1 protein levels were significantly increased in the lacrimal glands of

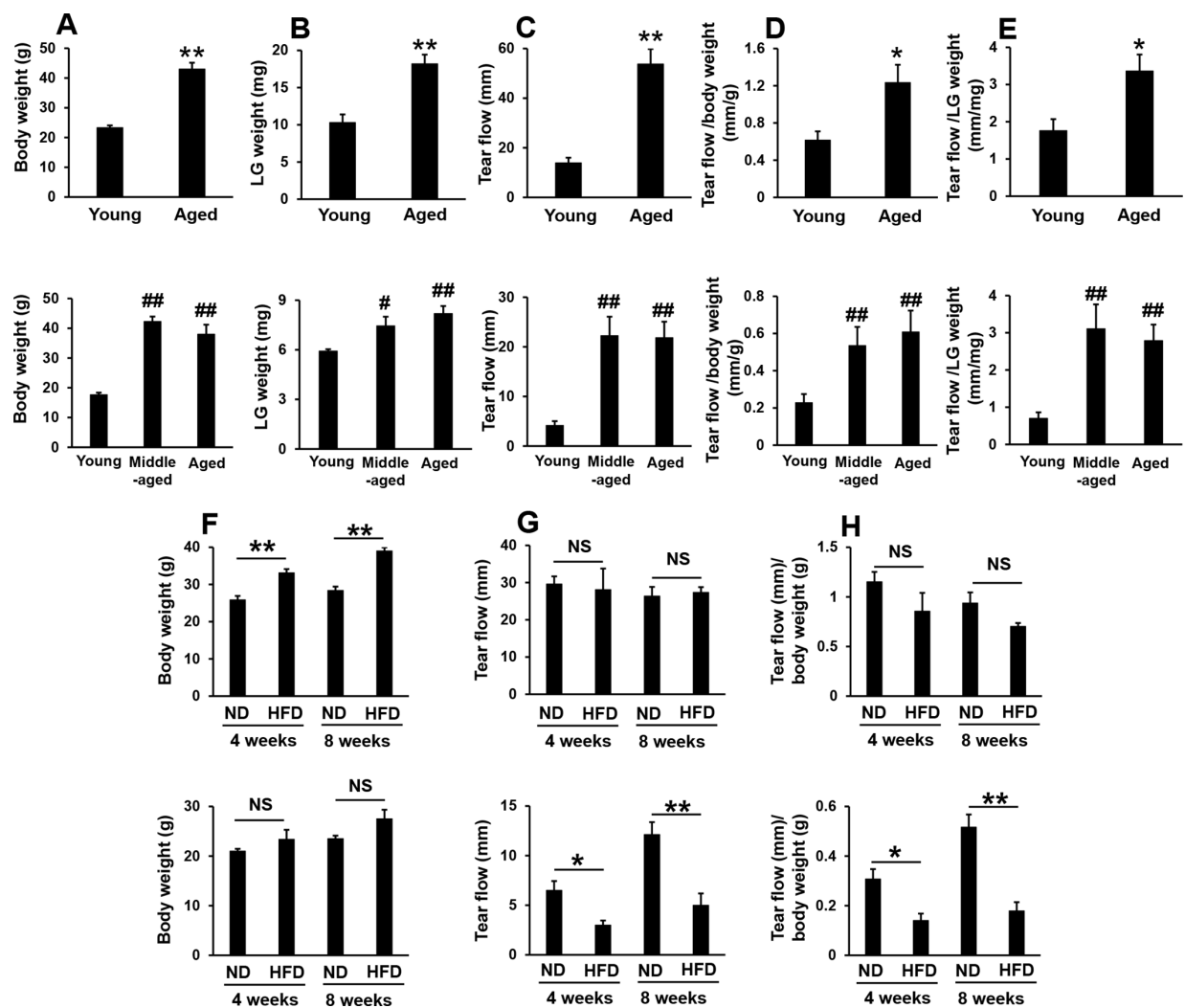


Figure 1. Pilocarpine-stimulated tear secretion increased in aged mice, but not in high-fat diet-fed mice. (A and B) Body weights and the weights of the lacrimal glands (LG) in young, middle-aged, and aged mice. Upper and lower graphs show male (N=5) and female mice (N=4-6), respectively. (C-E) Absolute volume of tear flow (C), adjusted by body weight (D) or LG weight (E). Upper and lower graphs show male (N=6) and female mice (N=4-6), respectively. (F) Body weight in normal diet (ND)- or high-fat diet (HFD)-fed mice for the indicated period (N=4). Upper and lower graphs show male and female mice, respectively. (G and H) Absolute volume of tear flow (G) adjusted by body weight (H) in ND or HFD-fed mice for the indicated period (N=4). Upper and lower graphs show male and female mice, respectively. Values are presented as means \pm SEM. * p <0.05 and ** p <0.01 (an unpaired Student's t -test). # p <0.05 and ## p <0.01 versus young mice (Dunnett's multiple comparison test).

aged mice (Figure 4D), and PPAR γ was detected in both the cytoplasm and nuclei, with higher expression levels in the cytosol of acinar cells (Figure 4E). A previous study reported that adiponectin mRNA levels in adipose tissue significantly decreased in high-fat diet-fed mice and obese volunteers [35]. However, although body weight and the volume of white adipose tissue in mice increased with age, adiponectin mRNA levels significantly increased in the white adipose tissue of aged mice (Figure 4F). Since a PPAR γ ligand and adiponectin have been shown to enhance tear secretion [24, 25], the present results indicate that increases in PPAR γ expression levels in the lacrimal glands and in adiponectin expression levels in white adipose tissue are involved in age-related increases in tear secretion in mice.

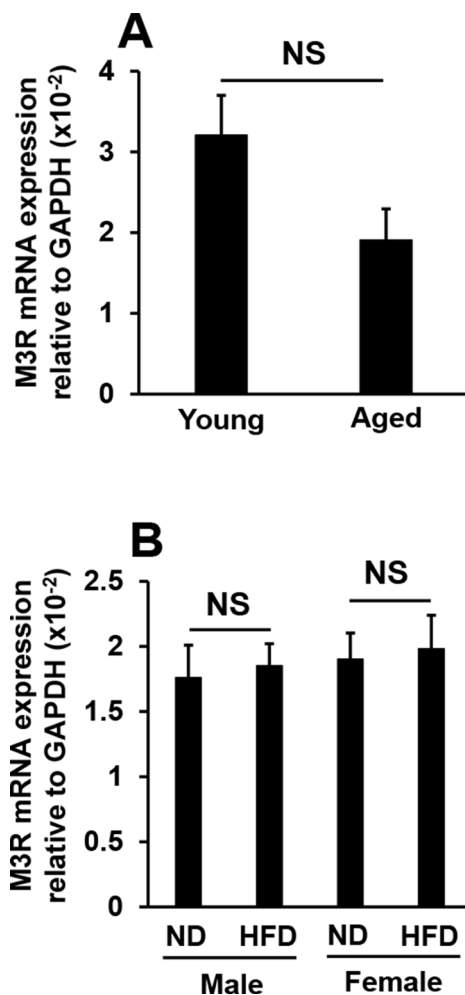


Figure 2. Effects of aging or high-fat diet feeding on M3R mRNA expression in lacrimal glands. M3R mRNA expression levels in young and aged mice (N=7-8) (A), and in mice fed a normal diet (ND) or high-fat diet (HFD) for 8 weeks (N=4-5) (B). Values are presented as means \pm SEM. NS, not significant (an unpaired Student's *t*-test).

Effects of aging and high-fat diet feeding on adiponectin, adipoR1, and adipoR2 expression levels in lacrimal glands

AdipoR1 and AdipoR2 are expressed in murine lacrimal glands [25], and the administration of 5-aminoimidazole-4-carboxamide ribonucleoside (AICAR), which is an activator of adenosine monophosphate-activated protein kinase (AMPK), similar to adiponectin, induced tear secretion in mice [36]. Therefore, we investigated adiponectin, adipoR1, and adipoR2 expression levels in the lacrimal glands of aged and high-fat diet-fed mice. The mRNA expression levels of adiponectin significantly increased in aged mice, but not in high-fat diet-fed male or female mice (Figure 5A). No significant changes were observed in adipoR1 mRNA expression levels in aged or high-fat diet-fed mice (Figure 5B). The mRNA expression levels of adipoR2, which is mainly activated by full-length adiponectin and, in turn, activates AMPK, were significantly increased in aged mice, but not in high-fat diet-fed mice (Figure 5C). In a Western blotting analysis, we confirmed that AdipoR2 protein levels were markedly increased in the lacrimal glands of aged mice (Figure 5D). Moreover, EpCAM-positive cells expressed AdipoR2 in the lacrimal glands of aged mice, particularly in duct cells and the basal membrane of acinar cells (Figure 5E). Based on the results shown in Figure 4, age-related increases in tear secretion may be due to elevated expression levels of PPAR γ , adiponectin, and adipoR2 in the lacrimal glands as well as increased adiponectin expression levels in white adipose tissue.

DISCUSSION

Although age and female sex are the greatest risk factors for dry eye in humans, we and other researchers [8, 37] showed that aqueous and pilocarpine-stimulated aqueous tear production both paradoxically increased with age in mice. The plasma levels of high-molecular-weight adiponectin, which may represent the most biologically active form of adiponectin [38, 39], were previously shown to decrease with age in women only [40], whereas high-molecular-weight adiponectin levels in plasma [41] and adiponectin mRNA expression in white adipose tissue (Figure 4F) both increased with age in mice. These discrepancies between human and murine adiponectin levels may result in paradoxical tear secretion with age. We also confirmed that the volume of tears secreted significantly decreased in high-fat diet-fed female, but not male mice (Figure 1G, H). Comb et al. reported that increases in plasma adiponectin levels during sexual maturation were 2.5-fold larger in female mice than in male mice [42]. In the present study, we fed mice a normal or high-fat diet from 4 weeks of age for 4 or 8 weeks, and sexual maturation occurred during this period. Since adiponectin mRNA levels in adipose

tissue significantly decreased in high-fat diet-fed mice [35], plasma adiponectin levels may markedly decrease if feeding of the high-fat diet starts before or during sexual maturation in female mice, resulting in reductions in tear secretion presumably via an adiponectin-mediated pathway.

In addition to previous findings showing mild or moderate lymphocytic infiltration in the lacrimal glands of aged mice [8, 43], we also noted an increase in the accumulation of SA-T cells in the lacrimal glands with age (Figure 3). The elevated tear volume in aged mice suggests that this level of inflammation is not sufficient to decrease secretory function. SA-T cells express PD-1, which a negative costimulatory receptor for T-cell receptor (TCR) signaling [44], and CD153, which is a tumor necrosis factor (TNF) superfamily protein [45]. SA-T cells show compromised proliferation and express large amounts of proinflammatory cytokines, such as osteopontin [28]. We demonstrated that the number of SA-T cells was approximately four-fold higher in female aged mice than in male aged mice (Figure 3D).

However, McClellan et al. reported that the CD4⁺ T-cell population was larger in 24-month-old male mice than in female mice of the same age [8]. In humans [46] and mice [47], senescent CD4⁺ T cells have been shown to play a role in the pathogenesis of rheumatoid arthritis and systemic lupus erythematosus, which are female-dominant systemic autoimmune diseases. These findings indicate that the systemic conditions of females may be more inducible to senescent CD4⁺ T cells than those of males. In the present study, we evaluated CD153 mRNA levels as a marker for SA-T cells (Figure 3E). In mice, CD153 has been detected on activated CD4⁺ T cells and dendritic cells [48]. Infiltrated CD4⁺ T cells in the lacrimal glands of aged mice were composed of the naïve or memory phenotype (Figure 3A). We confirmed that CD8⁺ and naïve CD4⁺ T cells did not express CD153 using a flow cytometric analysis (Supplementary Figure 1). Regarding DC, McClellan et al. previously reported that CD11b⁺ major histocompatibility complex (MHC) II⁺ cells and CD11c⁺ MHC II⁺ cells decreased [8], and we also confirmed that CD11b⁺ CD11c⁺ cells significantly

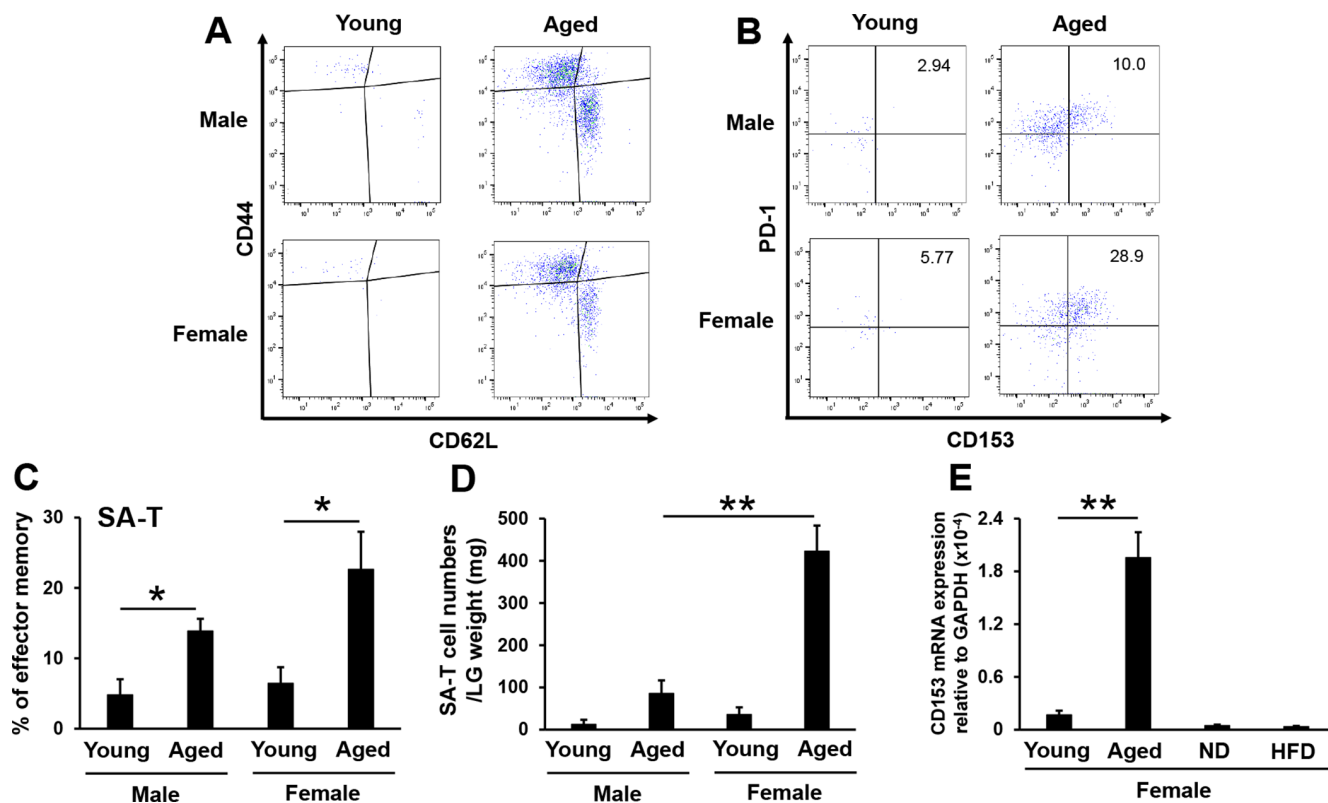


Figure 3. SA-T cells accumulate in lacrimal glands of aged mice, particularly in female mice. (A and B) Naïve (CD44^{lo}CD62L^{hi}) and effector memory (CD44^{hi}CD62L^{lo}) expression in CD4⁺ T cells (A), or PD-1⁺CD153⁺ expression in effector memory CD4⁺ T cells (B) in the lacrimal glands of young and aged mice. Results are representative of those from each group of mice. (C and D) Proportions (N=5) (C) and numbers adjusted by the lacrimal gland (LG) weight (N=4) (D) of PD-1⁺CD153⁺ cells gated on effector memory CD4⁺ T cells in the LG of young and aged mice. (E) CD153 mRNA expression levels in the LG of young and aged female mice, and of female mice fed a normal diet (ND) or high-fat diet (HFD) for 8 weeks (N=4-5). Values are presented as means ± SEM. *p<0.05 and **p<0.01 (an unpaired Student's *t*-test).

decreased in the lacrimal glands of aged mice (Supplementary Figure 2). Based on these results, it is reasonable to consider CD153 mRNA expression levels as a SA-T cell marker in the lacrimal glands using a real-time PCR analysis.

In recent years, evidence has been accumulating to support the potential benefits of PPAR γ , which

attenuates or prevents eye diseases. Chen et al. [24] reported that the expression of PPAR γ was down-regulated in the conjunctiva of mice with dry eye, and they also found that pioglitazone, a synthetic PPAR γ ligand, exerted therapeutic effects to increase tear fluid production and enhance tear film stability. Moreover, the localization of PPAR γ was shown to be involved in age-related changes in the meibomian glands, resulting

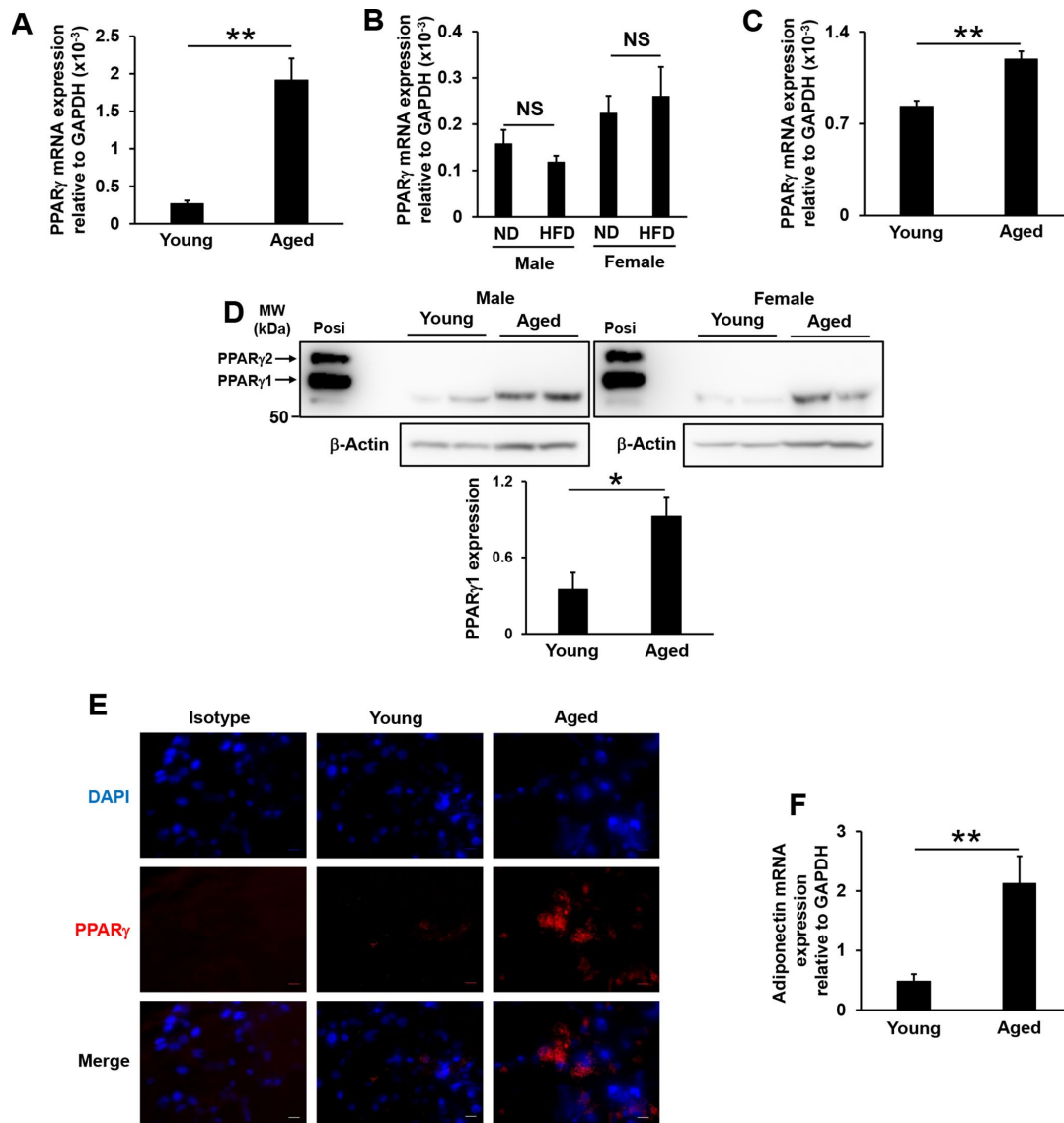


Figure 4. PPAR γ expression in lacrimal glands and adiponectin mRNA expression in the white adipose tissue of aged and high-fat diet-fed mice. (A and B) PPAR γ mRNA expression levels in the lacrimal glands of young and aged mice (N=7-8) (A), or of mice fed a normal diet (ND) or high-fat diet (HFD) for 8 weeks (N=4-5) (B). (C) PPAR γ mRNA expression levels in the epithelial cells of the lacrimal glands of young and aged mice (N=4). (D) Detection of the PPAR γ protein by Western blotting. Lysates prepared from the lacrimal glands of young and aged mice were immunoblotted with anti-AdipoR2 and anti- β -Actin antibodies. Left and right images show male (N=2) and female mice (N=2), respectively. The positive control (Posi) is a lysate prepared from the subcutaneous fat of young mice. The bar graph shows integrated signal intensities in AdipoR2 normalized to that of β -Actin (N=4). (E) PPAR γ expression in the acinar cells of the lacrimal glands of young and aged mice as detected by immunofluorescence. Nuclei were stained with DAPI. Bars = 10 μ m. (F) Adiponectin mRNA expression levels in the mesenteric white adipose tissues of young and aged mice (N=4-5). Values are presented as means \pm SEM. NS, not significant. **p<0.01 (an unpaired Student's *t*-test).

in meibomian gland dysfunction [49, 50]. We and other researchers reported the accumulation of lymphocytes in the lacrimal glands of aged mice. PPAR γ is expressed on some immune cells, such as macrophages, B lymphocytes, and T lymphocytes [51–53]. By isolating epithelial cells from the lacrimal

glands, we revealed that PPAR γ mRNA expression levels were up-regulated in aged mice (Figure 4C). Further experiments are needed to elucidate the underlying molecular mechanisms and demonstrate the efficacy of PPAR γ ligands for the treatment of dry eye diseases.

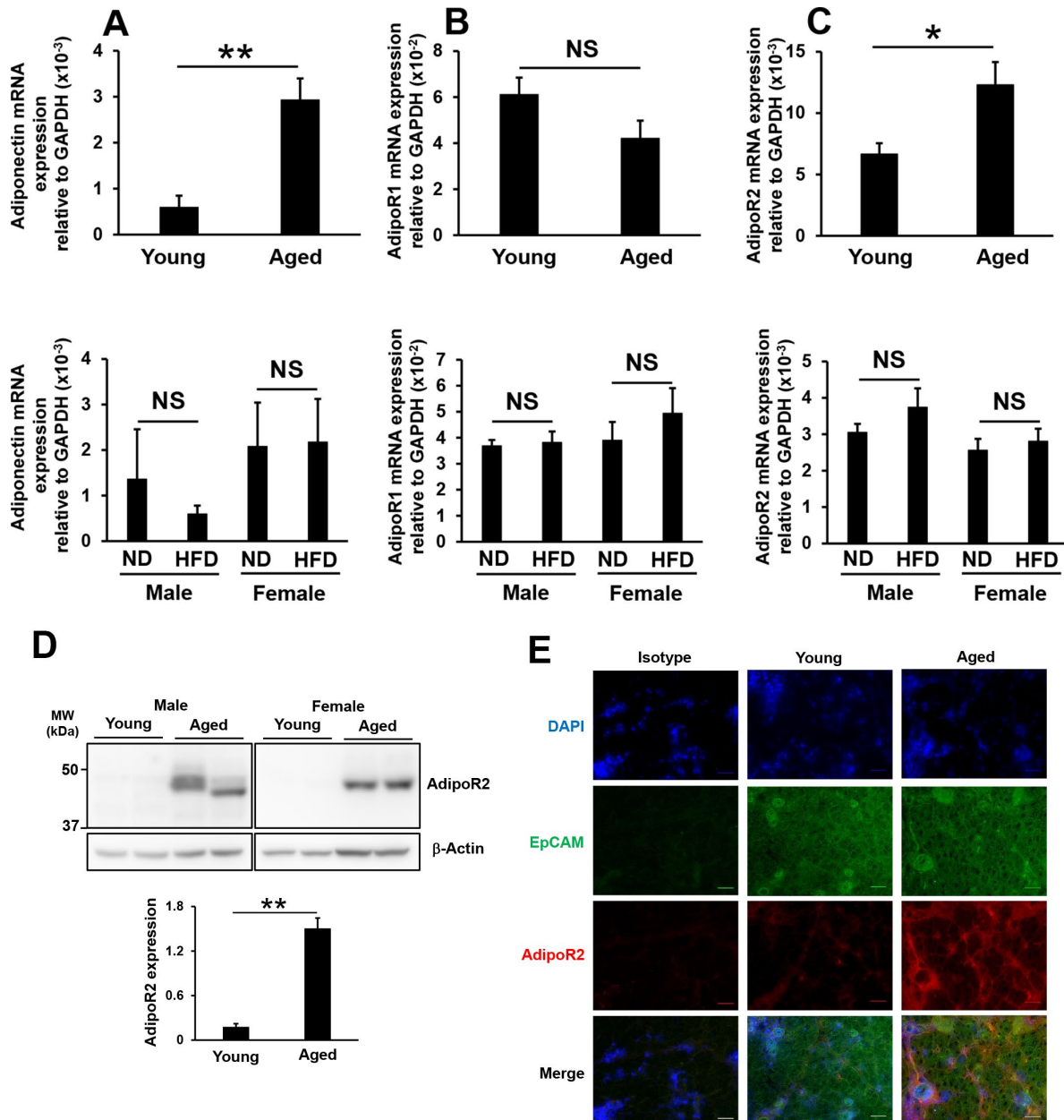


Figure 5. Influence of aging or high-fat diet feeding on adiponectin, adipoR1, and adipoR2 expression in lacrimal glands. Adiponectin (A), adipoR1 (B), and adipoR2 (C) mRNA expression levels in lacrimal glands. Upper and lower graphs show results in young and aged mice (N=7-8), and in mice fed a normal diet (ND) or high-fat diet (HFD) for 8 weeks (N=4-5), respectively. (D) Detection of the AdipoR2 protein by Western blotting. Lysates prepared from the lacrimal glands of young and aged mice were immunoblotted with anti-AdipoR2 and anti- β -Actin antibodies. Left and right images show male (N=2) and female mice (N=2), respectively. The bar graph shows integrated signal intensities in AdipoR2 normalized to that of β -Actin (N=4). (E) AdipoR2 expression in the lacrimal glands of young and aged mice as detected by immunofluorescence. Nuclei were stained with DAPI. Bars = 40 μ m. Values are presented as means \pm SEM. NS, not significant. * p <0.05 and ** p <0.01 (an unpaired Student's *t*-test).

IL-6 and TNF- α contribute to the senescence-associated secretory phenotype (SASP) [54], and their concentrations were found to be increased in the serum of both high-fat diet fed [55] and aged [56] mice. Moreover, the levels of these cytokines in tear fluid were shown to be higher in dry eye patients than in control subjects [57–59]. Leptin is mainly produced by adipocytes and is regarded as a proinflammatory adipokine because it appears to contribute to the so-called low-grade inflammatory state in overweight and obese individuals [60]. Leptin concentrations were previously shown to be increased in the serum of high-fat diet fed and aged mice [61]. The present results showed that the volume of tears was increased in aged (Figure 1C–1E), but not high-fat fed (Figure 1G and 1H) mice even when IL-6, TNF- α , and leptin concentrations were elevated in the serum of these mice. Furthermore, no significant differences were observed in IL-6 mRNA levels (we were unable to detect leptin even when the threshold cycle value was more than 40 cycles) in the epithelial cells of lacrimal glands between young and aged mice, whereas IL-6 and leptin mRNA levels were significantly higher in the lacrimal glands of aged mice (Supplementary Figure 3), suggesting that the source of IL-6 and leptin mRNA is not epithelial cells (possibly infiltrated lymphocytes).

In conclusion, the present results demonstrated the accumulation of SA-T cells in aged mice, which occurred to a greater extent in female than in male mice. Furthermore, increased tear secretion in aged mice appeared to be mediated by PPAR γ and adiponectin-mediated signaling. These results may explain the discrepancy in the volume of tears secreted with age between humans and mice.

MATERIALS AND METHODS

Animals

All animal experiments were approved by and conducted in accordance with guidelines established by the National Center for Geriatrics and Gerontology Animal Ethics Committee. Young adult C57BL/6N mice (age: 8–10 weeks), middle-aged adult C57BL/6N mice (age: 12 months), and aged adult C57BL/6N mice (age: 22–25 months) were obtained from Japan SLC Inc. (young and middle-aged) or the Experimental Animal Facility at the National Center for Geriatrics and Gerontology (aged: Obu, Japan). In high-fat diet experiments, mice were fed a normal diet (CE-2) or high-fat diet (HFD-32) from 4 weeks of age, as described in the Figure legends. These diets were purchased from CLEA Japan, Inc. Mice were housed in specific pathogen-free conditions under a 12-h light-dark photocycle and had *ad libitum* access to water and

the diet. The temperature in the room was maintained at $23 \pm 2^\circ\text{C}$ and $50 \pm 10\%$ humidity.

Measurement of tear flow rates

The phenol red thread test was used to measure the stimulated flow rates of tears as previously described [62]. Briefly, individual mice were weighed, anesthetized, and intraperitoneally injected with 1 mg/kg of pilocarpine (Kanto Chemical Co., Inc.). Five min later, tear volumes were measured using a phenol red thread (ZONE-QUICK, Ayumi Pharmaceutical Corporation), which was placed on the medial canthus. The total volume of tears was normalized by body weight or the weight of the lacrimal glands, as described in the Figure legends.

Quantitative real-time PCR analysis

Total RNA was extracted from cells and tissues using an RNeasy mini kit or RNeasy Lipid Tissue Mini Kit (Qiagen), respectively, according to the manufacturer's instructions. Total RNA concentrations were measured using a Nanodrop spectrophotometer (Thermo Fisher Scientific), and cDNA was synthesized with the PrimeScript RT Master Mix (Takara Bio Inc.). PCR was performed on a LightCycler 96 system using FastStart Essential DNA Green Master (Roche Applied Science). The following primers were used for the amplification of specific genes: adiponectin, 5'- CAGGCATCCCAG GACATCC-3' (sense) and 5'- CCAAGAAGACCTGCA TCTCCTTT-3' (antisense); AdipoR1, 5'- AGTTCAT GTATAAGGTCTGGGAGG-3' (sense) and 5'- CACATCTACGGGATGACTCTCCA-3' (antisense); AdipoR2, 5'-TTCCTATTATGAAAATAGCCCCGA-3' (sense) and 5'-CATGATGGGAATGTAGGAGC-3' (antisense); GAPDH, 5'-GCCTTCCGTGTTCTACC C-3' (sense) and 5'-TGAAGTCGCAGGAGACAACC-3' (antisense); interleukin (IL)-6, 5'-CCACTTCACAAG TCGGAGGCTTA-3' (sense) and 5'-GCAAGTGCATC ATCGTTGTTTCATAC-3' (antisense); leptin, 5'- CAAGCAGTGCCTATCCAGA-3' (sense) and 5'- AAGCCCAGGAATGAAGTCCA-3' (antisense); M3R, 5'-AGAGCTGGAAGCCCAGTGC-3' (sense) and 5'- GTAGCTTGGTAGAGTTGAGGATGG-3' (antisense); PPAR γ , 5'-TTTTCAAGGGTGCCAGTTTC-3' (sense) and 5'-AATCCTTGGCCCTCTGAGAT-3' (antisense). The murine CD153 primer (Mm_Tnfsf8_1_SG QuantiTect Primer Assay) was obtained from Qiagen. The relative mRNA expression of each transcript was normalized against GAPDH mRNA.

Flow cytometric analysis

Immune cells from lacrimal glands were stained using PE-Cy7-conjugated anti-mouse CD4 mAb (GK1.5;

BioLegend), PE-Cy5-conjugated anti-mouse CD8a mAb (53-6.7; BioLegend), PE-Cy5-conjugated anti-mouse/human CD11b mAb (M1/70; BioLegend), allophycocyanin (APC)-Cy7-conjugated anti-mouse CD11c mAb (N418; BioLegend), PE-Cy7-conjugated anti-mouse CD45.2 (Ly5.2) mAb (104; BioLegend), APC-conjugated anti-mouse CD44 mAb (IM7; BioLegend), APC-Cy7-conjugated anti-mouse CD62L mAb (Mel-14; BioLegend), PE-conjugated anti-mouse CD153 mAb (RM153; BioLegend), fluorescein isothiocyanate (FITC)-conjugated anti-mouse CD279 (PD-1) mAb (29F; BioLegend), and FITC-conjugated anti-mouse CD326 (epithelial cell adhesion molecule; EpCAM) mAb (G8.8; BioLegend). A Canto II flow cytometer (BD Biosciences) was used to identify cell populations according to surface expression profiles. Flow cytometric data were analyzed using FlowJo software (BD Biosciences). The representative gating strategy for SA-T cells is shown in Supplementary Figure 4.

Isolation of epithelial cells from lacrimal glands using MACS

Lacrimal glands were minced in Dulbecco's modified Eagle medium (DMEM) containing 10% fetal bovine serum (FBS) and 100 U/ml Penicillin Streptomycin (Pen Strep, Thermo Fisher Scientific), and digested at 37°C for 40 min with 1 mg/ml collagenase type I (Wako), 1 mg/ml hyaluronidase type I (Sigma), 0.01 mg/ml DNase I (Roche), and 100 U/ml Pen Strep in DMEM. After being digested, they were filtered through a 70- μ m nylon mesh, centrifuged, and rinsed twice with DMEM containing 10% FBS. Epithelial cells from the cell suspension were collected by positive selection using Miltenyi mouse CD326 (EpCAM) MicroBeads. We confirmed that purity was more than 80% (Supplementary Figure 5).

Western blot analysis

Lacrimal glands or subcutaneous fat was lysed in RIPA buffer supplemented with a protease and phosphatase inhibitor cocktail (Thermo Fisher Scientific) using a disposable homogenizer (BioMasher II; Nippi Inc.). Lysates were centrifuged at 12,000 \times g at 4°C for 10 min, and supernatants were collected. Protein concentrations were assessed using the BCA protein assay kit (Thermo Fisher Scientific). Protein concentrations were adjusted, and samples were then diluted in 2 \times Laemmli Sample Buffer. After boiling at 95°C for 5 min, proteins were separated using sodium dodecyl sulfate-polyacrylamide gel electrophoresis and transferred to polyvinylidene difluoride membranes (Bio-Rad Laboratories). Membranes were incubated with antibodies against AdipoR2 (sc-514045, Santa Cruz Biotechnology), β -Actin (3598R-100, BioVision),

and PPAR γ (2443, Cell Signaling Technology). To detect AdipoR2 and PPAR γ , antibodies were diluted with Can Get Signal (Toyobo). Proteins were visualized with Immunostar (Wako) and Amersham Imager 680, and the optical densities of protein bands were measured with Amersham Imager 680 Analysis Software (GE Healthcare). Band intensities were normalized to that of β -Actin.

Immunofluorescence staining

Frozen sections of lacrimal gland tissue were fixed with methanol/acetone (1:1), blocked using 5% normal goat serum (WAKO)/0.3% Triton \times -100 (Sigma) in phosphate-buffered saline (PBS), and stained with FITC anti-mouse CD326 (EpCAM) (118207, BioLegend), AdipoR2 (sc-514045), and PPAR γ (2443) antibodies. Alexa Fluor594-conjugated anti-mouse IgG (H+L) (8890, Cell Signaling Technology) and Alexa Fluor 555-conjugated anti-Rabbit IgG (H+L) (A21428, Thermo Fisher Scientific) were used as secondary antibodies. These antibodies were diluted with Can Get Signal immunostain solution (Toyobo). After washing 3 times with PBS, nuclear DNA was stained with ProLong Diamond Antifade Mountant with DAPI (Thermo Fisher Scientific). Sections were observed using a fluorescence microscope (KEYENCE) at a magnification of 400 \times or 1000 \times .

Statistical analysis

The significance of differences was evaluated by an unpaired Student's *t*-test or Dunnett's multiple comparison test after an analysis of variance (ANOVA) using GraphPad InStat (version 3.10, GraphPad InStat Software Inc.). Values of *p* < 0.05 were considered to be significant.

AUTHOR CONTRIBUTIONS

Conceived, designed, and performed the experiments: YS, MK. Analyzed the data: YS, MK. Contributed reagents/materials/analysis tools: MK, MF. Drafted the manuscript: YS. Helped to draft the manuscript: MK. Revised the Manuscript: NI, KM. All authors read and approved the final manuscript.

ACKNOWLEDGMENTS

We thank N. Ogiso (Laboratory of Experimental Animal, National Center for Geriatrics and Gerontology, Japan) for providing aged mice.

CONFLICTS OF INTEREST

The authors declare that they have no conflicts of interest with the content of this manuscript.

FUNDING

This work was supported in part by Research Funding for Longevity Sciences from the National Center for Geriatrics and Gerontology (grant #29-19 to Y.S and #30-39 to M.K) and Joint Usage and Joint Research Programs, the Institute of Advanced Medical Sciences, Tokushima University (grant #B-14 to Y.S).

REFERENCES

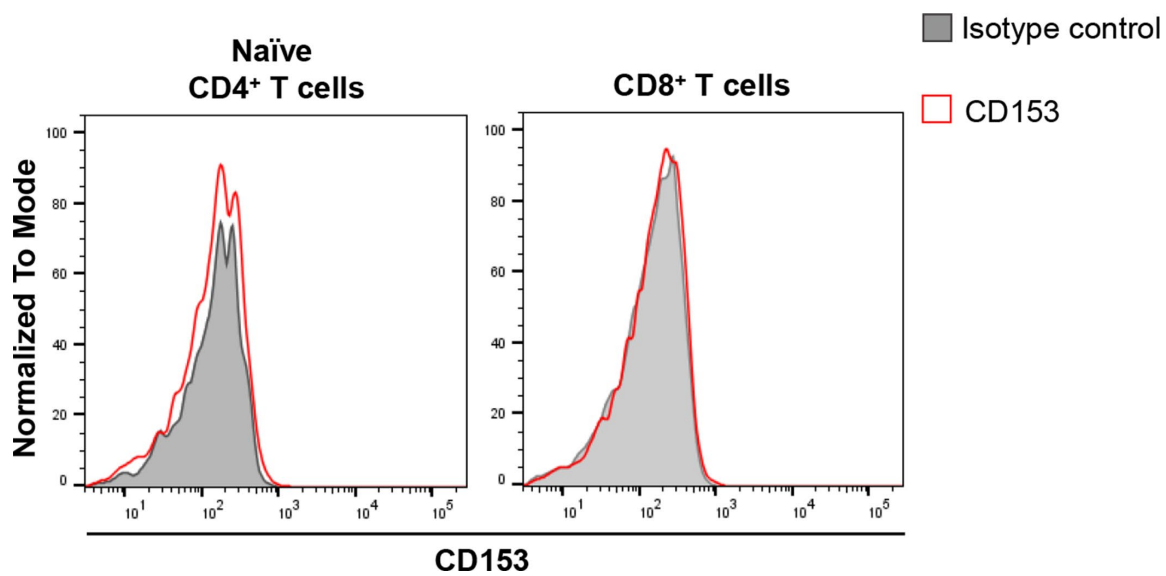
1. Schaumberg DA, Sullivan DA, Buring JE, Dana MR. Prevalence of dry eye syndrome among US women. *Am J Ophthalmol*. 2003; 136:318–26. [https://doi.org/10.1016/S0002-9394\(03\)00218-6](https://doi.org/10.1016/S0002-9394(03)00218-6) PMID:[12888056](https://pubmed.ncbi.nlm.nih.gov/12888056/)
2. Schaumberg DA, Dana R, Buring JE, Sullivan DA. Prevalence of dry eye disease among US men: estimates from the Physicians' Health Studies. *Arch Ophthalmol*. 2009; 127:763–8. <https://doi.org/10.1001/archophthalmol.2009.103> PMID:[19506195](https://pubmed.ncbi.nlm.nih.gov/19506195/)
3. Moss SE, Klein R, Klein BE. Incidence of dry eye in an older population. *Arch Ophthalmol*. 2004; 122: 369–73. <https://doi.org/10.1001/archopht.122.3.369> PMID:[15006852](https://pubmed.ncbi.nlm.nih.gov/15006852/)
4. Lamberts DW, Foster CS, Perry HD. Schirmer test after topical anesthesia and the tear meniscus height in normal eyes. *Arch Ophthalmol*. 1979; 97:1082–5. <https://doi.org/10.1001/archopht.1979.01020010536004> PMID:[444137](https://pubmed.ncbi.nlm.nih.gov/444137/)
5. McCarty CA, Bansal AK, Livingston PM, Stanislavsky YL, Taylor HR. The epidemiology of dry eye in Melbourne, Australia. *Ophthalmology*. 1998; 105:1114–19. [https://doi.org/10.1016/S0161-6420\(98\)96016-X](https://doi.org/10.1016/S0161-6420(98)96016-X) PMID:[9627665](https://pubmed.ncbi.nlm.nih.gov/9627665/)
6. Nasu M, Matsubara O, Yamamoto H. Post-mortem prevalence of lymphocytic infiltration of the lacrimal gland: a comparative study in autoimmune and non-autoimmune diseases. *J Pathol*. 1984; 143:11–15. <https://doi.org/10.1002/path.1711430104> PMID:[6737113](https://pubmed.ncbi.nlm.nih.gov/6737113/)
7. Obata H, Yamamoto S, Horiuchi H, Machinami R. Histopathologic study of human lacrimal gland. Statistical analysis with special reference to aging. *Ophthalmology*. 1995; 102:678–86. [https://doi.org/10.1016/S0161-6420\(95\)30971-2](https://doi.org/10.1016/S0161-6420(95)30971-2) PMID:[7724184](https://pubmed.ncbi.nlm.nih.gov/7724184/)
8. McClellan AJ, Volpe EA, Zhang X, Darlington GJ, Li DQ, Pflugfelder SC, de Paiva CS. Ocular surface disease and dacryoadenitis in aging C57BL/6 mice. *Am J Pathol*. 2014; 184:631–43. <https://doi.org/10.1016/j.ajpath.2013.11.019> PMID:[24389165](https://pubmed.ncbi.nlm.nih.gov/24389165/)
9. Cousen P, Cackett P, Bennett H, Swa K, Dhillon B. Tear production and corneal sensitivity in diabetes. *J Diabetes Complications*. 2007; 21:371–73. <https://doi.org/10.1016/j.jdiacomp.2006.05.008> PMID:[17967709](https://pubmed.ncbi.nlm.nih.gov/17967709/)
10. Imam S, Elagin RB, Jaume JC. Diabetes-associated dry eye syndrome in a new humanized transgenic model of type 1 diabetes. *Mol Vis*. 2013; 19:1259–67. <https://doi.org/10.1210/endo-meetings.2010.part2.p3.p2-115> PMID:[23805032](https://pubmed.ncbi.nlm.nih.gov/23805032/)
11. Meneilly GS, Elliott T. Metabolic alterations in middle-aged and elderly obese patients with type 2 diabetes. *Diabetes Care*. 1999; 22:112–18. <https://doi.org/10.2337/diacare.22.1.112> PMID:[10333911](https://pubmed.ncbi.nlm.nih.gov/10333911/)
12. Hotta K, Funahashi T, Arita Y, Takahashi M, Matsuda M, Okamoto Y, Iwahashi H, Kuriyama H, Ouchi N, Maeda K, Nishida M, Kihara S, Sakai N, et al. Plasma concentrations of a novel, adipose-specific protein, adiponectin, in type 2 diabetic patients. *Arterioscler Thromb Vasc Biol*. 2000; 20:1595–99. <https://doi.org/10.1161/01.ATV.20.6.1595> PMID:[10845877](https://pubmed.ncbi.nlm.nih.gov/10845877/)
13. Yamauchi T, Kamon J, Waki H, Terauchi Y, Kubota N, Hara K, Mori Y, Ide T, Murakami K, Tsuboyama-Kasaoka N, Ezaki O, Akanuma Y, Gavrilova O, et al. The fat-derived hormone adiponectin reverses insulin resistance associated with both lipoatrophy and obesity. *Nat Med*. 2001; 7:941–46. <https://doi.org/10.1038/90984> PMID:[11479627](https://pubmed.ncbi.nlm.nih.gov/11479627/)
14. Matsuda M, Shimomura I, Sata M, Arita Y, Nishida M, Maeda N, Kumada M, Okamoto Y, Nagaretani H, Nishizawa H, Kishida K, Komuro R, Ouchi N, et al. Role of adiponectin in preventing vascular stenosis. The missing link of adipo-vascular axis. *J Biol Chem*. 2002; 277:37487–91. <https://doi.org/10.1074/jbc.M206083200> PMID:[12138120](https://pubmed.ncbi.nlm.nih.gov/12138120/)
15. Okamoto Y, Kihara S, Ouchi N, Nishida M, Arita Y, Kumada M, Ohashi K, Sakai N, Shimomura I, Kobayashi H, Terasaka N, Inaba T, Funahashi T, Matsuzawa Y. Adiponectin reduces atherosclerosis in apolipoprotein E-deficient mice. *Circulation*. 2002; 106:2767–70. <https://doi.org/10.1161/01.CIR.0000042707.50032.19> PMID:[12451000](https://pubmed.ncbi.nlm.nih.gov/12451000/)
16. Pajvani UB, Du X, Combs TP, Berg AH, Rajala MW, Schulthess T, Engel J, Brownlee M, Scherer PE. Structure-function studies of the adipocyte-secreted hormone Acrp30/adiponectin. Implications for

- metabolic regulation and bioactivity. *J Biol Chem.* 2003; 278:9073–85.
<https://doi.org/10.1074/jbc.M207198200>
PMID:[12496257](https://pubmed.ncbi.nlm.nih.gov/12496257/)
17. Tsao TS, Murrey HE, Hug C, Lee DH, Lodish HF. Oligomerization state-dependent activation of NF- κ B signaling pathway by adipocyte complement-related protein of 30 kDa (Acrp30). *J Biol Chem.* 2002; 277:29359–62.
<https://doi.org/10.1074/jbc.C200312200>
PMID:[12087086](https://pubmed.ncbi.nlm.nih.gov/12087086/)
 18. Waki H, Yamauchi T, Kamon J, Ito Y, Uchida S, Kita S, Hara K, Hada Y, Vasseur F, Froguel P, Kimura S, Nagai R, Kadowaki T. Impaired multimerization of human adiponectin mutants associated with diabetes. Molecular structure and multimer formation of adiponectin. *J Biol Chem.* 2003; 278:40352–63.
<https://doi.org/10.1074/jbc.M300365200>
PMID:[12878598](https://pubmed.ncbi.nlm.nih.gov/12878598/)
 19. Fruebis J, Tsao TS, Javorschi S, Ebbets-Reed D, Erickson MR, Yen FT, Bihain BE, Lodish HF. Proteolytic cleavage product of 30-kDa adipocyte complement-related protein increases fatty acid oxidation in muscle and causes weight loss in mice. *Proc Natl Acad Sci USA.* 2001; 98:2005–10.
<https://doi.org/10.1073/pnas.98.4.2005>
PMID:[11172066](https://pubmed.ncbi.nlm.nih.gov/11172066/)
 20. Yamauchi T, Kamon J, Ito Y, Tsuchida A, Yokomizo T, Kita S, Sugiyama T, Miyagishi M, Hara K, Tsunoda M, Murakami K, Ohteki T, Uchida S, et al. Cloning of adiponectin receptors that mediate antidiabetic metabolic effects. *Nature.* 2003; 423:762–69.
<https://doi.org/10.1038/nature01705>
PMID:[12802337](https://pubmed.ncbi.nlm.nih.gov/12802337/)
 21. Anghel SI, Bedu E, Vivier CD, Descombes P, Desvergne B, Wahli W. Adipose tissue integrity as a prerequisite for systemic energy balance: a critical role for peroxisome proliferator-activated receptor gamma. *J Biol Chem.* 2007; 282:29946–57.
<https://doi.org/10.1074/jbc.M702490200>
PMID:[17699161](https://pubmed.ncbi.nlm.nih.gov/17699161/)
 22. Crossno JT Jr, Majka SM, Grazia T, Gill RG, Klemm DJ. Rosiglitazone promotes development of a novel adipocyte population from bone marrow-derived circulating progenitor cells. *J Clin Invest.* 2006; 116:3220–28.
<https://doi.org/10.1172/JCI28510> PMID:[17143331](https://pubmed.ncbi.nlm.nih.gov/17143331/)
 23. Maeda N, Takahashi M, Funahashi T, Kihara S, Nishizawa H, Kishida K, Nagaretani H, Matsuda M, Komuro R, Ouchi N, Kuriyama H, Hotta K, Nakamura T, et al. PPARgamma ligands increase expression and plasma concentrations of adiponectin, an adipose-derived protein. *Diabetes.* 2001; 50:2094–99.
<https://doi.org/10.2337/diabetes.50.9.2094>
PMID:[11522676](https://pubmed.ncbi.nlm.nih.gov/11522676/)
 24. Chen Y, Zhang X, Yang L, Li M, Li B, Wang W, Sheng M. Decreased PPAR- γ expression in the conjunctiva and increased expression of TNF- α and IL-1 β in the conjunctiva and tear fluid of dry eye mice. *Mol Med Rep.* 2014; 9:2015–23.
<https://doi.org/10.3892/mmr.2014.2041>
PMID:[24626526](https://pubmed.ncbi.nlm.nih.gov/24626526/)
 25. Li Z, Woo JM, Chung SW, Kwon MY, Choi JS, Oh HJ, Yoon KC. Therapeutic effect of topical adiponectin in a mouse model of desiccating stress-induced dry eye. *Invest Ophthalmol Vis Sci.* 2013; 54:155–62.
<https://doi.org/10.1167/iovs.12-10648>
PMID:[23211823](https://pubmed.ncbi.nlm.nih.gov/23211823/)
 26. Oh YS, Seo EH, Lee YS, Cho SC, Jung HS, Park SC, Jun HS. Increase of Calcium Sensing Receptor Expression Is Related to Compensatory Insulin Secretion during Aging in Mice. *PLoS One.* 2016; 11:e0159689.
<https://doi.org/10.1371/journal.pone.0159689>
PMID:[27441644](https://pubmed.ncbi.nlm.nih.gov/27441644/)
 27. Winzell MS, Ahrén B. The high-fat diet-fed mouse: a model for studying mechanisms and treatment of impaired glucose tolerance and type 2 diabetes. *Diabetes.* 2004 (Suppl 3); 53:S215–19.
https://doi.org/10.2337/diabetes.53.suppl_3.S215
PMID:[15561913](https://pubmed.ncbi.nlm.nih.gov/15561913/)
 28. Shimatani K, Nakashima Y, Hattori M, Hamazaki Y, Minato N. PD-1+ memory phenotype CD4+ T cells expressing C/EBPalpha underlie T cell immunodepression in senescence and leukemia. *Proc Natl Acad Sci USA.* 2009; 106:15807–12.
<https://doi.org/10.1073/pnas.0908805106>
PMID:[19805226](https://pubmed.ncbi.nlm.nih.gov/19805226/)
 29. Franceschi C, Bonafè M, Valensin S, Olivieri F, De Luca M, Ottaviani E, De Benedictis G. Inflamm-aging. An evolutionary perspective on immunosenescence. *Ann N Y Acad Sci.* 2000; 908:244–54.
<https://doi.org/10.1111/j.1749-6632.2000.tb06651.x>
PMID:[10911963](https://pubmed.ncbi.nlm.nih.gov/10911963/)
 30. Nikolich-Zugich J. Ageing and life-long maintenance of T-cell subsets in the face of latent persistent infections. *Nat Rev Immunol.* 2008; 8:512–22.
<https://doi.org/10.1038/nri2318> PMID:[18469829](https://pubmed.ncbi.nlm.nih.gov/18469829/)
 31. Farber DL, Yudanin NA, Restifo NP. Human memory T cells: generation, compartmentalization and homeostasis. *Nat Rev Immunol.* 2014; 14:24–35.
<https://doi.org/10.1038/nri3567>
PMID:[24336101](https://pubmed.ncbi.nlm.nih.gov/24336101/)
 32. Shirakawa K, Yan X, Shinmura K, Endo J, Kataoka M, Katsumata Y, Yamamoto T, Anzai A, Isobe S, Yoshida N, Itoh H, Manabe I, Sekai M, et al. Obesity accelerates T

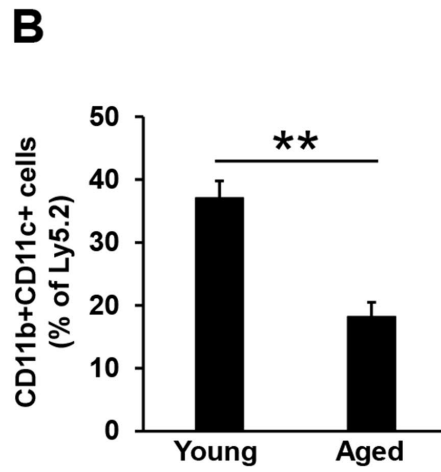
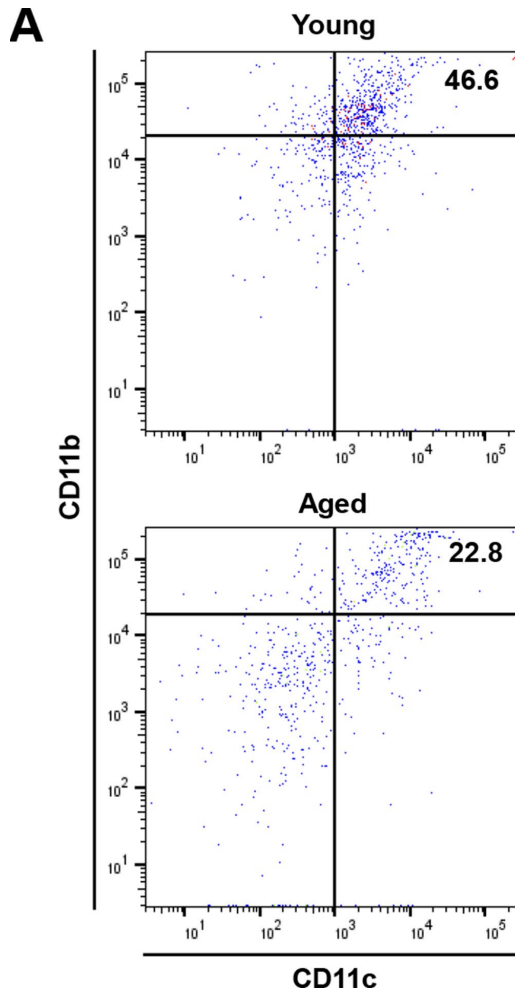
- cell senescence in murine visceral adipose tissue. *J Clin Invest*. 2016; 126:4626–39.
<https://doi.org/10.1172/JCI88606> PMID:[27820698](https://pubmed.ncbi.nlm.nih.gov/27820698/)
33. Ye P, Zhang XJ, Wang ZJ, Zhang C. Effect of aging on the expression of peroxisome proliferator-activated receptor gamma and the possible relation to insulin resistance. *Gerontology*. 2006; 52:69–75.
<https://doi.org/10.1159/000090951> PMID:[16508313](https://pubmed.ncbi.nlm.nih.gov/16508313/)
 34. Ahmadian M, Suh JM, Hah N, Liddle C, Atkins AR, Downes M, Evans RM. PPAR γ signaling and metabolism: the good, the bad and the future. *Nat Med*. 2013; 19:557–66.
<https://doi.org/10.1038/nm.3159> PMID:[23652116](https://pubmed.ncbi.nlm.nih.gov/23652116/)
 35. Landrier JF, Kasiri E, Karkeni E, Mihály J, Béke G, Weiss K, Lucas R, Aydemir G, Salles J, Walrand S, de Lera AR, Rühl R. Reduced adiponectin expression after high-fat diet is associated with selective up-regulation of ALDH1A1 and further retinoic acid receptor signaling in adipose tissue. *FASEB J*. 2017; 31:203–11.
<https://doi.org/10.1096/fj.201600263RR> PMID:[27729412](https://pubmed.ncbi.nlm.nih.gov/27729412/)
 36. Sano K, Kawashima M, Ito A, Inaba T, Morimoto K, Watanabe M, Tsubota K. Aerobic exercise increases tear secretion in type 2 diabetic mice. *Invest Ophthalmol Vis Sci*. 2014; 55:4287–94.
<https://doi.org/10.1167/iov.13-13289> PMID:[24876288](https://pubmed.ncbi.nlm.nih.gov/24876288/)
 37. Marko CK, Menon BB, Chen G, Whitsett JA, Clevers H, Gipson IK. Spdef null mice lack conjunctival goblet cells and provide a model of dry eye. *Am J Pathol*. 2013; 183:35–48.
<https://doi.org/10.1016/j.ajpath.2013.03.017> PMID:[23665202](https://pubmed.ncbi.nlm.nih.gov/23665202/)
 38. Zhu N, Pankow JS, Ballantyne CM, Couper D, Hoogeveen RC, Pereira M, Duncan BB, Schmidt MI. High-molecular-weight adiponectin and the risk of type 2 diabetes in the ARIC study. *J Clin Endocrinol Metab*. 2010; 95:5097–104.
<https://doi.org/10.1210/jc.2010-0716> PMID:[20719834](https://pubmed.ncbi.nlm.nih.gov/20719834/)
 39. Hara K, Horikoshi M, Yamauchi T, Yago H, Miyazaki O, Ebinuma H, Imai Y, Nagai R, Kadowaki T. Measurement of the high-molecular weight form of adiponectin in plasma is useful for the prediction of insulin resistance and metabolic syndrome. *Diabetes Care*. 2006; 29:1357–62.
<https://doi.org/10.2337/dc05-1801> PMID:[16732021](https://pubmed.ncbi.nlm.nih.gov/16732021/)
 40. Otsuka H, Yanai M, Kobayashi H, Haketa A, Hara M, Sugama K, Kato K, Soma M. High-molecular-weight adiponectin levels in healthy, community-dwelling, elderly Japanese volunteers: a 5-year prospective observational study. *Aging Clin Exp Res*. 2018; 30:791–98.
<https://doi.org/10.1007/s40520-017-0840-6> PMID:[29052034](https://pubmed.ncbi.nlm.nih.gov/29052034/)
 41. Miller KN, Burhans MS, Clark JP, Howell PR, Polewski MA, DeMuth TM, Eliceiri KW, Lindstrom MJ, Ntambi JM, Anderson RM. Aging and caloric restriction impact adipose tissue, adiponectin, and circulating lipids. *Aging Cell*. 2017; 16:497–507.
<https://doi.org/10.1111/acer.12575> PMID:[28156058](https://pubmed.ncbi.nlm.nih.gov/28156058/)
 42. Combs TP, Berg AH, Rajala MW, Klebanov S, Iyengar P, Jimenez-Chillaron JC, Patti ME, Klein SL, Weinstein RS, Scherer PE. Sexual differentiation, pregnancy, calorie restriction, and aging affect the adipocyte-specific secretory protein adiponectin. *Diabetes*. 2003; 52:268–76.
<https://doi.org/10.2337/diabetes.52.2.268> PMID:[12540596](https://pubmed.ncbi.nlm.nih.gov/12540596/)
 43. Ríos JD, Horikawa Y, Chen LL, Kublin CL, Hodges RR, Dartt DA, Zoukhri D. Age-dependent alterations in mouse exorbital lacrimal gland structure, innervation and secretory response. *Exp Eye Res*. 2005; 80:477–91.
<https://doi.org/10.1016/j.exer.2004.10.012> PMID:[15781275](https://pubmed.ncbi.nlm.nih.gov/15781275/)
 44. Yokosuka T, Takamatsu M, Kobayashi-Imanishi W, Hashimoto-Tane A, Azuma M, Saito T. Programmed cell death 1 forms negative costimulatory microclusters that directly inhibit T cell receptor signaling by recruiting phosphatase SHP2. *J Exp Med*. 2012; 209:1201–17.
<https://doi.org/10.1084/jem.20112741> PMID:[22641383](https://pubmed.ncbi.nlm.nih.gov/22641383/)
 45. Smith CA, Gruss HJ, Davis T, Anderson D, Farrah T, Baker E, Sutherland GR, Brannan CI, Copeland NG, Jenkins NA, Grabstein KH, Gliniak B, McAlister IB, et al. CD30 antigen, a marker for Hodgkin's lymphoma, is a receptor whose ligand defines an emerging family of cytokines with homology to TNF. *Cell*. 1993; 73:1349–60.
[https://doi.org/10.1016/0092-8674\(93\)90361-S](https://doi.org/10.1016/0092-8674(93)90361-S) PMID:[8391931](https://pubmed.ncbi.nlm.nih.gov/8391931/)
 46. Fessler J, Husic R, Schwetz V, Lerchbaum E, Aberer F, Fasching P, Ficjan A, Obermayer-Pietsch B, Duftner C, Graninger W, Stradner MH, Dejaco C. Senescent T-Cells Promote Bone Loss in Rheumatoid Arthritis. *Front Immunol*. 2018; 9:95.
<https://doi.org/10.3389/fimmu.2018.00095> PMID:[29472917](https://pubmed.ncbi.nlm.nih.gov/29472917/)
 47. Tahir S, Fukushima Y, Sakamoto K, Sato K, Fujita H, Inoue J, Uede T, Hamazaki Y, Hattori M, Minato N. A CD153+CD4+ T follicular cell population with cell-senescence features plays a crucial role in lupus pathogenesis via osteopontin production. *J Immunol*. 2015; 194:5725–35.

- <https://doi.org/10.4049/jimmunol.1500319>
PMID:[25972477](https://pubmed.ncbi.nlm.nih.gov/25972477/)
48. Kennedy MK, Willis CR, Armitage RJ. Deciphering CD30 ligand biology and its role in humoral immunity. *Immunology*. 2006; 118:143–52.
<https://doi.org/10.1111/j.1365-2567.2006.02354.x>
PMID:[16771849](https://pubmed.ncbi.nlm.nih.gov/16771849/)
49. Jester JV, Potma E, Brown DJ. PPAR γ Regulates Mouse Meibocyte Differentiation and Lipid Synthesis. *Ocul Surf*. 2016; 14:484–94.
<https://doi.org/10.1016/j.jtos.2016.08.001>
PMID:[27531629](https://pubmed.ncbi.nlm.nih.gov/27531629/)
50. Nien CJ, Massei S, Lin G, Nabavi C, Tao J, Brown DJ, Paugh JR, Jester JV. Effects of age and dysfunction on human meibomian glands. *Arch Ophthalmol*. 2011; 129:462–9.
<https://doi.org/10.1001/archophthalmol.2011.69>
PMID:[21482872](https://pubmed.ncbi.nlm.nih.gov/21482872/)
51. Asada K, Sasaki S, Suda T, Chida K, Nakamura H. Antiinflammatory roles of peroxisome proliferator-activated receptor gamma in human alveolar macrophages. *Am J Respir Crit Care Med*. 2004; 169:195–200.
<https://doi.org/10.1164/rccm.200207-740OC>
PMID:[14563653](https://pubmed.ncbi.nlm.nih.gov/14563653/)
52. Harris SG, Phipps RP. The nuclear receptor PPAR gamma is expressed by mouse T lymphocytes and PPAR gamma agonists induce apoptosis. *Eur J Immunol*. 2001; 31:1098–105.
[https://doi.org/10.1002/1521-4141\(200104\)31:4<1098::AID-IMMU1098>3.0.CO;2-I](https://doi.org/10.1002/1521-4141(200104)31:4<1098::AID-IMMU1098>3.0.CO;2-I)
PMID:[11298334](https://pubmed.ncbi.nlm.nih.gov/11298334/)
53. Padilla J, Leung E, Phipps RP. Human B lymphocytes and B lymphomas express PPAR-gamma and are killed by PPAR-gamma agonists. *Clin Immunol*. 2002; 103:22–33.
<https://doi.org/10.1006/clin.2001.5181>
PMID:[11987982](https://pubmed.ncbi.nlm.nih.gov/11987982/)
54. Tchkonina T, Zhu Y, van Deursen J, Campisi J, Kirkland JL. Cellular senescence and the senescent secretory phenotype: therapeutic opportunities. *J Clin Invest*. 2013; 123:966–72.
<https://doi.org/10.1172/JCI64098> PMID:[23454759](https://pubmed.ncbi.nlm.nih.gov/23454759/)
55. Hong EG, Ko HJ, Cho YR, Kim HJ, Ma Z, Yu TY, Friedline RH, Kurt-Jones E, Finberg R, Fischer MA, Granger EL, Norbury CC, Hauschka SD, et al. Interleukin-10 prevents diet-induced insulin resistance by attenuating macrophage and cytokine response in skeletal muscle. *Diabetes*. 2009; 58:2525–35.
<https://doi.org/10.2337/db08-1261> PMID:[19690064](https://pubmed.ncbi.nlm.nih.gov/19690064/)
56. Hu L, Mauro TM, Dang E, Man G, Zhang J, Lee D, Wang G, Feingold KR, Elias PM, Man MQ. Epidermal Dysfunction Leads to an Age-Associated Increase in Levels of Serum Inflammatory Cytokines. *J Invest Dermatol*. 2017; 137:1277–85.
<https://doi.org/10.1016/j.jid.2017.01.007>
PMID:[28115059](https://pubmed.ncbi.nlm.nih.gov/28115059/)
57. Enríquez-de-Salamanca A, Castellanos E, Stern ME, Fernández I, Carreño E, García-Vázquez C, Herreras JM, Calonge M. Tear cytokine and chemokine analysis and clinical correlations in evaporative-type dry eye disease. *Mol Vis*. 2010; 16:862–73.
<https://doi.org/10.1167/iovs.15-18615>
PMID:[20508732](https://pubmed.ncbi.nlm.nih.gov/20508732/)
58. Lam H, Bleiden L, de Paiva CS, Farley W, Stern ME, Pflugfelder SC. Tear cytokine profiles in dysfunctional tear syndrome. *Am J Ophthalmol*. 2009; 147:198–205.e1.
<https://doi.org/10.1016/j.ajo.2008.08.032>
PMID:[18992869](https://pubmed.ncbi.nlm.nih.gov/18992869/)
59. Massingale ML, Li X, Vallabhajosyula M, Chen D, Wei Y, Asbell PA. Analysis of inflammatory cytokines in the tears of dry eye patients. *Cornea*. 2009; 28:1023–27.
<https://doi.org/10.1097/ICO.0b013e3181a16578>
PMID:[19724208](https://pubmed.ncbi.nlm.nih.gov/19724208/)
60. Lago F, Gómez R, Gómez-Reino JJ, Dieguez C, Gualillo O. Adipokines as novel modulators of lipid metabolism. *Trends Biochem Sci*. 2009; 34:500–10.
<https://doi.org/10.1016/j.tibs.2009.06.008>
PMID:[19729309](https://pubmed.ncbi.nlm.nih.gov/19729309/)
61. Ahrén B, Månsson S, Gingerich RL, Havel PJ. Regulation of plasma leptin in mice: influence of age, high-fat diet, and fasting. *Am J Physiol*. 1997; 273:R113–20.
<https://doi.org/10.1152/ajpregu.1997.273.1.r113>
PMID:[9249540](https://pubmed.ncbi.nlm.nih.gov/9249540/)
62. Tsubota K, Fujita H, Tadano K, Takeuchi T, Murakami T, Saito I, Hayashi Y. Improvement of lacrimal function by topical application of CyA in murine models of Sjögren's syndrome. *Invest Ophthalmol Vis Sci*. 2001; 42:101–10.
PMID:[11133854](https://pubmed.ncbi.nlm.nih.gov/11133854/)

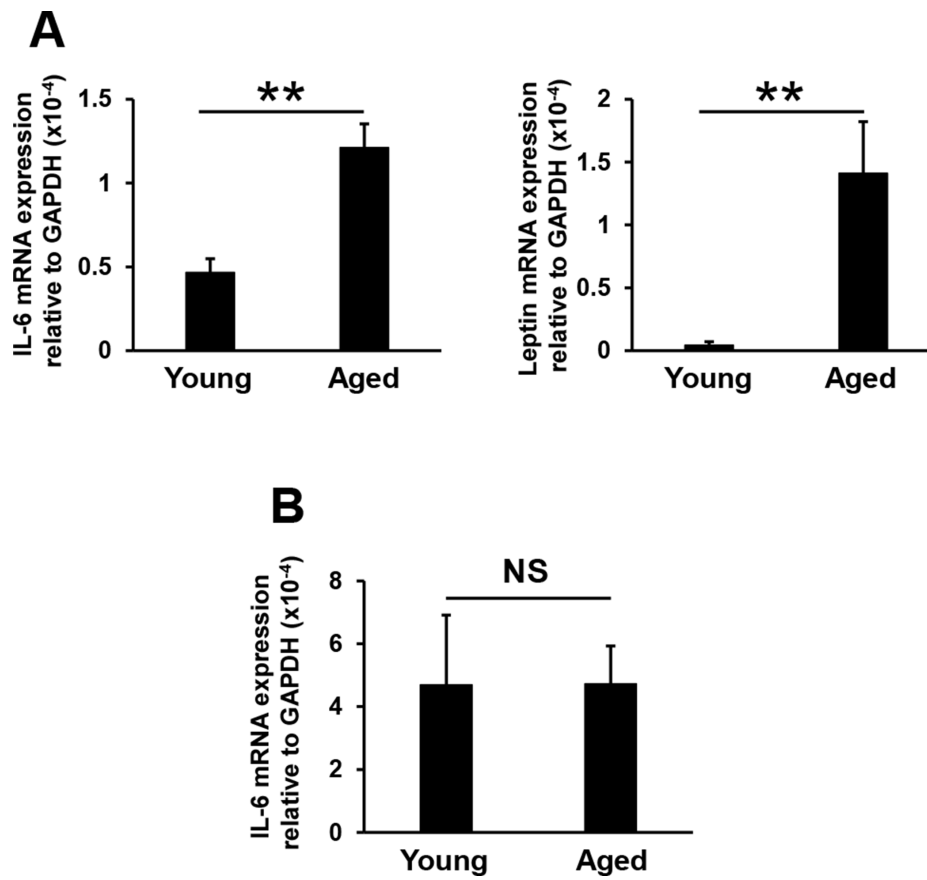
SUPPLEMENTARY MATERIALS



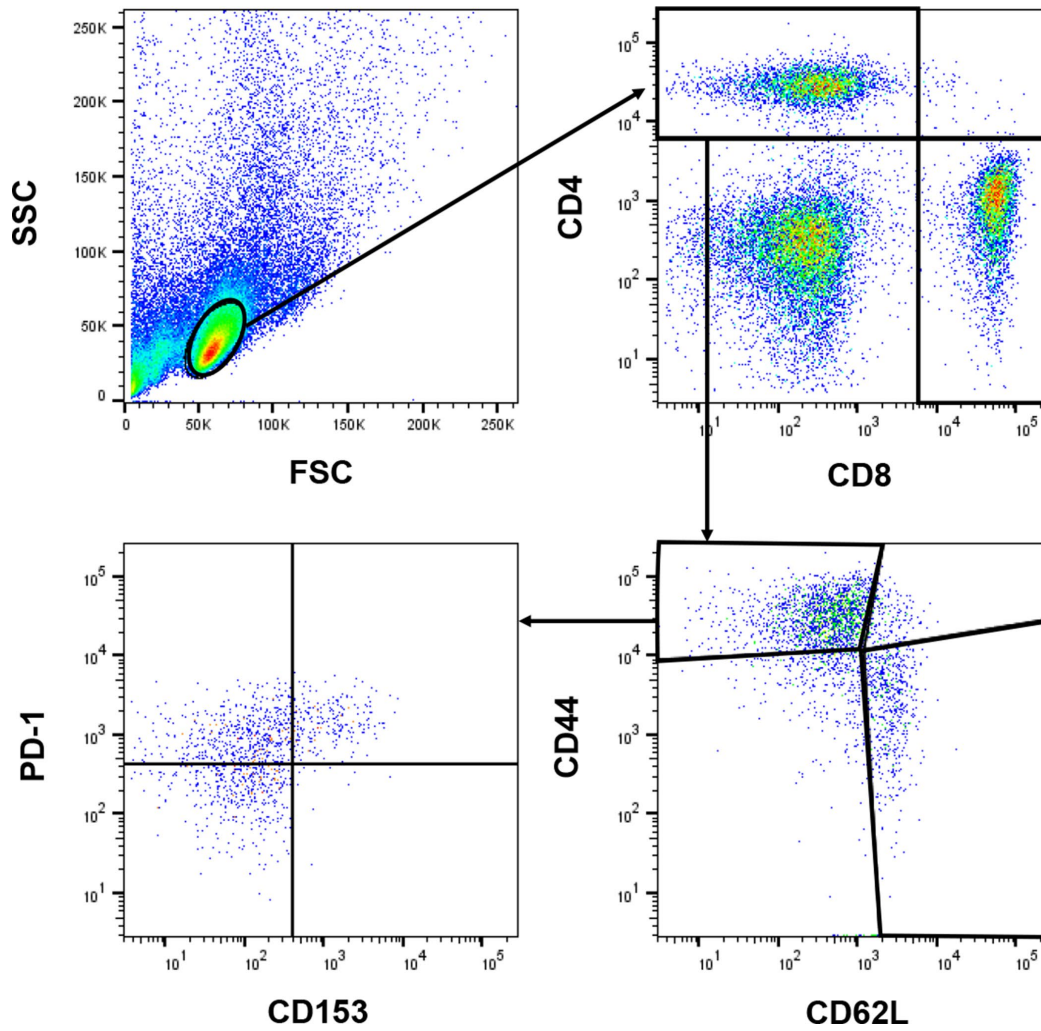
Supplementary Figure 1. CD153 expression in naïve CD4⁺ and CD8⁺ T cells. Flow cytometric analysis of CD153 expression on naïve (CD44^{lo}CD62L^{hi}) CD4⁺ and CD8⁺ T cells in the spleens of aged mice.



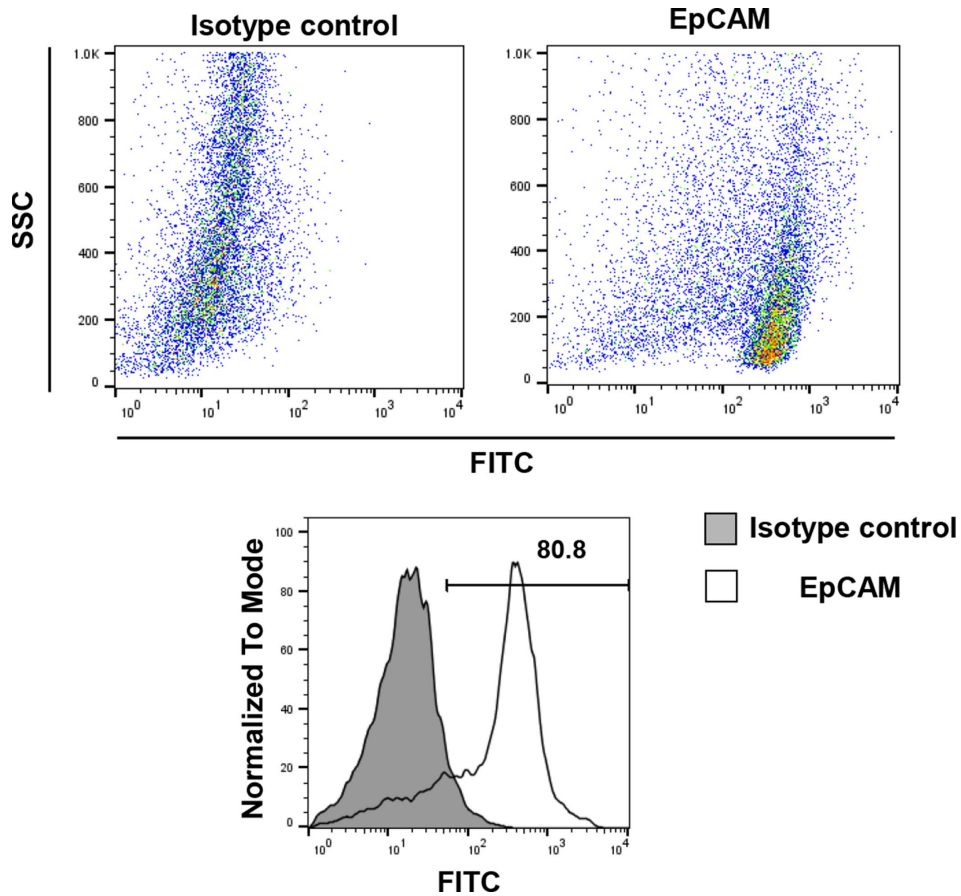
Supplementary Figure 2. CD11b⁺CD11c⁺ cells in lacrimal glands of young and aged mice. Proportion of CD11b⁺CD11c⁺ cells gated on Ly5.2⁺ cells in the lacrimal glands of young and aged mice (Male: N=5-6, Female: N=3-4). Cell debris and lymphocytes were excluded from the analysis based on scatter signals. Values are presented as means ± SEM. **p<0.01 (an unpaired Student's *t*-test).



Supplementary Figure 3. IL-6 and leptin mRNA expression in lacrimal glands. (A) IL-6 and leptin mRNA expression levels in the lacrimal glands of young and aged mice (N=7-8). (B) IL-6 mRNA expression levels in the epithelial cells of the lacrimal glands of young and aged mice (N=4). Values are presented as means \pm SEM. NS, not significant. ** $p < 0.01$ (an unpaired Student's *t*-test).



Supplementary Figure 4. Gating strategy for SA-T cells.



Supplementary Figure 5. Purity of CD326 (EpCAM)-positive cells isolated from lacrimal glands. Epithelial cells were isolated using CD326 (EpCAM) Microbeads from murine lacrimal glands. Cells were stained with an isotype control or FITC-conjugated CD326 (EpCAM) antibody, and analyzed by flow cytometry. Cell debris was excluded from the analysis based on scatter signals.

ALKBH5-mediated m⁶A demethylation of FOXM1 mRNA promotes progression of uveal melanoma

Lili Hao^{1,*}, Jiayang Yin^{1,*}, Hong Yang¹, Chaoxuan Li¹, Linxin Zhu¹, Lian Liu¹, Jingxiang Zhong¹

¹Department of Ophthalmology, The First Affiliated Hospital of Jinan University, Guangzhou 510632, Guangdong Province, China

*Equal contribution

Correspondence to: Jingxiang Zhong, Lian Liu; **email:** tzjx@jnu.edu.cn, lianliu@jnu.edu.cn

Keywords: uveal melanoma, ALKBH5, FOXM1, m⁶A demethylation

Received: March 4, 2020

Accepted: September 9, 2020

Published: January 10, 2021

Copyright: © 2021 Hao et al. This is an open access article distributed under the terms of the [Creative Commons Attribution License](https://creativecommons.org/licenses/by/3.0/) (CC BY 3.0), which permits unrestricted use, distribution, and reproduction in any medium, provided the original author and source are credited.

ABSTRACT

In this study, we found that ALKBH5, a key component of the N⁶-methyladenosine (m⁶A) methyltransferase complex, was significantly elevated in uveal melanoma (UM) cell lines and that ALKBH5 downregulation inhibited tumor growth *in vivo*. High ALKBH5 expression predicted worse outcome in patients with UM. EP300-induced H3K27 acetylation activation increased ALKBH5 expression. Downregulation of ALKBH5 inhibited UM cell proliferation, migration, and invasion and increased apoptosis *in vitro*. Besides, ALKBH5 may promote UM metastasis by inducing epithelial-to-mesenchymal transition (EMT) via demethylation of FOXM1 mRNA, which increases its expression and stability. In sum, our study indicates that ALKBH5-induced m⁶A demethylation of FOXM1 mRNA promotes UM progression. Therefore, ALKBH5 is a potential prognostic biomarker and therapeutic target in UM.

INTRODUCTION

Uveal melanoma (UM), which originates from melanocytes, is the most common primary intraocular malignancy in adults [1]. Although the primary tumor can be treated with resection, radiation therapy, and enucleation, up to 50% of UM patients will develop metastatic disease [2, 3]. The most common sites of UM metastasis are the liver (60.5%), lungs (24.4%), skin/soft tissue (10.9%), and bone (8.4%) [4]. Unfortunately, the 1-year survival rate of UM patients with metastases is only 15% [5]. Therefore, there is a pressing need to find useful prognostic biomarkers and therapeutic targets for this disease.

Although previous studies have revealed that distinct genetic alterations occur during the formation and progression of UM [6–8], genomic epigenetic modifications, such as histone modification, DNA modification, and RNA methylation, also play critical

roles in the tumorigenesis of UM [8–10]. N⁶-methyladenosine (m⁶A) methylation is the most prevalent modification in RNA, including mRNAs, lncRNAs, and circRNAs [11]. m⁶A modification is installed by a multicomponent methyltransferase complex consisting of METTL3, METTL14, and WTAP and is erased by FTO and ALKBH5. Moreover, specific RNA-binding proteins, such as YTHDF1, YTHDF2, and YTHDF3, bind to the m⁶A motif to modify RNA function [12, 13]. m⁶A modifications have been reported to affect multiple biological processes, such as RNA stability, splicing, transport, subcellular localization and translation efficiency, and RNA-protein interactions [11]. Recently, RNA methylation was shown to inhibit the progression of UM and ocular melanoma (OM), and decreased m⁶A levels were associated with a poor outcome in OM [14]. Conversely, METTL3-mediated m⁶A modification may promote UM progression by targeting c-Met and increasing its expression [15]. Therefore, understanding of the biological function of

m⁶A and potential regulatory mechanisms in human UM is still in its infancy.

Tumor metastasis requires a series of events within the tumor microenvironment, including cell proliferation, loss of cellular adhesion, degradation of the extracellular matrix, and cell migration and invasion [16]. In cancer, epithelial-to-mesenchymal transition (EMT) is a key process leading to tumor metastasis and aggression, stemness, and resistance to therapy [17]. m⁶A modifications have been shown to cause tumor progression via EMT and tumorigenesis. METTL3 induced an m⁶A modification in the coding sequence of Snail, a key transcription factor of EMT, which triggered polysome-induced translation of Snail mRNA in cancer cells [18]. In addition, METTL3-provoked m⁶A methylation of ZMYM1 mRNA facilitated EMT and gastric cancer metastasis [19]. Some studies have demonstrated that EMT promotes the metastasis and aggression of UM [20, 21]. However, the effect of m⁶A modifications on EMT in UM has yet to be explored.

Here, we verified that ALKBH5 overexpression promotes UM progression and found that ALKBH5 expression is increased by EP300-induced H3K27 acetylation activation. In addition, ALKBH5 promotes EMT of UM by upregulating FOXM1 expression via demethylating the m⁶A modification and further increasing the stability of FOXM1 mRNA.

RESULTS

High ALKBH5 expression is associated with worse prognosis in patients with UM and promotes UM growth *in vivo*

To obtain the clinical significance of ALKBH5 expression in patients with UM. The GEPIA database (<http://gepia.cancer-pku.cn>), which includes the data set from The Cancer Genome Atlas (TCGA), was used to evaluate the prognosis of ALKBH5 expression with a high or low level. As shown in Figure 1A, higher ALKBH5 expression was correlated with worse outcomes in patients with UM.

To investigate the association between ALKBH5 expression and UM, we measured ALKBH5 expression in two human UM cell lines (MuM-2B and C918). As shown in Figure 1B, the protein (Figure 1B, upper panel) and mRNA (Figure 1B, bottom panel) levels of ALKBH5 were significantly elevated in UM cells.

To study the effect of ALKBH5 on UM tumor progression *in vivo*, we used two short hairpin RNAs (shALKBH5#1 and shALKBH5#2) to decrease ALKBH5 expression. As expected, protein (Figure 1C, upper panel) and mRNA

(Figure 1C, bottom panel) expression of ALKBH5 was downregulated in MuM-2B and C918 cells that were transfected with two distinct shRNAs. Subsequently, ALKBH5-stable knockdown C918-shALKBH5#2 cells were established and injected subcutaneously into nude mice (Figure 1D, 1E). The results showed that the downregulation of ALKBH5 significantly suppressed tumor growth, as reflected by the tumor volumes (Figure 1E) and weight (Figure 1F) compared with tumors derived from control cells. In addition, IHC staining revealed that, compared with the normal control group, Ki-67 expression was dramatically suppressed and cleaved-caspase3 was increased in the C918-shALKBH5#2 group (Figure 1G). These results demonstrate that ALKBH5 expression is associated with UM tumorigenicity.

EP300-induced H3K27ac activation promotes ALKBH5 transcription in UM

To determine the cause of high ALKBH5 expression in UM cells, we analyzed melanoma data from the UCSC Genome Bioinformatics Site (<http://genome.ucsc.edu>) and found high enrichment and overlap of H3K27ac peaks at the promoter region of ALKBH5 in melanoma (Figure 2A), which suggests that ALKBH5 may be regulated by chromatin acetylation. It has been reported that H3K27ac is catalyzed by cAMP response element binding protein (CREB) binding protein (CREBBP) and EP300 in a bromodomain-dependent fashion [22]. By analyzing the TCGA data set, we found that EP300 (Figure 2B) and CREBBP (Figure 2C) mRNA expression was positively correlated with ALKBH5 expression in UM.

To verify the relationship between H3K27ac and ALKBH5, we treated UM cells with C646, the histone acetyltransferase inhibitor targeting EP300, and SGC-CBP30, a histone acetyltransferase inhibitor targeting CREBBP. The mRNA (Figure 2D) and protein (Figure 2E) levels of ALKBH5 were significantly decreased in C918 and MuM-2B cells after treating the cells with C646 for 24 hours. Although SGC-CBP30 decreased the expression of H3K27ac, ALKBH5 was not affected (Supplementary Figure 1). Furthermore, the ChIP assay results indicated that the promoter region of ALKBH5 was enriched in EP300 binding and H3K27ac signals, and inhibition of EP300 by C646 treatment could significantly decrease the enrichment of H3K27ac signals in the promoter of ALKBH5 (Figure 2F). These results indicate that EP300-induced H3K27ac activation increases ALKBH5 expression in UM.

ALKBH5 inhibition decreases proliferation and facilitates cell cycle arrest in UM cells

We performed a series of *in vitro* biological experiments to further assess the function of ALKBH5

in UM cells. Loss of ALKBH5 caused a significant decrease in cell viability in MuM-2B and C918 cells (Figure 3A) and induced G1 to S phase transition arrest (Figure 3B). The protein expression of the G1 to S phase checkpoint regulators cyclin D1 and cyclin E1 was downregulated in shALKBH5-transfected cells compared with the control vector-transfected cells (Figure 3D). These results confirm that ALKBH5 facilitates cell growth by promoting cell cycle progression in UM cells.

Loss of ALKBH5 promotes UM cell apoptosis

To further explore the effect of ALKBH5 on UM growth, we assessed the effect of ALKBH5 on cell apoptosis using flow cytometry after staining with annexin V and PI. Downregulation of ALKBH5 significantly increased cell apoptosis in MuM-2B and C918 cells (Figure 3C). Moreover, loss of ALKBH5 in MuM-2B and C918 cells significantly increased apoptosis marker protein levels, cleaved caspase-3, and

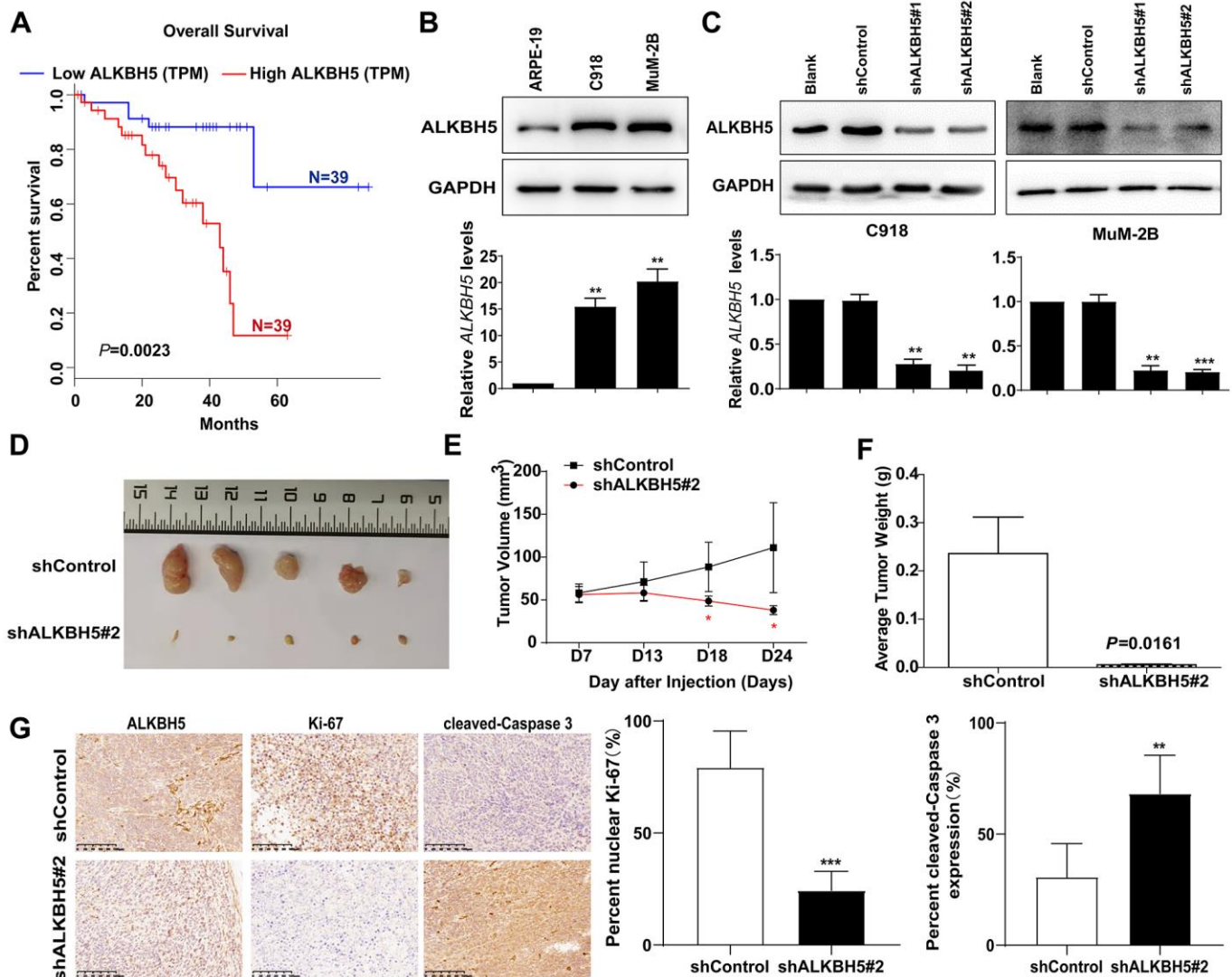


Figure 1. High ALKBH5 expression is associated with worse prognosis in patients with UM and promotes UM growth *in vivo* (A) Survival curves of UM patients expressing ALKBH5 at high and low levels in the TCGA cohort from the online GEPIA database ($P = 0.0023$). (B) Expression of ALKBH5 protein (upper panel) and mRNA (bottom panel) levels in UM cells was detected by western blot and qRT-PCR. (C) ALKBH5 knockdown efficiency was verified at the protein and mRNA levels in C918 (left panel) and MuM-2B (right panel) by western blot and qRT-PCR. (D) Knockdown of ALKBH5 effectively inhibited UM subcutaneous tumor growth in nude mice ($n=5$). (E) The growth curves of C918 stably transduced with shALKBH5 in nude mice were significantly dampened compared with those of C918 cells transduced with control plasmid. (F) Histogram shows the mean tumor weights from the shALKBH5 and control groups. (G) Sections of tumors were stained with anti-ALKBH5, anti-Ki67, and anti-cleaved-Caspase 3 antibodies by IHC staining. Mean \pm SEM, t-test, $*P < 0.05$, $**P < 0.01$, $***P < 0.001$.

decreased the expression of BCL-2, which is an antiapoptosis marker (Figure 3D).

Silencing ALKBH5 reduces migration and invasion of UM cells

Transwell migration and Matrigel invasion assays were performed to evaluate the effects of ALKBH5 on cell migration and invasion. As shown in Figure 4A,

knockdown of ALKBH5 significantly inhibited migration and invasion of MuM-2B and C918 cells. Western blot assay demonstrated that the downregulation of ALKBH5 reduced the expression of the tumor metastasis-related proteins matrix metalloproteinase 2 (MMP2), MMP7, and MMP9 in UM cells (Figure 4B). These findings indicate that ALKBH5 silencing reduces migration and invasion of UM cells.

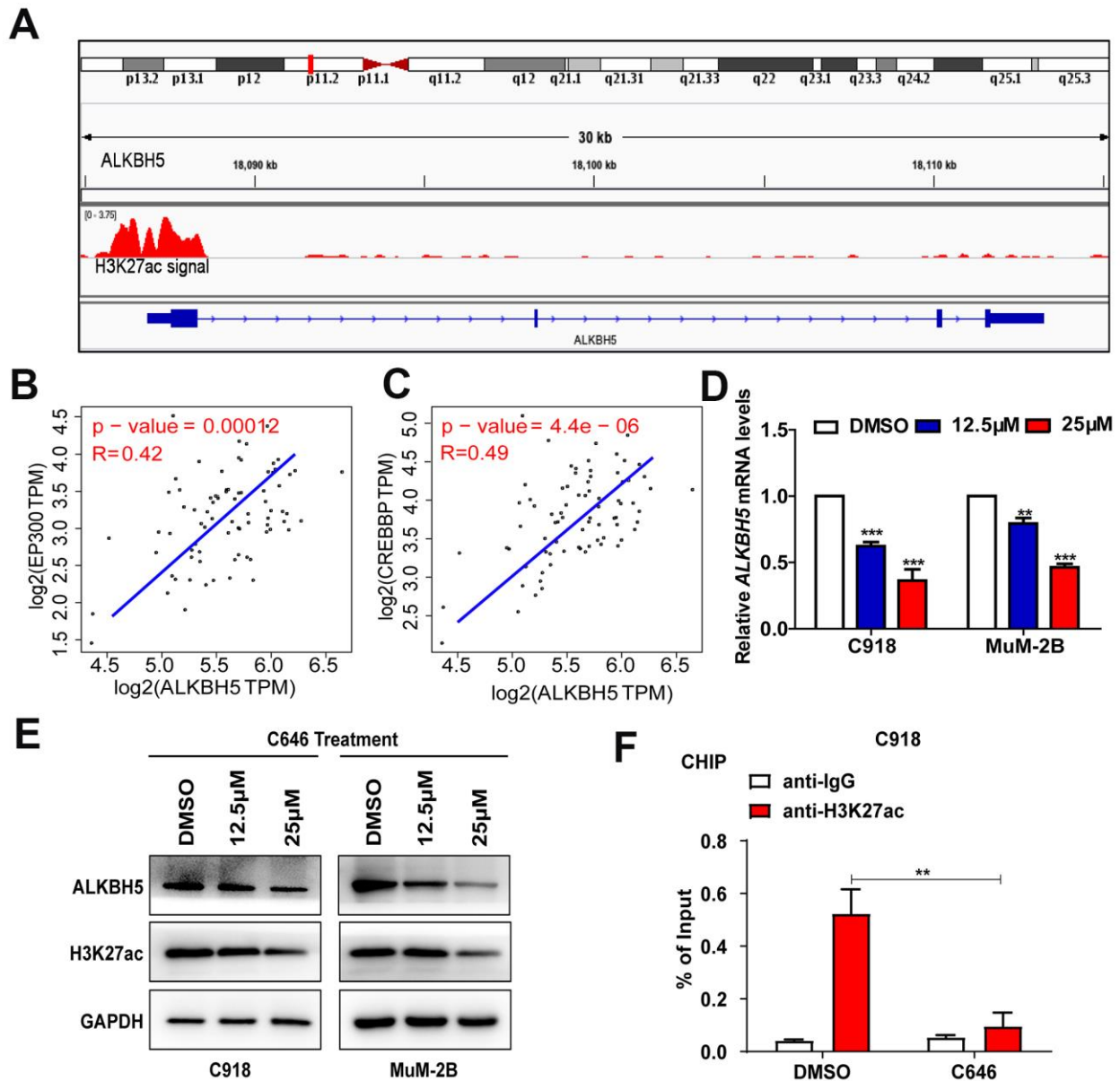


Figure 2. EP300-induced H3K27ac activation increased ALKBH5 expression in UM. (A) Data from the UCSC Genome Bioinformatics Site (<http://genome.ucsc.edu/>) showed high enrichment of H3K27ac in the promoter of ALKBH5 in melanoma. (B, C) ALKBH5 mRNA levels were positively correlated with EP300 (B) and CREBBP (C) in the UM data set from the TCGA database. (D–E) The mRNA (D) and protein (E) levels of ALKBH5 and H3K27ac were decreased when UM cells were treated with C646 for 24 hours. (F) ChIP assays were used to determine the enrichment of H3K27ac at the promoter of ALKBH5 after treating C918 cells with C646 and DMSO at 12.5µM for 12 hours. Mean ± SEM, t-test, * $P < 0.05$, ** $P < 0.01$, *** $P < 0.001$.

ALKBH5 promotes EMT of UM cells via m⁶A demethylation

Because EMT has been found to be a key process in tumor metastasis, we investigated the relationship between ALKBH5 and EMT in UM. As shown in Figure 4C, downregulation of ALKBH5 increased E-cadherin and decreased the protein levels of N-cadherin, Vimentin, Snail, Slug, and β -catenin (Figure 4C), which indicates that ALKBH5 affects the EMT of UM cells. In addition, overexpression of ALKBH5 not only significantly increased the migration and invasion of UM cells (Figure 4D, 4E, Supplementary Figure 2A), but also promoted UM cell EMT (Figure 4H). Moreover, IHC staining was used to detect EMT markers expression in tumors of nude mice assay of C918-shALKBH5#2 group and C918-shControl group. We found that Vimentin and Snail expressions were dramatically suppressed in the C918-shALKBH5#2

group than that in C918-shControl group (Supplementary Figure 2B).

ALKBH5, an m⁶A demethylase, can erase m⁶A mRNA modification and contribute to the progression of carcinomas [12]. Thus, we explored whether ALKBH5 upregulation and functional changes are a consequence of m⁶A demethylation. The reported catalytic inactive mutation ALKBH5 H204A (ALKBH5^{MUT}) plasmid and the wild-type ALKBH5 (ALKBH5^{WT}) plasmid were transfected into C918 and MuM-2B cells (Figure 4F). Compared with ALKBH5^{MUT}, ectopic expression of ALKBH5^{WT} increased cell migration and invasion (Figure 4G and Supplementary Figure 2C). Furthermore, cells with the catalytic inactive mutation of ALKBH5 showed lower N-cadherin, Vimentin, Snail, Slug, and β -catenin expression and higher E-cadherin expression (Figure 4I). These results indicate that ALKBH5-induced m⁶A demethylation is critical to EMT in UM.

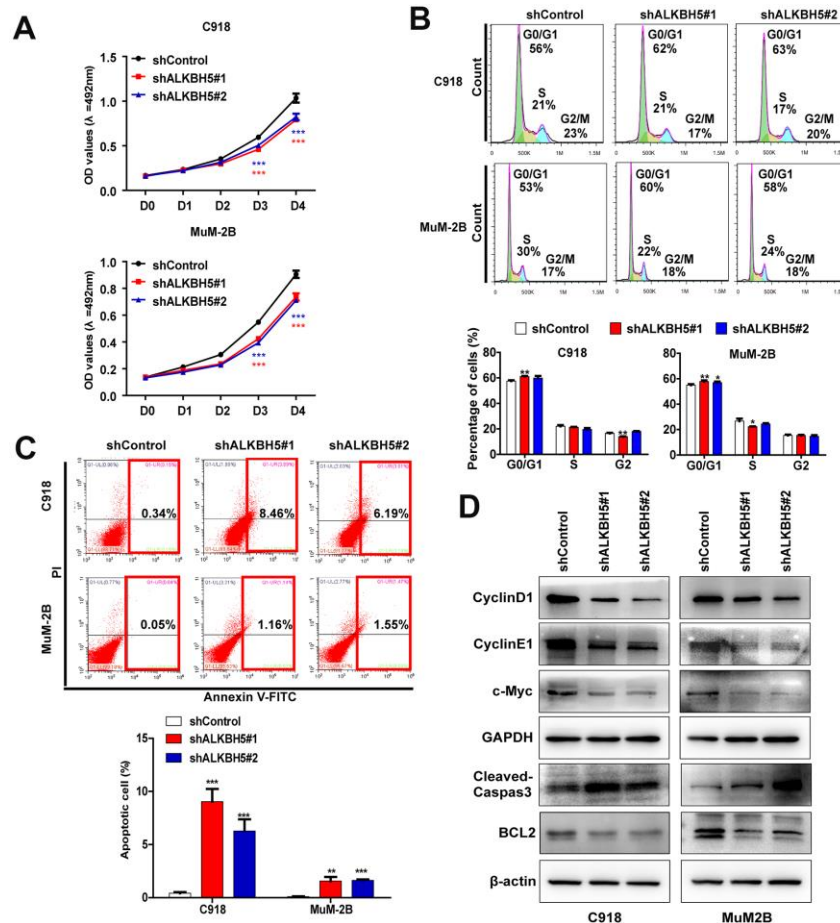


Figure 3. ALKBH5 knockdown inhibited UM cell growth. (A) Knockdown of ALKBH5 suppressed cell proliferation in UM cells as determined by MTT assay. (B) ALKBH5 shRNA treatment induced cell cycle arrest in G1/S phase in UM cells. (C) ALKBH5 elicited an apoptotic response in UM cells as determined by annexin V-FITC and PI staining and flow cytometry. (D) Western blot showed increased expression of apoptotic related protein, cleaved caspase-3, and decreased expression of BCL-2, c-Myc, cyclin D1 and cyclin E1 in ALKBH5-knockdown UM cells. Mean \pm SEM, t-test, * $P < 0.05$, ** $P < 0.01$, *** $P < 0.001$.

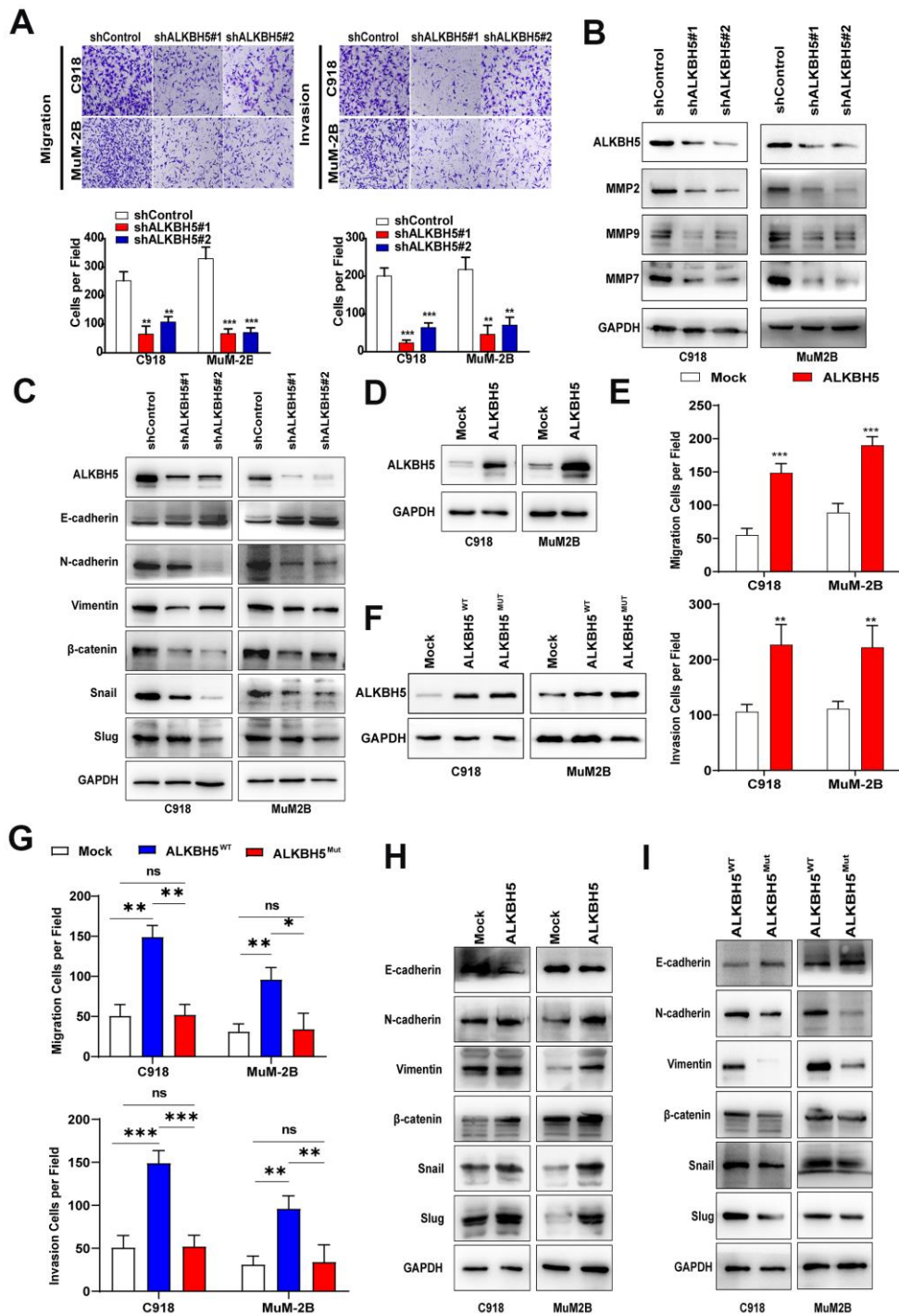


Figure 4. ALKBH5 promoted UM cell migration, invasion, and EMT. (A) After ALKBH5 knockdown plasmid transfection for 24 hours, the transwell migration assay and Matrigel invasion assay were used to determine cell migration and invasion ability, respectively, in C918 and MuM-2B cells. (B) After transfection with shRNA-targeted ALKBH5, the expression of MMP2, MMP7, and MMP9 was detected using western blot. (C) Knockdown of ALKBH5 decreased mesenchymal markers (N-cadherin, vimentin, Snail, Slug, and β -catenin) and increased epithelial marker (E-cadherin) in UM cells. (D) The ALKBH5 overexpression efficiency was verified at the protein level in UM cells by western blot assay. (E) Upregulation of ALKBH5 increased cell migration and invasion abilities in UM cells. (F) Western blot assay was used to detect the ALKBH5 protein level by transfecting UM cells with wild-type or catalytic inactive mutation plasmid of ALKBH5. (G) Compared with ALKBH5 wild-type plasmid transfection, catalytic inactive mutation of ALKBH5 decreased the migration and invasion of UM cells. (H) Overexpression of ALKBH5 increased the expression of EMT markers. (I) Loss of ALKBH5 catalytic activity suppressed the expression of EMT-related proteins in UM cells. Mean \pm SEM, t-test, * $P < 0.05$, ** $P < 0.01$, *** $P < 0.001$.

ALKBH5-induced m⁶A demethylation increases FOXM1 expression in UM cells

ALKBH5 has been reported to demethylate FOXM1 nascent transcripts and promote FOXM1 expression in glioblastoma [23]. Moreover, ALKBH5 downregulates the m⁶A enrichment on FOXM1 mRNA and promotes cell proliferation and invasion in lung adenocarcinoma [24]. Therefore, we firstly used the GSE22138, GSE73652, and TCGA data sets to investigate the relationship between FOXM1 and ALKBH5 in UM. We found that ALKBH5 expression is positively correlated with FOXM1 expression in UM tumors (Supplementary Figure 3A–3C). In addition, IHC staining also demonstrated that knockdown ALKBH5 could decrease FOXM1 expression *in vivo* (Supplementary Figure 3D). Furthermore, higher FOXM1 expression predicted poor prognosis in patients with UM in the TCGA data set (Supplementary Figure 3E).

To further confirm whether ALKBH5 could regulate FOXM1 expression, western blot assay was performed to detect protein levels of FOXM1 after transfection of ALKBH5 treated with different shRNAs. We found that FOXM1 expression increased after transfecting UM cells with ALKBH5^{WT} plasmid but did not change after treating UM cells with the catalytic inactive mutation of ALKBH5 (Figure 5A). Moreover, knockdown of ALKBH5 decreased the expression of FOXM1 (Figure 5B). We also used the MeRIP-qPCR assay to detect the effect of ALKBH5 on m⁶A levels of FOXM1 mRNA. As shown in Figure 5C, the downregulation of ALKBH5 increased the m⁶A level of FOXM1 mRNA in C918 cells (Figure 5C, left panel). In addition, m⁶A levels of FOXM1 mRNA were significantly increased in cells transfected with ALKBH5^{MUT} plasmids compared with wild-type plasmids (Figure 5C, right panel). Our results indicated that ALKBH5 demethylates the m⁶A modification on FOXM1 mRNA in UM cells.

Investigators have found that ALKBH5-induced m⁶A demethylation on mRNAs affects mRNA stability and translation [25, 26]. To investigate whether ALKBH5 increases FOXM1 expression by increasing its mRNA stability, we treated cells with the transcription inhibitor dactinomycin and detected the level of FOXM1 mRNA. As shown in Figure 5D (left panel), knockdown of ALKBH5 in C918 cells significantly decreased the FOXM1 mRNA level compared with control cells. Furthermore, the level of FOXM1 mRNA was notably reduced in C918 cells with catalytic inactive mutation of ALKBH5 after dactinomycin treatment (Figure 5D, right panel). Thus, these results demonstrated that ALKBH5 may upregulate FOXM1 expression and

increase the stability of FOXM1 mRNA via demethylating m⁶A modification.

FOXM1 is involved in ALKBH5-induced EMT in UM cells

FOXM1 is critical to the EMT/mesenchymal-epithelial transition (MET) process in carcinomas [27], but its role in UM remains unknown. In this study, we designed two different shRNAs to target FOXM1 and confirmed the knockdown efficiency by western blot (Figure 6A). Downregulation of FOXM1 significantly suppressed cell migration (Figure 6B) and invasion (Figure 6C). In addition, inhibition of FOXM1 in UM cells increased E-cadherin expression and decreased N-cadherin, vimentin, Snail, Slug, and β -catenin expression (Figure 6D).

To verify that m⁶A modification of FOXM1 mRNA is critical for ALKBH5-induced EMT, ALKBH5^{WT} and ALKBH5^{MUT} plasmids were transfected into ALKBH5-stable knockdown C918 cells. As expected, FOXM1 expression and EMT were markedly rescued by overexpression of the wild-type ALKBH5 but not the catalytic inactive mutation (Figure 6E). In addition, FOXM1-stable knockdown C918 cells were transduced with ALKBH5 overexpression and Control plasmid. As shown in Figure 6F, overexpression of ALKBH5 cannot rescue the deceleration of EMT caused by FOXM1 downregulation. Furthermore, the migration and invasion abilities of FOXM1-knockdown cells could not be promoted by ALKBH5 overexpression (Supplementary Figure 4). Taken together, our results suggest that ALKBH5 may promote UM EMT by upregulating FOXM1 expression in an m⁶A modification-dependent manner.

DISCUSSION

ALKBH5 has been shown to be involved in carcinogenesis and progression of a variety of cancers. However, the function of ALKBH5 in cancer is still controversial. In lung cancer [24, 28], gastric cancer [29], and epithelial ovarian cancer [30], ALKBH5 may act as an oncogene, whereas in colon cancer [31] and pancreatic cancer [32], ALKBH5 may inhibit tumor progression. However, few studies have investigated the role of ALKBH5 in UM. In this study, we demonstrated that inhibition of ALKBH5 suppresses tumor growth *in vivo* and that EP300-induced H3K27ac activation promotes ALKBH5 expression. A series of *in vitro* functional experiments verified that the downregulation of ALKBH5 inhibits cell proliferation, migration, and invasion and promotes cell apoptosis and G1 to S phase arrest. We also investigated the relationship between ALKBH5 and EMT. Western blot assay results showed

that knockdown or loss of m⁶A catalytic activity of ALKBH5 increased the epithelial cell phenotype marker E-cadherin and decreased mesenchymal phenotype markers (N-cadherin and Vimentin) compared with controls. Furthermore, ALKBH5 increases the expression and mRNA stability of FOXM1, a transcription factor found to promote EMT, via m⁶A modification.

ALKBH5 has been reported to have many biological functions. In epithelial ovarian cancer, ALKBH5 inhibits cell autophagy by enhancing the expression and stability of BCL-2 through m⁶A modification of BCL-2 mRNA [30]. ALKBH5 inhibits tumor motility and stemness by

demethylating TIMP3 [28], LncRNA NEAT1 [29], WIF1 [32], and LncRNA KCNK15-AS1 [33]. ALKBH5 regulates FOXM1 expression by demethylating the nascent transcripts of FOXM1 in glioblastoma stem-like cells [23]. However, in lung adenocarcinoma, ALKBH5 directly downregulates the m⁶A modification of FOXM1 mRNA and promotes FOXM1 expression under intermittent hypoxia [24]. In the present study, we demonstrated that ALKBH5 knockdown or loss of m⁶A catalytic activity had significantly decreased m⁶A enrichment of FOXM1 mRNA. Further studies should be performed to elucidate the oncogenic role of ALKBH5 in UM.

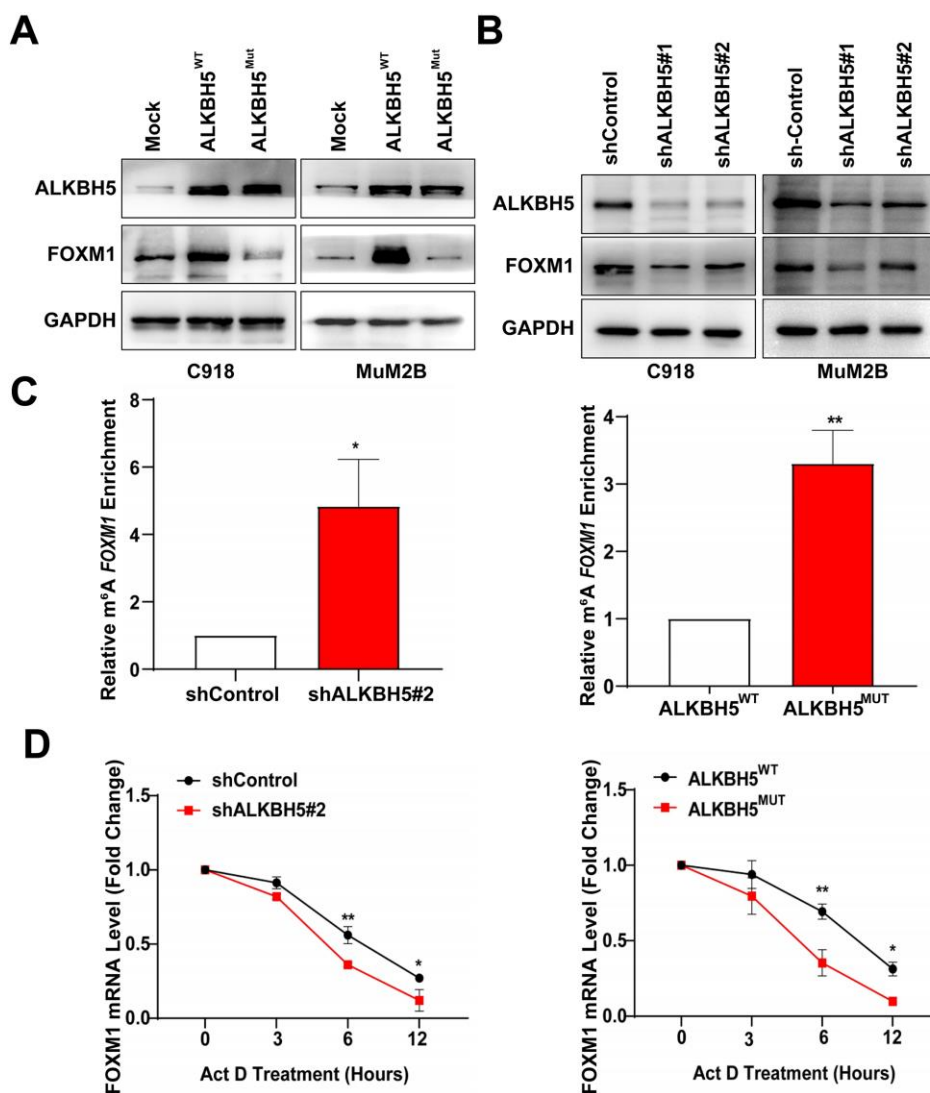


Figure 5. ALKBH5 increases FOXM1 expression and FOXM1 mRNA stability in UM cells. (A) The protein levels of FOXM1 in wild-type or catalytic inactive mutation ALKBH5-expressing UM cells were measured using western blotting. (B) ALKBH5 downregulation decreased FOXM1 expression in UM cells. (C) MeRIP-qPCR analysis was used to verify ALKBH5-induced FOXM1 m⁶A modification. The m⁶A modification of FOXM1 was increased on downregulation and catalytic inactive mutation of ALKBH5 in C918 cells. (D) C918 cells were treated with dactinomycin (Act D, 2 μg/mL) to block new RNA synthesis. The stability of FOXM1 was measured by qRT-PCR at different times. Mean ± SEM, t-test, **P* < 0.05, ***P* < 0.01, ****P* < 0.001.

Although the function of ALKBH5 has been widely investigated, few studies focus on the regulatory mechanism of abnormal ALKBH5 expression. In breast cancer, ALKBH5 is a direct target of hypoxia-inducible factor 1 α (HIF-1 α) and HIF-2 α and regulates breast cancer stem cell phenotype by downregulating the m⁶A modification on Nanog mRNA methylation [34]. It is well known that histone modifications involve a series of posttranslational modifications, including acetylation, methylation, and phosphorylation, that can impact gene expression by changing chromatin structure or recruiting histone modifiers [35, 36]. To further explore the relationship between histone modification and elevated ALKBH5 expression in UM, we analyzed the

data from UCSC Genome Bioinformatics Site and found high enrichments of H3K27ac peaks at the promoter of ALKBH5. Although the levels of both EP300 and CREBBP (the members of the EP300/CBP complex) were positively correlated with ALKBH5 in UM, we verified that EP300-induced H3K27ac activation promotes ALKBH5 transcription and increases ALKBH5 expression in UM. Our results provide new insight into the mechanisms involved in ALKBH5-related tumor progression.

FOXM1 has been reported to be involved in various tumor processes, including cancer growth and aggression, cancer differentiation, stem cell phenotype,

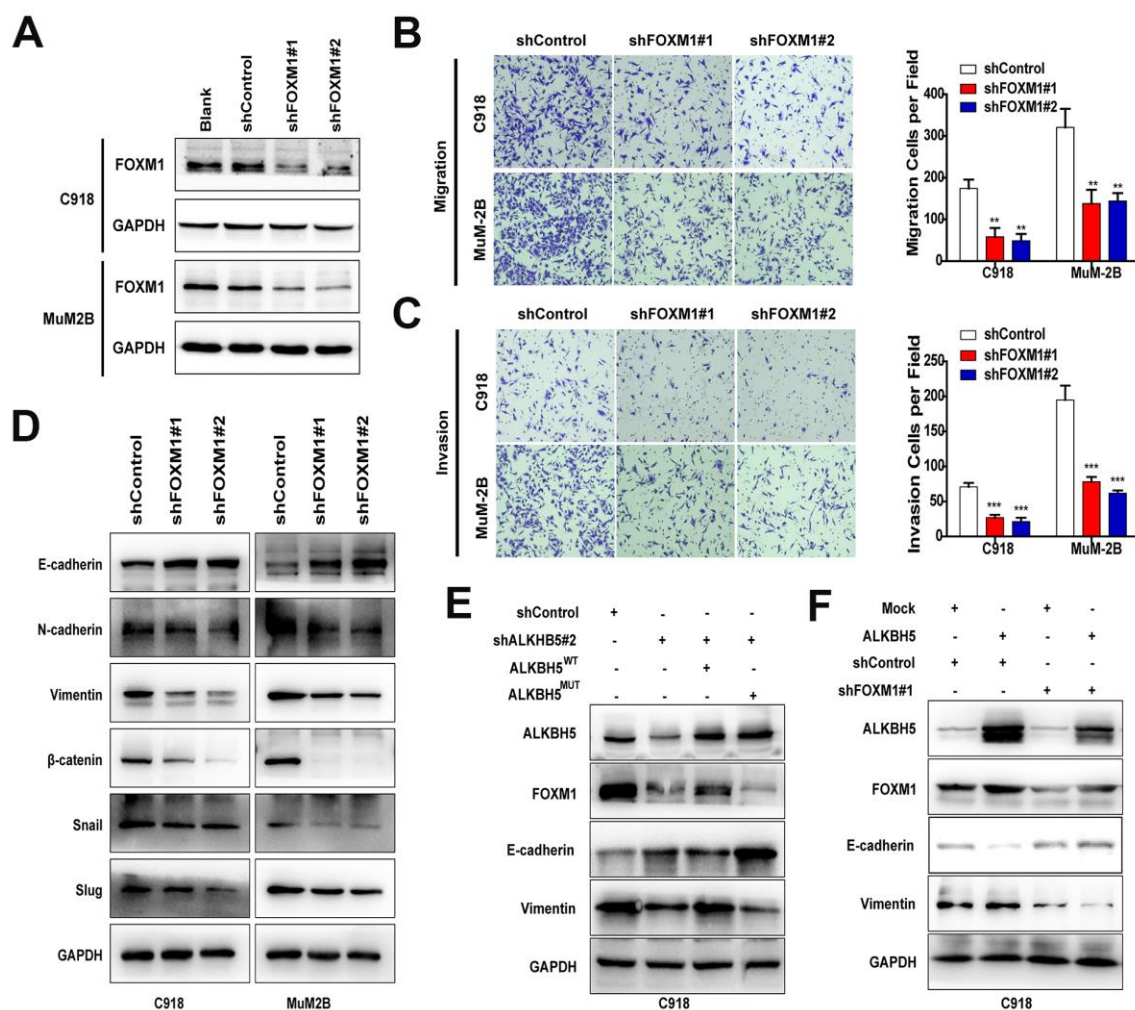


Figure 6. FOXM1 is involved in ALKBH5-induced EMT in UM cells. (A) The FOXM1 knockdown efficiency was verified at the protein level in UM cells by western blot assay. Downregulation of FOXM1 decreased cell migration (B) and invasion (C) of UM cells. (D) Downregulation of FOXM1 increased E-cadherin expression and decreased the protein levels of N-cadherin, vimentin, Snail, Slug, and β -catenin. (E) Western blot of FOXM1, E-cadherin, and vimentin in C918 cells with or without ALKBH5 stable knockdown transfected with wild-type or H204A mutation plasmid of ALKBH5. (F) The protein levels of E-cadherin and vimentin were measured using western blot in C918 cells stable transfected with shControl and shFOXM1 plasmid with or without ALKBH5 overexpression. Mean \pm SEM, t-test, * $P < 0.05$, ** $P < 0.01$, *** $P < 0.001$.

and EMT [37]. As a transcription factor, FOXM1 regulates the transcription of its downstream genes by directly binding to promoters of their DNA [27]. FOXM1 promotes EMT in pancreatic cancer by directly binding to the promoter region of the caveolin-1 gene and promoting its expression [38]. Snail and Slug, the transcription factors of EMT, are directly regulated by FOXM1 [39, 40]. In addition, FOXM1 not only regulates β -catenin expression but also reduces the nuclear accumulation and activity of β -catenin [41, 42]. In the current study, we observed that FOXM1 knockdown not only decreased the invasion and migration of UM cells, but also induced the downregulation of Snail, Slug, and β -catenin. In addition, the downregulation of FOXM1 in

UM cells decreased the expression of the mesenchymal markers Vimentin and N-cadherin and increased the expression of the epithelial marker E-cadherin. Finally, the expression of FOXM1 was upregulated by ALKBH5-induced m^6A demethylation, indicating that the ALKBH5/FOXM1 axis promotes UM EMT.

In conclusion, we demonstrate that ALKBH5, which is positively regulated by epigenetic modifications of H3K27 acetylation, promotes tumor progression by inducing tumor EMT and increasing FOXM1 expression via m^6A demethylation (Figure 7). Therefore, ALKBH5 is a potential target of UM molecular therapy.

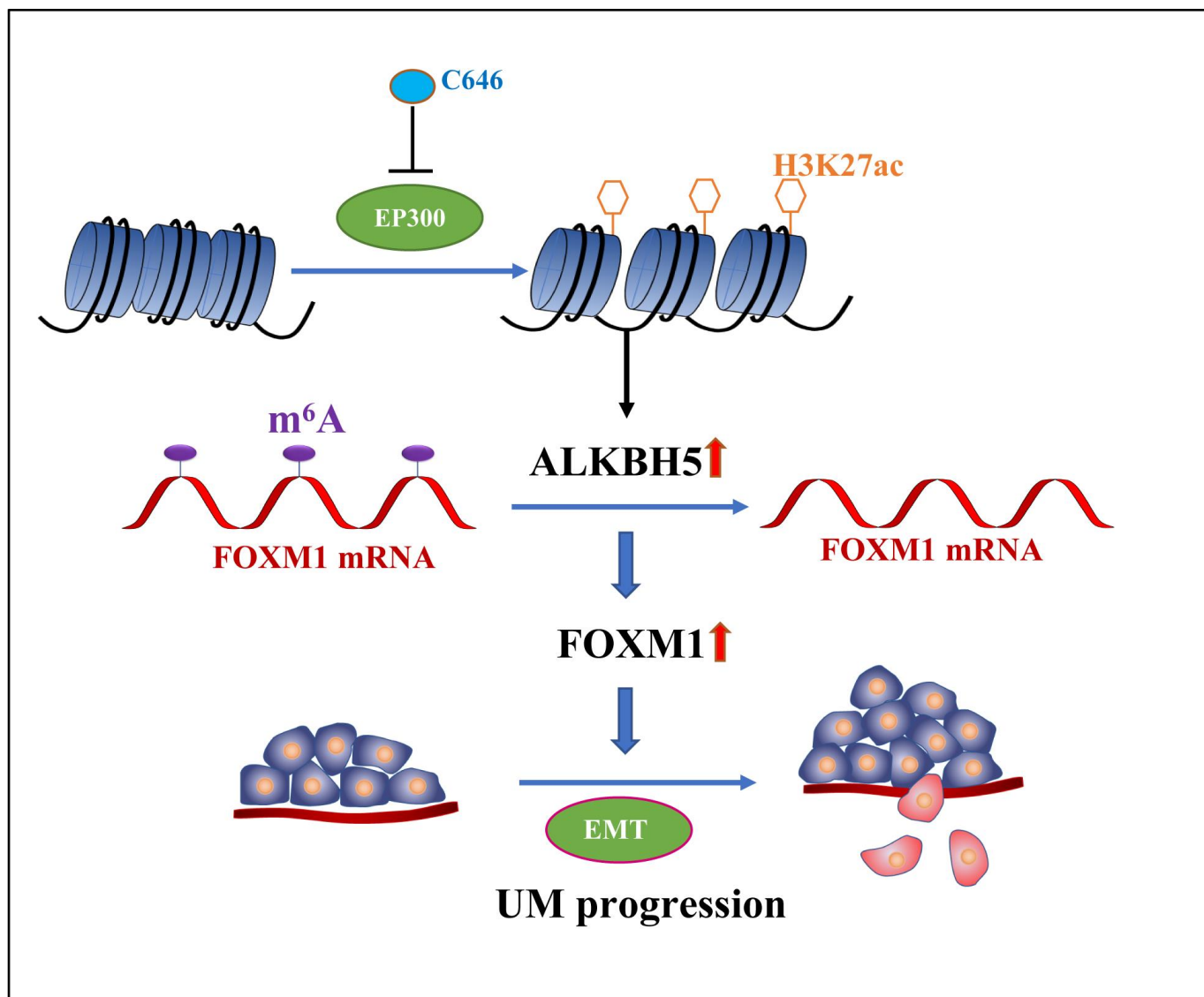


Figure 7. The graphic illustration of ALKBH5-mediated m^6A demethylation of *FOXM1* mRNA promotes progression of uveal melanoma.

MATERIALS AND METHODS

Cell culture and reagent

A human retinal pigment epithelium cell line (ARPE-19) was obtained from ATCC (ATCC CRL2302, Manassas, VA). Human UM cell lines (MuM-2B and C918) were obtained from the Cell Resource Center, Peking Union Medical College (Beijing, China). All cell lines were cultured in RPMI-1640 medium with supplementation of 10% fetal bovine serum (FBS; Invitrogen, Carlsbad, CA) and appropriate amounts of penicillin (100 U/mL) and streptomycin (100 mg/mL) in a humidified atmosphere of 5% CO₂ at 37° C. The histone acetyltransferase inhibitors C646, which targets EP300, and SGC-CBP30, which targets cAMP response element binding protein (CREB) binding protein (CREBBP), were purchased from Selleck (Shanghai, China).

Western blot

Proteins were collected from cells using the Whole Cell Lysis Assay Kit (KGP250, KeyGen, Nanjing, China). The protein concentration was determined using the bicinchoninic acid (BCA) method using the BCA Protein Quantitation Assay Kit (KeyGen, Nanjing, China). Protein was electrophoretically separated by 10% or 15% SDS-PAGE and transferred to PVDF membranes (Millipore, Billerica, MA). The membranes were blocked for 1 hour with 5% bovine serum albumin (BSA) in TBS-T and incubated with specific primary antibodies overnight at 4° C followed by incubation with rabbit or mouse radish peroxidase-coupled secondary antibodies for 1 hour. Antibody binding was detected using the enhanced chemiluminescence reagent (Millipore, Billerica, MA). The antibodies used in this study were as follows: ALKBH5 (ab195377, Abcam), H3K27ac (#8173, Cell Signaling Technology [CST]), cyclin D1 (#2978, CST), cyclin E1 (ab33911, Abcam), c-Myc (#5605, CST), caspase-3 (19677-1-AP, Proteintech), BCL-2 (12789-1-AP, Proteintech), MMP2 (#87809, CST), MMP7 (#71031, CST), MMP9 (#13667, CST), E-cadherin (#3195, CST), N-cadherin (#13116, CST), vimentin (#5741, CST), β -catenin (#8480, CST), Snail (ab53519, Abcam), Slug (ab27568, Abcam), β -actin (ab8227, Abcam), and GAPDH (#8884, CST).

Immunohistochemical staining

For immunohistochemical staining, deparaffinized sections were pretreated with 10 mM of sodium citrate buffer for antigen unmasking, blocked with 5% goat serum for 30 minutes, and incubated with antibodies at 4° C overnight. IHC staining was performed with horseradish peroxidase (HRP) conjugates using DAB, and the nuclei were stained with hematoxylin. Images

were taken with a Nikon microscopy and K-viewer system.

Plasmid construction and transfection

The shRNA sequences of ALKBH5 are as follows: shALKBH5#1, 5'-GAAAGGCTGTTGGCATCAATA-3'; shALKBH5#2, 5'-CCTCAGGAAGACAAGATTAGA-3'. The downregulation target sequences of FOXM1 are as follows: shFOXM1#1, 5'-CTCTTCTCCCTCAGATATA-3'; shFOXM1#2, 5'-GGACCACTTTCCTACTTT-3'. The catalytic inactive mutation site of ALKBH5 H204A was obtained from a previously published study [23]. Plasmids were transfected with Lipofectamine 2000 (Invitrogen, Carlsbad, CA) according to the manufacturer's instructions.

Lentiviral transduction for stable cell lines

Lentivirus plasmids of shRNA were co-transfected with the packaging plasmids pMD2.G and psPAX2 (Addgene) into HEK-293T cells to produce lentivirus. Two days after transfection, virus supernatants were collected, concentrated, and used to infect UM cells with polybrene (8 μ g/mL, Sigma, St. Louis, MO). After 3 days of transduction, cells were treated with 2 μ g/mL of puromycin (Sigma) for 4 to 7 days.

Quantitative real-time polymerase chain reaction (qRT-PCR)

Total RNA was isolated using RNA plus reagent (Takara, Japan). cDNA was prepared using Oligo(dT) primers according to the protocol supplied with the PrimeScript RT Reagent (Takara, Japan). The expression of ALKBH5 was determined by qRT-PCR using TB Green Advantage qPCR Premix (Takara, Japan). The primer sequences of ALKBH5, FOXM1, and GAPDH used in this study were as follows: ALKBH5, forward: 5'-GGTGTCGGAACCAGTGCTTT-3', reverse: 3'-CCAACCGGGGTGCATCTAAT-5'; FOXM1, forward: 5'-ACGTCCCCAAGCCAGGCTC-3', reverse: 5'-CTATGTAGCTCAGGAATAA-3'; GAPDH, forward: 5'-ACAACCTTTGGTATCGTGGAAGG-3', reverse: 3'-GCCATCACGCCACAGTTTC-5'.

Proliferation assay

Cell proliferation was assessed using the 3-(4,5-dimethylthiazol-2-yl)-2, 5-diphenyltetrazolium bromide (MTT) assay. Cells were plated into 96-cell plates (1000 cells per well). MTT solution (5 mg/mL) was added to the medium of each well. After incubation for 4 hours, the resultant formazan crystals were dissolved in dimethyl sulfoxide, and the absorbance intensity was measured using a microplate reader at 492 nm.

Migration and invasion assay

Cell migration assays were performed using 24-well transwell chambers (Costar-Corning, New York, USA) with an 8.0- μ m pore polycarbonate filter. The lower chamber was filled with 700 μ L of RPMI-1640 with 10% FBS, and cells (2.5×10^4 cells/well) pretreated with plasmid transfection of ALKBH5 were added into the upper chamber. After incubation for 5 hours, cells were fixed with methanol, stained with crystal violet, photographed, and counted. Cell invasion assay was performed similarly, except that transwell inserts were precoated with Matrigel and incubated for 10 hours.

Apoptosis and cell cycle assay

For cell apoptosis analysis, cells were serum-starved overnight and determined using the Annexin V-FITC Apoptosis Detection Kit (Beyotime, Shanghai, China). For cell cycle analysis, cells were fixed in 70% ethanol, stained with propidium iodide, and analyzed by flow cytometry.

m⁶A-RNA immunoprecipitation (MeRIP) assay

Total RNAs were extracted from stable ALKBH5 knockdown and catalytic inactive mutation C918 cells and their corresponding control cells. Chemically fragmented RNA (approximately 100 nucleotides) was incubated with m⁶A antibody (New England BioLabs) for immunoprecipitation according to the protocol of the Magna methylated RNA immunoprecipitation m⁶A kit (Merck Millipore). Enrichment of m⁶A-containing mRNA was analyzed using qRT-PCR.

Dactinomycin treatment

C918 cells were exposed to 2 μ g/mL of dactinomycin (Selleck, Shanghai, China) to block transcription for 0, 3, 6, and 12 hours. The cells were harvested, and the stability of *FOXMI* mRNA was analyzed using qRT-PCR assay.

Chromatin immunoprecipitation (ChIP)

ChIP analysis was carried out according to the standard method of the Simple ChIP Enzymatic Chromatin IP Kit (#9003, Cell Signaling Technology). Chromatin was immunoprecipitated with anti-H3K27ac (#8173, Cell Signaling Technology) or anti-IgG as a negative control. Finally, immunoprecipitated protein and DNA complexes were isolated and RT-PCR assay was carried out to examine the quantity of the specific proteins. The primers for the ALKBH5 promoters are listed as following: ALKBH5, forward: 5'-CGCGGGTTTCAGAACTTTCC-3', reverse: 3'-GGAGTTTCCGGAAGTCGGTT-5'.

Mice xenograft model

Animal experiments were approved by the Ethics Committee of Jinan University. The *in vivo* experiment method for transplantation of tumors was subcutaneous injection of 1×10^7 ALKBH5-stable knockdown C918 cells into BALB/c nude mice. The length and width of tumors were measured every 3 days to determine the tumor volume. After 4 weeks, the tumor-bearing mice were sacrificed, and the tumors were weighed.

Bioinformatics analysis

The gene expression profile GSE22138 and GSE73652 data sets were downloaded from the database and analyzed using R (V4.0, <https://cran.r-project.org/>) with the GEOquery Package. The GEPIA database (<http://gepia.cancer-pku.cn/index.html>) was used to analyze the interaction between ALKBH5, FOXM1, and clinical characteristics.

Statistical analysis

Data were analyzed for statistical significance using the t-test (IBM, NY). In these analyses, $P < 0.05$ was considered statistically significant. All *in vitro* experiments were confirmed three times.

AUTHOR CONTRIBUTIONS

L.L.H., J.X.Z. and L.L. conceived and designed this study; L.L.H. and J.Y.Y. performed experiments; L.L.H., H.Y., C.X.L. and L.X.Z. analyzed the data. L.L.H. prepared figures and drafted manuscript. L.L.H., J.Y.Y., H.Y., C.X.L., L.X.Z., L.L. and J.X.Z. approved the final version of the manuscript.

CONFLICTS OF INTEREST

The authors declare that they have no financial conflicts of interest.

FUNDING

This study was supported by the China Postdoctoral Science Foundation (2019M653288), National Natural Science Foundation of China (81970806), Postdoctoral Fund of the First Affiliated Hospital, Jinan University (801321), and the Short-term Research Abroad Program of Jinan University for the postdoctoral program (Lili Hao).

REFERENCES

1. Kaliki S, Shields CL. Uveal melanoma: relatively rare but deadly cancer. *Eye (Lond)*. 2017; 31:241–57.

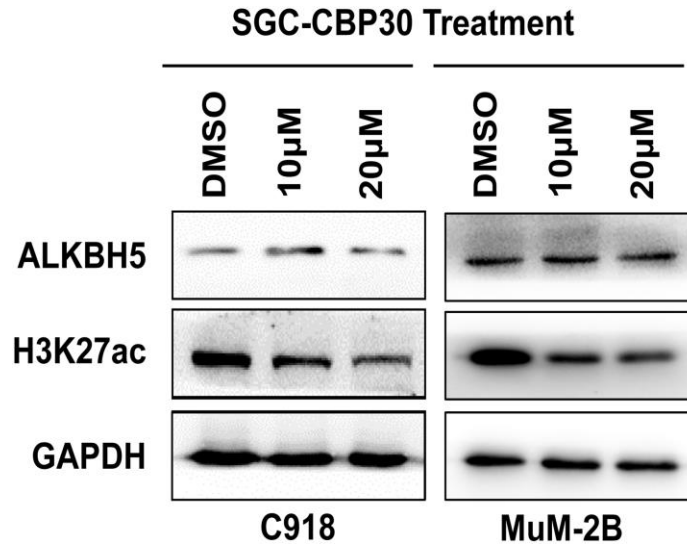
- <https://doi.org/10.1038/eye.2016.275>
PMID:[27911450](https://pubmed.ncbi.nlm.nih.gov/27911450/)
2. Krantz BA, Dave N, Komatsubara KM, Marr BP, Carvajal RD. Uveal melanoma: epidemiology, etiology, and treatment of primary disease. *Clin Ophthalmol.* 2017; 11:279–89.
<https://doi.org/10.2147/OPHTH.S89591> PMID:[28203054](https://pubmed.ncbi.nlm.nih.gov/28203054/)
 3. Carvajal RD, Schwartz GK, Tezel T, Marr B, Francis JH, Nathan PD. Metastatic disease from uveal melanoma: treatment options and future prospects. *Br J Ophthalmol.* 2017; 101:38–44.
<https://doi.org/10.1136/bjophthalmol-2016-309034>
PMID:[27574175](https://pubmed.ncbi.nlm.nih.gov/27574175/)
 4. Rietschel P, Panageas KS, Hanlon C, Patel A, Abramson DH, Chapman PB. Variates of survival in metastatic uveal melanoma. *J Clin Oncol.* 2005; 23:8076–80.
<https://doi.org/10.1200/JCO.2005.02.6534>
PMID:[16258106](https://pubmed.ncbi.nlm.nih.gov/16258106/)
 5. Lorenzo D, Ochoa M, Piulats JM, Gutiérrez C, Arias L, Català J, Grau M, Peñafiel J, Cobos E, Garcia-Bru P, Rubio MJ, Padrón-Pérez N, Dias B, et al. Prognostic factors and decision tree for long-term survival in metastatic uveal melanoma. *Cancer Res Treat.* 2018; 50:1130–39.
<https://doi.org/10.4143/crt.2017.171> PMID:[29198096](https://pubmed.ncbi.nlm.nih.gov/29198096/)
 6. Helgadottir H, Höiom V. The genetics of uveal melanoma: current insights. *Appl Clin Genet.* 2016; 9:147–55.
<https://doi.org/10.2147/TACG.S69210> PMID:[27660484](https://pubmed.ncbi.nlm.nih.gov/27660484/)
 7. Robertson AG, Shih J, Yau C, Gibb EA, Oba J, Mungall KL, Hess JM, Uzunangelov V, Walter V, Danilova L, Lichtenberg TM, Kucherlapati M, Kimes PK, et al, and TCGA Research Network. Integrative Analysis Identifies Four Molecular and Clinical Subsets in Uveal Melanoma. *Cancer Cell.* 2017; 32:204–220.e15.
<https://doi.org/10.1016/j.ccell.2017.07.003>
PMID:[28810145](https://pubmed.ncbi.nlm.nih.gov/28810145/)
 8. Sharma A, Stei MM, Fröhlich H, Holz FG, Loeffler KU, Herwig-Carl MC. Genetic and epigenetic insights into uveal melanoma. *Clin Genet.* 2018; 93:952–61.
<https://doi.org/10.1111/cge.13136>
PMID:[28902406](https://pubmed.ncbi.nlm.nih.gov/28902406/)
 9. Herlihy N, Dogrusöz M, van Essen TH, Harbour JW, van der Velden PA, van Eggermond MC, Haasnoot GW, van den Elsen PJ, Jager MJ. Skewed expression of the genes encoding epigenetic modifiers in high-risk uveal melanoma. *Invest Ophthalmol Vis Sci.* 2015; 56:1447–58.
<https://doi.org/10.1167/iovs.14-15250>
PMID:[25593028](https://pubmed.ncbi.nlm.nih.gov/25593028/)
 10. Li Y, Sun W, Sun D, Yin D. Ras-ERK1/2 signaling promotes the development of uveal melanoma by downregulating H3K14ac. *J Cell Physiol.* 2019; 234:16011–20.
<https://doi.org/10.1002/jcp.28259> PMID:[30770563](https://pubmed.ncbi.nlm.nih.gov/30770563/)
 11. Lee Y, Choe J, Park OH, Kim YK. Molecular mechanisms driving mRNA degradation by m⁶A modification. *Trends Genet.* 2020; 36:177–88.
<https://doi.org/10.1016/j.tig.2019.12.007>
PMID:[31964509](https://pubmed.ncbi.nlm.nih.gov/31964509/)
 12. Huang H, Weng H, Chen J. The biogenesis and precise control of RNA m⁶A methylation. *Trends Genet.* 2020; 36:44–52.
<https://doi.org/10.1016/j.tig.2019.10.011>
PMID:[31810533](https://pubmed.ncbi.nlm.nih.gov/31810533/)
 13. Ma S, Chen C, Ji X, Liu J, Zhou Q, Wang G, Yuan W, Kan Q, Sun Z. The interplay between m⁶A RNA methylation and noncoding RNA in cancer. *J Hematol Oncol.* 2019; 12:121.
<https://doi.org/10.1186/s13045-019-0805-7>
PMID:[31757221](https://pubmed.ncbi.nlm.nih.gov/31757221/)
 14. Jia R, Chai P, Wang S, Sun B, Xu Y, Yang Y, Ge S, Jia R, Yang YG, Fan X. m⁶A modification suppresses ocular melanoma through modulating HINT2 mRNA translation. *Mol Cancer.* 2019; 18:161.
<https://doi.org/10.1186/s12943-019-1088-x>
PMID:[31722709](https://pubmed.ncbi.nlm.nih.gov/31722709/)
 15. Luo G, Xu W, Zhao Y, Jin S, Wang S, Liu Q, Chen X, Wang J, Dong F, Hu DN, Reinach PS, Yan D. RNA m⁶A methylation regulates uveal melanoma cell proliferation, migration, and invasion by targeting c-Met. *J Cell Physiol.* 2020; 235:7107–19.
<https://doi.org/10.1002/jcp.29608> PMID:[32017066](https://pubmed.ncbi.nlm.nih.gov/32017066/)
 16. Schulz M, Salamero-Boix A, Niesel K, Alekseeva T, Sevenich L. Microenvironmental regulation of tumor progression and therapeutic response in brain metastasis. *Front Immunol.* 2019; 10:1713.
<https://doi.org/10.3389/fimmu.2019.01713>
PMID:[31396225](https://pubmed.ncbi.nlm.nih.gov/31396225/)
 17. Aiello NM, Kang Y. Context-dependent EMT programs in cancer metastasis. *J Exp Med.* 2019; 216:1016–26.
<https://doi.org/10.1084/jem.20181827>
PMID:[30975895](https://pubmed.ncbi.nlm.nih.gov/30975895/)
 18. Lin X, Chai G, Wu Y, Li J, Chen F, Liu J, Luo G, Tauler J, Du J, Lin S, He C, Wang H. RNA m⁶A methylation regulates the epithelial mesenchymal transition of cancer cells and translation of snail. *Nat Commun.* 2019; 10:2065.
<https://doi.org/10.1038/s41467-019-09865-9>
PMID:[31061416](https://pubmed.ncbi.nlm.nih.gov/31061416/)
 19. Yue B, Song C, Yang L, Cui R, Cheng X, Zhang Z, Zhao G. METTL3-mediated N⁶-methyladenosine modification is critical for epithelial-mesenchymal transition and metastasis of gastric cancer. *Mol Cancer.* 2019; 18:142.

- <https://doi.org/10.1186/s12943-019-1065-4>
PMID:[31607270](https://pubmed.ncbi.nlm.nih.gov/31607270/)
20. Gong C, Shen J, Fang Z, Qiao L, Feng R, Lin X, Li S. Abnormally expressed JunB transactivated by IL-6/STAT3 signaling promotes uveal melanoma aggressiveness via epithelial-mesenchymal transition. *Biosci Rep*. 2018; 38:BSR20180532.
<https://doi.org/10.1042/BSR20180532>
PMID:[29899166](https://pubmed.ncbi.nlm.nih.gov/29899166/)
21. Duan F, Lin M, Li C, Ding X, Qian G, Zhang H, Ge S, Fan X, Li J. Effects of inhibition of hedgehog signaling on cell growth and migration of uveal melanoma cells. *Cancer Biol Ther*. 2014; 15:544–59.
<https://doi.org/10.4161/cbt.28157> PMID:[24553082](https://pubmed.ncbi.nlm.nih.gov/24553082/)
22. Raisner R, Kharbanda S, Jin L, Jeng E, Chan E, Merchant M, Haverty PM, Bainer R, Cheung T, Arnott D, Flynn EM, Romero FA, Magnuson S, Gascoigne KE. Enhancer activity requires CBP/P300 bromodomain-dependent histone H3K27 acetylation. *Cell Rep*. 2018; 24:1722–29.
<https://doi.org/10.1016/j.celrep.2018.07.041>
PMID:[30110629](https://pubmed.ncbi.nlm.nih.gov/30110629/)
23. Zhang S, Zhao BS, Zhou A, Lin K, Zheng S, Lu Z, Chen Y, Sulman EP, Xie K, Böglér O, Majumder S, He C, Huang S. m⁶A demethylase ALKBH5 maintains tumorigenicity of glioblastoma stem-like cells by sustaining FOXM1 expression and cell proliferation program. *Cancer Cell*. 2017; 31:591–606.e6.
<https://doi.org/10.1016/j.ccell.2017.02.013>
PMID:[28344040](https://pubmed.ncbi.nlm.nih.gov/28344040/)
24. Chao Y, Shang J, Ji W. ALKBH5-m⁶A-FOXM1 signaling axis promotes proliferation and invasion of lung adenocarcinoma cells under intermittent hypoxia. *Biochem Biophys Res Commun*. 2020; 521:499–506.
<https://doi.org/10.1016/j.bbrc.2019.10.145>
PMID:[31677788](https://pubmed.ncbi.nlm.nih.gov/31677788/)
25. Li XC, Jin F, Wang BY, Yin XJ, Hong W, Tian FJ. The m⁶A demethylase ALKBH5 controls trophoblast invasion at the maternal-fetal interface by regulating the stability of CYR61 mRNA. *Theranostics*. 2019; 9:3853–65.
<https://doi.org/10.7150/thno.31868> PMID:[31281518](https://pubmed.ncbi.nlm.nih.gov/31281518/)
26. Tang C, Klukovich R, Peng H, Wang Z, Yu T, Zhang Y, Zheng H, Klungland A, Yan W. ALKBH5-dependent m⁶A demethylation controls splicing and stability of long 3'-UTR mRNAs in male germ cells. *Proc Natl Acad Sci USA*. 2018; 115:E325–33.
<https://doi.org/10.1073/pnas.1717794115>
PMID:[29279410](https://pubmed.ncbi.nlm.nih.gov/29279410/)
27. Bella L, Zona S, Nestal de Moraes G, Lam EW. FOXM1: a key oncofoetal transcription factor in health and disease. *Semin Cancer Biol*. 2014; 29:32–39.
<https://doi.org/10.1016/j.semcancer.2014.07.008>
PMID:[25068996](https://pubmed.ncbi.nlm.nih.gov/25068996/)
28. Zhu Z, Qian Q, Zhao X, Ma L, Chen P. N⁶-methyladenosine ALKBH5 promotes non-small cell lung cancer progress by regulating TIMP3 stability. *Gene*. 2020; 731:144348.
<https://doi.org/10.1016/j.gene.2020.144348>
PMID:[31927006](https://pubmed.ncbi.nlm.nih.gov/31927006/)
29. Zhang J, Guo S, Piao HY, Wang Y, Wu Y, Meng XY, Yang D, Zheng ZC, Zhao Y. ALKBH5 promotes invasion and metastasis of gastric cancer by decreasing methylation of the lncRNA NEAT1. *J Physiol Biochem*. 2019; 75:379–89.
<https://doi.org/10.1007/s13105-019-00690-8>
PMID:[31290116](https://pubmed.ncbi.nlm.nih.gov/31290116/)
30. Zhu H, Gan X, Jiang X, Diao S, Wu H, Hu J. ALKBH5 inhibited autophagy of epithelial ovarian cancer through miR-7 and BCL-2. *J Exp Clin Cancer Res*. 2019; 38:163.
<https://doi.org/10.1186/s13046-019-1159-2>
PMID:[30987661](https://pubmed.ncbi.nlm.nih.gov/30987661/)
31. Yang P, Wang Q, Liu A, Zhu J, Feng J. ALKBH5 holds prognostic values and inhibits the metastasis of colon cancer. *Pathol Oncol Res*. 2020; 26:1615–23.
<https://doi.org/10.1007/s12253-019-00737-7>
PMID:[31506804](https://pubmed.ncbi.nlm.nih.gov/31506804/)
32. Tang B, Yang Y, Kang M, Wang Y, Wang Y, Bi Y, He S, Shimamoto F. m⁶A demethylase ALKBH5 inhibits pancreatic cancer tumorigenesis by decreasing WIF-1 RNA methylation and mediating Wnt signaling. *Mol Cancer*. 2020; 19:3.
<https://doi.org/10.1186/s12943-019-1128-6>
PMID:[31906946](https://pubmed.ncbi.nlm.nih.gov/31906946/)
33. He Y, Hu H, Wang Y, Yuan H, Lu Z, Wu P, Liu D, Tian L, Yin J, Jiang K, Miao Y. ALKBH5 inhibits pancreatic cancer motility by decreasing long non-coding RNA KCN15-AS1 methylation. *Cell Physiol Biochem*. 2018; 48:838–46.
<https://doi.org/10.1159/000491915> PMID:[30032148](https://pubmed.ncbi.nlm.nih.gov/30032148/)
34. Zhang C, Samanta D, Lu H, Bullen JW, Zhang H, Chen I, He X, Semenza GL. Hypoxia induces the breast cancer stem cell phenotype by HIF-dependent and ALKBH5-mediated m⁶A-demethylation of NANOG mRNA. *Proc Natl Acad Sci USA*. 2016; 113:E2047–56.
<https://doi.org/10.1073/pnas.1602883113>
PMID:[27001847](https://pubmed.ncbi.nlm.nih.gov/27001847/)
35. Dutta A, Abmayr SM, Workman JL. Diverse activities of histone acylations connect metabolism to chromatin function. *Mol Cell*. 2016; 63:547–52.
<https://doi.org/10.1016/j.molcel.2016.06.038>
PMID:[27540855](https://pubmed.ncbi.nlm.nih.gov/27540855/)
36. Zhao S, Zhang X, Li H. Beyond histone acetylation-writing and erasing histone acylations. *Curr Opin Struct Biol*. 2018; 53:169–77.

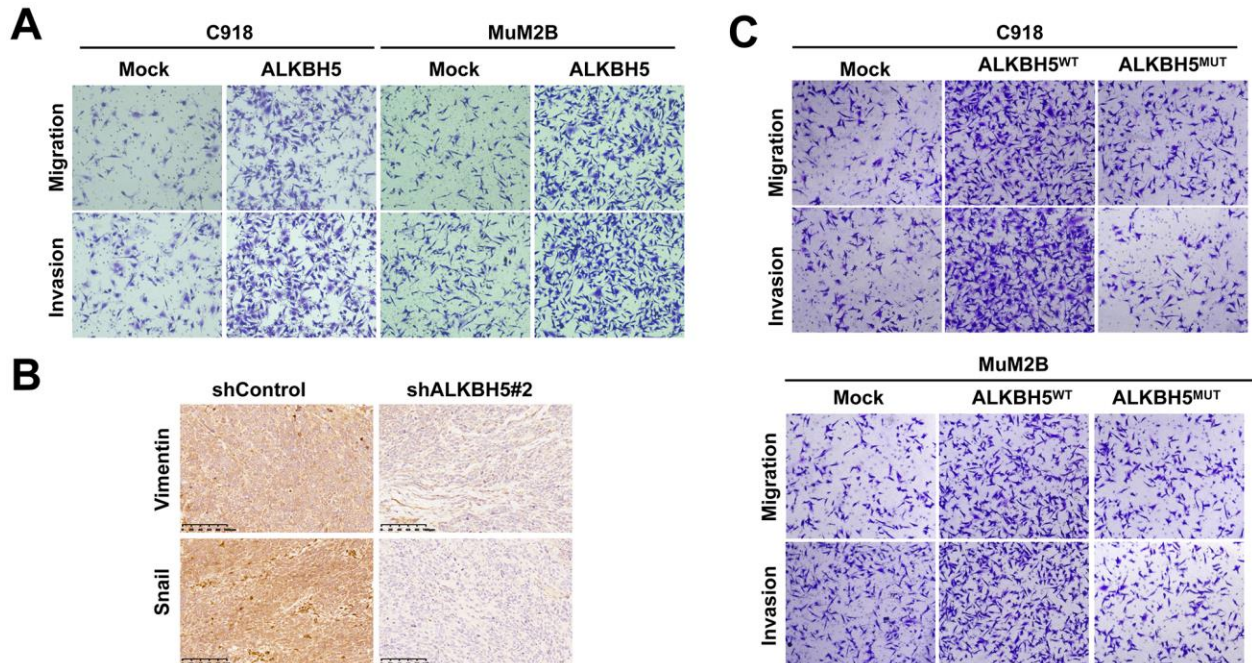
- <https://doi.org/10.1016/j.sbi.2018.10.001>
PMID:[30391813](https://pubmed.ncbi.nlm.nih.gov/30391813/)
37. Nandi D, Cheema PS, Jaiswal N, Nag A. FoxM1: repurposing an oncogene as a biomarker. *Semin Cancer Biol.* 2018; 52:74–84.
<https://doi.org/10.1016/j.semcancer.2017.08.009>
PMID:[28855104](https://pubmed.ncbi.nlm.nih.gov/28855104/)
38. Huang C, Qiu Z, Wang L, Peng Z, Jia Z, Logsdon CD, Le X, Wei D, Huang S, Xie K. A novel FoxM1-caveolin signaling pathway promotes pancreatic cancer invasion and metastasis. *Cancer Res.* 2012; 72:655–65.
<https://doi.org/10.1158/0008-5472.CAN-11-3102>
PMID:[22194465](https://pubmed.ncbi.nlm.nih.gov/22194465/)
39. Yang C, Chen H, Tan G, Gao W, Cheng L, Jiang X, Yu L, Tan Y. FOXM1 promotes the epithelial to mesenchymal transition by stimulating the transcription of slug in human breast cancer. *Cancer Lett.* 2013; 340:104–12.
<https://doi.org/10.1016/j.canlet.2013.07.004>
PMID:[23856032](https://pubmed.ncbi.nlm.nih.gov/23856032/)
40. Wei P, Zhang N, Wang Y, Li D, Wang L, Sun X, Shen C, Yang Y, Zhou X, Du X. FOXM1 promotes lung adenocarcinoma invasion and metastasis by upregulating SNAIL. *Int J Biol Sci.* 2015; 11:186–98.
<https://doi.org/10.7150/ijbs.10634>
PMID:[25561901](https://pubmed.ncbi.nlm.nih.gov/25561901/)
41. Jin B, Wang C, Li J, Du X, Ding K, Pan J. Anthelmintic niclosamide disrupts the interplay of p65 and FOXM1/ β -catenin and eradicates leukemia stem cells in chronic myelogenous leukemia. *Clin Cancer Res.* 2017; 23:789–803.
<https://doi.org/10.1158/1078-0432.CCR-16-0226>
PMID:[27492973](https://pubmed.ncbi.nlm.nih.gov/27492973/)
42. Chen Y, Li Y, Xue J, Gong A, Yu G, Zhou A, Lin K, Zhang S, Zhang N, Gottardi CJ, Huang S. Wnt-induced deubiquitination FoxM1 ensures nucleus β -catenin transactivation. *EMBO J.* 2016; 35:668–84.
<https://doi.org/10.15252/emboj.201592810>
PMID:[26912724](https://pubmed.ncbi.nlm.nih.gov/26912724/)

SUPPLEMENTARY MATERIALS

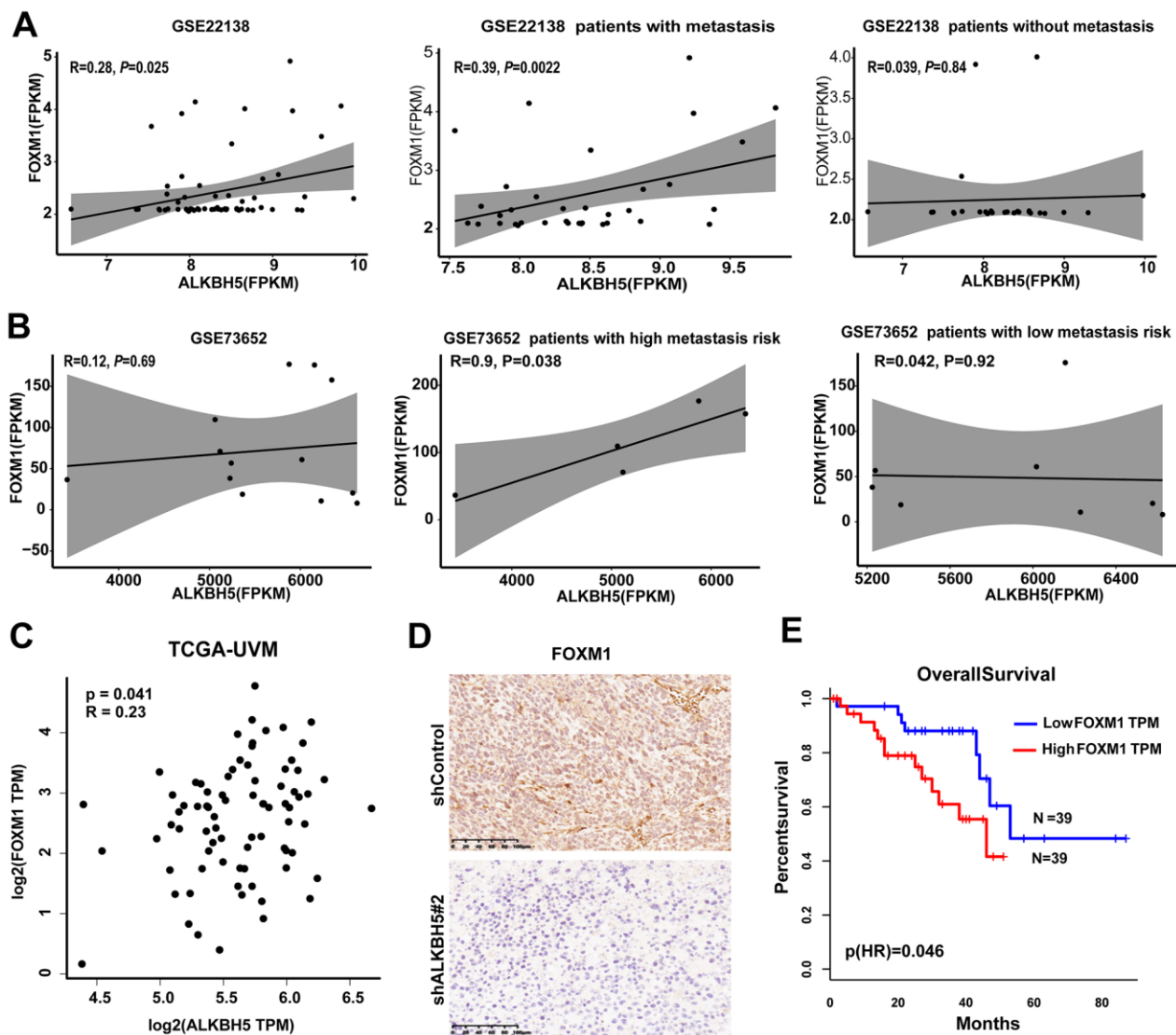
Supplementary Figures



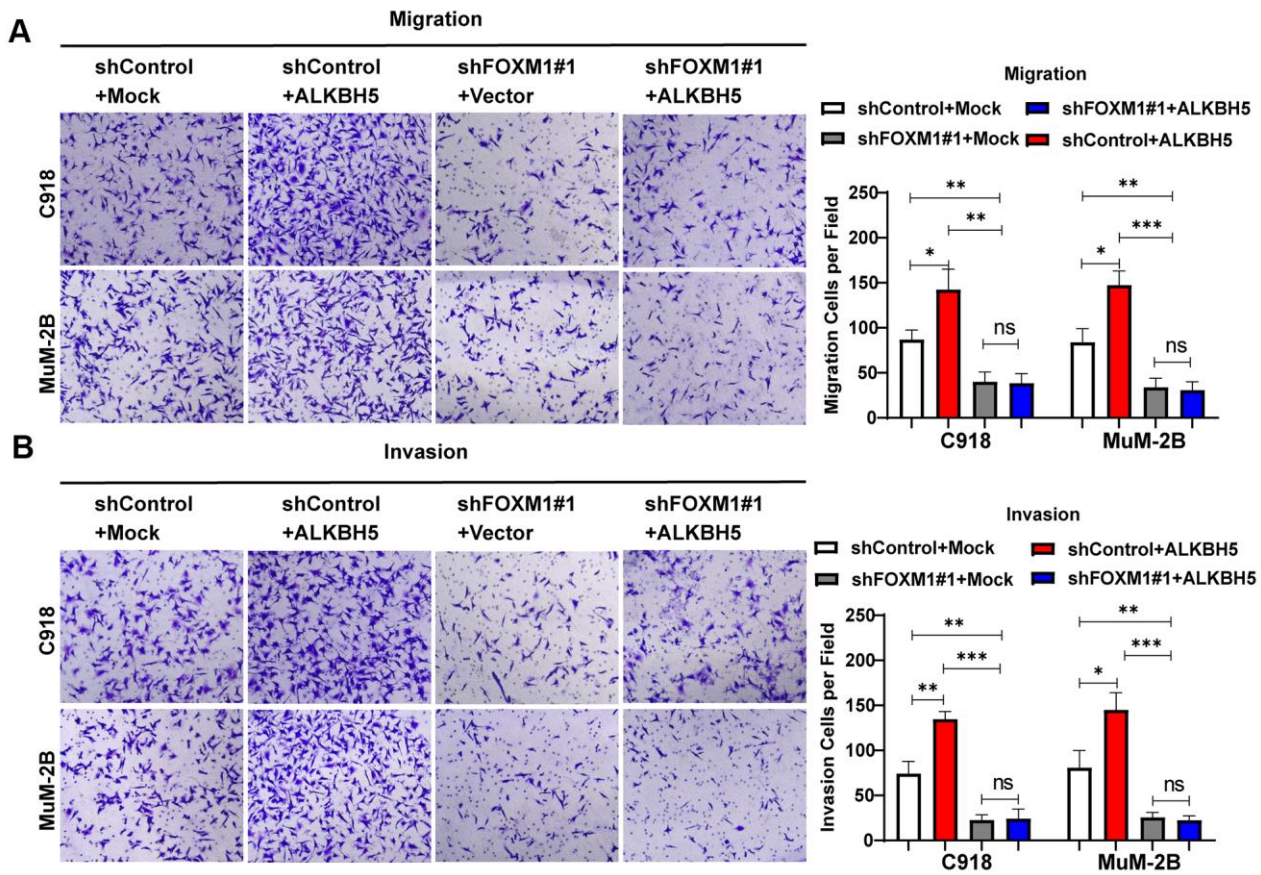
Supplementary Figure 1. After treating cells with SGC-CBP30 for 24 hours at different concentrations, the protein levels of ALKBH5 and H3K27ac were detected using western blot.



Supplementary Figure 2. ALKBH5 overexpression increased the abilities of migration and invasion in UM cells. (A) Upregulation of ALKBH5 increased cell migration and invasion in UM cells. (B) Vimentin and Snail expression were detected in C918-shALKBH5#2 and shcontrol group nude mice by IHC assay. (C) Compared with ALKBH5 wild-type plasmid transfection, cells with loss of catalytic activation ability of ALKBH5 could decrease the abilities of cell migration and invasion in UM.



Supplementary Figure 3. Public data on UM tissues were used to analyze the relationship between ALKBH5 and FOXM1. (A) ALKBH5 expression was significantly correlated with FOXM1 expression ($P = 0.025$) in the GSE22138 data set (left panel). ALKBH5 expression in primary tumors with distant metastasis was positively correlated with FOXM1 expression (middle panel). ALKBH5 expression in primary tumors without distant metastasis was not significantly related to FOXM1 expression in the GSE22138 data set (right panel). (B) Although ALKBH5 was not correlated with FOXM1 in the GSE73652 data set (left panel), its expression showed a positive correlation in the primary tumors of patients with high metastasis risk (middle panel), but not in the primary tumors of patients with low metastasis risk (right panel). (C) In the TCGA database of UM tissue, ALKBH5 expression was positively related to FOXM1 expression. (D) The expression of FOXM1 was detected in the C918-shALKBH5#2 group and the control group by IHC assay. (E) Patients with higher FOXM1 expression have worse outcomes compared with those with low FOXM1 expression.



Supplementary Figure 4. ALKBH5 could not rescue cell Migration (A) and Invasion (B) abilities caused by FOXM1 knockdown in UM cells. Mean \pm SEM, t-test, * $P < 0.05$, ** $P < 0.01$, *** $P < 0.001$.

Development and validation of an immune and stromal prognostic signature in uveal melanoma to guide clinical therapy

Qianwen Gong^{1,*}, Qi Wan^{2,*}, Anqi Li¹, Yubin Yu¹, Xiangyu Ding¹, Lei Lin¹, Xiaoliang Qi¹, Liang Hu¹

¹School of Ophthalmology and Optometry, Eye Hospital, Wenzhou Medical University, Wenzhou, Zhejiang, China

²State Key Laboratory of Ophthalmology, Zhongshan Ophthalmic Center, Sun Yat-Sen University, Guangzhou, China

*Equal contribution

Correspondence to: Liang Hu; email: liang_hu@live.cn, <https://orcid.org/0000-0003-1422-4008>

Keywords: uveal melanoma, immune, stromal, prognosis

Received: March 17, 2020

Accepted: July 14, 2020

Published: October 26, 2020

Copyright: © 2020 Gong et al. This is an open access article distributed under the terms of the [Creative Commons Attribution License](https://creativecommons.org/licenses/by/3.0/) (CC BY 3.0), which permits unrestricted use, distribution, and reproduction in any medium, provided the original author and source are credited.

ABSTRACT

The tumor microenvironment is known to play an important role in uveal melanoma. Reliable prognostic signatures are needed to aid high risk patients and improve prognosis. Uveal melanoma tissues from three public datasets were analyzed. RNA sequence data of uveal melanoma and corresponding clinical features were obtained from The Cancer Genome Atlas database. Immune and stromal scores were calculated by applying the “ESTIMATE” algorithm. The samples were divided into high and low immune or stromal score groups. We constructed prognostic models by using the ‘lasso’ package and tested them for 500 iterations. The cell signature was validated in another GSE44295 and GSE84976 datasets. We found that the median survival time of the low immune/stromal score group is longer than that of the high-score group. Thirteen immune cells and one stromal cell were concerned significant in predicting poor overall survival rate. Finally, a four-cell model was identified. Further validation revealed that the low-risk group has a significantly better survival than the high-risk group in another two datasets ($P < 0.05$). Moreover, the high-risk group is more sensitive to immunotherapy and chemotherapy. Summarizing, the proposed immune cells signature is a promising biomarker for estimating overall survival in uveal melanoma.

INTRODUCTION

Uveal melanoma (UM) is the most common type of malignant tumor of the adult eye, and 50% of patients with UM will eventually die as a result [1–3]. The prognosis for patients with UM remains poor, though there have been some certain advances in the diagnosis and treatment of UM [4]. Thus, there is an urgent need in this advancing field to further enhance prognostic accuracy and provide an efficient therapy [5].

In recent years, with the rapid development of immunotherapy, it has been reported that the tumor microenvironment (TME) plays a pivotal role in cancer progression and therapeutic responses [6–7]. Prognostic

or predictive biomarkers related to TME may hold great promise in identifying molecular targets and guiding patient management [8].

In the context of the tumor microenvironment, immune and stromal cells are two major types suggested as crucial for the diagnostic and prognostic assessment of tumors [9]. An increasing body of literature suggests that immune cell infiltration may co-evolve with the sequential genetic changes occurring in UM [10–13]. Early changes resulting in a gain of chromosome 8q are reported to activate macrophage infiltration, while sequential loss of BRCA1-associated protein-1 (BAP1) expression could drive T cell infiltration in UM [12]. Although increasing numbers of studies have explored

the microenvironment using differentially expressed genes, a comprehensive analysis with an overall landscape is still lacking. Fortunately, the availability of public large-scale datasets, such as the cancer genome atlas (TCGA), could be used to gain numerous amounts of RNA sequencing (RNA-seq) data to represent the tumor microenvironment [14–15]. And Yoshihara et al. designed the “ESTIMATE” (Estimation of STromal and Immune cells in Malignant Tumor tissue using Expression data) algorithm [16]. By analyzing specific gene expression signature of immune and stromal cells, immune and stromal scores can be calculated using the ESTIMATE algorithm to predict the infiltration of non-tumor cells. In recent years, the ESTIMATE algorithm has been reported to be applied in breast cancer, glioblastoma multiforme, etc., proving the effectiveness of such big-data-based algorithms [9, 17, 18]. Effective use of all this information would be helpful in improving clinical management.

In this study, we used a number of datasets with the ESTIMATE algorithm to identify the influence of immune and stromal cells in UM patients, and to develop and validate a prognostic signature to better guide the therapy and prognosis of UM.

RESULTS

Subgroup analysis of immune scores and stromal scores

A total of 15,187 generally changed mRNA expression values and clinicopathological characteristics of UM were obtained from TCGA. Based on the ESTIMATE algorithm, immune scores were distributed between -1600 and 1645 and stromal scores ranged from -2011 to -348, respectively. A subgroup analysis of clinical characteristics showed that only histological type has a significant difference in immune scores (Figure 1A).

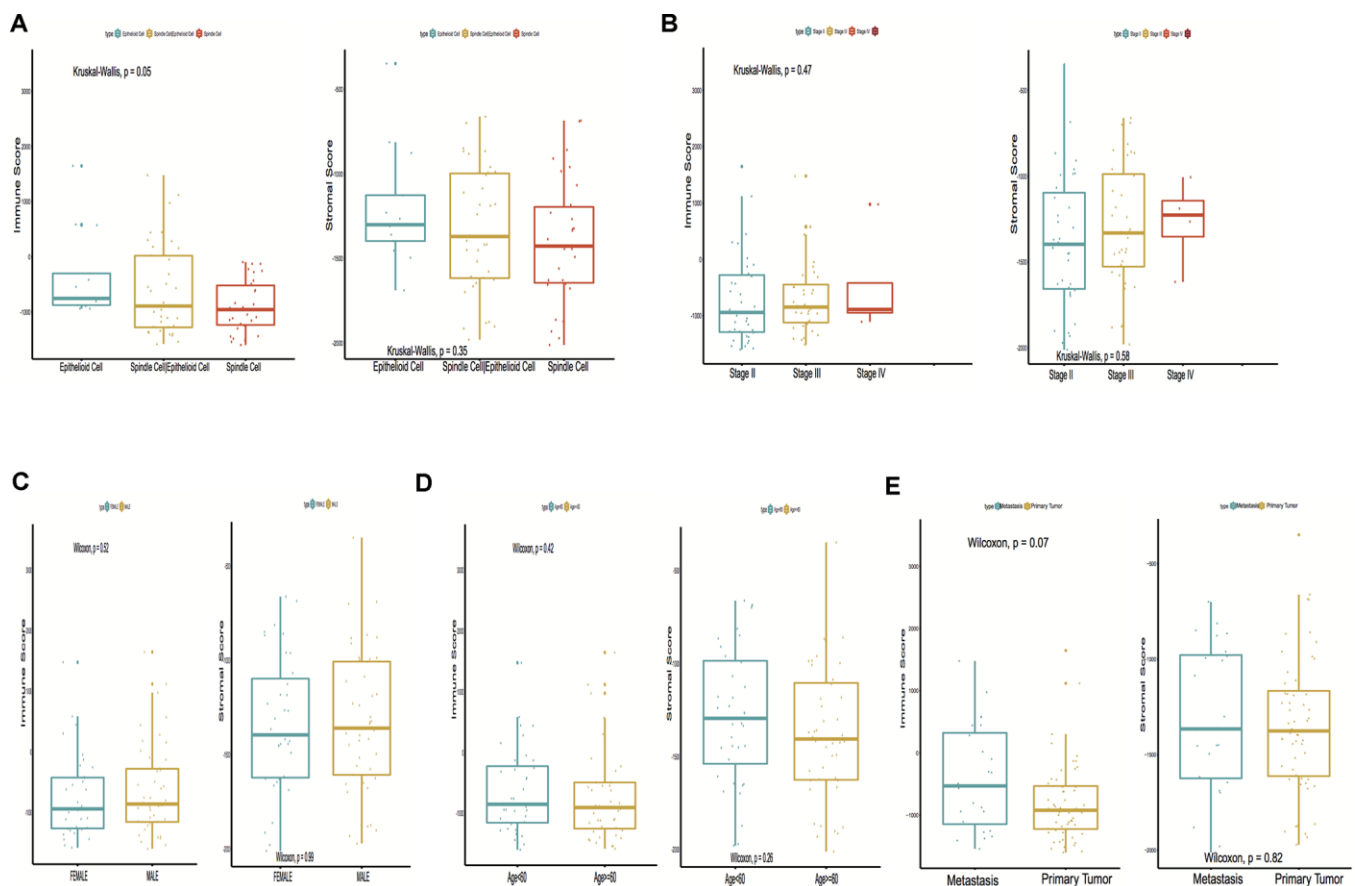


Figure 1. Immune scores and stromal scores are associated with Uveal Melanoma (UM) clinical subtypes, like histological type, metastasis, etc. (A) Distribution of immune scores and stromal scores of histological subtypes, Box-plot shows that there is a significant association between UM subtypes and the level of immune scores ($P = 0.05$); (B) Distribution of immune scores and stromal scores of stage subtypes; (C) Distribution of immune scores and stromal scores of sex subtypes; (D) Distribution of immune scores and stromal scores of age subtypes; (E) Distribution of immune scores and stromal scores of metastasis subtypes. Box-plot shows that there is no significant association between other subtypes and the levels of immune and stromal scores.

The subtype cases of epithelioid cells had the highest immune scores ($P = 0.05$). The clinical characteristics of stage, gender and age are statistically insignificant (Figures 1B–1D). Moreover, the metastatic UM showed a higher immune and stromal score, but this was statistically insignificant compared with the primary melanoma (Figure 1E). To determine the potential correlation of overall survival with immune scores and stromal scores, we divided the 80 UM samples of high and low immune or stromal score groups by median value. Kaplan-Meier survival curves show that the overall survival of samples with low immune scores and stromal scores is longer than that of the samples in the high score group (hazard ratio [HR], 5.35 [$P < 0.001$]; and 2.76 [$P = 0.02$], respectively) (Figure 2A, 2B).

Gene set variation analysis

To investigate the hallmark pathways shared by different immune or stromal groups, we performed gene set variation analysis (GSVA). According to the following criteria of P value < 0.05 and $|\text{GSVA score}| \geq 1$, four hallmark terms were commonly differently expressed in the high immune and stromal score group, and 12 hallmark terms were commonly differently regulated in the low immune and stromal score group. The same pathways are marked in red in Figure 2C, 2D.

Clustering for immune and stromal cells infiltration

To validate the above findings, the immune and stromal cells phenotypes expression profiles from UM were optimally clustered by applying the “ClassDiscovery” algorithm and the results are shown in Figures 3A, 3B. Cell infiltration in immune and stromal subtypes showed that the overall survival of the high infiltration group is significantly shorter than the low infiltration group (HR, 3.35; $P = 0.004$; and HR, 2.55; $P = 0.03$, respectively; Figure 3C, 3D).

Identification and confirmation of prognostic model

A log-rank test of Kaplan-Meier survival curves of 24 immune cells and 11 stromal cells showed that there was a total of 13 immune cells and 1 stromal cell capable of significantly predicting poor overall survival rate ($P < 0.05$). Moreover, we used LASSO modeling with 500 iterations to evaluate associations between the 14 selected cells and overall survival in the TCGA dataset. Finally, a four-cell (cytotoxic cells, Th1 cells, Th2 cells and myocytes cells) biomarker was screened out of the 14 selected cells to build a risk signature based on the criteria (Figure 4A). The risk score formula for overall survival was calculated as follows: risk score = $1.54 \times$ (expression value of Cytotoxic cells) + $1.20 \times$ (expression value of Th1 cells) + $2.80 \times$

(expression value of Th2 cells) - $0.46 \times$ (expression value of Myocytes). The risk system calculates a risk score for each patient. Applying the median cut-off value of the risk scores, 80 patients with UM were divided into high-risk and low-risk groups. Kaplan-Meier curve indicated that there was a significant difference between high-risk and low-risk group (HR, 6.39; 95% confidence interval (CI), 2.73 to 14.97; $P < 0.001$) (Figure 4B). The area under the curve (AUC) values for the four-cell model was 0.802. To verify the predictive ability of the four-cell model, validation analysis was performed using the GSE44295 and GSE84976 datasets. The AUC values of four cells were 0.681 and 0.658, respectively (Figure 5A, 5C). The Kaplan-Meier curve revealed that the low-risk group have a significantly better survival than the patients in high-risk group with log-rank test (HR, 2.54; $P = 0.03$ and HR, 4.01; $P = 0.003$, respectively) (Figure 5B, 5D). Results of the subgroup analysis of clinical characteristics of low- and high- risk groups are shown in Figure 6.

High-risk subgroup more sensitive to immunotherapy and chemotherapy

The correlations of cytotoxic T-lymphocyte-associated protein 4 (CTLA-4) and programmed death-ligand 1 (PD-L1) expression with low- and high- risk groups were analyzed. The results revealed that the expression in the high-risk group was generally higher than that in the low-risk group (Figure 7A). The relationships between risk score and previously established prognostic markers, such as tumor stage, chromosome 3 status, mutated BAP1 and molecular subtype, were explored. The box plots in Figure 7B show that BAP1 mutant, subtype D, and monosomy 3 have a higher risk score than BAP1 wildtype, subtype A and disomy 3, respectively. Compared with the 3 years AUC values of these established prognostic markers (BAP1 mutant, tumor stage, histological type, subtype and chromosome 3 status), our signature can achieve higher accuracy value (Figure 7C). Furthermore, we used subclass mapping to compare the expression profile of the two subgroups and another dataset containing details of 47 patients with cutaneous melanoma that responded to immunotherapies, published in the TIDE website. Interestingly, we found that the high-risk group is more promising to respond to anti-PD-1 therapy (Bonferroni corrected $P = 0.02$) (Figure 8H). To further explore the response to chemotherapy between high- and low-risk patients with UM, we performed “pRRophetic” algorithm to estimate the chemotherapeutic response based on half maximal inhibitory concentration (IC50) available in the Genomics of Drug Sensitivity in Cancer (GDSC) database. Seven chemotherapeutic drugs, including AZD6482, JNK Inhibitor VIII, Lapatinib,

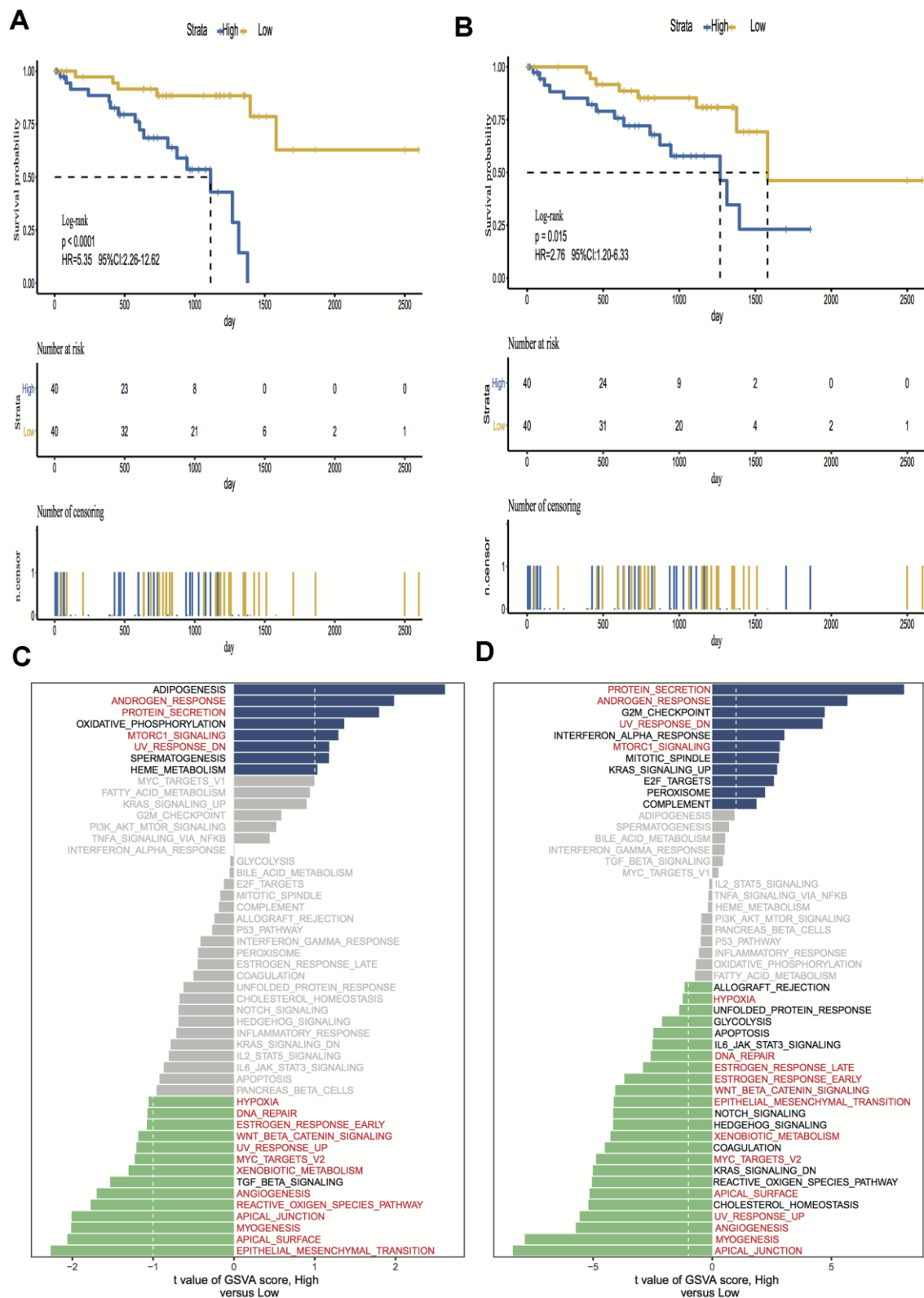


Figure 2. Kaplan-Meier survival analysis and Gene set variation analysis (GSVA) of high vs. low immune scores/stromal scores groups. (A, B) Overall survival among patients with uveal melanoma (UM) based on their immune and stromal scores; (C, D) Differential pathway activities between high and low immune and stromal scores groups, the same pathways are marked in red in the immune and stromal groups. Hazard ratios (HRs) and 95% CIs are for high vs low immune and stromal risk. The log-rank test was used to calculate P values in comparing risk groups.

Mitomycin C, PF.4708671, Temsirolimus and X17.AAG were identified as producing significant differences in the estimated IC50 between the high- and low-risk groups. Remarkably, we observed from the estimated IC50 of these chemotherapeutic drugs, that the high-risk group could be more sensitive to chemotherapies than those in low-risk group. (Figure 8A–8G).

DISCUSSION

To the best of our knowledge, this is the first study to investigate the UM tumor microenvironment using the ESTIMATE algorithm based on large public datasets, developing and validating the contribution of one stromal and three immune cells signatures in UM prognosis. Our prognostic signature can further stratify

clinically defined groups of patients (eg, age, stages I, II, III and IV UM, histological type) into subgroups with different risk analysis (Figure 6).

Previous studies mainly focused on the intrinsic genes of tumors [19], and some have provided elegant analyses on expression of immune-related genes or immune-infiltration in UM [11, 20]. However, a comprehensive analysis of the UM microenvironment consisting of larger cohorts is needed in studies of the UM microenvironment. In our study, we conduct the research with the help of numerous computational tools and public data, such as TCGA. The ESTIMATE algorithm was chosen for its compatible with RNA-Seq data and microarray data. The overall survival is correlated with immune scores and stromal scores, where the prognosis of low immune scores and stromal

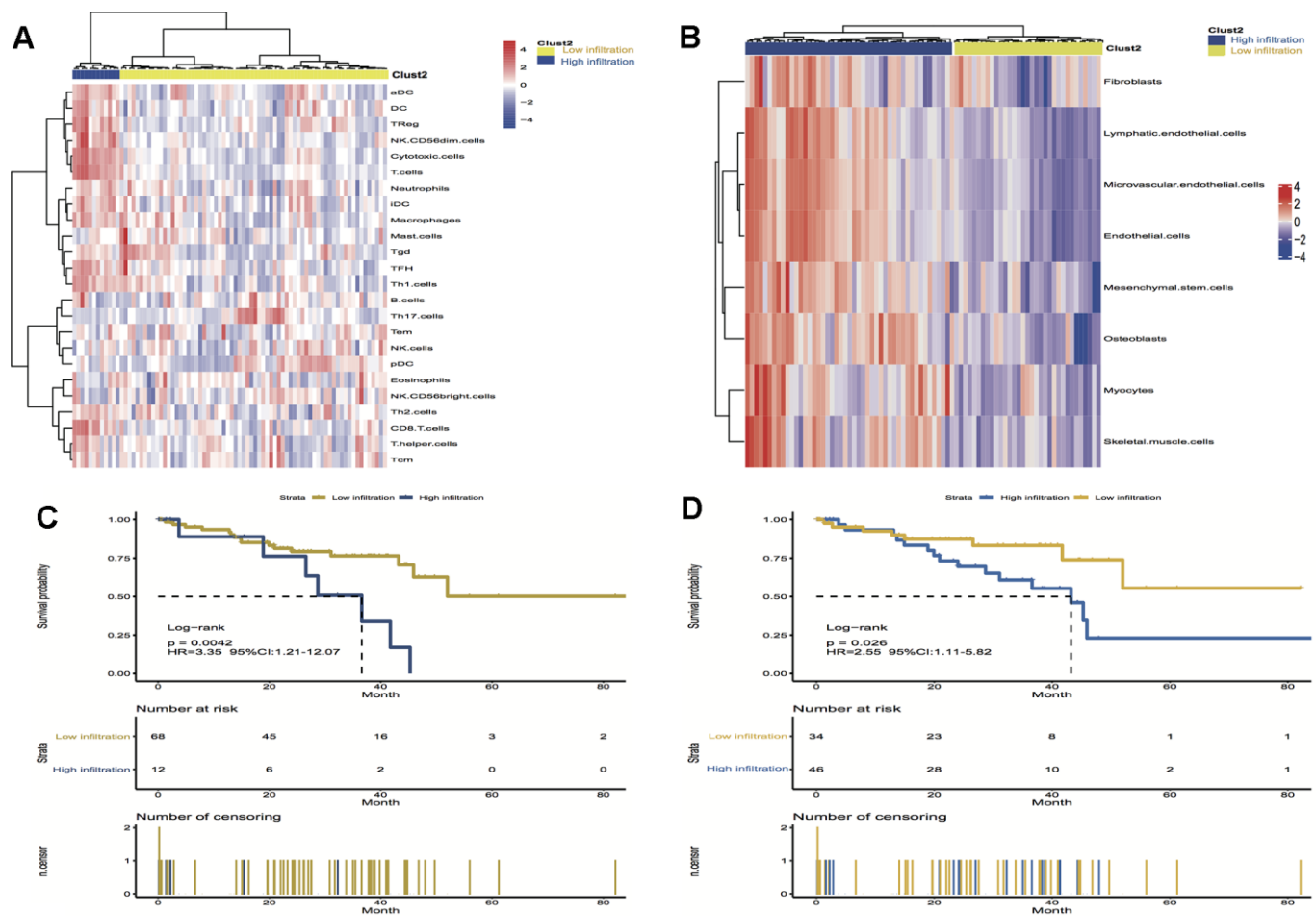


Figure 3. Unsupervised clustering of immune and stromal cells for 80 patients in the UM cohort. (A, B) The low infiltration and high infiltration cells in immune and stromal group; (C) Kaplan-Meier curves for overall survival (OS) of UM patients show that immune infiltration patterns are significantly associated with overall survival (log-rank test, $P = 0.004$); (D) Kaplan-Meier curves for OS of UM patients show that stromal infiltration patterns are significantly associated with overall survival (log-rank test, $P = 0.03$). Hazard ratios (HRs) and 95% CIs are for high or low immune and stromal infiltration risk.

scores is better than that of the high-score group. TME infiltration patterns also show that the low immune and stromal infiltration pattern has a better prognosis than the high infiltration pattern, which is consistent with the immune and stromal scores.

On further investigation, we found 13 immune cells and 1 stromal cell capable of significantly predicting poor overall survival rate in log-rank test, but which cell is more responsible than another and which common pathway is involved? Finally, signatures for three immune cell types - cytotoxic cells, Th1 cells, and Th2 cells - together with one stromal cell type - myocytes - were identified. Similarly, previous studies have reported that CD4+ T lymphocytes was present in UM inflammatory infiltrates. Moreover, CD4+CD25+ FoxP3+ Treg cells are capable of suppressing Th1 or

Cytotoxic T lymphocytes responses and represent a major mechanism of tumor escape in several cancers [2]. Our pathway research also found that myogenesis is significantly expressed in both the low immune and low stromal groups, which is consistent with the cells identification. In cardiac myocytes research, it has been demonstrated that fibroblast growth factor-2 (FGF-2) synthesis can be regulated at the transcriptional level [21], and FGF-2 was found to rescue UM cells from growth inhibition by bromodomain and extraterminal protein inhibitors [22]. It has been suggested that co-targeting of FGF receptor signaling is required to increase the responses of metastatic UM to BET inhibitors [22], which is a point we could consider with the stromal findings. The epithelial-to-mesenchymal transition (EMT) investigated is also a common pathway in low immune and stromal group of UM,

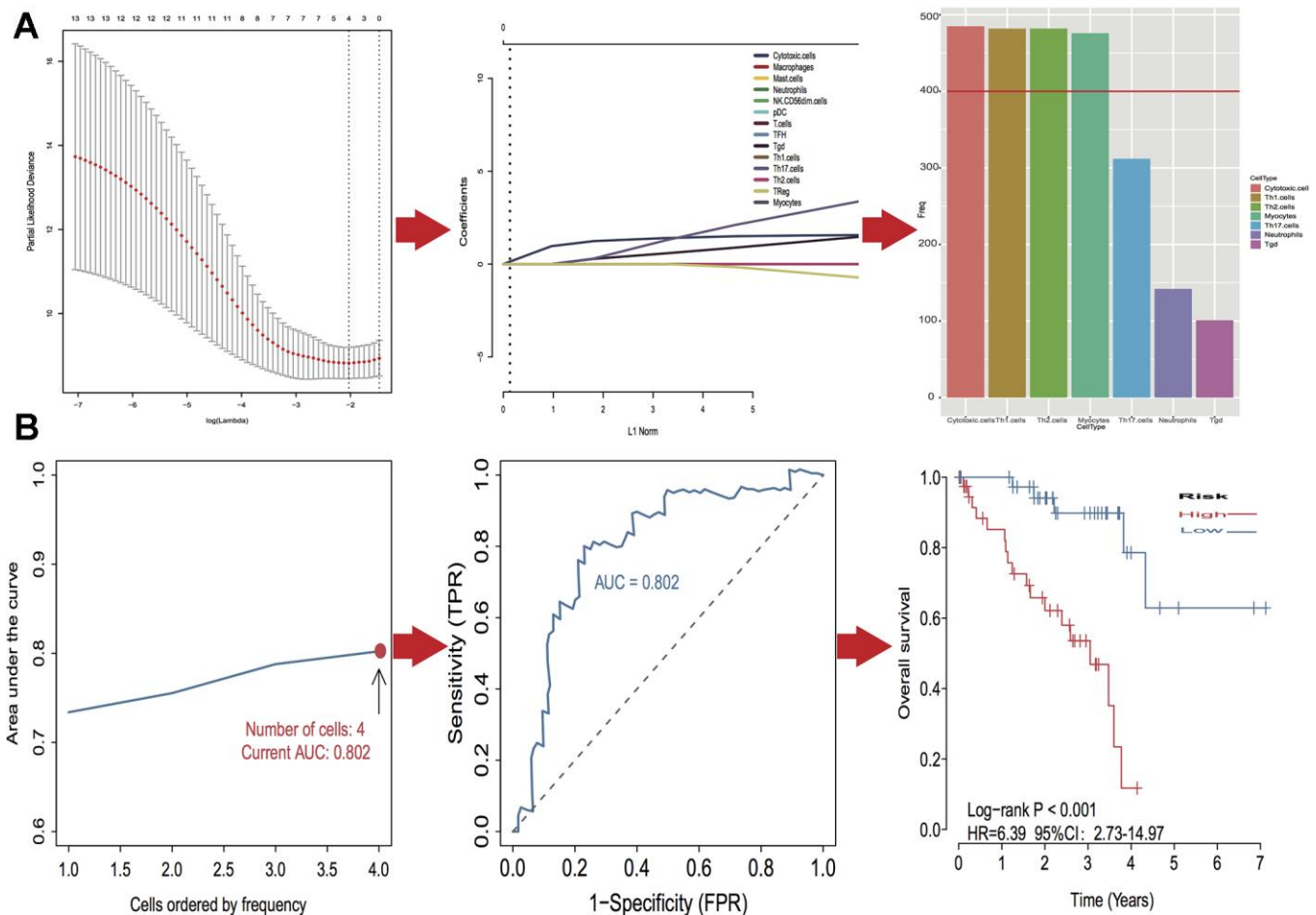


Figure 4. Identification of optimal cell signature for overall survival (OS) prediction. (A) The process of building the signature containing four cell types (3 immune cells and 1 stromal cell) and the coefficients calculated using the lasso method: from 500 iterations of lasso-penalized multivariate modeling, four cell types were reported as optimal for survival prediction more than 400 times; (B) The AUC curves of cell type models and Kaplan–Meier survival analysis of four-cell-type model in TCGA. Then the number of cells is four, the value of AUC is the highest (0.802). Kaplan–Meier curves indicated that there is a significant difference between high- and low-risk groups (log-rank $P < 0.001$).

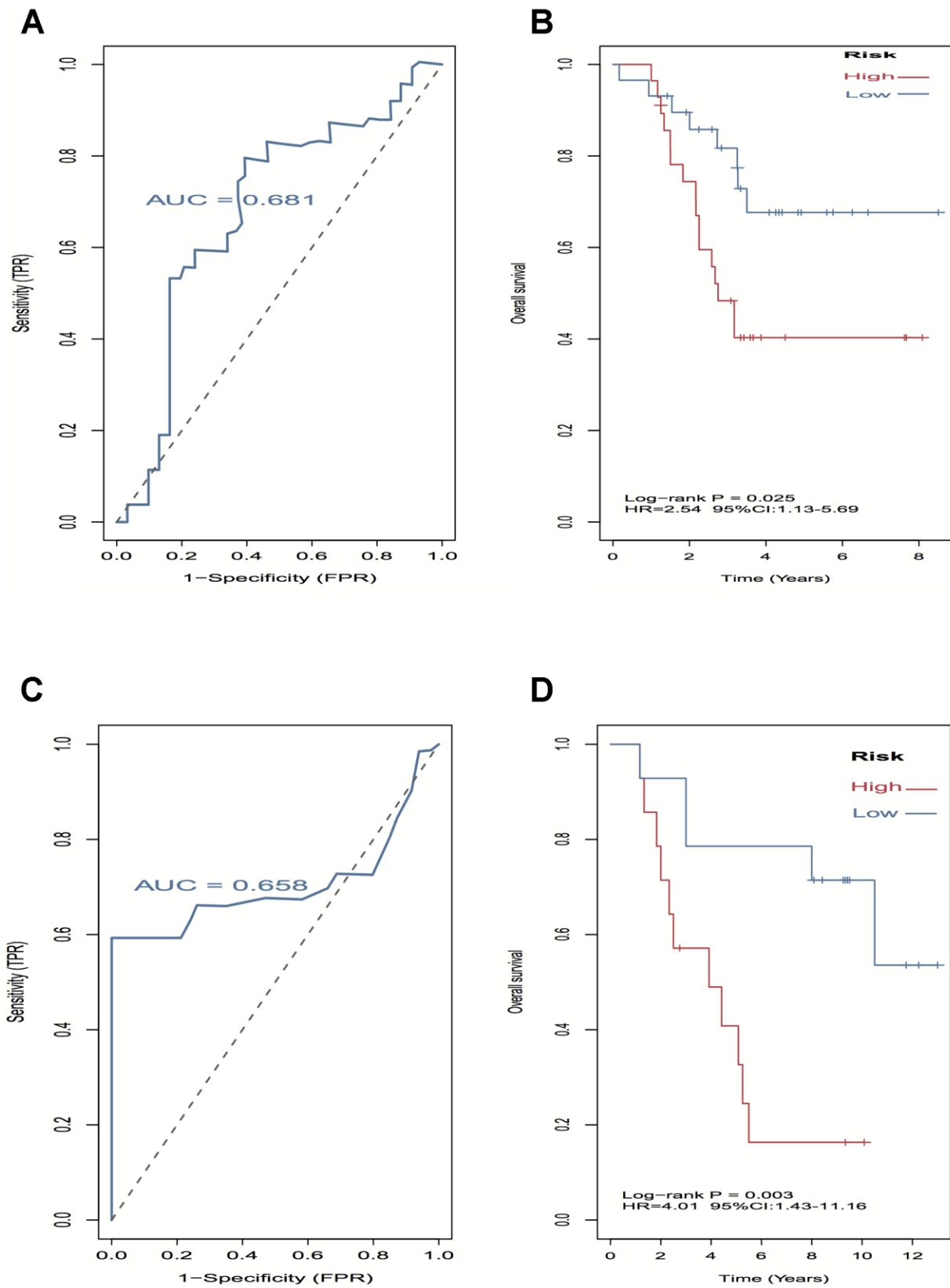


Figure 5. External validation of four-cell-type model in GSE44295 and GSE84976 datasets. (A–C) The AUC curves in GSE44295 and GSE84976 datasets. (B, D) Kaplan-Meier survival analysis in GSE44295 and GSE84976 datasets, revealed that the low-risk groups have a significantly better survival than the patients in high-risk group.

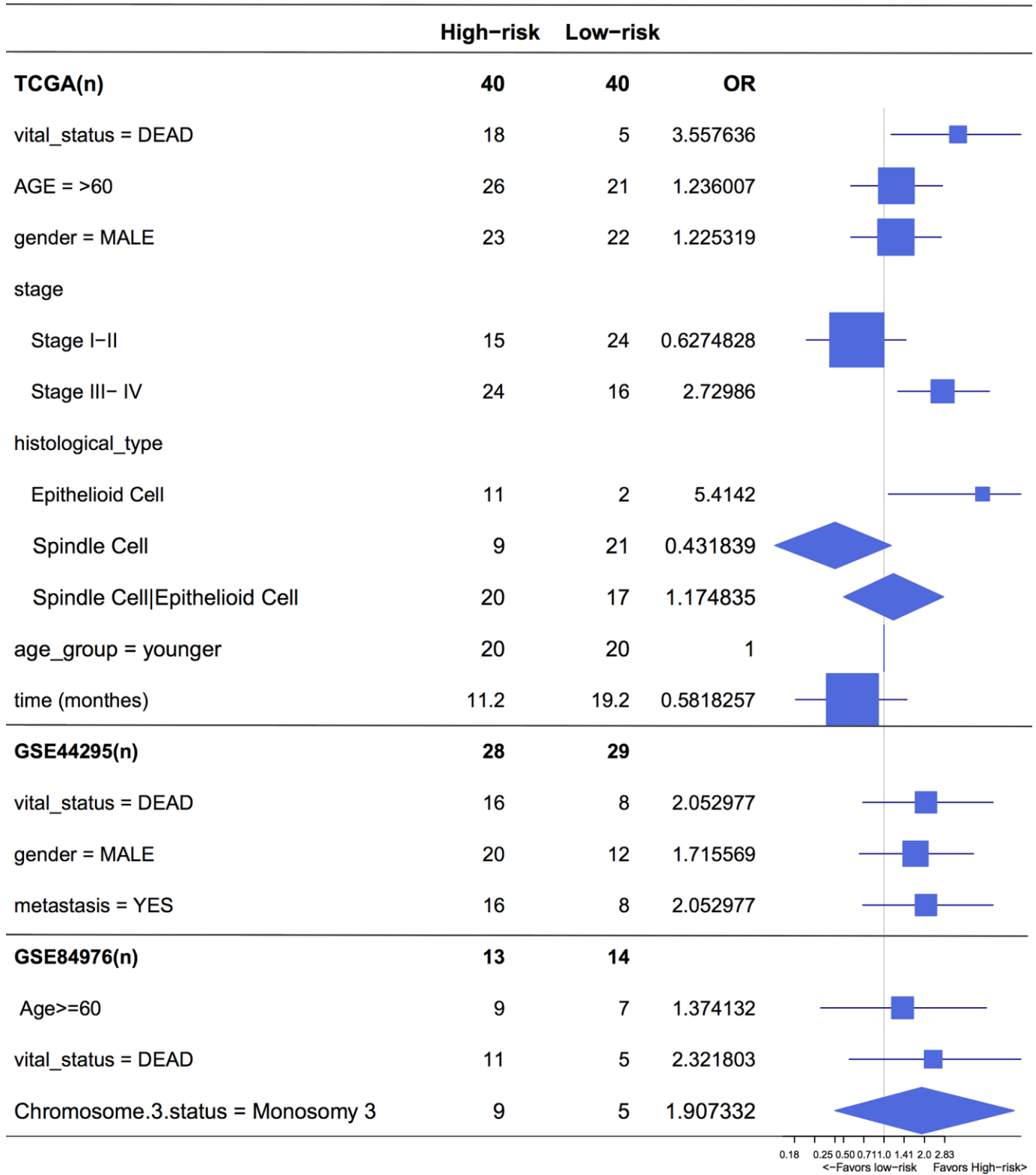


Figure 6. Forest plot for the odds ratio (OR) of high or low 4-cell-type model related risk groups. The length of the horizontal line corresponds to the confidence interval, and the size of the OR data marker is inversely proportional to the confidence interval. The vertical dotted line indicates OR of 1.0.

which is said to enable trans-differentiation of epithelial tumor cells, endowing them with migratory and invasive properties [23]. The EMT is demonstrated to be related to myogenesis [24]. Taken together, the myocyte expression is also an unusual phenomenon that deserves more attention and the risk score of prognostic signature is a tool that we could validate further in clinic.

All the three datasets showed that the correlation of CTLA-4 and PD-L1 expression with the low-risk group is significantly less than that of the high-risk groups. Thus, we were interested in investigating the response to treatment. It has been reported that the primary targets of immune checkpoint blockade (ICB) treatment are PD-1 and CTLA4 [25]. Previous studies have clarified that the success of anti-PD-1 and anti-CTLA-4 agents in UM has been much more limited [26–27]. Some of our results are consistent with the previous studies, but an interesting point is that the high-risk group is more responsive to

anti-PD-1 therapy and several chemotherapeutic drugs. Furthermore, we checked several more drugs like mitomycin C and lapatinib, which could also be used as supplementary or combined treatment agents [28]. However, more benchwork and clinical studies are needed to further validation. As aforementioned, we first developed the prognostic model and calculated the risk score. It would be more helpful to identify patients at high-risk in clinic and attempt the sensitive immunotherapy and chemo-treatment.

In summary, our study reveals a comprehensive landscape of the immune and stromal microenvironment in UM, and provides a promising prognostic signature for UM. Patients with the high risk scores could benefit more from anti-PD-1 therapy and chemotherapy. Further investigations are needed to verify the accuracy in estimating prognoses and to test its clinical utility in patient management.

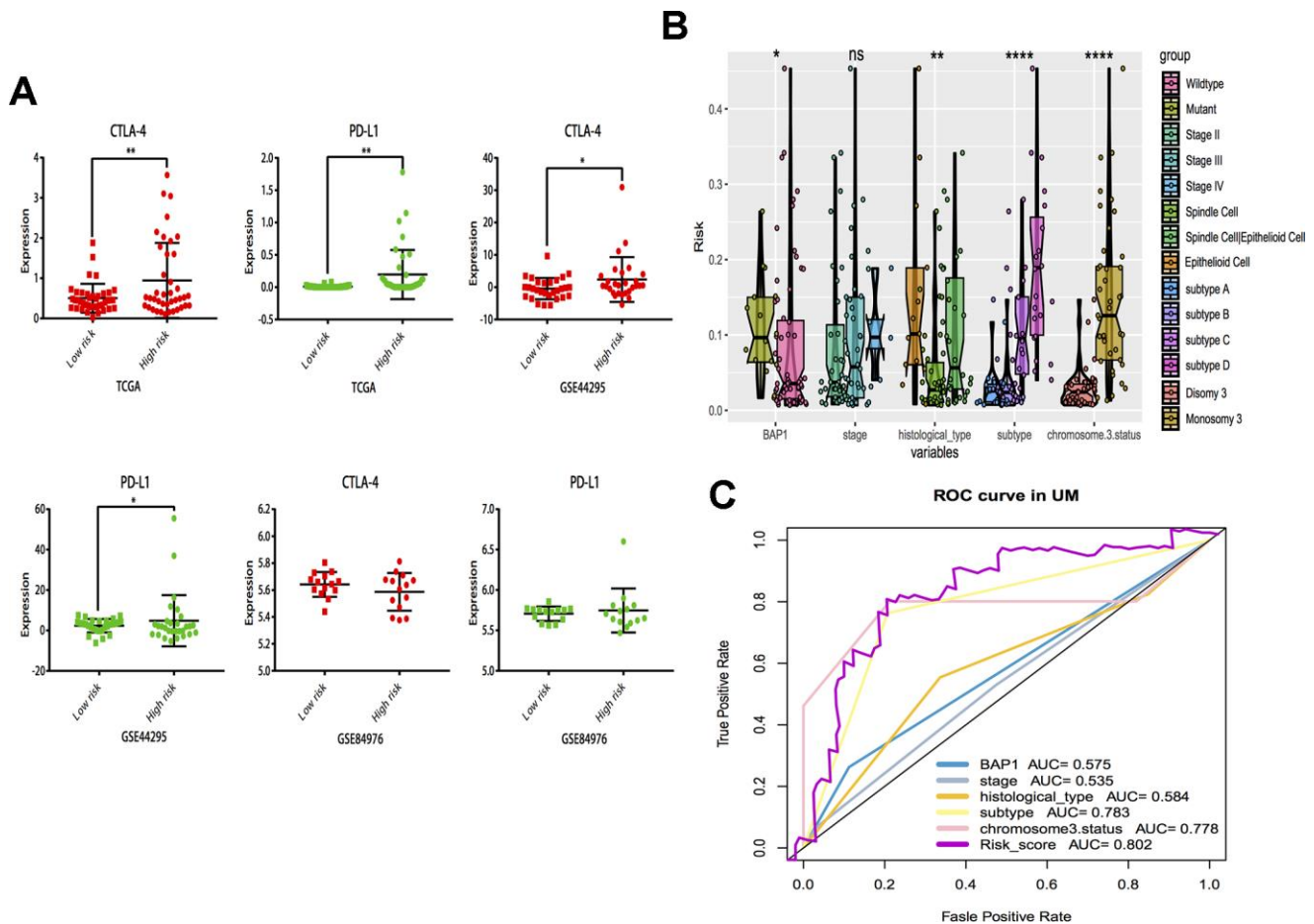


Figure 7. Subgroup analysis and risk score distribution. (A) Box-plot analysis of high and low groups in CTLA-4 and PD-L1 expression. (B) The association between risk score distribution and established prognostic markers, including BAP1 mutant, tumor stage, histological type, chromosome 3 status, and molecular subtype. (C) The 3 years area under the curve (AUC) of risk score and prognostic markers (BAP1 mutant, tumor stage, histological type, chromosome 3 status and molecular subtype) associated with OS in TCGA. * $P < 0.05$, ** $P < 0.01$, *** $P < 0.001$, **** $P < 0.0001$.

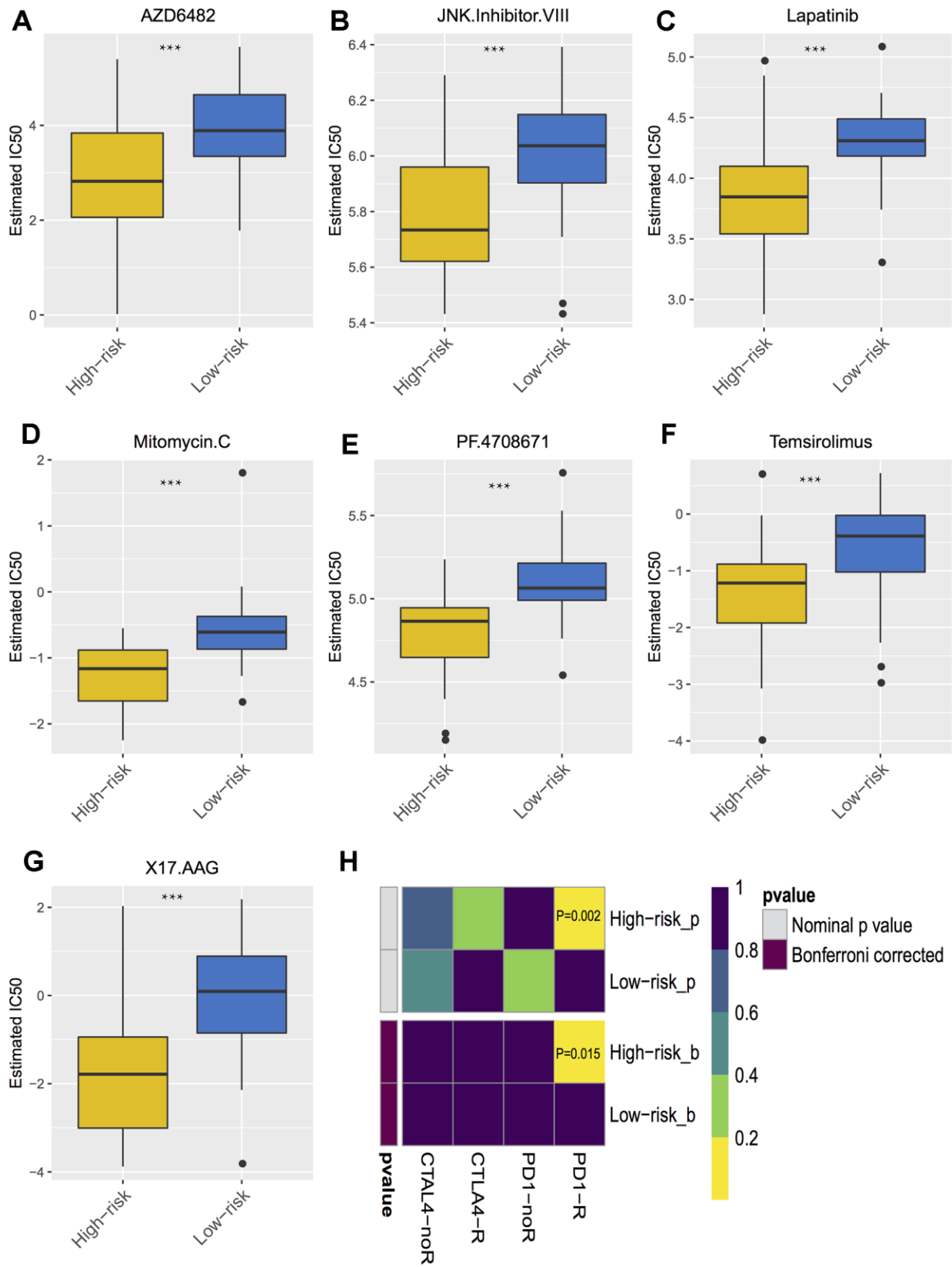


Figure 8. Differential putative chemotherapeutic and immunotherapeutic response. (A–G) The box plots of the estimated IC50 for the most sensitive chemotherapeutic drugs. (H) Submap analysis manifested that high risk group could be more sensitive to the programmed cell death protein 1 inhibitor (Bonferroni-corrected $P = 0.02$). *** $P < 0.001$.

MATERIALS AND METHODS

RNA and clinical data

The RNA sequencing dataset and corresponding clinical follow-up information of UM were obtained from the TCGA database. This dataset was derived from the tissue samples from 80 adult patients, and an integrative analysis by UM area consortia has also been conducting used this dataset [29]. Survival time was regarded as the time from tissue removal to death. Another two UM datasets (GSE44295 and GSE84976), consisting of 85 UM samples from the Gene Expression Omnibus, were used as external validation sets.

Tumor microenvironment estimation

Immune scores and stromal scores were calculated by applying the ESTIMATE algorithm in R package (“ESTIMATE”). By running ESTIMATE on TCGA RNA-Seq data, the immune scores and stromal scores of each uveal melanoma sample can be estimated. To quantify the proportions of immune and stromal cells in the UM samples, we first identified the biomarker genes of immune and stromal cells from the previously published articles [30, 31], and used single sample gene set enrichment analysis (ssGSEA) method to specifically discriminate 24 human immune cells and 11 stromal cells phenotypes using the R package (“GSVA”) to validate the ESTIMATE algorithm. The immune cells considered were dendritic cells (DCs), immature DCs (iDC), activated DCs (aDC), plasmacytoid DCs (pDC), natural killer (NK) cells, CD56dim NK cells, CD56bright NK cells, macrophages, neutrophils, eosinophils, mast cells, T cells, T central memory cells (Tcm), T effector memory cells, Tgd cells, CD8 T cells, regulatory T cells (Treg), T follicular helper cells (TFH), T helper cells, Th1, Th2, Th17, B cells, and cytotoxic cells. The stromal cells included fibroblasts, lymphatic endothelial cells, microvascular endothelial cells, endothelial cells, mesenchymal stem cells, osteoblasts, myocytes, and skeletal muscle cells.

Gene set variation analysis

The uveal melanoma samples were divided into high vs. low immune score/stromal score groups by the median value. Then, GSVA was used to evaluate the common pathways shared in the tumor-infiltrating immune and stromal groups. These 50 hallmark pathways described in the molecular signature database, exported using the “GSEABase” package. Next, pathway activity estimates were assigned to individual samples by using the R package (“GSVA”).

Heatmaps and clustering analysis

Heatmaps and clustering were generated using an R package (“pheatmap”).

Survival analysis of immune and stromal cells

The best separation survival analysis of immune and stromal cells was performed using the “survminer” package. Kaplan-Meier were plotted and the differences among groups were compared using log-rank tests.

Identification of prognostic model

The survival-related cells in primary selection are not suitable for clinical diagnosis. Therefore, a robust survival modeling approach was used to identify suitable cell signature. We constructed prognostic models by using the “lasso” package and ran the analysis for 500 iterations. Statistical stability under each model was evaluated and a frequency greater than 400 regarded as indicating a stable model. Kaplan–Meier survival curves were plotted and differences between the subgroups were compared using log-rank tests. Receiver operating characteristic curves [1] were drawn for the predicted 3-year overall survival (OS), and the AUC values was used to evaluate the specificity and sensitivity of the cell signature. Moreover, to prove the reliability of the result, this cell signature was further validated in another two independent datasets (GSE44295 and GSE84976).

Immuno- and chemotherapeutic response prediction

To explore the likelihood of an immune- or chemotherapeutic response, we predicted the chemotherapeutic response for each sample based on the Genomics of Drug Sensitivity in Cancer (GDSC) database (<https://www.cancerrxgene.org>) [32]. The most significant chemotherapeutic drugs were selected ($P < 0.0001$). The prediction process was implemented using the R package “pRRophetic”. Although immune checkpoint inhibitors have not yet been approved as routine drugs for UM, we also predicted the likelihood of response to immunotherapy by using the TIDE website tool (<http://tide.dfci.harvard.edu/>) [25].

Statistical analysis

All statistical analyses were conducted using the R package (version 3.5.2). For comparisons of two groups, the statistical significance for normally distributed variables was estimated using Student’s *t* tests, and non-normally distributed variables were analyzed using Mann-Whitney U tests (also called the Wilcoxon rank-sum test). For comparisons of more than

two groups, Kruskal-Wallis tests and one-way analysis of variance were used as non-parametric and parametric methods, respectively. The association between cell signature and clinicopathological characteristics was analyzed using Fisher's exact test.

Abbreviations

AUC: area under the curve; BAP1: BRCA1-associated protein-1; CI: confidence interval; CTLA-4: cytotoxic T-lymphocyte-associated protein 4; EMC: epithelial-to-mesenchymal transition; ESTIMATE: Estimation of STromal and Immune cells in MAlignant Tumor tissue using Expression data; FGF: fibroblast growth factor; GDSC: Genomics of Drug Sensitivity in Cancer; GSVA: gene set variation analysis; HR: hazard ratio; IC₅₀: half maximal inhibitory concentration; OR: odds ratio; PD-L1: programmed death-ligand 1; RNA: ribonucleic acid; TCGA: The Cancer Genome Atlas.

AUTHOR CONTRIBUTIONS

Conceptualization, QW. G, Q.W., and L.H.; Methodology, QW. G, Q.W.; Investigation, QW. G, Q.W., AQ. L., and YB. Y.; Writing – Original Draft, QW. G, Q.W., and L.L.; Writing – Review and Editing, XL. Q and L.H.; Funding Acquisition, L.H.; Supervision, L.H.

CONFLICTS OF INTEREST

No conflicting relationship exists for any author.

FUNDING

This work was supported by Natural Science Foundation of Zhejiang Province, China (Y17H120030). The sponsor or funding organization had no role in the design or conduct of this research.

REFERENCES

1. Singh AD, Turell ME, Topham AK. Uveal melanoma: trends in incidence, treatment, and survival. *Ophthalmology*. 2011; 118:1881–85. <https://doi.org/10.1016/j.ophtha.2011.01.040> PMID:21704381
2. Amaro A, Gangemi R, Piaggio F, Angelini G, Barisione G, Ferrini S, Pfeffer U. The biology of uveal melanoma. *Cancer Metastasis Rev*. 2017; 36:109–40. <https://doi.org/10.1007/s10555-017-9663-3> PMID:28229253
3. Kaliki S, Shields CL. Uveal melanoma: relatively rare but deadly cancer. *Eye (Lond)*. 2017; 31:241–57. <https://doi.org/10.1038/eye.2016.275> PMID:27911450
4. Kashyap S, Meel R, Singh L, Singh M. Uveal melanoma. *Semin Diagn Pathol*. 2016; 33:141–47. <https://doi.org/10.1053/j.semdp.2015.10.005> PMID:26972224
5. Jager MJ, Dogrusöz M, Woodman SE. Uveal melanoma: identifying immunological and chemotherapeutic targets to treat metastases. *Asia Pac J Ophthalmol (Phila)*. 2017; 6:179–85. <https://doi.org/10.22608/APO.201782> PMID:28399339
6. Quail DF, Joyce JA. Microenvironmental regulation of tumor progression and metastasis. *Nat Med*. 2013; 19:1423–37. <https://doi.org/10.1038/nm.3394> PMID:24202395
7. Su S, Chen J, Yao H, Liu J, Yu S, Lao L, Wang M, Luo M, Xing Y, Chen F, Huang D, Zhao J, Yang L, et al. CD10*GPR77* cancer-associated fibroblasts promote cancer formation and chemoresistance by sustaining cancer stemness. *Cell*. 2018; 172:841–56.e16. <https://doi.org/10.1016/j.cell.2018.01.009> PMID:29395328
8. Li B, Cui Y, Diehn M, Li R. Development and validation of an individualized immune prognostic signature in early-stage nonsquamous non-small cell lung cancer. *JAMA Oncol*. 2017; 3:1529–37. <https://doi.org/10.1001/jamaoncol.2017.1609> PMID:28687838
9. Jia D, Li S, Li D, Xue H, Yang D, Liu Y. Mining TCGA database for genes of prognostic value in glioblastoma microenvironment. *Aging (Albany NY)*. 2018; 10:592–605. <https://doi.org/10.18632/aging.101415> PMID:29676997
10. Jager MJ, Ly LV, El Filali M, Madigan MC. Macrophages in uveal melanoma and in experimental ocular tumor models: friends or foes? *Prog Retin Eye Res*. 2011; 30:129–46. <https://doi.org/10.1016/j.preteyeres.2010.11.004> PMID:21129496
11. Bronkhorst IH, Vu TH, Jordanova ES, Luyten GP, Burg SH, Jager MJ. Different subsets of tumor-infiltrating lymphocytes correlate with macrophage influx and monosomy 3 in uveal melanoma. *Invest Ophthalmol Vis Sci*. 2012; 53:5370–78. <https://doi.org/10.1167/iovs.11-9280> PMID:22743317
12. Gezgin G, Dogrusöz M, van Essen TH, Kroes WG, Luyten GP, van der Velden PA, Walter V, Verdijk RM, van Hall T, van der Burg SH, Jager MJ. Genetic evolution of uveal melanoma guides the development of an inflammatory microenvironment. *Cancer Immunol Immunother*. 2017; 66:903–12. <https://doi.org/10.1007/s00262-017-1991-1> PMID:28391358

13. Krishna Y, McCarthy C, Kalirai H, Coupland SE. Inflammatory cell infiltrates in advanced metastatic uveal melanoma. *Hum Pathol.* 2017; 66:159–66. <https://doi.org/10.1016/j.humpath.2017.06.005> PMID:[28655639](#)
14. Weinstein JN, Collisson EA, Mills GB, Shaw KR, Ozenberger BA, Ellrott K, Shmulevich I, Sander C, Stuart JM, and Cancer Genome Atlas Research Network. The cancer genome atlas pan-cancer analysis project. *Nat Genet.* 2013; 45:1113–20. <https://doi.org/10.1038/ng.2764> PMID:[24071849](#)
15. Jager MJ, Brouwer NJ, Esmali B. The cancer genome atlas project: an integrated molecular view of uveal melanoma. *Ophthalmology.* 2018; 125:1139–42. <https://doi.org/10.1016/j.ophtha.2018.03.011> PMID:[30032793](#)
16. Yoshihara K, Shahmoradgoli M, Martínez E, Vegesna R, Kim H, Torres-Garcia W, Treviño V, Shen H, Laird PW, Levine DA, Carter SL, Getz G, Stemke-Hale K, et al. Inferring tumour purity and stromal and immune cell admixture from expression data. *Nat Commun.* 2013; 4:2612. <https://doi.org/10.1038/ncomms3612> PMID:[24113773](#)
17. Priedigkeit N, Watters RJ, Lucas PC, Basudan A, Bhargava R, Horne W, Kolls JK, Fang Z, Rosenzweig MQ, Brufsky AM, Weiss KR, Oesterreich S, Lee AV. Exome-capture RNA sequencing of decade-old breast cancers and matched decalcified bone metastases. *JCI Insight.* 2017; 2:e95703. <https://doi.org/10.1172/jci.insight.95703> PMID:[28878133](#)
18. Zeng D, Li M, Zhou R, Zhang J, Sun H, Shi M, Bin J, Liao Y, Rao J, Liao W. Tumor microenvironment characterization in gastric cancer identifies prognostic and immunotherapeutically relevant gene signatures. *Cancer Immunol Res.* 2019; 7:737–50. <https://doi.org/10.1158/2326-6066.CIR-18-0436> PMID:[30842092](#)
19. Wan Q, Tang J, Han Y, Wang D. Co-expression modules construction by WGCNA and identify potential prognostic markers of uveal melanoma. *Exp Eye Res.* 2018; 166:13–20. <https://doi.org/10.1016/j.exer.2017.10.007> PMID:[29031853](#)
20. de Lange MJ, Nell RJ, Lalai RN, Versluis M, Jordanova ES, Luyten GP, Jager MJ, van der Burg SH, Zoutman WH, van Hall T, van der Velden PA. Digital PCR-based t-cell quantification-assisted deconvolution of the microenvironment reveals that activated macrophages drive tumor inflammation in uveal melanoma. *Mol Cancer Res.* 2018; 16:1902–11. <https://doi.org/10.1158/1541-7786.MCR-18-0114> PMID:[30093564](#)
21. Jin Y, Sheikh F, Detillieux KA, Cattini PA. Role for early growth response-1 protein in alpha(1)-adrenergic stimulation of fibroblast growth factor-2 promoter activity in cardiac myocytes. *Mol Pharmacol.* 2000; 57:984–90. PMID:[10779383](#)
22. Chua V, Orloff M, Teh JL, Sugase T, Liao C, Purwin TJ, Lam BQ, Terai M, Ambrosini G, Carvajal RD, Schwartz G, Sato T, Aplin AE. Stromal fibroblast growth factor 2 reduces the efficacy of bromodomain inhibitors in uveal melanoma. *EMBO Mol Med.* 2019; 11:e9081. <https://doi.org/10.15252/emmm.201809081> PMID:[30610113](#)
23. Smolkova B, Horvathova Kajabova V, Zmetakova I, Kalinkova L, Czanner G, Markova A, Furdova A. Role of epigenetic deregulation in hematogenous dissemination of Malignant uveal melanoma. *Neoplasma.* 2018; 65:840–54. https://doi.org/10.4149/neo_2018_180420N261 PMID:[30334454](#)
24. Sieiro D, Rios AC, Hirst CE, Marcelle C. Cytoplasmic NOTCH and membrane-derived β -catenin link cell fate choice to epithelial-mesenchymal transition during myogenesis. *Elife.* 2016; 5:e14847. <https://doi.org/10.7554/eLife.14847> PMID:[27218451](#)
25. Jiang P, Gu S, Pan D, Fu J, Sahu A, Hu X, Li Z, Traugh N, Bu X, Li B, Liu J, Freeman GJ, Brown MA, et al. Signatures of T cell dysfunction and exclusion predict cancer immunotherapy response. *Nat Med.* 2018; 24:1550–58. <https://doi.org/10.1038/s41591-018-0136-1> PMID:[30127393](#)
26. Heppt MV, Steeb T, Schlager JG, Rosumeck S, Dressler C, Ruzicka T, Nast A, Berking C. Immune checkpoint blockade for unresectable or metastatic uveal melanoma: a systematic review. *Cancer Treat Rev.* 2017; 60:44–52. <https://doi.org/10.1016/j.ctrv.2017.08.009> PMID:[28881222](#)
27. Komatsubara KM, Carvajal RD. Immunotherapy for the treatment of uveal melanoma: current status and emerging therapies. *Curr Oncol Rep.* 2017; 19:45. <https://doi.org/10.1007/s11912-017-0606-5> PMID:[28508938](#)
28. Gravells P, Hoh L, Canovas D, Rennie IG, Sisley K, Bryant HE. Resistance of uveal melanoma to the interstrand cross-linking agent mitomycin C is associated with reduced expression of CYP450R. *Br J Cancer.* 2011; 104:1098–105. <https://doi.org/10.1038/bjc.2011.56> PMID:[21386838](#)
29. Robertson AG, Shih J, Yau C, Gibb EA, Oba J, Mungall KL, Hess JM, Uzunangelov V, Walter V, Danilova L,

- Lichtenberg TM, Kucherlapati M, Kimes PK, et al, and TCGA Research Network. Integrative analysis identifies four molecular and clinical subsets in uveal melanoma. *Cancer Cell*. 2017; 32:204–20.e15.
<https://doi.org/10.1016/j.ccell.2017.07.003>
PMID:[28810145](https://pubmed.ncbi.nlm.nih.gov/28810145/)
30. Bindea G, Mlecnik B, Tosolini M, Kirilovsky A, Waldner M, Obenauf AC, Angell H, Fredriksen T, Lafontaine L, Berger A, Bruneval P, Fridman WH, Becker C, et al. Spatiotemporal dynamics of intratumoral immune cells reveal the immune landscape in human cancer. *Immunity*. 2013; 39:782–95.
<https://doi.org/10.1016/j.immuni.2013.10.003>
PMID:[24138885](https://pubmed.ncbi.nlm.nih.gov/24138885/)
31. Aran D, Hu Z, Butte AJ. xCell: digitally portraying the tissue cellular heterogeneity landscape. *Genome Biol*. 2017; 18:220.
<https://doi.org/10.1186/s13059-017-1349-1>
PMID:[29141660](https://pubmed.ncbi.nlm.nih.gov/29141660/)
32. Lu X, Jiang L, Zhang L, Zhu Y, Hu W, Wang J, Ruan X, Xu Z, Meng X, Gao J, Su X, Yan F. Immune signature-based subtypes of cervical squamous cell carcinoma tightly associated with human papillomavirus type 16 expression, molecular features, and clinical outcome. *Neoplasia*. 2019; 21:591–601.
<https://doi.org/10.1016/j.neo.2019.04.003>
PMID:[31055200](https://pubmed.ncbi.nlm.nih.gov/31055200/)

Loss of macroH2A1 decreases mitochondrial metabolism and reduces the aggressiveness of uveal melanoma cells

Sebastiano Giallongo^{1,2,3,*}, Michelino Di Rosa^{1,*}, Rosario Caltabiano⁴, Lucia Longhitano¹, Michele Reibaldi⁵, Alfio Distefano¹, Oriana Lo Re^{2,3}, Angela Maria Amorini¹, Lidia Puzzo⁴, Lucia Salvatorelli⁴, Stefano Palmucci⁵, Daniele Tibullo¹, Andrea Russo⁵, Antonio Longo⁵, Giacomo Lazzarino⁶, Giovanni Li Volti^{1,7}, Manlio Vinciguerra²

¹Department of Biomedical and Biotechnological Sciences, University of Catania, Catania, Italy

²Center for Translational Medicine (CTM), International Clinical Research Center (FNUSA-ICRC), St Anne's University Hospital, Brno, Czech Republic

³Department of Biology, Faculty of Medicine, Masaryk University, Brno, Czech Republic

⁴Department G.F. Ingrassia, Section of Anatomic Pathology, University of Catania, Catania, Italy

⁵Department of Ophthalmology, University of Catania, Catania, Italy

⁶UniCamillus-Saint Camillus International University of Health Sciences, Rome, Italy

⁷EuroMediterranean Institute of Science and Technology, Palermo, Italy

*Equal contribution

Correspondence to: Giovanni Li Volti, Manlio Vinciguerra; **email:** livolti@unict.it, manlio.vinciguerra@fnusa.cz

Keywords: macroH2A1, histones, uveal melanoma, metabolism, epigenetics

Received: January 29, 2020

Accepted: March 31, 2020

Published: May 12, 2020

Copyright: Giallongo et al. This is an open-access article distributed under the terms of the Creative Commons Attribution License (CC BY 3.0), which permits unrestricted use, distribution, and reproduction in any medium, provided the original author and source are credited.

ABSTRACT

Uveal melanoma (UM) is the most common primary intraocular tumour in adults. The most accurate prognostic factor of UM is classification by gene expression profiling. Currently, the role of epigenetics is much less defined compared to genetic mechanisms. We recently showed a strong prognostic role of the expression levels of histone variant macroH2A1 in UM patients. Here, we assessed the mechanistic effects of macroH2A1 on UM progression.

UM cell lines were stably knocked down (KD) for macroH2A1, and proliferation and colony formation capacity were evaluated. Mitochondrial function was assayed through qPCR and HPLC analyses. Correlation between mitochondrial gene expression and cancer aggressiveness was studied using a bioinformatics approach.

MacroH2A1 loss significantly attenuated UM cells proliferation and aggressiveness. Furthermore, genes involved in oxidative phosphorylation displayed a decreased expression in KD cells. Consistently, macroH2A1 loss resulted also in a significant decrease of mitochondrial transcription factor A (TFAM) expression, suggesting impaired mitochondrial replication. Bioinformatics analyses uncovered that the expression of genes involved in mitochondrial metabolism correlates with macroH2A1 and with cancer aggressiveness in UM patients. Altogether, our results suggest that macroH2A1 controls UM cells progression and it may represent a molecular target to develop new pharmacological strategies for UM treatment.

INTRODUCTION

Uveal melanoma (UM) is the most common primary intraocular tumour in adults [1, 2]. Metastasis is a frequent occurrence in UM with a 5 years survival of

~15%. It is estimated that 40-50% of UM patients will die of metastatic disease, even with early diagnosis and proper treatment [3]. By far the most common site of UM metastasis is the liver, reported in ~87% of metastasis cases [4]. Although both uveal and cutaneous melanomas

arise from melanocytes, UM is biologically and genetically distinct from the more common cutaneous melanoma [5]. In particular, UM lack mutations in BRAF, NRAS, or KIT, unlike cutaneous melanoma and it is characterized by activating mutations in the GPCR alpha subunits GNAQ or GNA11 [6]. Moreover, inactivating somatic mutations in the gene encoding BRCA-1 associated protein 1 (BAP1) have been observed in ~84% of metastasizing UM [7]. The frequency of BAP1 mutations in metastatic UM suggests that targeting the BAP1 pathway could be a valuable therapeutic approach. BAP1 is an enzyme that mediates epigenetic modifications like deubiquitination of histone H2A and host cell factor 1 (HCF-1) [8–10]. Epigenetic mechanisms controlling gene expression have long been known to have a role in cancer development [11]. In UM these include DNA methylation at CpG islands in promoters leading to decrease expression of p16/INK4a tumour suppressor protein [12]. However, compared with the genetic mechanisms, the role of epigenetics in UM carcinogenesis is poorly defined [13–16].

Histone variants confer unique biological functions to chromatin [17–19]. The H2A family is the most diverse and includes vertebrate-specific macroH2A1 (with splice variants mH2A1.1 and 1.2) and macroH2A2 [20–22], which are generally associated with transcriptionally repressed chromatin [23, 24]. However, macroH2A histones are widely distributed throughout chromatin, but may also exert positive effects [20–22, 25, 26]. Recent studies have examined the expression of macroH2A1 in solid tumours and its correlation with clinical pathological features, including cutaneous

melanoma [27–31]. MacroH2A1 appears to act as tumour suppressor or as an oncogene depending on the type of cancer and on the degree of stemness [21, 27, 28, 30]. Contrary to cutaneous melanoma [27], we demonstrated immunohistochemically that macroH2A1 expression is higher in metastatic UM than in not metastatic UM [32]. However, the role of macroH2A1 in UM development and progression is unknown. A better understanding of the epigenetic processes leading to UM progression, metastasis and mortality, is needed to identify new prognostic markers for the early diagnosis or response to treatment. The aim of the present study was to assess the role of histone macroH2A1 in UM progression and related metabolic pathways involved in cell proliferation and metastasis, using cell models and biopsies from UM patients.

RESULTS

MacroH2A1 silencing reduces cell proliferation and migration

The role of macroH2A1 was investigated by lentiviral mediated silencing in UM 92.1 cells. Control cells (CTL) were infected with a bicistronic construct expressing green fluorescent protein (GFP) and a scramble shRNA, while silencing of macroH2A1 was achieved through lentiviral infection of a bicistronic construct containing shRNA against macroH2A1 and a GFP cassette [29, 33] (knock-down, KD, Figure 1A). Lentiviral-mediated shRNA against macroH2A1 was confirmed by immunoblotting (Figure 1B). Our group already showed that loss of macroH2A1 leads to increased stemness and

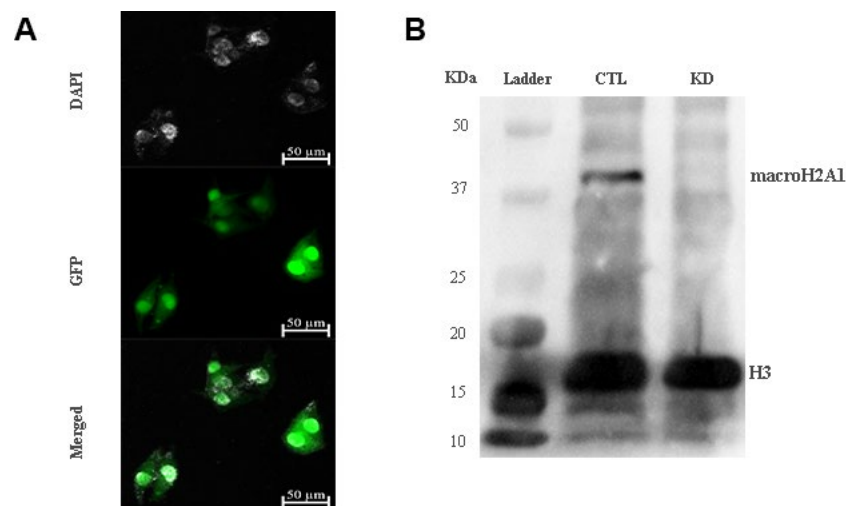


Figure 1. macroH2A1 silencing (knock-down, KD) in UM 92.1 cells. (A) Cells were infected with a lentivirus bearing a bicistronic construct expressing GFP and a macroH2A1-silencing shRNA. Control cells (CTL) were infected with lentivirus bearing a bicistronic construct

expressing GFP and a scramble shRNA (*data not shown*). (B) Western blot analysis showed a significant reduction of macroH2A1 in transfected cells.

decreased proliferation in liver cancer cells [29, 33]. Here, we generated cell growth curves for control and KD UM 92.1 cells using xCELLigence. Cells were seeded in wells carrying a gold electrode that measures electric impedance. The latter is related to cell density on the chip and is converted automatically into cell index by the device. Evaluation of cell index per each time point provides a direct quantification of cell proliferation [34]. XCELLigence analysis showed that macroH2A1 loss leads to a significant decrease of proliferation rate when compared to their control ($p < 0.01$) (Figure 2A). Interestingly, wound healing assay showed that silencing of macroH2A1 decreases wound closure ability of 92.1 UM cells (Figure 2B, Supplemental Figure 1). The difference became significant ($p < 0.01$) 24 hours after scrape introduction: at this time point the control and silenced cells differ for ~50% in wound closure (Figure 2B). Moreover, knockdown of macroH2A1 resulted into a decrease in migration in serum starved 92.1 UM cells (Figure 2C, Supplemental Figure 2). The difference in migration became highly significant ($p < 0.0001$) 6 hours after the introduction of the scrape. At this time point the number of KD cells migrated are a half compared with CTL cells (Figure 2C). These findings were further confirmed by clonogenic assay. Upon macroH2A1 knockdown 92.1 UM cells decreased

their colony formation capacity (Figure 3A). Moreover, the plate efficiency (% of cells inoculated at a low density that gave rise to colonies) of KD cells was significantly decreased compared with CTL cells (24.3 ± 4.81 versus 38.42 ± 4.04). Therefore, macroH2A1 silencing in UM cells significantly hampers their ability to proliferate and to migrate.

MacroH2A1 silencing decreases mitochondrial metabolism in UM cells

MacroH2A1 KD is able to increase lipid synthesis and to activate glycolytic pathways and in particular the pentose phosphate pathway (PPP) in HCC cells, rewiring energy metabolism to the needs of a cancer stem cell (CSC)-like state [29, 33, 35]. To study the role of macroH2A1 in the energy metabolism of UM cells, we next analyzed the endogenous metabolic profiles of control and macroH2A1 KD UM 92.1 cells. Metabolic profiling relies on the ability to determine changes in the total complement of metabolites in cells. In Figure 4A we report a heatmap representing all the changes in the levels of metabolites tested by high-performance liquid chromatography (HPLC), which allows the separation and quantification of most metabolites from glycolysis and the Krebs cycle including the high energy

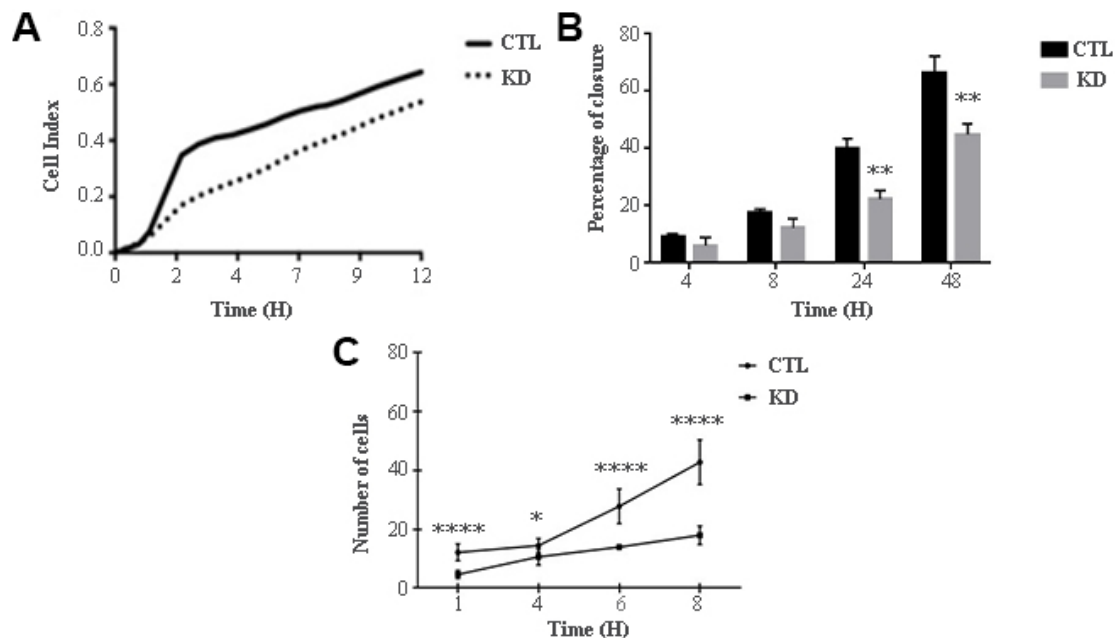


Figure 2. Proliferation and migration of UM 92.1 cells KD for macroH2A1. (A) Real time cell proliferation monitored by xCELLigence system. Cell index values were normalized at the time zero in order to obtain a normalized cell index. Each line is expressing the average of four different experiments. (B) Cell proliferation assay. Values are presented as percentage of the open wound following 4, 8, 24 and 48 hours (wound at time 0 was assumed as 100% and used as control). Values are expressed as the mean \pm SEM of three different experiments. ($p < 0.0001$ vs control). (C) The migration assay. Values are presented as number of migrating cells following 1, 4, 6 and 8 hours (wound at

time 0 was assumed without migrating cells and used as control). Values are expressed as the mean \pm SEM of three independent experiments. ($p < 0.0001$ vs control).

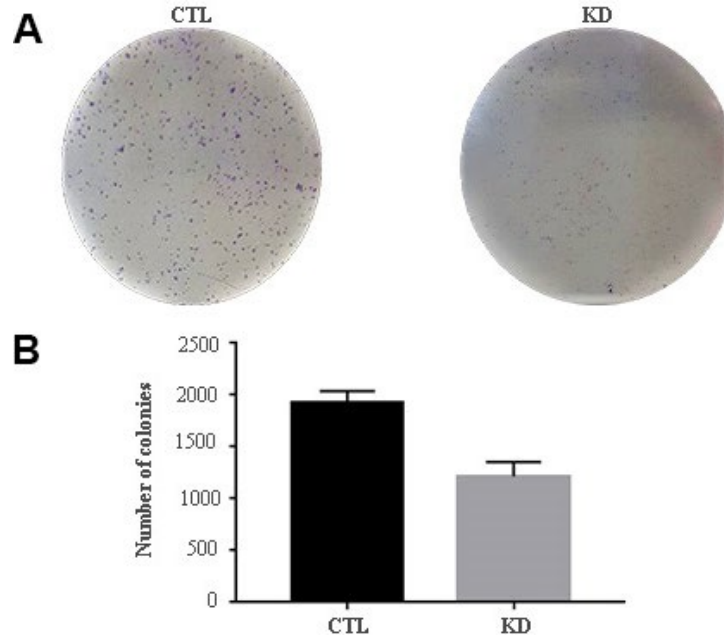


Figure 3. Colony formation capacity of UM 92.1 cells KD for macroH2A1. UM 92.1 cells were silenced for macroH2A1 expression as in Figure 1. (A) Images are representative of three separate experiments. (B) The number of colonies was manually counted and presented as the mean \pm SEM of three independent experiments. (* $p < 0.01$ vs control).

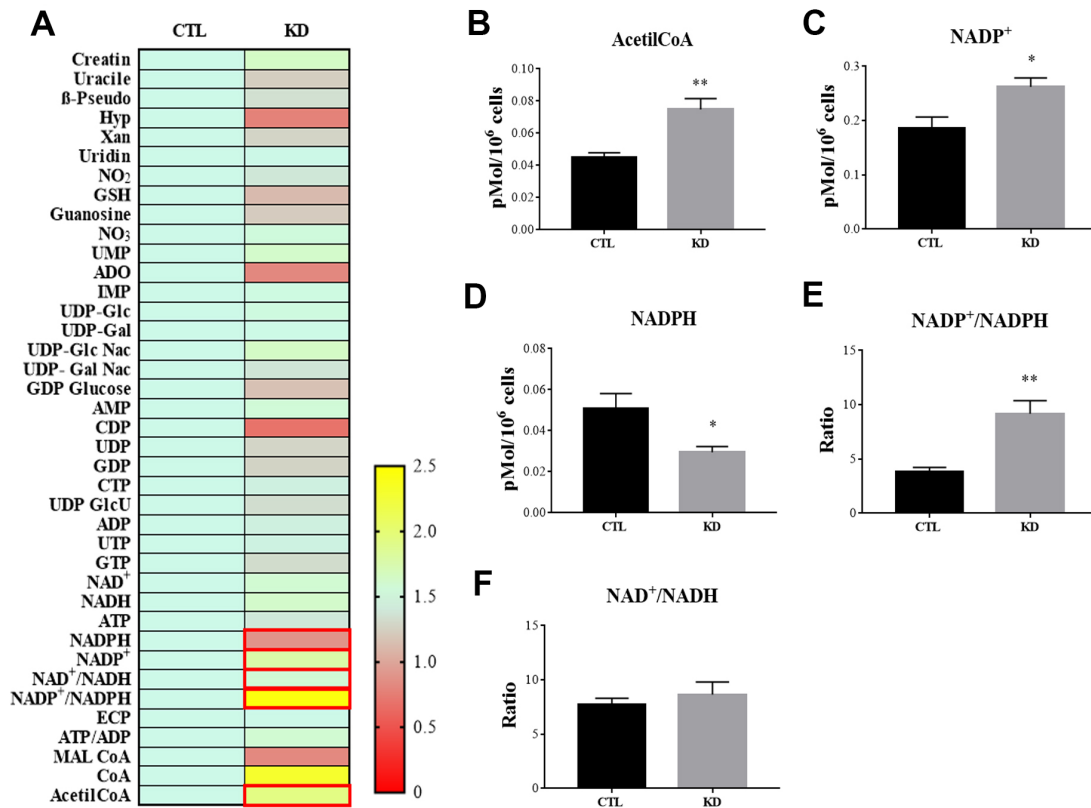


Figure 4. HPLC analysis of metabolites in CTL and macroH2A1 KD UM 92.1 cells. (A) Heatmap representing the levels of major classes of metabolites detected by HPLC. (B) Acetyl-co-A levels; (C) NADP⁺ levels; (D) NADPH levels; (E) NADP⁺/NADPH levels; (F) NAD⁺/NADH levels. Results are presented as the mean ± SEM of four independent experiments. (*p < 0.01; *** p < 0.001 vs control).

phosphates. Consistent with previous observations in HCC cells [33], macroH2A1 silencing resulted in a significant increase of acetyl-CoA (Figure 4B) and NADP⁺ (Figure 4C) content accompanied by a significant decrease of NADPH (Figure 4D), thus suggesting a switch to reductive biosynthesis and to lipid synthesis in KD cells. Consistent with this, the NADP⁺/NADPH ratio is increased in UM 92.1 cells knockdown for macroH2A1 (Figure 4E), while the ratio NAD⁺/NADH showed a trend to be higher upon macroH2A1 silencing (Figure 4F). As consequence, the impaired lipid biosynthesis reflected into a decreased efficiency of the pentose phosphate pathway (PPP) as also supported by the decreased trend of nucleic acid precursor CDP (cytosine diphosphate) and Hyp (hypoxanthine) (Figure 4A). MacroH2A1.1 isoform has been shown to boost mitochondrial respiration when overexpressed in muscle cells [36]. Conversely, we hypothesized that macroH2A1 KD in UM 92.1 cells might hamper the activity of mitochondria. We thus analyzed expression of genes involved in oxidative phosphorylation: the expression of MT-ND4, MT-CO2, COX4|1, MT-CYB, ATP5F1A and TFAM mRNAs were significantly decreased in KD UM cells compared to their controls (p < 0.001) (Figure 5A). The maintenance of an optimal NAD⁺/NADH ratio is essential for mitochondrial function [37]; UM 92.1 cells KD for macroH2A1 showed also a significant (p < 0.001) decrease in the mRNA levels of NMNAT1, NMNAT2, SIRT1 and NAMPT, key enzymes implicated in NAD⁺ turnover [38] (Figure 5B). In contrast, the mRNA levels

of NMNAT3 were increased of >1.5 in UM cells KD for macroH2A1 (Figure 5B). Interestingly, T-Fam transcript was also found significantly downregulated in UM 92.1 cells KD for macroH2A1 compared to CTL cells (p < 0.001) (Figure 5B). The TFAM gene encodes for the mitochondrial transcription factor A (TFAM), essential for replication and packaging of mitochondrial DNA into nucleoids, as well as critical for mitochondrial biogenesis [39]. Consistently, imaging for viable mitochondria co-stained with MitoTracker and TFAM antibody showed an impaired mitochondrial status in 92.1 UM cells deficient for macroH2A1 (Figure 5C).

MacroH2A1 gene expression (H2AFY) regulates the expression of genes involved in mitochondrial metabolism in UM patients

We recently conducted a retrospective study on macroH2A1 immunohistochemical expression in 55 UM patients, demonstrating a positive immunohistochemical correlation between macroH2A1 levels and UM aggressiveness [32]. Here we sought to analyse larger cohort to examine the correlation between the genes involved in mitochondrial metabolism and UM aggressiveness. To this aim, we took into account a total of 190 samples of patients with UM and 96 retinal pigment epithelium (RPE)-choroid of healthy control subjects, pooled from 6 different publicly available Gene Expression Omnibus (GEO) repositories [40] (GSE44295, GSE22138, GSE27831, GSE84976, GSE51880, GSE73652, GSE29801) (Table 1). From

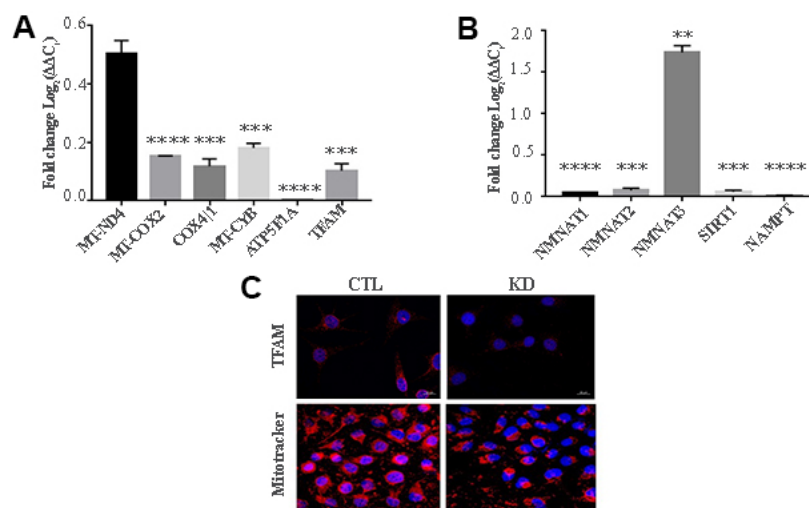


Figure 5. KD for macroH2A1 reprograms energy metabolism in UM 92.1 cells. (A) mRNA levels MT-ND4, MT-CO2, COX4|1, MT-CYB, ATP5F1A and TFAM were assessed by qPCR, and normalized to GAPDH levels. Values are presented as mRNA relative levels and they are expressed as the mean ± SEM of three different experiments. (p < 0.0001 vs control). (B) mRNA levels NMNAT1, NMNAT2, SIRT1 and NAMPT.

Values are presented as mRNA relative levels and they are expressed as the mean \pm SEM of three different experiments. (** $p < 0.01$ **** $p < 0.0001$ vs control). (C) Representative immunocytochemical images showing staining for TFAM (upper panels) and MitoTracker (lower panels) in CTL and in UM 92.1 cells KD for macroH2A1.

Table 1. List of GEO datasets selected.

GSE	GPL	Disease	Sample	Male	Female	Metastasis	No Metastasis
44295	6883	UM	57	32	25	24	33
22138	570	UM	63	39	24	35	28
27831	570	UM	29	17	12	11	18
84976	10558	UM	28	ns	ns	13	15
73652	10558	UM	13	ns	ns	5	8
29801	4133	UM	96	58	38	Not affected	Not affected

all the selected datasets we were able to obtain data regarding sex, age, presence of metastases, and survival rate. The GSE73652 dataset did not present information regarding sex. We divided the UM patients according to the presence or absence of metastases. Two groups of metastatic (88) and non-metastatic (102) patients were compared with each other and with the control group composed of healthy subjects (96), for the expression of the same panel of genes analyzed in

UM 92.1 cells KD for macroH2A1 and involved in mitochondrial respiration and NAD⁺ metabolism (Figure 5) (MT-ND4, MT-CO2, COX41, MT-CYB, ATP5A1 and TFAM, NMNAT1, NMNAT2, NMNAT3 SIRT1 and NAMPT). Our analysis highlighted that for NMNAT2, NMNAT3, COX41 and ATP5A1 expression levels were significantly increased in UM (metastatic/non metastatic [32]) patients compared to healthy controls (Figure 6A–6E). No differences were

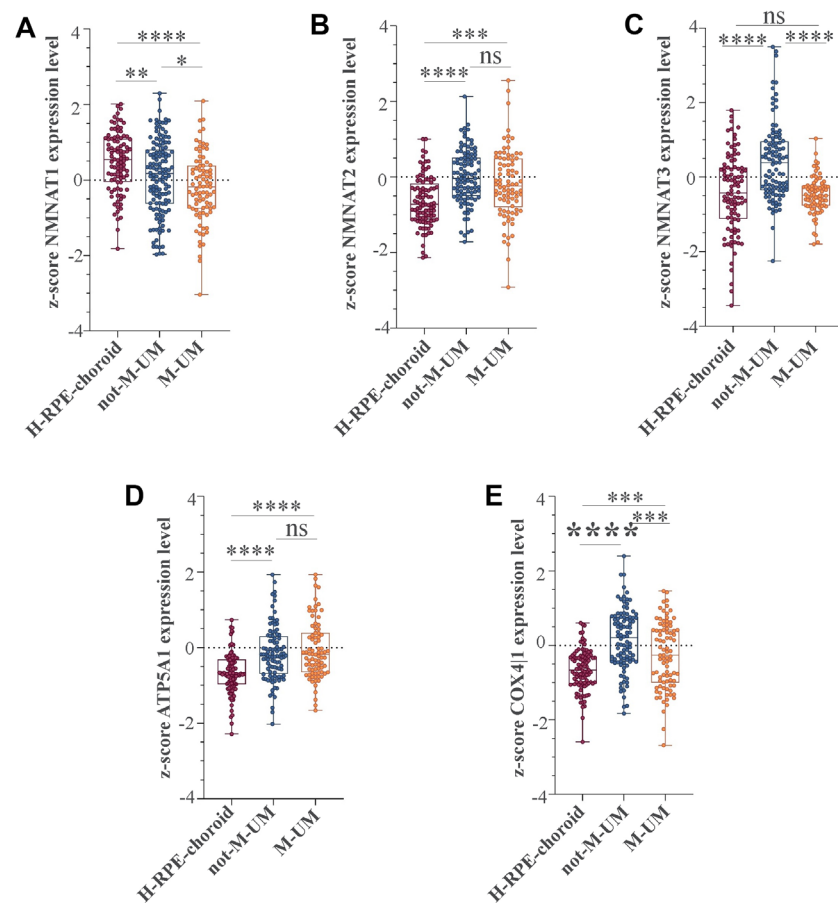


Figure 6. NMNAT1, NMAT2, NMNAT3, ATP5F1A, and COX4|1 mRNA expression levels in UM patients. Expression levels analysis of (A) NMNAT1, (B) NMAT2, (C) NMNAT3, (D) ATP5F1A, and (E) COX4|1 in 96 healthy control subjects (H-RPE-choroid), 88 metastatic (M-UM) and 102 non-metastatic (not-M-UM) UM patients. Data are expressed as z-score intensity expression levels and presented as vertical scatter dot plots. P values <0.05 were considered to be statistically significant (*p<0.05; **p<0.005; ***p<0.0005; ****p<0.00005).

observed for MT-ND4, MT-CO2, MT-CYB, TFAM, SIRT1 and NAMPT across the three categories (*data not shown*). Interestingly, when comparing metastatic versus non metastatic UM patients, we observed a down-regulation of the NMNAT1, NMNAT3 and COX4|1, but not of NMNAT2 and ATP5A1, mRNA levels (Figure 6A–6E). This is consistent and mirrors our data in macroH2A1 KD cells, less proliferative and aggressive, where we observed a general downregulation of the mRNA levels of the enzymes involved in NAD⁺ metabolism (Figure 5). Next, we sought to ascertain whether the expression levels of the selected genes were significantly correlated with the UM patient's survival rate. We found that only the COX4|1 expression levels were significantly positively correlated with the survival rate of metastatic patients ($r=0.3122$, $p=0.0041$) (Table 2A, Figure 7A). A nearly significant negative correlation between COX4|1 and survival was observed with non-metastatic patients ($r=-0.2035$, $p=0.0504$) (Table 2B, Figure 7B). Altogether these data demonstrate the importance of mitochondrial metabolism, as assessed by gene expression, in UM occurrence and aggressiveness.

DISCUSSION

Epigenetic changes cooperate actively with genetic alterations to drive the cancer phenotype. These changes involve DNA methylation, histone modifiers and readers, chromatin remodelers, ncRNA and other physical components of chromatin such as the histone variants [41]. During carcinogenesis, the result of the interplay between oncogenes and tumor suppressor genes can sometime code for histone variants [22, 42]. Others and we have shown that H2A histone variant macroH2A1 can act as oncogene or tumor suppressor depending on the blood or solid malignancy [27–31]. In the present study, we report for the first time that the loss of macroH2A1 inhibits UM cells proliferation and aggressiveness, while inducing an inhibition of mitochondrial metabolism and biogenesis through a gene expression signature that is also observed in UM patients. Therefore, consistent with previous clinical and histological studies on an Italian national reference cohort of biopsies from UM patients, where we showed the role of macroH2A1 as prognostic marker for UM progression [32], we conclude that macroH2A1 acts as an oncoprotein in UM. At the cellular level, UM shares the same lineage – the melanocytes – with cutaneous melanoma. However, the two melanomas differ in their etiologies, clinical features, and molecular abnormalities [43]. The size of the tumor and its degree of invasion are prognostic in both entities, but the patterns

of dissemination and metastasis differ: UM spreads through the blood, while cutaneous melanoma can spread through both the blood and the lymphatic system [44]. The most common site of metastasis of UM is the liver; cutaneous melanoma can instead spread to the lymph nodes, lung, brain, and soft tissue [32, 45].

The role of macroH2A1 in cutaneous melanoma has been well studied. Kapoor et al. reported 2010 that macroH2A proteins suppress progression of malignant cutaneous melanoma [27]. Loss of all macroH2A1 isoforms, positively correlated with increasing malignant phenotype of melanoma cells both in cell lines, in human tissue samples, and in animal models of cutaneous melanoma growth and metastasis; this phenotype could be restored by reintroduction of macroH2A1 [27]. The tumor suppression function of macroH2A1 in cutaneous melanoma was attributed to a large extent to the transcriptional suppression of CDK8, a known oncogene [27]. MacroH2A1 and CDK8 expression levels anti-correlate in human cutaneous melanoma patient samples [27]. Therefore, macroH2A1 functions as an oncogene in UM and as a tumor suppressor in cutaneous melanoma, highlighting the profound epigenetic differences between the two types of melanocyte-derived neoplasia. Genomic and transcriptomic approaches are required in parallel in cutaneous and UM experimental models and human biopsies to unravel the different dynamics of macroH2A1-dependent gene expression. The specific role of CDK8 in UM progression has not been investigated so far, although pan-CDK inhibition seems to be partially effective both in cutaneous melanoma and in UM [46].

Here we found that macroH2A1 loss in UM cells decrease their aggressiveness. This is supported by a distinct gene expression pattern, which is conserved between UM cultured cells and human UM datasets. The metabolite-binding macrodomain (present in macroH2A1.1 but not in macroH2A1.2) is required to sustain mitochondrial function but, interestingly is dispensable for gene regulation [36]. Resveratrol, a natural phenol, is able to inhibit tumor growth *in vitro* and in animal models of UM [47]. Consistent with our findings, an early event in resveratrol action is the direct targeting of mitochondria, which leads to a decrease in cell proliferation [47]. Similar findings were obtained with fisetin, a dietary flavonoid, and with another natural phenol, curcumin [48]. Resveratrol, fisetin and curcumin are contained in various fruits and vegetables. To date, however, there are no studies on dietary factors

and incidence of UM. Half of UM patients develop liver metastases, with a median survival of > 12 months [49]. The loss of one copy of chromosome 3 (Chr3) in a primary UM, referred to as monosomy 3 (M3), is

associated with metastasis and poor prognosis [50]. More than 90% of metastatic UM is M3. Consistent with our findings, M3 UM has a greater mitochondrial activity [51]. Our study identifies for the first time a

Table 2. Pearson correlation analyses between gene expression and survival in UM patients.

A					
Metastatic	surviving months vs. NMNAT1	surviving months vs. NMNAT2	surviving months vs. NMNAT3	surviving months vs. ATP5A1	surviving months vs. COX4I1
Pearson r	-0.1516	0.1291	0.1098	0.05273	0.3122
95% confidence interval	-0,3556 to 0,06628	-0,08907 to 0,3354	-0,1085 to 0,3179	-0,1648 to 0,2654	0,1035 to 0,4946
R squared	0.02297	0.01667	0.01205	0.00278	0.09748
P (two-tailed)	0.1714	0.2448	0.3233	0.6359	0.0041
P value summary	ns	ns	ns	ns	**
Significant (alpha = 0.05)	No	No	No	No	Yes
Number of XY pairs	83	83	83	83	83
B					
Non Metastatic	surviving months vs. NMNAT1	surviving months vs. NMNAT2	surviving months vs. NMNAT3	surviving months vs. ATP5A1	surviving months vs. COX4I1
Pearson r	0.1271	0.07544	0.04138	0.05706	-0.2035
95% confidence interval	-0,07869 to 0,3224	-0,1303 to 0,2749	-0,1637 to 0,2430	-0,1484 to 0,2578	-0,3910 to 0,0002075
R squared	0.01614	0.005691	0.001712	0.003255	0.04142
P (two-tailed)	0.2249	0.4723	0.6937	0.587	0.0504
P value summary	ns	ns	ns	ns	ns
Significant? (alpha = 0.05)	No	No	No	No	No
Number of XY pairs	93	93	93	93	93

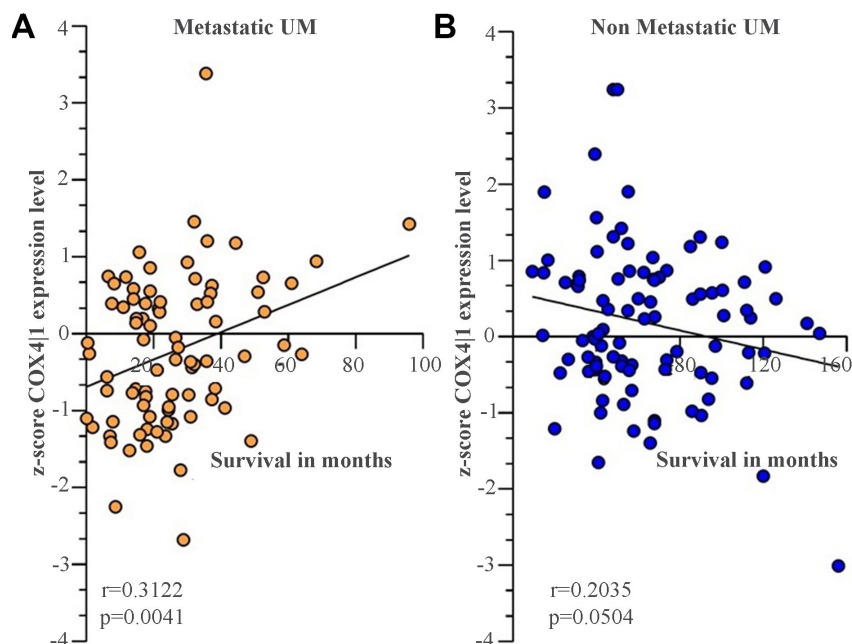


Figure 7. COX4|1 mRNA expression levels correlate with the surviving rate in UM metastatic patients. Correlation analysis of COX4|1 with surviving rate in (A) 88 metastatic (M-UM) and 102 (B) non-metastatic (not-M-UM) UM patients. Data are expressed as z-score intensity expression levels and presented as vertical scatter dot plots. Correlations were determined using Pearson's ρ correlation. P values <0.05 were considered to be statistically significant (* p <0.05; ** p <0.005; *** p <0.0005; **** p <0.00005).

correlation between the expression of COX4|1, key regulatory subunit of human cytochrome c oxidase, and UM patient survival, as observed in glioblastoma multiforme [52].

In conclusion, we suggest that strategies aiming at decreasing the expression of histone variant macroH2A1 [32], might effectively hamper the aggressiveness of UM cells, by inhibiting their mitochondrial phosphorylation. This could be a novel promising therapeutic strategy against UM [51].

MATERIALS AND METHODS

Cell culture

Human uveal melanoma cells (92.1) were purchased from ATCC Company (Milan, Italy). Cells were suspended in RPMI1640 culture medium containing 10% FBS, 100 U/mL penicillin, and 100 U/mL streptomycin. At 80% confluency, cells were passaged using trypsin-EDTA solution (0.05% trypsin and 0.02% EDTA).

Cell transfection was achieved using lentiviral particles [53] and carried out as previously described [28]. Cell proliferation and migration were studied using the "wound healing" assays [28]. The uncovered wound area was measured and quantified at different intervals with ImageJ 1.37v (NIH).

Immunoblotting

Histone protein isolation was achieved using ab113476 Histone Extraction Kit (Abcam, UK). Western blot analysis was performed as previously described [54, 55]. Rabbit MacroH2A1 and H3 antibodies were from Santa Cruz Biotechnology (CA, US). Anti-rabbit HRP linked was from Cell Signaling Technology (Praha, CZ).

Real time proliferation

xCELLigence experiments were performed using the RTCA (Real-Time Cell Analyzer) instrument (Roche Applied Science, Mannheim, Germany and ACEA Biosciences, San Diego, CA) [34]. First, the optimal seeding number was determined by cell titration and growth experiments. After seeding the optimal cell number (2500 cells/well), cells were automatically monitored every 15 min for 72h.

qPCR

Upon mRNA extraction and cDNA reverse transcription we evaluated expression of selected genes in 92.1 cells, CTL and KD. The quantitative analysis was performed using the One-Step Real-time PCR instrument and SYBR Green PCR master mix (Life Technology, Milan, Italy) [56]. GAPDH was used for normalization. Primer sequences were: GAPDH, forward 5'-CCGCATCTTC TTTTGCCTCG-3', reverse 3'-GACTCCGACCTTCAC CTTCC-5', MT-ND4, forward 5'-CAGCCACATAGC CCTCGTAG-3', reverse, 3'-TCGGGGTTGAGGGATA GGAG-5', MT-CO2, forward, 5'-GAACTATCCTGCC CGCCATC-3', reverse, 3'-AGGGATCGTTGACCTCG TCT-5', COX4|1, forward, 5'-GCGGTGCCATGTTCT TCATC-3', reverse, 3'-GGGCCGTACACATAGTGCT T-5', MT-CYB, forward 5'-TCTTGCACGAAACGGG ATCA-3', reverse 3'-TGATTGGCTTAGTGGGCGAA-5', ATP5F1A, forward, 5'-TGTGTGTAGTCTCACGT CACC-3', reverse, 3'-CTGCCTCATTATGGCCACT CC-5', NMNAT1, forward 5'-CCTTGAGGGATGGCG TCAA-3', reverse, 3'-CTTGGCCAGCTCAAACAA CC-5', NMNAT2, forward 5'-CATGACCGAGACCA CCAAGAC-3', reverse 3'-GTCGTGGACAGGGGAGA CAA-5', SIRT1, forward, 5'-CCAAGGCCACGGATA GGTC-3', reverse, 3'-ATTGTTTCGAGGATCTGTGCC-5', NAMPT, forward, 5'-GCTTGGGGGAAAGACCAT GA-3', reverse, 3'-GCTGACCACAGATACAGGCA-5'.

Clonogenic assay

Colony assays performed by seeding cells in 6-wells plates at low density (5000 cells/well) and allowing growth for 9 days. Colonies were fixed, stained with crystal violet (Sigma Aldrich) and quantified using ImageJ (NIH).

Immunofluorescence

Cells were grown directly on coverslips before immunofluorescence [57]. Briefly, after washing with PBS, cells were fixed in 4% paraformaldehyde (Sigma-Aldrich, Milan, Italy) for 20min at room temperature. Subsequently, cells were incubated with primary antibody against T-Fam we purchased from Thermo Fisher scientific (1:200), overnight at 4 °C. Cells were then washed three times in PBS for 5 min and incubated with secondary antibodies from Cell Signaling Technology. Nuclei were counterstained with DAPI (4',6-diamidino-2-phenylindole, Santa Cruz Biotechnology, CA, USA). Images were obtained using a Zeiss Axio Imager Z1 Microscope with Apotome 2 system (Zeiss, Milan, Italy).

simultaneous separation of high-energy phosphates (ATP, ADP, AMP, GTP, GDP, GMP, IMP, UTP, UDP, UMP, CTP, CDP, CMP), Coenzyme A and its

HPLC analysis of metabolites

Cellular packages were deproteinized to measure acid labile and easily oxidizable compounds [58]. The

Table 3. Probes set list.

N°	GSE	GPL	Probe set	Gene nomenclature
1	44295	6883	ILMN_1692413	NMNAT1
			ILMN_1742968	NMNAT2
			ILMN_2153485	NMNAT3
			ILMN_1652207	COX4I1
			ILMN_2341363	ATP5A1
2	22138 27831 51880	570	223692_at	NMNAT1
			1562818_at	NMNAT2
			228090_at	NMNAT3
			227323_at	COX4I1
			1569891_at	ATP5A1
3	84976 73652	10558	ILMN_1692413	NMNAT1
			ILMN_1742968	NMNAT2
			ILMN_2153485	NMNAT3
			ILMN_1652207	COX4I1
			ILMN_2341363	ATP5A1
4	29801	4133	3719	NMNAT1
			25564	NMNAT2
			20338	NMNAT3
			39732	COX4I1
			37865	ATP5A1

derivatives (Acetyl-CoA, Malonyl-CoA), nicotinic coenzymes (NAD⁺, NADH, NADP⁺, NADPH), reduced glutathione (GSH), malondialdehyde (MDA), nitrite and nitrate in the protein-free cell extracts, was carried out using established HPLC methods [58, 59]

Dataset selection and analysis

The NCBI Gene Expression Omnibus (GEO) database (<http://www.ncbi.nlm.nih.gov/geo/>) [40] was used to select microarray datasets. Mesh terms “Uveal Melanoma” and “eyes choroid” were used to identify datasets of interest. The obtained datasets were sorted by the number of samples (High to Low) and to available clinical data. Seven datasets were selected: GSE44295, GSE22138 [60], GSE27831 [61], GSE84976 [62], GSE51880 [63], GSE73652 [64], and GSE29801 [65] (Table 1). All the selected datasets were composed of samples from UM patients, divided according to sex and the presence of metastases. The samples were homogeneous for the age. Furthermore, the samples were selected based on survival rate. The GSE29801 dataset consisted of 151 samples from the

macular or extramacular region of donor eye retinal pigmented epithelium. Data processing: to identify significant differentially expressed genes (SDEG) in data sets, we used the MultiExperiment Viewer (MeV) software. In cases where multiple genes probes have insisted on the same GeneID NCBI, we have used those with the highest variance (Table 3). Statistical analysis was performed using GEO2R, applying a Benjamini and Hochberg (False discovery rate) to adjust P values for multiple comparisons [66–68].

Statistical analysis

Data are shown as means ± standard error of the mean (SEM). For statistical analysis, Prism 7 software (GraphPad Software, USA) was used. Significant differences between groups were assessed using the one-way ANOVA test. Correlations were determined using Pearson’s ρ correlation. All tests were two-sided, and significance was determined at $p < 0.05$. The analysis of microarray data by Z-score transformation was used in order to allow the comparison of

microarray data independent of the original hybridization intensities [34].

AUTHOR CONTRIBUTIONS

Conceptualization: G.L.V., M.V., R.C. and M.R.; methodology: D.T., S.G., M.D.R., A.M.A., G.L., O.L.R., R.C., L.P., L.S., S.P., L.L., D.A.; formal analysis: A.L., A.R., S.G., M.D.R.; investigation: M.R., R.C. and S.P.; resources, M.V., R.C., G.L.V.; data curation: M.D.R., O.L.R., A.R., A.L., S.G.; writing—original draft preparation: M.V., G.L.V.; writing—review and editing: M.V., D.T., R.C., M.R.; supervision: M.V., G.L.V. and R.C.

CONFLICTS OF INTEREST

The authors declare no conflicts of interest.

FUNDING

This research was funded by intradepartmental research plan 2016/2018 of the Department of Medical, Surgical, and Advanced Technology, University of Catania (funding number 5C722012114, 2018) and European Social Fund and European Regional Development Fund – Project MAGNET (No. CZ.02.1.01/0.0/0.0/15_003/0000492).

REFERENCES

1. Chang AE, Karnell LH, Menck HR. The national cancer data base report on cutaneous and noncutaneous melanoma: a summary of 84,836 cases from the past decade. The american college of surgeons commission on cancer and the american cancer society. *Cancer*. 1998; 83:1664–78.
[https://doi.org/10.1002/\(sici\)1097-0142\(19981015\)83:8<1664::aid-cnrc23>3.0.co;2-g](https://doi.org/10.1002/(sici)1097-0142(19981015)83:8<1664::aid-cnrc23>3.0.co;2-g)
PMID:9781962
2. Singh AD, Topham A. Incidence of uveal melanoma in the United States: 1973-1997. *Ophthalmology*. 2003; 110:956–61.
[https://doi.org/10.1016/S0161-6420\(03\)00078-2](https://doi.org/10.1016/S0161-6420(03)00078-2)
PMID:12750097
3. Kujala E, Mäkitie T, Kivelä T. Very long-term prognosis of patients with Malignant uveal melanoma. *Invest Ophthalmol Vis Sci*. 2003; 44:4651–59.
<https://doi.org/10.1167/iov.03-0538>
PMID:14578381
4. Kath R, Hayungs J, Bornfeld N, Sauerwein W, Höffken K, Seeber S. Prognosis and treatment of disseminated uveal melanoma. *Cancer*. 1993; 72:2219–23.
[https://doi.org/10.1002/1097-0142\(19931001\)72:7](https://doi.org/10.1002/1097-0142(19931001)72:7)

- [2219::aid-cnrc2820720725>3.0.co;2-j](https://doi.org/10.1002/1097-0142(19931001)72:7)
PMID:7848381
5. Pandiani C, Béranger GE, Leclerc J, Ballotti R, Bertolotto C. Focus on cutaneous and uveal melanoma specificities. *Genes Dev*. 2017; 31:724–43.
<https://doi.org/10.1101/gad.296962.117>
PMID:28512236
6. Van Raamsdonk CD, Griewank KG, Crosby MB, Garrido MC, Vemula S, Wiesner T, Obenaus AC, Wackernagel W, Green G, Bouvier N, Sozen MM, Baimukanova G, Roy R, et al. Mutations in GNA11 in uveal melanoma. *N Engl J Med*. 2010; 363:2191–99.
<https://doi.org/10.1056/NEJMoa1000584>
PMID:21083380
7. Harbour JW, Onken MD, Roberson ED, Duan S, Cao L, Worley LA, Council ML, Matattal KA, Helms C, Bowcock AM. Frequent mutation of BAP1 in metastasizing uveal melanomas. *Science*. 2010; 330:1410–13.
<https://doi.org/10.1126/science.1194472>
PMID:21051595
8. Scheuermann JC, de Ayala Alonso AG, Oktaba K, Ly-Hartig N, McGinty RK, Fraterman S, Wilm M, Muir TW, Müller J. Histone H2A deubiquitinase activity of the polycomb repressive complex PR-DUB. *Nature*. 2010; 465:243–47.
<https://doi.org/10.1038/nature08966>
PMID:20436459
9. Machida YJ, Machida Y, Vashisht AA, Wohlschlegel JA, Dutta A. The deubiquitinating enzyme BAP1 regulates cell growth via interaction with HCF-1. *J Biol Chem*. 2009; 284:34179–88.
<https://doi.org/10.1074/jbc.M109.046755>
PMID:19815555
10. Masoomian B, Shields JA, Shields CL. Overview of BAP1 cancer predisposition syndrome and the relationship to uveal melanoma. *J Curr Ophthalmol*. 2018; 30:102–09.
<https://doi.org/10.1016/j.joco.2018.02.005>
PMID:29988936
11. Sarkar S, Goldgar S, Byler S, Rosenthal S, Heerboth S. Demethylation and re-expression of epigenetically silenced tumor suppressor genes: sensitization of cancer cells by combination therapy. *Epigenomics*. 2013; 5:87–94.
<https://doi.org/10.2217/epi.12.68>
PMID:23414323
12. van der Velden PA, Metzelaar-Blok JA, Bergman W, Monique H, Hurks H, Frants RR, Gruis NA, Jager MJ. Promoter hypermethylation: a common cause of reduced p16(INK4a) expression in uveal melanoma. *Cancer Res*. 2001; 61:5303–06.
PMID:11431374

13. Liu J, Ma L, Li C, Zhang Z, Yang G, Zhang W. Tumor-targeting TRAIL expression mediated by miRNA response elements suppressed growth of uveal melanoma cells. *Mol Oncol*. 2013; 7:1043–55. <https://doi.org/10.1016/j.molonc.2013.08.003> PMID:[24001901](https://pubmed.ncbi.nlm.nih.gov/24001901/)
14. Sun L, Bian G, Meng Z, Dang G, Shi D, Mi S. MiR-144 inhibits uveal melanoma cell proliferation and invasion by regulating c-Met expression. *PLoS One*. 2015; 10:e0124428. <https://doi.org/10.1371/journal.pone.0124428> PMID:[25961751](https://pubmed.ncbi.nlm.nih.gov/25961751/)
15. Xu H, Gong J, Liu H. High expression of lncRNA PVT1 independently predicts poor overall survival in patients with primary uveal melanoma. *PLoS One*. 2017; 12:e0189675. <https://doi.org/10.1371/journal.pone.0189675> PMID:[29244840](https://pubmed.ncbi.nlm.nih.gov/29244840/)
16. Li Y, Jia R, Ge S. Role of epigenetics in uveal melanoma. *Int J Biol Sci*. 2017; 13:426–33. <https://doi.org/10.7150/ijbs.18331> PMID:[28529451](https://pubmed.ncbi.nlm.nih.gov/28529451/)
17. Bernstein E, Hake SB. The nucleosome: a little variation goes a long way. *Biochem Cell Biol*. 2006; 84:505–17. <https://doi.org/10.1139/o06-085> PMID:[16936823](https://pubmed.ncbi.nlm.nih.gov/16936823/)
18. Sarma K, Reinberg D. Histone variants meet their match. *Nat Rev Mol Cell Biol*. 2005; 6:139–49. <https://doi.org/10.1038/nrm1567> PMID:[15688000](https://pubmed.ncbi.nlm.nih.gov/15688000/)
19. Thambirajah AA, Li A, Ishibashi T, Ausió J. New developments in post-translational modifications and functions of histone H2A variants. *Biochem Cell Biol*. 2009; 87:7–17. <https://doi.org/10.1139/O08-103> PMID:[19234519](https://pubmed.ncbi.nlm.nih.gov/19234519/)
20. Giallongo S, Lo Re O, Vinciguerra M. Macro histone variants: emerging rheostats of gastrointestinal cancers. *Cancers (Basel)*. 2019; 11:676. <https://doi.org/10.3390/cancers11050676> PMID:[31096699](https://pubmed.ncbi.nlm.nih.gov/31096699/)
21. Lo Re O, Vinciguerra M. Histone MacroH2A1: a chromatin point of intersection between fasting, senescence and cellular regeneration. *Genes (Basel)*. 2017; 8:367. <https://doi.org/10.3390/genes8120367> PMID:[29206173](https://pubmed.ncbi.nlm.nih.gov/29206173/)
22. Buschbeck M, Hake SB. Variants of core histones and their roles in cell fate decisions, development and cancer. *Nat Rev Mol Cell Biol*. 2017; 18:299–314. <https://doi.org/10.1038/nrm.2016.166> PMID:[28144029](https://pubmed.ncbi.nlm.nih.gov/28144029/)
23. Costanzi C, Pehrson JR. Histone macroH2A1 is concentrated in the inactive X chromosome of female mammals. *Nature*. 1998; 393:599–601. <https://doi.org/10.1038/31275> PMID:[9634239](https://pubmed.ncbi.nlm.nih.gov/9634239/)
24. Zhang R, Poustovoitov MV, Ye X, Santos HA, Chen W, Daganzo SM, Erzberger JP, Serebriiskii IG, Canutescu AA, Dunbrack RL, Pehrson JR, Berger JM, Kaufman PD, Adams PD. Formation of MacroH2A-containing senescence-associated heterochromatin foci and senescence driven by ASF1a and HIRA. *Dev Cell*. 2005; 8:19–30. <https://doi.org/10.1016/j.devcel.2004.10.019> PMID:[15621527](https://pubmed.ncbi.nlm.nih.gov/15621527/)
25. Changolkar LN, Costanzi C, Leu NA, Chen D, McLaughlin KJ, Pehrson JR. Developmental changes in histone macroH2A1-mediated gene regulation. *Mol Cell Biol*. 2007; 27:2758–64. <https://doi.org/10.1128/MCB.02334-06> PMID:[17242180](https://pubmed.ncbi.nlm.nih.gov/17242180/)
26. Gamble MJ, Frizzell KM, Yang C, Krishnakumar R, Kraus WL. The histone variant macroH2A1 marks repressed autosomal chromatin, but protects a subset of its target genes from silencing. *Genes Dev*. 2010; 24:21–32. <https://doi.org/10.1101/gad.1876110> PMID:[20008927](https://pubmed.ncbi.nlm.nih.gov/20008927/)
27. Kapoor A, Goldberg MS, Cumberland LK, Ratnakumar K, Segura MF, Emanuel PO, Menendez S, Vardabasso C, Leroy G, Vidal CI, Polsky D, Osman I, Garcia BA, et al. The histone variant macroH2A suppresses melanoma progression through regulation of CDK8. *Nature*. 2010; 468:1105–09. <https://doi.org/10.1038/nature09590> PMID:[21179167](https://pubmed.ncbi.nlm.nih.gov/21179167/)
28. Borghesan M, Fusilli C, Rappa F, Panebianco C, Rizzo G, Oben JA, Mazzoccoli G, Faulkes C, Pata I, Agodi A, Rezaee F, Minogue S, Warren A, et al. DNA hypomethylation and histone variant macroH2A1 synergistically attenuate chemotherapy-induced senescence to promote hepatocellular carcinoma progression. *Cancer Res*. 2016; 76:594–606. <https://doi.org/10.1158/0008-5472.CAN-15-1336> PMID:[26772755](https://pubmed.ncbi.nlm.nih.gov/26772755/)
29. Lo Re O, Fusilli C, Rappa F, Van Haele M, Douet J, Pindjakova J, Rocha SW, Pata I, Valčíková B, Uldrijan S, Yeung RS, Peixoto CA, Roskams T, et al. Induction of cancer cell stemness by depletion of macrohistone H2A1 in hepatocellular carcinoma. *Hepatology*. 2018; 67:636–50. <https://doi.org/10.1002/hep.29519> PMID:[28913935](https://pubmed.ncbi.nlm.nih.gov/28913935/)

30. Park SJ, Shim JW, Park HS, Eum DY, Park MT, Mi Yi J, Choi SH, Kim SD, Son TG, Lu W, Kim ND, Yang K, Heo K. MacroH2A1 downregulation enhances the stem-like properties of bladder cancer cells by transactivation of Lin28B. *Oncogene*. 2016; 35:1292–301. <https://doi.org/10.1038/onc.2015.187> PMID:26028027
31. Bereshchenko O, Lo Re O, Nikulenkov F, Flamini S, Kotaskova J, Mazza T, Le Pann  rer MM, Buschbeck M, Giallongo C, Palumbo G, Li Volti G, Paziienza V, Cervinek L, et al. Deficiency and haploinsufficiency of histone macroH2A1.1 in mice recapitulate hematopoietic defects of human myelodysplastic syndrome. *Clin Epigenetics*. 2019; 11:121. <https://doi.org/10.1186/s13148-019-0724-z> PMID:31439048
32. Salvatorelli L, Puzzo L, Bartoloni G, Palmucci S, Longo A, Russo A, Reibaldi M, Vinciguerra M, Li Volti G, Caltabiano R. Immunoexpression of MacroH2a in Uveal Melanoma. *Applied Sciences*. 2019; 9:3244 <https://doi.org/10.3390/app9163244>
33. Lo Re O, Douet J, Buschbeck M, Fusilli C, Paziienza V, Panebianco C, Castracani CC, Mazza T, Li Volti G, Vinciguerra M. Histone variant macroH2A1 rewires carbohydrate and lipid metabolism of hepatocellular carcinoma cells towards cancer stem cells. *Epigenetics*. 2018; 13:829–45. <https://doi.org/10.1080/15592294.2018.1514239> PMID:30165787
34. Kho D, MacDonald C, Johnson R, Unsworth CP, O'Carroll SJ, du Mez E, Angel CE, Graham ES. Application of xCELLigence RTCA biosensor technology for revealing the profile and window of drug responsiveness in real time. *Biosensors (Basel)*. 2015; 5:199–222. <https://doi.org/10.3390/bios5020199> PMID:25893878
35. Lo Re O, Mazza T, Giallongo S, Sanna P, Rappa F, Vinh Luong T, Li Volti G, Drovakova A, Roskams T, Van Haele M, Tsochatzis E, Vinciguerra M. Loss of histone macroH2A1 in hepatocellular carcinoma cells promotes paracrine-mediated chemoresistance and CD4⁺ CD25⁺ FoxP3⁺ regulatory T cells activation. *Theranostics*. 2020; 10:910–24. <https://doi.org/10.7150/thno.35045> PMID:31903159
36. Posavec Marjanovi   M, Hurtado-Bag  s S, Lassi M, Valero V, Malinverni R, Delage H, Navarro M, Corujo D, Guberovic I, Douet J, Gama-Perez P, Garcia-Roves PM, Ahel I, Ladurner AG, Yanes O, Bouvet P, Suelves M, Teperino R, Pospisilik JA, Buschbeck M. MacroH2A1.1 regulates mitochondrial respiration by limiting nuclear NAD(+) consumption. *Nat Struct Mol Biol*. 2017;24:902–10. <https://doi.org/10.1038/nsmb.3481> PMID:28991266
37. Cant   C, Menzies KJ, Auwerx J. NAD(+) metabolism and the control of energy homeostasis: a balancing act between mitochondria and the nucleus. *Cell Metab*. 2015; 22:31–53. <https://doi.org/10.1016/j.cmet.2015.05.023> PMID:26118927
38. Stein LR, Imai S. The dynamic regulation of NAD metabolism in mitochondria. *Trends Endocrinol Metab*. 2012; 23:420–28. <https://doi.org/10.1016/j.tem.2012.06.005> PMID:22819213
39. Stiles AR, Simon MT, Stover A, Eftekharian S, Khanlou N, Wang HL, Magaki S, Lee H, Partynski K, Dorrani N, Chang R, Martinez-Agosto JA, Abdenur JE. Mutations in TFAM, encoding mitochondrial transcription factor A, cause neonatal liver failure associated with mtDNA depletion. *Mol Genet Metab*. 2016; 119:91–99. <https://doi.org/10.1016/j.ymgme.2016.07.001> PMID:27448789
40. Clough E, Barrett T. The gene expression omnibus database. *Methods Mol Biol*. 2016; 1418:93–110. https://doi.org/10.1007/978-1-4939-3578-9_5 PMID:27008011
41. Baylin SB, Jones PA. Epigenetic determinants of cancer. *Cold Spring Harb Perspect Biol*. 2016; 8:a019505. <https://doi.org/10.1101/cshperspect.a019505> PMID:27194046
42. Monteiro FL, Baptista T, Amado F, Vitorino R, Jer  nimo C, Helguero LA. Expression and functionality of histone H2A variants in cancer. *Oncotarget*. 2014; 5:3428–43. <https://doi.org/10.18632/oncotarget.2007> PMID:25003966
43. van den Bosch T, Kilic E, Paridaens D, de Klein A. Genetics of uveal melanoma and cutaneous melanoma: two of a kind? *Dermatol Res Pract*. 2010; 2010:360136. <https://doi.org/10.1155/2010/360136> PMID:20631901
44. Grossniklaus HE. Understanding uveal melanoma metastasis to the liver: the zimmerman effect and the zimmerman hypothesis. *Ophthalmology*. 2019; 126:483–87. <https://doi.org/10.1016/j.ophtha.2018.09.031> PMID:30910033
45. van der Kooij MK, Speetjens FM, van der Burg SH, Kapiteijn E. Uveal versus cutaneous melanoma; same origin, very distinct tumor types. *Cancers (Basel)*. 2019; 11:845. <https://doi.org/10.3390/cancers11060845> PMID:31248118

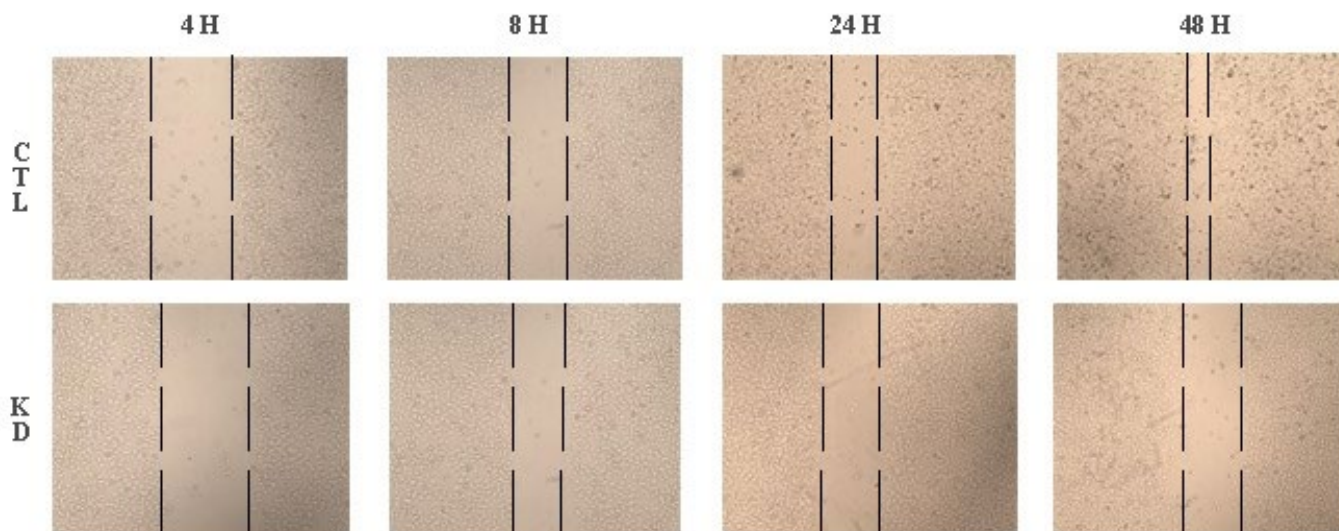
46. Heijkants R, Willekens K, Schoonderwoerd M, Teunisse A, Nieveen M, Radaelli E, Hawinkels L, Marine JC, Jochemsen A. Combined inhibition of CDK and HDAC as a promising therapeutic strategy for both cutaneous and uveal metastatic melanoma. *Oncotarget*. 2017; 9:6174–87.
<https://doi.org/10.18632/oncotarget.23485>
PMID:[29464063](https://pubmed.ncbi.nlm.nih.gov/29464063/)
47. van Ginkel PR, Darjatmoko SR, Sareen D, Subramanian L, Bhattacharya S, Lindstrom MJ, Albert DM, Polans AS. Resveratrol inhibits uveal melanoma tumor growth via early mitochondrial dysfunction. *Invest Ophthalmol Vis Sci*. 2008; 49:1299–306.
<https://doi.org/10.1167/iovs.07-1233>
PMID:[18385041](https://pubmed.ncbi.nlm.nih.gov/18385041/)
48. Lu C, Song E, Hu DN, Chen M, Xue C, Rosen R, McCormick SA. Curcumin induces cell death in human uveal melanoma cells through mitochondrial pathway. *Curr Eye Res*. 2010; 35:352–60.
<https://doi.org/10.3109/02713680903521944>
PMID:[20373902](https://pubmed.ncbi.nlm.nih.gov/20373902/)
49. Chattopadhyay C, Kim DW, Gombos DS, Oba J, Qin Y, Williams MD, Esmaeli B, Grimm EA, Wargo JA, Woodman SE, Patel SP. Uveal melanoma: from diagnosis to treatment and the science in between. *Cancer*. 2016; 122:2299–312.
<https://doi.org/10.1002/cncr.29727>
PMID:[26991400](https://pubmed.ncbi.nlm.nih.gov/26991400/)
50. Ewens KG, Kanetsky PA, Richards-Yutz J, Purrazzella J, Shields CL, Ganguly T, Ganguly A. Chromosome 3 status combined with BAP1 and EIF1AX mutation profiles are associated with metastasis in uveal melanoma. *Invest Ophthalmol Vis Sci*. 2014; 55:5160–67.
<https://doi.org/10.1167/iovs.14-14550>
PMID:[24970262](https://pubmed.ncbi.nlm.nih.gov/24970262/)
51. Chattopadhyay C, Oba J, Roszik J, Marszalek JR, Chen K, Qi Y, Eterovic K, Robertson AG, Burks JK, McCannel TA, Grimm EA, Woodman SE. Elevated endogenous SDHA drives pathological metabolism in highly metastatic uveal melanoma. *Invest Ophthalmol Vis Sci*. 2019; 60:4187–95.
<https://doi.org/10.1167/iovs.19-28082>
PMID:[31596927](https://pubmed.ncbi.nlm.nih.gov/31596927/)
52. Oliva CR, Markert T, Gillespie GY, Griguer CE. Nuclear-encoded cytochrome C oxidase subunit 4 regulates BMI1 expression and determines proliferative capacity of high-grade gliomas. *Oncotarget*. 2015; 6:4330–44.
<https://doi.org/10.18632/oncotarget.3015>
PMID:[25726526](https://pubmed.ncbi.nlm.nih.gov/25726526/)
53. Wilson AA, Kwok LW, Porter EL, Payne JG, McElroy GS, Ohle SJ, Greenhill SR, Blahna MT, Yamamoto K, Jean JC, Mizgerd JP, Kotton DN. Lentiviral delivery of RNAi for in vivo lineage-specific modulation of gene expression in mouse lung macrophages. *Mol Ther*. 2013; 21:825–33.
<https://doi.org/10.1038/mt.2013.19>
PMID:[23403494](https://pubmed.ncbi.nlm.nih.gov/23403494/)
54. Benegiamo G, Vinciguerra M, Mazzoccoli G, Piepoli A, Andriulli A, Paziienza V. DNA methyltransferases 1 and 3b expression in huh-7 cells expressing HCV core protein of different genotypes. *Dig Dis Sci*. 2012; 57:1598–603.
<https://doi.org/10.1007/s10620-012-2160-1>
PMID:[22526584](https://pubmed.ncbi.nlm.nih.gov/22526584/)
55. Sheedfar F, Sung MM, Aparicio-Vergara M, Kloosterhuis NJ, Miquilena-Colina ME, Vargas-Castrillón J, Febbraio M, Jacobs RL, de Bruin A, Vinciguerra M, García-Monzón C, Hofker MH, Dyck JR, Koonen DP. Increased hepatic CD36 expression with age is associated with enhanced susceptibility to nonalcoholic fatty liver disease. *Aging (Albany NY)*. 2014; 6:281–95.
<https://doi.org/10.18632/aging.100652>
PMID:[24751397](https://pubmed.ncbi.nlm.nih.gov/24751397/)
56. Sigala B, McKee C, Soeda J, Paziienza V, Morgan M, Lin CI, Selden C, Vander Borgh S, Mazzoccoli G, Roskams T, Vinciguerra M, Oben JA. Sympathetic nervous system catecholamines and neuropeptide Y neurotransmitters are upregulated in human NAFLD and modulate the fibrogenic function of hepatic stellate cells. *PLoS One*. 2013; 8:e72928.
<https://doi.org/10.1371/journal.pone.0072928>
PMID:[24019886](https://pubmed.ncbi.nlm.nih.gov/24019886/)
57. Paziienza V, Borghesan M, Mazza T, Sheedfar F, Panebianco C, Williams R, Mazzoccoli G, Andriulli A, Nakanishi T, Vinciguerra M. SIRT1-metabolite binding histone macroH2A1.1 protects hepatocytes against lipid accumulation. *Aging (Albany NY)*. 2014; 6:35–47.
<https://doi.org/10.18632/aging.100632>
PMID:[24473773](https://pubmed.ncbi.nlm.nih.gov/24473773/)
58. Lazzarino G, Amorini AM, Fazzina G, Vagnozzi R, Signoretti S, Donzelli S, Di Stasio E, Giardina B, Tavazzi B. Single-sample preparation for simultaneous cellular redox and energy state determination. *Anal Biochem*. 2003; 322:51–59.
<https://doi.org/10.1016/j.ab.2003.07.013>
PMID:[14705780](https://pubmed.ncbi.nlm.nih.gov/14705780/)
59. Romitelli F, Santini SA, Chierici E, Pitocco D, Tavazzi B, Amorini AM, Lazzarino G, Di Stasio E. Comparison of nitrite/nitrate concentration in human plasma and serum samples measured by the enzymatic batch griess assay, ion-pairing HPLC and ion-trap GC-MS: the importance of a correct removal of proteins in the griess assay. *J Chromatogr B Analyt Technol Biomed Life Sci*. 2007; 851:257–67.
<https://doi.org/10.1016/j.jchromb.2007.02.003>

PMID:[17324645](https://pubmed.ncbi.nlm.nih.gov/17324645/)

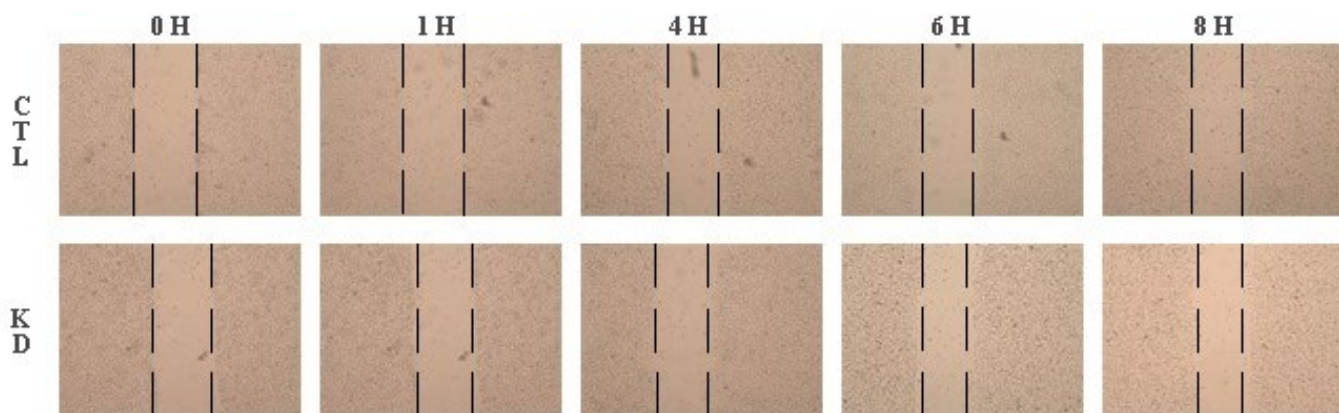
60. Laurent C, Valet F, Planque N, Silveri L, Maacha S, Anezo O, Hupe P, Plancher C, Reyes C, Albaud B, Rapinat A, Gentien D, Couturier J, et al. High PTP4A3 phosphatase expression correlates with metastatic risk in uveal melanoma patients. *Cancer Res.* 2011; 71:666–74.
<https://doi.org/10.1158/0008-5472.CAN-10-0605>
PMID:[21135111](https://pubmed.ncbi.nlm.nih.gov/21135111/)
61. Gangemi R, Mirisola V, Barisione G, Fabbi M, Brizzolara A, Lanza F, Mosci C, Salvi S, Gualco M, Truini M, Angelini G, Boccardo S, Cilli M, et al. Mda-9/syntenin is expressed in uveal melanoma and correlates with metastatic progression. *PLoS One.* 2012; 7:e29989.
<https://doi.org/10.1371/journal.pone.0029989>
PMID:[22267972](https://pubmed.ncbi.nlm.nih.gov/22267972/)
62. van Essen TH, van Pelt SI, Bronkhorst IH, Versluis M, Némati F, Laurent C, Luyten GP, van Hall T, van den Elsen PJ, van der Velden PA, Decaudin D, Jager MJ. Upregulation of HLA expression in primary uveal melanoma by infiltrating leukocytes. *PLoS One.* 2016; 11:e0164292.
<https://doi.org/10.1371/journal.pone.0164292>
PMID:[27764126](https://pubmed.ncbi.nlm.nih.gov/27764126/)
63. Amaro A, Mirisola V, Angelini G, Musso A, Tosetti F, Esposito AI, Perri P, Lanza F, Nasciuti F, Mosci C, Puzone R, Salvi S, Truini M, et al. Evidence of epidermal growth factor receptor expression in uveal melanoma: inhibition of epidermal growth factor-mediated signalling by gefitinib and cetuximab triggered antibody-dependent cellular cytotoxicity. *Eur J Cancer.* 2013; 49:3353–65.
<https://doi.org/10.1016/j.ejca.2013.06.011>
PMID:[23849826](https://pubmed.ncbi.nlm.nih.gov/23849826/)
64. Field MG, Decatur CL, Kurtenbach S, Gezgin G, van der Velden PA, Jager MJ, Kozak KN, Harbour JW. PRAME as an independent biomarker for metastasis in uveal melanoma. *Clin Cancer Res.* 2016; 22:1234–42.
<https://doi.org/10.1158/1078-0432.CCR-15-2071>
PMID:[26933176](https://pubmed.ncbi.nlm.nih.gov/26933176/)
65. Newman AM, Gallo NB, Hancox LS, Miller NJ, Radeke CM, Maloney MA, Cooper JB, Hageman GS, Anderson DH, Johnson LV, Radeke MJ. Systems-level analysis of age-related macular degeneration reveals global biomarkers and phenotype-specific functional networks. *Genome Med.* 2012; 4:16.
<https://doi.org/10.1186/gm315>
PMID:[22364233](https://pubmed.ncbi.nlm.nih.gov/22364233/)
66. Xiao J, Cao H, Chen J. False discovery rate control incorporating phylogenetic tree increases detection power in microbiome-wide multiple testing. *Bioinformatics.* 2017; 33:2873–81.
<https://doi.org/10.1093/bioinformatics/btx311>
PMID:[28505251](https://pubmed.ncbi.nlm.nih.gov/28505251/)
67. Smyth GK. Linear models and empirical bayes methods for assessing differential expression in microarray experiments. *Stat Appl Genet Mol Biol.* 2004; 3:Article3.
<https://doi.org/10.2202/1544-6115.1027>
PMID:[16646809](https://pubmed.ncbi.nlm.nih.gov/16646809/)
68. Davis S, Meltzer PS. GEOquery: A bridge between the gene expression omnibus (GEO) and BioConductor. *Bioinformatics.* 2007; 23:1846–47.
<https://doi.org/10.1093/bioinformatics/btm254>
PMID:[17496320](https://pubmed.ncbi.nlm.nih.gov/17496320/)

SUPPLEMENTARY MATERIALS

Supplementary Figures



Supplementary Figure 1. Proliferation of 92.1 UM cells control (CTL) or knock-down (KD) for macroH2A1, in presence of serum. The number of the cells in the area of wound was measured for all the fields and time points (4h, 8h, 24h, 48h) using Image J.



Supplementary Figure 2. Migration of 92.1 UM cells control (CTL) or knock-down (KD) for macroH2A1, with serum starvation. The number of the cells in the area of wound was measured for all the fields and time points (0h, 1h, 4h, 6h, 8h) using Image J.

Immunological analyses reveal an immune subtype of uveal melanoma with a poor prognosis

Hui Pan^{1,2,*}, Linna Lu^{1,2,*}, Junqi Cui^{3,*}, Yuan Yang^{1,2}, Zhaoyang Wang^{1,2}, Xianqun Fan^{1,2}

¹Department of Ophthalmology, Ninth People's Hospital, Shanghai JiaoTong University School of Medicine, Shanghai, China

²Shanghai Key Laboratory of Orbital Diseases and Ocular Oncology, Shanghai, China

³Department of Pathology, Ninth People's Hospital, Shanghai JiaoTong University School of Medicine, Shanghai, China

*Co-first authors

Correspondence to: Zhaoyang Wang, Xianqun Fan; **email:** zhaokekewzy@hotmail.com, fanxq@sjtu.edu.cn

Keywords: immune subtype, uveal melanoma, bioinformatics, immune cell fractions, TCGA

Received: October 20, 2019

Accepted: December 25, 2019

Published: January 18, 2020

Copyright: Pan et al. This is an open-access article distributed under the terms of the Creative Commons Attribution License (CC BY 3.0), which permits unrestricted use, distribution, and reproduction in any medium, provided the original author and source are credited.

ABSTRACT

Uveal melanoma is an aggressive intraocular malignancy that often exhibits low immunogenicity. Metastatic uveal melanoma samples frequently exhibit monosomy 3 or *BAP1* deficiency. In this study, we used bioinformatic methods to investigate the immune infiltration of uveal melanoma samples in public datasets. We first performed Gene Set Enrichment/Variation Analyses to detect immunological pathways that are altered in tumors with monosomy 3 or *BAP1* deficiency. We then conducted an unsupervised clustering analysis to identify distinct immunologic molecular subtypes of uveal melanoma. We used CIBERSORT and ESTIMATE with RNA-seq data from The Cancer Genome Atlas and the GSE22138 microarray dataset to determine the sample-level immune subpopulations and immune scores of uveal melanoma samples. The Kaplan-Meier method and log-rank test were used to assess the prognostic value of particular immune cells and genes in uveal melanoma samples. Through these approaches, we discovered uveal melanoma-specific immunologic features, which may provide new insights into the tumor microenvironment and enhance the development of immunotherapies in the future.

INTRODUCTION

Immune heterogeneity within the tumor microenvironment has been linked to the drug sensitivity and prognosis of patients with various cancer types [1, 2]. Thus, the profiling of immune signatures might uncover biomarkers for targeted therapy and clinical outcome assessment. Recently, datasets from The Cancer Genome Atlas (TCGA) have been used to depict the immune landscapes of multiple tumor types [1]. Researchers have used integrated approaches and multidimensional datasets to determine the infiltration levels and co-infiltration networks of various immune

cell populations in tumors [3, 4]. For instance, genomic data and hematoxylin & eosin image data were used to assess the total lymphocyte infiltration and immune cell fractions of the tumor microenvironment in different cancer types in TCGA [3]. This analysis revealed common immune subtypes, immune gene expression signatures and tumor-extrinsic features, which could be used to identify transcriptional regulatory networks in the tumor microenvironment. Moreover, an extensive immunogenomic analysis of PanCancer TCGA data from 33 diverse cancer types revealed six distinct immune subtypes and various tumor-immune cell interactions [1].

Uveal melanoma (UM) is the most common aggressive intraocular malignancy in adults, and originates from the uveal tract [5]. UM is characterized by different cytogenetic alterations than cutaneous melanoma (CM), and has the potential for hepatic metastasis [6]. Nevertheless, UM and CM share a common lineage that is determined by melanoma-specific neural crest genes [7]. Recently, a comprehensive analysis of 80 UM cases identified four molecularly distinct subtypes. Monosomy 3 (M3) tumors were found to be enriched for genes in immune pathways such as interferon signaling, T cell invasion and cytotoxicity [8]. Several reports have demonstrated that CM is highly infiltrated by immune cells such as CD4 and CD8 cells [9–11]. However, only a subset of UM patients exhibit similar lymphocyte infiltration of their tumors, suggesting that UM immune infiltration is heterogeneous [7]. In liver metastases, the tumor-infiltrating lymphocyte activity is lower in UM patients than in CM patients [5, 7, 12].

The inflammatory phenotype of UM is characterized by high infiltration of lymphocytes and macrophages, and by the expression of human leukocyte antigen (HLA) Class I and II antigens [13]. Mutation of GNA11/GNAQ was not found to significantly alter the immune infiltration and HLA Class I expression of primary UM [14]. However, the nuclear factor kappa-light-chain-enhancer of activated B cells (NF- κ B) pathway was found to be associated with the inflammatory phenotype and high HLA Class I expression, and was upregulated upon the inactivation of *BAP1* in UM. The levels of the NF- κ B pathway molecules NF- κ B1, NF- κ B2 and RELB were reported to correlate positively with the expression of HLA Class I and with the infiltration of T cells and macrophages in UM [15]. Moreover, one of the most significant UM studies revealed that lymphocyte infiltration and tumor-associated M2 macrophage levels were associated with a poor prognosis in primary UM after adjustment for other risk factors [16]. In another study, the authors used a digital PCR-based T cell quantification method to characterize the prognostic value of the T cell count and activated macrophage level in the microenvironment of UM [17]. Thus, characterizing the immunological features of UM may provide novel immune biomarkers for prognostic assessment and immunotherapy.

Immunotherapy through immune checkpoint blockades has displayed promising clinical efficacy in multiple tumor types [18–20]. Enhancing the cytolytic functions of infiltrating lymphocytes can significantly improve antitumor immunity [4]. However, due to the low levels of cytotoxic cells in the tumor microenvironment, non-responsiveness to immunotherapy remains a clinical

challenge. Thus, a deep comprehension of the interplay among the immune cell subsets in the tumor microenvironment is needed for the development of effective antitumor immune therapies. Here, we sought to identify the molecular immune subtypes and infiltrating immune cells of UM, in order to discover possible candidates for immunotherapy.

RESULTS

Identification of M3/*BAP1*-specific immunological pathways using GSEA

BAP1 is frequently mutated in metastatic UM, and is associated with chromosome 3 loss (M3) [16, 21]. Thus, we investigated whether *BAP1*-deficient UM samples exhibited distinct immune infiltration patterns from *BAP1*-intact samples in TCGA. Gene Set Enrichment Analysis (GSEA) was used to develop M3/*BAP1*^{null} aberrant gene signatures and reveal novel immune pathways. The immune-related gene signatures were then used to estimate the level of immune cell infiltration. Among the most significantly altered pathways in M3/*BAP1*^{null} tumors, those involving the CD8/T-cell-receptor, adaptive immune system, pre-B1 lymphocytes and differentiating T lymphocytes were significantly enriched in the M3 group (Figure 1A), consistent with a previous study [22]. In curating the differential gene expression data, we found significant gene expression changes in a variety of immune-associated processes, suggesting that M3/*BAP1*^{null} tumors highly express immune pathway genes.

Next, we performed Gene Set Variation Analysis (GSVA) to compare the sample-level infiltration of M3/*BAP1*^{null} tumors and disomy 3 (D3)/*BAP1*^{intact} tumors. The top 10 significantly enriched immune pathway gene sets were selected. As shown in the heatmap (Figure 1B), the “B-cell receptor signaling” pathway, the “IRF4 targets in plasma cells vs. mature B lymphocytes” pathway and the “peripheral blood mononuclear cell response to ionizing radiation (IR)” pathway were significantly enriched in M3/*BAP1*^{null} tumors, suggesting that IRF4 may enhance immunity in *BAP1* deficient UMs.

To further assess the immune cell subpopulations of M3/*BAP1*^{null} and D3/*BAP1*^{intact} tumors, we compared the relative abundance of immune cells between these two UM subtypes. As shown in Figure 1C, the levels of infiltrating CD8 T cells and T follicular helper cells were significantly higher in M3-subtype tumors (n = 42) than in D3 tumors (n = 38) (P < 0.01, Mann-Whitney test). Of note, D3 tumors were previously reported to have a better prognosis than M3 tumors. In contrast, monocytes and CD4 memory resting cell levels were

higher in D3 tumors than in M3 tumors ($P < 0.01$, Mann-Whitney test).

Hierarchical clustering of immune cell-associated gene expression in UM

We then performed an unsupervised clustering analysis of 730 immune-related genes in the UM dataset of TCGA, as described in a previous study [11]. The sample clustering revealed three clear groups of samples

that separated predominantly according to the gene expression of infiltrating immune cells, here termed the Immune Low (Immune L, $n = 54$, 67.5%), Immune Medium (Immune M, $n = 16$, 20%) and Immune High (Immune H, $n = 10$, 12.5%) groups (Figure 2A). As shown in the heatmap, the Immune H group expressed high levels of the majority of the immune-related genes, in contrast to the Immune L group. The Immune H group highly expressed genes associated with CD8 T cells, B cells and natural killer cells (Figure 2B). The

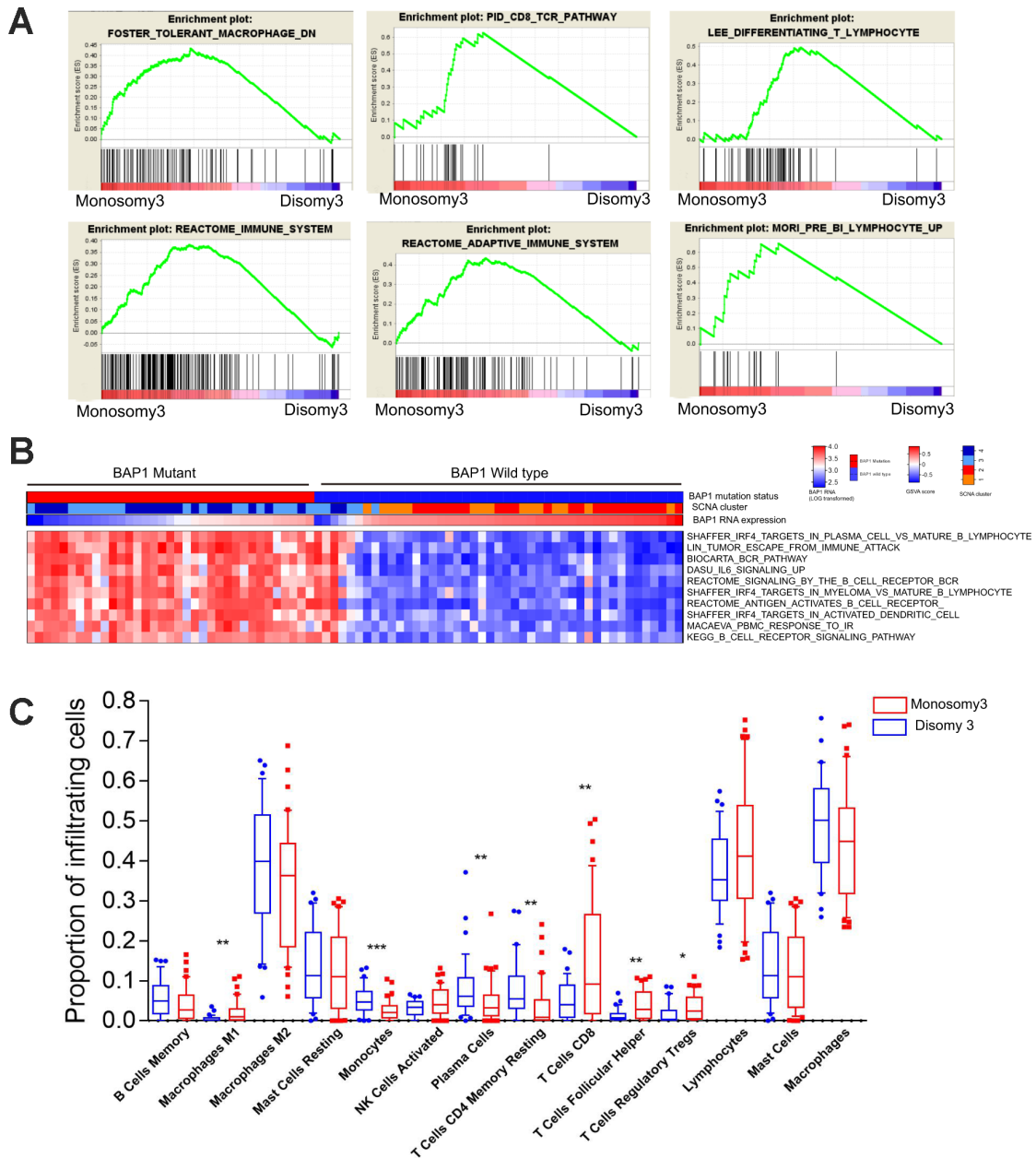


Figure 1. *BAP1*-mutant/M3 UM is enriched in immune signatures. (A) GSEA plots of gene ontology categories, including the immune response, immune system process, adaptive immune response, immune effector process, and regulation of immune system process. (B) GSVA analysis of differing immune pathways between *BAP1*^{wild type} and *BAP1*^{mutant} tumors. (C) Differential proportions of immune cells between D3 and M3 tumors.

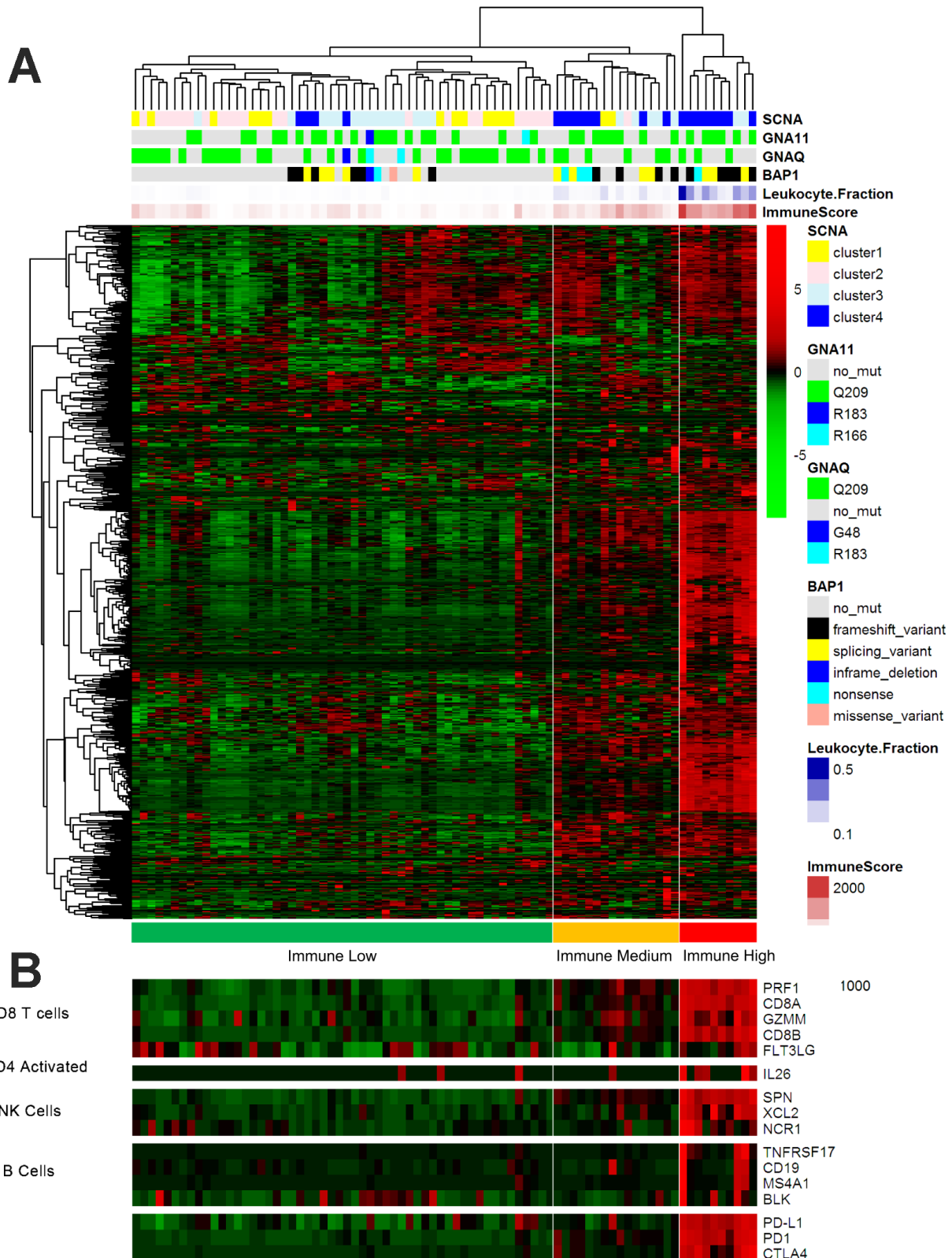


Figure 2. Immune-related gene expression in the UM dataset of TCGA. (A) Hierarchical clustering of 80 tumors based on 730 immune-related genes. Genes were median-centered. Each colored square represents the relative mean transcript abundance (\log_2 FPKM+1) for each sample, with the lowest levels shown in green, the median levels in black and the highest levels in red. The genetic mutation type, SCNA type, immune score, leukocyte fraction and *BAP1* mutation status are shown below the array tree. (B) The expression of selected gene signatures or genes is demonstrated below the heatmap.

inhibitory checkpoint molecules PD-1 and CTLA-4 and the genes directly associated with MHC CLASS I/II, Cytolytic Activity and co stimulatory Molecules were also highly expressed in the Immune H group and modestly expressed in the Immune M group (Supplementary Figure 2).

Next, we sought to determine the clinical and molecular features underlying the immune clustering. The age, American Joint Committee on Cancer stage (AJCC), sex and GNAQ/11 mutation status of the patients did not differ significantly between the Immune H group and the Immune L and M groups (Immune H vs. M vs. L). Interestingly, the *BAP1* mutation status differed significantly among the groups ($P < 0.0001$, Fisher's exact test, Immune H vs. M vs. L). Similarly, a significant difference in somatic copy number alteration (*SCNA1/2* vs. 3/4) was found among the groups ($P < 0.0001$, Fisher's exact test, Immune H vs. M vs. L) (Table 1). Our analysis suggested that *BAP1* mutations and chromosome alterations may determine the tumor immune state and immune infiltration of UM.

Immune subtypes correlated with immune infiltration and clinical outcomes

ESTIMATE (Estimation of STromal and Immune cells in MAlignant Tumor tissues using Expression data) is a tool for predicting tumor purity and assessing stromal/immune cell infiltration into tumor tissues based on gene expression data [23]. We used the ESTIMATE algorithm to calculate the immune score and stromal score for each UM sample from TCGA, and we compared the scores of the different immune subgroups. Since the immune score reflects the overall immune infiltration based on lymphocyte gene expression, we used this score to estimate the total immune cell infiltration of each sample. The Immune L group demonstrated the lowest immune and stromal scores, whereas the Immune M and Immune H groups displayed modest and high stromal and immune scores, respectively ($P < 0.0001$, analysis of variance [ANOVA], Immune H vs. M vs. L) (Figure 3A). The tumor purity calculated by the ESTIMATE algorithm revealed that the Immune L group was the purest subtype (mean 0.9373) and the Immune H group was the least pure subtype (mean 0.7649) ($P < 0.0001$, ANOVA) (Figure 3A).

To further examine the tumor microenvironment, we assessed the infiltration of distinct immune subpopulations in the three tumor subtypes. The Immune L group had the lowest levels of CD8 T cells and total lymphocytes, whereas the Immune M and Immune H subtypes displayed relatively high levels of these cell types ($P < 0.0001$, Immune H vs. M vs. L). In addition,

the Immune H group had lower levels of M2 macrophages and mast cells than the other two groups. The Immune L group also exhibited low infiltration of T follicular helper cells and regulatory T cells ($P < 0.0001$, Immune H vs. M vs. L) (Figure 3B), suggesting that there are distinct subtypes of UM with low or high T cell infiltration.

Next, we investigated the prognostic impact of immune clustering on patient survival. Interesting, we observed significantly worse overall survival (OS) and progression-free intervals (PFIs) in the Immune M and Immune H groups than in the Immune L group in the cohort from TCGA, suggesting that distinct immunological features correlate with the patient prognosis in UM (Figure 3C). However, the OS and PFI did not differ significantly between the Immune M and H groups (log-rank test, $P > 0.05$, Immune H vs. M).

Correlations of immune cells and immune scores in TCGA and Laurent datasets

Next, we performed a hierarchical clustering analysis of the pairwise correlations between the different immune subpopulations in UM samples from TCGA (Figure 4A). The heatmap revealed high correlations among several types of immune cells associated with cytotoxic T cell infiltration (i.e., lymphocytes, regulatory T cells, T follicular helper cells, M1 macrophages and CD8 T cells). We obtained similar results using Laurent microarray data (Figure 4B). Therefore, we concluded that the identified immune cells were significantly associated with immune infiltration in the tumor microenvironment.

We then examined the correlations between other immune parameters for UM patients in TCGA and Laurent UM dataset, and found a significant correlation between the immune score and the stromal score (Spearman's $r = 0.806$, 0.7789 , respectively; Supplementary Figure 4A and 4B). We also observed a strong correlation between the immune score and T cell infiltration (Spearman's $r = 0.7633$, 0.4993 , respectively; Supplementary Figure 4A and 4B). Additionally, a significant inverse correlation was found between the immune score and tumor purity (Spearman's $r = -0.9758$, $r = -0.9651$ Supplementary Figure 4A and 4B). In the Laurent UM dataset, the association between the immune score and CD8 T cell infiltration remained significant (Supplementary Figure 4A and 4B), supporting the ability of the immune score to predict immune infiltration. Therefore, the immune score based on immune marker gene expression reflected immune cell infiltration in both the UM TCGA RNA-seq dataset and an independent microarray dataset.

Table 1. Clinical–pathologic characteristics of the TCGA Dataset in this study.

N	N(%)
Age, median (range)	60 (22–86)
Sex	
Female	35(43.8%)
Male	45(56.2%)
AJCC Clinical Stage	
II	36(45%)
III/IV	44(55%)
Histological type	
Epithelioid cell dominant	23(28.8%)
Spindle Cell dominant	57(71.2%)
GNAQ/11 status	
Mutation	74(92.5%)
Wild type	6(7.5%)
BAP1 status	
Mutation	35(43.8%)
Wild type	45(56.2%)
Monosomy3	
Monosomy3/LOH	42(52.5%)
Disomy3	38(47.5%)
SCNA	
1/2	38(47.5%)
3/4	42(52.5%)

Prognostic value of immune cells and immune scores in TCGA and Laurent datasets

To assess the prognostic value of immune cells in UM, we first used a Univariate Cox regression model to investigate the associations of different immune subpopulations with the OS and PFI of patients in TCGA. The infiltration of M1 macrophages, activated natural killer cells and CD8 T cells was associated with a worse prognosis in the UM datasets (Figure 5A). On the contrary, the infiltration of monocytes was positively associated with patient survival (Figure 5A, 5B). In general, the infiltration of immune subpopulations involved in adaptive immunity is more likely to be an unfavorable prognostic factor than the infiltration of subpopulations involved in innate immunity.

To determine whether the immune score could predict the prognosis of UM patients in TCGA, we used a Kaplan-Meier curve and log-rank test to estimate the hazard ratios (HRs) of OS and the PFI. High immune scores and stromal scores were associated with worse OS in the datasets of TCGA (HR=6.721, P<0.0001, Figure 5B) and GSE22138 (HR=2.508, P=0.02,

Supplementary Figure 1A). Next, we determined the associations of different immune cells with the patient prognosis. Consistent with the Univariate Cox regression analysis, our survival analysis revealed that particular immune subpopulations (M1 and M0 macrophages, CD8 T cells and T follicular helper cells) were associated with a worse prognosis, whereas total CD4 cells were associated with a better prognosis in the UM dataset of TCGA. Similar results were obtained with the GSE22138 dataset (Supplementary Figure 1B). These results suggest that UM patients with greater infiltration of immune cells and effector molecules exhibit poorer survival and may benefit from immunotherapies.

Immune marker genes predict the prognosis of UM patients

Next, we examined the prognostic value of individual immune genes in predicting patient survival. Higher mRNA levels of *CD8A* (P<0.0001), *HLA-A* (P<0.0001), *HLA-B* (P=0.0001), *HLA-C* (P=0.0003) and *HLA-DRA* (P=0.0001) in TCGA samples were associated with significantly shorter OS and PFIs (Figure 6A, 6B). Similarly, higher levels of *HLA-A* (P=0.02), *HLA-B*

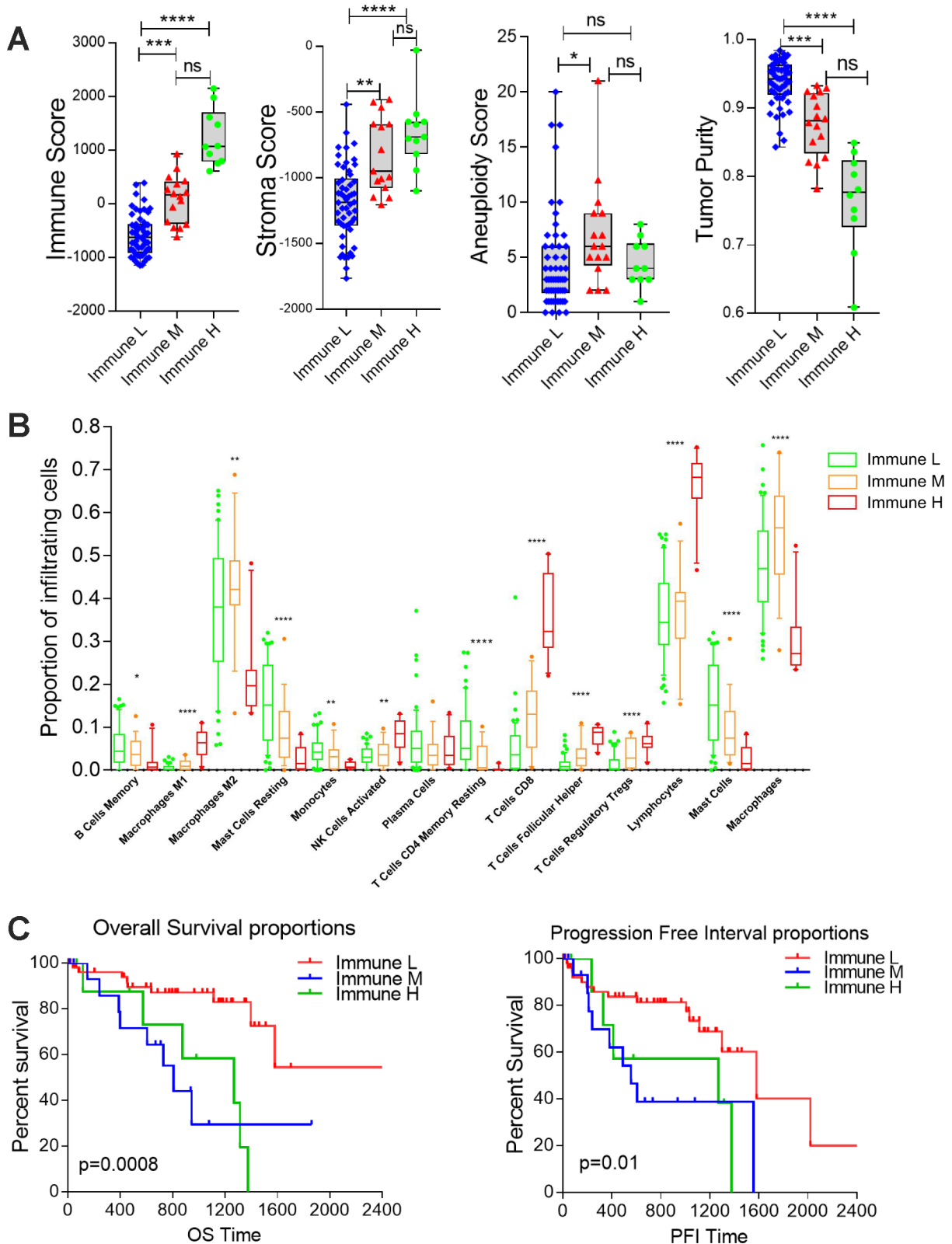


Figure 3. Differential infiltration of the immune subgroups. (A) Box plots comparing the distribution of immune infiltration measures in the three immune subtypes. Each box spans the interquartile range, with the lines representing the median for each group. Whiskers represent the absolute range. All outliers are included in the plot. (B) Differential proportions of immune cells in the immune subtypes. (C) Kaplan-Meier survival curves demonstrate that the Immune M and H groups of UM patients consistently exhibited worse OS and PFIs than the Immune L group (log-rank test, $P < 0.05$).

($P=0.002$), *HLA-C* ($P=0.007$) and *HLA-DRA* ($P=0.03$) were associated with significantly shorter metastasis-free survival in the 63 patients in the Laurent UM dataset (Figure 6C), and *CD8A* expression ($P=0.06$) displayed a similar but non-significant trend of association with metastasis-free survival.

DISCUSSION

TCGA has illuminated the genomic data from bulk tumor samples, and has provided detailed information about the tumor immune microenvironment [1, 24–26]. In previous studies, low immune cell infiltration has been associated with poor clinical outcomes for patients with different cancers [1, 27]. Through gene expression profiling, researchers can identify prognostic gene signatures and detect candidate genes for targeted therapies [27]. For example, an immune score based on gene expression data was found to correlate significantly with recurrence-free survival in thyroid cancer patients, regardless of their BRAF(V600E) status [28]. The fraction of immune cells in clinical tumor samples can be evaluated by multiple algorithms; indeed, aside from curating samples and performing basic pathologic characterization, investigators can analyze digitized hematoxylin & eosin-stained images of TCGA samples for tumor-infiltrating lymphocytes [3]. Using TCGA data, we identified three distinct immune subtypes of

UM, with prognostic implications for immunological cancer management. The immune score was strongly associated with immune infiltration and poor outcomes, regardless of the tumor genome ploidy of the UM tumor samples. The underlying mechanism needs to be explored.

Genomic and transcriptomic data have been used to detect immune infiltration and to determine the molecular subtypes of ovarian cancer, melanoma and pancreatic cancer [29–31]. For instance, DNA sequencing data have been used to connect the neoantigen load to the T cell response and to link somatic mutations to immune infiltration [1, 32]. More recently, deconvoluted expression data have been used to measure the cytolytic activity in the tumor microenvironment and to quantify the infiltration of individual immune cell subsets [33–35]. A common theme across these studies is the integration of several types of genomic and clinical data, allowing for associations to be made among immune activity, gene expression, the mutation burden and patient survival. In this study, we examined the immune infiltration of UM samples through a single-sample GSEA and deconvolution method based on publicly available data in TCGA and the Gene Expression Omnibus. Our results suggested that the infiltration of immune cells differs markedly among immune subtypes. This analysis may

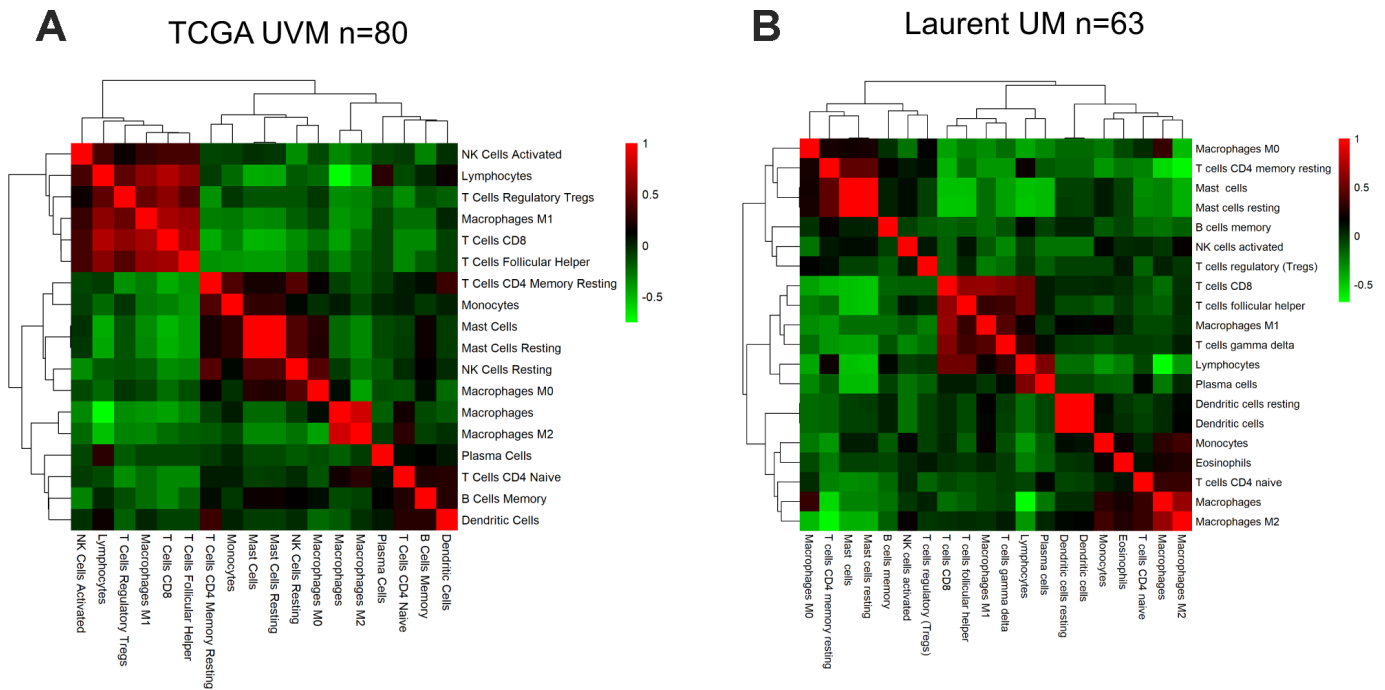


Figure 4. The correlation between the immune score and immune cell infiltration in UM. Pairwise correlation heatmap among immune cell-type scores in the datasets from TCGA (A) and GSE22138 (B).

ultimately reveal prognostic gene signatures and provide candidate genes for targeted therapies.

Despite the great success of immunotherapies against metastatic and late-stage melanoma [36, 37], immunotherapy has had limited success in UM [38]. UM

is considered to be an immunotherapy-resistant subtype of melanoma, and UM patients are frequently excluded from clinical trials of immunotherapies for metastatic melanoma [20, 39, 40]. Although higher cytotoxic expression patterns are associated with better anti-tumor response and better patient survival in many solid

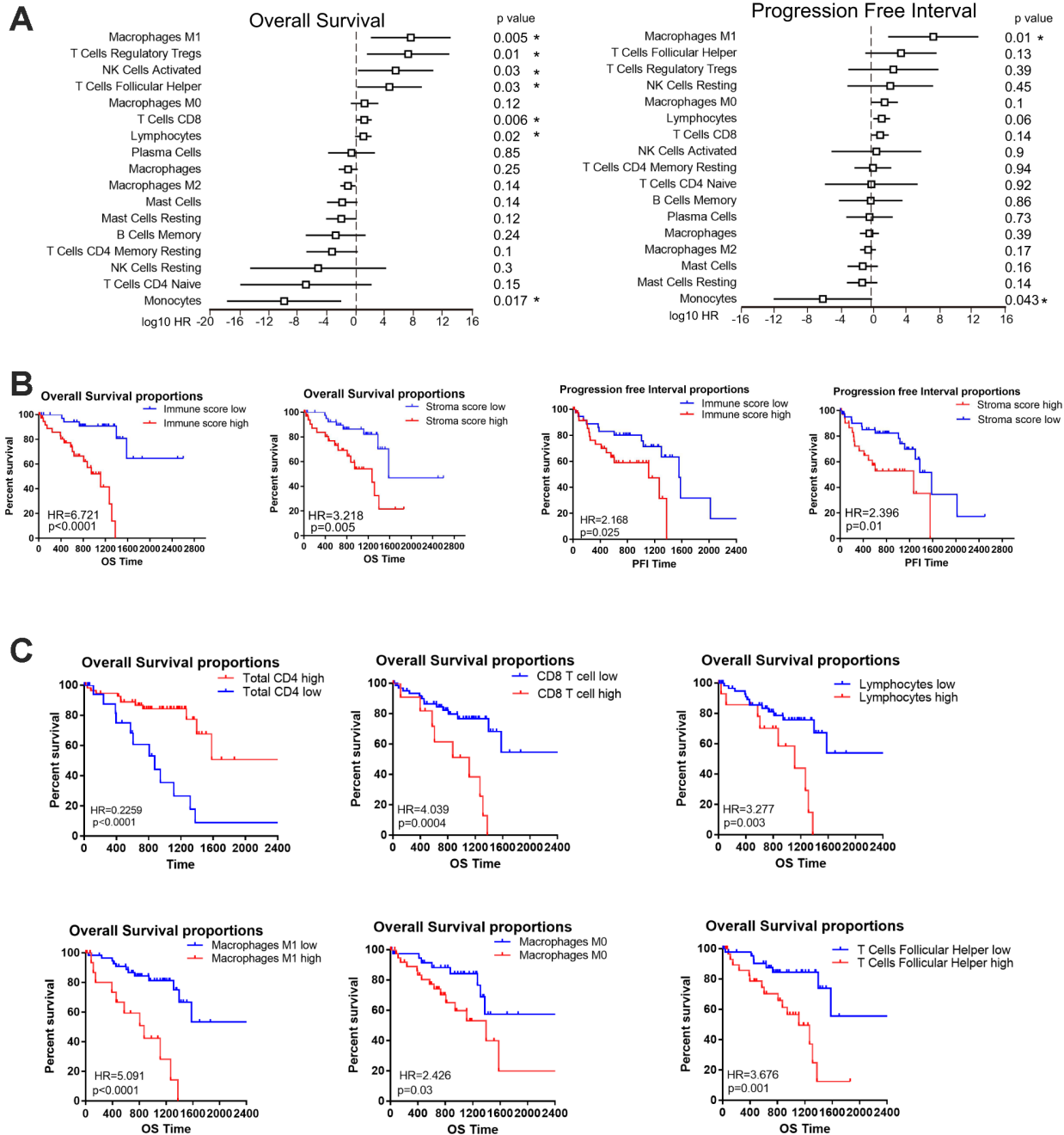


Figure 5. The prognostic value of the immune score and immune cell infiltration in UM. (A) HRs of OS and the PFI based on the infiltration of various immune cells (as continuous variables) in all patients (left); the horizontal bars represent the 95% confidence intervals of the HRs. Statistically significant variables are shown. Each cell type was evaluated individually and rank-ordered based on the estimated HR. (B) Kaplan-Meier survival analysis based on immune score and stroma score. Patients were divided into the high and low groups based on the level of immune score and stroma score. (C) Kaplan-Meier survival analysis based on selected immune cells. Patients were divided into the high and low groups based on their expression of each cell.

tumors [34, 41, 42], the prognostic effects of immune infiltration depend on the type of tumor, the location of the cells and the state of activation. In UM, high levels of immune cells are associated with poor prognostic factors, such as M3 and *BAP1* mutation [15, 17, 43]. Immune cell infiltration occurs more frequently in epithelioid-cell-type UM, which also has a poor prognosis [44]. Crosstalk in the tumor microenvironment can promote the inflammatory response in cancer cells. Cancer cells may also promote the type 2 differentiation of macrophages and neutrophils, and may attract myeloid-derived suppressor cells and regulatory T cells to tumor sites. Thus, we speculate that UM cells may utilize immune cells for their survival and protection from immunological attack. The immunomodulatory microenvironment in the liver could further protect escaped UM cells from systemic immune surveillance [5, 44, 45].

De Lange et al have used unsupervised clustering to investigate the gene expression profiles of 64 enucleated eyes from UM patients, and divided them into class I tumors with a good prognosis and class IIa and IIb

tumors with a poor prognosis [46]. Their study revealed an immune phenotype with a different prognosis. High expression of immune-related genes in class IIb UM suggested that the tumors were inflamed. Furthermore, study from TCGA of UM showed that the genes encoding chemotactic signals (e.g., *CXCL9* and *CXCL13*), MHC class I (A, B, C) and MHC class II (DP, DM, DOA, DOB, DQ and DR) were upregulated in M3 patients [22]. Consistent with the previous studies, we demonstrated that *BAP1* inactivation was associated with immune infiltration and immune marker gene set expression, indicating the *BAP1* may regulate tumor immunology. GSEA results suggested that *IRF4* targets and *BCR* pathways may be induced in *BAP1*-deficient tumors. Loss of *BAP1* expression is also associated with an increased infiltration of T cell follicular helper, Treg and CD8+ T cells, suggesting an inflammatory tumor microenvironment. Our data demonstrated that the immune cell subpopulations were differentially distributed between M3/*BAP1*null and D3/*BAP1*intact tumors, suggesting that *BAP1* null tumors might be prioritized for immune checkpoint blockade therapies in UM.

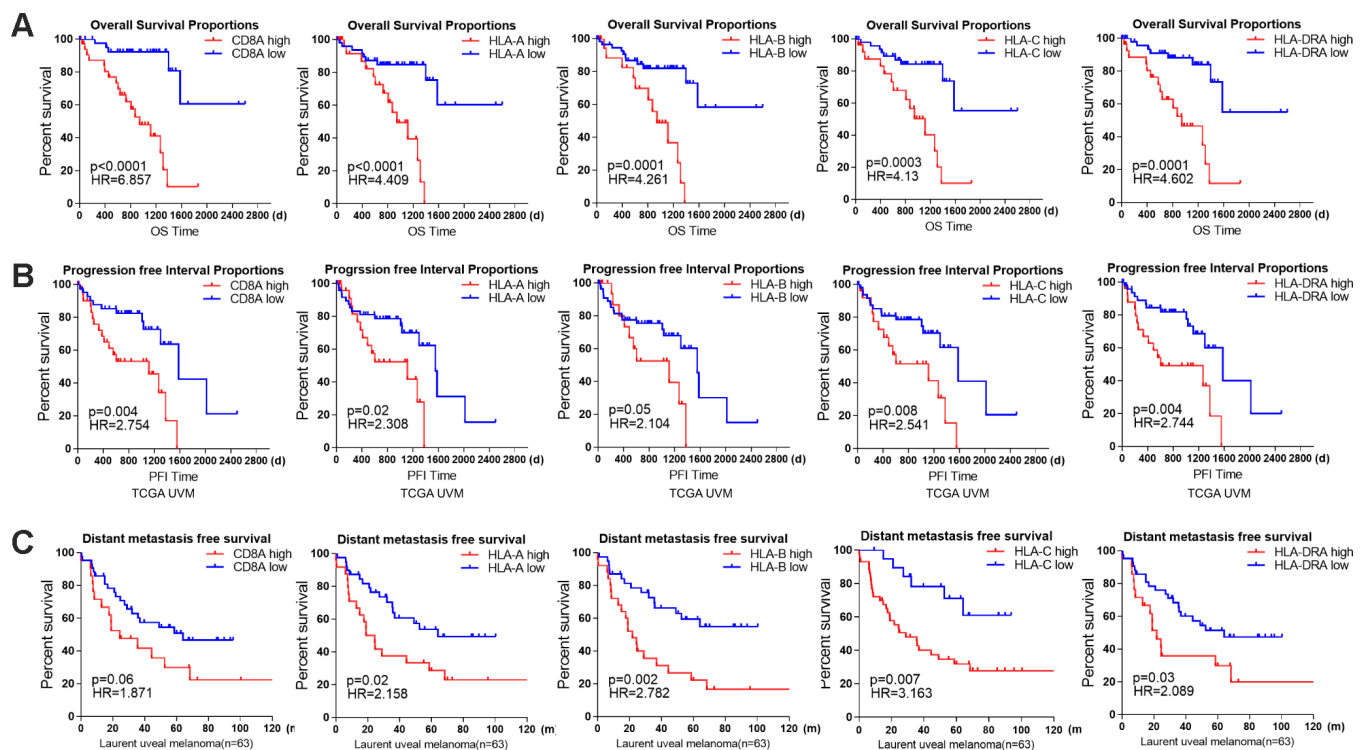


Figure 6. The prognostic value of individual immune genes in UM. (A) Kaplan-Meier survival curves demonstrate that elevated levels of CD8A ($P<0.0001$), HLA-A ($P<0.0001$), HLA-B ($P=0.0001$), HLA-C ($P=0.0003$) and HLA-DRA ($P=0.0001$) were consistently associated with worse OS in the UM dataset of TCGA. (B) Kaplan-Meier survival curves demonstrate that elevated levels of CD8A, HLA-A, HLA-B, HLA-C and HLA-DRA were consistently associated with a worse PFI in the UM dataset of TCGA (log-rank test, $P<0.05$). (C) Kaplan-Meier survival curves demonstrate that elevated levels of CD8A ($P=0.06$), HLA-A ($P=0.02$), HLA-B ($P=0.002$), HLA-C ($P=0.007$) and HLA-DRA ($P=0.03$) were consistently associated with worse metastasis-free survival in the Laurent UM dataset ($n=63$; log-rank test, $P<0.05$).

At the time of this work, large, publicly available gene expression profiling datasets of UM patients treated with immune checkpoint blockers were not available. In addition, clinical trials in immunotherapy are being deployed earlier in the course of the disease, whereas the cohort in TCGA is more representative of the clinical population. We hope that large sequencing data from UM patients undergoing immune checkpoint blocker treatment will emerge in the future. Nevertheless, our analysis of the available datasets has advanced the application of genomic data to tumor immunology. The immune features reported herein should be considered for integration into prognostic models, or explored as predictors of adjuvant immune therapy responsiveness in patients with *BAP1*-deficient UM.

MATERIALS AND METHODS

UM gene expression datasets

RNA-seq data for UM samples were generated by TCGA and downloaded from the Genomic Data Commons Data Portal (<https://portal.gdc.cancer.gov/>). This dataset includes normalized gene expression profiles for 80 tumor samples in FPKM (Fragments Per Kilobase of transcript per Million fragments mapped). We downloaded one additional microarray gene expression dataset from the Gene Expression Omnibus database (accession number: GSE22138 [6]; n=63) to verify the immune scores and gene signatures and to predict the patients' prognoses. GSE22138 included information on metastasis-free survival, while the UM dataset from TCGA included data on patients' OS and PFI from the supplemental file of a previous study [1]. The clinical information and molecular data for the UM samples from TCGA were also downloaded from the supplemental file of a previous study [8]. The clinical information included the age, sex, metastatic status, histology cell type, American Joint Committee on Cancer clinical stage, mutation data, SCNA data and vital status of the patients.

We used the complete linkage method for hierarchical clustering analysis of the tumor samples, immune cell types and genes. The hierarchical clustering algorithm is agglomerative in that it joins samples based on a measure of multivariate distance, and prevents the joined samples from clustering independently again. Pair-wise joins in samples are represented as combined branches of a tree in a Dendrogram Plot. Pearson's correlation distance method was used to determine whether samples clustered together [47].

ESTIMATE

ESTIMATE is a tool that predicts tumor purity and detects infiltrating stromal/immune cells in tumor tissues

based on gene expression data [23]. The ESTIMATE algorithm calculates the stromal and immune scores by performing single-sample GSEA for each sample. Data on the leukocyte fractions of the 80 tumor aliquots from TCGA were obtained from a previous study [1].

CIBERSORT (immune cellular fraction estimates)

The relative fractions of 22 immune cell types within the leukocyte compartment were estimated with CIBERSORT (Cell-type Identification By Estimating Relative Subsets Of RNA Transcripts) [33]. CIBERSORT requires a specialized knowledgebase of gene expression signatures, termed a "signature matrix," to deconvolute cell types of interest. CIBERSORT uses a set of 22 immune cell reference profiles (LM22) [33] to derive a base (signature) matrix that can be applied to mixed samples to determine the relative proportions of immune cells. LM22 is a signature matrix file consisting of 547 genes that can precisely distinguish 22 mature human hematopoietic populations (from peripheral blood or *in vitro* culture), including seven T cell types, naïve and memory B cells, plasma cells, natural killer cells, myeloid subsets, etc. LM22 can be applied to RNA-seq data as well as to microarray data. We used CIBERSORT to re-quantify several key immune gene signatures from GSE22138, and to identify the immune cells in the dataset from TCGA, as in a previous PanCancer immune study [1].

Predicting patient survival with the Cox proportional hazards model

A Cox proportional hazards regression model was used to investigate the effectiveness of immune cells in predicting patients' survival (PFI or OS). The optimal cut-off values of the proportions of immune cells in the cohort from TCGA were calculated based on their prognostic effects in X-Tile software [48]. The UM samples were then divided into high and low groups based on the cut-off point for the fraction level of each type of immune cell. In the subsequent scoring formula, the immune cell fraction level was given a value of 0 or 1. In STATA15, a univariate Cox proportional hazards model was used to evaluate the effects of significant prognostic immune cell fractions on survival outcomes. Kaplan-Meier plots were used to visualize the differences in survival between groups. The survival proportions of the different groups were compared through a log-rank test.

GSVA

GSVA was performed as previously described [49] with the curated gene set collection of the Molecular Signatures Database (Broad Institute, c2. CP CPG). We

searched for significant pathway gene sets that were differentially enriched between the *BAP1*^{null} and *BAP1*^{intact} groups (FDR≤0.01). The top 10 immune-related pathways were selected and shown in the heatmap.

GSEA

Gene set collections for canonical pathways (C2.CP canonical pathways) were downloaded from the Molecular Signatures Database version 6.2 (www.broadinstitute.org/gsea/msigdb/collections.jsp). Gene set enrichment scores were calculated [50] with GSEA package version 1.32.0 with RNA-seq parameters. Differential gene set enrichment was determined using the limma package. The thresholds for statistical significance are noted in the Results.

Statistical methods

All statistical analyses in this study were performed with R version 3.2.0 (R Foundation for Statistical Computing, Vienna, Austria) and SPSS Statistics 22.0. Survival curves were generated by the Kaplan-Meier method, and the log-rank test was used to compare the survival curves. The thresholds for each Kaplan-Meier plot were determined based on the unique score distribution of each dataset in X-Tile software [48]. We used Spearman's rank correlation coefficients to evaluate the correlation between the immune score and immune cell infiltration. The immune scores and stromal scores stratified by subgroup were compared by one-way ANOVA. A two-tailed P-value <0.05 was considered statistically significant.

Abbreviations

AJCC: American Joint Committee on Cancer stage; ANOVA, analysis of variance; CIBERSORT: Cell-type Identification By Estimating Relative Subsets Of RNA Transcripts; CM: cutaneous melanoma; D3: Disomy3; ESTIMATE: Estimation of STromal and Immune cells in MAlignant Tumor tissues using Expression data; FPKM: Fragments Per Kilobase of transcript per Million fragments mapped; GSEA/GSVA: Gene Set Enrichment/Variation Analysis; HR: hazard ratio; IR: Ionizing radiation; M3: Monosomy3; PFI: Progression-free interval; SCNA: somatic copy number alteration; TCGA: The Cancer Genome Atlas; UM: Uveal melanoma.

AUTHOR CONTRIBUTIONS

Pan H designed and drafted the manuscript; Lu L analyzed the data; Cui J and Yang Y reviewed and edited

the figures; Wang Z and Fan X discussed and approved the manuscript. All authors approved this manuscript.

CONFLICTS OF INTEREST

The author(s) declare that they have no conflicts of interest.

FUNDING

The work was supported by the National Key R&D Program of China (2018YFC1106100, 2018YFC1106101), The Science and Technology Commission of Shanghai (17DZ2260100, 19JC1410200), the National Natural Science Foundation of China (Grant U1932135, 81770934, 81702781), Shanghai Municipal Education Commission- Gaofeng Clinical Medicine Grant Support (20181810).

REFERENCES

1. Thorsson V, Gibbs DL, Brown SD, Wolf D, Bortone DS, Ou Yang TH, Porta-Pardo E, Gao GF, Plaisier CL, Eddy JA, Ziv E, Culhane AC, Paull EO, et al. The Immune Landscape of Cancer. *Immunity*. 2018; 48:812–830.e14. <https://doi.org/10.1016/j.immuni.2018.03.023> PMID:[29628290](https://pubmed.ncbi.nlm.nih.gov/29628290/)
2. Cesano A, Warren S. Bringing the next Generation of Immuno-Oncology Biomarkers to the Clinic. *Biomedicines*. 2018; 6:E14. <https://doi.org/10.3390/biomedicines6010014> PMID:[29393888](https://pubmed.ncbi.nlm.nih.gov/29393888/)
3. Saltz J, Gupta R, Hou L, Kurc T, Singh P, Nguyen V, Samaras D, Shroyer KR, Zhao T, Batiste R, Van Arnam J; Cancer Genome Atlas Research Network, Shmulevich I, et al. Spatial Organization and Molecular Correlation of Tumor-Infiltrating Lymphocytes Using Deep Learning on Pathology Images. *Cell Rep*. 2018; 23:181–193.e7. <https://doi.org/10.1016/j.celrep.2018.03.086> PMID:[29617659](https://pubmed.ncbi.nlm.nih.gov/29617659/)
4. Varn FS, Wang Y, Mullins DW, Fiering S, Cheng C. Systematic Pan-Cancer Analysis Reveals Immune Cell Interactions in the Tumor Microenvironment. *Cancer Res*. 2017; 77:1271–82. <https://doi.org/10.1158/0008-5472.CAN-16-2490> PMID:[28126714](https://pubmed.ncbi.nlm.nih.gov/28126714/)
5. Oliva M, Rullan AJ, Piulats JM. Uveal melanoma as a target for immune-therapy. *Ann Transl Med*. 2016; 4:172. <https://doi.org/10.21037/atm.2016.05.04> PMID:[27275485](https://pubmed.ncbi.nlm.nih.gov/27275485/)
6. Laurent C, Valet F, Planque N, Silveri L, Maacha S, Anezo O, Hupe P, Plancher C, Reyes C, Albaud B,

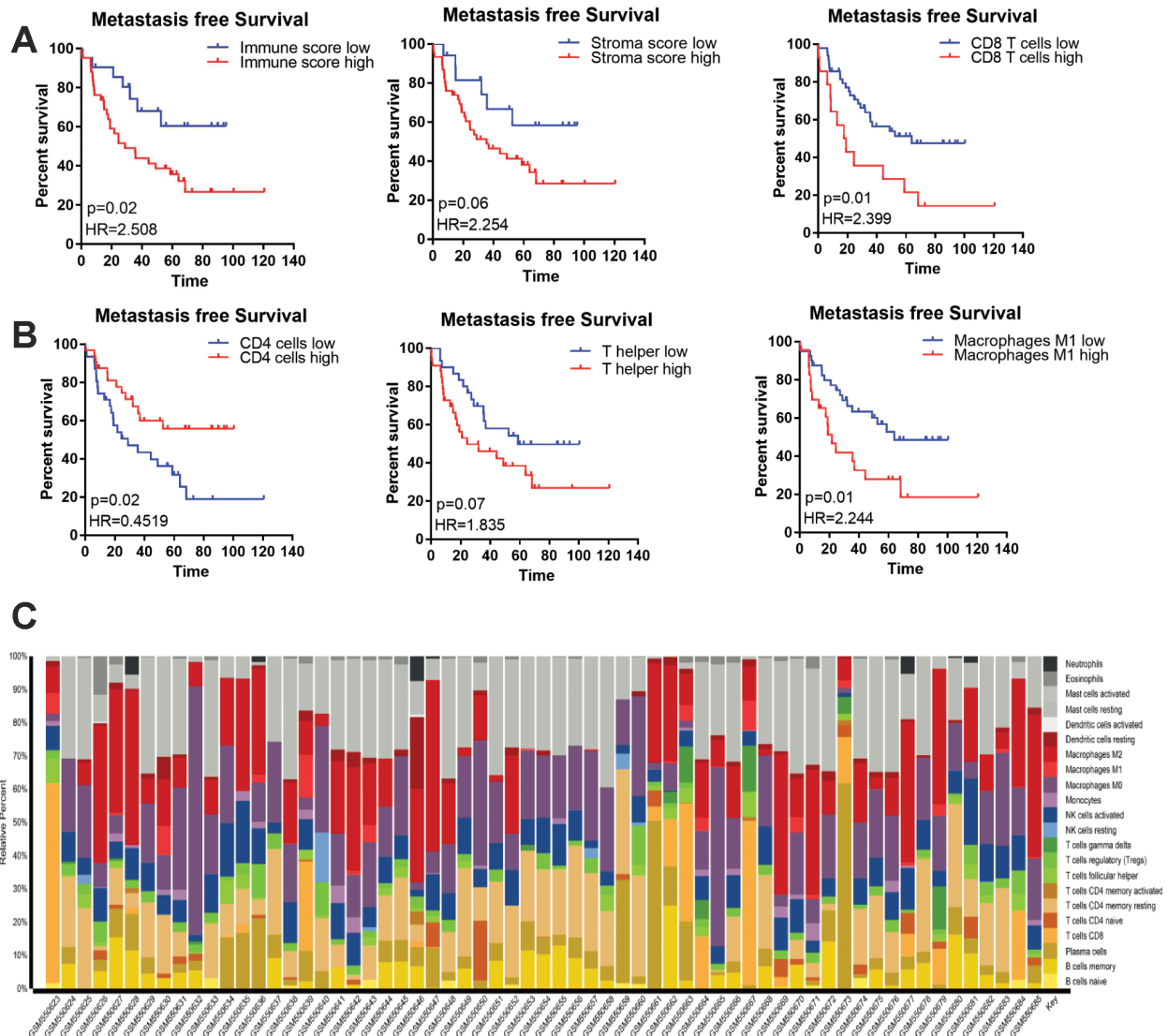
- Rapinat A, Gentien D, Couturier J, et al. High PTP4A3 phosphatase expression correlates with metastatic risk in uveal melanoma patients. *Cancer Res.* 2011; 71:666–74.
<https://doi.org/10.1158/0008-5472.CAN-10-0605>
PMID:[21135111](https://pubmed.ncbi.nlm.nih.gov/21135111/)
7. Rothermel LD, Sabesan AC, Stephens DJ, Chandran SS, Paria BC, Srivastava AK, Somerville R, Wunderlich JR, Lee CC, Xi L, Pham TH, Raffeld M, Jailwala P, et al. Identification of an Immunogenic Subset of Metastatic Uveal Melanoma. *Clin Cancer Res.* 2016; 22:2237–49.
<https://doi.org/10.1158/1078-0432.CCR-15-2294>
PMID:[26712692](https://pubmed.ncbi.nlm.nih.gov/26712692/)
 8. Robertson AG, Shih J, Yau C, Gibb EA, Oba J, Mungall KL, Hess JM, Uzunangelov V, Walter V, Danilova L, Lichtenberg TM, Kucherlapati M, Kimes PK, et al. Integrative Analysis Identifies Four Molecular and Clinical Subsets in Uveal Melanoma. *Cancer Cell.* 2017; 32:204–220.e15.
<https://doi.org/10.1016/j.ccell.2017.07.003>
PMID:[28810145](https://pubmed.ncbi.nlm.nih.gov/28810145/)
 9. Bertrand F, Montfort A, Marcheteau E, Imbert C, Gilhodes J, Filleron T, Rochaix P, Andrieu-Abadie N, Levade T, Meyer N, Colacios C, Ségui B. TNF α blockade overcomes resistance to anti-PD-1 in experimental melanoma. *Nat Commun.* 2017; 8:2256.
<https://doi.org/10.1038/s41467-017-02358-7>
PMID:[29273790](https://pubmed.ncbi.nlm.nih.gov/29273790/)
 10. Iglesia MD, Parker JS, Hoadley KA, Serody JS, Perou CM, Vincent BG. Genomic Analysis of Immune Cell Infiltrates Across 11 Tumor Types. *J Natl Cancer Inst.* 2016; 108:djw144.
<https://doi.org/10.1093/jnci/djw144>
PMID:[27335052](https://pubmed.ncbi.nlm.nih.gov/27335052/)
 11. Prat A, Navarro A, Paré L, Reguart N, Galván P, Pascual T, Martínez A, Nuciforo P, Comerma L, Alos L, Pardo N, Cedrés S, Fan C, et al. Immune-Related Gene Expression Profiling After PD-1 Blockade in Non-Small Cell Lung Carcinoma, Head and Neck Squamous Cell Carcinoma, and Melanoma. *Cancer Res.* 2017; 77:3540–50.
<https://doi.org/10.1158/0008-5472.CAN-16-3556>
PMID:[28487385](https://pubmed.ncbi.nlm.nih.gov/28487385/)
 12. Qin Y, Petaccia de Macedo M, Reuben A, Forget MA, Haymaker C, Bernatchez C, Spencer CN, Gopalakrishnan V, Reddy S, Cooper ZA, Fulbright OJ, Ramachandran R, Wahl A, et al. Parallel profiling of immune infiltrate subsets in uveal melanoma versus cutaneous melanoma unveils similarities and differences: A pilot study. *Oncoimmunology.* 2017; 6:e1321187.
<https://doi.org/10.1080/2162402X.2017.1321187>
PMID:[28680759](https://pubmed.ncbi.nlm.nih.gov/28680759/)
 13. Sourì Z, Wierenga AP, Mulder A, Jochemsen AG, Jager MJ. HLA Expression in Uveal Melanoma: An Indicator of Malignancy and a Modifiable Immunological Target. *Cancers (Basel).* 2019; 11:E1132.
<https://doi.org/10.3390/cancers11081132>
PMID:[31394860](https://pubmed.ncbi.nlm.nih.gov/31394860/)
 14. van Weeghel C, Wierenga AP, Versluis M, van Hall T, van der Velden PA, Kroes WG, Pfeffer U, Luyten GP, Jager MJ. Do GNAQ and GNA11 Differentially Affect Inflammation and HLA Expression in Uveal Melanoma? *Cancers (Basel).* 2019; 11:E1127.
<https://doi.org/10.3390/cancers11081127>
PMID:[31394807](https://pubmed.ncbi.nlm.nih.gov/31394807/)
 15. Sourì Z, Wierenga AP, van Weeghel C, van der Velden PA, Kroes WG, Luyten GP, van der Burg SH, Jochemsen AG, Jager MJ. Loss of BAP1 Is Associated with Upregulation of the NF κ B Pathway and Increased HLA Class I Expression in Uveal Melanoma. *Cancers (Basel).* 2019; 11:E1102.
<https://doi.org/10.3390/cancers11081102>
PMID:[31382450](https://pubmed.ncbi.nlm.nih.gov/31382450/)
 16. Bronkhorst IH, Vu TH, Jordanova ES, Luyten GP, Burg SH, Jager MJ. Different subsets of tumor-infiltrating lymphocytes correlate with macrophage influx and monosomy 3 in uveal melanoma. *Invest Ophthalmol Vis Sci.* 2012; 53:5370–78.
<https://doi.org/10.1167/iovs.11-9280>
PMID:[22743317](https://pubmed.ncbi.nlm.nih.gov/22743317/)
 17. de Lange MJ, Nell RJ, Lalai RN, Versluis M, Jordanova ES, Luyten GP, Jager MJ, van der Burg SH, Zoutman WH, van Hall T, van der Velden PA. Digital PCR-Based T-cell Quantification-Assisted Deconvolution of the Microenvironment Reveals that Activated Macrophages Drive Tumor Inflammation in Uveal Melanoma. *Mol Cancer Res.* 2018; 16:1902–11.
<https://doi.org/10.1158/1541-7786.MCR-18-0114>
PMID:[30093564](https://pubmed.ncbi.nlm.nih.gov/30093564/)
 18. Combe P, de Guillebon E, Thibault C, Granier C, Tartour E, Oudard S. Trial Watch: therapeutic vaccines in metastatic renal cell carcinoma. *Oncoimmunology.* 2015; 4:e1001236.
<https://doi.org/10.1080/2162402X.2014.1001236>
PMID:[26155388](https://pubmed.ncbi.nlm.nih.gov/26155388/)
 19. Hammers H. Immunotherapy in kidney cancer: the past, present, and future. *Curr Opin Urol.* 2016; 26:543–47.
<https://doi.org/10.1097/MOU.0000000000000338>
PMID:[27533501](https://pubmed.ncbi.nlm.nih.gov/27533501/)
 20. Wierenga AP, Cao J, Luyten GP, Jager MJ. Immune Checkpoint Inhibitors in Uveal and Conjunctival Melanoma. *Int Ophthalmol Clin.* 2019; 59:53–63.
<https://doi.org/10.1097/IIO.0000000000000263>
PMID:[30908279](https://pubmed.ncbi.nlm.nih.gov/30908279/)

21. Harbour JW, Onken MD, Roberson ED, Duan S, Cao L, Worley LA, Council ML, Matattal KA, Helms C, Bowcock AM. Frequent mutation of BAP1 in metastasizing uveal melanomas. *Science*. 2010; 330:1410–13.
<https://doi.org/10.1126/science.1194472>
PMID:[21051595](https://pubmed.ncbi.nlm.nih.gov/21051595/)
22. Robertson AG, Shih J, Yau C, Gibb EA, Oba J, Mungall KL, Hess JM, Uzunangelov V, Walter V, Danilova L, Lichtenberg TM, Kucherlapati M, Kimes PK, et al, and TCGA Research Network. Integrative Analysis Identifies Four Molecular and Clinical Subsets in Uveal Melanoma. *Cancer Cell*. 2018; 33:151.
<https://doi.org/10.1016/j.ccell.2017.12.013>
PMID:[29316429](https://pubmed.ncbi.nlm.nih.gov/29316429/)
23. Yoshihara K, Shahmoradgoli M, Martínez E, Vegesna R, Kim H, Torres-Garcia W, Treviño V, Shen H, Laird PW, Levine DA, Carter SL, Getz G, Stemke-Hale K, et al. Inferring tumour purity and stromal and immune cell admixture from expression data. *Nat Commun*. 2013; 4:2612.
<https://doi.org/10.1038/ncomms3612> PMID:[24113773](https://pubmed.ncbi.nlm.nih.gov/24113773/)
24. Bailey MH, Tokheim C, Porta-Pardo E, Sengupta S, Bertrand D, Weerasinghe A, Colaprico A, Wendl MC, Kim J, Reardon B, Kwok-Shing Ng P, Jeong KJ, Cao S, et al, and MC3 Working Group, and Cancer Genome Atlas Research Network. Comprehensive Characterization of Cancer Driver Genes and Mutations. *Cell*. 2018; 174:1034–35.
<https://doi.org/10.1016/j.cell.2018.07.034>
PMID:[30096302](https://pubmed.ncbi.nlm.nih.gov/30096302/)
25. Liu J, Lichtenberg T, Hoadley KA, Poisson LM, Lazar AJ, Cherniack AD, Kovatich AJ, Benz CC, Levine DA, Lee AV, Omberg L, Wolf DM, Shriver CD, et al. An Integrated TCGA Pan-Cancer Clinical Data Resource to Drive High-Quality Survival Outcome Analytics. *Cell*. 2018; 173:400–416.e11.
<https://doi.org/10.1016/j.cell.2018.02.052>
PMID:[29625055](https://pubmed.ncbi.nlm.nih.gov/29625055/)
26. Li B, Cui Y, Nambiar DK, Sunwoo JB, Li R. The Immune Subtypes and Landscape of Squamous Cell Carcinoma. *Clin Cancer Res*. 2019; 25:3528–37.
<https://doi.org/10.1158/1078-0432.CCR-18-4085>
PMID:[30833271](https://pubmed.ncbi.nlm.nih.gov/30833271/)
27. He B, Gao R, Lv D, Wen Y, Song L, Wang X, Lin S, Huang Q, Deng Z, Wang Z, Yan M, Zheng F, Lam EW, et al. The prognostic landscape of interactive biological processes presents treatment responses in cancer. *EBioMedicine*. 2019; 41:120–33.
<https://doi.org/10.1016/j.ebiom.2019.01.064>
PMID:[30799199](https://pubmed.ncbi.nlm.nih.gov/30799199/)
28. Geraldo MV, Kimura ET. Integrated Analysis of Thyroid Cancer Public Datasets Reveals Role of Post-Transcriptional Regulation on Tumor Progression by Targeting of Immune System Mediators. *PLoS One*. 2015; 10:e0141726.
<https://doi.org/10.1371/journal.pone.0141726>
PMID:[26536459](https://pubmed.ncbi.nlm.nih.gov/26536459/)
29. Zhao Y, Schaafsma E, Gorlov IP, Hernando E, Thomas NE, Shen R, Turk MJ, Berwick M, Amos CI, Cheng C. A Leukocyte Infiltration Score Defined by a Gene Signature Predicts Melanoma Patient Prognosis. *Mol Cancer Res*. 2019; 17:109–19.
<https://doi.org/10.1158/1541-7786.MCR-18-0173>
PMID:[30171176](https://pubmed.ncbi.nlm.nih.gov/30171176/)
30. Yoshihara K, Tsunoda T, Shigemizu D, Fujiwara H, Hatae M, Fujiwara H, Masuzaki H, Katabuchi H, Kawakami Y, Okamoto A, Nogawa T, Matsumura N, Udagawa Y, et al, and Japanese Serous Ovarian Cancer Study Group. High-risk ovarian cancer based on 126-gene expression signature is uniquely characterized by downregulation of antigen presentation pathway. *Clin Cancer Res*. 2012; 18:1374–85.
<https://doi.org/10.1158/1078-0432.CCR-11-2725>
PMID:[22241791](https://pubmed.ncbi.nlm.nih.gov/22241791/)
31. Danilova L, Ho WJ, Zhu Q, Vithayathil T, De Jesus-Acosta A, Azad NS, Laheru DA, Fertig EJ, Anders R, Jaffee EM, Yarchoan M. Programmed Cell Death Ligand-1 (PD-L1) and CD8 Expression Profiling Identify an Immunologic Subtype of Pancreatic Ductal Adenocarcinomas with Favorable Survival. *Cancer Immunol Res*. 2019; 7:886–95.
<https://doi.org/10.1158/2326-6066.CIR-18-0822>
PMID:[31043417](https://pubmed.ncbi.nlm.nih.gov/31043417/)
32. Matsushita H, Sato Y, Karasaki T, Nakagawa T, Kume H, Ogawa S, Homma Y, Kakimi K. Neoantigen Load, Antigen Presentation Machinery, and Immune Signatures Determine Prognosis in Clear Cell Renal Cell Carcinoma. *Cancer Immunol Res*. 2016; 4:463–71.
<https://doi.org/10.1158/2326-6066.CIR-15-0225>
PMID:[26980598](https://pubmed.ncbi.nlm.nih.gov/26980598/)
33. Chen B, Khodadoust MS, Liu CL, Newman AM, Alizadeh AA. Profiling Tumor Infiltrating Immune Cells with CIBERSORT. *Methods Mol Biol*. 2018; 1711:243–59.
https://doi.org/10.1007/978-1-4939-7493-1_12
PMID:[29344893](https://pubmed.ncbi.nlm.nih.gov/29344893/)
34. Narayanan S, Kawaguchi T, Yan L, Peng X, Qi Q, Takabe K. Cytolytic Activity Score to Assess Anticancer Immunity in Colorectal Cancer. *Ann Surg Oncol*. 2018; 25:2323–31.
<https://doi.org/10.1245/s10434-018-6506-6>
PMID:[29770915](https://pubmed.ncbi.nlm.nih.gov/29770915/)
35. Newman AM, Liu CL, Green MR, Gentles AJ, Feng W, Xu Y, Hoang CD, Diehn M, Alizadeh AA. Robust enumeration of cell subsets from tissue expression profiles. *Nat Methods*. 2015; 12:453–57.
<https://doi.org/10.1038/nmeth.3337> PMID:[25822800](https://pubmed.ncbi.nlm.nih.gov/25822800/)

36. Eggermont AM, Blank CU, Mandala M, Long GV, Atkinson VG, Dalle S, Haydon A, Lichinitser M, Khattak A, Carlino MS, Sandhu S, Larkin J, Puig S, et al. Prognostic and predictive value of AJCC-8 staging in the phase III EORTC1325/KEYNOTE-054 trial of pembrolizumab vs placebo in resected high-risk stage III melanoma. *Eur J Cancer*. 2019; 116:148–57. <https://doi.org/10.1016/j.ejca.2019.05.020> PMID:[31200321](https://pubmed.ncbi.nlm.nih.gov/31200321/)
37. Robert C, Ribas A, Schachter J, Arance A, Grob JJ, Mortier L, Daud A, Carlino MS, McNeil CM, Lotem M, Larkin JM, Lorigan P, Neyns B, et al. Pembrolizumab versus ipilimumab in advanced melanoma (KEYNOTE-006): post-hoc 5-year results from an open-label, multicentre, randomised, controlled, phase 3 study. *Lancet Oncol*. 2019; 20:1239–51. [https://doi.org/10.1016/S1470-2045\(19\)30388-2](https://doi.org/10.1016/S1470-2045(19)30388-2) PMID:[31345627](https://pubmed.ncbi.nlm.nih.gov/31345627/)
38. Heppt MV, Steeb T, Schlager JG, Rosumeck S, Dressler C, Ruzicka T, Nast A, Berking C. Immune checkpoint blockade for unresectable or metastatic uveal melanoma: A systematic review. *Cancer Treat Rev*. 2017; 60:44–52. <https://doi.org/10.1016/j.ctrv.2017.08.009> PMID:[28881222](https://pubmed.ncbi.nlm.nih.gov/28881222/)
39. Hou F, Huang QM, Hu DN, Jonas JB, Wei WB. Immune oppression array elucidating immune escape and survival mechanisms in uveal melanoma. *Int J Ophthalmol*. 2016; 9:1701–12. <https://doi.org/10.18240/ijo.2016.12.01> PMID:[28003967](https://pubmed.ncbi.nlm.nih.gov/28003967/)
40. Achberger S, Aldrich W, Tubbs R, Crabb JW, Singh AD, Triozzi PL. Circulating immune cell and microRNA in patients with uveal melanoma developing metastatic disease. *Mol Immunol*. 2014; 58:182–86. <https://doi.org/10.1016/j.molimm.2013.11.018> PMID:[24370793](https://pubmed.ncbi.nlm.nih.gov/24370793/)
41. Rooney MS, Shukla SA, Wu CJ, Getz G, Hacohen N. Molecular and genetic properties of tumors associated with local immune cytolytic activity. *Cell*. 2015; 160:48–61. <https://doi.org/10.1016/j.cell.2014.12.033> PMID:[25594174](https://pubmed.ncbi.nlm.nih.gov/25594174/)
42. Wakiyama H, Masuda T, Motomura Y, Hu Q, Tobo T, Eguchi H, Sakamoto K, Hirakawa M, Honda H, Mimori K. Cytolytic Activity (CYT) Score Is a Prognostic Biomarker Reflecting Host Immune Status in Hepatocellular Carcinoma (HCC). *Anticancer Res*. 2018; 38:6631–38. <https://doi.org/10.21873/anticancer.13030> PMID:[30504371](https://pubmed.ncbi.nlm.nih.gov/30504371/)
43. Bakhoun MF, Esmaeli B. Molecular Characteristics of Uveal Melanoma: Insights from the Cancer Genome Atlas (TCGA) Project. *Cancers (Basel)*. 2019; 11:E1061. <https://doi.org/10.3390/cancers11081061> PMID:[31357599](https://pubmed.ncbi.nlm.nih.gov/31357599/)
44. de Waard-Siebinga I, Hilders CG, Hansen BE, van Delft JL, Jager MJ. HLA expression and tumor-infiltrating immune cells in uveal melanoma. *Graefes Arch Clin Exp Ophthalmol*. 1996; 234:34–42. <https://doi.org/10.1007/BF00186516> PMID:[8750848](https://pubmed.ncbi.nlm.nih.gov/8750848/)
45. Barnes TA, Amir E. HYPE or HOPE: the prognostic value of infiltrating immune cells in cancer. *Br J Cancer*. 2018; 118:e5. <https://doi.org/10.1038/bjc.2017.417> PMID:[29315291](https://pubmed.ncbi.nlm.nih.gov/29315291/)
46. de Lange MJ, van Pelt SI, Versluis M, Jordanova ES, Kroes WG, Ruivenkamp C, van der Burg SH, Luyten GP, van Hall T, Jager MJ, van der Velden PA. Heterogeneity revealed by integrated genomic analysis uncovers a molecular switch in malignant uveal melanoma. *Oncotarget*. 2015; 6:37824–35. <https://doi.org/10.18632/oncotarget.5637> PMID:[26462151](https://pubmed.ncbi.nlm.nih.gov/26462151/)
47. Liu X, Zhu XH, Qiu P, Chen W. A correlation-matrix-based hierarchical clustering method for functional connectivity analysis. *J Neurosci Methods*. 2012; 211:94–102. <https://doi.org/10.1016/j.jneumeth.2012.08.016> PMID:[22939920](https://pubmed.ncbi.nlm.nih.gov/22939920/)
48. Camp RL, Dolled-Filhart M, Rimm DL. X-tile: a new bioinformatics tool for biomarker assessment and outcome-based cut-point optimization. *Clin Cancer Res*. 2004; 10:7252–59. <https://doi.org/10.1158/1078-0432.CCR-04-0713> PMID:[15534099](https://pubmed.ncbi.nlm.nih.gov/15534099/)
49. Hänzelmann S, Castelo R, Guinney J. GSVA: gene set variation analysis for microarray and RNA-seq data. *BMC Bioinformatics*. 2013; 14:7. <https://doi.org/10.1186/1471-2105-14-7> PMID:[23323831](https://pubmed.ncbi.nlm.nih.gov/23323831/)
50. Subramanian A, Tamayo P, Mootha VK, Mukherjee S, Ebert BL, Gillette MA, Paulovich A, Pomeroy SL, Golub TR, Lander ES, Mesirov JP. Gene set enrichment analysis: a knowledge-based approach for interpreting genome-wide expression profiles. *Proc Natl Acad Sci USA*. 2005; 102:15545–50. <https://doi.org/10.1073/pnas.0506580102> PMID:[16199517](https://pubmed.ncbi.nlm.nih.gov/16199517/)

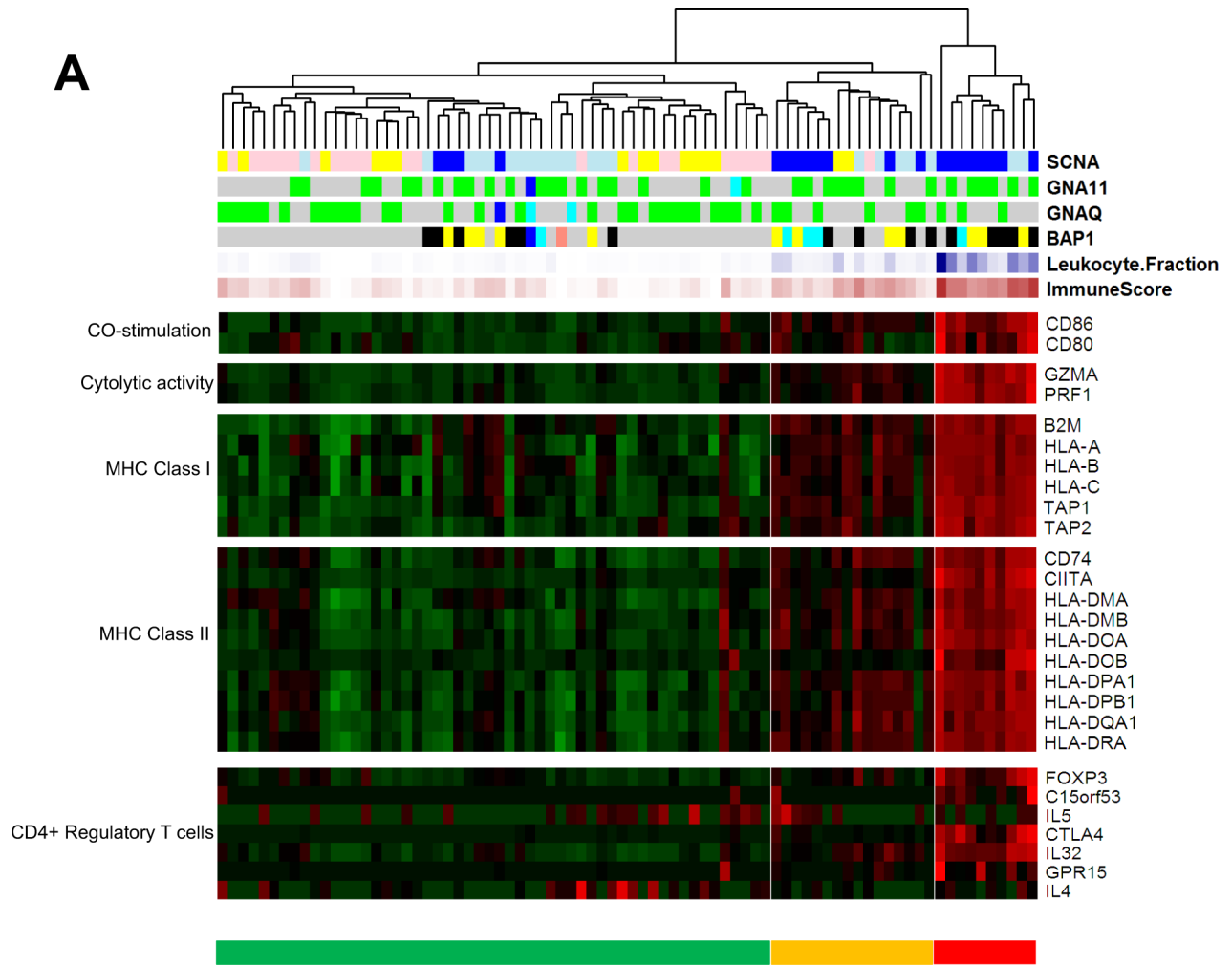
SUPPLEMENTARY MATERIALS

Supplementary Figures

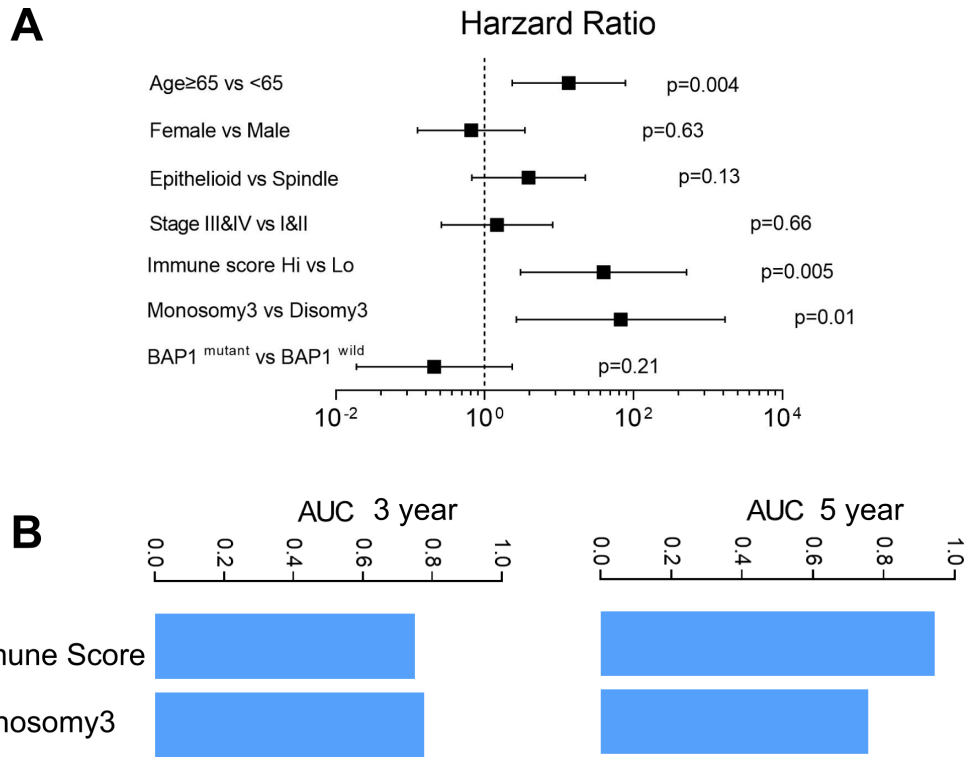


Supplementary Figure 1. The prognostic value of immune cell types in the Laurent UM dataset. (A) Kaplan-Meier survival analysis based on the immune score and stromal score. Patients were divided into high and low groups based on their value for each score. **(B)** Kaplan-Meier survival analysis based on immune cell types. Patients were divided into high and low groups based on their expression of each cell type. **(C)** The results of CIBERSORT in the Laurent UM dataset. n=63.

A

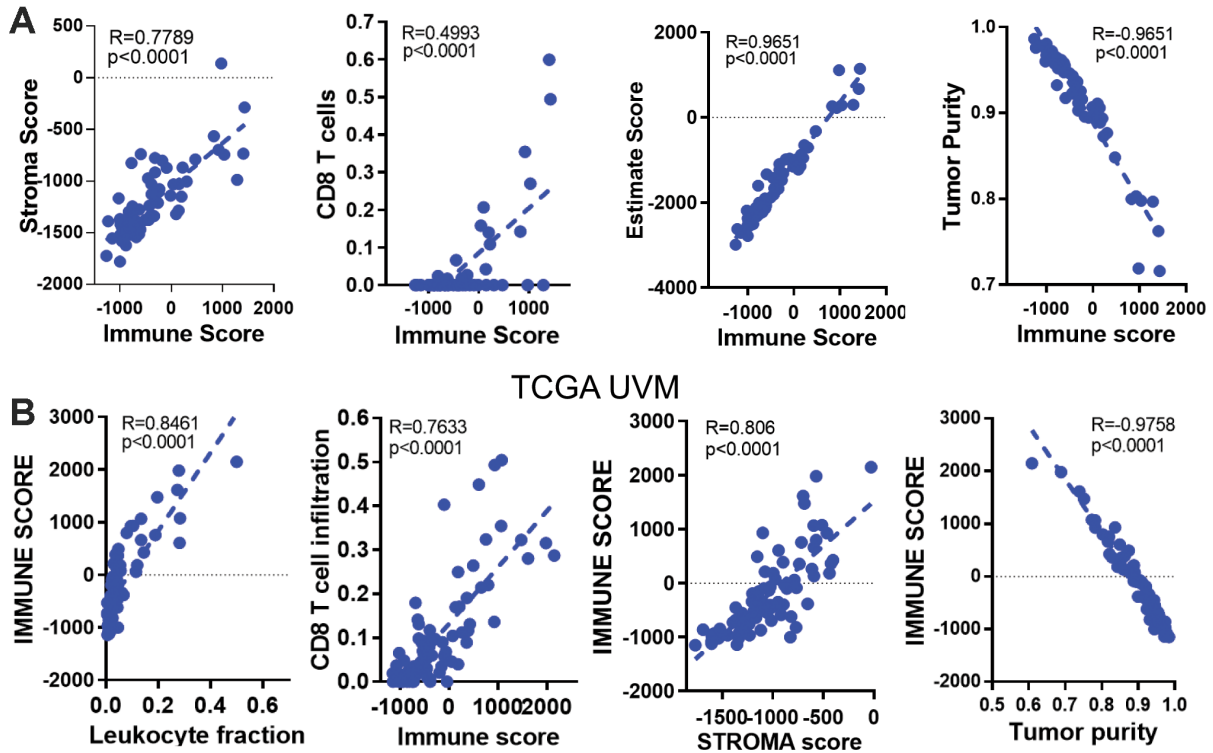


Supplementary Figure 2. Immune-related gene expression in the UM dataset of TCGA. (A) Hierarchical clustering of 80 tumors based on selected gene signatures or genes is shown.



Supplementary Figure 3. The prognostic power of the immune score in the UM dataset of TCGA. (A) HRs based on various clinical features in all patients; the horizontal bars represent the 95% confidence intervals of the HRs. Statistically significant variables are shown. **(B)** Area under the curve for the immune score and M3 in predicting survival among UM patients in TCGA.

Laurent uveal melanoma



Supplementary Figure 4. The correlation between the immune score and immune cell infiltration in UM. (A) Correlations among the estimate score, CD8 T cell infiltration, stromal score, tumor purity and immune score in the GSE22138 dataset. (B) Correlations among CD8 T cell infiltration, the stromal score, tumor purity and the immune score in the UM dataset of TCGA.